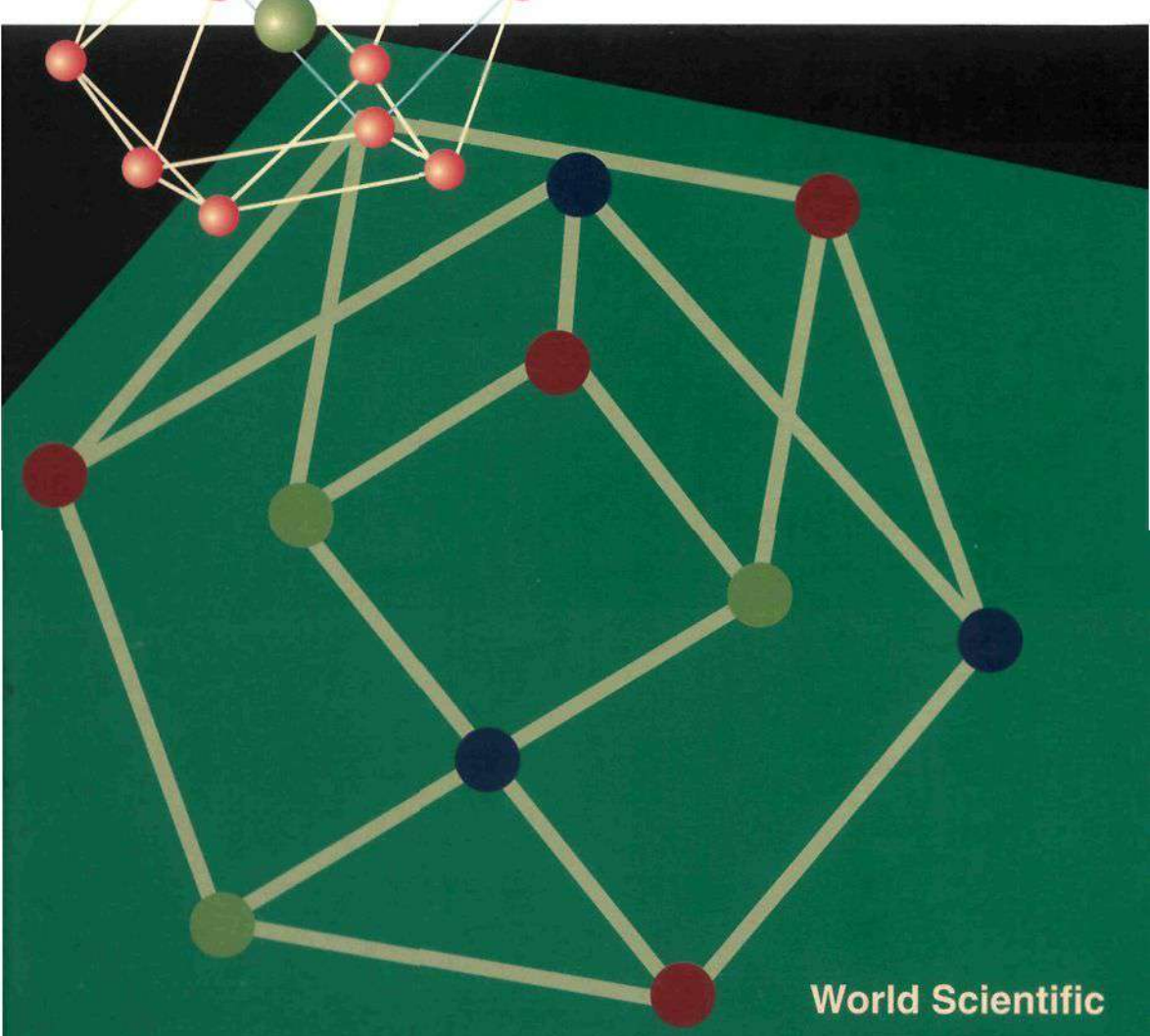


# Frontiers of Solid State Chemistry

Edited by S. H. Feng and J. S. Chen

Proceedings of the  
International Symposium on  
Solid State Chemistry in China



World Scientific

# **Frontiers of Solid State Chemistry**

This page is intentionally left blank

# **Frontiers of Solid State Chemistry**

**Proceedings of the International Symposium on  
Solid State Chemistry in China**

**Changchun, China      9 – 12 August 2002**

**Edited by**

**S. H. Feng and J. S. Chen**

**Jilin University, China**



**World Scientific**

*New Jersey • London • Singapore • Hong Kong*

*Published by*

**World Scientific Publishing Co. Pte. Ltd.**  
P O Box 128, Farrer Road, Singapore 912805  
**USA office:** Suite 1B, 1060 Main Street, River Edge, NJ 07661  
**UK office:** 57 Shelton Street, Covent Garden, London WC2H 9HE

**British Library Cataloguing-in-Publication Data**

A catalogue record for this book is available from the British Library.

**FRONTIERS OF SOLID STATE CHEMISTRY**

Copyright © 2002 by World Scientific Publishing Co. Pte. Ltd.

*All rights reserved. This book, or parts thereof, may not be reproduced in any form or by any means, electronic or mechanical, including photocopying, recording or any information storage and retrieval system now known or to be invented, without written permission from the Publisher.*

For photocopying of material in this volume, please pay a copying fee through the Copyright Clearance Center, Inc., 222 Rosewood Drive, Danvers, MA 01923, USA. In this case permission to photocopy is not required from the publisher.

**ISBN 981-238-105-8**

## Preface

Solid state chemistry has become a very important multidisciplinary area and it includes topics originated from the more conventional inorganic and physical chemistries. However, with the emerging of many new facets, solid state chemistry has undoubtedly reached beyond the area covered by inorganic and physical chemistries. In addition, solid state chemistry is closely related with solid state physics and materials science. Nowadays, solid state chemistry, playing an important role in the understanding, design and preparation of advanced solid materials, is generally considered as a sub-field of chemistry.

These proceedings are based on the contributions to the International Symposium on Solid State Chemistry in China in combination with the 8<sup>th</sup> National Conference on Solid State Chemistry and Inorganic Synthesis. In 1986, a number of distinguished chemists in China initiated a national conference focusing on solid state chemistry and inorganic synthesis, and this national conference has been held every two years since then. More and more researchers have been attracted to this conference, contributing their excellent research results in the field of solid state chemistry and inorganic synthesis. This year (2002) sees the 8<sup>th</sup> national conference of this series as a continuation of the previous seven ones held in Changchun (1986), Hefei (1988), Haerbin (1990), Tianjin (1992), Chengdu (1995), Fuzhou (1998) and Wuhan (2000), respectively. In order to extend the topics of the conference further, solid state chemists in China are strongly in favor of convening an international symposium in combination with the 8<sup>th</sup> national conference, and strong support has been obtained internationally. Therefore, researchers all over the world were invited to contribute to and to participate in the joint meeting. Contributions were poured to the organizers of the symposium after the first circular was announced to call for papers, and the most intriguing papers were selected, after scientific review, for inclusion in these proceedings.

In these proceedings, five parts preceded by three plenary contributions are arranged on the basis of the papers contributed to the symposium. Each part of the proceedings represents a unique sub-area of solid state chemistry. Thus, the first part of these proceedings covers topics of electrical, optical, magnetic solids and defects and mixed-valences in solids; the second part deals with porous solids and catalysts, and the third part involves hybrid inorganic-organic solids. In the fourth part of the proceedings, nano-materials and inorganic films are addressed whereas the fifth part is concerned with new synthetic methods, characterization and theory.

We would like to express our sincere gratitude to our colleagues, both in China and abroad, for their kind support and help. Most of them serve as a member of the advisory boards or the organizing committee. Naturally, without the contributions from the authors, these proceedings would not be possible and we also wish to acknowledge the efforts of the authors. Finally we thank the World Scientific Publishing Co. Ltd. for publication of these proceedings.

Shou-Hua Feng  
Jie-Sheng Chen  
(Editors)

This page is intentionally left blank

## Table of Contents

<b>Preface</b>	<b>v</b>
<b>Plenary papers</b>	<b>1</b>
Basic building units and self-assembly in inorganic open architectures <i>C. N. R. Rao</i>	3
Synthesis and characterization of the oxygen deficient double-perovskite $\text{Sr}_2\text{CrNbO}_{5.53}$ <i>G. M. Veith, M. Greenblatt, E. N. Caspi and J. D. Jorgensen</i>	13
Solvothermal synthesis of non-oxide nanomaterials <i>Y.-T. Qian and Y. L. Gu</i>	27
<b>Part I - Electrical, optical, magnetic solids and defects and mixed valences in solids</b>	<b>37</b>
Hydrothermal synthesis, structural characterization and ionic conductivity of Cu-Bi-V-O systems <i>S. H. Feng, Y. H. Shi, Y. W. Wang and Y. Li</i>	39
Synthesis, crystal structure and some properties of $\text{Ln}_2\text{MnTiO}_6$ phases ( $\text{Ln}$ = rare earth) <i>N. Kamegashira, M. Kobayashi and J. -I Saito</i>	47
Optical-induced Fréedericksz transition of nematic liquid crystal doped with porphyrinatozinc(II) <i>T. Li, C. -L. Ni, Y. Zhang, J. -W. Huang and L. -N. Ji</i>	53
Synthesis and properties of MBPO <sub>5</sub> : Pr (M=Ca, Sr, Ba) phosphors <i>X. T. Liu, G. X. Zhuang, J. H. Xiong, W. P. Wei, Y. Q. Luo, C. S. Shi and D. M. Xie</i>	59
Preparation, patterning and luminescence properties of rare earth-doped $\text{YVO}_4$ nanocrystalline phosphor films via sol-gel soft lithography <i>J. Lin and M. Yu</i>	65
Covalent grafting of luminescent rare earth complex onto MCM-41 by postsynthesis <i>F. Y. Liu, L. S. Fu, J. Wang, H. R. Li and H. J. Zhang</i>	73
A new anode material $\text{LiVMoO}_6$ for use in rechargeable Li-ion batteries <i>R. S. Liu, C. Y. Wang, S. F. Hu, L. Y. Jang and J. F. Lee</i>	79
Electronic ceramic $\text{BaTiO}_3$ : synthesis, dielectric and ferroelectric properties <i>W. Q. Lu, Z. Cai and Y. B. Feng</i>	85
X-ray absorption study of electronic, spatial structure and properties of $\text{BaLn}_2\text{Mn}_2\text{O}_7$ manganates <i>L. N. Mazalov, N. V. Bausk, V. V. Sokolov, V. N. Ikorskii, J. Meng, J. Feng, K. Fujita, H. Satoh and N. Kamegashira</i>	91

<b>Crystal growth and structural analysis of PrMnO<sub>3</sub> and TbMnO<sub>3</sub></b> <i>J. Meng, P. Che, T. Mori, R. Sasai, K. Fujita, H. Satoh, K. Aoki, N. Kamegashira, T. Shishido and T. Fukuda</i>	97
<b>A new nonlinear optical material for IR region: KHgBr<sub>3</sub>·H<sub>2</sub>O</b> <i>P. Ren, T. Liu, J. G. Qin, Y. C. Wu and C. T. Chen</i>	103
<b>Valency-variable cation Co-doping and Sn-Cl-doping in Bi-system 2223 phase superconductor</b> <i>R. F. Shen, F. Y. Wang, F. C. Xu and R. Xie</i>	109
<b>Topological properties and electronic structures of compounds with pyrite-type crystal structures</b> <i>A. C. Stückl, R. Weihrich and K.-J. Range</i>	117
<b>Synthesis and electrochemical performance of LiMn<sub>2-x</sub>Co<sub>x</sub>Y<sub>y</sub>O<sub>4</sub> cathode materials for lithium-ion secondary battery</b> <i>H. Tang, C. -Q. Feng, M. -K. Jia and K. -L. Zhang</i>	125
<b>A new orthorhombic phase of ZrW<sub>1.6</sub>Mo<sub>0.4</sub>O<sub>8</sub> at ambient pressure</b> <i>X. H. Zhao, W. Qi and H. Ma</i>	131
<b>Study on the synthesis, rare earth co-permeation and conductivity of complex K<sub>10</sub>H<sub>3</sub>[Y(SiW<sub>11</sub>O<sub>39</sub>)<sub>2</sub>]</b> <i>B. -B. Zhou, Y. -D. Wei, Z. -H. Li and Y. -R. Guo</i>	137
<b>Study on defected YVO<sub>4</sub> crystal</b> <i>Y. -Q. Zou, J. Xu, F. -X. Gan, X. -J. Li, Y. -L. Tian and W. -X. Huang</i>	143
<b>Long lasting phosphorescence, thermoluminescence and electron spin resonance property of Mn<sup>2+</sup> activated ZnO-Al<sub>2</sub>O<sub>3</sub>-SiO<sub>2</sub> ceramic</b> <i>J. Wang, C. Y. Li, S. B. Wang and Q. Su</i>	149
<b>Structural phase transition in the layered perovskite compound BaTb<sub>2</sub>Mn<sub>2</sub>O<sub>7</sub></b> <i>J. Meng, J. P. Wang, J. Feng, H. Satoh and N. Kamegashira</i>	159
<b>Processing and electrical properties of Sr- and Mn-doped lanthanum gallate</b> <i>Q. X. Fu, X. Y. Xu, D. K. Peng, X. Q. Liu, G. Y. Meng</i>	167
 <b>Part II - Porous solids and catalysts</b>	175
<b>Novel framework aluminium diphosphonates</b> <i>M. P. Atfield, H. G. Harvey and B. Slater</i>	177
<b>Synthesis of mesoporous phosphomolybdic acid</b> <i>L. Chu and Y. -M. Zhang</i>	185
<b>Preparation and characterization of hydroxyl-Zr bentonite</b> <i>Y. X. Jiang, C. G. Luo, Z. M. Li and Z. F. Tong</i>	191
<b>Dissipative forced intrusion of liquid in lyophobic porous materials: a new field of applications for MTS type materials</b> <i>B. Lefèvre, P. F. Gobin, T. Martin and F. Fajula</i>	197

Synthesis and characterization of Ti-Zr mesoporous oxides using mixed surfactants as templating agents <i>W. B. Li, X. F. Yang and Y. Zhang</i>	203
The studies on preparation and catalytic performance of superfine BaTiO <sub>3</sub> -supported Ni-based catalyst <i>X. C. Li, L. T. Luo, K. Q. Liu and Z. H. Lai</i>	211
Non-aqueous synthesis of novel low-dimensional zirconium phosphates <i>D. Wang, R. B. Yu, N. Kumada, N. Kinomura, K. Yanagisawa, Y. Matsumura and T. Yashima</i>	219
Postsynthesis hydrothermal treatment of double-mesopore silica molecular sieves in water <i>X. Z. Wang, T. Dou and B. Zhong</i>	227
Hydrothermal synthesis and characterization of zeolite-like crystal material CAS-1 <i>C. F. Xue, G. H. Liu, J. P. Li and J. X. Dong</i>	233
The synthesis and thermal stability study of mesoporous cerium (IV) oxide powders <i>R. Yang, J. H. Liu, M. Li and C. X. Yan</i>	241
Three-dimensional ordered macroporous hybrid silica materials functionalized with lacunary keggin-type polyoxometalates: preparation and characterization <i>Y. Yang, Y. H. Guo, C. W. Hu and E. B. Wang</i>	249
Hydrothermal formation of novel cerium materials with open-framework architectures <i>R. B. Yu, D. Wang, T. Takei, N. Kumada, N. Kinomura and M. Takano</i>	257
A study on catalytic wet oxidation of simulated wastewater succinic acid aqueous solution with Ru/TiO <sub>2</sub> catalyst <i>S. -H. Zhang, X. -Y. Tu, Z. -M. Yang, Z. -H. Li, P. -J. Hong, Y. Yang and B. Qian</i>	265
Synthesis and catalysis of mesoporous silica-heterostructured materials based on montmorillonite <i>C. H. Zhou, Q. W. Li, Z. H. Ge and X. N. Li</i>	275
Fabrication of three-dimensional large-pore mesoporous channels based on ordered mesoporous silica materials <i>J. Fan, C. Z. Yu, L. M. Wang, B. Tu and D. Y. Zhao</i>	283
<b>Part III - Hybrid inorganic-organic solids</b>	293
Study of the chiral transference and recognition effect in layered aluminophosphates templated by chiral cobalt complexes <i>Y. Li, J. H. Yu, Y. Wang and R. R. Xu</i>	295
Synthesis, structure and magnetism of a new imidazolate-bridged binuclear complex [Ni <sub>2</sub> (Im)(Phen) <sub>4</sub> ]·(NO <sub>3</sub> ) <sub>3</sub> ·3H <sub>2</sub> O <i>S. Y. Niu, J. Jin, G. D. Yang and L. Ye</i>	303

<b>Design of metal-carboxylate cavity-containing rectangular grids with 1,2,4,5-benzenetetracarboxylic acid</b>	311
<i>Q. Shi, R. Cao, D. F. Sun and M. C. Hong</i>	311
<b>[Mn(salAren)(H<sub>2</sub>O)]<sub>2</sub>[Fe(CN)<sub>5</sub>(NO)]·2CH<sub>3</sub>OH·3H<sub>2</sub>O: a new trinuclear complex with cyanide bridges and hydrogen bonds</b>	317
<i>S. -F. Si, Q. -L. Wang and D. -Z. Liao</i>	317
<b>Synthesis of nickel-organic complexes grafted on the surface of SiO<sub>2</sub> as catalysts for ethylene oligomerization reaction</b>	321
<i>D. B. Tagiyev, M. K. Munshiyeva and M. I. Rustamov</i>	321
<b>Synthesis and crystal structure of a new copper (II) complex containing fluoroquinolone</b>	327
<i>G. P. Wang and L. G. Zhu</i>	327
<b>Strategies for the construction of complexes based on metal clusters</b>	333
<i>R. H. Wang, M. C. Hong, Y. J. Zhao, R. Cao and J. H. Luo</i>	333
<b>Catalytic synthesis of <i>n</i>-amyl cinnamate with TiSiW<sub>12</sub>O<sub>40</sub>/TiO<sub>2</sub></b>	339
<i>S. J. Yang, X. Q. Yu, Y. G. Liang and J. T. Sun</i>	339
<b>Towards the construction of open framework structures of copper phosphonates and the magnetic studies</b>	345
<i>L. -M. Zheng</i>	345
<b>Three-dimensional network with cavities created by hydrogen bonds in protocatechuic acid/copper (II) system</b>	355
<i>L. -G. Zhu and S. Kitagawa</i>	355
<b>Porous crystalline materials constructed by complex cations and bulky arenedisulfonate counter anions</b>	361
<i>J. W. Cai, X. -P. Hu, J. Feng and X. -L. Feng</i>	361
<b>Part IV - Nano-materials and inorganic films</b>	367
<b>Characterization of sputtered thin films of indium tin oxide</b>	369
<i>H. -N. Cui and V. Teixeira</i>	369
<b>Size dependence of Curie temperature in PbZr<sub>1-x</sub>Ti<sub>x</sub>O<sub>3</sub> ultrafine particles</b>	377
<i>X. F. Cui, J. C. Li and Q. Jiang</i>	377
<b>ZnO thin film grown by metal-organic chemical vapor deposition</b>	383
<i>G. T. Du, X. Q. Wang, S. R. Yang, X. T. Yang, J. Z. Wang, Y. T. Zhang, D. Liu, Y. Ma, D. L. Liu and H. C. Ong</i>	383
<b>Preparation, structure and formation processes of nanometer-sized layered manganese oxides</b>	391
<i>Q. M. Gao and S. L. Suib</i>	391
<b>Self-assembly of iron nanoparticles with the assistance of binary surfactants under a solvothermal reaction</b>	399
<i>Y. -L. Hou, J. -F. Yu, S. Gao, G. -H. Wen and X. X. Zhang</i>	399

One-step, solid-state reaction at room temperature to the synthesis of polyoxometalate nanoparticles and nanorods <i>Z. H. Kang, E. B. Wang, Y. G. Li and C. W. Hu</i>	405
Nanocrystalline $\beta$ -SiC films grown by cat-CVD with pre-carbonization process <i>J. C. Li, Q. Zhao, M. Wang, X. M. Song, H. Wang, B. Wang and H. Yan</i>	411
Preparation and characterization of hybrid DODA/transition metal substituted heteropolybodiphosphate LB films <i>S. Z. Liu, L. Liu, X. H. Feng, Y. Fan, Z. G. Hu and Z. L. Du</i>	415
Preparation of nickel sulfide ultrafine particles by microemulsion <i>R. Luan and E. S. Han</i>	421
Chemistry in molecular approaches to microelectronic diffusion barrier materials <i>X. Z. Liu, H. Cai, Z. Z. Wu, Y. H. Yang, T. N. Chen, Z. L. Xue, C. E. Vallet, D. B. Beach and R. A. Zuhr</i>	427
Influence of crystallite size on the properties of $\text{SnO}_2$ nanocrystals <i>G. S. Pang, H. Y. Jin, Q. Wan, Y. Sun, S. H. Feng and A. Gedanken</i>	435
Metal salts as structure-directing agents for $\text{SiO}_2$ and $\text{TiO}_2$ nanotubes containing high amounts of encapsulated metal <i>L. R. Ren, U. Melville and M. Wark</i>	441
Temperature effects on formation of c-BN films by magnetron sputtering <i>B. Wang, H. Zhou, X. H. Li, R. Z. Wang, H. Wang and H. Yan</i>	447
Phase formation and transformation of nanostructured titania in solution <i>G. G. Wang, G. Lin, Y. L. Tu, X. F. Yang, J. B. Long, S. H. Feng, R. R. Xu and M. M. Wu</i>	453
Novel synthesis of nanosized $\text{Pd}/\text{Ce}_x\text{Zr}_{1-x}\text{O}_2$ catalysts <i>J. A. Wang, L. F. Chen, J. C. Guevara and L. Balderas-Tapia</i>	461
Effect of silicon dopant on the microstructure of titanium dioxide <i>Y. H. Zhang, O. Becher and A. Reller</i>	467
Microemulsion synthesis and magnetic properties of $\text{Co}@\text{Pt}$ core-shell nanoparticles <i>Y. N. Zhao, X. H. Li, M. Li, Z. H. Mai and Y. Yu</i>	473
Preparation and characterization of nanopowders and nanoceramics of vanadium oxides <i>C. M. Zheng, X. M. Zhang, L. Y. Wei, S. He and D. M. Lei</i>	479
Preparation of nanophase $\beta$ - $\text{Ni(OH)}_2$ powder for electrode materials <i>X. J. Han, C. Q. Xu, C. F. Zhang and L. Zhao</i>	487
Solid superacids of sulfated zirconia-silicon nanocrystals <i>H. Yang and R. Lu</i>	491

<b>Part V - New synthetic methods, characterization and theory</b>	<b>499</b>
Microwave hydrothermal particle growth of colloidal silica <i>C. Falamaki</i>	501
The method of determination of the surface composition of the Ir-Rh alloys <i>M. Q. Jia, N. I. Kudryashov and A. Meretsky</i>	507
The use of oxalates as precursors for the low temperature synthesis of LiNi <sub>1-x</sub> Co <sub>x</sub> VO <sub>4</sub> <i>Q. Y. Lai, J. Z. Lu, F. Y. Yan and X. Y. Ji</i>	515
Interface layer in colloid by SAXS <i>Z. H. Li, Y. J. Gong, M. Pu, D. Wu, Y. H. Sun, H. Zhao, J. Wang and B. Z. Dong</i>	523
Wicker-shaped silver particles prepared by extraction interface reduction <i>X. M. Li, S. X. Sun and Y. Z. Yang</i>	529
Rheological phase reaction method and its application <i>J. T. Sun, L. J. Yuan, Y. Y. Yang, Z. Y. Yuan, J. L. Wang and K. L. Zhang</i>	533
Nonequilibrium nondissipative thermodynamics and its application to modern inorganic synthesis <i>J. -T. Wang, D. W. Zhang and Z. -K. Liu</i>	541
Theoretical study on the reaction mechanisms of the imide formation in an N-(o-carboxybenzoyl)-L-amino acid <i>Z. J. Wu, F. Q. Ban and R. J. Boyd</i>	549
Synthesis and X-ray crystal structures of low-dimensional borates from hydrothermal and solvothermal systems <i>Z. -T. Yu, Y. He, Y. -S. Jiang, Z. Shi, W. Chen and J. -S. Chen</i>	555
Calculation of the electrostatic energy H <sub>e</sub> (fd) on 4f <sup>N-1</sup> 5d configuration of lanthanide ions <i>J. S. Shi, S. H. Zhong and S. Y. Zhang</i>	563
Enhancement of IR absorption of CO adsorbed on palladium nanoparticles prepared by ship-in-a-bottle in supercages of NaA zeolite <i>Y. -X. Jiang, N. Ding and S. -G. Sun</i>	571
Syntheses of mixed layered nickel hydroxide manganese oxides by hydrothermal intercalation reaction and exfoliation-restacking hydrothermal reaction <i>Y. H. Xu, S. H. Feng, W. Q. Pang, Q. Feng, K. Kajiyoshi and K. Yanagisawa</i>	577
Author Index	585
Subject Index	589

## **Plenary Papers**

This page is intentionally left blank

## BASIC BUILDING UNITS AND SELF-ASSEMBLY IN INORGANIC OPEN ARCHITECTURES

C. N. R. RAO\*

*CSIR Centre of Excellence in Chemistry and Chemistry and Physics of Materials Unit, Jawaharlal Nehru Centre for Advanced Scientific Research, Jakkur P.O., Bangalore 560 064, India*

Investigations of open-framework metal phosphates reveal that the formation of these complex architectures may involve a process wherein one-dimensional ladders or chains, and possibly zero-dimensional monomers, transform to higher dimensional structures. The one-dimensional ladder appears to be the primary building unit of these structures. At one stage of the building-up process, spontaneous self-assembly of a low-dimensional structure such as the ladder seems to occur, followed by crystallization of a two- or a three-dimensional structure. Accordingly, many of the higher dimensional structures retain structural features of the 1D structure, indicating the occurrence of self-assembly. The occurrence of a hierarchy of structures of zero- to three-dimensions is also found in open-framework metal oxalates.

### 1 Introduction

An important aspect related to complex inorganic materials that needs to be understood today pertains to their mode of formation. What is the secret of these fascinating three-dimensional architectures involving various types of networks and large channels? It is likely that structures such as the oxymolbdate wheels of 4 nm diameter or more are not formed by stepwise bond making and breaking [1]. It is possible that a basic structural motif self-assembles to yield many of the complex supramolecular inorganic chemical systems. This appears to be the case in zeolites and a variety of other materials [2]. In order to understand the processes involved in the creation of such materials, we have carried out investigations on inorganic open-framework materials and obtained results with implications in supramolecular inorganic materials chemistry. This is significant since the chemistry of supramolecular inorganic materials is not well understood as the chemistry of supramolecular organic materials.

Among the inorganic open-framework compounds, the family of phosphates is a large one [3]. A large variety of open-framework metal phosphates of different architectures have been synthesized in the last few years. They include one-dimensional (1D) linear chain and ladder structures, two-dimensional (2D) layer structures and three-dimensional (3D) channel structures [4]. In the linear chain and ladder structures, four-membered metal phosphate units of the type  $M_2P_2O_4$  share corners and edges respectively. Zero-dimensional four-membered zinc phosphates have been synthesised and characterized recently [5]. Several open-framework metal carboxylates have also been reported [6] and the presence of a hierarchy of zinc oxalates covering the monomer, dimer, chain, honeycomb-layer and 3D structures has indeed been established [7].

The open-framework phosphates, oxalates and other compounds are generally prepared under hydrothermal conditions in the presence of an organic amine which is considered to be a structure-directing agent. There are several intriguing aspects of these materials. Thus, under similar synthetic conditions, one obtains several 3D and other compounds, from the same pot. The use of different amines results in products with differing structures with no obvious relationship, and at the same time, the same amine can also yield compounds of various structures and dimensionalities [8]. While it is recognized that these reactions occur under kinetic control rather than thermodynamic

control, we are not able to understand many aspects of these reactions which give rise to such a rich variety structures.

How are these open architectures formed? What is the role of the organic amine which is considered to be a structure-directing agent? Is there a relationship amongst the structures of different dimensionalities? Can one identify a secondary building unit responsible for the ultimate formation of complex 3D structures? Is self-assembly, rather than a step-wise process, involved at some stage of the building process? We have attempted to answer these important questions in the case of open-framework phosphates [9] and I shall discuss some of the salient features of our findings in this article.

In Figure 1, we show typical 1D, 2D and 3D structures of open-framework metal phosphates. In the case of the 1D structures, we have shown a linear-chain structure containing corner-shared four-membered rings and a ladder structure with edge-shared four-membered rings. Looking at these 1D structures, it would appear that the four-membered ring is the primary building unit of these materials. Zero-dimensional (0D) monomeric zinc phosphates containing the four-membered ring have been prepared and characterized [5,10]. The availability of pure 0D, 1D and 2D compounds has enabled us to investigate the relationships amongst the metal phosphates of different dimensionalities and the transformations amongst them.

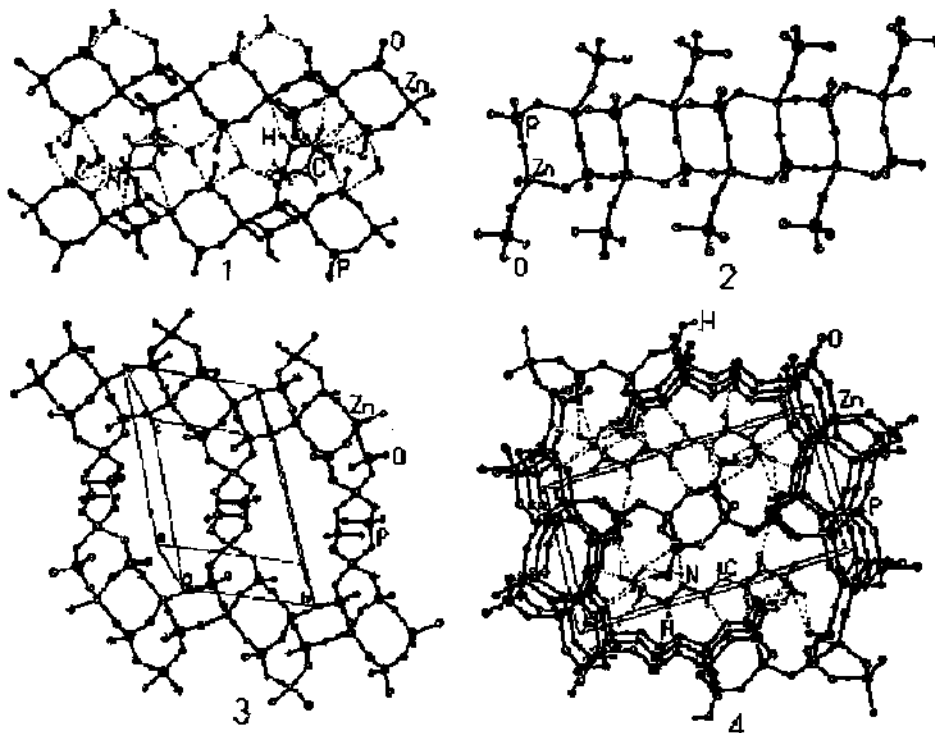


**Figure 1.** Open-framework metal phosphates of different dimensionalities: 1, 1D linear chain structure with piperazine,  $[C_4N_2H_{10}][Zn(HPO_4)_2] \cdot H_2O$ ; 2, 1D ladder structure,  $[C_6N_4H_{22}]_{0.5}[Zn(HPO_4)_2]$  with triethylenetetramine (TETA); 3, 2D layer phosphate with TETA,  $[C_6N_4H_{22}]_{0.5} [Zn_2(HPO_4)_3]$ ; 4, 3D structure with 16-membered channels with TETA,  $[C_6N_4H_{22}]_{0.5}[Zn_3(PO_4)_2(HPO_4)]$ .

## 2 Role of Amine phosphates

Before we examine the transformations of the low-dimensional (0D, 1D and 2D) metal phosphates, a few recent observations related to the role of the amine in the synthesis would be in order [8,11,12]. Organic amines are routinely used in the hydrothermal synthesis of these materials. While the pH of the medium, hydrogen bonding, and other factors may determine the role of the amine in the formation of open-framework metal phosphates, it seemed to us that the amines may be involved in a more direct manner as well. This is because we often find organic amine phosphates as side products in the hydrothermal synthesis of open-framework metal phosphates. These materials, being water soluble, are generally ignored since the preoccupation of most workers in the field has been to isolate open-framework structure compounds which come out as crystals on cooling the mother solutions. We considered it important to examine the possible role of amine phosphates [11,12]. We soon found out that amine phosphates react with metal ions such as Zn(II) and Co(II) under simple conditions to yield open-framework structures of different dimensionalities. Furthermore, the reactions could be carried out even at relatively low temperatures under ambient pressure. Thus, the reaction of 1, 3-diaminopropane phosphate with Zn(II) ions at room temperature gave ladder (1D) and layer (2D) phosphates (Figure 2). This is important not only because we can eliminate hydrothermal reaction conditions and carry out simple test tube reactions under mild conditions, but also because the amine phosphate route can be exploited to synthesize new and novel open-framework metal phosphates, including 0D and 1D materials<sup>12</sup>. The in-situ synchrotron X-ray diffraction experiments carried out recently on the reaction of piperazine phosphate with Zn(II) ions have shown that a one-dimensional phosphate is formed first followed by 3-dimensional structures [13]. This observation is indicative of a sequential building up process from low to high dimensional structures.

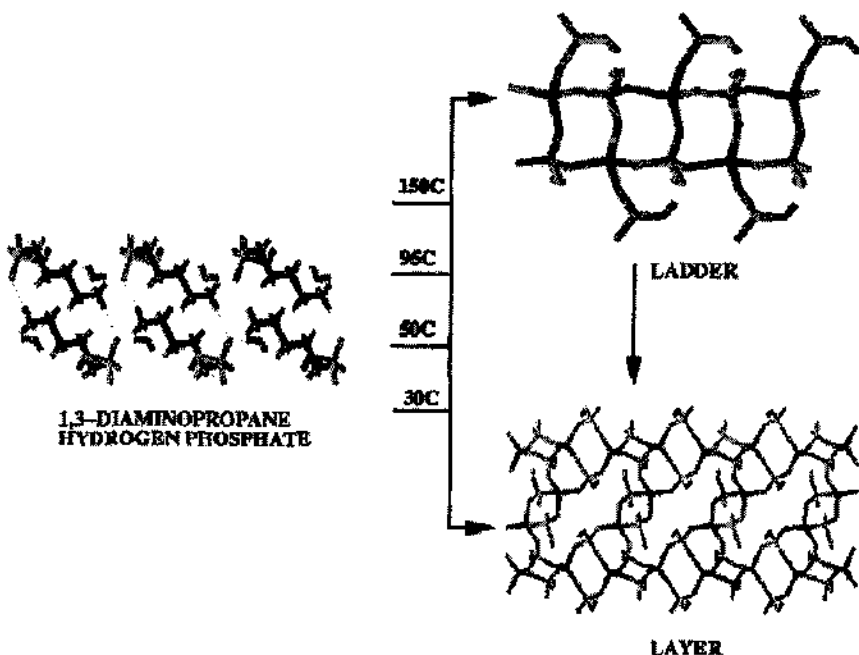


Figure 2. Reaction of an organic amine phosphate with Zn(II) ions to give a ladder and a layer phosphate.

### 3 Transformations of low-dimensional structures to higher dimensional structures

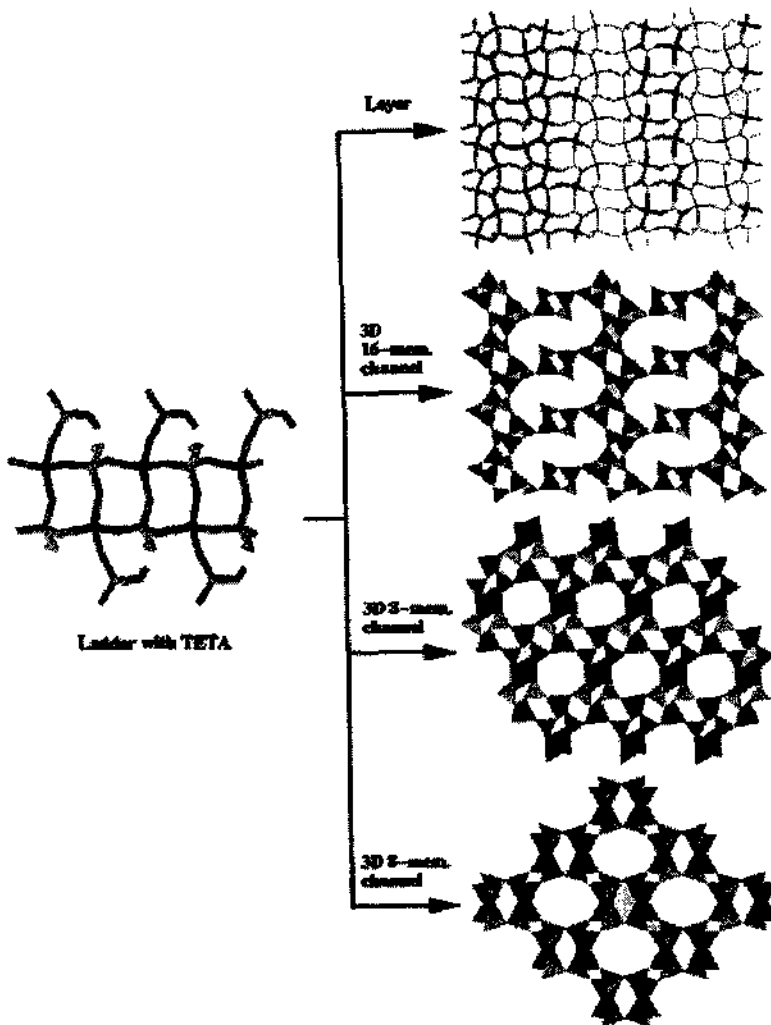
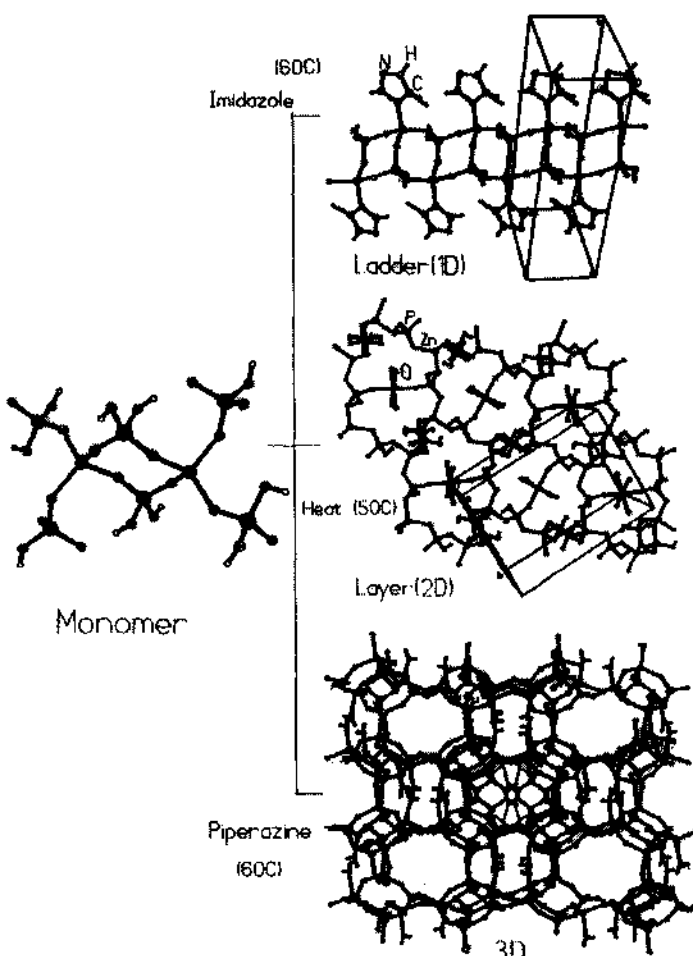


Figure 3. Transformations of a zero-dimensional monomeric zinc phosphate.

We now turn to examine the transformations of low dimensional structures to higher dimensional ones [9,10,14]. Zero-dimensional monomers of the type  $[C_6N_2H_{18}][Zn(HPO_4)(H_2PO_4)_2]$  transform under simple reaction conditions to 1D, 2D and 3D structures. The monomers comprising a 4-membered ring are not easy to isolate possibly because they readily transform to the more complex structures. In Figure 3, we show the transformations of a 0D monomer to higher dimensional structures. Such transformations may involve the elimination of  $H_3PO_4$ , rotation of bonds and condensation. One-dimensional ladder compounds of the type  $[C_6N_4H_{22}]_{0.5}[Zn(HPO_4)_2]$  transform to 2D layered compounds and 3D channel structures. In Figure 4, we show the transformations of a ladder phosphate. The transformations generally occur through the process of

deprotonation of the phosphoryl group, and the elimination of the  $\text{HPO}_4$  unit. Detailed transformation studies indicate that the one-dimensional ladder is most crucial for the building up of the complex open-framework structures. This is supported by a study of the transformations of two-dimensional layer structures. Having found that the 0D and 1D structures transform to higher-dimensional 2D and 3D structures under simple reaction conditions, it was of interest to find out whether the 2D layer structures transform to 3D structures. Systematic investigations of the transformations of layered zinc phosphates [15] show that on heating in water, the layered compounds transform to a 1D ladder structure along with a 3D structure or just a 1D ladder structure alone (Figure 5). On heating with amines such as piperazine, the 2D structures transform a 1D linear chain structure which gives rise to other 3D structures. The parent amine present in the 2D structure often gets replaced by the added amine. It appears that the primary product of the transformation of the 2D structures is the ladder structure which subsequently forms 2D or 3D structures. This observation reinforces the view that the ladder structure is probably the primary building unit of open-framework metal phosphates.



**Figure 4.** Transformations of a one-dimensional zinc phosphate with a ladder structure.

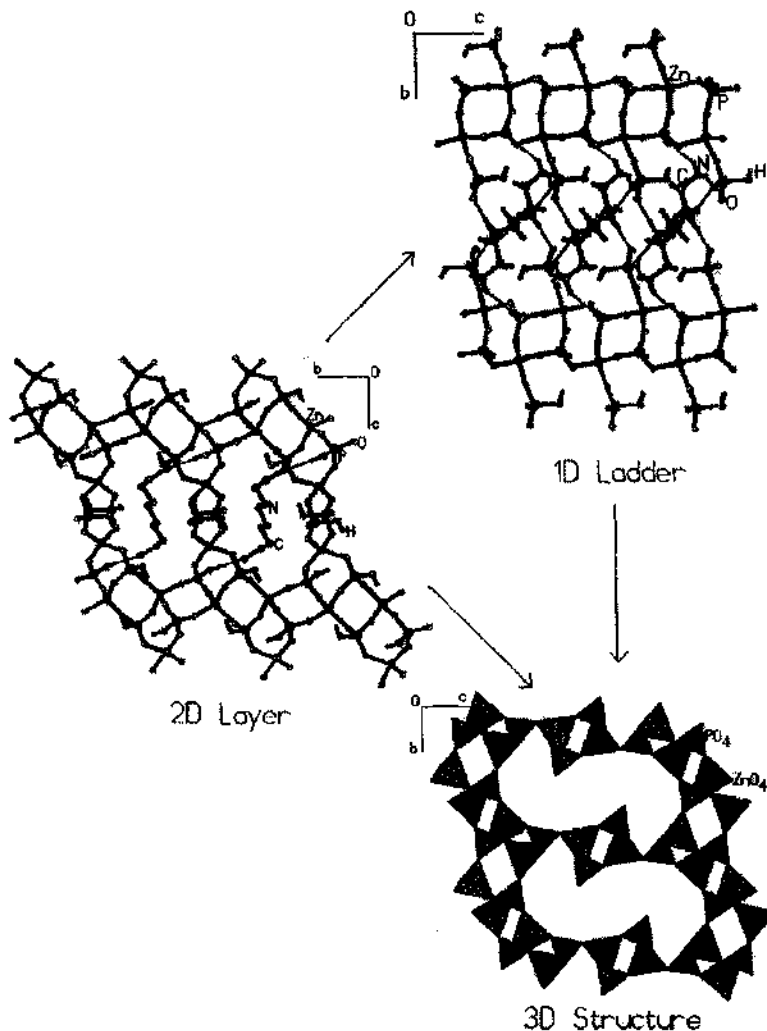


**Figure 5.** Transformations of a two-dimensional zinc phosphate with a layer structure.

#### 4 Is there Self-assembly?

A comment on the nature of the transformation of one-dimensional structures to more complex structures would be in order. Based on *in-situ* synchrotron X-ray diffraction studies [16], there is reason to believe that at some stage of the formation of complex 3D metal phosphates, there is spontaneous assembly. Our studies suggest that the ladder structure may indeed self-assemble to yield the 2D and 3D structures. Self-assembly here is not as simple as in organic compounds but involves the orientation of the building units followed by simple reactions such as deprotonation and condensation. Evidence for such self-assembly is found in the observation that the 2D and 3D structures retain the elements of the ladder structure. In Figure 6, we show how a ladder structure when connected by edge-sharing with a 4-membered ring can give rise to a 3D-structure with 8-

membered channels as in gismondine. Some of the 2D and 3D structures formed by the transformation of the 1D linear chain structures retain features of the chain. The linear chain may itself be formed from a ladder structure, rather than the other way as suspected earlier in the case of aluminum phosphates [17]. The linear chains do, however, transform under simple reaction conditions to 3D structures [15,18].

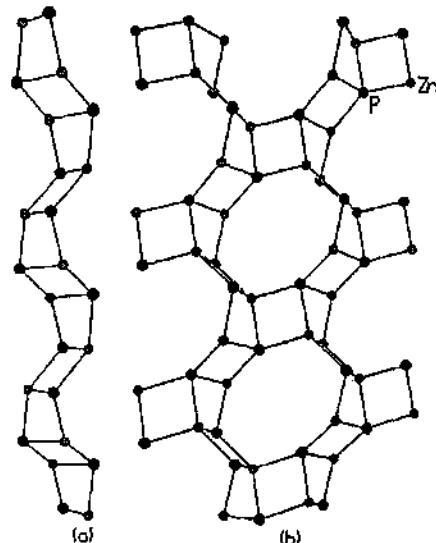
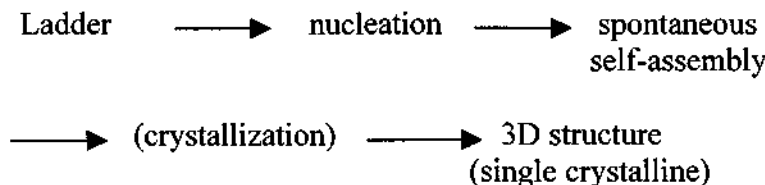


**Figure 6.** Relationship between the ladder structure and the 3D gismodine structure obtained on transformation.

## 5 Crystallization

A noteworthy feature in the transformations of 1D and 2D structures is that we readily obtain single crystals of the 3D structures as products, although we start with powders of the 1D/2D compounds, generally in solution. The ready crystallization of the 3D structures and the formation of single crystals is likely to be related to the process of self-assembly in these systems. We can represent the different steps as follows:



## 6 Hierarchy of structures in metal oxalates

Several open-framework metal oxalates have been synthesized and characterized in last two to three years. They include 1D, 2D and 3D structures. Following the success of the amine phosphate route to open-framework metal phosphates, reactions of organic amine oxalates with metal ions have been carried out. These reactions have yielded a hierarchy of zinc oxalates as shown in Figure 7. These different structures are mutually related.

Thus, it is easy to see how the dimer is related to the chain (1D) and the chain to the honeycomb structure (2D). Connecting the 2D layers by oxalate bridges gives the 3D structure.

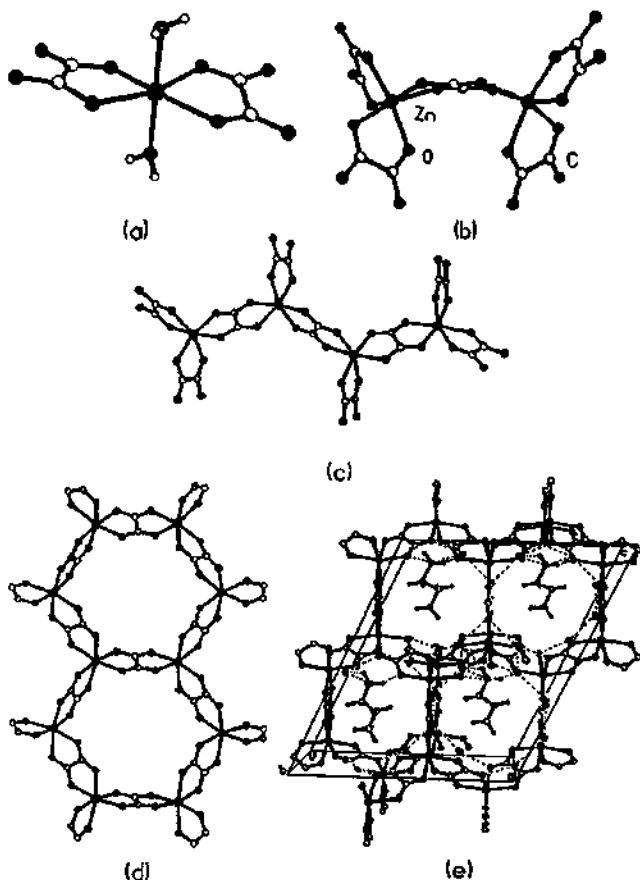


**Figure 7.** Hierarchy of zinc oxalate structures: (a) monomer, (b) dimer, (c) one-dimensional chain (d) two-dimensional honeycomb layer (e) three-dimensional structure.

## 7 Concluding Remarks

The various results from the studies of open-frame metal phosphates not only show the relationships between the structures of different dimensionalities, but also reveal a building up principle from low dimensional structures to higher dimensional ones. The transformations of 0D and 1D ladder structures to 2D and 3D structures is particularly significant and represents the first clear demonstration of such progressive building up of complex 2D and 3D structures starting from the low-dimensional structures. In Figure 8, we show the various transformations found hitherto. The occurrence of self-assembly during the building up process is of great significance. Thus, the study of the open-framework phosphates has thrown light on a problem of great current interest by showing the relation between basic building units of low dimensionality and open architectures of

higher dimensionality, and the role of self-assembly and crystallization in the formation of these structures. The presence of a hierarchy of zinc oxalates lends support to the idea of progressive build-up in these formation of open architectures.

### 0D Monomer

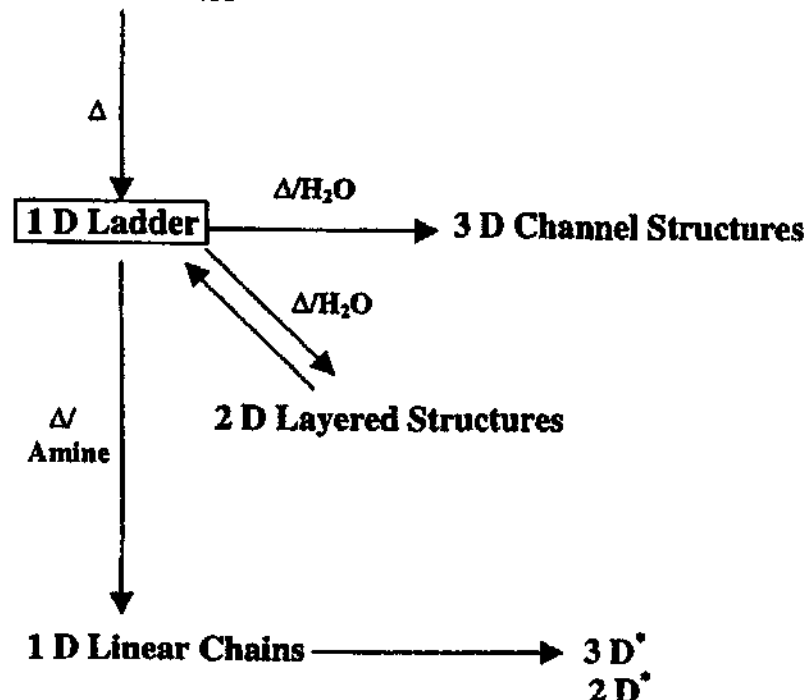


**Figure 8.** Chart showing various types of low D – high D transformations in open-framework zinc phosphates. Primacy of the 1D ladder structure can be seen.

### Acknowledgement

The author acknowledges close collaboration with Prof. A.K. Cheetham, Mr. A. Choudhury, Dr. S. Natarajan, Dr. S. Neeraj and Mr. R. Vaidhyanathan in this area of research.

### References

1. A. Miller, H. Reuter, S. Dillinger, *Angew. Chem. Int. Ed. Engl.*, 1995, **34**, 2328.
2. G. Ferey, *J. Solid State Chem.*, 2000, **152**, 37.
3. A. K. Cheetham, G. Ferey and T. Loiseau, *Angew. Chem. Int. Ed.*, 1999, **38**, 3268.
4. C. N. R. Rao, S. Natarajan, A. Choudhury, S. Neeraj and R. Vaidhyanathan, *Acta Cryst.*, 2001, **B57**, 1.
5. S. Neeraj, S. Natarajan and C. N. R. Rao, *J. Solid State Chem.*, 2000, **150**, 417.
6. C. Livage, C. Egger and G. Ferey, *Chem. Mater.*, 1999, **11**, 1546 and references therein.

7. R. Vaidhyanathan, S. Natarajan and C. N. R. Rao, *J. Chem. Soc. Dalton Trans.*, 2001, 699 and references therein.
8. A. Choudhury, S. Natarajan and C. N. R. Rao, *Inorg. Chem.*, 2000, **39**, 4295.
9. C. N. R. Rao, S. Natarajan, A. Choudhury, S. Neeraj and A. A. Ayi, *Acc. Chem. Res.*, 2001, **34**, 80.
10. A. A. Ayi, A. Choudhury, S. Natarajan, S. Neeraj and C. N. R. Rao, *J. Mater. Chem.*, 2001, **11**, 1181.
11. S. Neeraj, S. Natarajan and C. N. R. Rao, *Angew. Chem. Int. Ed.*, 1999, **38**, 3480.
12. C. N. R. Rao, S. Natarajan and S. Neeraj, *J. Am. Chem. Soc.*, 2000, **122**, 2810.
13. R. I. Walton, A.J. Norquist, S. Neeraj, S. Natarajan, C. N. R. Rao and D. O'Hare. To be published.
14. A. Choudhury, S. Neeraj, S. Natarajan and C. N. R. Rao, *J. Mater. Chem.*, 2001, **11**, 1537.
15. A. Choudhury, S. Neeraj, S. Natarajan and C. N. R. Rao, *J. Mater. Chem.* Communicated.
16. R. J. Francis, S. O'Brien, A. M. Fogg, P. S. Halasyamani, D. O'Hare, T. Loiseau and G. Ferey, *J. Am. Chem. Soc.*, 1999, **121**, 1002.
17. S. Oliver, A. Kuperman and G. A. Ozin, *Angew. Chem. Int. Ed.*, 1998, **37**, 46.
18. R. I. Walton, F. Millange, A. Le Bail, T. Loiseau, C. Serre, D. O'Hare and G. Ferey, *Chem. Commun.*, 2000, 203.

## SYNTHESIS AND CHARACTERIZATION OF THE OXYGEN DEFICIENT DOUBLE-PEROVSKITE $\text{Sr}_2\text{CrNbO}_{5.53}$

G. M. VEITH AND M. GREENBLATT\*

*Department of Chemistry and Chemical Biology, Rutgers the State University of New Jersey, 610 Taylor Road, Piscataway, NJ 08854-88087, USA  
Email: greenblatt@rutchem.rutgers.edu*

E. N. CASPI AND J. D. JORGENSEN

*Materials Science Division, Argonne National Laboratory, Argonne, IL 60439, USA*

We have synthesized the oxygen deficient double-perovskite  $\text{Sr}_2\text{CrNbO}_{5.53}$ , that forms in a monoclinically distorted double perovskite structure (S.G.  $I2/m$ ) as determined by analysis of time-of-flight powder neutron diffraction data. Cr and Nb partially order on Cr-rich ( $\text{Cr}/\text{Nb}(1)$ , occupancy, 63/ 37 %), and Nb-rich ( $\text{Cr}/\text{Nb}(2)$ , occupancy 37/63 %) sites. The oxygen vacancies occur in the apical positions. Below 150 K the Cr-rich octahedra undergo a large distortion and a concomitant large splitting of the  $t_{2g}$   $\text{Cr}^{3+}$  ( $d^3$ ) orbitals with a  $d^3$  ( $d_{xz}/d_{yz}$ ) and  $d^0$  ( $d_{xy}$ )  $S = \frac{1}{2}$  electronic configuration.  $\text{Sr}_2\text{CrNbO}_{5.53}$  is an insulator with a room temperature resistivity of *ca.* 250  $\Omega\cdot\text{cm}$ . Magnetic susceptibility measurements indicate spin-glass-type behavior with the transition temperature,  $T_g$  *ca.* 25 K. The magnetization data show evidence of ferromagnetic-like interactions from 5 to 110 K. The unexpectedly small magnetic moment of 0.15  $\mu_B$  in an applied field of 5 T at 5 K suggests the presence of frustrated magnetic interactions and is consistent with antiferromagnetic coupling between  $\text{Nb}^{4+}$  ( $d^1$ ) and a lone  $\text{Cr}^{3+}$  electron in a  $d_{xz}$  or  $d_{yz}$  orbital.

### 1 Introduction

Since the recent discovery of large negative magnetoresistance (MR) in the compound  $\text{Sr}_2\text{FeMoO}_6$  there has been a great deal of interest in compounds with the double-perovskite structure [1]. The double-perovskite,  $A_2\text{BB}'\text{O}_6$  structure consists of an array of corner-sharing  $\text{BO}_6$  and  $\text{B}'\text{O}_6$  metal octahedra [2]. The B and B' cations usually order crystallographically, if their formal oxidation states, number of valence electrons and ionic radii are considerably different [2]. The A cations are located in the 12-coordinate, cubo-octahedral positions of the three-dimensional (3D) octahedral network [2].  $\text{Sr}_2\text{FeMoO}_6$ , first reported on in 1963 by Patterson *et al.* [3], is a semimetal with an ordered array of  $\text{Fe}^{3+}$  ( $d^5$ ) and  $\text{Mo}^{5+}$  ( $d^1$ ) octahedra [3].  $\text{Sr}_2\text{FeMoO}_6$  orders ferrimagnetically around 410 K due to the alignment of the  $\text{Fe}^{3+}$  ( $d^5$ ) and  $\text{Mo}^{5+}$  ( $d^1$ ) spins in an anti-parallel arrangement [4].

Subsequently, numerous groups have investigated double-perovskite systems with magnetic interactions between the B and B' cations, in the search for materials with enhanced MR properties. For example, Moritomo *et al.* reported the synthesis of a series of molybdenum double-perovskites  $\text{Sr}_2\text{BMoO}_6$  (B = Cr, Mn, Fe and Co) [5]. They found that  $\text{Sr}_2\text{CrMoO}_6$  ordered ferrimagnetically around 300 K due to interactions between the  $\text{Cr}^{3+}$ ( $d^3$ ) and  $\text{Mo}^{5+}$ ( $d^1$ ) electrons, while the Co and Mn analogs were paramagnetic insulators [5]. Zeng *et al.* reported that  $\text{Sr}_2\text{CrMoO}_6$  is not a single phase and only the  $\text{Sr}_2\text{Cr}_{1.2}\text{Mo}_{0.8}\text{O}_{6.8}$  composition in this system forms as a single phase. The  $\text{Cr}^{3+}$ ( $d^3$ ) and  $\text{Mo}^{5+}$ ( $d^1$ ) electrons in  $\text{Sr}_2\text{Cr}_{1.2}\text{Mo}_{0.8}\text{O}_{6.8}$  order ferrimagnetically around 465 K [6]. This compound also exhibits large MR, albeit at 20 K in an applied field of 5T [6].

In this work we have attempted to prepare the oxygen deficient double-perovskite

$\text{Sr}_2\text{CrNbO}_{5.5}$ , with  $\text{Cr}^{3+}$  ( $d^3$ ) and  $\text{Nb}^{4+}$  ( $d^1$ ) formal oxidation states to investigate possible ferrimagnetic interactions between the Cr and Nb atoms similar to those present in  $\text{Sr}_2\text{FeMoO}_6$  [4]. The  $\text{Cr}^{3+}$  system was chosen instead of the  $\text{Fe}^{3+}$  system because previous work on compounds containing  $\text{Fe}^{3+}$  ( $d^5$ ) and  $\text{Nb}^{4+}$  ( $d^1$ ) revealed that the Fe is reduced to  $\text{Fe}^{2+}$  while Nb is oxidized to  $\text{Nb}^{5+}$  [7].

## 2 Experimental

### 2.1 Synthesis

$\text{Sr}_2\text{CrNbO}_{5.5}$  was synthesized by the solid-state reaction of stoichiometric mixtures of  $\text{SrO}$  (prepared by decomposing  $\text{SrC}_2\text{O}_4$ , Alfa, 95% Assay, at 1300 °C for 4 hours in air),  $\text{Cr}_2\text{O}_3$  (Fisher Certified, 99.9%), Nb (Alfa, 99.99%, Puratronic, -325 mesh),  $\text{Nb}_2\text{O}_5$  (Alfa, 99.99%, Optical Grade). The Nb was checked by powder X-ray diffraction prior to use to ensure that no oxides were present. All reagents were stored and thoroughly ground in an argon filled dry box. Pressed pellets were sealed in evacuated quartz tubes at a pressure of *ca.* 10<sup>-5</sup> torr. The tubes were heated at 550 °C for 24 hours then slowly ramped to 1050 °C over a period of 24 hours. After 24 hours at 1050 °C the samples were quenched to room temperature by removing the tubes from the furnace. The samples were reground in air, re-pressed into pellets, re-sealed in quartz tubes and sintered at 1200 °C for 48 hours, then quenched to room temperature. In order to obtain a single-phase product, the procedure was repeated and the sample was heated at 1200 °C for an additional 48 hours, and quenched as before. Samples kept in the ambient decompose in *ca.* 2 months; therefore they were stored in a dry box.

### 2.2 Structure

Powder X-ray diffraction (PXD) data were collected with a Scintag Pad V diffractometer with Ni-filtered  $\text{CuK}\alpha$  radiation and a Li-drifted germanium detector. Samples were finely ground and placed on a glass slide with petroleum jelly. Data were collected over a range of  $10^\circ \leq 2\theta \leq 120^\circ$ , with a step size of 0.02°. Lattice parameters were determined by Rietveld refinement with the program GSAS [8].

Time-of-flight powder neutron diffraction data was collected at the Intense Pulsed Neutron Source (IPNS), Argonne National Laboratory (ANL) with the Special Environment Powder Diffractometer (SEPD). The sample was sealed in a cylindrical vanadium can with helium exchange gas. Data were collected over a temperature range of 5 to 300 K with *ca.* 2 hour data collection time at each temperature except for 5 K, where a 5-hour data collection was made to look carefully for magnetic ordering. Rietveld refinements were performed using the program GSAS [8].

### 2.3 Oxygen Content

Thermogravimetric analysis (TGA) was performed with a TA Instrument 2050 thermal analyzer in order to determine the oxygen deficiency of the samples. The samples were ramped at 10°/min to 900 °C and remained isothermal in the presence of  $\text{O}_2$  gas until oxidation was complete. The oxidized powders were analyzed by PXD and the lattice parameters were compared to published values of  $\text{Sr}_2\text{CrNbO}_6$  [9] to confirm complete oxidation.

## 2.4 Magnetic and Electrical Properties

Temperature-dependent magnetic susceptibility,  $\chi$  measurements were made with a Quantum Design MPMS-XL SQUID magnetometer. The samples were cooled to 5 K, then a magnetic field of 100 gauss was applied and data were collected while heating from 5 to 400 K (ZFC) followed by re-cooling to 5 K (FC). Magnetization measurements were performed in fields of  $-5\text{T} \leq H \leq 5\text{T}$  at temperatures between  $5\text{ K} \leq T \leq 200\text{ K}$ . Temperature-dependent resistivity,  $\rho$  was measured with a conventional four-point probe technique.

## 3 Results and Discussion

Preliminary analysis of the PXD data indicated the formation of a pure phase. The oxygen deficiency determined from the TGA data was  $0.47 \pm 0.03$  moles (Figure 1). The temperature-dependent magnetic susceptibility data of  $\text{Sr}_2\text{CrNbO}_{5.53}$  in Fig. 2 shows a maximum at *ca.* 25 K. Analysis of the  $1/\chi$  vs T data (inset of Fig. 2) with the Curie-Weiss law, in the linear ranges of 370 - 200 K and 180 - 65 K, yielded effective magnetic moments ( $\mu_{\text{eff}}$ ) of  $2.81\text{ }\mu_{\text{B}}$  and  $2.44\text{ }\mu_{\text{B}}$ , and Weiss constants ( $\theta$ ) of  $-33\text{ K}$  and  $24\text{ K}$  respectively. The  $\mu_{\text{eff}}$  value determined for the higher range of temperature inverse susceptibility data is consistent with the predicted moment of  $2.87\text{ }\mu_{\text{B}}$  for  $S=1$ , assuming ferrimagnetic interactions between the  $\text{Nb}^{4+}$  ( $d^1$ ) and  $\text{Cr}^{3+}$  ( $d^3$ ) ions. The negative value of  $\theta$  indicates that the magnetic interactions are predominately antiferromagnetic (AFM), however below 180 K there is a crossover to a positive Weiss constant indicating that FM interactions are dominating. Both Weiss constants are consistent with the maximum seen in the susceptibility at *ca.* 25 K.

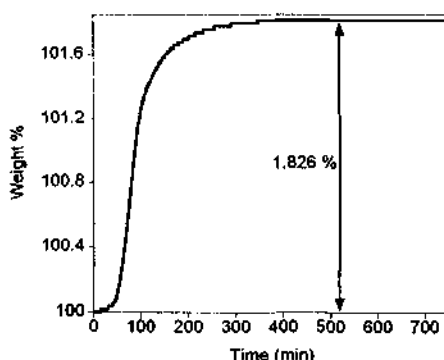


**Figure 1.** TGA data for the oxidation of  $\text{Sr}_2\text{CrNbO}_{5.53}$  to  $\text{Sr}_2\text{CrNbO}_6$ .

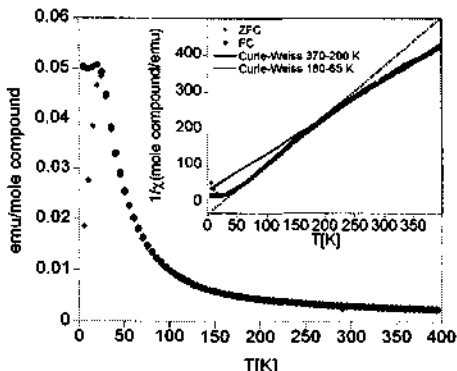


**Figure 2.** Magnetic susceptibility of  $\text{Sr}_2\text{CrNbO}_{5.53}$  as a function of temperature. Inset - inverse susceptibility as a function of temperature along with the Curie-Weiss plots.

According to the Curie-Weiss law the theoretically predicted paramagnetic moment for a  $d^3-d^1$  ferrimagnetic system should be around  $4.90\text{ }\mu_{\text{B}}$  rather than the observed  $\mu_{\text{eff}}$  of  $2.81\text{ }\mu_{\text{B}}$ . However, the analysis of reported magnetic susceptibility data for a variety of ferrimagnetic double-perovskites [6,10-13] shows that the observed paramagnetic

moment is close to or less than the calculated moment assuming anti-parallel spin alignment between the two transition metal ions above the ferrimagnetic ordering temperature. Due to the possibility of short range AFM correlations care should be taken in evaluating the inverse susceptibility data [14]. Also, according to Neél's mean-field theory, the  $1/\chi$  vs T curve is a hyperbola for T near  $T_c$  (where  $T_c$  is the Curie temperature) in the case of ferrimagnetic interactions. This could explain the observed divergence from linearity at *ca.* 180 K; however, fitting the data to the hyperbola version of the Curie-Weiss law did not produce more accurate results. For  $T \gg T_c$  the linear behavior of the Curie-Weiss law applies. More on the origin of the *ca.* 180 K anomaly will be discussed latter.

In Fig. 3, the field dependence of magnetization of  $\text{Sr}_2\text{CrNbO}_{5.53}$  at 5 K shows pronounced hysteresis, but no saturation of the magnetic moment even in an applied field of 5 T. The magnetic moment at 5 K is  $0.15 \mu_B$ , which is significantly smaller than the theoretically expected moment (*ca.*  $2 \mu_B$ ) for  $S = 1$  state, if ferrimagnetic ordering between  $d^3$  and  $d^1$  configurations is assumed. At 110 K a small hysteresis (not visible in the plot of Fig. 3) is observed, which suggests the presence of ferri/ferromagnetic interactions far above the magnetic transition temperature at *ca.* 25 K seen in the susceptibility data (Fig. 2). The small magnitude of the magnetic moment and the marked deviation between the FC and ZFC susceptibility data suggests spin-glass type magnetism [15,16]. Spin-glass type magnetism has been reported before in numerous other frustrated double-perovskites [17-19]. Spin-glass type magnetism is due to the competition between AFM  $\text{Cr}^{3+}\text{-O-Cr}^{3+}$  and  $\text{Nb}^{4+}\text{-O-Nb}^{4+}$  and the FM  $\text{Cr}^{3+}\text{-O-Nb}^{4+}$  interactions discussed below.

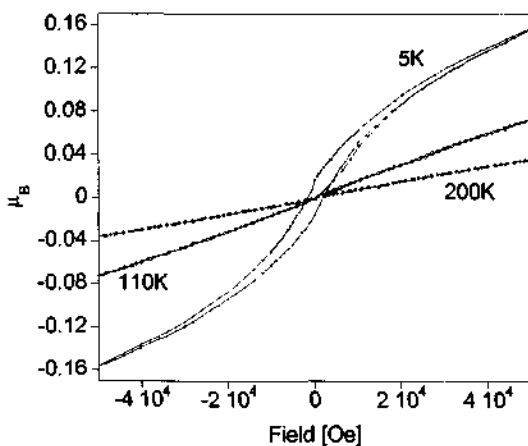
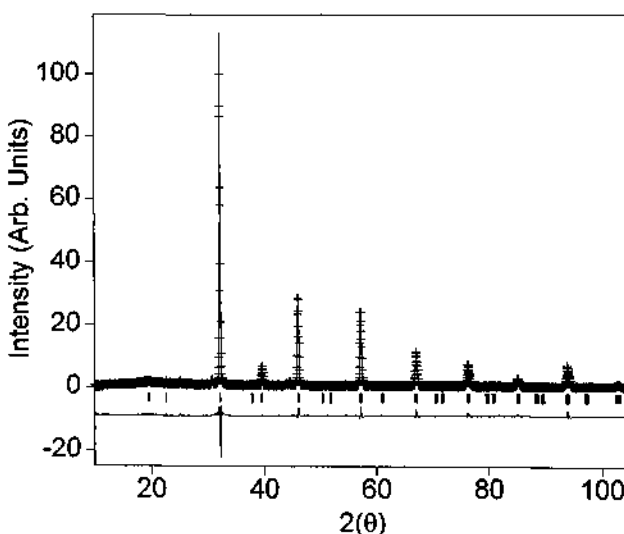


Figure 3. Magnetization as a function of applied field of  $\text{Sr}_2\text{CrNbO}_{5.53}$  measured at 5, 110 and 200 K.

$\text{Sr}_2\text{CrNbO}_{5.53}$  is a semiconductor with a room-temperature resistivity,  $\rho_{RT}$  of *ca.* 250  $\Omega\text{-cm}$ ;  $\rho$  increases rapidly with decreasing temperature and at low temperature  $\rho$  is larger than the limit of our instrument. Nevertheless,  $\rho_{RT}$  is significantly lower than that in the stoichiometric parent compound,  $\text{Sr}_2\text{CrNbO}_6$ ; this behavior is attributed to the additional electrons of  $\text{Nb}^{4+}$  in the reduced phase.

In order to better understand the magnetic properties of  $\text{Sr}_2\text{CrNbO}_{5.53}$  and to determine the effect of the oxygen deficiency on the structure, time-of-flight (TOF)

neutron diffraction experiments were carried out at 13 different temperatures in the range 5-300 K. Attempts to index the neutron diffraction data in the cubic space group  $Fm\bar{3}m$  reported by Choy *et al.* [9] for  $\text{Sr}_2\text{CrNbO}_6$ , were unsuccessful. Numerous other structural models from Woodward [20,21] were also tried, but these models resulted in either significantly larger goodness-of-fit values, unreasonable thermal parameters or simply failed to converge. The monoclinic space group  $I2/m$ , (tilt system -  $a^{\circ}b^{\circ}\bar{b}$  [22]) gave the best fit to the observed d-spacings. Simultaneous refinement of the room temperature X-ray (Fig. 4) and neutron models were used to determine the atomic positions and the most reliable fractional occupancies of the constituent ions. The total oxygen content was consistent with the value obtained from the TGA data (i.e. 5.53) and it was fixed to this value for all of the refinements based upon the neutron data sets. The refinement of the room-temperature model is consistent with vacancies in both of the oxygen positions, though the difference from unity for O(2), the equatorial oxygens, and from each other is just above the significance level. There was a small, unidentified impurity peak in the powder neutron diffraction pattern (PND) at 2.08 Å whose intensity did not change with temperature.



**Figure 4.** Room temperature PXD diffraction data for  $\text{Sr}_2\text{CrNbO}_{5.53}$ : observed (+), calculated (solid line), allowed reflections (tic) and difference plot (bottom).

Refinement of the data show that the structure of  $\text{Sr}_2\text{CrNbO}_{5.53}$  is made up of a partially ordered array of  $\text{CrO}_6$  and  $\text{NbO}_6$  corner-sharing octahedra (Fig. 5). The Cr/Nb(1) and Cr/Nb(2) site occupancy values are 63/37 and 37/63 % respectively (Table 1). The large amount of disorder between the Cr and Nb ions leads to AFM type magnetic interactions between identical neighboring transition metal ions. The presence of AFM type interactions leads to a reduction in the observed saturation magnetization moment and contributes to the observed spin-glass type behavior.

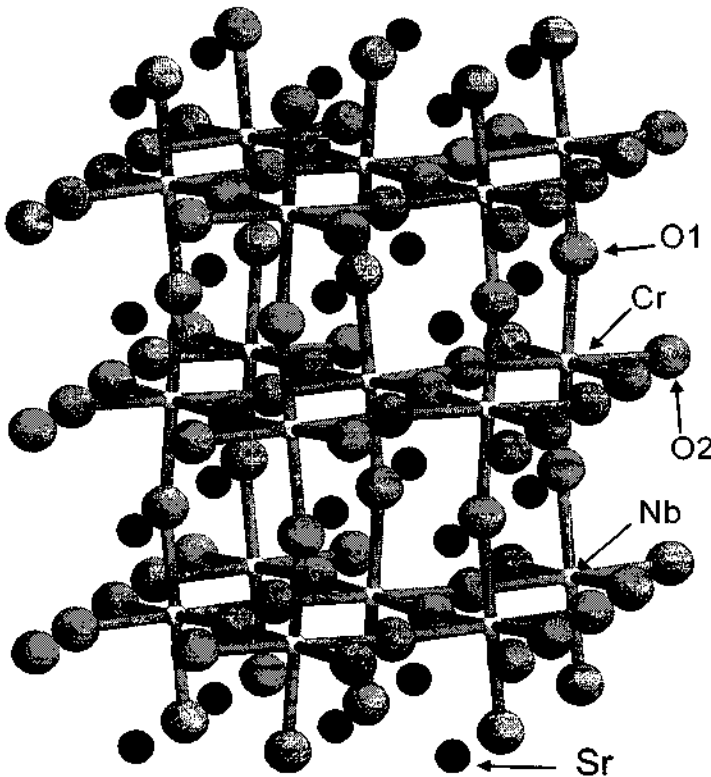


**Figure 5.** Schematic representation of  $\text{Sr}_2\text{CrNbO}_{5.53}$  (S.G.  $I2/m$ ). The black spheres represent Sr, the white spheres represent the two B cation sites, and the large grey spheres are O1 and O2.

There are two crystallographically unique Cr/Nb [Cr/Nb (1) at 2a and Cr/Nb (2) at 2c of  $I2/m$ ] and oxygens [axial-O(1) and equatorial-O(2)] (Fig. 5). The  $(\text{Cr}/\text{Nb})\text{O}_6$  octahedra are distorted with slightly longer axial than equatorial bond lengths (e.g. at 300 K: 1.981(11) and 1.973(9) Å; Table 1). The mean Sr-O (2.79 Å) and Cr/Nb(1)-O bond lengths are in good agreement with those previously reported for the double perovskite  $\text{Sr}_2\text{CrNbO}_6$  [9]. However, the mean Cr/Nb(2)-O bond distance for  $\text{Sr}_2\text{CrNbO}_{5.53}$  is slightly longer than that reported for  $\text{Sr}_2\text{CrNbO}_6$ , 1.979 vs 1.966 Å [9], respectively; this difference is consistent with the slightly larger effective ionic radius of  $\text{Nb}^{4+}$  compared to that of  $\text{Nb}^{5+}$  (0.82 vs 0.78 Å [23,24]). The Cr/Nb-O-Cr/Nb bond angles range between 168-176° and deviate significantly from those of the ideal double perovskite, i.e. 180°. The oxygen vacancies preferentially occupy the axial O(1) positions of the metal octahedra (Table 1). The room temperature PXD diffraction pattern including the raw data, fitted profile and the difference plot are shown in Fig. 4.

**Table 1.** Unit cell parameters<sup>a</sup>, atomic positions, occupation factors, thermal parameters, bond distances and angles as a function of temperature for Sr<sub>2</sub>CrNbO<sub>5.53</sub> - Space group *I2/m* (No.12-3), Z = 2.

T[K]	300	250	200	150	100
a (Å)	5.5795(3)	5.5761(3)	5.5738(3)	5.5719(3)	5.5699(3)
b (Å)	5.5747(3)	5.5715(3)	5.5692(3)	5.5669(3)	5.5650(3)
c (Å)	7.9036(2)	7.9021(2)	7.9000(2)	7.8984(2)	7.8975(2)
β (°)	90.162(3)	90.177(3)	90.176(3)	90.178(3)	90.184(3)
V (Å <sup>3</sup> )	245.832(18)	245.496(5)	245.230(5)	244.994(5)	244.795(5)
Sr(x)	0.5015(22)	0.5041(21)	0.5046(20)	0.5069(16)	0.5083(13)
Sr(z)	0.2487(18)	0.2491(14)	0.2487(13)	0.2492(10)	0.2502(9)
O(1) (x)	0.0278(9)	0.0325(7)	0.0346(6)	0.0356(6)	0.0369(5)
O(1) (z)	0.2500(13)	0.2502(11)	0.2505(10)	0.2512(9)	0.2515(9)
O(2) (x)	0.2504(15)	0.2501(14)	0.2496(12)	0.2498(12)	0.2508(12)
O(2) (y)	0.2496(24)	0.2485(18)	0.2491(17)	0.2478(16)	0.2465(15)
O(2) (z)	-0.0084(5)	-0.0089(5)	-0.0102(4)	-0.0110(34)	-0.0116(32)
Sr <sub>frac</sub> - 4m	1.00	1.00	1.00	1.00	1.00
Cr/Nb(1) <sub>frac</sub> - 2a	0.626/0.374(13)	0.626/0.374	0.626/0.374	0.626/0.374	0.626/0.374
Cr/Nb(2) <sub>frac</sub> - 2c	0.374/0.626(13)	0.374/0.626	0.374/0.626	0.374/0.626	0.374/0.626
O(1) <sub>frac</sub> - 4m	0.882(16)	0.882	0.882	0.882	0.882
O(2) <sub>frac</sub> - 8j	0.942(8)	0.942	0.942	0.942	0.942
Sr <sub>Uiso</sub> (Å <sup>2</sup> )	0.0118(2)	0.0112(3)	0.0101(3)	0.0093(3)	0.0079(3)
Cr/Nb(1) <sub>Uiso</sub> (Å <sup>2</sup> )	0.0034(17)	0.0028(15)	0.0036(10)	0.0035(14)	0.0028(14)
Cr/Nb(2) <sub>Uiso</sub> (Å <sup>2</sup> )	0.0062(17)	0.0078(17)	0.0055(12)	0.0058(15)	0.0056(14)
O(1) <sub>Uiso</sub> (Å <sup>2</sup> )	0.0076(10)	0.0064(6)	0.0049(5)	0.0042(3)	0.0031(4)
O(2) <sub>Uiso</sub> (Å <sup>2</sup> )	0.0075(4)	0.0073(3)	0.0065(3)	0.0063(3)	0.0060(3)
Sr-O(1)	2.643(12)	2.630(14)	2.620(13)	2.626(10)	2.626(8)
Sr-O(1)	2.936(12)	2.946(14)	2.954(13)	2.946(10)	2.944(8)
Sr-O(1) (x2)	2.7922(8)	2.7932(8)	2.7932(8)	2.7936(11)	2.7939(6)
<Sr-O(1)>	2.791	2.791	2.790	2.790	2.789
Sr-O(2) (x2)	2.831(12)	2.839(11)	2.848(11)	2.857(9)	2.863(8)
Sr-O(2) (x2)	2.734(9)	2.723(7)	2.714(6)	2.701(5)	2.692(6)
Sr-O(2) (x2)	2.747(12)	2.736(10)	2.726(11)	2.716(9)	2.709(8)
Sr-O(2) (x2)	2.856(9)	2.865(7)	2.872(6)	2.883(5)	2.891(6)
<Sr-O(2)>	2.792	2.791	2.790	2.789	2.789
Cr/Nb(1)-O(1) (x2)	1.981(11)	1.985(8)	1.981(8)	1.976(7)	1.996(7)
Cr/Nb(1)-O(2) (x4)	1.973(9)	1.966(8)	1.977(7)	1.980(7)	1.960(7)
<Cr/Nb(1)-O>	1.976	1.972	1.978	1.979	1.972
Cr/Nb(2)-O(1) (x2)	1.983(11)	1.983(8)	1.981(8)	1.976(7)	1.974(7)
Cr/Nb(2)-O(2) (x4)	1.973(9)	1.977(8)	1.977(7)	1.980(7)	1.981(7)
<Cr/Nb(2)-O>	1.976	1.979	1.978	1.979	1.979
Cr/Nb-O(1)-Cr/Nb (°)	171.03(28)	169.51(21)	168.85(19)	168.52(18)	168.12(17)
Cr/Nb-O(2)-Cr/Nb (°)	176.13(25)	175.90(22)	175.30(16)	174.92(16)	174.57(15)
$\chi^2$	4.673	3.057	3.028	3.105	3.247
wRp	7.28	8.01	8.03	8.08	8.28
Rp	4.98	5.36	5.43	5.48	5.66
Variables	39	37	37	37	37

**Table 1 (continued) - Space group  $I2/m$  (No.12-3),  $Z = 2$ .**

T[K]	50	40	32	25	20
a (Å)	5.5685(3)	5.5682(3)	5.5684(3)	5.5684(3)	5.5686(2)
b (Å)	5.5642(3)	5.5642(3)	5.5640(3)	5.5639(3)	5.5639(2)
c (Å)	7.8969(2)	7.8965(2)	7.8967(2)	7.8966(2)	7.8965(2)
$\beta$ (°)	90.191(3)	90.1864(4)	90.188(4)	90.190(4)	90.191(3)
V (Å <sup>3</sup> )	244.676(5)	244.654(5)	244.659(5)	244.655(5)	244.657(5)
Sr(x)	0.5099(10)	0.5092(11)	0.5087(12)	0.5088(12)	0.5086(10)
Sr(z)	0.2514(7)	0.2516(10)	0.2504(8)	0.2516(8)	0.2507(7)
O(1) (x)	0.0376(5)	0.0376(5)	0.0380(5)	0.0376(5)	0.0381(4)
O(1) (z)	0.2515(8)	0.2516(8)	0.2516(8)	0.2519(8)	0.2519(7)
O(2) (x)	0.2522(12)	0.2523(11)	0.2506(11)	0.2523(11)	0.2512(10)
O(2) (y)	0.2450(13)	0.2450(13)	0.2464(15)	0.2450(14)	0.2455(12)
O(2) (z)	-0.0115(33)	-0.0118(32)	-0.0123(30)	-0.0118(33)	-0.0121(27)
Sr <sub>frac</sub> - 4m	1.00	1.00	1.00	1.00	1.00
Cr/Nb(1) <sub>frac</sub> - 2a	0.626/0.374	0.626/0.374	0.626/0.374	0.626/0.374	0.626/0.374
Cr/Nb(2) <sub>frac</sub> - 2c	0.374/0.626	0.374/0.626	0.374/0.626	0.374/0.626	0.374/0.626
O(1) <sub>frac</sub> - 4m	0.882	0.882	0.882	0.882	0.882
O(2) <sub>frac</sub> - 8j	0.942	0.942	0.942	0.942	0.942
Sr <sub>Uiso</sub> (Å <sup>2</sup> )	0.0069(3)	0.0067(3)	0.0069(3)	0.0069(3)	0.0068(2)
Cr/Nb(1) <sub>Uiso</sub> (Å <sup>2</sup> )	0.0025(13)	0.0023(13)	0.0026(13)	0.0025(13)	0.0026(11)
Cr/Nb(2) <sub>Uiso</sub> (Å <sup>2</sup> )	0.0052(13)	0.0055(13)	0.0052(14)	0.0052(14)	0.0052(12)
O(1) <sub>Uiso</sub> (Å <sup>2</sup> )	0.0027(4)	0.0025(4)	0.0025(4)	0.0025(4)	0.0026(3)
O(2) <sub>Uiso</sub> (Å <sup>2</sup> )	0.0057(3)	0.0056(3)	0.0054(3)	0.0056(4)	0.0055(3)
Sr-O(1)	2.630(7)	2.626(7)	2.621(8)	2.624(7)	2.621(7)
Sr-O(1)	2.939(7)	2.942(7)	2.947(8)	2.944(7)	2.948(7)
Sr-O(1) (x2)	2.7940(6)	2.7944(6)	2.7942(6)	2.7941(6)	2.7941(6)
<Sr-O(1)>	2.789	2.789	2.789	2.789	2.789
Sr-O(2) (x2)	2.865(7)	2.866(7)	2.868(7)	2.865(7)	2.865(6)
Sr-O(2) (x2)	2.687(5)	2.687(5)	2.688(5)	2.689(5)	2.687(4)
Sr-O(2) (x2)	2.706(7)	2.706(7)	2.702(8)	2.706(7)	2.706(6)
Sr-O(2) (x2)	2.895(5)	2.894(5)	2.894(5)	2.893(5)	2.895(4)
<Sr-O(2)>	2.788	2.788	2.788	2.788	2.788
Cr/Nb(1)-O(1) (x2)	1.997(6)	1.997(6)	1.997(6)	2.000(6)	1.999(6)
Cr/Nb(1)-O(2) (x4)	1.959(7)	1.960(7)	1.959(7)	1.960(7)	1.958(6)
<Cr/Nb(1)-O>	1.972	1.972	1.972	1.973	1.972
Cr/Nb(2)-O(1) (x2)	1.974(7)	1.973(7)	1.974(7)	1.971(7)	1.972(7)
Cr/Nb(2)-O(2) (x4)	1.981(7)	1.981(7)	1.982(7)	1.981(7)	1.983(7)
<Cr/Nb(2)-O>	1.979	1.978	1.979	1.978	1.979
Cr/Nb-O(1)-Cr/Nb (°)	167.88(16)	167.90(16)	167.78(16)	167.89(16)	167.75(14)
Cr/Nb-O(2)-Cr/Nb (°)	174.45(16)	174.32(15)	174.26(14)	174.32(16)	174.29(13)
$\chi^2$	3.377	3.282	3.447	3.106	7.439
wRp	8.42	8.33	8.48	8.66	7.58
Rp	5.74	5.75	5.83	5.92	5.73
Variables	37	37	37	37	37

**Table 1 (continued) - Space group  $I2/m$  (No. 12-3),  $Z = 2$ .**

T[K]	15	10	5
a (Å)	5.5685(3)	5.5685(3)	5.5685(2)
b (Å)	5.5640(3)	5.5640(3)	5.5640(2)
c (Å)	7.8962(2)	7.8965(2)	7.8966(2)
$\beta$ (°)	90.188(4)	90.188(4)	90.192(3)
V (Å <sup>3</sup> )	244.647(5)	244.655(5)	244.663(5)
Sr(x)	0.5089(12)	0.5091(11)	0.5094(10)
Sr(z)	0.2508(8)	0.2508(7)	0.2514(6)
O(1) (x)	0.0375(5)	0.0373(5)	0.0378(4)
O(1) (z)	0.2519(8)	0.2518(8)	0.2516(7)
O(2) (x)	0.2515(12)	0.2511(11)	0.2520(10)
O(2) (y)	0.2454(14)	0.2456(14)	0.2450(12)
O(2) (z)	-0.0120(32)	-0.0123(31)	-0.0118(29)
$Sr_{\text{frac}} - 4m$	1.00	1.00	1.00
Cr/Nb(1) <sub>frac</sub> - 2a	0.626/0.374	0.626/0.374	0.626/0.374
Cr/Nb(2) <sub>frac</sub> - 2c	0.374/0.626	0.374/0.626	0.374/0.626
O(1) <sub>frac</sub> - 4m	0.882	0.882	0.882
O(2) <sub>frac</sub> - 8j	0.942	0.942	0.942
$Sr_{\text{Uiso}}$ (Å <sup>2</sup> )	0.0069(3)	0.0066(3)	0.0068(2)
Cr/Nb(1) <sub>Uiso</sub> (Å <sup>2</sup> )	0.0025(13)	0.0026(13)	0.0025(11)
Cr/Nb(2) <sub>Uiso</sub> (Å <sup>2</sup> )	0.0053(14)	0.0051(13)	0.0053(12)
O(1) <sub>Uiso</sub> (Å <sup>2</sup> )	0.0025(4)	0.0025(4)	0.0027(3)
O(2) <sub>Uiso</sub> (Å <sup>2</sup> )	0.0056(3)	0.0055(3)	0.0056(3)
Sr-O(1)	2.625(8)	2.627(7)	2.627(6)
Sr-O(1)	2.943(8)	2.942(7)	2.942(6)
Sr-O(1) (x2)	2.7940(6)	2.7940(6)	2.7945(5)
<Sr-O(1)>	2.789	2.789	2.790
Sr-O(2) (x2)	2.865(7)	2.868(7)	2.866(6)
Sr-O(2) (x2)	2.687(5)	2.686(5)	2.687(4)
Sr-O(2) (x2)	2.706(7)	2.703(7)	2.705(6)
Sr-O(2) (x2)	2.895(5)	2.896(5)	2.895(4)
<Sr-O(2)>	2.788	2.788	2.788
Cr/Nb(1)-O(1) (x2)	1.999(6)	1.998(6)	1.997(6)
Cr/Nb(1)-O(2) (x4)	1.959(7)	1.958(7)	1.959(7)
<Cr/Nb(1)-O>	1.972	1.972	1.972
Cr/Nb(2)-O(1) (x2)	1.971(7)	1.972(6)	1.974(6)
Cr/Nb(2)-O(2) (x4)	1.982(7)	1.983(7)	1.982(6)
<Cr/Nb(2)-O>	1.978	1.979	1.979
Cr/Nb-O(1)-Cr/Nb (°)	167.93(16)	167.97(16)	167.84(14)
Cr/Nb-O(2)-Cr/Nb (°)	174.30(15)	174.22(14)	174.34(13)
$\chi^2$	3.514	3.354	6.684
wRp	8.51	8.37	7.65
Rp	5.88	5.72	5.38
Variables	37	37	37

The Rietveld refinements of the low temperature data, 250 – 5 K, converged successfully with use of the room-temperature,  $I2/m$  structural model, Table 1. The occupations of the oxygen and Cr/Nb cation sites were fixed at the values obtained from the room-temperature refinement. When occupancy refinement was attempted with the neutron data their least squares shifts were highly correlated with those of the thermal parameters. The thermal parameters for all the atoms decreased smoothly with decreasing temperature. Magnetic reflections or magnetic intensity added to existing reflections were not observed at any temperature. Unit cell parameters, atomic positions, occupational and thermal parameters, bond distances and bond angles as a function of temperature are listed in Table 1.

The temperature variation of the unit cell parameters of  $\text{Sr}_2\text{CrNbO}_{5.53}$  in Figs. 6(a-c) show that the  $a$  and  $b$  lattice parameters decrease smoothly with decreasing temperature to a convergence at *ca.* 50 K. The thermal expansion co-efficients along the  $a$  and  $b$  directions were estimated to be  $4.7 \times 10^{-5} \text{ \AA/K}$  and  $4.8 \times 10^{-5} \text{ \AA/K}$ , respectively between 300 and 100 K. The  $c$  lattice parameter contracts smoothly with decreasing temperatures reaching a minimum at *ca.* 40 K; the thermal expansion coefficient is  $3.54 \times 10^{-5} \text{ \AA/K}$  (150-300 K; Fig. 6c) along the  $c$  axis. The monoclinic angle  $\beta$  increases slightly, *ca.*  $0.03^\circ$  with decreasing temperature (Fig. 6d). In Fig. 6f, the changes in lattice parameters from their 300 K value as a function of temperature show that the  $a$  and  $b$  axis contraction is almost twice as large as that of the  $c$  axis, as the temperature decreases. This behavior is attributed to a more flexible Cr/Nb-O(1)-Cr/Nb bond angle versus the Cr/Nb-O(2)-Cr/Nb angle and to the higher concentration of oxygen vacancies in the axial positions (O(1)). The Cr/Nb(1)-O-Cr/Nb(2) bond angles decrease smoothly with temperature (Fig. 7). However, the change in the axial Cr/Nb(1)-O(1)-Cr/Nb(2) bond angle is 1.8 times greater than the change in the equatorial Cr/Nb(1)-O(2)-Cr/Nb(2) one. The overall effect of decreasing temperature is increasingly distorted  $\text{Cr}/\text{NbO}_6$  octahedra, which further reduces the magnetic interactions.

Analysis of the Cr/Nb-O bond lengths reveals that for the Cr-rich site the axial Cr/Nb(1)-O(1) bond lengths abruptly expands below 150 K, while the equatorial Cr/Nb(1)-O(2) bonds simultaneously contract (Fig. 8). The Nb-rich site appears to undergo an elongation of the equatorial Cr/Nb(2)-O(2) bonds, with a concomitant shrinking of the axial Cr/Nb(2)-O(1) bonds below 150 K, although the mean Cr/Nb(2)-O bond length remains unchanged as a function of temperature (Table 1 and Fig. 8).

Originally we believed that the observed elongation/contraction was due to a crossover from a  $d^3/d^1$  system to a Jahn-Teller active  $d^4/d^0$  system below 180 K. However, the differences between the Cr/Nb(1)-O(1) and Cr/Nb(1)-O(2) bond lengths, *ca.*  $0.04 \text{ \AA}$ , are significantly smaller than the reported axial/equatorial Cr-O bond length differences for  $\text{Cr}^{2+}$ -O Jahn-Teller systems, *ca.*  $0.20$ - $0.40 \text{ \AA}$ , [25,26]. Moreover the presence of  $\text{Cr}^{2+}$  would result in significantly larger Cr-O bond lengths due to the larger  $\text{Cr}_{H.S.}^{2+} = 0.94 \text{ \AA}$  vs.  $\text{Cr}^{3+} = 0.755 \text{ \AA}$  [23,24]. Also a crossover from  $d^3$  to  $d^4$  should result in an increase in the effective magnetic moment, whereas we observed a decrease in the effective magnetic moment.

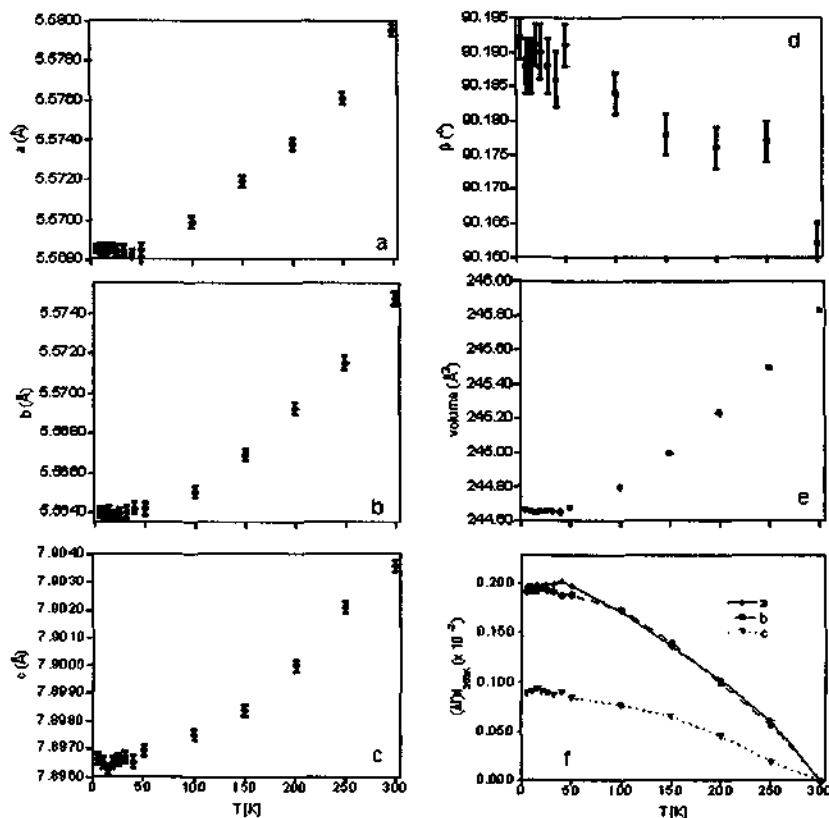


Figure 6. (a-c) lattice parameters; (d) monoclinic angle; (e) volume and (f) the change in lattice parameters as a function of temperature for  $\text{Sr}_2\text{CrNbO}_{5.53}$ .

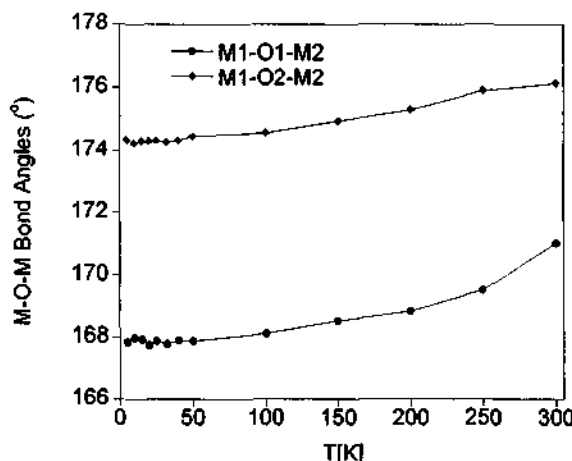


Figure 7. Cr/Nb-O-Cr/Nb bond angles of  $\text{Sr}_2\text{CrNbO}_{5.53}$  as a function of temperature. The error bars are smaller than the data point.

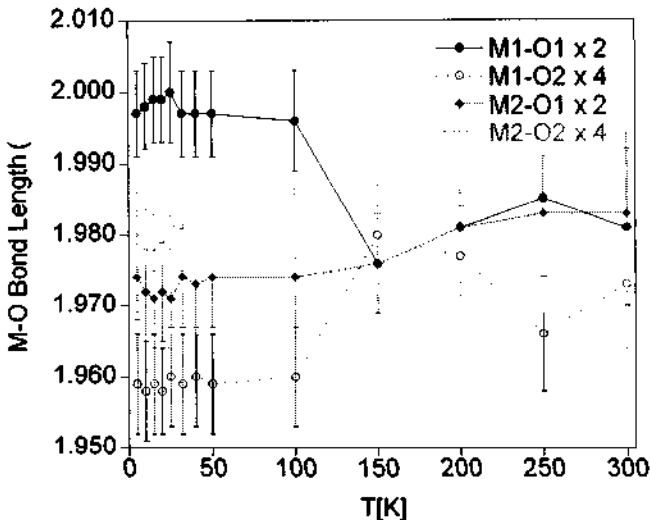


Figure 8. Cr/Nb -O bond lengths of  $\text{Sr}_2\text{CrNbO}_{5.53}$  as a function of temperature.

We propose that the distortion of the Cr-rich site is electronically driven, and is due to enhancement of the splitting of the Cr- $t_{2g}$  orbitals into low energy  $d_{xz}$  and  $d_{yz}$  orbitals and a higher energy  $d_{xy}$  orbital, at  $T < 150$  K as shown in Fig. 9, (i.e. in the monoclinic space group  $I2/m$  the orbitals are already non-degenerate). This is a highly unusual state, as the energy split between the  $d_{xz}/d_{yz}$  and  $d_{xy}$  states appears to be larger than the pairing energy, at least at  $T < 150$  K. Reports of a similar  $S = \frac{1}{2}$  ground state for octahedral  $\text{Cr}^{3+}$  ( $d^3$ ) electronic configuration was not found by extensive search of the literature. Thus the deviation of the magnetic susceptibility data from Curie-Weiss behavior below ca. 180 K (Fig. 2, inset), noted previously, is consistent with the enhanced splitting of the  $t_{2g}\text{Cr}^{3+}(d^3)$  states. Moreover, the frustrated FM type interactions observed in the magnetization data seen at 5 K in a field of 5 T is also consistent with FM coupling of  $\text{Nb}^{4+}$  ( $d^1$ ) and the lone spin of  $\text{Cr}^{3+}$  as depicted in Fig. 9.

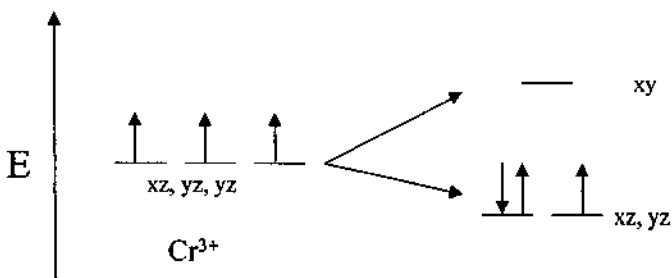


Figure 9. Schematic representation of the splitting of the  $\text{Cr}^{3+}(t_{2g})$  orbitals below 180 K.

#### 4 Conclusion

The oxygen deficient double-perovskite  $\text{Sr}_2\text{CrNbO}_{5.53}$  has been synthesized by solid-state high vacuum techniques. Simultaneous refinement of powder X-ray and neutron diffraction data reveals a preferential occupation of the oxygen vacancies in the apical position of the  $(\text{Cr}/\text{Nb})\text{O}_6$  octahedra and partial ordering of the Cr and Nb ions into Cr-rich and Nb-rich sites with 63/37 and 37/63 % occupation, respectively. Low temperature neutron diffraction data down to 5 K do not show evidence of magnetic ordering. However, the neutron data indicate at the Cr-rich site a dramatic contraction of the equatorial Cr/Nb-O bonds, with a concomitant elongation of the axial Cr/Nb-O bonds below *ca.* 150 K. This distortion of the  $\text{Cr}/\text{NbO}_6$  octahedra appears to be electronically driven and leads to a hitherto unobserved large splitting of the  $t_{2g}$  orbitals into  $d^3(d_{xz}, d_{yz})$  and  $d^6(d_{xy})$  states.  $\text{Sr}_2\text{CrNbO}_{5.53}$  is an insulator ( $\rho_{RT}$  *ca.* 250  $\Omega\text{-cm}$ ) and exhibits a spin-glass-like magnetic transition around 25 K. Magnetization measurements at 5 K show hysteresis, which is a signature of ferro/ferri magnetic interactions. The magnetization, at 5 K and  $H = 5$  T, is small,  $0.15 \mu_B$  and unsaturated. This unexpected low magnetization is attributed to frustrated FM interactions between the  $\text{Nb}^{4+}(d^1)$  and the lone  $\text{Cr}^{3+} d_{xz}$  or  $d_{yz}$  electron (Fig. 9). It appears that cation disorder on the octahedral sites, non-linear Cr/Nb-O-Cr/Nb bonds, oxygen vacancies, and orbital splitting prevent magnetic ordering in  $\text{Sr}_2\text{CrNbO}_{5.53}$ .

#### 5 Acknowledgments

We thank Dr. W. H. McCarroll for his critical reading of the manuscript before its submission, Dr. T. Emge for his thoughtful discussions related to the structural analysis, and S. Short for assistance with collection of the neutron diffraction data. We acknowledge Drs. M. Lobanov and B. McKernan for their editorial assistance. This work was supported by NSF-Solid State Chemistry Grant DMR 99-07963. The work at Argonne National Laboratory is supported by the US Department of Energy, Division of Basic Energy Science-Materials Sciences under contract No. W-31-109-ENG-38.

#### References

1. K.-I. Kobayashi, T. Kimura, H. Sawada, K. Terakura, *Nature* **395** (1998) 677.
2. M. T. Anderson, K. B. Greenwood, G. A. Taylor, K. R. Poeppelmeier, *Progress in Solid State Chemistry* **22** (1993) 197.
3. F. K. Patterson, C. W. Moeller, R. Ward, *Inorg. Chem.* **1** (1962) 196.
4. O. Chmaisssem, R. Kruk, B. Dabrowski, D. E. Brown, X. Xiong, S. Kolesnik, J. D. Jorgensen, C. W. Kimball, *Phys. Rev. B* **62** (2000) 14197.
5. Y. Moritomo, S. Xu, A. Machida, T. Akimoto, E. Nishibori, T. Takada, M. Sakata, *Phys. Rev. B* **61** (2000) R7827.
6. Z. Zeng, I. D. Fawcett, M. Greenblatt, M. Croft, *Mater. Res. Bull.* **36** (2001) 705.
7. G. M. Veith, M. Greenblatt, M. Croft, K. V. Ramanujachary, J. Hattrick-Simpers, S. E. Lofland, I. Nowik, *Chem. Mater.* Submitted.
8. GSAS-Generalized Crystal Structure Analysis System Los Alamos National Laboratory Report No. LA-UR-86-748.
9. J. H. Choy, S. T. Hong, K. S. Choi, *J. Chem. Soc. Faraday Trans.* **92** (1996) 1051.
10. C. P. Khattak, D. E. Cox, F. F. Y. Wang, *J. Solid State Chem.* **13** (1975) 77.

11. J. B. Goodenough, R. I. Dass, *Int. J. Inorg. Mater.* **2** (2000) 3.
12. J. Navarro, L. Balcells, B. Martinez, J. Fontcuberta, *J. Appl. Phys.* **89** (2001) 7684.
13. G. Popov, M. Greenblatt, M. Croft, *Phys. Rev. B* (2002) Submitted.
14. J. B. Goodenough Magnetism and the Chemical Bond, Interscience Publishers, New York, 1963.
15. P. D. Battle, S. J. Blundell, J. B. Claridge, A. I. Coldea, E. J. Cussen, L. D. Noailles, M. J. Rosseinsky, J. Singleton, J. Sloan, *Chem. Mater.* **14** (2002) 425.
16. G. M. Veith, I. D. Fawcett, M. Greenblatt, M. Croft, I. Nowik, *Int. J. Inorg. Mater.* **2** (2000) 513.
17. P. D. Battle, T. C. Gibb, C. W. Jones, F. Studer, *J. Solid State Chem.* **78** (1989) 281.
18. P. D. Battle, A. I. Coldea, N. Jordan, M. J. Rosseinsky, J. Singleton, *J. Mater. Chem.* **11** (2001) 1656.
19. A. I. Coldea, S. J. Blundell, I. M. Marshall, C. A. Steer, J. Singleton, F. L. Pratt, L. D. Noailles, M. J. Rosseinsky, L. E. Spring, P. D. Battle, *Phys. Rev. B* **65** (2001) 054402.
20. P. M. Woodward, *Acta Crystallogr.* **B53** (1997) 32.
21. P. M. Woodward, *Acta Crystallogr.* **B53** (1997) 44.
22. A. M. Glazer, *Acta Crystallogr.* **B28** (1972) 3384.
23. R. D. Shannon, C. T. Prewitt, *Acta Crystallogr.* **B25** (1969) 925.
24. R. D. Shannon, *Acta Crystallogr.* **A32** (1976) 751.
25. A. Schmidt, R. Glaum, J. Beck, *J. Solid State Chem.* **127** (1996) 331.
26. M. Saes, N. P. Raju, J. E. Greidan, *J. Solid State Chem.* **140** (1998) 7.

## SOLVOTHERMAL SYNTHESIS OF NON-OXIDE NANOMATERIALS

YI-TAI QIAN\* AND YUNLE GU

*Structure Research Lab & Department of Chemistry, University of Science and Technology of China, Hefei, Anhui 230026, P. R. China  
E-mail: ytqian@ustc.edu.cn*

Solvothermal process is a powerful route for preparing non-oxide nanomaterials. By using organic solvents under supercritical conditions as reaction media, chemical reaction and crystallization can be synchronously realized. Materials including diamond, carbon nanotubes, a series of carbides, nitrides, borides, phosphides, III-V and II-VI group semiconductor nanomaterials have been prepared via this method at conditions milder than those of traditional methods. As a low-temperature and convenient synthetic technique, solvothermal process is an exciting, promising approach for designing and preparing advanced materials.

### 1 Introduction

Inorganic non-oxide materials, such as III-V and II-VI group semiconductors, carbides, nitrides, borides, phosphides and silicides, are traditionally prepared by solid state reactions or gas-phase reaction at high temperatures. Some non-oxides have been prepared via liquid-phase precipitation or pyrolysis of organometallic precursors. However, amorphous phases are sometimes formed by these methods. Post-treatment at a high temperature is needed for crystallization. The products obtained by these processes are commonly beyond the manometer scale. Exploration of low temperature technique for preparing non-oxide nanomaterials with controlled shapes and sizes is very important in materials science.

Solvothermal process is now becoming a powerful technique for preparing nanomaterials. It is analogous to hydrothermal synthesis, except that non-aqueous solvents replace water as reaction medium. From the chemical reaction point of view, solvents in supercritical conditions play a significant role in reaction and crystallization. New materials, especially those having metastable phases and special nanostructures, can be obtained under mild conditions. By sealing the reaction system in an autoclave, the reactants and products prevent effectively from oxidation, hydrolysis and volatilization, and the reaction and crystallization can be realized synchronously.

Solvothermal method has been used in synthesis of a series of non-oxide nanomaterials, such as semiconductors [1,2], ceramic materials [3], and in fabricating special nanostructures [4]. It will be an exciting, promising field for designing and preparing advanced materials in the future. This paper focuses on some aspects of recent progress in solvothermal synthesis of non-oxides nanomaterials.

### 2 A new way to metastable structures

Metastable structure is one of the most important research directions in current physics, chemistry, materials and earth science fields. Under the conditions of supercritical solvent,

metastable structures can be prepared by solvothermal synthesis at pressures and temperatures milder than those of traditional methods.

We have developed solvothermal synthesis as an important method in research of metastable structures. In the benzene-thermal synthesis of nanocrystalline GaN at 280°C through the metathesis reaction of  $\text{GaCl}_3$  and  $\text{Li}_3\text{N}$ , the ultrahigh pressure rocksalt type GaN metastable phase, which was previously prepared at 37 GPa, was obtained at ambient condition [5]. Diamond crystallites were prepared from catalytic reduction of  $\text{CCl}_4$  by metallic sodium in an autoclave at 700°C (Fig.1) [6]. In our recent studies, diamond was also prepared via the solvothermal process. In the solvothermal catalytic metathesis reaction of carbides of transition metals and  $\text{CX}_4$  ( $X = \text{F}, \text{Cl}, \text{Br}$ ) at 600-700°C, Raman spectrum of the prepared sample shows a sharp peak at  $1330 \text{ cm}^{-1}$  (Fig. 1), indicating existence of diamond. In another process, multiwalled carbon nanotubes were synthesized at 350°C by the solvothermal catalytic reaction of  $\text{C}_6\text{Cl}_6$  with metallic potassium (Fig. 2) [7].

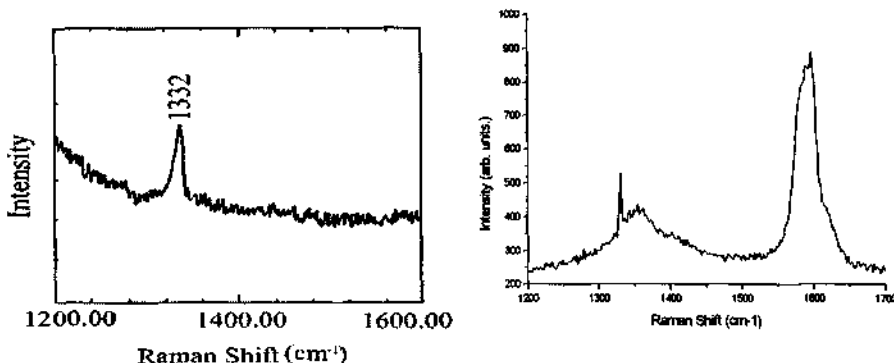


**Figure 1.** Raman spectra of the sample prepared by solvothermal process through the catalytic reduction [6] (left) and the catalytic metathesis reaction (right).

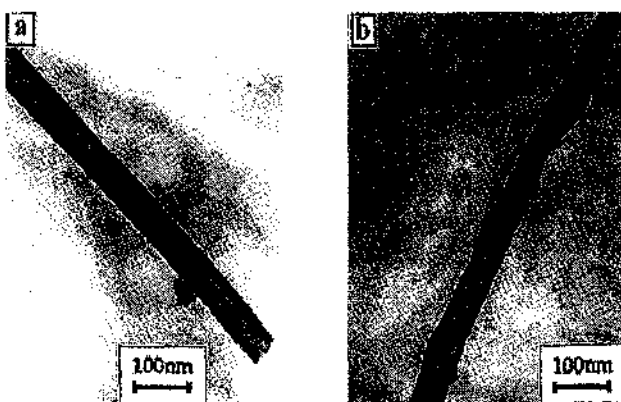


**Figure 2.** TEM images of multiwalled carbon nanotubes [7].

Cubic boron nitride is an important material that is widely used in cutting tools and as grinding, abrasive materials. Both Hu et al. [8] and Cui et al. [9] have synthesized cubic BN via this method. By using the solvothermal metathesis reaction of  $\text{BBr}_3$  and  $\text{Li}_3\text{N}$ , Cui and co-workers obtained better yield of cubic BN, and the TEM image and the XRD pattern are shown in Fig. 3. Some other metastable non-oxides have also been prepared and reported using solvothermal method, e.g. AlN [10-11] and  $\text{Si}_3\text{N}_4$  [12].

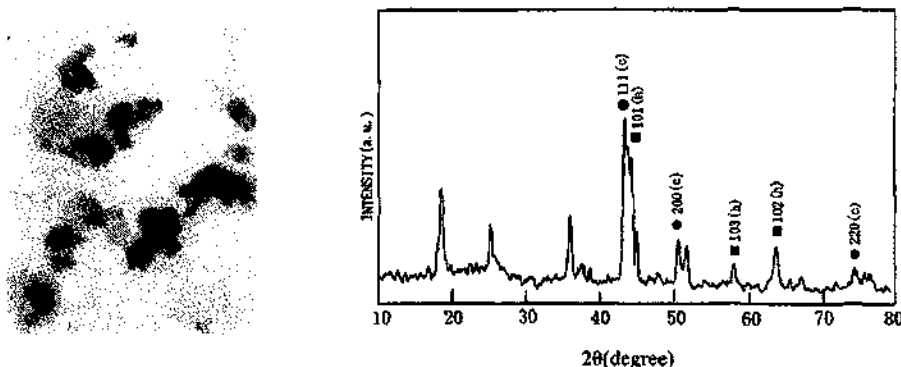


Figure 3. TEM image (left) and XRD patterns (right) of cubic BN [9].

Among the wide array of important properties, hardness is essential to many high-performance engineering applications. On the research for superhard materials, much effort has been made on the promising, hypothetical covalent C-N compound, which is suggested that its hardness might be comparable with that of diamond. Since Liu and Cohen [13,14] predicted theoretically the  $\beta\text{-C}_3\text{N}_4$ , several other structures of carbon nitride have been proposed (Fig. 4). Although the synthesis of graphitic- $\text{C}_3\text{N}_4$  via solvothermal process has been reported [17-19], no work has yet presented unambiguous evidence for the low-compressibility carbon nitrides with three-dimensional structures. Therefore, more efforts are needed in order to prepare metastable carbon nitrides by a solvothermal method.

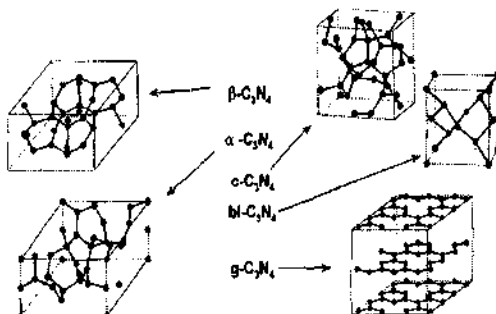
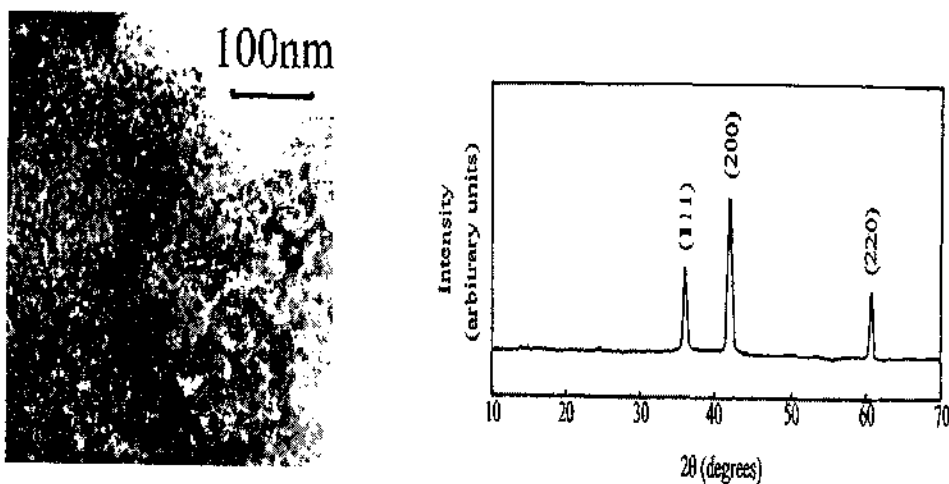


Figure 4. Different possible structures for hypothetical carbon nitrides [17]. ( $\beta\text{-C}_3\text{N}_4$ ,  $P3$  or  $P6_3/m$ ;  $\alpha\text{-C}_3\text{N}_4$ ,  $P3_1c$ ; face-centered cubic- $\text{C}_3\text{N}_4$ ,  $I-4_3d$  or  $P-4_2m$ ; pseudocubic- or  $bl\text{-C}_3\text{N}_4$ ,  $P-4_2m$ ; two-dimensional graphitic- $\text{C}_3\text{N}_4$ ,  $P-6m2$ ,  $R3m$ ) [15, 16].

### 3 A mild route to non-oxide ceramic nanomaterials

Non-oxide ceramic nanomaterials, such as carbides, nitrides, borides, phosphides and silicides, have received considerable attention due to their potential applications in electronics, optics, catalysis, and magnetic storage. In contrast with the traditional processes, such as solid state reactions, CVD, MOCVD and PVD, which involve using high temperatures, toxic organometallic precursors, or complicated reactions and post-treatments, solvothermal method is a low temperature route to these materials with controlled shapes and sizes.

Recently, we developed the solvothermal synthesis into an important solid-state synthetic method, by which a series of carbides, nitrides, borides were prepared. TiC nanocrystallites (Fig. 5) were synthesized at 450°C by reduction of  $\text{CCl}_4$  and  $\text{TiCl}_4$  using metallic sodium as the reductant [22]. By the reaction of  $\text{SiCl}_4$  and sodium azide ( $\text{NaN}_3$ ) at 600-700°C,  $\text{Si}_3\text{N}_4$  nanoparticles and nanorods (Fig. 6) were obtained [12]. In another process, hexagonal  $\text{TiB}_2$  nanoparticles were prepared by the reaction of  $\text{TiCl}_4$  and amorphous boron powders with metallic sodium at 400-500°C (Fig. 7a-b) [21]. Some other work was also reported, e.g.  $\text{SiC}$  [20],  $\text{ZrN}$  [23] and  $\text{TiN}$  [24]. All these reaction conditions are milder than those of traditional methods, showing good prospects in research of advanced non-oxide ceramic nanomaterials.



**Figure 5.** TEM image (left) and XRD patterns of TiC (right).

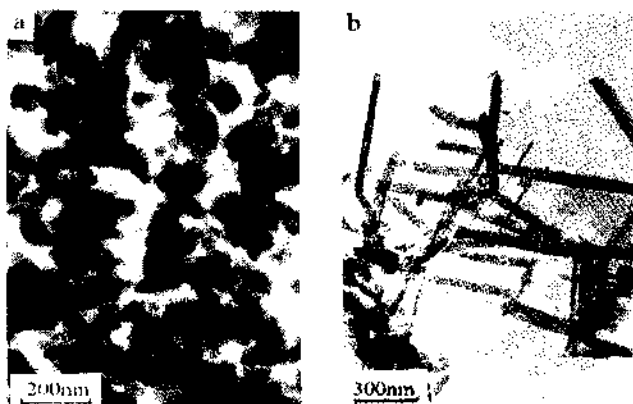


**Figure 6.** TEM images of Si<sub>3</sub>N<sub>4</sub> nanoparticles (left) and nanorods (right).

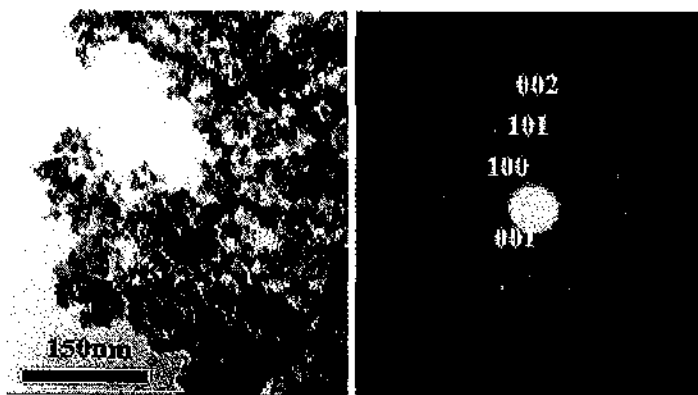


**Figure 7.** (a) TEM image (left) and TED pattern (right) of TiB<sub>2</sub> nanoparticles.

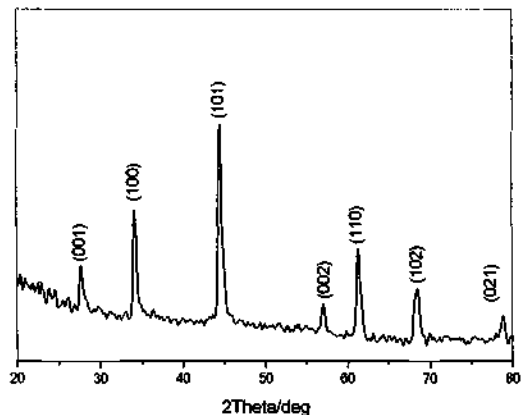


**Figure 7.** (b) XRD pattern of the TiB<sub>2</sub> sample.

#### 4 A convenient approach for controlling morphology

Nanomaterials with special morphology are attracting intense interest due to their remarkable optical, electrical and mechanical properties. Their potential uses ranging from microscopic probe to nanoelectronic devices. Therefore, current attention has focused on development of convenient approaches for preparing nanoscale structures with controlled shapes and sizes.

We have developed the solvothermal synthesis as a convenient approach for controlling morphology, by which non-oxides nanomaterials, such as nanoparticles, one-dimensional nanomaterials and those with very special shapes have been fabricated, which include nano-metered tubes, rods, wires, balls, hollow spheres and peanut-like nanostructures, etc.

In synthesis of III-V group (GaN, InAs and InP, etc.) and II-V group (i.e. CdE, ZnE, HgE, E = S, Se, Te) semiconducting nanocrystallites, materials such as 32 nm GaN [5], 12 nm InP [25] and 12 nm InAs [26], have been prepared via solvothermal method. Recently, we also prepared a series of binary and ternary chalcogenide semiconducting nanomaterials, e.g. MoS<sub>2</sub> [27], MnS [28], NiS [29], Cu<sub>2-x</sub>Se [30], MSe (M = Fe, Co, Ni)[31], Ag<sub>2</sub>E (E= S, Se, Te) [32], MAs (M = transition metals) [33], CuMS<sub>2</sub> (M=In, Ga) [34] and CuInE<sub>2</sub> (E=S, Se) [35].

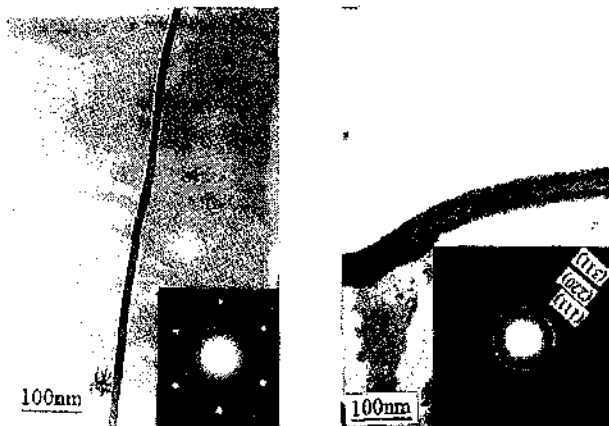


**Figure 8.** TEM images of SiC nanowire (left) and tubular structures (right).

In addition to the catalytic solvothermal synthesis of carbon nanotubes (Fig. 2) [7], SiC nanowires and tubular structures (Fig. 8) were prepared through a solvothermal reduction-carburization route using silicon powders and CCl<sub>4</sub> as Si and carbon sources [20], Si<sub>3</sub>N<sub>4</sub> nanorods were also prepared with a similar process [12].

By using polymer-controlled growth in ethylenediamine at 170°C, very long CdS nanowires (100μ×40 nm) were synthesized (Fig. 9a) [36]. Cadmium sulfide with different morphologies, such as nanoparticles and nanorods (Fig. 9b) [39], peanut-like nanostructures [37] and hollow nanospheres [38] (Fig. 9c) were prepared via solvothermal routes.

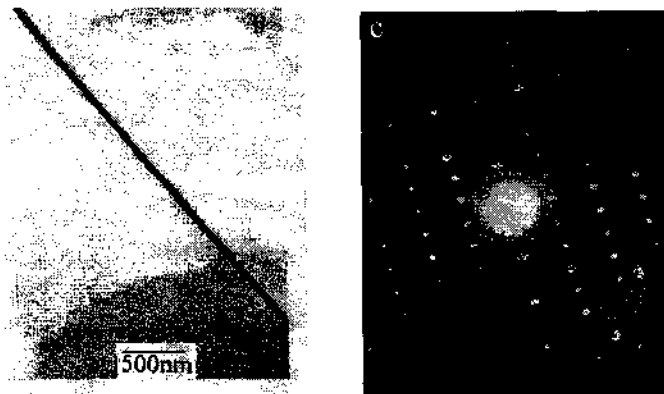


Figure 9. (a) TEM image (left) and SAED pattern (right) of CdS nanowires.

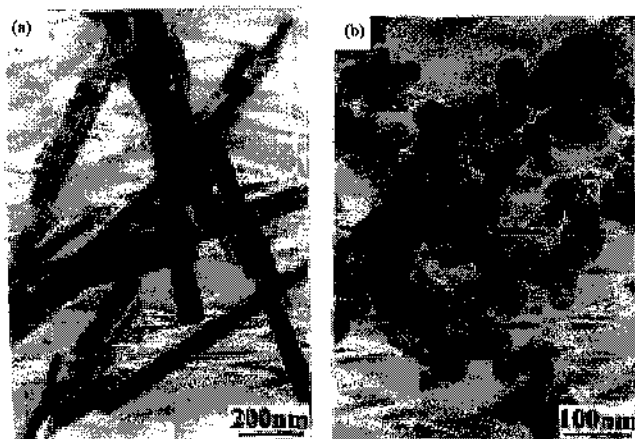


Figure 9. (b) TEM images of CdS nanorods (left) and CdS nanoparticles (right).

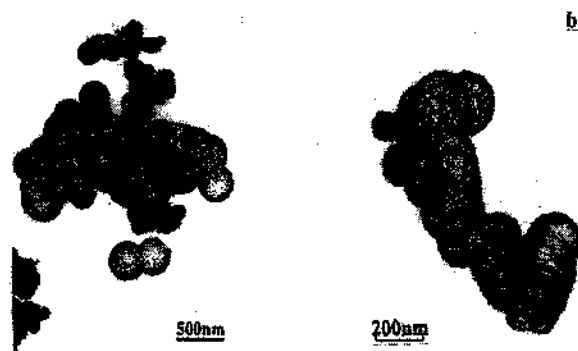


Figure 9. (c) TEM images of CdS hollow spheres and peanut-like nanostructures.

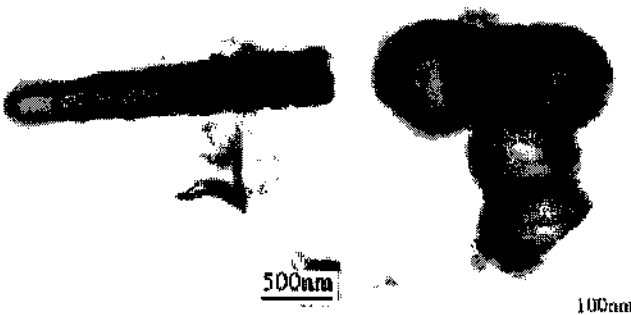


Figure 10. TEM images of tubular (left) and hollow-ball (right) structures of HPN<sub>2</sub>.

In another recent study, amorphous phosphorus nitride imide (HPN<sub>2</sub>), a ternary inorganic polymer, has also been prepared via a benzene-thermal reaction of PCl<sub>3</sub> and NaN<sub>3</sub> under mild conditions [40]. The products have interesting morphologies (Fig. 10) of microtubes, hollow balls and square frameworks. Their potential use for industrial application is now under investigation.

## References

1. Y. T. Qian, *Adv. Mater.* 1999, **11** (13), 1101.
2. L. Shu, S. H. Yu, Y. T. Qian, *Chinese J. Inorg. Chem.* 1999, **15** (1), 1-7.
3. S. H. Yu, *J. Ceram. Soc. Japan* 2001, **109**, S65-S75.
4. Y. Xie, *Chinese J. Inorg. Chem.* 2002, **18** (1), 1-7.
5. Y. Xie, Y. T. Qian et al., *Science* 1996, **272**, 1926.
6. Y. Li, Y. T. Qian et al., *Science* 1998, **281**, 246.
7. Y. Jiang, Y. Wu, S. Zhang, C. Xu, W. Yu, Y. Xie, Y. T. Qian, *J. Am. Chem. Soc.* 2000, **122**, 12383.
8. J. Q. Hu, Q. Y. Lu, K. B. Tang, S. H. Yu, Y. T. Qian et al., *J. Solid State Chem.* 1999, **148**, 325.
9. X. P. Hao, D. L. Cui et al., *Chem. Mater.* 2001, **13**, 2457.
10. Y. C. Lan, X. L. Chen, Y. G. Cao, Y. P. Xu et al., *J. Crystal Growth* 1999, **207** (3), 247-250.
11. N. Sonoyama, Y. Yasaki, T. Sakata, *Chem. Lett.* 1999, **3**, 203-204.
12. K. Tang, J. Hu, Q. Lu, Y. Xie, Y. T. Qian, *Adv. Mater.* 1999, **11**, 653-655.
13. A. Y. Liu, M. L. Cohen, *Science* 1989, **245**, 841.
14. A. Y. Liu, M. L. Cohen, *Phys. Rev.* 1990, **B41**, 10727.
15. D. M. Teter, R. J. Hemley, *Science* 1996, **271**, 53-55.
16. Thomas Malkow, *Mater. Sci. & Eng.* 2001, **A302**, 311-324.
17. H. Montigaud, B. Tanguy, G. Demazeau et al., *Diamond & Related Mater.* 1999, **8**, 1707-1710.
18. H. Montigaud, B. Tanguy, G. Demazeau et al., *J. Mater. Sci.* 2000, **35(10)**, 2547-2552.

19. H. Montigaud, S. Courjault, B. Tanguy, G. Demazeau et al., *High Pressure Res.* 2000, **18**(1-6), 213-219.
20. J. Q. Hu, Y. Lu, K. B. Tang, Y. T. Qian et al., *J. Phys. Chem. B* 2000, **104**, 5252.
21. Y. Gu, Y. T. Qian et al., *Chem. Commun.* Submitted.
22. Q. Lu, J. Hu, K. Tang, B. Deng, Y. T. Qian et al., *Chem. Phys. Lett.* 1999, **314**, 37-39.
23. J. Hu, Q. Lu, K. Tang, B. Deng, R. Jiang, Y. T. Qian, *Chem. Lett.* 2000, **5**, 74.
24. J. Q. Hu, Q. Y. Lu, K. B. Tang, S. H. Yu, Y. T. Qian et al., *J. Am Ceram. Soc.* 2000, **83**, 430.
25. P. Yan, Y. Xie, G. Xu, Y. J. Zhu, Y. T. Qian, *J. Mater. Chem.* 1999, **9**, 1831.
26. Y. D. Li, X. F. Duan, Y. T. Qian et al., *J. Am. Chem. Soc.* 1997, **119**(33), 7869-7870.
27. H. W. Liao, Y. F. Wang, S. Y. Zhang, Y. T. Qian et al., *Chem. Mater.* 2001, **13**(1), 6.
28. J. Lu, P. F. Qi, Y. Y. Peng, Y. T. Qian, et al., *Chem. Mater.* 2001, **13**(6), 2169-2172.
29. X. Jiang, Y. Xie, J. Lu, L. Zhu, W. He, Y. T. Qian, *Adv. Mater.* 2001, **13**, 1278-1281.
30. W. Zhang, X. Zhang, L. Zhang, J. Wu, Z. Hui, Y. Cheng, J. Liu, Y. Xie, Y. T. Qian, *Inorg. Chem.* 2000, **39**(7), 1838-1839.
31. J. Yang, G. H. Chen, J. H. Zeng, Y. T. Qian et al., *Chem. Mater.* 2001, **13**(3), 848-853.
32. X. C. Jiang, Y. Xie, J. Lu, Y. T. Qian et al., *J. Mater. Chem.* 2001, **11**(2), 584.
33. Y. Xie, J. Lu, P. Pan, X. C. Jiang, Y. T. Qian, *Chem. Lett.* 2000, **2**, 114.
34. Q. Lu, J. Hu, K. Tang, Y. T. Qian et al., *Inorg. Chem.* 2000, **39**, 1606.
35. Y. Jiang, Y. Wu, X. Mo, W. Yu, Y. Xie, Y. T. Qian, *Inorg. Chem.* 2000, **39**(14), 2946.
36. J. Zhan, X. Yang, D. Wang, Y. Xie, Y. Xia, Y. T. Qian, *Adv. Mater.* 2000, **12**, 1348.
37. Y. Xie, J. H. Huang, B. Li, Y. Liu, Y. T. Qian, *Adv. Mater.* 2000, **12**, 1523.
38. J. X. Huang, Y. Xie, B. Li, Y. Liu, Y. T. Qian et al., *Adv. Mater.* 2000, **12**(11), 808.
39. J. Yang, J. H. Zeng, S. H. Yu, L. Yang, G. Zhou, Y. T. Qian, *Chem. Mater.* 2000, **12**, 3259-3263.
40. Z. Meng, Y. Peng, Y. T. Qian, *Chem. Commun.* 2001, 469-470.

This page is intentionally left blank

## **Part I**

### **Electrical, Optical, Magnetic Solids and Defects and Mixed-Valences in Solids**

This page is intentionally left blank

# HYDROTHERMAL SYNTHESIS, STRUCTURAL CHARACTERIZATION AND IONIC CONDUCTIVITY OF Cu-Bi-V-O SYSTEMS

SHOUHUA FENG,\* YANHUI SHI, YONGWEI WANG AND YING LI

*State Key Laboratory of Inorganic Synthesis and Preparative Chemistry, College of Chemistry  
Jilin University, Changchun 130023, People's Republic of China  
E-mail: shfeng@mail.jlu.edu.cn*

Hydrothermal syntheses in Cu-Bi-V-O systems were carried out with an aim to search for fast oxygen ionic conductors. A novel phase with a formula of  $\text{Cu}_2\text{Bi}_4\text{V}_2\text{O}_{13}\cdot3\text{H}_2\text{O}$  was obtained from the hydrothermal system at 240 °C. This compound crystallizes in monoclinic system with cell parameters  $a=1.497(2)$  nm,  $b=0.3692(1)$  nm,  $c=1.1168(3)$  nm and  $\beta=107.32(2)^\circ$ . It undergoes a phase transformation at 441 °C to a high temperature phase. The high temperature phase showed considerably high oxygen ionic conductivity of  $1.02\times10^{-3}\text{ S}\cdot\text{cm}^{-1}$  at 600 °C. Powder X-ray diffraction, differential thermal and thermogravimetric analysis, infrared spectra and X-ray photoelectron spectroscopy, scanning electron microscopy, inductively coupled plasma, ac impedance spectroscopy were employed to characterize both the low and high temperature phases.

## 1 Introduction

Searching for solid state fast ionic conductors has increasingly been stimulating in both industrial and academic fields for their considerable applications to solid oxide fuel cells (SOFCs), solid batteries, chemical sensors, and oxygen pumps [1-3]. Such fast ionic conductors those are efficiently operated at lower temperatures are extremely needed [4]. Although yttria-stabilized zirconia (YSZ) was used in most SOFCs, its high activation energy for ionic conduction led to high operating temperature (~1000 °C) [5]. The required high temperature generates several problems, including detrimental chemical reactions with the electrodes and other components of the fuel cell, incompatibility of thermal expansion coefficients, and also a shortened fuel cell life span. Because of these drawbacks of operating a fuel cell at 1000 °C, solid electrolytes that exhibit high oxygen ion conductivity and low electronic conductivity at temperatures between 600 and 800 °C or even lower are being sought at replacements.

The metal-doped bismuth vanadium oxides (BIMEVOX) behave high ionic conductivities at low temperatures [6], which were conventionally synthesized by high temperature solid state reactions, although both sol-gel process and co-precipitation technique were reported [7]. With an aim toward developing soft synthesis routes to inorganic functional materials such as fast solid ionic conductors and chemical sensors, we have been performing mild hydrothermal syntheses in BIMEVOX and co-doped  $\text{CeO}_2$  systems [8-10], and it was found that in some cases hydrothermal routes are most effective for novel solid electrolytes and homogenous doping in ionically conducting solid solutions [11].

In this paper, we report the hydrothermal synthesis, structural characterization and ionic conductivity of a novel hydrated copper bismuth vanadate,  $\text{Cu}_2\text{Bi}_4\text{V}_2\text{O}_{13}\cdot3\text{H}_2\text{O}$  and its high temperature phase.

## 2 Experimental Section

$\text{Bi}(\text{NO}_3)_3 \cdot 5\text{H}_2\text{O}$  (A. R.),  $\text{BiCl}_3$  (A. R.),  $\text{Bi}_2\text{O}_3$  (A.R.),  $\text{NaVO}_3 \cdot 2\text{H}_2\text{O}$  (A. R.) and  $\text{CuCl}_2 \cdot 2\text{H}_2\text{O}$  (A.R.) were used as the starting materials in synthesis, and  $\text{NaOH}$  (A. R.) as a mineralizer. A typical procedure for a synthesis with a molar ratio of initial compositions of 0.45  $\text{Bi}_2\text{O}_3$ : 0.45  $\text{V}_2\text{O}_5$  : 0.5  $\text{CuO}$  : 5 $\text{Na}_2\text{O}$  : 550 $\text{H}_2\text{O}$  began with dissolving 0.426g  $\text{NaVO}_3 \cdot 2\text{H}_2\text{O}$  in 30mL 1.0 M  $\text{NaOH}$  to form a solution, to which 1.308g  $\text{Bi}(\text{NO}_3)_3 \cdot 5\text{H}_2\text{O}$  and 0.255g  $\text{CuCl}_2 \cdot 2\text{H}_2\text{O}$  were added with stirring to make a reaction mixture. The reaction mixture was sealed in a Teflon-lined stainless steel autoclave with a 80 % filling capacity and allowed to crystallize at 240 °C for 3 days. Greenish crystalline products were obtained. The crystals were recovered by filtering, washing with deionized water, sonicating (if necessary) and drying in air at ambient temperature.

Crystalline phases were identified by X-ray diffraction (XRD) on a SIEMENS D5005 diffractometer with Ni-filtered  $\text{CuK}\alpha$  radiation at room temperature. KCl powder was used as an internal standard for the determination of peak positions. XRD data were collected over 10-70° with a step interval of 0.02° and a preset time of 3s per step. The precise determination of peak positions, multipeak and  $\text{K}\alpha_2$  stripping were carried out by using a program available in a software package for line shape Fourier analysis. The indexing of XRD patterns and determination of cell parameters were performed by utilizing a computer program, DICVOL91 which is based on the successive dichotomy method and tackles any symmetry.

The compositions of the products were determined by inductively coupled plasma (ICP) with a Perkin-Elmer plasma 40 emission spectrometer. Simultaneous differential thermal analysis and thermogravimetric (DTA-TG) curves were carried out by using Perkin-Elmer DTA-7000, TGA-7 PC series thermal analysis instrument in air with a heating rate of 10 °C /min. The infrared (IR) spectra were recorded on an Impact 410 IR spectrometer on samples pelletized with KBr powder. Valence states were determined by X-ray photoelectron spectroscopy (XPS). The XPS for powder samples fixed on double sided tapes was measured on an ESCA-LAB MKII X-ray photoelectron spectrometer. The  $\text{C}_{1s}$  signal was used to correct the charge effects.

In electrical measurements, powder samples were pressed into a compact (6 mm in diameter and 3 mm in thickness) under 35 MPa. Sliver paste was painted on two sides of the disk as electrodes, and the disk with electrodes was sintered at 250 °C for 2h to erase the solvent. Platinum paste was painted on two sides of the disk sintered at 700 °C for 8h in air as electrodes, and the disk with electrodes was sintered again at 700 °C for 30 min to erase the solvent. The conductivity of the sintered disk was measured under different atmospheres: oxygen, air, nitrogen, and helium. The ionic conductivity measurements were performed by an *ac* complex impedance method at frequencies ranging from 1Hz to 1 MHz on a Solartron 1260 impedance/gain-phase analyzer. The *dc* (direct current) resistance measurement was conducted on a Solartron 1287 electrochemical interface. The current that appeared by applying the constant voltage (10 mV) on the two Pt electrodes was monitored as a function of time. The *dc* conductivity ( $\sigma_{dc}$ ) was calculated by the applied voltage, and the generated current, the surface area of the Pt electrode, and the thickness of the pellet.

### 3 Results and Discussion

#### 3.1 Hydrothermal Synthesis.

Main factors which affect a hydrothermal reaction are the initial composition, reaction temperature and time. In mild hydrothermal synthesis, reaction temperatures lower than 240 °C are respected for both safety of high pressure in normal autoclaves and protection of softness of Teflon line. In our specific synthesis system, high temperature favorites the reaction and the most important factor was the base concentration in the initial reaction mixtures. The reaction time associated with reaction temperature affected the reaction. Crystallization kinetic experiment for a typical reaction showed that a reaction time more than 10h gave well-crystallized product and the further crystal growth needed additional time. Table 1 lists the starting reaction compositions and phase identification of products obtained at 240 °C for 10h.

$\text{Cu}_2\text{Bi}_4\text{V}_2\text{O}_{13}\cdot3\text{H}_2\text{O}$  could be obtained from 1.0M NaOH solution with an initial Bi/V ratio of 0.5-1.5, when the mole ratio of  $\text{CuCl}_2\cdot2\text{H}_2\text{O}$  was fixed as unity. With a lower NaOH concentration,  $\text{BiVO}_4$  was obtained, whereas higher NaOH concentrations led to the formation of  $\text{Bi}_2\text{CuO}_4$ , which was also obtained by decreasing Bi/V ratio to smaller than 0.5. If the concentration of NaOH was higher than 3M,  $\text{Bi}_2\text{CuO}_4$  phase was formed at Bi/V ratios listed in Table 1. When the Bi/V ratio was fixed as unity, the mole ratios of 0.5-1.0 for  $\text{CuCl}_2\cdot2\text{H}_2\text{O}$  were needed for preparing a pure phase. If the mole ratios of  $\text{CuCl}_2\cdot2\text{H}_2\text{O}$  is larger than 1.5, the impurity phase, CuO was formed.

Table 1. Initial compositions of hydrothermal synthesis for  $\text{Cu}_2\text{Bi}_4\text{V}_2\text{O}_{13}\cdot3\text{H}_2\text{O}$ .

Bi/V	$\text{CuCl}_2\cdot2\text{H}_2\text{O}(\text{M})$	NaOH (M)	Product phases
1/1	0.5	1.0	A
1/1	1.0	1.0	A
1/1	1.5	1.0	A+CuO
1/1	2.0	1.0	A+CuO
6/4	1.0	1.0	A
5/4	1.0	1.0	A
4/4	1.0	1.0	A
3/4	1.0	1.0	A
2/4	1.0	1.0	A
1/4	1.0	1.0	$\text{Bi}_2\text{CuO}_4$
1/1	1.0	0.25	$\text{BiVO}_4$
1/1	1.0	0.5	$\text{BiVO}_4$ +A
1/1	1.0	1.0	A
1/1	1.0	1.5	$\text{Bi}_2\text{CuO}_4$
1/1	1.0	2.0	$\text{Bi}_2\text{CuO}_4$
1/1	1.0	2.5	$\text{Bi}_2\text{CuO}_4$

A:  $\text{Cu}_2\text{Bi}_4\text{V}_2\text{O}_{13}\cdot3\text{H}_2\text{O}$ .

**Table 2.** Effects of bismuth source on products.

Bismuth source	NaOH(M)	Products
BiCl <sub>3</sub>	0.5	A
BiCl <sub>3</sub>	1.0	A+unkown phase+amphouse
BiCl <sub>3</sub>	1.5	Bi <sub>2</sub> CuO <sub>4</sub>
BiCl <sub>3</sub>	2.0	Bi <sub>2</sub> CuO <sub>4</sub>
Bi <sub>2</sub> O <sub>3</sub>	0.25	A
Bi <sub>2</sub> O <sub>3</sub>	0.5	A+unkown phase+amphouse
Bi <sub>2</sub> O <sub>3</sub>	1.0	Bi <sub>2</sub> CuO <sub>4</sub>
Bi <sub>2</sub> O <sub>3</sub>	1.5	Bi <sub>2</sub> CuO <sub>4</sub>

Bi(NO<sub>3</sub>)<sub>3</sub>·5H<sub>2</sub>O, BiCl<sub>3</sub> or Bi<sub>2</sub>O<sub>3</sub> could be employed as bismuth source, but critical NaOH concentrations for each source were needed (see Table 2). If BiCl<sub>3</sub> was used, the concentration of NaOH was 0.5M. However, If Bi<sub>2</sub>O<sub>3</sub> was used, the concentration of NaOH was 0.25M.

The contents of Bi, V and Cu in product sample were determined by ICP after the sample was dissolved in HNO<sub>3</sub> aqueous solution. The ICP analyses of Bi, 59.3wt%, V, 7.2wt%, and Cu, 8.9wt%, which were combined with the determination for the valence of V and water content by XPX and TG, corresponded to a formula Cu<sub>2</sub>Bi<sub>4</sub>V<sub>2</sub>O<sub>13</sub>·3H<sub>2</sub>O.

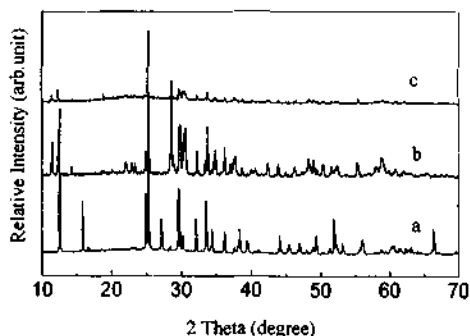


**Figure 1.** XRD patterns for (a) Cu<sub>2</sub>Bi<sub>4</sub>V<sub>2</sub>O<sub>13</sub>·3H<sub>2</sub>O, (b) the sample treated at 650°C, and (c) the sample treated at 820°C.

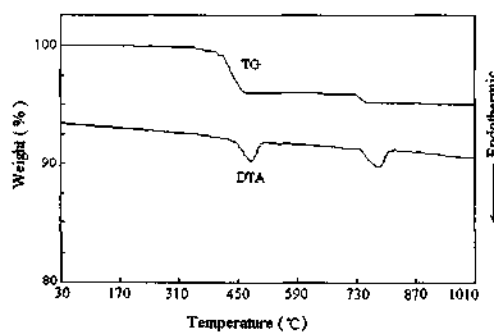


**Figure 2.** DTA-TG curves for Cu<sub>2</sub>Bi<sub>4</sub>V<sub>2</sub>O<sub>13</sub>·3H<sub>2</sub>O in air.

### 3.2 Characterization

Figure 1 shows XRD patterns of Cu<sub>2</sub>Bi<sub>4</sub>V<sub>2</sub>O<sub>13</sub>·3H<sub>2</sub>O(a), the samples heated at 650 °C(b) and 820 °C(c). All diffractions for Cu<sub>2</sub>Bi<sub>4</sub>V<sub>2</sub>O<sub>13</sub>·3H<sub>2</sub>O were well indexed in a monoclinic system with cell parameters  $a=1.497(2)$  nm,  $b=0.3692(1)$  nm,  $c=1.1168(3)$  nm,  $\beta=107.32(2)$  ° and  $V=0.6153(1)$  nm<sup>3</sup>. Table 3 lists X-ray diffraction data of Cu<sub>2</sub>Bi<sub>4</sub>V<sub>2</sub>O<sub>13</sub>·3H<sub>2</sub>O. Figure 2 shows DTA-TG curves of Cu<sub>2</sub>Bi<sub>4</sub>V<sub>2</sub>O<sub>13</sub>·3H<sub>2</sub>O in air. Two endothermic peaks at ca. 441 and 785 °C were clearly seen. A weight loss of 4.04% in 380 ~ 480 °C were attributed to the dehydration of the product, followed by

a structural transformation at 441 °C. IR spectrum for the sample heated at 441 °C indicates the decrease of absorption bands representative of lattice water, confirming the dehydration process.

**Table 3.** Powder X-ray diffraction data for  $\text{Cu}_2\text{Bi}_4\text{V}_2\text{O}_{13}\cdot3\text{H}_2\text{O}$

H	K	L	$D_{\text{OBS}}$	$D_{\text{CAL}}$	$I/I_0$	H	K	L	$D_{\text{OBS}}$	$D_{\text{CAL}}$	$I/I_0$
-2	0	1	7.033	7.036	56.6	-6	1	2	2.052	2.052	6.4
0	0	2	5.578	5.575	12.4	5	0	3	1.995	1.995	4.1
2	0	1	5.330	5.332	1.4	4	0	4	1.935	1.935	3.4
-1	0	3	3.893	3.890	1.0	-4	0	6	1.894	1.895	1.2
-2	0	3	3.799	3.791	1.1	-6	1	4	1.860	1.860	2.5
4	0	0	3.568	3.568	17.4	-7	1	2	1.844	1.845	5.0
-4	0	2	3.517	3.518	100	1	0	6	1.777	1.776	2.3
2	1	0	3.278	3.279	9.8	-8	0	4	1.758	1.759	10.8
-2	1	2	3.010	3.012	26.4	-2	1	6	1.721	1.721	3.4
2	0	3	2.954	2.955	4.9	4	0	2	1.640	1.639	6.7
0	0	4	2.786	2.787	9.3	-5	2	1	1.570	1.570	1.6
4	0	2	2.668	2.666	17.7	2	1	6	1.530	1.529	3.9
-4	0	4	2.604	2.605	7.7	-4	2	4	1.506	1.506	2.3
-6	0	1	2.481	2.482	7.0	-10	0	3	1.489	1.489	1.8
4	1	1	2.389	2.391	2.1	-10	0	1	1.472	1.472	2.3
-6	0	3	2.345	2.345	6.8	-10	0	5	1.407	1.407	7.6
-2	1	4	2.283	2.283	5.0	8	1	3	1.348	1.348	1.2
6	0	1	2.195	2.196	1.4	8	0	4	1.334	1.333	1.0

Figure 1(b) gives an XRD pattern for the high temperature phase after sintering  $\text{Cu}_2\text{Bi}_4\text{V}_2\text{O}_{13}\cdot3\text{H}_2\text{O}$  at 650 °C in air for 30 min. This phase lasted up to 730 °C. From 730 to 820 °C, another weight loss of 0.9% was observed, which apparently resulted from the loss of oxygen of the sample as in most cases of bismuth oxides. The losses of oxygen produced vacancies of oxygen, while its framework structure was kept the same as shown in Figure 1(c), though the crystallinity decreased. Thus, XRD and DTA-TG studies showed that the hydrothermally synthesized  $\text{Cu}_2\text{Bi}_4\text{V}_2\text{O}_{13}\cdot3\text{H}_2\text{O}$  has a phase transformation at 441 °C to a high temperature phase. The high temperature phase lost parts of oxygen at 730 °C and was stable until melting at 820 °C. This phase transformation was irreversible.

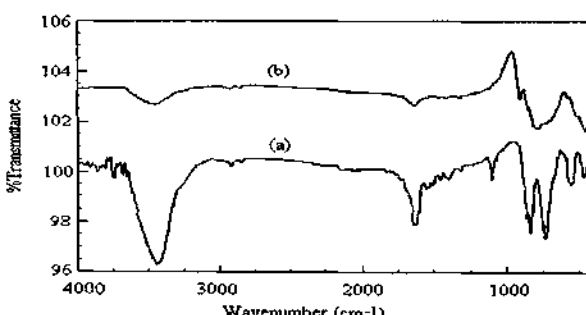


**Figure 3.** IR spectra for  $\text{Cu}_2\text{Bi}_4\text{V}_2\text{O}_{13}\cdot3\text{H}_2\text{O}$  (a) and the sample treated at 650 °C (b).

Figure 3 shows the infrared spectra within the 400-4000  $\text{cm}^{-1}$  region for  $\text{Cu}_2\text{Bi}_4\text{V}_2\text{O}_{13}\cdot 3\text{H}_2\text{O}$  (a) and its high temperature phase (b). In the spectra of  $\text{Cu}_2\text{Bi}_4\text{V}_2\text{O}_{13}\cdot 3\text{H}_2\text{O}$ , two very strong absorption band appears at ca. 3438 and 1635  $\text{cm}^{-1}$ , which were attributed to the stretching and bending vibrations of lattice water, respectively. The bands decrease markedly in intensity after the sample was evacuated at 650 °C for 30 min. The absorption bands at ca. 733 and 833  $\text{cm}^{-1}$ , which shift to about 781 and 892  $\text{cm}^{-1}$ , were due to V-O vibrations of the  $\text{VO}_4$  tetrahedron. This suggests that the structure of  $\text{Cu}_2\text{Bi}_4\text{V}_2\text{O}_{13}\cdot 3\text{H}_2\text{O}$  changed after heated at 650 °C and thus the distances between V and O become shorter.

XPS of  $\text{Bi}_{4f}$ ,  $\text{Cu}_{2p}$  and  $\text{V}_{2p}$  show that the binding energies of  $\text{Bi}_{4f5/2}$  and  $\text{Bi}_{4f7/2}$  are 163.9 and 158.6 eV, respectively. The binding energies of  $\text{Cu}_{2p1/2}$  and  $\text{Cu}_{2p3/2}$  are 954.1 and 934.2 eV, respectively. The binding energy of  $\text{V}_{2p}$  is 517.4 eV. These suggest trivalent Bi, divalent Cu and pentavalent V ions in the product.

$\text{Cu}_2\text{Bi}_4\text{V}_2\text{O}_{13}\cdot 3\text{H}_2\text{O}$  was synthesized in single phase and uniform crystals with a similar shape and this green plate crystal has an average dimension of 50  $\mu\text{m} \times 100 \mu\text{m} \times 30 \mu\text{m}$ . An attempt was made to measure its single crystal structure, but the collection of XRD intensity data was not suitable for the structure solution.

### 3.3 Electrical conductivity

AC impedance measurement of  $\text{Cu}_2\text{Bi}_4\text{V}_2\text{O}_{13}\cdot 3\text{H}_2\text{O}$  was performed in air in the temperature range of 200-500 °C. A typical complex impedance plot for  $\text{Cu}_2\text{Bi}_4\text{V}_2\text{O}_{13}\cdot 3\text{H}_2\text{O}$  at 350 °C was composed of successive semicircles. The bulk and grain boundary conductivity could not be distinguishable. Overall ionic conductivity was determined from the reciprocal of resistivity at the right-side intercept of the semicircular arc with the Z' axis of the Z'-Z'' plot. As the temperature increases, the ionic conductivity increases.

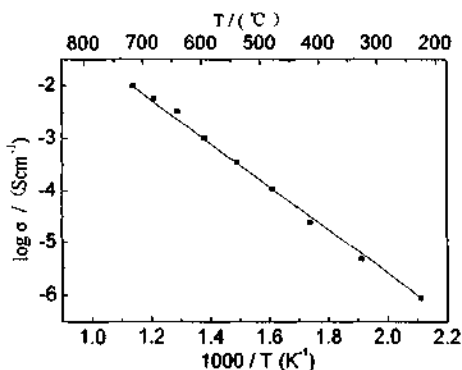


Figure 4. Arrhenius plot of ionic conductivity of the high temperature phase.

AC impedance measurements of the compound sintered at 700 °C were performed in air in the temperature range of 200-600 °C. The Arrhenius plots of the ionic conductivity are shown in Figure 4. The relationship between conductivity and the reciprocal of the absolute temperature is linear over the temperature range measured.

The activation energy for the sintered sample was  $82.62 \text{ KJ/mol}^{-1}$ . The highest ionic conductivity at  $600^\circ\text{C}$  was  $1.02 \times 10^{-2} \text{ S}\cdot\text{cm}^{-1}$ . To determine the ionic transference numbers of the heated sample, *dc* conductivity was measured as a function of time. The time dependence of *dc* conductivity at  $600^\circ\text{C}$  under oxygen, air, nitrogen and helium shows a clear polarizing behavior. The *dc* conductivity decreases abruptly in comparison to its *ac* conductivity and finally approaches a steady value. We, thus, observed that the polarization behavior increased with the decrease of oxygen pressure. The *dc* and *ac* conductivity ratio,  $\sigma_{dc}/\sigma_{ac}$  was not unity, even though the measurement was conducted in oxygen. The result was different from that of well-known oxygen ionic conductor [12] and indicated that, besides the oxygen ion conduction, there should exist other conduction species. As Pt was not a completely blocking electrode for oxygen ions, the ionic transference number ( $t_i$ ) was estimated from the polarization data measured in helium.

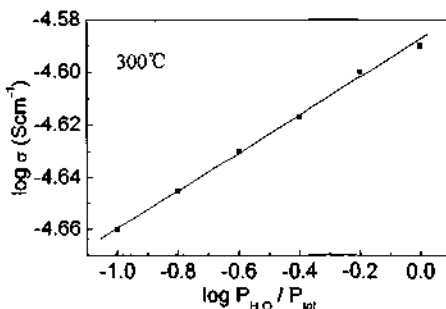


Figure 5. *ac* conductivity at  $600^\circ\text{C}$  as a function of water partial pressure.

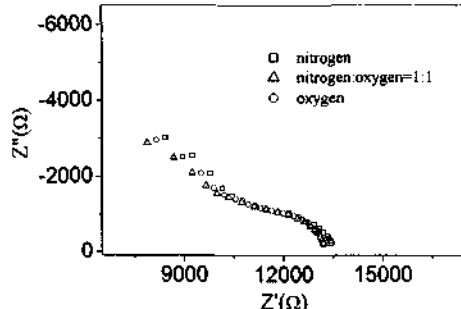


Figure 6. Impedance plots at  $600^\circ\text{C}$  for the high temperature phase in mixed nitrogen and oxygen.

The conductivity increased with increasing the water vapor pressure and a linear relationship could be obtained as shown in Figure 5. This proved that proton conduction exists in the compound. The reason for proton conduction is now not clear.

To investigate the influence of the gas atmosphere over the sample on its conductivity, oxygen and nitrogen were introduced into the measuring system. It was observed that the gas atmosphere had no effects on the conductivity, as shown in Figure 6. This result indicated a relatively pure ionic conductor.

#### 4 Conclusions

A novel hydrated copper bismuth vanadate,  $\text{Cu}_2\text{Bi}_4\text{V}_2\text{O}_{13}\cdot3\text{H}_2\text{O}$  was successfully synthesized by a mild hydrothermal method at  $240^\circ\text{C}$ . This compound undergone a phase transformation to a high temperature phase, of which the structure was unknown, but it showed high ionic conductivity. The highest ionic conductivity for the high temperature high at  $600^\circ\text{C}$  was  $1.02 \times 10^{-2} \text{ S}\cdot\text{cm}^{-1}$ , which was much higher than that of well-known Y-stabilized zirconia. Its ionic transference number was ca. 0.9. This material showed mixed proton and oxygen ionic conduction and belongs to one of the best ionic conductors.

## 5 Acknowledgment

This work was supported by the NSFC through the project of Hydrothermal Synthesis of Advanced Materials.

## References

1. Boivin J. C. and Mairesse G., Recent Material Developments in Fast Oxide Ion Conductors, *Chem. Mater.* **10**(10) (1998) pp. 2870-2888.
2. Steele B.C.H. and Angelika Heinzel, Materials for fuel-cell technologies, *Nature*. **414** (2001) pp. 345-352.
3. Kendall K.R., Navas C., Thoams J.K. and zur Loye H.-C., Recent Developments in Perovskite-based Oxide ion Conductors, *Solid State Ionics*. **82** (1995) pp. 215-223.
4. Lacorre Ph., Foutenoire F., Bohnke O., Retoux R. and Laligant Y., Designing fast oxide-ion conductors based on  $\text{La}_2\text{Mo}_2\text{O}_9$ , *Nature*. **404** (2000) pp. 856-858.
5. Riess I. In *Science and Technology of Fast Ion Conductors*, Plenum Press, New York, 1987.
6. Lee C. K., Ong C. S., Synthesis and characterisation of rare earth substituted bismuth vanadate solid electrolytes, *Solid State Ionics*. **117** (1999) pp. 301-310.
7. Bhattachary A. K. and Mallick K. K., Low temperature synthesis of a bismuth vanadium oxide isomorphous with  $\gamma\text{-Bi}_4\text{V}_2\text{O}_{11}$ , *Solid State Commun.* **91** (1994) pp. 357-360.
8. Feng S. H. and Xu R. R., Materials in hydrothermal synthesis, *Acc. Chem. Res.* **34** (2001) pp. 239-247.
9. Pang G., Feng S., Tang Y., Tan C. and Xu R., Hydrothermal synthesis, characterization, and ionic conductivity of vanadium-stabilized  $\text{Bi}_{17}\text{V}_3\text{O}_{33}$  with fluorite-related superlattice structure, *Chem. Mater.* **10** (1998) pp. 2446-2449.
10. Zhao H and Feng S, Hydrothermal synthesis and oxygen ionic conductivity of co-doped nanocrystalline  $\text{Ce}_{1-x}\text{MBi}_{0.4}\text{O}_{2.6-x}$ , M=Ca, Sr, Ba, *Chem. Mater.* **11** (1999) pp. 958-964.
11. Li G., Li L., Feng S., Wang M. and Yao X., An effect synthetic route for the novel electrolyte: nanocrystalline solid solutions of  $(\text{CeO}_2)_{1-x}(\text{BiO}_{1.5})_x$ , *Adv. Mater.* **11** (1999) pp. 146-149.
12. Kobayashi Y., Egawa T., Tamura S., Imanaka N. and Adachi G.-Y., Trivalent  $\text{Al}^{3+}$  Ion Conduction in Aluminum Tungstate Solid, *Chem. Mater.* **9** (1997) pp. 1649-1654.

# SYNTHESIS, CRYSTAL STRUCTURE AND SOME PROPERTIES OF $\text{Ln}_2\text{MnTiO}_6$ PHASES (Ln = RARE EARTH)

NAOKI KAMEGASHIRA

*Department of Materials Science, Toyohashi University of Technology, Tempaku-cho,  
Toyohashi, 441-8580, Japan  
E-mail: nkamegas@tutms.tut.ac.jp*

MIGAKU KOBAYASHI

*Department of Chemistry and Biochemistry, Numazu College of Technology, Ooka,  
Numazu, 410-8501, Japan  
E-mail: kobayasi@cab.numazu-ct.ac.jp*

JUN-ICHI SAITO

*Japan Science and Technology Corporation, 5-3, Yonbancho, Tokyo, 102-0081, Japan  
E-mail: jsaito@jst.go.jp*

Some compounds of  $\text{Ln}_2\text{MnTiO}_6$  (Ln = rare earth) were synthesized by the conventional solid state reaction method under low oxygen partial pressure in order to get the new perovskite type compounds with a combination of divalent manganese and tetravalent titanium ions. There exist three phases in this family for rare earth elements: orthorhombic and monoclinic with the perovskite structure, and hexagonal phases. The monoclinic phase is slightly different from the orthorhombic phase with several peaks split into double peaks. However the hexagonal phase is completely different from the perovskite type structure and B-site ions (Mn and Ti ions) are surrounded by five oxygen ions like the hexagonal  $\text{LnMnO}_3$  phase. Some of these compounds have antiferromagnetism at low temperature.

## 1 Introduction

The preparation of  $\text{La}_2\text{MnTiO}_6$  was reported by Rmanujachary and Swamy [1], but their x-ray data includes unassigned peaks and their calculated lattice constants did not correspond to the values cited on their table. In general,  $\text{LnMnO}_3$  (Ln = rare earth element) decomposes at high temperature under low oxygen partial pressure [2,3], while the formation of  $\text{LnTiO}_3$  needs much lower oxygen partial pressure to keep a valence state of Ti ion trivalent [4]. Therefore the formation of  $\text{Ln}(\text{Mn},\text{Ti})\text{O}_3$  is rather difficult because of difficulty to keep trivalent Mn and Ti ions in these compounds simultaneously. However it is rather realizable when a combination of divalent Mn and tetravalent Ti ionic states is carried out under an appropriate reduced atmosphere at high temperature during synthesis. In fact Rmanujachary and Swamy [1] concluded from their IR spectrum that these two valence states are included in their sample of  $\text{La}_2\text{MnTiO}_6$ .

$\text{Nd}_2\text{MnTiO}_6$  was synthesized in a reducing atmosphere by Nakano et al. [5] and all of the peaks in the powder X-ray diffraction patterns were

successfully indexed on the basis of orthorhombic unit cell, which was supported by electron diffraction results with the aid of high-resolution electron microscopy.  $\text{Sm}_2\text{MnTiO}_6$  was prepared by the authors [6] and monoclinic phase was identified by powder X-ray diffraction data with the Rietveld analysis. On the other hands  $\text{Yb}_2\text{MnTiO}_6$  has a hexagonal phase [7], although a small amount of impurity peaks ( $\text{MnO}$  or  $\text{Yb}_2\text{O}_3$ ) are included in the specimen from the results of powder X-ray diffraction patterns.

In this study synthesis of  $\text{Ln}_2\text{MnTiO}_6$  phase for several rare earths was tried, and phase behavior, crystal structure and magnetic properties are described.

## 2 Experimental

Polycrystalline samples of various  $\text{Ln}_2\text{MnTiO}_6$  phases were prepared by the solid-state reaction method. All the starting materials have 99.9 % purity, Kanto Chemicals Co. Ltd. and were pre-treated to adjust oxygen stoichiometry.  $\text{Ln}_2\text{O}_3$  was treated as described in other reports [3].  $\text{Pr}_2\text{O}_3$  was reduced from  $\text{Pr}_6\text{O}_{11}$  by the same method as previously described [3].  $\text{MnO}$  was prepared by reducing  $\text{Mn}_2\text{O}_3$  under hydrogen stream at 1273 K.  $\text{TiO}_2$  was annealed at 1273K in air for one day. Mixtures of  $\text{Ln}_2\text{O}_3$ ,  $\text{MnO}$  and  $\text{TiO}_2$  were pressed into pellet and heated at 1523 K for 2 days under 1 %  $\text{H}_2\text{-Ar}$  atmosphere. The grinding and heating process were repeated to get a homogeneous specimen.

X-ray powder diffraction data of the sample were collected with a MAC MXP18 powder diffractometer using  $\text{CuK}\alpha$  radiation equipped with a single-crystal graphite monochromator at room temperature. The  $2\theta$  range was  $20^\circ < 2\theta < 120^\circ$  with an increment  $0.04^\circ$  or  $0.05^\circ$ . The obtained data were analyzed by the Rietveld method using RIETAN program[7]. The overall isotropic thermal parameter was used for each calculation. Magnetic susceptibility was measured by Faraday and SQUID methods from liquid Helium temperature to room temperature.

## 3 Results and Discussion

$\text{La}_2\text{MnTiO}_6$  crystallized in an orthorhombic phase with the perovskite structure as described by Ramanujachary and Swamy [1].  $\text{Pr}_2\text{MnTiO}_6$  has an orthorhombic structure as  $\text{La}_2\text{MnTiO}_6$  [1] and  $\text{Nd}_2\text{MnTiO}_6$  [5]. X-ray diffraction patterns of orthorhombic phase are shown in Fig. 1 (a). The refinement of crystal structure of  $\text{Nd}_2\text{MnTiO}_6$  is shown in Table 1, where Mn and Ti atoms were assumed to be randomly distributed in the B site of the perovskite structure, so that a virtual atom ( $1/2 \text{ Mn} + 1/2 \text{ Ti}$ ) was used. The bond lengths and angles of  $\text{Nd}_2\text{MnTiO}_6$  were given in table 2. The typical monoclinic patterns are shown in Fig. 1(b) [6], where

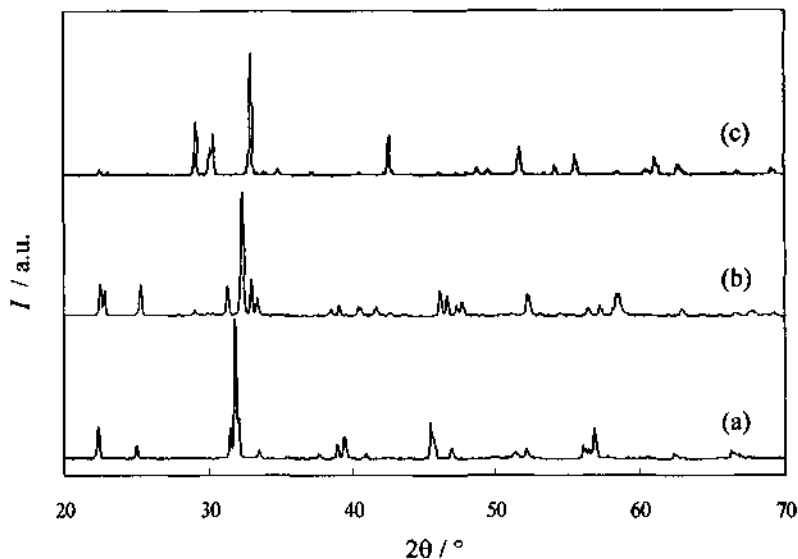


Fig. 1 Powder X-ray diffraction patterns for  $\text{Ln}_2\text{MnTiO}_6$  ;  
(a) orthorombic,(b) monoclinic and (c) hexagonal phases

Table 1 Atomic positions and isotropic thermal parameters for  $\text{Nd}_2\text{MnTiO}_6$

atom	site	<i>x</i>	<i>y</i>	<i>z</i>	<i>B</i> / nm <sup>2</sup>
Nd	4c	0.0566(1)	0.25	0.0125(2)	0.0070(2)
(Mn,Ti)	4b	0	0	0.25	0.0064(5)
O1	4c	0.462(2)	0.25	-0.104(2)	0.008(2)
O2	8d	0.199(1)	-0.0533(9)	-0.198(1)	0.009(2)

Table 2 Bond distances and bond angles for  $\text{Nd}_2\text{MnTiO}_6$

Nd-O1	× 1	0.241(1)	Nd-O1	× 1	0.3457(9)
Nd-O1	× 1	0.3300(9)	Nd-O1	× 1	0.231(1)
Nd-O2	× 2	0.2771(8)	Nd-O2	× 2	0.2357(6)
Nd-O2	× 2	0.2624(7)	Nd-O2	× 2	0.3586(6)
(Mn,Ti)-O1	× 1	0.2058(3)	(Mn,Ti)-O2	× 1	0.2058(6)
(Mn,Ti)-O2*	× 2	0.2077(6)			
$\angle(\text{Mn,Ti})-\text{O}1-(\text{Mn,Ti})$		145.3(5)	$\angle(\text{Mn,Ti})-\text{O}2-(\text{Mn,Ti})$		147.1(3)

Note : Distance (nm) and angle(° )

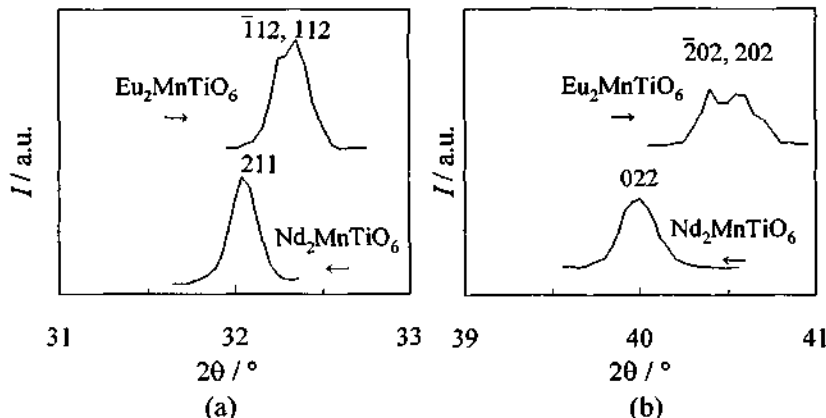


Fig. 2 Powder X-ray diffraction patterns for  $\text{Nd}_2\text{MnTiO}_6$  and  $\text{Eu}_2\text{MnTiO}_6$

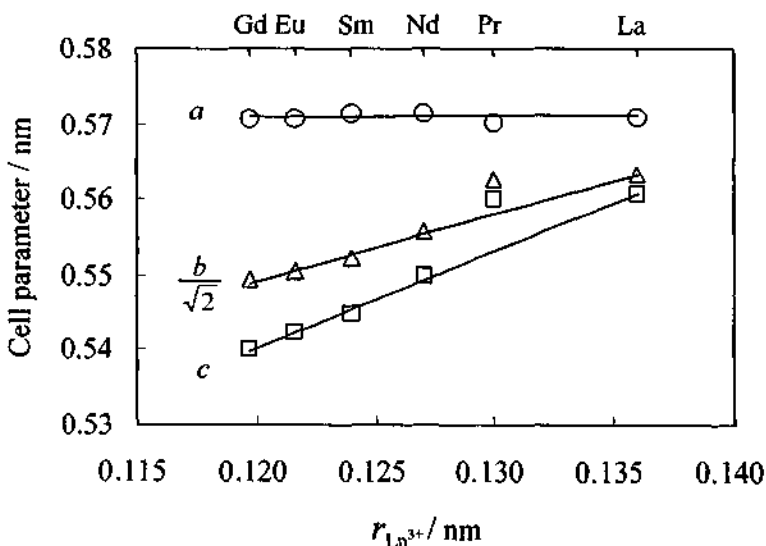


Fig. 3 Cell Parameters of  $\text{Ln}_2\text{MnTiO}_6$

several peaks split. These monoclinic phases were obtained for  $\text{Ln} = \text{Sm} - \text{Gd}$ , and for other rare earths peak splitting characteristic of monoclinic phase with perovskite structure were observed, although a considerable amounts of impurity phases were also included. Formation of single phases for these rare earths is rather difficult. An example of the difference of the typical peaks of X-ray diffraction patterns between orthorhombic and monoclinic phases are shown in Fig. 2. In the monoclinic phase Mn and Ti ions are distributed in ordered state (4b and 4c sites) [6], while in orthorhombic phase they are randomly distributed in

B-site. The variation of the lattice constants for orthorhombic and monoclinic phases with rare earths is shown in Fig. 3, where normalized lattice parameters are used. The cell volume decreases with decrease in ionic radius of rare earths as shown in Fig. 4. On the other hands, hexagonal  $\text{Yb}_2\text{MnTiO}_6$  has a completely different patterns as is shown in Fig. 1 (c). Only  $\text{Yb}_2\text{MnTiO}_6$  and  $\text{Lu}_2\text{MnTiO}_6$  have this structure with five coordinated oxygen ions surrounding a central manganese ion which is isostructural with hexagonal  $\text{LnMnO}_3$  ( $\text{Ln} = \text{Ho} - \text{Lu}, \text{Y}$  and  $\text{Sc}$ ).

The magnetic susceptibilities for several rare earths are shown in Fig.

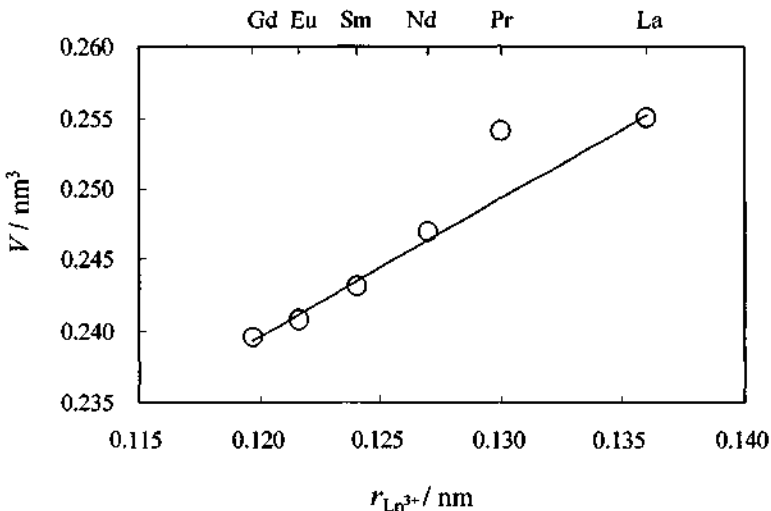


Fig. 4 Cell volume for  $\text{Ln}_2\text{MnTiO}_6$

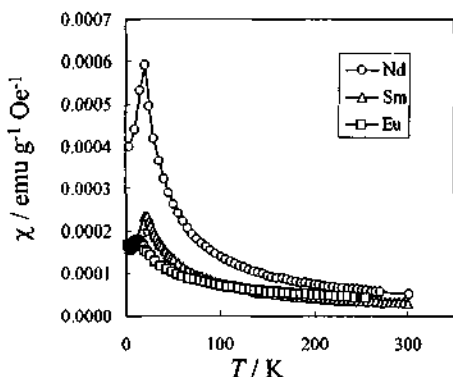


Fig. 5 Magnetic susceptibilities of  $\text{Ln}_2\text{MnTiO}_6$  as a function of temperature

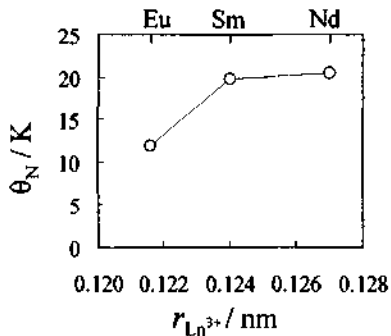


Fig. 6 Néel Temperature of  $\text{Ln}_2\text{MnTiO}_6$

5 and a typical antiferromagnetic behavior is observed only for Ln = Nd, Sm and Eu, where Néel temperature decreases as shown in Fig.6.

#### 4 Acknowledgements

This research was supported by the Grant-in-Aid for Scientific Research (B) (No. 13450259) by Japan Society for the Promotion of Science. Thanks are due to the Instrument Center, the Institute for Molecular Science, for assistance in obtaining the magnetic properties at low temperature.

#### 5 References

1. Ramanujachary K. V. and Swamy C. S., Preparation & characterization of  $\text{La}_2\text{TiMnO}_6$ . *Indian J. Chem.* 20A (1981) 96 - 97.
2. Nakamura T., Isothermal decomposition of ternary oxide  $\text{A}_x\text{B}_y\text{O}_z$  on an isobar stability of perovskite  $\text{ABO}_3$  ( A = La, Sm, Dy; B = Mn, Fe) in a reducing atmosphere. *J. Solid State Chem.* 38 (1981) pp.229 - 238.
3. Atsumi T., Ohgushi T., Kamegashira N., Studies on oxygen dissociation pressure of  $\text{LnMnO}_3$  ( Ln = rare earth) with the e.m.f. technique. *J. Alloys and Compounds* 238 (1996) pp.35 - 40..
4. McCarthy G. J., White W. B., Roy R., Preparation and structure of the rare earth titanates. *Mat. Res. Bull.* 4 (1969) pp. 251 - 256.
5. Nakano H., Nakazima N., Shirakami T. and Kamegashira N., Crystal structure of a new oxide,  $\text{Nd}_2\text{TiMnO}_6$ . *Mat. Res. Bull.* 34 (1999) pp. 1851 - 1858.
6. Kamegashira N., Nakajima N., Watanabe K. and Kobayashi M., Synthesis and crystal structure of  $\text{Sm}_2\text{MnTiO}_6$ . *J. Alloys and Compounds* 311 (2000) pp. 74 - 78.
7. Nakano H., Kamegashira N. and Urabe K., Structure analysis of a new oxide  $\text{Yb}_2\text{MnTiO}_6$ . *Mat. Res. Bull.* 36 (2001) pp. 57 - 68.
8. Izumi F., A software package for the Rietveld analysis of X-ray and neutron patterns. *J. Crystallogr. Jpn.* 27 (1985) pp.23 -31.

# OPTICAL-INDUCED FRÉEDERICKSZ TRANSITION OF NEMATIC LIQUID CRYSTAL DOPED WITH PORPHYRINATOZINC(II)

TAO LI\* AND CHUN-LIN NI

*Chemistry Dept., Three Gorges University, YiChang, HuBei Province, P. R. China  
Tel: 0717-6253073, E-Mail: chltl@x263.net*

YUAN ZHANG

*Life College, Zhongshan University, GuangZhou, P. R. China*

JIN-WANG HUANG AND LIANG-NIAN JI

*Chemistry Dept., Zhongshan University, GuangZhou, P. R. China*

The Optical-Induced Fréedericksz Transition of Nematic Liquid Crystal (5CB) doped with 1%(w/w) of 5, 10, 15, 20-tetraphenylporphyrinatozinc(II) (ZnTPP) were studied. Excited by Ti: Sappire laser with the 82MHz repetition rate and 100fs pulse duration, the optical Fréedericksz threshold of a 23.6 $\mu$ m-thickness planar alignment sample occurred at an intensity level of 0.35mW/mm<sup>2</sup> in contrast to the normally observed 83mW/mm<sup>2</sup> value for pure 5CB. The coordination-bonding interaction between 5CB and ZnTPP were discussed by UV-vis and fluorescence spectra. We attribute the reduction of the optical Fréedericksz threshold to the coordination-bonding interaction.

## 1 Introduction

Due to their large optical anisotropies, liquid crystals (LCs) have a large optical non-linearity which is the result of molecular reorientation (Fréedericksz transition) in an external field which exceeds the critical field [1]. The high external field inhibits the application of LCs, and decreasing the threshold as low as possible is a difficult task [2]. LCs doped with a small amount of absorbing dyes that could decrease the needed optical field intensity have been reported [3]. The basic assumption is that the anomalous reorientation of the director results from the interaction between the excited dye molecules and the host. However, this sample would easily degrade under the influence of laser radiation.

On the other hand, the electro-optical methods of high-density data storage and the electric-field induced surface photovoltaic spectroscopy based on a liquid crystal porphyrin have been studied [4,5]. It was found that upon light irradiation with simultaneous application of an electric field, electron-hole pairs were generated and separated within the liquid crystal porphyrin solid film. Information, as a form of trapped charge, can be written, read, and erased by the simultaneous application of an electric field and a light pulse. LCs also serve to slow down the rates of intramolecular electron transfer (IET) reactions in several supramolecular systems, thus allowing submicrosecond EPR spectroscopic techniques to be applied in the study of these systems. LCs were used as solvents to carry out a time-resolved EPR analysis of the IET process that occurs between the difference metalloporphyrins. The different paths of IET process can be controlled and differentiated by changing the environmental conditions, such as solvent and temperature. But the interaction between LCs and metalloporphyrins were not discussed.

In this paper, we first observed the optical-induced Fréedericksz transition of nematic liquid crystal (5CB) doped with 5, 10, 15, 20-tetraphenylporphyrinatozinc(II) (ZnTPP)

and the coordination interaction between 5CB and ZnTPP which are completely different with liquid crystal doped with a small amount of absorbing dye. The results show that the coordination interaction between 5CB and ZnTPP is an important cause of the optical-induced Fréedericksz transition.

## 2 Experimental

ZnTPP was synthesized in our laboratory and characterized by UV-vis, EA, <sup>1</sup>H-NMR, IR, MS and 5CB was from BDH (as shown in Figure 1). Two samples were studied in the experiment, 5CB and 5Cb doped with 1% (w/w) ZnTPP. The samples were sandwiched between two glass substrates with 23.6 $\mu$ m spacers, the two glass substrates were coated with polyimide and rubbed unidirectionally to give planar alignment.

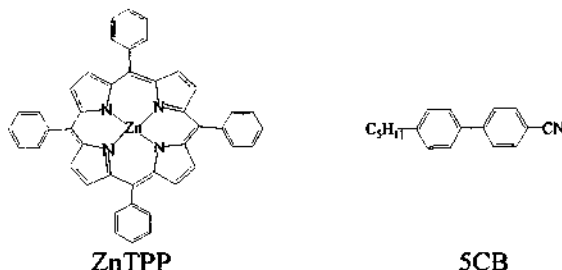


**Figure 1.** The molecular structures of ZnTPP and 5CB.

The optical phase retardation method was applied to probe the light transmission, which is an indicator of the LC twist reorientation under external field. The experiment arrangement is shown in Figure 2 with the temperature stabilized at 26°C. The probing light is a 655 nm laser beam generated by a cw semiconductor, as ZnTPP has no absorption of it. The probe laser beam polarized at 45° to the Y axis is normally incident to the sample, along the Z axis, d is the thickness of the sample. The orientation director  $n_0$  of 5CB (unperturbed) is along the Y axis. The output light is probed by a photo detector with an analyzer (P2) crossed to the polarizer (P1). The exciting laser was slightly focused with an  $e^2$  diameter of 2mm and was approximately normally incident on the samples. The polarization of the exciting laser beam is almost along X axis. When the exciting light intensity I is larger than the critical intensity  $I_c$ , the LC molecular will reorientate with twist angle  $\theta(z)$  in the X-Y plane, which results in the varying output light. The exciting laser used here is Ti: Sappire laser (made by Spectra-Physics) with the 82MHz repetition rate, 100fs pulse duration and 760-870nm adjusted wavelength. Using frequency doubled technique, the exciting laser beam can be acquired with wavelength ranging from 380nm to 435nm.

The UV-vis spectra were run on a SHIMADZU UV-2501PC. 5CB doped with ZnTPP in LC box was compared with 5CB in LC box, 5CB doped with ZnTPP film laid on the colorimetric cell was compared with 5CB film laid on the colorimetric cell, ZnTPP : 5CB (mol:mol=1:2000) in benzene was compared with the same amount 5CB.

The steady fluorescence spectra were measured on a HITACHI F-4500. The slit aperture of excitation and emission are all 5nm or 10 nm.

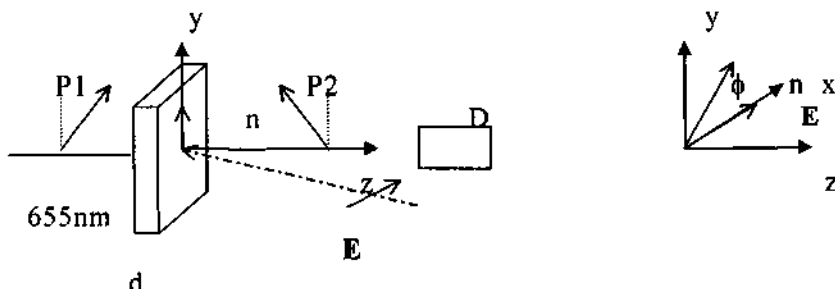


Figure 2. The experiment set-up of the optical phase retardation method.

### 3 Results and Discussion

#### 3.1 The optical-induced Fréedericksz transition

##### 3.1.1 $\lambda = 760\text{nm}$ (transparent region)

The corresponding  $I_c$  is  $84\text{mw/mm}^2$  for 5CB doped with ZnTPP. As for the pure 5CB, the corresponding  $I_c$  is  $83\text{mw/mm}^2$ . The dopant does not have any positive effect on the decrease of  $I_c$  because ZnTPP has no absorption.

##### 3.1.2 $\lambda = 435\text{nm}, 420\text{nm}$ and $380\text{nm}$ (absorption region)

The probe light transmission  $T$  vs. exciting laser intensity  $I$  at 435nm, 420nm, 380nm of 5CB doped with ZnTPP are shown in Figure 3, which revealed the optical property of dopant in detail. Compared to  $I_c=84\text{mw/mm}^2$  at 760nm in the transparent region,  $I_c$  is markedly reduced two orders as magnitude of  $I_c=0.35\text{mw/mm}^2$  at 435nm.

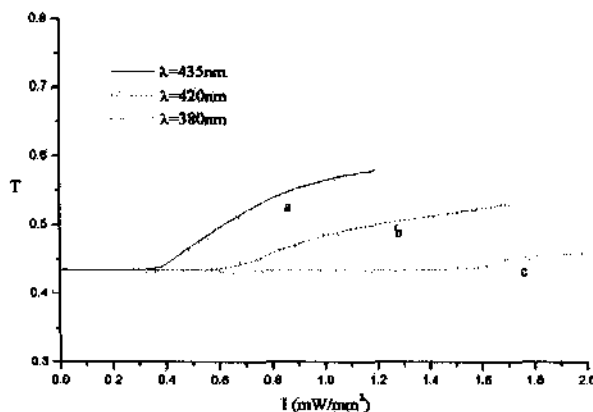
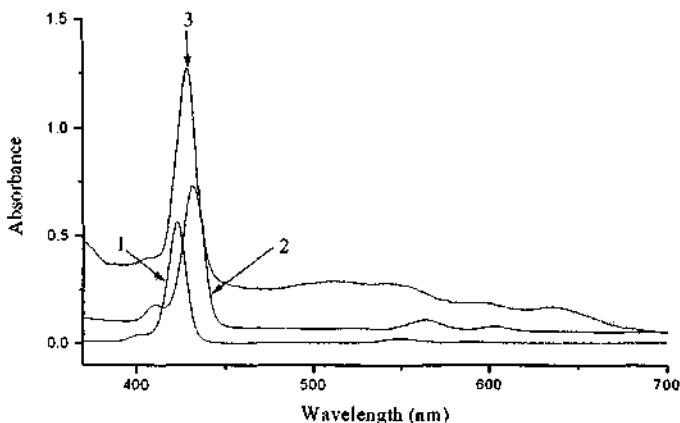


Figure 3. Light transmission  $T$  vs. light intensity  $I$  for planar alignment 5CB doped with 1% ZnTPP.

### 3.2 UV-vis spectra

The UV-vis spectra of ZnTPP are shown in Figure 4. The soret band and Q band of ZnTPP in benzene are 423.0nm, 547.9nm, 586.0nm, the UV-vis spectrum have no change when 2000-fold (mol:mol) 5CB was added. It means that 5CB has not coordinate with ZnTPP and the coordinate-bonding ability of 5CB is week.

In the 5CB doped with 1% ZnTPP film laid on the colorimetric cell, the soret band and Q band of ZnTPP are 432.0nm, 563.6nm, 602.6nm, but in the LC box, the soret band and Q band of ZnTPP are 428.8nm, 512.4nm, 544.7nm, 596.8nm, 632.8nm. The red shift of the soret band of ZnTPP means that 5CB coordinate with ZnTPP [6,7]. The UV-vis spectrum of ZnTPP in the LC box is different from that of ZnTPP film laid on the colorimetric cell. ZnTPP in the LC box is not the mixture of 4-coordinate and 5-coordinate because the UV-vis spectrum is not the superposition of 4-coordinate and 5-coordinate. We think that ZnTPP in the LC box maybe form the mixture of 5-coordinate and 6-coordinate [8,9].

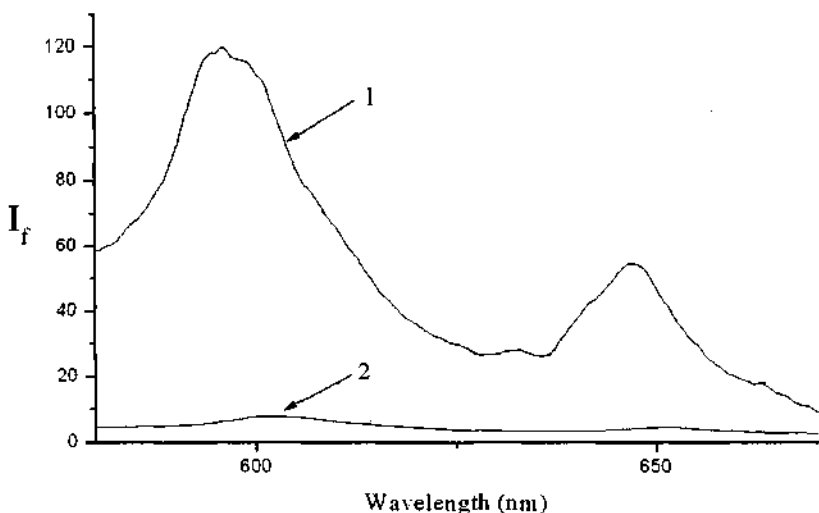


1. ZnTPP in benzene.
2. 5CB doped with 1% ZnTPP film laid on the colorimetric cell.
3. ZnTPP in the LC box.

**Figure 4.** The UV-vis spectra of ZnTPP.

### 3.3 Steady fluorescence spectra

In the 5CB doped with 1% ZnTPP film laid on the colorimetric cell, the fluorescence emission bands of ZnTPP are all 603.6nm, 651.8nm when the slits aperture of excitation and emission are all 5nm or 10nm. But in LC box, the fluorescence emission bands of ZnTPP are 603.2nm, 651.2nm when the slits aperture of excitation and emission are all 5nm. The fluorescence bands of ZnTPP box are 597.2nm, 647.2nm if the slits of excitation and emission are all 10nm (as shown in Figure 5).



1. the slits aperture of excitation and emission are all 10nm.
2. the slits aperture of excitation and emission are all 5nm.

Figure 5. The steady fluorescence spectra of ZnTPP in LC box.

In the LC box, metalloporphyrins can coordinate with 5CB [10,11]. Tetraphenylporphyrinatozinc have special property that the coordination interaction between ZnTPP and 5CB change, in other words, porphyrinatozinc changes from 5-coordinate (or 6-coordinate) to 4-coordinate because the transitions in the fluorescence spectra exhibit the corresponding absorption peaks [9,12]. We attribute this to that the excitation electron transfers from ZnTPP to 5CB and 5CB occurs optical-induced Fréedericksz transition so as to uncoordinate with ZnTPP (as shown in Figure 6).

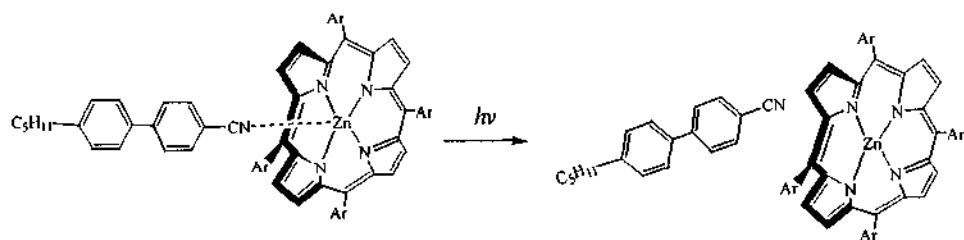


Figure 6. Optical-induced Fréedericksz transition of 5CB doped with ZnTPP.

#### 4 Acknowledgement

We thank the PhD's starting foundation of China Three Gorges University.

## References

1. Patel J.S., Lee Sin-Don and Goodby J. W. Physical Properties of Smectic Liquid Crystals and Novel Electro-optic Effects. Spatial Light Modulator Technology, Materials, Devices, and Applications (Uzi Efron, Marcel Dekker, New York, 1995).
2. Janossy I., Molecular interpretation of the absorption-induced optical reorientation of nematic liquid crystals. *Physicals. Review. E.* **49** (1994) pp. 2957-2963.
3. Marrucci L. and Paparo D. Photoinduced molecular reorientation of absorbing liquid crystals. *Physicals. Review. E.* **56** (1997) pp. 1765-1772.
4. Wróbel D., Goc J., and Ion R. M., Photovoltaic and spectral properties of tetraphenylporphyrin and metallotetraphenylporphyrin dyes. *Journal of Molecular Structure.* **450** (1998) pp. 239-246.
5. Chen Y. M., Cao C. S., Xie T. F., Wang X. Q., Lu R., Wang D. J., Bai Y.B. and Li T.J. Photovoltaic properties of a liquid crystal porphyrin solid film. *Supramolecular Science.* **5** (1998) pp. 461-463.
6. Hunter C. A. and Hyde R. K. Photoinduced Energy and Electron Transfer in Supramolecular Porphyrin Assemblies. *Angew. Chem., Int. Ed. Engl.* **35** (1996) pp. 1936-1939.
7. Gregory A. M. and F. A. Walker. Electronic Effects in Transition Metal Porphyrins. 5. Thermodynamics of Axial Ligand Addition and Spectroscopic Trends of a Series of Symmetrical and Unsymmetrical Derivatives of Tetraphenylporphinatozinc( II ). *Inorganica chimica Acta.* **91** (1984) pp. 95-102.
8. Brand U. and Vahrenkamp H. Zinc complexes of the new N, N, S ligand N-(2-mercaptopisobutyl) (picolyl) amine, *Inorganica chimica Acta.* **308** (2001) pp. 17-23.
9. Anderson H. A. Building molecular wires from the colours of life: conjugated porphyrin oligomers. *Chem. Commun.* (1999) pp. 2323-2330.
10. Xiang Y., Lin Z. Y., Li T., Shi J., Huang J. W. and Ji L. N., A homeotropic Alignment Nematic Liquid Crystal Doped with FeTPPCl will Dramatically Decrease the Critical Magnetic Field for the Bend Reorientation in a Static Magnetic Field. *Mol. Cryst. Liq. Cryst.* **339** (2000) pp. 139-143.
11. Li T., Xiang Y., Shi L. P., Huang J. W., Lin Z. Y., Shi J. and Ji L. N., Magnetic-field-induced Fréedericksz transition of a planar aligned liquid crystal doped with porphyrinatozinc( II ): influence of the substituent of the porphyrin ring. *Liquid Crystals.* **27** (2000) pp. 551-553.
12. Meot-Ner M. and Adler. A.D. Substituent Effects in Noncoplanar  $\pi$  Systems. Ms-Porphyrins. *Journal of the American Chemical Society.* **97** (1975) pp. 5107-5111.

## SYNTHESIS AND PROPERTIES OF MBPO<sub>5</sub>: Pr (M=Ca, Sr, Ba) PHOSPHORS

LIU XIAOTANG,<sup>1,3</sup> ZHUANG GUOXIONG,<sup>1</sup> XIONG JIANHUA,<sup>1</sup> WEI WEIPING,<sup>1</sup> LUO YAQIN,<sup>1</sup> SHI CHUNSHAN<sup>2</sup> AND XIE DEMIN<sup>3</sup>

<sup>1</sup> Department of Chemistry, Zhanjiang Normal College, Zhanjiang 524048, P. R. China

<sup>2</sup> Laboratory of Rare Earth Chemistry and Physics, Changchun Institute of Applied Chemistry, Chinese Academy of Science, Changchun 130022, P. R. China

<sup>3</sup> Faculty of Chemistry, Northeast Normal University, Changchun 130024, P. R. China

MBPO<sub>5</sub>: Pr (M=Ca, Sr, Ba) phosphors were synthesized in air atmosphere by solid-state reactions. The X-ray powder diffraction patterns show that all samples appeared to be a single phase. The synthetic temperature and doped concentration influence on luminescence. A better synthesis condition is that the synthetic temperature is 950°C and doped Pr<sup>3+</sup> concentration is 4mol%. The luminescence spectra of Pr<sup>3+</sup> ion in MBPO<sub>5</sub>: Pr (M=Ca, Sr, Ba) are presented. High-resolution excitation and emission spectra of Pr<sup>3+</sup> ion were measured at room temperature. These phosphors emission spectra can be divided into two parts. The first part is a weak broad band at wavelengths about 490nm. The second part consists of a number of emission peaks and the peak at 607nm is the strongest. The emission intensity of SrBPO<sub>5</sub>: Pr is strong. It is found that the intensity of the peak at 607nm, generated by Pr<sup>3+</sup> ion in SrBPO<sub>5</sub>, is about 15 times as high as that at 490nm. So we predict that the red emission can be made much stronger as long phosphorescence through use of additional phosphors showing a suitable absorption of the optical spectrum and emit light with long wavelength.

### 1 Introduction

The performance of rare earth phosphors is almost ideal in many applications. New impetus for research on phosphors is expected from new applications or phosphors showing new features [1].

In the last decade, for long phosphorescent phosphor, green or blue emitting alkaline earth metal aluminates doped with rare earth ions, have been invented and have a good performance. Their brightness and phosphorescent time are above thirty times as high as that of sulfide material system such as ZnS and SrS [2]. Recently, rare earth long phosphorescence has been dramatically improved. But the red emission long phosphorescence is rather lack and expected to obtain a novel one [3]. It is quite surprising that in Pr<sup>3+</sup> activated YF<sub>3</sub>, blue and red emission, originating from Pr<sup>3+</sup>, can be generated with a quantum efficiency of about 140%[4,5]. The red emission, generated by Pr<sup>3+</sup>, is located at about 620nm and therefore suitable for high quality fluorescent lamps. Srivastava et al reported the observation of the blue emission of Pr<sup>3+</sup> in oxidic materials [6]. In 1997, Dillo et al [7] found CaTiO<sub>3</sub>: Pr<sup>3+</sup> shows the properties of long afterglow luminescence. The luminescent mechanism of Pr<sup>3+</sup> ion had been investigated [8].

Therefore, we are interested in Pr<sup>3+</sup> and want to utilize the ability of Pr<sup>3+</sup> to develop novel red long phosphorescence. In this paper, we synthesized MBPO<sub>5</sub>: Pr (M=Ca, Sr, Ba) phosphors and made a tentative research.

## 2 Experimental

Samples with a  $\text{MBPO}_5$ : Pr (M=Ca, Sr, Ba) composition were synthesized by the classical solid-state reaction technique under an atmosphere of the air. The purity of  $\text{CaCO}_3$ ,  $\text{SrCO}_3$ ,  $\text{BaCO}_3$  and  $\text{H}_3\text{BO}_3$  was A.R., and that of  $\text{Pr}_6\text{O}_{11}$  was 99.99%. Stoichiometric amounts of the starting materials were thoroughly mixed and ground together, and excess 10% of the boric acid was used to compensate for the evaporation of  $\text{H}_3\text{BO}_3$  in high-temperature solid-state reaction. The mixture was heated at 200°C for 20 min, then ground and reheated at 950°C for another 6h. Then cooled them naturally to room temperature, and ground them and got white powder.

Crystal structures of samples were checked by means of a Rigaku Denki D/max-III A diffractometer using  $\text{Cu-K}\alpha$ . The X-ray powder diffraction pattern showed that the samples appeared to be a single phase. The observed d-values were identical with the JCPDS cards, and the cards' numbers are 18-283, 18-1270 and 19-96 respectively.

Luminescent properties of samples were evaluated on a SPEX FI-2 spectrofluorometer with a xenon arc lamp as excitation source at room temperature.

## 3 Results and Discussion

### 3.1 Luminescent properties of $\text{SrBPO}_5$ : Pr

The luminescent properties of phosphor  $\text{SrBPO}_5$ :0.04Pr activated by  $\text{Pr}^{3+}$  ion were investigated. Typical wide wavelength emission spectra of  $\text{SrBPO}_5$  doped with 4mol%  $\text{Pr}^{3+}$  ion, excited at 441 nm at room temperature, are shown in Figure 1.

The emission spectra of  $\text{Pr}^{3+}$  ion can be divided into two parts. The first part has a weak broad band at wavelength between 472nm and 507nm, whose maximum is at 487 nm. This broad band is corresponded to the  ${}^3\text{P}_0 \rightarrow {}^3\text{H}_4$  transition. The second part consists of strong emission lines at wavelength above 570nm. We found three groups of peaks; they are at 593, 607 and 622nm which are ascribed to the  ${}^3\text{P}_1 \rightarrow {}^3\text{H}_6$ ,  ${}^3\text{P}_0 \rightarrow {}^3\text{H}_6$  and  ${}^1\text{D}_2 \rightarrow {}^3\text{H}_4$  transitions, respectively. The  ${}^3\text{P}_0 \rightarrow {}^3\text{H}_6$  transitions is the strongest emission peak. The intensity of the  ${}^1\text{D}_2 \rightarrow {}^3\text{H}_4$  transitions at 622nm is relatively weak compared to the  ${}^3\text{P}_1 \rightarrow {}^3\text{H}_6$  luminescence intensity. Magnetic dipole allowed transitions will have greatest intensity when  $\Delta J=1$ , and electric dipole transitions will be most intense for  $\Delta J=0, 2, 4$  or 6, with the usual restrictions on  $\Delta J=0$  [8]. Emission from the  ${}^3\text{P}_1$  state of  $\text{Pr}^{3+}$  ion is quite noticeable, particularly the band at 593nm.

The electronic energies of  ${}^3\text{P}_1$  and  ${}^3\text{P}_0$  states, determined from the excitation spectra of  $\text{SrBPO}_5$ : $\text{Pr}^{3+}$  at room temperature ( $\lambda_{\text{em}}=607\text{nm}$ ), were found to be 441 and 478nm, respectively. (For details seen in Figure 2). The excitation spectra of  $\text{Pr}^{3+}$  exhibit two groups of excitation lines. One group consists of two peaks, and the strongest excitation peak is at 441nm. The other group has three sharp lines, and the strongest is at 477nm. These excitation lines are attributed to the 4f-5d transitions between the ground state of  $\text{Pr}^{3+}$  ion and its excited states.

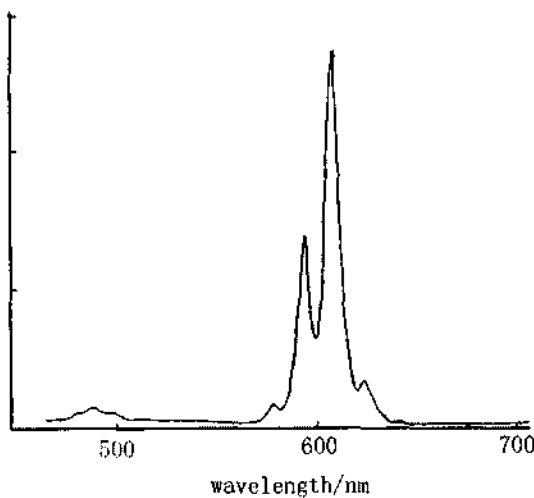


**Figure 1.** Photoluminescence emission ( $\lambda_{ex}=441\text{nm}$ ) spectra of  $\text{Pr}^{3+}$  in  $\text{SrBPO}_5:0.04\text{Pr}$ .

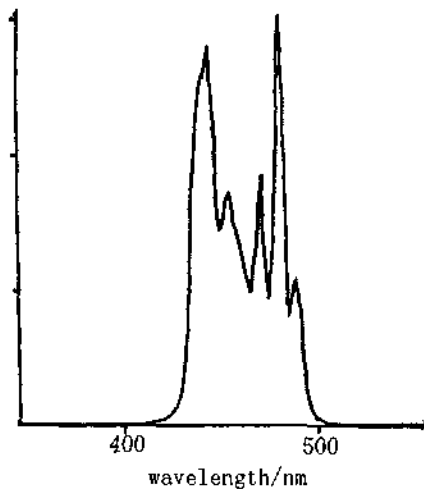


**Figure 2.** The excitation spectra of  $\text{Pr}^{3+}$  in  $\text{SrBPO}_5$  recorded at room temperature ( $\lambda_{em}=607\text{nm}$ ).

### 3.2 Luminescent properties of $\text{MBPO}_5:0.04\text{Pr}$ ( $M=\text{Ca}, \text{Sr}, \text{Ba}$ )

The phosphors emission spectra of  $\text{Pr}^{3+}$  ion in  $\text{MBPO}_5: \text{Pr}$  ( $M=\text{Ca}, \text{Sr}, \text{Ba}$ ) can be divided into two parts, as shown in Figure 3.

These emission spectra are very similar. In order to show more clearly, we list the fluorescent spectrum data of  $\text{MBPO}_5: \text{Pr}$  ( $M=\text{Ca}, \text{Sr}, \text{Ba}$ ) phosphors in Table 1.

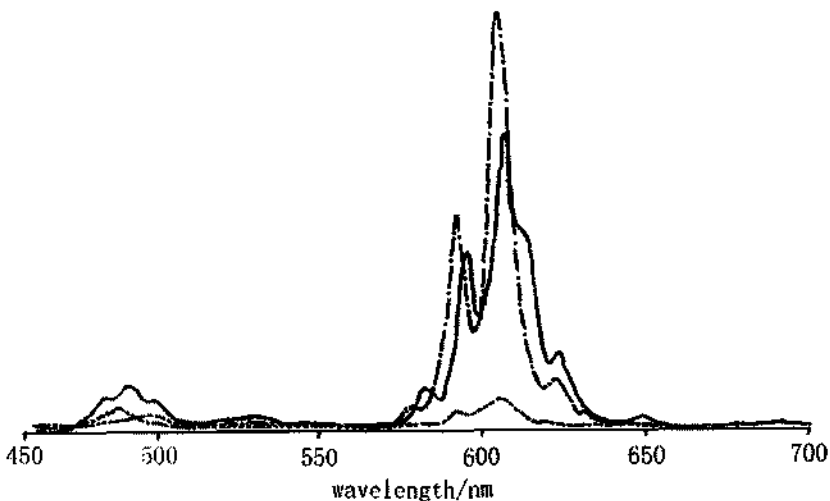


Figure 3. The emission spectra of  $\text{Pr}^{3+}$  in  $\text{MBPO}_5: \text{Pr}$  ( $\text{M}=\text{Ca}, \text{Sr}, \text{Ba}$ ) phosphors.

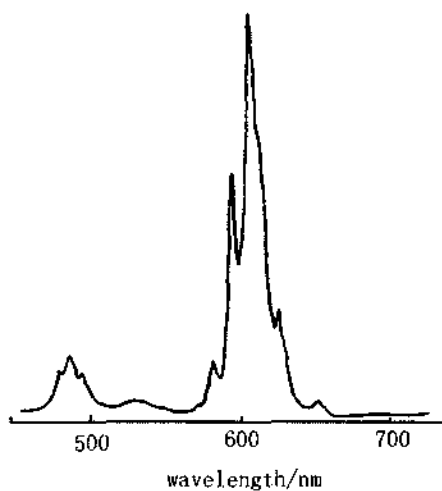
(—)  $\text{CaBPO}_5: \text{Pr}$  (— —)  $\text{SrBPO}_5: \text{Pr}$  (— · —)  $\text{BaBPO}_5: \text{Pr}$

Table 1. Fluorescent spectrum data of  $\text{MBPO}_5: 0.04\text{Pr}^{3+}$ .

Samples	Excitation spectra		Emission spectra	
	$\lambda_{\text{em}}/\text{nm}$	Wavelength/nm	$\lambda_{\text{ex}}/\text{nm}$	Wavelength/nm
$\text{CaBPO}_5:$ $\text{Pr}$	608	438, 472	438	490; 596, 608, 625
$\text{SrBPO}_5:$ $\text{Pr}$	607	441, 478	441	487; 593, 607, 622
$\text{BaBPO}_5:$ $\text{Pr}$	607	439, 477	439	496; 592, 607, 619

The first part consists of one weak emission peak at wavelengths about 490nm. The second part consists of three groups of emission peaks, which are at about 590nm, 607nm and 622nm respectively. In addition, broadband emission spectrum whose maximum is at 530nm is observed in  $\text{CaBPO}_5: 0.04\text{Pr}^{3+}$  phosphor under 438nm excitation. This is attributed to the  ${}^3\text{P}_1 \rightarrow {}^3\text{H}_5$  transitions in  $\text{Pr}^{3+}$  ion, as seen in Figure 4. The plot shown in Figure 5 illustrates the emission spectra of  $\text{BaBPO}_5: 0.04\text{Pr}^{3+}$  phosphor due to the  ${}^3\text{P}_0 \rightarrow {}^3\text{F}_2$  transition whose peak max wavelength is at 643nm.

We can see that the peak at 607nm is the strongest and its emission intensity is much higher than that of the others. The emission intensity of  $\text{SrBPO}_5: \text{Pr}$  is stronger than the others if the concentration of  $\text{Pr}^{3+}$  ion is same, and that of the peak at 607nm, generated by  $\text{Pr}^{3+}$  ion in  $\text{SrBPO}_5$ , is about 15 times as high as that at 490nm.



**Figure 4.** The emission spectra of  $\text{Pr}^{3+}$  in  $\text{CaBPO}_5$ :  $\text{Pr}$  phosphors.

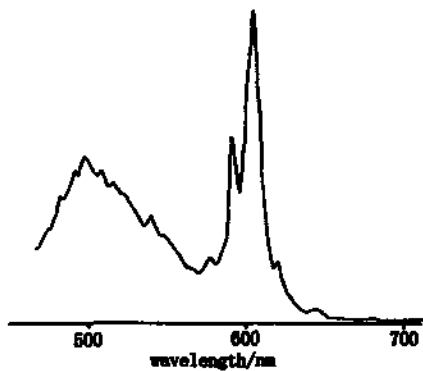


**Figure 5.** The emission spectra of  $\text{Pr}^{3+}$  in  $\text{BaBPO}_5$ :  $\text{Pr}$  phosphors.

### 3.3 The mechanism of luminescence

$\text{Pr}^{3+}$  ions metalepsis  $\text{M}^{2+}$  ions and form positive charge traps  $\text{Pr}_{\text{Ca}}^+$  [9]. These traps are luminescent centers. In addition, Pr is an element that leads to the easy formation of  $\text{Pr}^{4+}$  ion, so Pr may have already existed as mixed states of  $\text{Pr}^{3+}$  and  $\text{Pr}^{4+}$ .  $\text{Pr}^{3+}$  can possibly act as hole trapping centers while  $\text{Pr}^{4+}$  is known as electron trapping centers. The holes and electrons were trapped by defect centers, released by heat at room temperature, and recombined with electrons or holes trapped by other defect centers. The released energy, due to the recombination of holes and electrons, was transferred to the rare earth ions and excited the electrons at the ground state to an excited state of the rare earth ions, finally, leading to the characteristic rare earth ion emissions [10].

#### 4 Conclusions

$\text{MBPO}_5$ : Pr (M=Ca, Sr, Ba) phosphors can be synthesized in air atmosphere by solid-state reactions. The synthetic temperature and doped concentration influence on luminescence. The optimum experimental condition is that the synthetic temperature is 950°C and doped  $\text{Pr}^{3+}$  concentration is 4mol%.

The phosphors emission spectra of  $\text{Pr}^{3+}$  ion in  $\text{MBPO}_5$ : Pr (M=Ca, Sr, Ba) can be divided into two parts. The first part is a weak broad band at wavelengths about 490nm. The second part consists of a number of emission peaks and the peak at 607nm is the strongest. The emission intensity of  $\text{SrBPO}_5$ : Pr is stronger, and that of the peak at 607nm, generated by  $\text{Pr}^{3+}$  ion in  $\text{SrBPO}_5$ , is about 15 times as high as that at 490nm.

So we predict that the red emission can be made much stronger as long phosphorescence through use of additional phosphors showing a suitable absorption of the optical spectrum and emit light with longer wavelength.

#### 5 Acknowledgements

This work was supported by the Education Department of Guangdong Province.

#### References

1. C.R. Ronda, T. Jüstel, H. Nikol, Rare earth phosphors: fundamentals and applications, *J. Alloys. Compds.* 275-277 (1998) pp. 669-676.
2. Liu Yingliang, Meng Jianxin, Ding Hong, *The Development of Chinese Rare Earth Science and Technology*, 2000, Metallurgical Industry Press, 488490.
3. Liu Yingliang, Ding Hong, Research developments of long lasting phosphorescent materials, *Chinese J. Inorg. Chem.* 17 (2001) pp.181-187.
4. J.L Somerdijk, A. Bril, A.W. da Jager, *J. Lumin.* 1974, 8, 341.
5. J.L Somerdijk, A. Bril, A.W. da Jager, Luminescence of  $\text{Pr}^{3+}$ -activated fluorides, *J. Lumin.* 1974, 9, 288-296.
6. A.M. Srivastava, W.W. Beers, Luminescence of  $\text{Pr}^{3+}$  in  $\text{SrAl}_{12}\text{O}_{19}$ : Observation of two photon luminescence in oxide lattice, *J. Lumin.* 1997, 71, 285-290.
7. Lian Shi-xun, Lin Jian-hua, Su Mian-zeng, Syntheses and luminescent properties of  $\text{Ca}_{1-x}\text{Zn}_x\text{TiO}_3$ ;  $\text{Pr}^{3+}$ ,  $\text{R}^+$  ( $\text{R}^+ = \text{Li}^+, \text{Na}^+, \text{K}^+, \text{Rb}^+, \text{Cs}^+, \text{Ag}^+$ ), *J. Chinese Rare Earth Soc.* 19 (2001) pp. 602-605.
8. Z. Mazurak, A. Ratuszna, Ph. Daniel, Luminescence properties of  $\text{Pr}^{3+}$  and  $\text{Ce}^{3+}$  in  $\text{KCaf}_3$  single crystals, *J. Lumin.* 82 (1999) pp.163-171.
9. Vance E. R., Day R. A., Zhang Z., et al, Charge compensation in Gd-doped  $\text{CaTiO}_3$ , *J. Solid State Chem.* 124 (1996) pp. 77.
10. Jianrong Qiu, K. Miura, H. Inouye, et al, Femtosecond laser-induced three dimensional bright and long-lasting phosphorescence inside calcium aluminosilicate glasses doped with rare earth ions, *Appl. Phys.Lett.* 73 (1998) pp.1763-1765.

# PREPARATION, PATTERNING AND LUMINESCENCE PROPERTIES OF RARE EARTH-DOPED YVO<sub>4</sub> NANOCRYSTALLINE PHOSPHOR FILMS VIA SOL-GEL SOFT LITHOGRAPHY

J. LIN AND M. YU

*Key Laboratory of Rare Earth Chemistry and Physics, Changchun Institute of Applied Chemistry, Chinese Academy of Sciences, Changchun 130022, P. R. China.*

*E-mail: jlin@ns.ciac.jl.cn*

In this presentation, nanocrystalline YVO<sub>4</sub>:A (A=Eu<sup>3+</sup>, Dy<sup>3+</sup>, Sm<sup>3+</sup>, Er<sup>3+</sup>) phosphor films and their patterning were fabricated by a Pechini sol-gel process combined with a soft lithography (micro-molding in capillaries). XRD, FT-IR, AFM and optical microscope, absorption spectra, photoluminescence (PL) spectra as well as lifetimes were used to characterize the resulting films. The results of XRD indicated that the films began to crystallize at 400°C and the crystallinity increased with the increase of annealing temperatures. Transparent nonpatterned phosphor films were uniform and crack free, which mainly consisted of grains with an average size of 90nm. Patterned crystalline phosphor film bands with different widths (5-30 μm) were obtained. The doped rare earth ions (A) showed their characteristic emission in crystalline YVO<sub>4</sub> phosphor films due to an efficient energy transfer from vanadate groups to them. The Sm<sup>3+</sup> and Er<sup>3+</sup> ions also showed upconversion luminescence in YVO<sub>4</sub> film host. The optimum concentration for Eu<sup>3+</sup> was determined to be 7 mol% and those for Dy<sup>3+</sup>, Sm<sup>3+</sup>, Er<sup>3+</sup> were 2 mol% of Y<sup>3+</sup> in YVO<sub>4</sub> films, respectively.

## 1. Introduction

Displays with thin film phosphors have higher contrast and resolution, superior thermal conductivity as well as a high degree of uniformity and better adhesion. Efforts have been made to develop various kinds of luminescent films via sol-gel method in the past decade [1-3]. In most of the above cases, the sol-gel precursors used are metal alkoxides and/or organometallic compounds, which suffer from high cost, toxicity and difficulty in controlling the experimental processes. An alternative approach to form nanocrystalline thin film is the Pechini-type sol-gel process, which mainly employs the inorganic salts as precursors, citric acid as chelate ligand and polyethylene glycol (PEG) as crosslinking agent [4].

On the other hand, the patterning technologies of phosphor screens have a great effect on the resolution of flat panel display devices[5]. The current used patterning techniques for phosphor screens include electrophoretic deposition and screen printing based on photolithography, which needs the complicated and expensive photolithographic and etching equipment. Recently however, much attention has been paid to non-photolithographic patterning techniques collectively known as soft lithography, which have the potential of becoming versatile and low cost methods for creating micrometer and sub-micrometer size structures [6].

So far neither work of phosphor films via the Pechini-type sol-gel process nor their direct patterning via soft lithography have been reported in literature. Yttrium vanadate (YVO<sub>4</sub>) has been shown to be a useful host lattice for rare earth ions to produce phosphors emitting a variety of colors[7]. In this paper, we report a Pechini sol-gel synthesis of the nanocrystalline YVO<sub>4</sub>:A (A=Eu<sup>3+</sup>, Dy<sup>3+</sup>, Sm<sup>3+</sup>, Er<sup>3+</sup> ) thin phosphor films and their patterning via soft lithography (micro-molding in capillaries) as well as their

photoluminescence properties.

## 2. Experimental Section

Non-patterned thin-films of  $\text{YVO}_4$ : A ( $\text{A} = \text{Eu}^{3+}, \text{Dy}^{3+}, \text{Sm}^{3+}, \text{Er}^{3+}$ ) phosphor samples were prepared by a Pechini sol-gel and dip-coating method. The doping concentration of the rare earth ion (A) was 0.1-12 mol % that of  $\text{Y}^{3+}$  in  $\text{YVO}_4$  host. Stoichiometric amount of  $\text{Y}_2\text{O}_3$  (99.99%),  $\text{Eu}_2\text{O}_3$  (99.99%),  $\text{Dy}_2\text{O}_3$  (99.95%),  $\text{Sm}_2\text{O}_3$  (99.9%),  $\text{Er}_2\text{O}_3$  (99.9%) and  $\text{NH}_4\text{VO}_3$  (99%, A. R.) were dissolved in dilute  $\text{HNO}_3$  (A. R.), and then were mixed with a water-ethanol (v/v= 1:7) solution containing citric acid (A. R.) as chelating agent for the metal ions. The molar ratio of metal ions to citric acid was 1:2. Certain amount of polyethylene glycol (PEG, molecular weight = 10000, A. R.) was added as cross-linking agent. The solution was stirred for 1h to form a sol and then dip-coated on thoroughly cleaned silica glass substrates at a speed of 0.2cm/s. The coatings were dried at 100°C for 1h immediately. Then the dried films were annealed to the desired temperature (300-800°C) with a heating rate of 1°C /min and held there for 2h in air.

The patterning of the phosphor films was carried out by soft lithography as described previously [6]. First, polydimethylsiloxane (PDMS) stamp modes were fabricated by casting PDMS on masters having desired patterns. The PDMS modes were placed in conformal contact with thoroughly cleaned silicon wafer substrates. The channels of the mode thus formed capillaries with the silicon wafer substrate. The above sol for dip-coating was then dropped at the open end with a transfer pipette. The capillary force made the sol flow into the mold. Then the modes and substrates were dried at 100°C overnight. After careful removing the modes, the resulted patterned gel films were heated to 700°C with a heating rate of 1°C / min and held there for 2h in air.

The X-ray diffraction (XRD) of the film and powder samples was examined on a Rigaku-Dmax 2500 diffractometer using  $\text{Cu K}\alpha$  radiation ( $\lambda=0.15405\text{nm}$ ). The FT-IR spectra were measured with Perking-Elmer 580B infrared spectrophotometer with the KBr pellet technique. The thickness of the transparent non-patterned crystalline films was measured on a AUEL-III automatic laser ellipsometer. The morphology of the crystalline film sample was inspected using atomic force microscope (AFM, Seiko) with a taping mode. Patterned film pictures were taken on an Leica DMLP optical microscope. The UV/Vis absorption spectra were measured on a TU-1901 spectrophotometer. The excitation and emission spectra were taken on a SPEX FL-2T2 spectrofluorimeter equipped with a 450W xenon lamp as the excitation source. Luminescence lifetimes were measured with a SPEX 1934D phosphorimeter using a 7 W pulse xenon lamp as the excitation source with the pulse width of 3μs. All the measurements were performed at room temperature (RT).

## 3. Results and Discussion

### 3.1 Formation process and structures of the phosphor films

Fig. 1 shows the XRD profiles of the films annealed from 300 to 700°C (a-d) and that of the powder annealed at 500°C (e) as a comparison. For the film annealed at 300°C, no diffraction peak is observed except for the broad band at  $2\theta=22.02^\circ$ , which is ascribed to quartz glass substrate. This indicates that the film remains amorphous below this temperature. For the sample fired at 400°C, two weak and broad peaks at  $2\theta=24.92^\circ$  and

$33.48^\circ$  due to the (200) and (112) reflections of  $\text{YVO}_4$  are present, suggesting the starting of crystallization at this stage. After annealing at  $500^\circ\text{C}$  and  $700^\circ\text{C}$ , other diffraction peaks belonging to the crystalline  $\text{YVO}_4$  have been observed clearly (JCPDS Card 17-341). All the diffraction peaks due to  $\text{YVO}_4$  can be seen more obviously in the XRD pattern of the powder annealed at  $500^\circ\text{C}$ , as shown in Fig. 1(e). No second phase is detected. Note that the diffraction peaks of  $\text{YVO}_4$  film are a little broader and higher degree shift than the counterparts of  $\text{YVO}_4$  powder, indicating that the size of the crystalline grains in the film is smaller than that in the powder. In fact, the calculated crystal cell parameters ( $a=0.702\text{nm}$ ,  $c=0.619\text{nm}$ ,  $V=0.305\text{nm}^3$ ) for crystalline  $\text{YVO}_4$  in the film are a little smaller than those ( $a=0.725\text{nm}$ ,  $c=0.629\text{nm}$ ,  $V=0.330\text{nm}^3$ ) in the powder. This may be caused by slightly different crystallization behaviors between the film and powder samples. Furthermore, it can be seen clearly that the  $\text{YVO}_4$  film crystallized with (200) preferred orientation on the silica glass substrate, as observed previously [8].

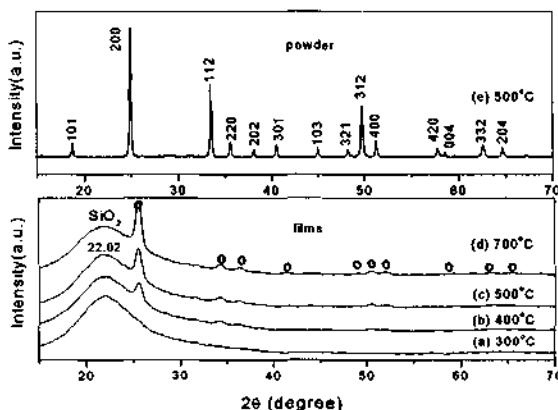


Figure 1. X-ray diffraction patterns for  $\text{YVO}_4:0.04\text{Eu}$  films and powder annealed at different temperatures.

The FT-IR spectra of the crystalline  $\text{YVO}_4$  films ( $500\text{-}700^\circ\text{C}$ ) show a very strong absorption band at  $823\text{cm}^{-1}$  and a weak band at  $450\text{cm}^{-1}$  were observed, which are attributed to the V-O stretching vibration and bending vibration from  $\text{VO}_4^{3-}$  groups, respectively. A weak broad band from  $500\text{cm}^{-1}$  to  $700\text{cm}^{-1}$  due to Y-O stretching can also be detected in the FT-IR spectra.

### 3.2 AFM and optical micrographs

The  $700^\circ\text{C}$  annealed transparent film (non-patterned, dip-coating) had a thickness of  $150\text{nm}$ . The AFM image of the transparent film annealed at  $700^\circ\text{C}$  is shown in Fig. 2. It is known from planar image that the film, which is uniform and crack-free, mainly consists of closely packed fine particles with an average grain size of  $90\text{nm}$  with a RMS roughness of  $4.55\text{nm}$ .

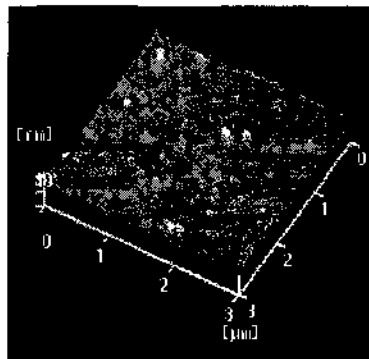


Figure 2. AFM images of the transparent  $\text{YVO}_4:0.04\text{Eu}$  film annealed at  $700^\circ\text{C}$ .

The patterning of the phosphor films was performed in  $\text{Eu}^{3+}$ -doped  $\text{YVO}_4$  system. Fig. 3a shows optical micrographs for the patterned structures of crystalline film annealed at  $700^\circ\text{C}$ . The actual width of the crystalline film band derived from the mode with  $21\mu\text{m}$  wide channel is only about  $14\mu\text{m}$ , i.e., a 30-40% shrinkage in width has occurred after crystallization. The edge lines between the film band and space caused by the shrinkage can also be seen clearly. This is not surprising, for it is well known that the evaporation and pyrolysis of organic compounds in a gel is accompanied by significant shrinkage. Additionally, owing to the shrinkage the surface of the crystalline film bands is not as smooth as that of gel film bands. Even narrow crystalline film bands with  $7\mu\text{m}$  width and space have been obtained, and no obvious defects can be detected, as shown in Fig. 3b. The crystalline patterned  $\text{YVO}_4:\text{Eu}$  films shows a strong red emission under the irradiation of UV light, and the emission intensity seems to increase with decreasing the width of film bands.

### 3.3 Optical properties

The patterned and non-patterned phosphor films show similar optical properties. So all the characterizations for the optical properties were performed on the non-patterned films due to their relatively easy availability.

Fig. 4 displays the absorption spectra for  $\text{YVO}_4$  (a) and  $\text{YVO}_4:0.02\text{Dy}$  (c), and PL excitation (b) and emission (d) spectra for  $\text{YVO}_4:0.02\text{Dy}$  as well as PL emission spectrum (e) for  $\text{YVO}_4:0.04\text{Eu}$ . A strong absorption band with maximum values at  $276\text{nm}$  is observed for both  $\text{YVO}_4$  and  $\text{YVO}_4:0.02\text{Dy}$  films. Obviously, this band is ascribed to a charge transfer from the oxygen ligands to the central vanadium atom inside the  $\text{VO}_4^{3-}$  ion. The  $700^\circ\text{C}$  annealed  $\text{YVO}_4:0.02\text{Dy}$  transparent film shows a strong yellow emission (close to white) under UV excitation. The excitation spectrum (Fig. 4b) consists of an intense band with a maximum at  $276\text{nm}$  due to the  $\text{VO}_4^{3-}$  absorption, which agrees well the absorption spectra (Fig. 4a, c). Excitation into the vanadate group at  $276\text{nm}$  yields the emission spectrum (Fig. 4d) which contains exclusively the characteristic transition lines of  $\text{Dy}^{3+}$ , i.e.,  $^4\text{F}_{9/2}-^6\text{H}_{15/2}$  ( $482\text{nm}$ , blue),  $^4\text{F}_{9/2}-^6\text{H}_{13/2}$  ( $573\text{nm}$ , yellow) and  $^4\text{F}_{9/2}-^6\text{H}_{11/2}$  ( $664\text{nm}$ , red). No emission from  $\text{VO}_4^{3-}$  is detected, indicating an efficient energy transfer from  $\text{VO}_4^{3-}$  to  $\text{Dy}^{3+}$  in the phosphor films. The same situation holds for that of crystalline  $\text{YVO}_4:0.04\text{Eu}$  film, which shows a strong red emission under UV excitation. The

excitation spectrum monitored with 618nm emission of Eu<sup>3+</sup> (<sup>5</sup>D<sub>0</sub>-<sup>7</sup>F<sub>2</sub>) is similar to that of YVO<sub>4</sub>:0.02Dy film (Fig. 4b). In this emission spectrum (Fig. 4e), not only the characteristic transition lines from the lowest excited <sup>5</sup>D<sub>0</sub> level of Eu<sup>3+</sup> are observed, but also those from higher energy levels (<sup>5</sup>D<sub>1</sub>, <sup>5</sup>D<sub>2</sub> and <sup>5</sup>D<sub>3</sub>) of Eu<sup>3+</sup> are detected with a very weak intensity. The locations of the emission lines of Eu<sup>3+</sup> and their assignments are indicated in the figure. Obviously, the strong emission of Eu<sup>3+</sup> is also due to an efficient energy transfer from the VO<sub>4</sub><sup>3-</sup> group to the Eu<sup>3+</sup> in YVO<sub>4</sub>:0.04Eu films.

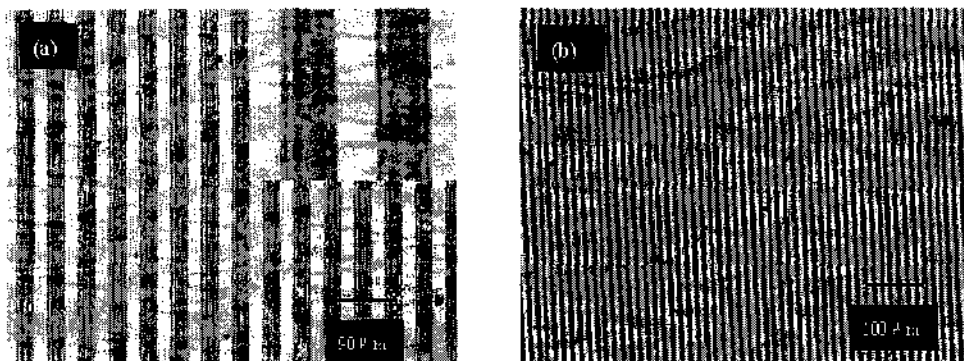


Figure 3. Optical micrographs of the patterned YVO<sub>4</sub>:0.04Eu phosphor films annealed at 700°C.

The excitation and absorption spectra for crystalline YVO<sub>4</sub>:Sm and YVO<sub>4</sub>:Er films are very similar to those in Fig. 4 (a)(b)(c), i.e., only a strong band with a maximum at 276nm due to VO<sub>4</sub><sup>3-</sup> group has been observed. Excitation into the vanadate group at 276nm yields the characteristic red-orange emission of Sm<sup>3+</sup> at 567nm (<sup>4</sup>G<sub>5/2</sub>-<sup>6</sup>H<sub>5/2</sub>), 605nm(<sup>4</sup>G<sub>5/2</sub>-<sup>6</sup>H<sub>7/2</sub>), 649nm (<sup>4</sup>G<sub>5/2</sub>-<sup>6</sup>H<sub>9/2</sub>) and green emission of Er<sup>3+</sup> at 525nm (<sup>2</sup>H<sub>11/2</sub>-<sup>4</sup>I<sub>15/2</sub>), 545nm, 553nm (<sup>4</sup>S<sub>3/2</sub>-<sup>4</sup>I<sub>15/2</sub>), respectively, as shown in Fig. 5(a). This indicates that, similarly to the situations for Eu<sup>3+</sup> and Dy<sup>3+</sup>, an efficient energy transfer also occurs from the VO<sub>4</sub><sup>3-</sup> to Sm<sup>3+</sup> and Er<sup>3+</sup> in YVO<sub>4</sub> film.

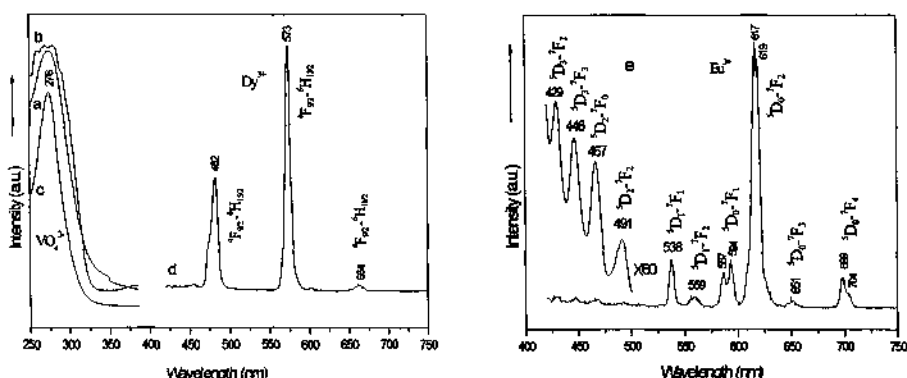
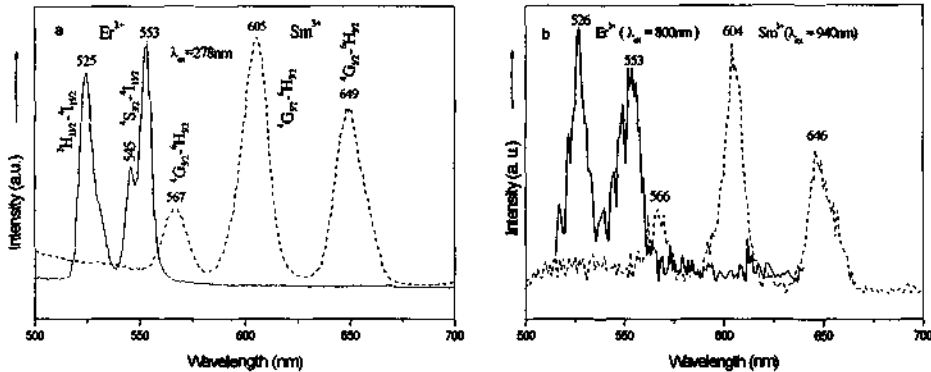


Figure 4. Absorption spectrum for YVO<sub>4</sub> film (a), excitation (b,  $\lambda_{\text{em}} = 573\text{nm}$ ), absorption (c) and emission (d,  $\lambda_{\text{ex}} = 276\text{nm}$ ) spectra for YVO<sub>4</sub>:0.02Dy film and emission spectrum for YVO<sub>4</sub>:0.04Eu film (e,  $\lambda_{\text{ex}} = 276\text{nm}$ ).



**Figure 5.** Downconversion (a) and upconversion (b) emission spectra of YVO<sub>4</sub>:0.02Sm and YVO<sub>4</sub>:0.02Er films.

Furthermore, the upconverted luminescence phenomena of Er<sup>3+</sup> and Sm<sup>3+</sup> have been observed in YVO<sub>4</sub> film. Fig. 5(b) shows the upconverted emission spectrum of Er<sup>3+</sup> excited with 800nm and that of Sm<sup>3+</sup> excited with 940nm. The characteristic green emission (520-560nm) of Er<sup>3+</sup> and red emission (560-670nm) of Sm<sup>3+</sup> have been clearly observed in these emission spectra. The Er<sup>3+</sup> is well known rare earth ion having upconversion luminescence properties, and the green upconverted emission of Er<sup>3+</sup> in YVO<sub>4</sub> crystals has been reported, whose mechanism has been well established[9]. It is the first observation for the upconversion phenomenon of Sm<sup>3+</sup> in YVO<sub>4</sub> (film) host. Under infra red light 940nm excitation, the <sup>4</sup>G<sub>5/2</sub> excited state of Sm<sup>3+</sup> can be populated by two possible approaches: the excited state absorption (EAS) and energy transfer (ET) processes. For the EAS process, after a first excitation to the <sup>6</sup>F<sub>11/2</sub> level, a second photon is absorbed by the same ion, exciting it to <sup>4</sup>I<sub>11/2</sub> state, i.e., <sup>6</sup>H<sub>5/2</sub> → <sup>6</sup>F<sub>11/2</sub> → <sup>4</sup>I<sub>11/2</sub>; for the ET process, one of the two coupled Sm<sup>3+</sup>, simultaneously excited through the ground state absorption by infra-red photons to the <sup>6</sup>F<sub>11/2</sub> state, transfer its energy to the neighboring ion leaving it in the higher excited states (<sup>4</sup>I<sub>11/2</sub> etc.). Both approaches excite the Sm<sup>3+</sup> to <sup>4</sup>I<sub>11/2</sub> (or <sup>4</sup>G<sub>7/2</sub>, <sup>4</sup>F<sub>3/2</sub>) state, from which <sup>4</sup>G<sub>5/2</sub> energy level is populated by multiphonon de-excitation. As a result, anti-stokes emissions from <sup>4</sup>G<sub>5/2</sub> excited state to the ground states (<sup>6</sup>H<sub>5/2</sub>, <sup>6</sup>H<sub>7/2</sub>, <sup>6</sup>H<sub>9/2</sub>) are observed. In view of the short lifetime (the order of 10ns) of <sup>6</sup>F<sub>11/2</sub> level of Sm<sup>3+</sup>, EAS transitions from this level are not likely to occur. So the most probable mechanism for the upconversion luminescence of Sm<sup>3+</sup> in YVO<sub>4</sub> film host is energy transfer between two Sm<sup>3+</sup> ions.

By varying the content of the rare earth ions A (A=Eu<sup>3+</sup>, Dy<sup>3+</sup>, Sm<sup>3+</sup>, Er<sup>3+</sup>) in Y<sub>1-x</sub>A<sub>x</sub>VO<sub>4</sub> films, we determined the compositions with the highest PL emission intensity. It is found that the PL emission intensity of Eu<sup>3+</sup>, Dy<sup>3+</sup>, Sm<sup>3+</sup>, Er<sup>3+</sup> increases with the increase of their concentrations (x) first, reaching a maximum value at x = 7mol% for Eu<sup>3+</sup> and at x = 2mol% for Dy<sup>3+</sup>, Sm<sup>3+</sup>, Er<sup>3+</sup> respectively, and then decrease with increasing their contents (x) due to the concentration quenching. Thus the optimum concentration for Eu<sup>3+</sup> is 7mol% and those for Dy<sup>3+</sup>, Sm<sup>3+</sup>, Er<sup>3+</sup> are 2mol% in YVO<sub>4</sub> films, respectively. Note that the optimum concentration of Eu<sup>3+</sup> is determined to be 7mol% in both the 500°C and 700°C annealed samples, indicating that the optimum concentration is independent of the annealing temperature. Except for the Er<sup>3+</sup>, the optimum concentrations for Eu<sup>3+</sup>, Dy<sup>3+</sup>, Sm<sup>3+</sup> agree well with those derived from the change of their lifetimes as a function of their

doping concentration ( $x$ ) in  $\text{YVO}_4$  films. The lifetimes of  $\text{Er}^{3+}$  in  $\text{Y}_{1-x}\text{VO}_4$ : $x\text{Er}$  films decrease monotonously with increasing its concentration ( $x$ ) in the studied concentration range although its emission intensity shows a maximum value. A similar situation has been observed before for  $\text{Er}^{3+}$  in  $\text{BaTiO}_3$  films[9]. Because the cross-relaxation processes in close  $\text{Dy}^{3+}$ - $\text{Dy}^{3+}$ ,  $\text{Sm}^{3+}$ - $\text{Sm}^{3+}$  and  $\text{Er}^{3+}$ - $\text{Er}^{3+}$  pairs play an important role in their luminescence quenching, their optimum concentrations are much lower than that of  $\text{Eu}^{3+}$  in the same host lattice, as observed in the current  $\text{YVO}_4$  films. In addition, the typical nonlinear variation of the PL intensity provides further evidence that the film sample consists of doped particles and not of a mixture of  $\text{AVO}_4$  ( $A=\text{Eu, Dy, Sm, Er}$ ) and  $\text{YVO}_4$  particles. In the latter case the PL intensity is expected to increase steadily with increasing the rare earth ion ( $A$ ) concentration.

#### 4. Conclusion

Nanocrystalline  $\text{YVO}_4$ :  $A$  ( $A=\text{Eu}^{3+}$ ,  $\text{Dy}^{3+}$ ,  $\text{Sm}^{3+}$ ,  $\text{Er}^{3+}$ ) phosphor films were successfully prepared by the Pechini sol-gel process using the cheap and nontoxic inorganic compounds as main precursors. These phosphor films can be patterned into ordered bands with different widths (5-30  $\mu\text{m}$ ) by soft lithography technique (micro-molding in capillaries). The patterned phosphor film bands present significant shrinkage during heat treatment process. Upon excitation into the  $\text{VO}_4^{3-}$  group at 276nm, the rare earth ions  $\text{Eu}^{3+}$ ,  $\text{Dy}^{3+}$ ,  $\text{Sm}^{3+}$  and  $\text{Er}^{3+}$  show their characteristic red ( $^5\text{D}_0$ - $^7\text{F}_2$ ), yellow ( $^4\text{F}_{9/2}$ - $^6\text{H}_{13/2}$ ), orange ( $^4\text{G}_{5/2}$ - $^6\text{H}_{7/2}$ ) and green ( $^4\text{S}_{3/2}$ - $^4\text{I}_{15/2}$ ) strong emissions in crystalline  $\text{YVO}_4$  phosphor films, respectively, due to an efficient energy transfer from  $\text{VO}_4^{3-}$  group to the rare earth ions. The  $\text{Sm}^{3+}$  and  $\text{Er}^{3+}$  ions have also shown upconversion luminescence properties in  $\text{YVO}_4$  film host under infra red excitation at 940nm and 800nm, respectively. The current methods can be extended to prepare various other phosphor films and their patterning.

#### 5. Acknowledgements

This project was financially supported by the foundation of "Bairen Jihua" of Chinese Academy of Sciences, the Outstanding Youth Fund of Jilin Province, Personnel and Educational Ministry of China, Nanometer Center of Changchun Institute of Applied Chemistry, Chinese Academy of Sciences.

#### References

- Choe J. Y., Ravichandran D., Biomquist S. M., Morton D. C., Kirchner K. W., Ervin M. H. and Lee U., Alkoxy sol-gel derived  $\text{Y}_{3(1-x)}\text{Al}_5\text{O}_{12}\text{:Tbx}$  thin films as efficient cathodoluminescent phosphors, *Appl. Phys. Lett.* **78**(2001) pp. 3800-3802.
- Rabinovich E. M., Shmulovich J., Fratello V. J. and Kopyov N. J., Sol-gel deposition of  $\text{Tb}^{3+}\text{:Y}_2\text{SiO}_5$  cathodoluminescent layers, *Am. Cer. Soc. Bull.* **6**(1987) pp. 1505-1509.
- Ravichandran D., Roy R., Chakhovskoi A. G., Hunt C. E., White W. B. and Erdei S., Fabrication of  $\text{Y}_3\text{Al}_5\text{O}_{12}\text{:Eu}$  thin films and powders for field emission display

- application, *J. Lumin.* **71**(1997) pp. 291-297.
- 4. Zhang Y. W., Yang Y., Jin S., Tian S. J., Li G. B., Jia J. T., Liao C. S. and Yan C. H., Sol-gel fabrication and electrical properties of nanocrystalline  $(RE_2O_3)_{0.08}(ZrO_2)_{0.92}$  ( $RE=Sc, Y$ ) thin films, *Chem. Mater.*, **13**(2001) pp. 372-378.
  - 5. Jang J. E., Gwak J. -H., Jin Y. W., Lee S. J., Park S. H., Jung J. E., Lee N. S and Kim J. M., High resolution phosphor screening method for full-color field emission display application, *J. Vac. Sci. Tech. B* **18**(2000) pp. 1106-1110.
  - 6. Seraji S., Wu Y., Jewell-Larson N. E., Forbess M. J., Limmer S. J., Chou T. P. and Cao G., Patterned microstructure of sol-gel derived complex oxides using soft lithography, *Adv. Mater.* **12**(2000) pp. 1421-1424.
  - 7. Huignard A., Gacoin T. and Boilot J. P. , Synthesis and luminescence properties of colloidal  $YVO_4:Eu$  phosphors, *Chem. Mater.* **12**(2000) pp. 1090-1094.
  - 8. Hirano S., Yogo T., Kikuta K., Sakamoto W. and Koganei H., Synthesis of Nd:YVO<sub>4</sub> thin films by sol-gel method, *J. Am. Ceram. Soc.* **79**(1996) pp. 3041-3044.
  - 9. Zhang H. X., Kam C. H., Zhou Y., Han X. Q., Buddhudu S., Xiang Q., Lam Y. L. and Chan Y. C., Green upconversion luminescence in  $Er^{3+}:BaTiO_3$  films, *Appl. Phys. Lett.* **77**(2000) pp. 609-611.

# COVALENT GRAFTING OF LUMINESCENT RARE EARTH COMPLEX ONTO MCM-41 BY POSTSYNTHESIS

F. Y. LIU, L. S. FU, J. WANG, H. R. LI AND H. J. ZHANG\*

*Key Laboratory of Rare Earth Chemistry and Physics, Changchun Institute of Applied Chemistry,  
Chinese Academy of Sciences, Changchun 130022, P. R. China  
E-mail: hongjie@ciac.jl.cn*

New luminescent hybrid mesoporous material was prepared by covalent anchoring rare earth complex onto MCM-41 by a postsynthesis approach. The monomer (referred to here as PABI) which plays double roles, i.e., as a ligand for lanthanide ion and as an organic functional molecule to modify MCM-41 is synthesized and characterized by  $^1\text{H}$  NMR and MS. The fluorescence spectra show clearly that the hybrid mesoporous material possesses excellent luminescence characteristics. The hybrid mesoporous material retains the structure of MCM-41 after modification.

## 1. Introduction

Since the exciting discovery of the novel class of MCM-41 mesoporous molecular sieves by Mobil researchers [1], much attention has been focused on tailoring the chemical composition of these materials for application in catalysis, adsorption, sensors and host materials for large guest molecules. One approach to modify the surface of MCM-41 is postsynthesis grafting. Many organic functional groups such as amino groups, thiol groups have been successfully grafted onto MCM-41. Mann and co-workers first reported covalent coupling of an organic chromophore into MCM-41 by template-directed co-condensation [2]. Ganschow et al. developed a technique for anchoring dye molecules onto MCM-41 using microwave-assisted hydrothermal co-condensation [3]. Since dye molecules were covalently linked to the framework of MCM-41, they can be dispersed and isolated from each other, which for some systems for example with rhodamine derivatives, should minimize intermolecular quenching of fluorescence properties.

As well-known excellent luminescent materials, rare earth organic complexes have been widely used in the field of optical materials because their photoluminescence exhibits high quantum yields and very sharp spectral bands [4]. The embedding of rare earth organic complexes in silica gels by using the sol-gel process has been much investigated [5-7]. The resulting organic-inorganic hybrid optical materials were shown to exhibit good luminescence properties. However, up to now and to the best of our knowledge, very few paper concerning the preparation of mesoporous materials by covalent anchoring rare earth complexes onto the walls of MCM-41 has been reported [8].

In this work, we present a new silylated ligand, which plays double roles, i.e., as a ligand for lanthanide ion and as an organic functional molecule to modify MCM-41. The luminescent mesoporous material is obtained first by grafting the silylated ligand to MCM-41, then coordinated with terbium chloride in ethanol. The luminescent properties of the hybrid mesoporous material will be described.

## 2. Experimental Section

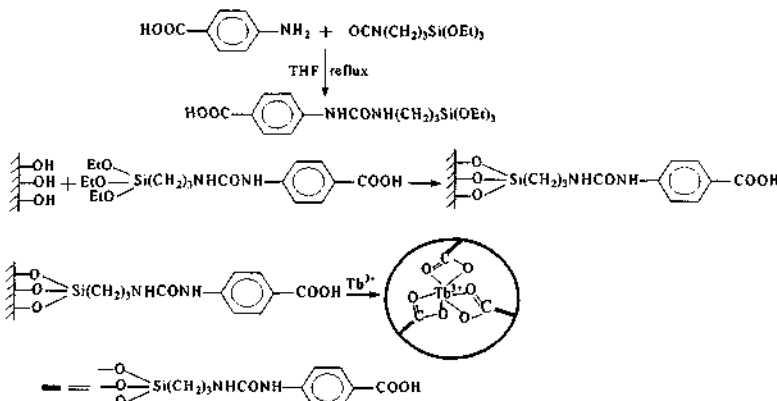
<sup>1</sup>H NMR spectra were recorded on a Bruker AC 400 spectrometer with tetramethylsilane (TMS) as internal reference. Infrared spectra were obtained as KBr pellets on a Perkin-Elmer 580 B FT-IR spectrometer. Electrospray (ES) mass spectra were recorded on an LCQ Finnigan Mat spectrometer. The excitation and emission spectra were obtained on a SPEX FL-2T2 spectrofluorimeter with slit at 0.8 mm and equipped with a 450 W lamp as the excitation source. Luminescence lifetimes were measured with a SPEX 1934D phosphorimeter using a 7 W xenon lamp as the excitation source with the pulse width at 3  $\mu$ s. Powder X-ray diffraction patterns were recorded on Rigaku D/Max-IIIB diffractometer using Cu-K $\alpha$  radiation.

Terbium oxide ( $Tb_4O_7$ , 99.99%) were obtained from Yue Long Chemical Plant (Shanghai, China). *p*-aminobenzoic acid (99.0%) were purchased from Beijing Chemical Company (Beijing, China). Isocyanatopropyltriethoxysilane (ICPTES) was obtained from Aldrich (USA).

PABI was prepared as follows: 5 mmol of *p*-aminobenzoic acid was dissolved in 15 ml of dry tetrahydrofuran (THF). To this solution 7.5 mmol of ICPTES was then added. The resulting solution was refluxed for 8 h. Then white precipitate was produced when 50 ml of petroleum ether was added to the solution. The precipitate was filtrated and washed with petroleum ether to remove the excess of ICPTES. Finally, the precipitate was dried on a vacuum line to get 1.8 g of PABI in a 95% yield.

<sup>1</sup>H NMR (DMSO, 400 MHz)  $\delta$  (ppm) 12.45 (1H, bs, COOH), 8.79 (1H, s, NH), 7.78 (2H, d, ArH,  $J=8.8$  Hz), 7.47 (2H, d, ArH,  $J=8.8$  Hz), 6.31 (1H, t, NH,  $J=5.6$  Hz), 3.75 (6H, q, OCH<sub>2</sub>,  $J=6.8$  Hz), 3.07 (2H, q, NCH<sub>2</sub>,  $J=6.4$  Hz), 1.48 (2H, quint, CH<sub>2</sub>,  $J=8.0$  Hz), 1.15 (9H, t, CH<sub>3</sub>(OEt),  $J=6.8$  Hz), 0.56 (2H, t, SiCH<sub>2</sub>,  $J=6.8$  Hz). MS (ES) m/e = 407.4(M+Na<sup>+</sup>)

The hybrid mesoporous material was prepared as follows: first, MCM-41 was modified by PABI by mixing PABI with MCM-41 in THF for 12 h, the solid was obtained by filtered the mixture. The product was designated as p-MCM-41. Then the complexation reaction was carried out by mixing p-MCM-41 with Tb<sup>3+</sup> ion in ethanol under stirring. The white solid was filtered after 24 h and washed by ethanol. The hybrid material was designated as p-Tb-MCM-41 (see Scheme 1).



Scheme 1. Preparation of luminescent hybrid mesoporous material.

### 3. Results and Discussion

Powder X-ray diffraction patterns for calcined pure MCM-41, p-MCM41 and p-tb-MCM-41 are shown in Fig. 1. They all exhibited three peaks characteristic of the MCM-41 structure that is known to consist of hexagonal arrays of uniform channel-like pores. An intensive peak observed at  $2\theta=2.1-2.4$  for these samples corresponds to the (100) diffraction peak. The XRD pattern is in very good agreement with that reported by Kresge et al. However, after MCM-41 was modified with monomer PABI and  $Tb^{3+}$ , the intensity of the (100) diffraction peaks of p-MCM-41, p-tb-MCM-41 are lower and broader than that of MCM-41, indicating that the mesoporous structures of MCM-41 become less uniform upon the introduction of monomer PABI and  $Tb^{3+}$  ion.

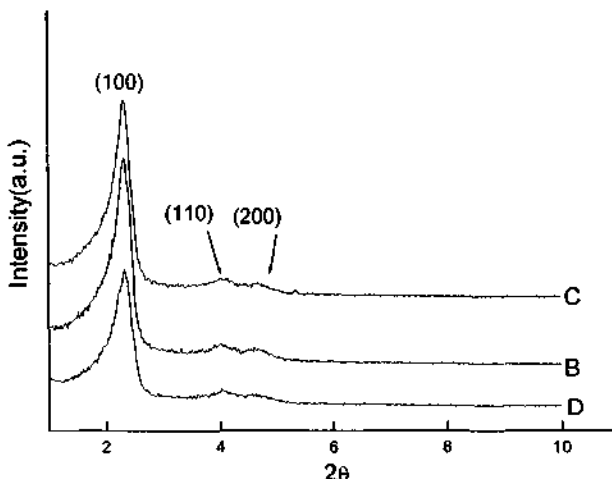


**Figure 1.** X-ray diffraction patterns of B) pure MCM-41, C) p-MCM-41, D) p-tb-MCM-41.

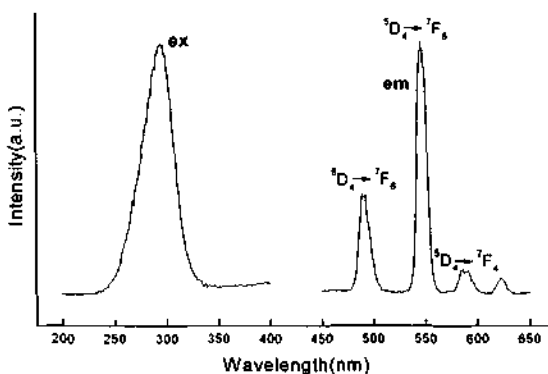


**Figure 2.** Fluorescence spectra of hybrid mesoporous material.

FTIR experiments were performed on monomer PABI as well as hybrid mesoporous material. The  $\nu(\text{Si-C})$  and  $\nu(\text{Si-OEt})$  absorption bands characteristic of trialkoxysilyl functions appear at 1193, 1080 cm<sup>-1</sup>, respectively. The sharp bands located at 1652, 1565, 1592 cm<sup>-1</sup> corresponding to urea NH-CO-NH function give strong evidence that ICPTES has been successfully grafted on to *p*-aminobenzoic acid. The stretching  $\nu(\text{C=O})$  of carboxylic acid function was detected at 1689 cm<sup>-1</sup>. After complexation with Tb<sup>3+</sup> ion, the characteristic stretching  $\nu(\text{C=O})$  of carboxylic acid function disappears, and new absorption bands appear at 1556 cm<sup>-1</sup> ( $\nu_{\text{as}}\text{COO}^-$ ) and 1417 cm<sup>-1</sup> ( $\nu_s\text{COO}^-$ ) that result from the formation of coordinated bonds between the carboxylic group and the Tb<sup>3+</sup> ion. Fig.2 shows the fluorescence spectra of hybrid mesoporous material. The excitation spectrum was recorded by monitoring the  $^5\text{D}_4 \rightarrow ^7\text{F}_5$  transition at 545 nm. The spectrum is dominated by a broad excitation band centered at 292 nm, which is assigned to the absorption of the ligand. Emission spectrum is recorded at room temperature by direct excitation of the ligand at 292 nm. A strong green emission was observed in their emission spectra, which indicated that the surrounding aromatic ligand absorbed energy and transferred energy to the chelated Tb<sup>3+</sup> ion. The line-emissions of the hybrid thin films of Tb<sup>3+</sup> were assigned to the transitions from the  $^5\text{D}_4$  level to the  $^7\text{F}_j$  ( $j = 6, 5, 4, 3$ ) levels at 485, 545, 584, 621 nm, respectively, with  $^5\text{D}_4 \rightarrow ^7\text{F}_5$  emission as the most prominent band. From the spectrum, both strong emission intensity and narrow half emission width (below 15 nm) were observed, showing the excellent luminescence characteristics of the resulting hybrid mesoporous material.

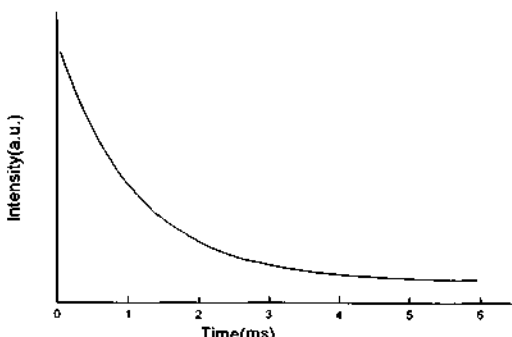


Figure 3. The decay curve of the hybrid mesoporous material with Tb<sup>3+</sup>.

Fig.3 presents the decay curve of the hybrid mesoporous material with Tb<sup>3+</sup>. The decay curve was singly exponential, showing that the Tb<sup>3+</sup> ion lies in the same average chemical environment. The resulting lifetime is in the millisecond range (1.2 ms). However, it appears that the lifetime in hybrid material is slightly lower than those in the organic complexes. This can be attributed to a possible quenching by silanol groups of MCM-41.

#### 4. Conclusion

We have synthesized a new monomer PABI, which acts a ligand for lanthanide ion and as an organic functional molecule to modify MCM-41 by grafting *p*-aminobenzoic acid to ICPTES. Luminescent hybrid mesoporous material has been prepared and characterized by XRD, FTIR. Fluorescence spectra show clearly that the hybrid mesoporous material possesses excellent luminescence characteristics.

#### 5. Acknowledgements

We are grateful to the "973"-National Key Project for Fundamental Research of Rare Earth Functional Materials of China, National Natural Science Foundation of China (No. 29731010, No. 29971030)

#### References

1. Kresge C. T., Leonowicz M. E., Roth W. J., Vartuli, J. C. and Beck, J. C. Ordered mesoporous molecular sieves synthesized by a liquid-crystal template mechanism, *Nature*, **359** (1992) pp. 710-712.
2. Fowler C. E., Lebeau B. and Mann S. Covalent coupling of an organic chromophore into functionalized MCM-41 mesophases by template-directed co-condensation, *Chem. Commun.* (1998) pp. 1825-1826.
3. Ganschow M., Wark M., Wohrle D. and Schulz-Ekloff G. Anchoring of functional dye molecules in MCM-41 by microwave-assisted hydrothermal co-condensation, *Angew. Chem. Int. Ed.*, **39** (2000) pp.161-163.
4. Capecchi S., Renault O., Moon D.Y., Halim M., Etchells M., Dobson P. J., Salata O. V. and Christou V., High-efficient organic electroluminescent devices using an organoterbium emitter, *Adv. Mater.* **12** (2000) pp. 1591-1594.
5. Fu L., Zhang H., Wang S., Meng Q., Yang K. and Ni J. Preparation and luminescence properties of the ternary europium complex incorporated into an inorganic/polymer matrix by a sol-gel method, *J. Sol-Gel Sci. Technol.* **15** (1999) pp. 49-55.
6. Yan B., Zhang H., Lin J., Wang S. and Ni J. Luminescence properties of the ternary rare earth complexes with  $\beta$ -diketones and 1,10-phenanthroline incorporated in silica matrix by a sol-gel method, *Mater. Chem. Phys.* **51** (1997) pp.92-95.
7. Serra O. A., Nassar E. J. and Rosa I. L. V.  $Tb^{3+}$  Molecular photonic devices supported on silica gel and functionalized silica gel, *J. Lumin.* **72-74** (1997) pp. 263-265.
8. Anwander R., Gorlitzer H. W., Gerstberger G., Palm C., Runte O. and Spiegler M. Grafting of bulky rare earth metal complexes onto mesoporous silica MCM-41, *J. Chem. Soc., Dalton Trans.* (1999) pp. 3611-3615.

This page is intentionally left blank

# A NEW ANODE MATERIAL LiVMoO<sub>6</sub> FOR USE IN RECHARGEABLE Li-ION BATTERIES

R. S. LIU AND C. Y. WANG

*Department of Chemistry, National Taiwan University, Taipei, Taiwan*

*E-mail: rsliu@ccms.ntu.edu.tw*

S. F. HU

*National Nano Device Laboratories, Hsinchu, Taiwan*

L. Y. JANG AND J. F. LEE

*Synchrotron Radiation Research Center, Hsinchu, Taiwan*

The lithiated transition metal oxide LiVMoO<sub>6</sub> has been synthesized by solid state reaction. This is the first report of this compound to be studied as an anode material. The synthesized LiVMoO<sub>6</sub> powder has been studied by means of X-ray diffraction (XRD) and X-ray absorption near edge structure (XANES) spectroscopy. The electrochemical characteristics of the prepared electrodes assembled in coin cells were also investigated in terms of half-cell performance. It is observed that the cell exhibits three stages of discharge plateaus in the ranges 2.1-2.0 V, 0.6-0.5 V and 0.2-0.01 V, respectively. The total discharge capacity, averaged over several test runs, is about 1250 mAh/g. This value is much higher than the capacities exhibited by many kinds of anode materials.

## 1 Introduction

Rechargeable batteries have been considered an attractive power source for a wide variety of applications and in particular, lithium-ion batteries are emerging as the technology of choice for portable electronics. One of the main challenges in the design of these batteries is to ensure that the electrodes maintain their integrity over many discharge and recharge cycles. Michael *et al.* have reported that LiVMoO<sub>6</sub> can be synthesized by a soft-combustion (wet chemical) method [1]. However, the XRD pattern of LiVMoO<sub>6</sub> reported by them was not indexed. On the other hand, Gopalakrishnan *et al.* have shown [2] that LiVMoO<sub>6</sub> as well as its reduced product, LiVMoO<sub>5</sub>, obtained by the solid-state reaction method can be identified by their XRD patterns. Also, many measurements on the physical properties of these materials were performed by the authors. In the present work, we focus on finding a moderate method for preparing LiVMoO<sub>6</sub> and on understanding the factors that influence its electrochemical properties.

## 2 Experimental

### 2.1 Synthesis of LiVMoO<sub>6</sub>

The LiVMoO<sub>6</sub> sample was synthesized by solid state reaction of Li<sub>2</sub>CO<sub>3</sub>, V<sub>2</sub>O<sub>5</sub> and MoO<sub>3</sub>. Well ground mixtures of the starting materials were sintered at 550°C in air for 24 h. X-ray diffraction (XRD) analyses were carried out with a SCINTAG (X1) diffractometer (Cu K<sub>α</sub> radiation,  $\lambda = 1.5406 \text{ \AA}$ ) at 40 keV and 30 mA. Data for the Rietveld refinement were collected in the 2θ range 10–110° with a step size of 0.02° and a count time of 10 s per step. The program GSAS [3] was used for the Rietveld refinement in order to obtain

information about the crystal structure of LiVMoO<sub>6</sub>.

## 2.2 Measurement of the valences of V and Mo

The valences of V and Mo were determined by the X-ray absorption technique. The experiments for V and Mo were carried out by using synchrotron radiation with the electron beam energy of 1.5 GeV at the Synchrotron Radiation Research Center (SRRC) in Taiwan and the 8 GeV SPring-8 facility in Japan, respectively. The spectra were recorded by measuring the ratio  $I/I_0$  ratio, where  $I_0$  is the intensity of the incident beam. According to the attenuation law  $I = I_0 \exp(-\mu x)$ ,  $\ln(I/I_0)$  is proportional to the absorption function  $\mu$ . Based on the transmission mode, the thickness  $x$  of the sample has to be adjusted such that  $\mu \cdot x = 1$ , where  $\mu$  is the absorption cross-section of the element of interest. The incident photon flux ( $I_0$ ) was monitored simultaneously by an ion-chamber which was positioned after the exit slit of the monochromator. The intensity of the transmitted X-ray monitored in the same way was considered as  $I_0$  of the standard metal foil for calibrating the energy of the beam. All the measurements were performed at room temperature. The photon energies were calibrated to an accuracy of 0.1 eV via the theoretical values of the V and Mo metal K-edge absorption energies.

## 2.3 Electrochemical experiments

Electrochemical characterization was performed using coin-type cells. The method of assembling the cell was as follows. The sheets were prepared by spreading a slurry mixture of 85 wt.% LiVMoO<sub>6</sub>, 9 wt.% carbon black and 6 wt.% polyvinylidene fluoride (PVDF) dissolved in 1-methyl-2-pyrolidinone (NMP) on an aluminum or copper foil. The prepared sheets were then placed into a vacuum oven to evaporate the solvent at 90~100°C for 12 hours. The electrode disks (1/2 inch o.d.) were punched from the sheets, with an average weight of 3 mg of active material. The cell consisted of an electrode disk and a lithium metal foil with a porous polyethylene film as a separator. The electrolyte used was 1 M LiPF<sub>6</sub> in a mixture of ethylene carbonate (EC) and dimethyl carbonate (DMC) in the volume ratio of 1:1. The cell was assembled in an argon-filled dry box and tested at room temperature. The charge and discharge experiments were performed with a Maccor battery cycling instrument. The cell was cycled at current density values between 0.3 and 3 mA/cm<sup>2</sup> in the voltage range 2.80~4.25 V or 0.01~3.00 V.

## 3 Results and Discussion

### 3.1 X-ray diffraction study

The powder XRD pattern of LiVMoO<sub>6</sub> and the structural parameters calculated with Rietveld refinement are presented in Fig. 1 and Table 1, respectively. The pattern of LiVMoO<sub>6</sub> could be indexed on the basis of a monoclinic cell [ $a = 9.3443(4)$  Å,  $b = 3.64610(14)$  Å,  $c = 6.63636(25)$  Å,  $\alpha = \gamma = 90^\circ$  and  $\beta = 111.6382(10)^\circ$ ] and the space group of its crystal structure is  $C12/m1$ . The sample could be synthesized successfully in single phase, as evidenced from the XRD refinement results. The layered structure of LiVMoO<sub>6</sub> plotted with ATOMS software is shown in Fig. 2. LiVMoO<sub>6</sub> crystallizes in the brannerite (ThTi<sub>2</sub>O<sub>6</sub>) structure which consists of edge- and corner-sharing MO<sub>6</sub> (M = V or Mo) octahedra. The negative charges on the M<sub>2</sub>O<sub>6</sub> sheets are compensated by additional cations (Li) which reside in the interlayer space [2]. From the viewpoint of the crystal

structure, Li ions might be extracted from the lattice driven by the input of electrical power. Then the  $\text{Li}_{1-x}\text{VMoO}_6$  ( $x < 1$ ) compound could be intercalated by lithium ions accompanied by the output of the current by the external circuit. Consequently it could play the role of cathode material like  $\text{LiCoO}_2$  with a layered crystal structure in Li-ion batteries.

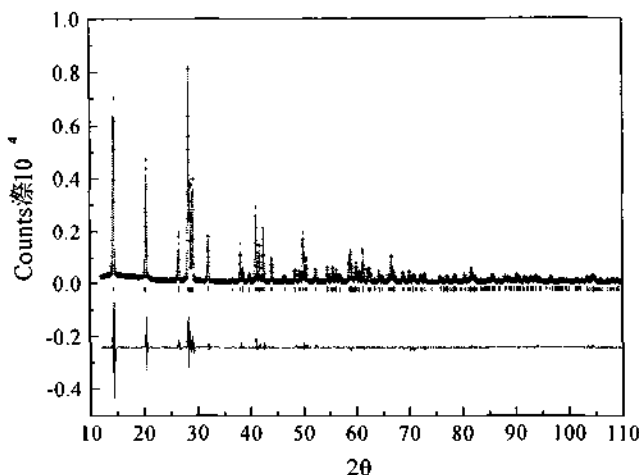


**Figure 1.** Observed (cross) and calculated (solid line) X-ray powder diffraction patterns of  $\text{LiVMoO}_6$ . Small bars indicate the positions of Bragg reflections for  $\text{LiVMoO}_6$ . The difference between the calculated and experimental patterns is plotted along the bottom.

**Table 1.** Refined fractional atomic positions, unit cell parameters and reliability factors (%) of  $\text{LiVMoO}_6$  having space group  $C12/m1$  at room temperature.

atoms	x	y	z	fraction	$U_i/U_e \times 100$
Li	0.00000	0.00000	0.00000	1	5.4(17)
V	0.18577(15)	0.00000	0.65371(21)	0.5	2.52(6)
Mo	0.18577(15)	0.00000	0.65371(21)	0.5	2.52(6)
O	0.9676(7)	0.00000	0.2783(8)	1	3.85(26)
O	0.3329(7)	0.00000	0.8957(9)	1	4.20(26)
O	0.3124(7)	0.00000	0.4309(9)	1	5.24(30)
space group: $C12/m1$		Reliability factor		bond distances (Å)	
lattice parameters:		$R_p = 7.25\%$		1.6839	
$a = 9.3443(4)$ Å		$R_{wp} = 10.69\%$		1.7180	
$b = 3.64610(14)$ Å		$\chi^2 = 2.11$		V(Mo)-O	
$c = 6.63636(25)$ Å				2.1833	
				1.8894	

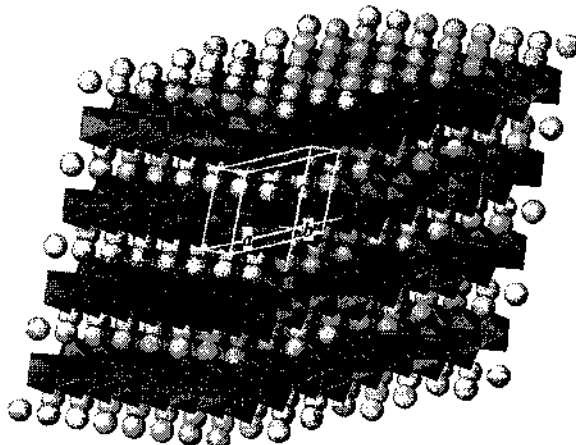


**Figure 2.** Ideal crystal structure of  $\text{LiVMoO}_6$  with monoclinic cell (space group:  $C12/m\bar{1}$ ). Unit cell is shown in the center. Part of each  $\text{V}(\text{Mo})\text{O}_6$  octahedra is shaded.

### 3.2 The valences of V and Mo in $\text{LiVMoO}_6$

Based on the studies of the XANES (X-ray absorption near edge structure) spectra of  $\text{LiVMoO}_6$  and the standard samples (such as  $\text{V}_2\text{O}_5$ ,  $\text{VO}_2$ ,  $\text{MoO}_3$ ,  $\text{MoO}_2$ , etc) at the V and Mo K-edges, we can determine the valence of the vanadium ion is about 4.5 while that of molybdenum ion is 6.

### 3.3 The electrochemical behavior of $\text{LiVMoO}_6$

Coin type cells were assembled and cycled using a Maccor automatic cycling/data recording system between 4.25 and 2.80 V. The cells were cycled with 0.3 mA of the charging and discharging current and the cycling results plotted in the form of potential vs. capacity are shown in Fig. 3. It is observed that although the ratio of the discharge capacity to charge in each cycle remains almost 95% for 30 cycles, the absolute values of the capacities were very low, 0.12 mAh/g.

Based on the chemical formula of  $\text{LiVMoO}_6$  that is used for a cathode material, the theoretical capacity is calculated to be 107 mAh/g, while the practical utilizable capacity was 92 mAh/g for the first cycle, which was reported by Michael *et al.* [1]. They also mentioned that their work could confirm that layered  $\text{LiVMoO}_6$  might be classified amongst 4-V class cathode materials for use in rechargeable Li-ion batteries. However, based on our experimental results presented above, we feel that  $\text{LiVMoO}_6$  is not suitable as a cathode material in rechargeable Li-ion batteries. The reasons are as follows: First, since de-intercalation of positive lithium ions from the crystal structure must be electrically compensated by oxidation of  $\text{V}^{4.5+}$  or  $\text{Mo}^{6+}$ , this suggests that even for layered structure phase, only the amount of  $\text{V}^{4.5+}$  contributes to the charge-discharge capacity. As a result, the initial capacity of  $\text{LiVMoO}_6$  is limited by the intrinsic amount of  $\text{V}^{4.5+}$  in the material. On the other hand, the expected capacity owing to V ions that can be oxidized seem to be much less than the experimental result of Michael *et al.* Second, as we know,

$\text{LiVMoO}_6$  is a crystal with layered structure. When it is used for the cathode material in the Li-ion batteries and the charging current is passed, the Li-ions are extracted during this period. But it is reasonable to expect that the layered structure needs a sufficient amount of Li ions in the lattice to maintain the structure or else, the structure would break down. Furthermore, that might be an irreversible process.

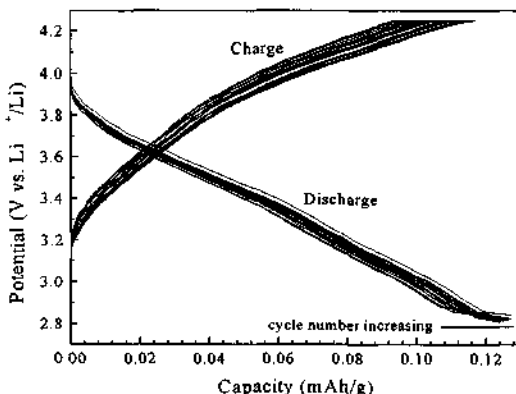


Figure 3. Typical charge and discharge curves of  $\text{LiVMoO}_6$  at a voltage of 2.80-4.25 V.

Therefore, coin type cells of  $\text{LiVMoO}_6$  were also assembled and cycled between 3.00 and 0.01 V (Fig. 4). During the first three cycles (the discharging current is 0.3 mA), the potential rapidly drops to reach a plateau, and then continuously decreases down to 0.01 V. The amplitudes of three plateaus are about 2.1-2.0 V, 0.6-0.5 V and 0.2-0.01 V, respectively. The total discharge capacity, averaged over several test runs, is about 1250 mAh/g. This value is much higher than the capacities exhibited by many kinds of anode materials. Further work therefore needs to focus on the identification of the changing crystal structures during the cycling, and based on such that a reasonable mechanism of the electrochemical reaction can be realized. Furthermore, increasing the reversible capacity of  $\text{LiVMoO}_6$  is also important.

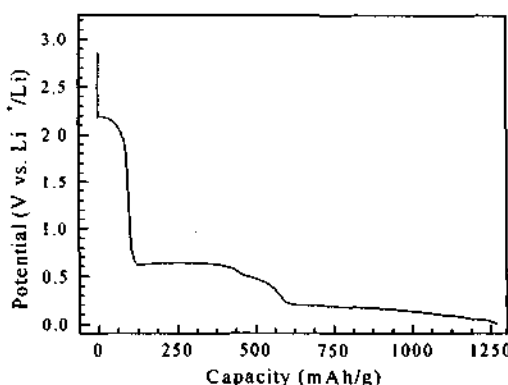


Figure 4. Typical charge and discharge curves of  $\text{LiVMoO}_6$  at a voltage of 3.00-0.01 V.

#### 4 Conclusion

$\text{LiVMoO}_6$  was successfully synthesized using the conventional solid-state reaction method, and its chemical and physical properties were examined by several analytical methods. We have shown that  $\text{LiVMoO}_6$  does not possess good structural characteristics for a lithium half cell ( $\text{Li}/\text{LiVMoO}_6$ ) as a cathode in non-aqueous electrolyte environment. Furthermore, we suggest that  $\text{LiVMoO}_6$  may instead be considered as an anode material of choice for developing rechargeable lithium-ion battery technology.

#### 5 Acknowledgements

This research has been supported by the SYNergy ScienTech Corporation, and the National Science Council under the grant number NSC90-2113-M-002-048.

#### References

1. Michael M. S., Fauzi A. and Prabaharan S. R. S., Soft-combustion (wet-chemical) synthesis of a new 4-V class cathode-active material,  $\text{LiVMoO}_6$ , for Li-ion batteries. *Int. J. Inorg. Mater.* **2** (2000) pp. 261-267.
2. Gopalakrishnan J., Bhuvanesh N. S. P., Vijayaraghavan R. and VasanthaCharya N. Y., A new charge density wave oxide,  $\text{LiVMoO}_5$ , and its tungsten analogue obtained by topotactic reduction of  $\text{LiVMO}_6$  ( $M = \text{Mo}, \text{W}$ ) brannerites. *J. Mater. Chem.* **7** (1997) pp. 307-310.
3. Larson A. C. and von Dreele R. B., Generalized Structure Analysis System, Los Alamos National Laboratory, Los Alamos, NM, (1994).

# ELECTRONIC CERAMIC BaTiO<sub>3</sub>: SYNTHESIS, DIELECTRIC AND FERROELECTRIC PROPERTIES

WENQING LU, ZHENG CAI AND YUEBING FENG

College of Chemistry and Environment Science, Materials Science Laboratory, Nanjing Normal University, Nanjing 210097, P. R. China

National Key Laboratory of Solid State Microstructures, Nanjing University,

Nanjing, 210093, P. R. China

E-mail: adjin@njnu.edu.cn

Dielectric and ferroelectric properties of BaTiO<sub>3</sub> ceramics are reported in this paper. Barium titanate (BaTiO<sub>3</sub>) powder was prepared by barium hydroxide (Ba(OH)<sub>2</sub>·8H<sub>2</sub>O) and titanium butoxide (Ti(OC<sub>4</sub>H<sub>9</sub>)<sub>4</sub>) precursors by a sol-gel technique using stearic acid as solvent, annealing gel at 750 °C in air for 1 hour. The as-grown powder is found to be amorphous, which crystallized as a tetragonal phase after annealing at 750°C. X-ray fluorescence and chemical analysis were used to investigate the chemical content Ba: Ti≈1. The grain size is about 40 nm, detected by TEM. LKY-3 apparatus and laser scatter particle size analyzer were used to determine the particle size distribution. Ceramic samples were prepared by pressing the powder using a pressure 8 MPa and sintering at 1 300 °C in air for 2 hour. Then the ceramic samples were prepared by electrodeing the sintered discs with silver paint. The ceramics show well-saturated polarization-field ( $P-E$ ) hysteresis loops at room temperature detected by RT 6 000 ferroelectric detecting system. The values of the spontaneous polarization ( $P_s$ ), remnant polarization ( $P_r$ ) and coercive field ( $E_c$ ) of the ceramics are found to be 5.512, 12.285  $\mu C\cdot cm^{-2}$  and 3 342  $V\cdot cm^{-1}$  respectively. The value of the dielectric constant ( $\epsilon_r$ ) of the bulk ceramics (200~150 000Hz) is found to be 2713.

## 1 Introduction

Ferroelectric ceramics and single crystals have found wide applications in many electronic, acoustooptic and piezoelectric devices [1,2]. Perovskites represent one of the most important classes of inorganic powders that are of great interest in functional ceramics used for electronic components; among them BaTiO<sub>3</sub> is a typical and most frequently used representative.

BaTiO<sub>3</sub> powder is used widely to make electronic components such as layered capacitor, printed circuit block, integrated circuit and piezoelectric ceramic etc. Moreover, it can be used in the field of computer and mobile telephone and satellite communications.

The most common method for preparing BaTiO<sub>3</sub> powder is the conventional solid state reaction [3], alternative methods have been developed [12], such as alkoxide hydrolysis [4], hydrothermal synthesis [5], colloid method [6], and so on.

In this work, sol-gel method was used to prepare BaTiO<sub>3</sub> powder, then ceramic electrode was made using this powder after removing binder, sintering and firing silver. Finally, the ceramics are used for the study of ferroelectric and dielectric properties.

## 2 Experimental Procedure

### 2.1 Processing [13]

$\text{Ba}(\text{OH})_2 \cdot 8\text{H}_2\text{O}$  was dissolved in stearic acid slowly, stirred and heated at a certain temperature. The barium stearate formed after some hours, to which a stoichiometric amount of tetrabutyl titanate ( $\text{Ti}(\text{OC}_4\text{H}_9)_4$ ) was added with stirring. The reaction mixture was kept at a certain temperature for hours to form white sol. The sol was dried in the air for 24 hours, and then the gel with a three-dimensional net-like structure was formed. The  $\text{BaTiO}_3$  powder was obtained by annealing the gel at 750 °C in the air for 1 h by using a conventional furnace.

The ceramic circular discs (1 cm diameter, 0.1 cm thick) were prepared by pressing the powder, using a pressure of 8 MPa, with adding in 8 % PVA solution as binder, and sintering at 1 300 °C for 2 hours. Then the ceramic samples were prepared by electrodeing the sintered disc with silver paint.

$\text{Ba}(\text{OH})_2 \cdot 8\text{H}_2\text{O}$ ,  $\text{Ti}(\text{OC}_4\text{H}_9)_4$  and  $\text{CH}_3(\text{CH}_2)_{16}\text{COOH}$  used for the experiment were all analytical grade (A.R.). The molten stearic acid serves as a solvent, a complexant and a surfactant. Some metal ions were mixed uniformly in it.

### 2.2 Characterization

The chemical content of Ba: Ti was determined by X-ray fluorophotometer (Shimadazu VF-320, Japan).

The structure of the ceramic powder was characterized by XRD using a Rigaku (D/MAX-RC) X-ray diffractometer.

The morphology of the powder was examined by TEM (Hitachi JEM-200CX).

The particle size distribution was tested by LKY-3 particle size analyzer and Malvern laser scatter particle size analyzer.

The dielectric properties were measured by using an alternating current impedance analysis apparatus (HP-4294A).

The polarization-field hysteresis was measured using radiant technologies (RT 6 000 HVS) apparatus.

## 3 Results

### 3.1 Microstructure

The X-fluorescence analysis shows that the Ba/Ti ratio is about 0.96. Fig. 1 shows the X-ray diffraction (XRD) pattern of  $\text{BaTiO}_3$  powder after annealing at 750 °C for 1 hour. The results indicate that the  $\text{BaTiO}_3$  crystal has formed and the XRD peak positions are in good agreement with that of JCPDS card. The crystal is tetragonal system. The peaks of  $\text{TiO}_2$  and  $\text{BaTi}_2\text{O}_5$  are not found. However, it can be seen that there are peaks of  $\text{BaCO}_3$  crystal, maybe it is due to the reaction of  $\text{CO}_2$  from air with  $\text{Ba}(\text{OH})_2 \cdot 8\text{H}_2\text{O}$  materials forming the  $\text{BaCO}_3$  substance. Such powders prepared by sol-gel exhibit high purity. Although the powder is tetragonal crystal, the split of the peaks is not obvious. Perhaps it is because that the particles are too small to split and that the peaks are much broad. Based on (200), (002) splitting, it can be calculated,  $a_0=4.019 \times 10^{-10}$  m,  $c_0=4.041 \times 10^{-10}$  m,  $a_0/c_0=1.005$ .

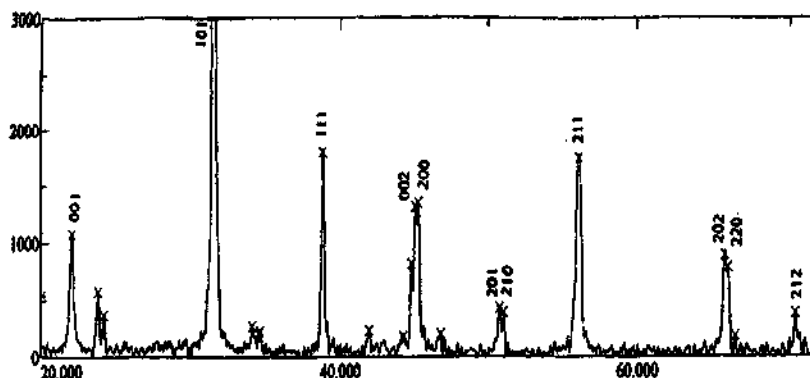


Figure 1. A XRD patterns of  $\text{BaTiO}_3$  annealing for 1 h at 750 °C.

### 3.2 The morphology and size distribution

Fig. 2 is the TEM photograph amplified by  $1 \times 10^5$  times. The  $\text{BaTiO}_3$  powder was annealed at 750 °C in air for 1 hour. There are some aggregates. The distracted particles are elliptical sphere and the particle sizes are in the range of 20~40 nm. LKY-3 particle size analyzer and laser scattering particle size analyzer determines particle size and its distribution (Table 1).  $D_{50}$  means median diameter size and  $D_n$  means number average size.  $\text{BaTiO}_3$  powders at certain concentration with dispersing agent of  $(\text{NaPO}_3)_6$  were supersonically dispersed for 15 minutes. The subsided liquid is made by glycerine-water solution. Table 2 and Fig. 3 show the experimental results by LKY-3.

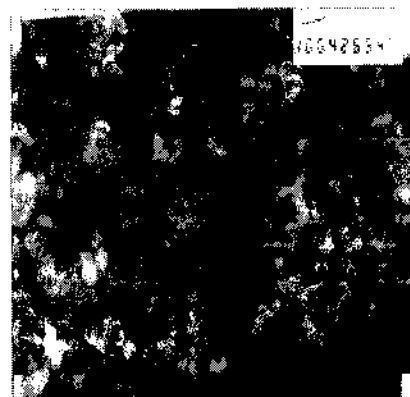


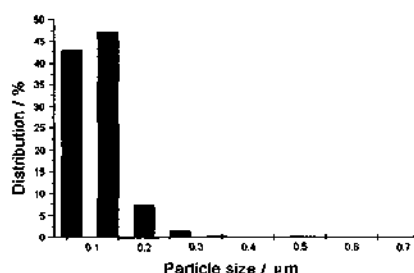
Figure 2. A TEM ( $\times 100 000$ ) picture of  $\text{BaTiO}_3$  nanocrystal annealing for 1 h at 750 °C

Table 1. Results of diameter analysis.

	TEM	LKY-3	Laser Scatter
$D_{50}$ / (nm)	/	190	151
$D_n$ / (nm)	20~40	140	179

**Table 2.** Differential diameter distribution by LKY-3.

No.	$D_i - D_{i+1}$ ( $\mu\text{m}$ )	dN(%)
1	0.06---0.13	42.96
2	0.13---0.20	47.40
3	0.20---0.27	7.62
4	0.27---0.34	1.46
5	0.34---0.41	0.37
6	0.41---0.48	0.11
7	0.48---0.55	0.04
8	0.55---0.62	0.02
9	0.62---0.69	0.01
10	0.69---0.76	0.01

**Figure 3.** Pattern of particle size distribution.

### 3.3 Ferroelectric properties (P-E)

The room-temperature polarization-field hysteresis of the ceramics shows well-saturated loops. The values of remnant polarization, spontaneous polarization and coercive field determined are reported in Table 3. The data of single crystal previously reported are also listed in Table 3.

**Table 3.** Ferroelectric properties of  $\text{BaTiO}_3$  single crystal and ceramic.

sample	remanent polarization $P_r$ / ( $\mu\text{C}/\text{cm}^2$ )	spontaneous polarization $P_s$ / ( $\mu\text{C}/\text{cm}^2$ )	coercive field ( $(\text{P}-\text{E}) E_c$ ) / (V/cm)	dielectric constant $\epsilon$
Single crystal	20.0[7]	26.0[7]	1 000[8]	4 000[9]
Ceramic	5.512	12.285	3 342	2 713

### 3.4 Dielectric properties

At room-temperature, from the capacitance-frequency and loss tangent ( $\tan \delta$ )-frequency figures, it can be seen that the dielectric constant  $\epsilon$  and the loss tangent ( $\tan \delta$ ) of  $\text{BaTiO}_3$  ceramics can keep constant. Their properties are stable, at the range of certain frequency (200~150 000 Hz) (Fig. 5). Based on the equation:

$$\epsilon = \frac{4\pi K C d}{S} \quad K = 9.0 \times 10^9 \text{ N}\cdot\text{m}^2/\text{C}^2$$

C--- capacity      d---ceramics thick      S---ceramics area,

the calculated value of  $\epsilon$  is 2713. The value of  $\tan \delta$  is 0.05 from Fig. 5.

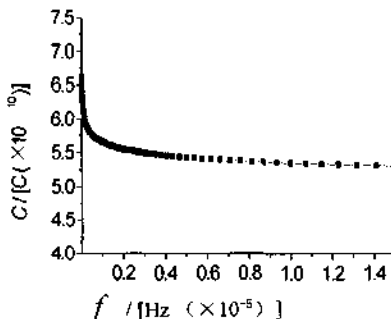


Figure 4. Capacitance-frequency characteristics of  $\text{BaTiO}_3$  ceramic.

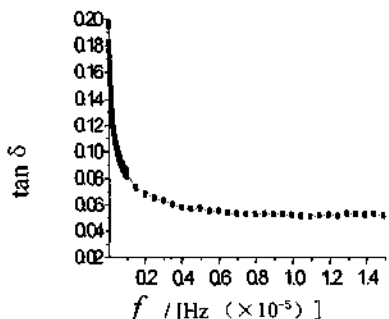


Figure 5. Loss tangent ( $\tan \delta$ ) of  $\text{BaTiO}_3$  ceramic with frequency.

#### 4 Discussion

We find that results by LKY-3 particle size analyzer and laser scatter particle size analyzer are different from the TEM. The diameter of the particle ( $750^\circ\text{C}$ ) is  $20\text{--}40\text{ nm}$  by TEM. This result is one order of magnitude lower than those of LKY-3 and laser scatter particle size analyzers (Table 1). The reason is that, what we observed was only the primary particles by TEM. Correspondingly, the two kinds of size analyzers tested all the particles, including primary particles and agglomerates, although it is hard to measure the primary particle distribution [10]. In the experiment, 10% glycerine-water solution is used as subsided solution, so perhaps its polarity enhances the agglomerates of the particles partly. Therefore the tested size is larger than the reality.

Compared to other methods, TEM is more reliable, accurate and intuitive. Meanwhile it can observe two-dimensional and three-dimensional forms of the particles. However, it only observes the particles in limited range, so it does not have statistical meaning. Based on centrifugal subsidence method, the particle size analyzer can get all kinds of the particles and the differential and cumulative diameter distribution curves of them. In order to dominate or avoid the particles agglomerate, the key is the suspension method in the test. In summary, the three methods are compensated for each other.

From the data listed in Table 3, it may be noted that the polarization values of the ceramics are lower than that of the single crystal [7,8] whereas the coercive field is higher. This may be attributed to the existence of the non-ferroelectric layers at the metal-ferroelectric interfaces and grain boundaries. In other way, when the anisotropy of the crystal get stronger, the displacement of ions, which is demanded by polarization inversion, get larger, the coercive field will be stronger.

The value of  $\epsilon$  of the  $\text{BaTiO}_3$  ceramics is lower than that reported for  $\text{BaTiO}_3$  single crystal [9] (along [100]  $\epsilon = 4\ 000$ ). This may be due to the structural and compositional variances. Meanwhile, the size of crystalline particle may affect the dielectric constant  $\epsilon$ , that is, when the particle size is lower than certain value, the constant will decrease with the decrease of the size. In addition to those mentioned above, porosity and the existence of low dielectric constant affect the non-ferroelectric layers at the metal-ferroelectric interface and the grain boundaries.

The effects of frequency change on the dielectric constant  $\epsilon$  and the  $\tan \delta$  of the ceramics was investigated. Fig. 4 and Fig. 5 show the variation of  $\epsilon$  and  $\tan \delta$  of the ceramics at the range of 200 to 15 000 Hz. The value of  $\epsilon$  and  $\tan \delta$  are less changeable.

$\text{BaTiO}_3$  powder has been prepared by sol-gel technique. The as-grown powder is found to be amorphous, which is crystallized to tetragonal phase after annealing at 750 °C in air for 1 hour. The size of tetragonal crystal is 20~40 nm by TEM. Compared with the conventional method, sol-gel technique can produce nano-crystalline  $\text{BaTiO}_3$ . At room-temperature, through measuring the ceramics polarization-field hysteresis, the values of the spontaneous polarization ( $P_s$ ), remnant polarization ( $P_r$ ) and coercive field ( $E_c$ ) of the ceramics are found to be 5.512, 12.285  $\mu\text{C}/\text{cm}^2$  and 3342 V/cm, respectively. The value of the dielectric constant ( $\epsilon$ ) is found to be 2713 (200~150 000 Hz). The value of  $\epsilon$  at room temperature is much higher than those reported in refs [7] and [11]. From the dielectric-frequency figure, when the frequency is between 200 and 150 000 Hz, the ceramics has good stability and the loss tangent is small. So the ceramics can be used to make some electronic components.

## 5 Acknowledgements

This work was supported by the Foundation of National Key Laboratory of Solid State Microstructures, Nanjing University (M 011609).

## References

1. Fan Fukang and Qiu Tai, Present situation and developing tendency of electronic ceramics. Bulletin of the Chinese Ceramic Society, 4(1995) pp. 29-36.
2. Leslie E., Cross, Dielectric, piezoelectric and ferroelectric components. Ceramic Bulletin. 63 (1984) pp. 585-590.
3. Templeton K. L. and Joseph A. P., Formation of  $\text{BaTiO}_3$  from  $\text{BaCO}_3$  and  $\text{TiO}_2$  in air and in  $\text{CO}_2$ . The American Ceramics Society. 42(5), 1959 pp. 212-216.
4. Kirby K. W., Alkoxide Synthesis Techniques for  $\text{BaTiO}_3$ . Mat. Res. Bull, 23(6) 1988 pp. 881-890.
5. Li Wenjun, Shi Erwei and Zheng Yanqing, Preparation of  $\text{BaTiO}_3$  powder by hydrothermal synthesis. J. the Chinese Ceramic Society, 27(6),1999 pp. 714-719.
6. Lu Wenqing, Cheng Baorong and Deng Haishan, Preparation and characterizations of colloidal  $\text{BaTiO}_3$  superfines. J. Wuhan University (Natural Science Edition). 46(2000) pp. 245-248.
7. Basantakumar Sharma and Sarma H. N. K., A Mansingh, Ferroelectric and dielectric properties of sol-gel processed barium titanate ceramics and thin film. J. Materials Science. 34(1999) pp. 1385-1388.
8. Herbert J. M., Ferroelectric materials, Chemistry in Britain. 9(1983), pp. 728-730.
9. Merz W. J., The electric optical behavior of  $\text{BaTiO}_3$  single-domain crystals. Physical Review. 76(1949) pp.1221-1225.
10. Shi Jianlin, Modern Inorganic Nonmetallic Materials Technology. Jilin Scientific Publish (Changchun, 1993), pp. 75-103.
11. Ding Shiwen, Ma Guangcheng and Shen Panwen, Synthesis and ceramics preparation of  $\text{BaTiO}_3$  superfine powder. J. Functional Materials, 29(1998) pp.72-74.
12. Larry L. H. and West J. K., The Sol-gel processes. Chem. Rev. 90 (1990), pp.33-72.
13. Cheng Baorong, Lu Wenqing, Huang Jinfan and Jin Anding, Preparation and characterization of  $\text{BaTiO}_3$  nanocrystal. J. Nanjing Normal University (Natural Science Edition) 23(1), 2000, pp. 49-53.

## X-RAY ABSORPTION STUDY OF ELECTRONIC, SPATIAL STRUCTURE AND PROPERTIES OF $\text{BaLn}_2\text{Mn}_2\text{O}_7$ MANGANATES

L. N. MAZALOV, N. V. BAUSK, V. V. SOKOLOV AND V. N. IKORSKII

*Institute of Inorganic Chemistry of SB RAS, Novosibirsk, 630090, Russia*

*Email: kamarz@che.nsk.su*

JIAN MENG AND JING FENG

*Key Laboratory of Rare Earth Chemistry and Physics, Changchun Institute of Applied Chemistry,*

*Chinese Academy of Sciences, Changchun, 130022, P.R. of China*

*Department of Materials Science, Toyohashi University of Technology, 441-8580, Japan*

*Email: jmeng@ns.ciac.jl.cn*

K. FUJITA, H. SATOH AND N. KAMEGASHIRA

*Department of Materials Science, Toyohashi University of Technology, 441-8580, Japan*

*Email: nkamegas@tutms.tut.ac.jp*

$\text{BaLn}_2\text{Mn}_2\text{O}_7$  ( $\text{Ln} = \text{Nd}, \text{Sm}, \text{Eu}$ ) have the tetragonal symmetry with the  $I4/mmm$  space group  $a = 0.3897 \text{ nm}$  and  $c = 2.0651 \text{ nm}$  for Nd,  $a = 0.3893 \text{ nm}$  and  $c = 2.0482 \text{ nm}$  for Sm,  $a = 0.3883 \text{ nm}$  and  $c = 2.0382 \text{ nm}$  for Eu. Their X-ray XANES and EXAFS-spectra were investigated using the X-ray K-spectra Mn,  $L_3$ -spectra of rare earths (Nd, Sm, Eu),  $L_3$ -spectra Ba. The energy level of the appropriate line can be connected with the charge state of absorbing atom. X-ray absorption data show that electronic density on Ba atom in a range of examined compositions depends on a nature Ln (Nd, Sm, Eu) and decreases in a direction Eu > Nd > Sm. The location of  $L_3$  edge of absorption of Ln was also testified about various charging state of rare earths in these compounds. At the same time charging state of Mn atoms remains constant. On the base of the analysis of EXAFS-spectra of these compounds the data on most typical interatomic distances are received.

### 1 Introduction

The manganates of  $\text{BaLn}_2\text{Mn}_2\text{O}_7$  belong to one of the Ruddlesden-Popper type of  $A_{n+1}\text{B}_n\text{O}_{3n+1}$  compounds with bi-layer ( $n=2$ ) perovskite structure [1]. Perovskite rare earth manganates are generally known to possess special physical and chemical properties due to having various structural phase transitions. There are novel electrical and magnetic properties accompanied with the phase transition [2-4]. Especially, the studies of distorted structure have a very interesting content owing to the Jahn-Teller effect of  $\text{Mn}^{3+}$  ion. But it is very difficult to obtain the pure phase containing  $\text{Mn}^{3+}$  ion only [5]. There are many parameters, for instance, temperature control, rate of increasing and decreasing temperature, ionic vacancy or defects etc. N. Kamegashira's laboratory has found that the structural phase transition is very strongly dependent on the preparation conditions [6, 7].

Properties and behavior of the  $\text{BaLn}_2\text{Mn}_2\text{O}_7$  compounds are very sensitive to Ba:Ln ratio and chemical nature of Ln. For the rare earth ions ( $\text{Ln} = \text{Pr} - \text{Tb}$ ) tetragonal phase with the space group  $I4/mmm$  is well known. For  $\text{BaLn}_2\text{Mn}_2\text{O}_7$  compounds the formation of orthorhombic phases in space group  $Fm\bar{m}m$  for Sm and Eu or  $I\bar{m}mm$  for Gd and Tb can be also obtained. Probably the oxygen non-stoichiometry of  $\text{BaLn}_2\text{Mn}_2\text{O}_{7+x}$  compounds has an influence on structural ordering of these compounds (for example, existing of  $\text{BaGd}_2\text{Mn}_2\text{O}_7$  in Sm type or in superstructure of tetragonal phase with space group  $P4/mmm$  or in monoclinic phase) [8, 9].

With the aim to study the features of an electronic and spatial structure of  $\text{BaLn}_2\text{Mn}_2\text{O}_7$ , ( $\text{Ln} = \text{Nd, Sm and Eu}$ ) the X-ray XANES and EXAFS-spectra of atoms of metals that are included in structure of these compounds and magnetic properties were investigated.

## 2 Experimental Methods

$\text{BaLn}_2\text{Mn}_2\text{O}_7$ , ( $\text{Ln} = \text{Nd, Sm and Eu}$ ) were prepared from the conventional solid state reaction method. The starting materials,  $\text{BaCO}_3$ ,  $\text{Ln}_2\text{O}_3$  and  $\text{Mn}_2\text{O}_3$ , were mixed with an appropriate molar ratio and pressed into pellets followed by heating finally at 1623 K in purified Ar.

The X-ray diffraction (XRD) patterns for the samples were recorded on a Rigaku D/max-II B Powder X-ray Diffractometer.

The X-ray K- spectra Mn,  $\text{L}_{2,3}$ -spectra of rare earths (Nd, Sm and Eu),  $\text{L}_{2,3}$ -spectra Ba were obtained using synchrotron radiation of EXAFS-station of Budker Institute of Nuclear physics of SB RAN (Novosibirsk). The typical operating conditions of the storage ring were as follows: electron beam energy  $E=2$  GeV, current  $I=100\text{mA}$ .

The X-ray emission Mn  $\text{L}_{\alpha}$  and  $\text{K}_{\beta}$  spectra were recorded using the X-ray ultrasoft (hypersoft) SPECTROMETER "Steorat". The X-ray electron spectra of Ba, Ln, Mn, and O in the compounds were measured on the VG-Microtext spectrometer.

The magnetic properties of the samples were measured by Faraday method in the temperature range of 78–300 K and in magnetic fields up to 10.9 kOe.

## 3 Results and Discussion

From powder X-ray diffraction data of prepared samples the unit parameters were calculated by the CELL program [10] and refined by the RIETAN program [11]. The lattice constants were  $a = 0.3897$  nm and  $c = 2.0651$  nm for Nd,  $a = 0.3893$  nm and  $c = 2.0482$  nm for Sm,  $a = 0.3883$  nm and  $c = 2.0382$  nm for Eu.

Analysis of XANES Ba ( $\text{L}_{2,3}$ ) spectra (Figure 1) shows a shift of the white line to short-waves region. It means that the electron density on the Ba atom in the series of the manganates decreases from Eu to Nd to Sm. The XANES ( $\text{L}_{2,3}$ ) edge of rare earth elements (Figure 2) is also characterized by "bright" white line, which is situated at different energy levels in accordance with the nature of Ln element. The white line of Nd and Sm  $\text{L}_{2,3}$  spectra in the compounds shift to a short-waves region, however this effect may be caused by a difference in energy of inner levels of these elements.

The presence of an intensive "white" line caused by transitions of excited X-ray electron on the free levels of system is characteristic for all spectra. The energy level of the appropriate line can be connected with charge state of absorbing atom.

X-ray absorption data show that electronic density on Ba atom in a range of examined compositions depends on a nature Ln (Nd, Sm and Eu) and decreases in a direction Eu > Nd > Sm. The location of  $\text{L}_{2,3}$  absorption edge of Ln in perovskites, was also testified about various charging state of rare earths in these compounds.

At the same time charging state of Mn atoms in a considered compound remains constant. The character before edge structure of K – spectra of Mn allows us to analyze the change of the chemical bonding in octahedral  $\text{MnO}_6$  dependant on the nature of out-spherical cations.

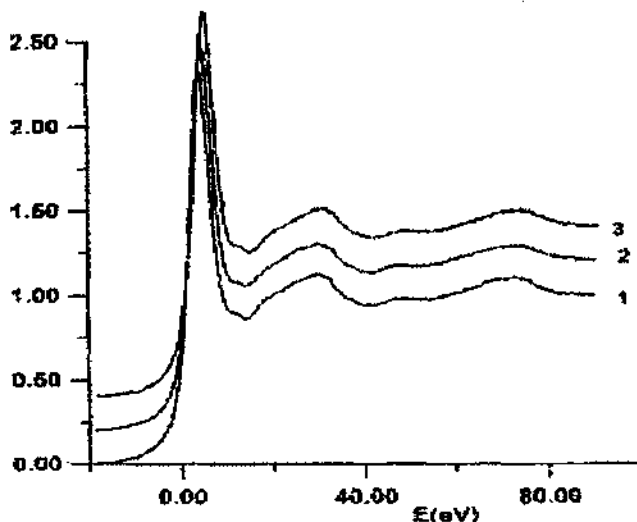


Figure 1. BaL<sub>3</sub> edge of absorption for BaLn<sub>2</sub>Mn<sub>2</sub>O<sub>7</sub>; 1 – Eu, 2 – Nd, 3 – Sm.

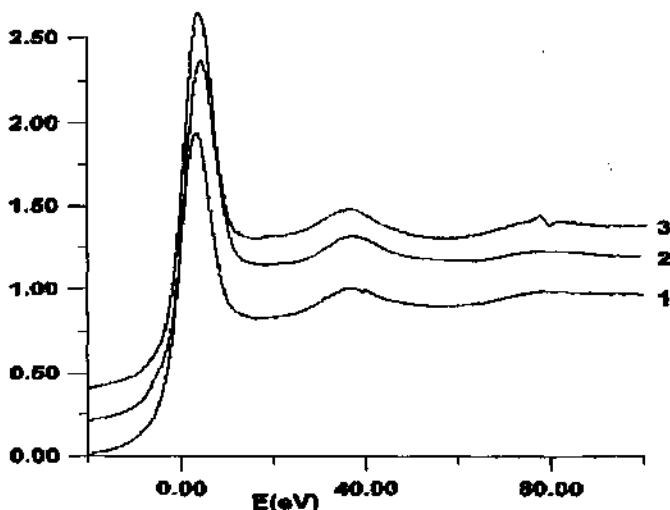


Figure 2. RL<sub>3</sub> edge of absorption for BaLn<sub>2</sub>Mn<sub>2</sub>O<sub>7</sub>; 1 – Eu, 2 – Nd, 3 – Sm.

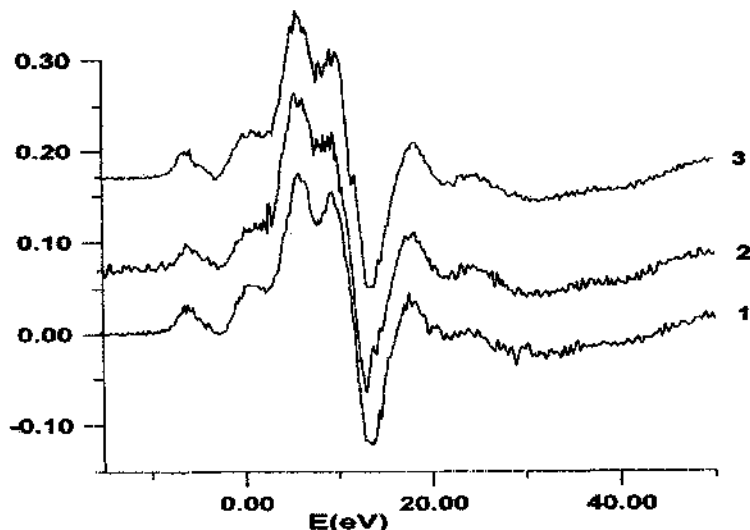


Figure 3. First derivation of Mn K edge absorption for  $\text{BaLn}_2\text{Mn}_2\text{O}_7$ : 1 – Eu, 2 – Nd, 3 – Sm.

Mn XANES K spectra are practically identical and independent of nature of cations in the compounds. Studying the pre-threshold structure of the spectra (Figure 3) shows that the system of non-occupied MO in the Mn clusters does not vary in the series of the manganates. It is evident that any noticeable covalent interaction between the Mn complex anion and its cation environment is absent.

Based on the spectra studied, it is concluded that the interaction between cation and anion sublattices in the manganates is mainly electrostatic interaction.

That magnetic susceptibilities of the samples depend on magnetic field in the temperature range indicates the presence of ferromagnetic ordering below 140 K. The results are in progress.

#### 4 Acknowledgements

This research was supported by the Grant-in-Aid for Scientific Research (B) (No. 13450259) by Japan Society for the Promotion of Science and State Key Program of Basic Research (G1998061311) and the National Natural Science Foundation of China (29831010).

#### References

1. Ruddlesden S. N. and Popper P., *Acta Crystallogr.* **11** (1958) pp. 541.
2. Seshadri R., Maignan A., Hervieu M., Nguyen N. and Raveau B., Complex Magnetotransport in  $\text{LaSr}_2\text{Mn}_2\text{O}_7$ , *Solid State Commun.*, **6** (1997) pp.453-457.

3. Peter D. B., Julie E. M., Matthew J. R., Lauren E. S., Jaap F.V. and Paolo G.R., Neutron Diffraction Study of the Structural and Electronic Properties of  $\text{Sr}_2\text{HoMn}_2\text{O}_7$  and  $\text{Sr}_2\text{YMn}_2\text{O}_7$ , *Chem. Mater.*, **9** (1997) pp.3136-3143.
4. Kimura T., Kumai R., Tokura Y., Li J.Q. and Matsui Y., Successive Structural Transition Coupled with Magnetotransport Properties in  $\text{LaSr}_2\text{Mn}_2\text{O}_7$ , *Phys. Rev.B*, **58** (1998) pp.11081-11084.
5. Aleksandrov K.S. and Barotolome J., Octahedral Tilt Phases in Perovskite-like Crystals with Slabs Containing an Even Number of Octahedral Layers, *J. Phys.: Condens. Matter.*, **6** (1994) pp.8219-8235.
6. Kamegashira N., Satoh H. and Horikawa M., Another Type of Orthorhombic Distortion in  $\text{BaGd}_2\text{Mn}_2\text{O}_7$  Phase, *Mater. Lett.*, **10** (1994) pp.494-496.
7. Meng J., Satoh H. and Kamegashira N., Crystal Structure Refinement of Tetragonal  $\text{BaTb}_2\text{Mn}_2\text{O}_7$ , *J. Alloys & Compds.*, **244** (1996) pp.75-78.
8. Meng J., Murase A., Satoh H. and Kamegashira N., Synthesis of a New Monoclinic Phase of  $\text{BaGd}_2\text{Mn}_2\text{O}_7$ , In *Proceeding of the 4<sup>th</sup> International Conference on Rare Earth Development and Application* ed. by Yu Zongsen, Yan Chunhua, Xu Guangyao, Niu Jingkao and Chen Zhanheng (Metallurgical Industry Press, Beijing, 2001) pp.183.
9. Meng J., Kamegashira N., Murase A., Satoh H., Liang H.W. and Feng J., Phase Transition and Absorption Spectrum of  $\text{BaLn}_2\text{Mn}_2\text{O}_7$  ( $\text{Ln}=\text{Eu}$  and  $\text{Gd}$ ), *Proceeding of the 4<sup>th</sup> International Conference on Rare Earth Development and Application* ed. by Yu Zongsen, Yan Chunhua, Xu Guangyao, Niu Jingkao and Chen Zhanheng (Metallurgical Industry Press, Beijing, 2001) p.213.
10. Takaki Y., Taniguchi T., Nakata K. and Yamaguchi H., Program for Finding the Unit-cell Constants and the Space Group from X-ray Powder Diffraction Data – The Case Where Approximate Unit-cell Contants are Known, *J.Ceram. Soc. Jpn.*, **97** (1989) pp.763-766.
11. Izumi F., RIETAN – a Software Package for the Rietveld Analysis and Simulation of X-ray and Neutron Diffraction Patterns, *J. Crystallogr. Soc. Jpn.*, **27** (1985) pp.23-26.

This page is intentionally left blank

## CRYSTAL GROWTH AND STRUCTURAL ANALYSIS OF $\text{PrMnO}_3$ AND $\text{TbMnO}_3$

JIAN MENG AND PING CHE

*Key Laboratory of Rare Earth Chemistry and Physics, Changchun Institute of Applied Chemistry,  
Chinese Academy of Sciences 130022, Changchun, P.R. China  
E-mail: jmeng@ns.ciac.jl.cn*

TAKANORI MORI, RYOUSUKE SASAI, KOUJI FUJITA, HIROHISA SATOH, KATSUYUKI  
AOKI AND NAOKI KAMEGASHIRA

*Department of Materials Science, Toyohashi University of Technology, Tempaku-cho, Toyohashi,  
441-8580, Japan  
E-mail: nkamegas@tutms.tut.ac.jp*

TOETSU SHISHIDO AND TUGUO FUKUDA

*Institute for Materials Research (IMR), Tohoku University, 2-1-1, Katahira-cho, Aoba-ku, Sendai  
980-8577, Japan  
E-mail: shishido@imr.tohoku-u.ac.jp*

Single crystals of  $\text{PrMnO}_3$  and  $\text{TbMnO}_3$  were grown by floating zone method and the crystal structure was determined by single crystal X-ray diffractometry. The structure of these compounds belongs to the orthorhombic system (space group is  $Pnma$ , No. 62) with the lattice parameters  $a \approx \sqrt{2} \cdot a_p$ ,  $b \approx 2 \cdot a_p$ ,  $c \approx \sqrt{2} \cdot a_p$  and  $Z = 4$ , where  $a_p$  is ideal cubic perovskite cell parameter.

### 1 Introduction

The electrical transport properties of rare earth manganites with perovskite-type structure have been extensively studied in recent years because of the colossal magnetoresistance (CMR) effect or potential applications as catalysts. In most cases the general formula of rare earth manganites used in these studies are  $\text{Ln}_{1-x}\text{A}_x\text{MnO}_3$ , where A is a divalent ion (A = Ba, Sr, Ca, Pb) substituting for La.

$\text{LnMnO}_3$  ( $\text{Ln}$  = rare earth) has an orthorhombic perovskite structure with  $\text{GdFeO}_3$  type at room temperature [1]. A common feature of this structure consists of the oxygen octahedron and this octahedron distorts and also tilts against each other in general. This kind of distortion of oxygen octahedron in rare earth manganites is caused by the Jahn-Teller effect of trivalent manganese ion surrounded by six oxygen ions. There are several reports on growth of single crystalline  $\text{LnMnO}_3$  ( $\text{Ln}$  = rare earth) [2] but no other paper has been seen on the structural analysis of single crystal of  $\text{LnMnO}_3$  with perovskite structure.

Recently we have reported the analysis of crystal structures of single crystals of  $\text{DyMnO}_3$  [3] and  $\text{LnMnO}_3$  ( $\text{Ln}$  = Nd, Sm, Eu and Gd) [4] using a four cycle X-ray diffractometer. In this study the growth of single crystals of  $\text{PrMnO}_3$  and  $\text{TbMnO}_3$  and the refined crystal structures are described. Since praseodymium and terbium have several valence states, some considerations about the atmospheric conditions are necessary.

## 2 Experimental

The single crystals were grown through zone-melting with a rotation of sintered pellet of  $\text{PrMnO}_3$  and  $\text{TbMnO}_3$ .  $\text{Pr}_2\text{O}_2\text{CO}_3$  was used as the praseodymium source and  $\text{Tb}_2\text{O}_3$  was reduced from  $\text{Tb}_2\text{O}_5$  in hydrogen at 1273K.  $\text{Mn}_2\text{O}_3$  was formed by heating under air at 1073K [3]. These starting materials and  $\text{Mn}_2\text{O}_3$  were weighed and mixed in an agate mortar. Then the mixtures were pressed into pellets and heated in Ar atmosphere at 1573K for three days. After identification of the formation of single phases of these rare earth manganites, the specimen was pulverized again and hydrostatically pressed in a rubber tube into rod-shape with 4mm diameter and 50 mm length. The rod was set to the upper and lower feed rods, which were rotated at each speed in the opposite direction. The sintered rod was melted in a bi-ellipsoidal halogen-lamp image furnace in argon. The zone passing was carried out downwards at each rate of 5 mm/h with 1 rpm, and the molten zone of about 3.5 mm in diameter and 3.5 mm height was maintained. The single crystals were cut from the solidified rod.

A suitable single crystal was selected and mounted on Rigaku-AFC7R X-ray four-circle diffractometer. These sizes were about  $0.15 \times 0.15 \times 0.15$  mm. The absorption effect was adjusted by program. Refined profiles were measured with graphite-monochromated Mo K $\alpha$  radiation. Intensities of three standard reflections, monitored throughout data collection, were constant within 4% of their respective mean intensities. The structures were analyzed by direct methods using the SHELXS-86 program [5] and refined by full-matrix least square on  $F^2$  using SHELXL-93 program [6].

## 3 Results and Discussion

Well-crystallized specimens were obtained for  $\text{PrMnO}_3$  and  $\text{TbMnO}_3$ . All crystals had black color and were obtained as a single phase. The measurement data of  $\text{PrMnO}_3$  and  $\text{TbMnO}_3$  are shown in Table 1. The conditions of systematic absences of X-ray peaks for each sample were  $k + l \neq 2n$  for  $0kl$ ,  $h \neq 2n$  for  $hk0$ ,  $h \neq 2n$  for  $h00$ ,  $k \neq 2n$  for  $0k0$  and  $l \neq 2n$  for  $00l$ . The possible space groups compatible with the above reflection conditions were centrosymmetric  $Pnma$  and acentrosymmetric  $Pn2_1a$ . The orthorhombic space group  $Pnma$  was chosen for the initial refinement.

From an expectation, these compounds would be isostructural with the  $\text{LnMnO}_3$  ( $\text{Ln} = \text{La, Nd, Sm, Eu, Gd}$ ) that are described in the space group  $Pnma$  [3,4]. There are four formula units per unit cell. The 4 rare earth atoms are in special positions  $4c$  ( $x, 1/4, z$ ), the 4 manganese atoms are in the special positions  $4b$  ( $0, 0, 1/2$ ), 4 of the 12 oxygen atoms are in the special positions  $4c$  ( $x, 1/4, z$ ), and 8 are in general positions. Unit weight was given to all the observed reflections. The atomic scattering factors for neutral atoms and the real part of the dispersion correction factors were taken from International Tables for X-ray Crystallography [7].

The final positional parameters and thermal parameters are shown in Tables 2 and 3 for  $\text{PrMnO}_3$  and  $\text{TbMnO}_3$ , respectively. The interatomic distances and angles for the samples are given in Table 4 together with their estimated standard deviation.

There are three kinds of Mn-O distances within each oxygen octahedron surrounding a central manganese ion; two of them are shorter (0.191 and 0.195 nm for  $\text{PrMnO}_3$ , and 0.194 and 0.190 for  $\text{TbMnO}_3$ ) and the other is a little longer (0.222 nm for  $\text{PrMnO}_3$  and 0.223 nm for  $\text{TbMnO}_3$ ). Thus each oxygen octahedron distorts and tilts each other, which are caused by the Jahn-Teller effect of trivalent manganese ion. Each rare

earth ion (Pr and Tb) is coordinated by twelve oxygen ions; three long, one medium and eight short length.

**Table 1.** Experimental and refinement data.

Molecular formula	PrMnO <sub>3</sub>	TbMnO <sub>3</sub>
Formula weight	243.8439 g/mol	261.8616 g/mol
Preparation method	FZ method	FZ method
<b>Crystal data</b>		
Space group	<i>Pnma</i> (62)	<i>Pnma</i> (62)
<i>a</i>	0.58249(6) nm	0.5856(7) nm
<i>b</i>	0.75705(8) nm	0.7448(1) nm
<i>c</i>	0.54454(8) nm	0.5342(3) nm
<i>V</i>	0.24013 nm <sup>3</sup>	0.2329 nm <sup>3</sup>
<i>Z</i>	4	4
<i>D<sub>c</sub></i>	6.747 g/cm <sup>3</sup>	7.442 g/cm <sup>3</sup>
Crystal size	0.15×0.15×0.15 nm <sup>3</sup>	0.15×0.15×0.15 nm <sup>3</sup>
Color	Black	Black
<b>Experiment method</b>		
Diffractometer	Rigaku AFC7R	
$\lambda$ (Mo K $\alpha$ )	0.071069 nm	
2 $\theta$	5 - 120°	5 - 120°
No. observations	1306	1372
( $I > 4.00 \sigma(I)$ )		
<b>Refinement</b>		
Refinement	Full-matrix least-square	
Thermal parameter	Anisotropic	Anisotropic
Residuals: R; R <sub>w</sub> ,	0.0846 ; 0.2279	0.0804 ; 0.2213
Program	SHELXS-86	SHELXS-93

**Table 2.** Positional and anisotropic displacement parameters for PrMnO<sub>3</sub>.

Atom	Pr	Mn	O(1)	O(2)
Site	4c	4b	4c	8d
x	0.00655(2)	0.0000	0.478(2)	0.319(1)
y	0.25000(7)	0.0000	0.2500	0.041(1)
z	-0.0121(2)	0.5000	0.085(3)	-0.287(1)
U <sub>eq</sub>	0.0066(6)	0.0060(9)	0.011(2)	0.009(2)
U <sub>11</sub>	0.0000(8)	0.000(1)	0.000(4)	0.000(3)
U <sub>22</sub>	0.0135(8)	0.012(1)	0.017(6)	0.019(4)
U <sub>33</sub>	0.0063(8)	0.006(2)	0.160(7)	0.008(4)
U <sub>12</sub>	0.0000	0.000(1)	0.0000	-0.003(3)
U <sub>13</sub>	-0.0007(2)	0.0013(7)	0.003(6)	0.000(2)
U <sub>23</sub>	0.000	-0.0000(8)	0.0000	0.003(4)

**Table 3.** Positional and anisotropic displacement parameters for  $\text{TbMnO}_3$ .

Atom	Tb	Mn	O(1)	O(2)
site	4c	4b	4c	8d
x	0.0779(6)	0.0000	0.472(2)	0.175(7)
y	0.2500	0.0000	0.2500	0.5497(8)
z	0.9843(7)	0.5000	0.100(3)	0.208(9)
U <sub>eq</sub>	0.0052(7)	0.0052(9)	0.008(7)	0.007(4)
U <sub>11</sub>	0.07(1)	0.08(3)	0.01(1)	0.08(1)
U <sub>22</sub>	0.02(1)	0.01(2)	0.00(1)	0.04(1)
U <sub>33</sub>	0.07(1)	0.05(3)	0.1(2)	0.09(1)
U <sub>12</sub>	0.000	0.01(2)	0.000	-0.001(9)
U <sub>13</sub>	-0.007(8)	0.01(2)	-0.04(2)	0.01(9)
U <sub>23</sub>	0.000	0.00(1)	0.08(8)	-0.001(8)

**Table 4.** Bond lengths (nm) and angles (deg.) for  $\text{TbMnO}_3$  and  $\text{PrMnO}_3$ .

Pr-O(1)	0.24681(1) 0.238(1) 0.346(1) 0.316(1)	Tb-O(1)	0.2308(7) 0.2339(5) 0.3180(7) 0.3602(8)
Pr-O(2)	0.2393(9)×2 0.2631(9)×2 0.3546(9)×2 0.2612(9)×2	Tb-O(2)	0.2339(5)×2 0.2389(7)×2 0.3642(5)×2 0.2595(4)×2
Mn-O(1)	0.1952(4)×2	Mn-O(1)	0.1943(2)×2
Mn-O(2)	0.1911(9)×2 0.2215(9)×2	Mn-O(2)	0.1903(5)×2 0.2236(4)×2
O(1)-Mn-O(1)	180.0°	O(1)-Mn-O(1)	180.0°
O(2)-Mn-O(2)	180.0° 89.4(1)° 90.6(1)°	O(2)-Mn-O(2)	180.0° 88.9(7)° 91.1(7)°
O(1)-Mn-O(2)	90.1(5)° 89.9(5)° 92.2(4)° 87.8(5)°	O(1)-Mn-O(2)	89.6(2)° 90.4(2)° 92.8(3)° 87.2(2)°
Mn-O(1)-Mn	151.6(9)°	Mn-O(1)-Mn	146.7(4)°
Mn-O(1)-Mn	150.0(5)°	Mn-O(1)-Mn	146.5(3)°

#### 4 Acknowledgements

This work was supported by the Grant-in-Aid for Scientific Research (B) (No. 13450259) by the Japan Society for the Promotion of Science and State Key Program of Basic Research (G1998061311) and the National Natural Science Foundation of China (29831010).

#### References

1. Khattak C. P. and F. F. Y. Wang F. F. Y., Perovskites and garnets. In Gschneidner, Jr. K. A. and Eyring L. (ed.) *Handbook on the Physics and Chemistry of Rare Earths*, (North-Holland, Amsterdam, 1979) Chapter 29, pp. 525 -607.
2. Hashimoto T., Ishizawa N., Mizutani N. and Kato M., Crystal growth and characterization of  $\text{La}_{1-x}\text{M}_x\text{MnO}_3$  ( $\text{M} = \text{Ca}, \text{Sr}$ ). *J. Crystal Growth* **84**, (1987) 207-211.
3. Mori T., Aoki K., Kamegashira N., Shishido T. and Fukuda T., Crystal structure of  $\text{DyMnO}_3$ . *Mater. Lett.*, **42**, (2000) pp.387-389.
4. Mori T., Kamegashira N., Aoki K., Shishido T. and Fukuda T., Growth and crystal structure of  $\text{LnMnO}_3$  ( $\text{Ln} = \text{Nd}, \text{Sm}, \text{Eu}, \text{Gd}$ ), *Mater. Lett.*, in press.
5. Sheldrick G. M., "SHELXS-86: A Program for the Determination of Crystal Structures from Diffraction Data," University of Göttingen, Germany (1990).
6. Sheldrick G. M., "SHELXL-93: A Program for the Refinement of Crystal Structures from Diffraction Data," University of Göttingen, Germany (1993).
7. Hahn T., "International Tables of Crystallography", Vol A (Kluwer, Boston, 1992).

This page is intentionally left blank

# A NEW NONLINEAR OPTICAL MATERIAL FOR IR REGION: KHgBr<sub>3</sub>·H<sub>2</sub>O

PENG REN, TAO LIU AND JINGUI QIN\*

*Department of Chemistry, Wuhan University, Wuhan 430072, China*

*E-mail: jgqin@whu.edu.cn*

YICHENG WU AND CHUANGTIAN CHEN

*Beijing Center for Crystal Research and Development, Chinese Academy of Science, Beijing 100080, China*

A new second-order nonlinear optical (NLO) material KHgBr<sub>3</sub>·H<sub>2</sub>O has been found. It is characterized by IR and X-ray powder diffraction (XPD). It is transparent in most of the IR region in spite of the absorption peaks in 3582 cm<sup>-1</sup> and 1613 cm<sup>-1</sup> which belong to the stretch frequencies of the crystalline water. Kurtz technique shows that the powder second harmonic generation (SHG) effect of KHgBr<sub>3</sub>·H<sub>2</sub>O is 1.5 times as large as that of KDP. The thermo-gravimetric analysis (TGA) measurement shows that KHgBr<sub>3</sub>·H<sub>2</sub>O is very stable up to 120 °C. These features make KHgBr<sub>3</sub>·H<sub>2</sub>O a potentially applicable second-order NLO material in IR region.

## 1 Introduction

Second-order nonlinear optical materials have played a key role in optical fields such as laser frequency conversion and optical parameter oscillator [1,2]. An excellent second-order nonlinear optical crystal material must exhibit the following properties: (1) relatively large SHG (second harmonic generation) coefficients. (2) wide transparency region. (3) proper birefringence. (4) high laser damage threshold. (5) good chemical stability and mechanical properties. Up to now several materials used in UV and visible regions have been found, such as KDP, KTP, BBO, LBO etc. But in IR region the current materials, such as AgGaSe<sub>2</sub>, ZnGeP<sub>2</sub>, are not so good for applications mainly due to their low laser damage threshold, as their band gaps are narrow. So the search for new nonlinear optical materials in IR region has become one of the most important issues due to their potentially wide applications in the fields such as scot and molecular spectrum [3].

In order to get materials with high laser damage threshold, we choose halide compounds as our jumping-off point because of their excellent insulation characters comparing to conventional sulfide and chalcogenides, which will be beneficial to the improvement of the laser damage threshold. In the guidance of this principle, we and an American research group have independently found an excellent NLO material CsGeCl<sub>3</sub>, whose SHG is five times as large as that of KDP [4,5], and its damage threshold reaches 200 mW·cm<sup>-2</sup> [6].

As continuation to the research of ternary halides for second-order nonlinear optical materials application, we have investigated large amounts of ternary halides with the formula ABX<sub>3</sub> (A=alkali metal; B=post transition metal; X=Cl, Br, I) in the guidance of the so-called anionic group theory. In this paper, we present the synthesis and properties of another NLO-active material for IR region: KHgBr<sub>3</sub>·H<sub>2</sub>O. Its powder SHG is 1.5 times as large as that of KDP, and it is transparent in most of the IR region, which make it a potential IR NLO material.

## 2 Experimental

### 2.1 Synthesis

The preparation of  $\text{KHgBr}_3 \cdot \text{H}_2\text{O}$  was performed according to the literature [7]. KBr and  $\text{HgBr}_2$  (mole ratio 1:1) were dissolved in hot distilled water and stirred for about 1h. While cooling, white sharp needle crystals were separated out, which was then filtered off and dried under vacuum for about 4h.

### 2.2 Physical measurements

The infrared spectrum of the  $\text{KHgBr}_3 \cdot \text{H}_2\text{O}$  in compressed pellet (with KBr) was recorded on a NICOLET 170SX FT-IR spectrophotometer with pellet in the region  $4000\text{-}400\text{ cm}^{-1}$ . X-ray powder diffraction (XRD) of the product was obtained using a SHIMAZU XRD6000 powder diffractometer with  $\text{Cu K}_{\alpha 1}$  radiation ( $\lambda=1.54056\text{nm}$ ) by a graphic monochromator. The scanning step width of  $0.02^\circ$  and the scanning speed of  $4^\circ\text{min}^{-1}$  were applied to record the patterns in the  $2\theta$  range of  $10\text{-}80^\circ$ . The thermo-gravimetric analysis (TGA) measurement on  $\text{KHgBr}_3 \cdot \text{H}_2\text{O}$  powder in static air was performed on a Shimadzu DT-40 at a scan rate of  $20^\circ\text{C/min}$ .

### 2.3 SHG measurement

The optical SHG effect was investigated using Kurtz powder technique. A Nd:YAG laser was utilized to generate fundamental  $1064\text{nm}$  light. Microcrystalline KDP served as the standard. The SHG signal was detected by a photomultiplier and read on an oscilloscope. The samples were put between two glass plates.

## 3 Results and Discussion

### 3.1 IR spectrum

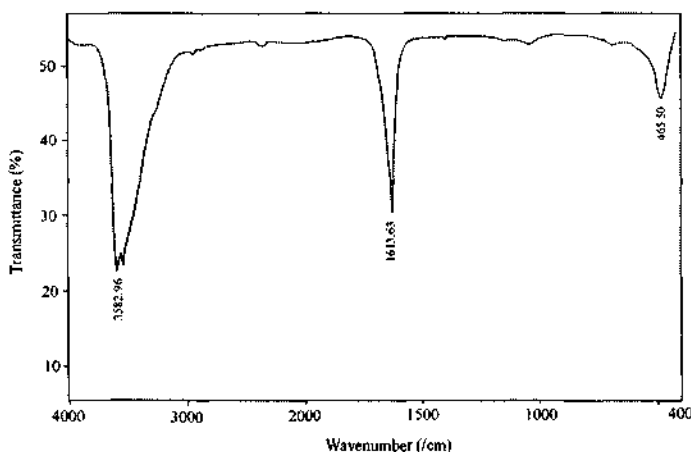


**Figure 1.** IR spectrum of  $\text{KHgBr}_3 \cdot \text{H}_2\text{O}$ .

Figure 1 shows the IR spectrum of  $\text{KHgBr}_3\cdot\text{H}_2\text{O}$ . The absorption peaks in  $3582\text{cm}^{-1}$  and  $1613\text{cm}^{-1}$  are the stretch vibration peaks of crystalline water. It is clear that there are no other peaks between  $400\text{ cm}^{-1}$  and  $4000\text{ cm}^{-1}$ , indicating that the transparent ranges of  $\text{KHgBr}_3\cdot\text{H}_2\text{O}$  are  $2.5\text{-}2.7$ ,  $2.9\text{-}5.8$  and  $6.5\text{-}25\text{ }\mu\text{m}$ . It is noteworthy that  $\text{KHgBr}_3\cdot\text{H}_2\text{O}$  is transparent between  $3\text{-}5\mu\text{m}$ , which is of vital importance to many fields such as scout and other civil applications [8].

### 3.2 X-ray powder diffraction (XPD) pattern

Figure 2 shows the X-ray powder diffraction (XPD) pattern of  $\text{KHgBr}_3\cdot\text{H}_2\text{O}$ .

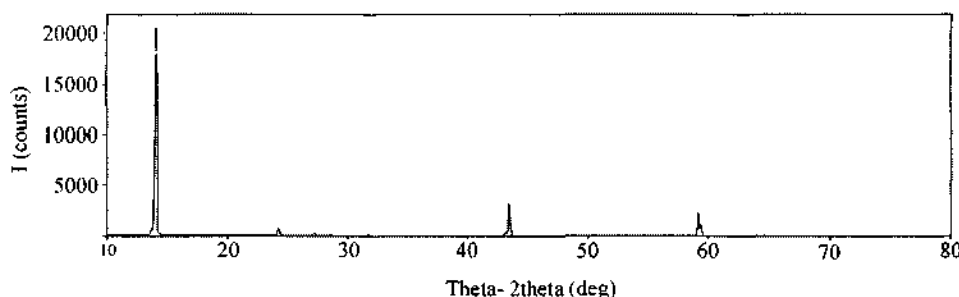


Figure 2. XPD pattern of  $\text{KHgBr}_3\cdot\text{H}_2\text{O}$ .

### 3.3 Thermo-gravimetric analysis (TGA) measurement

Figure 3 shows the thermo-gravimetric analysis (TGA) curve of  $\text{KHgBr}_3\cdot\text{H}_2\text{O}$ . The compound is stable up to about  $120\text{ }^{\circ}\text{C}$ , Then the compound begins to decompose. Between  $120\text{ }^{\circ}\text{C}$  and  $258\text{ }^{\circ}\text{C}$  weight loss is  $88.98\%$ , while between  $258\text{ }^{\circ}\text{C}$  and  $393\text{ }^{\circ}\text{C}$  the weight loss is  $11.12\%$ , which means that most of the weight has been lost.

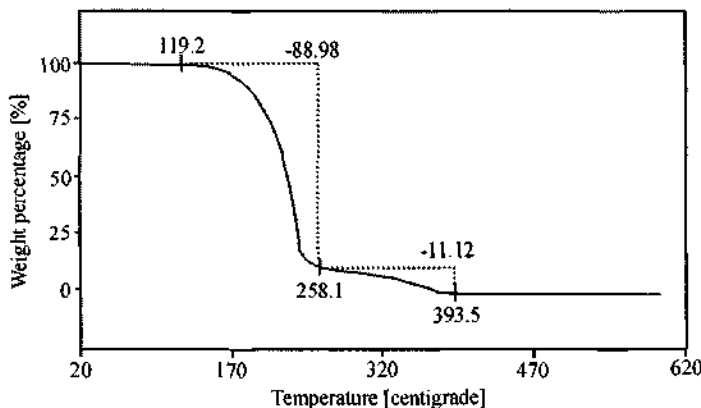
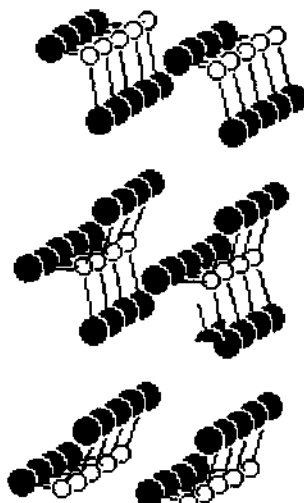


Figure 3. TGA curve of  $\text{KHgBr}_3\cdot\text{H}_2\text{O}$ .

### 3.4 Structure of $\text{KHgBr}_3 \cdot \text{H}_2\text{O}$

The space group of  $\text{KHgBr}_3 \cdot \text{H}_2\text{O}$  is Cmc21 (orthorhombic). Figure 4, 5 and 6 are the crystal structure of  $[\text{HgBr}_3]^-$  anion group in  $\text{KHgBr}_3 \cdot \text{H}_2\text{O}$  along x, y, z direction respectively [9]. Four bromide atoms are coordinated to one mercury atom to form a tetrahedron, and these tetrahedrons are connected together by bromide atoms to make up one-dimensional long chain. The mercury-bromide chains are parallel to each other. The bond length analysis shows that the bond lengths of mercury with two dangling bromide atoms, Hg–Br (1) and Hg–Br (2), are  $2.497\text{\AA}$  and  $2.499\text{\AA}$  respectively, while the bond lengths of mercury with the two bridging bromide atoms, Hg–Br (3) and Hg–Br (4), are both  $2.836\text{\AA}$ . So there is distortion within one mercury–bromide tetrahedron. Furthermore, the distortion directions of all of the mercury–bromide tetrahedrons are the same. According to the so-called anionic group theory [10], this packing mode is favorable to the accumulation of microscopic second order NLO coefficient so as to exhibit a relatively strong bulk NLO effect.



**Figure 4.** The crystal packing along  $\alpha$  direction.

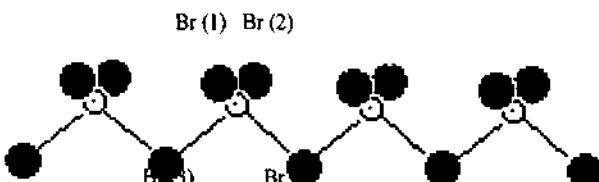


**Figure 5.** The crystal packing along the  $b$  direction.

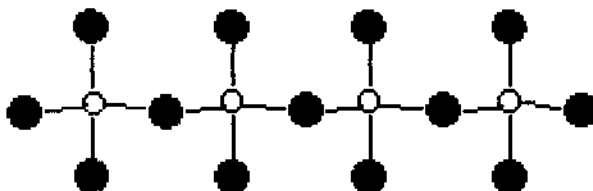


**Figure 6.** The crystal packing along the *c* direction.

### 3.5 SHG measurement

The Kurtz powder SHG measurement shows that the SHG signal of  $\text{KHgBr}_3\cdot\text{H}_2\text{O}$  is about 1.5 times as strong as that of KDP. Considering its wide transparent ranges in IR region and its relatively high stability,  $\text{KHgBr}_3\cdot\text{H}_2\text{O}$  can be expected to be a new candidate for NLO applications.

### 4 Acknowledgements

The authors are grateful to the National Key Fundamental Research Program of China (973 program) for financial support.

### References

- Chen C. T., Ye N., Lin J., Jiang J., Zeng W. R. and Wu B. C., Computer-assisted search for nonlinear optical crystals. *Adv. Mater.* **11** (1999), pp. 1071–1080.
- Qin J., Liu D., Dai C., Chen C., Wu B., Yang C. and Zhan C., Influence of the molecular configuration on second-order nonlinear optical properties of coordination compounds. *Coord. Chem. Rev.* **188** (1999), pp. 23–34.
- Dmitriev V. G., Gurzadyan G. G. and Nikojoyan D. N., *Handbook of Nonlinear Optical Crystals*, Springer-Verlag, third edition, 1999.
- (a) Zhang J., M. Sc. Thesis, Wuhan University, 1995. (b) Zhang J., Su N., Yang C., Qin J., Ye N., Wu B., and Chen C., A new NLO material in IR region:  $\text{CsGeCl}_3$ . *Proceedings of SPIE* **3556** (1998), pp. 1–3.
- Ewbank M. D., Cunningham F., Borwick R., Rosker M. J., and Gunter P., CLEO'97 CFA7, 462 (1997).
- Gu Q., Pan Q., Wu X., Shi W., and Fang C., Study on a new IR nonlinear optics crystal  $\text{CsGeCl}_3$ . *J. Crystal Growth* **212** (2000), pp. 605–607.
- Terao H., Okuda T., Uyama S., Negita H., Dou S. Q., Fuess H. and Weiss A., Crystal structure refinement and single crystal (81) Br Zeeman NQR study of  $\text{KHgBr}_3\cdot\text{H}_2\text{O}$ . *Z. fuer Naturforschung, A: Phys. Sci.*, **51** (1996), pp. 1197–1202.
- Zhang J., M. Sc. Thesis, Wuhan University, 1995.

9. Entry 83360, Inorganic crystal structure database (ICSD), Gmelin Institute, FIZ Karlsruhe, 1997.
10. (a) Chen C. T., The anion-group theory of electro-optical and nonlinear optical effects in oxides. *Sci. in China* **6** (1977), pp. 579–593. (b) Chen C. T., Wang Y. B., Wu B. C., Wu K. C., Zeng W. R. and Yu L. H., Design and synthesis of an ultraviolet-transparent nonlinear optical crystal  $\text{Sr}_2\text{Be}_2\text{B}_2\text{O}_7$ . *Nature* **373** (1995), pp. 322–324.

## VALENCY-VARIABLE CATION Co-DOPING AND Sn-Cl-DOPING IN Bi-SYSTEM 2223 PHASE SUPERCONDUCTOR

R. F. SHEN, F. Y. WANG, F. C. XU AND R. XIE

*Department of Chemistry, Xiamen University, Xiamen 361005, China*

The effects of doping cations and anions on superconducting phase structure, chemical bond and 2223 phase formation were investigated in this study. On the basis of XRD, XPS and SEM-EDAX detection, valence variation of Co and Sn, and their substitution in the 2223 phase of Bi-system superconductor were discussed. The XPS analysis showed that the Cu existed as both valence states +1 and +2, while the Bi as +3 and +4 in high  $T_c$  2223 phase of Bi-system superconductor. The inductive period of high  $T_c$  2223 phase formation at sintering was obviously reduced by doping of cation  $\text{Sn}^{4+}$  and anion  $\text{Cl}^-$ , and by valence-variable cation Co-doping, respectively.

### 1 Introduction

Concerning high  $T_c$  superconductor of Bi-system, recent studies [1-4] on its microstructure, crystal grain size, the effect of the preparation condition on its properties, phase transformation, preparation of pure 2223 phase and doping etc were reported.

In Bi-system, there exist a series of superconducting phases. Among them the Bi-system 2223 phase possesses relatively high  $T_c$  ( $T_c=110\text{K}$ ). It is a prospective superconductor material in practical application of large electric current. Therefore, the mechanism of superconductivity and formation of the 2223 phase have been of interest for a long time.

There are many factors which influence the formation of the 2223 phase of Bi-system superconductor, e.g. preparation condition, chemical composition etc. In order to study the effects of doping on the  $T_c$  and on the formation of high  $T_c$  2223 phase in the Bi-system, the high  $T_c$  phase development must be studied under specific conditions. The time when the high  $T_c$  phase appears at a sintering temperature is an important factor in the study of the doping effect on the Bi-system. It is well known that the Cu-O plane is the main origin of superconductivity in high  $T_c$  superconductor. It consists of valence-variable cations. Therefore, studies on doping with the valence-variable cation and on the induction period of 2223 phase formation after the doping are useful to reveal the mechanism of formation of the 2223 phase and its superconductivity in Bi-system. There are many reports on single cation doping, but few on the mixed doping of both cation and anion. In addition, we also reported the role of doping with both cation and anion in the formation of the high  $T_c$  2223 phase of Bi-system.

### 2 Methods

The samples were prepared by solid-state reactions. The Bi, Pb, Sr, Ca, Cu, and M (M=Co and Sn) nitrates, and Sn as chloride  $\text{SnCl}_2$  of A.R. grade, were used for the sample preparation. The chemicals were mixed in a molar ratio of Bi: Pb: Sr: Ca: Cu: M=1.7: 0.3: 2: 2: 3: 0, designated as "(1.7)(0.3) 2230", so as "(1.7) (0.3) 22 (2.91)(0.09)" and "(1.7)(0.3) 22(2.97)(0.03)", respectively. These mixtures were dissolved in an aqueous nitric acid solution, evaporated to dryness and heated at  $700^\circ\text{C}$  except for  $\text{SnCl}_2$ . The

chemicals were ground, subjected to a series of heating treatments and finally pressed into round disks.

The samples, with different sintering times at 850°C, were characterized at room temperature with XRD (Japan Riga Rot flax D/mix's), SEM (Hitachi S-520), EDAX (Philips PV9100) and XPS (Britain V.G. Com EXCA MK II XPS), respectively. Every binding energy  $E_b$  in the XPS analysis was calibrated by  $C_{1s}$ ,  $E_b=284.8\text{eV}$ . The curves of electric resistance versus temperature were determined by standard four-electrode method, in which the electric resistance at low temperature was measured in the range of liquid nitrogen temperatures.

### 3 Results and Discussion

#### 3.1 Doping effects

The samples in the experiment were all sintered at 850°C for 4h, 8h, 12h, 52h, 76h, 144h, ... and 360h, respectively, before XRD analysis. Figure 1 shows the XRD patterns of the samples sintered for 8h at 850°C, when the high  $T_c$  2223 superconducting phase appeared in the samples doped with Pb-Co and Pb-Sn-Cl ions, "(1.7) (0.3) 22(2.91) (0.09)", respectively, but not in the sample doped with Pb only in the starting composition "(1.7) (0.3) 2230". In the latter sample, high  $T_c$  2223 phase did not appear until being sintered for 76h at 850°C. The XRD spectra clearly indicate that the dopants Pb-Co or Pb-Sn-Cl have speeded up the formation of the high  $T_c$  2223 phase.

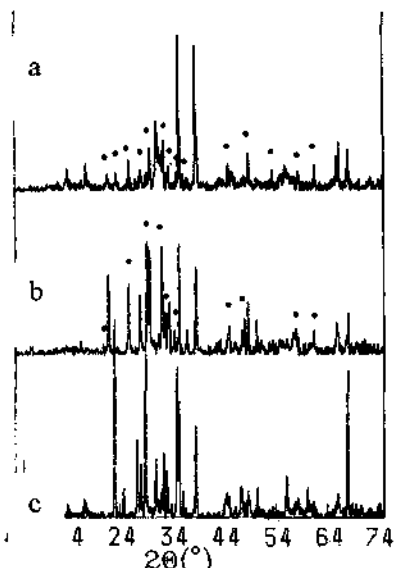


**Figure 1.** The XRD patterns of the samples sintered for 8h at 850°C: (a) doping with Pb-Sn-Cl, (b) doping with Pb-Co, (c) doping with only Pb. ●: 2223 phase.

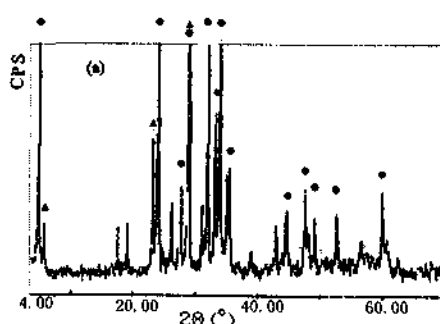


**Figure 2.** XRD pattern, the 2223 phase is over 90% in sample doped with Co ion. ●: 2223 phase, ▲: 2212.

### 3.2 Ionic valence in the high $T_c$ 2223 phase of Bi-system

When the samples were sintered at 850°C for 280h, over 90% 2223 phase was obtained, as shown in XRD Figure 2. The samples were also tested by XPS. Figure 3 (a) shows the XPS spectrum of the sample doped with Pb-Co for "(1.7) (0.3) 22 (2.91) (0.09)". Figure 3 (a) indicates that the Co [2P<sub>3/2</sub>] XPS peak has a binding energy,  $E_b$  (Co 2P<sub>3/2</sub>)=779.5 eV. The binding energy value corresponds to both valence states, Co<sup>2+</sup> and Co<sup>3+</sup>. These mixed valence states of cobalt ions may be formed through the following reaction:



In this reaction, the Co<sub>3</sub>O<sub>4</sub> is a mixture of the compounds Co<sub>2</sub>O<sub>3</sub> and CoO, and it consists of Co<sup>3+</sup> and Co<sup>2+</sup> ions. From Figure 3(b), the Cu [2P<sub>3/2</sub>] XPS peaks can be seen to have binding energies  $E_{b1}$  (Cu 2P<sub>3/2</sub>)=932.3eV and  $E_{b2}$  (Cu 2P<sub>3/2</sub>)= 933.6eV, respectively. The two values of the binding energies  $E_{b1,2}$  correspond to two valence states, Cu<sup>1+</sup> and Cu<sup>2+</sup>, respectively. The amount of Cu<sup>2+</sup> is estimated to be two thirds of that of the Cu ions in the 2223 phase.

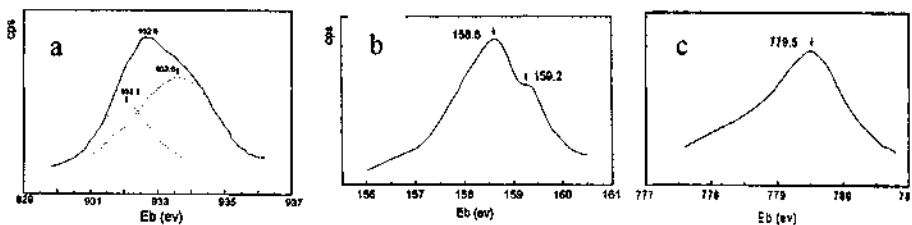


Figure 3. (a) Co[2P<sub>3/2</sub>] XPS spectrum peak, (b) Cu[2P<sub>3/2</sub>] XPS spectrum peak and (c) Bi[4f<sub>7/2</sub>] XPS peaks.

Figure 3 (C) shows two XPS peaks of Bi 4f<sub>7/2</sub>. Values of the binding energies are  $E_{b1}=158.5\text{eV}$  and  $E_{b2}=159.1\text{eV}$ , respectively. They correspond to valence states of Bi as Bi<sup>3+</sup> and Bi<sup>1+</sup>. The amount of Bi<sup>1+</sup> is larger than that of Bi<sup>3+</sup> in the Bi ions of the 2223 phase. The experiment results showed that the Cu exists as +2 and +1 valences in the 2223 phase. There are no Cu ions with a +3 valence. The Bi is presents in +3 and +4 valences. Doping of Sn-Cl or Co ions has been found to obviously reduce the induction period of the 2223 phase appearance at the sintering temperature.

### 3.3 Substitution ability of the doping ions

From SEM-EDAX analysis it is revealed that in the sample doped with Pb-Co "(1.7) (0.3) 22 (2.91) (0.09)", sintered for 144h at 850°C, the 2223 phase has a chemical formula of Bi<sub>1.7</sub>Pb<sub>0.3</sub>Sr<sub>2</sub>Ca<sub>2</sub>(Cu<sub>1-x</sub>Co<sub>x</sub>)<sub>3</sub>O<sub>y</sub>, where x=0.050.

It was confirmed that the Co ions enter the lattice in the formation reaction of the high  $T_c$  2223 phase, substituting for Cu<sup>2+</sup> and Cu<sup>+</sup> in both 5-coordination and 4-coordination, and occupying sites of Cu ions in the lattice in the superconductive planes of 2223 phase. Figure 4 is the SEM micrograph of the high  $T_c$  2223 phase for the sample doped with Pb-Co. From Figure 4, it can be seen that the crystal morphology of the 2223 phase is layer-like. Why did the doping Co ions get into the crystal lattice during the formation of the high  $T_c$  2223 phase, substituting for 4-coordination and 5-coordination Cu<sup>2+</sup> as well 4-

coordination Cu<sup>+</sup> in the crystal lattice?

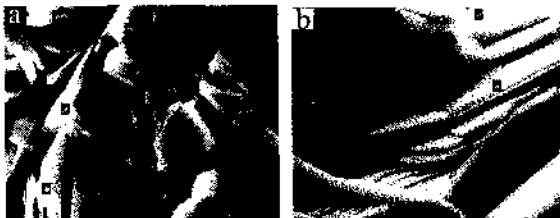


**Figure 4.** SEM micrograph of high T<sub>c</sub> 2223 phase.  
(a) doping with Pb-Co and (b) doping with Pb-Sb-Cl.

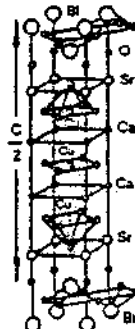


**Figure 5.** Structure of half of the single cell of the 2223 phase for the Bi-system.

On the basis of the important factors influencing substitution ability, such as their outer shell electron structure, radii and chemical properties, it is obvious that the doping Co<sup>2+(3+)</sup> ions can substitute for Cu ions easily. Figure 5 is the structure of one half of a single cell of the 2223 phase in the Bi-system [5]. First of all, from the above experiment results, it has been proved that the Co and Cu ions exist as mixed valence states, respectively, in the 2223 phase. Their ionic radii are close to each other. The radius of 4-coordination Cu<sup>2+</sup> is 0.057 nm and 4-coordination Cu<sup>+</sup> 0.060 nm., while 4-coordination Co<sup>3+</sup> radius is 0.0572 nm and 4-coordination Co<sup>2+</sup> 0.058 nm. 5-coordination Cu<sup>2+</sup> is 0.065 nm and 5-coordination Co<sup>2+</sup> is 0.067 nm [6]. Secondly, the outer shell electron configuration of Cu and Co ions is analogous to each other. That of Cu<sup>+</sup> ion is a typical type of the outer shell electron structure, (3d<sup>10</sup>). This type is considered as copper type. The outer shell electron structure of Cu<sup>2+</sup> is close to copper type. The Co<sup>3+</sup>(3s<sup>2</sup> 3p<sup>6</sup> 3d<sup>6</sup>) also belongs to transitional type and is close to copper type, too. So does Co<sup>2+(3d<sup>7</sup>)</sup>. Thirdly, the chemical properties of the cobalt ions are close to those of the copper ions as well. Therefore, Co<sup>2+(3+)</sup> ions are easy to substitute for Cu ions, i.e. the Co ions have greater substitution ability for Cu ions.

### 3.4 The factors in speeding up 2223 phase formation

The valence number of Co<sup>3+(2+)</sup> is higher than that of Cu<sup>2+(1+)</sup>. The substitution of Co<sup>2+(3+)</sup> for Cu<sup>2+(1+)</sup> is one in which the higher valence ion replaces the lower one. This substitution will increase the crystal lattice energy of the 2223 phase. Therefore after doping with the higher valence ions, the substitution improves the crystal stability of the 2223 phase and speeds up its the formation.

Secondly, superconductivity relates to the variable valence of Cu and Bi ions. From XPS analysis mentioned above, in Figure 3(b), the Cu [2P<sub>3/2</sub>] have two peaks, indicating that the Cu cations exist as both valence states, Cu<sup>2+</sup> and Cu<sup>+</sup>, in the high T<sub>c</sub> 2223 phase. Figure 3(c) also shows that there are two valence states of Bi, Bi<sup>3+</sup> and Bi<sup>4+</sup>. The two kinds of ions, Cu<sup>2+(1+)</sup> and Bi<sup>3+(4+)</sup> are of the variable valence, and exist as mixed valence states, respectively, in the 2223 phase. The doping Co ion is valence-variable and exists as the

mixed valence states,  $\text{Co}^{3+}$  and  $\text{Co}^{2+}$ , which are satisfied for the superconductive structure. These mixed valence states are likely to exchange with each other, respectively, in the 2223 phase.  $\text{Co}^{3+(2+)}$  substitutes for  $\text{Cu}^{2+(1+)}$  ions and occupies Cu ion sites of the Cu-O plane, increasing possibility of formation of 2223 phase in Bi-system. Consequently, it speeds up the formation of the 2223 phase. The Cu-O plane is the main origin of superconductivity in high  $T_c$  2223 phase of the Bi-system.

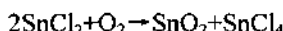
### 3.5 The Pb-Sn-Cl doping

Table I shows the intensity "I" and the relative intensity " $I/I_0$ " values of the XRD characteristic peak (002) of the high  $T_c$  2223 phase. When the samples were sintered for 8h at 850°C and the 2223 phase just appeared, the peak value for the sample doped with Pb-Sn-Cl ions,  $I=19$ ,  $I/I_0=5$ , was even greater than that for Pb-Co ions,  $I=5$ ,  $I/I_0=1$ . It illustrates that doping with Pb-Sn-Cl is even better and faster than Pb-Co doping to speed up the formation of 2223 phase, as follows:

**Table I.** The XRD data of 2223 superconductor phase in different ion-doping samples sintered at 850°C for 8h.

Original composition	Doping with metal ion	2223 phase	hkl	I	$I/I_0$
"(1.7)(0.3)2230"	Pb	—	002	—	—
"(1.7)(0.3)22(2.91)(0.09)"	Pb,Sn	Yes	002	19	5
"(1.7)(0.3)22(2.91)(0.09)"	Pb,Co	Yes	002	9	1

From SEM-EDAX analysis, the chemical stoichiometric formula of the high  $T_c$  2223 phase was obtained as  $\text{Bi}_{1.7} \text{Pb}_{0.3} \text{Sr}_2 \text{Ca}_2(\text{Cu}_{1-x}\text{Sn}_x)_3\text{O}_y\text{Cl}_z$ ,  $x=0.055$  for the sample doped with Pb-Sn-Cl, "(1.7)(0.3)22(2.91)(0.09)", sintered at 850°C for 144h. The experimental results confirmed that the substitution of  $\text{Sn}^{4+}$  for Cu ion in the Cu-O plane was realized. Sn ion may exist as  $\text{Sn}^{4+}$  in the high  $T_c$  2223 phase. The  $\text{Sn}^{4+}$  would be formed by the following reaction, when  $\text{SnCl}_2$  was heated during the sintering process of formation of 2223 phase:



The reasons for doping with Sn ion to speed up the formation of 2223 phase are the same as for doping with Co ion. The radii of 4-coordination and 5-coordination  $\text{Sn}^{4+}$  are 0.055 nm and 0.062 nm, respectively, being close to that of 4-coordination  $\text{Cu}^+$  of 0.060 nm, 4-coordination  $\text{Cu}^{2+}$  of 0.057 nm and 5-coordination  $\text{Cu}^{2+}$  of 0.065 nm. Their ionic radii are close to each other. Therefore,  $\text{Sn}^{4+}$  can be substituted for 4-coordination  $\text{Cu}^+$  or  $\text{Cu}^{2+}$  and for 5-coordination  $\text{Cu}^{2+}$ . Moreover, the  $\text{Sn}^{4+}$  outer shell electron structure,  $n^2np^6nd^{10}$  is the same as  $\text{Cu}^+$ , and they belong to copper type and are close to the  $\text{Cu}^{2+}$  outer shell electron structure ( $nd^9$ ). It is easier to substitute  $\text{Sn}^{4+}$  for 4-coordination  $\text{Cu}^+$  and  $\text{Cu}^{2+}$  and easier to form Sn-O square plane of 4-coordination  $\text{Sn}^{4+}$ . So the possibility of formation of 2223 phase is increased and the formation of the 2223 phase is obviously speeded up by doping with  $\text{Sn}^{4+}$ . As mentioned above, the substitution reduces the system energy and increases the crystal lattice energy, because the substitution of  $\text{Sn}^{4+}$  for  $\text{Cu}^+$  and  $\text{Cu}^{2+}$  is one of higher valence ion for lower one. The crystal of the 2223 phase becomes

more stable. The substitution of  $\text{Sn}^{4+}$  also speeds up the formation of the high  $T_c$  2223 phase. In addition, the radius of  $\text{Sn}^{4+}$  is smaller than that of the Co ion. Therefore, the diffusion rate of  $\text{Sn}^{4+}$  ion is faster during sintering reaction and the formation of the 2223 phase is speeded up.

The chemical stoichiometric formula of the 2223 phase determined by SEM-EDAX has approached to a theoretical one.

### *3.6 Effect of Doping on interplanar spacing and formation of 2223 phase*

From the XRD pattern given in Figure 1, it can be seen that when the specimen doped with Pb-Sn-Cl (1.7)(0.2)22(2.91)(0.09) was sintered at 850°C for 8h, the interplanar spacing (0012) along the *c*-axis was 0.3089(2) nm in the 2223 phase crystal. But for the specimen doped with Pb only the spacing was 0.3083(2) nm. The experimental value of the interplanar spacing was the same under different sintering duration for the same specimen. The experimental result showed that the interplanar spacing value of the 2223 phase along the *c*-axis was increased after doping with Pb-Sn-Cl. It implies that the anion  $\text{Cl}^-$  got into the lattice and occupied certain positions in the crystal lattice of the 2223 phase. In the lattice the anion  $\text{Cl}^-$  might be located in two possible sites. First, the  $\text{Cl}^-$  was substituted for  $\text{O}^{2-}$ , and occupied the  $\text{O}^{2-}$  sites. Secondly, the  $\text{Cl}^-$  is sandwiched between the layers in a single cell of the 2223 phase crystal. In the crystal cell of the 2223 phase, the layer sequence along the *c*-axis can be represented as

...BiO SrO CuO<sub>2</sub> Ca CuO<sub>2</sub> Ca CuO<sub>2</sub> SrO Bi<sub>2</sub>O<sub>2</sub> SrO CuO<sub>2</sub> Ca CuO<sub>2</sub> Ca CuO<sub>2</sub> SrO BrO..... as shown in Figure 5. If  $\text{Cl}^-$  substitutes for  $\text{O}^{2-}$  in the Cu-O square plane or pyramid bottom Cu-O plane, and occupies the position of the  $\text{O}^{2-}$  ion, the Cu-Cl or Bi-Cl bond will be formed in high  $T_c$  2223 phase. The crystal interplanar spacing would be expanded, because the radius of  $\text{Cl}^-$  ion is larger than that of  $\text{O}^{2-}$  (0.181 nm for 6-coordinational  $\text{Cl}^-$  and 0.140 nm for  $\text{O}^{2-}$ ), but without forming Cu-Cl and Bi-Cl bond. And when the  $\text{Cl}^-$  is sandwiched between layers in the single cell, it also enlarges the distance between the layers. On the contrary,  $\text{Sn}^{4+}$  radius is slightly smaller than those of  $\text{Cu}^+$  and  $\text{Cu}^{2+}$ , as mentioned above, and substitution of  $\text{Sn}^{4+}$  for Cu ions will results in reduction of the interplanar spacing, but the reducing value is less than expanding value made by the  $\text{Cl}^-$ . Therefore, as a result of double actions of the cation  $\text{Sn}^{4+}$  and the anion  $\text{Cl}^-$ , the experimental value of the interplanar spacing is larger than that of the sample doped with Pb only along the *c*-axis in the 2223 phase crystal.

### *3.7 The behavior of $\text{Cl}^-$ anion*

It is to point out that doping with  $\text{Cl}^-$  ion has no influence on both Cu 2p<sub>3/2</sub> and Bi 4f<sub>7/2</sub> binding energies of Cu-O and Bi-O bonds in the 2223 phase, as shown in Figure 3. From the XPS results, it can be seen that the Cu2p<sub>3/2</sub> binding energy is  $\text{Cu}^+$   $E_{\text{b}1}=932.4$  eV and  $\text{Cu}^{2+}$   $E_{\text{b}2}=933.6$  eV, respectively. The binding energy of Bi 4f<sub>7/2</sub> is  $E_{\text{b}1}=158.5$  eV and  $E_{\text{b}2}=159.1$  eV, respectively. The values are unvaried, either in the specimen doped with Pb-Sn-Cl, or in the other specimen doped with Pb only without doping with  $\text{Cl}^-$ , and/or doped with Pb-Co etc. The result proves that there are no Cu-Cl and Bi-Cl bonds in the 2223 phase doped with Pb-Sn-Cl., though  $\text{Cl}^-$  got into the lattice. The  $\text{Cl}^-$  ion may be sandwiched between the Bi-O double layers, and between the Cu-O square plane and Cu-O pyramid bottom plane. Because there are larger free spaces there (The distance between Bi-O double layers is ~0.340nm. The length of the Bi-O bond in the Bi-O layer is ~

0.271 nm. The distance from the Cu-O square plane to the Cu-O pyramid bottom plane is  $\sim 0.351$  nm. The Cu-O bond length in the Cu-O plane is  $\sim 0.192$  nm [7]). The Cl<sup>-</sup> entered between layers in the crystal cell of the 2223 phase, enlarging the interplanar spacing along the  $c$ -axis, but not being substituted for O<sup>2-</sup>.

Moreover, the energy coefficient of a divalent anion O<sup>2-</sup> is larger than that of a monovalent anion Cl<sup>-</sup> in the crystal. If the substitution of monovalent anion Cl<sup>-</sup> for O<sup>2-</sup> proceeded, the crystal lattice energy would be decreased. Consequently the crystal of the high T<sub>c</sub> 2223 phase would become less stable and the possibility of the formation of the high T<sub>c</sub> 2223 phase would be reduced. So, the doping Cl<sup>-</sup> anion prefers to be sandwiched between the layers along the  $c$ -axis rather than substituting for O<sup>2-</sup>. In addition, it can increase the degree of crystal disordering in the single cell of the high T<sub>c</sub> superconducting 2223 phase if Cl<sup>-</sup> has been sandwiched between layers. Consequently, the thermodynamic entropy value of the system increases and obviously the value of the Gibbs free energy  $\Delta G$  in the formation reaction of 2223 phase decreases, making the value more negative. The doping Cl<sup>-</sup> enables the 2223 phase to form more easily; The doping Cl<sup>-</sup> expands the interplanar spacing, making cations easily diffuse into suitable positions of the crystal lattice during thermal reaction. Cl<sup>-</sup> promotes the formation of the 2223 phase, too.

Figure 6 provides the XRD patterns of the samples doped with Pb-Sn-Cl, sintered at 850°C for 144h, when high T<sub>c</sub> 2223 phase is the predominant phase in the samples. Figure 7 shows the R-T curves of the samples of the high T<sub>c</sub> 2223 phase as the predominating phase. Figure 7 (a) is for the samples doped with Pb-Co and Figure 7 (b) for the ones doped with Pb-Sn-Cl.

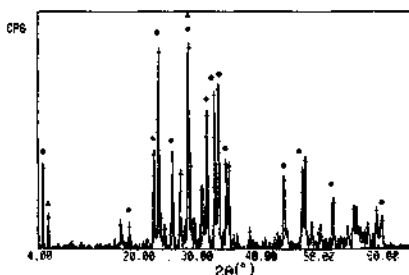


**Figure 6.** XRD pattern of the sample doped with Pb-Sn-Cl. ●: 2223 phase, ▲: 2212.

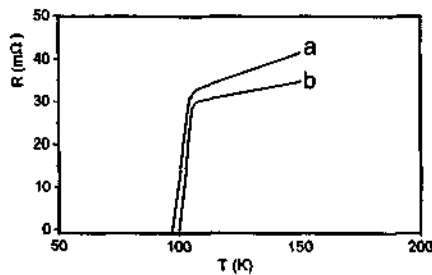


**Figure 7.** R-T curves of the samples for high T<sub>c</sub> 2223 phase: (a) doping with Pb-Co, (b) doping with Pb-Sn-Cl.

#### 4 Conclusions

Doping of valence-variable cation Co speeds up the formation of the high T<sub>c</sub> 2223 phase in Bi-system. Doping with both cation Sn<sup>4+</sup> and anion Cl<sup>-</sup> speeds up the formation of high T<sub>c</sub> 2223 phase further. There are Cu<sup>2+</sup>, Cu<sup>+</sup>, Bi<sup>3+</sup> and Bi<sup>4+</sup> cations in the high T<sub>c</sub> 2223 phase, but Cu<sup>3+</sup> is not found.

## References

1. Rinaudo G., Allasia D., Volpe P., Benzi P. and Agostino A., *Physica C*, **353** (2001) pp. 184-194.
2. Caillat R., Gomina M., *Superconductor Science & Technology*, **14** (2002) pp. 712-716.
3. Halim S. A., Saleh Al-K., Azhan H., Mohamed S. B., Khalid K. and Suradi J., *J. Mater. Sci.*, **35** (2000) pp. 3043-3046.
4. Hamid N. A. and Shukor R., *J. Mater. Sci.*, **35** (2000) pp. 2325-2329.
5. Tsuneyuki K., Tomoichi K. and Shin-Pei M., *Jpn. J. Appl. Phys.* **28** (1989), L551.
6. Shannon R. D., *Acta Cryst.*, **A32** (1976) p. 751
7. Lu W., Zhang Y. et al., *Acta Phys. Chim. Sinica*, **5** (1989), pp. 129-134.

## TOPOLOGICAL PROPERTIES AND ELECTRONIC STRUCTURES OF COMPOUNDS WITH PYRITE-TYPE CRYSTAL STRUCTURES

A. C. STÜCKL, R. WEIHRICH AND K. -J. RANGE

*Institut für Anorganische Chemie, Universitätstr. 31, D-93040 Regensburg, Deutschland, Germany*  
*E-mail: ac\_stueckl@yahoo.de*

$\text{SiP}_2$ ,  $\text{FeS}_2$ , and  $\text{AuSb}_2$  crystallize with pyrite structure. The structural topologies of the three compounds are comparable, while their constituting elements belong to very different groups of the periodic system of the elements. This fact motivates our interest in finding some criteria for the stability of their atomic arrangements. We used density functional methods (LCAO-CO Ansatz) to characterize the topological properties of the electron density: in addition to the results from theoretically determined structural parameters, band structures, and the electron localization function, the electronic charges of the corresponding atoms are calculated on the basis of Bader's zero-flux surface approach. It is shown, that charge transfer between the constituting elements of the pyrite structure is a characteristic feature of the structural stability in the title compounds. The detailed results on the partial density of states for all studied compounds finally allow the explanation of the theoretically determined density topology on the atomic level.

### 1 Introduction

$\text{AX}_2$  compounds with crystal structures belonging to the pyrite type ( $\text{C}2$ ) are well documented in the literature. Due to the constant interest in the electronic, optical, and magnetic properties of these materials, there exists extended experimental and theoretical work. Among the title compounds, synthetic or natural pyrites,  $\text{FeS}_2$ , turn out to be very well studied, like other transition metal disulphides, in both respects [1-5], while the electronic structures of pyrite-type  $\text{SiP}_2$  [6,7] and  $\text{AuSb}_2$  [8] are only partially known, and no theoretical study exists for the latter.

In trying to explain the stability of the  $\text{C}2$  structure in case of  $\text{SiP}_2$ ,  $\text{FeS}_2$ , and  $\text{AuSb}_2$ , an interesting question arises. Why do these binary compounds crystallize with topologically equal structures, where the constituting elements stem from very different groups of elements of the periodic system, and the electronic properties differ significantly from each other?  $\text{FeS}_2$  is a narrow gap semiconductor,  $\text{AuSb}_2$  shows metallic conductivity and even superconductivity with  $T < 0.58$  K, and  $\text{SiP}_2$  has semimetallic properties. The stability of transition metal chalcogenides and pnictides with pyrite structure were intensively discussed in the literature [5,9-12], looking at the different building blocks like the octahedral and tetrahedral coordination surrounding of the A- and X-elements, respectively, and the sublattices of A (cubic face centered arrangement) and X (molecular dumb-bells). Important concepts like ligand field- and MO-theory [9], the valence electron concentration (VEC) [10], and the electroneutrality principle [11] were used to find out systematic connections between the crystal structure and the electronic structure of these compounds. In this context, often also highly ionic limiting structures had to be discussed. The synopsis of the experimental observations on the trends of  $\text{X}_2$  charge densities in  $\text{FeS}_2$ ,  $\text{MnS}_2$  and  $\text{SiP}_2$  [7] however, where only small amounts of charge were found, led to the conclusion, that charge transfer between A and  $\text{X}_2$  might take place to reduce the local charge and cause stabilization.

To pick up this topic in a more general and quantitative way, we have chosen a quantum chemical approach. In contrast to published theoretical work on this subject, we

used density functional methods [13] to characterize the topological properties of the electron density [14,15]. At first, structural parameters obtained by the calculations are presented. The band structures and densities of states will give more details on the electronic structure of SiP<sub>2</sub> and new results on AuSb<sub>2</sub> with pyrite structure. Atom charges will be derived in the context of the zero-flux surface approach of Bader. In addition, the result of the electron localization function [17] is analyzed. The density functional approach yields for the title compounds a systematic trend without the restrictions of the former concepts, as it is e.g. the exclusion of metallic compounds like AuSb<sub>2</sub> from the stability considerations by the ligand field theory [10] or the VEC [11].

## 2 Calculation Methods

The calculations were performed within the framework of density functional theory as implemented in the CRYSTAL98 code [16]. The local density approximation (LDA) [13] was mainly used and compared with different approaches and functionals, e.g. B3LYP and GGA [13,16]. The valence electron configurations 3s<sup>2</sup>3p<sup>2</sup>, 3s<sup>2</sup>3p<sup>3</sup>, and 3s<sup>2</sup>3p<sup>4</sup> were considered by the choice of the basissets for Si, P, and S, as well as the 5s<sup>2</sup>5p<sup>3</sup>-configuration for Sb, all improved by polarization functions of d-character. Fe was described with a 3d<sup>6</sup>4s<sup>2</sup> configuration and polarization functions of s- and p-character. For Au, the 5s<sup>2</sup>5p<sup>6</sup>5d<sup>10</sup>6s<sup>1</sup> configuration, extended by p-polarization functions, was considered. All-electron basissets and valence electron basissets with Durand-Barthelat-pseudopotentials were optimized and compared for the atoms Si, P, S, Fe, and Sb. The Au basis set was optimized for the free atom using a suitable effective core potential (ECP) of Hay and Wadt, including relativistic effects. To prepare the electronic structure calculations of the chemical compounds in the solid state, the coefficients of the more diffuse functions were re-optimized with respect to the loss of the outer diffuse shells, that had to be removed as well as the f-states of Au in the bulk. Throughout this work, crystal orbitals were constructed from linear combinations of atomic orbitals (LCAO-CO *Ansatz*) with the aim to calculate partial atomic and orbital densities of states (DOS). Sufficient numbers of k-points for reliable self consistent results were obtained by a set of calculations on different grids in the reciprocal space, using the symmetry of space group No. 205 [18] and the Monkhorst-Pack scheme. Band structures were calculated along paths connecting several special points: X, R, M, and  $\Gamma$ . For the topological analysis, the zero-flux condition is applied to the gradient vector field of the electron density  $\rho(\mathbf{r})$ ,

$$\nabla \rho(\mathbf{r}) \cdot \mathbf{n}(\mathbf{r}) = 0,$$

where from the unit vectors  $\mathbf{n}(\mathbf{r})$ , normal to the surface at  $\mathbf{r}$ , the shape of the topological atoms can be constructed. The calculation and integration of the zero-flux surfaces, as well as the analysis of the electron localization function (ELF), was performed with the program TOPOND [17]. For the construction of the graphical zero flux surfaces, the program MAPLE V [19] was used. The color-coded ELF plots were visualized with ORIGIN4.1 [20].

## 3 Results and Discussion

The characteristic structure parameters of the pyrite structure, as obtained by the DFT calculations, are given in Tab. I in comparison to the experimental values. For the measured lattice parameters  $a$ , FeS<sub>2</sub> has a minimum. The position parameters increase

from 0.376 ( $\text{AuSb}_2$ ) and 0.385 ( $\text{FeS}_2$ ) to 0.391 ( $\text{SiP}_2$ ), and cross the value 0.38, for which the distances A-X and X-X equalize. The coordination angles, e.g. X-A-X, A-X-A, and X-X-A, deviate more strongly from the ideal octahedral or tetrahedral environment in going from the lighter elements to the heavier atoms A and X. In  $\text{AuSb}_2$ , on the other hand, X-X-A and X-A-X are therefore quite similar.

The LDA results describe the experimental trends quite well. It is noticed, that the distances X-X and A-X as well as the lattice parameters are underestimated for  $\text{AuSb}_2$  and  $\text{FeS}_2$ , a typical effect of the local density approximation. The theoretical unit cell of  $\text{SiP}_2$  is slightly expanded in comparison to the experimental result, which was assumed to be a high pressure phase [7]. All position parameters u are reproduced with sufficient precision.

**Table 1.** Structure parameters of  $\text{AuSb}_2$ ,  $\text{FeS}_2$ , and  $\text{SiP}_2$  obtained by LDA and experiment (d [ $\text{\AA}$ ], angles [ $^\circ$ ]).

$\text{AX}_2$	a [ $\text{\AA}$ ]	u (x,x,x)	d (XX)	d (AX)	$d(\text{AX})/d(\text{XX})$	(AXA)	(XXA)	(XAX)	Lit.
<b><math>\text{AuSb}_2</math></b>									
exp.	6.658	0.3760	2.860	2.762	0.97	116.9	100.3	95.1	[22]
calc.	6.644	0.3760	2.854	2.756	0.96	116.9	100.3	95.1	-
<b><math>\text{FeS}_2</math></b>									
exp.	5.428	0.3850	2.162	2.269	1.05	115.7	102.1	94.4	[23]
calc.	5.403	0.3830	2.152	2.258	1.05	115.5	102.4	94.3	-
<b><math>\text{SiP}_2</math></b>									
exp.	5.707	0.3906	2.162	2.397	1.11	114.6	103.7	93.9	[8]
calc.	5.720	0.3900	2.180	2.402	1.10	114.7	103.5	93.9	-

The electronic structures of the title compounds were determined on the basis of the optimized structure parameters with LDA, and are shown in Fig. 1. All energy values are related to the calculated Fermi energies ( $T=0\text{K}$ ). The resulting band gaps, being slightly underestimated by the chosen approach, confirm the experimental results on the material properties of the studied compounds in general.  $\text{FeS}_2$ , however, did not show a band gap at all, when the optimized structure parameters were used, as mentioned in [3]. A band structure calculation for the experimental cell ( $a = 5.42 \text{ \AA}$ ) is therefore used for the graphics depicted in Fig. 1. The resulting DOS of  $\text{FeS}_2$  corresponds almost quantitatively to the results of former studies [3-5]:  $\sigma$  and  $\sigma^*$  ( $\text{S} 3s$ ) levels are found between energies of -0.65 and -0.40 H, followed by the states of  $\sigma$ ,  $\pi$  and  $\pi^*$  character (mainly  $\text{S} 3p$ , accompanied by small amounts of  $\text{Fe} 4s$ ,  $4p$ ,  $3d$ ) at energies from -0.3 to -0.05 H. The Fe  $3d$  levels are well separated from the crystal orbitals of S and split up in two sets ( $t_{2g}$  and  $e_g$ , if the oversimplified picture of  $\text{O}_h$  site symmetry is used). At higher energies, S  $\sigma^*$  ( $3p$ ) orbitals mix slightly with the virtual  $e_g$  levels.

In contrast to this result, where the transition metal d orbitals of an octahedral coordination environment and the MOs of the  $\text{S}_2$  dumb-bells are nicely identified, the band structure and DOS analysis on  $\text{SiP}_2$  yields a strong mixing between all contributing valence orbitals of Si and P in the region between -0.32 and -0.02 H. The calculated total density of states fits extremely well to the measured  $\text{L}_{2,3^-}$  and  $\text{K}_\beta$ -spectra (X-ray emission) and underlines the results of Farberovich *et al.* [6], obtained by an orthogonalized plane wave (OPW) method in 1975. Their detailed interpretation of the emission peaks, concerning e.g. the strong P (3s) contribution to the lowest valence states, can now be supported by the actual calculation of the partial DOS, where the P (3s) orbitals indeed dominate the band with  $\sigma$  (P-P bond) character between -0.56 and -0.45 H. At higher energies, admixture of Si (3s, 3p) orbitals is found.

The electronic structure of  $\text{AuSb}_2$  yielded a complex picture of electron donating and accepting levels by experimental studies. Due to this fact, Ahn *et al.* [8] cleared up the Fermi surface only for certain symmetry directions and gave strong arguments for the modification of the usual nearly free electron (NFE) model in that case.

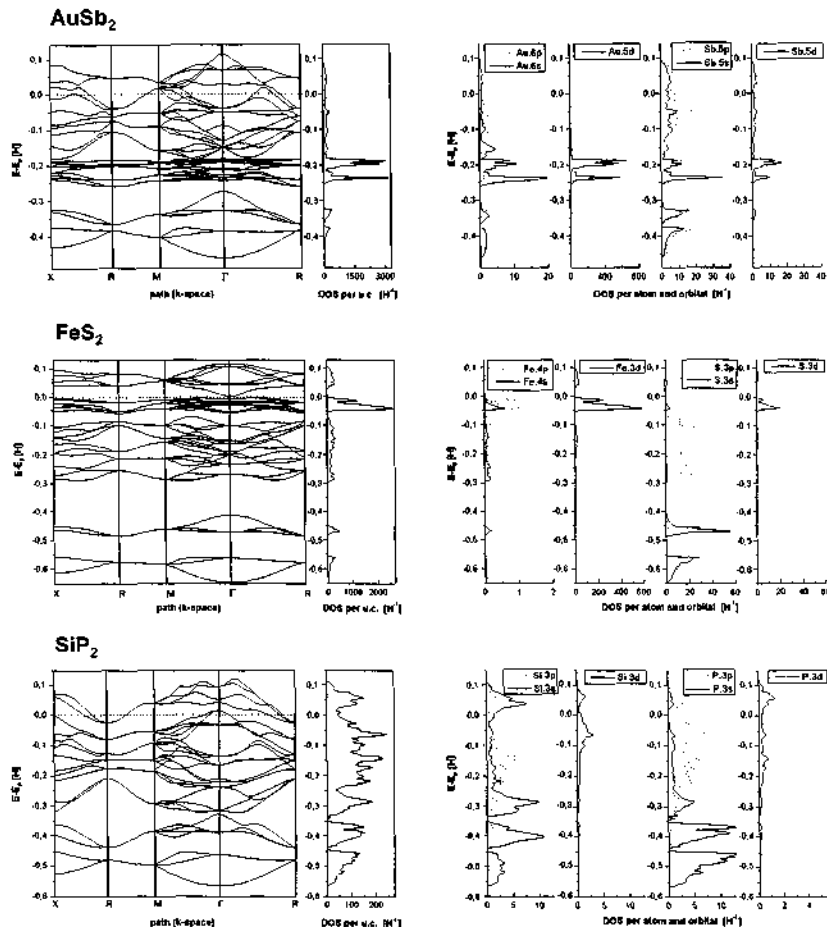
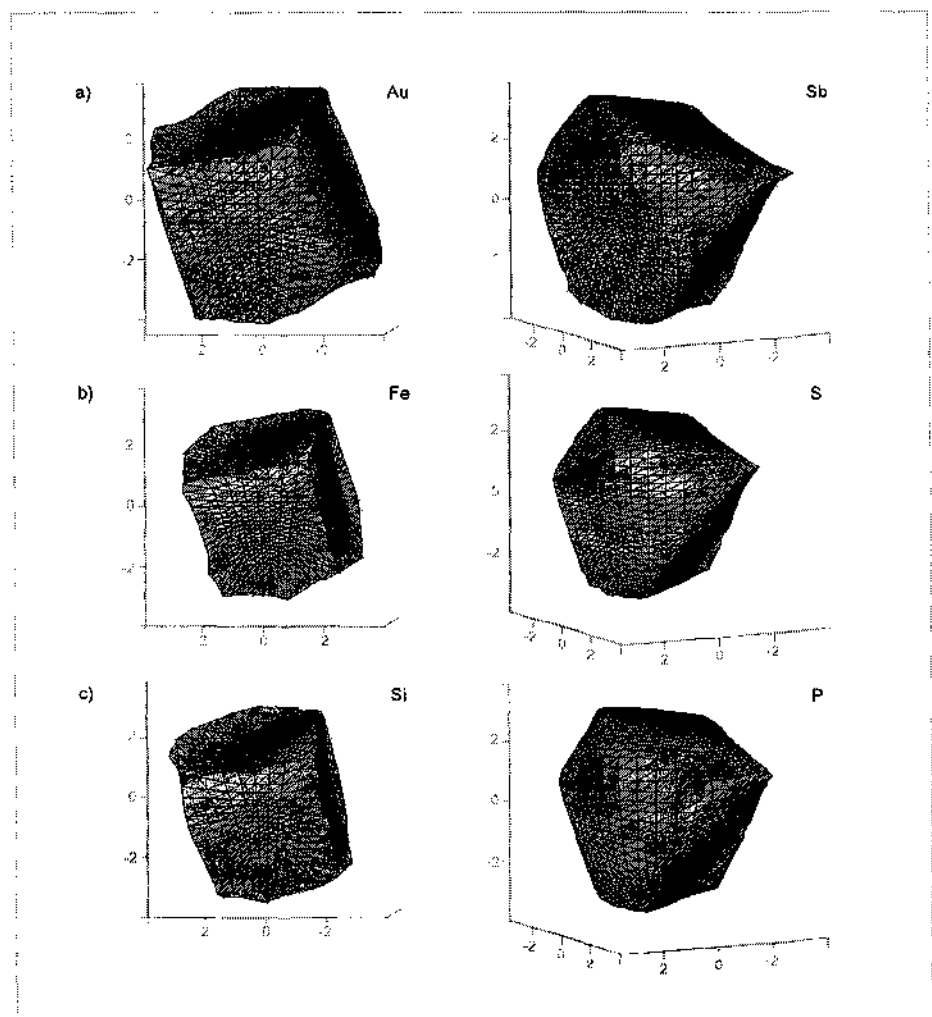


Figure 1. DFT band structures and DOS of  $\text{AuSb}_2$ ,  $\text{FeS}_2$ , and  $\text{SiP}_2$ .

The DFT calculation, as shown in Fig. 1, results in the following assignment. As already seen for  $\text{FeS}_2$  and  $\text{SiP}_2$ , the bands at lowest energies (from -0.46 to -0.27 H) have  $\sigma$  and  $\sigma^*$  character and are predominantly formed by Sb 5s orbitals. The contributions of Sb 5p and 5d states to the crystal orbital linear combinations with  $\sigma_p$ ,  $\pi_p$ - and  $\pi_p^*$ -character of the  $\text{Sb}_2$  dumb-bells are found at higher energies, between -0.18 and +0.02 H. They are obviously separated from the Sb 5s orbitals by the Au 5d states which form a band of about 0.07 H bandwidth, centered at -0.22 H. From there, the contribution of Au d-states to all  $\text{Sb}_2$  dumb-bell orbitals (the enlarged intensity scale is not shown in the figure)

continues. Another new feature in this bandstructure is the band with  $\pi^*$  character, which is not completely filled and crossed by the Fermi level in all sections of the chosen path.

The total charge distribution was revealed according to Bader's approach of zero-flux surfaces [14,15]. Different basis sets and functionals were tested for each compound. The calculated charge per atom varied only over a small range at the same unit cell size. On the other hand, significant differences within the charge distributions are found, if the unit cell volume is varied.



**Figure 2.** Zero-flux surfaces of  $\text{AuSb}_2$  (a),  $\text{FeS}_2$  (b), and  $\text{SiP}_2$  (c) (as obtained by solid state calculations for space group Nr. 205; scaling: a.u.).

Depicted graphically in Fig. 2, a very similar shape of the zero-flux surface is observed for all the elements Au, Fe, and Si of type A in  $\text{AX}_2$ . For X, according to the different site symmetry, the contour of the surface changes, again being comparable for the three different elements. The interatomic surface of X is essentially shared with the neighboring X atom, but the remaining atoms of the distorted tetrahedral coordination

sphere are separated from X by parts of the zero-flux surface, too. The interatomic surfaces of the A-type atoms are constructed by almost regular contacts to its six direct neighbors.

**Table 2.** Integration of zero-flux surfaces in  $\text{AuSb}_2$ ,  $\text{FeS}_2$ , and  $\text{SiP}_2$  from LDA calculations.  
(The  $\beta$ -sphere radius, the atomic volumes and charges, and the resulting amount of charge transfer is given.)

$\text{AX}_2$	$a [\text{\AA}]$	$u(x,x,x)$	$r_\beta [\text{\AA}]$	$r_\beta(X)/r_\beta(A)$	$V [\text{\AA}^3]$ , calc.	N (electrons)	CT (electrons)
$\text{AuSb}_2$	6.644	0.3760	1.47 1.40	0.95 1.04	293.019 160.484	20.12 25.42	-1.12 +0.56
$\text{FeS}_2$	5.420	0.3850	1.03 1.07	1.10	187.275 10.380	12.76 6.29	+0.58 -0.29
$\text{SiP}_2$	5.720	0.3900	0.97 1.07	1.10	18.219	5.62	+1.24 -0.62

The integration results are collected in Tab. 2. Au, the noble metal with high electronegativity on Pauling's scale, attracts from each Sb atom about 0.56 electrons. In  $\text{FeS}_2$ , the S atoms obtain additional charge density (0.29 electrons) as well as each P in  $\text{SiP}_2$  (0.62 electrons).

A different aspect of the bonding situation, supporting the DOS results, is given by the analysis of electron localization (ELF). Compared to the values of the homogeneous electron gas in the three compounds, all A-X and X-X regions give raise to find localized electron pair density. However, no common saddle point was seen for the Sb-Sb bond. Au and Sb<sub>2</sub> "bath" in an environment, where localization is only slightly enhanced with respect to the free electron gas, a typical feature of metallic interactions. S<sub>2</sub> has a saddle point in the Laplacian of the electron density. The relatively high value for localized pair density strongly supports a characteristic dumb-bell bond. Some electron pairs are oriented towards Fe. The transition metal shows delocalization in its surrounding, too. All A-X as well as the X-X bonds have a large covalent character in  $\text{SiP}_2$ , which is shown by remarkably high values of ELF in the bonding regions.

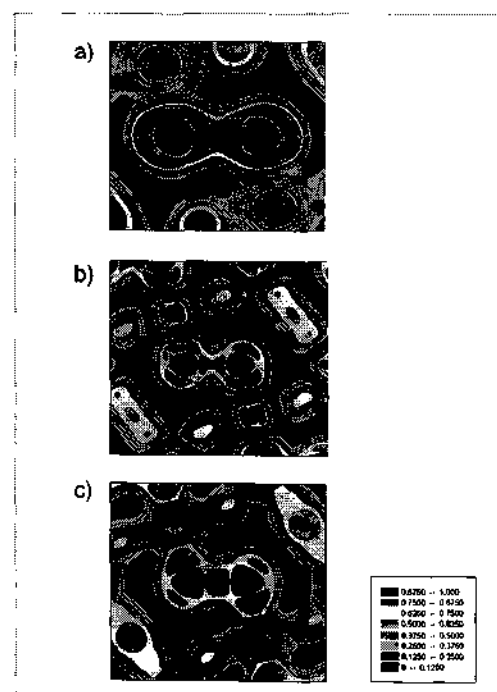


**Figure 3.** ELF plots of the (1-11)-plane in pyrite-type  $\text{AuSb}_2$ (a),  $\text{FeS}_2$ (b), and  $\text{SiP}_2$ (c).

#### 4 Charge transfer – topological versus quantum chemical approach?

The similar topology of the electron densities in compounds with pyrite-type structures is a consequence of the similar atomic arrangements. Only, if the elements under consideration are proper candidates to build up such an electron density distribution, there will crystallize a stable phase of this structure and composition in the equilibrium.

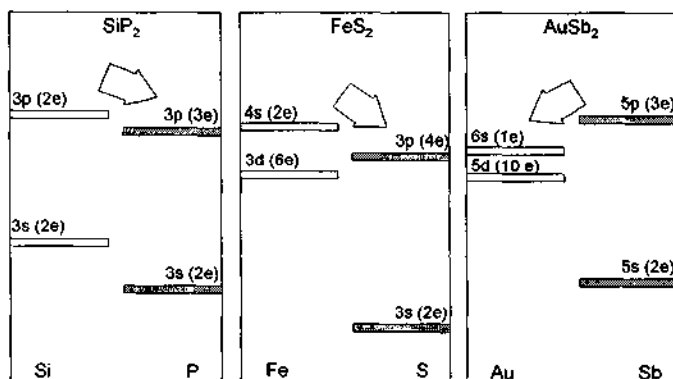
Following the actual concepts on the electronegativity  $\chi$  of atoms, as obtained by DFT calculations [13] from the ionization potentials I and the electron affinities A with

$$\mu \approx -0.5(I+A), \text{ where } \chi = 0.5(I+A), \text{ and hence } \mu \approx \chi,$$

the calculated striking trend of the charge transfer is found again when comparing the  $\chi$ -values of the studied elements:

Atoms	Sb, Au	S, Fe	P, Si
$\Delta\chi$ [14]	-0.92	+2.16	+0.85

Because of the known connection between electronegativity values and the one electron levels of the corresponding atoms, a direct link exists to predict charge transfer properties of compounds on the basis of the quantum chemical characteristics of the contributing elements. Simplifying the approach, the eigenvalues of the atomic levels have been calculated (relativistic effects are considered at Au and Sb) for the title compounds to predict the charge transfer path of these "open shell systems" schematically.



#### 5 Acknowledgements

The financial support of this work by the Deutsche Forschungsgemeinschaft and the Fonds der Chemischen Industrie is gratefully acknowledged.

#### References

1. Suga S., Kimura A., Matsushita T., Sekiyama A., Imada S., Mamiya K., Fujimori A., Takahashi H., and Mori N., 2p resonance photoemission and Auger features in NiS<sub>2</sub> and FeS<sub>2</sub>, *Phys. Rev. B* **60** (1999) pp. 5049-5054.

2. Lauer S., Trautwein A. X., and Harris F. E., Electronic-structure calculations, photoelectron spectra, optical spectra, and Mössbauer parameters for the pyrites  $M S_2$  ( $M=Fe, Co, Ni, Cu, Zn$ ), *Phys. Rev.* **B29** (1984) pp. 6774-6783.
3. Opahle I., Koepernik K., and Eschrig H., Full-potential band structure calculation of iron pyrite, *Phys. Rev.* **B60** (1999) pp. 14035-14041.
4. Zeng Y. and Holzwarth N. A., Density-functional calculation of the electronic structure and equilibrium geometry of iron pyrite ( $FeS_2$ ), *Phys. Rev.* **B50** (1994) pp. 8214-8220.
5. Raybaud P., Hafner J., Kresse G., and Toulhoat H., *Ab initio* density functional studies of transition-metal sulphides: II. Electronic structure, *J. Phys. Condens. Matter* **9** (1997) pp. 11107-11146.
6. Farberovich O. V. and Domashevskaya E. P., Band structure and density of states in  $SiP_2$ , *Phys. Stat. Sol. (b)* **72** (1975) pp. 661-665.
7. Chattopadhyay T. K. and von Schnering, H. G., Pyrite-type silicon diphosphide  $p$ - $SiP_2$ : Structural parameters and valence electron density distribution, *Z. f. Kristallographie* **167** (1984) pp. 1-12.
8. Ahn J. and Sellmyer D. J., Fermi surface of  $AuSb_2$ . II. de Haas-van Alphen and de Haas-Shubnikov effects, *Phys. Rev.* **B1** (1970) pp. 1285-1296.
9. Hulliger F., Crystal chemistry of the chalcogenides and pnictides of the transition elements, *Structure and Bonding* **4** (1968) pp. 83-229.
10. Parthé E., Valence-electron concentration rules and diagrams for diamagnetic, non-metallic ionic-covalent compounds with tetrahedrally coordinated anions, *Acta Cryst.* **B29** (1973) pp. 2808-2815.
11. Pauling L., Covalent chemical bonding of transition metals in pyrite, cobaltite, skutterudite, millerite and related minerals, *Canadian Mineralogist* **16** (1978) 447-452.
12. Brese N. E. and von Schnering, H. G., Bonding trends in pyrites and a reinvestigation of the structures of  $PdAs_2$ ,  $PdSb_2$ ,  $PtSb_2$  and  $PtBi_2$ , *Z. anorg. allg. Chem.* **620** (1994) pp. 393-404.
13. Parr R. G., Yang W., Density-functional theory of atoms and molecules (Oxford University Press, Oxford, 1989), and refs. therein.
14. Bader R. F. W., Atoms in molecules. A quantum theory (Oxford University Press, Oxford, 1990).
15. Bader R. F. W., The zero-flux surface and the topological and quantum definitions of an atom in a molecule, *Theor. Chem. Acc.* **105** (2001) pp. 276-283.
16. Saunders V. R., Dovesi R., Roetti C., Causa M., Harrison N. M., Orlando R., Zicovich-Wilson C. M., CRYSTAL98, User's manual (Torino, 1999), and Towler M., [http://www.tcm.phy.com.ac.uk/mdi26/basis\\_sets](http://www.tcm.phy.com.ac.uk/mdi26/basis_sets).
17. Gatti C., TOPOND98, User's manual (Milano, 1999), and refs. therein.
18. Hahn T., International tables for crystallography, Vol. A (D. Reidel Publishing Company, Dordrecht, 1987).
19. Maple V, Release 5, for Unix/Windows (Waterloo Maple Inc., Star Division, 1998).
20. Origin 4.1 (Microcal Software, Northampton, USA, 1991).
21. Furuseth S., Selte K., Kjekshus A., Redetermined crystal structures of  $PdAs_2$ ,  $PdSb_2$ ,  $PtP_2$ ,  $PtAs_2$ ,  $PdAs_2$ ,  $PtSb_2$ ,  $\alpha$ - $PtBi_2$ , and  $AuSb_2$ , *Acta Chem. Scand.* **19** (1965) pp. 735-741.
22. Finklea S., Cathey L., Amma E., Investigation of the bonding mechanism in pyrite using the Mössbauer effect and X-ray crystallography, *Acta Crystallogr.* **A32** (1976) pp. 529-537.

# SYNTHESIS AND ELECTROCHEMICAL PERFORMANCE OF LiMn<sub>2-x-y</sub>Co<sub>x</sub>Y<sub>y</sub>O<sub>4</sub> CATHODE MATERIALS FOR LITHIUM-ION SECONDARY BATTERY

TANG HAO, FENG CHUAN-QI, JIA MAN-KE AND ZHANG KE-LI\*

*College of Chemistry and Molecular Sciences, Wuhan University, Wuhan 430072, China*  
*E-mail: kdzhang@whu.edu.cn*

The complex LiMn<sub>2-x-y</sub>Co<sub>x</sub>Y<sub>y</sub>O<sub>4</sub> cathode materials with spinel-type structure were synthesized by rheological phase reaction method. The coordination precursors were prepared by rheological phase reaction and the cathode materials LiMn<sub>2-x-y</sub>Co<sub>x</sub>Y<sub>y</sub>O<sub>4</sub> were obtained by heating precursors at certain temperatures. These materials were characterized by XRD. The result demonstrated that the synthesized materials have complete spinel structure, the same as the parent LiMn<sub>2</sub>O<sub>4</sub> spinel. Their electrochemical behavior has also been examined in cells with lithium metal as anode and 1 mol.L<sup>-1</sup> LiClO<sub>4</sub>/PC as an electrolyte. A remarkable enhancement of the cyclability was observed, with a retention of the initial capacity>90% after 60 cycles at current density (IC). The synthesis, characterization and electrochemical properties of the cathode materials LiMn<sub>2-x-y</sub>Co<sub>x</sub>Y<sub>y</sub>O<sub>4</sub> are presented in this paper.

## I Introduction

The spinel LiMn<sub>2</sub>O<sub>4</sub> is regarded as one of the best-known compounds used as an insertion cathode in 4V rechargeable lithium batteries due to their low cost, abundance, and non-toxicity compared with layered oxide such as LiCoO<sub>2</sub> and LiNiO<sub>2</sub> [1-3]. The capacity of this cathode, however, decreases with cycling in the 4V range [4]. The capacity fade in spinel LiMn<sub>2</sub>O<sub>4</sub> is described as being due to a J-T effect of Mn<sup>3+</sup> and the weaker Mn-O bond in an octahedron. This capacity drop has been addressed by exploring alternatives to classic ceramic synthetic method [5-6] and by doping the spinel with various elements such as Mg, Zn, Cu, Ni, Co, Cr, Fe, Al and Ga, in order to improve its stability against cycling [7-15]. Among these element cobalt seems to be one of the most promising dopants investigated so far [11]. Although higher cobalt doping ( $x > 0.1$ ) is reported to be the best for cycle stability [11,16], replacement of Mn by the more expensive Co not only adds to the cost of material synthesis but also reduce the initial capacity of the electrode. There also attempts on the partial replacement of the Mn ions in LiMn<sub>2</sub>O<sub>4</sub> by Y<sup>3+</sup> [17-18]. Choi [18] found that the dopant of yttrium can improve the cyclability, but because the large Y<sup>3+</sup> radius, it is hard to form pure spinel structure and the initial capacity is also low. Recently, a few multiple substitutions of elements have been found to improve the cathode behavior of LiMn<sub>2</sub>O<sub>4</sub> and show good performance [19-20]. However, the co-doping ions were limited in one kind cation with another kind anion. Multiple cation substitution of Mn in the spinel LiMn<sub>2</sub>O<sub>4</sub> has rarely been reported. In this paper, we synthesized the Co and Y co-doped compound LiCo<sub>x</sub>Y<sub>y</sub>Mn<sub>2-x-y</sub>O<sub>4</sub> at small x and y values using rheological phase reaction method and studied its electrochemical performance as a cathode. The complex LiCo<sub>x</sub>Y<sub>y</sub>Mn<sub>2-x-y</sub>O<sub>4</sub> with various x and y values were prepared. Presently, results on phase with x=0.02, y=0.00,0.005,0.01,0.015 are reported.

## 2 Experimental

The complex  $\text{LiCo}_x\text{Y}_y\text{Mn}_{2-x-y}\text{O}_4$  was synthesized using rheological phase reaction method. The rheological phase reaction method is a process of preparing compounds or materials from solid-liquid rheological mixture. That is, the solid reactants were fully mixed in a proper molar ratio, made up by adding a proper amount of water or other solvent to a solid-liquid rheological body in which the solid particles and liquid substance were uniformly distributed. Then after reaction under suitable conditions, the product was obtained. Under the solid-liquid rheological state, many substances have new reaction properties, which are reported in our earlier work [21-23]. This synthesis method is inexpensive and simple. On the other hand, the resultant powders prepared by this method show perfect crystal structures and excellent electrochemical performance. In this paper, the synthesis, characterization and the further electrochemical property studies of the prepared  $\text{LiCo}_x\text{Y}_y\text{Mn}_{2-x-y}\text{O}_4$  powders are presented.

The complex  $\text{LiCo}_x\text{Y}_y\text{Mn}_{2-x-y}\text{O}_4$  studied in this work were prepared using lithium acetate  $\text{CH}_3\text{COOLi}\cdot 2\text{H}_2\text{O}$  and proper stoichiometric amounts of cobalt acetate  $(\text{CH}_3\text{CO}_2)_2\text{Co}\cdot 4\text{H}_2\text{O}$ , manganese acetate  $(\text{CH}_3\text{CO}_2)_2\text{Mn}\cdot 4\text{H}_2\text{O}$  and yttrium oxide  $\text{Y}_2\text{O}_3$  as the starting materials. The  $\text{CH}_3\text{COOLi}\cdot 2\text{H}_2\text{O}$ ,  $(\text{CH}_3\text{CO}_2)_2\text{Mn}\cdot 4\text{H}_2\text{O}$ ,  $(\text{CH}_3\text{CO}_2)_2\text{Co}\cdot 4\text{H}_2\text{O}$  and  $\text{Y}_2\text{O}_3$  were mechanically mixed in proper mole ratios, then add a proper quantity of citric acid (the amount equals to the mole sums of the total metal ions). After the powders were mixed homogeneously, a proper quantity of water was added. A solid-liquid rheological body was made by slightly milling the solid and liquid mixtures. Then a precursor was obtained from the solid-liquid rheological body in a closed container at 70-90°C for 8-10h. The spinel  $\text{LiCo}_x\text{Y}_y\text{Mn}_{2-x-y}\text{O}_4$  was obtained by thermal decomposition of the precursors at 750°C for 5-6 h in air.

Powder X-Ray diffraction was employed to identify the crystalline phase of the prepared powder samples. Rietveld refinement was then performed on the XRD data to obtain the lattice constants. The electrochemical properties of  $\text{LiCo}_x\text{Y}_y\text{Mn}_{2-x-y}\text{O}_4$  powders were characterized in  $\text{Li}/\text{LiCo}_x\text{Y}_y\text{Mn}_{2-x-y}\text{O}_4$  cells. The working electrodes were prepared by mixing polyvinylidene fluoride(PVDF), carbon black and  $\text{LiCo}_x\text{Y}_y\text{Mn}_{2-x-y}\text{O}_4$  powders in the ratio of 8:12:80% w/w, respectively. Electrochemical measurements were performed using lithium metal as counter and reference electrodes. The electrolyte was 1.0M anhydrous  $\text{LiClO}_4$  dissolved in a 1:1 v/v ethylene carbonate and dimethyl carbonate mixture. The cell was cycled at a current rate of 0.2C between 3.6 and 4.3V, unless otherwise specified.

## 3 Discussion

$\text{LiMn}_2\text{O}_4$  and co-doped  $\text{LiCo}_x\text{Y}_y\text{Mn}_{2-x-y}\text{O}_4$  ( $x=0.02, y=0.005, 0.01, 0.015$ ) have been prepared using rheological phase reaction method. They are well-crystalline and black in color. XRD data showed that pure single-phase materials have formed for the above referred x and y. And they all possess the same cubic structure (space group: Fd3m) as the parent compound  $\text{LiMn}_2\text{O}_4$  (see Figure 1). Compounds with higher y values were found to contain impurity phase and hence were not pursued further. The Rietveld refinement method was used to calculate the lattice parameters from the XRD data. The value of  $\text{LiMn}_2\text{O}_4$ :  $a=8.244\text{\AA}$ , which is in good agreement with that reported in the literature [24].

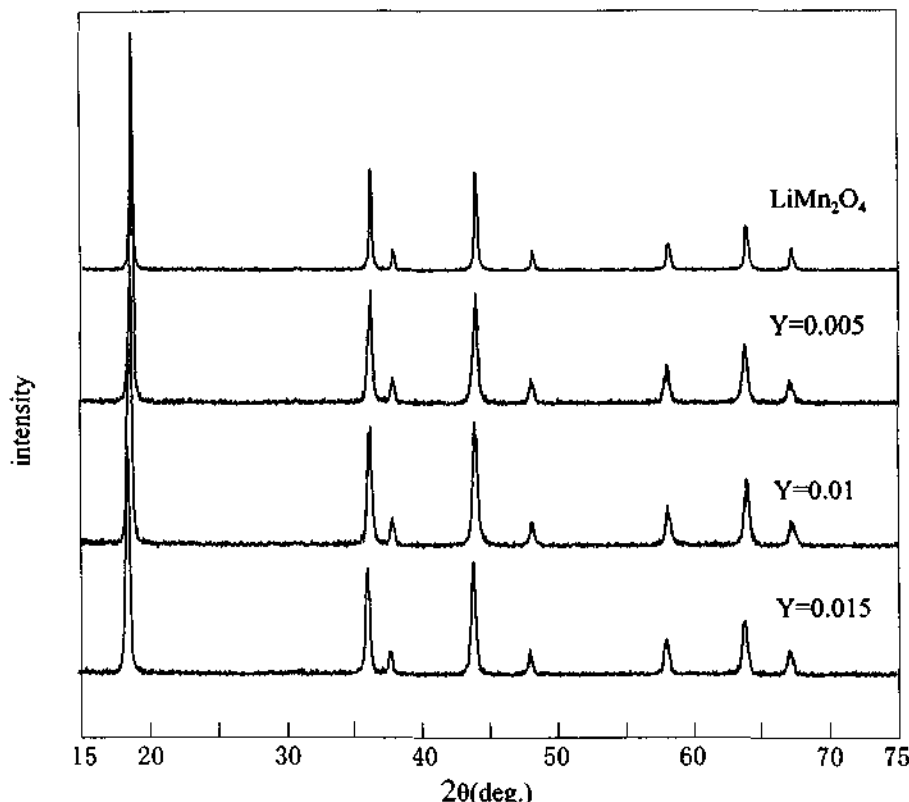


Figure 1. XRD patterns of  $\text{LiMn}_2\text{O}_4$  and  $\text{LiMn}_{2-y}\text{Co}_{0.02}\text{Y}_y\text{O}_4$  ( $y=0.005, 0.01, 0.015$ ) powders annealed at 750°C.

For  $y=0.005$ ,  $a=8.241\text{\AA}$ ;  $y=0.01$ ,  $a=8.233\text{\AA}$ ;  $y=0.015$ ,  $a=8.227\text{\AA}$ . The lattice parameters show a decrease with Co and Y doping. This is perhaps due to the effects of the Co-O bond and Y-O bond in the octahedron when the cations are incorporated into the spinel structure.

Galvanostatic charge-discharge curves have been recorded for the voltage window 3.6–4.3V versus Li metal at current rate of 0.2C for the cathodes up to 60 cycles. The current ratings were calculated from the actual currents and the weights of the active cathode material. In previous studies [25–28], doping of cations in  $\text{LiMn}_2\text{O}_4$  show a trade-off between capacity and cycleability, i.e. doping prevents capacity fading, but decreases the initial capacity. The trade-off relationship is also observed in this study. All the Co and Y co-doped spinel powders show lower initial capacity than undoped  $\text{LiMn}_2\text{O}_4$ , but better cycleability. The first charge capacity of  $\text{LiCo}_x\text{Y}_y\text{Mn}_{2-x-y}\text{O}_4$  varied from 118 to 125 mAh/g for the composition with different  $y$  values (Table 1). The irreversible capacity loss after the first discharge ranged from 5 to 7 mAh/g. The charge-discharge capacities in the range 5–60 cycles remained the same ( $\pm 2\%$ ) for all the compounds indicating excellent reversibility of the cathodes. After 60 cycles, the capacity retention ranged from 86% to 95%. As can be seen, the smaller Co and Y co-doped compound shows very good

cyclability, giving a constant higher discharge capacity up to 60 cycles. Pure  $\text{LiMnO}_4$ , on the other hand, shows a capacity fading with only 75% retention after 60 cycles.

**Table 1.** Cathode charge-discharge and irreversible capacities of the compounds,  $\text{Li}(\text{Co}_{0.02}\text{Y}_y\text{Mn}_{1.98-y})\text{O}_4$  at 0.2 C rate from 3.6-4.3 V (values are in mAh/g).

	$\text{LiMn}_2\text{O}_4$	$y=0.005$	$y=0.01$	$y=0.015$
First charge capacity	137	132	128	123
First discharge capacity	130	125	122	118
Irreversible discharge capacity	7	7	6	5
Reversible capacity after 60 cycles	98	108	113	112
Discharge capacity retention after 60 cycles	75%	86%	93%	95%
Reversible capacity after 60 cycles (1C rate)	79	93	102	108

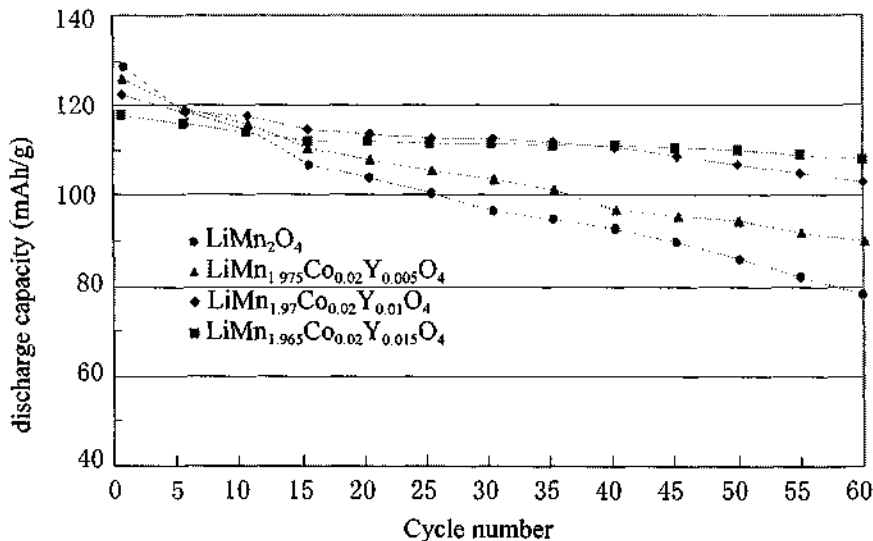


**Figure 2.** Plots of discharge capacity vs. the number of charge-discharge cycles for the cathodes:  $\text{LiMn}_2\text{O}_4$  and  $\text{LiMn}_{2-y}\text{Co}_{0.02}\text{Y}_y\text{O}_4$  ( $y=0.005, 0.01, 0.015$ ) prepared by rheological phase reaction method. Voltage window is 3.6-4.3 V (vs. Li-metal). Tests were done at 0.2C rate for 1-4th cycle, 0.5C rate for 5-14th cycle and finally at 1C rate for 15-60th cycle.

In order to explore the high-rate capacity of the cathodes, which is of relevance in the practical lithium-ion cells, tests were done on another batch of cells in the voltage range 3.6-4.3V using the following procedure, viz. charge-discharge cycling at 0.2C rate for the 1-4th cycle, 0.5 C rate for 5-14th cycle, and finally at 1 C rate for 15-60th cycle. Results are shown in Figure 2. The effect of Y-doping is clearly seen in giving consistently large cathodic capacities even at the 1 C rate, and the  $y=0.015$  shows the best behavior with the first discharge of 118 mAh/g and >90% retention after 60 cycles. Again the charge-

discharge capacities in the range 5-60 cycles were found to remain within  $\pm 2\%$  even at these high current ratings.

#### 4 Conclusion

The rheological phase reaction method offers a new and simple way to prepare compounds and materials. The prepared compounds  $\text{LiCo}_x\text{Y}_y\text{Mn}_{2-x-y}\text{O}_4$  show excellent capacity and cycleability. The cathode behavior of the  $\text{LiMn}_2\text{O}_4$  can be greatly improved by simultaneous doping of cobalt and yttrium, and our results on  $\text{LiCo}_x\text{Y}_y\text{Mn}_{2-x-y}\text{O}_4$  show that the composition with  $x=0.02$ ,  $y=0.015$  exhibits the best high current rate (1C) capacity up to 60 cycles. The compound after optimization may find potential application in practical lithium-ion cells.

#### 5 Acknowledgement

This work was supported by The National Nature Science Foundation of China (No.20071026).

#### References

1. T. Ohuzuku, M. Kitagawa, and T. Hirai, *J. Electrochem. Soc.*, **137** (1990) pp. 760.
2. W. J. Macklin, R. J. Neat, and R. J. Powell, *J. Power Sources*, **34** (1991) pp. 39.
3. D. Guyomard and J. M. Tarascon, *Solid State Ionics*, **69** (1994) pp. 222.
4. A. Momchilov, V. Manev, A. Nassalevska, and A. Kozawa, *J. Power Sources*, **41** (1993) pp. 305.
5. P. Barboux, J. M. Tarascon, and F. K. Shokoohi, *J. Solid State Chem.*, **94** (1991) pp. 18.
6. Y. Xia and M. Yoshio, *J. Electrochem. Soc.*, **143** (1996) pp. 825.
7. G. Pistoia, A. Antonini, R. Rosati, C. Bellitto, G. M. Ingo, *Chem. Mater.*, **9** (1997) pp.1443.
8. N. Hayashi, H. Ikuta, M. Wakihara, *J. Electrochem. Soc.*, **146** (1999) pp. 1351.
9. J. M. Tarascon, E. Wang, F. K. Shokoohi, W. R. McKinnon, S. Colson, *J. Electrochem. Soc.*, **138** (1991) pp. 2859.
10. D. Song, H. Ikuta, T. Uchida, and M. Wakihara, *Solid State Ionics*, **117** (1999) pp.151.
11. L. Guohua, H. Ikuta, T. Uchida, and M. Wakihara, *J. Electrochem. Soc.*, **143** (1996) pp. 178.
12. A. D. Robertson, S. H. Lu, W. F. Averill, W. F. Howard Jr, *J. Electrochem. Soc.*, **144** (1997) pp. 3500.
13. L. Hernan, J. Morals, L. Sanchez, J. Santos, *Solid State Ionics*, **118** (1999) 179.
14. M. Y. Song, D. S. Ahn, S. G. Kang, S. H. Chang, *Solid State Ionics*, **111** (1998) pp.237.
15. Q. Zhang, A. Bonakdarpour, M. Zhang, Y. Gao, and J. R. Dhan, *J. Electrochem. Soc.*, **144** (1997) pp. 205.
16. J. M. Amarilla, J. L. Martin de Vidales, and R. M. Rojas, *Solid State Ionics*, **127** (2000) pp. 73.

17. A. D. Robertson, S. H. Lu, W. F. Averill, and W. F. Howard, *J. Electrochem. Soc.*, **144** (1997) pp.3500.
18. H. J. Choi., K. M. Lee, and J. G. Lee, *J. Power Sources*, **103**, (2001) pp.154.
19. Y. K. Sun and I. H. Oh, *J. Power Sources*, **94** (2001) pp.132.
20. S. H. Park, K. S. Park, S. S. Moon, Y. K. Sun and K. S. Nahm, *J. Power Sources*, **92** (2001) pp.244.
21. J. T. Sun, X. Wei, L. J. Yuan, K. L. Zhang, and Q. Y. Wang, *Mater. Sci. Eng.*, B, **64**, (1999) pp. 157.
22. K. L. Zhang, M. K. Jia, H. Tang, J. B. Yuan, L. J. Yuan, and J. T. Sun, *J. Wuhan University (Natural Science Edition)*, **47**, (2001) pp. 657.
23. K. L. ZHANG, Y. ZHANG, L. P. ZHANG, L. J. YUAN and J. T. SUN, *J. Wuhan University (Natural Science Edition)*, **46** (2000) pp.77.
24. D. H. Jang, Y. J. Shin, and S. M. Oh, *J. Electrochem. Soc.*, **143**, (1996) pp.2204.
25. A. Kock, E. Ferg, R. J. Gummow, *J. Power Sources*, **70** (1998) pp.247.
26. M. Wohlfart-Mehrens, A. Buts, R. Oesten, G. Arnold, R. P. Henmer, R.A. Huggins, *J. Power Souces*, **68** (1997) pp.582.
27. M. Okada, Y.-S. Lee, M. Yoshio, *J. Power Souces*, **90** (2000) pp.196.

# A NEW ORTHORHOMBIC PHASE OF $\text{ZrW}_{1.6}\text{Mo}_{0.4}\text{O}_8$ AT AMBIENT PRESSURE

XINHUA ZHAO AND WANG QI

*Department of Chemistry, Beijing Normal University, Beijing 100875, P. R. China*  
*E-mail:xinhua@bnu.edu.cn*

HUI MA

*Analyzing and Testing Center, Beijing Normal University, Beijing 100875, P. R. China*

Nanocrystallite  $\delta'$ - $\text{ZrW}_{1.6}\text{Mo}_{0.4}\text{O}_8$  was prepared through a precursor route. The characterization by powder X-ray diffraction (XRD) and selected area electron diffraction (SAED) shows that the compound is orthorhombic crystal system with cell parameters:  $a=0.8969(7)$  nm,  $b=0.7011(8)$  nm,  $c=0.596(1)$  nm. The possible space group is Pnnm (58) or Pnn2 (34). The compound is a metastable phase depending on temperature and time.

## 1 Introduction

$\text{ZrW}_2\text{O}_8$  presents a few models of structures. The first report was by Graham et al. [1] and confirmed by Chang et al. [2] in pseudobinary phase diagram of  $\text{ZrO}_2$ - $\text{WO}_3$  system at atmospheric pressure. Cubic zirconium tungstate,  $\text{ZrW}_2\text{O}_8$ , possesses the acentric  $P2_13$  structure ( $\alpha$  form,  $a = 0.91575$  nm at 293K) [3] and is transformed to disordered centric  $\text{Pa}(-3)$  structure ( $\beta$  form,  $a = 0.91371$  nm, at 483 K) [3]. The precise transition temperature of  $\alpha$  to  $\beta$  form is 448 K determined by neutron HRPD data [4]. The linear coefficient of thermal expansion is about  $-9 \times 10^{-6}$  K $^{-1}$  with the cubic structure from 0.3-1050K and 1378-1530K [3-5]. It was suggested that the negative thermal expansion (NTE) property resulted from the unique structural characteristic [6].

The compound  $\text{ZrMo}_2\text{O}_8$  was until 1998 only known to occur in trigonal [7, 8] ( $\alpha$  form,  $P(-3)c$ ,  $a = 1.01391$  nm,  $c = 1.17084$  nm) and monoclinic [9, 10] ( $\beta$  form,  $C2/c$ ,  $a = 1.14309$  nm,  $b = 0.79376$  nm,  $c = 0.74619$  nm,  $\beta = 122.323^\circ$ ) forms. A new polymorph of  $\text{ZrW}_2\text{O}_8$  ( $P(-3)c$ ,  $a = 0.981$  nm,  $c = 1.173$  nm) which is similar to trigonal- $\text{ZrMo}_2\text{O}_8$  structure was prepared using nonhydrolytic sol-gel chemistry [11]. This implies that there are often similarities of the structural chemistry between molybdenum and tungsten.

In 1998, the strongly structural similarity of W and Mo led Lind et al. [12] to prepare a metastable cubic  $\gamma$ - $\text{ZrMo}_2\text{O}_8$  with a structural closely related to that of cubic  $\beta$ - $\text{ZrW}_2\text{O}_8$ . The lattice constant at 298K was determined to be  $a = 0.91304$  nm and the linear coefficient of thermal expansion was  $-5 \times 10^{-6}$  K $^{-1}$  from 11-573K. The molybdate properties offer advantages over  $\text{ZrW}_2\text{O}_8$  in the lower density, the lack of a discontinuity in thermal expansion at  $\sim 428$ K and the absence of a low-pressure phase transition [12]. Therefore, the modification of  $\text{ZrW}_2\text{O}_8$  by Mo was interest for application.

The Mo-substituted  $\text{ZrW}_2\text{O}_8$  was obtained by a precursor route at low temperature [13, 14]. The powder X-ray diffraction (XRD) patterns of  $\text{ZrW}_{2-x}\text{Mo}_x\text{O}_8$  ( $x=0.4, 0.6$ ) showed  $\alpha$ - $\text{ZrW}_2\text{O}_8$  form after calcination at 873 K. However, for  $x=0.7-1.5$ , the powder XRD patterns of  $\text{ZrW}_{2-x}\text{Mo}_x\text{O}_8$  only showed the  $\beta$ - $\text{ZrW}_2\text{O}_8$  form at temperature as low as 723 K [13, 14].

In this work, we report a new phase of  $\text{ZrW}_{1.6}\text{Mo}_{0.4}\text{O}_8$  (hereafter  $\delta'$ - $\text{ZrW}_{1.6}\text{Mo}_{0.4}\text{O}_8$  form) occurring during the crystallizing process in the precursor rout synthesis [13]. It is a

poor crystal shown from the broad X-ray peaks and is a metastable phase proved by the change of the patterns after prolonging a period of time.

## 2 Experimental

The precursor  $ZrW_{1.6}Mo_{0.4}O_7(OH)_2 \cdot (H_2O)_2$  was prepared using the starting materials ( $Na_2WO_4 \cdot 2H_2O$  (AR),  $Na_2MoO_4 \cdot 2H_2O$  (AR) and  $ZrOCl_2 \cdot 8H_2O$  (AR) were mixed stoichiometrically) in strongly acidic aqueous solution at reflux temperature according to the way mentioned in the reference [15]. Precipitate was isolated by centrifuge and the product was dried at 378 K. The precipitate was examined to be crystalline  $ZrW_{1.6}Mo_{0.4}O_7(OH)_2 \cdot (H_2O)_2$  by powder XRD after drying. The composition of the compound was determined as titled formula for W, Mo and Zr using base melted-sulfocyanide spectrophotometric and ICP-AES methods, respectively. The mother liquor were analyzed to check the metal elements by ICP. The absence of significant quantities of Zr, W and Mo in mother liquor also confirmed the Zr, W and Mo ratio in the compound. The weight-lose percentage of  $H_2O$  by thermogravimetric analysis corresponds with that of the calculated one from the formula  $ZrW_{1.6}Mo_{0.4}O_8 \cdot 3H_2O$ . After dehydration at 430K and annealing at 723K for one day,  $ZrW_{1.6}Mo_{0.4}O_8$  was taken off from the furnace cooled to room temperature.

The crystal was characterized by powder XRD on a Rigaku Dmax-3A instrument (Cu  $K_\alpha$  radiation and Ni filter) and selected area electron diffraction (SAED) with Hitachi H-600 TEM (HV = 100 kV,  $\lambda = 0.0037$  nm).  $SiO_2$  ground to 38-43  $\mu m$ , was used as an internal standard of the sample for correcting powder XRD data with SOS (I) program [16]. The samples for the SAED patterns were prepared by mild grinding of the powder sample, dispersed in alcohol and then distributed on Formvar films, which were coated on carbon-coated copper grids. Little gold powder was sprayed on the film as an internal standard.

## 3 Results and Discussion

### 3.1 The Characterization of $ZrW_{1.6}Mo_{0.4}O_8$ by x-ray Diffraction

The powder XRD pattern was recorded from  $10^\circ$  to  $40^\circ$  for characterizing the compound. The distinctly broad powder XRD pattern of  $ZrW_{1.6}Mo_{0.4}O_8$  grown up from an amorphous envelope was shown in Figure 1. The pattern was tried to index with known crystal structural models of both  $ZrW_2O_8$  and  $ZrMo_2O_8$ , and the pressure-induced system,  $\gamma$ - $ZrW_2O_8$  [17] (orthorhombic system,  $P2_12_12_1$ ,  $a = 0.9067$  nm,  $b = 2.7035$  nm,  $c = 0.8921$  nm). However, the pattern can not be indexed with any of those known structures. The reflections were also compared with monoclinic system [9, 10], but the indices 110 and 101 can not be indexed obviously. The indices 110 and 101 are the key feature of the pattern as shown in the inset of Figure 1.

Then TREOR (4) program [18] was used to index the pattern automatically and finally all peaks were indexed by orthorhombic system, resulting in the figure of merit,  $M(10)=32$ ,  $F(10)=21$ . SOS (II) program [16] was performed to refine the cell edges ( $a = 0.8969(7)$  nm,  $b = 0.7011(8)$  nm,  $c = 0.596(1)$  nm) and calculated out more indices of the reflections. The cell volume is about half of that of cubic modification. So the orthorhombic system (hereafter  $\delta'$ - $ZrW_{1.6}Mo_{0.4}O_8$ ) is a new crystal structure other than the pressure-induced orthorhombic  $\gamma$ - $ZrW_2O_8$  structural model.

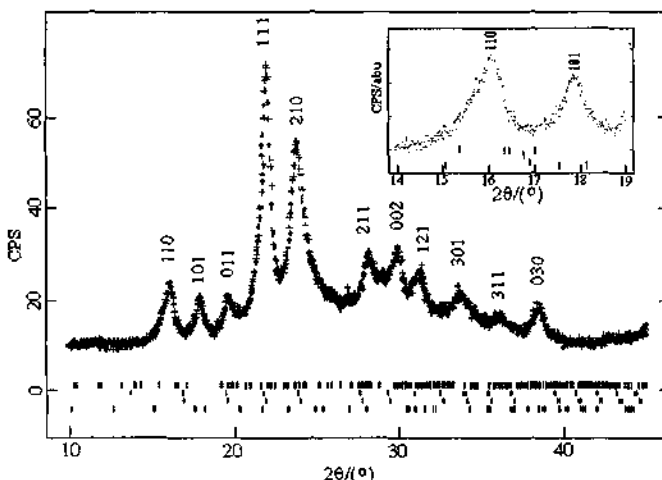


Figure 1

**Figure 1.** The indexing of  $\delta'$ -ZrW<sub>1.6</sub>Mo<sub>0.4</sub>O<sub>8</sub>. The indices were calculated from the TREOR program. The tick marks under the pattern were demonstrations of the failed index by known structural models. The tick marks were the allowed Bragg reflection positions of space groups of P(-3)c (the lowest), Pa(-3) (middle low), P2,3 (middle up) and P<sub>2</sub>,<sub>2</sub><sub>1</sub>,<sub>2</sub><sub>1</sub> (top) models of ZrW<sub>2</sub>O<sub>8</sub> or ZrMo<sub>2</sub>O<sub>8</sub>. The inset emphasizes that both indices 110 and 101 can not be indexed by any structure.

The FWHM of the reflections 111 and 210 were computed by Stokes' equation to determine the size of the nanocrystallite. The dependence of the crystallite size on the temperature and time was shown in Figure 2. It was shown that the samples are favorable to increase in size from about 10 nm to 20 nm when they were annealed at the high temperature or held on a long time. Further observation of the orthorhombic sample showed that the cubic form appear above 773 K. After prolonging as long as one year in ambient conditions, the sample was transformed to an unknown modification indicated by a changed powder XRD pattern. This implies that  $\delta'$ -ZrW<sub>1.6</sub>Mo<sub>0.4</sub>O<sub>8</sub> is a more or less kinetically stable phase during the crystallization process in the temperature range.

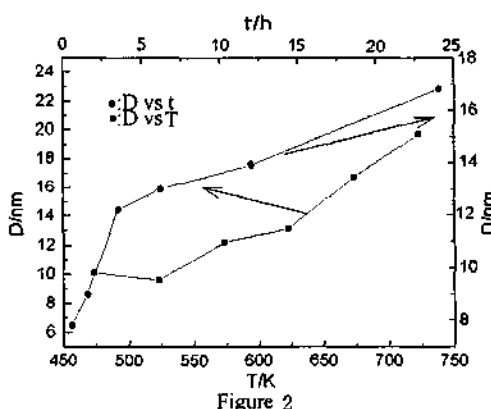
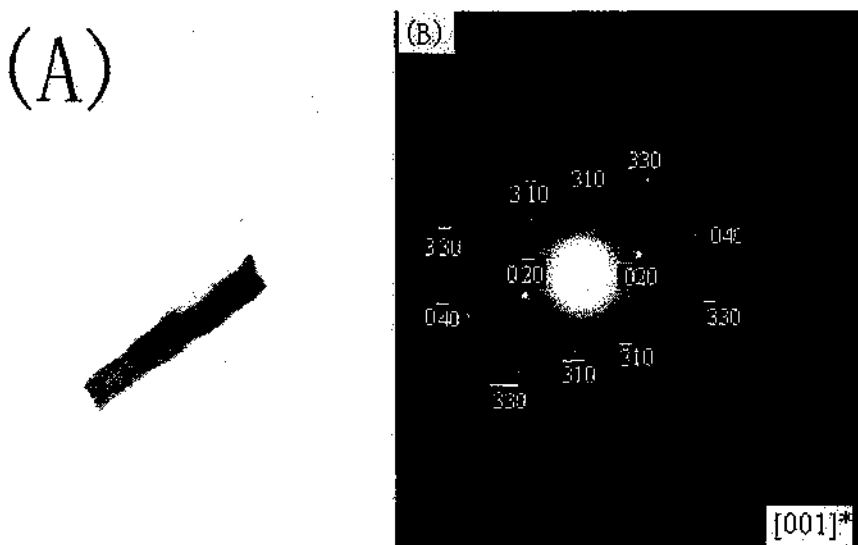


Figure 2. The dependence of crystallite size (D) on annealing temperature (T/K) and times (t/h), respectively.

### 3.2 The Characterization of $\delta$ -ZrW<sub>1.6</sub>Mo<sub>0.4</sub>O<sub>8</sub> by the Selected Area Electron Diffraction (SAED)

The transmission electron microscopy (TEM) image of the sample is shown in Figure 3 (A). This image displays a rod-like nanocrystallite ( $50\text{ nm} \times 350\text{ nm}$ ). The SAED patterns of the sample were taken in different projection. One of the patterns is parallel to the ab plane as shown in Figure 3 (B).

The reflections were indexed with the cell parameters of  $\delta'$ -ZrW<sub>1.6</sub>Mo<sub>0.4</sub>O<sub>8</sub> determined from x-ray diffraction. Meanwhile the indices were checked by comparing inter-planar angles between  $(h,k,l_1)$  and  $(h,k,l_2)$  in direct space with included angle between reciprocal vectors  $R_1^*$  and  $R_2^*$  in reciprocal lattice plane  $(uvw)^*$ . Hence the ED patterns are advantages in resolution for nanocrystallites because reflections can be distinguished in two-dimension in SAED pattern while reflections with closed d-spacing values were merged in a broad band in powder XRD pattern in one - dimension. Such as reflections (2 0 0) and (-2 0 0) are appeared and assigned in the [010]<sup>\*</sup> SAED pattern clearly, but reflection 011, assigned in powder XRD pattern, was extinct in the SAED pattern according to the zonal equation although their d values are closed. So combining a SAED and a XRD pattern, some reflections were emerged from dim x-ray diffraction bands. Therefore in the case, the ED patterns will be helpful to recognize the more indices of the reflections as shown in table 1. The numbers of reflections were increased to 31 indices other than 10 indices coming from XRD pattern as shown in Figure 1.



**Figure 3.** The image (A) and the indices of the spots on the selected area electron diffraction pattern of the [001]<sup>†</sup> zone (B) of  $\delta\text{-ZrW}_{1.6}\text{Mo}_{0.4}\text{O}_8$ . (The rings in (B) are the gold reflections as internal standard. The camera constant is  $K=3.003\text{mm}\cdot\text{nm}$ ).

**Table 1.** The indices of  $\delta'$ -ZrW<sub>1.6</sub>Mo<sub>0.4</sub>O<sub>8</sub> by XRD and SAED.

<i>h k l</i>	d <sub>exp</sub> /nm	d <sub>cal</sub> /nm	I/I <sub>0</sub>	K/mm·nm
1 1 0 (110, -1-10)*	0.5522	0.5524	25	2.991
1 0 1	0.4959	0.4964	27	
0 1 1	0.4534	0.4541	30	
(200, -200)*	0.438	0.44845		2.96
1 1 1 (111, -1-1-1, -1-11, 11-1)*	0.4056	0.4051	100	2.991
2 1 0	0.3771	0.3778	69	
(020, 0-20)*	0.343	0.35055		3.003
2 1 1	0.3191	0.3191	36	
0 0 2 (002, 00-2)*	0.2983	0.2980	44	2.991
1 2 1	0.2865	0.2864	33	
(310, 3-10, -3-10, -310)*	0.286	0.27501		3.003
3 0 1	0.2674	0.2672	27	
(202, -20-2)*	0.247	0.2482		2.96
212	0.2338	0.23397	23	
(330, 3-30, -3-30, -330)*	0.185	0.18412		3.003
(040, 0-40)*	0.172	0.17527		3.003

\*: Denote the d<sub>exp</sub> – values with the indices in round brackets are calculated from the formula  $d_i = K/R_i$ , where K is a camera constant and R<sub>i</sub> is a distance (mm) between a spot and origin. The indices in round bracket were assigned the spot on SAED pattern according to the indexed results from powder XRD.

The indices 212 and 030 have a similar lattice spacing (d<sub>212</sub> = 0.23397 nm, d<sub>030</sub> = 0.2337 nm) which were derived from the orthorhombic model. Which indices can we assign the 38.48° (20, d = 0.2338 nm) reflection to? The observation of reflection 030 should be found in the [001]<sup>+</sup> pattern according to the zonal equation if 030 reflection occurs. But there is no spot between 020 and 040 spots. So the only choice of the d-spacing 0.2338 nm from XRD is indexed to indices 212. After indexing all the reflections in Table 1 with orthorhombic system and the cell edges of  $\delta'$ -ZrW<sub>1.6</sub>Mo<sub>0.4</sub>O<sub>8</sub> we found that they obey the extinction conditions compatible with the space group D<sub>2h</sub><sup>12</sup>-Pnnm (58) or C<sub>2v</sub><sup>10</sup> - Pnn2 (34): h0l, h+l = 2n; 0kl, k+l = 2n.

In summary, samples in the ZrW<sub>2-x</sub>Mo<sub>x</sub>O<sub>8</sub> (x=0.4-1.2) system were prepared in different temperatures. They were analogous as  $\delta'$ -ZrW<sub>1.6</sub>Mo<sub>0.4</sub>O<sub>8</sub> not only in structure but also in kinetically stable properties. The further investigation of ZrW<sub>2-x</sub>Mo<sub>x</sub>O<sub>8</sub> is in progress.

#### 4 Acknowledgments

We gratefully acknowledge the financial support from the National Natural Science Foundation of China: NSFC 29871006. We also thank Gu Zhou for taking the ED photographs in the Analyzing and Testing Center, Beijing Normal University.

## References

1. Graham J. and Wadsley A. D., Weymouth J. H., et al., *J. Am. Ceram. Soc.*, **42** (11), 570 (1959).
2. Chang L. L. Y., Scroger M. G. and Phillips B., *J. Am. Ceram. Soc.*, **50** (4), 211 (1967).
3. Evans J. S. O., Mary T. A., Vogt T. et al., *Chem. Mater.*, **8**, 2809 (1996).
4. Evans J. S. O., David W. I. F. and Sleight A. W., *Acta Cryst. B* **55**, 333 (1999).
5. Evans J. S. O., *J. Chem. Soc., Dalton Trans.*, 3317 (1999).
6. Marry T. A. Evans J. S. O., Vogt, T. et al., *Science*, **272**, 90 (1996).
7. Auray M., Quarton M. and Tarte P., *Acta Cryst.*, **C42**, 257 (1986).
8. Mittai R., Chaplot S. L., Lallo N. P. et al., *J. Appl. Cryst.*, **32**, 1010 (1999).
9. Auray M., Quarton M. and Tarte P., *Powder Diffract.*, **4**, 29 (1989).
10. Serezhkin V. N., Efremov V. A. and Trunov V. K., *Russ. J. Inorg. Chem.*, **32**, 1566 (1987).
11. Wilkinson A. P., Lind C. and Patnaik S., *Chem. Mater.*, **11**, 101 (1999).
12. Lind C., Wilkinson A. P., Hu Z. et al., *Chem. Mater.*, **10**, 2335 (1998).
13. Zhang S., Zhao X., Ma H. et al., *Chinese J. Chem.*, **18** (4), 571 (2000).
14. Closmann C., Sleight A. W. and Haygarth J. C., *J. Solid State Chem.*, **139**, 424 (1998).
15. Clearfield A. and Blessing R. H., *J. Inorg. Nucl. Chem.*, **34**, 2643 (1972).
16. Scoose J., Meyer G., SOS: *Programme Zur Antwortung Von Guiner-Aufnahmen* Justus-Liebig-Universität, Giessen, 1980.
17. Evans J. S. O., Hu Z., Jorgensen J. D. et al., *Science*, **275**, 61 (1997).
18. Wernwe P. E., Kriksson L. and Wesdahl M., *J. Appl. Crystallogr.*, **18**, 367 (1985).

## STUDY ON THE SYNTHESIS, RARE EARTH CO-PERMEATION AND CONDUCTIVITY OF COMPLEX $K_{10}H_3[Y(SiW_{11}O_{39})_2]$

ZHOU BAI-BIN,<sup>1,2</sup> WEI YONG-DE,<sup>1</sup> LI ZHONG-HUA<sup>1</sup> AND GUO YUAN-RU<sup>1,2</sup>

<sup>1</sup> Department of Applied Chemistry, Harbin Institute of Technology, Harbin 150001, China  
E-mail: e\_lzh@0451.com

<sup>2</sup> Department of Chemistry, Harbin Normal University, Harbin 150080, China  
E-mail: zgzb@0451.com

The title compound has been synthesized by means of degradation. Its composition has been determined by chemical analysis, TG and ICP. The studies of IR, UV, XRD, <sup>183</sup>W-NMR indicate that the compound has the Keggin structure, and the results of TG-DTA show that the stable temperature of this compound is up to 400–450°C. We also studied the rare earth chemical thermal diffusion of the complex and found that the rare earth element can permeate into the surface, interface and the body cavity of the prepared material. The conductivity of the permeated sample is  $1.935 \times 10^{-2} \Omega^{-1} \cdot \text{cm}^{-1}$ , which is  $10^3$  times higher than that of the parent  $K_{10}H_3[Y(SiW_{11}O_{39})_2]$ .

### 1 Introduction

Lanthanide heteropoly complexes have been reported extensively since their first preparation by Peacock and Weakly in 1970s [1-4]. For their excellent properties in catalysis and anti-virus, they have received much attention [5,6], however, few people have studied their conductivities [7,8]. Polyoxometalates are proton conductors. Their conductivities are below  $10^{-3} \text{ S} \cdot \text{cm}^{-1}$ , and there are some difficulties for them to act as solid electrolytes of hydrogen-oxygen fuel cells. Therefore, it is significant to develop new polyoxometalates which have practical use in electro-color equipment, water wipe-off device and solid electrolyte of hydrogen-oxygen fuel cell. Because the physical and chemical properties of yttrium are similar to lanthanides, it is possible to prepare new complexes similar to lanthanide heteropoly complexes. According to our work at present, yttrium can substitute for tungsten to form new complexes. In this paper,  $K_{10}H_3[Y(SiW_{11}O_{39})_2]$  has been prepared and characterized by IR, UV, XRD, <sup>183</sup>W-NMR, and the data indicate that the complex retains the Keggin structure and Ce, Lu can permeate into the body of  $K_{10}H_3[Y(SiW_{11}O_{39})_2]$ . After permeation, the conductivity of the compound is improved remarkably, offering a new way for applying and preparing solid-electrolytes.

### 2 Experimental

#### 2.1 Instruments and reagents

The IR spectra were recorded on a 1730-FTIR (P.E. U.S.A.) spectrophotometer using KBr (S.P. grade) pellets. The XRD patterns were recorded on a D/MAX-3C diffractometer with a Cu target,  $K\alpha$  radiation ( $\lambda=0.15418 \text{ nm}$ ). The conductivities were obtained on a FLUKE 8505A Digital Multimeter (U.S.A.) conductivity measurement system. Thermal analyses were conducted on a LCT-1 thermogravimetric balance (China). The rate of rising temperature was  $10^\circ\text{C}/\text{min}$  and  $N_2$  was used as a protection atmosphere. A Varian Unity-400 NMR spectrometer (U.S.A.) was used to record the NMR signals using  $D_2O$  as

a source of lock signal.  $^{183}\text{W}$  spectra were obtained and referenced externally to  $\text{Na}_2\text{WO}_4$ ; the elemental analyses were performed on a IRIS ICP-AES (U.S.A.) quantometer. All the reagents used were of analytical grade.

## 2.2 Component analysis

The yttrium content was determined gravimetrically by ethanedioic acid and the tungsten content was determined gravimetrically by tannic acid-cinchonine. The silicon content was determined capacimetrically by potassium fluo-silicate whereas the potassium amount was obtained gravimetrically by sodium tetraphenyl-borate. The results of cation exchange resin, conductimetric analysis and ICP agree with those of elemental analysis.

## 2.3 Preparation of the title compound

15g  $\text{H}_4\text{SiW}_{12}\text{O}_{40} \cdot 20\text{H}_2\text{O}$ , which was prepared by ethyl ether extraction method, was dissolved in 150ml water, then  $\text{Y}(\text{NO}_3)_3$ , which was a little more than stoichiometry, was added into the solution. Monitored with an acidimeter, the solution of KAc-HAc buffer (while  $\text{KAc:H}_2\text{O:HAc} = 15\text{g}:30\text{ml}:1\text{ml}$ ) was slowly added dropwise bringing the pH to 4.6-5.0. The filtrate from the solution was placed in refrigerator at 0-3°C for 3 hours, then the resulting crystal was precipitated. Pure products were obtained by twice recrystallization from the mother solution  $\text{K}_{10}\text{H}_3[\text{Y}(\text{SiW}_{11}\text{O}_{39})_2]25\text{H}_2\text{O}$  (Theoretic values: Y: 1.42, Si: 0.89, W: 64.38, K: 6.22, H<sub>2</sub>O: 7.16; Experimental values: Y: 1.45, Si: 1.02, W: 64.42, K: 6.34, H<sub>2</sub>O: 6.85).

## 2.4 Rare-earth co-permeation

$\text{K}_{10}\text{H}_3[\text{Y}(\text{SiW}_{11}\text{O}_{39})_2]$  was compacted into a round piece (diameter=10mm, high=3mm) under 12MPa. The permeable reagent was self-made [9]. The equipment was a crucible cementation furnace with the XMT-101 fine temperature controller. The DP temperature was 550°C and the DP time was 2h. The system was cooled down naturally. The conductivity measurement was performed on a conductivity measuring system and the permeated rare-earth was determined by ICP, and the structure of the sample was detected by IR, XRD spectrometer.

## 3 Results and Discussion

### 3.1 IR spectra

The IR spectra are shown in Figure 1(a); all the characteristic peaks are in the range of 470-1000cm<sup>-1</sup>, which are similar to those of tungstosilicates. This indicates that the new complex still maintains the Keggin structure, and these peaks can be ascribed to the following vibrations according to Claude [10]:  $\nu_{as}\text{W-Od}$ : 1011.71;  $\nu_{as}\text{W-Od}$ : 952.36;  $\nu_{as}\text{Si-Oa}$ : 890.27;  $\nu_{as}\text{W-Oc-W}$ : 882.22, 770.19, 719.16;  $\nu_{as}\text{O-Si-O}$ : 522.74 cm<sup>-1</sup>. Comparing to those of the precursor, the IR spectrum of the new complex has the following characteristics: (1) the  $\nu_{as}\text{W-Od}$  and the  $\nu_{as}\text{Si-Oa}$  frequencies have an Einstein shift, and the yttrium coordinates with the mother HOMs, resulting in the enlargement of the structure and the lessening of force constant and the decrease of vibrational frequency; (2) the  $\nu_{as}\text{W-Ob-W}$  frequency disappears, and the  $\nu_{as}\text{W-Oc-W}$  splits, because the force constant of W-Oc-W ( $f=3.91$ ) is lower than that of W-Ob-W ( $f=4.0$ ) [11]; the

corresponding IR absorptions are unchanged and are covered up by that of the  $v_{as}$ -Si-Oa. However, the  $v_{as}$ -W-Oc-W has an Einstein shift and splits, implying that after coordinating with yttrium, the precursor changes its structure.  $\text{Y}^{3+}$  is not only in the position of W, but also coordinates with two Oc atoms and two Ob atoms, forming a sandwich heteropolyanion, indicating that the  $\text{SiW}_{11}\text{O}_{39}^{8-}$  bonds with  $\text{Y}^{3+}$  in a quadridentate form, resulting in a 1:1:1 coordinate compound.

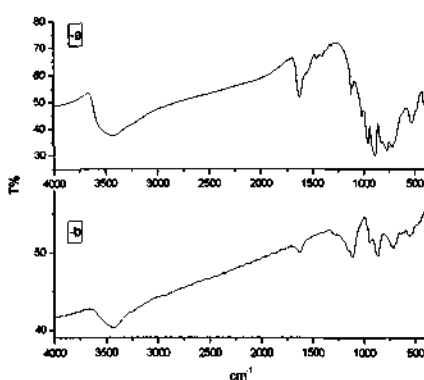


**Figure 1.** IR spectra of  $\text{K}_{10}\text{H}_3[\text{Y}(\text{SiW}_{11}\text{O}_{39})_2]$ .  
a. before permeation b. after permeation.

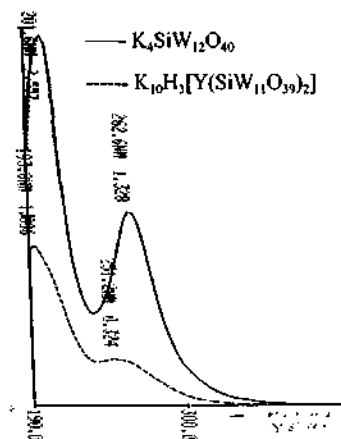


**Figure 2.** UV spectra of the heteropoly complex.

### 3.2 Electronic spectra

The electronic spectra of  $\text{K}_{10}\text{H}_3[\text{Y}(\text{SiW}_{11}\text{O}_{39})_2]$  are shown in Figure 2. The results indicate that the new complex, despite exhibiting an Einstein shift, has two peaks in the range of 190–400nm, similar to that of the saturated polyanion. These peaks can be ascribed to the Od→M (193.8nm) and Ob, Oc→M (251.2nm) transitions. This result is in accordance with that of the IR spectra. The broad and weak band associated with yttrium in the range of <500nm has been covered up by the strong absorption of the ligand.

### 3.3 $^{183}\text{W-NMR}$

$^{183}\text{W-NMR}$  is a powerful tool of characterizing HOMs, and can discriminate different isomers. The  $^{183}\text{W-NMR}$  spectrum of the title complex characterized using the Varian Unity-400 spectrometer is shown in Figure 3. The spectrum has only one peak for the reason that the W atoms have the same chemical environment in the Keggin heteropolyanion  $\text{SiW}_{12}\text{O}_{40}^{4-}$ . After losing a WO group, the  $\text{SiW}_{12}\text{O}_{40}^{4-}$  produces four types of isomers such as  $\alpha$ -,  $\beta_1$ -,  $\beta_2$ -,  $\beta_3$ -, and the symmetry of the compound changes from  $Td$  to  $Cs$  when forming  $\alpha$ -,  $\beta_1$ -,  $\beta_2$ - $[\text{Y}(\text{SiW}_{11}\text{O}_{39})_2]^{13-}$ . Therefore, the 11 W atoms in six chemical environment results in six peaks [12]. However, when it comes to  $\beta_2$ - $[\text{Y}(\text{SiW}_{11}\text{O}_{39})_2]^{13-}$ , the symmetry changes to  $Cl$ , and the 11 W atoms in different

chemical environments leads to 11 peaks in the NMR spectrum. This result gives sufficient evidence for the formation of the title complex.

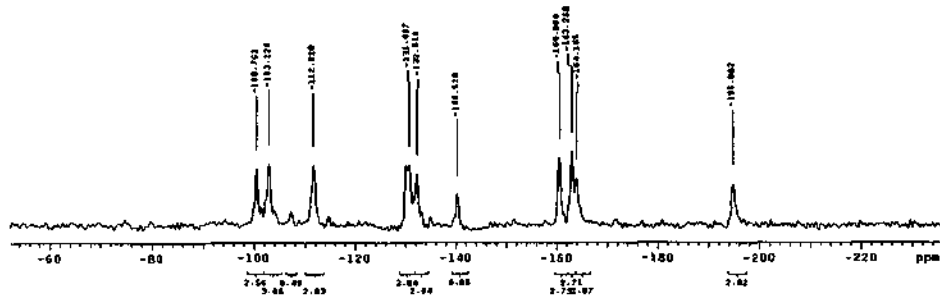


**Figure 3.**  $^{183}\text{W}$ -NMR spectrum of  $\text{K}_{10}\text{H}_3[\text{Y}(\text{SiW}_{11}\text{O}_{39})_2]$ .

### 3.4 XRD characterization

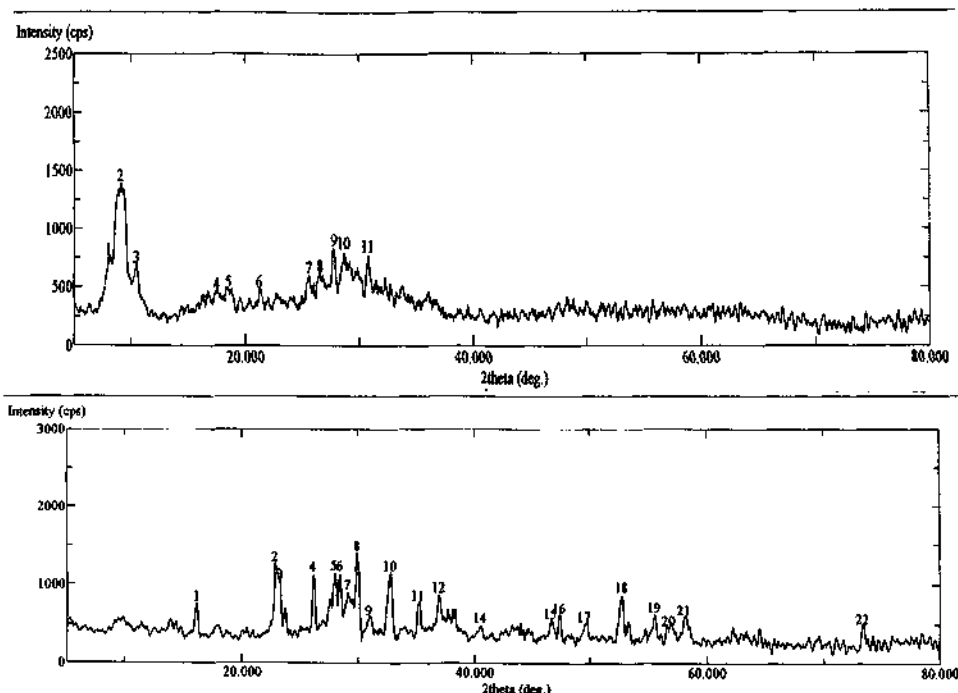


**Figure 4.** X-ray powder diffraction patterns of  $K_{10}H_5[Y(SiW_{11}O_{39})_2]$ . (a) before permeation, (b) after permeation.

The XRD pattern of the new complex in the range of  $5^\circ \leq 2\theta \leq 80^\circ$  is shown in Figure 4(a). The pattern resembles that of ammonium tungsten silicate. This indicates that they have the same crystal structure. There are three characteristic peaks in the range of  $8^\circ\text{-}10^\circ$ ,  $17^\circ\text{-}20^\circ$  and  $25^\circ\text{-}30^\circ$  suggesting that this new complex maintains the Keggin structure.

### 3.5 Thermal stability of the complex

The TG-DTA curves of  $K_{10}H_3[Y(SiW_{11}O_{39})_2] \cdot 25H_2O$  are shown in Figure 5. There are two steps of weight loss in the TG curve corresponding to the DTA curve. The two endothermic peaks provide evidence for the loss of water. The complex loses 23 water molecules before  $402^\circ C$ , and loses 2 structural water molecules at  $502^\circ C$ . Before  $400^\circ C$ , the IR spectrum and the XRD pattern at different temperatures does not change, implying that structure of the compound has not been destroyed, and still maintain Keggin structure. However, the situation is different at  $450^\circ C$ , and the IR absorptions at  $842.22$ ,  $770.19$ ,  $719.16\text{cm}^{-1}$  of  $v_{as}W\text{-Oe-W}$  disappear. The XRD pattern at different temperatures change remarkably, evidencing that the Keggin structure has been destroyed, and the decomposing temperature ranges from  $400^\circ C$  to  $450^\circ C$ . This result is in accordance with the occurrence of the first exothermic peak in the DTA curve ( $413^\circ C$ )[13].

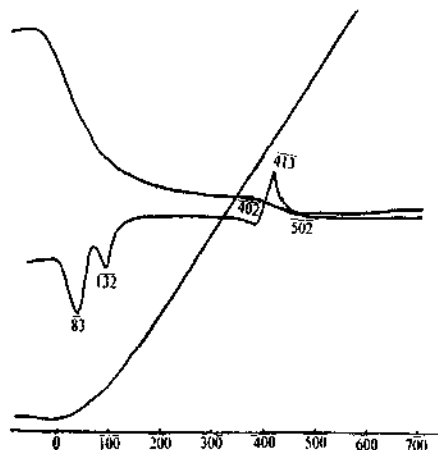


Figure 5. TG-DTA analysis curves of  $K_{10}H_3[Y(SiW_{11}O_{39})_2] \cdot 25H_2O$ .

### 3.6 Rare-earth co-permeation and conductivity

The elemental analysis of the permeated sample on IRIS ICP gives rise to the following results: La:0.15%, Sm:0.13%, Dy:0.24%. This confirms that a small amount of rare-earth elements can permeate into the surface, the interface and the body of the title complex. The IR spectrum and the XRD pattern of the permeated sample are shown in Figures 1(b) and 4(b). After comparing them with Figure 1(a) and 4(a), we know that after permeation the Keggin structure has been changed, and new phases are formed. The conductivities of these two samples have been measured. Before permeation, the conductivity value  $\sigma$  is  $2.69 \times 10^{-7} \Omega^{-1}\text{-cm}^{-1}$ , and after the permeation the value is  $1.935 \times 10^{-2} \Omega^{-1}\text{-cm}^{-1}$ , an

enhancement of about  $10^5$  times. The permeation with rare-earth elements improves the conductivity of this new complex markedly, and it is promising to obtain a new type of conductive material through this approach.

## References

1. Peacock R. D. and Weakley T. J. R., Heteropolytungstate complexes of the lanthanide Elements. Part 1.Preparation and reaction, *J. Chem. Soc. (A)*, **18** (1971) pp. 1836.
2. Wang E.-B., Hu C.-W. And Xu L., *Introduction of Polyacid Chemistry*, Chemical Industry Press, Beijing, 1998, pp. 4 (in Chinese) .
3. Feng J.-H., Li X.-J., Jing F.-Y., Pei F.-K., Synthesis, characterization, stability and relaxation behaviors of rare earth heteropolymetalates, *Acta Chim. Sinica*, **58** (2000) pp. 423 (in Chinese).
4. Baker L. C. W. and Glick D. C., Present general status of understanding of heteropoly electrolytes and a tracing of some major highlights in the history of their elucidation., *Chem. Rev.*, **8** (1998) pp. 4.
5. Lin S., Zheng Y., Xu L.-M. and Wang S.-M., Synthesis, characterization and catalytic activity for phenol hydroxylation of rare earth molybdoanadophosphate tetrabasic heteropoly complexes with Keggin structure., *Chem. J. Chinese Univ.*, **21** (2000) pp. 1248 (in Chinese).
6. Liu J., Zhang M.-L., Wang L.-J. and Wang E.-B., Synthesis, properties and antiviral of Keggin molybdogemmum heteropoly blues, *Chinese J. Inorg. Chem.*, **21** (2000) pp. 1791 (in Chinese).
7. Yu X.-W., Liu S.-X., Wang G., Wang X.-L. and Wang E.-B., Studies on magnetism and conductivity of trisubstituted tungstogalliumate containing transition metal, *Acta Chim. Sinica*, **54** (1996) pp. 864 (in Chinese).
8. Wang, L., Liu Z.-R., Zhou Y.-S. and Wang E.-B., Studies on the conductivity and magnetic properties of substituted heteropoly tungstogallates, *Chem. J. Chinese Univ.*, **18** (1997) pp. 846(in Chinese).
9. Wei Y.-D., Liu Z.-R. and Wang C.-Y., A note on coating of surface diffusion-Infiltration of RE on steel 20 and armco iron by chemical process. *Acta Metallurgica Sinica*, **19** (1983) pp. B197-199.
10. Rocchiccioli-Deltcheff C., Fournier M. , Franck R. et al., Vibrational investigation of polyoxometalates, *Inorg. Chem.*, **22** ( 1983) pp. 207.
11. Kazanskii L. P., Molecular and electronic structure of heteropoly complexes., *Izv. An. Sssr, Ser. Khim.* (1977) pp. 502.
12. Liu J.-F., Wang W.-Q., Meng L. and Liu Y.,  $^{183}\text{W}$  NMR characterization of rare earth heteropolymetalates in aqueous solution., *Chem. J. Chin. Univ.*, **17** (1996) pp. 179 (in Chinese).
13. Wang Z.-P., Niu J.-Y., Xu L. and Wang E.-B., Study on thermal property of heteropolyacids with Keggin structure, *Acta Chim. Sinica*, **53** (1995) pp. 757 (in Chinese).

## STUDY ON DEFECTED YVO<sub>4</sub> CRYSTAL

YU-QI ZOU,\* JUN XU AND FU-XI GAN

*Shanghai Institute of Optics and Fine Mechanics, Chinese Academy of Sciences, Shanghai 201800,  
P. R. China  
E-mail: yqzou@mail.shcnc.ac.cn*

XIN-JUN LI

*Shanghai University, Shanghai 201800, P. R. China  
E-mail: zyqzl6924@citiz.net*

YU-LIAN TIAN WAN-XIA HUANG

*Beijing Institute of High Energy Physics, Chinese Academy of Sciences, Beijing 100039, P. R.  
China  
E-mail: huangwx@mail.ihep.ac.cn*

In this paper Synchrotron Radiation X-Ray White-beam Topography (SRXWT) was used to investigate the defects of yttrium orthovanadate crystal. dislocations, inclusions and stress area were found in (001) and (100) wafers. Analysis showed that inclusions were the main cause of dislocations and stress area. Electronic Probe Microscopic Analysis (EPMA) indicated that these inclusions resulted from impurities appearing on the annealed (001) wafer, which revealed that there lied small amount of ferrum and aluminium.

### 1. Introduction

Yttrium orthovanadate (YVO<sub>4</sub>) crystallizes in the zircon-type and belongs to the tetragonal space group  $D_{4h}^{19}$ -I4<sub>1</sub>/amd and with the lattice constants of  $a=b=7.1192\text{ \AA}$ ,  $c=6.2898\text{ \AA}$ ,  $\alpha=\beta=\gamma=90^\circ$  [1]. The YVO<sub>4</sub> crystal is a strongly birefringent uniaxial crystal ( $n_o=1.958$ ,  $n_e=2.168$  at 1064nm) with a high optical transparency in the 400-5000nm region. It has been widely used as isolator, circulator, WDM (Wave Division Multiplexer) in optical communication areas. YVO<sub>4</sub> crystal doped with Nd<sup>3+</sup> ion was a promising crystal for its low threshold and large laser emission cross section [2-4]. In this paper synchrotron radiation X-ray topograph and Electronic Probe Microscope Analysis were utilized to investigate the defects of YVO<sub>4</sub> crystal.

### 2. Experimental

#### 2.1 Sample Preparation

YVO<sub>4</sub> crystal sample, grown by the Czochralsky method along the [001] direction, was cut into two wafers along [001] and [100] directions respectively with the size of 10mm×10mm×1mm. Errors on each facet were controlled within 30' by using X-ray directional apparatus. Wafers with the density of 0.3mm were obtained after a series of techniques such as grinding, polishing and chemical polishing. No nicks were found on the surface under a microscope.

## 2.2 Topography

X-ray white-beam synchrotron radiation topograph was carried on with the energy 2.2013GeV, beam intensity 82.4mA, lifetime 23.8h in the Beijing Synchrotron Radiation Faculty (BSRF). The exposure time was fixed to be 3-6 seconds according to the distance between wafers and slit, area and beam intensity. Photos with different sizes were obtained by adjusting the size of the film and slit.

## 2.3 EPMA Experiments

Errors were limited within 30' on the (001) facet and no spots were detected by an optical microscope after orientation. The samples were cut and polished, annealed for 72hours at 1000°C and then coated with carbon for EPMA. The apparatus was EPMA-8705QH2 of Japan with the energy of 20.0kv and a resolution ratio of 5μm.

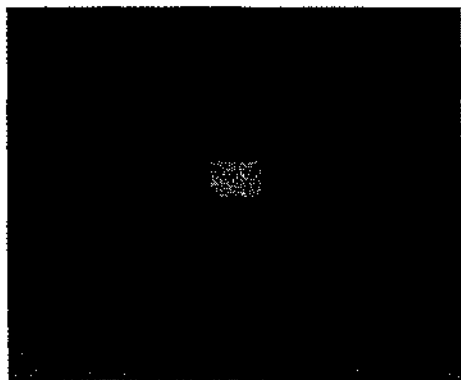


**Figure 1.** The (001) Laue spots.

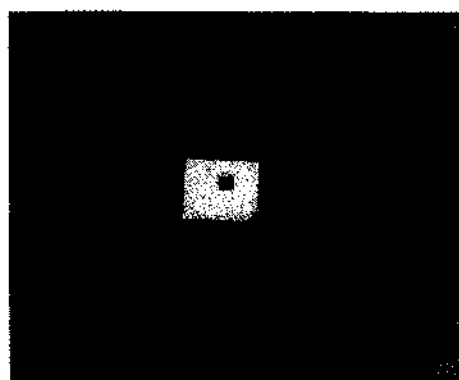


**Figure 2.** The polycrystal Laue spots.

## 3. Results and Discussion

Figure 1 shows the Laue spots of the [001] wafer, through which YVO<sub>4</sub> crystal could be tested to be a tetragonal system. Figure 2 presents the irregular Laue spots that could be regarded as the evidence for the existence of polycrystals that were created by the control of small angle grain boundary. Figure 3 shows the mosaic structures that possess a hexagonal geometry. The symbol T indicates a dislocation that orients towards the [010] direction. Obviously it originates from the mosaic structure and ends at the edge of the crystal. The symbol S represents the normal region.

The stress area is found in Figure 4. The induction of impurities into the melts during crystal growth led to local lattice distortion resulting in irregular stress area. It is clearly shown by the contrast in color. The dislocations were induced by this area and showed irregular directions. In Figure 5 a dislocation along the [100] direction is shown.

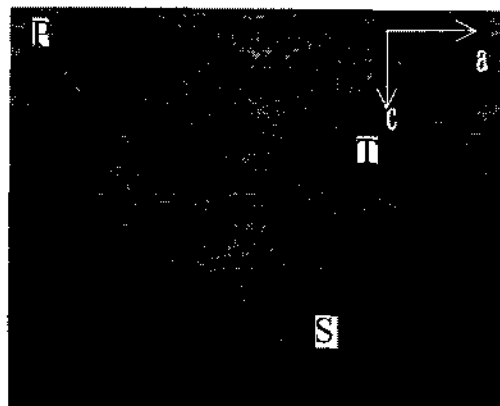


Figure 3. The [100] dislocation and mosaic structure.



Figure 4. Micrograph of the [001] stress area.

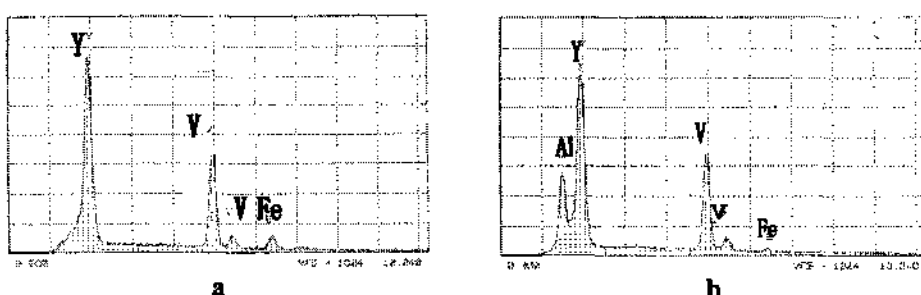


Figure 5. The [001] dislocation.

Qualitative and quantitative analyses were performed in four parts of the crystal by using EPMA as shown in Figure 5. A trace amount of ferrum was detected in the white region as shown by symbols I and III, while black region of symbol III indicated that there exists aluminum which was attributed to the refractory materials. Symbol II represents larger part of this surface without any dots or impurities. The results show no existence of impurities here. The analysis reveals that the emergence of ferrum is due to the impurity of raw materials. As for the small amount of ferrum in region II, it can be ascribed to the accumulation of ferrum brought by the expelling of impurities. After physical process and annealing, impurities show up on the top of the crystal.



**Figure 6.** Domain structure of C-cut plate  $\text{YVO}_4$  under EPMA.



**Figure 7.** EMPA X-ray energy spectrum of defect domain.

#### 4. Conclusions

Synchrotron radiate white-beam X-ray topography and EPMA were combined to investigate the defects of the  $\text{YVO}_4$  crystal. Dislocations and stress area were found on some wafers showing that the inclusions brought by impurities were the major reason. Since super cooling components were included inside the crystal, when cooled, they precipitated nearby and grew inside. So inclusions possessed a certain shape. Qualitative results given by EPMA showed that the impurities contained ferrum and aluminum.

#### References

1. Erdei S., Growth of oxygen deficiency-free  $\text{YVO}_4$  single crystal by top-seeded solution growth technique. *J.Crystal Growth*, **134** (1993), pp. 1-13.
2. Erdei S. and Ainger F.W., Crystal growth of  $\text{YVO}_4$  using LHPG technique. *J. Crystal Growth*, **128** (1993), pp.1025-1030.
3. O'Conner J.R., Unusual Crystal-field energy level efficient laser properties of  $\text{YVO}_4\text{:Nd}$ , *Appl. Phys. Lett.* **9** (!996), pp. 407.
4. Yaney P. P. and Deshazer L. G., Spectroscopic studies and analysis of the laser states of  $\text{Nd}^{3+}$  in  $\text{YVO}_4$ ., *J. Opt. Soc. Am.* **6** (1976), pp. 1405.

This page is intentionally left blank

# LONG LASTING PHOSPHORESCENCE, THERMOLUMINESCENCE AND ELECTRON SPIN RESONANCE PROPERTY OF Mn<sup>2+</sup> ACTIVATED ZnO-Al<sub>2</sub>O<sub>3</sub>-SiO<sub>2</sub> CERAMIC

JING WANG,<sup>a</sup> CHENGYU LI,<sup>a</sup> SHUBIN WANG<sup>a</sup> AND QIANG SU<sup>a,b</sup>

<sup>a</sup>Key Laboratory of Rare Earth Chemistry and Physics, Changchun Institute of Applied Chemistry, Chinese Academy of Sciences, Changchun, Jilin 130022, P. R. China  
E-mail: suqiang@ns.ciac.jl.cn

<sup>b</sup>State Key Laboratory of Optoelectronic Materials and Technology, School of Chemistry and Chemical Engineering, Sun Yat-sen University, Guangzhou, Guangdong 510275, P. R. China  
E-mail: cedc25@zsu.edu.cn

The long lasting phosphorescence (LLP) phenomenon in Mn<sup>2+</sup>-doped ceramic based on ZnO-Al<sub>2</sub>O<sub>3</sub>-SiO<sub>2</sub> (ZASM) is observed. After irradiation by a UVP standard mercury lamp peaking at 254 nm with a power of 0.6 mW/cm<sup>2</sup> for 15 min, the ceramic sample emits a bright green light peaking at 519 nm, which can be seen in the dark even 15 h after the removal of UVP standard mercury lamp by the naked eyes whose limit of light perception is 0.32 mcd/m<sup>2</sup>. The initial afterglow intensity reaches about 1900 mcd/m<sup>2</sup>, and the color coordinate (X, Y) is (0.2280, 0.5767) at about 10 s after stopping irradiation. The thermoluminescence (TL) spectra show that there are at least three kinds of trap centers with different trap levels while electron spin resonance (ESR) spectra indicate that there are electron- and hole-trapping centers induced after irradiation by a UVP standard mercury lamp. Based on these measurements, the LLP is considered to be due to the recombination of electrons and holes at trapping centers with different levels, which are firstly thermally released back to Mn<sup>2+</sup> and then give rise to the bright green LLP at room temperature.

## 1 Introduction

Recently, especially since the LLP phenomenon in SrAl<sub>2</sub>O<sub>4</sub>: Eu<sup>2+</sup>, Dy<sup>3+</sup> was reported in 1996 [1], LLP materials have been extensively investigated due to its potential application in display in the dark, energy storage, enhancement of the conversion efficiency of solar cell and the fabrication of re-writable three-dimensional optical memory devices, etc [2-5].

As far as the activators that can give rise to LLP is concerned, most reports, to the best of our knowledge, focus on the RE ions, such as Ce<sup>3+</sup>, Tb<sup>3+</sup>, Pr<sup>3+</sup>, especially Eu<sup>2+</sup> [6,7]. Few researches are reported on LLP phenomenon of transitional metal ions except Cu, Mn ions. With respect to Cu, ZnS:Cu once was a well-known green LLP phosphor but its applications are limited due to several shortcomings, i.e. extremely sensitivity to moisture due to the unstable sulphide-based matrix and radioactivity to environment when co-doped with Pm to prolong the afterglow time [8]; For Mn ion, the researches of LLP are just conducted in sodium borate glasses reported by Qiu J.R. etc. al. and ZnGa<sub>2</sub>O<sub>4</sub>: Mn<sup>2+</sup> reported by Uheda K. and co-workers [5,9]. So LLP materials with the properties such as strongest intensity, longest decay time, excellent chemistry stability, and non-radioactivity etc are being strongly expected in the field of application. Furthermore it is also important to explore new system of LLP materials with new activators beyond RE ions for purpose of researches on theory of LLP.

In the present paper, we first synthesize an intensive green LLP ceramic based on Mn<sup>2+</sup> doped ZnO-Al<sub>2</sub>O<sub>3</sub>-SiO<sub>2</sub> (designated ZASM) with the properties of strong brightness, longer decay time, excellent chemistry stability and non-radioactivity. The luminescence and defects properties of the material on photoluminescence (PL), LLP, TL and ESR are systematically investigated. Based on these measurements, a possible mechanism of LLP is proposed.

## 2 Experimental

Appropriate amounts of reagent-grade ZnO, Al<sub>2</sub>O<sub>3</sub>, SiO<sub>2</sub>, and MnCO<sub>3</sub> were mixed thoroughly. Then the mixed batches were sintered at 1550 °C for 6 h under ambient atmosphere condition. The photoluminescence spectra of the samples were recorded on a HITACHI F-4500 Spectrofluorometer. The LLP emission of the sample at ~ 10s after irradiation by a UVP standard mercury lamp peaking at 254nm with a power of 4.07 mW/cm<sup>2</sup> for 5 min was recorded by the photomultiplier of HITACHI F-4500 Spectrofluorometer. For determination of the LLP decay curve, Minolta CS-100A Chromameter equipped with Minolta DP-101 Data processor was used and the data were collected by every 10 s after irradiation by a UVP standard mercury lamp peaking at 254 nm with a power of 0.6 mW/cm<sup>2</sup> for 15 min. With respect to TL, the sample was measured on an FJ-427A thermoluminescence-meter (Beijing Nuclear Instrument Factory) at the temperature range from 20°C to 500°C in the heating rate of 2°C per second. The ESR measurement was performed using a TEOL model TES-FE-3AX ESR spectrometer (made in Japan) at X-band (9.438GHz). All measurements except TL spectra were determined at room temperature.

## 3 Results

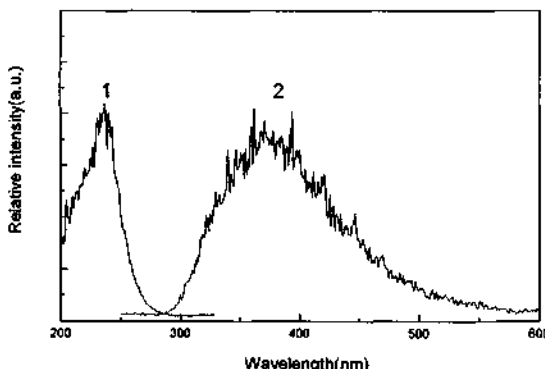
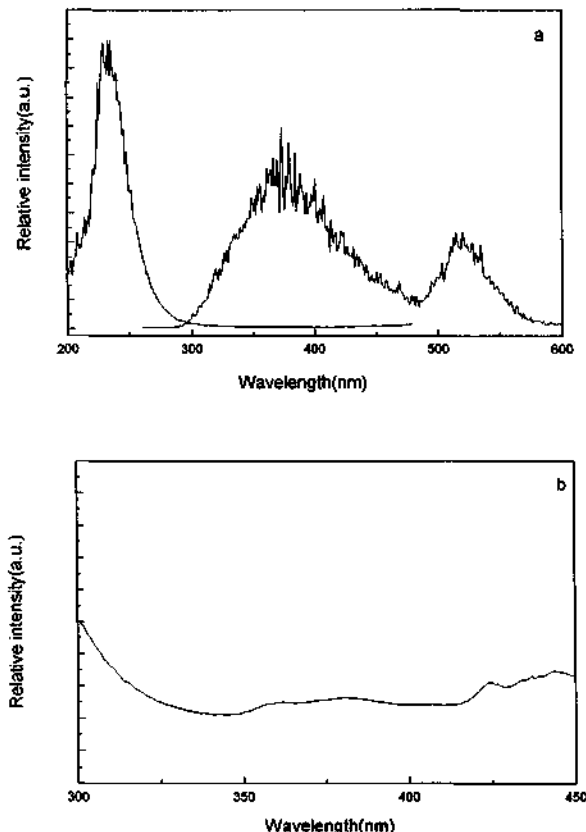


Figure 1. The excitation ( $\text{em}=380 \text{ nm}$ ) and emission ( $\text{ex}=230 \text{ nm}$ ) spectra of the sample ZAS.

Figure 1 shows the excitation and emission spectra of the host  $\text{ZnO-Al}_2\text{O}_3-\text{SiO}_2$  (designated ZAS for brevity). It can be found that a broad excitation band appears in the wavelength range of 200 to 300 nm with a maximum at  $\sim 230\text{nm}$ . The emission spectrum consists of a broad band predominating at  $\sim 380$  under the excitation at 230 nm. These excitation and emission spectra originate from the self-activated luminescence of the host like  $\text{ZnGa}_2\text{O}_4$  and  $\text{Zn}_4\text{B}_6\text{O}_{13}$ , etc [10,11].



**Figure 2.** The excitation ( $\text{em}=520\text{ nm}$ ) and emission ( $\text{ex}=230\text{ nm}$ ) spectra of ZASM [a] and a local enlargement of the excitation spectra at wavelength range of 300 to 450 nm [b].

The luminescence spectra of the  $\text{Mn}^{2+}$ -doped  $\text{ZnO-Al}_2\text{O}_3-\text{SiO}_2$  are shown in Figure 2a and Figure 2b. It can be seen that ZASM shows more bands in either excitation or emission spectrum with comparison to ZAS in Figure 1. When monitoring the emission wavelength at

around 520 nm, the excitation spectra consist of a strong band at ~ 230 nm in Figure 2a and another two weaker bands from 320 nm to 450 nm as observed in Figure 2b. Compared with excitation spectrum of ZAS, the band at 230 nm should be ascribed to the host absorption while the latter two weaker bands can be assigned to  $3d^5 \rightarrow 3d^5$  forbidden transition of  $Mn^{2+}$  on the consideration of their weak intensity [12]. The transitions at wavelength range of 320 to 450 nm are resulted from the splitting of the  $^4D$  and  $^4G$  levels of  $Mn^{2+}$  by the crystalline field. The first weaker band between 320 and 400 nm may be assigned to the  $^6A_1 \rightarrow ^4D$  transition while another between 410 and 450 nm to the  $^6A_1 \rightarrow ^4G$  transition. The emission spectrum of ZASM consists of two bands with maxima at ~ 380 and 520 nm. The former emission band is due to the self-activated emission of the host as shown in Figure 1, and the later one to the forbidden  $^4T_{1g} \rightarrow ^6A_{1g}$  transition of  $Mn^{2+}$ .

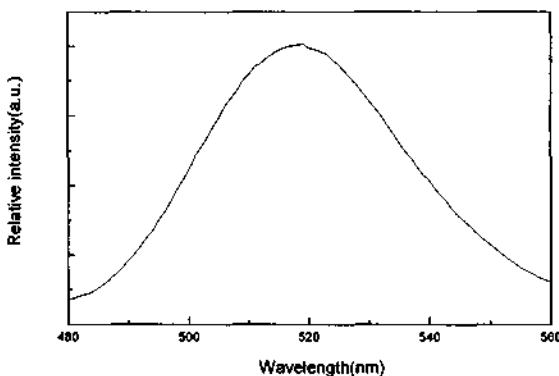


**Figure 3.** The emission spectra of LLP of the sample ZASM at about 10 s after irradiation by a UVP standard mercury lamp peaking at 254 nm with a power of  $4.07 \text{ mW/cm}^2$  for 5 min.

Figure 3 shows the emission spectra of LLP of the sample ZASM at about 10 s after irradiation by a UVP standard mercury lamp peaking at 254 nm with a power of  $4.07 \text{ mW/cm}^2$  for 5 min. The green long lasting phosphorescence peaking at 519 nm is clearly observed at about 10 s, which is almost the same with the emission of  $Mn^{2+}$  at 520 nm under normal static excitation in Figure 2. It indicates that the LLP in ZASM is derived from the  $^4T_{1g} \rightarrow ^6A_{1g}$  transition of  $Mn^{2+}$ .

Figure 4 shows the decay curve of LLP based on the sample ZASM after irradiation by a UVP standard mercury lamp peaking at 254 nm with a power of  $0.6 \text{ mW/cm}^2$  for 15 min. The initial intensity of the LLP reaches  $1990 \text{ mcd/m}^2$  at 10 s and then drops down to  $10 \text{ mcd/m}^2$  at 590 s after irradiation. The phosphorescence can be seen in the dark even 15 h after the removal of UVP standard mercury lamp by the naked eyes whose limit of light perception is  $0.32 \text{ mcd/m}^2$ . From the LLP decay curve, it can be roughly separated into a fast component

and a slow one that determines the LLP time at room temperature. The time dependence of the inverse of the intensity of LLP is also presented in the Figure 4. The intensity of LLP seems to be inversely proportional to time, which indicates the electron-hole recombination mechanism [5] and is consistent with ESR results.

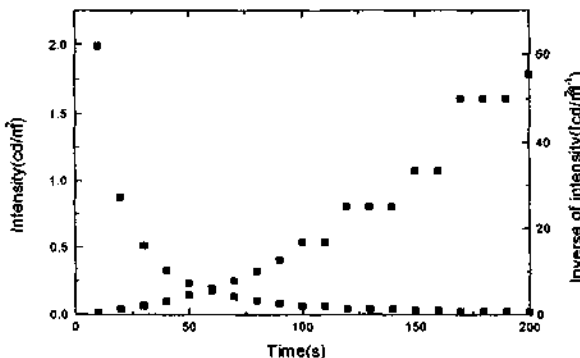


Figure 4. The decay curve and the time dependence of the inverse of the intensity of the LLP based on the sample ZASM at 519 nm after irradiation by a UVP standard mercury lamp peaking at 254 nm with a power of  $0.6 \text{ mW/cm}^2$  for 15 min.

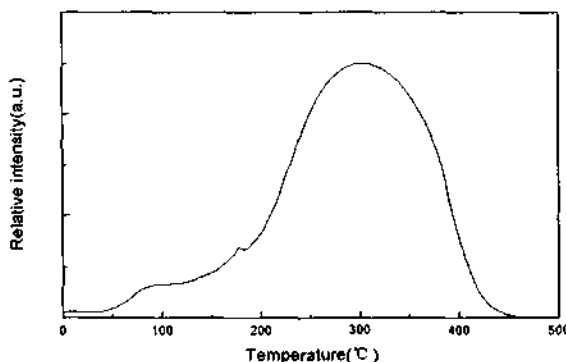
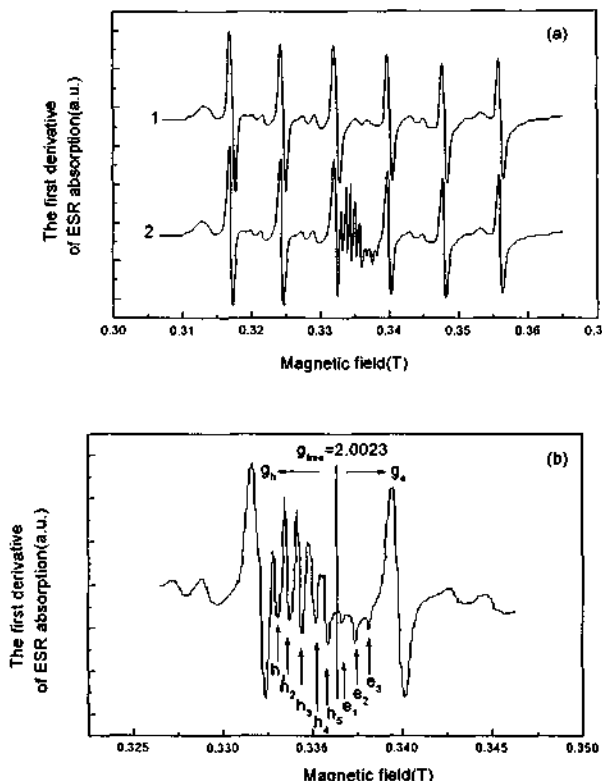


Figure 5. The TL spectra of the sample ZASM at the heating rate of  $2^\circ\text{C/s}$  after irradiation by a UVP standard mercury lamp peaking at 254 nm with a power of  $4.07 \text{ mW/cm}^2$  for 5min

Figure 5 shows TL spectra of the sample ZASM. Before irradiation by mercury lamp, no peaks are found in TL spectra of the sample while after irradiation, three broad peaks are induced in TL spectra of the samples which are treated at round 99°C, 178°C and 302°C, respectively. The results imply that there are at least involved with three kinds of electron or hole trap centers with different trap depth in the ceramic, which finally leads to the LLP.



**Figure 6.** X-band ESR spectra of the powder sample ZASM before and after irradiation by a UVP standard mercury lamp peaking at 254 nm with a power of  $4.07 \text{ mW/cm}^2$  for 5 min: before irradiation [curve 1 in (a)]; after irradiation [curve 2 in (a)]. Figure 6b is the local enlargement of the curve 2 in (a).

Figure 6 shows the X-band ESR spectra of the sample ZASM. Before irradiation, no ESR signals can be detected other than six signals in curve 1 of Figure 6(a), which is ascribed to the hyperfine spin interaction of  $\text{Mn}^{2+}$  ions ( $3d^5$ ) with the total electron spin  $S=5/2$  in the sample. Whereas after irradiation by UVP standard mercury lamp, a complex spectrum with eight

signals beside those of the  $Mn^{2+}$  ions is observed in curve 2 of Figure 6(a) and Figure 6 (b). Based on  $g = h\nu/\beta H_r$ , (where  $h$ ,  $\nu$ ,  $\beta$  and  $H_r$  are Plank constant, microwave frequency, Bohr magnetron and the magnetic field at which the maximum amplitude of a signal is observed.), the  $g$ -values of eight signals ( $h_1$ ,  $h_2$ ,  $h_3$ ,  $h_4$ ,  $h_5$ ,  $e_1$ ,  $e_2$ ,  $e_3$ ) are calculated and listed in Table 1. According to the value of  $\Delta g = g - g_{\text{free}}$  (where the  $g$ -value of the free electron,  $g_{\text{free}}$ , is 2.0023), those signals can be classified into two type spin centers. If  $g - g_{\text{free}} > 0$ , the signal is attributed to hole-trapping centers. If  $g - g_{\text{free}} < 0$ , the signal is identified as electron-trapping centers [13]. So the signals  $h_1$ ,  $h_2$ ,  $h_3$ ,  $h_4$  and  $h_5$  induced by UV in the present sample can be assigned to hole-trapping centers, and the signals  $e_1$ ,  $e_2$  and  $e_3$  are assigned to electron-trapping centers.

**Table 1.**  $g$ -value of ESR centers in sample ZASM after irradiation

Label	$h_1$	$h_2$	$h_3$	$h_4$	$h_5$	$e_1$	$e_2$	$e_3$
$g$ -value	2.0200	2.0162	2.0117	2.0080	2.0038	1.9985	1.9943	1.9897

#### 4 Discussion

The phenomenon of LLP is a complicated behavior that varies from materials to materials. Up to now, there are several models such as electron or hole transfer model, configurational coordinate model and energy transfer model proposed to try to describe the process of LLP phenomenon in details [14]. In the present article, we propose a thermal-assistant recombination mechanism of electrons and holes to illustrate the LLP phenomenon with combination to the results of measurements above obtained in the sample.

Before description of LLP behavior of the sample ZASM in detail, two illustrations should be given.

The first one is whether the higher valence of manganese exists in the ceramic. Before irradiation by the UVP mercury lamp, the body of the ceramic sample shows a milk white color, which indicates the existence of  $Mn^{2+}$  instead of other higher valence of manganese in the as-prepared ceramic. The result is also proved by the typical ESR spectra of  $Mn^{2+}$  shown in curve 1 of Figure 6(a). After irradiation, no evidence implies the optical characteristics of higher valent manganese but  $Mn^{2+}$  in Figure 2 and Figure 3. Furthermore, it is well known that the intensity of the spin signal is proportion to the concentration of spin species. Whereas no change of the position and amplitude of  $Mn^{2+}$  spin signals is observed before and after irradiation. It indicates the absence of higher valence of manganese with lower spin. Based on the discussions mentioned above, the conclusion can be obtained that manganese ion in ZASM almost exist in divalent whenever before or after irradiation.

The second is on the nature of trapping centers. Upon exposure to ultraviolet radiation, the body of the ceramic sample presents a cyan-white color. The phenomenon of photochromism is expected to originate from electrons or hole captured at corresponding trapping centers, which is also described by Qiu J. R. et al. [3]. As shown in ESR spectra in Figure 6., the signals with  $g$ -value smaller and larger than the  $g_{\text{free}}$  likewise indicate the co-existence of electron- and hole-trapping centers, which is also expected by the proportional dependence of the inverse intensity of LLP on time as shown in Figure 4. The hole-trapping center may be attributed to bridging oxygen [6], or zinc vacancy [9] in the ceramic fabricated

at the higher temperature while the electron-trapping center attributed to the oxygen vacancy, which is always present in the oxides [11,14,15]. The results from the TL spectra show that these hole- and electron- trapping centers have different trap depth.

Based on the discussions mentioned above, the LLP behavior can be illustrated as follows. During irradiation, electrons and holes are formed. Then they are directly trapped by oxygen vacancy and the bridging oxygen or zinc vacancy with different trap depth near Mn<sup>2+</sup> rather than directly excited into conductive and valence band because the latter process involves with the existence of higher valence of manganese, which is impossible as discussed above in detail. And then electrons and holes at corresponding trapping centers are thermally released back to Mn<sup>2+</sup> and finally recombined to give rise to the bright green LLP at the room temperature.

In conclusion, we have first synthesized and reported on the bright green LLP phenomenon of Mn<sup>2+</sup> doped ZnO-Al<sub>2</sub>O<sub>3</sub>-SiO<sub>2</sub> ceramic. After irradiation by a UVP standard mercury lamp peaking at 254 nm with a power of 0.6 mW/cm<sup>2</sup> for 15 min, the ceramic sample emits a bright green light peaking at 519 nm, which is derived from the <sup>4</sup>T<sub>1g</sub>→<sup>6</sup>A<sub>1g</sub> transition of Mn<sup>2+</sup> and can be seen in the dark even 15 h after the removal of UVP standard mercury lamp by the naked eyes whose limit of light perception is 0.32 mcd/m<sup>2</sup>. The initial afterglow intensity with the color coordinate (0.2280, 0.5767) reaches about 1900 mcd/m<sup>2</sup> at 10 s after stopping irradiation. From TL and ESR spectra, it is indicated that there are several electron- and hole- trapping centers with different trap depths in the ceramic induced by UV irradiation, which finally lead to the LLP. The mechanism of LLP based on Mn<sup>2+</sup> doped ZnO-Al<sub>2</sub>O<sub>3</sub>-SiO<sub>2</sub> ceramic is considered to be due to thermal-assistant recombination of the trapped electrons and holes, which are formed during irradiation at room temperature.

## 5 Acknowledgment

This work is supported by the State Key Project of Basic Research (G1998061312) of China.

## References

1. Matsuzawa T., Aoki Y., Takeuchi N. and Murayama Y., A new long phosphorescence phosphor with high brightness, SrAl<sub>2</sub>O<sub>4</sub>: Eu<sup>2+</sup>, Dy<sup>3+</sup>, *J. Electrochem. Soc.* **143** (1996) pp. 2670-2673.
2. Tianzhi Z. and Qiang S., Rare earth materials for use in the dark, *J. SID.* **8** (2000) pp. 27-30.
3. Qiu J. R. and Hirao K., Long lasting phosphorescence in Eu<sup>2+</sup>-doped calcium aluminoborate glass, *Solid. State. Commun.* **106** (1998) pp. 795-798.
4. Qiu J. R., Miura K., Inouye H., Kondo Y. and Mitsuyu T., Femtosecond laser-induced three dimensional bright and long lasting phosphorescence inside calcium aluminosilicate glass doped with rare earth ions, *Appl. Phys. Lett.* **73** (1998) pp. 1763-1765.
5. Qiu J. R., Kondo Y., Minra K., Mitsuyu T. and Hirao K., Infrared femtosecond laser induced visible long lasting phosphorescence in Mn<sup>2+</sup> doped sodium borate glasses, *Jpn. J. Appl. Phys.* **38** (1999) pp. L649-L651.

6. Kodama N., Tanii Y. and Yamaga M., Long lasting phosphorescence in Ce<sup>3+</sup>-doped Ca<sub>2</sub>Al<sub>2</sub>SiO<sub>7</sub> and CaYAl<sub>3</sub>O<sub>7</sub> crystals, *Appl. Phys. Letters.* **75** (1999) pp. 1715-1717.
7. Takeru K. and Hideo H., Materials design and example of long lasting phosphorescence glasses utilizing electron trapped centers, *J Non-Cryst Solids.* **274** (2000) pp. 257-263.
8. Lin Y. H., Tang Z. L. and Zhang Z. T., Preparation of long-afterglow Sr<sub>4</sub>Al<sub>14</sub>O<sub>25</sub>-based luminescent material and its optical properties, *Materials Letters* **51** (2001) pp. 14-18.
9. Ueda K., Maruyama T., Takizawa H. and Endo T., Synthesis and long-period phosphorescence of ZnGa<sub>2</sub>O<sub>4</sub>: Mn<sup>2+</sup>, *J. Alloy. Compd.* **60-64** (1997) pp. 262-263.
10. Suresh K. S. and James F. C., Optical properties of zinc aluminate, zinc gallate and zinc aluminogallate spinels, *J. Am. Ceram. Soc.* **81** (1998) pp. 649-654.
11. Meijerink A., Blasse G. and Clasbeek M., Photoluminescence, thermoluminescence and EPR studies on Zn<sub>4</sub>B<sub>6</sub>O<sub>13</sub>, *J. Phys: Condens. Mater.* **2** (1990) pp. 6303-6313.
12. Linwood S. and Wegl J., On the luminescence of divalent manganese in solids, *J. Opt. Soc. Am.* **42** (1952) pp. 910-916.
13. Qiu J. R., Shimizugawa Y., Kojima K., Tanaka K. and Hirao K., Relaxation of ultraviolet-induced structure and long-lasting phosphorescence in Eu<sup>2+</sup>-doped strontium alumiosilicate glass, *J. Mater. Res.* **16** (2001) pp. 88-92.
14. Liu Y. L. and Ding H., Research developments of long lasting phosphorescent materials, *Chinese. J. Inorg. Chem.* **17** (2001) pp. 181-187.
15. Haddad, M., Vignaud, G. and Berger, R., ESR of x-ray irradiated boracites, *J. Phys. Chem. Solids.* **46** (1985) pp. 997-1005.
16. Schirmer, O. F., Trapped-hole centers containing lithium in MgO, CaO and SrO, *J. Phys. Chem. Solids.* **32** (1971) pp. 499-509.

This page is intentionally left blank

# STRUCTURAL PHASE TRANSITION IN THE LAYERED PEROVSKITE COMPOUND $\text{BaTb}_2\text{Mn}_2\text{O}_7$

JIAN MENG, JINGPING WANG AND JING FENG

*Key Laboratory of Rare Earth Chemistry and Physics, Changchun Institute of Applied Chemistry,  
Chinese Academy of Sciences 130022, Changchun, P. R. China  
E-mail: jmeng@ns.ciac.jl.cn*

HIROHISA SATOH AND NAOKI KAMEGASHIRA

*Department of Materials Science, Toyohashi University of Technology, Tempaku-cho, Toyohashi,  
441-8580, Japan  
E-mail: nkamegas@tutms.tut.ac.jp*

A distorted layered perovskite compound  $\text{BaTb}_2\text{Mn}_2\text{O}_7$  was synthesized by the solid state reaction in pure argon. There is a structural phase transition in the  $\text{BaTb}_2\text{Mn}_2\text{O}_7$  compound. The phase transition was characterized by the DSC and high temperature X-ray diffraction. The heat capacity of  $\text{BaTb}_2\text{Mn}_2\text{O}_7$  was calculated. The thermal anomaly corresponding to the phase transition was observed at about 740K. The lattice parameters were calculated by the CELL program for  $\text{BaTb}_2\text{Mn}_2\text{O}_7$ . It has Tb-type orthorhombic symmetry with  $a = 0.3908 \text{ nm}$ ,  $b = 0.3866 \text{ nm}$ ,  $c = 2.0163 \text{ nm}$ , and space group  $I\bar{m}mm$  at room temperature. With the increase of temperature, the lattice parameters gradually increase until 673K. From 723K to 973K, the compound translates to tetragonal with  $a = 0.39078 \text{ nm}$ ,  $c = 2.0277 \text{ nm}$  and S.G.  $I4/mmm$ . This result is fairly in accordance with that of heat capacity.

## 1 Introduction

The richness of structural change and physical properties displayed by manganite layered perovskites has attracted a lot of recent attention because of potential applications of theory calculation and colossal magnetoresistance displayed by the systems [1-3]. Especially, the studies of distorted structures have a very interesting content owing to the John-Teller effect of  $\text{Mn}^{3+}$  ion. But it is very difficult to obtain the pure phase containing  $\text{Mn}^{3+}$  ion only. There are a number of factors in controlling the distortion structure and behavior of the perovskite-related Ruddlesden-Popper (RP) phase, which have the general formula  $\text{BaLn}_2\text{Mn}_2\text{O}_7$ , such as cation size, cation disorder and cation acidity.  $\text{BaLn}_2\text{Mn}_2\text{O}_7$ , in general, always have the tetragonal symmetry with  $I4/mmm$  space group. But they are associated with two kinds of orthorhombic phases, so-called Sm-type with space group  $Fmmm$  for  $\text{BaSm}_2\text{Mn}_2\text{O}_7$  and  $\text{BaEu}_2\text{Mn}_2\text{O}_7$  [4] and Tb-type with space group  $I\bar{m}mm$  for  $\text{BaGd}_2\text{Mn}_2\text{O}_7$  and  $\text{BaTb}_2\text{Mn}_2\text{O}_7$  [5] under different prepared conditions and different kinds of reaction gas.

In contrast to the situation in the 3-dimensional perovskite structure, two distinct sites are available for Ln and Ba cations, in this quasi-2-dimentional crystal structure. A 12-coordinate site (Ba/La1) is situated within the perovskite-like blocks, and a 9-coordinate (Ba/Ln2) is situated on the edge of the blocks referred to as the rock-like layer. The availability of these two sites introduces an additional parameter, which has an influence over the properties of this phase, namely, the degree of cation ordering on the Ba/Ln sublattice [6]. Therefore, it is worthy that the pure phase containing  $\text{Mn}^{3+}$  ion only is

obtained and their structural transport and the situation site occupied random by Ba or Ln ions are investigated. In this paper, we report the phase transition with temperature in  $\text{BaTb}_2\text{Mn}_2\text{O}_7$  compound.

## 2 Experimental Detail

The  $\text{BaTb}_2\text{Mn}_2\text{O}_7$  sample was prepared by the usual solid state reaction from mixtures of  $\text{BaCO}_3$ ,  $\text{Tb}_2\text{O}_3$  and  $\text{Mn}_2\text{O}_3$ . These raw materials were all of 99.99% purity (Kanto Chem. Co. Ltd.).  $\text{Tb}_2\text{O}_3$  was got by the reduction of  $\text{Tb}_4\text{O}_7$  at 1273K in pure  $\text{H}_2$  for 24 hours. The pretreatment of the other reagents was similar to the method described in a previous study [7]. Mixtures of these powders were pressed into pellets and calcined in pure Ar at 1173K for 24 hours to exclude  $\text{CO}_2$  gas and subsequently at 1627K for 72 hours. Then, the sample was slowly cooled to room temperature in the furnace to control the oxygen nonstoichiometry. The as-prepared sample was identified by powder X-ray diffractometer.

The high temperature X-ray diffraction was carried out on an MAC MXP<sup>18</sup> powder X-ray diffractometer using  $\text{Cu K}\alpha$  radiation. The TG/DTA was carried out on SEIKO 400 apparatus. The DSC apparatus used in the heat capacity measurements was a DSC 200 model of SEIKO Electronic Industry Co. Ltd. The measurements were carried out from room temperature to 850K under flowing Ar gas. Reference and pans were made on Al pans covered with Al lids and the empty pan was put on the reference cell side during this experiment. For each cycle of the heating pattern, three sets of the quantities of heat of another empty pan, standard  $\alpha\text{-Al}_2\text{O}_3$  and the specimen were measured against the reference. DSC measurements were achieved by repeating these procedures from 300 to 850K. At a given temperature, the DSC data are overlapped twice for every run of the blank, the standard  $\alpha\text{-Al}_2\text{O}_3$  and the sample. Therefore, eight measures of heat capacities can be calculated at each temperature from a combination of these three kinds of DSC data. For all the values of these calculated heat capacities in the measured temperature range, except for the region of thermal anomaly, multiple regression analysis was carried out with the following equation [8]:

$$\text{Cp}_{\text{ex}} = a + bT + cT^2$$

Where  $\text{Cp}_{\text{ex}}$  is the expected values of the heat capacity, T the absolute temperature and a, b and c are constants. At each temperature, the best-fit value to  $\text{Cp}_{\text{ex}}$  from eight calculated heat capacities was chosen as the observed heat capacity.

## 3 Results and Discussion

The TG/DTA were measured from room temperature to 1573K for  $\text{BaTb}_2\text{Mn}_2\text{O}_7$  and the results were given in Fig.1. In the TG/DTA curves, it is obvious that there are a sharp weak exothermic peak around 625K and smaller peaks at 1071K, 1175K and 1299K, respectively. The exothermic peak at 1071K and 1175K should be related with the decomposition of carbonate into oxides. Accompanying with the change of DTA, the TG curve shows a weight lose of 6% gradually until 1300K. It suggests that the steady structure phase can be synthesized above 1300K.

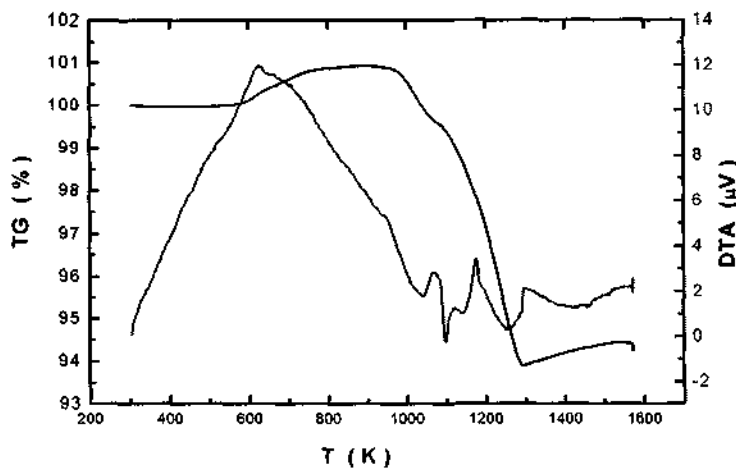


**Figure 1.** The TG/DTA curves for  $\text{BaTb}_2\text{Mn}_2\text{O}_7$ .

The precision of the present measurement of the heat capacity was checked by measuring the heat capacity of a standard  $\alpha\text{-Al}_2\text{O}_3$  sample. The precision of measurement was within  $\pm 2.5\%$  below 380K and above 800K and within  $\pm 1.0\%$  between these two temperatures.

The heat capacity of  $\text{BaTb}_2\text{Mn}_2\text{O}_7$  was measured and the result was shown in Figure 2. It is obvious that the thermal anomaly corresponding to the phase transition was observed in the range from 680K to 800K. The transition temperature was about 740K. It is considered that there is a phase transition at about the temperature in  $\text{BaTb}_2\text{Mn}_2\text{O}_7$ . In this compound, the metal vacancy is a probable defect.

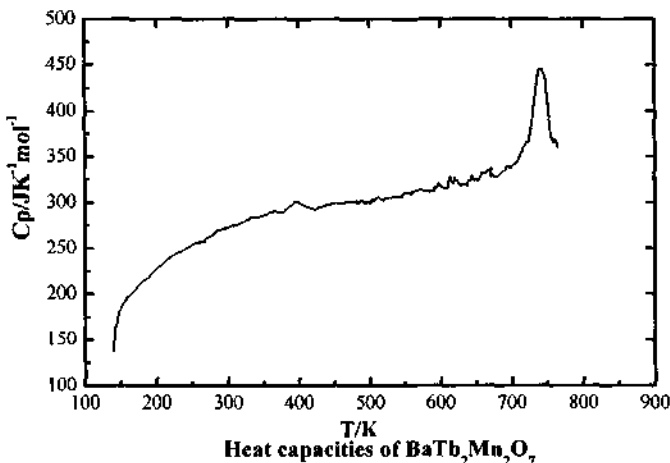


**Figure 2.** Heat capacities for  $\text{BaTb}_2\text{Mn}_2\text{O}_7$ .

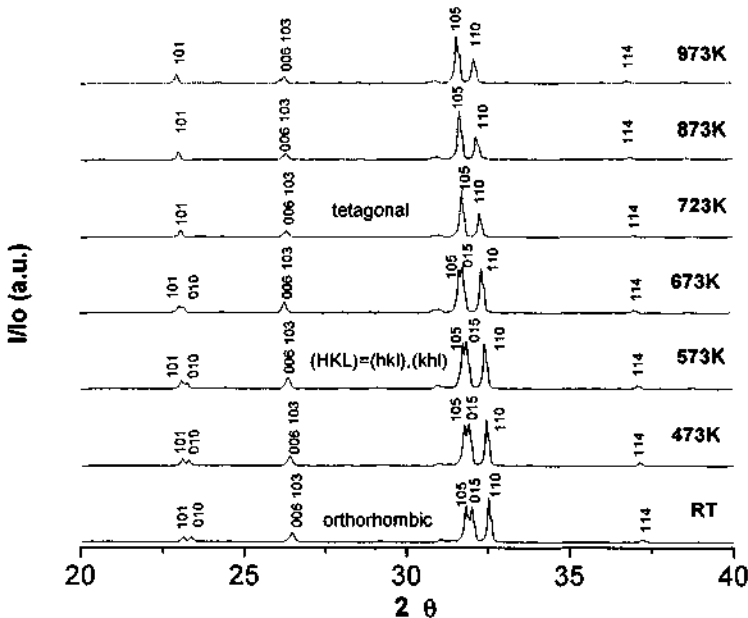


**Figure 3.** The X-ray patterns of  $\text{BaTb}_2\text{Mn}_2\text{O}_7$  from 20 to 40 degrees (two theta angle).

In order to confirm that there is the phase transition in this compound we measured the high temperature X-ray diffraction and the experiment patterns are shown in Figure 3 and Figure 4.

From Figures 3 and 4, it is seen that there are two different kinds of diffraction patterns. Comparison of both patterns indicates that the  $(hh\bar{l})$  reflections in Miller indices are invariant between both phases, while the  $(h\bar{k}l)_{\text{tet}}$  reflection lines split into double peaks with a nearly equal intensity,  $(h\bar{k}l)_{\text{orth}}$  and  $(khl)_{\text{orth}}$ , when  $h \neq k$ . The extinctions of  $h+k+l \neq 2n$  lines are also hold in the orthorhombic phase. It is the characteristic of Tb-type orthorhombic phase. For example, double peaks  $(101)_{\text{orth}}$ ,  $(010)_{\text{orth}}$ ,  $(105)_{\text{orth}}$ ,  $(015)_{\text{orth}}$ ,  $(200)_{\text{orth}}$ ,  $(020)_{\text{orth}}$  and  $(215)_{\text{orth}}$ ,  $(125)_{\text{orth}}$  correspond to the  $(101)_{\text{tet}}$ ,  $(105)_{\text{tet}}$ ,  $(200)_{\text{tet}}$  and  $(215)_{\text{tet}}$ , respectively. Therefore, it belongs to the orthorhombic phase below 673K and it undergoes a phase transition to the tetragonal symmetry with  $I4/mmm$  space group. Therefore, there is a phase transition in  $\text{BaTb}_2\text{Mn}_2\text{O}_7$  at about 723K.

The lattice parameters were calculated by the CELL program [9] for  $\text{BaTb}_2\text{Mn}_2\text{O}_7$  and the results are listed in Table 1. It has a Tb-type orthorhombic symmetry with  $a = 0.3908$  nm,  $b = 0.3866$  nm,  $c = 2.0163$  nm, space group  $I\overline{m}\overline{m}\overline{m}$  at room temperature. With the increase of temperature, the lattice parameters gradually increase until 673K. From 723K, the compound transforms from orthorhombic to tetragonal with  $a = 0.39078$  nm,  $c = 2.0277$  nm and S.G.  $I4/mmm$ . Within 723K and 973K,  $\text{BaTb}_2\text{Mn}_2\text{O}_7$  retains the tetragonal structure but the lattice parameters gradually increase with temperature. This result is fairly in accordance with that of heat capacity. We consider that the structural phase transition arises from the distortion of  $\text{MnO}_6$  octahedron containing John-teller  $\text{Mn}^{3+}$  ion along the  $c$  axis and the  $[110]_t$  direction of the fundamental cell because of the

### **influence of temperature.**

The crystal structure was initially analyzed by RIETAN program [10]. The structural model around the Mn site is shown in Figure 5. According to the initial model, it is seen that there is distortion in the  $\text{MnO}_6$  octahedron. The O3-Mn and O4-Mn bonds are somewhat lengthened along the  $b$  axis. Moreover, the O1-Mn and O5-Mn have the longest bond distances. Therefore, the  $\text{MnO}_6$  octahedron was distortedly extended along the  $c$  axis. We consider that the distortion of the  $\text{MnO}_6$  octahedron results from the John-Teller effect because of the existence of  $\text{Mn}^{3+}$  ion. Further structural refinement is in progress.

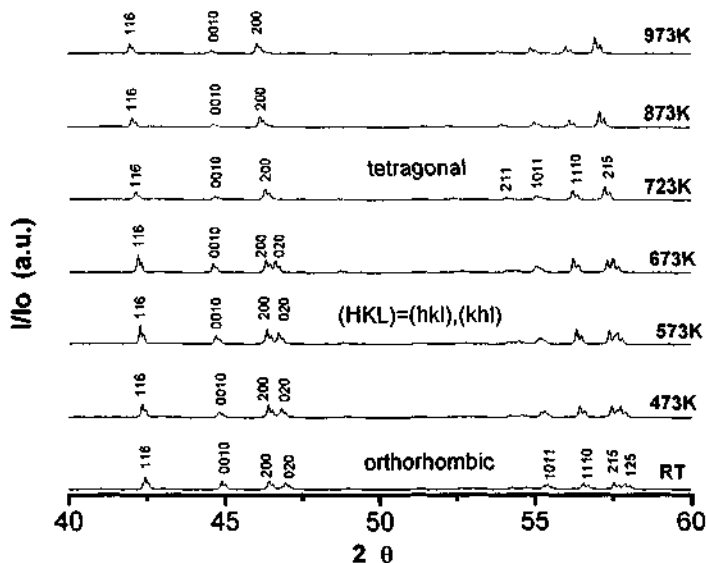


**Figure 4.** The X-ray patterns of BaTb<sub>2</sub>Mn<sub>2</sub>O<sub>7</sub> from 40 to 60 degrees (two theta angle).

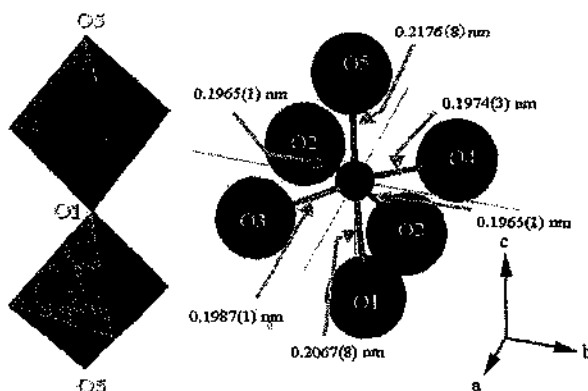


**Figure 5.** The oxygen octahedral ( $MnO_6$ ) in  $BaTb_2Mn_2O_7$ .

**Table I.** High temperature X-ray diffraction results for BaTb<sub>2</sub>Mn<sub>2</sub>O<sub>7</sub>.

Temp. (K)	Phase	<i>a</i> (Å)	<i>b</i> (Å)	<i>c</i> (Å)
298	Orth.	3.9079	3.8657	20.1629
373	Orth.	3.9104	3.8696	20.1844
423	Orth.	3.9109	3.8730	20.1989
473	Orth.	3.9110	3.8766	20.2033
523	Orth.	3.9119	3.8810	20.2218
573	Orth.	3.9148	3.8830	20.2373
623	Orth.	3.9169	3.8873	20.2473
673	Orth.	3.9174	3.8919	20.2622
723	Tetr.	3.9078		20.2768
773	Tetr.	3.9176		20.2582
873	Tetr.	3.9292		20.2732
973	Tetr.	3.9373		20.3090

#### 4 Acknowledgements

This work was supported by the Grant-in-Aid for Scientific Research (B) (No. 13450259) by Japan Society for the Promotion of Science and State Key Program of Basic Research (G1998061311) and National Natural Science Foundation of China (29831010).

#### References

1. Liu R. S., Jang L. Y., Chen J. M., Wu J. B., Liu R. G., Lin J. G. and Huang C. Y., X-ray absorption new edge structure studies of colossal magnetoresistance ferromagnet (La<sub>1.4</sub>Sr<sub>1.6</sub>)Mn<sub>2</sub>O<sub>7</sub>, *Solid State Commun.*, **9** (1998) pp.605-608.
2. Deschizeaux Cheruy M. N. and Joubert J. C., Donnees cristallographiques sur une nouvelle serie de manganites mixtes de terre rare et d'alcalino-terreux, *J. Solid State Chem.*, **40** (1981) pp.14-19.
3. Seshadri R., Maignan A., Hervieu M., Nguyen N. and Raveau B., Complex Magnetotransport in LaSr<sub>2</sub>Mn<sub>2</sub>O<sub>7</sub>, *Solid State Commun.*, **6** (1997) pp.453-457.
4. Ueno S., Meng J., Kamegashira N., Saito-Nakano H. and Enami K., Crystal structure of a layered perovskite, Barium Europium manganese Oxide[BaEu<sub>2</sub>Mn<sub>2</sub>O<sub>7</sub>], *Mater. Res. Bull.*, **31** (1996) pp.497-502.

5. Kamegashira N., Shimono A. and Horikawa M., Synthesis and transition of the orthorhombic  $\text{BaGd}_2\text{Mn}_2\text{O}_7$ , *Mater. Chem. Phys.*, **24** (1990) pp.389-397.
6. Peter D.B., Julie E.M., Matthew J.R., Lauren E.S., Jaap F.V. and Paolo G.R., Neutron Diffraction Study of the Structural and Electronic Properties of  $\text{Sr}_2\text{HoMn}_2\text{O}_7$  and  $\text{Sr}_2\text{YMn}_2\text{O}_7$ , *Chem. Mater.*, **9** (1997) pp.3136-3143.
7. Meng J., Satoh H. and Kamegashira N., Crystal Structure Refinement of Tetragonal  $\text{BaTb}_2\text{Mn}_2\text{O}_7$ , *J. Alloys Compds.*, **244** (1996) pp.75-78.
8. Satoh H., Horikawa M. and Kamegashira N., Measurement of the heat capacity of  $\text{BaEu}_2\text{Mn}_2\text{O}_7$ , *J. Alloys Compds.*, **192** (1993) pp.99-101.
9. Takaki Y., Taniguchi T., Nakata K. and Yamaguchi H., Program for Finding the Unit-cell Constants and the Space Group from X-ray Powder Diffraction Data – The Case Where Approximate Unit-cell Contants are Known, *J.Ceram. Soc. Jpn.*, **97** (1989) pp.763-766.
10. Izumi F., RIETAN – a Software Package for the Rietveld Analysis and Simulation of X-ray and Neutron Diffraction Patterns, *J. Crystallogr. Soc. Jpn.*, **27** (1985) pp.23-26.

This page is intentionally left blank

## PROCESSING AND ELECTRICAL PROPERTIES OF Sr- AND Mn-DOPED LANTHANUM GALLATE

QINGXI FU, XINGYAN XU, DINGKUN PENG, XINGQIN LIU AND GUANGYAO MENG\*

*Department of Materials Science & Engineering, University of Science and Technology of China,  
Hefei 230026, P. R. China  
E-mail: mgym@ustc.edu.cn*

Sr- and Mn-doped lanthanum gallate powders ( $\text{La}_{0.9}\text{Sr}_{0.1}\text{Ga}_{1-x}\text{Mn}_x\text{O}_{3-\delta}$ , LSGMn) were prepared by glycine/nitrate combustion synthesis. X-ray diffraction patterns indicate that the perovskite structure is formed without any second phases after sintering the powders at 1000°C for 4h. Compacts of powders synthesized under stoichiometric combustion were sintered to densities over 95% of theoretical values. The electrical conductivity of this material in air and H<sub>2</sub> are characterized using AC impedance spectroscopy. It shows that the conductivity in H<sub>2</sub> atmosphere is lower than that in air due to *p*-type conduction in this material, and the electrical conductivity increases with increasing manganese content. The chemical stability of  $\text{La}_{0.9}\text{Sr}_{0.1}\text{Ga}_{1-x}\text{Mn}_x\text{O}_{3-\delta}$  in H<sub>2</sub> atmosphere at 750°C as well as the relatively high conductivity makes it a possible anode material for Sr- and Mn-doped lanthanum gallate (LSGM)-based Solid Oxide Fuel Cells.

### 1 Introduction

In recent years, strontium- and magnesium-doped lanthanum gallate perovskite oxides (LSGM) have been proposed as possible electrolyte materials for medium-temperature solid oxide fuel cells (SOFCs) [1]. Compared to high temperature SOFCs based on YSZ electrolytes, the performance of intermediate-temperature SOFCs depends more on the electrode-electrolyte interfaces, since the interfacial polarization of a solid state cell increases rapidly as the operating temperature is reduced [2]. In LSGM-based SOFCs, Sr-doped LaCoO<sub>3</sub> [3] and Sr-doped SmCoO<sub>3</sub> are often used as the cathode materials, and nickel-based materials, such as metallic Ni, NiO-LSGM cermet [4,5], NiO-SDC (Sm<sub>2</sub>O<sub>3</sub>-doped CeO<sub>2</sub>) composite [5,6] and Ni-doped CeO<sub>2</sub> (DCO) composite, have been reported as anode materials. Due to interactions of a LSGM electrolyte with anode material, the anode polarization increases rapidly, so anode performance is influenced greatly. Therefore, it is necessary to search for anode materials that show both high catalytic activity for fuel oxidation and chemical compatibility with the LSGM electrolyte.

If the electrode is made of mixed ionic-electronic conductors (MIECs), which have a perovskite structure, the reaction sites will be expanded beyond the TPBs to the whole MIEC/gas interface. The use of these MIECs as electrode materials for LSGM-based SOFCs offers at least two advantages. First, they are compatible both chemically and physically with LSGM electrolytes, minimizing interfacial reactions due to interdiffusion or chemical reaction. Second, they should have thermal expansion coefficients similar to that of LSGM, minimizing thermally induced stresses at the interface during thermal cycling and, thus improving adhesion of the electrode to the electrolyte [6]. Lanthanum gallates doped with transition metal elements usually exhibit mixed ionic/electronic conduction [7-9], thus these materials may be used as anode materials for LSGM-based SOFCs, assuming these materials have good chemical stability, sufficient electrical conductivity and high catalytic activity. It is also well known that the conductivity of transition metal doped lanthanum gallate increases with increasing transition metal doping [7]. Among the transition metal doped lanthanum gallates, most have bad chemical

stability in reducing atmosphere [10], rendering them inappropriate for anode materials. One material, Sr- and Mn-doped lanthanum gallate (denoted as LSGMn), was reported to have good chemical stability and ever used as anode materials for LSGM-based SOFCs [9]. However, due to low dopant concentration (only 20mol%), the material exhibits mainly ionic conduction and the whole electrical conductivity is relatively low [9]. Therefore, we propose to improve the conductivity of LSGMn by increasing Mn content. If the conductivity is increased without the loss of chemical stability, the higher manganese doped lanthanum gallate may be used as a good anode material.

The glycine/nitrate process (GNP) is a self-combustion method using glycine as fuel and the nitrates of metal components of the material to be synthesized as oxidant, which can prepare a high specific surface powder with single phase composition in very short time. It is especially appropriate for the fabrication of multi-component system such as doped perovskite compounds [11]. Moreover, this process is easily operated and cost-effective.

In this paper, we report the preparation of Sr- and Mn-doped lanthanum gallate powders ( $\text{La}_{0.9}\text{Sr}_{0.1}\text{Ga}_{1-x}\text{Mn}_x\text{O}_{3-\delta}$ ,  $x=0.2, 0.35, 0.43$ ) by a glycine nitrate process. The electrical properties of sintered pellets from as-prepared powders at different atmospheres, as well as their chemical stability under  $\text{H}_2$  atmosphere were characterized.

## 2 Experimental

### 2.1 Sample synthesis

The super fine powders with composition of  $\text{La}_{0.9}\text{Sr}_{0.1}\text{Ga}_{1-x}\text{Mn}_x\text{O}_{3-\delta}$  ( $x=0.2, 0.35, 0.43$ ) were synthesized by GNP. The starting materials were glycine (as the fuel), La-, Sr-, Ga- and Mn nitrates (as oxidants). The glycine was added into the mixed nitrate solution in a molar ratio of 1:1 for fuel: oxidant (stoichiometric combustion). The mixed solutions were heated until sufficient water was removed for combustion to occur. The resulting ash was “precalcined” at 350°C in air for 2h to remove residual organic substances. Subsequent calcinations were performed at 1000°C in air. The calcined powders were compacted in a steel die and sintered at 1500°C for 4h. The densities of the sintered pellets were measured by the Archimedes method. Phase development was determined by X-ray diffraction(XRD) analysis using Cu  $\text{K}_\alpha$  radiation (Rigaku D/Maz- $\gamma_A$ ).

### 2.2 Microstructure

The morphology or microstructure of powders and well-polished pellets was observed with TEM (H-800) and SEM (Hitachi X-650). Au coating was applied on the surfaces or fracture surfaces to prevent charging before observation and photo-taken.

### 2.3 Electrical conductivity

The conductivity of sintered pellets was obtained from two-probe impedance spectroscopy. Platinum electrodes were applied on both surfaces of pellets by coating platinum paste and then firing at 850°C for 0.5h. Measurements were made with an computer-interfaced impedance analyzer (GenRad 1689 Precision RLC Digibridge) over a frequency range of 12-10<sup>5</sup> Hz in the temperature range of 500°C-800°C. Each sample was measured in air and  $\text{H}_2$  atmospheres, respectively.

## 2.4 Chemical stability in reducing atmosphere

The sintered pellets were exposed to H<sub>2</sub> at 750°C for 5 h, followed by XRD measurement and SEM observation to examine whether there is any change on both phase structure and microstructure after heat treatment in a strong reducing atmosphere.

## 3 Results and Discussion

In this paper, La<sub>0.9</sub>Sr<sub>0.1</sub>Ga<sub>1-x</sub>Mn<sub>x</sub>O<sub>3-δ</sub> compositions are designated by the abbreviation LSGMn. The numbers following the abbreviation refer to the relative proportions of Sr and Mn in the material. For example, La<sub>0.9</sub>Sr<sub>0.1</sub>Ga<sub>0.8</sub>Mn<sub>0.2</sub>O<sub>2.85</sub> is designated LSGMn-1020.

### 3.1 X-ray diffractograms

The results of the X-ray diffraction patterns for the LSGMn-1020, LSGMn-1035 and LSGMn-1043 are shown in Fig. 1. It can be seen that all powders with different manganese contents produced by "stoichiometric" combustion followed by calcination at 1000°C for 4h exhibited almost complete perovskite structure. Compared with the traditional solid reaction, by which the perovskite formation temperature is usually above 1300°C, and often with impure second phases, the glycine nitrate process can remarkably lower the formation temperature. The X-ray diffraction patterns of the sintered pellets before and after heat treatment in H<sub>2</sub> are shown in Fig. 2 (A) and (B) respectively. It showed that the phase structures for all compositions investigated here remain unchanged after heat treatment in H<sub>2</sub>, indicating the samples are chemically stable in H<sub>2</sub> atmosphere at least below 750°C.

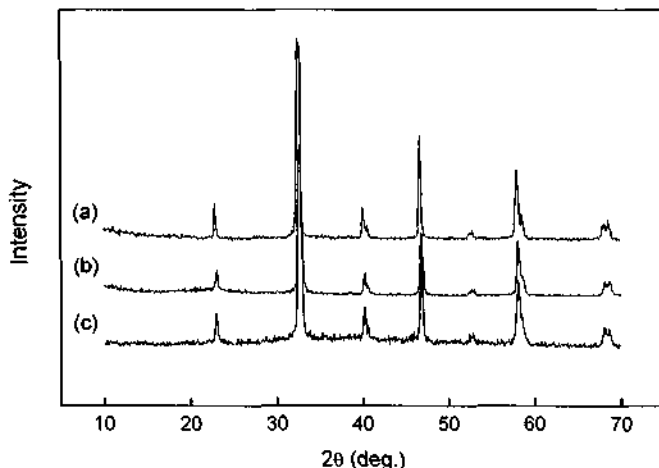


**Figure 1.** X-ray diffraction patterns of powders produced by GNP, calcined at 1000 °C. (a) LSGMn-1020, (b) LSGMn-1035 and (c) LSGMn-1043.

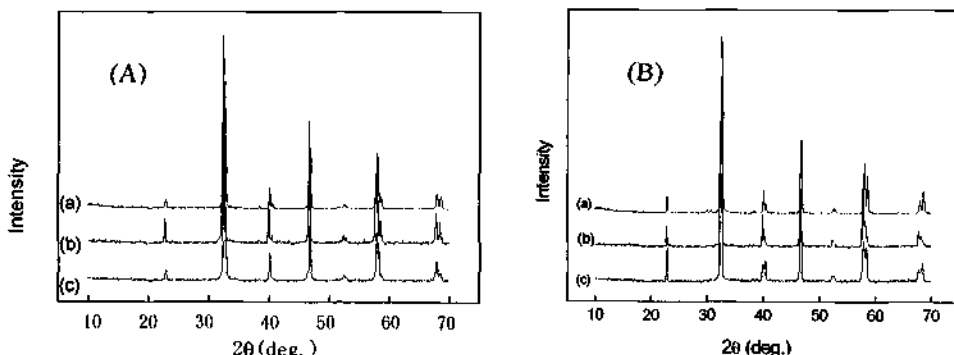


**Figure 2.** XRD patterns of pellets sintered at 1500°C in air (A) and after heat treatment in H<sub>2</sub> at 750°C for 5h (B): (a) LSGMn-1020 (b) LSGMn-1035 (c) LSGMn-1043.

### 3.2 Microstructure

The TEM micrographs for GNP prepared powders calcined at 1000°C are shown in Fig. 3. It can be found that the powder is mostly composed of agglomerates, but the primary particles are uniform with the size around 40nm. During GNP synthesis, one end of the glycine molecules is linked to La<sup>3+</sup> and Sr<sup>2+</sup> ions and the other (amine groups) is linked to Ga<sup>3+</sup> and Mn<sup>2+</sup> ions. These metal ions may be linked to several glycine functional groups, therefore the complexed precursors of the powder should be net-like and the combustion products would be of agglomerates. The temperature of the combustion reaction is generally low and the time is very short, therefore the agglomerates should be soft and may be broken up by ball-milling.

SEM photographs of the surfaces of the sintered samples are shown in Fig. 4 (A). The surface microstructure reveals uniform and fine grain growth about 2-3μm. No pores were observed on the surface of the sample, but there were some pores from the fracture surface of the sample, as shown in Fig. 4 (C). The sintered density is 6.6 g/cm<sup>3</sup>, which is over 95% of the theoretical value. The residual pores may be partly attributed to the agglomerates in the source powders that lowered the sinterability of the green bodies. It can also be seen that there are no great changes between the pellets sintered in air before and after heat treatment at 750°C for 5h in H<sub>2</sub>. This result is in accordance with that of XRD. It confirms that the samples are chemically stable in H<sub>2</sub> atmosphere at least below 750°C.

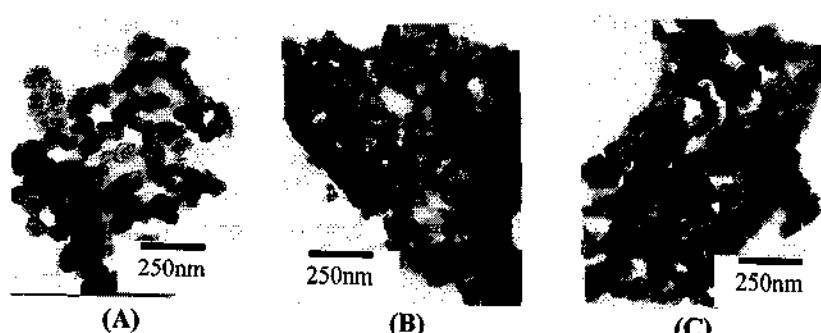


**Figure 3.** TEM micrograph of LSGMn powder calcined at 1000°C: (A) LSGMn-1020 (B) LSGMn-1035(C) LSGMn-1043.

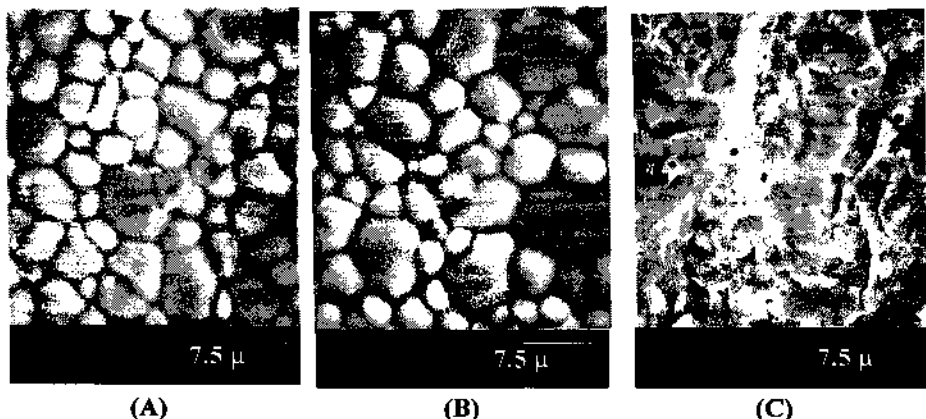
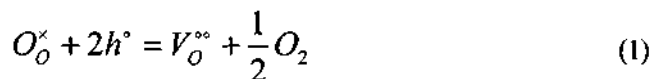


**Figure 4.** Microstructure of the surfaces and fracture of LSGMn pellets. (A) LSGMn-1043 after sintering at 1500°C in air without treatment in H<sub>2</sub> at 750°C; (B) with treatment in H<sub>2</sub> at 750°C and (C) fracture in air.

### 3.3 Electrical conductivity

The temperature dependence of the electrical conductivity of LSGMn-1020, LSGMn-1035, LSGMn-1043 in air and H<sub>2</sub> atmosphere is shown in Fig. 5. It can be seen that the electrical conductivity in H<sub>2</sub> is lower than that in air. The transition metal doped lanthanum gallate mainly exhibits *p*-type electronic conduction, and the mechanism of electronic transport is most likely to be hopping of *p*-type charge carriers [12]. Under reducing atmospheres, the following defect reaction may occur, which reduces the concentration of charge carriers – electronic holes, hence reduces the electrical conductivity.



It is well known that the electronic conductivity of transition metal doped LaGaO<sub>3</sub> increases with increasing transition metal-cation content. When the transition metal dopant concentration exceeds a certain value, a ‘percolation limit’ (30–35%), electron transport transfers from the *p*-type small polaron mechanism to metallic behavior [13]. In our work, for the sample LSGMn-1043, the conductivity at high temperature also becomes metallic-like, as seen in Fig. 5(A). So with Mn content increasing, the conductivity is improved greatly. The conductivity of LSGMn-1020, LSGMn-1035 and LSGMn-1043 in H<sub>2</sub> is 0.020, 0.069, 0.303 at 800°C, respectively.

An important requirement for anode materials is phase stability under reducing atmospheres. From the above XRD and SEM results, we can see that the lightly as well as heavily doped samples do not have any phase or microstructure changes after H<sub>2</sub> treatment at 750°C, a suitable operating temperature for LSGM-based mediate temperature SOFCs. Therefore, we can conclude that they are chemically stable at SOFC anode atmospheres.

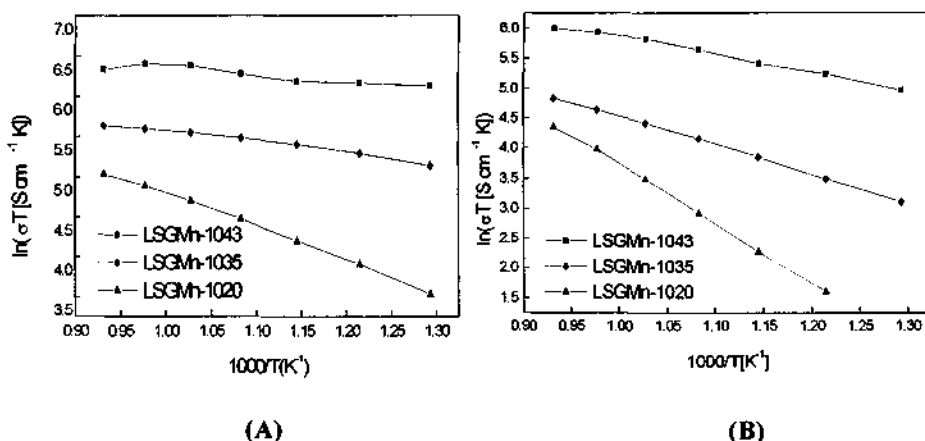


**Figure 5.** Temperature dependence of electrical conductivity of LSGMn samples doped with different quantities of Mn at 800°C: (A) in air and (B) in  $H_2$ .

#### 4 Conclusions

$La_{0.9}Sr_{0.1}Ga_{1-x}Mn_xO_{3-\delta}$  ( $x=0.2, 0.35, 0.43$ ) were synthesized by GNP. A single perovskite phase powder calcined at 1000°C for 4h was obtained. The relative density reaches  $6.6\text{g}/\text{cm}^3$  for the LSGMn pellets sintered at 1500°C for 5h. The conductivity was greatly increased with increasing manganese content. Due to *p*-type electronic conduction, the conductivity in  $H_2$  atmosphere is lower than that in air. The chemical stability in  $H_2$  at 750°C as well as relatively high conductivity makes them possible anode materials for Sr- and Mg-doped lanthanum gallate (LSGM)-based SOFCs. The performance of SOFCs based on such anode materials will be reported later.

#### 5 Acknowledgements

The authors would like to thank the National Natural Science Foundation of China (Grant No. 20071029) and the Ministry of Science and Technology of China (Grant No.G-2000026409 and 2001AA323090) for financial support.

#### References

1. Stevenson J. W., Armstrong T. R., Pederson L. R., Li J., Lewinohn C. A. and Baskaran S., *Solid State Ionics* **113-115** (1998) pp. 571-583.
2. Chen F. L. and Liu M. L., *J. Solid State Electrochem.* **3** (1998) pp.7-14.
3. Maric R., Ohara S., Fukui T., Yoshida H., Nishimura M., Inagaki T. and Miura K., *J. Electrochem. Soc.* **146 (6)** (1999) pp. 2006-2010.
4. Zhang X. G., Ohara S., Maric R., Okawa H., Fukui T., Yoshida H., Inagaki T. and Miura K., *Solid State Ionics* **133** (2000) pp. 153 -160.
5. Huang P. N., Horley A. Petric A., *J. Am. Ceram. Soc.* **82(9)** (1999) pp. 2402-2406.

6. Zhang X. G. Ohara S., Maric R. and Mukai K., *J. Power Sources* **83** (1999) pp.170-177.
7. Trofimenco N. and Ullmann H., *Solid State Ionics* **118** (1999) pp. 215-227.
8. Thangadurai V., Sukla A. K. and Goplakrishnan J., *Chem. Commun.* (1998) pp. 2647-2648.
9. Chen F. L. and Liu M.L., *J. Solid State Electrochem.* **3**(1) (1998) pp. 7-14.
10. Ming Q., Nersesyan M. D., Wagner A., Ritchie J., Richardson J. T., Luss D., Jacobson A. J. and Yang Y. L., *Solid State Ionics* **122** (1999) pp. 113-121.
11. Chick L. A., Pederson L. R., Maupin G. D. and Bates J. L., *Mater. Lett.* **10** (1990) pp. 6-12.
12. Kharton V.V., Viskup A. P., Naumovich E. N. and Lapchuk N. M., *Solid State Ionics* **104** (1997) pp. 67-78.
13. Kharton V. V., Yaremchenko A. A. and Viskup A. P., *Solid State Ionics* **132** (2000) pp. 119-130.

This page is intentionally left blank

**Part II**

**Porous Solids and Catalysts**

This page is intentionally left blank

## NOVEL FRAMEWORK ALUMINIUM DIPHOSPHONATES

MARTIN P. ATTFIELD,<sup>a,b</sup> HOWARD G. HARVEY<sup>a</sup> AND BEN SLATER<sup>a</sup>

<sup>a</sup>Davy-Faraday Research Laboratory, Royal Institution of Great Britain, 21 Albemarle Street, London, W1S 4BS, UK

<sup>b</sup>School of Crystallography, Birkbeck College, University of London, Malet Street, London, WC1E 7HX, UK

E-mail: m.attfield@mail.cryst.bbk.ac.uk

The aluminium diphosphonates,  $\text{Al}_2[\text{O}_3\text{PC}_2\text{H}_4\text{PO}_3](\text{H}_2\text{O})_2\text{F}_2\cdot\text{H}_2\text{O}$  (*I*) and  $\text{Al}_2[\text{O}_3\text{PC}_2\text{H}_4\text{PO}_3](\text{H}_2\text{O})_2\text{F}_2\cdot\text{H}_2\text{O}$  (*II*), have been prepared under solvothermal conditions from a HF/pyridine solvent system and their structures determined. The structures consists of chains of corner sharing  $\text{AlO}_4\text{F}_2$  octahedra with bridging F atoms linking the octahedra. The chains of octahedra are linked together in two directions perpendicular to the chain direction by the alkylidendiphosphonate groups. The resulting structures contain a one-dimensional channel system in which extra-framework water molecules reside, there being one type of channel in *I* and two in *II*. A study of the energetics affecting the structure adopted by these materials reveals that one of the major contributions to the driving force that dictates the formation of a particular structure is the configuration of the organic moiety and this provides a chemical means to control the pore structure of this system and of hybrid inorganic / organic materials.

### 1 Introduction

The chemistry of metal phosphonates has received much interest in recent years because of the wide variety of accessible structures possible and their potential for use as sorbents, catalysts and optical materials [1, 2]. The main attraction of such materials stems from the inclusion of an organic moiety into the compound that may be modified to impart particular chemical functionality and structure on the material and introduce a high degree of hydrophobicity. The latter property can lead to improvements in catalytic performances in particular systems [3, 4]. Initially, synthetic work focused primarily on using phosphonic acids for the synthesis of new materials, this has been extended to include the utilization of diphosphonic acids ( $[(\text{HO})_2\text{OPRPO}(\text{OH})_2]$ , where R is an organic group). The attraction of incorporating the diphosphonic acid is that through careful selection of the R group the interlamellar distance, pore size, and potentially the shape selective properties within the resulting structure can be controlled. In this respect, the chemical manipulation of the R group, when included into a system that forms the same type of structure when R is changed, may be used to form designed structures. Metal diphosphonates containing various metal cations have been reported [1]. We are interested in the aluminium diphosphonate system, a system that has received scant attention, which is surprising considering the possible chemical similarities between this type of material and the important aluminophosphate family of compounds. As far as the authors are aware, our paper on the synthesis and structure of aluminium ethylenediphosphonate is the first to be reported for this family [5]. The structure of this material,  $\text{Al}_2[\text{O}_3\text{PC}_2\text{H}_4\text{PO}_3](\text{H}_2\text{O})_2\text{F}_2\cdot\text{H}_2\text{O}$ , was determined using data collected on a twinned crystal without de-twinning the data [5]. To confirm this structure, we present the Rietveld refinement of this material using synchrotron X-ray powder data. In addition, the preliminary structural findings of the next homologue in

this series is described and a study of the energetics which dictate the structure adopted by these materials is presented.

## 2 Experimental Details

The synthesis of the  $\text{Al}_2[\text{O}_3\text{PC}_2\text{H}_4\text{PO}_3](\text{H}_2\text{O})_2\text{F}_2\cdot\text{H}_2\text{O}$  (*I*) was performed by mixing  $\text{Al}_2(\text{SO}_4)_3\cdot 18\text{H}_2\text{O}$  (Aldrich), ethylenediphosphonic acid (Lancaster), HF/ pyridine (70 wt % HF, Aldrich), pyridine (Aldrich), and de-ionised water in the molar ratio 1: 2.16: 8.7: 54: 144. The reaction mixture (initial pH = 6) was sealed in a Teflon-lined steel autoclave and heated under autogenous conditions at 170 °C for 5 days.  $\text{Al}_2[\text{O}_3\text{PC}_3\text{H}_6\text{PO}_3](\text{H}_2\text{O})_2\text{F}_2\cdot\text{H}_2\text{O}$  (*II*) was synthesized using a similar synthesis procedure. The obtained crystalline products were separated by suction filtration, washed in distilled water and acetone, and dried in air.

A 0.5 mm diameter Lindemann glass capillary of sample *I* was mounted on the powder diffractometer at station 2.3 at CCLRC Daresbury Laboratory, Synchrotron Radiation Source and room temperature synchrotron X-ray data were collected. The mean wavelength used was 1.2999 Å and data were collected from 6 to 80° 2θ. The diffractometer operated with a Si(111) monochromator, parallel foils prior to the detector and a scintillation detector. The sample was spun during data collection to minimise preferred orientation and sampling effects. Data were collected on sample *II* in a similar manner but at a wavelength of 1.3000 Å.

The starting model for the Rietveld refinement of (*I*) was the twinned crystal structure of  $\text{Al}_2[\text{O}_3\text{PC}_2\text{H}_4\text{PO}_3](\text{H}_2\text{O})_2\text{F}_2\cdot\text{H}_2\text{O}$  [5] using the space group  $P2_1/m$ . The background was fitted using a simple interpolation formula with 36 terms. The profile peak shape was described using a pseudo-Voigt function with an additional term to allow for anisotropic particle size broadening effects. The final cycle of least squares refinement included the scale factor, detector zero point, background coefficients, unit cell parameters, peak shape width variation terms and positional and isotropic thermal parameters for all atoms. The isotropic thermal parameters of the Al and P atoms were constrained to have the same shift, as were those of the O, F and C atoms and an absorption correction was applied to the data. Final observed, calculated and difference profile plots are shown in Figure 1, and the final atomic coordinates and isotropic thermal parameters are given in Table I. The Rietveld refinement was performed using the GSAS package [6].

Laboratory powder diffraction data was used to determine the orthorhombic unit cell ( $a = 4.917$  Å,  $b = 12.080$  Å,  $c = 19.178$  Å) of (*II*) from the first 20 low-angle Bragg reflections using the auto-indexing program TAUP [7] within the Crysfire suite of programs [8]. The synchrotron data was used to provide an initial structure solution, using the program SIRPOW [9], and for structure refinement, using the GSAS package [6], in space group  $P2_2_12_1$ . The Rietveld refinement of the structure gave final residues of  $R_p = 6.49\%$ ,  $R_{wp} = 7.9\%$  and  $\chi^2 = 1.341$ . Further studies are continuing to verify the space group assignment and preliminary structure of *II* and will be presented in full elsewhere.

A preliminary study of the energetics of this system has been performed to understand the driving forces that give rise to the structures adopted by both *I* and *II* in

contrast to other polymorphs constructed from the same inorganic and organic chains. All calculations were performed using plane wave density functional methods embodied in the CASTEP code [10].

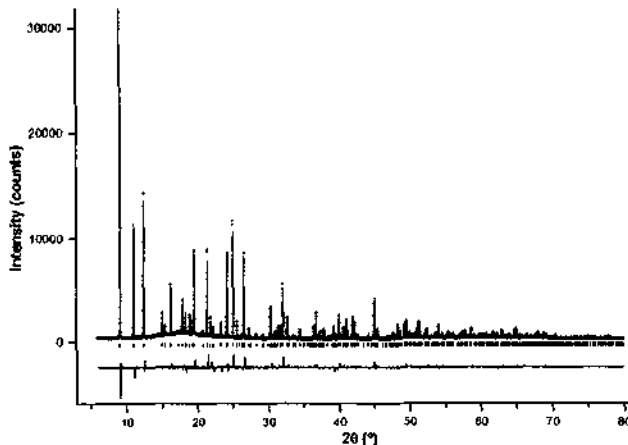


**Figure 1.** The final observed (crosses), calculated (line) and difference plot for the Rietveld refinement of  $\text{Al}_2[\text{O}_3\text{PC}_2\text{H}_4\text{PO}_3](\text{H}_2\text{O})_2\text{F}_2\cdot\text{H}_2\text{O}$ .

**Table I.** Final atomic coordinates and isotropic thermal parameters for  $\text{Al}_2[\text{O}_3\text{PC}_2\text{H}_4\text{PO}_3](\text{H}_2\text{O})_2\text{F}_2\cdot\text{H}_2\text{O}^a$ .

Atom	x	y	z	$U_{\text{iso}} (\text{\AA}^2)$
Al(1)	0.5000	0.5000	0.0000	0.0164(3)
Al(2)	0.2439(7)	0.2500	0.1452(4)	0.0164(3)
P(1)	0.0077(4)	0.4853(3)	0.2397(5)	0.0164(3)
O(1)	0.0411(8)	0.3585(3)	0.2397(5)	0.0097(4)
O(2)	0.2055(7)	0.5433(3)	0.1209(5)	0.0097(4)
O(3)	-0.2822(7)	0.5191(3)	0.1915(4)	0.0097(4)
O(4)	0.503(1)	0.2500	0.3296(6)	0.0097(4)
O(5)	0.011(1)	0.2500	-0.0554(6)	0.0097(4)
O(6)	0.434(1)	0.2500	-0.3456(6)	0.0097(4)
F(1)	0.4514(7)	0.3524(2)	0.0477(4)	0.0097(4)
C(1)	0.088(1)	0.5304(5)	0.4468(7)	0.0097(4)

<sup>a</sup> $a = 4.97722(2) \text{\AA}$   $b = 12.01318(5) \text{\AA}$   $c = 8.18106(4) \text{\AA}$   $\beta = 92.052^\circ$ ;  $R_{wp} = 8.59\%$ ,  $R_p = 6.73\%$ ,  $R_I = 6.77\%$   $\chi^2 = 3.83$

### 3 Results and Discussion

The crystal structure of  $\text{Al}_2[\text{O}_3\text{PC}_2\text{H}_4\text{PO}_3](\text{H}_2\text{O})_2\text{F}_2\cdot\text{H}_2\text{O}$  (*I*) is shown in Figure 2 (top). The structure consists of chains of corner sharing  $\text{AlO}_4\text{F}_2$  octahedra running parallel to the [010] direction with bridging fluorine atoms linking the octahedra. These chains contain two types of  $\text{AlO}_4\text{F}_2$  octahedra. The first type contains aluminium, Al(1), coordinated to two fluorine atoms (2x Al(1)-F(1) 1.833(3) Å) in a *trans* configuration

with the other corners of the octahedron being occupied by four of the oxygen atoms of the diphosphonate groups, (2x Al(1)-O(2) 1.871(4) Å; 2x Al(1)-O(3) 1.887(4) Å). The second octahedron consists of a central aluminium atom, Al(2), bound to two fluorine atoms in a *cis* fashion (2x Al(2)-F(1) 1.810(4) Å) with the other two equatorial positions being occupied by two diphosphonate oxygen atoms (2x Al(2)-O(1) 1.837(4) Å). The remaining axial positions are filled by two water molecules (Al(2)-O(4) 1.950(6) Å; Al(2)-O(5) 1.976(6) Å). The Al-O, Al-F and Al-OH<sub>2</sub> distances observed are similar to those reported in the literature [11]. The internal bond angles of the AlO<sub>4</sub>F<sub>2</sub> octahedra all fall within the range 85.7 – 92.6° and 174.5 – 180° as expected for octahedral units.

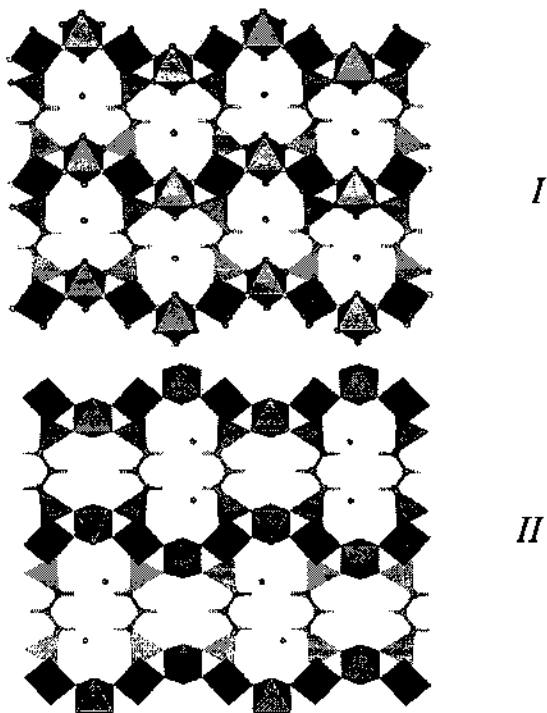


**Figure 2.** Polyhedral views of  $\text{Al}_2[\text{O}_3\text{PC}_2\text{H}_4\text{PO}_3](\text{H}_2\text{O})_2\text{F}_2\text{H}_2\text{O}$  (*I*) (top) and  $\text{Al}_2[\text{O}_3\text{PC}_3\text{H}_6\text{PO}_3](\text{H}_2\text{O})_2\text{F}_2\text{H}_2\text{O}$  (*II*) (bottom) looking along the channel direction. Dark grey - AlO<sub>4</sub>F<sub>2</sub> octahedra; lighter grey - PO<sub>3</sub>C tetrahedra; alkyl chains shown as ball and stick model. The possible physically reasonable permutations of water molecule arrangements are shown in the large channels of *II*.

The ethylenediphosphonate groups link the octahedral chains in the [100] and [001] directions to form a structure containing small channels running along the [100] direction. Within these channels are found extra-framework water molecules, O(6). The bond lengths (P(1)-O(1) 1.532(4) Å, P(1)-O(2) 1.547(4) Å, P(1)-O(3) 1.529(4) Å and P(1)-C(1) 1.845(6) Å) and internal tetrahedral bond angles (range 104.4 – 113.1°) of the phosphonate group all lie within the range expected for the geometry of such moieties [12]. The bond lengths and angles described above are all in agreement, allowing for the estimated standard deviations for each value, with those obtained

initially using the twinned crystal data except for the P(1)-C(1) distance which is slightly longer than that reported previously (1.845(6) Å in this study and 1.780(8) Å in the former report) but still within the range of P-C bond distances observed in phosphonate materials [13]. This indicates that the structure obtained using the twinned micro-crystal data had the correct geometry even though the final residuals were somewhat higher than is usually expected from single crystal X-ray diffraction structure determinations.

The crystal structure of  $\text{Al}_2[\text{O}_3\text{PC}_3\text{H}_6\text{PO}_3](\text{H}_2\text{O})_2\text{F}_2 \cdot \text{H}_2\text{O}$  (*II*) is shown in Figure 2 (bottom). It consists of the same components as *I*, that is, chains of corner sharing  $\text{AlO}_4\text{F}_2$  octahedra bridged in two directions by the propylene diphosphonate groups. However, unlike *I* where adjacent inorganic chains are arranged in a "herringbone" (**H**) arrangement (see Figure 2), the chains in *II* are arranged in an "anti-herringbone" (**AH**) fashion (see Figure 2) in which the chains are displaced half a unit cell along the *b* axis relative to each other. This latter (**AH**) arrangement results in two types of channel being formed in *II*, one that contains the extra-framework water and one that is empty.

The structures of *I*, *II*, *III* and *IV* were energy minimized using plane wave density functional methods. The energy minimized structure *III* is shown in Figure 3 (top) and is a hypothetical structure related to *I*, but in which there is an **AH** arrangement of the inorganic chains. The energy minimized structure *IV* is shown in Figure 3 (bottom) and is a hypothetical structure related to *II*, but in which there is a **H** arrangement of the inorganic chains.

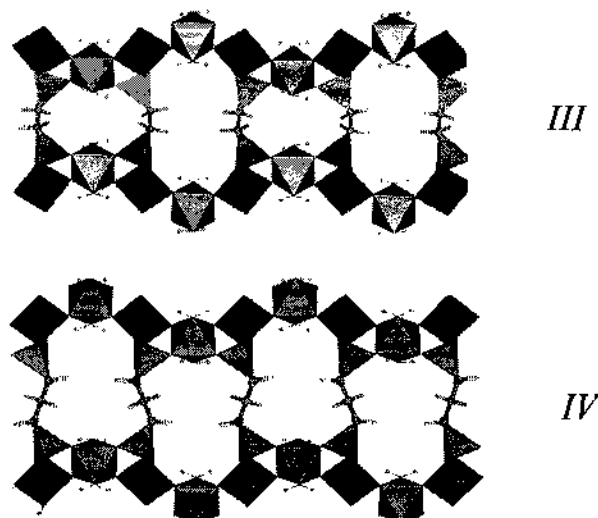


**Figure 3.** Polyhedral views of the hypothetical structures of  $\text{Al}_2[\text{O}_3\text{PC}_2\text{H}_4\text{PO}_3](\text{H}_2\text{O})_2\text{F}_2$  (*III*) (top) and  $\text{Al}_2[\text{O}_3\text{PC}_3\text{H}_6\text{PO}_3](\text{H}_2\text{O})_2\text{F}_2$  (*IV*) (bottom) looking along the channel direction. Dark grey -  $\text{AlO}_4\text{F}_2$  octahedra; lighter grey -  $\text{PO}_3\text{C}$  tetrahedra; alkyl chains shown as ball and stick model.

The total energy calculations on both the ethyl- and propyl-containing systems indicated that the hypothetical structures (*III* and *IV*) were between 115 and 85 kJ mol<sup>-1</sup> less stable than the experimentally observed structures (*I* and *II*, respectively).

The unit cells of structures *I*–*IV* were deconstructed in order to determine the

origin of the total energy differences between the observed and hypothetical structures. This was done by taking the optimised cell for each structure and removing the alkyl component, saturating under coordinated phosphorous atoms with hydrogen atoms, and calculating the single point total energy of the remaining cell contents. Similarly, the inorganic chains were removed and the unsaturated carbon atoms capped with hydrogen, and again the single point total energy calculated. The energy difference calculations for these possibilities allowed the contributions of the inorganic or organic components of the cell to the stability or instability of the observed and hypothetical structures to be determined.

The cell deconstruction calculations revealed that for the ethylene diphosphonate structure the most stable arrangement of the inorganic chains is **H** (as in *I*) and that in the observed structure (*I*) the configuration of the ethyl backbone is more stable. For the propylene diphosphonate system, we again find that it is thermodynamically more favourable to align the inorganic sheets in a **H** arrangement (as in *IV*) and that in the observed structure (*II*) the configuration of the propyl backbone is more stable energetically.

These cell deconstruction calculations reveal that the actual structure adopted in these materials arises, predominantly, from a competition between the energies resulting from the non-local forces between the inorganic chains, which favour **H** alignment, and the torsional forces within the organic component linking the inorganic chains, that favour a *trans* arrangement. For the observed ethylene diphosphonate structure (*I*), both the inorganic and organic components of the cell are more energetically stable than the configuration in the hypothetical structure (*III*). For the observed propylene diphosphonate structure (*II*), the inorganic structure is less stable than that in the hypothetical structure (*IV*), but the driving force which gives rise to the experimentally observed crystal structure is the configuration of the organic moiety, which is far more energetically stable in the observed structure (*II*).

The results demonstrate that the layering of these materials is heavily influenced by the most energetically favourable configuration of the organic component, particularly for the longer alkyl chain. Thus by modifying the organic component of the diphosphonic acid in the reaction mixture it should be possible to dictate the structure produced. Hence, by careful selection of the number of carbons in the alkyl chain, a material with one or two types of channel can be formed with a particular channel height. Use of computer simulation techniques allows us to predict which of the two configurations is most likely to be adopted by the material for a particular alkyl chain diphosphonic acid. Thus, for this particular system we have developed a chemical strategy to control the pore structure of these hybrid inorganic/organic materials.

#### 4 Acknowledgements

MPA would like to thank the Royal Society for provision of a University Research Fellowship and HGH would like to thank EPSRC for provision of a quota award and for funding. We would like to thank EPSRC for funding the computer facilities used in this work and Accelrys for use of their visualization software.

## References

1. Clearfield A., Metal Phosphonate Chemistry. In *Progress in Inorganic Chemistry*, ed. by Karlin K. D. (Wiley, 1998) pp 371-510.
2. Vermeulen L. A. and Thompson M. E., Stable photoinduced charge separation in layered viologen compounds, *Nature* (1992) **358** pp. 656-658.
3. Rhijn W. M. V., De Vos D. E., Sels B. F., Bossaert W. D. and Jacobs P. A., Sulfonic acid functionalised ordered mesoporous materials as catalysts for condensation and esterification reactions, *Chem. Commun.* (1998) pp. 317-318.
4. Bhaumik A., Mukherjee P. and Kumar R., Triphase catalysis over titanium-silicate molecular sieves under solvent-free conditions - I. Direct hydroxylation of benzene, *J. Catal.* (1998) **178** pp. 101-107.
5. Harvey H. G., Teat S. J. and Attfield M. P.,  $\text{Al}_2[\text{O}_3\text{PC}_2\text{H}_4\text{PO}_3](\text{H}_2\text{O})_2\text{F}_2\cdot\text{H}_2\text{O}$ : a novel aluminium diphosphonate, *J. Mater. Chem.* (2000) **10** pp. 2632-2633.
6. Larsen A. and von Dreele R. B., GSAS – General Structure Analysis System, Tech. Rept. LA-UR-86-748 (Los Alamos National Laboratory, USA, 1987).
7. Taupin D., A Powder-Diagram Automatic-Indexing Routine, *J. Appl. Cryst.* (1973) **6** pp. 380-385.
8. Shirley R., The CRYSFIRE System for Automatic Powder Indexing: User's Manual (The Lattice Press, 41 Guildford Park Avenue, Guildford, Surrey GU2 5NL, England, 1999).
9. Altomare A., Cascarano G., Giacovazzo C., Guagliardi A., Burta M. C., Polidori G. and Camalli M., SIRPOW-92 – a program for automatic solution of crystal structures by direct methods optimised for powder data, *J. Appl. Cryst.* (1994) **27** pp. 435-436.
10. Payne M. C., Teter M. P., Allan D. C., Arias T. A., Joannopoulos J. D., Iterative minimization techniques for ab initio total-energy calculations - molecular-dynamics and conjugate gradients CASTEP 4.2, *Rev. Mod. Phys.* (1992) **64** pp. 1045-1097.
11. Simon N., Guillou N., Loiseau T., Taulelle F., and Ferey G., Synthesis and ab initio structure determination from X-ray powder diffraction of MIL-12, a new layered fluoroaluminophosphate templated with 1,3 diaminopropane:  $[\text{N}_2\text{C}_3\text{H}_{12}]\text{Al}_2(\text{PO}_4)_x(\text{OH})_{8-x}\text{F}_{5-x}$  ( $x \sim 2$ ), *J. Solid State Chem.* (1999) **147** pp. 92-98.
12. Soghomonian V., Diaz R., Haushalter R. C., O'Connor C. J. and Zubieta J., Hydrothermal syntheses and crystal-structures of 2 oxovanadium-organodiphosphonate phases  $[\text{H}_2\text{N}(\text{C}_2\text{H}_4)_2\text{NH}_2][\text{(VO)}_2(\text{O}_3\text{PCH}_2\text{CH}_2\text{CH}_2\text{PO}_3\text{H})_2]$ , a stair structure incorporating an organic cationic template, and  $[(\text{VO})(\text{H}_2\text{O})(\text{O}_3\text{PCH}_2\text{NH}(\text{C}_2\text{H}_4)_2\text{NHCH}_2\text{PO}_3)]$ , a layered structure pillared by a piperazinium-tethered diphosphonate, *Inorg. Chem.* (1995) **34** pp. 4460-4466.

This page is intentionally left blank

## SYNTHESIS OF MESOPOROUS PHOSPHOMOLYBDIC ACID

CHU LEI AND ZHANG YUAN-MING

*Department of Chemistry, Jinan University, Guangzhou 510632, P. R. China*

*E-mail: tzhangym@jnu.edu.cn*

Mesoporous phosphomolybdic acid has been hydrothermally synthesized with the surfactant template cetyltrimethylammonium bromide, phosphomolybdic acid and tetraethyl orthosilicate as the silicon source. The parent materials are extracted in a solvent to remove the organic structure-directing agent. The materials have been characterized by chemical analysis, X-ray diffraction, TEM, Infrared spectra and nitrogen BET surface measurement. After extraction of the silica-modified salts with HCl/EtOH, the surface area of the mesoporous material is up to  $140 \text{ m}^2/\text{g}$ , and the pore diameter is  $30\sim40 \text{ nm}$ .

### 1 Introduction

As a silica-based mesoporous material, M41S is of great interest for being attractive as adsorbents and supports for catalysts [1,2]. The attraction of new prospects for industrial utility explains to a great extent the impact that the discovery of the first family of silica-based mesoporous molecular sieves (denoted M41S) had in the scientific community. Following the announcement of the Mobil researchers' success, based on the use of long-chain quaternary ammonium surfactants as structural directing agents [3], a large amount of related work was published in a very short time [4,5]. This new family of mesoporous materials possess uniform and large pores ( $2\sim10 \text{ nm}$ ), a large surface area over  $1000 \text{ m}^2/\text{g}$  and a large adsorption capacity. However it has several limitations due to the lattice of silica. From this viewpoint, a number of groups have successfully incorporated various metal ions such as Al, Ti, V, Ga, and B [6] into the silica framework of MCM-41. Metal oxides with porous structures have been synthesized by using structure-directing agents similar to the templates used in the synthesis of M41S. Some efforts were made to obtain porous heteropoly acids, but none was accomplished due to the low thermal stability of the heteropoly anions [7].

Stein et al. and Janauer et al. have synthesized layered mesostructured materials of  $(\text{C}_{19}\text{H}_{42}\text{N})_6(\text{H}_2\text{W}_{12}\text{O}_{40})$  and  $[\text{C}_{12}\text{H}_{25}\text{N}(\text{CH}_3)_3]_6(\text{H}_2\text{W}_{12}\text{O}_{40})$ , respectively [2,8]. These materials are of great interest because their walls are made of cluster anions, in contrast to the amorphous walls of the other materials. The tungsten, vanadium, niobium, and molybdenum oxide precursors reacting with cationic surfactants, often form similar cluster ion salts with lamellar structures [2].

In our studies we synthesized surfactant salts of phosphomolybdic acid (PMA) and reacted them with tetraethyl orthosilicate (tetrabutyl titanate) in a "salt-gel" reaction in order to obtain a three-dimensional tunnel structure. It is based on the hydrothermal reaction using cetyltrimethylammonium bromide as a structure-directing agent. Phosphomolybdic acid is unstable when the temperature is over 723 K. Calcination to decompose the template will make the inorganic portion of the structure to collapse invariably and to form dense  $\text{MoO}_{3-x}$  phases. Therefore, we

removed the template by extraction with the solvent instead of calcination.

## 2 Experimental

### 2.1 Synthesis

#### 2.1.1 Synthesis of $(C_{19}H_{42}N)_3(PMo_{12}O_{40})$

The solution of surfactant was prepared by dissolving  $CH_3(CH_2)_{15}N(CH_3)_3Br$  (CTAB) in the distilled water and to the solution was added the appropriate amount of  $H_7[P(Mo_2O_7)_6].xH_2O$  (PMA) with vigorous stirring. After being stirred at room temperature for 1 h, the resulting mixtures were allowed to react in a Teflon-lined autoclave at 368K from 24 to 96 h. The resultant yellow solid products were filtered, washed with distilled water, and dried in air. Elementary analysis: C, 25.08%; H, 4.86%; N, 1.22%; calculated for  $(C_{19}H_{42}N)_3(PMo_{12}O_{40})$ : C, 25.47%; H, 4.69%; N, 1.56%.

#### 2.1.2 Reaction with tetraethyl orthosilicate (TEOS)

Silicate was introduced into the salts by reacting 3g of the cluster/surfactant salt with 3g TEOS at 433K for 24 h in a Teflon-lined autoclave. The product was collected by filtration, wash with 95% ethanol, and dried in air. The product is marked as S<sub>1</sub>.

#### 2.1.3 Extraction of template

The cationic surfactant was removed by stirring in 150 ml of 1M HCl/EtOH at room temperature for 48h. The product was collected by filtration, wash with ethanol, and dried in air. The product is marked as S<sub>2</sub>.

### 2.2 Product characterization

Elementary analysis for C, H, and N were carried out with an Elementar Inc., Vario EL, GA. X-ray diffraction (XRD) data were collected using a Rigaku Corporation D/max - IIIA diffractometer with Cu K $\alpha$  radiation (35kV, 25mA). Fourier transform infrared spectra were collected on a Bruker Equinox 55 FTIR spectrometer, using KBr pellets of the samples. Transmission electron microscopy were performed using a JEM-100CX II /T transmission electron microscope operating at 100 kV. Specimens were prepared for TEM examination by crushing the starting materials to a fine powder and dispersing the resulting particles on a holey carbon film supported by a copper mesh grid. The BET surface area measurements were carried out using a Quantachrome NOVA 1000 instrument.

### 3 Results and Discussion

#### 3.1 Infrared spectrum

The IR spectrum of  $(C_{19}H_{42}N)_3(PMo_{12}O_{40})$  is compared with those of PMA and the samples treated by TEOS in Fig.1. The bands in the IR spectrum of  $(C_{19}H_{42}N)_3(PMo_{12}O_{40})$  correspond well to those of PMA, showing the typical features of Keggin anions. The four absorption bands at 1062, 957, 881, 800  $\text{cm}^{-1}$  are assigned to the  $\nu(\text{P}-\text{O})$ ,  $\nu(\text{Mo}-\text{O}_t)$  ( $\text{O}_t$  refers to the terminal oxygens),  $\nu(\text{Mo}-\text{O}_c-\text{Mo})$  ( $\text{O}_c$  refers to the corner oxygens) and  $\nu(\text{Mo}-\text{O}_e-\text{Mo})$  ( $\text{O}_e$  refers to the edge oxygens) respectively. The red-shift of the bands of  $(C_{19}H_{42}N)_3(PMo_{12}O_{40})$  compared with those of PMA suggests some interaction between the cluster anions and the cationic headgroups of the surfactant. The IR spectrum of TEOS-treated samples exhibit several absorption bands in the region between 1100 and 500  $\text{cm}^{-1}$ . It is different from the PMA and  $(C_{19}H_{42}N)_3(PMo_{12}O_{40})$ . The bands of heteropoly acid near 800 and 880  $\text{cm}^{-1}$  disappeared, which implied that the Mo-O-Mo bond was destroyed. Only the peak near 960  $\text{cm}^{-1}$  can show the existence of the heteropoly acid. The peak at 700  $\text{cm}^{-1}$  is assigned to the  $\nu(\text{Mo}-\text{O}-\text{Si})$ . After the extraction of the template with HCl/EtOH, the IR spectrum corresponds well to the product before the extraction, showing the structure remains intact.

#### 3.2 X-ray diffraction

The XRD pattern of the  $(C_{19}H_{42}N)_3(PMo_{12}O_{40})$  is shown in Fig.2, and the (hkl) indexes are also indicated with the corresponding diffraction peaks. There are several sharp peaks at low angles (less than 10°), while the XRD pattern only shows broad lumps at angles greater than 10°. These features are again reminiscent of MCM-41, which shows sharp low-angle lines and diffuse high-angle lines, indicative of long-range ordering of channels but a locally glassy aluminosilicate framework [3]. However, the peaks are different from those for MCM-41 but similar to those for the layer compounds at low angles [3,6,9], which indicates that the salt has the layer structure. The interlamellar distance can be calculated from the 001 index as  $d_{001}=3.00 \text{ nm}$ .

The XRD patterns of S<sub>1</sub>, S<sub>2</sub> are shown in Fig.3. The peak near 2.9° changes to 3.4° for the TEOS-treated sample, which means the interlamellar distance decreases when treated with TEOS. And the strength of the peaks at low angles becomes less sharp than the salt. It is contrast to the increase surface area of the material. We can deduce that the addition of Si leads to the bending of the layers, and at last results in the transformation of the lamellar salt into a porous structured compound through the

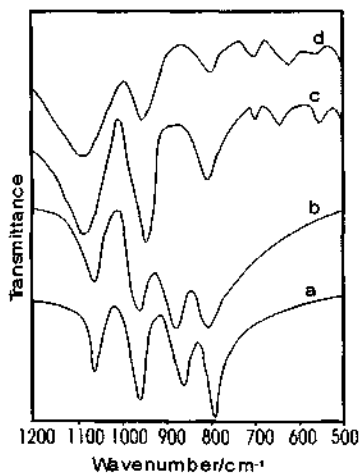
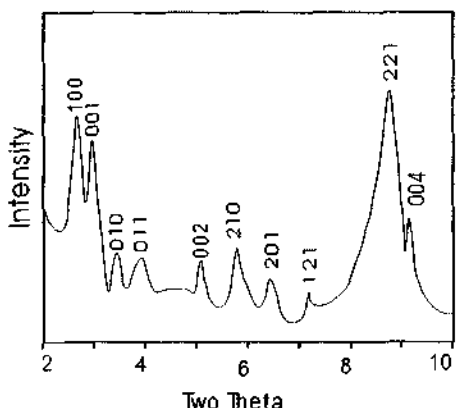
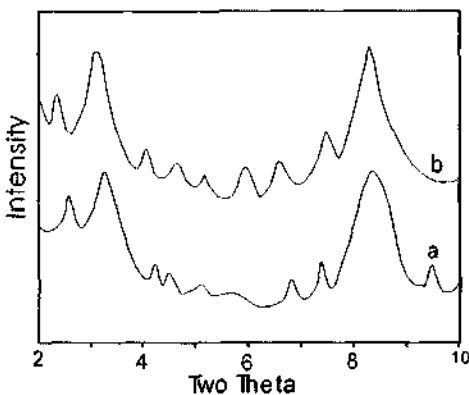


Figure 1. IR spectra of (a) PMA, (b)  $(C_{19}H_{42}N)_3(PMo_{12}O_{40})$ , (c) S<sub>1</sub>, (d) S<sub>2</sub>.

interaction between the surfactant / heteropoly-acid and the silicate.



**Figure 2.** XRD pattern of  $(C_{19}H_{42}N)_3(PMo_{12}O_{40})$ .



**Figure 3.** XRD patterns of (a) S<sub>1</sub>, (b) S<sub>2</sub>.

### 3.3 Transmission electron microscopy

Fig.4 is the TEM image of S<sub>2</sub>. The porous structure can be seen on the surface of the compound and the pore diameter is 30~40 nm. The XRD and TEM measurements reveal that the TEOS-treated sample after solvent extraction is a mesoporous material.

### 3.4 BET surface area

With the surfactant molecules in the structure, S<sub>1</sub> was nonporous ( $0.05\text{ m}^2/\text{g}$ ). After partial removal of the template, the surface area increases to  $140\text{ m}^2/\text{g}$ . The bands around  $3000$  and  $1500\text{ cm}^{-1}$  assigned to the stretching and bending vibrations of C-H of the surfactants are observed in the IR spectrum, indicating that some surfactant was still present and the extraction was uncompleted. Even in the elementary analysis the component of the element N decreased from 1.02% to 0.77%. If HCl/EtOH extraction is complete, the BET surface area may be more than  $140\text{ m}^2/\text{g}$ . A particle size determination by TEM shows an average diameter of 2 um, indicating that the high surface area cannot be attributed to the size of small, dense spherical particles.



**Figure 4.** TEM micrograph of S<sub>2</sub>.

### 3.5 The formation of the porous PMA

The hydrolysis product of the tetraethyl orthosilicate is the SiO<sub>2</sub> xerogel. In our experiment, when phosphomolybdic acid was hydrothermally reacted with TEOS at

368K, the quantity of the water (mostly molecular water and crystal water) is very small, the molar ratio of the water and the TEOS is less than 0.05:1, in which the PMA is the acid catalyst. The whole system is heterogeneous, while the hydrolysis is homogenous. In the system there is no deposit produced. The hydrogen bonds on the surface of  $\text{SiO}_2$  xerogel are few, hence the product  $\text{SiO}_2$  has no intense linkage with the PMA. When the product was washed in ethanol solution, PMA was observed to be dissolved in the solvent and a virescent solution was obtained. The insoluble white product in the solution was certified to be amorphous  $\text{SiO}_2$ , which indicates that the adsorption of heteropoly acid on  $\text{SiO}_2$  is reversible and the PMA can get desorbed from the surface of  $\text{SiO}_2$  in this case (Fig. 5a).

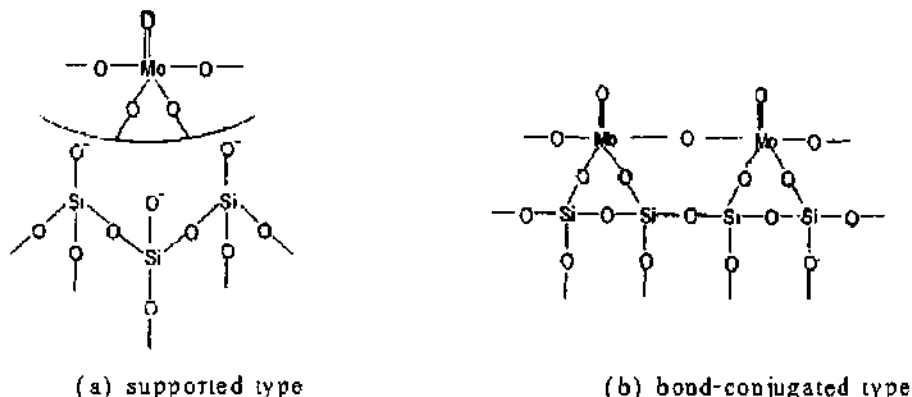


Figure 5. Surface structure models of PMA- $\text{SiO}_2$ .

On the other hand, the “salt-gel” process was used to connect prestructured cluster arrays. In the reaction water is little and TEOS is hydrolyzed, finally the products of large BET surface area are obtained. It indicates that firstly PMA reacted with cationic surfactants get a salt with stratification structure, the hydrolysate  $\text{SiO}_2$  of TEOS can be absorbed into the interlaminar salt by the organophilic part ( $\text{C}_{19}\text{H}_{42}\text{N}^+$ ) of the surfactants, then linkage with bridge oxygen to form Mo-O-Si bond and results inner pore structures in the phosphomolybdic acid.  $\text{S}_2$  was washed by ethanol solution for several times and for days without any obvious change. No HPA was observed to be dissolved in the solvent. It suggests that PMA is adsorbed on  $\text{SiO}_2$  mainly by bond-conjugated type (Fig. 5b) and Mo-O-Si bond is formed between the PMA and  $\text{SiO}_2$ .

We also used the surfactant salts of phosphomolybdic acid (PMA) to react with tetrabutyl titanate instead of TEOS in order to obtain a containing-titania mesoporous phosphomolybdic acid. However, after the solvent extraction, the titania-modified samples exhibited a BET surface area of only  $7\sim13 \text{ m}^2/\text{g}$ , which indicated that there are no inner pores in it. We think that it may be due to the difficulty in the formation of the Mo-O-Ti bonds.

#### 4 Conclusion

Several conclusions may be drawn from these data. (1) Weakly ordered mesoporous structures with high surface areas were obtained after the surfactant template was removed from TEOS-treated phosphomolybdate salts by solvent extraction. (2) IR and XRD data confirm that the silicate was indeed incorporated in the salt structures and changed these structures. Finally the Mo-O-Si bond was formed. (3) In contrast to the formation of the Mo-O-Si, the Mo-O-Ti bond is difficult to form in the same reaction conditions. So we only obtained a silica-containing mesoporous PMA. A significant breakthrough may be the appearance of good catalytic activity with the synthesis of the porous phosphomolybdic acid. The applications of the material in catalytic reaction are also being studied in our future work.

#### 5 Acknowledgement

The project was supported by the National Natural Science Foundation of China (No. 29903004).

#### References

1. Behrens P., Ordered molecular arrays as templates, a new approach to synthesis of mesoporous materials, *Adv. Mater.* **5** (1993) pp. 127-132.
2. Stein A., Fendorf M., Jarvie T. P. et al., Salt-gel synthesis of porous transition metal oxides, *Chem. Mater.* **7** (1995) pp. 304-313.
3. Kresge C., Leonowicz M., Roth W. et al., Ordered mesoporous molecular sieves synthesized by a liquid-crystal template mechanism, *Nature* **359** (1992) pp. 710-712.
4. Corma A., From microporous to mesoporous molecular sieve materials and their use in catalysis, *Chem. Rev.* **97** (1997) pp. 2373-2419.
5. Sayari A., Catalysis by crystalline mesoporous molecular sieves, *Chem. Mater.* **8** (1996) pp. 1840-1852.
6. Akira T., Takayuki A. and Masakazu I., Non-silica-based mesostructured material. 2 Synthesis of hexagonal superstructure consisting of 11-tungstophosphate anions and dodecyltrimethylammonium cations, *Microporous and Mesoporous Materials* **21** (1998) pp. 387-393.
7. Yang P., Zhao D., Margolese D. I. et al., Generalized syntheses of large-pore mesoporous metal oxides with semicrystalline frameworks, *Nature* **396** (1998) pp. 152-155.
8. Janauer G. G., Dobley A., Guo J. et al., Novel tungsten, molybdenum, and vanadium oxides containing surfactant ions, *Chem. Mater.* **8** (1996) pp. 2096-2101.
9. Ravikovich P. I., Wei D., Chueh W. T. et al., Evaluation of pore structure parameters of MCM-41 catalyst supports and catalysts by means of nitrogen and argon adsorption, *J. Phys. Chem.* **B101** (1997) pp. 3671-3679.

## PREPARATION AND CHARACTERIZATION OF HYDROXYL-Zr BENTONITE

JIANG YUEXIU, LUO CHENGGANG, LI ZHONGMIN AND TONG ZHANGFA\*

*School of Chemistry and Chemical Engineering, Guangxi University, Nanning, 530004, China  
E-mail: hgx@gxy.edu.cn*

Hydroxyl-Zr bentonite catalyst for esterification was prepared. Effects of the preparation conditions (calcination temperature, calcination time and ageing time) on interlayer distance, specific surface area and surface total acidity of catalyst have been studied. XRD, BET method and potentiometric titration were respectively used to determine interlayer distance, specific surface area and surface total acidity of catalyst. Scanning Electron Microscopy was performed to observe the images of samples.

### 1 Introduction

Pillared clays, which are an interesting class of microporous materials with high surface area, have been studied extensively for application as catalysts [3,5] and sorbents for gas separations. Pillared clays are obtained by exchanging the charge-compensating cations between the clay layers with larger inorganic hydroxyl cations, which are oligomeric hydroxyl metal cations formed by hydrolysis of its metal salts. After calcination, these metal hydroxyl cations undergo dehydration and dehydroxylation and then transform into robust oxide particles as pillars, which expand the layers of the clay.

Bentonite, whose main ingredient is montmorillonite, is one kind of layer structure clay mineral. It is an ideal material for preparation of pillared clays. If metal cations with high catalytic activity were intercalated in the interlayers of montmorillonite, a new type of solid acid catalyst can be obtained. The catalytic activity of the catalyst is closely associated with its porosity, specific surface area and surface total acidity. One of the effective ways to enhance catalytic activity is to prepare catalyst with appropriate metal cations and structure.

In this paper, we report the preparation and characterization of a new catalyst for esterification, hydroxyl-Zr bentonite, which was prepared by using Ningmin bentonite as starting material. XRD, BET and potentiometric titration [2] were respectively used to determine the interlayer distance, specific surface area and surface total acidity of the catalyst. Scanning Electron Microscope (SEM) was taken to observe the images of the samples. In order to prepare bentonite catalyst with good structure, the effects of calcination temperature, calcination time and ageing time on interlayer distance, specific surface area and surface total acidity of the catalyst have also been investigated.

### 2 Experimental Method

#### 2.1 Material

Bentonite was obtained from Ningmin County, Guangxi Zhuang Autonomous Region, which holds one of the largest bentonite deposits in China. Its chemical composition [1] is given in Table 1.

**Table I.** The chemical composition of Ningming bentonite.

Composition	SiO <sub>2</sub>	Al <sub>2</sub> O <sub>3</sub>	Ti O <sub>2</sub>	Fe <sub>2</sub> O <sub>3</sub>	Ca O	Mg O	K <sub>2</sub> O	Na <sub>2</sub> O
Content / %	64.53	17.86	0.38	3.23	1.69	3.05	1.17	1.27

## 2.2 Pretreatment of material

### 2.2.1 Purification and Na-exchange

The coarse particle in the bentonite was removed to make the clay free from other non-clay matter by use of the sedimentation technique. Then NaCl was added to the clay suspension in water to carry out the intercalation reaction at 90 °C for 2h under vigorous stirring.

### 2.2.2 Acid activation

A clay slurry was prepared by adding the Na-exchanged clay to the 15% H<sub>2</sub>SO<sub>4</sub> solution and was refluxed for 3 h. Then the solid in the slurry was separated, washed with the distilled water till the PH of the filtrate reaches 3 to 4. Finally the filtrated cake was dried at 110°C for 10h. The resulting product is atlapulgite (acid-activated clay).

### 2.2.3 Sample preparation

A 0.5 mmol/L oligomeric hydroxyl-Zr solution was prepared by adding a certain quantity of ZrOCl<sub>2</sub>·8H<sub>2</sub>O to the distilled water, then it was aged for 24 h at room temperature under constant agitation until there was no precipitation. A 3% (by weight) atlapulgite slurry was prepared by adding acid-activated clay to the distilled water. Then the slurry was slowly added to the oligomeric solution under stirring at a Zr/clay ratio of 4 mmol Zr per gram of clay. The mixture was kept under stirring for 4 h before it was aged and then it was filtered. After the filtered cake was washed, it was dried in an oven overnight at 110°C. Finally the dried filtered cake was ground into power and then calcined in a furnace.

### 2.2.4 Sample characterization

The X-ray diffraction data were obtained by using 3015 Rigaku/ MAX 2500 V DCX diffractometer, with a copper tube as radiation source ( $\lambda = 1.54178 \text{ \AA}$ ) and operating at 40 kV and 120 mA, Its profiles were recorded at 2° (2θ) per minute. The BET equation was used to calculate the specific surface areas from the nitrogen adsorption isotherms at liquid N<sub>2</sub> temperature, the total acidity of samples was determined by using a ZD-3 automatic potentiometric titrator. SEM images of samples were taken at a magnification of 10000 times with Hitachi S-750 at a voltage of 25 kV.

### 3 Results and Discussion

#### 3.1 The SEM images of hydroxyl-Zr bentonite

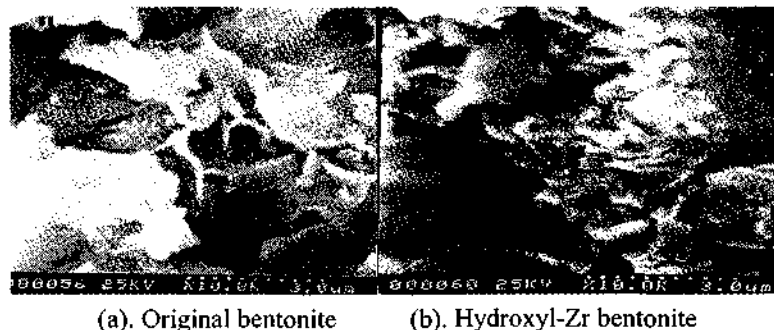


Figure 1. SEM picture of the original bentonite and hydroxyl-Zr bentonite.

Figure 1 presents the two SEM pictures of the original bentonite and hydroxyl-Zr bentonite calcined at 573K for 2h. It was observed that the SEM image of the hydroxyl-Zr bentonite, which is of puff lamellar structure, is similar to that of the original bentonite. Therefore, the introduction of hydroxyl Zr did not affect the image of bentonite.

#### 3.2 The effects of preparation conditions on the interlayer distance

The changes in "d" values of the hydroxyl-Zr bentonite aged for 2 h and calcined at different temperatures for 2 h are listed in Table 2. For comparison purposes, the datum of the interlayer distance of atlapulgite is also listed in the Table 2. From the table it can be seen that atlapulgite shows the lowest interlayer distance among all materials, which conformed that hydroxyl-Zr had already introduced among the layers of montmorillonite, and thus expanded the basal spacing of bentonite. On the other hand, the interlayer distance can also give us information on the resistance of the pillared bentonite to thermal treatment. No significant decrease of the "d" values was observed after calcinations. When calcination temperature increase from 473 K to 773 K, the interlayer distances of hydroxyl-Zr bentonite had decreased only by 0.5Å. Suggesting that the hydroxyl-Zr pillars can effectively reduce the number of protons which migrate to the octahedral layers of montmorillonite during the pillar dehydroxylation, therefore the interaction between pillars and the montmorillonite layers was strengthened [4].

Table 2. Effects of the different calcination temperatures ( $T$ ) on interlayer distances ( $d$ )

$T/K$	hydroxyl-Zr bentonite				atlapulgite
	200	300	400	500	
$d/\text{\AA}$	16.55	16.28	16.19	16.05	13.80

With the variation in calcination time, the interlayer distances of hydroxyl-Zr bentonite remain nearly constant (see Table 3).

**Table 3.** Effects of the different calcination times (*t*) on interlayer distances (*d*)

<i>t/h</i>	1	2	3	4
<i>d / Å</i>	16.55	16.55	16.39	16.32

Calcination temperature : 473K, ageing time : 2h

However, the interlayer distance of hydroxyl-Zr bentonite varies inversely with the ageing time. When the ageing time is over 2h, the basal spacing decreases gradually, as it can be seen from Table 4.

**Table 4.** Effects of the different ageing times (*t*) on interlayer distances (*d*)

<i>t/h</i>	2	4	6	10
<i>d / Å</i>	16.55	16.55	15.84	15.78

Calcination temperature: 473K, calcination time: 2h

### 3.3 The effects of preparation conditions on the surface total acidity

From Table 5 and Table 6 it can be seen that all the samples of different calcination time and aging time possess nearly the same acidity at a particular calcination temperature, revealing the negligible effect of the calcination time and aging time on the surface total acidity. However, Table 7 shows that the total number of acid sites and the number of the Brönsted acid sites on the catalysts decrease with an increase in calcination temperature. It is known that the surface acid sites of hydroxyl-Zr bentonite mainly stem from surface hydroxyl and exposed metal cation [6], and the Brönsted acid sites result from protons on the surface of the octahedral layers. When the calcination temperature increases, the migration of protons to the octahedral layers of montmorillonite will become easier, leading to the decrease of the number of Brönsted acid sites.

**Table 5.** Effects of the different calcination time (*t*) on the total acidity (*n*).

<i>t/h</i>	1	2	3	4
<i>n/mmol.g<sup>-1</sup></i>	1.08	1.08	1.07	1.04

Calcination temperature: 473 K, ageing time: 2h.

**Table 6.** Effects of the different aging time (*t*) on the total acidity (*n*).

<i>t/h</i>	2	4	6	10
<i>n/mmol.g<sup>-1</sup></i>	1.08	1.08	1.06	1.06

Calcination temperature: 473 K, calcination time: 2h.

**Table 7.** Effects of calcination temperature (*T*) on the total acidity (*n*) and the number of B acid sites (*n<sub>B</sub>*).

<i>T/K</i>	200	300	400	500
<i>n /mmol.g<sup>-1</sup></i>	1.08	0.91	0.88	0.76
<i>n<sub>B</sub> /mmol.g<sup>-1</sup></i>	0.41	0.22	0.18	0.10

*n<sub>B</sub>*: the number of B acid sites, calcination time: 2 h, aging time : 2 h.

### 3.4 The effects of preparation conditions on the specific surface area

The specific surface area for each sample calcined at a particular temperature for 2h is given in Table 8. From it we can see that the specific surface area decreased with the increase of calcination temperature. This may be explained by the agglomeration of the fine particles. Fine particles have tendency to agglomerate due to their high surface energy. This tendency become stronger when calcination temperature increases, so the specific surface area of catalyst decreased.

**Table 8.** Effects of the different calcination temperature ( $T$ ) on specific surface area ( $S$ ).

$T/K$	200	300	400	500
$S/m^2g^{-1}$	164.5	156.0	138.4	121.2

Calcination time: 2h, ageing time : 2h.

Specific surface area of the samples at different ageing time is presented in Table 9. The results show the increase in specific surface area with the increase in the ageing time. The increase of the specific surface area may be attributed to the further division of bentonite into thinner slices after long time interaction with water molecules.

Calcinations time has no effect on specific surface area of the samples, as can be seen from Table 10.

**Table 9.** Effects of the different ageing time ( $t$ ) on the specific surface area ( $S$ ).

$t/h$	2	4	6	10
$S/m^2g^{-1}$	164.5	167.5	171.8	177.0

Calcination temperature: 473 K, calcination time: 2h.

**Table 10.** Effects of the different calcination time ( $t$ ) on the specific surface area ( $S$ ).

$t/h$	1	2	3	4
$S/m^2g^{-1}$	164.8	164.5	164.7	164.6

Calcination temperature: 473K, aging time : 2h

## 4 Conclusion

Hydroxyl-Zr bentonite catalyst was prepared and characterized in our laboratory. The results show that the hydroxyl-Zr bentonite possesses good thermal stability. The interlayer distance of the modified bentonite decreased with the increase of aging time; and its the specific surface area varies inversely with the calcination temperature but increases with the increase of aging time. The surface total acidity and the number of Brönsted acid sites of hydroxyl-Zr bentonite are reduced with the increase of calcination temperature.

## 5 Acknowledgement

This work was supported by the National Natural Science Foundation of China (No.

29806004) and the Natural Science Foundation of Guangxi (No. 9912029).

## References

1. Li Xuanhai, Huang Zuqing, Pan Liuping et al., Researches on the technology of purification of Ningming bentonite by means of wet-way, *Industrial Minerals and Processing*, **29** (2000) pp. 5-8
2. Liu Xiayao, *Characterization of industrial catalysts*. (Hydrocarbon processing Press, 1990), pp. 87.
3. Suhas P. Katdare, Veda Ramaswamy and A. V. Ramaswamy, *Catalysis Today*, **49** (1999) pp. 313-320
4. Sun Laisheng, Li Dongfan, Zhang Yingzhen et al., *Chinese Journal of Catalysis*, **18** (1997) pp. 135-139.
5. Trilochan Mishra, Kulamani Parida, *Applied Catalysis A: General* **174** (1998) pp. 91-98.
6. Wu Yue, *Chemistry Advance*, **10** (1998) pp.159-169.

## DISSIPATIVE FORCED INTRUSION OF LIQUID IN LYOPHOBIC POROUS MATERIALS : A NEW FIELD OF APPLICATIONS FOR MTS TYPE MATERIALS

B. LEFEVRE AND P. F. GOBIN

*Laboratoire G.E.M.P.P.M., UMR 5510, INSA de LYON, Bât. Blaise Pascal, 20, av. Albert Einstein,  
69621 VILLEURBANNE, France  
E-mail: benoit.lefeuvre@insa-lyon.fr*

T. MARTIN AND F. FAJULA

*Laboratoire de Matériaux Catalytiques et Catalyse en Chimie Organique, UMR 5618, 8, rue de l'Ecole Normale, 34296 MONTPELLIER Cedex 05, France  
E-mail: tmartin@cit.enscm.fr*

Recently microporous and mesoporous materials were found to be particularly suitable for a new type of applications in the mechanical field. This paper reports experimental features about the dissipative forced intrusion of water in highly hydrophobic mesoporous materials: this phenomenon can be used to develop a new type of dampers and/or actuators. Silica-based materials behavior was investigated. Among them, MCM-41 exhibits original and interesting properties towards the potential developments of dampers and appears to be of great interest for the comprehension of energy dissipation mechanisms.

### 1 Introduction

In the last decade, a variety of microporous and mesoporous materials have been developed for applications in catalysis, chromatography and adsorption. Great attention has been paid to the control of (i) pore surface chemistry and (ii) textural properties such as pore size distribution, pore size and shape. Recently, a new field of applications for these materials has been highlighted [1-3]: by forcing a non-wetting liquid to invade a porous solid by means of an external pressure, mechanical energy can be converted to interfacial energy. The capillary pressure,  $P_{CAP}$ , required for pore intrusion can be written from the Laplace-Washburn relation,

$$P_{CAP} = -\frac{2\gamma \cos\theta_a}{r}$$

$\gamma$  being the liquid surface tension,  $r$  the pore radius and  $\theta_a$  the advancing contact angle between the liquid and the solid surface. This stored energy can then be completely or partially restored once the system recovers the initial extruded state. Depending on the texture and surface properties of the matrix, the considered system could be applied for either energy storage (springs, actuators) or dissipation (damping). Actually, the possibility to dissipate mechanical energy depends on the presence of pressure hysteresis in the intrusion-extrusion process.

The physical principle is in fact close to porosimetry experiments based on mercury injection. However, because of evident environmental disadvantages of mercury manipulation, it appeared convenient to find other (solid-liquid) systems. This difficulty was overcome by using hydrophobic solids and water [4].

The first results were obtained using modified mesoporous silica gels [4-8]. For such systems, water intrusion typically occurs between 10 MPa and 60 MPa, whereas extrusion occurs at relatively low pressures, from 8 MPa down to atmospheric pressure, providing a

high dissipative power. In 2001, Eroshenko and co-workers [2] obtained interesting results using two hydrophobic zeolites, for which no hysteresis was observed: intrusion and extrusion take place at higher pressures (80 and 100 MPa).

The present report focuses on the intrusion-extrusion characteristics of grafted silica-based materials: conventional chromatography adsorbents and Micelle-Templated-Silica materials (MCM-41) [3]. Finally, the mechanisms of energy dissipation will be analyzed in terms of general thermodynamic considerations.

## 2 Materials and Methods

For reverse-phase chromatography purposes, silica sorbents are commonly modified by hydrophobic ligands by means of silanes. These systems are therefore particularly suitable for water intrusion experiments [7]. We studied the influence of the chain nature (perfluorinated, alkyl), the chain length and the type of bonding chemistry (mono or trifunctional, chloro- or alkoxy-silanes) on the hydrophobic properties of silica gels.

In the present paper, we will focus in a first step, on the results obtained using the same parent support (silica gel) modified by alkyl-dimethyl chlorosilanes of various alkyl chain length: 1, 4, 8 and 18 carbon atoms. This material presents a disordered mesoporous texture [8].

Then, two MCM-41 materials modified by octyl-dimethyl chlorosilanes were tested. The parent MCM-41 matrices were synthesized by conventional route using hexadecyl-trimethylammonium bromide (sample MTS2) and octadecyl-trimethylammonium bromide (sample MTS1). They exhibit typical peaks of hexagonal ordered mesoporous materials in X-ray diffraction patterns.

Nitrogen sorption isotherms of the three parent silica supports are presented in Figure 1, and computed textural properties are reported in Table 1. Pore radii were determined by means of Barrett-Joyner-Halenda (BJH) and Broekhoff-De-Boer (BdB) calculations. Chain loadings  $n_g$  are reported in Table 2.

Table I. Textural properties of parent silica supports.

Material	Pore volume/ml.g <sup>-1</sup>	Pore radius/nm
Silica gel	0.78	2.4 <sup>BJH</sup>
MTS1	0.74	2.0 <sup>BdB</sup>
MTS2	0.70	1.8 <sup>BdB</sup>

Water intrusion runs were carried out according to a procedure described elsewhere [8]. Full intrusion-extrusion runs were completed within 3 minutes. Several successive cycles were recorded for each system with a 10-minute pause at atmospheric pressure between 2 cycles.

## 3 Results

The intrusion-extrusion reports reveal three distinct behaviors:

- (1) Only one intrusion occurs, meaning that water did not expel from the porosity even after a storage of several weeks at atmospheric pressure: sample S1.
- (2) Numerous cycles can be registered, but changes between the first and the followings (referred to as stable) are observed: samples S4, S18, g-MTS1 and g-MTS2.

(3) Cycles are completely reproducible: sample S8.

The intrusion-extrusion data are presented as pressure vs  $\Delta V$  plots, where  $\Delta V$  is the volume variation of the system due to water penetration in the porosity. Derivative representations  $d(\Delta V)/dP$  of the intrusion curves allow to determine precisely the range of injection pressures.  $\Delta V$  values are expressed in  $\text{mm}^3$  per gram of bare silica.

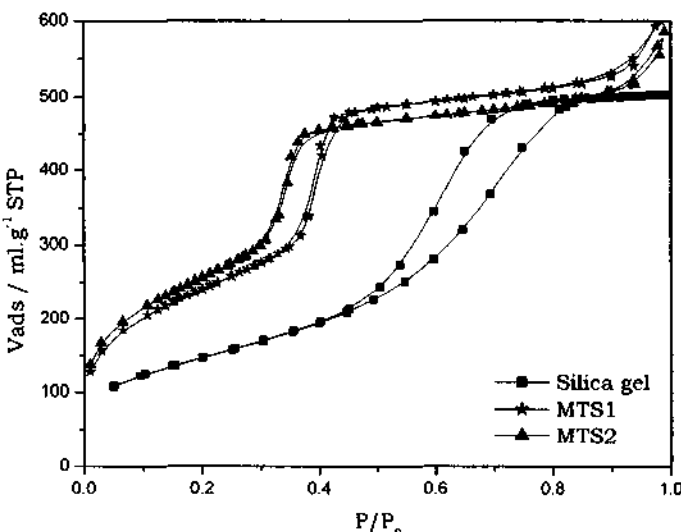


Figure 1. Nitrogen isotherms at 77 K of parent silica supports.

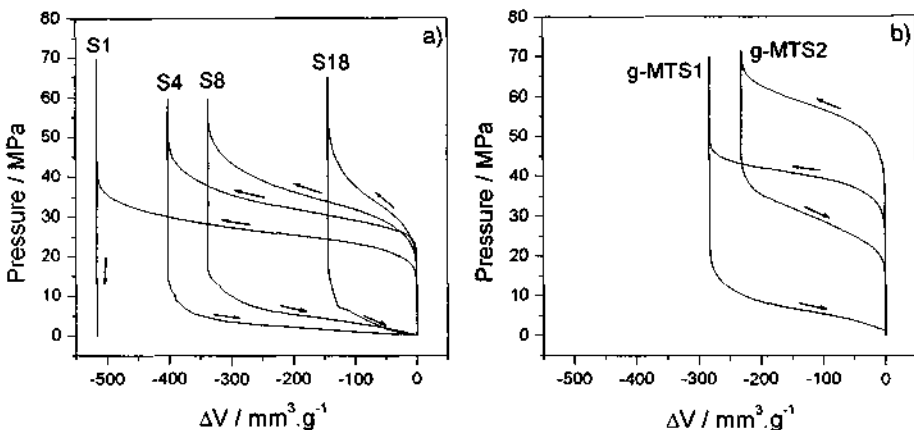
### 3.1 Grafted silica gel :

Figure 2a) represents stable cycles for samples S4, S8 and S18 and the first intrusion for sample S1. Derivative representation of successive intrusions are reported in Figure 3a). These results are in agreement with anterior studies. The mean conclusions are:

- The disordered structure (cf. pore size distribution) of the sample accounts for the injection pressure dispersion.
- The best hydrophobicity is obtained when the screening of the residual silanols is optimal. For the present series, it appears that sample S8 develops the strongest repellent power as no evolution was observed for successive cycles. As a consequence, this type of modification was used to modified MTS samples.
- Total intruded volumes decreases dramatically as the chain length is increased. This diminution is due to the presence of the grafted phase. The consequence is a loss of disposable volume. The choice of the surface modifier is therefore a compromise: on one hand, the layer should provide high hydrophobicity, which is obtained by a high carbon loading, but on the other hand, long chains reduce the available volume, and, as a consequence, the dissipative efficiency of the system ( $E \approx \Delta P \times \Delta V$ ).
- Finally, extrusion occurs at low pressure (<8 MPa). As far as damping devices are concerned, this low pressure characteristic implies the pressure to be decreased down to atmospheric pressure to allow cyclic use, which is a constraining aspect for operational devices design.

### 3.2 Grafted MTS materials

Stable cycles obtained on grafted MCM-41 materials are gathered in Figure 2b). For sample g-MTS1, phenomena occur in the range of pressure of grafted silica gel, whereas sample g-MTS2 exhibits a distinct behavior: intrusion and extrusion take place at above 15 MPa.



**Figure 2.** Water intrusion and extrusion cycles : (a) first intrusion for S1 and stable cycles for S4, S8 and S18, (b) stable cycles for g-MTS1 and g-MTS2.

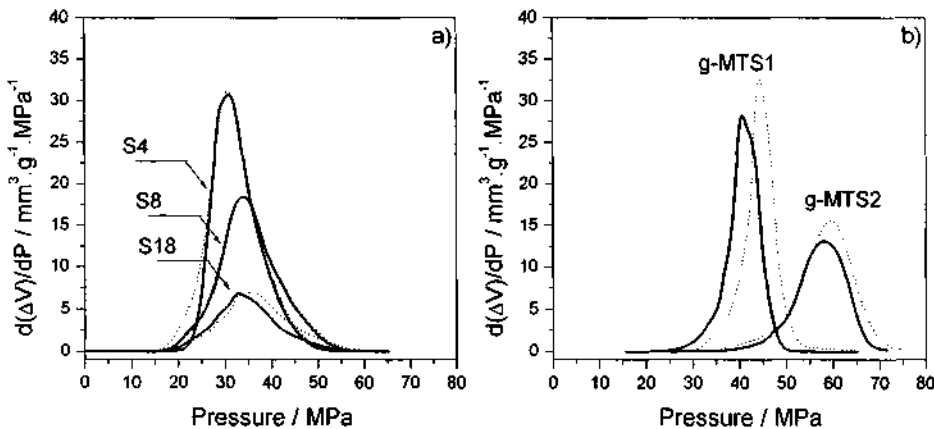


**Figure 3.** Derivative representations of intrusion plots: from stable cycles (plain line), from the first cycle (dotted line).

Figure 3 reveals a diminution of both (1) injection pressure and (2) total intruded volume from the first to further intrusions. As nitrogen sorption analysis of the materials after water intrusion experiments did not reveal any damage of textural properties, partial alteration of surface hydrophobicity may consist the origin of such evolutions. We believe

that water molecules can interact with residual silanols and kept trapped at the pore surface at the end of intrusion, even if no chemical deterioration of the bonded phase occurred. As a consequence, advancing contact angle  $\theta_a$  and accessible volume may be reduced for further intrusion runs. The lowest grafting ratios obtained on MTS materials argue for this apparent hydrophobicity alteration.

As expected from the monodispersity of pore size for such model materials, both intrusion and extrusion pressure ranges are relatively small. Values of pressure dispersion  $\Delta P_{int}/P_{int}$  are reported in Table 2.

**Table 2.** Chain loading, pore radius, intrusion and extrusion pressures and calculated contact angles  $\theta_a$  and  $\theta_r$ .

Sample	$r_p/\text{nm}$	$n_g/\text{nm}^{-2}$	$P_{int}/\text{MPa}$	$\theta_{int}/^\circ$	$P_{ext}/\text{MPa}$	$\theta_r/^\circ$	$\Delta P_{int}/P_{int}$
S8	1.7 <sup>BdB</sup>	1.40	34.1	114	3.7	92	1
g-MTS1	1.6 <sup>BdB</sup>	1.24	41	116	6.3	94	0.4
g-MTS2	1.3 <sup>BdB</sup>	1.35	58	119	30.2	105	0.4

#### 4 Discussion

A classical description of the intrusion and extrusion pressures is achieved by considering the Laplace-Washburn relation. This relation allows the calculation of advancing and receding contact angles  $\theta_a$  and  $\theta_r$  from the values of pore radius assuming that the surface tension of the liquid is constant and unaffected by confinement (see Table 2). For the three octyl-modified samples,  $\theta_a$  is roughly constant, meaning that during stable cycles the apparent hydrophobicity of the different grafted layers is similar in spite of small variations of chain loading. By contrast,  $\theta_r$  differs from 92° and 94° for sample S8 and sample g-MTS1 respectively to 105° for g-MTS2.

Contact angle hysteresis is usually attributed to surface properties such as roughness or chemical heterogeneity [9]. In the case of grafted MCM-41 materials, as the values of  $\theta_a$  are closed, these two samples are supposed to have comparable surface properties. Therefore, the difference of calculated contact angles  $\theta_r$  for g-MTS1 and g-MTS2 is surprising. However, other aspects may be considered in order to understand the origin of the pressure hysteresis. For disordered structures such as silica gel, the presence of ink-bottle pores may consist a source of volume hysteresis. This contribution is typically considered to explain the hysteresis loops in mercury porosimetry and gas adsorption experiments [10]. But, if we consider that the mechanisms leading to hysteresis in capillary condensation and forced intrusion are similar, the pore size can also have a strong influence on the amplitude of the phenomena. Indeed, studies on the adsorption of gases on ordered mesoporous adsorbents revealed that the adsorption isotherms become reversible as the pore size is decreased to a threshold value [11,12]. In the case of forced intrusion, hysteresis loop is decreased from g-MTS1 to g-MTS2 and, as an extreme case, it vanishes in the case of micropores [2] as previously mentioned. The concept of phase metastability in confined geometry developed for the treatment of capillary condensation seems to apply to forced intrusion experiments. Furthermore, the reduction of pressure hysteresis in water intrusion experiments as the temperature is increased confirms the similitude of both phenomena.

As far as mechanical applications are concerned, the use of grafted MCM-41 materials represents a real improvement: first, high pressure extrusions allow cyclic use without complete discharge of the operational device. Secondly, low intrusion pressure

dispersion and easy tailoring of pore size (by changing the surfactant chain length during the synthesis of the parent material) allow to adjust the intrusion pressure according to the required value.

In conclusion, the study of the influence of grafted chain length on the hydrophobicity of silica gel allowed us to choose a convenient surface treatment, which was successfully transposed to MCM-41 materials. These former materials were demonstrated to be particularly suitable for the considered new field of applications, and to present advantages compared to silica gels. Finally, Micelle-Templated-Silica materials represent a class of useful models for a comprehensive study of the mechanisms of energy dissipation during forced intrusion and more generally of the physical chemistry of surfaces.

## References

1. Eroshenko V., *US Pat.*, 6 052 992 (2000).
2. Eroshenko V., Regis R.C., Soulard M. and Patarin J., *J. Am. Chem. Soc.*, **123** (2001) pp. 8129-8130.
3. Martin T., Lefevre B., Brunel D., Galarneau A., Di Renzo F., Fajula F., Gobin P.F., Quinson J.F. and Vigier G., *Chem. Comm.*, (2002) pp. 24-25.
4. Gusev V.Y., *Langmuir*, **10** (1994) pp. 235-240.
5. Fadeev A.Y. and Eroshenko V., *J. Colloid Interface Sci.*, **187** (1997), pp. 275-282.
6. Eroshenko V. and Fadeev A.Y., *Colloid Journal*, **57** (1995) pp. 446-449.
7. Gomez F., Denoyel R. and Rouquerol J., *Langmuir*, **16** (2000) pp. 4374-4379.
8. Lefevre B., Charlaix E., Gobin P.F., Perriat P. and Quinson J.F., *2<sup>nd</sup> International Conference on Silica Science and Technology Silica 2001*, (2001) Proceedings Cd-Rom, Mulhouse, France.
9. Israelachvili J., *Intermolecular and Surface Forces*, (1992) Academic Press, London, pp. 323.
10. Gregg S.J. and Sing K.S.W., *Adsorption Surface Area and Porosity*, (1967) Academic Press, London and New York, pp. 145.
11. Evans R., Marini Bettolo Marconi U. and Tarazona, *J. Chem. Phys.*, **84** (1986) pp. 2376.
12. Morishige K. and Shikimi M., *J. Chem. Phys.*, **108** (1998) pp. 7821.

## SYNTHESIS AND CHARACTERIZATION OF Ti-Zr MESOPOROUS OXIDES USING MIXED SURFACTANTS AS TEMPLATING AGENTS

WEIBIN LI,\* XUFEI YANG AND YU ZHANG

*Department of Environmental Science and Engineering, Tsinghua University, Beijing 100084,  
China*  
*E-mail:* [wbli@mail.tsinghua.edu.cn](mailto:wbli@mail.tsinghua.edu.cn)

A series of experiments have been conducted in an attempt to improve the thermal stability of the Ti-Zr mesoporous mixed oxide prepared from inorganic precursors. The results show that the crystallinity of the Ti-Zr mesoporous mixed oxide depends strongly on the Ti/Zr molar ratio in the gel mixtures, and a better crystalline mesoporous structure can be obtained on the sample with the 1:1 Ti/Zr molar ratio. It is also found that surfactant content, addition of sulfate species and auxiliary organic additive such as DDA, TritonX-100, triethanolamine and ethanol would play a key role in tailoring the mesopore structures and improving thermal stability of the obtained materials. In addition, the mixing order of organic surfactants, i.e., CTAB and DDA, also affects the the crystallinity of the product.

### 1 Introduction

Mesoporous materials are very attractive in the fields of catalysis and gas adsorption because of their unique pore structures [1]. However, there are few literature reports on transition metal mesoporous molecular sieves as compared with a great number of reports on MS41 type mesoporous materials containing silica or aluminum, which is partly due to their easily collapsed crystalline structures after removing organic templates. Several attempts have been made to stabilize the mesoporous structures including introduction of phosphoric acid during reaction by Ying et al [2], or conducting a post-synthetic treatment with phosphoric acid by Chen et al [3]. But it is difficult to remove phosphor species from the final samples, which are believed to be poisoning components for many catalytic reactions or gas adsorption, and hence limit the applications of thus obtained materials to some extent [4].

In this presentation, several synthesis parameters have been investigated in order to improve the thermal stability of the Ti-Zr containing phosphorus-free mesoporous oxides by using either single surfactant, i.e., cetyltrimethylammonium bromide (CTAB) or mixed surfactants, i.e., CTAB and dodecylamine (DDA) as the templating agent under hydrothermal conditions.

### 2 Experimental

The Ti-Zr mesoporous mixed oxides were synthesized from titanium sulfate and zirconium nitrate through templating by CTAB and other auxiliary organic components, i.e. dodecylamine (DDA), triethanolamine, TritonX-100, in aqueous solution at 100-110°C for 2 days; the Ti/Zr molar ratio in the starting gel mixture was varied from 20-80 mol% of the titanium; the  $\text{SO}_4^{2-}/\text{Ti-Zr}$  molar ratio was varied from 1.5 to 5.0 by adjusting with the addition of various amounts of  $(\text{NH}_4)_2\text{SO}_4$  into the gel mixture. After stirring for 2 hours, the Ti-Zr containing gel mixtures were transferred into Teflon autoclave, and subsequently heated at 100°C for 2 days. After filtration

and washing, the powders were dried at 100°C in air, a part of dried sample was chosen for small angle XRD test, the remaining part of the sample were further calcined at 350 or 450°C in nitrogen followed by in oxygen.

Small angle X-ray diffraction (XRD) patterns were obtained on a Rigaku D/max RB X-ray diffractometer using Cu K $\alpha$  radiation in the region of 1-8° at a speed of 2° min<sup>-1</sup> in 2 $\theta$ . TEM images were obtained on a JEM-200C transmission microscope with acceleration voltage 200kV and resolution 0.5nm. Thermogravimetric analysis (TGA) was performed with a TA instruments TGA 51 thermogravimetric analyzer in nitrogen with heating rate of 10°C/min.

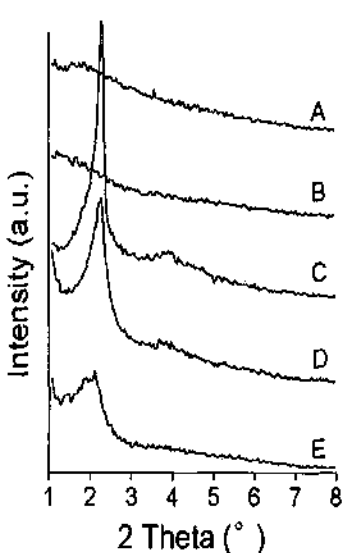


**Figure 1.** XRD patterns of the Ti-Zr Samples dried at 100°C with various Ti molar percentage: 20% (A), 35% (B), 50% (C), 65% (D), 80% (E).

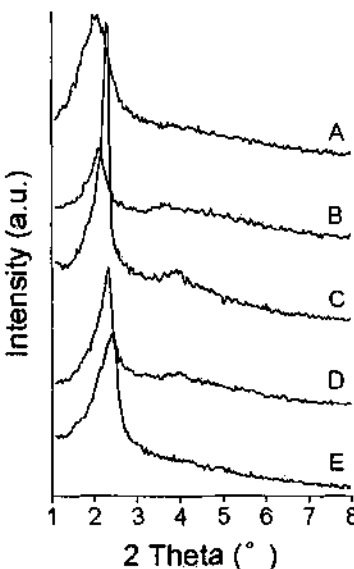


**Figure 2.** XRD patterns of the Ti-Zr Samples dried at 100 °C with various CTAB/(Ti+Zr) molar ratios: 0.75 (A), 0.64 (B), 0.54 (C), 0.43 (D), 0.32 (E).

### 3 Results and Discussion

#### 3.1 Effect of the Ti/Zr ratio

Figure 1 shows the XRD patterns of the Ti-Zr samples with various Ti/Zr molar ratios dried at 100°C in air, indicating that the crystallinity depends strongly on the Ti/Zr molar ratio in the gel mixtures. The results show that the intensity of the XRD peak first increased and then decreased with an increase in the Ti/Zr ratio. The most intense and sharp peak at 2.3° (2 $\theta$ ), with  $d_{100}=3.84$  nm was observed on the sample with the Ti/Zr molar ratio of 1/1. It is likely that the better ordered mesostructure could be obtained on the Ti-Zr mixed oxides as compared with that on the pure Ti or

Zr oxide. Recently, Chen et al also reported that doping with 10 mol % titania could significantly increase the thermal stability of  $\text{TiO}_2\text{-ZrO}_2$  mixed sample after post treatment with phosphoric acid solution [5]. Hereafter the 1:1 molar ratio was chosen to synthesize the Ti-Zr samples.

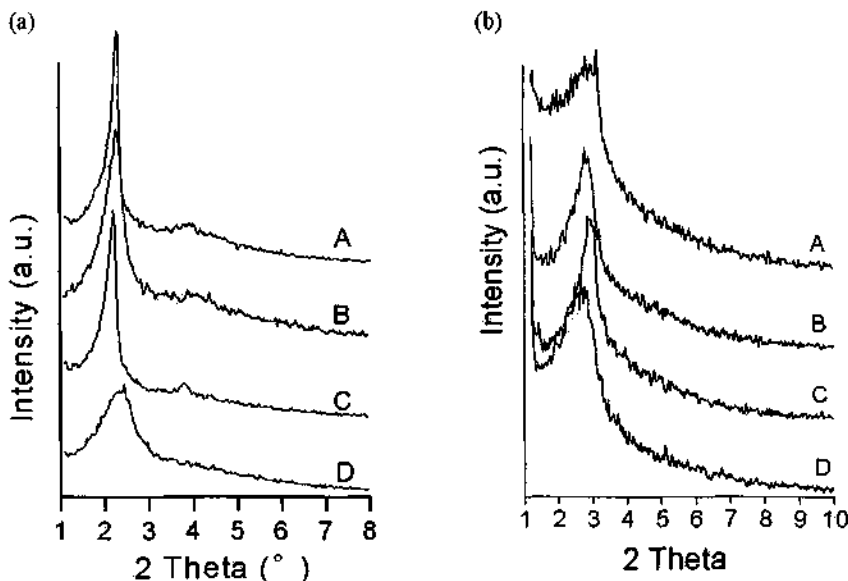


**Figure 3.** XRD patterns of the Ti-Zr Samples dried at 100°C(a) and calcined at 350°C(b) with various ethanol/water volume ratios: 0/30 (A), 5/25 (B), 10/30 (C), 15/15 (D).

### 3.2 Effect of template content

Figure 2 shows the XRD patterns of the Ti-Zr samples as a function of CTAB content. The results indicate an increase in CTAB content would result in shifting of  $2\theta$  value to low angel and d-spacing to high value according to the Bragg equation. The highest intensity of XRD peak was observed at the 0.54:1 CTAB/Ti-Zr ratio, which was chosen for the following experiments unless stated otherwise.

### 3.3 Effect of auxiliary organic components

It is well known that some auxiliary organic components such as mesitylene can expand the mesopores of titania [6] and silica [7]. Here, DDA, TritonX-100, triethanolamine and ethanol were chosen to control the mesophase structure of the Ti-Zr samples. Considering the fast condensation of Ti- or Zr- components, these organic components may help to slow down the condensation and improve the thermal stability.

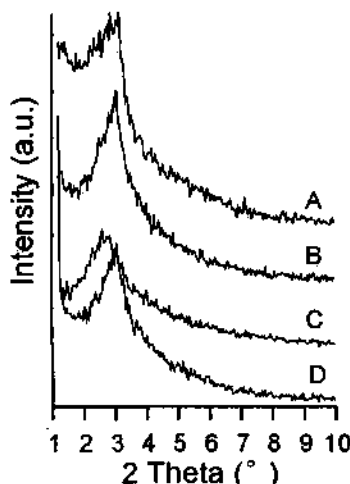


**Figure 4.** XRD patterns of the Ti-Zr samples prepared with and without (A) auxiliary organic components after calcination at 350°C: DDA (B), triethanolamine (C), TritonX-100 (D).

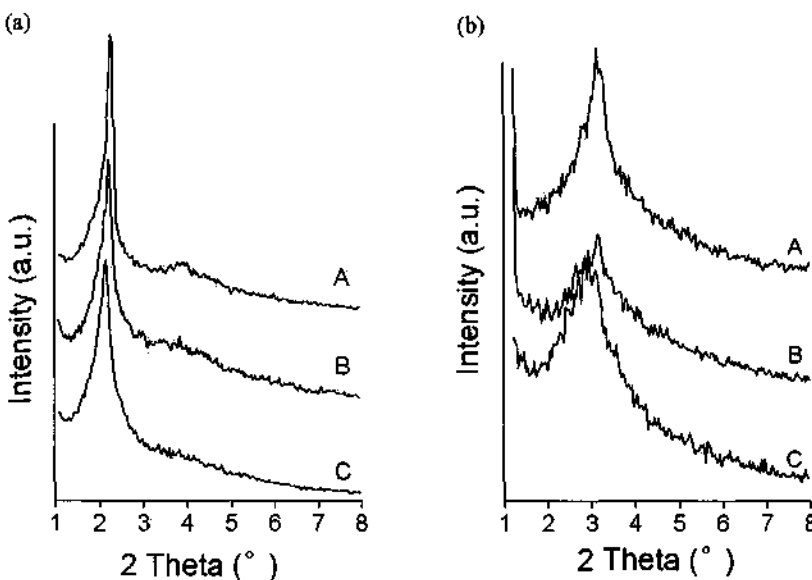


**Figure 5.** XRD patterns of Ti-Zr samples prepared with different mixing orders: (A) addition of CTAB followed by DDA, (B) addition of CTAB and DDA simultaneously, (A) addition of DDA followed by CTAB after dried at 100°C (a) or calcined at 350°C(b).

The effect of addition of ethanol was first investigated on the Ti-Zr samples with different volume ratio of H<sub>2</sub>O to ethanol for the dried or calcined form. As can be seen in Figure 3a, a large amount of ethanol would decrease the crystallinity for the samples dried at 100°C; While thermal stability could be increased compared with

that without addition of ethanol as shown in Figure 3b. Alcohol has been used as a co-surfactant or solvent to change the interaction between surfactant and metal oxide matrices [8]. Here, the effect of addition of other auxiliary organic components, i.e., DDA, Triton X-100 and triethanolamine on the thermal stability of the Ti-Zr samples was shown in Figure 4. As compared with the pure CTAB surfactant, addition of organic components can increase the thermal stability of the products, and the best crystallinity are obtained on the sample prepared with the addition of DDA.

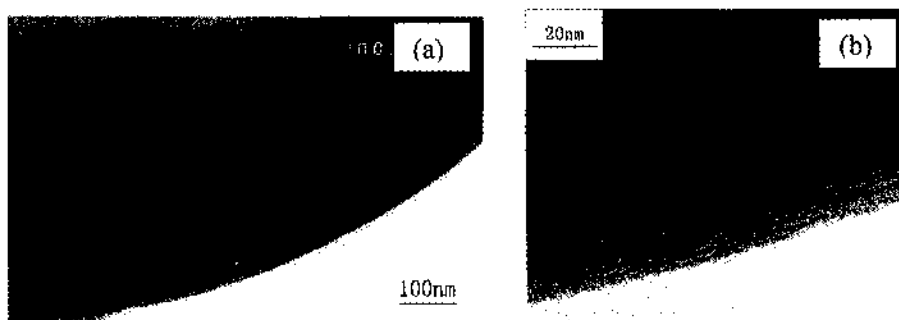


**Figure 6.** TEM images of the Ti-Zr sample (a) and its enlarged photo (b) prepared by mixing inorganic components CTAB followed by DDA after calcination at 350°C.

The effect of mixing order of DDA and CTAB on the thermal stability based on XRD patterns at 100°C and 350°C is shown in Figure 5. The results show that the peak intensities were higher for the sample prepared by mixing inorganic precursor successively with either CTAB or DDA than that prepared from the mixture of CTAB and DDA. As we know that both condensation in the inorganic components and the interaction at boundary between the surfactant and the inorganic components were essential to control the thermal stability of the final product. Obviously, the mixing order would affect the interaction between inorganic components and organic templating components, and hence affect the mesostructures of the obtained sample. Further tuning the interaction is believed to improve the thermal stability.

A typical TEM image of the sample prepared by adding CTAB followed by DDA after calcination at 350°C was shown in Figure 7A, indicating a well defined lamellar structure with big domains. The enlarged part of this image was also shown in Figure 7B, the lamellar structures are much clearly evidenced. As compared with that for DDA-free sample, it suggests that the presence of DDA can improve the lamellar mesophase during the synthesis conditions.

### 3.4 Effect of sulfate on the thermal stability

It is reported that ammonium sulfate can produce the negatively charged oligomers through sulfate bridges, which induced the electrostatic interaction with the surfactant and therefore facilitate the formation of zirconia/CTAB mesophase [9]. Since  $Ti(SO_4)_2$  was used as Ti precursor in the present study, a various amounts of  $(NH_4)_2SO_4$  was added into the CTAB solution in order to investigate the sulfate effect

on the thermal stability of the Ti-Zr samples, the result is shown in Figure 7. It is obvious that addition of sulfate could increase the thermal stability at 350°C as shown in Figure 7b, and the mesophase structure was still retained in the sample at 450°C as shown in Figure 7c. However there was no apparent shifting of  $2\theta$  value for the samples calcined at 450°C in contrast to the pure mesoporous zirconia sample reported by Ciesla et al. [10].

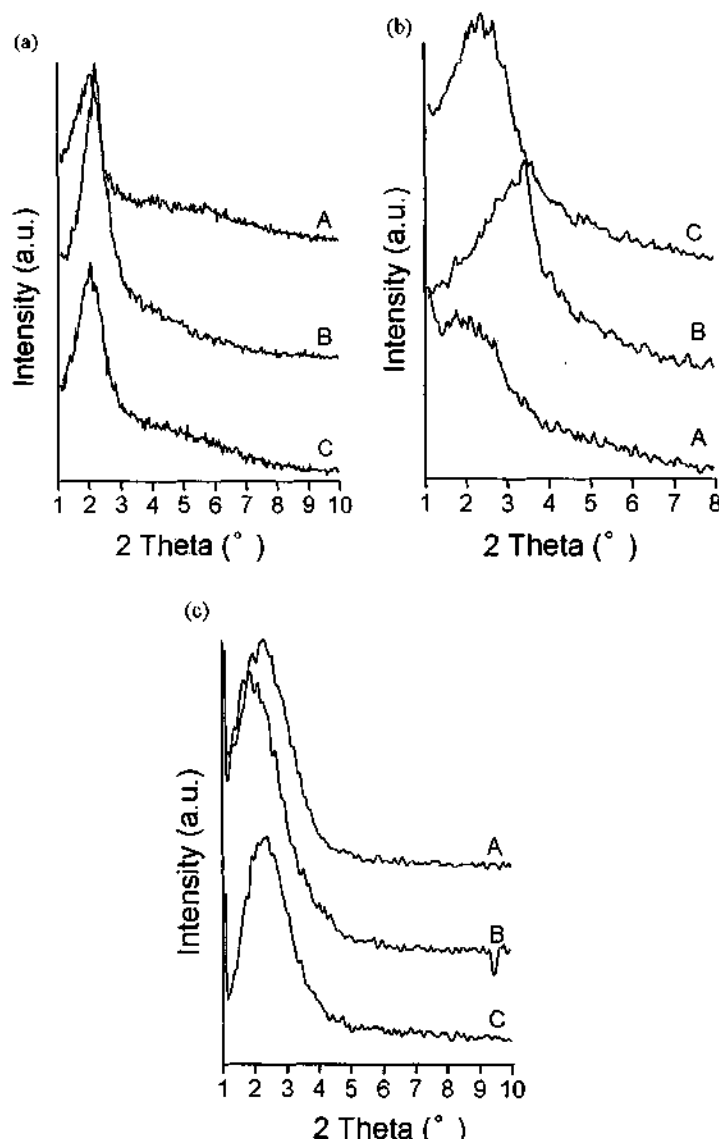


**Figure 7.** XRD patterns of the Ti-Zr samples dried at 100°C(a) and calcined at 350°C(b) or 450°C(c) prepared with the various  $\text{SO}_4^{2-}/\text{Ti-Zr}$  molar ratios: 1.5(A), 3.0(B), 5.0(C).

TGA was also employed to investigate the thermal stability of these samples as shown in Figure 8. The weight loss was between 44-52%, and the highest weight loss was observed on the sample with the  $\text{SO}_4^{2-}/\text{Ti-Zr}$  molar ratio of 1:3. The derivative curves exhibited two peaks: The first peak occurred at 270°C can be related with the desorption of organic components, which was further confirmed by its disappearance after further extraction treatment. Whereas the second peak at 400°C was assigned to the decomposition of the organic components. As suggested by sayari et al[11], the larger the peak related with adsorption of organics, implied the larger the pores associated with the well ordered mesopores. Indeed, the larger weight loss on the sample with the  $\text{SO}_4^{2-}/\text{Ti-Zr}$  ratio of 3:1 is in the agreement with the sharp peak of the Figure 7a. It seems that the sulfate species with the present concentration can only slightly improve the thermal stability of Ti-Zr mixed oxide, which is different from the pronounced effect on the thermal stability on the pure zirconia reported by Ciesla et al. [9].

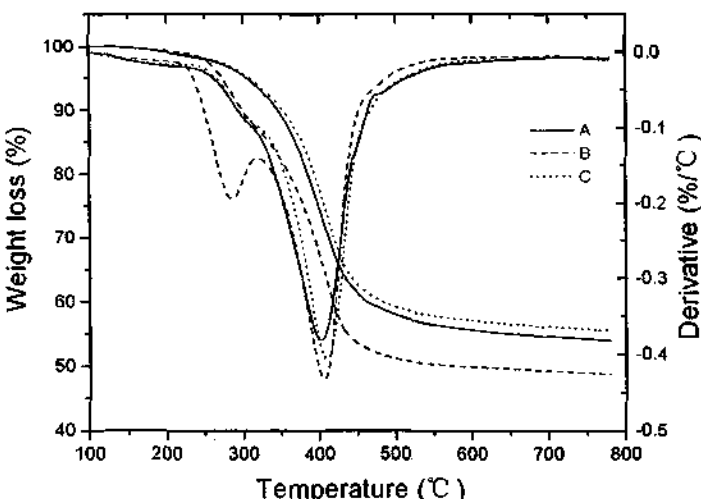


Figure 8. TGA profiles and their derivative curves of the Ti-Zr samples prepared with the various  $\text{SO}_4^{2-}/\text{Ti-Zr}$  molar ratios: 1.5(A), 3.0(B), and 5.0(C).

#### 4 Conclusion

In conclusion, a series of experiments have been conducted in an attempt to improve the thermal stability of the Ti-Zr mesoporous mixed oxide prepared from inorganic precursors. Several synthesis parameters including the Ti/Zr molar ratio, surfactant content, the effect of auxiliary organic additive and sulfate on the crystallinity and the thermal stability of the Ti-Zr mesoporous mixed oxide were investigated. The results show that the crystallinity of the Ti-Zr mesoporous mixed oxide depends strongly on the Ti/Zr molar ratio in the gel mixtures. Introduction of some auxiliary organic components such as DDA, TritonX-100, triethanolamine and ethanol can improve the thermal stability of the Ti-Zr mesoporous mixed oxides. As for the DDA dopant, the

mixing order also affects the crystallinity of the Ti-Zr mesoporous mixed oxides. It seems that the sulfate species with the present concentration can improve the thermal stability of Ti-Zr mixed oxide, which was not as pronounced as that for pure zirconia reported in the literature [10].

## 5 Acknowledgements

This work was supported by the National Natural Science Foundation of China (No. 29907003) and the Basic Research Foundation of Tsinghua university (No. JC1999009).

## References

1. Corma A., From microporous to mesoporous molecular sieve materials and their use in catalysis, *Chem. Rev.* **97** (1997) PP. 2373-2419.
2. Antonelli D. M., Ying J. Y., Synthesis of hexagonally packed mesoporous  $TiO_2$  by a modified sol-gel method, *Angew. Chem. Int. Ed. Engl.* **34** (18) (1995) pp. 2014-2017.
3. Chen H. R., Shi J. L., Hua Z. L., Ruan M. L., Yan D. S., Parameter control in the synthesis of ordered porous zirconium oxide, *Mater. Lett.* **51** (3) (2001) pp. 187-193.
4. Fujii H., Ohtaki M., Eguchi K., Synthesis and photocatalytic activity of lamellar titanium oxide formed by surfactant bilayer templating, *J. Am. Chem. Soc.* **120** (1998) pp. 6832-6833.
5. Chen H. R., Shi J. L., Yu J., Wang L. Z. and Yang D. S., Synthesis of titanium-doped ordered porous zirconium oxide with high-surface-area, *Microporous and Mesoporous Materials* **39** (2000) pp. 171-176.
6. Miyake Y., Kondo T., Mesoporous titania prepared in the presence of alkylamine, *J. Chem. Eng. Jp.* **34** (3) (2001) pp. 319-325.
7. Beck J. S., Vartuli J. C., Roth N. J., et al., A new family of mesoporous molecular sieves prepared with liquid crystal templates, *J. Am. Chem. Soc.* **114** (1992) pp. 1267-1269.
8. Tanev P. T., Pinnavaia T. J., Biomimetic of porous lamellar silicas by vesicular surfactant assemblies, *Science* **271** (5253) (1996) pp. 1267-1269.
9. Ciesla U., Schacht S., Stucky G. D., Unger K. K., and Schüth F., Formation of a porous zirconium oxo phosphate with a high surface area by a surfactant-assisted synthesis, *Angew. Chem. Int. Ed. Engl.* **35** (1996) 541-543.
10. Ciesla U., Fröba M., Stucky G., Schüth F., Highly ordered porous zirconias from surfactant-controlled syntheses: Zirconium oxide-sulfate and zirconium oxo phosphate, *Chem. Mater.* **11** (1999), 227-234.
11. Kruk M., Jaroniec M., Sayari A., New insights into pore-size expansion of mesoporous silicates using long-chain amines, *Microporous and Mesoporous Materials* **35-36** (2000) PP. 545-553.

# THE STUDIES ON PREPARATION AND CATALYTIC PERFORMANCE OF SUPERFINE BaTiO<sub>3</sub>-SUPPORTED Ni-BASED CATALYST

LI XIANCAI, LUO LAITAO, LIU KANGQIANG AND LAI ZIHUA

*Institute of Chemistry and Material Science, Nanchang University, Nanchang Jiangxi, 330047,  
P. R. China*

SUPERFINE BaTiO<sub>3</sub> support has been prepared by sol-gel method. Sol is formed under certain conditions with titanate, absolute alcohol, glacial acetic acid and barium acetate as starting materials. Subsequently, the sol transforms into transparent gel and ultrafine BaTiO<sub>3</sub> powders are formed by further calcination of dry gel which has been dried in oven. DTA-TG has been carried out to study the thermal decomposition mechanism of the dry gel. The powder x-ray diffraction (XRD) patterns of BaTiO<sub>3</sub> are recorded. The powder size is measured by transmission electron microscopy (TEM). The surface area is also measured. The influence of several factors on BaTiO<sub>3</sub> particle size and surface area is discussed. Optimum parameters for preparing ultrafine BaTiO<sub>3</sub> support are achieved. When the molar ratio of water volume for hydrolysis to titanate is about 25.0 and the pH value is 4.0, ultrafine BaTiO<sub>3</sub> with smallest size and largest surface area can be prepared. Superfine Ni-based catalyst is prepared by impregnating aqueous solution of Ni (NO<sub>3</sub>)<sub>2</sub>·6H<sub>2</sub>O onto ultrafine BaTiO<sub>3</sub> powders prepared by sol-gel process. This catalyst is used to the reaction of CO<sub>2</sub> reforming CH<sub>4</sub> to syngas (CH<sub>4</sub>+CO<sub>2</sub>=2H<sub>2</sub>+2CO) and shows excellent activity and high selectivity which still keep stable under high temperature. The conversion of CH<sub>4</sub> and CO<sub>2</sub> can both reach as high as over 90 percent under the reaction conditions: temperature, 1073K, the GHSV , 12000ml/(hg-cat), CO/H<sub>2</sub> molar ratio is close to 1.0.

## 1 Introduction

Barium titanate (BaTiO<sub>3</sub>), a perovskite-type electro-ceramic material, has been extensively studied and utilized due to its dielectric and ferroelectric properties. The wide applications of barium titanates include multilayer capacitors in electronic circuits, nonlinear resistors, thermal switches, passive memory storage devices, and transducers. In addition, barium titanate can be used for chemical sensors due to its surface sensitivity to gas adsorption.

Compared to conventional solid-state reaction and co-precipitation method [1,2], sol-gel method offer promising approaches for preparing ultrafine, homogeneous, high-purity powders at temperatures far below other required methods. Currently, there are no literatures reporting that nanometer BaTiO<sub>3</sub> was used as support to prepare catalyst. In this paper, performance of the catalyst with nanometer BaTiO<sub>3</sub> as support in the reaction of CO<sub>2</sub> reforming CH<sub>4</sub> to syngas was described.

## 2 Experimental

### 2.1 Synthesis procedure

At first, homogeneous and transparent solution is prepared by mixing 0.0147 mol titanate and 10 ml alcohol solvent, after stirring vigorously for 20 min, 10 ml glacial acetic acid is added into the solution at room temperature. Subsequently, certain volume of barium acetate solution is dropped into the prepared solution with the mole ratio of Ba/Ti=1.0 followed by continuing stirring for 30 min to promote complete hydrolysis reaction. The pH value is kept 4~5. At last, the mixture solution is put into water-bath with temperature of 343K to start the process of formation of sol and transformation of sol into gel.

Amorphous barium titanate gel is obtained in couple of minutes. The gel is then dried in vacuum at temperature of 333K for 24 h, and nanometer BaTiO<sub>3</sub> is prepared by calcining the dry gel at 973-1073K for 2h.

## 2.2 Characterization

The powder morphology is observed with TEM (Japan H-600). Thermal analyses are carried out by using TG/DTA (Shimadzu DT-40). The powder x-ray diffraction patterns of BaTiO<sub>3</sub> is recorded with XRD (D/max-3B diffractometer), Surface area is measured with ST-08 surface area apparatus.

## 2.3 Preparation and test of catalyst

The catalyst sample of Ni/BaTiO<sub>3</sub> is prepared by wet impregnation of an aqueous solution of Ni (NO<sub>3</sub>)<sub>2</sub>·6H<sub>2</sub>O onto nanometer BaTiO<sub>3</sub> obtained by sol-gel method for 24 h. After being dried, the sample is calcined in air at 923K for 3h (the content of Ni in catalyst is 5.0%). The calcined catalyst is made into particles of 60~80 mesh. Before the catalyst test, the catalyst was reduced in situ at 773K for 1 h, the catalytic reaction is conducted in a fix-bed reactor under atmospheric pressure, The catalyst bed contains 150 mg Ni/BaTiO<sub>3</sub>, the catalytic reaction is performed with a feed of 1:1 CH<sub>4</sub>/CO<sub>2</sub> unless otherwise specified , the flow rate of the feed is GHSV=1.2×10<sup>4</sup>ml/(h.g.cat.), product gases are immediately injected into a gas chromatograph for analysis.

## 3 Results and Discussion

### 3.1 Thermal decomposition mechanism of the dry gel

Essential content of the dry gel is formed by the combination of Ti<sub>6</sub>(μ<sub>3</sub>-O)<sub>2</sub>(μ<sub>2</sub>-O)(μ<sub>2</sub>-OC<sub>4</sub>H<sub>9</sub>)<sub>2</sub>(μ-CH<sub>3</sub>COO)<sub>8</sub>(OC<sub>4</sub>H<sub>9</sub>)<sub>6</sub> and Ba<sub>4</sub>(Ac)<sub>8</sub> tetramer through acetic acid radical [ 3 ].

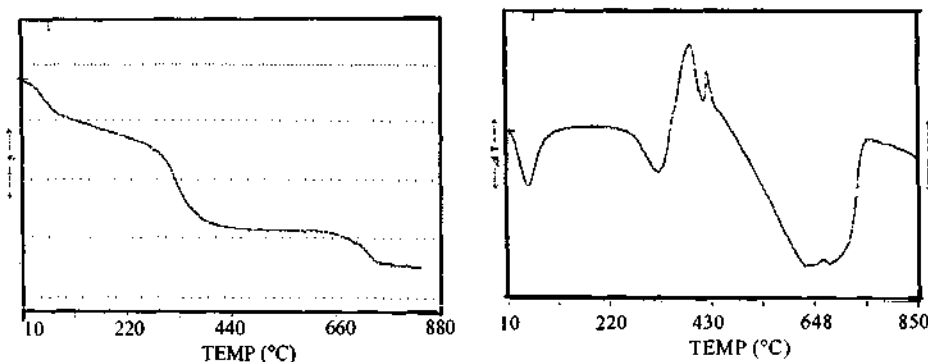


**Figure 1.** TG/DTA curves for the dry gel.

It can be seen that thermal decomposition process can be divided into four steps (Figure1). The original weight loss occurs gradually to from 283K to 390K, percentage of weight loss is 8.235%. In the same temperature range, a endothermic peak around 328K is

observed in DTA curves. This step is thought to be due to the evaporation of physically absorbed water and the reserved organic content.

In the second step, percentage of weight loss is 24.11% from 390K to 673K, meanwhile, an endothermic peak around 597.9K and two following exothermic peaks around 661K and 698.6K respectively can be seen in DTA curves. The endothermic peak is attributed to the evaporation of some organic groups such as ethoxy group, acetic acid radical and butoxy group. Two exothermic peaks are resulted from the following oxidation of these organic groups and a series of reactions related to the formation of  $\text{BaCO}_3$  and  $\text{TiO}_2$ .

In the third step at temperatures from 673K to 896K, there is no weight loss shown in TG curve. There are also no apparent endothermic peaks or exothermic peaks in DTA curves, which is thought to be due to the transformation of disorder nanometer  $\text{BaCO}_3$  and  $\text{TiO}_2$  into their order phase.

In the fourth step at temperatures from 896K to 993K, percentage of weight loss is 8.529%. A large endothermic peak can be observed in DTA curve. In this step,  $\text{BaCO}_3$  and  $\text{TiO}_2$  react to form  $\text{BaTiO}_3$ .

### 3.2 Calcination of dry gel

The dry gel is calcined at 923K, 973K and 1073K respectively after it is ground. Apparent color of powders calcined at 923K is white and grayish, which may be caused by a little organic matter without decomposing completely. The samples calcined at 973K and 1073K show pure white. Their powder diffraction patterns are shown in Figure 2.

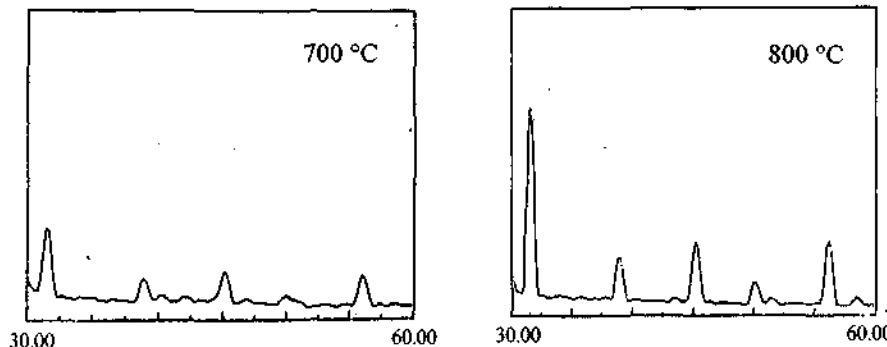
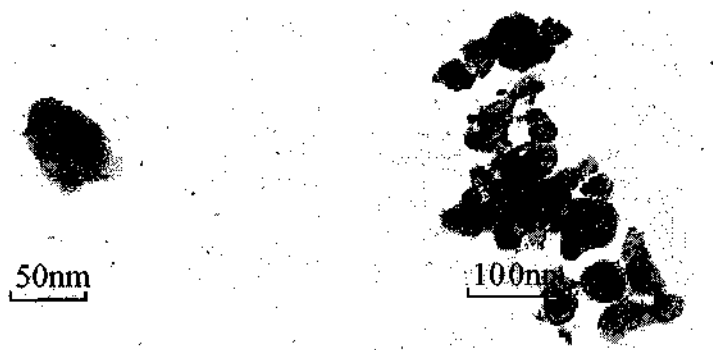


Figure 2. XRD patterns of  $\text{BaTiO}_3$ .

It can be seen from Figure 2 that  $\text{BaTiO}_3$  whose major phase is cubic phase is prepared at 973K far below that required for conventional solid-state reaction over 1373K. TEM morphology of  $\text{BaTiO}_3$  powders shown in Figure 3 reveals that besides a little conglomeration, there are many well-dispersed single particles which are spherical in form and 25~60 nm in diameter.



**Figure 3.** TEM morphology of BaTiO<sub>3</sub> powers.

### 3.3 Factors influencing powder quality

#### 3.3.1 Influence of water volume

The structure of final product prepared by sol-gel method is in shape preliminarily in solution, and following process is relevant to the characteristic of sol directly. So the characteristic of sol is very important. The essential reason for transformation of homogeneous solution into sol is the hydrolysis of alcoholate and the condensation polymerization. Controlling conditions for hydrolysis of alcoholate is the key to the preparation of sol with promising quality.

Research revealed that water volume has great effect on the structure of alcoholate polymer. There are a little alkoxy group formed by hydrolysis under small water volume, and products with low cross-linking level are easy to form by condensation polymerization of molecules related to hydrolysis reaction. On the contrary, when water volume is large, products with high cross-linking level are easy to form. In the experiment, when barium acetate solution is dropped into the solution prepared by dissolution of Ti(OR)<sub>x</sub>(OAc)<sub>y</sub> (OR is n-butyl alcohol or alcohol, OAc is acetate) in absolute alcohol, the compound of Ti(OH)<sub>x</sub>(OAc)<sub>y</sub> can be formed because of faster hydrolysis rate of alkoxy group than that of acetate, and the compound is able to be dissolved in excess water. Sol particles are not formed in the process of hydrolysis of Ti(OR)<sub>x</sub>(OAc)<sub>y</sub> to Ti(OH)<sub>x</sub>(OAc)<sub>y</sub>. The formation of sol was next to the rapid transformation of sol into gel. That is to say there is no apparent boundary between them. The process of transformation carried out in water-bath includes the formation and the transformation of sol. When different volumes of water used, there are different gel times (the time lasts from starting heating to ending gel formation). That is to say, that water volume will affect greatly the formation of final sol particles and the transformation of sol into gel, and influence powder quality. Relationship between water volume and powder quality is shown in Table 1.

It is known from Table 1 that gel time increases with the increase of water volume for hydrolysis. Transparent gel body can be obtained under 10 ml or 20 ml of water, whereas it would become opaque and show light white when water volume increases to 40 ml. The structure of gel body will become loosen and a little solution will bleed under the following drying, gel can not be formed when water volume rises up to 50 ml, white

precipitate is obtained under continuing heating in water-bath at 343K, which may be due to the less concentration of compound of  $Ti(OH)_4(OAc)_6$ , under more water volume and the resulted weaker interaction force among compound molecules which causes the formation of sol body and transformation of sol into gel to slow down. When water volume increases to 50 ml, the interaction force among sol nucleus weakens to the degree that they can't aggregate, which makes the gel not be formed. The compound of  $Ti(OH)_4(OAc)_6$  continues to be hydrolyzed and  $TiO_2 \cdot 2H_2O$  is formed in the end.

**Table 1.** Relationship between water volume of hydrolysis and powder quality.

Sample	Water volume (ml)	Gel time (min)	Particle size (nm)	Surface area ( $m^2/g$ )
A	50	Without gel		
B	40	Loosen gel		
C	30	33	85	8.78
D	20	25	70	9.04
E	10	17	25~60	10.76
F	4	10	100	8.18

Particle size rises with the increase of water volume, surface area reaches its maximum and particle size is minimum when water volume is 10 ml. Samples prepared under minimum water volume feels bad, and there are much hard conglabation and soft conglabation.

### 3.3.2 Selection of solvent

Solvent is important to preparation of sol. -OR group in alcoholate is easy to exchange with -OR' group in solvent, which results in the variation of activity of hydrolysis of alcoholate. If the same alcoholate chooses different solvent, its hydrolysis rate and gel time will follow to be different. In the experiment, three kinds of solvent are selected: alcohol, isopropanol and n-butyl alcohol. The research result reveals that sol will be formed in all occasions, but gel time was greatly different. Particle size and surface area also vary slightly. That is because that polarity, pole moment, and achievement ability to active proton result in different effects on the exchange reaction in sol.

**Table 2.** Relationship between solvent and powder quality.

Solvent	Gel time (min)	Particle size (nm)	Surface area ( $m^2/g$ )
Alcohol	17	25~60	10.76
Iso-panol	20	85	10.43
n-butyl alcohol	44	145	8.25

### 3.3.3 Influence of pH value on gel time

The experimental result reveals that pH value has great effect on gel time. From the result shown in Table 3, it can be seen that gel time increases with the fall of pH value. When pH value is equal or down to 3, it is not gel body but white precipitate that is obtained when mixing solution is heated in water-bath at 343K for 8 h. When the pH value is 4~5, transparent gel can be obtained.

**Table 3.** Influence of pH value on gel time.

pH	Gel time (min)	Gel state
2	Without gel	White precipitate
3	Without gel	White precipitate
4	17	Transparent gel
5	16	Opaque gel

The solubility and stability in mixing solution of  $Ti(OH)_4(OAc)_2$  vary with surrounding temperature. Temperature has great effect on the formation and transformation of sol. Experiment result is shown in Table 4.

**Table 4.** Relationship between gel time and gel temperature.

Gel temperature (K)	283	293	323	343	353
Gel time	White precipitate	>120h	120min	20min	17min

It is known from Table 4 that the gel time increased with the fall of gel temperature and it is more difficult to form gel under lower temperature.

### 3.4 Activity of $Ni/BaTiO_3$ catalyst

There is a general interest in recent years in the more efficient use of natural gas (methane) and in the reduction of  $CO_2$  in the atmosphere. The production of syngas ( $CO$  and  $H_2$ ) by  $CO_2$  reforming of  $CH_4$  over heterogeneous catalyst is one of the attractive routes for the utilization of the methane and  $CO_2$  resources [4,5].  $Ni/BaTiO_3$  catalyst can be used to the reaction and has excellent performance which is shown in Table 5.

**Table 5.** Catalytic activity of catalyst  $Ni/BaTiO_3$ .

Temperature (K)	Conversion (X%)			Content of dry product (%)		
	$CH_4$	$CO_2$	$CH_4$	$CO_2$	CO	$H_2$
973	80.1	82.3	8.0	8.5	43.7	39.8
1073	94.4	93.3	3.5	2.7	48.3	45.5
1123	99.2	98.9	0.4	0.5	50.6	48.5

It can be seen that Ni/BaTiO<sub>3</sub> catalyst possesses high activity and does not deactivate for a long time under high reactive temperature. Whereas, though Ni based catalysts such as Ni/ $\gamma$ -Al<sub>2</sub>O<sub>3</sub> also show high activity, they often deactivate rapidly due to carbon deposition or the crystal structure transformation of the support occurring at high reactive temperature, which hinders the process from industrial applications.

#### 4 Conclusion

BaTiO<sub>3</sub> precursor can be formed by sol-gel method under appropriate condition, and nanometer BaTiO<sub>3</sub> is prepared by further calcining the precursor at 973K. Solvent, temperature, pH value and water volume for hydrolysis have great effect on the quality of BaTiO<sub>3</sub> powders in the process of preparing precursor. Nanometer BaTiO<sub>3</sub> is used as support to prepare Ni based catalyst, and the catalyst has high activity in the reaction of CO<sub>2</sub> reforming CH<sub>4</sub> to syngas.

#### References

1. M. Z. C. Hu , G. A. Miller et al., Homogeneous co-precipitation of inorganic salts for synthesis of monodispersed barium titanate particles, *J. Mater. Sci.* 35(2000) pp. 2927-2936.
2. John Wang, Jiye Fang et al., Ultrafine barium titanate powders via microemulsion proressing routes. *J. Am. Ceramic Soc.* 82(1999) pp.873-881.
3. S. L. Wu, H. P. Li et al., Sol-gel preparation and characteristic on ultrafine BaTiO<sub>3</sub>, and Semiconducting BaTiO<sub>3</sub>, Ceramics doped with yttrium, *Functional Material*, 26(1995) pp. 427-430.
4. M. C. J.Bradford, and M. A.Vannice, CO<sub>2</sub> reforming of CH<sub>4</sub>, *Catal.Rev.-Sci.Eng.* 41(1999) pp.1-42.
5. Jun-Mei Wei, Bo-Qing Xu et al., Highly active and stable Ni/ZrO<sub>2</sub> catalyst for syngas production by CO<sub>2</sub> reforming of methane, *Appl. Catal.* 196(2000) pp.167-172.

This page is intentionally left blank

# NON-AQUEOUS SYNTHESIS OF NOVEL LOW-DIMENSIONAL ZIRCONIUM PHOSPHATES

D. WANG, R. B. YU, N. KUMADA AND N. KINOMURA

*Institute of Inorganic Synthesis, Faculty of Engineering, Yamanashi University,  
Miyamae-cho 7, Kofu 400-8511, JAPAN*

K. YANAGISAWA

*Laboratory of Hydrothermal Chemistry, Faculty of Science, Kochi University, 2-5-1  
Akebono-Cho Kochi, JAPAN*

D. WANG, Y. MATHMURA AND T. YASHIMA

*Research Institute of Innovative Technology for the Earth, 9-2 Kizugawadai, Kizu-cho,  
Soraku-gun, Kyoto 619-0292, JAPAN  
E-mail: danwang1@rite.or.jp*

Three novel zirconium phosphates, 2-D  $[\text{NH}_4]_2[\text{H}_3\text{N}(\text{CH}_2)_2\text{NH}_3]_2 [\text{Zr}_3(\text{OH})_6(\text{PO}_4)_4]$  ( $\text{ZrPO-1}$ ), 2-D  $[\text{NH}_4]_2[\text{Zr}(\text{OH})_3(\text{PO}_4)]$  ( $\text{ZrPO-2}$ ), 1-D  $[\text{NH}_4]_3[\text{Zr}(\text{OH})_2(\text{PO}_4)] (\text{HPO}_4)$  ( $\text{ZrPO-3}$ ), have been synthesized in non-aqueous media and characterized by means of single-crystal X-ray analysis.

## 1 Introduction

Metal phosphates have been known for a long time and were extensively investigated with respect to crystal chemistry, various properties and many potential applications in a wide area of materials [1]. Since the discovery of open-framework aluminum phosphates in 1982 [2], hydrothermal chemistry of metal phosphates, in particular transition metal phosphates, have attracted a great deal of active researches. Correspondingly, a great number of phosphates of Zn [3, 4], V [5, 6], Fe [7, 8], Zr [9, 10], and Co [11], etc. have been synthesized by using organic amines as the structure-direction agent.

Although the study of organically templated zirconium phosphates was conspicuous and some inspiring results were recently achieved, there were still few examples of them. In 1994, Clearfield et al. reported a layered zirconium phosphate fluoride [12]. A one-dimensional double-stranded polymer  $[\text{enH}_2]_{1.5}[\text{Zr}(\text{PO}_4)(\text{HPO}_4)\text{F}_2]$  was solvothermally synthesized in 1995 [13]. In the following year, a zirconium phosphate fluoride containing organic template with a three-dimensional cage structure was obtained for the first time [14]. More recently, a series of zirconium phosphate fluorides were prepared [15]. But up to now, only two low-dimensional zirconium phosphates free from fluoride element have been reported, one is one-dimensional  $[\text{enH}_2][\text{Zr}(\text{HPO}_4)_3]$ , the other is two-dimensional  $[\text{enH}_2]_{0.5}[\text{Zr}(\text{PO}_4)(\text{HPO}_4)]$  which is the ion-exchanged analogue of  $\gamma\text{-ZrP}$  [16].

It is known that non-aqueous synthesis has been effectively applied in the preparation of various metal phosphates, including amine-containing aluminum, gallium, indium, zinc and cobalt phosphates with three-dimensional open-framework structures [17-24]. Moreover, phosphates with a layered or chain structure can be crystallized from non-aqueous media [25, 26]. Since the fluoride ions mineralizer was introduced into the synthesis of zirconium phosphates, several zirconium phosphate fluorides with novel structures have also been developed.

In the present work, we studied the non-aqueous synthesis and characterizations of novel zirconium phosphates with the aim to open up a new synthetic system for this class of compounds and obtain some new structures. Three zirconium phosphates with layered and chain structures,  $[\text{NH}_4]_2[\text{H}_3\text{N}(\text{CH}_2)_2\text{NH}_3]_2[\text{Zr}_3(\text{OH})_6(\text{PO}_4)_4]$  (ZrPO-1),  $[\text{NH}_4]_2[\text{Zr}(\text{OH})_3(\text{PO}_4)]$  (ZrPO-2) and  $[\text{NH}_4]_3[\text{Zr}(\text{OH})_2(\text{PO}_4)(\text{HPO}_4)]$  (ZrPO-3), have been prepared in  $\text{ZrOCl}_2 \cdot \text{H}_3\text{PO}_4$  - organic amine -  $\text{NH}_4\text{F}$  - organic solvent systems. Herein, we will discuss the synthesis, structures, and properties of these compounds in detail.

## 2 Synthesis and Characterizations

### 2.1 Synthesis

The low dimensional compounds were synthesized from a reaction mixture of composition of  $\text{ZrOCl}_2 / \text{H}_3\text{PO}_4 / \text{organic amine} / \text{NH}_4\text{F} / \text{organic solvent}$ . In a typical synthesis procedure,  $\text{ZrOCl}_2 \cdot 8\text{H}_2\text{O}$  (C.R.) was dissolved in ethylene glycol to form a solution, to which phosphoric acid (85%) was added, then the mixture gelled. Ammonium fluoride was added to the gel to form a sol under stirring with a glass stick, then ethylenediamine was added dropwise to the sol under vigorous stirring. The reaction mixture was stirred with a magnetic stirrer for 120 min and then was transferred into a Teflon-lined stainless steel autoclave to a filling fraction of 60%. The crystallization was carried out under autogenous pressure at 160-190 °C for 3-6 days. The colorless crystalline product was filtered and washed with deionized water and ethanol, and then dried in air at ambient temperature.

### 2.2 X-ray Structure Determination

All measurements were performed on a Rigaku AFC7R diffractometer with graphite monochromated Mo K $\alpha$  radiation and a rotating anode generator. The crystal structure was solved by direct method and expanded by Fourier techniques. The non-hydrogen atoms were refined anisotropically. All calculations were performed using the teXsan crystallographic software package. Further details of crystal data are summarized in Table 1.

Table 1. Crystal Data and Structure Refinement.

Empirical formula	$H_{34}Zr_3P_4O_{22}N_6C_4$	$H_{11}ZrPO_7N_2C_4$	$H_{15}ZrP_2O_{10}N_3$
Formula weight	915.91	273.29	370.30
Crystal System	triclinic	monoclinic	triclinic
Space Group	$P\bar{1}$ (No. 2)	$P2_1/n$ (No. 14)	$P\bar{1}$ (No. 1)
Lattice Parameters			
a (Å)	9.383(3)	7.661(2)	8.1432(8)
b (Å)	9.923(3)	9.699(2)	12.718(2)
c (Å)	8.342(2)	10.473(2)	5.2463(6)
$\alpha$ (°)	97.85(2)		91.85(1)
$\beta$ (°)	111.75(2)	95.16(2)	92.16(1)
$\gamma$ (°)	113.01(2)		74.25(1)
V (Å <sup>3</sup> )	627.0(4)	775.1(3)	522.4(1)
Z value	1	4	2
D <sub>calc</sub> (g/cm <sup>3</sup> )	2.426	2.426	2.354
Residuals: R; R <sub>w</sub>	0.051; 0.056	0.065; 0.077	0.057; 0.061
Goodness of Fit	1.63	1.93	1.82

### 3 Results and Discussion

#### 3.1 Synthesis conditions

##### 3.1.1 Influence of the solvent

In this work, alcoholic solvents were used as the reaction medium, and three novel zirconium phosphates have been synthesized in these reaction system. From Table 2 it can be seen that under similar starting materials molar ratio, solvents critically influence the formation of the products. By changing alcoholic solvent into water only, very different product  $Zr_4P_6O_{23}$  [27] and  $NH_4Zr_2(PO_4)_3$  [28] were easily obtained.

##### 3.1.2 Influence of the starting materials

Three zirconium sources were used for the synthesis.  $Na_2ZrF_6$  and  $ZrOCl_2$ , exhibited higher reaction activity. Under the same starting materials molar ratio as that for formation of  $ZrPO \cdot 1$ ,  $Na_2ZrF_6$  gave another known zirconium phosphate fluoride [13]. However, because of relatively complicated alcoholysis of  $(C_4H_9O)_4Zr$ , by using it as the zirconium source, the reaction conditions were difficult to be controlled, and amorphous phases were formed. (Table 3.)

Table 2. Influence of the solvent on the preparation of zirconium phosphates.

Starting materials molar ratio					Product
ZrOCl <sub>2</sub>	H <sub>3</sub> PO <sub>4</sub>	Organic amine	NH <sub>4</sub> F	Solvent	
1.0	1.0	1.0 [NH <sub>2</sub> (CH <sub>2</sub> ) <sub>3</sub> NH <sub>2</sub> ]	4.0	110 H <sub>2</sub> O	Zr <sub>4</sub> P <sub>6</sub> O <sub>23</sub>
1.0	1.0	1.5 [NH <sub>2</sub> (CH <sub>2</sub> ) <sub>3</sub> NH <sub>2</sub> ]	4.0	110 H <sub>2</sub> O	NH <sub>4</sub> Zr <sub>2</sub> (PO <sub>4</sub> ) <sub>3</sub>
1.0	1.0	2.0 [NH <sub>2</sub> (CH <sub>2</sub> ) <sub>3</sub> NH <sub>2</sub> ]	4.0	110 H <sub>2</sub> O	Zr <sub>4</sub> P <sub>6</sub> O <sub>23</sub>
1.0	1.0	1.0 [NH <sub>2</sub> (CH <sub>2</sub> ) <sub>2</sub> NH <sub>2</sub> ]	4.0	110 H <sub>2</sub> O	Zr <sub>4</sub> P <sub>6</sub> O <sub>23</sub>
1.0	1.0	1.0 [NH <sub>2</sub> (CH <sub>2</sub> ) <sub>2</sub> NH <sub>2</sub> ]	4.0	110 EG	ZrPO·1
1.0	1.0	1.0 [NH <sub>2</sub> (CH <sub>2</sub> ) <sub>3</sub> NH <sub>2</sub> ]	4.0	110 EG	ZrPO·2
1.0	1.0	1.0 [NH <sub>2</sub> (CH <sub>2</sub> ) <sub>2</sub> NH <sub>2</sub> ]	4.0	110DEG	ZrPO·3

Table 3. Influence of zirconium source on the products.

Starting materials molar ratio					Product
Zr source	H <sub>3</sub> PO <sub>4</sub>	Organic amine	NH <sub>4</sub> F	Solvent	
1.0 Na <sub>2</sub> ZrF <sub>6</sub>	1.0	1.0 en	4.0	110EG	[Zr(HPO <sub>4</sub> )(PO <sub>4</sub> )F <sub>2</sub> ]1.5en
1.0 ZrOCl <sub>2</sub>	1.0	1.0 en	4.0	110EG	ZrPO·1
1.0 (C <sub>4</sub> H <sub>9</sub> O) <sub>4</sub> Zr	1.0	1.0en	4.0	110EG	am.*

\* am.: amorphous.

Organic diamines are effective structure-direction agents for metal phosphates. Therefore, in this work, organic diamines were used mainly. By using ethylene glycol as the solvent, ZrPO·1 and ZrPO·2 are synthesized. Except for ethylenediamine, almost all other kinds of amines we used could give ZrPO·2 as the product. (Table 4)

In the synthesis of these zirconium phosphates, F<sup>-</sup> ions were chosen as the mineralizer. NH<sub>4</sub>F, NaF, and KF can provide F<sup>-</sup> ions for the synthetic system, but the experiment results indicated that the presence Na<sup>+</sup>, K<sup>+</sup> cations is not good for product crystallization. On one hand, Na<sup>+</sup>, K<sup>+</sup> cations could increase the basicity, which is not suitable for the product formation. On the other hand, NH<sub>4</sub><sup>+</sup> cations also have certain function as template.

Table 4. Influence of organic amine on the products.

ZrOCl <sub>2</sub>	H <sub>3</sub> PO <sub>4</sub>	Starting materials molar ratio	Organic amine	NH <sub>4</sub> F	Solvent	Product
1.0	1.0	1.0	[NH <sub>2</sub> (CH <sub>2</sub> ) <sub>2</sub> NH <sub>2</sub> ] <sub>2</sub>	4.0	110EG	ZrPO·1
1.0	1.0	1.5	[NH <sub>2</sub> (CH <sub>2</sub> ) <sub>3</sub> NH <sub>2</sub> ] <sub>2</sub>	4.0	110EG	ZrPO·2
1.0	1.0	1.0	[NH <sub>2</sub> (CH <sub>2</sub> ) <sub>4</sub> NH <sub>2</sub> ] <sub>2</sub>	4.0	110EG	ZrPO·2
1.0	1.0	1.0	[NH <sub>2</sub> (CH <sub>2</sub> ) <sub>5</sub> NH <sub>2</sub> ] <sub>2</sub>	4.0	110EG	ZrPO·2
1.0	1.0	1.0	[NH <sub>2</sub> (CH <sub>2</sub> ) <sub>6</sub> NH <sub>2</sub> ] <sub>2</sub>	4.0	110EG	ZrPO·2
1.0	1.0	1.0 CH <sub>3</sub> NH <sub>2</sub>		4.0	110EG	ZrPO·2
1.0	1.0	1.0 CH <sub>3</sub> CH <sub>2</sub> NH <sub>2</sub>		4.0	110EG	ZrPO·2
1.0	1.0	1.0 CH <sub>3</sub> (CH <sub>2</sub> ) <sub>2</sub> NH <sub>2</sub>		4.0	110EG	ZrPO·2
1.0	1.0	1.0 NH <sub>2</sub> CH <sub>2</sub> CH <sub>2</sub> OH		4.0	110EG	am.
1.0	1.0	1.0 N(CH <sub>2</sub> CH <sub>2</sub> OH) <sub>3</sub>		4.0	110EG	am.

### 3.1.3 Influence of the reaction temperature and duration

In this work, synthesis of zirconium phosphates was carried out in two alcoholic media. The suitable reaction temperature and duration are 180°C and 3·5 days.

## 3.2 Crystal Structure

### 3.2.1 Structure of ZrPO·1

The structure of this crystal is based on a network of zirconium-centered octahedra and phosphorus-centered tetrahedra. The structure consists of macroanionic [Zr<sub>3</sub>P<sub>4</sub>O<sub>22</sub>H<sub>6</sub>]<sup>6-</sup> sheets separated by organic diprotonated ethylenediamine and inorganic ammonium cations. The sheet lying in the crystallographic *ab* plane is built up from corner-sharing ZrO<sub>4</sub>(OH)<sub>2</sub> octahedra and PO<sub>4</sub> tetrahedra. Whereas four vertices of the ZrO<sub>4</sub>(OH)<sub>2</sub> octahedron are shared by adjacent PO<sub>4</sub> units, three vertices of the PO<sub>4</sub> tetrahedron are linked to adjacent ZrO<sub>4</sub>(OH)<sub>2</sub> units with the remaining corresponding to the P=O group, leading to a P/Zr ratio of 4/3.

### 3.2.2 Structure of ZrPO·2

The structure of ZrPO·2 is based on a sheet of zirconium-centered octahedra and phosphorus-centered tetrahedra. The structure consists of

macroanionic  $[\text{ZrPO}_7\text{H}_3]^{2-}$  sheets separated by inorganic ammonium cations.  $\text{ZrO}_2(\text{OH})_3$  octahedra link up with  $\text{PO}_4$  tetrahedra via corner-sharing in a strictly alternating manner to give rise to an infinite layer. Similar to  $\text{ZrPO}\cdot 1$ , there are eight- and four-membered rings in the sheet. However, the four-membered rings each are surrounded by eight-membered rings, in a way very different from that for  $\text{ZrPO}\cdot 1$  (Figure 1). Three vertices of the  $\text{ZrO}_3(\text{OH})_3$  octahedron are shared by adjacent  $\text{PO}_4$  units, and three vertices of the  $\text{PO}_4$  tetrahedron are linked to adjacent  $\text{ZrO}_3(\text{OH})_3$  units with the remaining corresponding to the  $\text{P}=\text{O}$  group, leading to a  $\text{P}/\text{Zr}$  ratio of 1. Only inorganic ammonium cations are incorporated in the interlayer and lie above and below the windows within the layers.

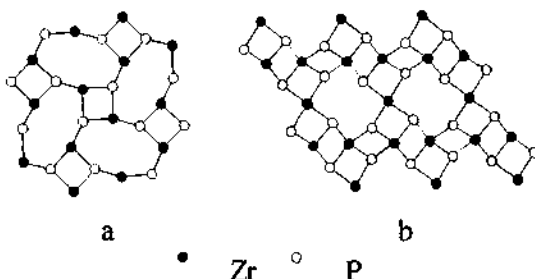


Figure 1. Different layer structures of (a)  $[\text{NH}_4]_2[\text{Zr}(\text{OH})_3(\text{PO}_4)]$  and (b)  $[\text{NH}_4]_2[\text{enH}_2]_2[\text{Zr}(\text{enH}_2)_6(\text{PO}_4)_4]$ .

### 3.2.3 Structure of $\text{ZrPO}\cdot 3$

Up to now, only two one-dimensional zirconium phosphates have been reported. One is  $[\text{enH}_2][\text{Zr}(\text{HPO}_4)_8]$  [16], and the other is zirconium phosphate fluoride  $[\text{enH}_2]_{1.5}[\text{Zr}(\text{PO}_4)(\text{HPO}_4)\text{F}_2]$  [13] with double-stranded chains. The simple models of one-dimensional chain inorganic polymers are shown schematically in Figure 2.  $\text{ZrPO}\cdot 3$  has a chain structure similar to the one-dimensional aluminum phosphate,  $[\text{AlP}_2\text{O}_8\text{H}]^{2-}$  [29].

The compound consists of macroanionic chains (empirical formula  $[\text{ZrP}_2\text{O}_{10}\text{H}_3]^{3-}$ ), separated by  $\text{NH}_4^+$  cations. The octahedral Zr atoms are bridged with  $\text{PO}_4$  and  $\text{HPO}_4$  groups via Zr-O-P-O-Zr linkages. Thus each  $\text{ZrO}_6$  octahedron shares four  $\text{PO}_4$  tetrahedra with each of its neighbors on either corner.

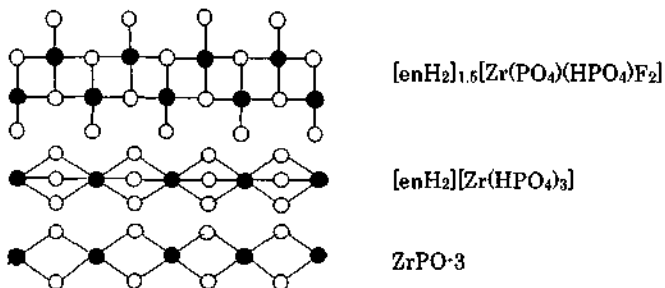


Figure 2. One-dimensional chain structures for zirconium phosphates.

#### 4 Summary

Three kinds of novel zirconium phosphates, 2-D  $[\text{NH}_4]_2[\text{H}_3\text{N}(\text{CH}_2)_2\text{NH}_3]_2[\text{Zr}_3(\text{OH})_6(\text{PO}_4)_4]$  (ZrPO·1), 2-D  $[\text{NH}_4]_2[\text{Zr}(\text{OH})_3(\text{PO}_4)]$  (ZrPO·2), 1-D  $[\text{NH}_4]_3[\text{Zr}(\text{OH})_2(\text{PO}_4)_2(\text{HPO}_4)]$  (ZrPO·3), have been synthesized in non-aqueous media and have been structurally characterized.

Through the investigation of various synthetic conditions, the actions of non-aqueous solvents, organic amines and F<sup>-</sup> cations for product crystallization are further clarified. Moreover, the probable reaction mechanisms for the formations of the compounds were estimated. These mechanisms need to be proved or corrected via further investigation. Additionally, with cations located at the interspaces of the structures, the compounds will probably have some ion-exchange properties, researches about which are now in progress.

#### 5 Acknowledgement

Ranbo Yu acknowledges the JSPS Research Fellowships for Young Scientists for financial support.

#### References

1. F. Nozaki, T. Sodesawa, *The surface Science Society of Japan*, 23 (1985) 400.
2. S. T. Wilson, B. M. Lok, C. A. Messina, T. R. Cannan and E. M. Flanigen, *J. Am. Chem. Soc.*, 104 (1982) 1146.
3. T. E. Gier and G. D. Stucky, *Nature*, 349 (1991) 508.
4. S. Neeraj, S. Natarajan and C. N. R. Rao, *Chem. Mater.* 11 (1999) 1390.
5. V. Soghomonian, Q. Chen, R. C. Haushalter, J. Zubieta and C. J. O'Connor, *Science*, 259 (1993) 1509.
6. T. Loiseau and G. Ferey, *J. Solid State Chem.*, 111 (1994) 416.

7. J. R. D. DeBord, W. M. Reiff, R. C. Haushalter, and J. Zubieta, *J. Solid State Chem.*, **125** (1996) 186.
8. J. R. D. DeBord, W. M. Reiff, C. J. Warren, R. C. Haushalter, and J. Zubieta, *Chem. Mater.*, **9** (1997) 1994.
9. D. M. Poojary, B. Zhang, and A. Clearfield, *J. Chem. Soc., Dalton Trans.* (1994) 2453.
10. D. Wang, R. Yu, N. Kumada, and N. Kinomura, *Chem. Mater.*, **12** (2000) 956.
11. P. Feng, X. Bu, G. D. Stucky, *Nature*, **388** (1997) 735.
12. D. M. Poojary, B. Zhang, and A. Clearfield, *J. Chem. Soc., Dalton Trans.*, (1994) 2453.
13. M. B. Hursthouse, K. M. A. Malik, J. M. Thomas, J. Chen, J. Xu, T. Song, and R. Xu, *Russ. Chem. Bull.*, **43** (1994) 1787.
14. E. Kemnitz, M. Wloka, S. Troyanov, and A. Stiewe, *Angew. Chem., Int. Ed. Engl.*, **35** (1996) 2677.
15. M. Wloka, S. I. Troyanov, and E. Kemnitz, *J. Solid State Chem.*, **135** (1998) 293-301.
16. H. H-Y. Sung, J. Yu, and I. D. Williams, *J. Solid State Chem.*, **140** (1998) 46-55.
17. M. E. Davies, C. Saldarriaga, C. Montes, J. Garces, and C. Crowder, *Nature*, **331** (1988) 698.
18. Q. Huo, R. Xu, S. Li, Z. Ma, J. M. Thomas, R. H. Jones, and A. M. Chippindale, *J. Chem. Soc., Chem. Commun.*, (1992) 875.
19. M. Estermann, L. B. McCusker, C. Baerlocher, A. Merrouche, and H. Kessler, *Nature*, **352** (1991) 25.
20. G. Yang, S. Feng, R. Xu, and J. Chen, *J. Chem. Soc., Chem. Common*, (1987) 1254.
21. A. M. Chippindale, S. J. Brech, A. R. Cowley, and W. M. Simpson, *Chem. Mater.*, **8** (1996) 2259.
22. T. Song, M. B. Hursthouse, J. Chen, J. Xu, K. M. A. Malik, R. H. Jones, R. Xu, and J. M. Thomas, *Adv. Mater.*, **69** (1994) 679.
23. J. Chen, R. H. Jones, S. Natarajan, M. B. Hurthhouse, and J. M. Thomas, *Angew. Chem. Int. Ed. Engl.*, **33** (1994) 6.
24. P. Feng, X. Bu, and G. D. Stucky, *Nature*, **388** (1997) 735.
25. A. M. Chippindale, S. Natarajan, and J. M. Thomas, *J. Solid State Chem.*, **111** (1994) 18.
26. Q. Gao, J. Chen, S. Li, R. Xu, J. M. Tomas, M. Light, and M. B. Hursthouse, *J. Solid State Chem.*, **127** (1996) 145.
27. A. Ono, Y. Yajima, *Bull. Chem. Soc. Jpn.*, **59** (1986) 2761.
28. A. Ono, *J. Mater. Sci. Lett.*, **4** (1985) 936.
29. I. D. Williams, J. Yu, Q. Gao, J. Chen, and R. Xu, *Chem. Commun.* (1997) 1273.

## POSTSYNTHESIS HYDROTHERMAL TREATMENT OF DOUBLE-MESOPORE SILICA MOLECULAR SIEVES IN WATER

X. Z. WANG<sup>a,b</sup> AND T. DOU

<sup>a</sup>*Institute of Special Chemicals, Taiyuan University of Technology, Taiyuan 030024, P. R. China*

*E-mail: wangxiaozhong@tyut.edu.cn*

B. ZHONG

<sup>b</sup>*State Key Laboratory of Coal Conversion, Institute of Coal Chemistry, the Chinese Academy of Sciences, Taiyuan 030001, P. R. China*

Double-mesopore silica (DMS) molecular sieves were synthesized with a mixture composed of tetraethylorthosilicate, ammonia, cetyltrimethylammonium bromide in water at room temperature, and the effect of postsynthesis hydrothermal treatment in water, which was used previously in mediating the pore size of MCM-41 mesoporous materials, on their mesoporous framework structure was assessed using different analytical techniques such as XRD,  $^{29}\text{Si}$  MAS NMR and  $\text{N}_2$  adsorptions. In comparison with the normal preparation, the sample undergoing low temperature water treatment exhibits a trend of higher long-range order and a promoted wall polymerization or local atomic arrangement. However, increasing water treatment temperature up to 423K, the structure transformation of DMS sample from double-mesopore to single mesopore occurs, resulting from the further condensation of surface silanol groups on the pore wall of larger secondary mesopores.

### 1 Introduction

The synthesis of inorganic frameworks with hierarchically structured pores, and an accurately controlled pore texture at different length scales is of potential importance in catalysis, separation technology and biomaterials engineering. Since the first synthesis of mesoporous MCM-41 materials [1,2], there has been intense activity in the design and synthesis of a variety of mesoporous solids with different structural features. At present, the surfactant-templated synthetic procedures have been extended to include a wide range of compositions, and a variety of conditions have been developed for exploiting the structure-directing functions of surfactant. In earlier investigations, we showed that careful controlling alkalinity affords a novel porous materials with well-defined double-mesopore size distribution at room temperature in a conventional system which used usually to prepared mesoporous MCM-41 materials [3,4]. The materials contain randomly distributed hexagonal and stripe-like mesoporous channels with uniform pore sizes and exhibit very large surface areas and pore volumes. So far, relatively little work has been reported for the pore size mediation of DMS silica mesostructures and no convincing mechanism for such specific mesostructural formation has been put forward. Undoubtedly, the ability to control framework double-mesopore distribution can be of great value in designing DMS materials as catalysts, adsorbents and sensor materials. Accordingly, in the present work we have examined the effect of the postsynthesis hydrothermal treatment in water, which was used previously in mediating the pore size of MCM-41 mesoporous materials [5,6] at different temperatures, on DMS silica mesoporous framework structure using different analytical techniques such as XRD,  $^{29}\text{Si}$  MAS NMR and  $\text{N}_2$  adsorptions, which allows us to obtain a better understand for the difference between DMS silicas and MCM-41 molecular sieves. At the same time we give a full account of the trend of pore structure variation of DMS materials and extend on our hitherto proposed formation mechanism.

## 2 Methods

### 2.1 Synthesis and postsynthesis hydrothermal treatment of DMS silicas

The synthesis procedure for DMS silicas was described elsewhere [3,4]. The postsynthesis hydrothermal treatment was carried out by replacing the mother liquor with pure water after the normal synthesis. Typically, the as-synthesized DMS silica was mixed with a certain amount of pure water, which was equivalent to about 20ml of water per gram of dried uncalcined samples, transferred into an autoclave, and kept in the oven maintained at 373K and 423K, respectively, for different periods of time. Finally, the solid product was filtered, washed, dried, and calcined as in the normal preparation.

### 2.2 Characterization

The powder X-ray diffraction patterns (XRD) were recorded using a D/max-2500 powder diffractometer with Cu-K $\alpha$  radiation (40kV, 100mA), 0.02° step size and 1 s step time over the range  $1^\circ < 2\theta < 8^\circ$ . The  $^{29}\text{Si}$  MAS NMR spectra were acquired at 79.4MHz with 90° radiofrequency pulses and 600s' recycle delays using a Bruker DRX-400 spectrometer and zirconia rotors 7.5mm in diameter spun in air at 4KHz. The chemical shifts are given in ppm from external tetramethylsilane.  $\text{N}_2$  adsorption isotherms were measured at -196°C using a ASAP2000 analyser. The volume of adsorbed  $\text{N}_2$  was normalized to standard temperature and pressure. Prior to the experiments, samples were dehydrated at 350°C for 12h. The pore-size distribution was calculated using the desorption branches of the  $\text{N}_2$  adsorption isotherm and the Barrett-Joyner-Halenda (BJH) formula.

## 3 Results and Discussion

### 3.1 XRD patterns

Figure 1 provides the representative X-ray powder diffraction patterns for the two series of samples typically treated in water at 373K and 423K, respectively, for 1 day, and at the same time makes a comparison with the normally synthesized and calcined DMS silicas sample. As can be seen in Figure 1, the normally synthesized DMS sample exhibits a single very low angle reflection, which seems to display less ordering in the mesostructure with a large unit-cell size. However, the water-treated DMS samples exhibit a more higher XRD intensities than that does normally prepared sample, and at the same time a clear shoulder peak was examined. This suggests that postsynthesis hydrothermal treatment can improve obviously the long-rang order of DMS silica mesostructure. Different from the water-treatment results of MCM-41 mesoporous materials treated in similar conditions [6], the interplanar spacing  $d_{100}$  (or unit cell  $a_0$ ) of water-treated DMS samples seems to be of the trend of shifting gradually toward higher  $2\theta$  angle (see Table 1). This may be concerned with the difference

**Table 1.** Characteristics of normally prepared and water-treated DMS silica samples.

sample	Water treatment	$a_0$ before calcined(Å)	$a_0$ after calcined(Å)	$\Delta a_0$
a	No	60.0	53.1	6.9
b	Yes	56.7	52.1	4.6
c	Yes	54.3	52.6	1.7

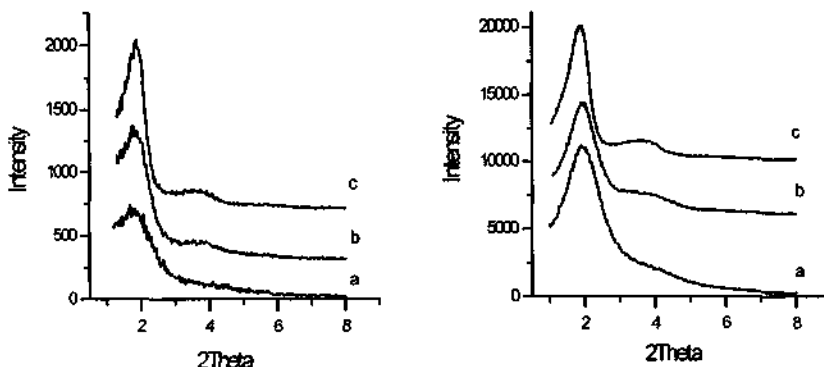


**Figure 1.** XRD patterns of as-synthesized (left) and calcined (right) double-mesopore silica samples for a normally prepared DMS silica (a) and postsynthesis hydrothermally treated at 373K (b) and 423K (c), respectively, for 1 day.

of framework mesostructure between MCM-41 and DMS silica materials.

There are no significant changes upon calcination, except for the expected increase in XRD peak intensity and lattice contraction due to the higher removal of the contrast-matching surfactant. This result may be consistent with the retention of the framework double-mesopore structure upon complete removal of the surfactant from the framework. However, one significant difference between the uncalcined DMS silicas obtained by a normal synthesis and a water treatment is the extent of the unit cell shrinkage during calcination (see table 1). It was found that the water-treated sample showed much less shrinkage upon calcination. For example, the shrinkage of  $a_0$  was 11.5% for the as-synthesized sample at room temperature in its mother liquor, while it was only 8.1% and 3.1% for the as-synthesized sample and then treated in water at 373K and 423K, respectively, for 1 day and calcined at 823K in air for 6 h. It is reasonable to suggest that the less shrinkage of the unit cell for the water-treated sample is as a result of better wall polymerization.

### 3.2 $N_2$ adsorptions

Important trends of double-mesopore structural development resulting from the water-treatment are revealed in Figure 2 by the  $N_2$  adsorption-desorption isotherms and the corresponding BJH pore size distribution based on the desorption branch for the representative samples mentioned above. The isotherm of the normally synthesized DMS simple shows a typical irreversible type IV adsorption isotherm with two separate, well-expressed H1 hysteresis loops as defined by IUPAC at relative pressures  $p/p_0$  of 0.2-0.45 and that of 0.8-1.0, respectively. The first condensation step on the isotherm at  $p/p_0=0.2-0.45$  is similar to that for usual MCM-41 materials, however, obviously, this inflection at higher relative pressures differs completely from that of previously-synthesized mesoporous materials in the aspect of their effects on the mesoporous frameworks of the product, namely, this material is of a clear double mesopore size distribution. After 1 day of postsynthesis hydrothermal treatment, the properties of the samples changed dramatically. Compared with the normally synthesized DMS sample, the water-treated sample at 373K shows more steep adsorption steps at 0.25-0.4 $p/p_0$  and 0.8-1.0 $p/p_0$ , respectively, suggesting that double-

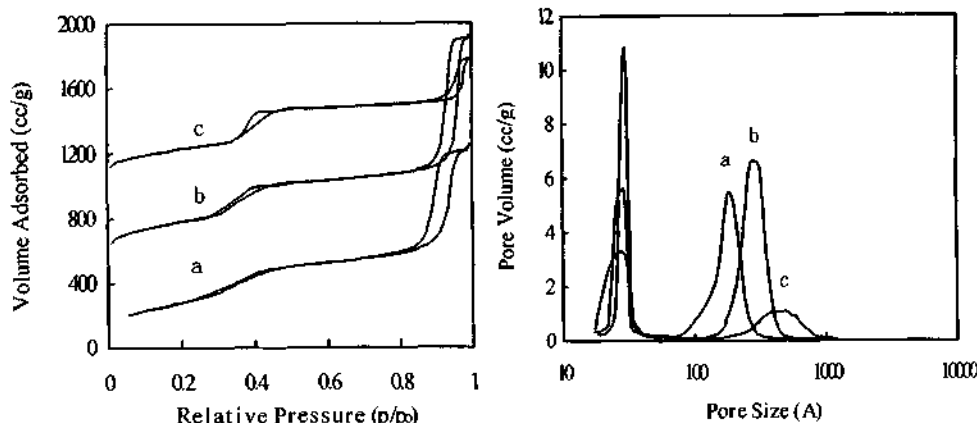


**Figure 2.** N<sub>2</sub> adsorption-desorption isotherms and corresponding pore size distribution of the normally synthesized (a) and water-treated DMS samples after a total of 1 day treatment at 373K (b) or 423K (c).

mesopore size distribution of DMS sample becomes more narrower. At the same time the two adsorption steps shift gradually toward higher relative pressure, indicating that water-treatment results in a concurrent increase of the primary mesopore size and its secondary mesopore size, the both mesopore volume increased to 0.68cm<sup>3</sup>/g and 1.45cm<sup>3</sup>/g, while the BET surface area decreased to 1018.7m<sup>2</sup>/g and 212.7m<sup>2</sup>/g, respectively (see Table 2). However, the development of DMS mesostructure are even more pronounced if the water-treated temperature is increased from 373K to 423K. Though the adsorption step at lower relative pressure becomes even more steeper and shifts toward even more high relative pressure, indicating that the primary mesopore size further increases and becomes more narrower than that of normally synthesized and water-treated samples at lower temperature, one may notice that secondary mesopore size distribution tends to become disappearance only after 1 day water treatment at 423K. This may indicate that increasing water-treatment temperature can lead to further condensation of surface silanol groups on the pore wall of larger secondary mesopore to form smaller primary mesopore.

### 3.3 <sup>29</sup>Si MAS NMR

To further examine the effect of the postsynthesis hydrothermal treatment on the extent of double-mesopore framework cross-linking, we employed the <sup>29</sup>Si MAS NMR. It can be seen from Figure 3 that the Q4 (Si(OSi)<sub>4</sub>) to Q3 (Si(OSi)<sub>3</sub>(OH)) ratio of the water-treated (at 373K) uncalcined DMS is higher than that of the normally prepared one. The high portion of

**Table 2.** Effect of a water treatment (b-373K and c-423K, 24h) on the characteristics of DMS silicas

sample	Water treatment	unit cell a <sub>0</sub> (Å)	Primary mesopore			Secondary mesopore		
			A <sub>BET</sub> m <sup>2</sup> /g	pore size (Å)	pore volume (cm <sup>3</sup> /g)	A <sub>BET</sub> m <sup>2</sup> /g	pore size (Å)	pore volume (cm <sup>3</sup> /g)
a	no	53.1	1064.6	26.1	0.66	243.1	189	1.18
b	yes	52.1	1018.7	29.8	0.68	212.7	274	1.45
c	yes	52.6	978.6	30.0	0.72	\	\	\

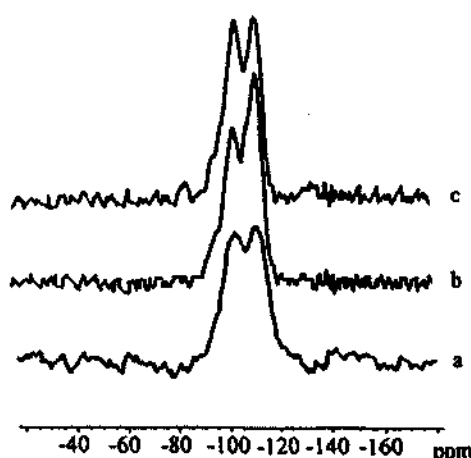


**Figure 3.**  $^{29}\text{Si}$  MAS NMR spectra of normally prepared DMS silica (a) and water-treated uncalcined samples at 373K (b) and 423K (c), respectively, for 1 day.

Q4 in the water-treated DMS sample is an indication of a high degree of polymerization of the silicate wall or a better local atomic arrangement. However, for the DMS sample treated in water at higher temperature such as 423K, the ratio of Q4/Q3 do not variety obviously compared with the normally synthesized DMS sample. This may be concerned with the different trend of mesostructural development resulting from the difference of water-treated temperature, *i.e.* the water treatment at higher temperature may mainly result in the framework mesostructural transformation from double-mesopore structure to single mesopore structure, and its effect on the condensation degree of framework is not evident. The detailed reason is not still very distinct and further studies are needed to fully understanding the nature of the observed phenomena.

Further experimental results show that the effects of lengthening water treatment time such as 373K for 10 days and 423K for 5 days, respectively, on double-mesopore structure is not essential, in other words, it is that water treated temperature but time is crucial for double-mesopore structural development. In a typical synthesis of DMS silica under our conditions, the pH of the initial synthesis gel mixture was *ca.* 9.5 and the synthesis process was completed in a very short time (*ca.* 7-10min). In such a short reaction time, the surfactant micelles formed in the initial reaction mixtures may possess different size and shape, and the hydrolysis of TEOS and the condensation of the hydrolyzed products are incomplete, and thus the hydrolyzed  $\text{SiO}_2$  species are not enough to condense around every surfactant micelle. This may make some adjacent surfactant micelle interconnect and lead to the formation of mesopore framework of alternating hexagonal pore and stripe-like pore. When the mother liquor was replaced with water, the pH of the resulting mixture was in the range 7-8 depending upon the amount water added. It has been known that a low pH is favorable for the condensation of silanol groups. The returning of the synthesis gel to a pH lower than 9 favors the condensation of silanols and the redeposition of silicate anions[7]. Possibly the as-synthesized material with defective anionic sites and terminal silanol groups restructured toward a higher polymerization to form more  $\text{Si}(\text{OSi})_4$  bonds at a lower pH[6]. The promoted condensation of silanols leads to a higher order of local atomic arrangement. Hence, it is inferred that the lowering of the pH by the replacement of the mother liquor with

water is responsible for the better polymerization of the silicate wall.

#### 4 Conclusions

The present study demonstrates that the postsynthesis hydrothermal treatment method reported by Huo *et al* [5] is a convenient way to improve the quality not only of MCM-41 mesoporous materials but also of our DMS silicas. However, different from the conventional MCM-41 mesoporous materials, the double-mesopore structure of our DMS silica is extremely sensitive to the water treatment temperature but not to the water treatment time. For example, at lower water treatment temperature (e.g., 373K) for short or long periods of time (e.g., 1 day to 10 days), the sample of DMS obtained in this way shows more highly crystalline (a more narrower main peak and a clear shoulder peak were examined), has more large pore sizes, big pore volumes, and has a small unit cell shrinkage on calcination, but a slight decrease in surface area. In contrast, the water-treated sample at higher temperature (e.g., 423K) for even short periods of time (e.g., 1 day) shows the mesostructure transformation from double-mesopore structure to a single mesopore structure, resulting from the further condensation of surface silanol groups on the pore wall of larger secondary mesopore.

#### 5 Acknowledgement

This research was supported by the National Natural Science Foundation of China (Grant No.20073029).

#### References

1. Kresge C. T., LeonowiczM. E., Roth W. J., Vartuli J. C. and Beck J. S., Ordered mesoporous molecular sieves synthesized by a liquid-crystal template mechanism, *Nature*, **359** (1992) pp.710-712.
2. Beck J. S., Vartuli J. C., Roth W. J., Leonowicz M. E., Kresge C. T., Schmitt K.D., Chu C. T. W., Olson D. H., Sheppard E. W., McCullen S. B., Higgins J. B. and Schlenkere J. L., A new family of mesoporous molecular sieves prepared with liquid crystal templates, *J. Am. Chem. Soc.*, **114** (1992) pp.10834-10843.
3. Wang X. Z., Dou T. and Xiao Y. Z., Synthesis of double-mesopore silica using aqueous ammonia as catalyst, *Chem.Commun.*, 1998 pp.1035-1036.
4. Wang X. Z., Dou T., Xiao Y. Z. and Zhong B., Formation of double-mesopore silica and its transformation into MCM-41, *Stud. Surf. Sci. Catal.*, **135** (2001) pp.199.
5. Huo Q., Margolese D. I. and Stucky G. D., Surfactant control of phases in the synthesis of mesoporous silica-based materials, *Chem. Mater.*, **8** (1996) pp.1147-1160.
6. Chen L., Horiuchi T., Mori T. and Maeda K., Postsynthesis hydrothermal restructuring of M41S mesoporous molecular sieves in water, *J. Phys. Chem. B*, **103**(1999) pp.1216-1232.
7. Iler R.K., *The Chemistry of Silica*, Wiley: New York, 1979.

## HYDROTHERMAL SYNTHESIS AND CHARACTERIZATION OF ZEOLITE-LIKE CRYSTAL MATERIAL CAS-1

CHUN FENG XUE, GUANGHUA LIU, JINPING LI AND JINXIANG DONG

*Research Institute of Special Chemicals, Taiyuan University of Technology,*

*79 Yingze West Street, Taiyuan 030024, Shanxi, P. R. China*

*E-mail: jxdong@public.ty.sx.cn*

The calcosilicate zeolite-like crystal material CAS-1 was hydrothermally synthesized and the thermal stability of the samples were investigated. The effects of composition of raw materials, reaction temperature and alkali metals on the synthesis of CAS-1 were addressed. Cation exchange reactions and their influences on the thermal stability of CAS-1 framework structure were also studied. The samples were characterized by XRD, TEM, SEM, DT-TGA, AAS and chemical analysis. The results showed that CAS-1 could be obtained from a wide range of composition of raw materials and reaction conditions. The cations have great influence on the thermal stability of the CAS-1 framework structure.

### 1 Introduction

Zeolites have increasingly found applications as catalysts, adsorbents and ion exchangers [1]. Their microporous properties of the inorganic host-guest systems are based primarily on the structure of the tetrahedral framework built from the  $\text{TO}_4$  tetrahedral and the possible variation of T atoms (Si, Al, P, Zr, Sn, Ti, Ga, B, etc.). The guest species such as organic and/or inorganic cations fill the pore space of the framework to achieve electroneutrality.

The preparation of zeolite molecular sieves with substitutions of Al and/or Si by the other tri- or tetravalent elements in the tetrahedral positions (T) is an active research subject. In addition to synthesizing unknown zeolites with new chemical compositions, the presence of heteroatoms in the synthesis mixture plays an important role in the forming of new topologies. However, the frameworks of molecular sieves containing the divalent heteroatoms are rare. Although the synthesis of new materials by silicate sols containing heteroatoms has been confirmed with the divalent heteroatoms  $\text{Zn}^{2+}$  and  $\text{Be}^{2+}$ , the reports on the research of divalent heteroatoms acting as the molecular sieve framework should be accelerated. Among the zeolite minerals the berylliosilicate lovdarite [2] is of particular interest because its structure contains the spiro-5 building unit built from three-membered rings, which occur only very rarely in tetrahedral framework. But the many beryllium compounds are highly toxic and thus make them undesirable thing to work with. Brunner and Meier showed that there is a correlation between the minimum ring size in a framework topology and the framework density [3]. They suggested that synthesis tailored to produce three-rings might produce very open framework structures. As all to known, the more large pore volume zeolite frameworks are more benefit to expose catalytically active centers and adsorb molecular to participate in the reactions and alleviate the jug of the pore opening so that prolong the life-span of catalyst. In 1991, the zincosilicate molecular sieve VPI-7 was hydrothermally synthesized from the silicate sols containing the heteroatom zinc [4]. And its framework also contains three-membered ring units just as that of berylliosilicate lovdarite. After that, a series of zincosilicate synthesis including the molecular sieve

VPI-8 [5], VPI-9 [6], VPI-10 [7], RUB-17 [8] and Zn-SOD [9] were reported. From the previous report on the hydrothermal synthesis of microporous zincosilicate molecular sieves, it could be found that the inorganic cation is the main factor determining the nature of the phase formed.

In the attempt to synthesize molecular sieves with isomorphous substitutions of Al and/or Si by the divalent calcium element in the tetrahedral positions, we obtained a new calcium silicate phase by inclusion of heteroatom calcium into silicate sols. The characterization results showed that as-synthesized calcium silicate, named CAS-1 (Calcium silicate No. 1), was a novel zeolite-like crystal material with the cation reversibly exchangeable and selectively adsorptive properties. In this paper, the effects of composition of raw materials, reaction temperature and the different alkali ion on the hydrothermal synthesis of calcosilicate crystal material CAS-1 were investigated and the uptake of different cation on the thermal stability of CAS-1 structure was also examined. The sample was characterized by XRD, TEM, SEM, DT-TGA, BET, AAS and chemical analysis.

## 2 Experimental

### 2.1 Synthesis

In our experiments, the reagents used were the following: calcium nitrate tetrahydrate,  $\text{Ca}(\text{NO}_3)_2 \cdot 4\text{H}_2\text{O}$  ( $\geq 96\text{wt\%}$ , Beijing Hongxin Chemical Factory), colloidal silica,  $\text{SiO}_2$  (6.05mol /L *aq.* solution, Qingdao Chemical Factory), potassium hydroxide, KOH ( $\geq 82\text{wt\%}$ , Beijing Chemical Factory), sodium hydroxide, NaOH ( $\geq 95\text{wt\%}$ , Beijing Chemical Factory), lithium hydroxide, LiOH ( $\geq 90\text{wt\%}$ , Beijing Chemical Factory), tetraethylammonium hydroxide, TEAOH ( $\geq 25\text{wt\%}$  *aq.* solution, China National Medicine Group Shanghai Corporation), tetramethylammonium hydroxide, TMAOH ( $\geq 25\text{wt\%}$  *aq.* solution, China National Medicine Group Shanghai Corporation), tetraethylammonium bromide, TEABr ( $\geq 98\text{wt\%}$ , Beijing Xingfu Special Chemical Research Department), tetramethylammonium bromide, TMABr ( $\geq 98\text{wt\%}$ , Beijing Xingfu Special Chemical Research Department) and n-butylamine,  $\text{BuNH}_2$  ( $\geq 99.5\text{wt\%}$ , China National Medicine Group Shanghai Corporation).

In a typical synthesis, distilled water, calcium nitrate tetrahydrate, colloidal silica, potassium hydroxide and tetraethylammonium hydroxide were added as a recipe of 0.2TEAOH: 0.3K<sub>2</sub>O: 0.15CaO: SiO<sub>2</sub>: 30H<sub>2</sub>O in turn and stirred using a stainless muddler at room temperature for half an hour. The resulting homogeneous sol was sealed in a Teflon-lined stainless autoclave and held at 493K for ten days in a convection oven. The solid product was separated by centrifuge, washed with distilled water for six times and dried in air at around 373K.

### 2.2 Analysis

The X-ray powder diffraction patterns (XRD) were obtained on a Rigaku D/Max 2500 diffractometer fitted with a fine-focus copper X-ray tube and operated at 100kV and 40mA, respectively. The relative crystallization intensity (RCI) of CAS-1 was calculated following the procedures: the five XRD diffraction peaks of the sample

(see the typical experiment) at  $2\theta=7.38, 14.76, 27.24, 29.72, 30.58$  were selected as reference peaks, and the summation of their intensities was considered as a reference. The ratio of the summation of the other sample to the reference was the RCI.

The transmission electron microscopy (TEM) images were acquired using a Phillips CM200FEG microscope operated at 100kV. The scanning electron microscopy (SEM) photograph was obtained on a JEOL, JSM-35C microscope operated at 25kV.

Thermogravimetric analysis (TGA) and differential thermal analysis (DTA) were performed in air at a heating rate of 10K/min. on a PTC-10A thermogravimetric analyzer. The adsorption isotherms for vapor-phase water and ethanol were measured using the BET method. The saturation pressures,  $P_0$ , of water and ethanol at 299K are 758 mmHg. Prior to the adsorption experiments, the samples were dehydrated at 673K in air for 4 h.

Chemical analysis was carried out as following: the content of Si was analyzed by the gravitational method and that of Ca was measured by volume method. The atomic absorption spectrophotometer (AAS) is for the analysis of K and Na.

The cation exchange reactions were conducted by following the procedure: 3g of the CAS-1 were equilibrated in the beaker with 100 ml chloride solution of  $\text{Na}^+$ ,  $\text{K}^+$ ,  $\text{NH}_4^+$  or  $\text{Mg}^{2+}$  of 1 mol/L. The concentration of  $\text{Mg}^{2+}$  aqueous solution was 0.5 mol/L. With continual stirring, the reactions were carried out at 298K for 1 h. The process was repeated for six times. Finally, the samples were washed with the distilled water to remove the excess of  $\text{Cl}^-$  and dried in air at around 373K. And the filtrates were analyzed for  $\text{Cl}^-$  by the 0.1 mol/L  $\text{AgNO}_3$  aqueous solution.

### 3. Results

#### 3.1 Synthesis

The calcosilicate zeolite-like crystal material CAS-1 could be hydrothermally synthesized using a very wide range of synthetic conditions (Table 1). These reaction conditions include the use of five organic additives of different sizes and shape, as well as a broad range of Si/Ca ratios (4-20) and a range of crystallization temperatures (423-493K). However, the range of Si/Ca of initial sols for synthesizing CAS-1 is influenced because of the addition of the different organics at 493K. CAS-1 could be obtained from the initial gel with the range of Si/Ca from 4 to 20 when using TEAOH; the range of Si/Ca from 4 to 10 for using TMAOH; the range of Si/Ca from 4 to 8 for using TMABr; the range of Si/Ca from 6 to 8 for using or without using  $\text{ButNH}_2$ . Although CAS-1 could be obtained when using the alkali NaOH, its crystallization intensity is very poor. We could only obtain the quartz when using alkali LiOH. And CAS-1 with different crystallization intensity could also be obtained over a wide range of temperature for different reaction time.

**Table 1.** Representative synthesis conditions for the crystallization of CAS-1.

a. Synthesis with different organic, composition: 0.8KOH : 0.4R : 0.15Ca(NO<sub>3</sub>)<sub>2</sub>·4H<sub>2</sub>O : SiO<sub>2</sub> : wH<sub>2</sub>O

R	W	Temperature (K)	Time (days)	Phase
TEAOH	40	493	8	CAS-1
TMAOH	40	493	8	CAS-1
TEABr	30	473	10	CAS-1
TMABr	30	473	10	CAS-1
ButNH <sub>2</sub>	30	493	10	CAS-1
Without	30	493	15	CAS-1
ButNH <sub>2</sub>	30	423	30	CAS-1

b. Synthesis with TEAOH, 493K, composition: mMOH : rTEAOH : z Ca(NO<sub>3</sub>)<sub>2</sub>·4H<sub>2</sub>O : SiO<sub>2</sub> : wH<sub>2</sub>O.

M	m	r	z	w	Time (days)	Phase
K	0.6	0	0.1	30	10	CAS-1
K	0.8	0	0.2	30	10	Amorphous
K	0.8	0.4	0.2	30	10	CAS-1
K	0.2	0.2	0.05	30	5*	CAS-1
K	0.9	0.4	0.25	30	10	CAS-1
Na	0.8	0.4	0.15	30	10	CAS-1
Li	0.8	0.4	0.15	30	10	Quartz

- Reaction temperature is 453K.

### 3.2 Characterization

The XRD patterns of calcosilicate zeolite-like crystal material CAS-1 have been indexed (Figure 1). The sample has very fine crystallization intensity. The data of XRD data for CAS-1 was also indexed in Table 2. The data showed that the product CAS-1 may be a crystal material with new topology structure.

As-synthesized CAS-1 can be calcined in air to 873K for an hour in order to remove the organics possibly occluded within the pores during synthesis. But during and after calcination, the sample is always white and hardly any structure collapse is detected by XRD. TGA of calcined and rehydrated sample shows that the as-synthesized CAS-1 loses weight only up to 533–583K. This weight loss is not analogous to that of organic-containing zeolites and molecular sieves. The TGA data can be used to calculate the amount of water occluded in CAS-1 and conclude the organics were not occluded within the pores of CAS-1 during synthesis, by considering that the organic additive should remain at temperatures above 583K. This water loss is up to 11.2wt% and reversible. However, it was not possible to record a nitrogen or ethanol adsorption isotherm of CAS-1 probably because its pores are smaller than the kinetic diameter of nitrogen and ethanol. The maximum uptake of the BET surface area of CAS-1 measured at water adsorption was 11.1wt%.

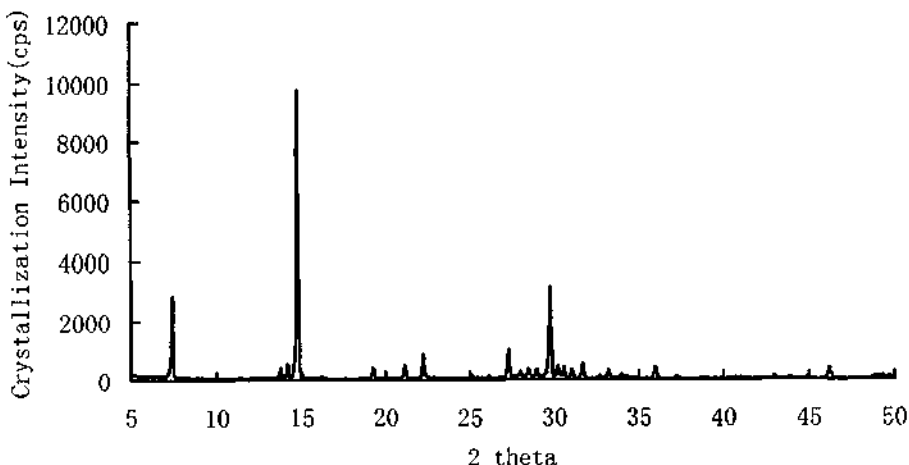


**Figure 1.** X-ray powder diffraction pattern of K-CAS-1.

**Table 2.** The XRD data for K-CAS-1.

Peak No.	2theta	d-value	I/I <sub>0</sub>	Peak No.	2theta	d-value	I/I <sub>0</sub>
1	7.38	11.968	25	13	28.94	3.0827	5
2	14.16	6.2495	7	14	29.72	3.0035	36
3	14.76	5.9968	100	15	30.58	2.9210	23
4	19.24	4.6093	6	16	31.06	2.8769	7
5	21.10	4.2070	7	17	31.66	2.8238	9
6	22.20	4.0010	9	18	32.66	2.7396	2
7	22.80	3.8971	4	19	33.18	2.6978	6
8	25.06	3.5505	4	20	35.96	2.4954	8
9	26.14	3.4062	5	21	37.20	2.4154	2
10	27.24	3.2711	15	22	41.04	2.1974	2
11	27.98	3.1862	3	23	42.94	2.1045	3
12	28.48	3.1314	13	24	46.16	1.9649	7

From the SEM's of the as-synthesized CAS-1 indexed in Figure 2, it is noticed that the synthesis products are long sticks of long platelike crystals. Figure 3 shows the TEM images for CAS-1. As with the adsorption data mentioned above, the micrograph clearly suggests that CAS-1 possesses a 1-dimensional small pore channel system. Based on the water adsorption measurement and TEM image result, it can be classified as a microporous material. It is analogous to AV-6 shown to adsorb water but not nitrogen [10].

Chemical analysis and AAS data of well crystalline, pure forms of CAS-1, K-CAS-1 and Na-CAS-1 were summarized in the Table 2. The Ca and Si had incorporated in the framework of CAS-1 because they were unexchangeable during the cation exchange reaction. But the K and Na cations present in the as-synthesized CAS-1 are reversibly exchangeable, like in other molecular sieves, for such cations as Li<sup>+</sup>, Na<sup>+</sup> or NH<sub>4</sub><sup>+</sup>. The Na<sup>+</sup> present in the as-synthesized CAS-1 is introduced by the addition of the colloidal silica.



**Figure 2.** Scanning electron micrograph of CAS-1.

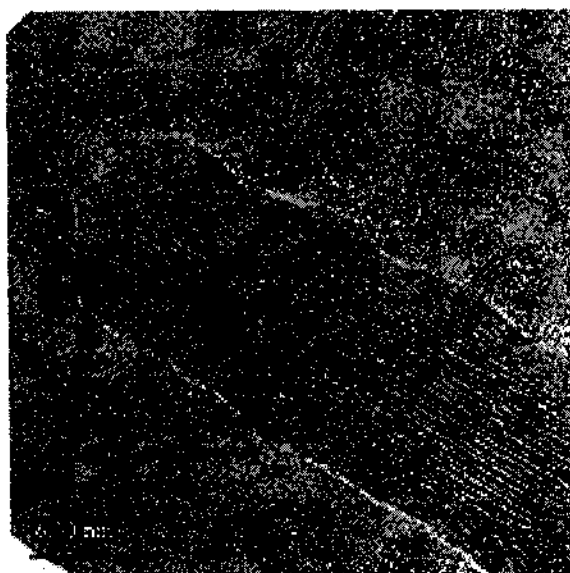


**Figure 3.** Transmission electron micrograph of CAS-1.

**Table 3.** Chemical analysis results of CAS-1.

Samples (molar ratio)	SiO <sub>2</sub> /CaO	K <sup>+</sup> /CaO	Na <sup>+</sup> /CaO
CAS-1	4.86	1.0851	0.1357
Na-CAS-1	4.86	0.3727	0.8485
K-CAS-1*	4.87	1.0911	0.1219

\*The sample was exchanged with NaCl aqueous solution first and then re-exchanged with a KCl solution.

The as-synthesized CAS-1 and cation-exchanged samples were calcined at 673K and 873K for 4 h, respectively. The structural collapse of the samples was investigated by the XRD technique. The thermal stability of the samples was estimated by comparing their RCI. The RCI of samples uncalcined and calcined at 673K and 873K were summarized in Table 3. The XRD patterns reveal the difference of the thermal stability between the samples. The thermal stability of the K-CAS-1 was the strongest one and that of the NH<sub>4</sub>-CAS-1 was the poorest one among the five samples. However, a calcination at 673K for 4 h for NH<sub>4</sub>-CAS-1 provokes the transformation of CAS-1.

**Table 4.** RCI of samples calcined at 673K and 873K.

Samples	CAS-1	Na-CAS-1	K-CAS-1*	NH <sub>4</sub> -CAS-1	Mg-CAS-1
Exchanged	100%	100%	100%	100%	100%
673K	95%	75%	100%	Transformed	87%
873K	48%	1%	79.1%	Amorphous	23%

\*The sample was exchanged with NaCl aqueous solution firstly; then re-exchanged with KCl one.

#### 4. Discussion

CAS-1 with very high crystallinity can be prepared by numerous methods over a wide range of Si/Ca ratios. Since CAS-1 could be obtained with or without TEAOH, TMAOH, TEABr, TMABr or ButNH<sub>2</sub> that have differences in size and shape, the organics must not play a template agent, or even a structure-directing role on the crystallization of CAS-1. Most likely, the addition of all the organics serve only to speed the rate of crystallization and they are incorporated into the product CAS-1. Different alkali metals have critical influence on the synthesis of CAS-1. The absence of KOH allows the crystallization of very poorly crystalline CAS-1 or quartz. KOH plays an important role in the formation and thermal stability of CAS-1.

The difference in thermal stability between framework structures of different samples indicated that CAS-1 had the capability of reversible ion exchange and the cations greatly influenced the thermal stability of CAS-1. The thermal stability of K-CAS-1, which were obtained from Na-CAS-1 equilibrated with KCl, is much stronger than that of Na-CAS-1. At the same time, the fact that the thermal stability of the as-synthesized CAS-1 between that of Na-CAS-1 and K-CAS-1 reveals the presence of Na<sup>+</sup> in the as-synthesized CAS-1. And the results well correspond to those from the chemical analysis, suggesting that the as-synthesized CAS-1 contains Na<sup>+</sup> cations introduced by the addition of colloidal silica.

#### 5. Conclusion

CAS-1 is the first microporous calcosilicate zeolite-like crystal material and can be easily synthesized with or without organics. The reversible cation-exchangeability and the selectively adsorptive properties of CAS-1 are analogous to those for zeolites and molecular sieves. CAS-1 can withstand high temperature calcination indicating that it has a good thermal stability that is common for zeolites.

## 6. Additional Note

We have found that CAS-1 exhibits catalytic activity in the preparation of polyethylene nanometer composite material and the details will be presented elsewhere.

## 7. Acknowledgements

We thank Prof. Jianhua Zhu for the measurement of water and ethanol adsorption. We thank Dr. Qing Chen for his assistance in the TEM data collection. And we also thank Prof. Fengshou Xiao for his constructive advice on structure discussion.

## References

1. Davis M. E. and Lobo R. L., Zeolite and molecular sieve synthesis., *Chem. Mater.*, **4** (1992) pp. 756–768.
2. Merlin S., Lovdarite,  $K_4Na_{12}(Be_{28}O_{72})\cdot 18H_2O$ , a zeolite-like mineral structural features and OD character., *Eur. J. Miner.*, **2** (1990) pp. 809–817.
3. Brunner G.O. and Meier W.M., Framework density distribution of zeolite-type tetrahedral nets., *Nature*, **337** (1989) pp. 146–147.
4. Annen M.J., Davis M. E., Higgins J. B. and Schlenker J. L., VPI-7: the first zirconosilicate molecular sieve containing three-membered T-atom rings., *J. Chem. Soc. Chem. Commun.*, (1991) pp. 1175–1176.
5. Camblor M. A., Yoshikawa M., Zones S. I. and Davis M. E., Synthesis of VPI-8: the first large pore zirconosilicate., *Synthesis of Porous Mater.*, **69** (1997) pp. 243–261.
6. Annen M. J. and Davis M. E., Raman and  $^{29}Si$  MAS NMR spectroscopy of framework materials containing three-membered rings., *Microporous Mater.*, **1** (1993) pp. 57–65.
7. Camblor M. A. and Davis M. E.,  $^{29}Si$  MAS NMR spectroscopy of tectozirconosilicates., *J. Phys. Chem.*, **98** (1994) pp. 13151–13156.
8. Röhrig C. and Gies H., A new zirconosilicate zeolite with nine-ring channels., *Angew. Chem. Int. Ed. Engl.*, **34** (1995) pp. 63–65.
9. Camblor M. A., Lobo R. L., Koller H. and Davis M. E., Synthesis and characterization of zirconosilicate with the SOD topology., *Chem. Mater.*, **6** (1994) pp. 2193–2199.
10. Lin Z., Rocha J. and Valente A. Synthesis and characterization of a framework microporous stanosilicate., *Chem. Commun.*, (1999) pp. 2489–2490.

# THE SYNTHESIS AND THERMAL STABILITY STUDY OF MESOPOROUS CERIUM (IV) OXIDE POWDERS

RU YANG, JIANHONG LIU, MIN LI AND CAIXIA YAN

*The Key Laboratory of Science and Technology of Controllable Chemical Reactions, BUCT,  
Ministry of Education, Beijing 100029, People's Republic of China  
E-mail: yangru@public.bta.net.cn*

Mesoporous cerium (IV) oxides with high surface area and crystalline pore wall of cubic crystal structure were synthesized. The material has been characterized by small and large angle X-ray diffraction (XRD), nitrogen physisorption and high-resolution transmission electron microscopy (HRTEM). XRD patterns show that an intense peak at low angle ( $2\theta < 10^\circ$ ) and at the same time the special diffraction peak of  $\text{CeO}_2$  with the cubic fluorite structure at wider angle ( $2\theta > 10^\circ$ ) could be observed. HRTEM images show no ordered stacking of the pores but some spongy image. After the samples were calcined at 873K for 3h, the surfactant was removed and the low angle diffraction peak still existed. When the temperature rose to 1083K, the crystal of  $\text{CeO}_2$  rapidly grew up and the mesoporous structure collapsed. Adsorption analysis showed that the isotherm of the  $\text{CeO}_2$  powder is of type IV according to the IUPAC classification. After calcined at 873K, the mesopore structure changes from type H<sub>2</sub> to H<sub>1</sub>.

## I Introduction

In recent years ordered mesoporous materials have attracted great attention [1] for their interesting property [2] and these materials have numerous potential applications in many fields such as separation, catalysis, and biomaterial engineering [3,4]. Much interest is being focused on the preparation of transition-metal oxides using several templating pathways besides silica-based materials.

For chemical processes requiring heterogeneous catalysts a high density of surface exposed active sites in a given reactor volume is desirable. This can be achieved by using porous materials, either as catalysts or as supports for small clusters of a catalytic material. For catalytic processes with large molecules, the pore dimensions are of interest; in particular, for liquid phase catalysis multidimensional pore with diameters exceeding 2.0nm may be required.

$\text{CeO}_2$  is an important functional material, exhibiting special catalysis activity and selectivity. Earlier study on  $\text{CeO}_2$  oxide revealed that the material shows enhanced redox and oxygen storage properties [5], improved thermal resistance and better catalytic activity at lower temperature [6]. Cerium (IV) oxide with a mesostructure may provide a good catalyst support for well-dispersed and stable metal particles upon calcination and reduction. Several approaches have been suggested to synthesize the mesostructured surfactant oxide composites. In some cases a regular pore structure was retained even after template removal [7], while the majority suffered from collapse during the high temperature calcination. It was assumed that the existence of several relatively stable oxidation states of the metal centers results in oxidation and/or reduction during calcination [8]. Mesoporous structures prepared from nonionic surfactant as template have relatively thicker pore wall and can improve the thermal and hydrothermal stability of mesoporous framework. However, the ability of self-assembling of most a nonionic surfactant is worse than an ionic surfactant. In this paper, we report a precipitation method using polyethylene glycol (PEG) and  $(\text{CH}_3\text{CH}_2)_3\text{N}$  as double templates for the preparation

of mesoporous CeO<sub>2</sub> with cubic fluorite structure.

## 2 Experimental

### 2.1 Sample preparation

In this experiment, mesoporous cerium (IV) oxide was synthesized by employing polyethylene glycol PEG and cationic surfactant (CH<sub>3</sub>CH<sub>2</sub>)<sub>3</sub>N as templates. The molecular weights of PEG are 600, 6000, and 19000, respectively. The composition corresponding to a molar ratio of 1Ce: 2(CH<sub>3</sub>CH<sub>2</sub>)<sub>3</sub>N was prepared by adding the (CH<sub>3</sub>CH<sub>2</sub>)<sub>3</sub>N to Ce(SO<sub>4</sub>)<sub>2</sub> solution. In a typical synthesis, 4g PEG-6000 was dissolved in the 0.2M Ce(SO<sub>4</sub>)<sub>2</sub> solution. To the solution, 14ml (CH<sub>3</sub>CH<sub>2</sub>)<sub>3</sub>N (0.1mol) was added, and the mixture was stirred for 5min. An orange, clear solution was obtained. After the temperature rose to 353K, 31mL amine solution of 25% mass concentration was dropped under intense stirring. Immediately, a large gray matter appeared and became straw yellow after a while. When the reaction was over, stirring was continued for another one hour. Then the precipitate was allowed to age for 12h. The solid prepared was separated by centrifuging and was washed with deionized water and anhydrous ethanol, and then air-dried at room temperature.

### 2.2 Characterization

Powder X-ray diffraction (XRD) patterns of the samples were recorded on a Rigaku Rotoflex Dmaxa X-ray diffractometer using CuK $\alpha$  radiation.

HRTEM images were obtained on a Jeol JEM2010 ultra high-resolution analytical electron microscope equipped with an emission cathode operated at 200KV in bright field mode. The samples were examined with a magnification of 400,000. The ex situ treated samples were supported holey carbon coated copper grids for the experiment.

Nitrogen adsorption-desorption isotherms were used to determine the BET surface areas of the samples using a sorption analyzer AUTOSORB-1 (manufacturer: American Quantachrome Corporation). The total pore volume of the materials and mesopore size distribution were also determined.

## 3 Results and Discussion

### 3.1 Mesoporous CeO<sub>2</sub> with crystalline framework

Table 1 shows the various reactants and their dosages for each sample. In the preparation course, two surfactants of (CH<sub>3</sub>CH<sub>2</sub>)<sub>3</sub>N and PEG were used as template, and the sample was named CPN-X (X=1, 2, 3; the corresponding PEG molecular weight is 600, 6000, 19000). If only one template, PEG or (CH<sub>3</sub>CH<sub>2</sub>)<sub>3</sub>N, was employed, the samples was named CP and CN respectively, and the synthesis conditions are summarized in Table 1. Figure 1 shows the X-ray diffraction patterns of the samples. In the XRD patterns of CN and CPN-2 a single intense peak at a low angle, characteristic of a mesophase with a pore system lacking long-range ordering [9], can be observed. But this low-angle peak does not exist in the pattern of CP. Therefore, it may be concluded that not PEG, but (CH<sub>3</sub>CH<sub>2</sub>)<sub>3</sub>N is the essential species for the mesoporous CeO<sub>2</sub>. In the higher angle XRD pattern, shown in Fig. 1b, the special diffraction peak of CeO<sub>2</sub> with the cubic fluorite structure can be

observed. It means that not only mesoporous structure but also crystal character exist in the CeO<sub>2</sub> powders prepared. It can be attributed to the accelerating reaction of hydrothermal treatment at 353K for crystal formation. Moreover, the synthesis in the hydrothermal condition can enhance the thermal stability of mesostructure [10].

Table 1. The various reactants and their dosages for every sample.

Sample	Ce(SO <sub>4</sub> ) <sub>2</sub> (mol/L)	PEG MW <sup>a</sup>	(CH <sub>3</sub> CH <sub>2</sub> ) <sub>3</sub> N (mol/L)	Synthesis Reaction (K)	Reaction Time (min)
CP	0.2	6000	0.016	none	353 180
CPN-1	0.2	600	0.016	0.4	353 180
CPN-2	0.2	6000	0.016	0.4	353 180
CPN-3	0.2	19000	0.016	0.4	353 180
CN	0.2	None		0.4	353 180

a: MW, PEG Molecular Weight.

Figure 2 is the HRTEM images of air-dried and calcined at 673K of CPN-2. From the images, it appears that the synthesized materials do not display any regular pore stacking and only a sponge-like texture can be seen. However, the clear lattice fringe observed in the HRTEM image indicated that the crystallinity of mesoporous CeO<sub>2</sub> was fine. It is consistent with the XRD patterns of CPN-2.

The nitrogen adsorption-desorption isotherm and the pore-size distribution plots of the sample CPN-2 are shown in Figure 3. According to the classification of IUPAC [11], the isotherm should be ascribed to be of type IV. The BET surface area of the example sample is 215.39m<sup>2</sup>. The pore size distribution (Fig. 3b) can be calculated from the desorption branch of the isotherms. The most probable pore size of the sample is 5nm and the pore volume of the pores with a diameter less than 606Å at relative pressure of 0.967 is 0.2376cm<sup>3</sup>/g.

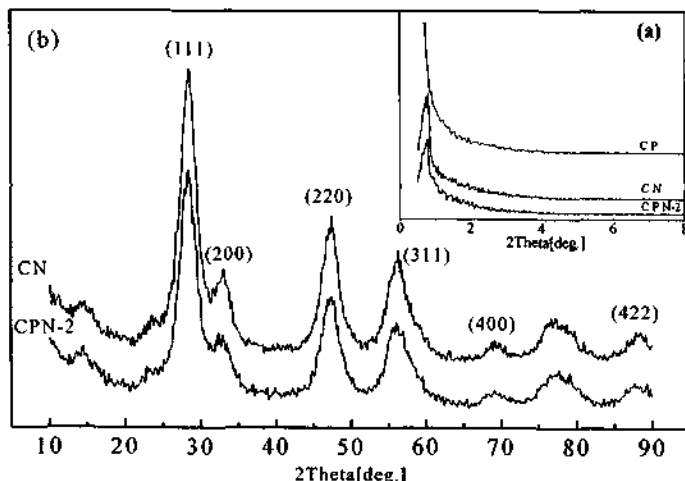
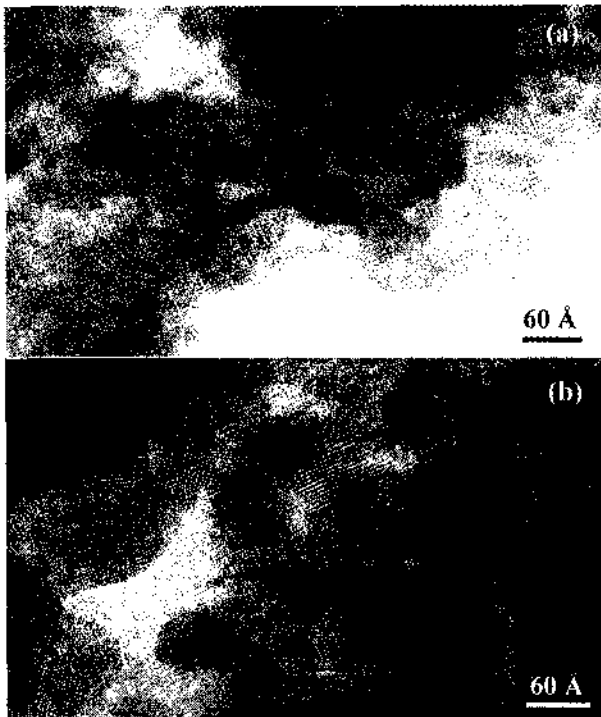


Figure 1. XRD patterns of mesoporous cerium (IV) oxide at (a): low-angles and (b): large-angles.



**Figure 2.** HRTEM images of the sample CPN-2: (a) air-dried and (b) calcined at 673K.

### 3.2 Effects of PEG molecular weight

In order to investigate the effects of molecular weight, several PEG molecules with various molecular weights of 600, 6000, 19000 were employed to synthesize the mesoporous CeO<sub>2</sub>. Figure 4 shows the small angle XRD profiles of the mesopore CeO<sub>2</sub> synthesized using various molecular weights of PEG. The XRD patterns of these samples show a common character of a single intense peak at the low-angle region. The intensity of the low-angle diffraction peaks decreases as the molecular weight of PEG increases. Figure 5 shows the variation trend of BET surface area with the change of the PEG molecular weight. It is not difficult to find that the surface area of the mesopore CeO<sub>2</sub> powder is enlarged with the reduction of the molecular weight of PEG. Recent report [13] illustrated that the morphology and the texture structure of the precipitated powder were attributed not only to the precursor and the solvent, but also to the non-polar additive. Polyethylene glycol (PEG), which contains hydroxyl groups at each end of the ethyleneglycol chain, is prone to form loose chelate ring with metal ions in the solution. After removing PEG by washing and/or calcination, it may be inclined to form a structure system of fewer pores, thus the surface area of the obtained micropores decreases correspondingly.

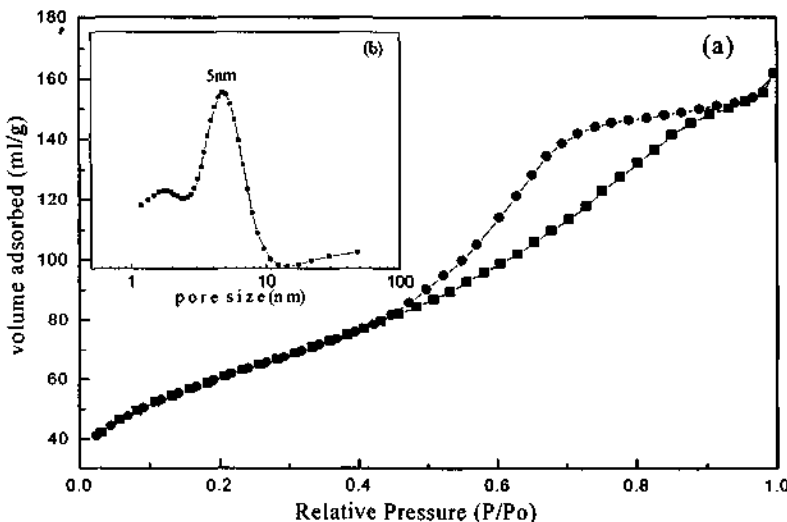
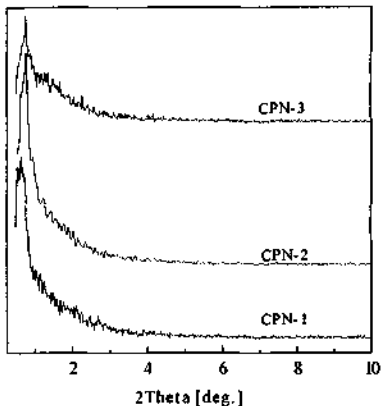


Figure 3. N<sub>2</sub> adsorption and desorption isotherm curve of CPN-2 (insert is the pore size distribution).

### 3.3 The thermal stability of the mesoporous CeO<sub>2</sub> powders

The thermal stability of the sample CPN-2 calcined at various temperatures for 3h was tested by X-ray diffraction analysis, high-resolution electron microscopy and N<sub>2</sub> adsorption-desorption measurements.

Figure 6 shows the small angle XRD profiles of the sample CPN-2 calcined at different temperatures. It was found that up to the calcination temperature of 873K the characteristic small angle XRD peak was retained. When the temperature rose to 1073K, the crystal of CeO<sub>2</sub> rapidly grew up and the mesoporous structure collapsed. Figure 7 shows the large angle XRD profiles of the mesoporous CeO<sub>2</sub> calcined at different temperatures. It can be found that the crystal structures were improved by elevating the calcination temperature. The crystallization process was accompanied by a loss of mesoporosity of the materials. Figure 2b shows the HRTEM image of a sample calcined at 673K. The same spongy image was maintained and the particles grew up and the lattice fringe became clearer. Figure 8 shows the N<sub>2</sub> adsorption-desorption isotherms of the mesoporous CeO<sub>2</sub> calcined at different temperatures. After calcination at a high temperature, the adsorption-desorption isotherms were invariably of type IV. The hysteresis loops presented the trend from type H<sub>2</sub> to type H<sub>1</sub>. It meant that in the calcination courses, the pore structure was improved from some complex and interconnected networks with different pore-sizes and shapes to a system with narrow distribution of uniform pores [11]. Figure 9 shows the BJH pore size distribution of the mesoporous CeO<sub>2</sub>. The narrow distribution of pores with radii of 5nm was maintained for calcination up to 673K. After calcination at 873K, the most probable pore size was enlarged to 10nm, and the pore size distribution became wider. The calcination at high temperatures also resulted in the decrease of surface area and pore volume of the mesoporous CeO<sub>2</sub>. In the whole pore structure, there were some micropores (<2nm) and macropores (>50nm) existing in the pore system. As the calcination temperature rises, the micropores and macropores disappear whereas the mesopores are retained.



**Figure 4.** Small angle XRD profiles of mesoporous  $\text{CeO}_2$  synthesized using various molecular weight of PEG.

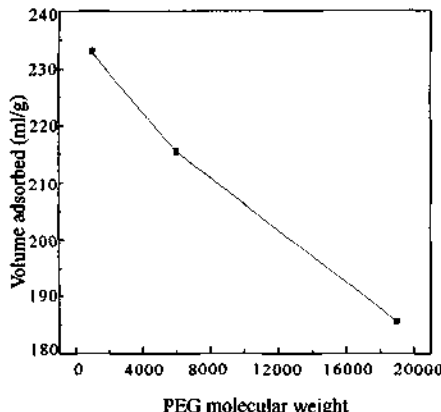


**Figure 5.** BET surface area of mesoporous  $\text{CeO}_2$  synthesized using various molecular weight of PEG. The samples are the same as those in Figure 4.

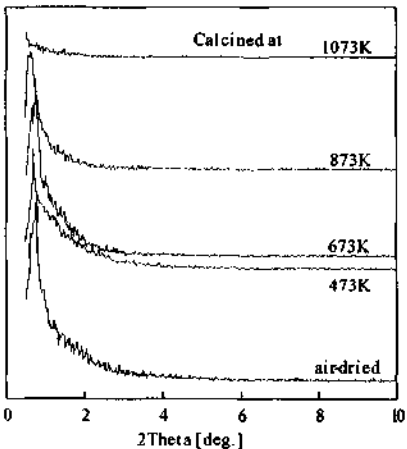


**Figure 6.** Small angle XRD patterns of the sample CPN-2 calcined at different temperatures

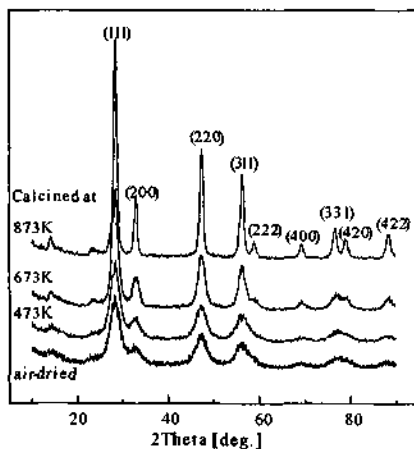


**Figure 7.** Large angle XRD patterns of the sample CPN-2 calcined at different temperatures. The samples are the same as the Figure 6.

Therefore, it is conceivable that the micropore and macropore are interparticle pores, while the mesopore presumably is the intra-particle pore. During the course of calcination, the connection of interparticle was destroyed and this finally resulted in the vanishing of macropore. Because the mesopore was the intraparticle pores, it had relative fine thermal stability though the pore size was enlarged in the calcination. The reasons may be attributed to the steric dispersant effect of non-ionic surfactant PEG [12]. In the synthesis course, PEG gave steric hindrance to the assembling of mesophase and improved the pore structure.

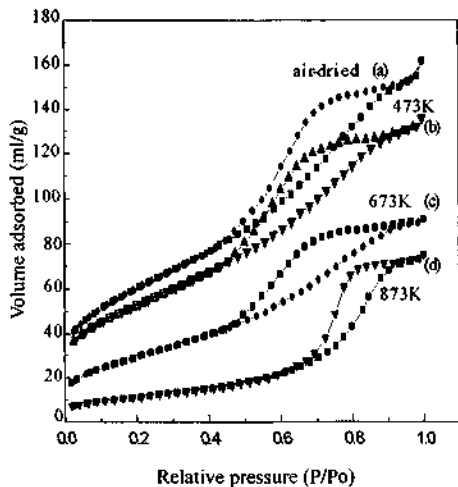


**Figure 8.**  $N_2$  adsorption-desorption isotherm of the sample CPN-2 calcined at different temperatures.

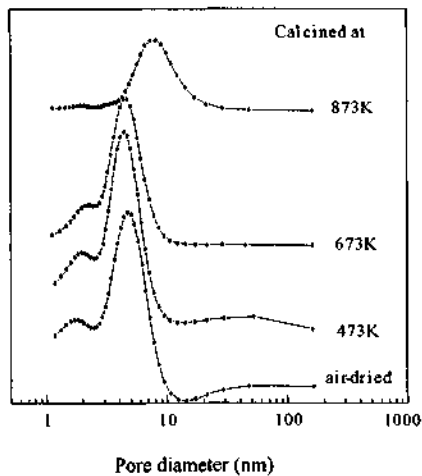


**Figure 9.** BJH pore size distribution profiles of the sample CPN-2 calcined at different temperatures. The samples are the same as the Figure 8.

The effect of PEG on thermal stability of the mesostructured  $CeO_2$  powders has been observed by comparing the difference of properties between the samples CPN-2 and CN. Figure 10 shows the small angle XRD patterns of the samples CPN-2 and CN. After calcination at 673K, the low-angle diffraction peak in the XRD pattern of CN disappeared, but still existed in that of CPN-2. This may be attributed to the thermal stability improvement deriving from non-ionic surfactant PEG.

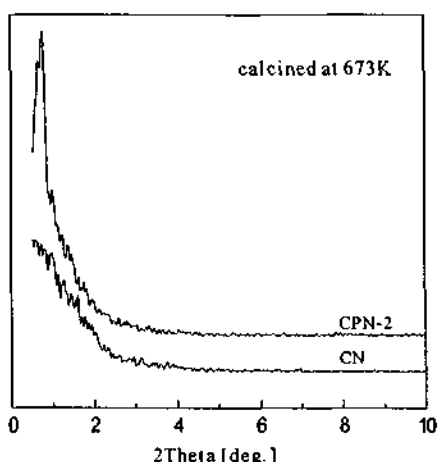


**Figure 10.** Small angle XRD patterns of the samples CPN-2 and CN.

In this study, it is found that the effects of  $(CH_3CH_2)_3N$  on the formation of mesopore structures and the effects of the PEG on the thermal stability of the precipitated powders are very interesting. The results show that the  $CeO_2$  powders prepared by the precipitation method are mesoporous with crystalline walls. The mesoporous structure can be maintained upon calcination up to 873K. The mesoporous  $CeO_2$  synthesized from the system in the presence of non-ionic surfactant PEG exhibits better thermal stability than that prepared using one template of  $(CH_3CH_2)_3N$  only.

#### 4 Acknowledgements

We gratefully acknowledge the financial support from the Science and Technology Key Projects (Project NO.00016) of Ministry of Education of China.

#### References

1. Ciesla U. and Schüth F., Order mesoporous materials. *Micro. & Meso. Mater.* **27** (1996) pp. 131-149.
2. Monnier A., Schüth F., Huo Q., Kumar D., Margolese D., Maxwell R. S., Stucky G. D., Krishnamurty M., Petrolf P., Firouzi A., Janicke M. and Chmelka B. F., Cooperative formation of inorganic-organic interfaces in the synthesis of silicate mesostructure. *Science* **261** (1993) pp. 1299-1303.
3. Davis S. A., Burkett S. L., Mendelson N. H. and Mann S., Bacterial templating of ordered macrostructures in silica and silica-surfactant mesophases. *Nature* **385** (1997) pp. 420-423.
4. Huo Q., Margolese D. I., Ciesla U., Feng P., Gler T. E., Sieger F., Leon R., Petrolf P. M., Schüth F. and Stucky G. D., Generalized synthesis of periodic surfactant/inorganic composite materials. *Nature* **368** (1994) pp. 317-312.
5. Fronasiero P., Balducci G., Monte R. D., Kaspar J., Sergio V., Gubitosa G., Ferrero A. and Graziani M., Modification of the redox behaviour of CeO<sub>2</sub> induced by structural doping with ZrO<sub>2</sub>. *J. Catal.* **164** (1996) pp. 173-183.
6. Zamar F., Trovarelli A., Leitenburg C. and de Dolcetti G., CeO<sub>2</sub>-based solid solution with the fluorite structure as novel and effective catalysts for methane combustion. *J. Chem. Soc. Chem. Commun.* (1995) pp. 965-966.
7. Ciesla U., Schacht S., Stucky G., Unger K. K. and Schüth F., Formation of a porous zirconium oxo phosphate with a high surface area by a surfactant-assisted synthesis. *Angew. Chem. Int. Ed. Eng.* **35** (1996) pp. 541-543.
8. Ciesla U., Demuth D., Leon R., Petrolf P., Stucky G., Unger K. and Schüth F., Surfactant controlled preparation of mesostructured transition-metal oxide compounds. *Chem. Commun.*, (1994) pp. 1387-1388.
9. Bagshaw S. A., Prouzet E. and Pinnavaia T. J. Templating of mesoporous molecular sieves by nonionic polyethylene oxide surfactants. *Science*, **269** (1995) pp. 1242-1247.
10. Liu P., Liu J. and Sayari A., Preparation of porous hafnium oxide in the presence of a cationic surfactant. *Chem. Commun.*, (1997) pp. 577-578.
11. Rouquerol F., Rouquerol J. and Sing K., Adsorption by Powders and Porous Solids, Principles, Methodology and Applications (Academic Press, Harcourt Brace & Company, 1999).
12. Park H. K., Moon Y. T., Kim D. K. and Kim C. H., Formation of monodisperse spherical TiO<sub>2</sub> powders by thermal hydrolysis of Ti(SO<sub>4</sub>)<sub>2</sub>. *J. Am. Ceram. Soc.*, **79** (1996) pp. 2727-2732.
13. Park, H. K., Kim D. K. and Kim C. H., Effect of Solvent on Titania Particle Formation and Morphology in Thermal Hydrolysis of TiCl<sub>4</sub>, *J. Am. Ceram. Soc.*, **80** (1997) pp. 743-749.

# THREE-DIMENSIONAL ORDERED MACROPOROUS HYBRID SILICA MATERIALS FUNCTIONALIZED WITH LACUNARY KEGGIN-TYPE POLYOXOMETALATES: PREPARATION AND CHARACTERIZATION

Y. YANG, Y. H. GUO, C. W. HU AND E. B. WANG

*Institute of Polyoxometalate Chemistry, Faculty of Chemistry, Northeast Normal University,  
Changchun 130024, People's Republic of China  
E-mail: huchw@nenu.edu.cn*

Three-dimensional ordered macroporous silica hybrid materials functionalized with mono-lacunary Keggin-type molybdates including  $[X'''Mo_{11}O_{39}]^{(12-n)}$  (abbreviated XM<sub>11</sub>, X'''=Si<sup>4+</sup>, Ge<sup>4+</sup>, P<sup>5+</sup>) have been prepared via sol-gel as well as polystyrene (PS) templating technique. The structural integrity of XM<sub>11</sub> cluster in the composites were characterized by UV diffuse reflectance spectra (UV/DRS), infrared spectra (IR), and solid-state MAS NMR spectra, indicating that the primary Keggin structures remained intact in the hybrid materials, and chemical interaction existed between POM molecules and the silica matrix. The porous structures of the composites were characterized by scanning electron microscopy (SEM) and transmission electron microscopy (TEM), indicating that the products had three-dimensional ordered macroporous and their average pore diameter was  $300 \pm 50$  nm. Three different colored materials were chosen to test the absorption behaviors of XM<sub>11</sub>-SiO<sub>2</sub>.

## 1 Introduction

The development of methods for the preparation of macroporous inorganic materials based on silica or other oxides is thriving due to their potential for wide practical applications in separation processes, large-molecule catalysis, host-guest system, thermal or electrical insulator and photonic crystals with tunable band gaps [1-10]. Using inorganic or organic templates, materials with periodic pores such as macroporous oxides (oxides of Si, Ti, Zr, Al, Sb, W, Fe and mixture of these), silicates, aluminophosphate, hybrid organosilicates and polymers (polyacrylamide and polyurethane) have been synthesized [11-14]. Templating methods provide conventional preparation for well-defined macroporous materials with narrow pore size distribution. These macroporous materials are obtained by filling the spaces between close-packed arrays of polystyrene with a precursor fluid, which forms a solid skeleton around spheres. After the templating agents are removed by either calcination or solvent extraction, the porous structures are maintained with diameters from tens to hundreds of nanometers [15-18].

Polyoxometalates have found applications in analytical and clinical chemistry, catalysis (including photocatalysis), biochemistry (electron transport inhibition), medicine (antitumoral, antiviral, and even anti-HIV activity), and solid-state device [19,20]. Recently, three-dimensional ordered materials are modified by the incorporation of POM into wall structures using a direct synthesis approach [21,22]. The motivation for the work lies in the novel properties that POM is introduced into silica networks [19,20]. The incorporation is that the POM is linked to silica matrix by covalent grafting. A class of POM that are particularly attractive for the preparation of hybrid materials are the lacunary POM. Lacunary POMs include the mono and divacant unsaturated Keggin fragments  $[X'''W_{11}O_{39}]^{(12-n)}$  (X'''=B<sup>3+</sup>, Si<sup>4+</sup>, Ge<sup>4+</sup>, P<sup>5+</sup>) [22],  $[Y\text{-SiW}_{10}O_{36}]^8$  [21]. Lacunary POMs have potential for forming hybrid materials due to nucleophilic surface oxygen atoms at the vacant site of them, which allow the covalent grafting of electrophilic group

(such as  $\text{RSi}^{3+}$ ,  $\text{RPO}^{2+}$  and  $\text{RSn}^{3+}$ ) by E-O-W ( $\text{E} = \text{Si}^{4+}$ ,  $\text{P}^{5+}$ ,  $\text{Sn}^{4+}$ ) bridges to form inorganic-organic hybrid materials.

In the current work, three-dimensional ordered macroporous silica materials functionalized by lacunary  $\text{XM}_{11}$  were prepared for the first time. The process included hydrolysis of tetraethoxysilane (TEOS) in the presence of  $\text{XM}_{11}$  under acidic conditions formed sol and then reacted directly with mono-lacunary  $\text{XM}_{11}$  followed by condensation around polystyrene (abbreviated PS) colloidal crystals. As-synthesized PS latex spheres coated with  $\text{XM}_{11}\text{-SiO}_2$  were immersed in toluene for *ca.* 30 min. to remove the PS spheres, resulting in macroporous hybrid  $\text{XM}_{11}\text{-SiO}_2$  materials. The resulting compositions were characterized by UV/DRS spectra, IR spectra, and solid-state MAS NMR spectra. The results showed the primary Keggin structures were retained after hybrid macroporous materials forming, and the bond connecting lacunary  $\text{XM}_{11}$  to the silica networks is Mo-O-Si bridge. The macroporous structures were described based on the images of SEM and TEM, their average pore diameter were  $300 \pm 50\text{ nm}$ . In order to test the adsorption behaviors of  $\text{XM}_{11}\text{-SiO}_2$  hybrid materials, three different dyes Rhodamine B, indophenol, and methyl violet were chosen. We studied adsorption behaviors of  $\text{XM}_{11}\text{-SiO}_2$  porous materials via detecting the changes of the concentrations of the solutions of dyes.

## 2 Experimental

### 2.1 Materials

Monodisperse PS spheres were synthesized and packed into colloidal crystals by centrifugation as described previously [6]. PS spheres used in the synthesis had diameter of *ca.* 500 nm. Regents used as follows  $\text{Na}_2\text{MoO}_4\cdot 2\text{H}_2\text{O}$ ,  $\text{Na}_2\text{HPO}_4\cdot 9\text{H}_2\text{O}$ ,  $\text{Na}_2\text{SiO}_3\cdot 9\text{H}_2\text{O}$ ,  $\text{MoO}_3$ ,  $\text{GeO}_2$ , styrene,  $\text{K}_2\text{S}_2\text{O}_8$ , ethanol (EtOH), tetraethoxysilane (TEOS), toluene, Rhodamine B, indophenol, and methyl violet. All chemicals were used as received without further purification. Doubly distilled water was used in all experiments.

### 2.2 Synthesis

The 1:11 series of POM were prepared as follows.  $\text{Na}_4\text{PM}_{11}\text{O}_{39}$  ( $\text{PM}_{11}$ ),  $\text{Na}_8\text{SiM}_{11}\text{O}_{39}$  ( $\text{SiM}_{11}$ ),  $\text{Na}_4\text{GeM}_{11}\text{O}_{39}$  ( $\text{GeM}_{11}$ ) were prepared according to the method reported [23]. The experimental conditions of the preparation of  $\text{XM}_{11}\text{-SiO}_2$  are listed in Table 1. The typical procedure was as follows. 2.8 g  $\text{XM}_{11}$  ( $\text{X}=\text{Si, Ge, P}$ ) was stirred with water at room temperature. A small amount of  $\text{HNO}_3$  (4 mol/L) was added dropwise in order to increase the solubility of  $\text{XM}_{11}$ , but the pH of the solution should not lower than 3. TEOS and EtOH were thoroughly mixed in a separate container and then added dropwise to  $\text{XM}_{11}$  mixture with vigorous stirring. The pH of the resulting was adjusted to *ca.* 2.5 with  $\text{HNO}_3$  (4 mol/L) and the reaction solution was stirred for *ca.* 90 min. until homogeneous silica sol functionalized with  $\text{XM}_{11}$  was formed. The clear sol was then applied dropwise to completely cover the millimeter-thick layer of dried PS spheres, which were crushed and deposited on filter paper in a Büchner funnel with suction applied. The composite sample was allowed to dry in air at room temperature for 24 h. and PS spheres were removed from samples by extraction for 30 min in toluene. The green-blue powder products were recovered by filtration and washed by toluene.

**Table 1.** Experimental conditions for the synthesis of XM<sub>0.11</sub>-SiO<sub>2</sub>

Inorganic precursor	Reactor molar ratio POM: H <sub>2</sub> O: TEOS: EtOH	pH <sup>a</sup>	Product
SiMo <sub>0.11</sub>	1: 525: 47.2: 180	2.3±0.2	SiMo <sub>0.11</sub> -SiO <sub>2</sub>
GeMo <sub>0.11</sub>	1: 524: 47.6: 181.4	2.8±0.2	GeMo <sub>0.11</sub> -SiO <sub>2</sub>
PMo <sub>0.11</sub>	1: 520: 46.8: 178.3	3.3±0.2	PMo <sub>0.11</sub> -SiO <sub>2</sub>

<sup>a</sup>Acidity of the reaction solution during TEOS hydrolysis in the presence of different POM precursor.

### 2.3 Characterization

The infrared spectra were performed on a Nicolet Magna-IR 560 spectrophotometer with mid-IR capability and the spectra were obtained using the powder samples in FT-IR grade KBr pellets. The UV/DRS spectra were recorded on a Shimadzu UV-2201 UV-Vis spectrophotometer and the samples for UV/DRS were prepared by diluting the green powder with BaSO<sub>4</sub>. <sup>31</sup>P and <sup>29</sup>Si MAS NMR spectra were obtained on a Varian Unity-400 NMR spectrometer. Scanning electron micrographs (SEM) were obtained on a Hitachi S-570 scanning electron microscope. Samples for SEM were prepared by dusting the powders with Au. Transmission electron micrographs (TEM) were obtained on a Hitachi H-600 transmission electron microscope. Samples for TEM were prepared by sonicating the powders in absolute ethanol for 30 min. and depositing one and two drops of the suspension on a holey polymer film.

### 2.4 Adsorption Behaviors Testing

The XM<sub>0.11</sub>-SiO<sub>2</sub> materials were tested for adsorption behaviors and three colored materials Rhodamine B, indophenol, and methyl violet were chosen. Solid porous XM<sub>0.11</sub>-SiO<sub>2</sub> materials were added to the ethanol solutions of dyes. The suspension of the solution of dyes (0.02g/L) and XM<sub>0.11</sub>-SiO<sub>2</sub>(0.02g) were shaken in dark for 5 days. The adsorption isotherms were obtained by detecting the changes of concentrations in upper clear solutions by 756CRT UV-VIS spectrophotometer.

## 3 Result and Discussion

The purpose of selecting XM<sub>0.11</sub>-SiO<sub>2</sub> as the inorganic precursor is that they are chemically active toward siloxanes. At first the hybrid XM<sub>0.11</sub>-SiO<sub>2</sub> sols were prepared via hydrolysis of TEOS in the presence of XM<sub>0.11</sub> under acidic conditions. A little amount of nitric acid was added to the solution in order to increase the solubility of XM<sub>0.11</sub> and still remained the mono lacunary structures. Second, the sols of the hybrid materials were introduced into the spaces between the templating PS sphere arrays (with suction applied); subsequently, a solid hybrid material skeleton was constructed via in situ sol-gel transformation. The PS templates were removed by extraction with toluene solution.

Characterization of the XM<sub>0.11</sub>-SiO<sub>2</sub> materials indicated that the synthesis produced three-dimensional ordered macroporous materials with highly dispersed polyoxometalates covalently incorporated within the wall structures. IR, UV/DRS, solid-state MAS NMR spectra confirmed that the polyoxometalates remained intact in the hybrid macroporous silica materials. At first, three solid XM<sub>0.11</sub>-SiO<sub>2</sub> materials all exhibited two absorptions with maxima at ca. 200 and 260 nm, respectively (Figure1). The former is stronger and

the latter is weaker, attributed to oxygen-to-molybdenum charge-transfer at Mo=O and Mo-O-Mo bands, respectively. But it is not enough to confirm whether the transformation from 1:11 complexes to 1:12 complexes happened or the 1:11 complexes still remained. Therefore, IR and solid-state NMR spectra were used to confirm XM<sub>11</sub>-SiO<sub>2</sub> composites further.

### 3.1 Structural Integrity of Compositions

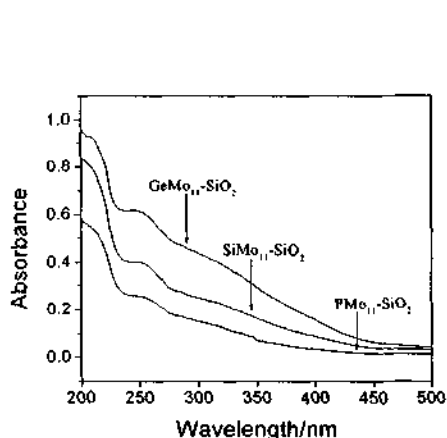


**Figure 1.** UV diffuse reflectance spectra of the macroporous hybrid silica materials based on lacunary XM<sub>11</sub>.

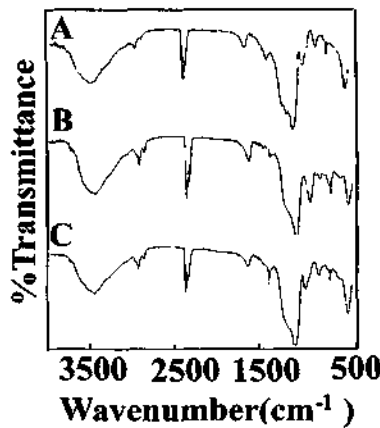


**Figure 2.** Mid-IR spectra of (A) SiMo<sub>11</sub>-SiO<sub>2</sub>, (B) PMo<sub>11</sub>-SiO<sub>2</sub>, (C) GeMo<sub>11</sub>-SiO<sub>2</sub>.

**Table 2.** Main relevant mid-IR data (cm<sup>-1</sup>) of the starting XM<sub>11</sub>s and their corresponding XM<sub>11</sub>-SiO<sub>2</sub> hybrid materials.

Sample	$\nu$ as (X-O)	$\nu$ as (Mo=O <sub>d</sub> )	$\nu$ as (Mo-O <sub>c</sub> -Mo)	$\delta$ (O-X-O)
SiMo <sub>11</sub>	890	928	810, 764, 729	531, 494
SiMo <sub>11</sub> -SiO <sub>2</sub>	895	930	798, 750, 715	533, 500
GeMo <sub>11</sub>	799	937	776, 731	466
GeMo <sub>11</sub> -SiO <sub>2</sub>	800	955	776, 733	458
PMo <sub>11</sub>	1080, 1035	934	821, 768, 730	595, 503, 476
PMo <sub>11</sub> -SiO <sub>2</sub>	1079	906	799, 773, 710	605, 508, 458

Pure mono-lacunary molybdate XM<sub>11</sub> (X=Si, Ge, P) displays a characteristic infrared fingerprint in the region from *ca.* 1000 to 700 cm<sup>-1</sup> [19]. From Table 2 and Figure 2, it can be observed that XM<sub>11</sub>-SiO<sub>2</sub> (X=Si, Ge, P) materials have vibration bands similar to the corresponding pure XM<sub>11</sub> (X=Si, Ge, P), suggesting that the starting XM<sub>11</sub> structures remained intact regardless of the functionality of the polyanions. At the same time it is also observed that the stretching vibration bands are shifted to higher frequency in comparison with the primary pure POMs due to the interaction between

$\text{XMn}_{11}$  molecules and the surface silanol groups in the silica framework. The polyanion fingerprint is obscure in the  $\text{XMn}_{11}\text{-SiO}_2$  materials because of strong IR bands from the silica framework. Intense and broad Si-O-Si vibration band of silica framework at 1080  $\text{cm}^{-1}$  covered Si-O from central  $\text{SiO}_4$  unit vibration band of polyoxometalate. So from the peaks at mid-IR region, we cannot confirm the structural integrity of  $\text{SiMn}_{11}$  has been preserved after  $\text{SiMn}_{11}\text{-SiO}_2$  formed. Solid-state  $^{29}\text{Si}$  MAS NMR spectrum of  $\text{SiMn}_{11}\text{-SiO}_2$  composite indicated that the resonance at  $\delta$  -73.99 ppm [Figure 3A] originated from central  $\text{SiO}_4$  unit of  $\text{SiMn}_{11}$  similar to that of precursor  $\text{SiMn}_{11}$  ( $\delta$  -68.3 ppm), suggesting that Si-O in central  $\text{SiO}_4$  unit of  $\text{SiMn}_{11}$  existed in the hybrid materials. The rest of the resonance signals were originated from  $\text{Si(OSi)}_4$ ,  $\text{Si(OSi)}_3(\text{OH})$ ,  $\text{Si(OSi)}_2(\text{OH})_2$  and  $\text{Si(OSi)}(\text{OH})_3$ , respectively, indicating that surface silica existed in the hybrid materials. Solid-state  $^{31}\text{P}$  MAS NMR spectrum showed that one resonance at  $\delta$  -5.985 ppm appeared [Figure 3B]. The determined  $^{31}\text{P}$  NMR signals for the pure saturated and monovacant Keggin-type molybdophosphates were  $\delta$  -6.07 and -5.31 ppm, respectively. Therefore, the Keggin unit of  $\text{PMn}_{11}\text{-SiO}_2$  tends to be saturated due to grafting of the organosiloxane. According to the above analysis results, we conclude that the primary  $\text{XMn}_{11}$  structures remained intact after the  $\text{XMn}_{11}$  containing hybrid silica materials.

### 3.2 Macroporous Structures of Composition

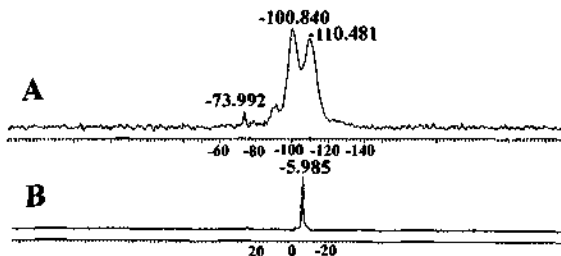
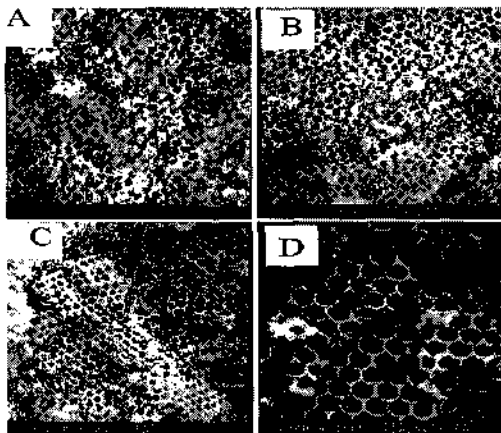


Figure 3. A)  $^{29}\text{Si}$  MAS NMR spectrum of  $\text{SiMn}_{11}\text{-SiO}_2$ ; B)  $^{31}\text{P}$  MAS NMR spectrum of  $\text{PMn}_{11}\text{-SiO}_2$ .

Macroporous structures of the  $\text{XMn}_{11}\text{-SiO}_2$  hybrid materials were formed after the PS templates and the materials walls were composed of silica functionalized with  $\text{XMn}_{11}$  ( $X=\text{Si, Ge, P}$ ). The mechanism of formation of macroporous POM [21] is similar to that of the macroporous oxides [5,6]. SEM and TEM were used to characterize the porous structures of  $\text{XMn}_{11}\text{-SiO}_2$  hybrid materials, and the results are shown in Figure 4 and Figure 5. From the SEM images, the average porous diameters were estimated from 280 to 350 nm, and the wall thickness ranged from 30 to 90 nm. In general, the porous size should be equal to the diameter of PS sphere (ca. 500). However, the resulting value is lower than the expected one ( $300 \pm 50\text{nm}$ ), attributed to the shrinkage of the structures during extraction. Wall thickness of the composite is related to the concentration of the inorganic precursor, hydrolysis time, and extraction conditions. Some areas in the SEM image showed point defect and some PS templates remained in the pores of the hybrid materials because extraction conditions were not perfect and the water-solubility of

$\text{XM}_{11}$  was not good. The TEM image of  $\text{SiMo}_{11}\text{-SiO}_2$  also showed that the pores of the hybrid materials were well-ordered (TEM images of the other two  $\text{XM}_{11}\text{-SiO}_2$ s were similar to that of  $\text{SiMo}_{11}\text{-SiO}_2$ ). The light areas represent the pores and the dark areas represent the walls of the hybrid materials.



**Figure 4.** SEM images of the macroporous hybrid silica materials based on lacunary POMs: (A)  $\text{SiMo}_{11}\text{-SiO}_2$ , (B)  $\text{GeMo}_{11}\text{-SiO}_2$ , (C)  $\text{PMo}_{11}\text{-SiO}_2$ , (D)  $\text{PMo}_{11}\text{-SiO}_2$  with high magnification .

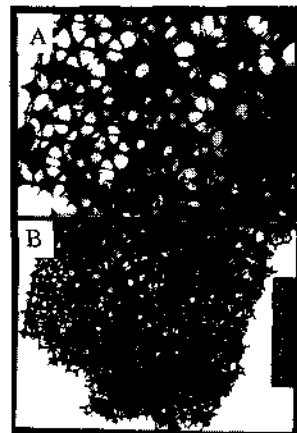


**Figure 5.** TEM images of the  $\text{Si Mo}_{11}\text{-SiO}_2$  with high (A) high and (B) low magnification

### 3.3 Adsorption Behaviors of Macroporous Materials

In order to test the adsorption behaviors of this kind of macroporous materials, three colored materials Rhodamine B, indophenol, and methyl violet were chosen. The changes of concentrations of the solutions of dyes in a period were detected by UV-VIS spectrometer. The adsorption isotherms are shown in Figure 6. From the adsorption isotherms we can see that the adsorption behaviors of macroporous materials are not good. The reason may be (I) that the surface areas of macroporous materials are low (*ca.*  $100\text{m}^2/\text{g}$ ) and the active sites are few; (II) the solvent ethanol was adsorbed by the hybrid materials. The adsorption isotherms of three colored materials were different. Methyl violet was an alkaline indicator and the adsorption of methyl violet and hybrid materials may correspond to a chemisorption. Acid indicator Rhodamine B was not adsorbed by the adsorbent and the solvent ethanol was adsorbed instead. Therefore, after reaction the concentration of the solution increased and the adsorption capacity appeared negative. Compared with the former two, indophenol molecule is smaller and is easy to be absorbed. Therefore, its adsorption behavior is stronger relatively.

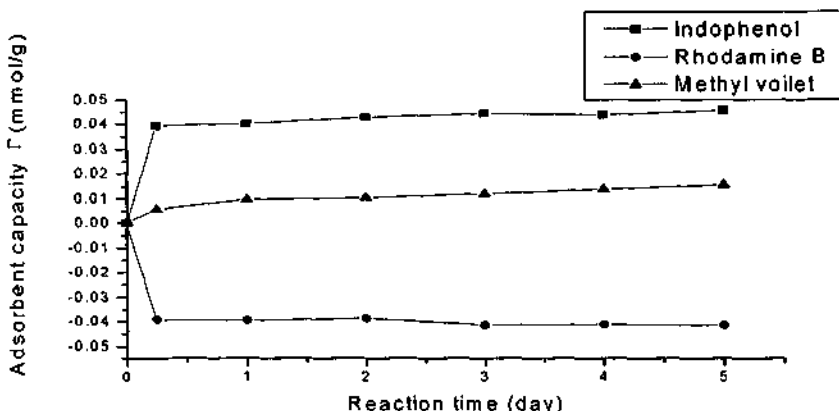


**Figure 6.** Adsorption isotherm of macroporous SiMo<sub>11</sub>-SiO<sub>2</sub>

$\Gamma = (C_0 - C) * V / m$   $C_0$ : the changeable values of concentrations of dyes solutions;  $V$ : solutions volume;  $m$ : the quality of adsorbent SiMo<sub>11</sub>-SiO<sub>2</sub>.

#### 4 Conclusion

A templating method was presented to fabricate novel three-dimensional ordered macroporous silica materials functionalized by polyoxometalates. Characterization of the products indicated that the starting XM<sub>o</sub><sub>11</sub> remained intact regardless of the functionality of the polyanions, and their primary lacunary structures tended to get saturated. The future development of the method holds promise for the formation of advanced new materials with more novel properties, which can be applied in more wide fields.

#### 5 Acknowledgment

The National Natural Science Foundation of China is acknowledged for financial support (No. 20071007).

#### References

1. Holland B. T., Blanford C. F., Stein A., Synthesis of macroporous minerals with highly ordered three-dimensional arrays of spheroidal voids, *Science* **281** (1998) pp. 538-540.
2. Wijnhoven J. E. G. J., Vos W. L., Preparation of photonic crystals made of air spheres in titania, *Science* **281** (1998) pp. 802-804.
3. Stein A., Fendorf M., Jarvie T. P., et al., Salt-gel synthesis of porous transition-metal oxides, *Chem. Mater.* **7** (2) (1995) pp.304-313.
4. Velev O. D., Jede T. A., Lobo R. F., Lenhoff A.M., Microstructured porous silica obtained via colloidal crystal templates, *Chem. Mater.* **10** (1998) pp. 3579-3602.

5. Subramanian G., Manoharan V. N., Thorne J. D., Pine D. J., Ordered macroporous materials by colloidal assembly: a possible route to photonic bandgap materials, *Adv. Mater.* **11** (15) (1999) pp. 1261-1265.
6. Holland B. T., Blanford C. F., Do T., Stein A., Synthesis of highly ordered, three dimensional, macroporous structures of amorphous or crystalline inorganic oxides, phosphates, and hybrid composites, *Chem. Mater.* **11** (1998) pp. 795-805.
7. Diddams P., *Inorganic supports and catalysis*; Smith K., Ed.; Ellis Horwood: New York (1992) pp. 3-39
8. Blanco A., Chomski E., Grabtchak S., et al., Large-scale synthesis of a silicon photonic crystal with a complete three-dimensional bandgap near 1.5 micrometres, *Nature* **405** (2000) pp. 437-440.
9. Holland B.T., Abram L., Stein A., Dual templating of macroporous silicates with zeolitic microporous frameworks, *J. Am. Chem. Soc.* **121** (1999) pp. 4308-4309.
10. Yang P. D., Deng T., Zhao D. Y., et al., Hierarchically ordered oxides, *Science* **282** (1998) pp. 2244-2246.
11. Velev O. D., Jede T. A., Lobo R. F., Lenhoff A. M., Porous silica via colloidal crystallization, *Nature* **389** (1997) pp. 447-448.
12. Xia Y.; Fabrication of three-dimensional macroporous membranes with assemblies of microspheres as templates, *Chemistry of Materials* **10**(7) (1998) pp. 1745-1747.
13. Mayer C. R., Thouven R., New hybrid covalent network based on polyoxometalae: part 1, hybrid networks based on poly (ethylmethacrylate) chains covalent cross-linked by heteropolyanions: synthesis and swelling properties, *Chem. Mater.* **12** (2) (2000) pp. 257-260.
14. Imhof A., Pine D. J., Uniform macroporous ceramics and plastics by emulsion templating, *Adv. Mater.* **10** (9) (1998) pp. 697-700.
15. Velev O. D., Tessier P. M., Lenhoff A. M., Kaler E.W. Materials: a class of porous metallic nanostructures, *Nature* **401** (1999) pp. 548-551.
16. Johnson S. A., Ollivier P. J., and Mallouk T. E., Ordered mesoporous polymers of tunable pore size from colloidal silica templates, *Science* **283** (1999) pp. 963-968.
17. Jiang P., Hwang K. S., Mittleman D.M., Bertone J.F., and Colvin V.L., Template-directed preparation of macroporous polymers with oriented and crystalline arrays of voids, *J. Am. Chem. Soc.* **121** (50) (1999) pp. 11630-11637.
18. Guo Y. H., Wang Y. H., Hu C. W., Wang Y. H., Wang, E. B., Microporous polyoxometalates POM/SiO<sub>2</sub>: synthesis and photocatalysis degradation of aqueous organochlorine pesticides, *Chem. Mater.* **12** (2) (2000) pp. 3501-3508.
19. Pope M. T., *Heteropoly and isopoly oxometalates*; Springer Verlage: Berline (1983)
20. Pope, M. T., Müller A., Polyoxometalate chemistry: an old field with new dimensions in several disciplines, *Angew. Chem. Int. Ed. Engl.* **30** (1991) pp. 34-48.
21. Schroden R. C., Stein A., et al., Direct synthesis of ordered macroporous silica materials functionalized with polyoxometalate clusters, *Chem. Mater.* **13** (2001) pp. 1074-1081.
22. Guo Y. H., Yang Y., Hu C. W., Ordered macroporous hybrid silica based on lacunary Keggin-type polyoxometalates: preparation, characterization and photochemical behavior, (*in press*).
23. Par M<sup>me</sup> Claude Tourné, Gilbert Tourné, Les sries d'h tropolyanions de type XW<sub>11</sub>, XZW<sub>11</sub>, X<sub>2</sub>W<sub>17</sub>, X<sub>2</sub>ZW<sub>17</sub>, et leurs homologues molybdiques, *Bull. Soc. Chim. Fr.* N°4 (1969) pp. 1124-1136.

# HYDROTHERMAL FORMATION OF NOVEL CERIUM MATERIALS WITH OPEN-FRAMEWORK ARCHITECTURES

RANBO YU,<sup>\*\*</sup> DAN WANG,<sup>\*\*\*</sup> TAKAHIRO TAKEI,<sup>\*</sup> NOBUHIRO KUMADA,<sup>\*</sup>  
NOBUKAZU KINOMURA<sup>\*</sup> AND MIKIO TAKANO<sup>\*\*</sup>

*\*Institute of Inorganic Synthesis, Faculty of Engineering, Yamanashi University,  
Miyamae-cho 7, Kofu 400-8511, Japan*

*\*\*Institute for Chemical Research (ICR), Kyoto University, Gokasho, Uji, Kyoto 611-  
0011, Japan*

*\*\*\*Research Institute of Innovative Technology For the Earth (RITE), 9-2 Kizugawada,  
Kizu-cho, Soraku-gun, Kyoto 619-0292, Japan  
E-mail: danwang1@rite.or.jp*

Two novel open-framework cerium materials, cerium phosphate fluoride  $(\text{NH}_4)[\text{Ce}^{\text{IV}}\text{F}_2(\text{PO}_4)]$  (I), cerium oxyfluoride  $\text{H}_{25.5}(\text{NH}_4)_{10.5}\text{Ce}_9\text{O}_{27}\text{F}_{18}$  (II), have been synthesized under hydrothermal conditions, and characterized by means of single-crystal X-ray diffraction, ion chromatography analysis, infrared spectroscopy, and thermal analysis. In these compounds, two kinds of cerium-centered polyhedra  $\text{CeO}_4\text{F}_4$  and  $\text{CeO}_6\text{F}_2$  are incorporated into the structures as novel basic building units. The structure of (I) contains corrugated chains along the *b*-axis formed by  $\text{CeO}_4\text{F}_4$  polyhedra link via  $\text{Ce}_2\text{F}_2$  rings, and these chains are tetrahedrally connected via  $\text{PO}_4$  groups to create the 3-D network with 1-D channel. In the structure of compound (II), six  $\text{CeO}_6\text{F}_2$  dodecahedra link to form an octahedral  $\text{Ce}_6\text{O}_{24}\text{F}_{12}$  cage, which connect one another via bridging oxygen atoms to give rise to a three-dimensional channel system with eight-ring pore opening. Both of these two compounds accommodate  $\text{NH}_4^+$  cations at the intersection of the channels to balance the framework negative charge.

## 1 Introduction

Lanthanide materials with potential applications as ion exchanger, moisture sensor, fluorescence material, and ion conductor, have attracted considerable research attentions [1-2]. Synthesis of open-framework lanthanide materials is of great interest because the interspaces of three-dimensional channels would be capable of enhancing some properties of this class of compounds, such as ion conductivity and ion exchange, and widening the application area as well [3, 4].

We are interested in exploring the synthesis of lanthanide materials for a number of reasons. First, lanthanide elements could give the high coordination numbers and the variety of coordination geometries, and hydrothermal synthesis in the presence of template organic molecules could be expected to result in the formation of new, complex framework architectures. Some inspirited results have been achieved in investigation of related field about actinide materials [5-11]. Second, lanthanide materials may be envisioned to exhibit useful catalytic, ion-exchange and intercalation properties. Finally, the existence of manifold stable oxidation

states in lanthanide, in particular cerium, offers the possibility of synthesizing materials with useful magnetic properties.

Studies on open-framework lanthanide material started long time ago, however, the desirable results are rather few. [12-17]

In this work, we focus on hydrothermal synthesis of open-framework cerium materials. By using fluoride ions mineralizer, two novel open-framework cerium materials, cerium phosphate fluoride  $(\text{NH}_4)[\text{Ce}^{\text{IV}}\text{F}_2(\text{PO}_4)]$  (I), cerium oxyfluoride  $\text{H}_{25.5}(\text{NH}_4)_{10.5}\text{Ce}_9\text{O}_{27}\text{F}_{18}$  (II), have been prepared in presence of  $\text{F}^-$  ion. Both of them exhibited unique structural features, which is so different from traditionally porous materials, including zeolites and some metal phosphates.

## 2 Experimental

A mixed phase of compound (I) and (II) could be synthesized together from the starting composition of  $1.0 \text{ Ce}(\text{SO}_4)_2 / 0.5 \text{ H}_3\text{PO}_4 / 1.5 \text{ H}_2\text{N}(\text{CH}_2)_2\text{NH}_2 / 4.0 \text{ NH}_4\text{F} / 150\text{H}_2\text{O}$ . This mixture was heated at  $180^\circ\text{C}$  for 3-8 days in Teflon-lined stainless steel autoclaves. After the crystallization, the product was filtered and washed with deionized water and ethanol, and then dried in air at ambient temperature. The yield of compound (I) was 20-30%. Further investigation of the reaction conditions indicated that pure phase of the cerium phosphate fluoride,  $(\text{NH}_4)[\text{CeF}_2(\text{PO}_4)]$ , could be obtained by change of the starting composition.

Powder X-ray diffraction patterns were taken on a Mac Science MXP<sup>3</sup> X-ray diffractometer, using Ni-filtered  $\text{Cu K}\alpha$  radiation. Thermo-gravimetric analysis (TGA) was carried out on a Rigaku Thermoflex TAS 200 thermal analysis system with a heating rate of  $10^\circ\text{C}/\text{min}$  over 20- $1000^\circ\text{C}$  temperature range. Infrared absorption spectra (IR) were recorded on a JASCO FT/IR-410 spectrometer using transparent KBr pellets: 1.2 mg of the sample was crushed and mixed with 300 mg KBr. CHN elemental analysis was carried out on a Yanaco MT-5 CHN CORDER, by using antipyrine as the standard sample. Ion chromatography analysis of fluoride ion was carried out on an IC 7000 SERIES Ion Chromatographic Analyzer equipped with a Yokogawa ICS AZG+ICS-A23 (4.6mm×75mm) column by using NaF aqueous solution as the standard solution. The sample used for measurement was prepared as follows: ca. 0.2 g of as-synthesized product was dissolved in 10 ml of 5N  $\text{H}_2\text{SO}_4$  at ambient temperature. Then the solution was further diluted with deionized water to the  $\text{F}^-$  ion concentration of 1-10 ppm.

A crystal of (I) with dimensions of  $0.2 \times 0.2 \times 0.2 \text{ mm}^3$  and a transparent tetrahedral crystal of (II) with approximate dimensions of  $0.12 \times 0.12 \times 0.12 \text{ mm}^3$  were isolated and mounted on glass fibers, respectively. Single crystal X-ray diffraction data were collected with a Rigaku AFC7R diffractometer equipped with graphite monochromated Mo

K $\alpha$  radiation ( $\lambda = 0.71069 \text{ \AA}$ ).

Table 1. Crystal data and structure refinement for the two compounds.

Empirical formula	CePO <sub>4</sub> NH <sub>4</sub> F <sub>2</sub>	Ce <sub>9</sub> O <sub>27</sub> F <sub>18</sub> N <sub>10.5</sub> H <sub>67.50</sub>
Formula weight	219.13	2250.14
Crystal system	monoclinic	trigonal
Space group	P2 <sub>1</sub> /m (No.11)	R̄3 (No.148)
Lattice parameters		
a (Å)	6.660(2)	15.252(8)
b (Å)	5.875(2)	
c (Å)	7.177(3)	10.749(4)
$\beta$ (°)	114.31(2)	
V (Å <sup>3</sup> )	255.9(2)	2165(1)
Z	2	3
D <sub>calc</sub> (g/cm <sup>3</sup> )	3.777	5.176
Radiation	Mo K $\alpha$ ( $\lambda=0.71069 \text{ \AA}$ )	Mo K $\alpha$ ( $\lambda=0.71069 \text{ \AA}$ )
No. of reflection measured	Total: 2364 Unique: 2243 (R <sub>int</sub> = 0.033)	Total: 2364 Unique: 2243 (R <sub>int</sub> = 0.033)
No. of observations (I > 3.00(I))	1810	2466
No. of variables	83	67
Residuals: R, R <sub>w</sub>	0.039, 0.045	0.045, 0.051
GOF indicator	1.69	1.90

For compound (I), the systematic absence ( $0k0=2n+1$ ) was consistent with either space group P2<sub>1</sub> or P2<sub>1</sub>/m. Successful solution and refinement led to the choice of the centrosymmetric space group. 2243 of the total 2364 collected reflections were unique ( $R_{int} = 0.033$ ), and equivalent reflections were merged. The crystal structure was solved by direct methods (SAPI90) and expanded using Fourier techniques. The non-hydrogen atoms were refined anisotropically. The final cycle of full-matrix least-squares refinement was based on 1810 observed reflections ( $I > 3.00(I)$ ) and 83 variable parameters and converged with unweighted and weighted agreement factors of  $R = 0.039$ ,  $R_w = 0.045$ . For compound (II), the space group R̄3 could be assigned uniquely after a careful inspection of all reciprocal lattice points for which  $2\theta < 90^\circ$ . 3971 of the total 4257 collected reflections were unique, and equivalent reflections were merged. The structure was solved by heavy-atom Patterson methods and expanded using Fourier techniques. The non-hydrogen atoms were refined anisotropically. The final cycle of full-matrix least-squares refinement was based on 2466 observed reflections ( $I > 3.00\sigma(I)$ ) and 67 variable parameters and converged with unweighted and weighted agreement

factors of  $R = 0.045$  and  $R_w = 0.051$ . All calculations were performed using the teXsan [18] crystallographic package. Hydrogen atoms were added to balance the negative charges of the framework. Further details of crystal data and structure refinement of these compounds are summarized in Table 1.

### 3 Results and Discussion

#### 3.1 Crystal structure of cerium phosphate fluoride.

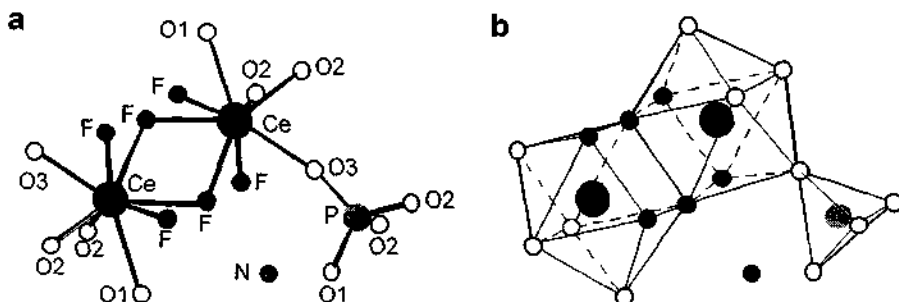
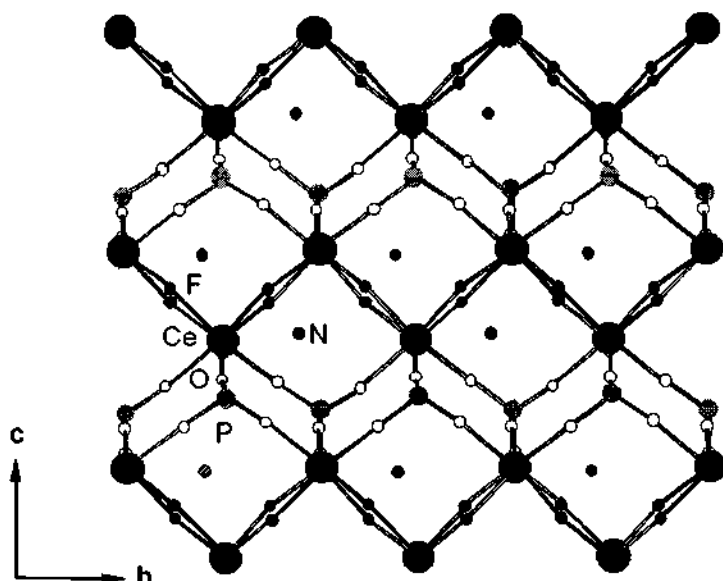


Figure 1. Stick-ball (a) and polyhedral (b) representation of the asymmetric unit of compound (I) with the atoms labeled.

The cerium phosphate fluoride (I) was found to contain framework fluoride atoms coordinated to cerium atoms, giving rise to the structure formula (NH<sub>4</sub>)<sub>2</sub>[Ce<sup>IV</sup>F<sub>2</sub>(PO<sub>4</sub>)]. The structure of this crystal is based on a network of phosphorus-centered tetrahedral PO<sub>4</sub> and edge-sharing cerium-centered polyhedra CeO<sub>4</sub>F<sub>4</sub>, which is new type of basic building unit that has never been found in open-framework structures before (Figure 1). Along the *b*-axis of the structure, there are corrugated chains formed by CeO<sub>4</sub>F<sub>4</sub> polyhedra via Ce<sub>2</sub>F<sub>2</sub> rings. They are further tetrahedrally connected via PO<sub>4</sub> groups to create the 3-D open-framework structure (Figure 2). There is a six-ring channel system along the *b*-axis of the structure as shown in Figure 3. Each six-ring channels contains four CeO<sub>4</sub>F<sub>4</sub> polyhedra and two PO<sub>4</sub> tetrahedra with the polyhedron arrangement as -Ce-Ce-P-Ce-Ce-P- and has diagonals varied between 4.26 and 6.71 Å, which are almost as large as the dimension of eight-ring window in zeolite NaA [19]. Three types of four-ring windows are found in the structure. In the planes vertical to the *a*-axis, there are four-ring four-ring windows containing three CeO<sub>4</sub>F<sub>4</sub> polyhedra and one PO<sub>4</sub> tetrahedron with diagonals varied between 4.03 and 4.07 Å. The other two kinds of windows vertical to the *c* and *b* axis, in which CeO<sub>4</sub>F<sub>4</sub> dodecahedra and PO<sub>4</sub> tetrahedra are strictly alternated, have diagonals of 2.95-4.47 Å and 3.31-4.17 Å, respectively. NH<sub>4</sub><sup>+</sup> cations are accommodated

in the interspace of these four-ring windows as well as that of the six-ring channels and hydrogen bond to framework O(1), O(3) and F atoms.



**Figure 2.** Projection of the structure of compound (I) along the *a* axis, showing the four-membered windows and corrugated chains formed by  $\text{CeO}_4\text{F}_4$  polyhedra.

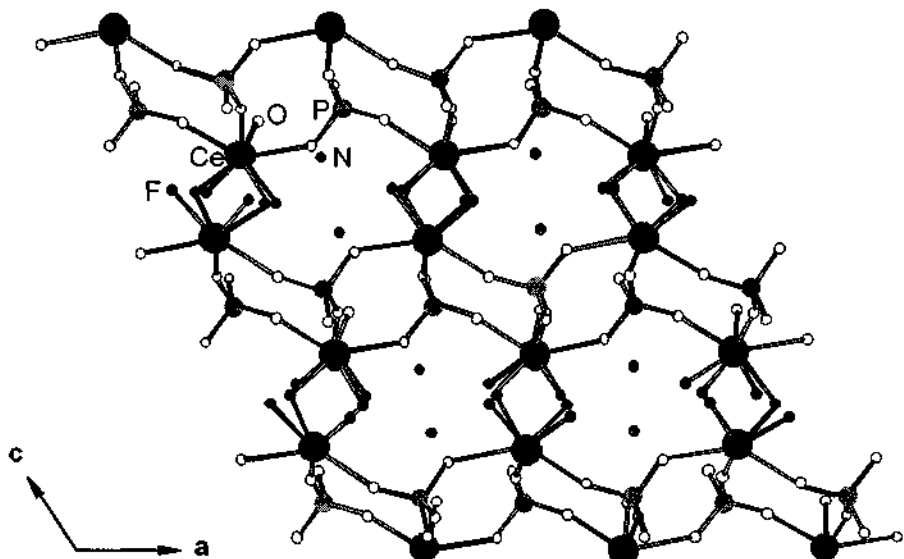


**Figure 3.** Projection of the structure of compound (I) along the *c* axis, showing the channel system with six-membered window.

### 3.2 Crystal structure of cerium oxyfluoride

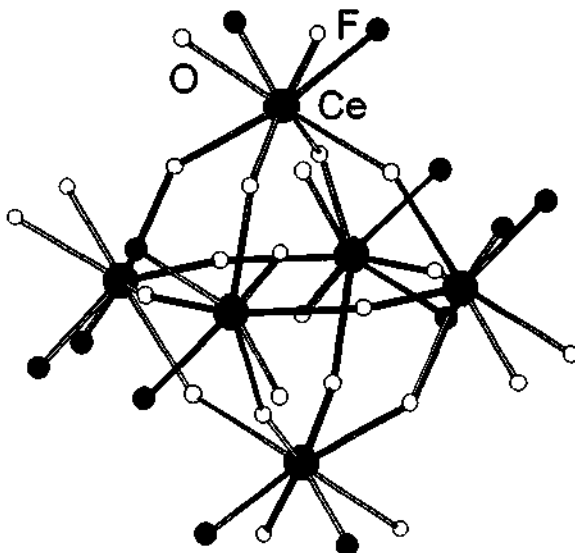


Figure 4. Octahedral cage of the structure of compound (II) formed by CeO<sub>6</sub>F<sub>2</sub> dodecahedron.

The framework of the cerium oxyfluoride (II) consists of cerium-centered CeO<sub>6</sub>F<sub>2</sub> dodecahedron, which is a new type of basic building unit incorporated in open-framework structures. Six of cerium-centered CeO<sub>6</sub>F<sub>2</sub> dodecahedra formed an octahedral cage via corner sharing, which contains eight three-rings as show in Figure 4. Although the octahedral cage is made up of dodecahedra with large volume, it has a large body diagonal of 5.8 Å from O to O, because that the polyhedra connection is corner sharing, and the Ce-O bond length (*ca* 2.4 Å) is relatively long. This kind of octahedral cage has never been found in previous structure types of open-framework materials. The framework can be described as a hexagonal arrangement of octahedral cages connected by bridging oxygen atoms (Figure 5). The octahedral cages connect each other by sharing edges of the dodecahedra to give rise to a framework structure with a three-dimensional channel system. At the intersection of these channels, there are large supercages with the body diagonal of 13.17 Å from O to O. The channel system goes through the opposite faces of the supercage in the [331], [331], and [301] directions, and has the elliptical eight-ring windows with O···O distance varied between 6.3 and 9.7 Å and F···F distance varied between 3.7 and 4.4 Å as shown in Figure 5. NH<sub>4</sub><sup>+</sup> cations are accommodated in the channels to balance the framework negative charge.

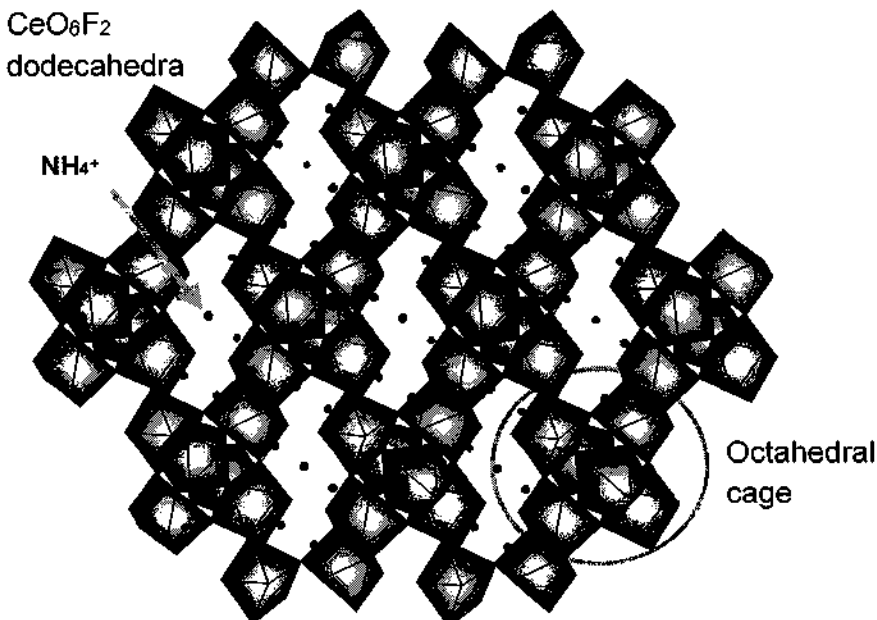


Figure 5. Structure of the compound (II) showing the channel system with eight-membered window and location of the NH<sub>4</sub><sup>+</sup> cations.

Although the dodecahedron occupies much more space than the usual tetrahedron, the structure of the new open-framework cerium oxyfluoride is very open. The most important reason for it is considered that in the structure of the compound large cerium-centered polyhedra connect each other through corner- and edge-sharing, but not face-sharing. Therefore, the structure has relatively large Ce···Ce distances. In addition, the structure possesses a great deal of three-rings. The formation of these kinds of small rings (3- or 4-rings) in traditional aluminosilicate zeolites was considered as a dominant factor for their very open structures [20]. In the case of this cerium oxyfluoride, with the long Ce-O distances (the average Ce-O distance is 2.3061 Å), formation of three-rings is easily realized. The long distances of Ce-O and Ce-F bonds (average bond length is 2.1619 Å) are suggested to attribute to the very open framework of this cerium oxyfluoride to a degree.

#### 4 Acknowledgements

Ranbo Yu acknowledges the Grant-in-Aid for JSPS Fellows and JSPS Research Fellowship for Young Scientists for financial support.

## References

1. G. J. McCarthy, W. B. White, D. E. Pfoertsch, *Mater. Res. Bull.* **13** (1978) 1239.
2. I. Szczygiel, T. Znamierowska, *J. Solid State Chem.* **95** (1991) pp. 260.
3. H. Y.-P. Hong, *Mater. Res. Bull.* **11** (1976) pp. 173.
4. M. A. Subramanian, P. R. Rudolf, A. Clearfield, *J. Solid State Chem.* **60** (1985) pp. 172.
5. R. J. Francis, M. J. Drewitt, P. S. Halasyamani, C. Ranganathachar, D. O'Hare, W. Clegg, S. J. Teat, *Chem. Commun.* (1998) pp. 279.
6. R. J. Francis, P. S. Halasyamani, D. O'Hare, *Angew. Chem., Int. Ed. Engl.* **37** (1998) pp. 2214.
7. P. S. Halasyamani, S. M. Walker, D. O'Hare, *Chem. Mater.* **121** (1999) pp. 7415.
8. P. S. Halasyamani, R. J. Francis, S. M. Walker, D. O'Hare, *Inorg. Chem.* **38** (1999) pp. 271.
9. D. Grohol, M. A. Sumbamanian, D. M. Poojary, A. Clearfield, *Inorg. Chem.* **35** (1996) pp. 5264.
10. D. M. Poojary, D. Grohol, A. Clearfield, *Angew. Chem., Int. Ed. Engl.* **34** (1995) pp. 1508.
11. D. M. Poojary, D. Grohol, A. Clearfield, *J. Phys. Chem. Solids* **56** (1995) pp. 1383.
12. R. C. L. Mooney, *Acta Crystallogr.* **3** (1950) pp. 337.
13. M. Vlasse, *Acta Crystallogr.* **38** (1982) pp. 2328.
14. C. Parent, P. Bochu, A. Daoudi, G. Leflem, *J. Solid State Chem.* **43** (1982) pp. 190.
15. L. P. Keller, G. J. McCarthy, R. G. Garvey, *Mater. Res. Bull.* **20** (1985) pp. 459.
16. G. Wu, M. Jansen, K. Konigsten, *J. Solid State Chem.* **98** (1992) pp. 210.
17. Y. Xu, S. Feng, W. Pang, G. Pang, *Chem. Commun.* (1996) pp. 1305.
18. *Crystal Structure Analysis Package*, Molecular Structure Corporation (1985 & 1990).
19. D. W. Breck, *Zeolite Molecular Sieves: Structure, Chemistry, and Use*, Wiley-Interscience, Toronto (1974).
20. G. O. Brunner, W. M. Meier, *Nature* **337** (1989) pp. 146.

# A STUDY ON CATALYTIC WET OXIDATION OF SIMULATED WASTEWATER SUCCINIC ACID AQUEOUS SOLUTION WITH Ru/TiO<sub>2</sub> CATALYST

SHI-HONG ZHANG, XUE-YAN TU, ZHONG-MIN YANG,  
ZI-HONG LI AND PIN-JIE HONG

*Chemistry Department, Yunnan University, Kunming 650091, China  
E-mail:xytu@yun.edu.cn*

YING YANG AND BIAO QIAN

*Yunnan High-Tech Environmental Protection Co. Ltd., 650032, China*

TiO<sub>2</sub> supports and Ru/TiO<sub>2</sub> catalysts were characterized with the compression strength, specific area and crystalline structure. Activities of Ru/TiO<sub>2</sub> catalysts in catalytic wet oxidation of succinic acid aqueous solution were studied. When loading the same content of Ru on the support, the larger of specific area and pore volume of the support, the higher the catalytic activity is. Activities of catalysts made by surface treated support are higher than those of the un-treated supports (COD removal increases by about 10%). The reaction is greatly influenced by temperature and pH value. When the reaction conditions are 270°C, pH=11.00, starting pressure 2.3MPa, reacting pressure 7.1MPa, 30min, the COD removal is in the range of 67.4-95.4%. The catalysts remain high activities and stability after 12 times of reaction in an autoclave and keep COD removal rate greater than 99%, whereas the NH<sub>3</sub>-N removal rate reaches 100% for a month running on a 200L/d reactor.

## 1 Introduction

Catalytic wet oxidation (CWO) is an efficient method for the treatment of refractory organic waste water. This technology has been widely investigated in recent years [1-5]. Organic pollutants are converted to CO<sub>2</sub>, H<sub>2</sub>O and N<sub>2</sub> in the process of CWO without producing second pollution. Today, CWO is mainly developed in three aspects as follows. First, CWO under supercritical conditions in which temperature is always higher than 344 °C and pressure greater than 22 MPa, so the pollutants are quickly degraded in a few seconds or minutes [6-10]. However, it demands highly strong instruments to support. Next, CWO is under medium conditions such as 200-300°C and 10-20 MPa using various of catalysts (for example, noble metals [11,12], Mn [13] and Cu [14]). The main researches are focused on developing high activation catalysts. Third, CWO is combined with other techniques (such as biological methods). However, many studies on CWO are still in the stage of laboratory and most catalysts are of powder. The shaping and strength of catalyst and its longevity are seldom considered. In industrial application, Osaka Gas developed a series of ripe technology. However, it costs too much in one time. This paper is focused on the industrial application of CWO to resolve the problems of support shaping, strength and catalyst activity and longevity.

## 2 Methods

### 2.1 Preparation of supports and catalysts

Metatitanic acid is the precursor of making TiO<sub>2</sub> supports. The rough steps of this technique are as follows. First, carbonate and binders are added into the material and then the mixture is shaped by wet compression to obtain a spherical product. The product is dried and calcined to give a spherical TiO<sub>2</sub> support ( $\Phi \approx 4.5\text{mm}$ ). Ru/TiO<sub>2</sub> catalyst is

made by the soaking method using a solution of RuCl<sub>3</sub>. After soaking the solution is filtered. A concentration of NaOH is used to precipitate Ru<sup>3+</sup> and the Ru(OH)<sub>3</sub> is reduced by chemical method, and then the Ru/TiO<sub>2</sub> catalysts are washed with water and finally dried at 100°C.

## 2.2 Characterization of supports and catalysts

In our experiment, the compression strength of supports was tested by an intellect strength tester (Model ZQJ, China). Specific areas, pore volume and average pore diameters were measured by a static physical absorber (Model ASAP-2000, America). The surface of catalyst was observed under an electron microscope (Model JEM-1200EX). The crystal structure was detected by an X-ray fluorescence spectrometer (Model 3015, Japan). The content of Ru was detected by a plasma spectrum instrument (Model ICPS-1000II).

## 2.3 Determination of catalytic activities

### 2.3.1 Apparatus and agents

A schematic diagram of the autoclave (Model CJF-025) is shown in Figure 1. It is made of stainless steel with 250mL of volume and design temperature within 350°C, and the temperature accuracy is  $\pm 3^\circ\text{C}$ . The design pressure is within 22 Mpa; impel moment 120N·cm and heating power 0.8kW. A continuous fixed bed reactor (Model STU, Osaka Gas) with a treating capacity of 200L/d is also employed in our experiment.

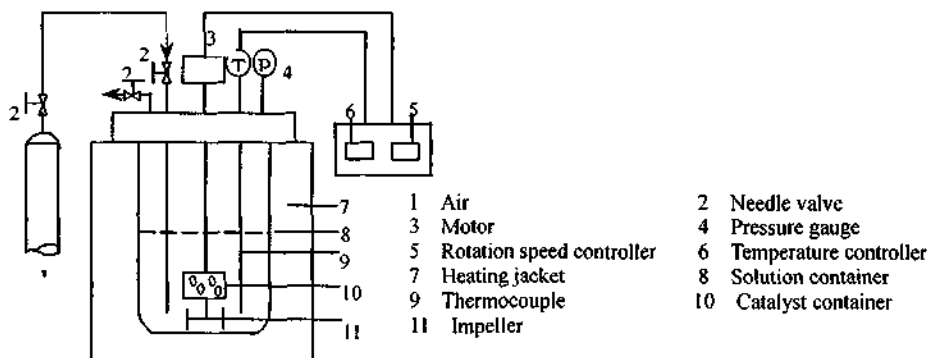


Figure 1. Schematic diagram of experimental apparatus.

The simulated wastewater is a solution of 7.4g/L succinic acid (COD $\approx$ 7000mg/L). Coking wastewater in which the COD was 4500-5000mg/L and the NH<sub>3</sub>-N was about 1000mg/L was taken from Kunming coking factory. All the agents are of A. R. purity.

### 2.3.2 The procedures of treating wastewater

When the reaction was carried out in the autoclave, 10g of Ru/TiO<sub>2</sub> catalyst was put in the catalyst container and 100mL of simulated wastewater was injected in the solution container and the pH value of the wastewater was adjusted by adding solid NaOH when necessary. Then, the reactor was sealed up and a initial pressure of air was injected in the

reactor (here, the theoretical initial pressure of air was calculated based on the reaction equation  $\text{HO}_2\text{C}(\text{CH}_2)\text{CO}_2\text{H} + 3.5\text{O}_2 \rightarrow 4\text{CO}_2 + 3\text{H}_2\text{O}$ , and the amount of air injected was 1.5 times that of the theory value). The reactor was heated to a certain temperature at the rate of 7°C/min with a impelling speed of 800r/min. The reaction was hold for 30min at the temperature and then the solution container was taken out from the heating jacket and cooled at a rate of 5°C/min. After cooling to room temperature, the COD and  $\text{NH}_3\text{-N}$  were detected.

### 3 Results and Discussion

#### 3.1 Characterization of supports and catalysts

The CWO process is always carried out at high temperatures and pressures and the wastewater is always an acidic or basic system, so it demands that the support have a high strength and can endure the corrosion of acid or base. In our experiments, zeolites and  $\text{Al}_2\text{O}_3$  were used as supports; however, they are unsuitable because of low strength or leaching in acid or base solution.  $\text{TiO}_2$  supports prepared in our laboratory show advantages in strength and anti-acidity (or base). It is a suitable support for CWO process. Six kinds of  $\text{TiO}_2$  supports and two Ru-TiO<sub>2</sub> catalysts are characterized in Table 1. Figure 2 is a TEM photograph of the Ru-TiO<sub>2</sub> catalysts. The compression strength is in the range of 96-146N and the specific area is 14-26m<sup>2</sup>/g; pore volume 0.086-0.16mL/g and average pore diameter 21.6-26.2nm. The pore volume increases with specific area. Support TiO<sub>2</sub>:3\* is made of TiO<sub>2</sub>:3 via surface treatment and it gives a larger specific area and pore volume. According to their higher catalytic activity in comparison with other catalysts (see Table 3), Ru/TiO<sub>2</sub>:3 and Ru/TiO<sub>2</sub>:3\* are chosen as further study in our experiment.

Table 1. Characteristics of supports and catalysts.

Sample	Compression strength (N)	Specific area ( $S_{\text{BET}}$ ) (m <sup>2</sup> /g)	Pore volume (mL/g)	Average pore diameter (nm)
TiO <sub>2</sub> : 1	96	14	0.086	21.6
TiO <sub>2</sub> : 2	98	16	0.094	26.2
TiO <sub>2</sub> : 3	110	25	0.15	24.0
TiO <sub>2</sub> : 3*	112	26	0.16	24.5
TiO <sub>2</sub> : 4	130	23	0.14	23.7
TiO <sub>2</sub> : 5	146	22	0.12	22.7
Ru/TiO <sub>2</sub> :3	108	24	0.14	23.1
Ru/TiO <sub>2</sub> :3*	114	26	0.16	23.3

\* Via surface treating

The XRD analysis results of the supports and catalysts are shown in Table 2. Figure 3 is the XRD pattern of the catalyst. The results indicate that TiO<sub>2</sub> mainly exists in the form of anatase at the content of 93-95% and exists as rutile if the content is less than 1.0%. The content of BaSO<sub>4</sub> is about 2.9-4.5% and rest is about 1%. The content of Ru in the catalyst is approximately 2%. The crystal structure of the surface-treated support is the same as the un-treated one. When 2% of Ru is loaded on the supports, the diffraction

peak of rutile disappears. Ru exists in a hexagonal form in the catalysts.

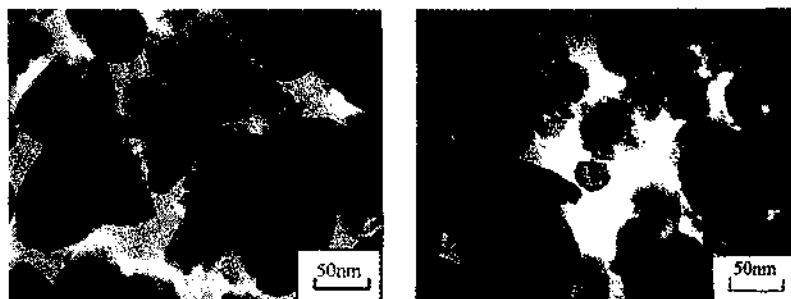


Figure 2. TEM photographs of catalysts: (left) Ru/TiO<sub>2</sub>;3\*; (right) Ru/TiO<sub>2</sub>; 3.

Table 2. Crystalline structure of supports and catalysts.

Sample	TiO <sub>2</sub> (%)				Other content (%)
	Anatase (tetragonal system)	Rutile (tetragonal system)	BaSO <sub>4</sub> (%)	Ru (hexagonal system) (%)	
TiO <sub>2</sub> ; 1	93.49	<1.00	4.51	-	1.00
TiO <sub>2</sub> ; 2	93.67	<1.00	4.33	-	1.00
TiO <sub>2</sub> ; 3	94.54	<1.00	3.46	-	1.00
TiO <sub>2</sub> ; 4	94.76	<1.00	3.24	-	1.00
TiO <sub>2</sub> ; 5	95.04	<1.00	2.96	-	1.00
TiO <sub>2</sub> ; 3*	94.45	<100	3.55	-	1.00
Ru/TiO <sub>2</sub> ;3	94.17	-	2.82	2.01	1.00
Ru/TiO <sub>2</sub> ; 3'	94.22	-	2.82	1.96	1.00

### 3.2 Catalytic activities in autoclave and mini-200L/d continuous reactor

Table 3. presents the abatement results of simulated wastewater succinic acid solution with different catalysts in CWO process. The reactions were carried out in an autoclave under the same reaction conditions. The content of Ru in the catalysts is approximately 2%. Among the tested catalyst, Ru/TiO<sub>2</sub>;3\* has the highest COD removal rate. This may be due to the contribution of surface treatment on the support. The specific area, pore volume and average pore diameter are enlarged after the treatment, resulting in the Ru concentration increase on the surface of the support and accelerating the reaction speed. Further study on the Ru/TiO<sub>2</sub>;3\* is still underway, and new results will be reported elsewhere.

**Table 3.** Catalytic activity of various catalysts.

Catalysts	Ru (%)	COD in treated water (mg/L)	COD removal (%)
Ru/TiO <sub>2</sub> :1	2.11	2281.3	67.4
Ru/TiO <sub>2</sub> :2	2.05	2225.3	68.2
Ru/TiO <sub>2</sub> :3	2.01	1009.4	85.6
Ru/TiO <sub>2</sub> :4	2.08	1143.8	83.7
Ru/TiO <sub>2</sub> :5	2.04	1344.0	80.0
Ru/TiO <sub>2</sub> :3'	1.96	325.0	95.4

Reaction condition: 270°C, pH=11.00, starting pressure 2.3 MPa, reaction pressure 7.1 MPa, 30min.

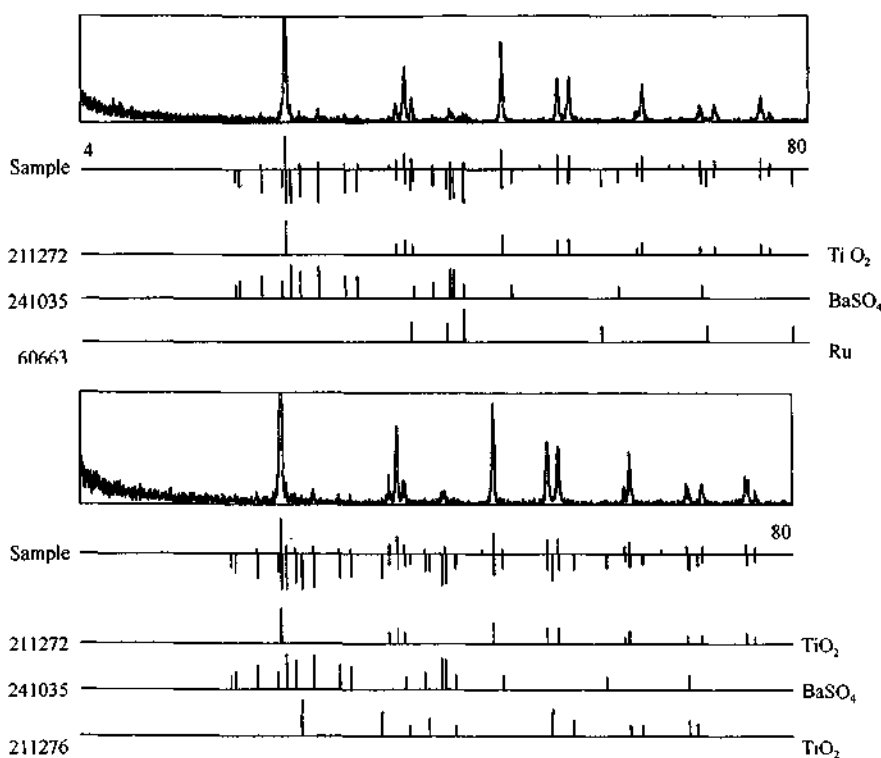
**Figure 3.** XRD patterns for TiO<sub>2</sub> support (top) and Ru/TiO<sub>2</sub>:3 catalyst (bottom).

Figure 4 shows the result of using Ru-TiO<sub>2</sub>:3 to treat the simulated wastewater succinic acid in a 200L/d continuous reactor under different conditions. When the water ran at a speed of 4L/h and the O<sub>2</sub> content is 20%, the COD and NH<sub>3</sub>-N removal rate increases with temperature and pressure. When the temperature is down to 200°C, the COD removal is nearly zero. However, the NH<sub>3</sub>-N can be partly removed. This may indicate that 200°C is an activating temperature for the catalyst Ru/TiO<sub>2</sub>:3. The reaction speed is greatly influenced by temperature. When the temperature increases to 250°C, at 7.0MPa, the COD removal rate is greater than 99% and the NH<sub>3</sub>-N removal rate reaches

100% in 15min of reaction.

In this work, a coking wastewater was treated in a continuous reactor using Ru/TiO<sub>2</sub>:3. The results of one month running are shown in Figure 5. The reactions proceed at 250°C, 7.0MPa, O<sub>2</sub> content 20%, water speed 4L/h, 30min. The COD removal rate remained greater than 99% and the NH<sub>3</sub>-N removal rate was nearly 100%.

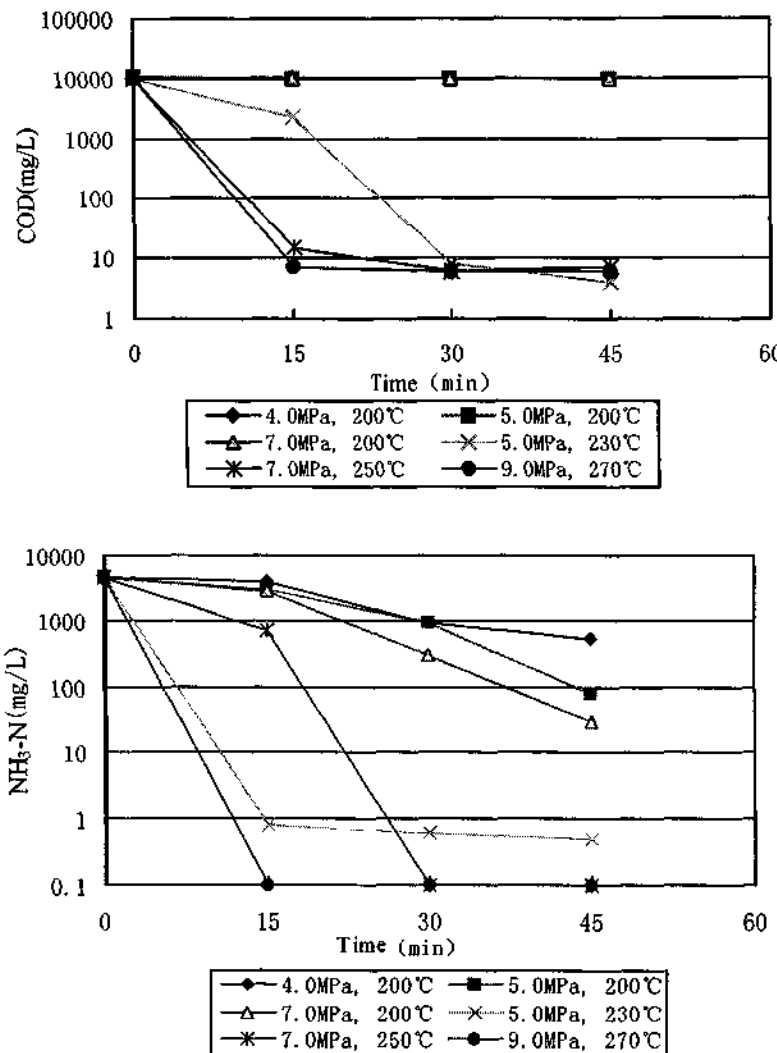


Figure 4. The results of using Ru/TiO<sub>2</sub> : 3 to treat simulated wastewater.

The relationship between COD removal and temperature is shown in Table 4. The COD removal increase with temperature is attributed to that the solubility of O<sub>2</sub> in water increases with the temperature and a high speed impelling accelerates the mass transport.

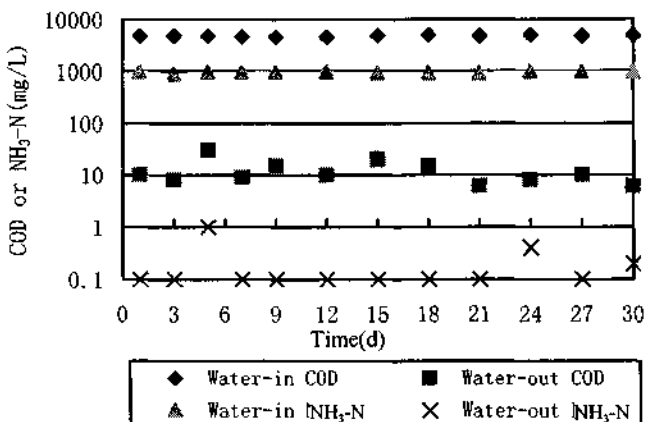


Figure 5. The results of treating coking wastewater in a month using the catalyst Ru/TiO<sub>2</sub>·3.

Table 4. The influence of temperature on COD removal.

Temperature (°C)	COD in treated water (mg/L)	COD removal (%)
210	6081.2	13.1
230	3631.2	48.1
250	1443.8	79.4
270	931.2	86.7

Reaction conditions are the same as in Table 3 except for temperature.

The experimental results indicate that the COD removal is greatly influenced by the initial pH value of the succinic acid solution. The results are shown in Figure 6. The COD removal rate is higher in the range of pH 2.7-5.0 and pH 9.0-12.0. However it decreases to the lowest value at pH 7.0. In our experiment, pH=11.00 was chosen as the initial value which can decrease the corrosion to the reactor. The reaction solution always turns to acidic when the initial pH value is lower than 11.00. However, it becomes a neutral system when the initial pH value is greater than 11.00.

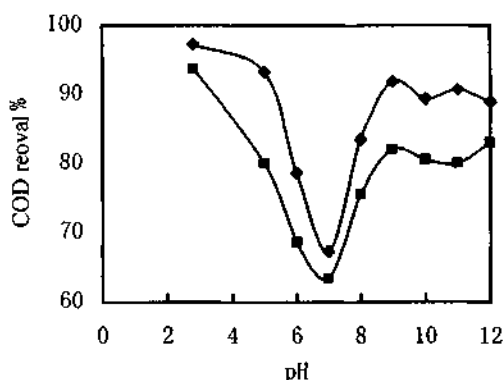


Figure 6. The influence of pH value on COD removal. Reaction conditions are the same as in Table 3 except for pH value (◆: Ru/TiO<sub>2</sub>·3\*, ■: Ru/TiO<sub>2</sub>·3).

The compression strength is regarded as an important mechanical property of support which directly influences the life of catalyst. However, compression strength and specific area is a pair of contradictions. To make a high strength support needs the sacrifice of the specific area. In this work, the compression strength of support was controlled in the range of 100-120N. The COD removal results of different specific area supports loading the same content of Ru are shown in Table 5. As one sees, the Ru/TiO<sub>2</sub>:3\* material exhibits a high COD removal rate (higher than that of Ru/TiO<sub>2</sub>:3 by about 10%). The results indicate that the larger the specific area the higher the COD removal rate.

**Table 5.** The influences of specific area and pore volume on COD removal rate.

Support name	Catalyst	Specific area (S <sub>BET</sub> ) (m <sup>2</sup> /g)	Pore volume (mL/g)	COD removal (%)
TiO <sub>2</sub> :1	Ru/TiO <sub>2</sub> :1	14	0.086	67.4
TiO <sub>2</sub> :2	Ru/TiO <sub>2</sub> :2	16	0.094	68.2
TiO <sub>2</sub> :3	Ru/TiO <sub>2</sub> :3	25	0.15	85.6
TiO <sub>2</sub> :3*	Ru/TiO <sub>2</sub> :3*	26	0.16	95.4
TiO <sub>2</sub> :4	Ru/TiO <sub>2</sub> :4	.23	0.14	83.7
TiO <sub>2</sub> :5	Ru/TiO <sub>2</sub> :5	22	0.12	80.0

Reaction conditions are the same as in Table 3.

The leaching of several ions in the reaction solution has also been studied (see Table 6). Fe, Ti, Ru are leached out at pH 3-9, but the leaching becomes very weak when the pH value is greater than 10.00. Therefore, choosing pH=11.00 as the initial pH is reasonable. Repeating the reaction for 12 times with the same catalyst Ru/TiO<sub>2</sub>:3 has been conducted to test the catalyst stability. The results indicate that a small amount of Ru and Ti can be detected in the reaction solution, but the COD abatement still remains at 85% without losing the activity of the catalyst.

**Table 6.** The concentration of main ions in the reaction solution at different pH values.

pH	Fe (μ g/mL)	Ti (μ g/mL)	Ru (μ g/mL)
3.0	248.06	1.89	4.50
5.0	319.00	1.96	6.66
7.0	286.37	27.90	9.08
9.0	206.31	11.75	5.76
10.0	4.51	0.89	N.D.
11.0	3.78	N.D.	0.11
12.0	3.82	1.75	1.18

Reaction conditions are the same as in Table 3 except for pH value.

### 3.3 The mechanism of CWO

The mechanism of CWO is complex until now and there is still no final conclusion. A common opinion is that an  $O_2^-$  free radical appears in the reaction [15,16]. Yang et al. [10] proved the free radical mechanism under supercritical conditions. The research of Li [15] and Pintar [16] indicates that  $TiO_2$  may first interact with  $O_2$  to produce superoxide radical  $O_2^-$ . These radicals can initiate a free radical reaction. The final products are  $CO_2$  and  $H_2O$ . The surface of  $TiO_2$  becomes an oxygen deficient surface when the superoxide radical  $O_2^-$  is derived from the stoichiometric composition, and the number of surface vacant sites for oxygen activation is a function of the specific area. This would explain the relationship between the specific area and the catalytic activity. The larger the specific area the more the number of superoxide radical  $O_2^-$ . The adding of Ru could increase the catalytic activity, because Ru may function in the cycle of  $Ru_2O_3/Ru$  and thus to activate oxygen to produce  $O_2^-$  or form OXO metal complexes [16]. On the other hand, different  $Ru/TiO_2$  catalysts exhibit the lowest COD removal rate at pH=7.0 and a higher COD removal rate at acidic or basic conditions. Consequently, the mechanism should be related with  $H_3O^+$  and  $OH^-$  species, and we believe that the reaction is an acid or base catalyzed one [17].

## 4 Conclusion

The  $Ru/TiO_2$  catalyst prepared in our laboratory shows high catalytic activity in CWO of succinic acid solution. It retains a COD removal rate greater than 99% and an  $NH_3-N$  removal rate close to 100% in the treatment of coking wastewater. The catalyst is stable for long time running.

## 5 Acknowledgements

This work was financially supported by the high-tech. industrial project of the National Project Committee and Osaka Gas Co. Ltd.

## References

1. Levec J., Wet oxidation processes for treating industrial wastewaters. *Chem. Biochem. Eng.*, **11** (1997) pp.47-58.
2. Josef Prousek, Advanced oxidation processes for water treatment. *Chem. Process. Chem. Listy*, **90** (1996) pp. 229-237.
3. Luck F., A review of industrial catalytic wet oxidation processes. *Catal. Today*, **27** (1996) pp. 195-202.
4. Zhong Y. D., Michael A. F. et. al., Catalytic wet oxidation in supercritical water. *Ind. Eng. Chem. Res.*, **35** (1996) pp. 3257-3279.
5. Earnest F. Gloyna and Lixiong Li, Supercritical water oxidation research and development update. *Environ. Progress*, **14** (1995) pp. 182-192.
6. Rofer C. K., Supercritical water oxidation for treatment of mixed wastes. *Proc. Inc. Symp. Ist.*, (1991) pp. 278-291.
7. Gloyna E. F., Li, L., Supercritical oxidation: an engineering update. *Waste Manage*, **13** (1993) pp. 379-387.

8. Welbley P. A., Tester J. W., Holgate H. R., Oxidation kinetics of ammonia and ammonia-methanol mixtures in supercritical water in the temperature range 530-700 °C at 246bar. *Ind. Eng. Chem. Res.*, **30** (1991) pp. 1745-1754.
9. Li. R., Savage P. E. D., Szmukler, D. et al., The 2-chlorophenol oxidation in supercritical water: global kinetics and reaction products. *Environ. Energy Eng.*, **39** (1993) pp. 178-186.
10. Yang. H. H., Eckert C. A., Homogeneous catalysis in the oxidation of p- chlorophenol in supercritical water. *Ind. Eng. Chem. Res.*, **27** (1998) pp. 2009-2018.
11. Qin J. Y., Zhang Q. L., Karl. T. Chuang K. T., Catalytic wet oxidation of p- chlorophenol over supported noble metal catalysts. *Appl. Catal. B: Environ.*, **29** (2001)pp. 115-123.
12. Delanoë F., Acedo B., Karpel N., Leitner V., Legube B. et al., Relationship between the strucrre of Ru/CeO<sub>2</sub> catalysts and their activity in the catalytic ozonation of succinic acid aqueous solution. *Appl. Catal. B: Environ.*, **29** (2001)pp. 315-325.
13. YLiu Y., Lou M., Wei Z., Xin Q., Ying P. L., Li C., Catalytic oxidation of chlorobenzene on supported manganese oxide catalysts. *Appl. Catal. B: Environ.*, **29** (2001) pp. 61-67.
14. Hočevá S., Krašovce U. O., Orel B., Aricó A. S., Kim H., CWO of phenol on two differently prepared CuO-CeO<sub>2</sub> catalysts. *Appl. Catal. B: Environ.*, **28** (2000) pp. 113-125.
15. Li, C., Domen, K. Maruya K. L., Onishi T. et al., Oxygen exchange reaction over cerium oxide: an FI-IR study, *J. Catal.*, **123** (1990) pp. 436-442.
16. Pintar A., Besson M., Gallezot P., Catalytic oxidation of Kraft bleaching plant effluents in the presence of titania and zirconia supported ruthenium, *Appl. Catal. B: Environ.*, **30** (2001) pp. 123-139 .
17. Wu Y., *Catalytic Chemistry*, Science Press, (1990) pp. 171-176.

## SYNTHESIS AND CATALYSIS OF MESOPOROUS SILICA-HETEROSTRUCTURED MATERIALS BASED ON MONTMORILLONITE

CHUNHUI ZHOU,\* QINWEI LI, ZHONGHUA GE AND XIAONIAN LI

*Laboratory of Advanced Catalyst Materials, College of Chemical Engineering, Zhejiang University of Technology, Hangzhou 310014, China  
E-mail: catalysis8@yahoo.com.cn*

Based on ion-exchange and self-assembly techniques, a novel nanoporous silica-montmorillonite heterostructured material which exhibits a basal spacing of 37.1 Å, gallery height 27.5 Å, a BET surface area of 661 m<sup>2</sup>/g and average pore size 25 Å has been synthesized. According to XRD, FTIR, TEM and TG results, a new type of porous material is thought to be formed by *in situ* silica intercalation and assembly. Both the clay:DDA:TEOS molar ratio and reaction time have important effects on the  $d_{001}$  value and the crystallinity of the final materials. The synthetic material is a potentially effective solid acid catalysts for the Friedel-Crafts alkylation of catechol with tert-butyl alcohol to synthesize butyl 4-tert-butylcatechol (4-TBC). The results show that the brönsted acidity favors the conversion of catechol, but the pore structure controls the selectivity. Over synthetic nanoporous material the selectivity of 4-TBC is 21.2% and the conversion of catechol 77.1% under experimental conditions. All of results indicate that the silica -montmorillonite heterostructure has great potential applications for larger molecule adsorption and acid catalysis.

### 1 Introduction

Over the past four decades, considerable synthetic efforts have been devoted to developing frameworks with larger pore diameters. The largest synthesized mesoporous molecular sieves designated as M41S have been discovered early in 1990s [1-5]. Although M41S possesses specific properties which have great potential applications in catalysis and sorption, these materials still suffer some drawbacks which have been the limiting factors in their industrial applications [1]. As an alternative approach to obtain thermally stable porous materials, various inorganic oxo-cations have been intercalated into layered solids such as smectite clays and phosphates [2-4]. Calcination of these cation-intercalated materials formed inorganic pillared solids with different characteristics. Especially such pillaring of layered aluminosilicates has given rise to many attempts to prepare new high surface area materials which can be used for separations, sorption and catalysis.

In most of the reported layered clay pillared by inorganic pillars such as aluminum Keggion ions and tetrameric zirconium cations, the gallery heights are comparable to the van der Walls thickness of the host layers [3,4]. Silica also is one of the most commonly used pillars. Although silica pillared clays have been discovered, the process of preparation is very complicated and inconvenient [5]. It was noted that recently a new method has been developed [6] for preparation of porous clay materials which possess the pore size distributions in the supermicropore to small mesopore (14-25 Å). The new approach to designing porous clay materials is based on the use of intercalated quaternary ammonium cations and neutral amines as co-surfactants to direct the interlamellar hydrolysis and condensation polymerization of neutral inorganic precursor within the galleries of an ionic lamellar solid. Several layered host structures such as fluorohectorite, synthetic saponite [6], magadiite [7], and beidellites [8] have been used for conducting relative investigation, but all starting layered hosts are man-made.

Based on ion-exchange and self-assembly techniques, in this paper we try to synthesize porous silica-montmorillonite heterostructured materials, starting with natural sodium montmorillonite which are ubiquitous so their cost effectiveness will continue to be lower than any synthetic competitive materials. The silica will be orderly assembled within gallery of layers, using the template-directing action. Through the catalytic alkylation reaction of catechol to produce polymerization inhibitor 4-tertbutylcatechol, the catalytic properties of porous silica-montmorillonite heterostructure were evaluated.

## 2 Experimental

The synthesis procedure for the new porous materials from sodium montmorillonite (source Clays, from Ningan Zhejiang, China) is typically as follows. Organic intercalating was achieved using the <2 $\mu$ m sodium montmorillonite fractions collected by usual sedimentation. 14.6 gram of cetyltrimethylammonium bromide (CTAB) in 50mL deionized water was mixed with 2% aqueous suspension of montmorillonite (20g) and the mixture was stirred for 1 day. The solid was filtered, then followed by washing and drying at 90°C. 5 gram of organomontmorillonite was added to a solution of dodecyl amine (6.25g). Tetraethyl orthosilicate (TEOS) was added to above reaction mixture under vigorously stirring for 8 hours at room temperature. After that, the solid was separated by filtration, aged and finally dried in air on a glass plate and calcined at 550°C under N<sub>2</sub> flow for 4 hours to removed the templated surfactant. H-clay are prepared by acidifying original sodium montmorillonite with 15% H<sub>2</sub>SO<sub>4</sub> for 8 h.

The X-ray powder diffraction spectra(XRD) was recorded on a Philips X'Pert instrument using Cu K $\alpha$  radiation ( $\lambda=1.5404\text{ \AA}$ ). Nitrogen adsorption-desorption isotherms were obtained using a Coulter Omnisorp 100CX. The specific surface areas were calculated by the BET method. The FTIR spectra were recorded on a Shimadzu 8300 spectrometer in a Nujol matrix and the KBr wafer technique was used. Thermogravimetric analysis were taken with Shimadzu TG-50, using 10°/min heating rate. For transmission electron microscopy a JEOL 1200EX instrument was used. The catalytic performance and its acidity were checked by probe reaction of the alkylation of catechol (CAT) with tert-butyl alcohol (TBA) to synthesize 4-tert-butylcatechol (4-TBC). The catalytic reactions were carried out in a glass batch reactor. The products were analyzed by HPLC with Zorbax ODS25ml×4.6mm i.d. column and UV detector. All reagents were analytically pure and were used without further treatment.

## 3 Results and Discussion

### 3.1 The effect of preparation conditions

The corresponding formula for starting Na-montmorillonite is Na<sup>+</sup><sub>0.66</sub>[Al<sub>2.97</sub>Fe<sub>0.37</sub>Mg<sub>0.66</sub>](Si<sub>8.00</sub>)O<sub>20</sub>(OH)<sub>4</sub>. The effects of synthetic conditions on the samples were investigated by the XRD technology to trace the change of basal spacing value. The basal spacing  $d_{001}$  of starting montmorillonite is 12.2 Å ( $2\theta=7.24^\circ$ ), and after calcined at 500°C the  $d_{001}$  value decrease to 9.86 Å ( $2\theta=8.96^\circ$ ). CTAB readily intercalates montmorillonite and increases the interlayer distance to 22.1 Å ( $2\theta=4.00^\circ$ ). After the organoclay reacted with DDA, the basal spacing reached 47.9 Å ( $2\theta=1.84^\circ$ ), which was approximately equal to the value of the 9.6 Å thickness of the clay layer plus C<sub>16</sub>H<sub>33</sub>N(CH<sub>3</sub>)<sub>3</sub><sup>+</sup> chain length (21.5 Å) and C<sub>12</sub>H<sub>25</sub>NH<sub>2</sub> chain length (16.5 Å). The results

revealed that organo montmorillonite not only changed the character of interlamellar surface from hydrophilic to hydrophobic, but also expanded the gallery to facilitate the accessibility of amine. After the host further reacted with Si sources and calcination at 550°C for 4 hours, the basal spacing  $d_{001}$  of the as-synthesized samples decreased to 37.1 Å ( $2\theta=2.38^\circ$ ) under 1:20:150 molar ratio of clay:DDA:TEOS, owing to the organic template decomposition and formation of new silica structure [Figure 1(c)]. The XRD results showed that both the clay:DDA:TEOS molar ratio and reaction time have important effects on the  $d_{001}$  value and crystallinity of the final materials [Figure 1 and Figure 2]. Only when the amounts of co-template amines and reaction time were suitable can the heterostructured materials take shape.

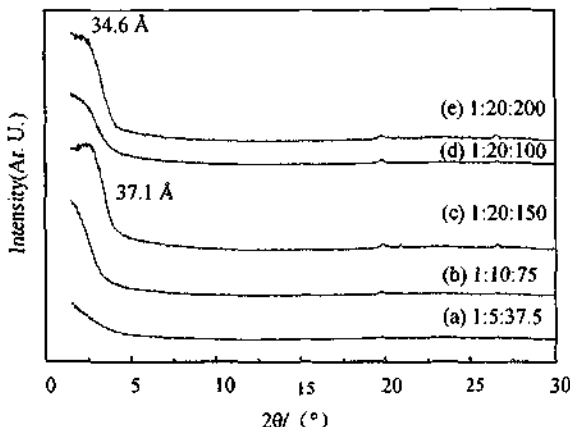


Figure 1. Effect of different maolar ratio of organoclay/DDA/TEOS (reaction time: 8 h).

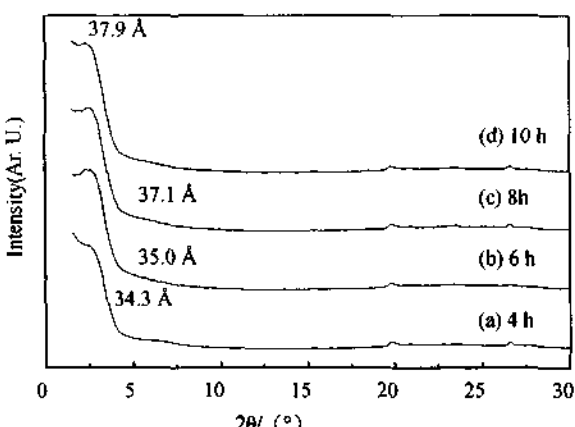
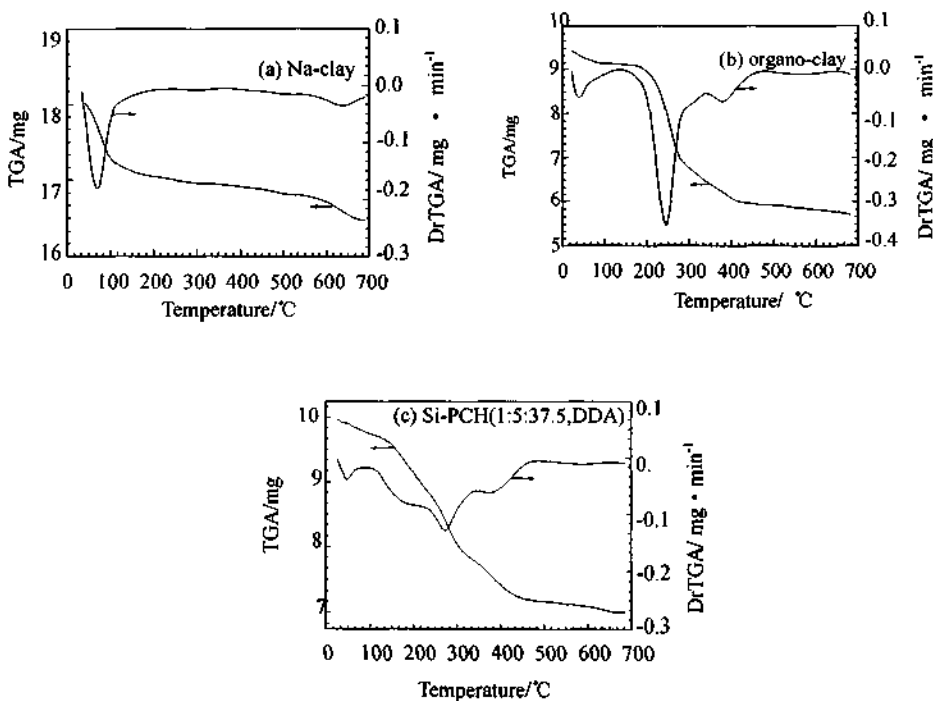


Figure 2. Effect of different reaction time (molar ratio of organoclay/DDA/TEOS: 1:20:150).

### 3.2 The analysis of TG of samples

The thermogravimetric analysis curves of Na original clay, organo clay and the as-synthesized sample were shown in Figure 3. The thermogravimetric analysis of this as-synthesized sample revealed about 36.76% total weight loss on heating to 700°C. The percentage of weight loss is much higher than that of CTAB surfactant in complex  $[C_{16}H_{33}N(CH_3)_3]^{+}_{0.66}[Al_{2.97}Fe_{0.37}Mg_{0.66}]Si_{8.00}O_{20}(OH)_4$ , thus revealing the intercalation of neutral amine. Compared with Na clay and organo clay, more distinguishing weight loss was observed in the curve of as-synthesized sample and could be divided into three parts. The first part before 100°C is attributed to the release of adsorbed water, the second including temperature ranges of 100-185°C, 185-330°C, 330-460°C to the desorption and decomposition of neutral amine and CTAB, and the third after 460°C decreasing slowly to dehydroxylation of silica within gallery (Figure 3). Combining TG results with XRD patterns, it is deduced that amine and air-drying arouse the interlamellar hydrolysis and condensation polymerization of Si precursor within the galleries of montmorillonite. Therefore a nano scale silica montmorillonite heterostructure with gallery height 27.24 Å ( $=37.1-9.86\text{ \AA}$ ) has been obtained after calcination at 550°C indeed.



**Figure 3.** Weight loss and derivative curves from TGA (run in nitrogen atmosphere) of synthetic samples.

### 3.3 The analysis of infrared spectra of samples

The FTIR spectra of the final sample, air-dried sample, organo clay and original clay are shown in Figure 4. In the spectrum of Na-Clay, the peaks at  $470\text{cm}^{-1}$ ,  $524\text{cm}^{-1}$ ,  $916\text{cm}^{-1}$

and  $1039\text{cm}^{-1}$  can be ascribed to montmorillonite Si-O bending vibration, Al-O stretching vibration, Al-OH-Al bending vibration and Si-O stretching vibration respectively. The peaks at  $1635\text{cm}^{-1}$ ,  $3431\text{cm}^{-1}$  and  $3628\text{cm}^{-1}$  are assigned to hydroxyl HOH, -OH vibrations. Organoclay exhibits bands at  $2853\text{cm}^{-1}$ ,  $2923\text{cm}^{-1}$  and  $1467\text{cm}^{-1}$ . The presence of these peaks is considered to be a strong evidence for the intercalation of CTAB into the layer of clay. A similar stronger band is also observed in the as-synthesized samples, because of amine intercalation. After calcinations, all peaks of organic groups disappeared, thus confirming the organic template decomposition and formation of new silica structure. The new band at  $960\text{ cm}^{-1}$  is considered to be Si-O in the interlayer and the band at  $3629\text{cm}^{-1}$  which can not be observed in the final sample, air-dried samples are attributed to hydrolysis in the interlayer region of the as-synthesized sample. The above results further illustrate that intercalation, hydrolysis and condensation took place within gallery and a new porous material came into being.

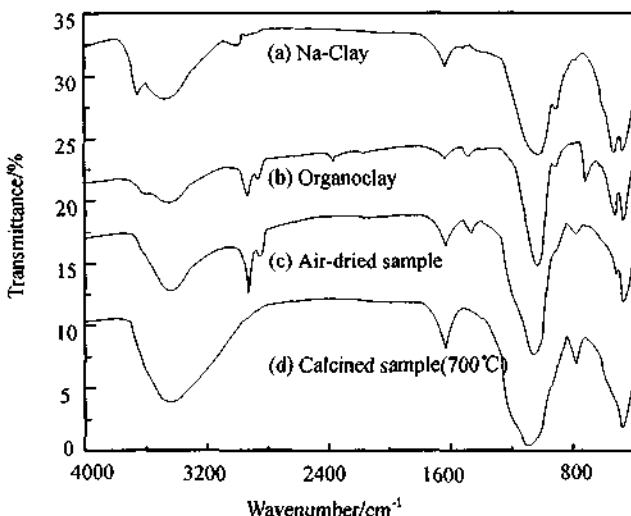


Figure 4. FTIR spectra of different samples.

### 3.4 The analysis of TEM and adsorption-desorption of samples

Using transmission electron microscopy the lattice fringe image can be seen. Also the scanning electron microscopy image showed that the montmorillonite layer structures still remained after Si-heterostructure and no occluded clay by  $\text{SiO}_2$  is observed. The results further indicate the expansion of the basal spacing.

The porosity of montmorillonite is greatly increased by *in situ* intercalation of silica. The BET specific surface area of the material reaches  $661\text{m}^2/\text{g}$ . The pore-size distribution is measured by the BJH method using the desorption curve, which has an average value of  $25\text{ \AA}$ . The original montmorillonite is actually a non-porous solid with a surface area of experimental value  $75\text{m}^2/\text{g}$ , which is significantly lower than those calculated for single layer particles, evidencing that only external surface is accessible to nitrogen [9].

A dense silica phase completely filling the interlayer region would not give rise to the observed high surface areas. Considering these facts, a new type of porous material is thought to be formed by silica intercalation and assembly. The specific surface area of the as-synthesized samples outgassed at 120°C is also very low, probably due to overcrowding of interlayer space and filling of the micropores by organic cations. The shape of nitrogen adsorption-desorption isotherms for the synthetic sample has a hysteresis loop which is typical for micro-mesoporous structure which belong to a Type-IV isotherms(see Figure 5 ).The results are also in good agreement with the specific surface area measurements.

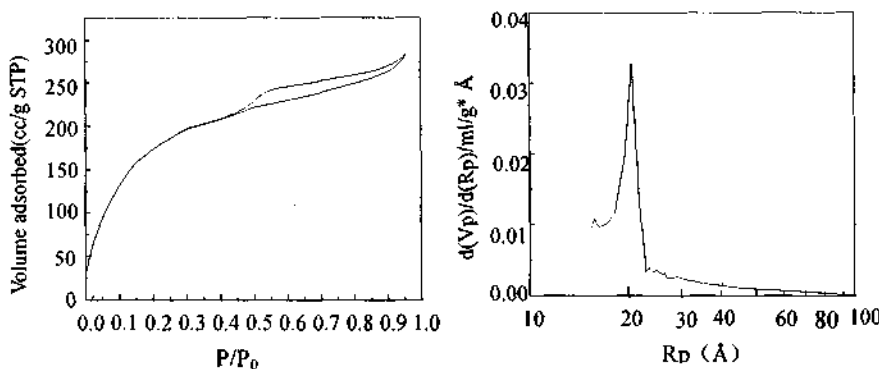


**Figure 5.** Nnitrogen adsorption-desorption curves (a) and pore size distribution curves (b) of Si-heterostructured montmorillonite sample.

### 3.5 The catalytic performances of synthetic samples

The possibility of using this materials for shape selective and acid catalysis was investigated by probe reaction of alkylation of catechol with tert-butyl alcohol to produce 4-tert-butylcatechol (4-TBC), compared with the H-clay and other solid acid molecule sieve catalyst. Catechol alkylation with tert-butyl alcohol is a typical Friedel-Crafts alkylation and can be catalyzed by acid sites. From the data (see Table 1), it is clear that the performance is governed by acidity and pore structures. Because of calcinations at 800°C and 900°C, the catalyst gallery shrunk and the pore size was decreased or damaged, so the selectivity decreased. Over the silica-montmorillonite which was calcinated at 700°C the catechol conversion and 4-TBC selectivity are 77.1% and 21.2% respectively, which are the best among the tested catalysts. H-clay showed lower conversion and selectivity under the same reaction conditions. It was illustrated that the silica-montmorillonite heterostructure has not only stronger acid catalytic properties but also larger and well-defined pore structure. It is speculated that a significant enhancement of acidity is achieved by the novel silica-montmorillonite. The main reason is probably extra formation of protons resulted from the surfactant and cocompound removal from the as-synthesized solids. Although traditional liquid acid catalyst also has good result in conversion of catechol, it gives rise to many problems concerning corrosion and pollution, which can be overcome by environmentally friendly solid acid catalysts.

**Table I.** Catalytic properties of samples calcined at different temperatures.

catalysts	Null	600°C	700°C	800°C	900°C
Con. of Catechol /%	0	83.8	77.1	95.2	95.3
Sel. of 4-TBC /%	0	19.3	21.2	13.2	9.7
Yield of 4-TBC /%	0	16.2	16.3	12.5	9.2

(catalyst samples producing conditions: organoclay/DDA/TEOS=1:20:150, reaction time:8 h. catalytic reaction condition: catalyst 500mg, catechol 5g/ tert-butyl alcohol = 1:1.5 molar ratio, reaction time 2h, temperature 135°C, solvent: m-xylene 30ml)

In conclusion, the silica-montmorillonite heterostructured material prepared here is facile to be obtained. More importantly, it possesses a higher surface and larger pore than conventional  $\text{Al}_{13}$  pillared montmorillonite [10]. During the formation of new silica-montmorillonite heterostructure, acidity has been tuned to enable its application at alkylation of larger reactant molecular and transitional states. If over the nanoporous silica-montmorillonite the catalytic alkylation reaction condition is further investigated, it will be of great significance to use this solid acid catalyst to replace polluted liquid acid in catalysis to produce fine chemicals. Further systematic investigation on this material is under way.

#### 4 Acknowledgement

Financial supports of the Natural Science Foundation No.201057 of Zhejiang Province (China) are gratefully acknowledged.

#### References

1. F. Agnes, K. Imre, S-I. Niwa, M. Toba, Y. Kiyozumi, F. Mizukami. mesoporous materials synthesized by intercalation of silica tubes between magadiite layers. *Appl. Catal. A*:176(1999), pp.L153-L158.
2. T. J. Pinnavaia, Intercalated clay catalysts. *Science*, 220(1983), pp.365-371.
3. F. Figueras, Pillared clays as catalysts. *Catal. Rev. Sci. Eng.* ,30(1988), pp.457.
4. C. X. Guo,W. H. Hou, M Guo, Q. J. Yan and Y. Chen. Synthesis of a new solid acid: silica pillared lanthanum niobate with a supergallery. *Chem. Commun.*, 1997, pp.801-802.
5. R. M. Lewis, K. C. Ott , R. A. Van Santen. USP, 4510257, 1985.
6. M. Polverejan, Y. Liu, and T. J. Pinnavaia. Mesostructured clay catalysts: a new porous clay heterostructure(PCH) derived from synthetic saponite, *Stud. Surf. Sci. Catal.*, 129(2000), pp.401-408.
7. F. Agnes , K. Imre, S-I. Niwa, M. Toba, Y. Kiyozumi, F. Mizukami. Mesoporous materials synthesized by intercalation of silica tubes between magadiite layers. *Appl. Catal. A*:176(1999), pp.153-157.
8. J. A. Matens,E Benazzi, J. B. Rendle, S. Lacombe and R. L. Dred. Catalytic performances of pillared beidellites compared to ultrastable Y zeolites in hydrocracking and hydroisomerisation reactions. *Stud. Surf. Sci. Catal.*, 130(2000), pp.293-298.

9. A. Vaccari, Clays and catalysis:a promising future, *Appl. Clay Sci.*, 14(1999): pp.161-198.
10. Z. H. Ge, D. Y. Li, T. J. Pinnavaia, Preparation of alumina-pillared montmorillonites with high thermal stability, regular microporosity and Lewis/Brönsted acidity. *Microporous Mater.*, 3(1994), pp.165-175.

## FABRICATION OF THREE-DIMENSIONAL LARGE-PORE MESOPOROUS CHANNELS BASED ON ORDERED MESOPOROUS SILICA MATERIALS

JIE FAN, CHENGZHONG YU, LIMIN WANG, BO TU AND DONGYUAN ZHAO\*

*Department of Chemistry, Fudan University, Shanghai 200433, P. R. China*

*E-mail: dyzhao@fudan.edu.cn*

A novel method for fabricating three dimensional (3D) large-pore mesoporous channels based on original ordered mesoporous silica materials is demonstrated, which involves the introduction of organic co-solvents such as 1,3,5-trimethylbenzene, *n*-butanol and *n*-hexane followed by a high temperature hydrothermal process. The resulted 3D SBA-15 has interconnecting 3D networks with an average structure of space group (*P*6<sub>mm</sub>) symmetry. Many randomly distributed mesotunnels can be formed between the main channels. The sizes of the mesotunnels can be as large as approximate to the cylindrical channel size (*ca.* 8 nm). For caged cubic mesoporous SBA-16, its previous small caged windows (2.3 nm) of the mesostructures can be opened up to 10.8 nm, whereas the original cubic mesostructure is retained. We have also utilized negative diluted Au nanocrystals prepared from opened SBA-16 as the hard templates to determine the window dimension. This method can also directly "image" the connecting manner of each spherical cavity through the windows, which can not be obtained by the sorption method.

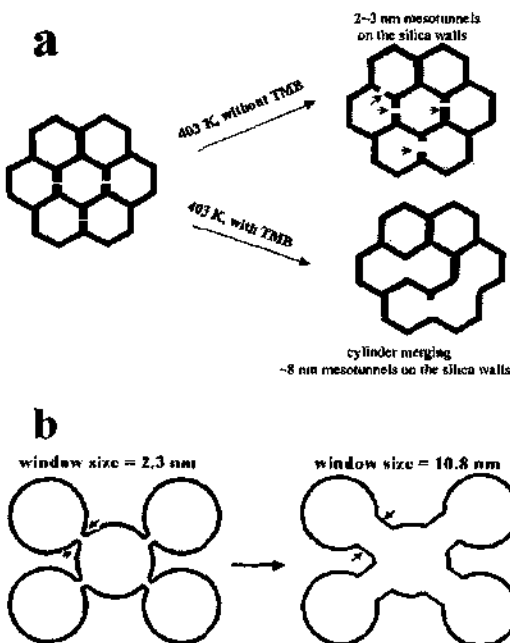
### 1 Introduction

The synthesis of molecular sieves with large pores is of great importance for many applications such as catalysis, separation, adsorption and fabrication of various quantum materials [1-7]. With the recent discovery of hexagonal and cubic large pore mesoporous materials (SBA-15, SBA-16, FDU-1) [2,3], block copolymers have turned out to be valuable supramolecular templates for the synthesis of ordered large pore mesoporous materials because of their facile structure-directing ability, low-cost commercial availability and biodegradability.

Compared to one-dimensional (1D) hexagonal mesoporous materials (MCM-41 and SBA-15), 3D ordered mesoporous materials have the advantage in the diffusion and transport of large molecules for their interconnecting networks [4]. Except bicontinuous cubic (space group *Ia3d*) MCM-48 [1,5], 3D mesoporous materials including cubic *Pm3n* (SBA-1) [6a], 3D hexagonal *P6<sub>3</sub>/mmc* (SBA-2 and SBA-12) [9,13b] and cubic *Im3m* (SBA-16 and FDU-1) structures [8,9], have caged mesostructures. Two methods have successfully been used to determine the window sizes of the cavities. One is high-resolution transmission electron microscopy (HRTEM) based on different directions, and another is determination of N<sub>2</sub> adsorption capability [7]. Unfortunately, both of them have revealed that these 3D caged mesoporous materials, such as SBA-16 and FDU-1, have much small size windows (<3 nm) that block the large pore channels. Moreover, these caged mesoporous materials after functionalized with long-chain organic groups may lose the adsorption, separation and catalysis capabilities involving large molecules. Though Stucky and co-workers have reported a mesofoam structure (MCF) with large pore size [8], but the mesofoam has randomly disordered mesostructure and limited its application. Therefore, it is of great significance to overcome the pore structure limitation for ordered 1D and 3D caged mesoporous materials, and to generate 3D large pore products, simultaneously, retaining their ordered mesostructures [9].

In this paper, we demonstrate a novel method to generate 3D large-pore mesoporous channels, which involved the introduction of organic co-solvents followed by a high

temperature hydrothermal process. With this approach, a resulting 3D mesoporous SBA-15 and very opened cubic mesoporous SBA-16 are obtained. Their pore structures are described in Scheme 1. We have also utilized negative diluted Au nanocrystals prepared from caged mesoporous SBA-16 as the hard templates to determine the window dimension. This method can also directly "image" the connecting manner of each spherical cavity through the windows, which can not be obtained by the sorption method [14b].



Scheme 1. Schematic illustration for the pore structure of a) 3D mesoporous SBA-15 and b) window enlargement of 3D cubic caged mesoporous silica SBA-16.

## 2 Experimental Section

**Synthesis:** In a typical synthesis of 3D mesoporous SBA-15, 2.0 g of triblock copolymer Pluronic P123 ( $\text{EO}_{20}\text{PO}_{70}\text{EO}_{20}$ , BASF, MW 5800) was dissolved in 75 mL of 1.6 M HCl at 313 K. Then 4.3 g of tetraethyl orthosilicate (TEOS) was added into that solution under stirring. After the mixture was stirred for 65 min at 313 K, a cloudy solution was obtained, implying that an embryo mesostructured SBA-15 was formed. The solution was immediately filtered. The obtained precipitate was dispersed in a solution of 1 g of P123 and 75 mL of 1.6 M HCl. To this mixture 2 g of 1,3,5-trimethylbenzene (TMB) was added. In order to avoid the leaching out of the copolymer and to emulsify TMB, the solution containing P123 is necessary. After stirring for 24 h at 313 K, the mixture was transferred into an autoclave and heated at 403 K for 24 h. Solid products were collected by filtration and dried at room temperature in air. The resulted powders were calcined at 823 K for 6 h in order to obtain mesoporous silica materials.

A typical synthesis of caged cubic mesoporous SBA-16 with ultra-large windows (designed as SBA-16L) is described as follows. Triblock copolymers ( $\text{EO}_{106}\text{PO}_{70}\text{EO}_{106}$ , F127, BASF, 2.0 g), 2.0 g TMB, and 5.0 g KCl were dissolved in 120 ml of 2 M HCl. To this solution, 8.3 g of TEOS was added under stirring. After stirring for 24 h at 313 K, the mixture was transferred into an autoclave and heated at 413 K for 24 h. Solid products were collected by filtration and dried at room temperature in air. The resulted powders were calcined at 823 K for 6 h in order to obtain mesoporous silica materials.

Au nanocrystals were prepared as following: 50 mg calcined mesoporous silica was immersed in 100 mL aqueous solution of  $\text{HAuCl}_4 \cdot 3\text{H}_2\text{O}$  (3 mg / 100 mL). The solvent was evaporated in a rotary evaporator, and subsequently, 100 mL  $\text{CH}_2\text{Cl}_2$  was added to induce the outer surface bound metal precursors to move into the channels of mesoporous silica.  $\text{CH}_2\text{Cl}_2$  was also removed by evaporation. The obtained solids were dried at room temperature and reduced in a constant  $\text{H}_2$  flow at 773 K for 3 h. Silica frameworks were dissolved using a 10 wt% solution of HF to obtain unsupported Au nanoparticles.

*Characterization:* Powder X-ray diffraction patterns (XRD) were recorded with a Rigaku D/Max-IIA diffractometer with  $\text{Cu K}\alpha$  radiation. TEM images were taken on a JEM-2010 microscope (JEOL), operated at 200 kV. Scanning electron microscopy (SEM) was obtained with a Philip XL30. Nitrogen adsorption measurements were performed at 77 K using a Micromeritics Tristar 3000 analyzer. The samples were pretreated at 473 K under the blow of the  $\text{N}_2$  for at least 3 h.

### 3 Results and Discussion

#### 3.1 3D Mesoporous SBA-15

The ordered hexagonal arrangements with interconnected channels for 3D SBA-15 materials prepared at high hydrothermal temperature (403 K) show well-resolved XRD patterns (Figure 1a). The four well resolved diffraction peaks can be clearly observed and assigned to (100), (110), (200) and (210) diffractions of 2D hexagonal space group ( $P6m$ ), similar to that of conventional SBA-15 prepared at low temperature ( $\leq 373$  K) (Figure 1b). The cell parameter ( $a = 13.0$  nm) for calcined 3D SBA-15 prepared with TMB is much larger than that for calcined conventional SBA-15 ( $a = 10.4$  nm) (Table 1). The morphology of 3D SBA-15 with TMB is similar to that of conventional SBA-15, further suggesting that hexagonal ordered mesostructure of the 3D SBA-15 is retained.

$\text{N}_2$  sorption measurements for calcined 3D SBA-15 without and with addition of TMB show typical IV isotherms with large type  $\text{H}_1$  hysteresis loops and relative narrow mesopore distributions at mean size of 10.7 and 17.6 nm, respectively. It is interesting that the mean pore sizes calculated from the adsorption branches for 3D SBA-15 are much larger than that from the desorption branches. However, the mean pore sizes for conventional SBA-15 ( $< 373$  K) have almost the same values calculated from both adsorption and desorption branches, indicating that latter have perfect cylinder channels while the former do not. Furthermore, the cell parameters (13.0 or 10.4 nm) for 3D SBA-15 products with or without TMB are smaller than the pore sizes (17.6 or 10.7 nm). These results imply that 3D SBA-15 products have interconnections of channels.

HRTEM images (Figure 2) reveal that calcined 3D SBA-15 samples (without TMB) at 403 K have ordered hexagonal pore arrangements and the center-to-center distance of adjacent channels is 10.2 nm, in accordance with XRD results. Figure 2a clearly shows some mesotunnels with the size of 2~3 nm randomly distributed on the silica wall of 3D SBA-15. After addition of TMB, HRTEM images also show that the size of the tunnels

approximates to the cylindrical channel size (~8 nm), implying that the hexagonal channels for 3D SBA-15 can be completely interconnected. HRTEM images along [110] direction (Figure 2b) also show that 3D SBA-15 has modulated gourd-like channels and some randomly distributed mesotunnels between the main channels are clearly observed.

Table 1. Physical data for mesoporous silica SBA-15 samples prepared under different conditions.

No.	Hydrothermal Temperature (K)	Pa (nm)	Pd (nm)	Unit Cell Parameter (nm)	Pore Volume (cm <sup>3</sup> /g)	BET Area (m <sup>2</sup> /g)	Surface
Without TMB							
1	313	4.0	4.0	9.5	0.47	448	
2	333	4.9	4.9	9.7	0.51	459	
3	353	8.0	7.6	10.1	1.08	789	
4	373	9.6	8.0	10.4	1.04	521	
5	403	10.7	7.6	10.4	1.11	417	
With TMB							
6	373	10.7	9.0	12.0	1.52	767	
7	393	12.7	9.2	12.5	1.40	538	
8	403	17.6	12.7	13.0	1.43	324	
9	413	22.3	12.6	13.0	1.25	254	

Pore size Pa and Pd were calculated from nitrogen sorption isotherm based on BJH model from adsorption branch and desorption branch, respectively.

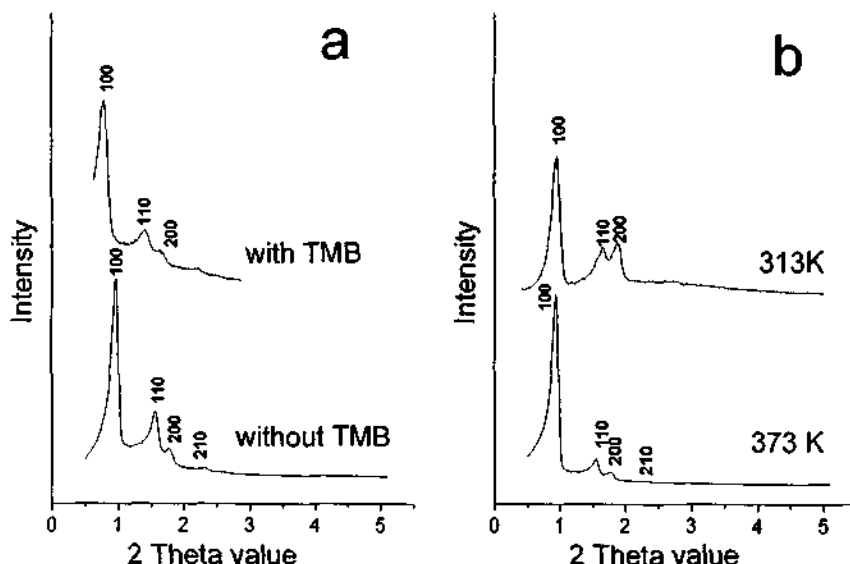
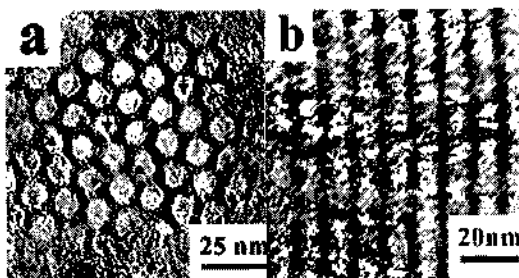
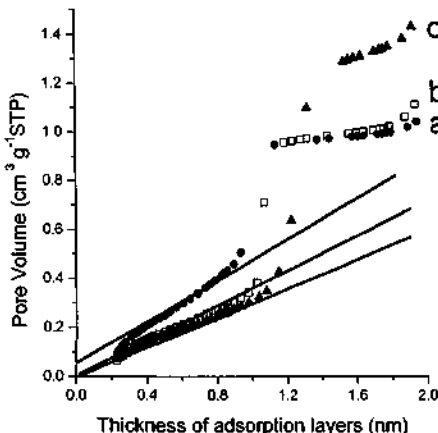


Figure 1. XRD patterns of a) calcined 3D mesoporous SBA-15 prepared at 403 K and b) conventional SBA-15.



**Figure 2.** HREM images and electron diffraction patterns of calcined 3D mesoporous SBA-15 prepared at 403 K without TMB viewed along a) [100] and b) [110] direction.



**Figure 3.** t-Plots of nitrogen adsorption isotherms for mesoporous materials: (a) conventional SBA-15 prepare at 373 K, (b) calcined 3D SBA-15 prepare at 403 K (without TMB) and (c) calcined 3D SBA-15 prepare at 403 K (with TMB).

The t-plots calculated from N<sub>2</sub> adsorption isotherms for mesoporous materials are shown in Figure 3. The t-plots for calcined 3D SBA-15 prepare at 403 K (without TMB and with TMB) give two straight lines at  $t = 0.4\text{--}0.75\text{ nm}$  and the extrapolation lines go through the origin, indicating that the 3D SBA-15 products have no micropores. For conventional SBA-15 the extrapolation line cuts the y-axis at  $0.07\text{ cm}^3/\text{g}$ , suggesting the presence of the micropores.

The formation of disordered mesotunnels may be related to the change of hydrophobic/hydrophilic property of the block copolymers with temperature. When the hexagonal mesostructure is formed at low temperature, the hydrophilic PEO chains have strong interaction with the silica species and are partially occluded into silica wall [15]. The high temperature process would result in volume expansion of the block copolymer because the PEO chains become hydrophobic. The microporous void space in the wall would be attacked by the copolymer and become expanded, resulting in formation of the mesotunnels. It is also expected that by addition of TMB, the number and size of the mesotunnels increase because of larger volume expansion of the block copolymer caused from TMB.

The time to add organic co-solvent is a key factor for the formation of 3D SBA-15. In order to avoid the formation of disordered MCFs, TMB should be added after the

“embryo” mesostructure is formed. When SBA-15 mesostructure is completely formed after a long reaction time, the addition of TMB has no effect on the size of the mesotunnels. The best time for the addition of TMB is 65 min after the reaction starts. The hydrothermal temperature also has great effect on the size of the mesopores and mesotunnels (Table 1). The mesotunnel size increases with the temperature. Other organic co-solvents, such as *n*-butanol and *n*-hexane can also be used as the co-solvents for formation of 3D SBA-15. When the same amount of *n*-butanol or *n*-hexane cosolvent (in molar) as TMB is used, the size of the mesotunnels is smaller than that from TMB.

### 3.2 3D Large Window Mesoporous SBA-16L

The as-synthesized and calcined SBA-16L at 373 K hydrothermal temperature show well-resolved XRD patterns (Figure 4a). Five well-resolved diffraction peaks can be assigned to (110), (200), (211), (310) and (420) diffractions, respectively, indicating excellent structural ordering for a cubic space group (*Im3m*) with a cell parameter (*a*) of 21.8 nm. Even after a high temperature (413 K) hydrothermal treatment, the well-resolved XRD patterns are also observed (Figure 4b), suggesting that the high ordered cubic caged mesostructure is retained. A slight enlargement of cell parameter is found with the increase of hydrothermal temperature, suggesting high stability and flexibility of ordered mesostructure.

The SEM images of the as-synthesized SBA-16L (413 K) shows a crystal-like morphology with a uniform size of ~ 5  $\mu$ m. The crystals consist of 20 clear crystal faces with 2 hexagons, 12 trapeziums and 6 rectangles. Similar to that reported by Che *et al.*, the crystal faces of the particles increase with the hydrothermal temperature [10].

The TEM images and corresponding Fourier diffractograms viewed along [100], [110] directions for calcined large window sized SBA-16L (413 K) are shown in Figure 2a, b. The highly ordered cubic regular periodicity over large domains suggests that the crystal-like products have a uniform, well-defined body center cubic mesostructure (*Im3m*).

Table 2. Physicochemical properties of SBA-16 samples.

No.	Hydrothermal temperature (K)	Cavity size (nm)	Window size (nm)	Cell parameter (nm)	Pore volume (cm <sup>3</sup> /g)	Surface area (m <sup>2</sup> /g)
SBA-16	373	7.9	2.3 <sup>[a]</sup>	13.0	0.56	461
SBA-16L1	373	10.6	3.8 <sup>[b]</sup>	19.0	0.65	564
SBA-16L2	393	12.7	5.8 <sup>[b,c]</sup>	19.5	0.73	535
SBA-16L3	403	14.5	7.4 <sup>[b,c]</sup>	20.1	0.86	480
SBA-16L4	413	15.9	10.8 <sup>[b,c]</sup>	20.6	0.78	281

[a] determined from the model of TEM measurement [14a]

[b] calculated from the corresponding Au nanocrystal images

[c] calculated from the desorption branch of the N<sub>2</sub> adsorption/desorption isotherms based on BdB model

N<sub>2</sub> sorption measurements for calcined mesoporous silica SBA-16L (413 K) with large window confirm that the window size of the cages can be opened. A representative isotherm for calcined conventional SBA-16 prepared without TMB shows a type IV isotherm with typical H<sub>2</sub> hysteresis loops, suggesting that the material consists of large cages connected with small size windows (<4 nm). It should be noted that the window

size could not be calculated from desorption branch for the instability of the meniscus of the condensed nitrogen in the pores [11]. However, calcined large window mesoporous silica SBA-16L (413 K) has a type H<sub>1</sub> hysteresis loop. The sizes of the cavities and windows can be calculated from the desorption and adsorption branches to be 15.4 and 10.8 nm respectively (Table 2) [12]. Compared to conventional SBA-16, the pore size, more importantly, the window dimension is much larger, suggesting that the window of the cavities can be opened to 10.8 nm.

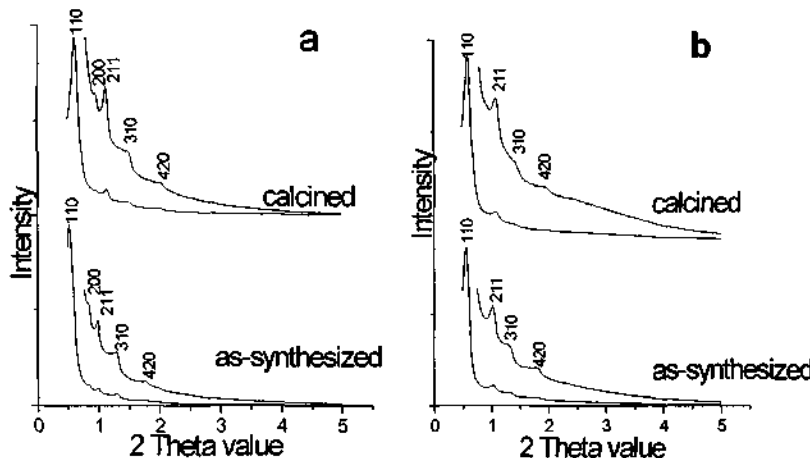


**Figure 4.** XRD patterns of as-synthesized and calcined 3D large window mesoporous silica SBA-16L under a) 373 K and b) 413 K hydrothermal treatment.

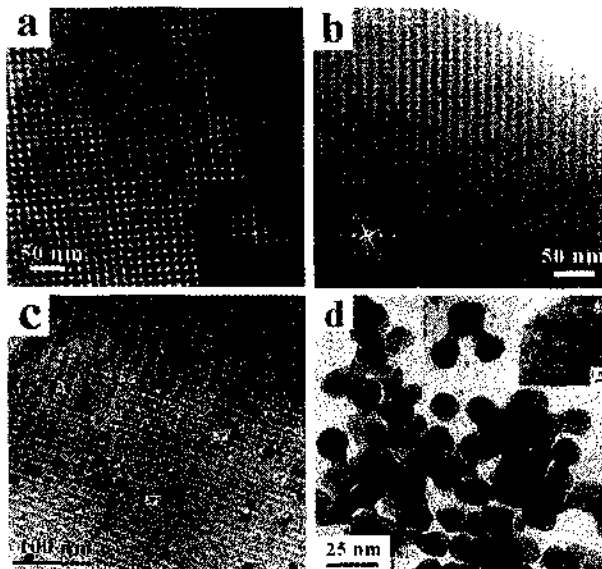


**Figure 5.** TEM images and corresponding Fourier diffractogram (inset) for calcined large window mesoporous silica SBA-16L (413 K) viewed in a) [100] and b) [110] directions. TEM images for c) Au/SBA-16L, d) unsupported Au nanocrystals, and a single Au nanocrystal in high resolution together with the corresponding Fourier transform (d. inset).

In order to directly image the connectivity of each spherical cavities, as well as the window dimension, we have utilized dispersed Au nanocrystals prepared by using the large window mesoporous silica SBA-16L as a hard template according to an easily loading approach [13]. Figure 5c shows a HRTEM image of Au/SBA-16 taken in [110] direction, which indicates that all Au nanoparticles are well confined in the cages. Occasionally, two or three Au nanoparticles locating in neighboring cages aggregate through the window (indicated by small arrows). After the removal of silica frameworks, these aggregated Au nanoparticles show a dumbbell-like morphology (Figure 5d). The Au "balls" with the diameter size of 15.0 nm are connected by a bridge with the width of 9.5 nm, in accordance with the cavity dimension and window size calculated from nitrogen sorption results, further confirming that the window size can be opened by incorporation of TMB and high temperature hydrothermal treatment in the present of inorganic salts. HRTEM image (Figure 5d inset) shows that the Au particles are highly crystalline nanocrystals.

The enlargement of window size of caged mesoporous silica may also be related to a volume expansion of the block copolymers under the high temperature hydrothermal treatment. From the illustration of SBA-16 pore structure by Terasaki and co-workers, the wedge-shaped silica wall forming the windows is relatively thinner than that at other locations, and has the highest curvature. In this case, it's feasible to be attacked by the volume expansion of organic splices under high temperature. The inorganic salts service as a stabilizer for the mesostructure and ordering during the process, which may relate to the increase of the interaction between the block copolymers and silicate species by the introduction of inorganic salts.

#### 4 Conclusions

Two 3D ordered large pore mesoporous silica structures have been synthesized based on original 2D hexagonal SBA-15 and cubic caged SBA-16: a) 3D SBA-15 has interconnecting 3D networks with an average structure of space group ( $P6m$ ) symmetry. b) Crystal-like SBA-16L has tunable window sizes (2.3~10.8 nm) while retaining original cubic mesostructure ( $I\bar{m}3m$ ) simultaneously. The unblocked 3D large mesopore networks would much facilitate diffusion and transport of molecules between the channels and further extend the catalysis, adsorption, separation, and sensing applications. Also the new mesostrucutures would be promising nanoreactors for the synthesis of other metal and semiconductor quantum dots and wires.

#### 5 Acknowledgements

This work was supported by NSF of China (Grant No. 29925309 and 29873012), Shanghai Sci. Tech. Committee (Grant No. 00JC14014), State Key Basic Research Program of PRC (G2000048001). We thank Prof. O. Terasaki for TEM measurements and helpful discussion.

#### References

1. Kresge, C. T.; Leonowicz, M. E.; Roth, W. J.; Vartuli, J. C.; Beck, J. S. *Nature* 1992, **359**, 710.
2. Yu, C.; Yu, Y.; Zhao, D. *Chem. Commun.* 2000, 575.

3. Zhao, D.; Feng, J.; Huo, Q.; Melosh, N.; Fredrickson, G. H.; Chmelka, B. F.; Stucky, G. D. *Science* 1998, **279**, 548.
4. a) Morey, M. S.; Davidson, A.; Stucky, G. D.; *J. Porous Mater.* 1998, **5**, 195. b) Dai, L.-X.; Teng, Y.-H.; Tabata, K.; Suzuki, Tatsumi, E.; T. *Microporous Mesoporous Mater.* 2001, **43**, 573.
5. a) Sayari, A. *J. Am. Chem. Soc.* 2000, **122**, 6504. (b) Kim, J. M.; Kim, S. K.; Ryoo, R. *Chem. Commun.* 1998, 259.
6. a) Huo, Q.; Margolese, D.; Ciesla, U.; Feng, P.; Gier, T. E.; Sieger, P.; Leon, R.; Petroff, P. M.; Schuth, F.; Stucky, G. D. *Nature* 1994, **368**, 317; b) Huo, Q.; Leon, R.; Petroff, P. M.; Stucky, G. D. *Science* 1995, **268**, 1324.
7. a) Sakamoto, Y.; Kaneda, M.; Terasaki, O.; Zhao, D. Y.; Kim, J. M.; Stucky, G.; Shin, H. J.; Ryoo, R. *Nature* 2000, **408**, 449. b) M. Kruk, V. Antochshuk, J. R. Matos, L. P. Mercuri, M. Jaroniec, *J. Am. Chem. Soc.* 2002, **124**, 768.
8. Schmidt-Winkel, P.; Lukens, W. W.; Zhao, D. Y.; Yang, P. D.; Chmelka, B. F.; Stucky, G. D. *J. Am. Chem. Soc.* 1999, **121**, 254.
9. Fan, J.; Yu, C.; Wang, L.; Tu, B.; Zhao, D.; Sakamoto, Y.; Terasaki, O. *J. Am. Chem. Soc.* 2001, **123**, 12113.
10. Che, S.; Sakamoto, Y.; Terasaki, O.; Tatsumi, T.; *Chem. Mater.* 2001, **13**, 2237.
11. a) Gregg, S. J.; Sing, K. S. W. *Adsorption, Surface Area and Porosity*; Academic Press: London, 1982; b) Galarneau, A.; Desplantier, D.; Dutartre, R.; Di Renzo, F. *Microporous Mesoporous Mater.* 1999, **27**, 297; c) Inoue, S.; Hanzawa, Y.; Kaneko, K. *Langmuir* 1998, **14**, 3079.
12. a) Broekhoff, J. C. P.; de Boer, J. H. *J. Catal.* 1967, **9**, 8; b) Broekhoff, J. C. P.; de Boer, J. H. *J. Catal.* 1968, **10**, 153; c) Broekhoff, J. C. P.; de Boer, J. H. *J. Catal.* 1968, **10**, 368.
13. Han, Y.-J.; Kim, J. M.; Stucky, G. D. *Chem. Mater.* 2000, **12**, 2068.

This page is intentionally left blank

## **Part III**

### **Hybrid Inorganic-Organic Solids**

This page is intentionally left blank

# STUDY OF THE CHIRAL TRANSFERENCE AND RECOGNITION EFFECT IN LAYERED ALUMINOPHOSPHATES TEMPLATED BY CHIRAL COBALT COMPLEXES

YI LI, JIHONG YU, YU WANG AND RUREN XU

*State Key Lab of Inorganic Synthesis and Preparative Chemistry, College of Chemistry, Jilin University, Changchun 130023, P. R. China  
E-mail: rr xu@mail.jlu.edu.cn*

In this work, we have discussed the chiral transference and recognition effect occurring in several layered aluminophosphates templated by optically pure or racemic mixture of chiral cobalt complexes. These aluminophosphates are  $\text{Co}(\text{tn})_3\text{Al}_3\text{P}_4\text{O}_{16}\cdot 2\text{H}_2\text{O}$  (1),  $d\text{-Co}(\text{en})_3\text{Al}_3\text{P}_4\text{O}_{16}\cdot 3\text{H}_2\text{O}$  (2),  $trans\text{-Co(dien)}_2\text{Al}_3\text{P}_4\text{O}_{16}\cdot 3\text{H}_2\text{O}$  (3) and  $\text{Co}(\text{en})_3\text{Al}_3\text{P}_4\text{O}_{16}\cdot 3\text{H}_2\text{O}$  (4). All these layered structures are featured by a series of chiral inorganic structural motifs. It is found that the absolute configuration of the complex template determines that of the inorganic structural motif. A  $\Delta$  or  $\Lambda$  configuration metal complex can accordingly induce a  $\Delta$  or  $\Lambda$  configuration inorganic structural motif, and a pair of enantiomers of chiral metal complexes can induce a pair of enantiomers of chiral inorganic structural motifs. The chiral recognition effect is studied by molecular mechanical calculation in terms of the host-guest non-bonding interaction.

## 1 Introduction

In recent years, chiral compounds are playing more and more important roles in many fields such as pharmaceuticals, enantioselective separation and catalysis. The synthesis of optically pure chemicals especially chiral microporous materials is of great challenge. So far, only a few chiral compounds have been synthesized, such as zincophosphate CZP [1,2] and some layered aluminophosphates templated by chiral Co(III) complexes [3-6]. It is found that the chiral metal complex plays an important structure-directing role in the formation of chiral materials. Notable example is a chiral layered structure templated by an optically pure metal complex [4]. In addition, it is found that the chirality of metal complexes can be locally imprinted into the inorganic framework as demonstrated in our previously reported two zinc phosphates  $[\text{Co}^{II}(\text{en})_3]_2[\text{Zn}_8\text{P}_8\text{O}_{32}\text{H}_8]$  and  $[\text{Co}^{III}(\text{en})_3]_2[\text{Zn}_8\text{P}_6\text{O}_{24}\text{Cl}] \cdot 2\text{H}_2\text{O}$  [7] using a racemic mixture of chiral complexes as the template. It is believed that there exists molecular recognition between the host and the guest that allows the chirality of the metal complex transferring into the inorganic framework through H-bond interaction. It is of significance to understand the structure-directing ability of the chiral metal complexes. In this work, the chiral transference and recognition effect occurred in several aluminophosphates templated by chiral cobalt complex has been discussed by using molecular mechanical calculations, and we find that the absolute configuration of chiral cobalt (III) complexes determines the absolute configuration of the chiral structural motifs through molecular recognition.

## 2 Methodology

### 2.1 The Force Field and Parameters

Our calculation is based on the Burchart1.01-Dreiding2.21 force field that combines the Burchart force field [8], which is used to treat the frameworks of zeolites, and Dreiding II

force field [9], which is used to treat the intra- and intermolecular interactions. Because the energy terms of Co(III) are not addressed in this force field, we divide them into the bonding terms and the non-bonding terms. For the bonding terms, we derive them from UFF generator, since the Universal force field facilitates the optimization of the configuration of the metal complexes. For the non-bonding terms, we use Lennard-Jones 6-12 potential function to express the van der Waals energy. Some parameters which are not available in the force field are added according to the reference [10]: Co-O:  $D_0=0.055$  kcal/mol,  $R_0=3.18\text{\AA}$ ; Co-H:  $D_0=0.055$  kcal/mol,  $R_0=2.16\text{\AA}$ . Other parameters are the same as those used in the Burchart1.01-Dreiding2.21 force field given in Cerius<sup>2</sup> package [11].

## 2.2 Building Models

The experimental structures of the aluminophosphates are built up according to their crystal data using Cerius<sup>2</sup> package. For the substituted hypothetical structures, we change the Co complexes to their enantiomorph ( $\Delta \rightarrow \Lambda$  or  $\Lambda \rightarrow \Delta$ ) with the positions of the Co atoms unchanged.

## 2.3 Energy Calculation.

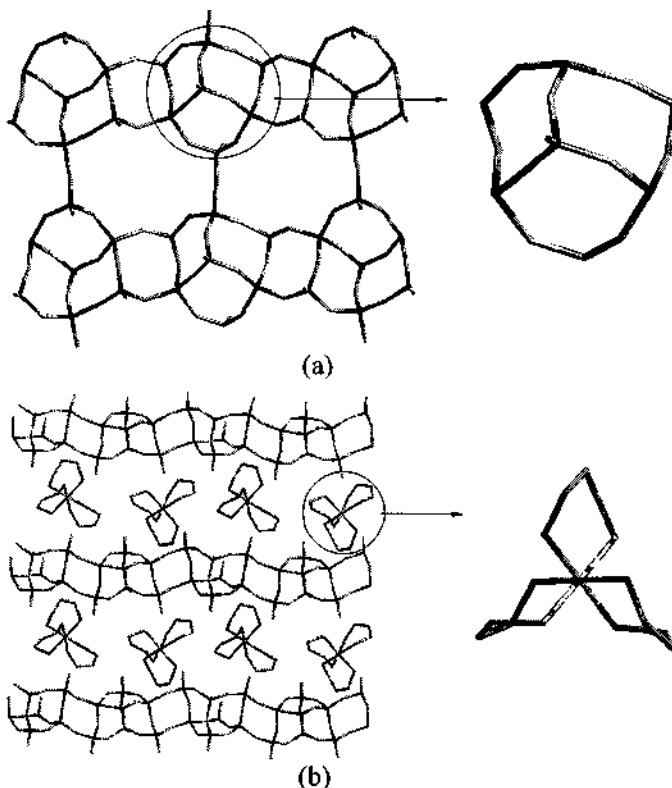
In this paper, the energy we considered is mainly van der Waals and H-bonding energy between the host and the guest. We optimize the experimental structures and the substituted hypothetical structures by energy minimization. During the energy minimization, the inorganic networks are fixed, the Co complexes are considered as rigid bodies and the positions of Co atoms are fixed. Water molecules in the interlayer region are ignored.

## 3 Results and Discussion

So far, there are four layered aluminophosphates [3-6] reported which are templated by an optically pure or a racemic mixture of chiral cobalt metal complex. Their structural features are listed in Table 1. The chiral layered aluminophosphate  $\text{Co}(\text{tn})_3 \cdot \text{Al}_3\text{P}_4\text{O}_{16} \cdot 2\text{H}_2\text{O}$  (1) consists of 4.6.8-net inorganic sheets stacking in an AAAA sequence. As seen in Figure 1, the chiral templates with only  $\Delta$  configuration reside in the interlayer region. The inorganic sheet is characteristic of a capped 6-membered ring (MR) which is chiral. It is noted that all the structural motifs are exclusively with  $\Delta$  configuration. The layered aluminophosphate  $d\text{-Co}(\text{en})_3 \cdot \text{Al}_3\text{P}_4\text{O}_{16} \cdot 3\text{H}_2\text{O}$  (2) consists of 4.6-net inorganic sheets stacking in an ABAB sequence, which is featured by a [3.3.3] propellane-like chiral structural motif. The chiral templates reside in the interlayer region with only  $\Lambda$  configuration. Corresponding to the  $\Lambda$  configuration complex, the inorganic chiral structural motifs are all with  $\Lambda$  configuration (Figure 2).

**Table 1.** Structural features of four layered AlPOs templated by cobalt complexes.

Formula	Space Group	Inorganic Sheets	Templates	Chiral Motifs	Ref.
<b>1</b> $\text{Co}(\text{tn})_3 \cdot \text{Al}_3\text{P}_4\text{O}_{16} \cdot 2\text{H}_2\text{O}$	$P2_1$	4.6.8-net, AAAA-stacking	$\Delta\text{-Co}(\text{tn})_3$	$\Delta$ -capped 6MR	3
<b>2</b> $d\text{-Co}(\text{en})_3 \cdot \text{Al}_3\text{P}_4\text{O}_{16} \cdot 3\text{H}_2\text{O}$	$C222_1$	4.6-net, ABAB-stacking	$\Lambda\text{-Co}(\text{en})_3$	$\Lambda$ -[3.3.3] propellane-like motif	4
<b>3</b> $trans\text{-Co}(\text{dien})_2 \cdot \text{Al}_3\text{P}_4\text{O}_{16} \cdot 3\text{H}_2\text{O}$	$P6_{3}22$	4.6-net, helical-stacking	$trans\text{-Co}(\text{dien})_2$	$\Lambda$ -[3.3.3] propellane-like motif	5
<b>4</b> $\text{Co}(\text{en})_3 \cdot \text{Al}_3\text{P}_4\text{O}_{16} \cdot 3\text{H}_2\text{O}$	$Pna2_1$	4.6-net, ABAB-stacking	$\Delta, \Delta\text{-Co}(\text{en})_3$	$\Delta, \Delta$ -[3.3.3] propellane-like motif	6

**Figure 1.** (a) the inorganic network and the  $\Delta$ -chiral motif of **1** and (b) the  $\Delta\text{-Co}(\text{tn})_3^{3+}$  cations located between the layers in **1**.

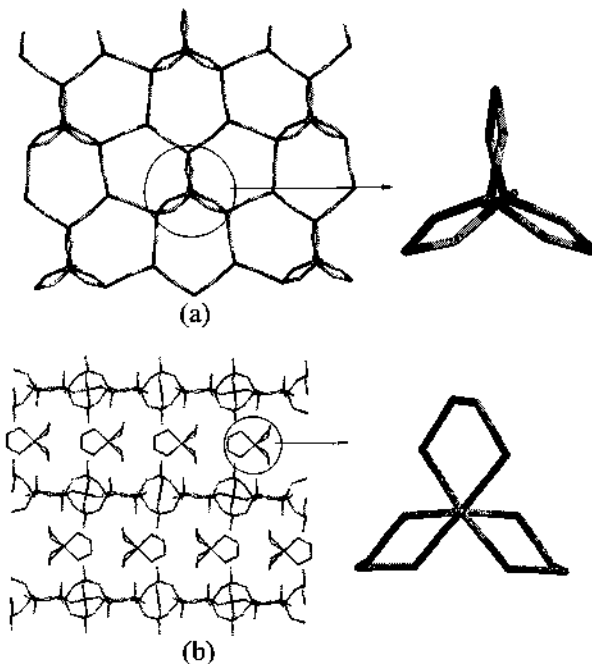


**Figure 2.** (a) the inorganic network and the  $\Delta$  chiral motif of 2 and (b) the  $\Delta$   $\text{Co}(\text{en})_3^{3+}$  cations located between the layers in 2.

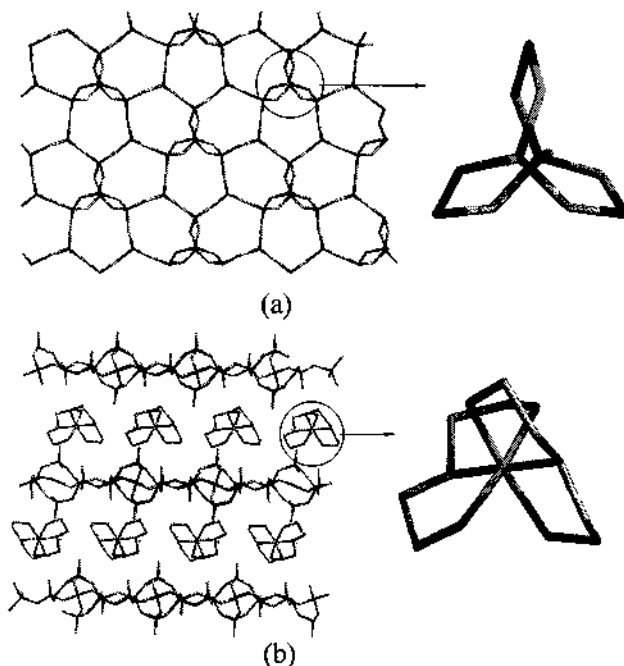


**Figure 3.** (a) the inorganic network and the  $\Delta$  chiral motif of 3 and (b) *trans*- $\text{Co}(\text{dien})_2^{3+}$  between the layers in 3.

The layered aluminophosphate *trans*-Co(dien)<sub>2</sub>·Al<sub>3</sub>P<sub>4</sub>O<sub>16</sub>·3H<sub>2</sub>O (**3**) consists of 4.6-net inorganic sheets stacking in a 6<sub>3</sub> helical fashion. As shown in Figure 3, between the layers, there are Co(dien)<sub>2</sub> complexes with only one kind of isomers. Correspondingly, the inorganic sheet contains a series of [3.3.3] propellane-like chiral motifs exclusively with  $\Lambda$  configuration. The layered aluminophosphate Co(en)<sub>3</sub>·Al<sub>3</sub>P<sub>4</sub>O<sub>16</sub>·3H<sub>2</sub>O (**4**) consists of inorganic 4.6-net sheets stacking in an ABAB sequence. A pair of enantiomers of complex cations locates in the interlayer region, corresponding to which, a pair of enantiomers of chiral structural motifs exist (Figure 4).

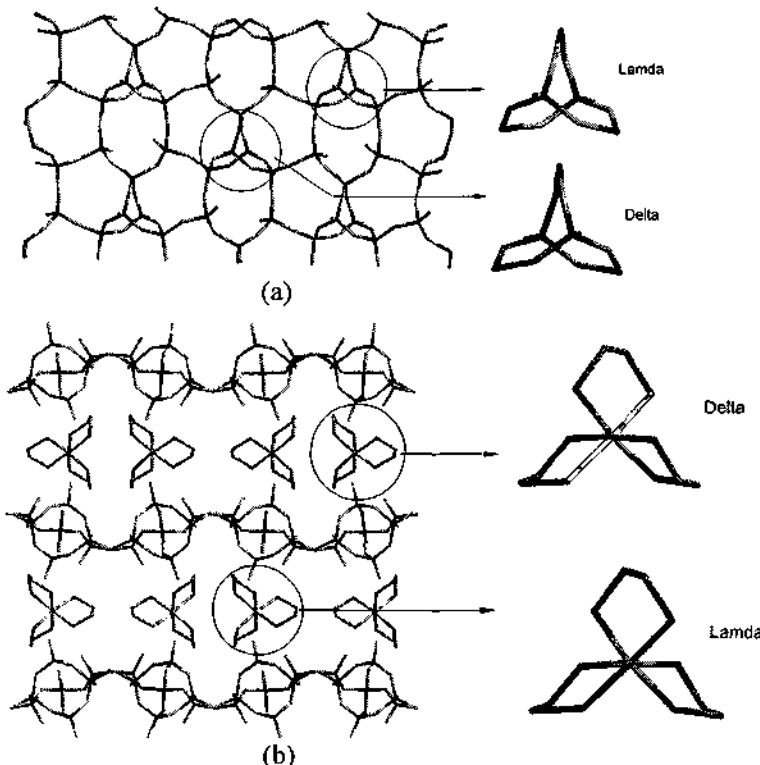


**Figure 4.** (a) the inorganic network and the chiral motif of **4** and (b) the chiral Co(en)<sub>3</sub><sup>3+</sup> cations between the layers in **4**.

From above discussion, we find that the chirality of metal complexes can locally pass onto the inorganic networks because of the chiral recognition effect between the host and the guest. A  $\Delta$  or  $\Lambda$  configuration metal complex can induce a  $\Delta$  or  $\Lambda$  configuration inorganic structural motif. Accordingly, a pair of enantiomers of chiral metal complexes can induce a pair of enantiomers of chiral inorganic structural motifs. This reflects a chiral discrimination effect: Chiral discrimination energies are central for understanding and determining the mechanisms of chiral recognition, enantioselective reactions, and a multitude of chirally discriminating effects in chemistry and biology. We investigate this chiral discrimination effect in terms of the non-bonding interaction energies of the host and the guest. The results of the calculation are listed in Table 2. Here we define the “chirodiastaltic energy” as  $\Delta E = E_{\text{experimental}} - E_{\text{substituted}}$ . For **1**, in the experimental

structure, templates and inorganic motifs are all with  $\Delta$  configuration; while in the substituted hypothetical structure, templates are of  $\Lambda$  configuration. The host-guest interaction energy of the experimental structure  $E_{\Delta\text{complex}/\Delta\text{motif}}$  is of -25.90 kcal/mol, and the substituted structure  $E_{\Lambda\text{complex}/\Delta\text{motif}}$  ( $= E_{\Delta\text{complex}/\Delta\text{motif}}$ ) is of -10.88 kcal/mol. The energy difference  $\Delta E$  ( $E_{\Delta\text{complex}/\Delta\text{motif}} - E_{\Delta\text{complex}/\Delta\text{motif}}$ ) is of -15.02 kcal/mol. This suggests that the  $(\Delta_{\text{complex}}/\Delta_{\text{motif}})$  induction is in favor of the  $(\Delta_{\text{complex}}/\Lambda_{\text{motif}})$  induction. That is to say, in **1**, the templates with  $\Delta$  configuration favor the formation of the inorganic motifs with  $\Delta$  configuration. In **2**, which contains  $\Lambda$  motifs in the networks, the experimental structure templated by  $\Delta$   $\text{Co}(\text{en})_3^{3+}$  complex are more stable than the substituted hypothetical structure templated by  $\Delta$   $\text{Co}(\text{en})_3^{3+}$  complex ( $\Delta E = -25.80$  kcal/mol). This implies that in **2**, the  $(\Delta_{\text{complex}}/\Delta_{\text{motif}})$  induction is in favor of the  $(\Delta_{\text{complex}}/\Delta_{\text{motif}})$  induction. Similarly, in **3**, the templates have only one configuration, which induce motifs with only  $\Lambda$  configuration in the networks. The substituted hypothetical structure is with higher energy than the experimental structure. The reason why the energy difference  $\Delta E$  of 168.79 is so high is that the substituted structures should be in space group  $P6_22$  but not  $P6_522$  and thus the substituted hypothetical structure violates the symmetry rules. In the experimental structure of **4**, the chiral templates are racemic. Energy calculation result indicates that the energy difference between the experimental and the substituted hypothetical structures is relatively small. This is because in **4**, a pair of enantiomers of chiral templates induces a pair of enantiomers of chiral motifs synergically, therefore the chiral recognition effect is not as obvious as the structures discussed above.

**Table 2.** The calculated non-bonding interaction energy ( kcal/mol per  $\text{Al}_3\text{P}_4\text{O}_{16}^{3-}$  unit).

Compound	$E_{\text{exp}}$	$E_{\text{sub}}$	$\Delta E$
<b>1</b>	-25.90	-10.88	-15.02
<b>2</b>	-29.10	-3.30	-25.80
<b>3</b>	-15.29	+153.5	-168.79
<b>4</b>	-16.00	-10.09	-5.91

#### 4 Conclusions

In this paper, the “chirodiastaltic energy” between the inorganic host and the complex guest is calculated using the molecular mechanics. The results imply that there is chiral recognition effect between the inorganic chiral motifs and chiral complex templates. The absolute configuration of the chiral templates determines that of the chiral motifs in the networks.

#### References

1. Rajic, N., Logar, N. Z., Kaucic, V. *Zeolites*, 1995, **15**, pp672-678.
2. Harrison, W. T. A., Gier, T. E., Stucky, G. D., Broch, R. W., Bedard, R. A. *Chem. Mater.*, 1996, **8**, pp.145-151.

3. Bruce, D. A.; Wilkinson, A. P.; White, M. G.; Bertrand, J. A. *J. Chem. Soc., Chem. Commun.*, 1995, pp.2059-2060.
4. Gary, M. J.; Jasper, J. D.; Wilkinson, A. P.; Hanson, J. C. *Chem. Mater.*, 1997, **9**, pp.976-980
5. Bruce, D. A.; Wilkinson, A. P.; White, M. G.; Bertrand, J. A. *Journal of solid state chemistry* 1996, **125**, pp.228-233
6. Morgan, K.; Gainsford, G.; Milestone, N. *J. Chem. Soc., Chem. Commun.*, 1995, pp.425-426.
7. Yu, J.; Wang, Y.; Shi, Z.; Xu, R. *Chem. Mater.*, 2001, **13**, pp.2972-2978
8. de Vos Burchart, E. *Studies on Zeolites; Molecular Mechanics, Framework Stability and Crystal Growth. Ph. D. Thesis*, Thchnische Universiteit Delft, 1992.
9. Mayo, S. L.; Olafson, B. D.; Goddard, W. A. *J. Phys. Chem.* 1990, **94**, pp.8897.
10. Ramirez-Cuesta, A. J.; Mitchell, C. H.; Rodger, P. M. *J. Chem. Soc., Faraday Trans.*, 1998, **94**(15), pp.2249-2255.
11. Cerius2, Molecular Simulations/Biosym Corporation, 1995.

This page is intentionally left blank

# SYNTHESIS, STRUCTURE AND MAGNETISM OF A NEW IMIDAZOLE-BRIDGED BINUCLEAR COMPLEX $[\text{Ni}_2(\text{Im})(\text{Phen})_4]\cdot(\text{NO}_3)_3 \cdot 3\text{H}_2\text{O}$

SHU YUN NIU\* AND JING JIN

*Department of Chemistry, Liaoning Normal University, Dalian 116029, P. R. China*

*E-mail: syniu@sohu.com*

GUANG DI YANG AND LING YE

*Key Lab of Supramolecular Structure and Spectroscopy, Jilin University, Changchun 130023, P. R. China*

In  $\text{C}_2\text{H}_5\text{OH}$  and  $\text{H}_2\text{O}$  as a solvent with  $\text{Ni}(\text{NO}_3)_2 \cdot 6\text{H}_2\text{O}$ , imidazole and phenanthroline (phen) acting as starting materials, the binuclear complex  $[\text{Ni}_2(\text{im})(\text{phen})_4]\cdot(\text{NO}_3)_3 \cdot 3\text{H}_2\text{O}$  was synthesized. The complex crystallizes in triclinic space group  $P-1$  with  $a = 13.294(5)\text{\AA}$ ,  $b=13.725(5)\text{\AA}$ ,  $c=16.823(2)\text{\AA}$ ,  $\alpha=89.67(2)^\circ$ ,  $\beta=69.11(13)^\circ$ ,  $\gamma=63.43(3)^\circ$ ,  $V=2520.8(13)\text{\AA}^3$  and  $Z = 2$ . The structure consists of the dimeric  $[\text{Ni}_2(\text{im})(\text{phen})_4]^{3+}$  ion with the imidazolate ion bridging the two  $\text{Ni}(\text{phen})_2$  moieties. The lattice contains three water molecules and three nitrate anions. Each  $\text{Ni}(\text{II})$  ion is five coordinated, and the coordination geometry is a distorted square pyramid. Cryomagnetic investigations (4.5~300K) reveal an antiferromagnetic coupling between two  $\text{Ni}(\text{II})$  ions in the complex with  $J = -30.43\text{cm}^{-1}$ ,  $g = 1.98$ . The UV-VIS-NIR and IR spectra of the complex were determined and assigned.

## 1 Introduction

Studies of imidazolate-bridged complexes of transition metal M(II) (M=Cu, Zn, Ni, Co) have received more and more attention since Kolks et al. [1,2] reported several imidazolate-bridged binuclear or polynuclear Cu(II) complexes in 1976. This is maybe due to the relevance of the complexes to some bioenzymes. For example, the studies of bovine erythrocyte superoxide dismutase (SOD) reveals the presence of imidazolated-bridged copper(II)-zinc(II) center (Cu/Zn-SOD) at the active site, and it can catalyze some biological reaction [2]. J. P. Costes et al. [3-9] reported new routes to bimetallic imidazolate-bridged complex. In these reports the syntheses, structures and properties on electronic spectroscopy, IR, NMR, ESR, electrochemistry and magnetism etc. of binuclear or polynuclear imidazolate-bridged complexes have been fully studied. Although all of these works provided important references to further research of this field, the center metals in these complexes are only 4-coordinated with a square-planar geometry. In addition, the studies of binuclear Cu(II) complexes bridged imidazolate ion with 5 coordination in another reports also obtained many significant results [10-17]. But, to our knowledge, there are few reports for imidazolate-bridged Ni(II) binuclear complex which is 5-coordinated [18,19].

Here we present a novel binuclear Ni(II) complex with imidazolate-bridged ligand. The two Ni(II) ions in the complex are pentacoordinated, and the geometry around each Ni(II) ion is a distorted square pyramid. The complex possesses weak antiferromagnetic property at low temperature.

## 2 Experimental

### 2.1 Physical measurement

The element contents were measured on a PE-240C elemental analyzer and TLASMA-II ICP. The infrared spectrum was recorded on a Nicolet Nexus 470 FT/IR spectrometer with

pressed KBr pellet and UV-VIS-NIR spectrum (diffuse reflectance spectrum) on an UV-3100 spectrophotometer using BaSO<sub>4</sub> pellet as reference. The magnetic susceptibilities were measured with an MPMS-7 Superconducting Quantum Magnetometer in the temperature range of 4.5 ~300K and on magnetic field of 0.1 T.

## 2.2 Synthesis of [Ni<sub>2</sub>(im)(phen)<sub>4</sub>]·(NO<sub>3</sub>)<sub>3</sub>·3H<sub>2</sub>O

Quantities of 0.7g (10mmol) imidazole and 0.4g (10mmol) NaOH were dissolved in 20mL of water under full stirring. Then 0.2g (1mmol) MnCl<sub>2</sub>·4H<sub>2</sub>O were added to the above solution. A khaki color appeared at once. After 20 minutes, 0.3g (1mmol) Ni(NO<sub>3</sub>)<sub>2</sub>·6H<sub>2</sub>O, 10mL of water and 20mL of ethanol were added under heating and stirring. In the solution a small amount of yellow precipitate appeared. After 3 hours, a solution of 0.2g (2.0mmol) phenanthroline dissolved in 10mL of ethanol was added. The reaction continued for 4 days. The solution became blue. The reaction was stopped and filtered, and the filtrate was kept at room temperature. The blue crystals were observed in two months. Found(%): C, 52.73; H, 3.59; N, 15.87; Ni, 10.13. Calc. for C<sub>51</sub>H<sub>41</sub>N<sub>13</sub>Ni<sub>2</sub>O<sub>12</sub>: C, 53.48; H, 3.61; N, 15.90; Ni, 10.25. IR (cm<sup>-1</sup>): 3480s(v<sub>OH</sub>); 3030w(v<sub>Ar,C-H</sub>); 1610m(v<sub>C=N</sub>); 1595w, 1575w, 1505w(v<sub>Ar-H, C=C</sub>); 1415s(δ<sub>OH</sub>); 1370vs(v<sub>NO<sub>3</sub></sub>); 1080s(v<sub>C-N</sub>); 840s, 815m, 770m, 710s(δ<sub>Ar, CH</sub>); 420w and 310w (v<sub>N-Ni</sub>). UV-VIS-NIR(nm): The d-d transition bands of Ni(II) ions in the complex apparently occur: 875 (<sup>3</sup>B<sub>1</sub>→<sup>3</sup>B<sub>2</sub>+<sup>3</sup>E) and 642(<sup>3</sup>B<sub>1</sub>→<sup>3</sup>A<sub>2</sub>+<sup>3</sup>E). In addition, the strong bands in the region 400~230 nm are overlap of bands of the π→π\* transitions of the ligands and the bands of charge transferring of Ni (II)←N in the complex.

Table 1. Crystal data and structure refinement for the complex.

Compound	[Ni <sub>2</sub> (im)(phen) <sub>4</sub> ]·(NO <sub>3</sub> ) <sub>3</sub> ·3H <sub>2</sub> O
Empirical formula	C <sub>51</sub> H <sub>41</sub> N <sub>13</sub> Ni <sub>2</sub> O <sub>12</sub>
Molecular weight	1145.38
Crystal system	Triclinic
Space group	P-1
a (Å), α°	13.294(5), 89.67(2)
b (Å), β°	13.723(5), 69.11(3)
c (Å), γ°	16.823(2), 63.43(3)
Volume(Å <sup>3</sup> ), Z	2520.9(3), 2
Density (cal.)	0.755 g/cm <sup>3</sup>
F(000)	590
Absorption coefficient	0.412 mm <sup>-1</sup>
θ range, Scan type	1.69~24.11, ω
Limiting indices	-1 ≤ h ≤ 15, -14 ≤ k ≤ 15, -18 ≤ l ≤ 19
Reflection collection	9105
Independent reflections	7935 (R <sub>int</sub> = 0.0669)
Quantity minimized	Σw(F <sub>o</sub> -F <sub>c</sub> ) <sup>2</sup>
Weighting scheme	w <sup>-1</sup> =[σ <sup>2</sup> (F <sub>o</sub> ) <sup>2</sup> +(0.06P) <sup>2</sup> ] (P=(F <sub>o</sub> <sup>2</sup> +2F <sub>c</sub> <sup>2</sup> )/3)
Final R indices (I>2σ(I))	R1 = 0.0827, wR2 = 0.1408
R indices (all data)	R1 = 0.2147, wR2 = 0.2169
Goodness-of-fit on F <sup>2</sup>	1.040
Largest diff. peak and hole	0.376 e·Å <sup>-3</sup> , -0.428 e·Å <sup>-3</sup>

### 2.3 X-ray crystallography

A blue single crystal with dimensions  $0.38 \times 0.36 \times 0.30$  mm was used for indexing and intensity data collection on a Bruker R3 four circle diffractometer with graphite-monochromated Mo-K $\alpha$  radiation ( $\lambda=0.71073$  Å) at 293K. All the crystallographic data are summarized in Table 1. L-P factor and empirical absorption corrections were applied for the complex. The structure was solved by heavy atom methods and refined with a full matrix least-squares program. All the atomic positions were obtained by Fourier-difference synthesis. All the calculations were performed using the SHELXTL program system. Selected bond lengths and angles are listed in Table 2.

## 3 Results and Discussion

### 3.1 Description and discussion of structure

The structure analysis shows that the formula of the complex is  $[\text{Ni}_2(\text{im})(\text{phen})_4]\cdot(\text{NO}_3)_3\cdot3\text{H}_2\text{O}$ . The feature of the crystal structure concentrates on the  $[\text{Ni}_2(\text{im})(\text{phen})_4]^{3+}$  ion (Figure 1). In the cation, the  $[\text{Ni}(\text{phen})_2]$  moieties are bridged by one imidazolate ion and each crystallographically independent Ni(II) ion is five-coordinate with a distorted square pyramidal geometry. Four of the five coordinate nitrogen atoms for each Ni(II) ion are from two phen and one from bridging imidazolate. Three of the phen nitrogens on each Ni(II) ion ( $\text{N}_4$ ,  $\text{N}_7$ ,  $\text{N}_8$  on  $\text{Ni}_1$  and  $\text{N}_2$ ,  $\text{N}_5$ ,  $\text{N}_6$  on  $\text{Ni}_2$ ) and one of the bridging imidazolate nitrogen atoms ( $\text{N}_{10}$  to  $\text{Ni}_1$  and  $\text{N}_9$  to  $\text{Ni}_2$ ) occupy the four sites of the basal plane of the square pyramid. The eight Ni-N distances range from 1.962(8) Å to 2.045(9) Å. The remaining one nitrogen ( $\text{N}_3$  to  $\text{Ni}_1$  and  $\text{N}_1$  to  $\text{Ni}_2$ ) of the phen group occupies the apical position of the distorted square pyramid. The two Ni-N separations are 2.244(8) Å and 2.226(9) Å, respectively. The  $\text{Ni}_1$  and  $\text{Ni}_2$  ions are not on the basal plane, but are 0.16 Å and 0.13 Å respectively above the distorted square plane. This slight difference between the two deviations may be due to the effect of the  $\text{NO}_3^-$  group. The  $\text{Ni}_1\text{-Ni}_2$  distance is 0.5857(5) Å. The bond lengths and angles in the phen and imidazolate ligands are normal. The packing of molecules in the unit cell is shown in Figure 2.

Table 2. Selected bond lengths (Å) and angles (°) for the complex.

Ni(1)-N(10)	1.962(8)	Ni(2)-N(9)	1.972(8)
Ni(1)-N(8)	2.028(8)	Ni(2)-N(2)	2.022(9)
Ni(1)-N(7)	2.031(7)	Ni(2)-N(6)	2.029(9)
Ni(1)-N(4)	2.040(8)	Ni(2)-N(5)	2.045(9)
Ni(1)-N(3)	2.244(8)	Ni(2)-N(1)	2.226(9)
N(10)-Ni(1)-N(8)	166.2(3)	N(9)-Ni(2)-N(2)	93.9(3)
N(10)-Ni(1)-N(7)	93.7(3)	N(9)-Ni(2)-N(6)	94.0(3)
N(8)-Ni(1)-N(7)	81.0(3)	N(2)-Ni(2)-N(6)	171.6(3)
N(10)-Ni(1)-N(4)	93.1(3)	N(9)-Ni(2)-N(5)	161.7(3)
N(8)-Ni(1)-N(4)	91.4(3)	N(2)-Ni(2)-N(5)	92.2(4)
N(7)-Ni(1)-N(4)	171.9(3)	N(6)-Ni(2)-N(5)	81.1(4)
N(10)-Ni(1)-N(3)	95.7(3)	N(9)-Ni(2)-N(1)	97.9(3)
N(8)-Ni(1)-N(3)	98.0(3)	N(2)-Ni(2)-N(1)	78.7(4)
N(7)-Ni(1)-N(3)	104.5(3)	N(6)-Ni(2)-N(1)	97.4(3)
N(4)-Ni(1)-N(3)	79.1(3)	N(5)-Ni(2)-N(1)	100.2(3)

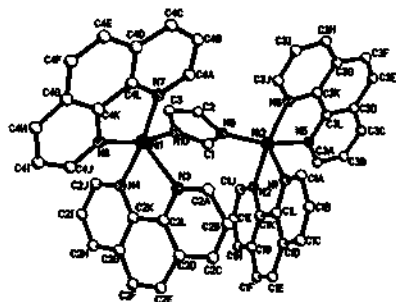


Figure 1. The molecular structure of the complex.

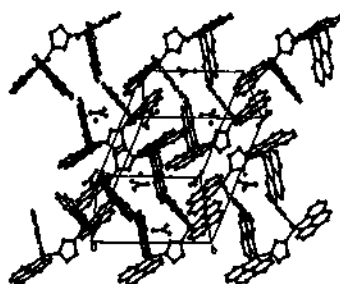


Figure 2. The packing of molecule in the unit cell.

In the present paper, the binuclear Ni(II) ( $d^8$ ) complex with imidazolate-bridged ligand has obvious characteristic compared with the relevant complexes in the literature. The comparison of the configurations, coordinations and geometries of the relevant complexes are listed in Table 3.

Table 3. The comparison of the configurations, coordinations and geometries of the relevant complexes.

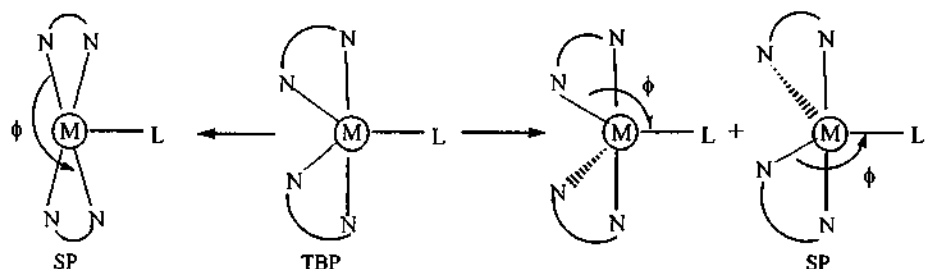
Center metals (M-M')	Bridged ligand	Terminal ligand	Coor. numb er	$d^n$	Coordination geometry	Magnetism	Ref
Cu(II),Cu(II)	im	AE	4	$d^9$	square- planar	antiferromagnetic $J=-21.5\text{cm}^{-1}$	3
Cu(II),Ni(II)	im	AE	4	$d^9, d^{10}$	square- planar	antiferromagnetic $J=-24\text{cm}^{-1}$	6
Ni(II),Ni(II)	im	AE	4	$d^8$	square- planar	diamagnetic	8
Cu(II),Cu(II)	im	tren	5	$d^9$	trigonal bipyramidal		17
Cu(II),Zn(II)	im	trien	5	$d^9, d^{10}$	tetrahedral pyramid		12
Cu(II),Zn(II)	im	tren	5	$d^9, d^{10}$	trigonal bipyramidal		12
Cu(II),Cu(II)	im	phen	5	$d^9$	tetrahedral pyramid	antiferromagnetic $J=-24\text{cm}^{-1}$	13
Cu(II),Cu(II)	im	TMDT	5	$d^9$	tetrahedral pyramid	antiferromagnetic $J=-25.8\text{cm}^{-1}$	16
Cu(II),Cu(II)	im	pip	4	$d^9$	square- planar	antiferromagnetic $J=-26.74\text{cm}^{-1}$	2
Ni(II),Ni(II)	bilm	tren	5	$d^8$		antiferromagnetic $J=-2.9\text{cm}^{-1}$	18
Ni(II),Ni(II)	im	phen	5	$d^8$	tetrahedral pyramid	antiferromagnetic $J=-30.43\text{cm}^{-1}$	This paper

AEH = 7-amino-4-methyl-5-aza-3-hepten-2-onato; tren = tris(2-aminoethyl)amine; phen = phenanthroline; trien = triethylenetetramine; TMDT = 1,1,7,7-tetramethyldiethylenetriamine; im = imidazolate; pip = 2-[2-(2-pyridyl)ethyl-iminomethyl]pyridine.

In Table 3 if the metal ion in the complex is 4 coordinated, its coordination geometry is square plane. According to the valence bond theory, the hybrid orbital of the metal ion should be  $dsp^2$ . As far as the Ni(II) ( $d^8$ ) ion is concerned, when it adopts the form of  $3d4s4p^2$  hybridization, the Ni(II) complex with a square planar geometry will be diamagnetic and stable. On the other hand, if the metal ion is 5 coordinated, there will be two possible coordination geometries around the metal ion, trigonal bipyramidal and square pyramid. In the former, the metal ion adopts  $dsp^3$  hybridization and the latter is  $d^2sp^2$ . These two configurations of a  $d^8$  ion possess approximate energy and they can be interconverted to each other under some condition:

(1) In the light of the distortion ( $\Delta$ ) of coordination polyhedron, the coordination polyhedron is a regular square pyramid if  $\Delta=1$  and a regular trigonal bipyramid if  $\Delta=0$ .

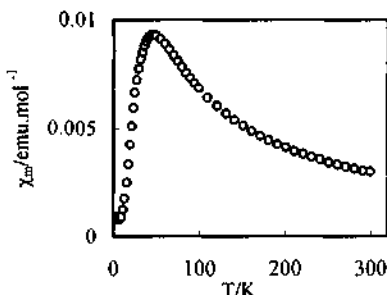
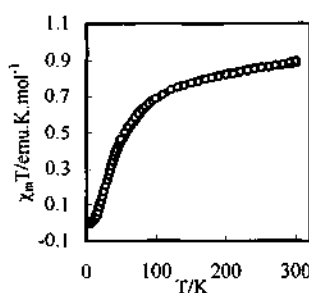
(2) The trigonal bipyramid (TBP) — square pyramid (SP) interconversion can take place by an elongation of either a Ni-N<sub>eq</sub> or a Ni-L<sub>eq</sub> bond, as the angle  $\phi$  opposite that bond in the equatorial plane becomes greater than  $120^\circ$  (see following Figure )[13].



In the title complex two Ni(II) ( $d^8$ ) ions probably adopt  $4s4p^24d^2$  hybrid orbital to accept the electrons of the ligands. In this complex, although the energy of hybrid orbital of the Ni(II) ions is higher than that of the  $3d^24s4p^2$ , the possibility of the conversion of coordination geometry from SP to TBP is decreased. This favors to the stability of the complex and the paramagnetism of the Ni(II) ions.

### 3.2 Magnetic properties of the complex

In the light of the magnetic moments of the complex of measurement, we obtained the molar susceptibility ( $\chi_m$ ) and the effective magnetic moment ( $\mu_{eff} = 2.829 \sqrt{\chi_m T}$ ) of the complex. The temperature dependence of  $\chi_m$  and  $\chi_m T$  is shown in Figures 3 and 4. In Figure 3, the plot of  $\chi_m$  vs.  $T$  passes through a maximum at ca. 48 K and decreases again. This behavior indicates that the sample possesses obvious phase change at 48K. The plot of  $\chi_m T$  vs.  $T$  in Figure 4 quickly drops at 48K then turns to zero when  $T$  approaches 0K. These behaviors reveal that the complex possesses antiferromagnetic feature at low temperature, i.e., there is an antiferromagnetic interaction between the two Ni(II) ions in the complex.

Figure 3. Temperature dependence of  $\chi_m$ .Figure 4. Temperature dependence of  $\chi_mT$ .

According to the Heisenberg model, the antiferromagnetic interaction can be further analyzed in the theory. The Hamiltonian of the magnetic interaction between the two paramagnetic ions can be written as,  $\hat{H} = -2JS_1S_2$ , where  $S_1$  and  $S_2$  stand for the spins of two Ni(II) and  $J$  is the exchange integral. It is ferromagnetic interaction between ions if  $J > 0$  and antiferromagnetic if  $J < 0$ . By means of the model, the title complex has two Ni(II) ions of  $S_1 = 1$  and  $S_2 = 1$ , so that the following expression of  $\chi_m$  can be deduced theoretically:

$$\chi_m = \frac{Ng^2\beta^2}{KT} \cdot \left( \frac{e^{J/KT} + 5e^{3J/KT}}{1 + e^{J/KT} + 5e^{3J/KT}} \right)$$

where  $N$  is Avogadro constant,  $K$  is Boltzmann constant,  $\beta$  denotes Bohr magneton,  $J$  and  $g$  are magnetic parameters for evaluation,  $T$  is absolute temperature. By using the origin 5.0 procedure, a very good fitting of the  $\chi_mT$  (exp.) with  $\chi_mT$  (theory) has been attained (Figure 4). And the magnetic parameters has been yielded:  $J = -30.43\text{cm}^{-1}$  and  $g = 1.98$ . The signal and magnitude of  $J$  demonstrate that there is an antiferromagnetic interaction between two Ni(II) ions in the complex.

## References

1. Kolks G., Frihart C. R., Rabinowitz H. N. and Lippard S. J., Imidazolate-bridged complexes of copper(II), *J. Am. Chem. Soc.*, **98** (1976) pp. 5720-5721.
2. Kolks G. and Lippard S. J., Magnetism exchange interactions in imidazolate bridged copper(II) complexes, *J. Am. Chem. Soc.*, **99** (1977) pp. 5804-5806.
3. Costes J. P., Serra J. F., Dahan F. and Laurent J. P., Synthesis and solid-state properties of a homodinuclear complex, *Inorg. Chem.*, **25** (1986) pp. 2790-2795.
4. Costes J. P., Commenges G. and Laurent J. P., NMR study of dinickel complexes. Importance of the non-bonded interactions, *Inorg. Chim. Acta*, **134** (1987) pp. 237-244.
5. Costes J. P. and Laurent J. P., Solution properties of dinuclear copper and nickel complexes and their mononuclear precursors, *Inorg. Chim. Acta*, **134** (1987) pp. 245-248.

6. Costes J. P. and Fernandez Garcia M. I., Synthesis and characterization of homobinuclear and heterobinuclear imidazolate-bridged complexes, *Inorg. Chim. Acta*, **173** (1990) pp.247-254.
7. Costes J. P. and Laurent J. P., Spin delocalization in pyridine adducts of mononuclear and dinuclear nickel(II) complexes: a <sup>1</sup>H NMR study, *Inorg. Chim. Acta*, **177** (1990) pp. 277-282.
8. Costes J. P., Dahan F. and Laurent J. P., Structural and magnetic consequences of steric effects in mono- and dinuclear Ni(II) and Cu(II) complexes, *Inorg. Chem.*, **30** (1991), pp. 1887-1892.
9. Costes J. P., Dahan F., Fernandez Fernandez M. B., Fernandez Garcia M. I., Garcia Deibe A. M. and Sanmartin J., General synthesis of 'salicylaldehyde half-unit complexes', *Inorg. Chim. Acta*, **274** (1998) pp. 73-81.
10. Coughlin P. K. and Lippard S. J., Magnetic, ESR, electrochemical, and potentiometric titration studies of the imidazolate-bridged dicopper(II) ion, *Inorg. Chem.*, **23** (1984) pp. 1446-1451.
11. Fu D. G., Xu B., Wang G. X., Tang W. X., Yu K. B. and Zhou Z. Y., Studies of structure and magnetism of the Cu-Co complex, *Science in China (series B)*, **24** (1994) pp.225-231.
12. Mao Z. W., Chen M. Q., Tan X. S., Liu J. and Tang W. X., Synthesis, crystal structure, and properties of a new imidazolate-bridged copper-zinc heterbinuclear complex, *Inorg. Chem.*, **34** (1995) pp. 2889-2893.
13. Morehouse S. M., The crystal and molecular structure of 1*H*-imidazolzobis[bis-(1-10phenanthroline)copper(II)] nitrate, *Inorg. Chim. Acta*, **243** (1996) pp. 327.
14. Zhu H. L., Zheng L. M., Fu D. G., Huang P., Bu W. M. and Tang W. X., Synthesis, structure and magnetism behavior of a tetracopper(II) complex, *Inorg. Chim. Acta*, **287** (1999) pp. 52-60.
15. Patel R. N., Pandey H. C. and Pandeya K. B., X-band e.p.r. spectra of imidazole/imidazolate bridged polynuclear copper(II) complexes, *Transition Met. Chem.*, **24** (1999) pp. 35-37.
16. O'Young C. L., Dewan J. C., Lilenthal H. R. and Lippard S. J., Electron spin resonance, magnetic, and structure of copper(II) complex, *J. Am. Chem. Soc.*, **100** (1978) pp. 7291-7300.
17. Lu Z. L., Duan C. Y., Tian Y. P. and You X. Z., Synthesis and crystal structure of an imidazolate-bridged dicopper complex, *Transition Met. Chem.*, **22** (1997) pp. 549-552.
18. Haddad M. S. and Hendrickson D. N., Magnetic exchange interactions in binuclear transition-metal complexes 15, *Inorg. Chem.*, **17** (1978) pp. 2622-2630.
19. Zhu H. L., Bu W. M. and Tang W. W., Synthesis and crystal structure of N,N-bis(2-aminoethyl)-1,3-propyldiamine complexes with nickel(II), *Chinese J. Inorg. Chem.*, **15** (1999) pp. 423-428.

This page is intentionally left blank

# DESIGN OF METAL-CARBOXYLATE CAVITY-CONTAINING RECTANGULAR GRIDS WITH 1,2,4,5-BENZENETETRACARBOXYLIC ACID

QIAN SHI, RONG CAO,\* DAOFENG SUN AND MAOCHUN HONG\*

*State Key Laboratory of Structural Chemistry, Fujian Institute of Research on the Structure of Matter, the Chinese Academy of Sciences, Fuzhou, 350002, P. R. China*

Four 1,2,4,5-benzenetetracarboxylate Cu(II) complexes were designed and synthesized in the presence of a second ligand, namely,  $[\text{Cu}_2(\text{btec})(\text{H}_2\text{O})_4 \cdot 2\text{H}_2\text{O}]_n$  (2),  $[\text{Cu}_2(\text{btec})_{4/4} \{\text{Cu}(\text{Hbtec})_{2/2}(4,4'\text{-Hbpy})(\text{H}_2\text{O})_2\}_2 \cdot 4\text{H}_2\text{O}]_n$  (3),  $[\text{Cu}_2(\text{btec})(\text{hmt})(\text{H}_2\text{O})_4 \cdot 8\text{H}_2\text{O}]_n$  (4) and  $[\text{Cu}_2(\text{btec})(\text{OH})_2]_n$  (5). The complexes are characterized by crystal X-ray diffraction and IR spectra. The four complexes all contain rectangular grid-like structures in spite of the different coordination fashions of the carboxylate groups in 1,2,4,5-benzenetetracarboxylic acid.

## 1 Introduction

The design of metal-organic materials with large channels and cavities has been deeply researched, due to their intriguing structural diversity and potential functions as microporous solids for molecular adsorption, ion exchange, and heterogeneous catalysis.[1-3] 1,2,4,5-Benzenetetracarboxylate acid ( $\text{H}_4\text{btec}$ ) appears to be a good choice in the forming of rectangular grids due to its rich coordination modes and high symmetry. The size of the cavities depends on the coordination fashion of the carboxylate groups in  $\text{H}_4\text{btec}$ .[4-6] In our recent work, we found it is interesting that the second ligands, present in the reaction system, contribute to the construction of the porous frameworks.[7,8]

Considering the special bioactive and biocatalytic functions of copper(II) carboxylate complexes,[9] along with the magnetic properties and various coordination fashions of Cu(II) ion,[10-12] we focused our work on the Cu(II) and  $\text{H}_4\text{btec}$  system. Based on the layer structure of  $[\text{Cu}_2(\text{btec})(\text{H}_2\text{O})_6 \cdot 4\text{H}_2\text{O}]_n$  (1),[13] in which the Cu(II) atom with bi-pyramidal configuration is coordinated by two monodentate carboxyl O atoms and three aqua molecules, part of the coordinated aqua molecules of Cu(II) is possible to be replaced by some bridging spacers, such as pyrazine, 4,4'-bipyridine (4,4'-bpy) and the related species, and to construct 2-D and 3-D open-frameworks with variable cavities and channels.

The results we got are somewhat unprecedented. The coordination modes of  $\text{H}_4\text{btec}$  and Cu(II) are changed along with the addition of the second ligands. In the presence of pyrazine, an unexpected complex  $[\text{Cu}_2(\text{btec})(\text{H}_2\text{O})_4 \cdot 2\text{H}_2\text{O}]_n$  (2) was obtained, in which pyrazine are not present in the solid product. We also have tried to synthesize 2 in the same condition without pyrazine, but what we got is the same as 1. Complex  $[\text{Cu}_2(\text{btec})_{4/4} \{\text{Cu}(\text{Hbtec})_{2/2}(4,4'\text{-Hbpy})(\text{H}_2\text{O})_2\}_2 \cdot 4\text{H}_2\text{O}]_n$  (3), obtained with the replacement pyrazine by 4,4'-bpy, is constructed by the paddle-wheel  $[\text{Cu}_2(\text{OOCR})_4]$  building units in the layer and constrained by Cu-Hbtec-Cu-L ( $L = 4,4'\text{-Hbpy}$ ) chains in both sides of the layer. When hexamethylenetetramine (hmt) was added into the original system,  $[\text{Cu}_2(\text{btec})(\text{hmt})(\text{H}_2\text{O})_4 \cdot 8\text{H}_2\text{O}]_n$  (4) produced, in

which the coordination mode of btec<sup>4+</sup> is similar to that in **1**, and only one of the Cu-O(aqua) bond is replaced by Cu-N(hmt) bond.

Further, we wanted to use solvothermal method to prepare some new materials. High dimension and unexpected structures were always produced using such method. Unfortunately, the ligands mentioned above (pyrazine, 4,4'-bpy and hmt) process redox reactions with Cu(II) at high temperature, and only mixture were obtained in our experiments. When another stable ligand imidazole (imH) is placed in the system, a new species was formed in high yield,  $[Cu_3(btec)(OH)_2]_n$  (**5**). In **5**, the microporous transition-metal-containing species produced based on Cu(II) hydroxide structural members, joined together by btec<sup>4+</sup> ions. The attempt to synthesize **5** in the absent of imH was failed, only with powder products, which indicates that imH plays an important role in the reaction.

Here in, we report the preparation and crystal structures of complexes **2**, **3**, **4** and **5**.

## 2 Experimental Section

### 2.1 General methods.

Elemental analyses of carbon, hydrogen and nitrogen were carried out with an Elementar Vario ELIII. The infrared spectroscopy on KBr pallets was performed on a Nicolet Magna FT-IR 750 spectrometer in the range of 200-4000 cm<sup>-1</sup>. All reagents were commercially available and used as received.

### 2.2 Synthesis

**[Cu<sub>2</sub>(btec)(H<sub>2</sub>O)<sub>4</sub>·2H<sub>2</sub>O]<sub>n</sub>** (**2**). To an aqua solution (30cm<sup>3</sup>) of H<sub>4</sub>btec (0.12g, 0.5mmol), a solution of CuCl<sub>2</sub>·2H<sub>2</sub>O (0.17g, 1.0mmol) in 10cm<sup>3</sup> H<sub>2</sub>O was slowly added and boiled for 15min. A MeOH solution of pyrazine (0.08g, 1.0mmol) was diffused into the above solution, and the solution was adjusted to pH = 4 by the addition of dilute NaOH solution. The mixture was filtered and stood at room temperature for a week to give green crystals of **2** (yield 48% based on CuCl<sub>2</sub>·2H<sub>2</sub>O). *Anal.* Calc. for C<sub>10</sub>H<sub>14</sub>Cu<sub>2</sub>O<sub>14</sub>: C, 24.74; H, 2.89. Found: C, 24.85; H, 2.82%.

**[Cu<sub>2</sub>(btec)<sub>4/4</sub>{Cu(Hbtec)<sub>2/2</sub>(4,4'-Hbpy)(H<sub>2</sub>O)<sub>2</sub>}·4H<sub>2</sub>O]<sub>n</sub>** (**3**). This complex was prepared similar to **2** with the exception that the pH value was adjusted to 2. Dark-green crystals of **3** were obtained after standing at room temperature for several weeks (yield 52% based on CuCl<sub>2</sub>·2H<sub>2</sub>O). *Anal.* Calc. for C<sub>50</sub>H<sub>42</sub>Cu<sub>4</sub>N<sub>4</sub>O<sub>32</sub>: C, 40.95; H, 2.87; N, 3.83. Found: C, 40.49; H, 2.83; N, 3.95%.

**[Cu<sub>2</sub>(btec)(hmt)(H<sub>2</sub>O)<sub>4</sub>·8H<sub>2</sub>O]<sub>n</sub>** (**4**). This complex was prepared similar to **2** and blue-green crystals of **4** were formed after standing at room temperature only for one day (yield 82% based on CuCl<sub>2</sub>·2H<sub>2</sub>O). *Anal.* Calc. for C<sub>16</sub>H<sub>38</sub>Cu<sub>2</sub>N<sub>4</sub>O<sub>20</sub>: C, 26.19; H, 5.18; N, 7.64. Found: C, 26.12; H, 5.15; N, 7.72%.

**[Cu<sub>3</sub>(btec)(OH)<sub>2</sub>]<sub>n</sub>** (**5**). CuCl<sub>2</sub>·2H<sub>2</sub>O (0.08g, 0.5mmol), H<sub>4</sub>btec (0.12g, 0.5mmol), imH (0.04g, 0.5mmol) and NaOH (0.04g, 1mmol) were added to a 1:1 (V/V) MeOH-H<sub>2</sub>O solution (20cm<sup>3</sup>) in a Teflon-lined stainless-steel reactor. The mixture was heated at 140°C for 2 days and green block-like crystals were formed after the mixture cooled to room temperature (yield 87% based on CuCl<sub>2</sub>·2H<sub>2</sub>O). *Anal.* Calc. for C<sub>10</sub>H<sub>4</sub>Cu<sub>3</sub>O<sub>10</sub>: C, 25.29; H, 0.84. Found: C, 25.25; H, 0.90%.

### 2.3 X-ray crystallography.

X-ray intensities of the four complexes were collected on a Siemens Smart CCD diffractometer with graphite-monochromated Mo-K $\alpha$  radiation ( $\lambda = 0.71073 \text{ \AA}$ ) with the  $\omega$ -2 $\theta$  scan mode. Empirical absorption correction was applied to the data using SADABS program.[14] The structures were solved by direct methods.[15] Non-hydrogen atoms were refined anisotropically. Hydrogen atoms in **2** were generated in idealized positions. In **3** and **4**, the hydrogen atoms for the C and N atoms were generated from successive difference Fourier syntheses, while those for the O(aqua) atoms were generated in idealized positions. In **5**, all the other hydrogen atoms were generated in idealized positions, except that for the hydroxide group was generated from difference Fourier synthesis. All calculations were performed using the SHELXTL program.[16]

## 3 Results and Discussion

### 3.1 IR spectra.

The difference in  $v_{as}(\text{COO})$  and  $v_s(\text{COO})$  ( $\Delta\nu$ ), compared to the corresponding values in sodium carboxylate ( $95\text{cm}^{-1}$  in  $\text{Na}_4\text{btec}$ ), is currently employed to determine the corresponding mode of carboxylate group. In complex **2**, the values of  $\Delta\nu$  show that the carboxylate groups coordinate to the Cu(II) atoms both in monodentate ( $201\text{cm}^{-1} > 95\text{cm}^{-1}$ ) and in bidentate ( $72\text{cm}^{-1} < 95\text{cm}^{-1}$ ) fashions. In **3**, besides the two coordination fashions as in **2** ( $\Delta\nu = 216$  and  $74\text{cm}^{-1}$ ), an un-coordinated protonated carboxylate group is present with the characteristic absorption at  $1739\text{cm}^{-1}$ . The absorption at  $3510\text{cm}^{-1}$  is assigned as  $v_{N-H}$  of the protonated N atom in *4,4'-Hbpy*. As for **4** and **5**, the values of  $\Delta\nu$  ( $190$  and  $212\text{cm}^{-1}$  respectively) indicate that the carboxylate groups coordinate to the Cu(II) atoms only as a monodentate ligand.

### 3.2 Descriptions of the crystal structures.

In **2**, the 2D step structure with grids is constructed by the monodentate carboxylate groups in  $\text{btec}^{4+}$  and the bi-nuclear Cu(II) units as shown in Fig. 1a. The square-pyramidal configuration of the Cu(II) atom is completed by two carboxyl O atoms from two  $\text{btec}^{4+}$  ligands and two aqua O atoms in the equatorial plane, and one carboxyl O atom from the third  $\text{btec}^{4+}$  ligands in the axial position. In the plane, the bond lengths of Cu(II)-O are in the range of  $1.955(4)$ - $1.977(5) \text{ \AA}$  and the bond angles of O-Cu(II)-O are varied from  $81.89(19)$  to  $93.87(18)^\circ$ . The bond of Cu(II)-O(axial) is some longer than that in the plane with the value of  $2.245(4) \text{ \AA}$ , and the bonds of O(axial)-Cu(II)-O(equatorial) are  $102.81(16)$ ,  $87.95(16)$ ,  $90.84(16)$  and  $100.6(2)^\circ$  respectively. The carboxylate groups of  $\text{btec}^{4+}$  show two coordination fashions in the structure, in which two bidentate groups chelate two Cu(II) atoms forming a binuclear unit and the monodentate carboxylate groups link the binuclear units into a 2D step structure with grids of  $6.5\text{\AA} \times 4.5 \text{ \AA}$ . Numerous hydrogen bonding interactions are present between O(aqua) $\cdots$ O(carboxyl) and O(carboxyl) $\cdots$ O(carboxyl), forming a 3D structure with channels (Fig. 1b).

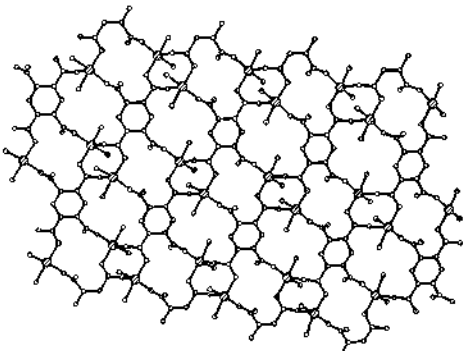


**Figure 1a.** Pack structure for **2** along *a* axial.

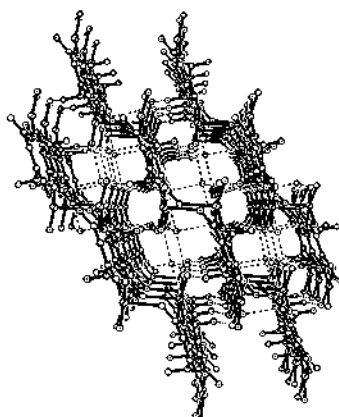


**Figure 1b.** Pack structure for **2** along *c* axial.

The crystal structure analysis reveals that **3** is a neutral 2D polymer, tetranuclear species [ $\text{Cu}_2(\text{btec})_{4/4}\{\text{Cu}(\text{Hbtec})_{2/2}(4,4'\text{-Hbpy})(\text{H}_2\text{O})_2\}_2$ ] constitutes the basic building block, which is composed of one  $\text{Cu}_2$  paddle-wheel secondary building unit (SBU) and two mononuclear  $\text{Cu}(\text{II})$  motifs (Fig. 2a). The paddle-wheel SBU is completed by four carboxylate groups, two from  $\text{btec}^{4-}$  and two from  $\text{Hbtec}^{3-}$ , with a  $\text{Cu}-\text{Cu}$  distance being  $2.6926(16)$  Å. Two coordination modes for benzenetetracarboxylate ligands are present: *a*, All carboxyl groups are deprotonated ( $\text{btec}^{4-}$ ), two *para* ones take part in the organization of two SBUs in bidentate bridging mode, while the remaining two link the other two SBUs at axial positions in a monodentate mode. Hence, each  $\text{btec}^{4-}$  ligand connects four SBUs and *vice versa*, forming an infinite 2D layer with rectangular pores ( $6\text{\AA} \times 7\text{\AA}$ ), and two guest water molecules per pore are present; *b*, Only three carboxyl groups are deprotonated ( $\text{Hbtec}^{3-}$ ) and take part in the coordination, the protonated one remains free. The carboxylate group *para* to the protonated carboxyl group is used to complete the paddle-wheel SBU in bidentate bridging mode. The other two carboxylate groups link two mononuclear copper motifs in monodentate mode and each of such motifs attaches to two  $\text{Hbtec}^{3-}$ , generating 1D chains that can be viewed as paralleled Cu-Hbpy barriers on the two sides of the SBU layer (Fig. 2b).

The structure of **4** formed just as our expectation, in which the N atom from the hmt ligand replace the position of the O atom of one aqua molecule coordinate to the  $\text{Cu}(\text{II})$  atom as in **1**. The  $\text{Cu}(\text{II})$  atom is surrounded by two O atoms from two monodentate carboxylate groups of two, one O atom from an aqua molecule and one N atom from hmt in the equatorial plane, and one O atom from aqua in the axial position, forming a square-pyramidal configuration. The 4+4 grid in the complex is constructed by four  $\text{btec}^{4-}$  ligands at the corner and four  $\text{Cu}(\text{II})$  atoms in the sides, with the size of  $10.1\text{\AA} \times 11.8\text{\AA}$  (Fig. 3). The hmt ligands link the grids into a 3D network with numerous hydrogen bonding of  $\text{O}(\text{carboxyl})\cdots\text{O}(\text{aqua})$ ,  $\text{O}(\text{carboxyl})\cdots\text{O}(\text{carboxyl})$  and  $\text{O}(\text{aqua})\cdots\text{O}(\text{aqua})$  dotted in the grids.

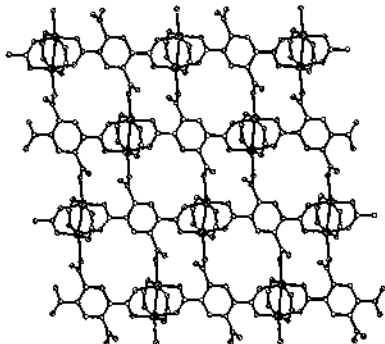


**Figure 2a.** View of the layer structure formed by Cu<sub>2</sub> SBUs in 3. The copper motifs outside the layer are omitted for clarity.

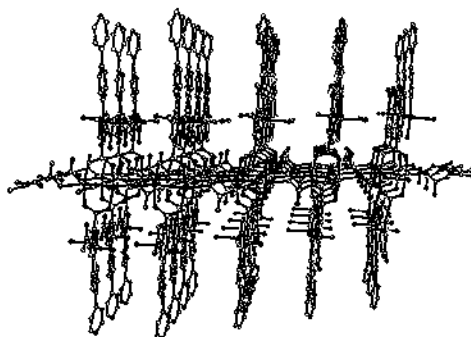


**Figure 2b.** Packing structure along a axis for 3.

The microporous structure in 5 is produced based on Cu(II) hydroxide structural members joined together by the btec<sup>4-</sup> ligands (Fig. 4). The complex can be viewed as being made up from assemblies of tubes with rectangular sections in which the metal hydroxide chains are the walls of the tube and the btec<sup>4-</sup> ligands act as spacers. The Cu(II) atoms are all four coordinated (two carboxyl O atoms and two aqua O atoms) with square-plane configuration with two types. In one type, two carboxyl O atoms are in *para* position, while in the other type they are in *trans* place.

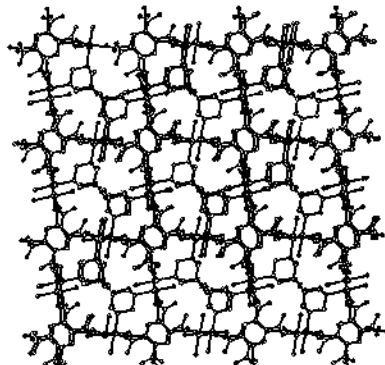


**Figure 3.** Packing structure for 4 along a axial.

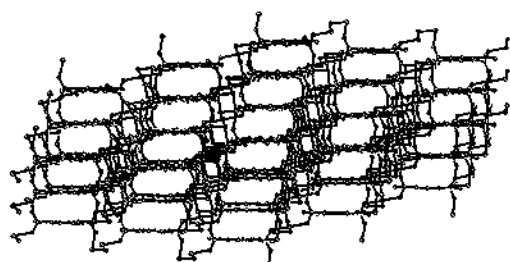


**Figure 4.** Packing structure for 5 along c axial.

#### 4 Acknowledgement

The authors thank the NNSFC and the CAS for financial support.

## References

- Zaworotko M. J., Superstructural diversity in two dimensions: crystal engineering of laminated solids. *J. Chem. Soc., Chem. Commun.* (2001) pp. 1-9.
- Eddaoudi M., Moler D. B., Li Hailian, Chen Banglin, Reineke T. M., O'Keeffe M. and Yaghi O. M., Modular Chemistry: Secondary building units as a basis for the design of highly porous and robust metal-organic carboxylate frameworks, *Acc. Chem. Res.* **34** (2001) pp. 319-330.
- Chui S. S.-Y., Lo S. M.-F., Charmant J. P.-H., Orpen A. G. and Williams L. D., A chemical functionalizable nanoporous material  $[\text{Cu}_3(\text{TMA})_2(\text{H}_2\text{O})_2]_n$ , *Science* **283** (1999) pp. 1148-1150.
- Plater M. J., Foreman M. R. St J., Howie R. A., Skakle J. M. S. and Slawin A. M. Z., Hydrothermal synthesis of polymeric metal carboxylates from benzene-1,2,4,5-tetracarboxylic acid and benzene-1,2,4-tricarboxylic acid, *Inorg. Chim. Acta* **315** (2001) pp. 126-132.
- Murugavel R., Krishnamurthy D. and Sathyendiran M., Anionic metal-organic and cationic layer alternation in the coordination polymers  $[(\{\text{M(BTEC)}(\text{OH}_2)_4\} \cdot \{\text{C}_4\text{H}_{12}\text{N}_2\} \cdot 4\text{H}_2\text{O})_n]$ , *J. Chem. Soc., Dalton Trans.* (2001) pp. 34-39.
- Gutschke S. O. H., Price D. J., Powell A. K. and Wood P. T., Rational design of oper-framework coordination solids-synthesis and structure of  $[\text{Co}_3(\text{OH})_2\{1,2,4,5-(\text{O}_2\text{C})_4\text{C}_6\text{H}_2\}_2(\text{H}_2\text{O})_4] \cdot x\text{H}_2\text{O}$ , *Eur. J. Inorg. Chem.* (2001) pp. 2739-2741.
- Shi Q., Cao R., Sun D.-F., Hong M.-Ch. and Liang Y.-C., Solvothermal syntheses and crystal structures of two metal coordination polymers with double-chain structures, *Polyhedron* **20** (2001) pp. 3287-3293.
- Sun D.-F., Cao R., Liang Y.-C., Shi Q., Su W.-P. and Hong M.-Ch., Hydrothermal syntheses, structures and properties of terephthalate-bridged polymeric complexes with zig-zag chain and channel structure, *J. Chem. Soc., Dalton Trans.* (2001) pp. 2335-2340.
- King R. B., *Encyclopedia of Inorganic Chemistry* (Wiley, New York), 1994.
- Maji T. K., Mukherjee P. S., Mostafa G., Mallah T., Cano-Boquera Joan and Chaudhuri N. R., First observation of a ferromagnetic interaction through and end-to-end azido bridging pathway in a 1D copper(II) system, *J. Chem. Soc., Chem. Commun.* (2001) pp. 1012-1013.
- Xu Zh.-Q., Thompson L. K. and Miller D. O., A self-assembled novel Cu(II) 'pin-wheel' cluster exhibiting ferromagnetic coupling, *J. Chem. Soc., Chem. Commun.* (2001) pp. 1170-1171.
- Carlucci L., Ciani G., Proserpio D. M. and Rizzato S., Interlinked molecular squares with  $[\text{Cu}(2,2'\text{-bipy})]^{2+}$  corners generating a three-dimensional network of unprecedented topological type, *J. Chem. Soc., Chem. Commun.* (2001) pp. 1198-1199.
- Usubaliev B. T., Shnulin A. N. and Mamedov Kh. S., *Koord. Khim.* **8** (1982) pp. 1532.
- Sheldrick G. M., SADABS, *Program for Empirical Absorption Correction of Area Detector Data*, University of Göttingen, 1996.
- Sheldrick G. M., SHELXS 97, *Program for Crystal Structure Solution*, University of Göttingen, 1997.
- Sheldrick G. M., SHELXS 97, *Program for Crystal Structure Refinement*, University of Göttingen, 1997.

**[Mn(salAren)(H<sub>2</sub>O)]<sub>2</sub>[Fe(CN)<sub>5</sub>(NO)]·2CH<sub>3</sub>OH·3H<sub>2</sub>O: A NEW TRINUCLEAR COMPLEX WITH CYANIDE BRIDGES AND HYDROGEN BONDS**

SHU-FENG SI, QING-LUN WANG AND DAI-ZHENG LIAO

*Department of Chemistry Nankai University, Tianjin 300071, P. R. China*

*Email: coord@nankai.edu.cn*

The coordination compound [Mn(salAren)(H<sub>2</sub>O)]<sub>2</sub>[Fe(CN)<sub>5</sub>(NO)]·2CH<sub>3</sub>OH·3H<sub>2</sub>O (1) has been synthesized and structurally characterized. (1) crystallizes in the triclinic space group P-1 ( $a = 11.019(4)$  Å,  $b = 11.269(4)$  Å,  $c = 11.395(4)$  Å,  $\alpha = 101.666(6)$  °,  $\beta = 115.424(6)$  °,  $\gamma = 104.868(7)$  °). One dimensional chain was constructed from trinuclear units via hydrogen bonds. The magnetic measurement indicates this complex exhibiting antiferromagnetic behavior.

## 1. Introduction

Mn<sup>III</sup> complexes based upon Schiff bases of the type salen (N,N'-ethylenebis(salicylideneaminato)) have been used as paramagnetic building blocks in the research of magnetic materials and magnetism [1]. This kind of complexes has shown a good ability to form bimetallic compounds with [M(CN)<sub>m</sub>]<sup>n-</sup> anions [2-4]. Nitrosylpantacyanoferrates, commonly known as nitroprussides, are members of the polycyanide metal complexes. It has been widely studied in connection with their properties as molecular sieves, cation exchangers, and to carry out some catalytic reactions [5, 6]. The complex [Mn(Br-salen)]<sub>2</sub>[Fe(CN)<sub>5</sub>(NO)] bearing the long-lived metastable state has been reported [7]. As an extension of those studies, in the present paper, the synthesis, crystal structure and magnetic properties of the title complex has been studied.

## 2. Experimental

**General:** All starting materials were of analytical grade. Elemental analyses (C, H, N) were performed on a Perkin-Elmer 240 analyser. IR spectra were recorded on a Shimadzu IR-408 spectrometer as KBr pellets. Variable-temperature magnetic susceptibilities were measured on a Quantum Design MPMS-7 SQUID magnetometer. Diamagnetic corrections were made with Pascal's constants for all the constituent atoms.

**Preparation of (1):** The complex [Mn(salAren)(H<sub>2</sub>O)]<sub>2</sub>ClO<sub>4</sub>·3H<sub>2</sub>O was prepared by a literature method[8]. Well shaped single crystals of (1) suitable for X-ray crystallography were obtained in an H tube at room temperature, by slow diffusion between the two solutions, [Mn(salAren)(H<sub>2</sub>O)]<sub>2</sub>ClO<sub>4</sub>·3H<sub>2</sub>O (112mg, 0.2mmol) in CH<sub>3</sub>OH in one side and Na<sub>2</sub>[Fe(CN)<sub>5</sub>(NO)]·3H<sub>2</sub>O (26mg, 0.1mmol) in water in the other side. Elemental analysis for C<sub>47</sub>H<sub>40</sub>FeMn<sub>2</sub>N<sub>10</sub>O<sub>9</sub>, (calcd)%: C 54.20(54.32), N 13.12(13.28), H 3.79(3.82),

**X-Ray Crystallography:** Determination of the unit cell and data collection were performed at room temperature on an Enraf-Nonius CAD4 diffractometer, using a graphite-monochromated Mo-Kα radiation ( $\lambda = 0.71073$  Å). The structures were solved by direct methods using Siemens SHELXS-97 and refined by least-squares procedures on F<sub>o</sub><sup>2</sup> with SHELXL-97 by minimizing the function  $\Sigma w(F_o^2 - F_c^2)^2$ , where F<sub>o</sub> and F<sub>c</sub> are the

observed and calculated structure factors respectively. The crystallography indicate: chemical formula:  $C_{47} H_{40} Fe Mn_2 N_{10} O_9$ ,  $M_r = 1054.62$ , crystal system: Triclinic, Space group: P-1, Unit cell dimensions:  $a = 11.019(4)$  Å,  $b = 11.269(4)$  Å,  $c = 11.395(4)$  Å,  $\alpha = 101.666(6)$  °,  $\beta = 115.424(6)$  °,  $\gamma = 104.868(7)$  °,  $V = 1153.4(7)$  Å<sup>3</sup>,  $Z = 1$ ,  $F(000) = 540$ , 4075 unique reflections,  $R_1 = 0.0562$ ,  $wR_2 = 0.1285$

### 3. Results and Discussion

**Crystal structure of (1).** The structure of (1) consisting of neutral trinuclear core is illustrated in Figure 1. Selected bond distances and angles are listed in Table 1. One  $[Fe(CN)_3(NO)]^{2-}$  anion linked to two  $[Mn(salAren)(H_2O)]^+$  through two trans CN<sup>-</sup> ligands. In the linkage of Fe – C – N – Mn, There is a bend with the angle of C(21) - N(3) - Mn(1) = 148.2(4)°, the distance of Mn … Mn is 10.38 Å. Bonds of Mn – O, Mn – N of salAren is normal according to previous literature [3]. Given the restriction of middle phenyl ring, all atoms of Schiff Based complex lie in the equatorial plane (see angles in Table 1.). Dihedral angles between plane of N2O2 and two kinds of phenol plane (such as plane C1, C2, C3, C4, C5 C6 and plane C8, C9, C10, C11, C12, C13) are 1.4 and 0.5° respectively. The Manganese(III) atom is in a slightly distorted octahedral environment and deviated from plane of N2O2 by 0.0283 Å. The two axial positions are occupied by one N atom from a CN<sup>-</sup> bridging ligand of nitroprusside and one water molecule. One dimensional chain has been formed through H bonds of axial oxygen atoms and oxygen atoms of neighbor salAren. The water and methane molecules are positioned in the vicinity of the chain. Figure 2 shows the molecule-packing diagram of the Mn<sub>2</sub>Fe unit.

Table 1. Selected Bond Distances (Å) and Angles (deg) for (1)

Mn(1)-O(1)	1.865(3)	Fe(1)-C(21)	1.926(5)
Mn(1)-O(2)	1.891(3)	Fe(1)-N(6)	1.943(5)
Mn(1)-N(2)	1.993(3)	Fe(1)-C(23A)	1.943(5)
Mn(1)-N(1)	1.994(3)	N(3)-C(21)	1.164(6)
Mn(1)-O(3)	2.255(3)	N(5)-C(23A)	1.157(6)
Mn(1)-N(3)	2.317(4)	N(6)-O(4)	1.157
O(1)-Mn(1)-N(3)	92.08(14)	C(21)-Fe(1)-C(23A)	89.29(19)
O(1)-Mn(1)-O(3)	90.21(13)	Fe(1)-C(21)-N(3)	177.8
N(1)-Mn(1)-O(3)	90.23(12)	Mn(1)-N(3)-C(21)	148.2
N(1)-Mn(1)-N(3)	90.60(14)		

**Spectroscopic characterization.** The infrared spectrum shows three strong band group: The band at 2140, with the shoulder at 2135cm<sup>-1</sup>, are attributed to the C≡N stretching vibration, 1895cm<sup>-1</sup> to the stretching vibration of NO in  $[Fe(CN)_3(NO)]$ , and 1600cm<sup>-1</sup>, to the stretching vibration of C=N in salAren.

**Magnetic properties.** The magnetic behavior of the complex is shown in Figure 3 in the form of  $\chi_M$  Vs.  $T$  and  $\mu_{eff}$  Vs.  $T$  plots ( $\chi_M$  being the magnetic susceptibility for a Mn<sub>2</sub>Fe unit). The  $\mu_{eff}$  at room temperature, 7.09  $\mu_B$ , is slightly lower than the spin-only value of 7.18  $\mu_B$ , expected for the magnetically isolated unit. The magnetic moment does not show the distinct trend of decrease in the scope of 300K and 20K. Below 20K, the  $\mu_{eff}$  value decreases sharply, and reaches a minimum 2.30  $\mu_B$  at 2.0K. This behavior is probably due

to intramolecular antiferromagnetic interaction between two paramagnetic Mn ions.

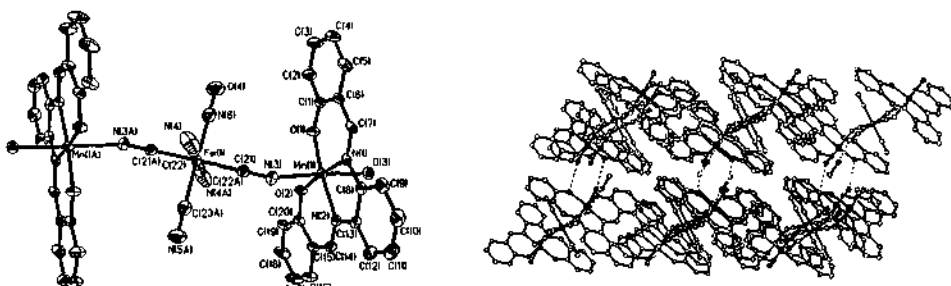


**Figure 1.** ORTEP view of the trinuclear complex.

**Figure 2.** The molecule-packing diagram of (1).

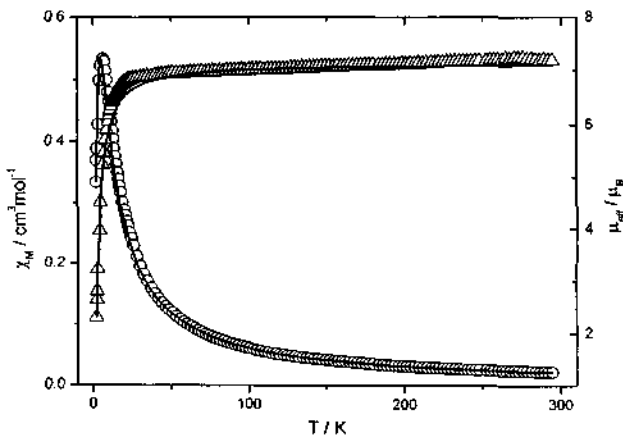


**Figure 3.** The magnetic behavior of the title complex.

To fit magnetic data we used the spin Hamiltonian(*eq.1.*):

$$\hat{H}_{ex} = -2J\hat{S}_1\hat{S}_2 \quad 1$$

Where  $J$  is the exchange integral and  $S_1 = S_2 = 2$  (local spins).  $[\text{Fe}(\text{CN})_6(\text{NO})]$  portion act as exchange channels only. So,  $\chi_M$  may be expressed as (*eq.2.*):

$$\chi_M = \frac{2Ng^2\beta^2}{KT} \frac{A}{B} \quad 2$$

$$A = 30 + 14\exp\left(\frac{-8J}{KT}\right) + 5\exp\left(\frac{-14J}{KT}\right) + \exp\left(\frac{-18J}{KT}\right)$$

$$B = 9 + 7\exp\left(\frac{-8J}{KT}\right) + 5\exp\left(\frac{-14J}{KT}\right) + 3\exp\left(\frac{-18J}{KT}\right) + \exp\left(\frac{-20J}{KT}\right)$$

Where the symbols have their usual meanings. The solid line in Fig. 3 shows the result of this fit. The fitting parameters are  $J = -0.55 \text{ cm}^{-1}$ , and  $g_{Mn} = 2.05$  with the agreement factor  $R = \sum(\chi_{obsd} - \chi_{cacl})^2 / \sum \chi_{obsd}^2 = 4.1 \times 10^{-3}$ . The exchange interaction occurs between two Mn atoms through diamagnetic  $[\text{Fe}(\text{CN})_5(\text{NO})]$ . The distance between two Mn atoms is long ( $\text{Mn} \cdots \text{Mn} = 10.38 \text{ \AA}$ ), so the complex shows weak antiferromagnetic interaction ( $J = -0.55 \text{ cm}^{-1}$ ).

### Acknowledgement

This work was supported by the National Natural Science Foundation of China (No.20071019, No. 50172021, and No. 90101028).

### References

1. Ohba M, Okawa H., *Coord. Chem. Rev.*, **198** (2000) p. 313.
2. Miyasaka H, Matsumoto N, Okawa H, Re N., Gallo E., Floriani C., *J. Am. Chem. Soc.*, **118** (1996) p. 981.
3. Miyasaka H, Matsumoto N, Okawa H, Re N., Gallo E., Floriani C., *Angew. Chem. Int. Ed. Engl.*, **34** (1995) p. 1446.
4. Miyasaka H, Matsumoto N, Okawa H, Re N., Gallo E., Floriani C., *Inorg. Chem.*, **37** (1998) p. 255.
5. Gutlich P., Garcia Y., Woike T., *Coord. Chem. Rev.*, **219-221** (2001) p. 839.
6. Woike Th., Krasser W., Bechthold P. S., Haussuhl S., *Phys. Rev. Lett.*, **53** (1984) p. 1767.
7. Clemente-Leon M., Coronado E., Galan-Mascaros J. R., Woike Th., Clemente-juan J. M., *Inorg. Chem.*, **40** (2001) p. 87.
8. Matsumoto N., Takemoto N., Ohyoshi A., Okawa H., *Bull. Chem. Soc. Jpn.*, **61** (1988) p. 2984.

## SYNTHESIS OF NICKEL-ORGANIC COMPLEXES GRAFTED ON THE SURFACE OF SiO<sub>2</sub> AS CATALYSTS FOR ETHYLENE OLIGOMERIZATION REACTION

D. B. TAGIYEV, M.K.MUNSHIYEVA AND M. I. RUSTAMOV

*Institute of Petrochemical Process, National Academy of Sciences of Azerbaijan  
30, N. Rafiyev St., 370025, Baku, Azerbaijan Fax: 99412-90-35-20  
E-mail: anipep@dcacs.ab.az, dtagihev@hotmail.com*

Heterogeneous metal-complexes of the zero-valent nickel have been synthesized by ligand exchange between triphenylphosphine or hexaethyltriamidophosphine Ni(0) complex and chemically modified by method of immobilization support – silica, containing complex forming –  $\text{NPR}_2$ -group, where R is Ph or  $\text{NEt}_2$ . The comparative characteristics of the activity of these catalysts and their homogeneous analogues in ethylene oligomerization are given. It is shown that various factors (pressure, temperature, molar correlation Al/Ni) do not significantly influence the selectivity of this process in the presence of investigated heterogeneous metal-complexes.

### **1. Introduction**

Available vast information in the scientific literature on synthesis and mechanism of heterogeneous metal-complex catalysts (HMC) action points to combination of advantages in both homogeneous and heterogeneous catalysts. The catalytic activity of HMC has been investigated in a series of processes, including oligomerization of lower olefins [1]. However, in connection with limitations of physicochemical methods of research of HMC, the data on formation of catalytic active centers on the surface of the support and on mechanism of their action are not numerous and are contradictory.

Therefore, the aim of the present research is to work out the method of grafting triphenylphosphine and hexaethyltriamidophosphine complexes of Ni(0) to the surface of the support – silica, to investigate the process of forming the active centers in the case of homogeneous analogue, and to compare the catalytic activities of these HMC and their homogeneous analogues in ethylene oligomerization.

### **2. Experimental**

Silica with a specific surface area – 120  $\text{m}^2/\text{g}$  was used as a support. Before modifying, the silica was calcined by way of keeping it in a vacuum (10-2 torr) at 600 °C for 6 hours.

The density of stickiness of the modifier on the support is defined by the titrimetric method, processing it by  $(\text{EtO})_3\text{Si}(\text{CH}_2)_3\text{NH}_2$  [2].

The heterogeneous Ni-complexes were obtained by the method of ligand exchange of phosphine groups stuck to the surface of the support and ligands in  $\text{Ni}(\text{PR}_3)_n$ , where R is Ph or  $\text{NEt}_2$ .

The amount of nickel on the surface of the studied supports was determined by the polarography method. It ranges within 0.75-0.8 wt%.

$\text{Ni}(\text{PR}_3)_n$  with R-Ph was obtained by method [3] and with R-  $\text{NEt}_2$  according to [4].

The IR-spectra of diffuse reflection were recorded on the spectrometer Hitachi M-430 at room temperature.  $^1\text{H}$  and  $^{13}\text{C}$  NMR spectra were measured on the spectrometer Bruker WP-200 SY at 22 °C in  $\text{C}_6\text{D}_6$  or  $\text{CDCl}_3$ , taken as a solvent.

$^{31}\text{P}$ -{ $^1\text{H}$ } NMR spectra were registered on a Bruker HX-90 NMR spectrometer (with 85%  $\text{H}_3\text{PO}_4$  as an external standard).

Ethylene oligomerization was conducted in the reactor, which served as a vessel of stainless steel in a volume of 250 cm<sup>3</sup> tested for the pressure of 100 atm. Into the reactor filled with argon a certain amount of catalyst in the corresponding solvent was introduced. Following that, the system while intermixing, was filled with ethylene up to the pressure of 10 atm and the an activator  $\text{AlEt}_2\text{Cl}$  was added.

GLC analysis of the reaction products was carried out on an LHM-8MD chromatograph, equipped with flame-ionizing detector, using a 2m×3mm column (5% SE-chezasorb AW-HMDS as filler and helium as carrier gas) with temperatures ranging from 50 to 250 °C.

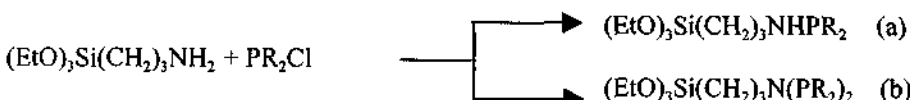
All the experiments were carried out under an argon atmosphere using absolute solvents, which were distilled under argon prior to use.

### 3. Results and Discussion

To obtain the chemically modified support the method of surface collection or immobilization is used. The first method consists of interaction of dehydrated silica with  $(\text{EtO})_3\text{Si}(\text{CH}_2)_3\text{NH}_2$  with further processing by benzene solution of  $\text{PPh}_3\text{Cl}$  or  $\text{P}(\text{NEt}_2)_2\text{Cl}$ , from which it follows that on the surface of silica the heterogeneous compounds can be located due to its heterogeneity and taking into consideration the steric factors. Therefore, in our subsequent research we used only the method of immobilization, consisting of single-stage stickiness to the surface of silica of preliminarily prepared modifier – the product of interaction of  $(\text{EtO})_3\text{Si}(\text{CH}_2)_3\text{NH}_2$  with  $\text{PPh}_3\text{Cl}$  or  $\text{P}(\text{NEt}_2)_2\text{Cl}$ .

For purpose of obtaining more full information on processes proceeding on the surface of the support, the attempt of carrying out the identical reaction with homogeneous analogues (contrary synthesis) has been undertaken.

The contrary synthesis of the initial modifier for subsequent immobilization on silica has shown that reaction can proceed in two directions with formation of mono-(a) and two-substituted (b) product, where R is Ph or  $\text{NEt}_2$ :



The results of elementary analysis, NMR and IR spectroscopic studies witness formation of two-substituted product. Thus, the absence of bands of the absorption at 3300-3370 cm<sup>-1</sup> points to absence of N-H bond in the synthesized compounds. Data of  $^1\text{H}$  NMR spectra confirm this conclusion that in the field typical for NH group the signals are not observed. In  $^{13}\text{C}$  NMR - spectra of the obtained product  $(\text{EtO})_3\text{Si}(\text{CH}_2)_3\text{N}(\text{PPh}_2)_2$  notable removal of the signals of  $-\text{CH}_2-$  to side of the weaker field is observed. Attention is paid to the fact that the chemical shift of  $\text{CH}_2\text{N}$ -group (56.45 ppm) in  $^{13}\text{C}$  NMR spectra approaches the chemical removal of  $\text{CH}_2\text{O}$ -group (58.38 ppm).

The same spectra identified splitting the signal of this group on phosphorous atom with constant of splitting (11.0±0.6 Hz). Identification of  $^1\text{H}$  and  $^{13}\text{C}$  NMR – spectra of

$(EtO)_3Si(CH_2)_3N[P(NEt_2)_2]_2$  is somewhat difficult because the superposition of own vibrations of  $CH_2N$  and  $CH_2C$ -groups of ligand on vibrations of these groups in  $(EtO)_3Si(CH_2)_3NH_2$  occurs (Table 1).

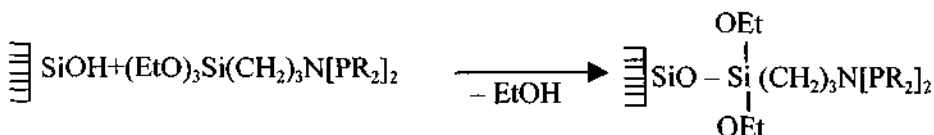
Table 1.  $^{13}C$  and  $^{31}P\{-^1H\}$  NMR chemical shifts of  $(EtO)_3Si(CH_2)_3NH_2$ , the synthesized product and related compounds [5,6].

Substance	$^{13}C$ $\delta$ , ppm.					$^{31}P\{-^1H\}$ $\delta$ , ppm
	$CH_3C$	$CH_2O$	$CH_2$	$-CH_2-$	$CH_2N$	
$(EtO)_3Si(CH_2)_3NH_2$	18.48	58.31	8.01	27.31	45.44	
$(EtO)_3Si(CH_2)_3N(PPh_2)_2$	18.52	58.30	8.21	25.33	56.45	63.11
$(EtO)_3Si(CH_2)_2N[P(NEt_2)_2]_2$	18.51	58.0	8.2	23.17	51.62	119.74
$Me(CH_2)_2N(PPh_2)_2$					53.3	48.20
$EtNHPPh_2$					45.0	40.04
$EtN(PPh_2)_2$					50.9	61.80

In the  $^{31}P\{-^1H\}$  NMR spectra of the product of interaction of  $(EtO)_3Si(CH_2)_3NH_2$  with  $P(NEt_2)_2Cl$  one single signal is observed at  $\delta$  119.79 ppm which, taking into consideration the data of the work [6], should be referred to the obtained compound  $(EtO)_3Si(CH_2)_3N[P(NEt_2)_2]_2$ . After 12 hours of keeping this compound at 80 °C no change has been observed. It is a white gel-like material.

The total data obtained when studying reaction of phosphining  $NH_2$ -groups permit to draw a conclusion that, as a result of aforementioned reaction, substitution of both hydrogen atoms of  $NH_2$ -group with creation of two-substituted compound takes place.

By interaction of calculated amounts of pretreated at 600 °C ( $10^{-2}$  torr) silica with  $(EtO)_3Si(CH_2)_3N[PR_2]_2$  in boiling benzene there was obtained chemically modified silica containing  $N[PR_2]_2$  group, characterized by significant electron-donor capability.



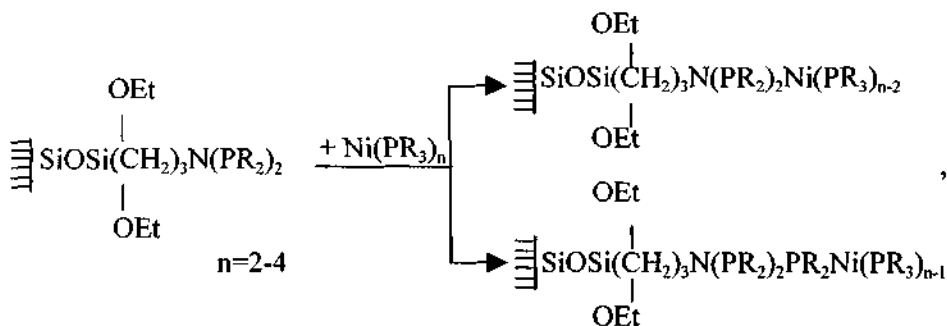
From the known physicochemical methods of research restriction only by study of IR-spectra of diffuse reflection can we obtain limited information on creation of the active centers on the surface of the support. In the IR-spectra of diffuse reflection of the silica samples chemically modified by  $(EtO)_3Si(CH_2)_3N[PPh_2]_2$ , the main changes are observed in the region of vibrations of CH-bonds. Two high frequency bands of absorption appear at 3055 and 3010  $\text{cm}^{-1}$  as well as at 2965, 2940 and 2860  $\text{cm}^{-1}$ , which belong to the aromatic rings. In the spectra of the silica samples of chemically modified by  $(EtO)_3Si(CH_2)_3N[P(NEt_2)_2]_2$  besides bands of absorptions at 3750-3600  $\text{cm}^{-1}$ , typical for OH-group of silica, there are strong bands at 2970-2865  $\text{cm}^{-1}$ , belonging to the ethyl fragments, and at 2250  $\text{cm}^{-1}$ , typical for  $-N<$ .

The suggested method of preparation of chemically modified silica helps us to obtain support, which contains the similar compounds and avoids the influence of the steric factors, because the preliminarily prepared modifier immobilizes on the surface of support. The obtained data have most important theoretical and practical significance, and as suggested in the literature [7], the phosphining of amino groups contained in chemically

modified silica with the creation of the two-substituted product is very difficult for steric reasons.

To obtain the HMC as an active component zero-valent nickel complexes of the general formula -  $\text{Ni}[\text{PR}_3]_n$  ( $n=2-4$ ), where R was Ph or  $\text{Et}_2\text{N}$ , characterized by high activity in oligomerization of lower olefins in homogeneous conditions were taken. Heterogenization of these complexes was conducted by method of ligand exchange. In the literature there are examples of carbonyl complexes of palladium prepared by this method, which show activity in propylene dimerization [8]. However, we have failed to find data on such nickel catalysts in the literature.

The ligand exchange has been carried out according to the following scheme:



One or two  $\text{PR}_2$ - ligands of Ni-complex are substituted for phosphine groups stuck to the surface of the support. Unfortunately, identification of nickel on the surface of the support by the present spectral methods is not possible. In this connection determination of nickel and also the process of formation of Ni-HMC was conducted by method of polarography. For the control of completeness of ligand exchange proceeding the samples of the same series of support have been treated by benzene solution of Ni-complex with identical nickel concentration during the different time. To achieve the equilibrium 3-4 hours are quite enough.

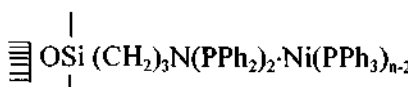
It was shown by experiments that these complexes totally collapsed at  $80^\circ\text{C}$ . Therefore, the formation of Ni-HMC was carried out at room temperature. For purpose of comparison of activity, selectivity and duration of work, the catalytic properties of Ni-HMC and its homogeneous analogues -  $(\text{EtO})_3\text{Si}(\text{CH}_2)_3\text{N}(\text{PR}_2)_2\text{Ni}(\text{PR}_3)_{n-2}$  in the identical conditions in combination with activator  $\text{AlEt}_2\text{Cl}$  have been studied (Table 2).

The catalytic experiments have shown the essential difference both in productivity and selectivity of the process of oligomerization for catalysts of different kinds. During the early stage of work homogeneous catalysts were more active. Their initial activity exceeds the heterogeneous analogues by 3-3.5 times and for systems on  $\text{Ni}[\text{P}(\text{NEt}_2)_3]_2$  base it reaches  $11-16 \text{ kmol C}_2\text{H}_4/\text{molNi}\cdot\text{min}$ . However, the time of their active work does not exceed 10-15 min. At the same time the heterogeneous sample in one hour of work, in practice, has entirely preserved the initial activity. The amount of ethylene entering in the reaction on compared systems for 1 hour of work made up 102.2 and 46.7 g correspondingly, i.e. the difference in yields of product on these systems even in 1 hour of work is significantly less [9,10].

**Table 2.** The activity and selectivity of Ni - HMC and their homogenous analogues in ethylene oligomerization.

Ni-complex	[Ni], M·10 <sup>-5</sup>	Al/Ni (mol)	The reacted C <sub>2</sub> H <sub>4</sub> , g/h	Selectivity (%)		
				ΣC <sub>4</sub>	ΣC <sub>6</sub>	others
Ni(PPh <sub>3</sub> ) <sub>n</sub>	6.1	50	79.8	85.5	14.4	0.1
Ni[P(NEt <sub>2</sub> ) <sub>3</sub> ] <sub>2</sub>	3.3	30	64.4	83.4	16.6	-
Ni(PPh <sub>3</sub> ) <sub>n</sub> <sup>+</sup> (EtO) <sub>2</sub> Si(CH <sub>2</sub> ) <sub>3</sub> N(PPh <sub>2</sub> ) <sub>2</sub>	6.0	50	102.2	91.4	4.4	4.2
Ni[P(NEt <sub>2</sub> ) <sub>3</sub> ] <sub>2</sub> <sup>+</sup> (EtO) <sub>2</sub> Si(CH <sub>2</sub> ) <sub>3</sub> N[P(NEt <sub>2</sub> ) <sub>2</sub> ] <sub>2</sub>	3.0	30	77.6	94.7	5.2	0.1
Ni(PPh <sub>3</sub> ) <sub>n</sub>   SiO <sub>2</sub> -PPh <sub>2</sub> *	6.0	50	46.7	98.2	1.8	-
Ni[P(NEt <sub>2</sub> ) <sub>3</sub> ] <sub>2</sub>   SiO <sub>2</sub> -P(NEt <sub>2</sub> ) <sub>2</sub> *	6.1	50	52.0	91.6	8.3	0.1

n=2-4; \* Brief notation of

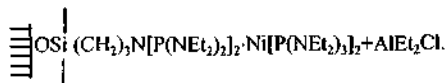


The compared catalytic systems show differences also in selectivity of the process. In case of homogeneous analogues the amount of dimers in the products of reaction does not exceed 83-85%. The heterogeneous samples are characterized by higher content of butene, which reaches 91-98%. In addition, selectivity, according to butene-1 in C<sub>4</sub>-fraction, for homogeneous and heterogeneous catalysts makes up 15 and 49.5% correspondingly.

It should be noted that the heterogeneous complexes on Ni[P(NEt<sub>2</sub>)<sub>3</sub>]<sub>2</sub> base, showing at the early stage of work higher activity in ethylene oligomerization and better selectivity in respect to butene-1, are less steady in comparison with such complexes on Ni(PPh<sub>3</sub>)<sub>n</sub> base.

It was established that in the presence of the investigated Ni-HMC various factors, such as pressure, temperature, molar correlation Al/Ni do not significantly influence the selectivity of oligomerization process, but the olefin conversion and the yield of product are very dependent on these factors (Table3).

Thus, by modifying the Ni-HMC with specific exchangeable ligands its efficiency can be increased and the selectivity of reaction can be regulated.

**Table 3.** The influence of various factors on the ethylene oligomerization in the presence of system

Catalyst, g	[Ni], M·10 <sup>-5</sup>	Al/Ni (mol)	Pressure of C <sub>2</sub> H <sub>4</sub> (atm.)	Temperature, °C	Time (min)	The yield of product, kg/[Ni], g/h
0,61	3,9	38	10	20	60	2,40
0,58	3,6	42	10	22	40	2,26
0,58	3,6	42	10	30	40	2,20
0,32	2,5	65	20	32	60	2,01
0,4	3,0	52	10	35	50	1,99
0,62	3,9	20,5	5	22	60	0,51
0,67	4,0	9	8	22	30	0,53

## References

- Whitehurst D. D., Catalysis by heterogenized transition metal complexes, *Chem. Technol.*, No.1 (1980) p.44.
- Lisichkin G.V. and Yuffa A. Ja. Heterogeneous metallocomplex catalysts, *Chemistry*, Moscow, (1981) p.160.
- Wade R., Holah D. G., Hughes A. N. and Hui B. C., Catalytically active borohydride-reduced nickel and cobalt systems, *Catal. Rev.*, No.2 (1976), 211.
- Tagiev D.B., Furman D.B., Munshieva M.K. et al. Catalytic conversion of C<sub>n</sub>-cyclic defines in the presence of metallocomplexes. *Russ. Chem. Bull.*, No.3 (1991), 541.
- Schraml J., Nguyen-Duc-Chuy, Chvalovsky V. et al., NMR study of organosilicon compounds. *Org. Magn. Reson.*, No.7 (1975) p.379.
- Van Linthoudt J. P., Van der Berghe E. V., Van der Kelen G. P. NMR study (<sup>1</sup>H, <sup>13</sup>C, <sup>31</sup>P) of the [(C<sub>2</sub>H<sub>5</sub>)<sub>2</sub>N]<sub>n</sub>P<sub>3-n</sub>X compound (X=Cl, C<sub>2</sub>H<sub>5</sub>; n=0, 1, 2, 3)., *Spectrochim. Acta*, No.3 (1980) p.315.
- Dovganjuk B. D., Lafer L. I., Isaeva V. I., Sharf V. Z. et al., Structure and catalytic activity of supported metallocomplexes., *Russ. Chem. Bull.*, No.12 (1987) p.2660.
- Mitchell T.O., Whitehurst D. D. Organic compounds conversion, US Patent No 4053534 (1977).
- Furman D. B., Ivanov A. O., Munshieva M. K. et al., Metallocomplexes in the catalytic conversion of olefins. *Russ. Chem. Bull.*, No.3 (1990) p.516.
- Munshieva M. K., Heterogeneous Ni(0) complexes in the ethylene oligomerization. *Azerb. Chem. J.*, No.2 (1999) p.104.

## SYNTHESIS AND CRYSTAL STRUCTURE OF A NEW COPPER(II) COMPLEX CONTAINING FLUOROQUINOLONE

GUO PING WANG AND LONG GUAN ZHU

*Department of Chemistry, Zhejiang University, Hangzhou 310027, P. R. China*

The structural property of a new copper (II) complex of  $[\text{Cu}(\text{cip})(\text{bpy})\text{Cl}] \cdot 2\text{H}_2\text{O}$  ( $\text{bpy}=2,2'$ -bipyridyl,  $\text{cip}=1\text{-cyclopropyl-6-4-oxo-1,4-dihydroquinoline-3-carboxylic acid}$ ) obtained during the synthesis of the copper complex with ciprofloxacin, has been investigated. The complex crystallizes in the triclinic system, space group  $P\bar{1}$  (#2). The cell dimensions are:  $a=10.329(2)$  Å,  $b=10.225(3)$  Å,  $c=10.225(3)$  Å,  $\alpha=95.77(3)^\circ$ ,  $\beta=99.10(2)^\circ$ ,  $\gamma=98.65(2)^\circ$ ,  $V=1167.6(6)$  Å<sup>3</sup>, and  $Z=2$ . The Cu (II) ion displays a five-coordinate square pyramidal coordination with two nitrogen donors from bpy, the 4-keto and 3-carboxylate oxygen donors from cip, and Cl<sup>-</sup> anion occupying the fifth site. There is a stack effect between cip ring and bpy ring from another molecule, where the stacking distance is about 3.5 Å.

### 1 Introduction

Many drugs possess modified pharmacological and toxicological properties administered in the form of metallic complexes. Probably the most widely studied cation in this respect is Cu<sup>2+</sup>, since a host of low-molecular-weight copper complexes has been proved beneficial in several diseases such as tuberculosis, rheumatoid, gastric ulcers and cancers [1-4]. There has been tremendous growth of drugs from quinolone family. It began with the discovery of nalidixic acid (Hnal) 40 years ago. Since then, the exponential growth of this family has produced more than ten thousands of analogues [5]. The coordination chemistry of these drugs with metal ions of biological and pharmaceutical importance is of considerable interest. Ciprofloxacin was considered the best of quinolone family of the third generation. There have been several reports about the synthesis and crystal structure of metal complexes with cpf [6-9]. Recently, we have found that, during the synthesis of copper complex containing fluoroquinolone ligand, the cpf ligand is changed interestingly into cip. The crystal structure of this compound was thus characterized and is reported in this paper.

### 2 Experimental

cpf·HCl (pure powder, 99.9%) was kindly donated by Xinchang Pharmaceutical Factory. All other chemicals used were of analytical reagent grade.

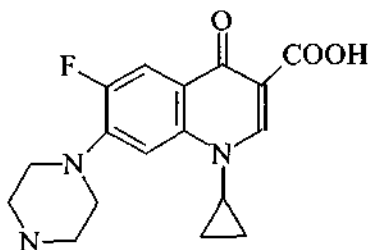


Figure 1. The structure of cpf.

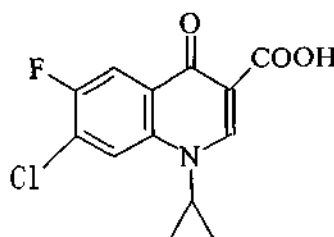


Figure 2. The structure of cip.

### 2.1 Synthesis of $[Cu(cip)(bipy)Cl] \cdot 2H_2O$

1 mmol of bpy dissolved in 5ml of ethanol was added to 10 mL of aqueous solution containing 1mmol of  $Cu(NO_3)_2 \cdot 3H_2O$ . To this mixture was then added a solution prepared by dissolving 1mmol of cpfHCl in 100 mL of water containing 1mmol of NaOH; its pH was adjusted to 7.0~8.0 with HCl. The resulting blue solution was slowly evaporated at room temperature, and blue crystals suitable for X-ray structure determination were formed finally after a period of 2 months.

Anal. Calc. for  $C_{23}H_{20}O_5N_3FCuCl_2$ : C, 48.30; H, 3.52; N, 7.35. Found: C, 48.47; H, 3.54; N, 7.58%.

### 2.2 Crystallographic data and structure determination

The crystal data and refinement parameters of the title complex are summarized in Table 1. A Rigaku AFC7R diffractometer with graphic monochromated Mo-K $\alpha$  radiation and a 12 kW rotating anode generator was used for the determination of the unit cell and data collection. The data were collected using the  $\omega$ -2 $\theta$  scan technique to a maximum 2 $\theta$  value of 50.0°. The linear absorption coefficient,  $\mu$ , for Mo-K $\alpha$  radiation was 12.13 cm $^{-1}$ . An empirical absorption correction based on azimuthal scans of several reflections was applied which resulted in transmission factors ranging from 0.63 to 1.00. The data were corrected for Lorentz and polarization effects. A correction for secondary extinction was applied (coefficient =  $3.46614 \times 10^{-7}$ ). The structure was solved by direct methods using SHELXS86 and expanded using Fourier techniques. The non-hydrogen atoms were refined anisotropically. Hydrogen atoms were included but not refined. The final cycle of full-matrix least-squares refinement was based on 2918 observed reflections ( $I > 3.00\sigma(I)$ ) and 317 variable parameters and converged with unweighted and weighted agreement factors of  $R = \sum ||F_0| - |Fc|| / \sum |F_0| = 0.050$  and  $R_w = [\sum \omega(|F_0| - |Fc|)^2 / \sum \omega F_0^2]^{1/2} = 0.061$ . The weighting scheme,  $\omega = 1/(\sigma^2(F_0))$ . Neutral atom scattering factors were taken from Cromer and Waber [10]. Anomalous dispersion effects were included in  $F_{\text{calc}}$ . All calculations were performed using the teXsan crystallographic software package of Molecular Structure Corporation.

### 3 Results and Discussion

The atomic coordinates and equivalent isotropic thermal parameters for non-H atoms are given in Table 2. Figure 3 and Figure 4 show the coordination of the metal and the atomic numbering scheme for the complex, and the crystal packing in the unit cell, respectively. The copper (II) atom is coordinated to the keto and the carboxylic acid oxygen of the cip to form a six-membered ring. The copper atom displays a five-coordinate square pyramidal coordination with two nitrogen donors from 2,2'-bpy, the 4-keto and 3-carboxylate oxygen donors, and Cl<sup>-</sup> anion occupying the fifth site. Previous studies for the structures of copper (II) complexes with 2,2'-bpy, or 1,10-phenanthroline and a quinolone ligand except ciprofloxacin or its derivative have indicated that while the Cu-O (acid) distances are kept constant, the Cu-O(keto) distance varies from one to another, such as  $[(\text{Cu}(\text{phen})(\text{nal})]^+$ , 1.914 and 1.934 Å;  $[\text{Cu}(\text{phen})(\text{cnx})]^+$  ( $\text{cnx}=\text{cinoxacinato}$ ), 1.913 and 1.914 Å;  $[\text{Cu}(\text{bpy})(\text{oxo})]^+$  (oxo=oxolinate), 1.914 and 1.936 Å, and  $[\text{Cu}(\text{cpf})(\text{bpy})(\text{Cl})_{0.7}(\text{NO}_3)_{0.3}]$ , 1.920(3) and 1.924(3) Å, respectively [9,11-13]. In the present study, however, we find that the Cu-O distances of 1.923(3)(acid) and 1.976(3)(keto) do not fall in the middle of 1.913~1.936 Å as Wallis concluded [11].

**Table 1.** Crystal data and structure refinement for  $[\text{Cu}(\text{cip})(\text{bpy})\text{Cl}] \cdot 2\text{H}_2\text{O}$  complex.

Empirical formula	$\text{C}_{23}\text{H}_{26}\text{O}_5\text{N}_3\text{FCuCl}_2$	Volume of unit cell	1167.6(6) Å <sup>3</sup>
Formula weight	571.88	Z	2
Temperature	293(1) K	Density (calculated)	1.627 g·cm <sup>-3</sup>
Mo-Kα	0.71069 Å	F(000)	582
μ (Mo-Kα)	12.13 cm <sup>-1</sup>	Crystal size	0.20×0.20×0.30 mm
Crystal system	Triclinic	2θ range	6° to 50°
Space group	P $\overline{1}$ (#2)	Reflections collected	3882
Unit-cell dimensions	a = 10.329(2) Å b = 10.225(3) Å c = 10.225(3) Å α = 95.77(3)° β = 99.10(2)° γ = 98.65(2)°	Independent reflections	3636( $R_{\text{int}}=0.022$ )
		Goodness of Fit Indicator	2.37
		Final R indices [I > 3.00σ (I)]	R = 0.050 wR = 0.061
		Max. peak in final diff. Map	0.62e <sup>-1</sup> /Å <sup>3</sup>
		Min. peak in final diff. Map	-0.81e <sup>-1</sup> /Å <sup>3</sup>

The dihedral angle between the two ligands in the complex  $[\text{Cu}(\text{cip})(\text{bpy})\text{Cl}] \cdot 2\text{H}_2\text{O}$  is 8.32°. There is a stack effect between cip rings from two neighbor molecules, and the distance is about 3.68 Å. Also there is a stack effect between cip ring and bpy ring from another molecule with a distance of about 3.5 Å. The observed stacking in these molecules are indicative of a π~π interaction at a distance that is similar with those encountered in the base stacking of DNA [14]. Also, this distance is encountered in some compounds like  $[\text{Cu}(\text{phen})(\text{cnx})(\text{H}_2\text{O})]\text{NO}_3 \cdot \text{H}_2\text{O}$  [15], where the stacking distance between cnx ring and phen ring from another molecule is about 3.5 Å, and in some intercalated compounds like 5-iodouridyl-(3'-5')-adenosine:ethidium [16], where the stacking distances are: 3.3 Å (adenine-ethidium) and 3.4 Å (uracil-ethidium). It is important to notice that the arrangement in the crystal packing is dependent on the environment

of the metal ion, and this should be relevant in any proposal of intercalation processes. The data suggests that this type of compound could act as an intercalate agent and also that the mechanism of action should be by a metal-quinolone complex. Supporting evidence of this idea is given by the Shen model [17], which proposes a direct interaction between the quinolones and DNA.

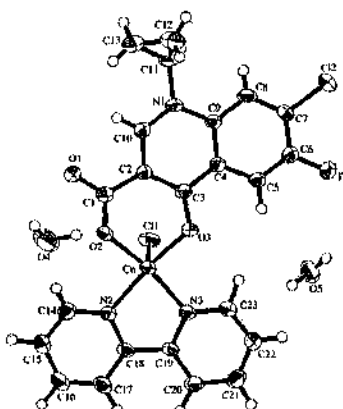


Figure 3. Structure of the complex.

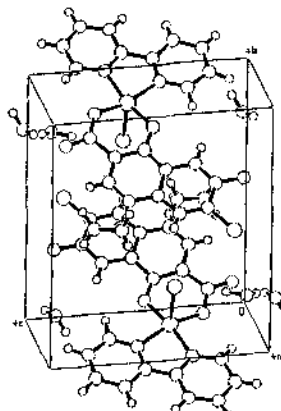


Figure 4. Packing drawing of the complex.

Table 3. Some selected bond lengths ( $\text{\AA}$ ), angles ( $^{\circ}$ ), and e.s.d.s. (in parentheses) for the  $[\text{Cu}(\text{cip})(\text{bpy})\text{Cl} \cdot 2\text{H}_2\text{O}]$  complex.

Cu-Cl(1)	2.507(1)	Cu-O(2)	1.923(3)
Cu-O(3)	1.976(3)	Cu-N(2)	2.020(4)
Cu-N(3)	1.992(4)	C(1)-O(1)	1.234(6)
C(1)-O(2)	1.290(6)	C(3)-O(3)	1.274(5)
C(1)-C(2)	1.495(6)	C(2)-C(3)	1.419(6)
N(1)-C(11)	1.471(6)	C(11)-C(12)	1.464(8)
C(11)-C(13)	1.467(8)	C(12)-C(13)	1.451(9)
C(7)-Cl(2)	1.719(5)	N(2)-C(18)	1.348(6)
N(2)-C(14)	1.345(6)	N(3)-C(19)	1.358(6)
N(3)-C(23)	1.350(6)	C(18)-C(19)	1.472(6)
Cl(1)-Cu-O(2)	98.5(1)	Cl(1)-Cu-O(3)	93.8(1)
Cl(1)-Cu-N(2)	98.6(1)	Cl(1)-Cu-N(3)	97.2(1)
O(2)-Cu-O(3)	91.5(1)	O(2)-Cu-N(2)	91.3(1)
O(2)-Cu-N(3)	163.2(1)	O(3)-Cu-N(2)	166.7(1)
O(3)-Cu-N(3)	93.3(1)	N(2)-Cu-N(3)	80.5(2)
Cu-O(2)-C(1)	126.5(3)	Cu-O(3)-C(3)	122.3(3)
Cu-N(2)-C(18)	114.9(3)	Cu-N(3)-C(19)	115.5(3)
C(9)-N(1)-C(10)	119.5(4)	C(9)-N(1)-C(11)	119.2(4)
N(1)-C(11)-C(12)	120.0(4)	N(1)-C(11)-C(13)	120.5(5)
Cl(2)-C(7)-C(8)	120.6(4)	F-C(6)-C(7)	118.6(4)
C(6)-C(7)-C(8)	120.1(5)	N(2)-C(18)-C(19)	114.5(4)
C(14)-N(2)-C(18)	118.6(4)	C(17)-C(18)-C(19)	123.5(4)

## References

1. Sorenson J.R.J., *J. Med. Chem.* **19** (1976) pp.35.
2. Brown D. H., Smith W. E., and Teape J. W., *J. Med. Chem.* **23** (1980) pp.729.
3. Williams D.R., *The Metals of Life*, Van Nostrand Reinhold, London (1971).
4. Ruiz M., Perello L., Ortiz R. et al., *J. Inorg. Biochem.* **59**(1995) pp.801-810.
5. Castillo-Blum S. E. and Barba-Behrens N., *Coord. Chem. Rev.* **196** (2000) pp.3-30.
6. Turel I., Leban I. and Bukovec N., *J. Inorg. Biochem.* **66(4)** (1997) pp.241-245.
7. Turel I., Golic L. and Bukovec P. et al., *J. Inorg. Biochem.* **71(1,2)** (1998) pp. 53-60.
8. Yang P., Li J. B. and Tian Y. N. et al., *Chinese Chem. Lett.* **10(10)** (1999) pp. 879-880.
9. Wang G. P., Cai G. Q. and Zhu L. G., *Chin. J. Inorg. Chem.* **6** (2000) pp.987-990.
10. Cromer D. T. and Waber J. T., "International Tables for X-ray Crystallography", Vol.IV, The Kynoch Press, Birmingham, England, Table 2.2 A (1974).
11. Wallis S. C., Gahan L. R. and Charles B. G. et al., *J. Inorg. Biochem.* **62** (1996) pp.1-16.
12. Wallis S. C., Gahan L. R. and Charles B. G. et al., *Polyhedron* **14(20~21)** (1995) pp.2835-2840.
13. Berman H. M. and Shieh Huey-Sheng, in *Topics in Nucleic Acid Structure*, S. Neidle, Ed., MacMillan Publishers LTD., London (1981) pp.17-32.
14. Voet D. and Judith G.. V., *Biochemistry*, John Wiley& Sons, New York, (1990) pp.795.
15. Mendoza-Diaz G., Martinez-Aguilera L. M. R. and Moreno-Esparza R. et al., *J. Inorg. Biochem.*, **50** (1993) pp.65-78.
16. Chun-che T., Shri-C J., and Sobell H. M., *Proc. Natl. Acad. Sci. USA*, **92** (1975) pp.628.
17. Shen L. L., Miitscher L. A., Sharma P. N. et al., *Biochemistry* **28(9)** (1989) pp.886.

This page is intentionally left blank

## STRATEGIES FOR THE CONSTRUCTION OF COMPLEXES BASED ON METAL CLUSTERS

RUIHU WANG, MAOCHUN HONG,\* YINGJUN ZHAO, RONG CAO\* AND JUNHUA LUO

*State Key Laboratory of Structural Chemistry, Fujian Institute of the Research on the Structure of Matter, Chinese Academy of Sciences, Fuzhou, Fujian, 350002, China*

E-mail: hmc@ms.fjirsm.ac.cn

Supramolecular chemistry is today a major research area, and most of supramolecular complexes are based on the use of metal atoms or ions as key elements. Considerable success has already been achieved by employing metal clusters or metal-organic secondary building units (SBUs) instead of single metal atoms or ions. Considering that a lot of molecular complexes or metal entities have been obtained by using mono-functional organic ligands, to construct complexes based on metal clusters, we used di-functional diamine ligands with suitable spacers, such as, 4,4'-diaminodiphenylmethane (DADPM) and 4,4'-diaminodiphenylether (DADPE), instead of mono-functional aniline derivatives in single cubane-like  $\text{Cu}_4\text{I}_4$  complexes and obtained two discrete macrocyclic complexes  $[(\text{Cu}_4\text{I}_4)(\text{MeCN})_2(\text{DADPM})] \cdot 2\text{MeCN}$  (1) and  $[(\text{Cu}_4\text{I}_4)(\text{MeCN})_2(\text{DADPE})] \cdot 2\text{MeCN}$  (2). We also used dicarboxylate ligands, such as nitroterephthalic acid ( $\text{H}_2\text{NTPA}$ ) and diphenic acid ( $\text{H}_2\text{DPA}$ ), instead of mono-functional carboxylates ligands in the discrete dimeric dicarboxylatotetraorganodistannoxane complexes  $[(\text{R}_2\text{Sn}(\text{O}_2\text{CR}')_2\text{O}]_2$  (3) and obtained a one-dimensional polymer  $[(\text{Me}_2\text{Sn})_2(\mu_3\text{-NTPA})(\mu_3\text{-O})]_n$  (3) and a two-dimensional polymer  $\{(\text{Me}_2\text{Sn})_4(\mu_3\text{-DPA})(\mu_4\text{-DPA})(\mu_3\text{-O})_2\}_n$  (4).

### 1 Introduction

The construction of supramolecular architectures are currently of great interest in coordination chemistry and supramolecular chemistry owing to their intriguing structural versatility and potential application in various materials, while the majority of supramolecular species have been constructed from organic ligands and metal ions by spontaneous self-assembly [1,2]. Recently much effort has been devoted to design and construction of new supramolecular frameworks by using metal clusters or metal-organic secondary building units (SBUs) as building blocks [3-6]. The assembly of such building blocks and multi-functional organic ligands led to a number of interesting structural topologies and a more extensive application in material sciences. At the same time, they might be designed to direct the formation of target structures as well as to impart desired physical properties to solid materials. Our work has been focused on the designed construction of extended frameworks from soluble molecular building blocks in order to seek modular materials since they are constructed from discrete molecular complexes or cluster entities which can be modified to have well-defined function. In this paper, we have presented synthetic strategies to construct complexes from two kinds of discrete metal cluster complexes.

### 2 The cubane-like $\text{Cu}_4\text{I}_4$ cluster

It has been known that the reaction of copper(I) iodide with Lewis bases, such as aniline derivatives, produced complexes with single cubane-like  $\text{Cu}_4\text{I}_4$  cluster, in which the aniline derivatives act as the terminal ligands coordinating to the copper(I) centers [7-10]. Thus, it is reasonable to expect macrocyclic or extended complexes constructed by  $\text{Cu}_4\text{I}_4$  cluster units through replacing aniline derivatives with ditopic

diamine ligands with suitable spacers. Considering the flexibility and electronic structures of 4,4'-diaminodiphenylmethane (DADPM) and 4,4'-diaminodiphenylether (DADPE), and the coordination geometry of Cu(I) ions. Assembly of DADPM, DADPE and CuI in MeCN/H<sub>2</sub>O has resulted in two discrete macrocyclic complexes  $[(\text{Cu}_4\text{I}_4)(\text{MeCN})_2(\text{DADPM})]_2 \cdot 2\text{MeCN}$  (**1**) and  $[(\text{Cu}_4\text{I}_4)(\text{MeCN})_2(\text{DADPE})]_2 \cdot 2\text{MeCN}$  (**2**), respectively. To our best knowledge, they are the first two discrete macrocyclic complexes constructed by cubane-like Cu<sub>4</sub>I<sub>4</sub> metal cluster building blocks. Single-crystal X-ray diffraction analyses reveal that they possess a distorted metallomacrocycle enclosed by two cubane-like Cu<sub>4</sub>I<sub>4</sub> cluster units and two bridging diamine ligands DADPM for **1** and DADPE for **2** (Fig. 1 and 2). Each diamine ligand acts as a  $\mu_2$ -bridge linking two cubane-like Cu<sub>4</sub>I<sub>4</sub> units through its two nitrogen atoms. The bond angles of C(4)-C(5)-C(6) in the DADPM and C(4)-O(1)-C(5) in the DADPO are 112.7(10) $^\circ$  and 117.1(7) $^\circ$ , respectively. The cavities of the distorted rhombus are 10.53 x 4.04 $\text{\AA}$  for **1** and 9.99 x 3.88 $\text{\AA}$  for **2**, respectively, which are different from that of 8.36 x 4.10 $\text{\AA}$  from DADPM and Cu(II) ions [11]. Two uncoordinated MeCN molecules lie in two sides of the cavity as space fillers. Each Cu<sub>4</sub>I<sub>4</sub> unit displays a cubane-like arrangement. No apparent difference of the bond distances and angles in the Cu<sub>4</sub>I<sub>4</sub> cluster units from those in the reported Cu<sub>4</sub>I<sub>4</sub>L<sub>2</sub>(MeCN)<sub>2</sub> complexes (L = aniline derivative) are observed [7-10]. This result depicts that the topology of cubane-like Cu<sub>4</sub>I<sub>4</sub> cluster units is maintained during the assembly process and is not influenced by the linker ligands used.

### 3 The dimeric dicarboxylatotetraorganodistannoxane SBUs

The discrete dimeric dicarboxylatotetraorganodistannoxane complexes  $\{[\text{R}_2\text{Sn}(\text{O}_2\text{CR}')_2\text{O}]_2\}$  have been extensively studied due to their wide application in biology and catalysis, but most of them have been obtained by assembly of mono-functional carboxylate ligands and organotin. [12-16] To the best our knowledge, only two organotin polymers containing the dimeric tetraorganodistannoxane units, obtained through hydrolyzate of Me<sub>2</sub>Sn(OAc)<sub>2</sub> [17] and the hydrothermal reaction of trimethyltin chloride and 4-hydroxyl-3-methoxybenzoic acid, respectively, have been reported [18]. This prompted us to construct extended structures by using bi-functional dicarboxylate ligands instead of mono-functional carboxylates ligands in the discrete dimeric dicarboxylatotetraorganodistannoxane complexes. Assembly of two dicarboxylate ligands, nitroterephthalic acid (H<sub>2</sub>NTPA) and diphenic acid (H<sub>2</sub>DPA), and trimethyltin chloride resulted in two novel organotin polymers  $[(\text{Me}_2\text{Sn})_2(\mu_3\text{-NTPA})(\mu_3\text{-O})]_n$  (**3**) and  $\{(\text{Me}_2\text{Sn})_4(\mu_3\text{-DPA})(\mu_4\text{-DPA})(\mu_3\text{-O})_2\}_n$  (**4**), consisting of different dimeric dicarboxylatotetraorganodistannoxane SBUs, respectively.

Complex **3** is a one-dimensional chain coordination polymer (Fig. 3). The SBU in **3** is the predominant structural form in five types of the dimeric dicarboxylatotetraorganodistannoxane in which each Sn atom is in a distorted trigonal bipyramidal geometry. [12] It consists of a central planar (Me<sub>2</sub>Sn)<sub>2</sub>O<sub>2</sub> four-membered ring and two peripheral Me<sub>2</sub>Sn units attached to two  $\mu_3$ -bridging oxygen atoms. NTPA<sup>2-</sup> acts as a tridentate ligand. NO<sub>2</sub> in NTPA<sup>2-</sup> has a great effect on the formation of the polymer and is not involved in coordination to Sn atoms. All bond distances and bond angles are comparable to those in this type of the dimeric dicarboxylatotetraorganodistannoxane complexes [12-16]. The structural feature of **3** is quite different from that of  $\{[\text{Me}_2\text{Sn}(\text{OAc})_2\text{O}]_2\}_n$ , the only known one-dimensional organotin polymer in which

acetate in a tetradentate mode links the dimeric tetraorganodistannoxane units [17].

Complex **4** is a two-dimensional corrugated sheet polymer which is made up of the dimeic tetraorganodistannoxane units and bridging DPA<sup>2-</sup> ligands. As shown in Fig. 4, the SBU is different from that in complex **3** and similar to the only known that in  $\{[\text{Me}_2\text{Sn}(\text{OAc})_2\text{O}]_2\}_n$ . All bond distances and bond angles in the SBU are comparable to those in  $\{[\text{Me}_2\text{Sn}(\text{OAc})_2\text{O}]_2\}_n$  [17]. DPA<sup>2-</sup> is a chiral ligand and the dihedral angles of two phenyl rings are 99.4° for the tridentate mode and 87.1° for the tetradentate mode, respectively. In this complex, u<sub>4</sub>-bridging DPA<sup>2-</sup> links the dimeric tetraorganodistannoxane units forming a helical chain and u<sub>3</sub>-bridging DPA<sup>2-</sup> links the helical chains by coordinating to remaining coordination sites of the dimeric tetraorganodistannoxane units forming a two-dimensional sheet structure with curvature (Fig. 5). The structural feature of **2** is quite different from that of a two-dimensional rhombohedral grid polymer composed of ladder-type dimeric tetraorganodistannoxane units and 4-hydroxyl-3-methoxybenzoic acid dianion [18].

#### 4 Conclusion

By using bi-functional linker ligands instead of mono-functional ligands in molecular complexes, we have successfully obtained two discrete macrocyclic complexes and two organotin polymers consisting of the dimeric dicarboxylatotetraorganodistannoxane SBUs based on single cubane-like Cu<sub>4</sub>I<sub>4</sub> complexes and discrete dimeric dicarboxylatotetraorganodistannoxane complexes, respectively. Moreover, the topology of cluster units is maintained during the assembly process and is not influenced by the linker ligands used. This study may open a new approach to assemble different types of discrete metal clusters or molecular complexes into macrocyclic complexes or extended polymers through using di- or multi-functional ligands instead of mono-functional ligands as linkers. It might be helpful to seek modular materials with desirable physical and chemical properties by structural modification. The syntheses of related complexes and the studies of properties are in progress.

#### 5 Acknowledgements

We acknowledge financial support from the National Nature Science Foundation of China and the Key Project of Chinese Academy of Science.

#### References

- Holliday B. J. and Mirkin C. A., Strategies for the construction of supramolecular compounds through coordination chemistry, *Angew. Chem., Int. Ed.* **40** (2001) pp. 2022-2043.
- Hagman P. J., Hagman D. and J. Zubieta, Organic-inorganic hydrid materials, from "simple" coordination polymers to organodiamine-templated molybdenum oxides, *Angew. Chem., Int. Ed.* **38** (1999) pp. 2638-2684.
- Cotton F. A., Lin C. and Murillo C. A., Supramolecular array based on dimetal building units, *Acc. Chem. Res.* **34** (2001) pp. 759-771 and references therein.
- Zhang Q.-F., Niu Y., Leung W.-H., Song Y., Williams I. D. and Xin X., Synthesis of a 2D polymeric cluster  $\{[\text{NEt}_4]\text{[Mo}_2\text{O}_2\text{S}_6\text{Cu}_6\text{I}_{(4,4'\text{-bipy})}_3]\text{MeOH}\text{H}_2\text{O}\}_n$  with a

- significant improvement of optical limiting effect, *Chem. Commun.* (2001) pp. 1126-1127.
5. Eddaoudi M., Moler D. B., Li H., Chen B., Reineke T. M., O'Keeffe M. and Yaghi O. M., Modular Chemistry: secondary building units as a basis for the design of highly porous and robust metal-organic carboxylate frameworks, *Acc. Chem. Res.* **34** (2001) pp. 319-330 and references therein.
  6. Bourne S. A., Lu J., Mondal A., Moulton B. and M. Zaworotko J., Self-assembly of nanometer-scale secondary building units into an undulating two-dimensional network with two types of hydrophobic cavity, *Angew. Chem., Int. Ed.* **40** (2001) pp. 2111-2113.
  7. Rath N. P., Holt E. M. and Tanimura K., Fluorescent copper(I) complexes: structural and spectroscopic characterization of bis(*p*-toluidine)bis(acetonitrile)tetraiodotetracopper and bis(*p*-chloroaniline)(acetonitrile)diiododicopper, tetrameric complexes of mixed ligands character, *Inorg. Chem.* **24** (1985) pp. 3934-3938.
  8. Hu G., Mains G. J. and Holt E. M., Correction of structure and emission in solid state copper(I) complexes;  $Cu_4I_4(CH_3CN)_2(L)_2$ , L = aniline derivates. *Inorg. Chem. Acta* **240** (1995) pp. 559-565.
  9. Schaefer W. P., Crystal structure of bis(*p*-toluidine)bis(acetonitrile)tetraiodotetracopper: correction of space group, *Inorg. Chem.* **25** (1986) pp. 2665.
  10. Rath N. P., Jasinski J. and Holt E. M., Fluorescent copper(I) cluster systems, *Acta Crystallogr., Sect. A* **40** (1984) pp. C316.
  11. Zhang Y., Nishiura M., Li J., Wei D. and Imamoto T., New Maze-Type Network Assembled by Copper(II) and 4,4'-Diaminodiphenylmethane:  $\{[Cu(C_{13}H_{14}N_2)(C_6H_4O_4Cl)]Cl\}_2$ , *Inorg. Chem.* **38** (1999) pp. 825-827.
  12. Tiekink E. R. T., Gielen M., Bouhdid A., Biesemans M. and Willem R., Crystal structure of the dimeric bis(*p*-fluoro- and pentafluorophenylacetato)tetra-n-butyltin distannoxanes, *J. Organomet. Chem.* **494** (1995) pp. 247-253.
  13. Ribot F., Sanchez C., Meddour A., Gielen M., Tiekink E. R. T., Biesemans M. and Willem R., On the assignment of  $^{119}Sn$  resonances of bis[dicarboxylatotetraorganodistannoxanes] in solution and solid state  $^{119}Sn$  NMR spectra, *J. Organomet. Chem.* **552** (1998) pp. 177-182.
  14. Narula S. P., Kaur S., Bharadwaj S. K. and Chadha R. K., Crystal and molecular structure of 1,2,3,4-di- $\mu$ -O-methyl/o-chlorobenzoato-OO'1,3-bis(o-methyl/o-chlorobenzoato-O)-1,2,4;2,3,4-di- $\mu$ \_3-oxotetrakis[di-n-butyltin(IV)] and molecular structure of 1,2,3,4-di- $\mu$ -hydroxylbenzoato-OO'-1,3-bis(o-hydroxylbenzoato-O)-
  15. 1,2,4;2,3,4-di- $\mu$ \_3-oxo-oxotetrakis[di-n-butyltin(IV)] compounds, *J. Organomet. Chem.* **506** (1996) pp. 181-190.
  16. Petrosyan V. S., Yashina N. S., Drovetskaia T. V., Yatsenko A. V., Aslanov L. A. and Pellerito L., Synthesis and structures of some diethyl- and diphenyltin bishydroxamates, *Appl. Organometallic Chem.*, **10** (1996) pp. 523-528.
  17. Blie J. A., Howie R. A., Wardell J. L. and Cox P. J., Crystal structures of  $[(IMe_2SnOSnMe_2OEt)_2]$  and  $[\{Pr(O_2)Me_2SnMe_2O_2(Pr)_2\}_2]$ , *Polyhedron* **16** (1997) pp. 881-888.
  18. Lockhart T. P., Manders W. F. and Holt E. M., Solution and solid-state molecular structures of  $Me_2Sn(OAc)_2$  (I) and its hydrolyzate ( $[Me_2Sn(OAc)_2O]$ , (II), by solution and solid-state  $^{13}C$  NMR. X-ray diffraction study of II, *J. Am. Chem. Soc.* **108** (1986) pp. 6611-6616.
  19. Xiong R.-G., Zuo J.-L., You X.-Z., Fun H.-K. and Raj S. S., A novel rhombohedral

grid based on tetraorganodistannoxane as corner unit, *Organometallics* 19 (2000) pp. 4183-4186.

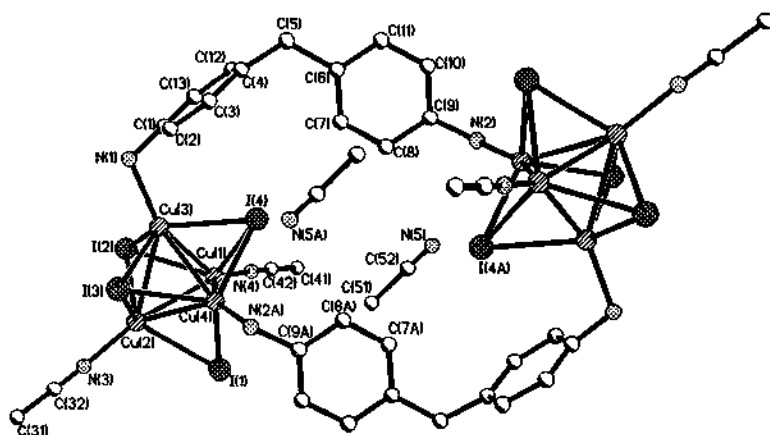


**Figure 1.** A view of the macrocyclic structure of 1.

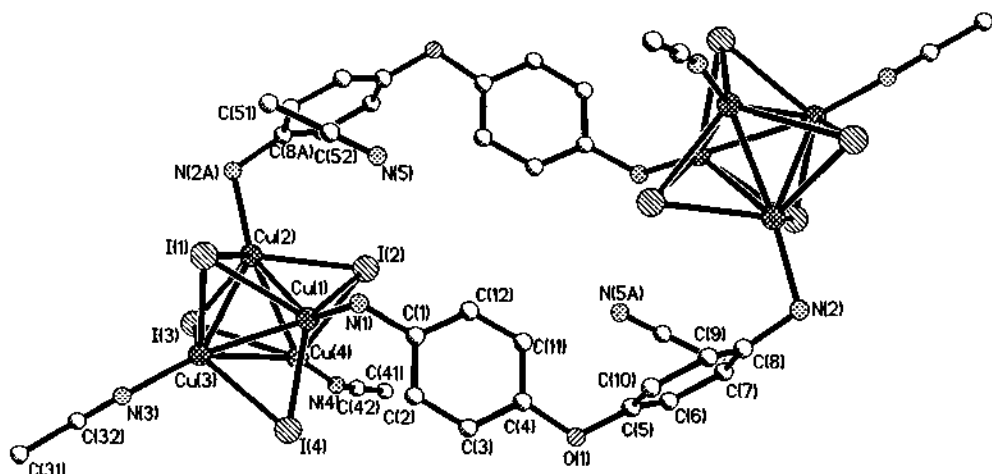


**Figure 2.** A view of the macrocyclic structure of **2**.

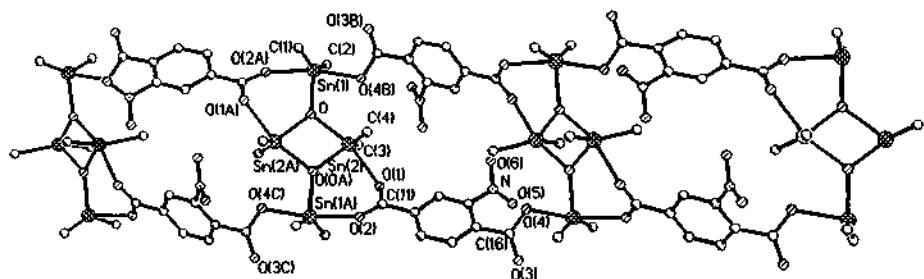


Figure 3. View of one-dimensional chain in 3 with atomic numberings.

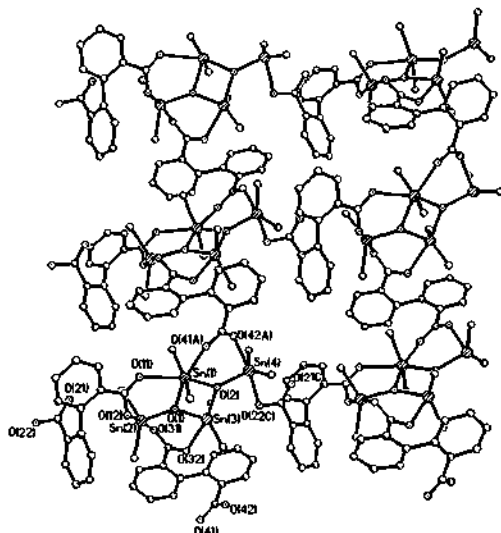


Figure 4. View of two-dimensional sheet along *b* axis in 4 with atomic numberings.

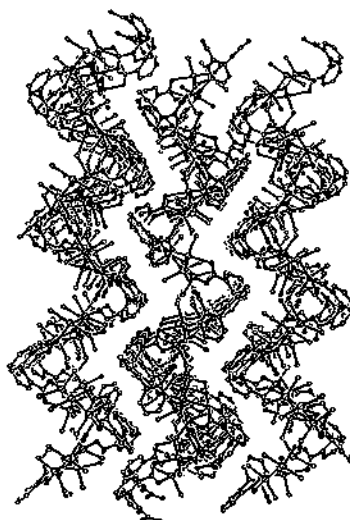


Figure 5. View of the corrugated sheet along *c* axis in 4.

# CATALYTIC SYNTHESIS OF N-AMYL CINNAMATE WITH $\text{TiSiW}_{12}\text{O}_{40}/\text{TiO}_2$

SHUIJIN YANG<sup>1,2</sup>, XIEQING YU<sup>2</sup>, YONGGUANG LIANG<sup>2</sup> AND JUTANG SUN<sup>1</sup>

<sup>1</sup>*College of Chemistry and Molecular Sciences, Wuhan University, Wuhan 430072, P. R. China*  
E-mail: jtsun@whu.edu.cn

<sup>2</sup>*Department of Chemistry and Environmental Engineering, Hubei Normal University, Huangshi 435002, P. R. China*  
E-mail: yangshuijin@163.com

The catalytic activities of  $\text{TiSiW}_{12}\text{O}_{40}/\text{TiO}_2$  in synthesizing *n*-amyl cinnamate are reported. It has been demonstrated that  $\text{TiSiW}_{12}\text{O}_{40}/\text{TiO}_2$  is an excellent catalyst. Various factors concerned in this reaction have been investigated. The optimum conditions have been found. That is, the molar ratio of alcohol to acid is 4:1; the mass ratio of the catalyst used to the reactants is 2.0 %, the reaction temperature 122-126 °C, and the reaction time 1.5 h. Under this condition, the yield of *n*-amyl cinnamate is 93.3 %.

## 1 Introduction

The *n*-amyl cinnamate is a very important perfume material [1,2]. Until now, there are many methods to synthesize this compound. Conventionally  $\text{H}_2\text{SO}_4$  is used as catalyst in factories, but it causes many problems, such as the erosion of equipments, difficulty for after-treatment, low quality of the products, etc. The catalytic function of heteropoly compounds of tungsten and molybdenum has recently attracted much attention for various industrial processes, such as oxidation, hydration, esterification [3-6] etc, particularly in the last two decades, because their acidic and redox properties can be controlled at atomic/molecular levels. Mizuno and Misono [7-9] and Pope [10] and Kozhevnikov [11] and Wang Enbo [12,13] have reviewed the homogeneous catalysis and fine organic synthesis catalyzed by heteropoly compounds. However, there is no report on the synthesis of *n*-amyl cinnamate catalyzed by  $\text{TiSiW}_{12}\text{O}_{40}/\text{TiO}_2$ . In this paper, the synthesis of *n*-amyl cinnamate by using  $\text{TiSiW}_{12}\text{O}_{40}/\text{TiO}_2$  as catalyst were studied with *n*-amyl alcohol and cinnamic acid as reactants, and the reaction conditions were examined.

## 2 Experimental

### 2.1 Reagents and apparatus

Cinnamic acid and *n*-amyl alcohol were of analytical reagent grade. The IR spectra were obtained using an IMP 410 IR spectrometer. The X-ray powder diffraction pattern of the powder sample was measured by a Rigaku model D/MAX-3C X-ray diffractometer employing  $\text{CuK}\alpha$  radiation. The accelerating voltage and the applied current were 40 kV and 20 mA, respectively.

## 2.2 Preparation of the catalysts

$\text{TiSiW}_{12}\text{O}_{40}/\text{TiO}_2$  was prepared according to the literature [14] and identified by means of IR and XRD.

## 2.3 Esterification reaction

The reaction was carried out in a three-necked flask equipped with a stirrer, a water segregator with a reflux condense and a thermometer. To the flask were added a certain amounts of *n*-amyl alcohol, cinnamic acid and the catalyst, which was heated to boiling and refluxed until no water flowed off. The purified product was analyzed by means of IR.

## 3 Results and Discussion

### 3.1 Infrared absorption spectra of catalyst

Fig.1 shows the IR spectra of  $\text{TiO}_2 \cdot x\text{H}_2\text{O}$ ,  $\text{H}_4\text{SiW}_{12}\text{O}_{40} \cdot x\text{H}_2\text{O}$  and  $\text{TiSiW}_{12}\text{O}_{40}/\text{TiO}_2$ .

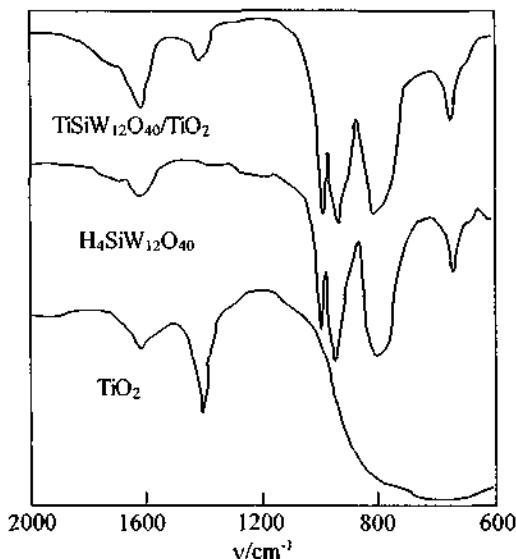


Figure 1. IR spectra of  $\text{TiO}_2 \cdot x\text{H}_2\text{O}$ ,  $\text{H}_4\text{SiW}_{12}\text{O}_{40} \cdot x\text{H}_2\text{O}$  and  $\text{TiSiW}_{12}\text{O}_{40}/\text{TiO}_2$ .

In the infrared spectra, the characteristic peak of  $\text{TiO}_2 \cdot x\text{H}_2\text{O}$  shows up at  $1401\text{cm}^{-1}$ , and those of  $\text{H}_4\text{SiW}_{12}\text{O}_{40} \cdot x\text{H}_2\text{O}$  at  $1631, 1021, 984, 935, 891, 785$  and  $549\text{cm}^{-1}$ . The infrared spectrum of the reaction product ( $\text{TiSiW}_{12}\text{O}_{40}/\text{TiO}_2$ ) suggests the absorption bands at  $1618, 1021, 984, 928, 885, 791$  and  $543\text{cm}^{-1}$  to be assigned to the bending vibrations of H-O-H bonds, the stretching vibrations of Si-O-Si, W-Od, Si-O, W-Ob-W, W-Oc-W and Si-O-Si bonds, respectively. The IR spectral data show that  $\text{H}_4\text{SiW}_{12}\text{O}_{40} \cdot x\text{H}_2\text{O}$  and  $\text{TiSiW}_{12}\text{O}_{40}/\text{TiO}_2$  have the same Keggin structure.

### 3.2 Studies on the reaction condition

#### 3.2.1 The effect of the amount of the catalyst on the yield

The effect of the amount of the catalyst on the yield is shown in Table 1.

**Table 1.** The effect of the catalyst amount on the yield\*.

Amount of catalyst/%	1.0	1.5	2.0	2.5
Yield/%	83.3	90.0	93.3	93.3

\*cinnamic acid: 0.05 mol; the ratio of alcohol to acid: 4:1 mol; reaction time: 1.5 h.

From Table 1, we can see that the yield increases when the catalyst concentration increases. When the mass ratio of the catalyst to the reactants was 2.0 %, the yield was 93.3 %. The yield did not vary greatly when more catalyst was added. Therefore, the mass ratio of the catalyst to the reactants was 2.0 % for these experiments.

#### 3.2.2 The effect of the ratio of alcohol to acid

Table 2 shows the effect of the ratio of alcohol to acid on the yield. The ratio of alcohol to acid directly influence the yield.

**Table 2.** The effect of the ratio of alcohol to acid on the yield\*.

Ratio of alcohol to acid	2:1	3:1	4:1	5:1
Yield/%	64.4	76.7	93.3	75.6

\*cinnamic acid: 0.05 mol; mass ratio of catalyst to reactants: 2.0 %; reaction time: 1.5 h

The yield increases with the ratio of the alcohol to the acid. When the ratio is 4:1, the yield is the highest. To increase the ratio of alcohol to acid will cause a lower yield, because of the lowering of the temperature. Thus the optimum ratio of alcohol to acid is 4:1.

#### 3.2.3 The effect of reaction time on the yield

Reaction time is also an important factor for the reaction. Table 3 shows the effect of the reaction time on the yield. We can see from Table 3 that the yield increases with increase of time. After 1.5 h, the yield does not show obvious changes. Therefore, we choose 1.5 h as the optimum reaction time.

**Table 3.** The effect of the reaction time on the yield\*.

the reaction time /h	1.0	1.5	2.0	2.5
Yield/%	92.2	93.3	94.4	93.3

\*cinnamic acid: 0.05 mol; ratio of alcohol to acid: 4:1 mol; mass ratio of catalyst to reactants: 2.0 %.

### 3.2.4 The effect of reaction temperature on the yield

The reaction may proceed quite differently at different temperatures. It proceeds very slowly or does not take place at all at low temperatures. Yet a high temperature will cause the by-products to increase. The temperature can be controlled by adding a certain amount of a water-carrying agent. Cyclohexane can be used to keep the temperature between 122-126 °C in this experiment.

### 3.3 Comparison of catalytic activities of catalysts

Table 4 presents the catalytic activity data of PVC-FeCl<sub>3</sub> [2], NH<sub>4</sub>Fe(SO<sub>4</sub>)<sub>2</sub> [15] and TiSiW<sub>12</sub>O<sub>40</sub>/TiO<sub>2</sub>.

**Table 4.** Catalytic activity data of PVC-FeCl<sub>3</sub>, NH<sub>4</sub>Fe(SO<sub>4</sub>)<sub>2</sub> and TiSiW<sub>12</sub>O<sub>40</sub>/TiO<sub>2</sub>.

Catalyst	ratio of alcohol to acid	reaction time /h	yield/%
PVC-FeCl <sub>3</sub>	10:1	2.0	75.7
NH <sub>4</sub> Fe(SO <sub>4</sub> ) <sub>2</sub>	10:1	2.0	84.9
TiSiW <sub>12</sub> O <sub>40</sub> /TiO <sub>2</sub>	4:1	1.5	93.3

From Table 4 we can obtain the following conclusion: all of the catalysts have certain catalytic activities for this reaction. The catalytic activity of TiSiW<sub>12</sub>O<sub>40</sub>/TiO<sub>2</sub> is the highest among all the catalysts. The results imply that the catalytic activities of TiSiW<sub>12</sub>O<sub>40</sub>/TiO<sub>2</sub> for the esterification of cinnamic acid with *n*-amyl alcohol are related to the acidity of the heteropolyacids.

### 3.4 Analysis and identification of the product

A purified product was analyzed by means of IR spectrum. The IR spectrum shows peaks at 1714 cm<sup>-1</sup> (=C=O) and 1310, 1171cm<sup>-1</sup> (C-O-C) which are in accordance with those in the standard IR spectrum of *n*-amyl cinnamate, n<sub>D</sub><sup>20</sup>=1.5370.

### 3.5 The repeated application of the catalyst

A good catalyst should be able to be used repeatedly. We found that the catalytic activities of our catalyst are almost unchanged after it has been used for five times.

## 4 Conclusion

The optimum conditions are: molar ratio of *n*-amyl alcohol to cinnamic acid is 4:1, the mass ratio of catalyst to reactants is equal to 2.0 %, the reaction temperature 122-126 °C, and reaction time 1.5 h. Under this condition, the yield of *n*-amyl cinnamate can reach over 93.3 %. From the above results and discussion, we can see that the synthesis of *n*-amyl cinnamate catalyzed by TiSiW<sub>12</sub>O<sub>40</sub>/TiO<sub>2</sub> instead of H<sub>2</sub>SO<sub>4</sub> has a great prospect of application.

## 5 Acknowledgements

We acknowledge the National Natural Science Foundation of China (No. 29971024) and the Natural Science Foundation of Hubei Province (No. 99J064) for financial support.

## References

1. Jinan qingong yanjiusuo bianyi, Hecheng shiyong xiangliao shouce (Qinggongye chubanshe, Beijing, 1985), pp. 636-641.
2. Ding L., Yu S. and Wen R., Catalytic synthesis of cinnamates with polyvinyl chloride-ferric chloride. *Journal of Shanxi University* **24** (2001) pp. 133-135.
3. Dupont P., Vedrine J. C., Paumard E., et al., Heteropolyacids supported on activated carbon as catalysts for the esterification of acrylic acid by butanol. *Appl. Catal. A-Gen* **129** (1995) pp. 217-227.
4. Yang S., Liang Y., Yu X. et al., Catalytic synthesis of Nipagin esters with  $TiSiW_{12}O_{40}/TiO_2$ . *China Surfactant Detergent and Cosmetics* **30** (2000) pp. 20-21.
5. Yang S. and Liang Y., Study of catalytic synthesis of glucose esters with  $TiSiW_{12}O_{40}/TiO_2$ . *Fine Chemicals* **18** (2001) pp. 408-410.
6. Yang S., Liang Y., Yu X. et al., Synthesis of glucose pentaacetate by using  $TiSiW_{12}O_{40}/TiO_2$  as catalyst. *Huaxue Shijie* **41** (2000) pp. 650-652.
7. Misono M., Heterogeneous catalysis by heteropoly compounds of molybdenum and tungsten. *Catal. Rev.-Sci. Eng.* **29** (1987) pp. 269-321.
8. Mizuno N. and Misono M., Heteropolyacid catalysts. *Current opinion in solid state and materials science* **2** (1997) pp. 84-89.
9. Shikata S., Okuhara T. and Misono M., Gas phase synthesis of methyl tert-butyl ether over heteropolyacids. *J. Mol. Catal.* **100** (1995) pp. 49-59.
10. Pope M. T., *Heteropoly and isopoly oxometalates* (Springer-Verlag, New York, 1983), p. 23.
11. Kozhevnikov I. V., Heteropolyacids and related compounds as catalysts for fine chemical synthesis. *Catal. Rev.-Sci. Eng.* **37** (1995) pp. 311-352.
12. Zheng R. and Wang E., Polyacid chemistry of molybdenum and tungsten. *Huaxue Tongbao* **9** (1984) pp. 12-18.
13. Xu L., Hu C and Wang E, Progress in the research of heteropolyacid catalysts in recent five years. *Shiyou Huagong* **26** (1997) pp. 632-638.
14. Yu X., Zhang J., Zhang S. and Wang E., Synthesis of dioctyl phthalate using catalyst  $TiSiW_{12}O_{40}/TiO_2$ . *J.I Northeast Normal Univer.* **2** (1995), pp. 59-61.
15. Wen R., Luo X., Yu S. et al., Catalytic synthesis of cinnamate with ammonium ferric sulfate. *Hecheng Huaxue* **9** (2001) pp. 269-271.

This page is intentionally left blank

# TOWARDS THE CONSTRUCTION OF OPEN FRAMEWORK STRUCTURES OF COPPER PHOSPHONATES AND THE MAGNETIC STUDIES

LI-MIN ZHENG

*State Key Laboratory of Coordination Chemistry, Coordination Chemistry Institute, College of Chemistry and Chemical Engineering, Nanjing University, Nanjing 210093, P. R. China  
E-mail: lmzheng@netra.nju.edu.cn*

With the aim of gaining novel copper phosphonate compounds with open framework structures, a series of copper phosphonates based on 1-hydroxyethylidenediphosphonate (hedp) have been synthesized in this laboratory through two approaches. One is by template influences on the structures of the final products, and the other is to introduce a second bridging ligand. So far, twelve Cu-hedp compounds have been prepared in this way, some of which exhibit open framework structures. Magnetic property investigations reveal that antiferromagnetic interactions are observed between the magnetic centers in all these compounds. A few of them show interesting metamagnetism at low temperatures.

## 1 Introduction

The metal phosphonate compounds usually adopt layered or pillared layered structures with the organic moieties filling in the inter-layer spaces [1-4]. The layered nature makes them interesting candidates to host intercalation reactions. Furthermore, the potential for the organic moieties to be modified by functional groups allows for the preparation of a number of new materials that have possible applications in areas such as catalysis, ion exchange, sensing and ion conduction [1,4-7].

Although efforts were initially focused on phosphonates of group 4 and 14 elements, increasing attention has been paid to transition metal phosphonates due to their solubility in acidic aqueous solutions and their ability for crystallization [3]. Among the transition metal phosphonates, the copper compounds are unique because of several reasons: (1) The versatile coordination capabilities of Cu ions could provide many unusual structure types. The copper atom can have coordination numbers up to six. In copper phosphonates, the 4- or 5- coordination modes are commonly observed, making one or two coordination sites available. (2) The presence of the available sites could make these phosphonates exhibiting interesting intercalation and/or catalytic properties. (3) They are magnetically interesting. Each Cu(II) has a single unpaired electron, thus provides the simplest cases for a study on the magneto-structural relationships of metal phosphonates. (4) The redox property of copper ions also makes the copper phosphonates electronically interesting. So far, the syntheses and characterization of new copper phosphonates with extended structures have been carried out in several research groups. A limited number of compounds have been obtained through direct reactions between Cu(II) ions and the phosphonic acids. Examples of monophosphonates include Cu(RPO<sub>3</sub>)·H<sub>2</sub>O (R = C<sub>6</sub>H<sub>5</sub>, C<sub>2</sub>H<sub>5</sub>, CH<sub>3</sub>) [8, 9], Cu(C<sub>2</sub>H<sub>5</sub>PO<sub>3</sub>) [9], β-Cu(CH<sub>3</sub>PO<sub>3</sub>) [10], Cu<sub>3</sub>O(CH<sub>3</sub>PO<sub>3</sub>)<sub>2</sub>·2H<sub>2</sub>O [10], NaCu(O<sub>2</sub>CCH<sub>2</sub>NHCH<sub>2</sub>PO<sub>3</sub>)·3.5H<sub>2</sub>O [11], Cu<sub>2.5</sub>(NH<sub>3</sub>CH<sub>2</sub>CH<sub>2</sub>PO<sub>3</sub>)(OH)<sub>2</sub>(SO<sub>4</sub>) [12], Cu<sub>2</sub>(NH<sub>2</sub>CH<sub>2</sub>CH<sub>2</sub>PO<sub>3</sub>)(OH)(NO<sub>3</sub>)·H<sub>2</sub>O [12], Cu<sub>2</sub>(4-pyridylphosphonate)<sub>2</sub>·2H<sub>2</sub>O [13] and Na[Cu(O<sub>3</sub>PCH<sub>2</sub>CH<sub>2</sub>CO<sub>2</sub>)] [14]. Their structures range from one-dimensional chain, two-dimensional layer to three-dimensional open framework. Copper diphosphonate materials have also been explored, including Cu<sub>2</sub>[(O<sub>3</sub>PC<sub>2</sub>H<sub>4</sub>PO<sub>3</sub>)(H<sub>2</sub>O)<sub>2</sub>], Cu<sub>2</sub>[(O<sub>3</sub>PC<sub>3</sub>H<sub>6</sub>PO<sub>3</sub>)(H<sub>2</sub>O)<sub>2</sub>]·H<sub>2</sub>O [15],

$\text{Cu}_2[(\text{O}_3\text{PC}_6\text{H}_4\text{PO}_3)(\text{H}_2\text{O})_2]$  and  $\text{Cu}[\text{HO}_3\text{P}(\text{C}_6\text{H}_4)_2\text{PO}_3\text{H}]$  [16]. Our interest in the copper phosphonate chemistry is two-fold: first, to construct new materials with open framework or even porous structures; secondly, to understand the magnetic properties of these compounds on the basis of their structures. The efforts have been targeted to compounds with 1-hydroxyethylidenediphosphonic acid [hedp<sub>H4</sub>,  $\text{CH}_3\text{CH}(\text{OH})(\text{PO}_3\text{H}_2)_2$ ]. As already reported, most diphosphonate compounds show pillared layered structures. The inter-layer separations vary with the size of cross-linking organic groups. Other structure types were also found for diphosphonates, depending on factors such as: (1) the length of the R tether in  $\text{H}_2\text{O}_3\text{P}-\text{R}-\text{PO}_3\text{H}_2$ ; and (2) whether the phosphonate oxygens are protonated. For M-hedp compounds where the two phosphorus atoms are separated by a single methyl group, the M-O-P-C-P-O six member rings are favored. Therefore, like methylenediphosphonate [17], structures other than the pillared layered are often formed.

Two approaches have been employed in this laboratory. One is through structure directing agents such as ammonium and organic diamines. This approach has been used extensively in synthesizing materials of zeolites and phosphates [18], but still relatively less in metal phosphonates. The template influences on the structures of some M-hedp compounds have been discussed in a previous review [19]. The other approach is through the introduction of a second bridging ligand. It has been reported by Alberti and Clearfield et al that spacers such as phosphites or phosphates may be introduced between the bisphosphonates in the cross-linked structures in order to create pores in these compounds [20]. Several microporous diphosphonates have been prepared in this way. For M-hedp compounds which usually do not show pillared layered structures, the introduction of a second bridging ligand may lead to the construction of novel open framework structures, which is found to be the case.

In order to find new magnetic materials based on copper phosphonates, our effort has also been devoted to the magnetic properties of the Cu-hedp compounds. In recent years, the magnetic properties of some metal phosphonate compounds have been studied. Although no true ferromagnet has yet been discovered in phosphonate system, weak ferromagnetism (canted antiferromagnetism) was observed in  $\text{Fe}(\text{RPO}_3)\cdot\text{H}_2\text{O}$  ( $\text{R} = \text{C}_2\text{H}_5, \text{C}_6\text{H}_5$ ) [21, 22],  $\text{Cr}(\text{CH}_3\text{PO}_3)\cdot\text{H}_2\text{O}$  [23],  $\text{Mn}(\text{C}_n\text{H}_{2n+1}\text{PO}_3)\cdot\text{H}_2\text{O}$  [24],  $\text{Co}_3(\text{O}_3\text{PC}_2\text{H}_4\text{CO}_2)_2$  [25] and  $\{\text{K}_2[\text{CoO}_3\text{PCH}_2\text{N}(\text{CH}_2\text{CO}_2)_2]\}_6\cdot\text{xH}_2\text{O}$  [26]. This area is still rich for exploration to better understand the magneto-structural relationships of the phosphonate compounds. Based on the structures of the Cu-hedp compounds, we have carried out a detailed study on the magnetic properties of these compounds. Some interesting results have been obtained.

This short review will present our work on both the structures and the magnetic properties of the Cu-hedp compounds synthesized in this laboratory.

## 2 Cu-hedp compounds involving organic templates

In the presence of structure-directing agents, we have succeeded in synthesizing seven Cu-hedp compounds with extended structures including  $[\text{NH}_3(\text{CH}_2)_2\text{NH}_3]\text{Cu}_2(\text{hedp})_2\cdot\text{H}_2\text{O}$  (1),  $[\text{NH}_3\text{CH}(\text{CH}_3)\text{CH}_2\text{NH}_3]\text{Cu}_2(\text{hedp})_2$  (2) [27],  $(\text{NH}_4)_2\text{Cu}_3(\text{hedp})_2(\text{H}_2\text{O})_4$  (3) [28],  $[\text{NH}_2(\text{CH}_2)_3\text{NH}_2]\text{Cu}_3(\text{hedp})_2\cdot3.5\text{H}_2\text{O}$  (4) [29],  $[\text{NH}_2(\text{CH}_2)_4\text{NH}_2]\text{Cu}_3(\text{hedp})_2\cdot2\text{H}_2\text{O}$  (5),  $[\text{NH}_2(\text{C}_2\text{H}_4)_2\text{NH}_2]\text{Cu}_3(\text{hedp})_2$  (6) [28] and  $\text{Na}_2\text{Cu}_{15}(\text{hedp})_6(\text{OH})_2(\text{H}_2\text{O})_7$  (7) [30].

Compounds 1 and 2 are closely related to each other. Both exhibit linear chain structures in which the  $\{\text{Cu}_2(\text{hedp})_2\}$  dimers are connected by edge-shared  $\{\text{CuO}_5\}$  square pyramids (Fig. 1a). Each hedp in the chains behaves as a bis(chelating) bridging ligand and links two copper ions in a *cis*-bridging mode. This is different from the *trans*-bridging mode

observed in compounds 3-7.

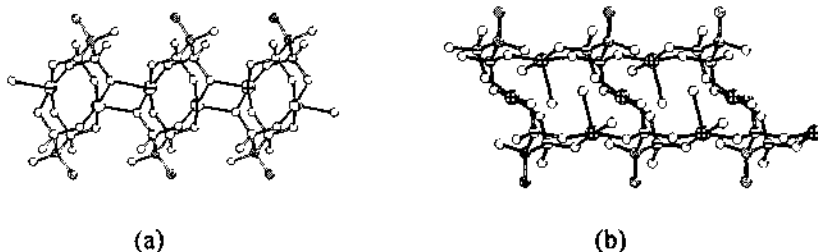


Figure 1. A fragment of the chain in structures 1 (a) and 3 (b).

In compounds 3-6, same building blocks, e.g. the  $\text{Cu}_3(\text{hेप})_2^{2-}$  trimer unit, are observed. When each trimer is linked to its two equivalents through corner-sharing of  $\{\text{CuO}_5\}$  tetragonal pyramids and the  $\{\text{CPO}_3\}$  tetrahedra, a ladder-like chain structure is built up, as found in compound 3 (Fig. 1b). When each trimer is linked to its four equivalent neighbors through vertex-sharing of  $\{\text{CuO}_4\}$  units and  $\{\text{CPO}_3\}$  tetrahedra, two dimensional layer structures are constructed, as found in compounds 4-6 (Fig. 2). These layers contain 4- and 8-membered rings, and are stacked on top of each other, resulting in one-dimensional channels. The diammonium counterions reside in the channels and occupy the interlayer spaces. The preference of a chain structure in compound 3 while a layer structure in compounds 4-6 could originate from the templates employed under very similar reaction conditions. The template effect depends on both its own properties and the nature of the anionic lattice. The properties of templates include the size, geometrical shape, hydrogen bonding ability with the other components and charge density and distribution. Clearly, the inorganic amine  $\text{NH}_3$  has a different property in all aspects from the organic diamines  $\text{NH}_2(\text{CH}_2)_n\text{NH}_2$  ( $n = 3, 4$ ) and  $\text{NH}(\text{C}_2\text{H}_4)_2\text{NH}$ , thus leading to a complete different structure of 3 compared with those of 4-6.

Compound 7 can be viewed as a pillared layered structure with two sets of inorganic layers (A and B) separated by nine-membered rings containing organic moieties (Fig. 3). Layer A is based on an equilateral triangle unit of  $\text{Cu}_3\text{O}$ , each is edge-shared with three other equivalents, forming a two-dimensional  $\{(\text{Cu}_3\text{O})_3\}$  network with 12-membered rings. The  $\{\text{CuO}_4\text{Na}\}$  sheet (layer B) contains similar 12-ring cavities generated from edge-shared  $\text{CuO}_4$  planes and  $\text{NaO}_6$  octahedra. Therefore, an interesting three-dimensional open-framework structure is established, with one-dimensional channels along the [001] direction. Although the template is not involved in the structure, it clearly plays an important role in directing the open framework structure of 7.

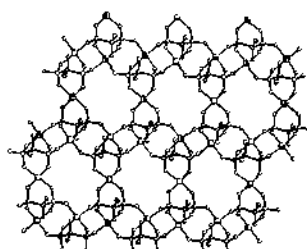
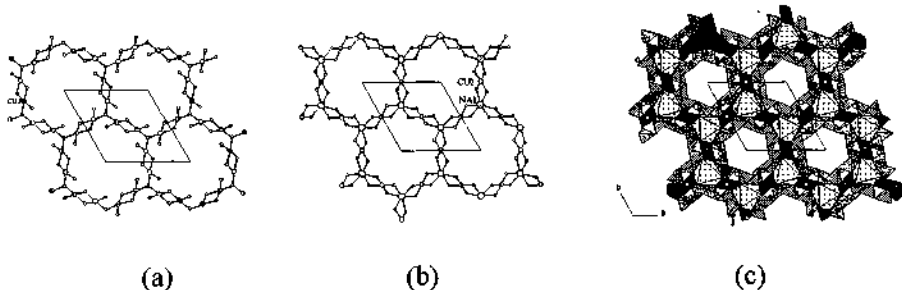


Figure 2. One layer of structure 4.



**Figure 3.** (a) Layer A, (b) layer B, and (c) packing diagram of structure 7.

### 3 Cu-hedp compounds involving second organic bridging ligands

By this approach, five Cu-hedp compounds with novel structures have been obtained by us including  $\text{Cu}_4(\text{hedp})_2(\text{pz})(\text{H}_2\text{O})_2$  (8) [31],  $\text{Na}_2\text{Cu}_3(\text{hedp})_2(\text{pz})(\text{H}_2\text{O})_2$  (9) [32],  $\text{Cu}_3(\text{hedpH})_2(4,4'\text{-bipy})_2(\text{H}_2\text{O})_2$  (10),  $\text{Cu}_3(\text{hedpH})_2(4,4'\text{-azpy})_2(\text{H}_2\text{O})_2$  (11) [33] and  $\text{Cu}_3(\text{hedpH}_2)_2(4,4'\text{-bipy})_2\cdot 2\text{H}_2\text{O}$  (12) [34], where pyrazine (pz), 4,4'-bipyridine (4,4'-bipy) and 4,4'-azobispyridine (4,4'-azpy) are used as second bridging ligands.

Figure 4 shows the structure of compound 8. The ladder-like chains of  $\{\text{Cu}_3(\text{hedp})_2(\text{H}_2\text{O})_2\}$  are again observed, reminiscent of that observed in compound 3. These double chains are connected through  $\{\text{Cu}(3)\text{O}_4\}$  units by sharing the remaining phosphonate oxygen [O(6)] of hedp, forming  $\{\text{Cu}_4(\text{hedp})_2(\text{H}_2\text{O})_2\}_n$  layers with zigzag fluctuation in the *ab* plane. The layers are linked by pyrazine bridging ligands, leading to a three dimensional open framework structure. The structure of compound 9 is very similar except that the Cu(3) atom is replaced by two sodium ions.

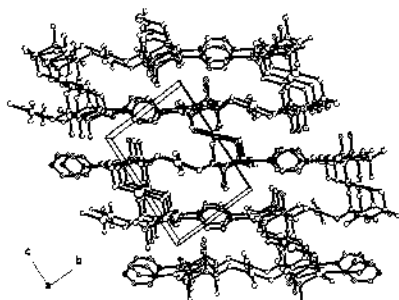


**Figure 4.** The structure of 8.

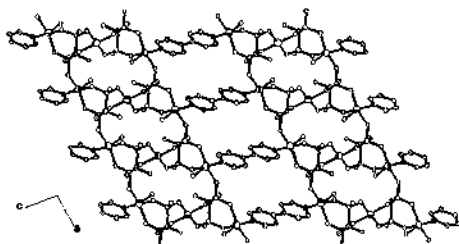


**Figure 5.** One layer of structure 10.

The substitution of pyrazine by a longer bifunctional ligand such as 4,4'-bipy and 4,4'-azpy destroys the three-dimensional structure of 8 in one direction. Therefore, compounds 10 and 11 with layer structures are resulted. The structures of these two compounds are quite similar. Each contains the ladder-like chains of  $\{\text{Cu}_3(\text{hedpH})_2(\text{H}_2\text{O})_2\}$  connected by 4,4'-bipy or 4,4'-azpy bridging ligands, forming zigzag layers with windows. Figure 5 shows one layer of compound 10. These layers are held together by strong interlayer hydrogen bonds, forming a three-dimensional open network structure with

channels generated along a-axis. The lattice water resides in these channels.

The observation of the ladder-like chain motif in one-dimensional compound 3, two-dimensional compounds 10-11 and three-dimensional open framework compounds 8-9 demonstrate that the  $\{\text{Cu}_3(\text{hedpH})_2\}$  anionic chain may serve as a useful building block in constructing a number of novel copper phosphonates with layer or open framework structures.

Under more acidic conditions, compound 12 containing mixed valence copper(I,II) ions was prepared. The compound has a two dimensional brick-wall like layer structure, composed of  $\{\text{Cu}^I_2\text{Cu}^{II}(\text{hedpH}_2)_2\}$  trimer units and 4,4'-bipyridine linkages (Fig. 6). The layers are stacked along [001] direction with inter-layer  $\pi$ - $\pi$  interactions between the pyridine rings and strong inter-layer hydrogen bonds between the phosphonate oxygens, forming a three-dimensional network structure. A significant feature of the structure 12 is that only molecular units of copper phosphonate are observed within the extended structure, which is rare among phosphonate compounds. This feature provides a potential for discrete copper phosphonate species to act as building units and involve in the construction of a great number of supramolecular complexes with interesting open framework structures.

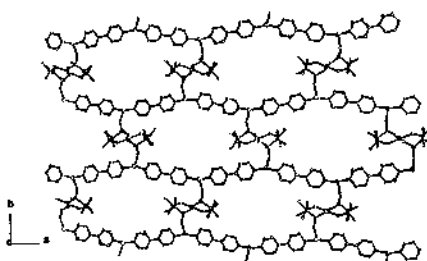


Figure 6. One layer of structure 12.

#### 4 Magnetic properties

The magnetic behaviors of compounds 1-11 have been investigated. A dominant antiferromagnetic interaction is observed for compounds 1 and 2. By considering their structures, the Cu(II) ions are bridged by O-P-O groups and oxygen atoms, alternatively (Fig. 1a). The magnetic susceptibility data were analyzed by the Bleaney-Bowers expression, assuming that the exchange coupling through the oxygen bridge is more efficient than that through the O-P-O bridge. The parameters thus obtained are  $g = 2.22$ ,  $J = -61.8 \text{ cm}^{-1}$ ,  $\rho = 0.00259$  for 1, and  $g = 2.17$ ,  $J = -57.3 \text{ cm}^{-1}$ ,  $\rho = 0.00118$  for 2, respectively.

For compounds 3, 10 and 11 in which the  $\{\text{Cu}_3(\text{hedpH})_2(\text{H}_2\text{O})_x\}$  double chains are separated either by ammonium cations or by long bridging ligands, antiferromagnetic interactions are also observed. This interaction however, is much weaker compared with that in compounds 1-2 because the copper(II) centers in 3, 10 and 11 are purely linked by O-P-O bridges (Fig. 1b). The weak antiferromagnetic exchange is evidenced by the lack of maximums in the  $\chi_M$  vs T curves down to 2 K.

For compounds 4-6 where copper (II) ions are bridged by O-P-O groups into a layer, very interesting metamagnetic behaviors are observed. Figure 7 shows the temperature dependent magnetic susceptibilities of compound 4 at 20 kOe, which is characteristic of a ferrimagnetic behavior. The  $\chi_M$  vs T curves measured at 20 kOe, 180 Oe and 30 Oe show a

sharp peak at *ca.* 4.7 K at a low field of 30 Oe (inset of Fig. 7), suggesting the occurrence of long range antiferromagnetic (AF) ordering. The field dependent magnetization of compound 4 measured at 1.8 K reveals a metamagnetic behavior: below *ca.* 50 Oe, the magnetization increases slightly with increasing field, subsequently it increases abruptly to a ferrimagnetic state, and reaching a saturation magnetization plateau above 5 kOe (Fig. 8). The hysteresis loop at 1.8 K is typical for a soft ferrimagnet.

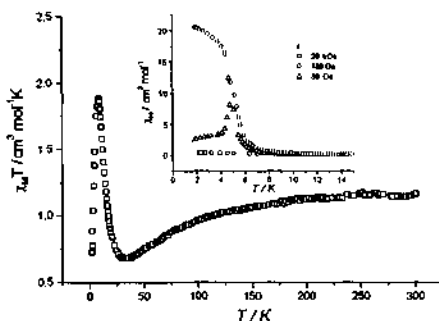


**Figure 7.** Temperature dependence of magnetic susceptibility of 4:  $\chi_M T$  ( $\square$ ) vs  $T$  plot at 20 kOe; inset,  $\chi_M$  vs  $T$  plots at 20 kOe ( $\square$ ), 180 Oe ( $\circ$ ), and 30 Oe ( $\Delta$ ).

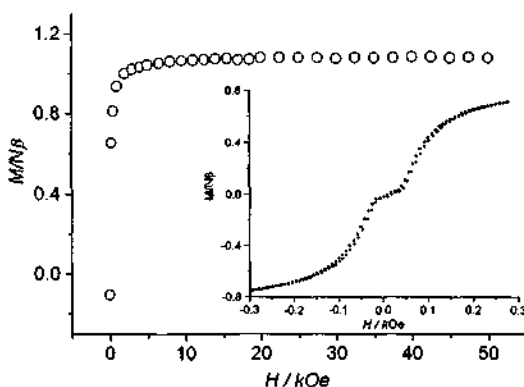


**Figure 8.** Field dependent magnetization and hysteresis loop (inset) for 4 at 1.8 K.

According to the structure, compound 4 contains  $\{\text{Cu}_3(\text{hedp})_2\}_{n}^{2n-}$  anionic layers separated by  $[\text{NH}_3(\text{CH}_2)_3\text{NH}_3]^{2+}$  cations and lattice water. Although the intra-layer interaction between the magnetic centers of copper is principally antiferromagnetic, the odd number of the Cu(II) ions in the trimer unit leads to a non-zero net magnetic moment, and hence an intra-layer ferrimagnetism in 4. At very low temperature, the antiferromagnetic interaction between the layers dominates, leading to an antiferromagnetic ground state at low external fields. This inter-layer antiferromagnetic interaction is so weak, however, when the external field approaches to a critical value (*ca.* 48 Oe for 4), the compound switches

from an AF ground state to a ferrimagnetic state. Similar metamagnetism is also observed in compound **5** with a critical field of *ca.* 185 Oe.

Compound **8** also shows metamagnetism at low temperature. The origin is, however, different from that for **4** and **5**. The structure **8** contains  $\{\text{Cu}_4(\text{hedp})_2(\text{H}_2\text{O})_2\}$  layers linked by pyrazine bridges. The exchange interactions within the phosphonate layer through the O-P-O bridges make a major contribution to the bulk magnetic behavior of **8**. An examination of the structure of the phosphonate layer reveals that it is composed of  $\{\text{Cu}_3(\text{hedp})_2(\text{H}_2\text{O})_2\}$  double chains linked by  $\{\text{Cu}(3)\text{O}_4\}$  units. The exchange within the  $\{\text{Cu}_3(\text{hedp})_2(\text{H}_2\text{O})_2\}$  double chain is antiferromagnetic, leading to non-zero net magnetic moment. The exchange between the chain and the Cu(3) atom, however, is ferromagnetic, indicated by the saturation magnetization of  $2.3 N\beta$  per Cu<sub>4</sub> unit at 1.93 K. At very low temperature, the inter-layer antiferromagnetic couplings through the pyrazine bridge and/or the space are dominant, yielding a weak three-dimensional AF ordering state below 4.2K. When a critical field of *ca.* 2-3 kOe is reached at 1.93 K, compound **8** switches from an AF ground state to a ferrimagnetic-like state.

For compound **7**, the dominant antiferromagnetic interactions are also observed. This interaction is mainly attribute to layer A, which is composed of equilateral triangle units of Cu<sub>3</sub>O, each edge-shared with three other equivalents. The predominant antiferromagnetic couplings within the Cu<sub>3</sub>O triangle of layer A are responsible to the spin frustration interfering with the magnetic ordering, as observed in compound **7**.

## 5 Conclusions

Twelve new Cu-hedp compounds have been prepared under hydrothermal conditions. Their structures range from one-dimensional chain to three-dimensional open framework. The results demonstrate that open framework copper phosphonates are feasible through either template approach or by introducing a second bridging ligand. Magnetic investigations on these compounds revealed interesting metamagnetism in several systems.

## 6 Acknowledgements

Support from the National Natural Science Foundation of China and the Natural Science Foundation of Jiangsu province is greatly acknowledged.

## References

1. Cao G., Hong H. and Mallouk T. E., Layered metal phosphonates: from crystals to monolayers, *Acc. Chem. Res.* 25 (1992) pp.420-427.
2. Alberti G., Layered metal phosphonates and covalently pillared diphosphonates, In *Comprehensive Supramolecular Chemistry*, ed. by Lehn J. M. (Pergamon, Elsevier Science, Ltd.: Oxford, U. K., 1996: vol. 7) pp. 151-187.
3. Clearfield A., Metal phosphonate chemistry. In *Progress in Inorganic Chemistry*, ed. by Karlin K. D. (John Wiley & Sons, Inc. New York, 1998, vol. 47) pp. 371-510.
4. Zhang B. and Clearfield A., Crown ether pillared and functionalized layered zirconium phosphonates: a new strategy to synthesize novel ion selective materials, *J. Am. Chem. Soc.* 119(1997) pp. 2751-2752.

5. Alberti G., Constantino U., Casciola M. and Vivani R., Layered and pillared metal(IV) phosphates and phosphonates, *Adv. Mater.* 8 (1996) pp. 291.
6. Snover J. L., Byrd H., Suponeva E. P., Vicenzi E. and Thompson M. E., Growth and characterization of photoactive and electroactive zirconium bisphosphonate multilayer films, *Chem. Mater.* 8 (1996) pp. 1490.
7. Zubieta J., Clusters and solid phases of the oxovanadium-phosphate and -organophosphonate systems, *Comments Inorg. Chem.* 16 (1994) pp. 153-183.
8. Zhang Y. and Clearfield A., Synthesis, crystal structures and coordination intercalation behavior of two copper phosphonates, *Inorg. Chem.* 31 (1992) pp. 2821-2826.
9. Le Bideau J., Bujoli B., Jouanneaux A., Payen C., Palvadeau P. and Rouxel J., Preparation and structure of  $\text{Cu}(\text{C}_2\text{H}_5\text{PO}_3)_2$ . structural transition between its hydrated and dehydrated forms, *Inorg. Chem.*, 32 (1993) pp. 4617-4620.
10. Le Bideau J., Payen C., Palvadeau P. and Bujoli B., Preparation, structure, and magnetic properties of copper(II) phosphonates.  $\beta\text{-Cu}(\text{CH}_3\text{PO}_3)_2$ , an original three-dimensional structure with a channel-type arrangement, *Inorg. Chem.* 33 (1994) pp. 4885-4890.
11. Clarke E. T., Rudolf P. R., Martell A. E. and Clearfield A., Structural investigation of the Cu(II) chelate of N-phosphonomethylglycine. X-ray crystal structure of  $\text{Cu}(\text{II})[\text{O}_2\text{CCH}_2\text{NHCH}_2\text{PO}_3]\text{Na}(\text{H}_2\text{O})_{3.5}$ , *Inorg. Chim. Acta*, 164 (1989) pp. 59-63.
12. Drumet S., Janvier P., Bujoli-Doeuff M. and Bujoli B., Synthesis and crystal structure of two members of a new type of layered compound: copper(II) hydroxyphosphonates, *Inorg. Chem.* 35 (1996) pp. 5786-5790.
13. Ayyappan P., Evans O. R., Foxman B. M., Wheeler K. A., Warren T. H. and Lin W., New open frameworks based on metal pyridylphosphonates, *Inorg. Chem.* 40 (2001) pp. 5954-5961.
14. Riou-Cavellec M., Sanselme M., Guillou N. and Ferey G., Hydrothermal synthesis and ab initio structural resolution from X-ray powder diffraction of a new open framework Cu(II) carboxyethylphosphonate:  $\text{Na}[\text{Cu}(\text{O}_3\text{P}-(\text{CH}_2)_2-\text{CO}_2)]$ , *Inorg. Chem.* 40 (2001) pp. 723-725.
15. Poojary D. M., Zhang B. and Clearfield A., Pillared layered metal phosphonates. Syntheses and X-ray powder structures of copper and zinc alkylenebis(phosphonates). *J. Am. Chem. Soc.* 119 (1997) pp. 12550.
16. Poojary D. M., Zhang B., Bellinghausen P. and Clearfield A. Synthesis and X-ray powder structures of two lamellar copper arylenebis(phosphonates), *Inorg. Chem.* 35 (1996) pp. 4942-4949.
17. Huan G., Johnson J. W., Jacobson A. J. and Merola J. S., Hydrothermal synthesis and single-crystal structural characterization of  $(\text{VO})_2[\text{CH}_2(\text{PO}_3)_2] \cdot 4\text{H}_2\text{O}$ , *J. Solid State Chem.* 89 (1990) pp. 220. Bonavia G., Haushalter R. C., O'Connor C. J. and Zubieta J., Structural variability of the vanadium-organodiphosphonate system: hydrothermal syntheses and structural characterizations of one-dimensional, two-dimensional, and three-dimensional phases, *Inorg. Chem.* 35 (1996) pp. 5603-5612. Gao Q., Guillou N., Nogues M., Cheetham A. K. and Ferey G., Structure and magnetism of VSB-2, -3, and -4 or  $\text{Ni}_4(\text{O}_3\text{PCH}_2\text{PO}_3)_2 \cdot (\text{H}_2\text{O})_n$  ( $n = 3, 2, 0$ ), the first ferromagnetic nickel(II) diphosphonates: increase of dimensionality and multiple coordination changes during a quasi topotactic dehydration. *Chem. Mater.* 11 (1999) pp. 2937-2947. Lohse D. L. and Sevov S. C.,  $\text{Co}_2(\text{O}_3\text{PCH}_2\text{PO}_3)_2 \cdot \text{H}_2\text{O}$ : a novel microporous diphosphonate with an inorganic framework and hydrocarbon-lined hydrophobic channels, *Angew. Chem. Int. Ed. Engl.* 36 (1997) pp. 1619.

18. Cheetham A. K., Ferey G. and Loiseau T., Open-framework inorganic materials, *Angew. Chem. Int. Ed.* 38 (1999) pp. 3268-3292. Lii K.-H., Huang Y.-F., Zima V., Huang C.-Y., Lin H.-M., Jiang Y.-C., Liao F.-L. and Wang S.-L., Syntheses and structures of organically templated iron phosphates, *Chem. Mater.* 10 (1998) pp. 2599-2609.
19. Zheng L.-M., Song H.-H. and Xin X.-Q., Syntheses and structures of transition metal-hedp compounds and the template influences (hedp = 1-hydroxyethylidenediphosphonate), *Comments Inorg. Chem.* 22 (2000) pp. 129-149.
20. Alberti G., Costantino U., Marmottini F., Vivani R. and Zappelli P., Zirconium phosphite (3,3',5,5'-tetramethyl-biphenyl)diphosphonate, a microporous, layered, inorganic-organic polymer, *Angew. Chem. Int. Ed. Engl.* 32 (1993) pp. 1357-1359. Clearfield A., Poojary D. M., Zhang B., Zhao B. and Derecskei-Kovacs A., Azacrown ether pillared layered zirconium phosphonates and the crystal structure of N,N'-bis(phosphonomethyl)-1,10-diaza-18-crown-6, *Chem. Mater.* 12 (2000) pp. 2745-2752.
21. Bujoli B., Pena O., Palvadeau P., Le Bideau J., Payen, C. and Rouxel J., Synthesis, structure and magnetic properties of a new lamellar iron phosphonate,  $\text{Fe}^{II}(\text{C}_2\text{H}_5\text{PO}_3)\cdot\text{H}_2\text{O}$ , *Chem. Mater.* 5 (1993) pp. 583.
22. Bellitto C., Federici F., Altomare A., Rizzi R. and Ibrahim S. A., Synthesis, X-ray powder structure, and magnetic properties of the new, weak ferromagnet iron(II) phenylphosphonate, *Inorg. Chem.* 39 (2000) pp. 1803-1808.
23. Bellitto C., Federici F. and Ibrahim S. A., Synthesis and magnetism of chromium(II) methylphosphonate,  $\text{Cr}(\text{MePO}_3)\cdot\text{H}_2\text{O}$ : a new weak ferromagnet, *Chem. Commun.* (1996) pp. 759-760.
24. Carling S. G., Visser D. and Kremer R. K., Weak ferromagnetic behavior of the manganese alkylphosphonate hydrates  $\text{MnC}_n\text{H}_{2n+1}\text{PO}_3\cdot\text{H}_2\text{O}$  ( $n = 1-4$ ), *J. Solid State Chem.* 106 (1993) pp. 111-119.
25. Rabu, P., Janvier, P. and Bujoli B., Magnetic properties of a new 3D-cobalt phosphonate:  $\text{Co}_3(\text{O}_3\text{PC}_2\text{H}_4\text{CO}_2)_2$ , *J. Mater. Chem.* 9 (1999) pp. 1323-1326.
26. Gutschke, S. O. H.; Price, D. J.; Powell, A. K.; Wood, P. T., Solvothermal synthesis of the canted antiferromagnet  $\{\text{K}_2[\text{CoO}_3\text{PCH}_2\text{N}(\text{CH}_2\text{CO}_2)_2]\}_6\cdot\text{xH}_2\text{O}$  *Angew. Chem. Int. Ed.* 38 (1999) pp. 1088-1090.
27. Song H.-H., Zheng L.-M., Liu Y.-J., Xin X.-Q., Jacobson A. J. and Decurtins S., Syntheses, structures and magnetic properties of two copper(II) diphosphonates:  $[\text{NH}_3(\text{CH}_2)_2\text{NH}_3]_2\text{Cu}_2(\text{hedp})_2\cdot\text{H}_2\text{O}$  and  $[\text{NH}_3\text{CH}(\text{CH}_3)\text{CH}_2\text{NH}_3]_2\text{Cu}_2(\text{hedp})_2$  (hedp = 1-hydroxyethylidenediphosphonate), *J. Chem. Soc. Dalton Trans.* (2001) pp. 3274-3278.
28. Zheng L.-M., Song H.-H., Duan C.-Y. and Xin X.-Q., Template directed one- and two-dimensional Copper diphosphonates:  $(\text{NH}_4)_2\text{Cu}_3(\text{hedp})_2\cdot(\text{H}_2\text{O})_4$ ,  $[\text{NH}_3(\text{CH}_2)_4\text{NH}_3]_2\text{Cu}_3(\text{hedp})_2\cdot2\text{H}_2\text{O}$  and  $[\text{NH}_2(\text{C}_2\text{H}_4)_2\text{NH}_2]_2\text{Cu}_3(\text{hedp})_2$  (hedp = 1-hydroxyethylidenediphosphonate) *Inorg. Chem.* 38 (1999) pp. 5061-5066.
29. Zheng L.-M., Gao S., Song H.-H., Decurtin S., Jacobson A. J. and Xin X. Q., Metamagnetic Copper(II) Diphosphonates with Layered Structures, *Chem. Mater.* In revision.
30. Zheng L.-M., Duan C.-Y., Ye X.-R., Zhang L.-Y., Wang C. and Xin X.-Q., Synthesis, crystal structure and magnetic properties of a novel mixed-valence copper phosphonate:  $\text{Na}_2\text{Cu}_{15}(\text{hedp})_6(\text{OH})_2(\text{H}_2\text{O})$  (hedp = 1-hydroxyethylidene-diphosphonate), *J. Chem. Soc., Dalton Trans.* (1998) pp. 905-908.
31. Yin P., Zheng L.-M., Gao S. and Xin X.-Q.,  $\text{Cu}_4\{\text{CH}_3\text{C}(\text{OH})(\text{PO}_3)_2\}_2(\text{C}_4\text{H}_4\text{N}_2)(\text{H}_2\text{O})_4$ :

- a novel three dimensional copper diphosphonate with metamagnetism, *Chem. Commun.* (2001) pp. 2346-2347.
- 32. Yin P., Zheng L.-M. and Xin X.-Q., unpublished results.
  - 33. Yin P., Zheng L.-M., Peng Y. and Xin X.-Q., unpublished results.
  - 34. Zheng L.-M., Yin P. and Xin X.-Q., A Novel Coordination Polymer Containing a Mixed Valence Copper(I,II) Phosphonate Unit:  $Cu^{I,II}_2(hedpH_2)_2(4,4'-bpy)_2 \cdot 2H_2O$  (hedp = 1-hydroxy-ethylidenediphosphonate), *Inorg. Chem.* in revision.

# THREE-DIMENSIONAL NETWORK WITH CAVITIES CREATED BY HYDROGEN BONDS IN PROTOCATECHUIC ACID/COPPER (II) SYSTEM

LONG-GUAN ZHU

*Department of Chemistry, Zhejiang University, Hangzhou 310027, P. R. China*

*E-mail: chezlg@zju.edu.cn*

SUSUMU KITAGAWA

*Department of Synthetic Chemistry and Biological Chemistry, Graduate School of Engineering,*

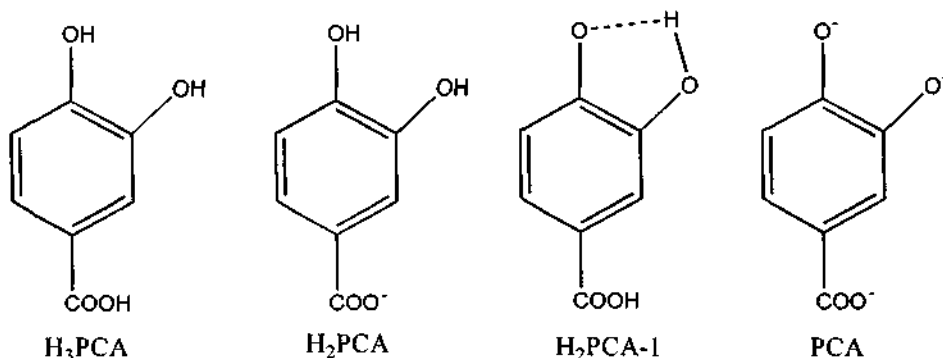
*Kyoto University, Kyoto 606-8501, Japan*

*E-mail: kitagawa@sbchem.kyoto-u.ac.jp*

A new complex,  $\{\text{Cu}_2(\text{phen})_6(\text{H}_3\text{PCA})_4(\text{NO}_3)_4 \cdot 2\text{H}_2\text{O}\}$  (1), was synthesized and structurally characterized. Crystal data for the complex 1 are as follows:  $\text{Cu}_2\text{C}_{100}\text{N}_{16}\text{O}_{30}\text{H}_{76}$ , FW=2108.88, monoclinic, space group Cc,  $a=1.0039(1)$  nm,  $b=3.9152(5)$  nm,  $c=2.41074(7)$  nm,  $\beta=102.0370(7)^\circ$ ,  $V=9.267(1)$  nm<sup>3</sup>,  $Z=4$ ,  $R_1=0.053$  and  $R_{\text{w}}=0.058$ . The complex is composed of copper cations, nitrate anions, 1,10-phenanthroline, protocatechuic acid and lattice water molecules. The structure of H<sub>3</sub>PCA, NO<sub>3</sub><sup>-</sup> and waters comprises packing of three-dimensional network by hydrogen bonds with cavities. The complex can be considered as a model of host/guest supermolecule. The three-dimensional hydrogen-bonding network is the host species. The Cu(phen)<sub>3</sub><sup>2+</sup> cations, guest species, occupy the cavities of the host.

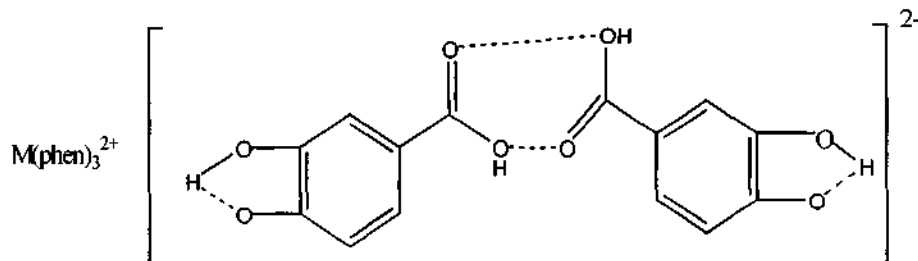
## 1 Introduction

Complexes of protocatechuic acid are of continuous interest from structural and biological viewpoints [1-2]. Protocatechuic acid (H<sub>3</sub>PCA, see scheme 1) is a multi-functional ligand and most of researches were done in solution [3-7] while limited solid complexes were reported [8-12]. Many efforts were devoted to obtain crystals of complexes of protocatechuic acid, but only one crystal structure was occasionally solved [13]. On the biological side, people have been motivated to study this ligand chiefly by the fact that in living systems, like plants or microorganisms, compounds bearing H<sub>3</sub>PCA serve as versatile ligands to chelate toxic and nutrient metal ions. On the structural side, there are some reasons for us to build polymeric networks used in



Scheme 1 Structural forms of protocatechuic acid and protocatechuates

gas adsorption using H<sub>3</sub>PCA ligand, for example, Gerega et al. [14] suggested several interesting structures of Cu<sub>3</sub>(PCA)<sub>2</sub>. Interestingly, two strange compounds, M(phen)<sub>3</sub>(PCAH<sub>2</sub>-1)<sub>2</sub>(2H<sub>2</sub>O) [M=Co, Ni], reported in reference [15] also raised our interest to check the coordination nature of the H<sub>3</sub>PCA ligand.



Scheme 2 The strange structure suggested by Iyer

## 2 Experimental

### 2.1 Synthesis

A mixture of 0.234 g Cu(NO<sub>3</sub>)<sub>2</sub>·3H<sub>2</sub>O, 0.539 g phen·H<sub>2</sub>O, 0.297 g H<sub>3</sub>PCA and 50 mL water was heated up to 70 °C with stirring. At that temperature the volume of the solution was reduced to ca. 10 mL. The solution at room temperature in the air was slow evaporated, after some days crystals were obtained. Elemental analysis for the compound of {Cu<sub>2</sub>(phen)<sub>6</sub>(H<sub>3</sub>PCA)<sub>4</sub>(NO<sub>3</sub>)<sub>4</sub>·2H<sub>2</sub>O}: C, 57.31%; N, 10.69%; H, 3.85%. Found: C, 57.00%; N, 10.58%; H, 3.72%. IR(cm<sup>-1</sup>): 1644(s), 1598(s), 1519(m), 1460(m), 1429(s), 1385(s), 1297(s), 1247(s), 1142(w), 1097(m), 948(w), 865(w), 846(s), 825(w), 768(m), 725(s), 638(w), 567(w), 461(w).

### 2.2 Crystallography

A green plate crystal having approximate dimensions of 0.5 mm×0.30 mm×0.10 mm was mounted on a glass fiber. The data were collected at 173 K on a Rigaku Mercury CCD diffractometer with graphite monochromated MoKα ( $\lambda=0.071069$  nm) radiation to a maximum 2θ value of 54.3°. A total of 33695 reflections were collected and 10181 were unique ( $R_{\text{int}}=0.018$ ). The data were corrected for Lorentz and polarization effects. The structure was solved by heavy-atom Patterson methods and expanded using Fourier techniques. The non-hydrogen atoms were refined anisotropically. Hydrogen atoms were included but not refined. The final cycle of full-matrix least-squares refinement was based on 7947 observed reflections ( $I>3.0\sigma(I)$ ) and 1338 variable parameters and converged with unweighted and weighted agreement factors of  $R=0.053$  and  $R_w=0.058$ . All computations are carried on an OS2 workstation using teXsan software [16]. Drawings were produced with ORTEP-3 program [17]. Crystal data for the complex are as follows: Cu<sub>2</sub>C<sub>100</sub>N<sub>16</sub>O<sub>30</sub>H<sub>76</sub>, FW=2108.88, the crystal is monoclinic, space group Cc, with  $a=1.0039(1)$  nm,  $b=3.9152(5)$  nm,  $c=2.41074(7)$  nm,  $\beta=102.0370(7)$ °,  $V=9.267(1)$

$\text{nm}^3$ ,  $Z=4$ ,  $D_c=1.511 \text{ g/cm}^3$ ,  $\mu(\text{MoK}\alpha)=5.54 \text{ cm}^{-1}$  and  $\text{GOF}=2.57$ .

### 3 Results and Discussion

The ORTEP viewing of the molecule is shown in Figure 1. The complex is composed of copper cations, nitrate anions, 1,10-phenanthroline, protocatechuic acid and lattice water molecules. The copper atom has an octahedral geometry and the average bond length of Cu-N is 0.2134(4) nm. The packing viewing of cations is depicted in Figure 2. The structure of  $\text{H}_3\text{PCA}$ ,  $\text{NO}_3^-$  and waters comprises packing of three-dimensional network by hydrogen bonds with cavities. In the hydrogen-bonding network there are four types of hydrogen bonds between water, nitrate and  $\text{H}_3\text{PCA}$  and listed in Table 1. The three-dimensional hydrogen-bonding network can be considered as the host species. The  $\text{Cu}(\text{phen})_3^{2+}$  cation, guest species, occupied the cavities of the host. The model of host/guest complex is shown in Figure 3.

From our synthetic and crystallographic results, it is obvious that Iyer et al. made a big mistake for their synthetic procedure and characterization. In this text, we used the starting material of  $\text{Cu}(\text{NO}_3)_2$ , however Iyer selected the starting material of  $\text{CuSO}_4$ . To get the clear understanding, we also used the starting material of  $\text{CuSO}_4$ . The experimental characterization and single-crystal X-ray analysis show us that the resulting compound is  $\text{Cu}(\text{SO}_4)(\text{phen})_3(\text{H}_3\text{PCA})_2 \cdot 8\text{H}_2\text{O}$ , in which the  $\text{H}_3\text{PCA}$  ligands are neutral. So we can conclude that systems of  $\text{Cu}(\text{NO}_3)_2/\text{phen}/\text{H}_3\text{PCA}$  or  $\text{CuSO}_4/\text{phen}/\text{H}_3\text{PCA}$  result in the compounds containing neutral  $\text{H}_3\text{PCA}$  ligand.

Table 1. Hydrogen bonds in complex 1.

Hydrogen bond	Bond length (nm)
$\text{O}(\text{NO}_3^-)\dots\text{H}-\text{O}(\text{w})$	0.2848, 0.283
$\text{O}(\text{NO}_3^-)\dots\text{H}-\text{O}(\text{H}_3\text{PCA})$	0.2778, 0.297
$\text{O}(\text{w})\dots\text{H}-\text{O}(\text{H}_3\text{PCA})$	0.2711, 0.2707
$\text{O}\dots\text{H}-\text{O}(\text{between two H}_3\text{PCA})$	0.261, 0.258

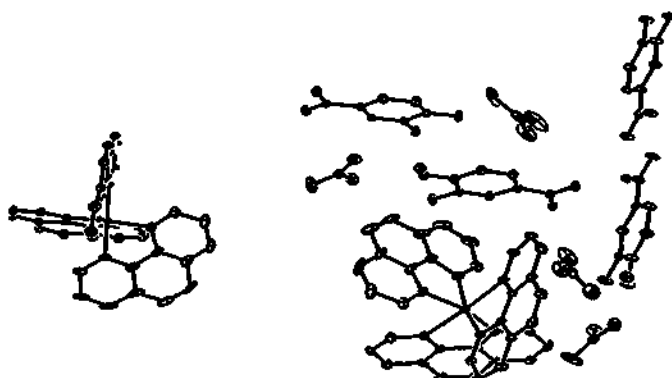


Figure 1. ORTEP viewing of the complex 1.

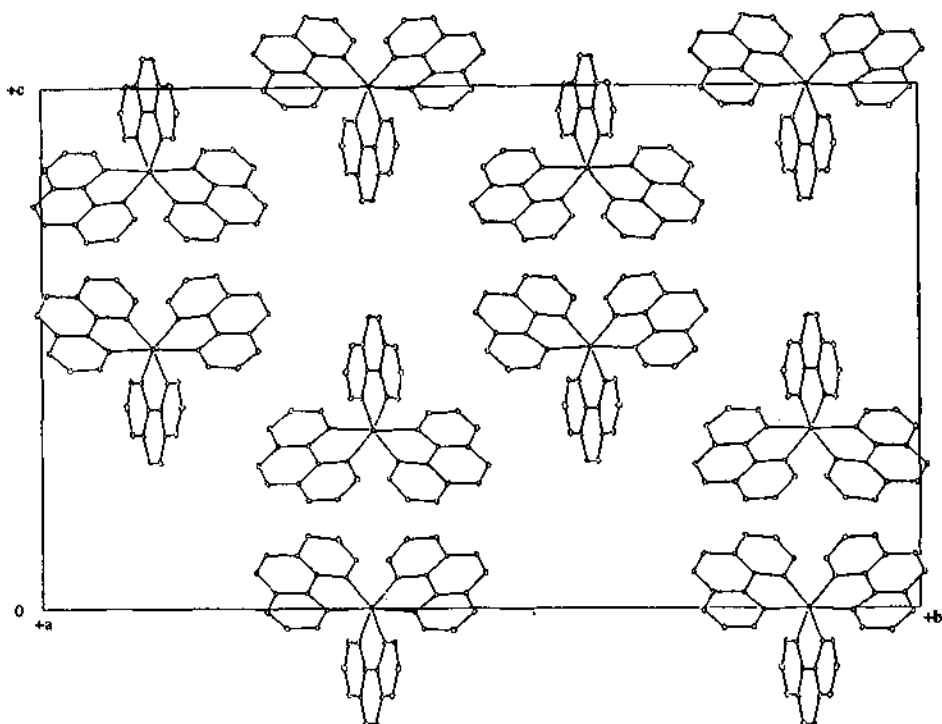


Figure 2. Packing viewing of  $[\text{Cu}(\text{phen})_3]^{2+}$  in the complex 1.

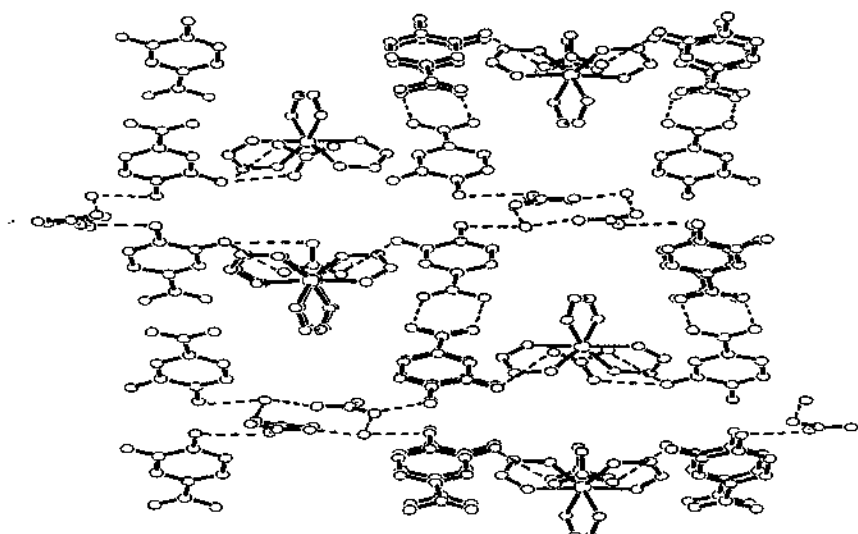


Figure 3. The hydrogen-bonding network of the complex 1.

#### 4 Acknowledgements

Dr Zhu thanks the financial supports from the National Natural Science Foundation of China (No. 50073019 ) and the State Key Laboratory of Inorganic Synthesis and Preparative Chemistry (No. 2000-005).

#### 5 References

1. Lu F. J., Tseng S. N., Li M. L and Shih S.R., In vitro anti-influenza virus activity of synthetic humate analogues derived from protocatechuic acid. *Archives of Virology* **147**(2002) pp.273-284.
2. Zheng Y., Massey V., Schaller A., Palfey B. A. and Carey P. R., Comparison of resonance Raman spectra of flavin-3,4-dihydroxybenzoate charge-transfer complexes in three flavoenzymes. *J. Raman Spectro.* **32** (2001) pp. 579-586.
3. Dhir L., Diwan B. D. and Mundhara G. L., Physico-chemical investigation on some mixed-ligand complexes of dioxouranium (VI). *Asian J. Chem.* **12**(2000) pp.1247-1254.
4. Sharma S., Vora J. J. and Joshi J. D., Equilibrium studies on some chelates of Nd(III), Ho(III), Yb(III) with phenols containing O-O donor atoms. *J.Indian Counc. Chem.* **13** (1997) pp.55-57.
5. Patel V. M. and Joshi J. D., Equilibrium study on the complex formation of europium-, terbium-, dysprosium- and thulium (III) with some oxyacids, thioacids and phenols. *J. Indian Chem. Soc.* **75** (1998) pp. 100-101.
6. Deng J. C., Zhong C. F., Zhao H. B. and Tong J., Coordination of rare earth elements with derivatives of catechol. *Chin. J. Inorg. Chem.* **12**(1996) pp. 362-367.
7. Chitale V. K. and Pitre K. S., A polarographic study of the composition and stability constants of benzoate, protocatechuate and salicylate complexes of neodymium (III). *Natl. Acad. Sci. Lett.* **4** (1981) pp. 247-248.
8. Ali S. F. M., Complexes of protocatechuic acid with lanthanides. *Curr. Sci.* **46** (1977) pp. 812-813.
9. Deng J. C., Xiang N. J., Li Z. F. and Chen Q. Y., Study on coordination and transformation reaction of iron (II) with 3,4-dihydroxybenzoic acid. *Natural Sci. J. Xiangtan University* **23** (2001) pp. 41-43.
10. Deng J. C., Zhu M. X., Zhong C. F. and Tong J., The coordination of rare earth elements with derivatives of catechol. *Chem. J. Chin. Universities* **19**(1998) pp. 1016-1019.
11. Deng J. C., Zhong C. F. and Tong J., Oxidation colouring mechanism of cerium with catechol derivatives. *J. Chin. Rare Earth Soc.* **15**(1997) pp. 252-256.
12. Karaliota A., Kamariotaki M., Hadjipanagioti D. and Aletras V., Molybdenum catecholates as models for Mo in biological systems. 1. Synthesis and spectroscopic study on Mo complexes with 3,4-dihydroxybenzoic and 3,4-dihydroxyphenylacetic acid. *J. Inorg. Biochem.* **69** (1998) pp. 79-90.
13. Aletras V., Hadjiliadis N., Stabaki D., Karaliota A., Kamariotaki M., Butler I., Plakatouras J. C. and Perlepes S., Preparation and characterization of the seven

- coordinate cadmium(II) complex  $[\text{Cd}(3,4\text{-dhb})_2(\text{H}_2\text{O})_3]\text{center dot HCl center dot}(3,4\text{-dhb})\text{center dot }2.5\text{H}_2\text{O}$ ; The first structural determination of a complex containing the 3,4-dihydroxybenzoato ligand. *Polyhedron* **16** (1997) pp. 1399–1402.
- 14. Gerega K. and Kozłowski H., Cupric complexes with 3,4-dihydroxybenzoic acid. *Inorg. Chim. Acta* **138**(1987) pp.31-34.
  - 15. Iyer H. P., Ramanathan P. S. And Venkateswarlu C., Tris(phenanthroline) compounds of cobalt and nickel with catechol and protocatechuic acid. *J. Inorg. Nucl. Chem.* **40**(1978) pp.1704-1705.
  - 16. Molecular Structure Corporation, teXsan: Crystal structure analysis package, 1999.
  - 17. Farrugia L J., ORTEP-3 for windows --- a version of ORTEP-III with a graphical user interface (GUI). *J. App. Cryst.* **30**(1997) pp. 30.

## POROUS CRYSTALLINE MATERIALS CONSTRUCTED BY COMPLEX CATIONS AND BULKY ARENEDISULFONATE COUNTER ANIONS

JIWEN CAI,\* XIAO-PENG HU, JUN FENG AND XIAO-LONG FENG

*School of Chemistry and Chemical Engineering, Sun Yet-Sen (Zhongshan) University, Guangzhou 510275, P. R. China  
E-mail: pscjw@zsu.edu.cn*

Crystal structures of  $[\text{Co}(\text{trien})(\text{phen})](1,5\text{nds})_{1,5}(\text{phen})_2(\text{H}_2\text{O})_8$  (1) and  $[\text{Co}(\text{en})_2(\text{phen})](1,5\text{nds})_{1,5}(\text{H}_2\text{O})_7$  (2) ( $1,5\text{nds}$  = 1,5-naphthalenedisulfonate) illustrate that porous crystalline materials which can intercalate large organic molecules can be constructed using complex cations and bulky organic counter anions.

### 1. Introduction

Promising application of porous crystalline materials include separation, shape-selective catalysis, trapping and storage of toxic materials, off-peak energy storage, and heterogeneous catalysis [1-3]. Efforts have been devoted to creating porous lattices which can accommodate guest molecules, in the meantime having certain kind of selectivity [4-6]. The general approach toward the construction of porous coordination network is the use of coordination polymerization to align inorganic complexes [7-9]. A number of boxes and a wide range of infinite frameworks, including diamondoid, honeycomb, grid, T-shaped, ladder, brick wall, and octahedral frameworks, have been generated with simple, linear spacers such as 4, 4'-bipyridine and pyrazine [10]. However, only a few of them have created efficient spaces to host guest molecules.

Previous studies about the structures of metal naphthalenesulfonate and benzenesulfonate salts have been carried out in order to produce structural analogs of metal-phosphates, a class of porous materials which have been heavily studied with two-dimensional metal-oxygen-nonmetal or metal-oxygen-metal frameworks [11-16], due to their potential use as host structures for various chemical process. However, these metal naphthalenesulfonate and benzenesulfonate salts have high tendency to segregate into layered structures [12-16]. Very recently, the Shimizu's group reported that silver sulfonates can intercalate guest molecules such as alcohol and MeCN [17,18], and the origin of the absorption is the flexible coordination behavior of the  $\text{SO}_3^-$  group. This result is in line with our observation that the coordination mode and strength of the sulfonate anions can be modified by other organic ligand, such as amines [19,20].

Herein we wish to report another approach, namely the use of the coordination complexes and bulky organosulfonate counter anions as building blocks, to generate porous ionic network which intercalates 1,10-phenanthroline or water guest molecules. The structures of adduct  $[\text{Co}(\text{trien})(\text{phen})](1,5\text{NDS})_{1,5}(\text{phen})_2(\text{H}_2\text{O})_8$  (1) and  $[\text{Co}(\text{en})_2(\text{phen})](1,5\text{NDS})_{1,5}(\text{H}_2\text{O})_7$  (2), (trien=triethylenetetraamine, en=ethylenediamine, phen=1,10-phenanthroline, 1,5nds=1,5-naphthalenedisulfonate) represents a novel example in which large organic guest molecules, such as 1,10-phenanthroline, can be clathrated into a porous network generated by bulky fragments of coordination complexes and organic counter ions.

## 2. Experimental

**Compound 1:** *cis*-[Co(trien)Cl<sub>2</sub>]Cl, phen and 1,5-naphthalenedisulfonate sodium salt were mixed in aqueous (molar ratio 1:1.5:1.5) solution, which was stirred and warmed at 50°C for 2 hours. The resulting solution was kept at room temperature and crystals suitable for x-ray analysis were obtained after a few days. Compound 2 was obtained using the same procedure as that of 1, except that *cis*-[Co(en)<sub>2</sub>Cl<sub>2</sub>]Cl was used instead of *cis*-[Co(trien)Cl<sub>2</sub>]Cl.

Crystal data. Compound 1: C<sub>57</sub>H<sub>67</sub>CoN<sub>10</sub>O<sub>17</sub>S<sub>3</sub>,  $M=1319.32$ , Monoclinic,  $C2/c$ ,  $\alpha=38.825(6)$ ,  $b=21.872(3)$ ,  $c=14.004(2)$  Å,  $\beta=90.211(3)^\circ$ ,  $U=11892(3)$  Å<sup>3</sup>,  $T=293$  K,  $z=8$ ,  $\rho=1.474$  Mg/m<sup>3</sup>,  $\mu(\text{MoK}\alpha)=0.474$  mm<sup>-1</sup>, 41137 reflections measured, 10139 unique ( $R_{\text{wu}}=0.0564$ ) which were used in all calculations. The final  $R_1$  and  $wR_2(F^2)$  are 0.0697, 0.2051 for strong reflections ( $I > 2\sigma(I)$ ), 0.1174 and 0.2450 for all data. Compound 2: C<sub>31</sub>H<sub>47</sub>CoN<sub>8</sub>O<sub>16</sub>S<sub>3</sub>,  $M=914.86$ , Triclinic,  $P-1$ ,  $a=12.455(2)$ ,  $b=13.417(2)$ ,  $c=13.942(2)$  Å,  $\alpha=83.757(3)$ ,  $\beta=69.208(3)$ ,  $\gamma=78.406(3)^\circ$ ,  $U=2131.9(6)$  Å<sup>3</sup>,  $T=293$  K,  $z=2$ ,  $\rho=1.425$  Mg/m<sup>3</sup>,  $\mu(\text{MoK}\alpha)=0.622$  mm<sup>-1</sup>, 12118 reflections measured, 8595 unique ( $R_{\text{wu}}=0.0307$ ) which were used in all calculations. The final  $R_1$  and  $wR_2(F^2)$  are 0.0631 and 0.1959 for strong reflections ( $I > 2\sigma(I)$ ), 0.0997 and 0.2199 for all data.

All diffraction data were collected on a Bruker Smart 1000 CCD diffractometer. Absorption correction was applied by SADABS [21]. In all cases, the structures were solved by direct methods and refined using full-matrix least-squares/difference Fourier techniques using SHELXTL [22]. All non-hydrogen atoms were refined with anisotropic displacement parameters. After that, all hydrogen atoms of the organic groups were placed at idealized positions and refined as riding atoms with the relative isotropic parameters of the heavy atoms to which they are attached. Hydrogens of water molecules were not located.

Crystallographic data (excluding structure factors) for the structures reported in this paper have been deposited with the Cambridge Crystallographic Data Center. Copies of the data can be obtained free of charge on application to CCDC, 12 Union Road, Cambridge CB2 1EZ, UK.

## 3. Results and Discussion

Compound 1 crystallizes with a large cell volume close to 12,000 Å<sup>3</sup>. The cobalt (III) atom is six-coordinated to 4 nitrogens from the trien ligand and two nitrogens from the phen ligand in a standard octahedral fashion, with bond lengths range from 1.954(4) to 1.970(4) Å. As indicated in Fig.1, channels running along the crystallographic *c* axes are generated between two layers of complex cations, which are supported by selective hydrogen bonding interaction formed between the amine hydrogen and sulfonate oxygen, as illustrated in Fig. 2. Each complex cation is involved in hydrogen bonding interactions with two 1,5-naphthalenedisulfonate ions. The 1,10-phenanthroline guest molecules are intercalated into the channel and stabilized by hydrogen bonds and π-π interactions with the host complexes (N4...N10=2.92 Å, shortest interplane atom-atom distance of the host and guest phen is 3.35 Å, the dihedral angle between the phen planes is 5.7°). The coordinated phen ligands and the clathrated phen molecules stack on top of each other and aggregate into columns along the crystallographic *a* axis via π-π interaction.

When the tetradeinate ligand trien is substituted by two bidentate ligands, namely ethylenediamine, the resulting compound 2 adopts another type of packing mode, in which each complex cation forms extensive hydrogen bonding interactions with 1,5-

naphthalenedisulfonate anions, and *vice versa*. However, because of the non-complementary topology of the complex cation and the organic anion, large cavities running along the crystallographic *b* axis are generated and filled by crystalline water molecules, as shown in Fig. 3.

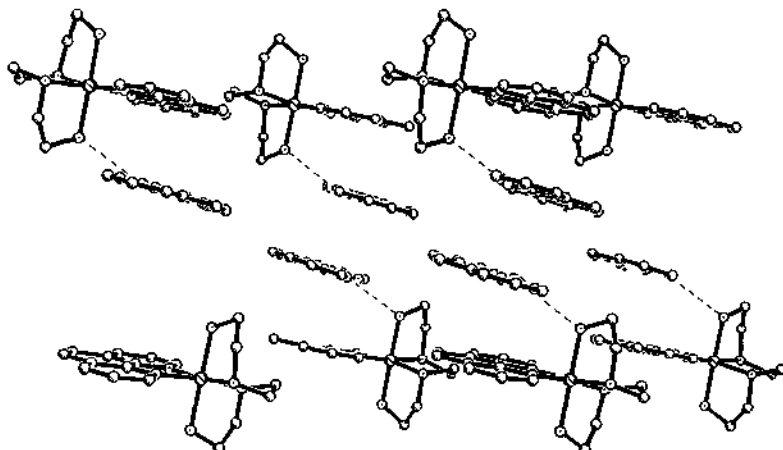


**Figure 1.** Intercalation of the guest phen molecules into the channel formed between two layers of complex cations observed in compound 1.

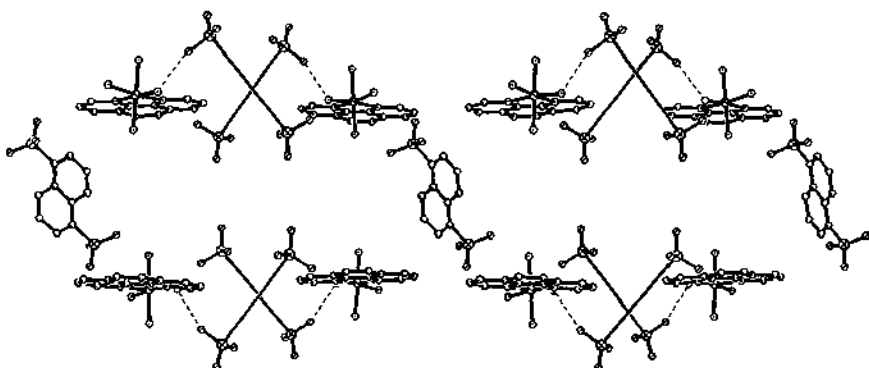


**Figure 2.** Illustration of the construction of porous structure by the complex cation and 1,5NDS anion in compound 1. The guest phen molecules, crystalline water, hydrogen and carbon atoms of the trien ligand are omitted, and the naphthalene rings of 1,5NDS anions between the complex cations are represented by lines drawn between the S atoms, for clarity.

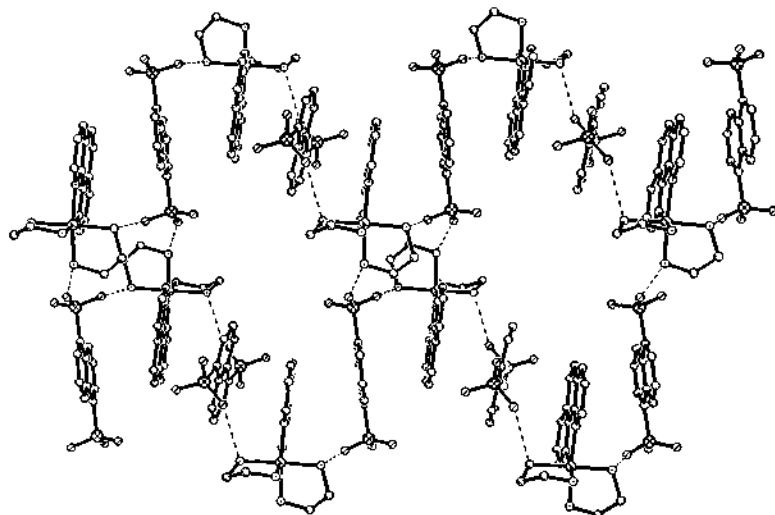


**Figure 3.** Packing feature of compound 2, illustrating the large pore when looking down along the  $\delta$  axis, which are packed with crystalline water molecules. Water molecules and hydrogen atoms are omitted for clarity.

Herein we have demonstrated that by incorporating organic ligands, metal naphthalenedisulfonate can form porous host framework, with the size and polarity tunable through the use of different organic groups.

#### 4. Acknowledgements

This work was supported by the Guangdong Provincial Natural Science Foundation of China (No.990208).

#### References

1. Fujita M., Kwon Y. J., Washizu S. and Ogura K., *J. Am. Chem. Soc.*, **116** (1994), 1151.
2. Yaghi O. M. and Li H., *J. Am. Chem. Soc.*, **117** (1995), 10401.
3. Endo K., Koike, T., Sawaki T., Hayashida O., Masuda, H. and Aoyama, Y., *J. Am. Chem. Soc.*, **119** (1997), 4117.
4. Russell V. A., Evans C. C., Li W. and Ward M. D., *Science*, **276** (1997), 575-579.
5. Swift J. A., Pivovar A. M., Reynolds A. M. and Ward M. D., *J. Am. Chem. Soc.*, **120** (1998), 5887-5894.
6. Swift J. A., Reynolds A. M. and Ward M. D., *Chem. Mater.*, **10**(1998), 4159-4163.
7. Zimmer S. C., *Science*, **276** (1997), 543-544.
8. Munakata M., Wu L. P., Yamamoto M., Kuroda-Sowa T., Maekawa M., *J. Am. Chem. Soc.*, **118** (1996), 3117-3124.
9. Hunter C. A., *Angew. Chem. Int. Ed. Engl.*, **34** (1995), 1079-1081.

10. Tong M-L., Ye B-H., Cai J., Chen X-M. and Ng S. W., *Inorg. Chem.*, **37** (1998), 2645-2650 and the references cited therein.
11. Thompson M. E., *Chem. Mater.*, **6** (1994), 1168-1175.
12. Gunderman B. J. and Squattrito P. J., *Inorg. Chem.*, **34** (1995), 2399-2406.
13. Kosnic E. J., McClymont E. L., Hodder R. A. and Squattrito P. J., *Inorg. Chim. Acta*, **201** (1992), 143-151.
14. Gunderman B. J. and Squattrito P. J., *Inorg. Chem.*, **33** (1994), 2924-2931.
15. Gunderman B. J., Kabell I. D., Squattrito P. J. and Dubey S. N., *Inorg. Chim. Acta*, **258** (1997), 237-246.
16. Shubnell A. J., Kosnic E. J. and Squattrito P. J., *Inorg. Chim. Acta*, **216** (1994), 101-112.
17. Côté A. P., Ferguson M. J., Khan K. A., Enright G. D., Kulynych A. D., Dalrymple S. A. and Shimizu, G. K. H., *Inorg. Chem.* **41** (2002), 287.
18. Mäkinen S. K., Melcer N. J., Parvez M. and Shimizu G. K. H., *Chem. Eur. J.*, **7** (2001), 5176.
19. Cai, J. W.; Chen, C. H.; Liao, C. Z.; Yao, J. H.; Hu, X. P.; Chen, X. M. *J. Chem. Soc., Dalton Trans.* (**2001**), 1137.
20. Cai J. W., Chen C. H., Liao C. Z., Feng X. L. and Chen X. M., *J. Chem. Soc., Dalton Trans.*, (**2001**), 2370.
21. Blessing R. *Acta Cryst.*, **A51**(1995), 33-38.
22. Sheldrick G. M., SHELX97, Program for X-ray Crystal Structure Solution and Refinement. Göttingen University, Germany, 1997.

This page is intentionally left blank

## **Part IV**

### **Nano-Materials and Inorganic Films**

This page is intentionally left blank

## CHARACTERIZATION OF SPUTTERED THIN FILMS OF INDIUM TIN OXIDE

H.-N. CUI<sup>a,b</sup> AND V. TEIXEIRA<sup>a</sup>

<sup>a</sup> IMAT-Materials Institute, Department of Physics, University of Minho, Campus de Gualtar, P-4710-057 Braga, PORTUGAL  
E-mail: vasco@fisica.uminho.pt

<sup>b</sup> Laboratory of Rare Earth Chemistry and Physics, Changchun Institute of Applied Chemistry, Chinese Academy of Sciences, Chang Chun, 130022, P. R. China  
E-mail: cui@fisica.uminho.pt

ITO films have been deposited onto glass substrates by d.c. reactive magnetron sputtering. The effects of thermal annealing on the properties of the films in air atmosphere were investigated from 25 °C to 700 °C. The transmittance, sheet resistance, surface roughness, structure, energy band gap and Figure of Merit of the films were discussed. The film, which exhibited high optical transmittance and conductivity, shows more practical application as electrode for most types of large area devices due to this fabricating method of high sputtering rate and less expense.

### 1 Introduction

Indium tin oxide thin films, commonly referred to as ITO, have a high transmittance to visible, a low electrical resistivity, good substrate adherence, certain hardness and chemical inertness. They have been found extensive applications in photoelectron devices, flat panel display, touch sensitive coating, sensor and electrochromic window. Though many deposition technologies have been used to fabricate ITO films, among the techniques available for ITO thin film production, sputtering is the most widely investigated. Although in our previous and other authors study it has reported the preparation of high conductive ITO films using low temperature (T) deposition processes by radio frequency (r.f.) sputtering [1-4], there are few reports for the purpose using direct current (d.c.) magnetron sputtering at room temperature (RT) [5]. The high transmittance and conductance is difficult to attain in ITO film that are prepared at RT or post-annealing at low T by magnetron sputtering [6, 7]. Using sputtering and electron beam evaporation at low T have often resulted in films with poor electrical properties. The attainments of good properties of ITO films are strongly dependent on the growth conditions such as oxygen partial pressure ( $P_{O_2}$ ) and temperature. The former determines the oxidation state, while the latter controls the activation of cation (Sn) and oxygen vacancies in the film. We have studied the effect of  $P_{O_2}$  [8] and low T (< 300 °C) annealing in air and vacuum atmosphere [9]. Here RT growing and high temperatures up to 700 °C post-annealing are studied.

### 2 Experimental

The ITO target used had a diameter of 85 mm, which contained pure  $In_2O_3$  and 10 wt %  $SnO_2$ -doped. This commercially available high purity (99.99%) targets was from Goodfellow Cambridge Limited. The base pressure of the vacuum chamber was pumped to less than  $1 \times 10^{-3}$  Pa. The total pressure during deposition was kept constant at  $2 \times 10^{-1}$  Pa

while the oxygen partial pressure  $P_{O_2} = P(O_2)/[P(O_2) + P(Ar)]$  (where  $P(O_2)$  and  $P(Ar)$  is the pressure of gas by penning) is chose to 10.4%. The sputtering power applied was 90 W. The deposition process took place at RT for 1 hour per sample. After deposition an annealing up to 760 °C was carried out in an air ambient atmosphere. The film transmittance, absorption, diffuse and specular reflectance were measured in UV-visible-near infrared (UV-Vis-NIR) region by a double beam spectrophotometer of Shimadzu UV-3101PC. The film thickness and morphology were measured or valued with SEM supplied by Leica-Cambridge S360 and spectra method. The sheet resistance was determined by using a four-point-probe-system. The microstructures of the films were determined by x-ray diffraction (XRD) diffractometer (Philips PW-1710 with Cu K $\alpha$  radiation) and energy dispersion of x-ray (EDX, Link eXLII -pentafet Oxford, UK) and atomic force microscopy (AFM, Multimode TM SPM 3, Digital Instruments Nanoscope).

### 3 Results and Discussion

#### 3.1 Sheet Resistance of the Films

The data of the sheet resistance ( $R_s$ ) treated in air is shown in Table 1. The 188 nm thickness films as deposited (sample 1) yielded the  $R_s$  of 121.5 Ω·m. The  $R_s$  decreased sharply with an increase in the range of annealing T less 220 °C in air [9]. They had much lower  $R_s$  than that of as-deposited film. After annealing of 220 °C, the  $R_s$  increased from 59.7 Ω·m to 234.3 Ω·m with increasing T. For the sample annealed in vacuum there is a similar regularity of the air annealing at lower T less than 300 °C [9]. If annealing T is above 300 °C, the  $R_s$  becomes bigger than that of the as-deposited ITO film, the biggest one reaches 234.3 Ω·m at 540 °C and the glass substrate begins deform from 620 °C. These results thus showed a regularity of the temperature effect on the conductivity of the films.

Table 1. The parameters of the ITO films annealed in air.

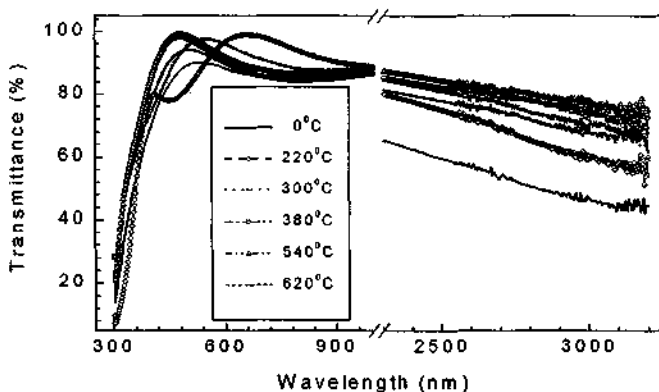
Samp.	Anne T (°C)	$R_s(\Omega \cdot m)$	$E_g(eV)$	$T_{max}(\%)$	$\delta(nm)$	$\Phi_{max}(10^{-3}\Omega^{-1})$
1	-	121.1	3.78	91	12.5	7.5
2	220	59.7	3.66	99	12.8	16.5
3	300	212.4	3.85	96	12.7	4.5
4	380	228.1	3.85	97	13.2	4.3
5	460	232.4	3.86	97	13.5	4.2
6	540	234.3	3.87	98	13.8	4.2
7	620	big	3.88	97	14.0	-
8	700	big	-	-	-	-

#### 3.2 Transmittance of ITO Film

The transmission spectra of ITO films as deposited and annealing are showed in Figure 1. All transmittance data of the samples at maximum ( $T_{max}$ ) is listed in Table 1. A maximum transmission of about 99 % is achieved in the visible spectral region after annealing. The optical properties of ITO films are determined to a large extent by the microstructure of

the film and hence by the preparation technique. The films have high minimum transmittance (>85%) at visible range. The transmittance of ITO increases with an increase of the annealing T. The edge of the transmission at the range of long wavelength shifts towards longer wavelength after increasing of the annealing T in the NIR range. The edge of the transmission of sample 2 at the range of short wavelength shifts towards longer wavelength after 220 °C annealing.

As we know, the slope of the edge of the transmission curve is steep or has a blue shift in accordance with a narrow distribution of particle sizes of the material. This is related to the forming of an ultrafine particles (UFP) microstructure, nanometer ultra thin film and having a larger relative ratio of crystalline/defect of the film. The absorption peak (transmission onset) is due to a 1s-1s quantum particle transition as suggested. A slight increase in the transmission and a slight shift of the absorption edge to a shorter wavelength had been also observed in the ultrafine particles (UFP) CdS materials [10]. Similarly, it is found as following fact in Figure 1. (1) The onset of the spectrum of sample 2 appears a 450 nm side absorption peak (or split). (2) The slope of the onset of the transmission is more steep than sample 1. (3) The onset of absorption split (or the maximum transmission peak) shifted towards longer wavelengths comparing the sample 1 and other samples. This means that the domain boundary (or grain boundary), thickness of thin film and relative ratio of crystalline/defect become larger at 220 °C annealing, but there are more narrow sizes of no crystalline UFP inside the film. A lateness discussion motioned that the film with weak (211) and (222) plane texturing at annealing T of below 250 °C. Due to above we can explain that the observed lower  $R_s$  of 59.7 Ω·m can be referred to the associated decrease in particle size, increase in the domain of crystalline and lower domain boundary scattering of the carrier in the annealed films. The bigger  $R_s$  is caused by decreasing of the ratio of crystalline/defect at annealing T of above 300 °C.



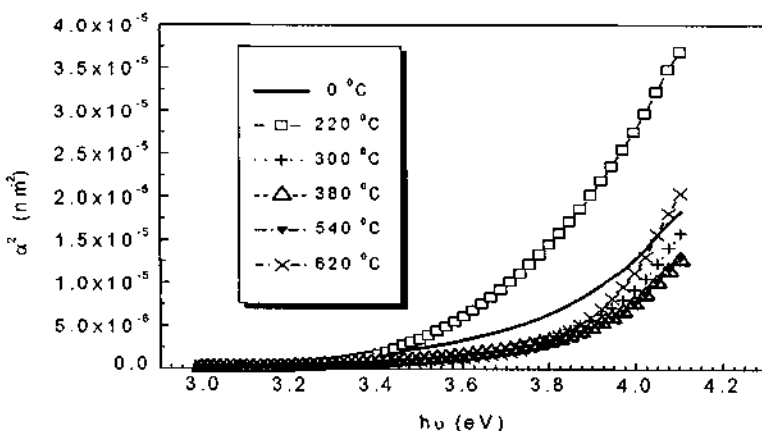
**Figure 1.** Transmittance spectra of films prepared in 10.4% oxygen partial pressure at different annealing temperature in air.

Table 1 also shows the Figure of Merit ( $\Phi_{TC} = T_{max}/R_s$ ) of the samples (where  $R_s$  is sheet resistance). Clearly the sample 2 has a better value of Figure of Merit.

### 3.3 Energy Band Gap ( $E_g$ )

In the strong and medium absorption region of short wavelength, the optical behavior of ITO is dominated by absorption from the valence electrons. The absorption coefficient  $\alpha$  can be determined by direct transition model [11]:  $\alpha^2 = C(h\nu - E_g)$ . The  $\alpha^2$  vs. the photo energy in different annealing T (Figure 2) are obtained from measurement of the absorption spectrum in order to get  $E_g$ . Table 1 gives  $E_g$  values of all ITO films. The intrinsic band gap is well known as 3.53 eV [12]. The obtained values vary between 3.88 and 3.66 eV for the ITO films. The  $E_g$  decreases as the annealing T increases from RT to 220 °C. The  $E_g$  increases as the annealing T further increase from 300 °C to 620 °C. At 620 °C the  $E_g$  reach the biggest 3.88 eV.

As the treated ITO samples show comparably high effective band gaps, we draw a conclusion as the following. A combination of Burstein-Moss-Shift and contributions of scattering [11] causes the increased  $E_g$ . It is not only a reason of Burstein-Moss-Shift like Bender et al mentioned [13].  $E_g = E_{g,0} + \Delta E_{BM} = E_{g,0} + \frac{\hbar(3\pi^2n_e)^{2/3}}{2m^{*}_{vc}} + \hbar\Sigma$ , Where  $E_g$  is the measured or varied effective band gap,  $E_{g,0}$  is the intrinsic band gap,  $m^{*}_{vc}$  representing the reduced effective mass and  $n_e$  is free electron density. The  $\hbar\Sigma$  represents the broadening of the band gap due to electron-electron scattering, electron-ion scattering and the width of the transition. If the transmission increases (or shifts towards longer wavelength) in the long wavelength region (NIR), this indicates a decrease of the density of free electrons in the film [13]. Because the transmission increases in NIR region (Figure 1), we think that the  $\Delta E_{BM}$  value comes from the contribution of  $\hbar\Sigma$  mainly. It is assumed that the  $\text{Sn}^{4+}$  ions behave as single charged point scatter.



**Figure 2.** Dependence of the absorption coefficient on the photoenergy.

### 3.4 Surface Morphology

The surface morphology of SEM were not observed for most ITO films, because the films were too smooth to observe using SEM. Here a spectra method was used to value the surface morphology. Figure 3 shows the diffuse reflectance (DR) and specular reflectance (SR) about the variation of annealing temperature of the films as a function of

wavelength. The intensity variation with wavelength of SR is similar to that of DR. The SR decreasing can lead to the increase of transmittance. The surface roughness ( $\delta$ ) can be calculated by total integrated scattering (TIS) (Figure 3c) [14].  $TIS = DR/(DR+SR) = 1 - \exp(-4\pi\delta\cos\theta_0/\lambda)^2$ , where  $\theta_0$  is the angle of incidence. The  $\delta$  as deposited and post annealed was range of 12.5-14.0 nm. It is confirmed by AFM (Figure 3d). The  $\delta$  as deposited film was 12.5 nm. The films annealed were rougher as indicated by high  $\delta$  value up to 14.0 nm. The light scattering is caused by the  $\delta$  and domain boundaries. Domain boundaries will grow after annealing. We deduce that the bigger roughness come from the increasing of boundaries. Table 1 shows the average surface  $\delta$  of the films at different annealing T. The results thus showed that annealing T has an effect on the morphology.

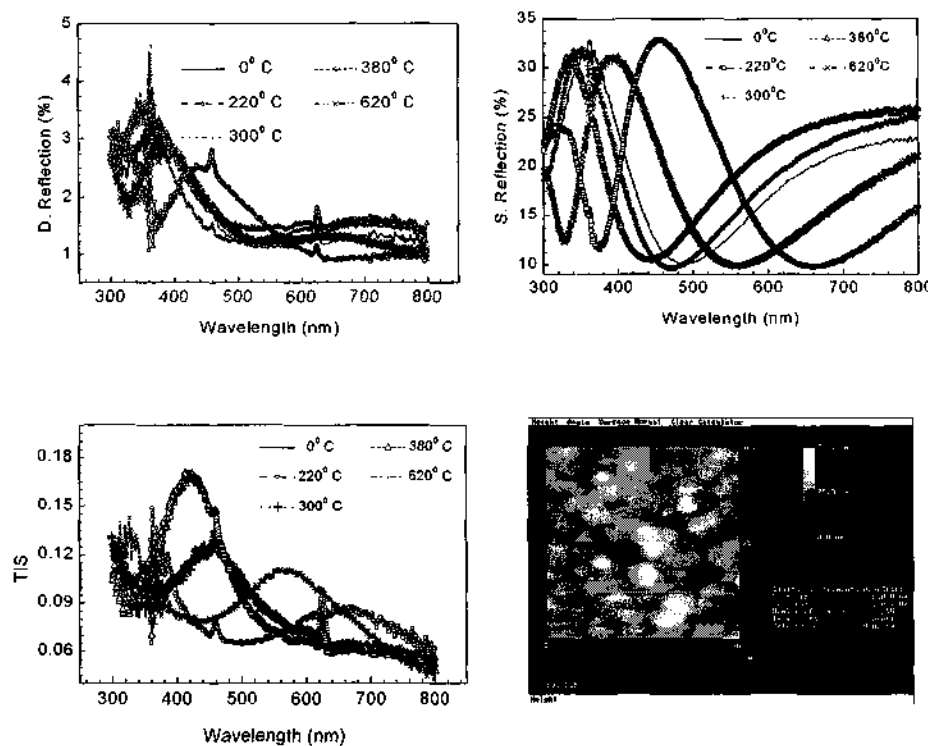


**Figure 3.** (a) Diffuse (D) reflectance, (b) specular (S) reflectance and (c) Total integrated scattering (TIS) of ITO films at different annealing temperature in air. (d) Topography of AFM of ITO films as deposited.

### 3.5 Structural Properties

Figure 4 shows the effects of annealing T on the XRD curves of ITO film. An amorphous film was obtained at RT, irrespective of the  $\text{SnO}_2$ -doping concentration in the film. The films show the (222) plane texturing. The ITO films prepared at low annealing T have no sharp peak in their X-ray diffraction spectra. Only a weak peak of  $\text{In}_2\text{O}_3$  (211), a mixing peak of  $\text{In}_2\text{O}_3$  (222) plus broad background from the glass substrate can be observed,

because the films were amorphous and the films were thin. There is no evidence of the pure  $\text{SnO}_2$  peak in the spectrum. This could be caused by the small amount of  $\text{SnO}_2$  in the ITO film. Our EDX results demonstrated that there are only less 6%  $\text{SnO}_2$  in the ITO film. No clear change was observed in the XRD on the annealing films at temperature lower than 250 °C. However, after annealing at 300 °C for 1 hour in air, the sharp peaks of (211), (222), (400), (411), (431), (440), (611), (622) and (800) peaks of  $\text{In}_2\text{O}_3$ , emerged from the amorphous XRD [4, 15]. The films show the (400) plane texturing. The better crystallisation was observed from the change in the predominant plane of crystallisation (222) and (400) plane after annealing. It demonstrates that the annealing ITO film is of much better polycrystalline structure.

Generally the  $\text{SnO}_2$  doping of  $\text{In}_2\text{O}_3$  films does not contribute to carrier generation at amorphous films [7, 16]. The electrical property of pure  $\text{In}_2\text{O}_3$  is known to rely entirely on the oxidation state of the metal constituent [4]. Since there are only less 6%  $\text{SnO}_2$  in the ITO film, hence the creation of oxygen vacancies contributed to the high carrier concentrations and is responsible for the low resistivity measured in the pure  $\text{In}_2\text{O}_3$  film and less 6%  $\text{SnO}_2$  doped ITO film. The decrease of  $R_s$  in the range of RT-250 °C is not due to the phase transformation of the ITO film determined by X-ray diffraction [1, 14] and Figure 4, because the XRD pattern did not show the difference at below 300 °C treating. The existence of a minimum  $R_s$  after annealing is a well known behaviour of ITO (1.0 wt %  $\text{SnO}_2$ -doped  $\text{In}_2\text{O}_3$ ), But for  $\text{In}_2\text{O}_3$  or  $\text{In}_2\text{O}_3$  doped with 6%  $\text{SnO}_2$  film it is accepted only in case of annealing below 250 °C.

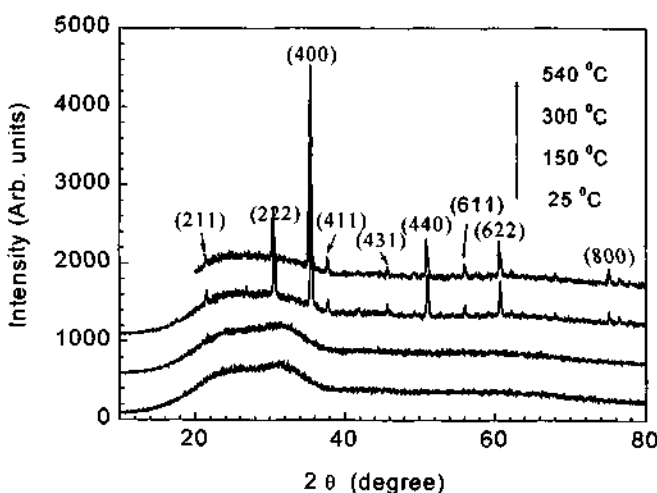


**Figure 4.** XRD patterns of ITO films of samples on glass substrate at different annealing temperature.

#### 4 Conclusion

Here RT growing of the ITO films and high temperature up to 700 °C post-annealing are studied. After the heat treatment of the film in air atmosphere there are some

improvement about the electron conductivity, transparency, microstructure and other characterizations.

The lowest  $R_s$  of  $59.7\Omega \cdot m$  was obtained for ITO film annealed at low T of  $220^\circ C$  in air, but at above annealing T of  $300^\circ C$  a rapid decline in the electron conductivity occurred. Strong domain boundary scattering of carriers, small ratio of crystalline/defect and severe loss of oxygen vacancies could cause the high resistivity. The Eg varies within  $3.66\text{ eV}$ - $3.88\text{eV}$ . The Eg increases as the annealing T further increase from  $300^\circ C$  to  $620^\circ C$ . The results showed that annealing T has some effect on the morphology of the ITO films. Minimum surface roughness of  $12.5\text{ nm}$  was obtained at RT. The film surface becomes rougher as the annealing T is increased. The films also exhibited high maximum optical transmittance (99%) and high minimum transmittance ( $> 85\%$ ) to visible light.

The film as deposited is amorphous and the better crystallisation was observed from the change in the predominant plane of crystallisation (222) and (400) plane after heat treatment. The sharp peaks of (211), (222), (400), (411), (431), (440), (611), (622) and (800) peaks of  $\text{In}_2\text{O}_3$  emerged from the amorphous XRD at  $300^\circ C$  annealing in air for 1 hour. The film that is improved in  $R_s$  after low annealing T less than  $250^\circ C$  is still amorphous. The film annealed at  $220^\circ C$  suits for the application of smart windows of electrochromic material or other functional multilayer films.

## 5 Acknowledgements

H.-N. Cui acknowledges the F.C.T. grant of Portugal. This work was partially financially supported by Fundação para a Ciência e Tecnologia under the PRAXIS program, research project 'Spectrally selective coatings for solar applications', PRAXIS/P/CTM/11235/98.

## References

1. Cui H.-N. and Xi S.-Q., The fabrication of dipped CdS and sputtered ITO thin films for photovoltaic solar cells, *Thin Solid Films* **288** (1996) pp. 325-329.
2. Meng L.-J. and Dos Santos M. P., Influence of the target-substrate distance on the properties of indium tin oxide films prepared by radio frequency reactive magnetron sputtering, *J. Vac. Sci. Technol. A18(4)* (2000) pp. 1668-1671.
3. Nanto H., Minami T., Orito S. and Takata S., Electrical and optical properties of indium tin oxide thin films prepared on low-temperature substrate by rf magnetron sputtering under an applied external magnetic field, *J. Appl. Phys.* **63** (1988) pp. 2711-2716.
4. Tahar R. B. H., T. Ban, Ohya Y. and Takahashi Y., Tin doped indium oxide thin films: Electrical properties, *J. Appl. Phys.* **83** (1998) pp. 2631-2645.
5. Shigesato Y., Takaki S. and Haranoh T., Electrical and structural properties of low resistivity tin-doped indium oxide films, *J. Appl. Phys.* **71** (1992) pp. 3356-3364.
6. Minami T., Sonohara H., Kakumu T. and Takata S., Physics of very thin ITO conducting films with high transparency prepared by DC magnetron sputtering, *Thin Solid Films*, **270** (1995) pp. 37-42.
7. Paine D. C., Whitson T., Janiae D., Beresford R. and Yang C. O., A study of low temperature crystallization of amorphous thin film indium-tin-oxide, *Appl. Phys.* **85** (1999) pp. 8445-8450.
8. Teixeira V., Cui H.-N., Monteiro A. and Bertran E., Characterization of sputtered ITO-WO<sub>3</sub> thin films for electrochromic devices, The Proceeding of International

Conference on Metallurgical Coatings and Thin Films (San Diego, USA, 2001) April 30- May 4.

9. Cui H.-N. and Teixeira V., Study of low temperature annealing of DC sputtered ITO films by optical methods. In Mechanics and Material Engineering for Science and Experiments, ed. by Y. Zhou, Y. Gu and Z. Li (Science Press, New York, 2001) pp.292-295.
10. Cui H-N, Wang R., Wang W. Y. and Xi S. Q. Preparation and photoluminescence of ultrafine cadmium sulfide particles, *J. Mater. Sci. Lett.* **17(11)** (1998) pp. 913-916.
11. Weijtens C.H.L. and Van Loon P.A.C., Influence of annealing on the optical properties of indium tin oxide, *Thin Solid Films* **196** (1991) pp. 1-10.
12. Ray S., Banerjee R., Basu N., Batabyal A. K. and Barua A. K., Properties of tin doped indium oxide thin films prepared by magnetron sputtering, *J. Appl. Phys.* **54** (1983) pp. 3497-3501.
13. Bender M., Seelig W., Daube C., Ocker B. and Stollenwerk J., Dependence of oxygen flow on optical and electrical properties of DC magnetron sputtered ITO films, *Thin Solid Films* **326** (1998) pp.72-77.
14. Chiou B. S and Hsieh S. T., R. f. magnetron-sputtered indium tin oxide film on a reactively ion-etched acrylic substrate, *Thin Solid Films* **229** (1993) pp. 146-148.
15. Terzini E., Thilakan P. and Minarini C., Properties of ITO thin films deposited by RF magnetron sputtering at elevated substrate temperature, *Mater. Sci. Engineer.* **B77** (2000) pp. 110-114.
16. Shigesato Y. and Paine D. C., Study of the effect of Sn doping on the electronic transport properties of thin film indium oxide, *Appl. Phys. Lett.* **62** (1993) pp.1268-1270.

# SIZE DEPENDENCE OF CURIE TEMPERATURE IN $\text{PbZr}_{1-x}\text{Ti}_x\text{O}_3$ ULTRAFINE PARTICLES

X. F. CUI, J. C. LI AND Q. JIANG

*Department of Materials Science and Engineering, Jilin University Changchun 130025, China  
E-mail: jiangq@jlu.edu.cn*

A simple quantitative model, with no adjustable parameters, is developed for the finite size effect of ferroelectric particles on the Curie transition temperature. As the size of ferroelectric particles decreases, the Curie temperature decreases. Based on our model for lattice contraction and the Landau-Ginsburg-Devonshire (LGD) phenomenological theory, size effects on Curie temperature of lead zirconate titanate  $\text{PbZr}_{1-x}\text{Ti}_x\text{O}_3$  (PZT,  $x \geq 0.6$ ) are considered. It is shown that Curie temperature of PZT ( $x \geq 0.6$ ) decreases with decreasing particle size. The predictions of our equation are in agreement with the experimental results.

## 1 Introduction

As the ferroelectric device elements become smaller and smaller with the dimension of ferroelectrics in the sub-micrometer range or even lower, the physical properties become size dependent and the particle size effect must be taken into consideration for optimizing the properties. One of the important properties is the size-dependence of Curie temperature.

It is well known that nanocrystals with free surfaces have considerable lattice contraction induced by the large surface/volume ratio. The lattice contraction increases as the size of the nanocrystals decreases. In this contribution, we have considered the size-dependence of the Curie temperature of PZT induced by lattice contraction when the particles size goes into nanometer range. Useful results have been obtained. However, we have neglected the extrinsic contributions on properties, which are caused by domain wall, defect motion, and/or surface charge, etc. The extrinsic properties are more or less affected by the materials processing technology and discussion of them is out of the scope of the present study.

## 2 Model

Recently, a quantitative model for the size-dependent Curie temperature  $T_c$  has been established based on mechanic and thermodynamic considerations using the Landau-Ginsburg-Devonshire (LGD) phenomenological theory by equalizing free energies of the ferroelectrics and paraelectrics phases [1-4],

$$T_c = T_{c0} + 3ca_0Q_h\sigma_p/4 \quad (1)$$

where  $T_{c0}$  is the bulk Curie temperature,  $c$  is the Curie constant,  $a_0$  is the vacuum dielectric permittivity,  $Q_h = Q_{11} + 2Q_{12}$  where  $Q_{11}$  and  $Q_{12}$  are the electrostrictive constants,  $\sigma_p$  denotes internal stress.

In equation (1), only unknown parameter is  $\sigma_p$ . It is known that  $\sigma_p = \varepsilon B$  where  $\varepsilon$  shows strain and  $B$  is bulk modulus. Thus, if  $\varepsilon$  can be determined,  $T_c$  may be determined. In this contribution, our developed  $\varepsilon$  function is introduced into equation (1). With the

function,  $T_c$  is predicted. The predicted result is in agreement with the known experimental and theoretical results.

$\varepsilon$  as a function of particle size  $D$  has been developed recently with the following form [5-6],

$$\varepsilon = -\frac{\sqrt{6\gamma_0 D_0 k}}{3D} \quad (2)$$

where  $\gamma_0$  is the solid-liquid interface energy of bulk crystals,  $k$  denotes compressibility,  $D_0$  is the particle diameter which almost all atoms of the particle are located on its surface and  $D_0=3h$  where  $h$  is lattice constant [5-6].

In equation (2),  $\gamma_0$  has been deduced according to Gibbs-Thomson equation [7],

$$\gamma_0(T) = 2hS_{vib}H_m(T)/(3V_mR) \quad (3)$$

where  $V_m$  is molar volume,  $R$  is the ideal gas constant,  $H_m(T)$  denotes the melting enthalpy of bulk crystals as a function of temperature  $T$ ,  $S_{vib}$  is the vibrational part of the overall melting entropy of crystals  $S_m$ . For compounds,  $S_{vib} \approx S_m - R$  is assumed [8].

According to the Helmholtz function,  $H_m(T)=g_m(T)-Tdg_m(T)/dT$  where  $g_m(T)$  is the volume Gibbs free energy and  $g_m(T)=H_m(T_m-T)/T(T_m)^2$  [9], and thus

$$H_m(T) = H_m/(T_m/T)^2 \quad (4)$$

where  $H_m$  is the melting enthalpy of bulk crystals,  $T_m$  is the melting point. Taking equations (4) and (3) into equation (2), it reads,

$$\varepsilon = \frac{2}{3(T_m/T)D} \sqrt{kD_0 h S_{vib} H_m / (R V_m)} \quad (5)$$

With equation (5), equation 1 is rewritten as,

$$T_c = T_{c0} - \frac{ca_0 Q_h B}{2[T_m/T_c(\infty)]D} \sqrt{kD_0 h S_{vib} H_m / R V_m} \quad (6)$$

**Table 1.** Values of the parameters in equation (6) for  $PbZr_{1-x}Ti_xO_3$  where  $T_{c0}$  and  $c$  [2] are transformed from Celsius scale to Kelvin temperature. Due to the difficulty of finding the melting enthalpy  $H_m$  and entropy  $S_m$  of lead zirconate titanate PZT, mean values of  $PbO$ ,  $TiO_2$  and  $ZrO_2$  consisted of the compound [12] are utilized.  $T_m$  of PZT (expect  $PbTiO_3$ ) can be obtained by using  $H_m=T_m S_m$ .  $V_m$  is obtained by  $M/\rho$  where molar mass  $M$  is cited from Ref [15] and it is reasonable that we chose the value of density  $\rho$  for PZT unanimously to be 7.38 g/cm<sup>3</sup> since compounds in PZT system have similar density [14].

	x=0.6	x=0.7	x=0.8	x=0.9	x=1.0
$T_{c0}$ (K) <sup>[2]</sup>	691.4	713.2	732.1	750.1	765.1
$a_1 (10^7 m^2 F^{-1})^{[2]}$	-8.340	-12.47	-14.84	-16.17	-17.08
$c (10^5 K)^{[2]}$	7.107	5.016	4.407	4.212	4.120
$Q_{11}(10^{-2} m^4 C^{-2})^{[2]}$	8.116	7.887	8.142	8.504	8.900
$Q_{12}(10^{-2} m^4 C^{-2})^{[2]}$	-2.950	-2.480	-2.446	-2.507	-2.600
$V_m$ (cm <sup>3</sup> mol <sup>-1</sup> )	43.42	42.83	42.24	41.66	41.07
$H_m$ (kJmol <sup>-1</sup> )	37.623	35.656	33.689		29.755
$T_m$ (K)	1803.5	1759.8	1716.0		1554.0 <sup>[14]</sup>
$S_m$ (Jmol <sup>-1</sup> K <sup>-1</sup> )	20.861	20.261	19.632		19.147
$S_{vib}$ (Jmol <sup>-1</sup> K <sup>-1</sup> )	12.547	11.947	11.318		10.833

### 3 Discussion

According to the above equation, the size dependence of Curie temperature of PZT particles depends on both electricity parameters and thermodynamics parameters. It has been shown that Curie temperature decrease with decreasing particles size. And with the increase of the content of titanium (Ti),  $T_c$  is increasing (see in Figure 1). In figure 2, the observed experimental data of  $T_c$  correspond to the prediction of equation (6) (the solid line) and the mechanics model (the dash line) perfectly and the Curie temperature is a liner decrease with the reciprocal particle diameter.

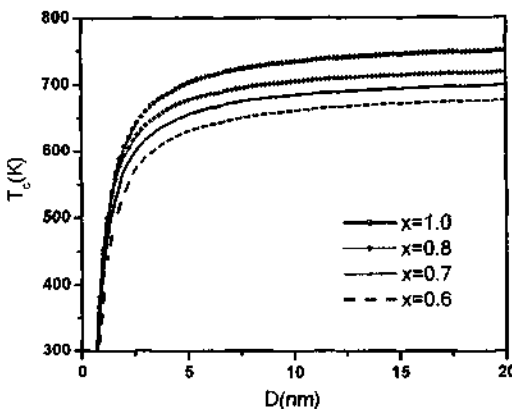


**Figure 1.** Shows Curie temperature  $T_c$  of PZT ( $x=0.6, 0.7, 0.8$  and  $1.0$ ) versus particle size in terms of equation (6). In equation 6, the vacuum dielectric permittivity  $\epsilon_0$  is  $8.85 \times 10^{-12} \text{ Fm}^{-1}$  [12],  $k=1/B$  where  $B$  is the bulk modulus and we chose the value of  $B$  of PZT to be the value of  $\text{PbTiO}_3$  is  $209 \text{ GPa}$  for their similar properties [13].  $D_0 = 3h$  and  $h$  is lattice parameter,  $h = 0.4 \text{ nm}$  from Ref [14].  $R$  is the ideal gas constant. All the other parameters are listed in table 1.

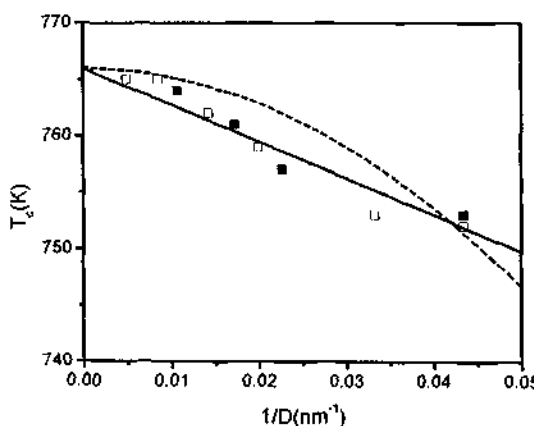


**Figure 2.** Gives  $T_c$  function of  $\text{PbTiO}_3$  ultra fine particles in terms of equation (6) and experiment results of the specific heat measurements; the symbol ■ derived from Ref [10], □ derived from ref [11]. The solid line is our model and the dash line is a mechanic and thermodynamic model in reference [1].

In summary, a model without any freedom adjustable parameter for the size-dependence of Curie temperature of PZT ( $x \geq 0.6$ ) is established and confirmed by the experimental results. And the results indicate that the value of Curie temperature is decreased with the decreasing particles size. The equation shows an expedient way to determine the size-dependence of Curie temperature in ferroelectrics and all the parameters in this equation are measurable.

#### 4 Acknowledgements

We thank the financial support from the NNSFC under Grant No. 59931030, 50071023, 50025101 and from the Trans-Century Training Program Foundation for the Talents by the Ministry of Education of China are acknowledged.

#### References

- Huang H., Sun C. Q. and Hing P., Surface bond contraction and its effect on the nanometeric sized lead zirconate titanate, *J. Phys.: Condens. Matter* **12** (2000) pp. L127-132.
- Haun M. J., Furman E., Jang S. J. and Cross L. E., Thermodynamic theory of the lead zirconate-titanate solid solution system, *Ferroelectrics* **99** (1989) 13 Parts I to V.
- Oh S. H. and Jang H. M., Enhanced thermodynamic stability of tetragonal-phase field in epitaxial Pb(Zr,Ti)O<sub>3</sub> thin films under a two-dimensional compressive stress, *Appl. Phys. Lett.* **72** (1998) pp.1457-1460.
- Huang H., Sun C. Q., Zhang T. and Hing P., Grain-size effect on ferroelectrics Pb(Zr<sub>1-x</sub>Ti<sub>x</sub>)O<sub>3</sub> solid solutions induced by surface bond contraction, *Phys. Rew. B* **63** (2000) pp.1184112 (1-9).
- Jiang Q., Liang L. H. and Zhao D. S., Lattice contraction and surface stress of fcc nanocrystals, *J. Phys. Chem. B* **105** (2001) pp.6275-6277.
- Jiang Q., Zhao D. S. and Zhao M., Size-dependent interface energy and related interface stress, *Acta Mater.* **49** (2001) pp. 3143-3147.
- Jiang Q., Shi H X. and Zhao M., Free energy of crystal-liquid interface, *Acta Mater.* **47** (1999) pp.2109-2112.
- Zhang Z., Zhao M. and Jiang Q., Melting temperatures of semiconductor nanocrystals in the mesoscopic size range, *Semicond. Sci. Tech.* **16** (2001) pp.L33-L35.
- Hoffman J. D., Thermodynamic driving force in nucleation and growth processes, *J. Chem. Phys.* **29** (1958) 1192-1193.
- Zhong W. L., Jiang B., Zhang P. L., Ma J. M., Chen H. M., Yang Z. H. and Li L., Phase transition in PbTiO<sub>3</sub> ultra fine particles of different sizes, *J. Phys.:Condens. Matter* **5** (1993) pp.2619-2624.
- Zhong W. L., Wang Y. G., Zhang P. L. and Qu B. D., Phenomenological study of the size effect on phase transitions in ferroelectrics particles, *Phys. Rew. B* **50** (1994) pp.698-703.
- Weast R. C (editor-in-chief), Astle M. J. and Beyer W. H (editor), *CRC Handbook of Chemistry and physics*, 69<sup>th</sup> edition, (CRC Press, Inc., Boca Raton, Florida, 1988), PP. B-225, PP. B-226, PP. B-227, pp. F-191
- King-Smith R. D. and Vanderbilt D., First-principles investigation of ferroelectricity in peroskite compounds, *Phys. Rew. B* **49** (1994) pp. 5828-5844.

14. Hellwege K. H (editer-in-chief),, *Landolt-Börnstein New Series on Crystals and Solid State Physics*, Group III Spring-Verlag, Berlin, **16/a** (1981) PP.77, pp.122-125.
15. Sargent-Welch Scientific Company 1980 *Table of periodic properties of the elements*: Skokie, Illinois, pp.1.

This page is intentionally left blank

## ZnO THIN FILM GROWN BY METAL-ORGANIC CHEMICAL VAPOR DEPOSITION

GUOTONG DU, XINQIANG WANG, SHUREN YANG, XIAOTIAN YANG, JINZHONG WANG,  
YUANTAO ZHANG, DAN LIU, YAN MA AND DALI LIU

*College of Electronic Engineering, State Key Lab. on Integrated Optoelectronics, Jilin University,  
Changchun, 130023, People's Republic of China  
E-mail: laserlab@mail.jlu.edu.cn*

H. C. ONG

*Department of Electrical Engineering, Chinese University of Hong Kong, Hong Kong*

High quality ZnO films were deposited on  $c$ -Al<sub>2</sub>O<sub>3</sub> substrate by metal-organic chemical vapor deposition. X-ray diffraction indicated that ZnO films were strongly  $c$ -oriented. Strong ultraviolet (UV) emission was observed with center peak at 3.29 eV. The full width at half maximum of UV emission was 99 meV. The deep level emission was too weak to be observed. Transmission spectrum indicated that ZnO film was highly transparent in visible range with an abrupt absorption edge in UV region. The calculated band-gap energy from transmission spectrum coincided with that of ZnO bulk well. Raman spectrum showed that ZnO film could be classified as high quality epitaxial layers of hexagonal ZnO. Optical pumped UV lasing was obtained at room temperature. The threshold was as low as 0.24  $\mu$ J with pumped beam diameter of 20  $\mu$ m.

### 1 Introduction

ZnO, a wide gap semiconductor with band-gap of 3.37 eV at room temperature, is attracting more attention because of the good optical, electrical and piezo-electrical properties. It has potential uses in optoelectronic systems such as light emitting diodes (LEDs) [1], photodetectors [2], electroluminescence devices [3] and solar cells [4]. Recently, several authors have reported optically pumped ultraviolet (UV) lasing of ZnO film by molecular beam epitaxy (MBE) and pulsed laser deposition [5-7]. GaN is known as a kind of good material for the fabrication of optical devices such as LEDs and laser diodes (LDs) [8]. ZnO not only has the same crystal structure as GaN, but also has a larger exciton binding energy of 60 meV, which is 2.4 times that of GaN. Furthermore, Yu et al. have shown that textured ZnO films might have higher quantum efficiency than GaN [9]. This indicates that ZnO becomes the most potential material to realize the next generation UV semiconductor laser. ZnO is also a kind of promising material for the surface acoustic wave (SAW) devices that are very important in this information age.

In order to fabricate the above-mentioned devices and realize its uses, what we should do firstly is to get high quality ZnO film. A lot of methods have been used to deposit ZnO films such as Molecule Beam Epitaxy (MBE) [10], Metal-organic Chemical Vapor Deposition (MOCVD) [11], Pulsed Laser Deposition (PLD) [12], Atomic Layer Epitaxy (ALE), Sputter and Thermal Evaporation. Among them, high quality ZnO films can be obtained by MBE, MOCVD and PLD. And MOCVD provides high growth rate and growth efficiency, large area uniformity and different doping processes. Therefore, MOCVD offers the advantage of industrial production.

In this paper, high quality ZnO films were deposited on sapphire substrate by MOCVD. X-ray diffraction measurement was taken to estimate the crystal structure of ZnO layer. The optical properties were investigated by transmission spectrum and photoluminescence (PL) spectrum. X-ray photoemission spectra were used to confirm the stoichiometry of ZnO film.

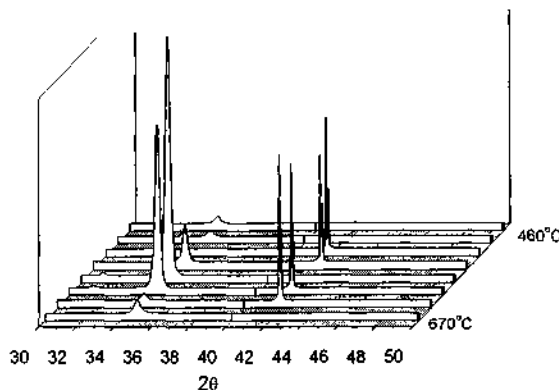
## 2 Experimental

ZnO films were deposited by MOCVD with rotating disk vertical reactor. The substrate holder could be rotated at a speed within a maximum of 1000 rpm. The best vacuum of our chamber was about  $1 \times 10^{-3}$  Pa. A resistive heater was placed below the wafer carrier and the heating was accomplished by radiation. A continuous flow of carrier gas (high purity N<sub>2</sub>) was introduced uniformly into chamber from the top. The precursors were diethyl zinc (DEZn) and O<sub>2</sub>. Ultrahigh purity Ar was passed through the DEZn bubbler which was maintained at temperature within the -10°C ~ 10 °C range. Since DEZn reacted vigorously with O<sub>2</sub> even at room temperature, they were introduced into chamber by two separated injectors to reduce the pre-reaction. In this method, uniform and high quality ZnO film could be obtained. The growth conditions of our sample were as follows: The chamber pressure was about 1 Torr. The N<sub>2</sub> flow was 600 sccm, and the O<sub>2</sub> flow was 90 sccm. Ar passed through the bubbler at 2~4 sccm. An additional Ar flow of 6~20 sccm was introduced into the DEZn line immediately at the exit of the bubbler to reduce the transit time of DEZn to the reactor. The growth temperature was 600°C. The thickness of ZnO film was 300nm.

We used SIEMENS D 5005 X-ray Diffractometer to investigate crystal structure and quality. PL spectrum was measured by 325 nm He-Cd laser. The PL signals from the sample were filtered by a monochromator and picked up computer. X-ray photoemission spectra (XPS) were performed on ESCALAB Mark II X-ray photoemission spectrometer.

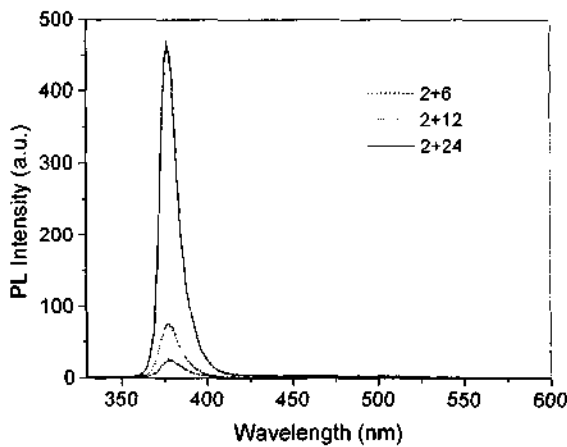
## 3 Results and Discussion

Figure 1 showed the X-ray diffraction patterns of ZnO films grown on *c*-Al<sub>2</sub>O<sub>3</sub> substrate at different growth temperature. The growth temperature was 460°C, 490°C, 520°C, 550°C, 580°C, 610°C, 640°C and 670°C respectively. From the spectra, we could find two diffraction peaks at 2θ 34.6° and 42°. The diffraction peak at 2θ 34.6° was ascribed to ZnO (002) diffraction peak while that at 42° was due to diffraction peak of sapphire. The intensity of (002) ZnO diffraction peak was the strongest at the growth temperature of 580°C, indicating the best quality of ZnO film. This showed that 580°C was the optimized growth temperature. The observation of ZnO (002) diffraction peak indicated that ZnO films were strongly *c*-oriented.



**Figure 1.** X-ray diffraction patterns of ZnO films at different growth temperature.

Room temperature photoluminescence spectra of ZnO films grown on *c*-Al<sub>2</sub>O<sub>3</sub> substrate with different Ar flows were shown in figure 2. The main flow of Ar gas passed through the DEZn bubbler was 2 sccm. The additional Ar flow which were introduced into the DEZn line at the exit of the bubbler were 6 sccm, 12sccm and 24 sccm, respectively. From the figure, UV emissions were observed in all samples with center peak of 377 nm (3.29 eV). Since the exciton binding energy of ZnO film was 60 meV at room temperature, the position of UV emission coincided with ZnO bulk well. The intensity of UV emission was the strongest when the additional Ar flow was 24 sccm. The full width at half maximum was 99 meV, which was comparative to that of ZnO films grown by MBE [13]. We could not find the deep level transition from the PL spectra. All these indicated that ZnO film was in high quality.



**Figure 2.** Room-temperature photoluminescence spectra of ZnO film on *c*-Al<sub>2</sub>O<sub>3</sub> at different Ar flow.

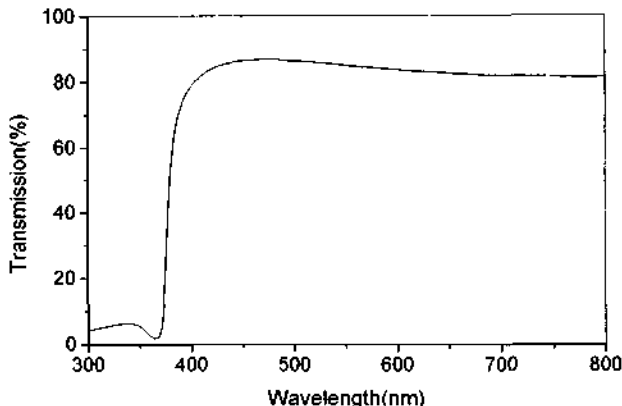
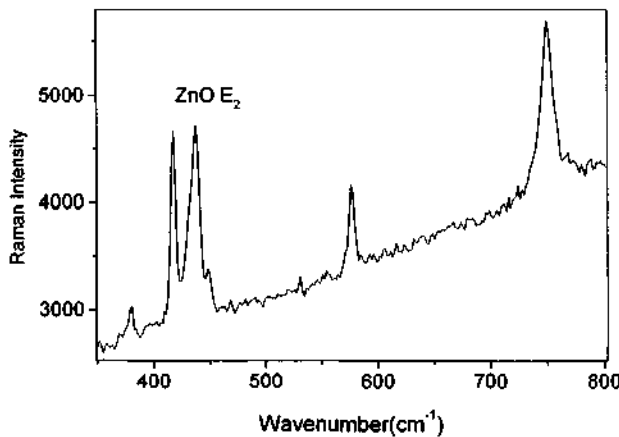


Figure 3. Transmission spectrum of ZnO film.

Figure 3 showed the transmission spectra of ZnO films at optimized growth condition, measured using by a Beckman Spectrophotometer. The contribution of sapphire substrate was excluded. The transmission in the visible region was over 80% and ZnO film was highly transparent. The transmission in the Ultraviolet region decreased sharply between 370 nm and 390 nm, resulting from a band-to-band transition. According to the transmission spectrum, the band gap energy of ZnO film was calculated from the spectral dependence of the transmission. By plotting  $\alpha^2 E^2$  as a function of  $E$  ( $\alpha$  is absorbance coefficient and  $E$  is incident photon energy) and extrapolating the linear position of the curves to plotting  $\alpha^2 E^2 = 0$ , the optical band gap obtained from the transmission spectrum was 3.29 eV. This coincided with the results of photoluminescence measurement well.

X-ray photoemission measurements were performed to confirm the stoichiometry of ZnO film. The results showed that ZnO films were Zn-rich.

Raman measurement was performed at room temperature in back-scattering configuration. ZnO has a hexagonal wurtzite structure and belongs to the  $C_{6v}$  symmetry group. The group theory predicts two  $A_1$ , two  $E_1$ , two  $E_2$ , and two  $B_1$  modes. Among them, one  $A_1$  and one  $E_1$  and two  $E_2$  modes are Raman active. In our back-scattering configuration,  $A_{1(\text{LO})}$  and  $E_2$  are Raman active. The peak at  $438 \text{ cm}^{-1}$  was due to  $E_2$  (high frequency) mode of ZnO film with a FWHM value of  $9 \text{ cm}^{-1}$ . Since the measure range of our micro-Raman system was from  $100 \text{ cm}^{-1} \sim 4000 \text{ cm}^{-1}$ , we could not obtain the low frequency  $E_2$  mode. The other scattering peaks were due to sapphire substrate. Since ZnO film was almost transparent in 514.5 nm, the wavelength of excitation laser, the scattering peaks from sapphire could be observed. The obtained Raman data clearly demonstrated that ZnO film of interest could be classified as high quality epitaxial layers of hexagonal ZnO.



**Figure 4.** Raman scattering of ZnO film.

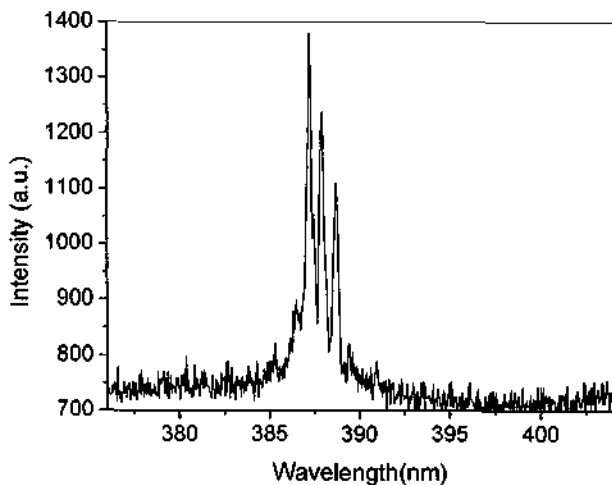


**Figure 5.** Optical pumped UV lasing spectrum of ZnO film.

Optical pumped UV lasing spectrum of ZnO film was observed as shown in figure 5. The samples were optically pumped by a frequency-tripled mode-locked Nd: YAG laser 355nm, 10Hz repetition rate, 15ps pulse width. The pump beam was focused to a spot with diameter of about 20  $\mu\text{m}$  on the surface of ZnO film. The threshold of lasing was as low as 0.24  $\mu\text{J}$ . From the lasing spectrum, we could find that much narrow lasing peak with line-width less than 0.6nm. This was due to self-formed resonator cavities [14].

#### 4 Conclusions

In this paper, high quality ZnO films were grown on *c*-Al<sub>2</sub>O<sub>3</sub> by MOCVD. Optimized growth condition was obtained by XRD and PL measurements. ZnO films were strongly *c*-oriented from XRD measurement. In room temperature PL spectra, we could find strong UV emission at 377nm. The deep level emission was too weak to be observed. Transmission spectrum showed that ZnO film was highly transparent in visible range while it has an abrupt absorption edge in UV region. The results obtained from transmission coincided with that of PL measurement well. In Raman spectrum, we found E<sub>2</sub> peak as predicted by group theory. This indicated that ZnO film could be classified as high quality epitaxial layers of hexagonal ZnO. Optical pumped UV lasing was observed at room temperature.

#### 5 Acknowledgements

This work was supported by NSFC-RGC (No.59910161983), NSFC (No. 60177007, 60176026) and 863 project with contract number of 2002AA311130.

#### References

1. X. L. Guo, J. H. Choi, H. Tabata and T. Kawai, Fabrication and optoelectronic properties of a transparent ZnO hemostructural light-emitting diode. *Jpn. J. Appl. Phys.* **40** (2001) pp. L177-L179.
2. S. Liang, H. Sheng, Y. Liu, Z. Hou, Y. Lu and H. Shen, ZnO schottky ultraviolet photodetectors. *J. Cryst. Growth* **225** (2000) pp.110–113.
3. H. Kim, C. M. Gilmore, J. S. Horwitz, A. Piqué, H. Murata, G. P. Kushto, R. Schlaf, Z. H. Kafafi and D. B. Chrisey, Transparent conducting aluminum-doped zinc oxide thin films for organic light-emitting devices. *Appl. Phys. Lett.* **76** (2000) pp. 259–261.
4. I. Luck, J. Kneisel, K. Siemer, J. Bruns, R. Scheer, R. Klenk, N. Janke, and D. Bräunig, Influence of Na on the properties of Cu-rich prepared CuInS<sub>2</sub> thin films and the performance of corresponding CuInS<sub>2</sub>/CdS/ZnO solar cells. *Solar Energy Materials & Solar Cells*, **67** (2001) pp.151-158.
5. D. C. Reynolds. D. C. Look and B. Jogai, Optically pumped ultraviolet lasing from ZnO, *Solid State Commun.* **99** (1996) pp.873–876.
6. D.M. Bagnall, Y. F. Chen, Z. Zhu et al., Optically pumped lasing of ZnO at room temperature. *Appl. Phys. Lett.* **70** (1997) pp. 2230–2232.
7. Z. K. Tang, G. K. L. Wong, P. Yu et al., Room-temperature ultraviolet laser emission from self-assembled ZnO microcrystalline thin films. *Appl. Phys. Lett.* **72** (1998) pp. 3270-3272.
8. S. Nakamura, The role of structural imperfections in InGaN-based blue light-emitting diodes and laser diodes. *Science* **281** (1998) pp. 956-961.
9. P. Yu, Z. K. Tang, G. K. L. Wong, M. Kawaski, A. Ohtomo and H. Koinuma, *Physics of Semiconductors*, edited by M. Scheffler and Zimmermann, (World

- Scientific 1996) p.1453.
- 10. S. K. Hong, Y. Chen, H. J. Ko, H. Wenisch, T. Hanada and T. Yao, ZnO and related materials: Plasma-assisted molecular beam epitaxial growth, characterization, and application. *J. Electron. Mater.* **30** (2001) pp. 647-658.
  - 11. X. Wang, S. Yang, J. Wang, M. Li, X. Jiang, G. T. Du, X. Liu and R. P. H. Chang, Nitrogen doped ZnO film grown by the plasma-assisted metal-organic chemical vapor deposition. *J. Cryst. Growth* **226** (2001) pp. 123-129.
  - 12. H. C. Ong, J. Y. Dai, A. S. K. Li, G. T. Du, R. P. H. Chang and S. T. Ho, Effect of Microstructure on the formation of self-assembled laser cavities in polycrystalline ZnO. *J. Appl. Phys.* **90** (2001) pp. 1664-1666.
  - 13. Y. Chen, D. M. Bagnall, H. Koh, et al. Plasma assisted molecular beam epitaxy of ZnO on c-plane sapphire: Growth and characterization. *J. Appl. Phys.* **84** (1998) pp. 3912-3916.
  - 14. H. Cao, Y. G. Zhao, H. C. Ong et al., Ultraviolet lasing in resonators formed by scattering in semiconductor polycrystalline films. *Appl. Phys. Lett.* **73** (1998) pp. 3656-3658.

This page is intentionally left blank

# PREPARATION, STRUCTURE, AND FORMATION PROCESSES OF NANOMETER-SIZED LAYERED MANGANESE OXIDES

GAO QIUMING<sup>\*1,2</sup> AND SUIB STEVEN L.<sup>2,3,4</sup>

<sup>1</sup>*State Key Lab of High Performance Ceramics and Superfine Structures, Shanghai Institute of Ceramics, Chinese Academy of Sciences, 1295 Dingxi Rd., Shanghai 200050, P. R. China E-mail: qmgao@mail.sic.ac.cn.* <sup>2</sup>*Department of Chemistry, <sup>3</sup>Department of Chemical Engineering and <sup>4</sup>Institute of Materials Science, University of Connecticut, Storrs, Connecticut 06269-4060, USA*

Stable colloids of nanometer-sized lamellar manganese oxides have been prepared by intercalation and self-assembly direct reduction methods. The structures, particle sizes, and optical properties of the materials have been described. Organic amine/ammonium species (TAA and DA) were used to intercalate birnessite H-OL-1 to prepare TAA-OL-1. Many kinds of structures and their formation processes were also described. The effects of organic ammonium cations and organic amines on the preparation of the manganese oxides were studied systematically.

## 1 Introduction

Much effort has been focused on semiconductor nanometer-crystalline materials including nanometer crystals of silicon and II-VI and III-V semiconductors [1-9]. Their potential utilization in the fields of catalysts and photocatalysts, battery materials, phosphors, and supports are due to their high surface area coupled with size-dependent electronic and optoelectronic properties, both of which, in the nanometer regime, are strongly related to size [10-15]. Manganese oxides are one of the most important materials, potentially utilized in the fields of ion-exchange, molecular adsorption, catalysis, electrochemistry, and magnetism [16-25]. The structure of two-dimensional layered birnessite is comprised of edge shared MnO<sub>6</sub> octahedra, with water molecules and/or metal cations occupying the interlayer region [26-32]. Nanometer crystalline manganese oxides [33, 34] may produce a new set of properties complementary to those in the bulk, improving or augmenting the applications for manganese oxide. We have undertaken a systematic study of the effects of organic ammonium cations and organic amines on the preparation of manganese oxides. Intercalation and direct reduction methods were reported here to successfully prepare the stable colloids of lamellar manganese oxides. Their structures, particle sizes, and optical properties will be described.

## 2 Experimental Section

### 2.1 Preparation

#### 2.1.1 Intercalation method

Reduction method was used to prepare potassium type manganese oxide birnessite K-OL-1. The solution of the mixture of ethanol and potassium hydroxide was added slowly to a beaker containing a solution of potassium permanganate with vigorous

stirring for a certain time. The resultant gel was aged in an oven for a certain time. The product was washed with distilled deionized water (DDW) to a pH lower than 9. This sample, still wet, was transferred into a beaker contained  $\text{HNO}_3$  and stirred at ambient temperature for one day. In a similar way, K-OL-1 was ion-exchanged with  $\text{H}^+$  three times to make sure the ion-exchange reaction was complete. The product was washed with DDW to a pH higher than 6. Kept wet, the H-OL-1 sample was used for further intercalation reactions.

The tetraalkylammonium hydroxides (TAA) including tetramethylammonium hydroxide (TMA), tetraethylammonium hydroxide (TEA), tetrapropylammonium hydroxide (TPA), and tetrabutylammonium hydroxide (TBA) and diamines (DA) like ethylenediamine (en), 1,6-diaminohexane (1,6-DHA), and 1,10-diaminoctane (1,10-DOA) were used to intercalate into the layers of H-OL-1. The TAA or DA was added to the gel of H-OL-1. The whole mixture was stirred for certain times and the resultant nanometer-sized and larger sized colloids or sols were characterized.

#### 2.1.2 Direct reduction method

Potassium permanganate was reacted with TAA to get TAA permanganate. The colloids or sols of nanometer-sized TAA manganese oxides were prepared in manganese concentrations of 0.05-0.1 M manganese by adding the appreciate  $\text{TAAMnO}_4$  salt to a mixture of DDW and 2-butanol or ethanol in a molar ratio of 1:1 and stirring for half an hour. Sols were aged for several days at room temperature to produce gels.

### 2.2 Characterization

The manganese and potassium amounts were determined with a Perkin-Elmer model 2380 flame absorption spectrometer and model P 40 inductively coupled plasma with an atomic emission spectrometer (ICP-AES). A Scintag XDS-2000 diffractometer utilizing  $\text{Cu K}\alpha$  radiation with a voltage of 45 kV and current of 40 mA was used to obtain diffraction patterns. Samples were prepared by pipetting small amounts of the sols/colloids onto glass slides and allowing the solvent to evaporate for a certain time at ambient temperature. SEM photographs were taken on an Amray 1810 scanning electron microscope. An Amray Model PV 9800 EDX system was used to obtain energy dispersive X-ray analyses. The FT-IR spectra were taken on a Nicolet Magna-IR System 750 FT-IR Spectrometer, using standard KBr pellet methods. A HP 8452A spectrophotometer was used to obtain the UV-vis spectra, using 1.0 cm quartz cells. The sols/colloids were diluted to concentrations of  $10^{-3}$ - $10^{-4}$  mol/l Mn for the measurements. Samples were prepared by placing a drop of  $10^{-2}$ - $10^{-3}$  mol/l Mn sols/colloids on carbon coated copper grids and allowing the water to evaporate at ambient temperature. TEM images were obtained at 100 kV using a Philips EM 420 electron microscope.

### 3 Results and Discussion

#### 3.1 Preparation of TAA- and DA-OL-1

Since potassium type OL-1 (K-OL-1) was not active for ion-exchange reactions of organic ammonium ions, ion-exchanged methods were chosen to prepare proton type birnessite (H-OL-1). XRD analyses of K-OL-1 prepared by reduction methods [35] and proton ion-exchanged H-OL-1 showed that the layered structures had basal spacing of 0.72 nm [34]. SEM images of them showed that both samples were plate-like pure birnessites. ICP and EDX analyses showed that H-OL-1 included trace K with a K/Mn ratio of 0.02, much lower than that of K-OL-1, whose K/Mn ratio was 0.31. These data showed that most potassium cations  $K^+$  of K-OL-1 were ion-exchanged by protons to form H-OL-1. Potassium ions intercalated between the layers of birnessite could not be totally ion-exchanged by protons, based on thermodynamic calculations [36]. More than 93% potassium of the original potassium type K-OL-1 samples was ion-exchanged by protons. H-OL-1 was used to ion-exchange with organic ammonium ions. FT-IR spectroscopy studies showed that DA was in the form of diammonium cations. Absorption bands characteristic of  $NH_3^+$  were clearly observed, instead of  $NH_2$ , for all of the dried TAA-OL-1 and DA-OL-1 samples.

Using 2-butanol or ethanol as reducing agents by direct reduction method [33], TAA permanganate precursors were reduced to form TAA-OL-1 manganese oxide colloidal solutions. The solid permanganate salts were added to a stirred mixture of 2-butanol and water, and manganese oxide sol formation occurred within half an hour. The reaction of 2-butanol with TAA permanganate in water is a two-phase reaction owing to the poor miscibility of the two solvents. The TAA permanganate salts have a low solubility in both water and 2-butanol, with the TMA salt being the most 2-butanol soluble. The manganese oxides of TMA-, TEA-, and TPA-OL-1 colloids form in the aqueous layer, whereas the colloid of TBA-OL-1 is mainly soluble in the 2-butanol layer.

#### 3.2 XRD characterization of freshly prepared TAA- and DA-OL-1

A very complex structure of TMA intercalated samples was found, compared with other members of the TAA-OL-1 system, since the XRD pattern peaks of TMA-OL-1 were not able to be indexed to any known structure [34]. OL-1 inorganic layers kept their original structures under intercalation conditions and the co-existence of two kinds of structures with different layer distances is likely. The peaks at 2.58, 0.86, 0.62, and 0.48 nm were indexed to the (001), (003), (004), and (005) reflections of the structure, respectively, using a trigonal or hexagonal crystal system. The d-values of the (001) crystal spacing reflections are related to the interlayer distances, so the interlayer distance of this structure is 2.58 nm. This structure was a little irregular because of the absence of (002) peaks and deviation of others. The others peaks at 1.18, 0.60, 0.40, and 0.30 nm were indexed to the (001), (002), (003), and (004) reflections of the structure with interlayer distances of 1.18 nm, respectively. Using the same analyses method, XRD results showed that the interlayer distances of TEA,

TPA, and TBA intercalated OL-1 were 1.72, 1.56, and 1.69 nm, respectively. Fig. 1 showed the XRD patterns of K-OL-1, H-OL-1, and DA-OL-1 samples. The first strong peaks at the lowest two-theta values were shifted to lower two-theta angle positions. The interlayer distances of en, 1,6-DHA, and 1,10-DOA intercalated OL-1 were 0.723, 1.48, and 1.86 nm, respectively.

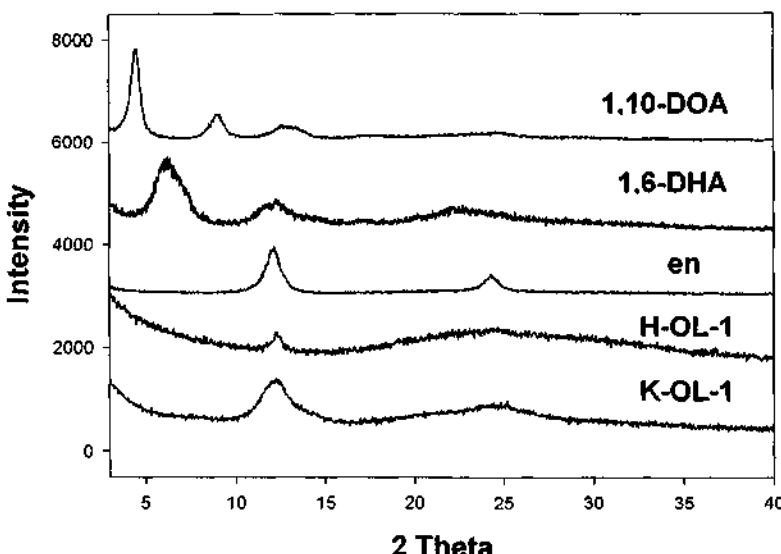


**Figure 1.** X-ray diffraction patterns of K-OL-1 (bottom), H-OL-1, en-OL-1, 1,6-DHA-OL-1, and 1,10-DOA-OL-1 (top).

Freshly prepared manganese oxide sols evaporated onto glass slides initially have broad XRD patterns. Sharpening of the XRD reflections was observed aging of the sols at room temperature for a few days, due to the increasing in the layer stacking order or crystallite size [33]. Two peaks XRD patterns of at 9.6 and 4.8 Å, respectively, were found for TMA-OL-1 manganese oxides, corresponding to the interlayer spacing of 9.6 Å. TEA-, TPA-, and TBA-OL-1 have the interlayer distances of 17.0, 16.0, and 16.6 Å, respectively, based on the same analytic method.

### 3.3 Structures of TAA- and DA-OL-1

Interlayer distance data of DA intercalated OL-1 samples show that only one layer of amines was intercalated into the layers with average intercalation angles of about 40, 69, and 61°, respectively, for en-OL-1, 1,6-DHA-OL-1, and 1,10-HOA-OL-1. TMA intercalated H-OL-1 had two kinds of interlayer distances of 2.58 and 1.18 nm. The larger interlayer structure may include two layers of TMA and three layers of water molecules according to diameters of these molecules/ions. The small one included one layer of TMA cations and one layer of water molecules corresponded to the type II model of TMA manganese oxide prepared by redox methods using tetramethylammonium permanganate [33]. The structures of TEA, TPA, and TBA

intercalated H-OL-1 corresponded to those of type III, II, and I models of related structures of redox reactions with TAA permanganates, respectively.

A layered structure of OL-1 with different interlayer distance of H-OL-1 was got when TMA permanganate was reduced by alcohol. TMA cations were not in between the layers according to the  $\text{TMA}^+$  ion diameter size. The structures of those samples of TEA-, TPA-, and TBA-OL-1, directly reduced by their TAA permanganates, were related to type III, II, and I models.

The shorter alkyl chains of TMA lead to more polar and strongly bound TAA cations. The interaction between TMA cations and negatively charged OL-1 inorganic layers was stronger than the others and more and more TMA cations were able to be intercalated into the spaces between the inorganic layers of OL-1. These structures are not stable [34], thus only H-OL-1 without TMA cations were found for TMA permanganate reduction product. The interaction of TEA was a little weaker than TMA, so only one layer of TEA cations and two layers of water molecules were in the layers of OL-1. For TPA and TBA the interactions were much weaker than that of TEA. Only a structure of one layer of TPA or TBA and one layer of water intercalated into the OL-1 layers was formed. Both products from intercalated method and direct reduction method are the same type of structures with a little different interlayer distance because of the different preparing methods.

According to C-C, C-N, and N-H bond distances and manganese oxide slab thickness, angles of organic ammonium ions between the layers were calculated [34]. In contrast to the TAA-OL-1 samples, the XRD patterns of diamine intercalated OL-1 had a typical character of intercalated structures with larger interlayer distances that correlate with longer molecular distances of different amines.

These two kinds of amines are very different based on electronic and steric factors. The electrical charge of TAA is at the center of the molecule, which is covered by hydrophobic groups. DA has double the electrical charge of TAA with a distribution at both ends of the molecule, very near the negatively charged layers of OL-1 leading to very strong interactions between DA and OL-1 layers. Two kinds of organic amines were utilized as templating and intercalating agents: tetraalkylammonium (TAA) hydroxide and diamine (DA) due to their different electronic and steric factors.

### *3.4 Particle Size Determination*

The UV-vis spectra of the colloids/sols of TAA-OL-1 and DA-OL-1 diluted to concentrations of  $10^{-4} \sim 10^{-3}$  mol l<sup>-1</sup> manganese were measured. One strong absorption band centered at 368 nm and one weak absorption band centered at 216 nm were found for TMA-OL-1 colloids. Based on the Beer-Lambert law, the molar absorption coefficients of TMA-OL-1 colloids with Mn concentrations of  $3.60 \times 10^{-5}$  mol l<sup>-1</sup> were  $2.41 \times 10^{-4}$  M<sup>-1</sup> cm<sup>-1</sup> and  $1.89 \times 10^{-4}$  M<sup>-1</sup> cm<sup>-1</sup> for the two absorption bands centered at 368 nm and 216 nm, respectively. Similar results were found for the other TAA-OL-1 colloids. The molar absorption coefficients of TAA-OL-1 colloids became smaller along with the longer alkyl chain TAA species intercalated into OL-1 layers. These results are similar to those of TAA manganese oxides reduced from TAA permanganate, whose UV-vis absorption peaks shift from lower to higher

positions along with the increasing ageing time. For example, the absorption peak shifts from 312 to 377 nm and from 294 to 334 nm for TEA and TPA manganese oxide colloids, respectively, with manganese concentrations of  $5.3 \times 10^{-4}$  and  $4.6 \times 10^{-4}$  M aged from initial to 22 days.

The two higher energy electronic absorption bands of TAA-OL-1 are the result of quantum confinement effects that arise when the size of the particles becomes smaller than the electron-hole pair in the bulk semiconductor material. The large band-gap was corresponded to nano-particle sizes of manganese oxide. TEM images of 0.1 M TAA manganese oxide colloids were obtained [33, 34]. The particle sizes are between 30~100 nm.

Electronic charge and steric factors affected both the structures and particle sizes. Only a strong absorption band centered at 425 nm was found for en-OL-1 and a band centered at 445 nm appeared for 1,6-DHA-OL-1 and 1,10-DOA-OL-1 sols, respectively. The one strong absorption band of en-OL-1, at lower energy, showed that its particles were bigger than those of TAA-OL-1 colloids. The adsorption bands at much lower energies for 1,6-DHA-OL-1 and 1,10-DOA-OL-1 sols showed that these materials have much larger particles. The molar absorption coefficients of TAA samples became lower as the alkyl groups of TAA ions became larger. The inorganic layers were separated by ammonium ions. These interactions between inorganic layer and ammonium ions became weaker as the chain length increased. The internal energy became smaller as the size of the TAA cations intercalated into the layers increased. Due to smaller surface areas of DA-OL-1, the molar absorption coefficients were much lower than those of TAA-OL-1 samples. The sequences of molar absorption coefficients for DA-OL-1 sols followed the same order of steric factors of diamines. The molar absorption coefficient of en-OL-1 was larger than those of 1,6-DHA-OL-1 and 1,10-DOA-OL-1 sols due to its higher particle surface areas and shorter distances between the inorganic layers.

### 3.5 Processes in TAA-OL-1 Systems

By intercalation method, tetraalkylammonium ions were present directly between the birnessite inorganic layers during those reactions. Relatively large particles of H-OL-1 materials were changed into nanometer-sized particles by ion-exchange methods. In the beginning of gel formation, the H-OL-1 kept its normal particle size of about 20-50  $\mu\text{m}$  based on SEM analyses of H-OL-1. Further intercalation of TAA ions led to larger distances between the inorganic layers. The number of stacks of layers are smaller at the same time, because the interactions between inorganic layers and TAA ions are weaker than those between inorganic layers and  $\text{K}^+$ ,  $\text{H}_3\text{O}^+$ , and DA ions. The layers are then easier to break. The particles became smaller colloids with nano-sized particles of manganese oxide formed after 3 d stirring. DA-OL-1 sols had typical bulk manganese oxide character, due to strong interactions between inorganic layers and DA ions, compared with those of TAA ions. Processes of TAA-OL-1 systems from direct reduction method [33], which described a process of self-assembly redox reactions between tetraalkylammonium and isopropanol and growth of very small particles, quite different from those of intercalation method. Firstly, unassociated particles were formed and freely floated in solution, secondly a little small particles

of layered structures with low crystallinity formed in small regions, and thirdly well ordered structure produced from heating the colloid in solution or annealing the thin films.

#### 4 Conclusions

Intercalation and self-assembly direct reduction methods were described to prepare TAA-OL-1. Organic amine/ammonium species (TAA and DA) were used to intercalate birnessite H-OL-1. Many kinds of structures were described and their formation processes were described.

#### 5 Acknowledgements

The financial support of the Chinese Academy of Sciences and Office of Basic Energy Sciences, Division of Chemical Sciences, of the U.S. Department of Energy are gratefully acknowledged.

#### References

1. Bley R. A. and Kauzlarich S. M., *J. Am. Chem. Soc.*, **118** (1996) pp.12461.
2. Zhang L., Coffer J. L., Xu W. and Zerda T. W., *Chem. Mater.*, **9** (1997) pp.2249.
3. Peng X., Wilson T. E., Alivisatos A. P. and Schultz P. G., *Angew. Chem. Int. Ed. Engl.*, **36** (1997) pp. 145.
4. Counio G., Esnouf S., Gacoin T. and Boilot J. P., *J. Phys. Chem.*, **100** (1996) pp.20021.
5. MacDougall J. E., Eckert H., Stucky G. D., Herron N., Wang Y., Moller K., Bein T. and Cox D., *J. Am. Chem. Soc.*, **111** (1989) pp.8006.
6. Micic O. I., Sprague J.R., Curtis C. J., Jones K. M., Machol J. L., Nozik A. J., Giessen H., Fluegel B., Mohs G. and Peyghambarian N., *J. Phys. Chem.*, **99** (1995) pp.7754.
7. Guzelian A. A., Katari J. E. B., Kadavanich A. V., Banin U., Hamad K., Juban E., Alivisatos A.P., Wolters R.H., Arnold C.C. and Heath J.R., *J. Phys. Chem.*, **100** (1996), pp.7212.
8. Li Y. D., Duan X. F., Dian Y. T., Li Y., Ji M. R. and Li C. W., *J. Am. Chem. Soc.*, **119** (1997) pp.7869.
9. Janik J. F., Wells R. L., Young V. G. Jr, Rheingold A. L. and Guzei I. A., *J. Am. Chem. Soc.*, **120** (1998) pp.532.
10. Sunstrom J. E., Moser W. R. and Marshik-Guerts B., *Chem. Mater.*, **8** (1996) pp.2061.
11. Yin J. S. and Wang Z. L., *J. Phys. Chem. B*, **101** (1997) pp.8979.
12. Masui T., Fujiwara K., Machida K., Adachi G., Sakata T. and Mori H., *Chem. Mater.*, **9** (1997) pp.2197.
13. Nyffenegger R. M., Craft B., Shaaban M., Gorer S., Erley G. and Penner R. M., *Chem. Mater.*, **10** (1998) pp.1120.

14. Steigerwald M. L. and Brus L. E., *Acc. Chem. Res.*, **23** (1990) pp.183.
15. Alivisatos A. P., *J. Phys. Chem.*, **100** (1996) pp.13226.
16. Tsuji M. and Abe M., *Solvent Extr. Ion Exch.*, **2** (1984) pp.253.
17. Shen Y. F., Zerger R. P., DeGuzman R. N., Suib S. L., McCurdy L., Potter D. I. and O'Young C. L., *Science*, **260** (1993) pp.511.
18. Yin Y. G., Xu W. Q., Shen Y. F. and Suib S. L., *Chem. Mater.*, **6** (1994) pp.1808.
19. Feng Q., Kanoh H., Ooi K., Tani M. and Nakacho Y., *J. Electrochem. Soc.*, **141** (1994) pp.135.
20. Feng Q., Karoh H., Miyai Y. and Ooi K., *Chem. Mater.*, **7** (1995) pp.148.
21. Feng Q., Kanoh H., Miyai Y. and Ooi K., *Chem. Mater.*, **7** (1995) pp.1226.
22. Feng Q., Kanoh H., Miyai Y. and Ooi K., *Chem. Mater.*, **7** (1995) pp.1722.
23. Koksbang R., Barker J., Shi H. and Saidi M.Y., *Solid State Ionics*, **84** (1996) pp.1.
24. Armstrong A. R. and Bruce P. G., *Nature*, **381** (1996) pp.499.
25. Rao C. N. R., Cheetham A. K. and Mahesh R., *Chem. Mater.*, **8** (1997) pp.2421.
26. Bricker O., *Am. Mineral.*, **50** (1965) pp.1296.
27. Pereira-Ramos J.P., Badour R., Bach S. and Baffier N., *Solid State Ionics*, **701** (1992) pp.3.
28. Bach S., Pereira-Ramos J. P. and Baffier N., *Electrochim. Acta*, **38** (1993) pp.1995.
29. Bach S., Pereira-Ramos J. P. and Baffier N., *J. Solid State Chem.*, **120** (1995) pp.70.
30. Bach S., Henry M., Baffier N. and Livage J., *J. Solid State Chem.*, **88** (1990) pp.325.
31. Parent J., Olazcuaga R., Devalette M., Fouassier C. and Hagenmuller P., *J. Solid State Chem.*, **3** (1971) pp.1.
32. Baser W., Graf P. and Feitknecht W., *Helv. Chim. Acta*, **37** (1954) pp.2322.
33. Brock S. L., Sanabria M., Suib S. L., Urban V., Thiagarajan P. and Dotter D. I., *J. Phys. Chem. B*, **103** (1999) pp. 7416. (Model I assumes the absence of a hydration layer between the TAA cations and manganese oxide layers, although water molecules may be present in the same plane as the TAA cations; model II corresponds to a total of one effective layer of water in addition to the TAA cations; and model III presents an expansion of two layers of water between the TAA cations and the manganese oxide slabs).
34. Gao Q., Giraldo O., Tong W. and Suib S. L., *Chem. Mater.*, **13** (2001) pp.778.
35. Ma Y., Luo J. and Suib S. L., *Chem. Mater.*, **11** (1999) pp.1972.
36. Liu Z. H., Ooi K., Kanoh H., Tang W. P. and Tomida T., *Langmuir*, **16** (2000) pp.4154.

# SELF-ASSEMBLY OF IRON NANOPARTICLES WITH THE ASSISTANCE OF BINARY SURFACTANTS UNDER A SOLVOTHERMAL REACTION

YANG-LONG HOU, JUN-FENG YU AND SONG GAO\*

*College of Chemistry and Molecular Engineering, State Key Laboratory of Rare Earths Materials Chemistry and Applications, Peking University, Beijing 100871, China  
E-mail: gaosong@pku.edu.cn*

GE-HUI WEN, X. X. ZHANG

*Department of Physics., The Hong Kong University of Science and Technology, Clear Water Bay, Kowloon, Hong Kong, China*

Self-assembly based on spontaneous control of non-covalent interaction, such as van de Waals forces,  $\pi - \pi$  interaction, electrostatic forces, can be applied to the fabrication of structured system at a molecular level. In this paper, binary surfactants (triethylphosphine oxide and oleic acid) were added when the iron complex  $\text{Fe}(\text{acac})_3$  was reduced to Fe nanoparticles by  $\text{N}_2\text{H}_4\text{OH}$  in ethylenediamine with PVP under a solvothermal reaction, resulting in spherical aggregates. The average size of the assembled sphere is about  $210 \pm 10$  nm. A similar reaction without the surfactants just gave smaller Fe-nanoparticles (ca. 60 nm) without such an aggregation. The magnetic properties of the spherical aggregates were investigated by a superconducting quantum interference device (SQUID) magnetometer. The particles show a bulk-like softmagnetic Fe behavior.

## 1 Introduction

The assembly of individual nanoparticle into structured system is of interest because of the potential application in magnetic recording, molecular recognition, biological label, electronic devices [1-4]. A number of techniques are exploited in assembly approaches of nanoparticles, such as aerosol assisted, thiol, DNA and recognition-mediated assembly, etc [5-8]. Among these, the building of organized magnetic metallic nanoparticles is a major issue in recent years [9,10]. However, conventional synthetic procedure of nanoscale materials limits to a discrete system. Self-assembly based on spontaneous control of non-covalent interaction, including van de Waals forces [11,12],  $\pi - \pi$  interaction [13], electrostatic forces [14,15], hydrogen bonding [16-18], provides a powerful route for the fabrication of structured system at a molecular level. Such polymer-functionalized nanoparticles were used as building block to fabricate structured system. Recently, Rotello and co-workers reported that monolayer polymer-protected gold nanoparticles were self-assembled into spherical aggregates through hydrogen bonding interaction [18]. The self-assembly of TTP-COOH coated  $\text{Fe}_3\text{O}_4$  through  $\pi - \pi$  interaction was also reported by L. Jiang [13]. However self-assembled aggregates of magnetic nanometals are rarely studied at the present time [19]. And these aggregates were not uniform in size and shape, which was governed by the polymer and the self-assemble process, and will possibly affects their use in electric devices.

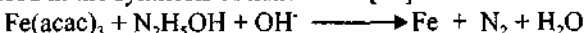
In this paper, we report an intriguing finding that binary surfactants helped self-assembly of magnetic particles into spherical aggregates. The self-assembly of magnetic nanometals occurs in a solvothermal reaction through the mortar of triethylphosphine oxide (TOPO) and oleic acid.

## 2 Experimental

The synthesis of metal nanoparticles was carried out in a polyfluoroethylene-lined stainless steel bomb (100 ml capacity) under autogenous pressure. In this experiment, 0.2g Fe(acac)<sub>3</sub>, 1.55g PVP, 2 ml 10%N<sub>2</sub>H<sub>5</sub>OH were put into the reaction vessel ,which had been already filled with ethylenediamine up to 90% capacity. In special, binary surfactants, that are Tri-n-octylphosphine oxide (TOPO) (0.2g, 99% purity) and Oleic acid (0.1ml), which were purchased from Acros organic company, were put into the vessel. The autoclave was maintained at 120-140 °C for 8-12h. After reaction, the autoclave was cooled to room temperature naturally. The precipitates were collected and washed with methanol/CHCl<sub>3</sub>, 1:1 and distilled water in sequence to remove the possible excess PVP, N<sub>2</sub>H<sub>5</sub>OH and by-products, then were dried in vacuum at 60°C for 12h. X-ray powder diffraction was performed on a Rigaku Dmax/2000 diffractometer under Cu K $\alpha$  radiation. Transmission electron microscopy (TEM) to determine the particle size and size distribution was collected by JEOL 200CX (200kV). Magnetic studies were carried out using a superconducting quantum interference device (SQUID) magnetometer.

## 3 Results and Discussion

Iron particles were synthesized by a solvothermal route, to the best of our knowledge, which is seldom used in the synthesis of nanometals[20].The reaction was as the follows :



The advantage of this reaction lies on the creation of nitrogen, which makes an inert ambience to prevent nanoparticle from further oxidation. So it is convenient route to make metal nanoparticles. The formation of the assembled iron particles can be directly seen by transmission electron microscopy (TEM) image (in Figure 1a), the average size of assembled spheres is about 210±10 nm. The X ray diffraction pattern of the products (Figure 1b) revealed the formation of cubic Fe [21].

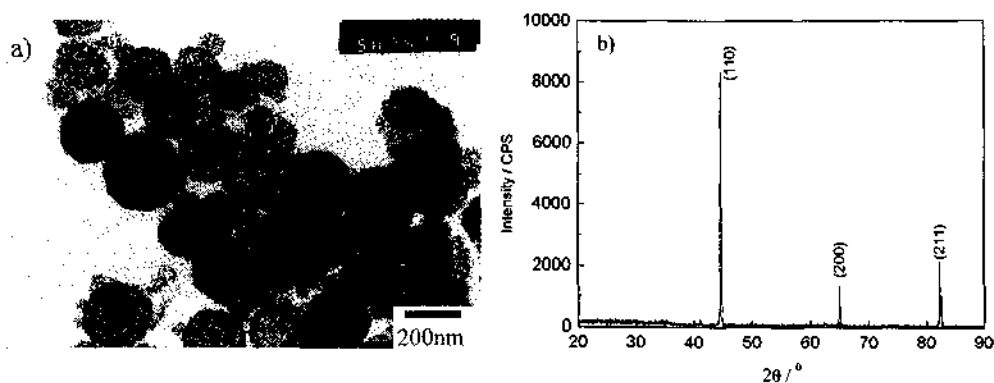
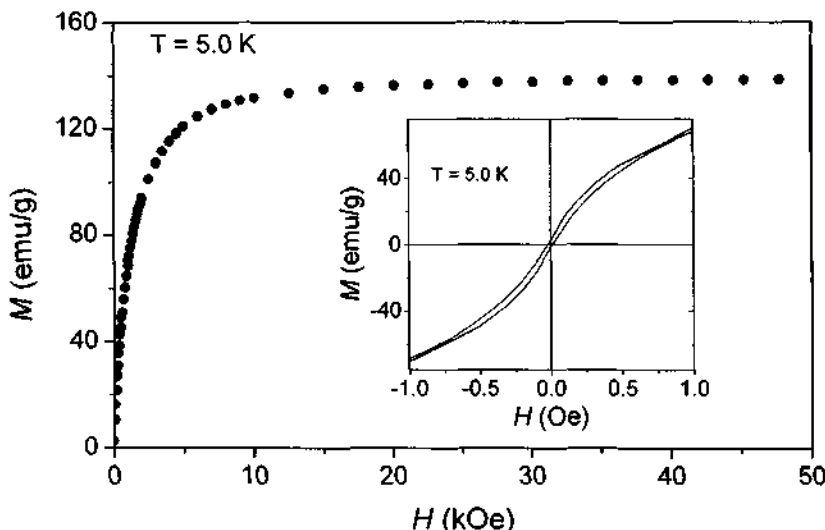


Figure 1. TEM images (a) and XRD pattern (b) for assembled iron nanoparticles

A similar reaction without the surfactants just gave smaller Fe-nanoparticles (ca. 60 nm) without such an aggregation [22], suggesting that the two surfactants have a key role

in the self-assemble process. Further studies are acquired to characteristic of the structure and the interaction between metals and surfactants in the assembled iron nanoparticles.

Field dependence of magnetization shows a rapid saturation, and with a very small hysteresis, suggesting that the particles have a bulk-like softmagnetic Fe behavior. The saturated magnetization of assembled iron particles is 138 emu/g at 5K, and it decreases slightly with increase of temperature, and reaches 135 emu/g at room temperature. Standard crystalline bcc Fe has a saturated magnetization of 222 emu/g at 298K [23], whereas bulk amorphous Fe saturates at 156 emu/g [24]. For the PVP-coated iron nanoparticles prepared form decomposition of  $\text{Fe}(\text{CO})_5$ , the saturated magnetization is 101 emu/g at 290K [25].



**Figure 2.** Field dependent magnetization of iron nanoparticles, measured at 5 K.

#### 4 Conclusion

In this work, a route to build an aggregate of nanoparticles through two surfactants as mortar is developed in organic solvent. The results reveal that the strategy of self-assembly is an efficient way to create a new nano-structured system. The average size of assembled sphere is about  $210 \pm 10 \text{ nm}$ . The sample has a bulk-like softmagnetic Fe behavior.

#### 5 Acknowledgement

Financial support from the State Key Project for Fundamental Research (G1998061305), and the National Science Fund for Distinguished Young Scholars (20125104) is gratefully acknowledged.

## References

1. Lieber C. M., One-dimensional nanostructures: chemistry, physics & applications. *Solid State Commun.* **107** (1998) pp. 607-616.
2. Bruchez Jr. M., Moronne M., Gin P., Weiss S. and Alivisatos A. P., Semiconductor nanocrystals as fluorescent biological labels. *Science* **281** (1998) pp. 2013-2015.
3. Sun S., Murray C. B., Weller D., Folks L. and Moser A., Monodisperse FePt nanoparticles and ferromagnetic FePt nanocrystal superlattices. *Science* **287** (2000) pp. 1989-1992.
4. Cui Y. and Lieber C. M., Functional nanoscale electronic devices assembled using silicon nanowires building blocks. *Science* **291** (2000) pp. 851-853.
5. Lu Y., Fan H., Stump A., Ward T. L., Rieker T. and Brinker C. J., Aerosol-assisted self-assembly of mesostructured spherical nanoparticles. *Nature* **398** (1999) pp. 223-226.
6. Motte L. and Pileni M. P., Self-assemblies of silver nanocrystals: influence of length of thiol-alkyl chains used as coating agent. *Applied Surface Science* **164** (2000) pp. 60-67.
7. Mucic R. C., Storhoff J. J., Mirkin C. A. and Letsinger R. L., DNA- directed synthesis of binary nanoparticles network materials. *J. Am. Chem. Soc.* **120** (1998) pp. 12674-12675.
8. Frankamp B. L., Uzun O., Ilhan F., Boal A. K. and Rotello V. M., Recognition-mediated assembly of nanoparticles into micellar structured with diblock copolymers. *J. Am. Chem. Soc.* **124** (2002) pp. 892-893.
9. Alivisatos A. P. et al., Organization of ‘nanocrystal molecular’ using DNA. *Nature* **382** (1996) pp. 609-611.
10. Peng X., Manna L., Yang W., Wickham J., Scher E., Kadavanich A. and Alivisatos A. P., Shape of CdSe nanocrystals. *Nature* **404** (2000) pp. 59-61.
11. Lehn J.-M., *Supramolecular chemistry* (VCH, Weinheim, 1995).
12. Andres R. P., Bielefeld J. D., Henderson J. I., Janes D. B., Kolagunta V. R., Kubiak C. P., Mahiney W. J. and Osifchin R. G., Self-assembly of a two-dimensional superlattice of molecularly linked metal clusters. *Science* **273** (1996) pp. 1690-1693.
13. Jin J., Iyoda T., Cao C., Song Y., Jiang L., Li T. J. and Zhu D. B., Self-assembly of uniform spherical aggregated of magnetic nanoparticles through  $\pi - \pi$  interactions. *Angew. Chem. Int. Ed.* **40** (2001) pp. 2135-2138.
14. Fye M. C. T. and Stoddart J. F., Synthetic supramolecular chemistry. *Acc. Chem. Res.* **32** (1999) pp. 278-286.
15. Caruso F., Caruso R. and Mohwald H., Nanoengineering of inorganic and hybrid hollow spheres by colloidal templating. *Science* **282** (1998) pp. 1111-1114.
16. Mirkin C. A., Letsinger R. L., Mucic R. C. and Storhoff J. J., DNA-based method for rationally assembling nanoparticles into macroscopic materials. *Nature* **382** (1996) pp. 607-609.
17. Rebek J., Reversible encapsulation and its consequences in solution. *Acc. Chem. Res.* **32** (1999) pp. 278-286.
18. Boal A. K., Ilhan F., Derouiche J. E., Thurn-Albercht T., Russell T. P. and Rotello V. M., Self-assembly of nanoparticles into structured spherical and network aggregates. *Nature* **404** (2000) pp. 746-748.
19. Black C. T., Murray C. B., Sandstrom R. L. and Sun S., Spin-dependent tunneling in self-assembled cobalt-nanocrystal superlattices. *Science* **290** (2000) pp. 1131-1134.

20. Gao S., Zhang J., Zhu Y. F. and Che C. M., A convenient solvothermal route to ruthenium nanoparticles. *New J. Chem.* **24** (2000) pp. 739-740.
21. Joint Committee on Powder Diffraction Standards files No.06-0696.
22. Hou Y. L. and Gao G., Solvothermal Synthesis and Magnetic Properties of Polymer Protected Iron and Nickel Nanocrystals, submitted to *J. Mater. Chem.*
23. Cullity B. D., Introduction to magnetic materials. Addison-Wiley: New York, 1972, pp. 171-190.
24. Rozenfeld O., Koltypin Y., Bamnolker H., Margel S. and Gedanken A., Self – assembled monolayer coatings on amorphous iron. *Langmuir* **11** (1994) pp.3919-3921.
25. Suslick K. S., Fang M. and Hyeon T., Sonochemical synthesis of iron colloids. *J. Am. Chem. Soc.* **118** (1996) pp. 11960-11961.

This page is intentionally left blank

# ONE-STEP SOLID-STATE REACTION AT ROOM TEMPERATURE FOR THE SYNTHESIS OF POLYOXOMETALATE NANOPARTICLES AND NANORODS

ZHENHUI KANG, ENBO WANG,\* YANGGUANG LI AND CHANGWEN HU

*Institute of Polyoxometalate Chemistry, Department of Chemistry, Northeast Normal University,  
Changchun, Jilin, 130024, P. R. China  
E-mail: wangenbo@public.cc.jl.cn*

A novel and simple one-step solid-state reaction in the presence of a suitable surfactant (PEG-400) has been developed to synthesize uniform polyoxometalate nanorods with an average diameter of *ca.* 20 nm and a length of up to 400 nm. Polyoxometalate nanoparticles were also prepared by one-step solid-state reaction at room temperature. The polyoxometalate nanorods and nanoparticles were characterized by IR, elemental analyses, XRD and TEM. The uniform nanoparticles have an average size of 8~10 nm. The possible formation mechanism of these polyoxometalate nanomaterials was speculated.

## 1 Introduction

Many peculiar and technologically important phenomena occur in nanosystems, such as quantized excitation, coulomb blockade, single-electron tunneling (SET) and metal-insulator transition, which have attracted intensive interest in recent years [1,2]. Nanosystems, with characteristic lengths between 1 and 100 nm, have become one of the most attractive subjects in physics, materials science, chemistry, and biology [3-5]. In this field, the exploration of novel nanomaterials is still the first and one of the most significant challenges to the realization of various applications. The preparations of nanostructural materials are currently the focus of considerable interest. Many methods have been used for the preparation of low dimensional nanomaterials [5]. However, to our knowledge, complex process control, high reaction temperature or long synthesis may be required for these approaches. In this paper, a series of novel polyoxometalates (POMs) nanoparticles and nanorods were prepared by one-step, solid-state reaction at room temperature for the first time.

Recently, POMs as one of typical metal oxide clusters have received much attention owing to their novel compositions, structures and applications in the fields of catalysis, medicine and electromagnetic materials [6-10]. In particular, the attracting properties of the POM related to the developing nanomaterials are (i) environmentally benign catalysis [11(a,b), 14-17], (ii) unusual magnetic properties rendered by the incorporation of metal-oxo clusters with various transition metal ions and the increasing of extra electron to become heteropoly blue [9,12,13], (iii) photochromism, electrochromism and luminescence properties [11(c)] and (iv) anti-HIV activities and the interactions with proteins [8]. It is obvious that POMs are one of extremely versatile inorganic entities for the construction of functionally active solids and the favorite candidates to be transformed into nanometer sized materials [12-21].

At present, the design and preparation of POMs-based nanomaterials are in infancy. Müller et al have ingeniously synthesized many giant clusters of POMs within the nanometer-scale, including novel kinds of large rings and wheel-shaped systems with 176 or even more Mo atoms [22-24]. Recently, Takerulto et al have studied the growing process of polyoxotungstate  $(\text{NH}_4)_3\text{PW}_{12}\text{O}_{40}$  crystalline nanoparticles [25]. Because numerous well characterized POMs are available [16-25], it is extremely significant to

develop new strategies for the preparation of POM nanomaterials so as to explore their interesting properties. In this paper, POM nanoparticles and nanorods were prepared by one-step, solid-state reaction at room temperature for the first time. The formation mechanism of these POM nanomaterials was presumed.

## 2 Experimental

### 2.1 Materials

$\text{Na}_2\text{WO}_4 \cdot 2\text{H}_2\text{O}$ ,  $\text{H}_3\text{PO}_4$ ,  $\text{CsCl}$ , hydrochloric acid, ether, PEG-400, and triton-X-100 were commercially available reagent grade without further purification.

### 2.2 Synthesis of $\text{H}_6\text{P}_2\text{W}_{18}\text{O}_{62} \cdot n\text{H}_2\text{O}$

Precursor of  $\text{H}_6\text{P}_2\text{W}_{18}\text{O}_{62} \cdot n\text{H}_2\text{O}$  was prepared by improved methods of published literatures [26,27]. The  $\text{Na}_6\text{P}_2\text{W}_{18}\text{O}_{62}$  is prepared according to the literatures [26,27]. Then the sodium salts of POMs are dissolved in distilled water (1 mmol/6mL), acidified by hydrochloric acid (12 mol/L, 4mL), and extracted by ether (4 mL). The heavy layer, added with half its volume of water, gave yellow crystals after desiccation. Elemental analyses gave the P:W = 1:9 IR spectra exhibited the characteristic peaks of Dawson structures [26,27].

### 2.3 Preparation of POM nanoparticles

A typical preparation of  $\text{Cs}_6\text{P}_2\text{W}_{18}\text{O}_{62}$  nanoparticles is as follows. The weighed reactants in a mole ratio of  $\text{CsCl}:\text{H}_6\text{P}_2\text{W}_{18}\text{O}_{62} \cdot 20\text{H}_2\text{O} = 5:1$  were put into an agate mortar followed with several drops of surfactant Triton-X-100. The mixture was thoroughly ground for 20 min, washed in a supersonic washing machine using absolute alcohol as dispersant, and centrifuged at a speed of 10000 rpm. The washing and centrifuging processes were repeated for 5 times. The wet nanoparticles of  $\text{Cs}_6\text{P}_2\text{W}_{18}\text{O}_{62}$  were obtained and dried in vacuum drying oven for 4 h (50-60 °C). The final yield of nanoparticles  $\text{Cs}_6\text{P}_2\text{W}_{18}\text{O}_{62}$  was 70% (based on W). Anal. Calcd. for the nanoparticles  $\text{Cs}_6\text{P}_2\text{W}_{18}\text{O}_{62}$  (%): Cs, 15.46; P, 0.12; W, 64.13; Found: Cs, 15.41; P, 0.18; W, 64.19. IR ( $\text{cm}^{-1}$ ): 1089 (s), 1002 (w), 956 (ms), 913 (ms), 797 (s).

### 2.4 Preparation of POM nanorods

The procedure employed by us for preparing POMs nanorods is as follows. In a typical synthesis of  $\text{Cs}_6\text{P}_2\text{W}_{18}\text{O}_{62}$  nanorods, 1 g  $\text{H}_6\text{P}_2\text{W}_{18}\text{O}_{62} \cdot n\text{H}_2\text{O}$  and 0.5g  $\text{CsCl}$  were ground for 10 min each, before mixing together, 3ml of polyethylene glycol (PEG) 400 was than added to the mixture. After 30min of grinding, the mixture was washed in an ultrasonic bath four times with EtOH to remove the PEG. Finally, the product was dried in air at 50 °C for 2 h. The yield was 90% (based on W).

### 2.5 Characterization

The IR spectra (KBr pellet; 4000-400  $\text{cm}^{-1}$ ) were recorded on a Mafna FT-IR 560 spectrophotometer. Ag, Cs, Mo, P, and W were determined by a Leaman inductively coupled plasma (ICP) spectrometer. The XRD patterns were obtained on a D/Max-RA diffractometer and D/Max 2500V PC X with Cu-K $\alpha$  radiation. Hitachi-H600

transmission electron microscope was used to examine the morphology of the POM nanomaterials. For the electron microscopy study, the powder was dispersed in absolute alcohol with an ultrasonic vibrator for 20 min, and then deposited on a copper grid covered with a perforated carbon film.

### 3 Results and Discussion

Element analyses results prove that these nanoparticles and nanorods still keep the compositions of POMs. In the IR spectra, intense bands at 1089, 956, 913, 797  $\text{cm}^{-1}$  are attributed to the vibration of  $\nu$  (P=Oa),  $\nu$  (W=Ot),  $\nu$  (W-Ob-W) and  $\nu$  (W-Oc-W), respectively. These characteristic peaks of the Dawson type structure further prove that the nanomaterials are composed of POMs. The XRD patterns of POM nanoparticles are shown in Figure 1. The sizes of these POM nanoparticles, 8-10 nm, were calculated from the data of broadened XRD peaks with the Scherer equation:  $D = 0.89 \lambda / \beta \cos \theta$ . As shown in the Figure 2, the uniform nanoparticles have an average size of 8~10 nm and nanorods have average diameter of ca.20nm and lengths of up to 400nm.

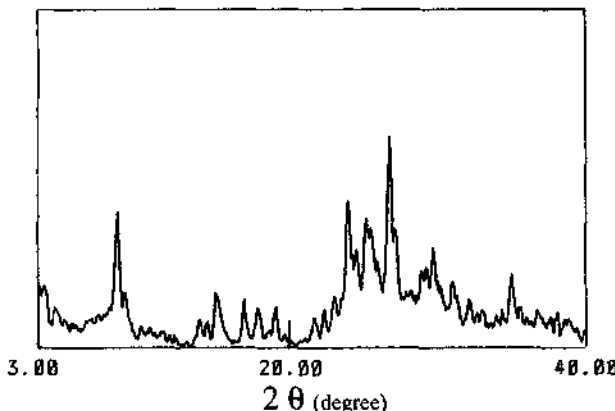


Figure 1. The XRD patterns of POM nanoparticles:  $\text{Cs}_6\text{P}_2\text{W}_{18}\text{O}_{62}$ .

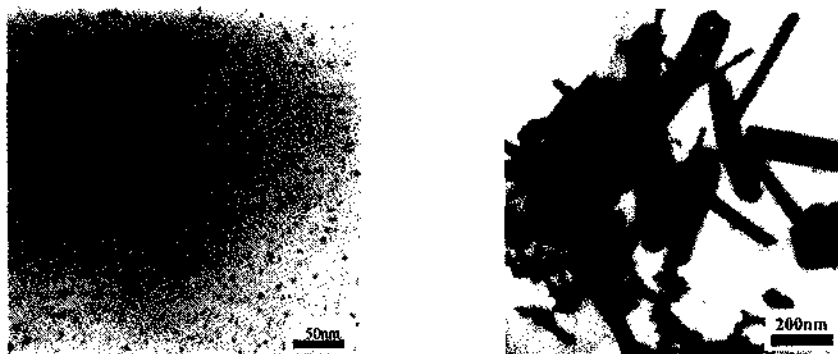
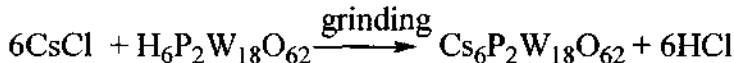


Figure 2. The TEM images of POMs nanoparticles and nanorods:  $\text{Cs}_6\text{P}_2\text{W}_{18}\text{O}_{62}$ .

Pseudo-liquid phase behavior is a unique phenomenon in the heteropolyacid (HPA) chemistry. Polar and basic molecules are rapidly absorbed into the solid lattice of the HPAs, these solids behaving in a sense like a concentrated solution. [28] During the preparation of POM nanoparticles *via* the solid-state reaction, such amorphous and flexible pseudo-liquid phase solids make reactions proceed rapidly and completely. In this paper,  $H_6P_2W_{18}O_{62}\cdot20H_2O$  were selected as precursors. The non-ionic surface-active agent Triton-X-100 was used in the preparation of POM nanoparticles. Only several drops of Triton-x-100 were added when the mixture of HPA and CsCl was ground in the agate mortar. During grinding at room temperature, a lot of water microcells could be formed in the reaction system owing to the interaction between the crystal water of HPA and the triton-X-100. These microcells are metastable and provide reaction fields for the formation of nanoparticles. If the reaction in microcells could be finished rapidly and completely, the shape and size of products could be controlled by these microcells in the triton-X-100 film. According to the different properties of A and B class of POMs [29], we select a series of metathetical reactions to synthesize the POM particles. The typical metathetical reaction is as follows:



On the one hand, these complete and rapid one-step solid-state reactions are due to the pseudo-liquid phase properties of solid-state HPAs. On the other hand, suitable crystal water of HPAs is important to the synthesis of POM nanoparticles. The HPA precursors with about twenty crystal water molecules are the best candidate for the preparation of uniform nanoparticles as observed in the TEM images (Figure 1). HPAs with excessive or lacking crystal water could not become the appropriate precursor.

A novel, one-step, solid-state reaction at room temperature was employed to synthesize the POM nanorods at ambient temperature, using PEG-400. It has been known that the surfactant PEG forms a chainlike structure due to the assembly in water. [30] Therefore, we can imagine that 1D nanomaterials could be formed in the field of the chainlike structure of PEG. During the preparation of 1D POM nanomaterials, the sticky solution is one of important factors, in which the uniform POM nanorods could be obtained and stably exist without agglomeration.

#### 4 Acknowledgments

We gratefully acknowledge the financial support of the National Natural Science Foundation of China (20171010).

#### References

1. Xia, Y. N.; Rogers, J. A.; Paul, K. E.; Whitesides, G. M. *Chem. Rev.*, **99** (1999) pp. 1823-1848.
2. Ball, P; Garwin L. *Nature*, **355** (1992) pp 761-766.
3. Duan, X. F.; Huang, Y.; Cui, Y.; Wang, J. F.; Lieber, C. M. *Nature*, **409** (2001) pp. 66-69.
4. Jana, N. R.; Latha, G. H.; Murphy, C. J. *Chem. Commun.*, (2001) pp. 617-618.
5. Huang, M. H.; Mao, S.; Feick, H.; Yan, H. Q.; Wu, Y. Y.; Kind, H.; Weber, E.; Russo, R.; Yang, P. D. *Science*, **292**, (2001), pp 1897-1899. Huang, M. H.; Mao, S.;

- Feick, H.; Yan, H. Q.; Wu, Y. Y.; Kind, H.; Weber, E.; Russo, R.; Yang, P. D. *Science*, **292**, (2001), pp 1897-1899. Chen, C. C.; Yeh, C. C.; Chen C. H.; Yu, M. Y.; Liu, H. L. et al. *J. Am. Chem. Soc.*, **123**, (2001), pp. 2791-2798. Kwan, S.; Kim, F.; Akana, J.; Yang, P. D. *Chem. Commun.* (2001) pp. 447-448.
6. Pope, M. T. *Heteropoly and Isopoly Oxometalates*; Springer, Berlin, (1983) pp. 30-33.
  7. Pope, M. T.; Müller, A. *Angew. Chem. Int. Ed. Engl.*, **30** (1991) pp. 34-48.
  8. (a) Rhule, J. T.; Hill, C. L.; Judd, D. A.; Schinazi, R. F. *Chem. Rev.*, **98** (1998) pp. 327-357. (b) Hill, C. L.; Weeks, M. S.; Schinazi, R. F. *J. Med. Chem.*, **33** (1990) pp. 2767-2772.
  9. Müller, A.; Petters, F.; Pope, M. T.; Gatteschi, D. *Chem. Rev.*, **98** (1998) pp. 239-272.
  10. Coronado, E.; Gomez-Garcia, C. J. *Chem. Rev.*, **98** (1998) pp. 273-296.
  11. (a) Weinstock, I. A. *Chem. Rev.*, **98**, (1998), pp 113-170. (b) Mizuno, N.; Misono, M. *Chem. Rev.*, **98**, (1998), pp 199-217. (c) Yamase, T. *Chem. Rev.*, **98** (1998) pp. 307-325.
  12. Bi, L. H.; Wang, E. B.; Peng, J.; Huang, R. D.; Xu, L.; Hu, C. W. *Inorg. Chem.*, **39** (2000) pp. 671-679.
  13. Bi, L. H.; Huang, R. D.; Peng, J.; Wang, E. B.; Wang, Y. B.; Hu C. W. *J. Chem. Soc., Dalton Trans.*, (2001) pp. 121-129.
  14. You, W. S.; Wang, E. B.; Xu, Y.; Li, Y. G.; Xu, L.; Hu, C. W. *Inorg. Chem.*, **40** (2001) pp. 5468-5471.
  15. Guo, Y. H.; Wang, E. B.; Zhou, Y. N.; Feng, S. H. *Chem. Mater.*, **12(11)**, (2000) pp. 3501-3508.
  16. Guo, Y. H.; Hu, C. W.; Wang, X. L.; Wang, E. B., Zhou, Y. N., Feng, S. H. *Chem. Mater.*, **13(11)** (2001) pp. 4058-4064.
  17. Guo, Y. H.; Li D. F.; Hu, C. W.; Wang, Y. H.; Wang, E. B. *Appl. Catal. B (Environment)*, **30(3-4)** (2001) pp. 337-349.
  18. Peng, G; Wang, Y. H.; Hu, C. W.; Wang, E. B. *Applied Catalysis A, General*, **218 (1-2)**, (2001), pp. 91-99.
  19. Peng, J.; Wang, E. B.; Zhou, Y. S.; Xing, Y.; Jia, H. Q.; Lin, Y. H. *J. Chem. Soc., Dalton Trans.*, (1998) pp. 3865-3870.
  20. Xu, L.; Sun, Y. Q.; Wang, E. B.; Shen, E. H.; Liu, Z. R.; Hu, C. W. *New J. Chem.*, **23** (1999) pp 1041-1044.
  21. Xu, L.; Sun, Y. Q.; Wang, E. B.; Shen, E. H.; Liu, Z. R.; Hu, C. W. *J. Solid State Chem.*, **146** (1999) pp. 533-537.
  22. Müller, A.; Shah, S. Q. N.; Bogge, H.; Schmidtmann, M. *Nature*, **397** (1999) pp. 48-50.
  23. Müller, A.; Kogerle, P.; Kuthmann, C. *Chem. Commun.*, (1999) pp. 1347-1358.
  24. Müller, A.; Samark, D.; Bögge, H.; Schmidtmann, M.; Botar, A.; Patrut, A. *Chem. Commun.*, (2001) pp. 657-658.
  25. Ito, T.; Inumaru, K.; Misono, M. *Chem. Mater.*, **13**, (2001), pp 824-831.
  26. Acerete, R.; Hammer, C. F.; Baker, L. C. W. *J. Am. Chem. Soc.*, **101**, (1979) pp. 267 and references there in.
  27. T. Osakai, S. Himeno, A. Saito, *J. Electroanal. Chem. Interfacial Electrochem.*, **332**, (1992) pp 169 and references therein.
  28. Shikata, S.; Misono, M. *Chem. Commun.*, (1998), pp 1293-1294.
  29. Misono, M. *Catal. Rev.-Sci. Eng.*, **30**, (1988) pp. 339-392.
  30. Sun, J. H.; Gong, Y. J.; Fan, W. H.; Sun, Y. H. *Chem. J. Chin. Univ.* **21**, (2000) pp. 95-99.

This page is intentionally left blank

# NANOCRYSTALLINE $\beta$ -SiC FILMS GROWN BY CAT-CVD WITH PRE-CARBONIZATION PROCESS

J. C. LI, Q. ZHAO, M. WANG, X. M. SONG, H. WANG, B. WANG AND H. YAN\*

*The Key Lab of Advanced Functional Materials of China Education Ministry, Beijing Polytechnic University, Beijing, China, 100022  
E-mail: hyan@bjpu.edu.cn*

Nanocrystalline cubic SiC ( $\beta$ -SiC) films were grown on silicon (100) substrate by catalytic chemical vapor deposition (Cat-CVD) at a temperature as low as 300°C with a pre-carbonization process. To enhance nucleation density of  $\beta$ -SiC, a buffer layer was made by carbonizing the substrate surface. From the comparison between both carbonized sample and non-carbonized sample, the pre-carbonization process has beneficial effects on the growth of nanocrystalline  $\beta$ -SiC films. Mechanistic interpretations are given to explain the carbonization process and catalyzing deposition process.

## 1 Introduction

With its wide band gap, high saturated electron drift velocity, high thermal conductivity and other promising properties, silicon carbide (SiC) films have exhibited great superiority for potential applications in the aspects of high-temperature, high-frequency, high-power conducting devices, hard wear resistant coatings for corrosion or thermal oxidation [1]. Considering the high quality of cubic-SiC ( $\beta$ -SiC) films on Si substrate,  $\beta$ -SiC films are more attractive in the integrated technology compatible with Si. However,  $\beta$ -SiC films are conventionally produced by chemical vapor deposition at high growth temperature (>1000°C), which suffers from structural damage and formation of voids [2~4]. Recently, a newly developed low-temperature deposition method, so called catalytic chemical vapor deposition (Cat-CVD), was proposed to obtain some thin films of device quality without using plasma [5,6].

There are some reports [7,8] about preparing  $\alpha$ -SiC and  $\beta$ -SiC films at low temperature by Cat-CVD and other methods, such as magnetron sputtering and plasma enhanced CVD (PECVD). In order to get high quality  $\beta$ -SiC films, the substrate temperatures are still high (400~600°C). Furthermore, the growth mechanism of  $\beta$ -SiC films by Cat-CVD is not well understood. In this work, by using Cat-CVD with pre-carbonization process, nanocrystalline  $\beta$ -SiC films were successfully synthesized on Si substrate at the low substrate temperature of 300°C.

## 2 Experimental

The gases used for the experiments were pure CH<sub>4</sub> (99.99%) as C source, pure SiH<sub>4</sub> (99.99%) as Si source and pure hydrogen (99.999%) as the dilution and etching gas. These gases were introduced into the reactor through the dispersal ring placed at the bottom of the reactor. The substrate was Si (100) wafers with a resistivity of 10~20 Ω·cm and the catalyst was made of high-purity tungsten wire of 0.4 mm diameter. A thermocouple attached on the substrate surface was used to monitor the substrate temperature.

Pre-carbonization process was performed at a substrate temperature of 300°C with flow rates of 5 sccm CH<sub>4</sub> and 100 sccm H<sub>2</sub> at a high pressure of 1000~2000Pa. Here, the carbonization time was about 5~10 min. The deposition was carried out at the hydrogen flow rate of 200 sccm, the ratio of CH<sub>4</sub> and SiH<sub>4</sub> flow rate of 1:1, the catalyst temperature of 2000°C, the substrate temperature of 300°C, and under a fixed reaction pressure of 100 Pa, respectively.

### 3 Results and Discussion

Figure 1 shows typical FTIR spectra of the carbonized sample and non-carbonized sample. The spectra display only the characteristic Si-C bond absorption within the range of 400~4000 cm<sup>-1</sup>. The absorption peak of the carbonized sample shifted slightly from 796cm<sup>-1</sup>, which is the characteristic absorption peak of  $\beta$ -SiC stretching mode [9], to 808cm<sup>-1</sup>, as compared with the non-carbonized sample. There are different explanations for the blue shift. The most important two aspects involved are as follows: one is size effect and the other is surface effect. Due to the decrease of the particle scale and the broadening of energy gap, the absorption band subsequently shifts to short wave. The width between molecular orbit energy levels occupied by electrons and those unoccupied (namely energy gap) increases with the decline of the particle diameter, which is the fundamental cause of blue shift [10]. Since the nanometer particles are very small, the great surface tension causes the distortion of the crystal lattice. Subsequently, the lattice constant decreases. According to nanometer oxide silicon and nanometer nitride silicon [11], the decrease in the bond length results in the increase of the vibration frequency of nanometer particle bands, namely the absorption band shifts to higher wavenumber. Therefore, the behavior of the blue shift indicates that the size of crystalline grains of the carbonized sample is smaller than that of the non-carbonized sample.

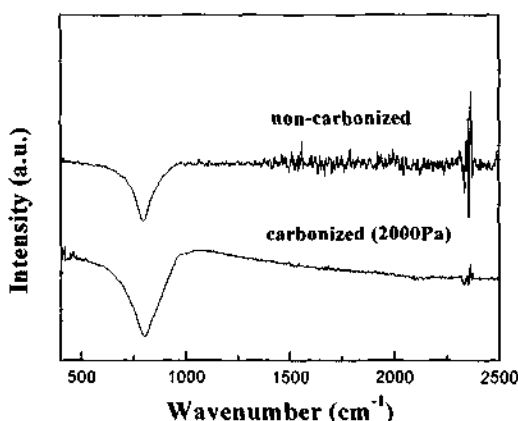


Figure 1. FTIR spectra of the carbonized sample and the non-carbonized sample.

The X-ray diffraction (XRD) patterns recorded for the carbonized sample and non-carbonized sample are plotted in Figure 2. As can be clearly seen, there are three peaks positioned at  $2\theta=35.7^\circ$ ,  $60.0^\circ$  and  $71.5^\circ$ , respectively, which correspond to (111), (220) and (311) of  $\beta$ -SiC [12]. As a result, the XRD measurement shows that the structure of

both the samples are  $\beta$ -SiC, consistent well with the FTIR measurements. Note that there is a slight increase of the full width at half maximum (FWHM) of the (111) peak in the carbonized sample, and the peak intensity of the other two planes is much stronger than the non-carbonized sample. According to Debeye-Scherrer formula [13], the crystal sizes of the carbonized sample and non-carbonized sample are 7nm and 35nm, respectively. Hence, the FTIR and XRD results demonstrate that the carbonization process has beneficial effects on decreasing  $\beta$ -SiC grain size.

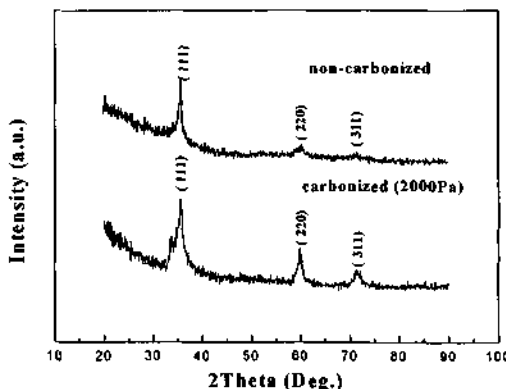


Figure 2. XRD patterns of the carbonized sample and the non-carbonized sample.

On the one hand, due to the low substrate temperature when using Cat-CVD, the critical nucleation free energy drops down and then the number of nuclei increase, which have benefits the formation of small grains. On the other hand, to enhance the nucleation density on Si substrate, the carbonization process is necessary. In this case, the surface of carbonized sample becomes rough and defect formation is enhanced [14]. Etch pits, hollow voids between the carbonization layer and the substrate are formed during the carbonization process and the subsequent film growth stage [15]. It is considered that the high nucleation density causes the growth of nanocrystalline  $\beta$ -SiC films to be more effective.

The catalyzed deposition also plays an important role in the growth of  $\beta$ -SiC film at a low temperature. However, the detailed decomposition mechanism of  $\text{CH}_4$  and  $\text{SiH}_4$  mixture at the catalyst is not clear. The decomposition of a  $\text{SiH}_4$  molecule is believed to follow the reaction [16] as: first, a  $\text{SiH}_4$  is absorbed on the surface of the catalyst M by forming  $\text{M-H-SiH}_3$ ; second,  $\text{M-H-SiH}_3$  dissociates to  $\text{M-H+SiH}_3$ . The deposition rate at the same temperature changes slightly after the catalyst begins to be covered with the film. Therefore, the deposition reaction cannot be said to be simple pyrolytic one, and it does include the catalytic reaction.

#### 4 Conclusion

Combined with the pre-carbonization process, nanocrystalline  $\beta$ -SiC films were deposited on (100) silicon by (Cat-CVD) at a low temperature ( $300^\circ\text{C}$ ). From the FTIR spectrum it is found that the carbonized sample is composed of  $\beta$ -SiC component which shows a blue shift, and the XRD patterns show that the grain-size of the carbonized sample is smaller.

## 5 Acknowledgements

This work was supported in part by the project of New Star Science & Technology of Beijing, the Natural Science Foundation of Beijing (No. 2992002).

## References

- Cole M. W., Joshi P. C., Hubbard C. W., Wood M.C., Ervin M. H., Greil B. and Ren F., Improvement Ni based composite ohmic contact to n-SiC for high temperature and high power device applications, *J. Appl. Phys.* **88** (2000) pp.2652-2657.
- Pring J. N. and Filelding W., *Chem. J. Soc.* **95** (1909) pp.1497-1501.
- Sano S., Nishino S. and Saraie J., *Proc. 6<sup>th</sup> Int. Conf. Silicon Carbide and Related Materials*, Kyoto, Japan, 1995, pp.209-214.
- Chassagne T., Ferro G., Gourbeyre C., Berre M. L., Barbier D. and Monteil Y., *Mater. Sci. For.* **155** (2001) pp.353-357.
- Matsumura H., Catalytic chemical vapor deposition (CTL-CVD) method producing high quality hydrogenated amorphous silicon, *Jpn. J. Appl. Phys.* **25** (1986) pp. L949-L952.
- Mahan A. H. and Gallagher,A., Mechanisms influencing 'hot wire' deposition of hydrogenated amorphous silicon, *J. Appl. Phys.* **69** (1991) pp.1909-1913.
- Kerdihes S., Rizk R., Gourblleau F., Perez-Rodriguez A., Garrido B., Gonzalez-Varona O. and Morante J. R., Low temperature direct growth of nanocrystalline silicon carbide films, *Mater. Sci. Eng. B* **69** (2000) pp.530-535.
- Lee S. W., Choi Y. S., Moon J. Y., Ahn S. S., Kim H. Y., Shin D. H., Growth of nanocrystalline silicon carbide thin films by plasma enhanced chemical vapor deposition, *J. Korean Phys. Soc.* **34** (1999) pp.562-565.
- Sun Y. and Miyasato T., Infrared absorption properties of nanocrystalline cubic SiC films, *Jpn. J. Appl. Phys.* **37** (1998) pp.5485-5491.
- Ball P., and Garwin L., Science at the atomix scale, *Nature*. **355** (1992) pp.761-763.
- Cai S., Men J., Zhang L. and Cheng B., *Acta Phys. Sinica* **41** (1992) pp.1620-1624 (in Chinese).
- Boo J. H., Yu K. S., Lee M. and Kim Y., *Appl. Phys. Lett.* **66** (1995) pp.3487-3491.
- Chayahara A., Kiuchi M., Kinomura A., Mokano Y., Horino Y. and Fuji K., *Jpn. J. Appl. Phys.* **32** (1993) pp.1287-1292.
- Mogab C. J. and Leamg H. J., Conversion of Si to epitaxial SiC by reaction with C<sub>2</sub>H<sub>2</sub>, *J. Appl. Phys.* **45** (1974) pp.1075-1080.
- Sun Y., Kirimoto K. and Miyasato T., Fabrication of nanoscale cubic SiC particle film, *Jpn. J. Appl. Phys.* **39** (2000) pp.6202-6207.
- Matsumura H., Low temperature deposition of silicon nitride by the catalytic chemical vapor deposition method, *Jpn. J. Appl. Phys.* **28** (1989) pp.2157-2160.

# PREPARATION AND CHARACTERIZATION OF HYBRID DODA/ TRANSITION METAL SUBSTITUTED HETEROPOLYMOLYBDOPHOSPHATE LB FILMS

S. Z. LIU, L. LIU, X. H. FENG AND Y. FAN

*Faculty of Chemistry and Material Science, Hubei University, Wuhan 430062, China*  
*E-mail: Lisz@public.wh.hb.cn*

Z. G. HU AND Z. L. DU

*Laboratory of Solid Surface, Henan University, Kaifeng 475001, China*  
*E-mail: zld@public.kfptt.ha.cn*

LB films of five new hybrid dimethyldioctadecylammonium/heteropolyanions DODA/HPA ( $\text{HPA}=[\text{PZ}(\text{H}_2\text{O})\text{Mo}_{11}\text{O}_{39}]$ , Z=Co, Cu, Mn, Zn, Ni) were prepared and characterized by  $\pi$ -A isotherms, UV-Vis absorption spectra, IR spectra, small-angle X-ray diffraction (SAXD), and atomic force microscope (AFM). The results show that these compounds have good film-forming property on the air-water interface. The collapse pressure of LB films is 28.7–37.5 mN/m. The area per molecule is  $28.18\sim49.07 \text{ nm}^2\text{ mol}^{-1}$ . The LB films have lamellar structures in which the monolayers of the heteropolyanions alternate with bilayers of DODA to form centrally symmetrical LB films.

## 1 Introduction

In recent years, the design and synthesis of functional molecular materials is a focus of active research in the fields of chemistry and materials science. Polyoxometalate anions constitute a distinctive class of compounds which are receiving increasing interest in catalysis, medicine and materials science. Their chemical, structural and electronic versatility make them act as electron acceptors and accommodate magnetic transition metal centers in their structures.

In 1997, Clemente-Leon *et al.* used polyoxometalate as inorganic components to construct hybrid organic-inorganic functional materials. They first used the LB technique to organize dimethyldioctadecylammonium cation and Keggin polyoxometalates  $[\text{X}^{n+}\text{W}_{12}\text{O}_{40}]^{(8-n)-}$  ( $\text{X}=2(\text{H}^+)$ , P<sup>V</sup>, Si<sup>IV</sup>, B<sup>III</sup>, Co<sup>II</sup>) Langmuir and Langmuir-Blodgett films [1,2,3]. Recently we have prepared organic-inorganic LB films by DODA and PW<sub>12</sub>Mo<sub>40</sub>, PW<sub>6</sub>Mo<sub>6</sub>, Ln(PW<sub>11</sub>)<sub>2</sub>, (Ln=La, Sm, Eu), PW<sub>12</sub>, PMo<sub>12</sub>, P<sub>2</sub>Mo<sub>18</sub>, respectively [4,5]. In this paper, we report the preparation and characterization of five novel hybrid DODA/transition metal ions substituted heteropolymolybdate LB films.

## 2 Experimental Section

### 2.1 Instruments and materials

Built-up films have been obtained by the vertical lifting method at room temperature with a 105 type LB trough. The IR spectra were recorded on a Nicolet FT-IR spectrometer, the UV-Vis spectra were measured using a Perkin-Elmer 330 spectrometer whereas the SAXD measurements were performed on a D/Max-rA X-ray diffractometer (CuK $\alpha$  radiation with  $\lambda = 0.15405 \text{ nm}$ ). The AFM images were obtained on an SAP 400 (Seiko Instrument Inc.) microscope.

Five heteropolyoxometalates used in this work, i.e.,  $\text{Na}_2\text{PMo}_{11}\text{MnO}_{40}\cdot\text{nH}_2\text{O}$ ,  $\text{Na}_2\text{PMo}_{11}\text{CoO}_{40}\cdot\text{nH}_2\text{O}$ ,  $\text{Na}_2\text{PMo}_{11}\text{NiO}_{40}\cdot\text{nH}_2\text{O}$ ,  $\text{Na}_2\text{PMo}_{11}\text{CuO}_{40}\cdot\text{nH}_2\text{O}$ , and  $\text{Na}_2\text{PMo}_{11}\text{ZnO}_{40}\cdot\text{nH}_2\text{O}$ , were synthesized according to the literature procedures. Their components and structures were confirmed by ICP, IR and CV measurements.

Dimethyldioctadecylammonium bromide was obtained from Kodak and used without further purification. Chloroform was used as the spreading solvent and was redistill before use. All other chemicals were of analytical grade and used as received. The water used as a subphase was of Milli-Q grade with a resistivity higher than 18 M  $\Omega\cdot\text{cm}$ .

## 2.2 Preparation of DODA/ $\text{H}_2\text{O}$ and DODA/ $\text{PMo}_{11}\text{ZO}_{39}$ ( $\text{Z}=\text{Mn, Co, Ni, Cu, Zn}$ ) LB films

The measurements of the surface pressure-area isotherms and the deposition of LB films were carried out by using a Langmuir trough. The compression was performed at  $10\pm0.5^\circ\text{C}$  using a continuous speed for the barrier of *ca* 6 cm/min. At least two measurements were done for each set of experimental conditions. Built-up films have been obtained by the vertical lifting mode method. The monolayer of the DODA was formed by spreading 630  $\mu\text{L}$  ( $10^{-3}\text{ mol}\cdot\text{L}^{-1}$ ) aqueous solution subphase. Transference (Y-type) of this more condensed Langmuir-film can be achieved at a surface pressure of 30 mN/m and a dipping speed of 10 mN/min. The LB films were transferred onto optically polished calcium fluoride for infrared measurements, mica for AFM experiments, and quartz for UV-Vis experiments, respectively.

## 3 Results and Discussion

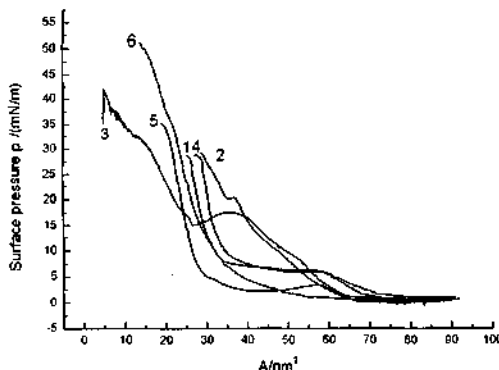
### 3.1 $\pi$ - $A$ curves

Figure 1 and Table 1 show the surface pressure-area isotherms ( $\pi$ - $A$  curves) and data from the isotherms for DODA on pure water and on  $10^{-5}\text{ mol}\cdot\text{L}^{-1}$  PZMo<sub>11</sub> subphases. The results indicate that DODA has good film-forming property at the air-water interface.

The monomolecular area of the Langmuir films of DODA/HPA obtained at mN/m are 28.18~49.07  $\text{nm}^2\cdot\text{mol}^{-1}$ . The monomolecular areas have been observed to decrease in the order of  $\text{Cu}>\text{Mn}>\text{Ni}>\text{Co}>\text{Zn}$ . The collapse pressures are 28.75~43.85 mN·m<sup>-1</sup>, indicating that the monolayer and multilayer prepared have good stability.

Table 1. Surface pressure-area isotherm date of the five Langmuir films.

Langmuir films	Cross section/( $\text{nm}^2\cdot\text{mol}^{-1}$ )	Collapse pressure/mN·m <sup>-1</sup>
DODA/PCoMo <sub>11</sub>	32.50	28.75
DODA/PCuMo <sub>11</sub>	49.07	29.25
DODA/PMnMo <sub>11</sub>	36.11	43.85
DODA/PNiMo <sub>11</sub>	34.16	28.75
DODA/PZnMo <sub>11</sub>	28.18	37.50



**Figure 1.** Compression isotherm of DODA on pure water and on  $10^{-5}$  mol·L $^{-1}$  HPA 1-Co, 2-Cu, 3-Mn, 4-Ni, 5-Zn, 6-H $_2$ O.

### 3.2 IR spectra

The IR spectra of DODA/HPA LB films show very strong bands at 2916, 2849 and 1467cm $^{-1}$ , which are assigned to the stretching and scissoring modes of CH bonds of DODA alkyl chains. The characteristic peaks of HPA are covered up by the strong absorption peaks of the quartz substrate.

### 3.3 UV-Vis spectra

The diffuse reflectance electronic spectra of the title LB films are given in Figure 2 and Table 2.

**Table 2.** Absorption spectra date of the five LB films (nm)

LB films	$O_d \rightarrow Mo$	$O_b(O_c) \rightarrow Mo$	$Mo^V \rightarrow Mo^{VI} + e$
DODA/PCoMo <sub>11</sub>	224	324,384	532
DODA/PCuMo <sub>11</sub>	224	324,384	580
DODA/PMnMo <sub>11</sub>	224	324,388	504
DODA/PNiMo <sub>11</sub>	224	324,384	—
DODA/PZnMo <sub>11</sub>	224	324,392	504

The absorption at *ca.* 504~532nm in the spectrum of the title LB film is ascribed to the IVCT ( $Mo^V \rightarrow Mo^{VI} + e$ ) band of the reduced anion  $PMo_{12}O_{40}^{4-}$ . The absorption band at *ca.* 324~392nm is ascribed to the  $O_{b,c} \rightarrow Mo$  band. The absorption bands of  $O_d \rightarrow Mo$  and  $O_{b,c} \rightarrow Mo$  have red-shifts after the heteropolyanion was reduced. These indicate that the charge-transfer effect occur in PZnMo<sub>11</sub> heteropolyanion and DODA.

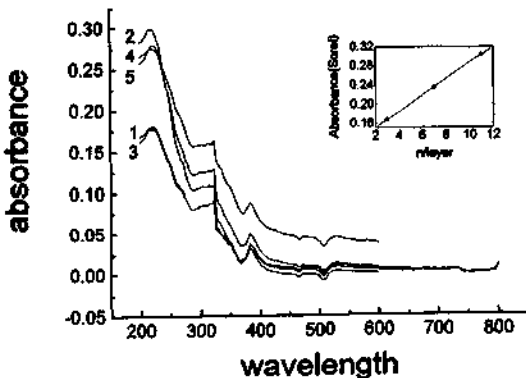


Figure 2. Absorption spectra of DODA/HPA LB films: 1-Co, 2-Ni, 3-Zn, 4-Cu, 5-Mn.

From Figure 2 we observed that with an increase of the number of layers the adsorption intensity is strengthened, but the absorption positions are not shifted. The Soret band absorbance of the DODA/HPA LB films is measured at 212~224nm. As shown in the insert of Figure 2, the absorbance changes linearly with the number of layers, indicating that the DODA/HPA LB films prepared have good structure homogeneity.

### 3.4 SAXD

Figure 3 shows the SAXD pattern of DODA/HPA LB films (13 Layers). Two Bragg peaks can be found in Figure 3. A well-defined Bragg diffraction peak occurs at  $2.3^\circ$ , which corresponds to the (001) Bragg peak. The other two peaks occur at angles below the (001) Bragg peak ( $2.3^\circ$ ). These results show that DODA/HPA LB films are of good interlayer order with a well-defined lamellar structure. According to Bragg's diffraction formula,  $n\lambda=2ds\sin\theta$ , where  $d$  is equal to 5.1nm, thus for Y-mode LB films,  $d/2$  being equal to a monolayer thickness of 2.55nm, one can estimate a thickness of *ca.* 1nm for the DODA/HPA LB film. In comparison with the radius of a Keggin polyanion (*ca.* 0.52nm), such a value clearly demonstrates that each inorganic layer consists of one polyanion monolayer alternating with bilayers of the organic surfactant (centrally symmetric LB film).

### 3.5 Atomic force microscopy

AFM has recently been used as an important tool for studying LB films because of its unprecedented ability to give information ranging from molecular resolution crystallography to surface morphology at length scales up to about  $100\mu\text{m}$  on films with any number of layers. Hence, AFM studies of DODA/HPA LB films may be an ideal method for checking the surface structure and defects in LB films. Parts A and B in Figure 4 show typical AFM images of one-layer LB films of DODA/H<sub>2</sub>O and DODA/HPA which were deposited on mica substrates, respectively. Parts C and D in Figure 4 represent the cross-section of parts A and B compared to parts C and D with the largest height difference on the sample surface being *ca.* 1.68nm. The roughness of 1.68nm demonstrates that for DODA/HPA LB films, an extremely flat surface

morphology is observed over the large area. On the other hand, we can conclude that the HPA is induced into the DODA matrices.

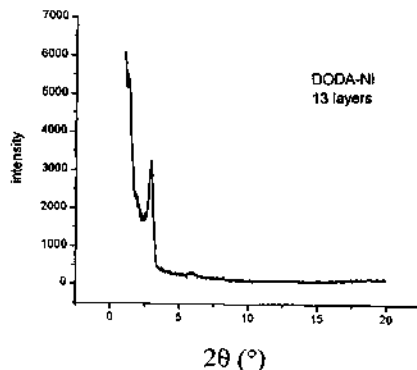


Figure 3. SAXD pattern of DODA/HPA LB films.

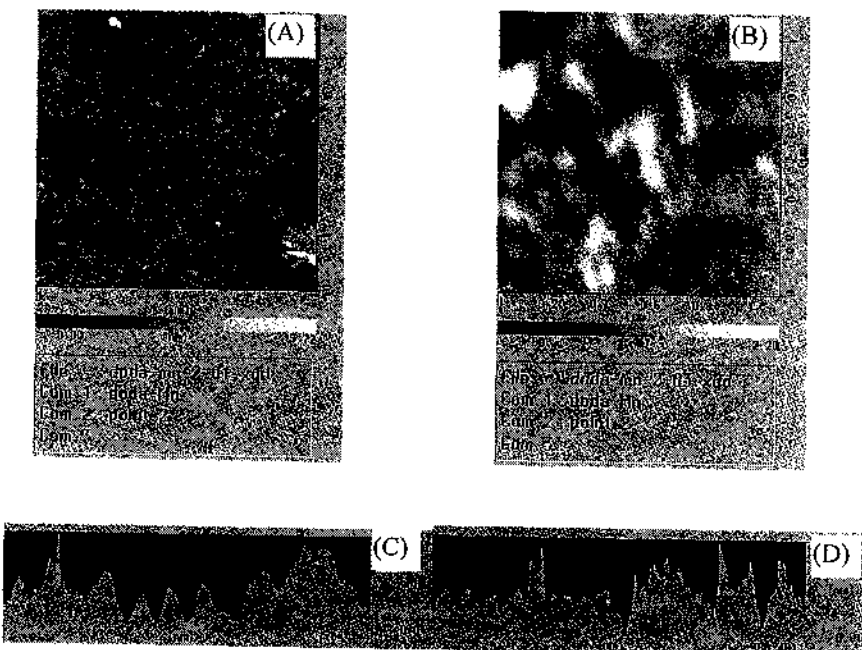


Figure 4. AFM images of LB films. A: DODA/ $\text{H}_2\text{O}$ , B: DODA/HPA, C: cross-section of (A), and D: cross-section of (B).

#### 4 Acknowledgements

This research was supported by the National Natural Science Foundation of China (Nos.29671011, 29971010) and the Natural Science Foundation of Hubei province (Nos.96J035, 99J066).

#### References

1. Clemente-Leon M, Mingotaud C., Agricole B., Gomez-Garcia C. J., Coronado E. and Delhaes P., Application of the Langmuir-Blodgett technique to polyoxometalates: towards new magnetic films, *Angew. Chem. Int. Ed. Engl.*, **36** (1997) pp. 1114-1116.
2. Clemente-Leon M , Agricole B., Mingotaud C., Gomez-Garcia C. J., Coronado E. and Delhaes P., Toward new organic/inorganic superlattices: Keggin polyoxometalates in Langmuir and Langmuir-Blodgett films, *Langmuir*, **13** (1997) pp. 2340-2347.
3. Coronado E and Gomez-Garcia C., Polyoxometalate-based molecular materials, *J. Chem. Rev.*, **98**(1998) pp. 273-296.
4. Liu S. Z., Zhang Z. W., Wang J., Du Z. L. and Dai S. X., Studies on the preparation, structure and properties of dilongchain alkyl group rare earth heteropoly compounds LB films, *Acta Chim. Sinica*, **59** (2001) pp.339-343.
5. Liu S. Z., Zhang Z. W., Wang J., Du Z. L. and Dai S. X., Studies on the preparation, structure and properties of LB films of 12-tungstomolybdophosphheteropolyacid with dimethyldiocta-decylammonium, *Chem. J. Chinese Unive.*, **23**(2002) pp.27-29.

## PREPARATION OF NICKEL SULFIDE ULTRAFINE PARTICLES BY MICROEMULSION

LUAN RUI AND HAN ENSHAN

*Department of Applied Chemistry, School of Chemical Engineering and Technology, Hebei University of Technology, Tianjin 300130, China  
E-mail: eshan@hebut.edu.cn*

The synthesis of nanosized nickel sulfide particles through a microemulsion-based method is reported in this paper. We used a UV-spectrophotometer to monitor the growth process of the particles and used TEM to confirm the sizes of the particles. By changing W, Ni/S molar ratios and the concentration of reactants, the effects of reaction conditions on particles have been investigated and we put forward the mechanism of growth of NiS particles.

### 1 Introduction

The inner core of microemulsion can dissolve water to form water core called water pool [1]. Little water pools of microemulsion surrounded by the single molecule interface formed by surfactants and co-surfactants can form particles whose sizes are from tens to hundreds of Å [2]. In this paper, a microemulsion-based method, and the formation conditions and growth mechanism of nanosized nickel sulfide particles are reported. This research is the base of application of ultrafine NiS particles on catalysis and optics.

The process of particle formation from dissolved ions can be represented in the following order: ions—monomers—nuclei—particles. After a stable nucleus is formed, it can grow by the following processes: (a) incorporation of ions and aggregation of primary particles or nuclei to form bigger particles. In order to form a stable nucleus, a cluster containing a critical number of monomer ( $N_c$ ) must form. An important parameter in this connection is the ion occupancy number, i.e., the number of reactant species in an inverse micelle. A nucleus is formed if the ion occupancy number is greater than  $N_c$  [3].

In most researches of the mechanism of ultrafine particle growth, researchers thought that the particle is resulted from the interaction of inter-micelles [5-8]. We found that there are many empty micelles in the test. This explains that the nucleus is formed by effect of inter-micelles, not of inner-micelles. The nucleation and initial growth of particles take place through collision, fusion, and splitting of inverse micelles.

When  $\text{Ni}^{2+}$  ions and  $\text{S}^{2-}$  ions are in the same micelles, nickel sulfide will precipitate. Here we assume that only one nucleus is formed in a water pool. The probability of the reactant species meeting in one water pool increases as the ion occupancy number increases; hence, an increase in the number of nuclei in the microemulsion with increasing ion occupancy number is to be expected.

### 2 Methods

**MATERIALS:** nonionic surfactant Triton X-100, n-hexane (99.7%), cyclohexane (99%), nickel nitrate (98%).

**PARTICLE SYNTHESIS:** The W/O microemulsion with Triton X-100/ n-hexane/ cyclohexane/  $\text{Ni}(\text{NO}_3)_2$  and  $\text{Na}_2\text{S}$  solution was prepared in  $30 \pm 0.1^\circ\text{C}$ . Two microemulsions that contain two reactants are mixed, and the reaction process is monitored by using a UV-spectrophotometer (Shimadzu Co. Ltd., UV-3000).

### 3 Results and Discussion

The UV-absorption spectra of metal sulfides have the following characteristics: a longer wavelength corresponds to a larger diameter.

#### 3.1 The effect of water to surfactant molar ratio ( $W$ ) on particles

The UV-absorption spectra of the microemulsion and the NiS particles are shown in Figures 1-4. From Figures 1, 3 and 5 we know that the micelles grow with time. Figures 2, 4 and 6 show that the NiS particles grow with time at early period of synthesis, but the particle diameter decreases at late period. The reason that the micelles grow with time is that the volumes of micelle increase after two microemulsions containing two reactants are mixed. Therefore the spectra are red-shifted. The reason that the particle diameter decreases at late period is that the micelles must be separated after they collide with each other.

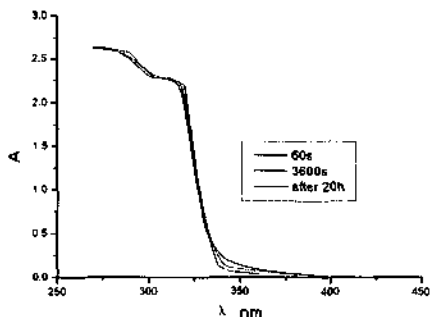


**Figure 1.** UV spectrum of  $W=3$  microemulsion whose disperse is 0.01 mol/L  $\text{Ni}(\text{NO}_3)_2/\text{Na}_2\text{S}$ .

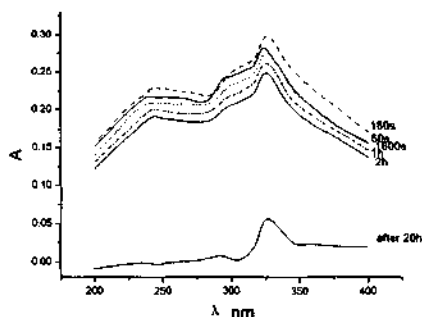


**Figure 2.** UV spectra of NiS synthesized by  $W=3$  microemulsion whose disperse is 0.01 mol/L  $\text{Ni}(\text{NO}_3)_2/\text{Na}_2\text{S}$ .

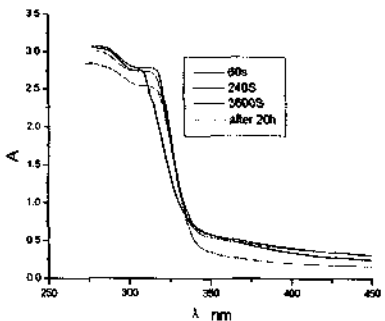


**Figure 3.** UV spectra of  $W=8$  microemulsion whose disperse is 0.01 mol/L  $\text{Ni}(\text{NO}_3)_2/\text{Na}_2\text{S}$ .

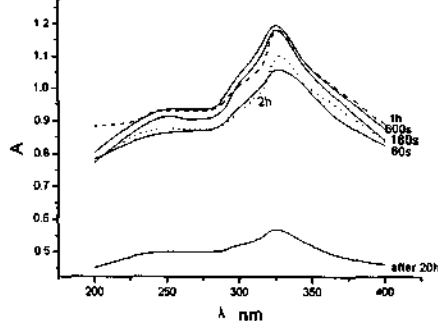


**Figure 4.** UV spectra of NiS synthesized by  $W=8$  whose disperse is 0.01 mol/L  $\text{Ni}(\text{NO}_3)_2/\text{Na}_2\text{S}$ .

Figures 7 and 8 show that the spectra of micelles and NiS particles have red-shifted when the molar ratio  $W$  of water to surfactant increases. The particle diameter increases

when the volume of micelle increases. Therefore, we can control the particle diameter by changing the value of W.

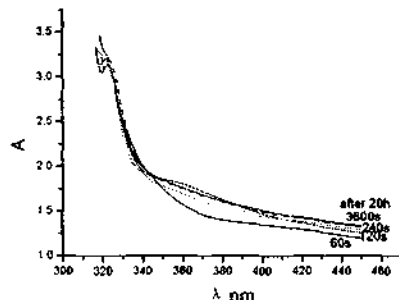


**Figure 5.** UV spectra of  $W=15$  microemulsion whose disperse is  $0.01\text{ mol/L}$   $\text{Ni}(\text{NO}_3)_2/\text{Na}_2\text{S}$ .

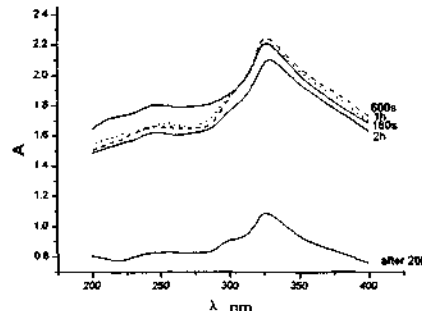


**Figure 6.** UV spectra of  $\text{NiS}$  synthesized by  $W=15$  microemulsion whose disperse is  $0.01\text{ mol/L}$   $\text{Ni}(\text{NO}_3)_2/\text{Na}_2\text{S}$ .

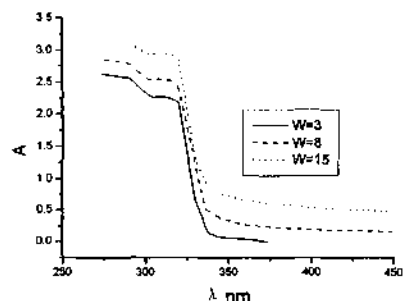


**Figure 7.** UV spectra of microemulsion whose  $W$  varies after 20h.

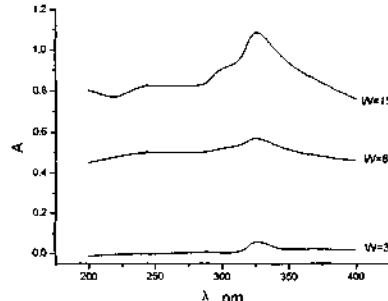


**Figure 8.** UV spectra of  $\text{NiS}$  particles whose  $W$  varies after 20h.

### 3.2 The effect of $\text{Ni/S}$ molar ratio ( $Y$ ) on particle diameter

Figures 9 and 10 show that the particles grow faster to larger sizes at higher  $Y$ . The result is interpreted in terms of the formation of unstable micelles containing  $\text{NiS}$  particles. At high  $Y$ , the produced  $\text{NiS}$  particles are probably coated with  $\text{S}^{2-}$  ions, resulting in a negatively charged surface. Conversely, the attractive interaction between  $\text{NiS}$  particles coated with  $\text{Ni}^{2+}$  ions and surfactant head groups contributes to the stability of the particles, restricting particle coagulation [3].

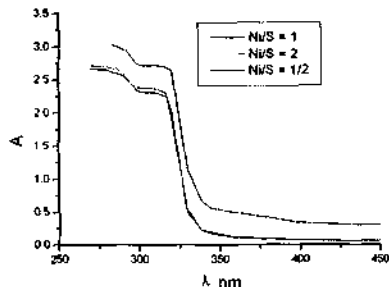


**Figure 9.** UV spectra of  $W=6$  microemulsion whose disperse is  $0.01\text{ mol/L}$   $\text{Ni}(\text{NO}_3)_2/\text{Na}_2\text{S}$  when the  $\text{Ni}/\text{S}$  molar ratio is varied.

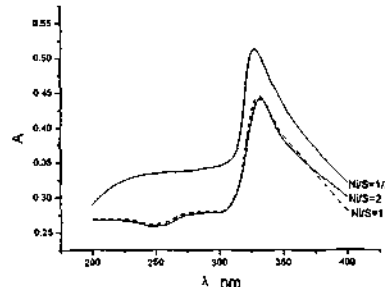
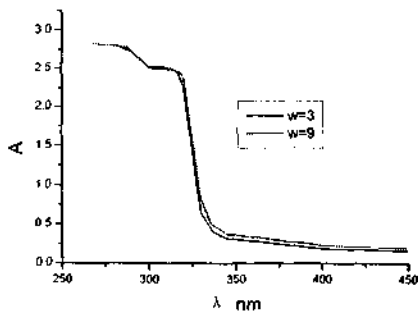


**Figure 10.** UV spectra of  $\text{NiS}$  synthesized by  $W=6$  microemulsion whose disperse is  $0.01\text{ mol/L}$   $\text{Ni}(\text{NO}_3)_2/\text{Na}_2\text{S}$  when  $\text{Ni}/\text{S}$  molar ratio is varied.

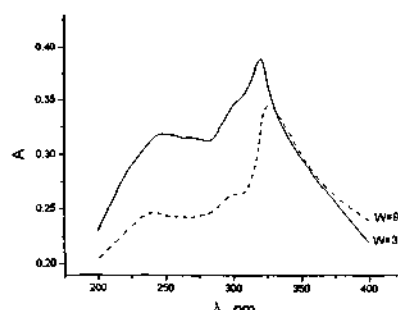
### 3.3 Origin of particle growth restraints

It is important to understand the origin of the restraint effect. In principle, we can imagine two kinds of origin for the presence of the stable size specific to  $W$ . One is of thermodynamic origin, i.e., the microemulsion micelles containing  $\text{NiS}$  particles is stable at a certain size. In this case, the formation of stable particles is reversible upon change in  $W$ . Another is of kinetics origin, i.e., the coalescence of the microemulsion droplets containing  $\text{NiS}$  particles becomes very slow over a certain size. In order to confirm this we conducted the following experiments [4].

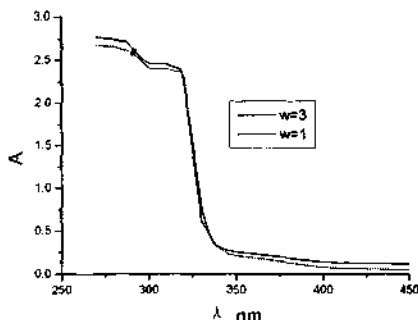
- Exp'1:  $\text{NiS}$  particles were formed under the conditions  $W=3$ . Then pure Triton X-100 was added to the system to convert the  $W$  from 3 to 1.
- Exp'2:  $\text{NiS}$  particles were formed when  $W=3$ , and then water was added to the system to convert the  $W$  from 3 to 9.
- Exp'3: Two kinds of  $\text{NiS}$  particles were separately formed beforehand when  $W=3$  and 8. The time for the preparation of the particles was over 2h. The microemulsion containing these particles were mixed to yield a microemulsion with  $W=5.5$ .



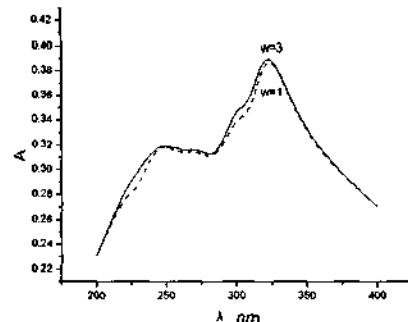
**Figure 11.** UV spectra of microemulsion before and after Triton X-100 is added.



**Figure 12.** UV spectra of  $\text{NiS}$  before and after Triton X-100 is added.



**Figure 13.** UV spectra of microemulsion before and after water is added.



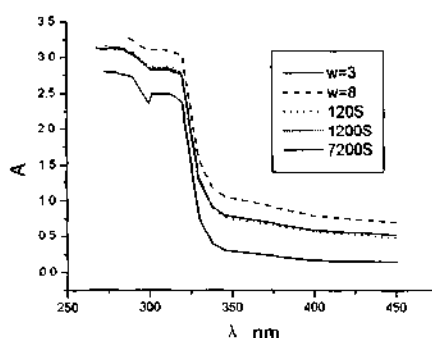
**Figure 14.** UV spectrum of NiS before and after water is added.

Figure 11 and Figure 12 show the result of Exp'1. The UV-spectra after adding Triton X-100 are the same as those before adding Triton X-100, when the dilution effect of NiS particles caused by the addition of Triton X-100 is taken into account. This result means that once particles grow over the diameter  $N_c$ , the particles never become smaller, even if the  $W$  changes to 1.

Figure 13 and Figure 14 show the result of Exp'2. The absorption spectra indicate red-shifts just after the increase of the  $W$  value. This result means that the particles grow rapidly after increasing  $W$ .

The result of Exp'3 is shown in Figures 15 and 16. After mixing these microemulsions, only the absorption at the lower wavelength changes with time, whereas for longer wavelength absorptions, no change is observed. This result means that the smaller NiS particles produced at  $W=3$  grow to larger sizes and the larger particles at  $W=8$  never changes with time.

These results strongly suggest that a stable size does not originate from thermodynamic stability of the NiS-microemulsion supramolecules, i.e., the particles having been formed at  $W_1$  are not divided into finer particles upon the alteration of  $W$  to  $W_2$  ( $W_1 < W_2$ ). The presence of the stable size arises from kinetics origin. Furthermore, smaller particles are not redistributed to larger particles.



**Figure 15.** UV spectra of microemulsions whose  $W=3$  and  $W=8$  are mixed to form  $W=5.5$ .

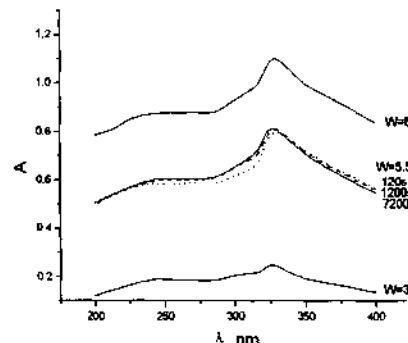


**Figure 16.** UV spectra of NiS whose  $W=3$  and  $W=8$  are mixed to form  $W=5.5$ .

### 3.4 Effect of concentration of $\text{Ni}(\text{NO}_3)_2$ solution on particles

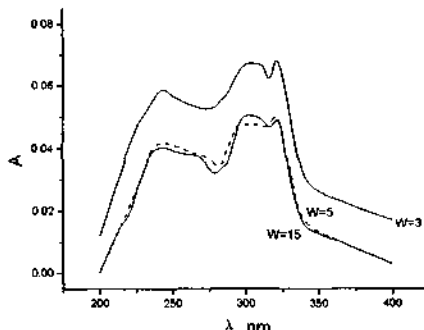


Figure 17. UV spectra of NiS whose disperse is 0.001 mol/L  $\text{Ni}(\text{NO}_3)_2/\text{Na}_2$  and W is varied.

Figure 17 shows that the particle diameter decreases with W when the concentration of reactant is very low (0.001 mol/L), conversely to Fig. 8. The reason is that relatively fewer water cores will contain the minimum number of ions required to form a nucleus. As a result, the nucleation process is relatively larger. These ions will be incorporated into the already formed nuclei via intermicellar communication and will contribute to growth, leading to larger particles.

## 4 Conclusion

Ultrafine nickel sulfide particles have been synthesized in Triton X-100/n-hexane/cyclohexane/water microemulsion. The experimental results indicate that careful control of the water to surfactant molar ratio W and ion occupancy number is vital in forming NiS particles.

## References

1. Wang J., Wu J. G. and Xu G. X., *Circular of Chemistry*, 9 (1995) pp. 1-4.
2. Shen X. H. and Gao H. C., *Circular of Chemistry*, 11 (1995) pp. 6-9.
3. Kiyoshi S., Noriaki M. and Makoto H., *J. Chem. Engineer. Japan*, 32 (1999) pp. 31-39.
4. Kiyoshi S., Makoto H. and Skihisa S., *J. Chem. Engineer. Japan*, 29 (1996) pp. 264-276.
5. Boakye E., Radovic L.R. and Osseo-Asare K., *J. Colloid Interf. Sci.*, 163 (1994) pp. 120-129.
6. Lianos P. and Thomas J. K., *J. Colloid Interf. Sci.*, 117 (1987) pp. 505-512.
7. Petit C. and Pileni M. P., *J. Phys. Chem.* 92 (1998) pp. 2282-2286.
8. Hanrama S. K., Mahadeshwar A. R. and Dixit S. G., *J. Phys. Chem.*, 100 (1996) pp. 5868-5873.

## CHEMISTRY IN MOLECULAR APPROACHES TO MICROELECTRONIC DIFFUSION BARRIER MATERIALS

XIAOZHAN LIU, HU CAI, ZHONGZHI WU, YIHUI YANG,  
TIANNIU CHEN AND ZILING XUE

*Department of Chemistry, The University of Tennessee, Knoxville, Tennessee 37996, U.S.A.  
E-mail: xue@novell.chem.utk.edu*

CATHERINE E. VALLET AND DAVID B. BEACH

*Chemical Sciences Division, Oak Ridge National Laboratory, Oak Ridge, Tennessee 37831, U.S.A.*

RAY A. ZUHR

*Surface Modification and Characterization Research Center, Oak Ridge National Laboratory, Oak Ridge, Tennessee 37831, U.S.A*

Ti-Si-N ternary thin films were prepared from the reactions of  $Ti(NMe_2)_4$  with  $SiH_4$  through chemical vapor deposition processes. Mechanistic studies revealed that these reactions between amides and hydrosilanes involved reversible amide-hydride exchanges to give “ $=Ti(NMe_2)H$ ” and amidosilanes  $H_nSi(NMe_2)_{4-n}$ . These two species then underwent separate pathways to give TiN and  $Si_3N_4$ , respectively. The isolation of an  $\eta^2$ -imine complex in the reactions of  $Ta(NMe_2)_5$  with silanes indicated that  $\beta$ -H abstraction between two amide ligands in  $M(NR_2)_n$  perhaps led to the formation of M-C bound species and C incorporation in CVD involving amide precursors.

### I Introduction

Over the past decade, shrinking dimensions in microelectronic devices have demanded modification or replacement of existing metallization technologies. With each generation of metallization technology, new interconnect schemes have evolved to meet the rapidly increasing performance demands. Copper is now used as a replacement for aluminum in interconnect schemes because it exhibits better electromigration resistance, a better thermal expansion coefficient, and a lower tendency to form hillocks [1-3]. The use of copper in integrated circuits provides several challenges for barrier and contact layers [1-3], as Cu deposited on a Si wafer reacts with Si through solid-state reactions (diffusion). Diffusion barrier layers are often introduced between the metal layer and semiconductor to suppress their interaction (Figure 1) [4]. TiN is an accepted diffusion barrier material for copper-based interconnect. Chemical vapor deposition (CVD) process has been used to give thin TiN films from  $Ti(NMe_2)_4$  or  $Ti(NEt_2)_4$  and  $NH_3$  [5]. These TiN films are often polycrystalline with grain-boundary diffusion, and the barrier properties of TiN films may be inadequate, particularly at a thickness below 20 nm.

Ternary amorphous metallic alloys such as Ti-Si-N are of intense current interest [1-3]. These phases have demonstrated superior diffusion barrier properties for copper and silicon. There is an increased motivation to deposit these amorphous barriers by CVD processes to permit conformal coatings (uniform coating of non-planar surfaces) of trenches and bias (vertical connections) [1-3]. Smith and Nicolet have studied various CVD processes with  $Ti(NEt_2)_4$ ,  $SiH_4$ , and  $NH_3$  as precursors to give Ti-Si-N ternary films [6-7]. We were particularly intrigued by the observations that these Ti-Si-N ternary films are mixtures of TiN and  $Si_3N_4$  (Figure 2); The compositions of these films were near or above the TiN and  $Si_3N_4$  tie-lines in Ti-N-Si ternary phase diagram [6-7], and there were no  $TiSi_n$  phases in the films. A key question is why the reactions of  $Ti(NEt_2)_4$  with  $SiH_4$

and  $\text{NH}_3$  gave  $\text{TiN}$  and  $\text{Si}_3\text{N}_4$  in the Ti-Si-N ternary phases [7]. In addition, C incorporation into metal nitride  $\text{MN}_x$  films in CVD using  $\text{M}(\text{NR}_2)_n$  is often observed [8]. In this presentation, our recent studies of the mechanistic pathways in CVD of  $\text{TiN-Si}_3\text{N}_4$  from  $\text{Ti}(\text{NMe}_2)_4$  and  $\text{SiH}_4$  and in the C incorporation in CVD of  $\text{MN}_x$  films from  $\text{M}(\text{NR}_2)_n$  are summarized [9-10].

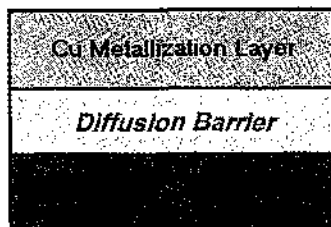


**Figure 1.** Diffusion barrier in Si-based microelectronic devices.

## 2 Preparation and Characterization of Ti-Si-N Ternary Thin Films and Powders

CVD was performed in an ultra high vacuum reactor shown in Figure 3. The precursor  $\text{Ti}(\text{NMe}_2)_4$  was placed in a bubbler attached to the CVD apparatus.  $\text{SiH}_4$  (99.999+%) was introduced to the CVD reactor through a separate inlet. A Si(100) wafer as substrate was placed in the middle heating zone. Ultra-high-purity Ar was used as carrier gas. The system was evacuated and purged for 30 min around 400 °C before each deposition. Under these conditions, analyses of the Ar outflow by residual gas analyzer (RGA) showed that it contained no  $\text{O}_2$ . The precursor  $\text{Ti}(\text{NMe}_2)_4$  was evacuated at -193 °C before each deposition. After each deposition, the film was annealed to 750 °C under vacuum for 2 hours.

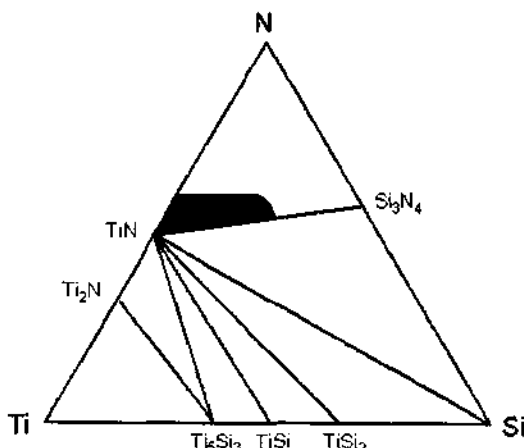


**Figure 2.** Compositions of the Ti-Si-N thin films from the CVD from  $\text{Ti}(\text{NMe}_2)_4$ ,  $\text{SiH}_4$ , and  $\text{NH}_3$  as precursors.

To avoid premature reaction between  $\text{SiH}_4$  and  $\text{Ti}(\text{NMe}_2)_4$ , we designed our system to only allow the two precursors to mix exactly above the substrate in the heating zone. One feature of our process was that the deposition was direction-oriented. When the substrate was placed parallel to the gas flow, no deposition occurred. The substrate was thus placed with one end slightly tilted in the direction of the gas flow to give the observed thin film deposition.

### UHV/CVD Reactor

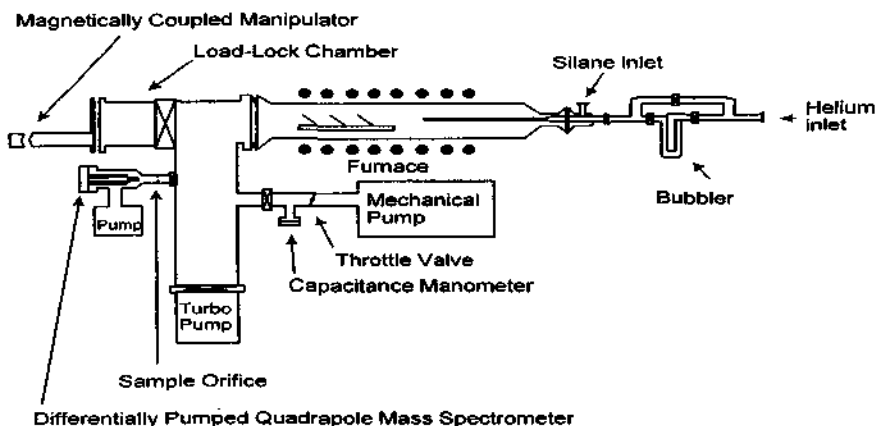


**Figure 3.** Schematic view of the CVD reactor used for the current studies.

Delivery temperatures of 264 °C and 350 °C were used to give films 1 and 2, respectively. In the formation of film 2 with a delivery temperature of 350 °C, premature precursor decomposition was observed in the delivery zone. Deposition temperature was also found to be a very important factor. The deposition at 300 °C gave a much thinner film. Films 1 and 2 deposited at 448-450 °C had a gold color and a dark blue black zone, reflecting some bluish gray light. Under the same conditions, films deposited on quartz substrates below 450 °C had very different appearances compared to those grown on a Si(100) wafer. They were very thin, transparent and quite yellow.

Several techniques including X-ray photoelectron spectroscopy (XPS) and Rutherford backscattering spectrometry (RBS) were used to analyze the films. The XPS chemical shifts of  $\text{Ti } 2\text{p}_{3/2}$  (455.50 eV),  $\text{Si } 2\text{p}$  (102.00 eV),  $\text{N } 1\text{s}$  (397.00 eV), and  $\text{O } 1\text{s}$  (531.00 eV) in film 1 after sputtering (Figure 4) are closed to those in the reported  $\text{TiSi}_{1.4}\text{N}$  alloy ( $\text{Ti } 2\text{p}_{3/2}$  (455.5 eV),  $\text{Si } 2\text{p}$  (102.5 eV),  $\text{N } 1\text{s}$  (397.8 eV) [11]). The RBS spectra of films 1 and 2 (Figure 5) showed that the  $\text{Ti} : \text{Si} : \text{N}$  ratios in these films were 16 : 13 : 30 and 16 : 17 : 19, respectively. Detailed analyses of the RBS spectra revealed that the films were not oriented since the random and aligned spectra for Ti, Si (in film), O, and N were identical.

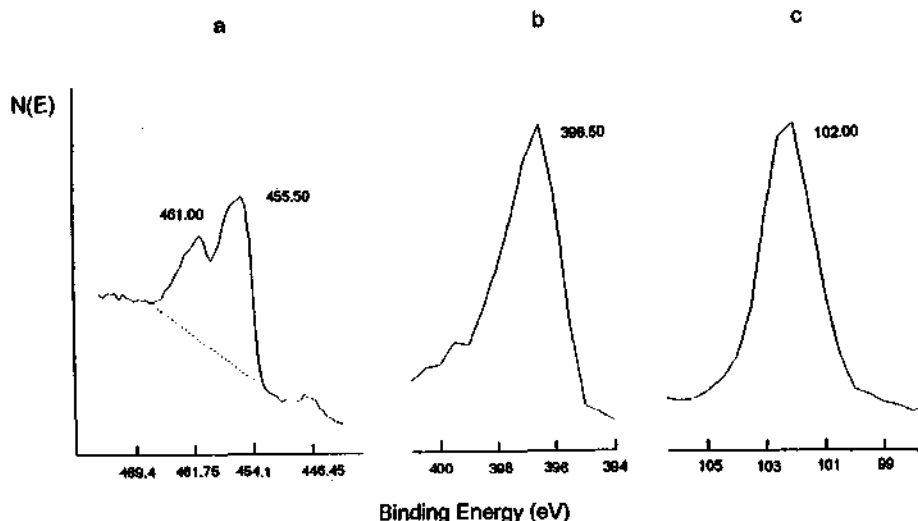


Figure 4. XPS of film 1 after sputtering: (a) Ti 2p<sub>3/2</sub>; (b) N 1s; (c) Si 2p.

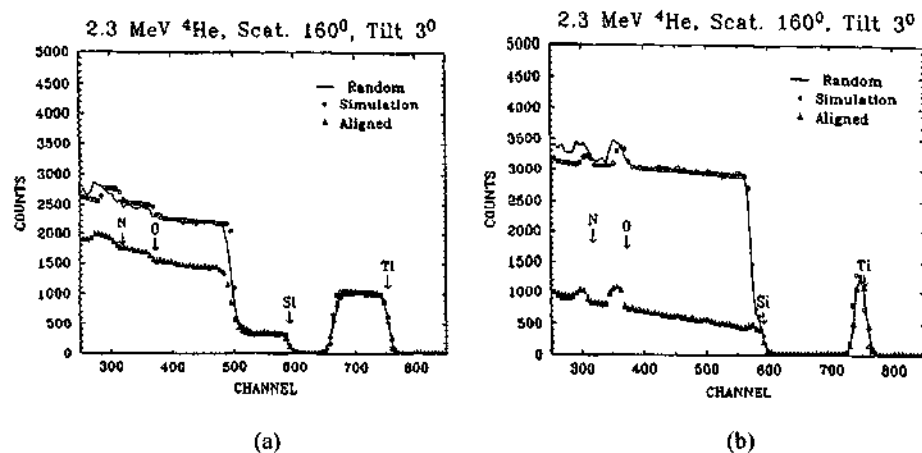


Figure 5. Rutherford backscattering spectra (RBS) of films 1 (a) and 2 (b) deposited on Si wafers.

The XPS analysis showed a large O content (20-35%) in the films. Since the precursors  $\text{Ti}(\text{NMe}_2)_4$  and  $\text{SiH}_4$  contain no oxygen, oxygen perhaps was incorporated during the deposition process. Similar O incorporation has been reported in the deposition of TiN films from  $\text{Ti}(\text{NMe}_2)_4$  and  $\text{SiH}_4$ , especially when not enough  $\text{NH}_3$  was supplied [12]. Since both Ti(IV) and Si(IV) are oxophilic, this is perhaps not surprising. Carbon impurity, mostly of hydrocarbons, was also observed in XPS of the films.

The ellipsometry analysis indicated that the thickness of film 1 was fairly uniform, giving an average of  $2168 \text{ \AA}$ . Scanning electron microscopy (SEM) showed that the film was smooth. No pattern was observed in powder X-ray diffraction of the film, indicating that the film was amorphous, a desired feature of diffusion barriers.

### 3 Reactions of $\text{Ti}(\text{NMe}_2)_4$ with Silanes - Preparation of Ti-Si-N Powders

Reactions of  $\text{Ti}(\text{NMe}_2)_4$  with  $\text{SiH}_4$  or  $\text{H}_3\text{SiPh}$  were also conducted at room temperature in a Schlenk system to better understand these reactions. Liquid  $\text{Ti}(\text{NMe}_2)_4$  at room temperature was exposed to  $\text{SiH}_4$  or  $\text{H}_3\text{SiPh}$  to give an immediate reaction with gas evolution. The gas was found to be  $\text{H}_2$ . The reaction mixture involving  $\text{Ti}(\text{NMe}_2)_4$  turned darker with the formation of a black solid and  $\text{HSi}(\text{NMe}_2)_3$ , or  $\text{HSi}(\text{NMe}_2)_2\text{Ph}$ . The black solid after heating gave amorphous powders with a metallic appearance under a microscope. The XPS chemical shifts of the powder were similar to those in film 1 and the reported  $\text{TiSi}_{1.4}\text{N}$  alloy.

The black solid from the reaction with  $\text{H}_3\text{SiPh}$  was found to give  $\text{DNMe}_2$ ,  $\text{H}_2$ ,  $\text{HD}$ , and  $\text{D}_2$  when exposed to  $\text{DCl}$ . Raman spectra of the solid showed M-N but no M-Si stretches. These results suggest that the black solid contained unreacted  $-\text{NMe}_2$  and  $-\text{H}$  ligands.

### 4 Reactions of Amides with Phenylsilanes – Isolation of Molecular Intermediates

Reactions of  $\text{Zr}(\text{NMe}_2)_4$  with  $\text{H}_2\text{SiRNPh}$  ( $\text{RN} = \text{H/D, Me, Ph}$ ) were found to yield  $[(\text{Me}_2\text{N})_3\text{Zr}(\mu\text{-H})(\mu\text{-NMe}_2)_2]_2\text{Zr}$  (3, Figure 6), which was characterized by NMR and X-ray diffraction [9]. In this reaction, an exchange between Zr-NMe<sub>2</sub> and Si-H led to the formation of this rare amide hydride complex [9]. This reaction was unusual as well, as known M-NR<sub>2</sub> reactions with active H-containing species such as  $\text{H}_2\text{O}$ , HOR,  $\text{HSnPh}_3$ , [13], and a silane  $\text{HSi}(\text{C}_6\text{F}_5)_3$ , [14], usually give amine  $\text{HNR}_2$ .

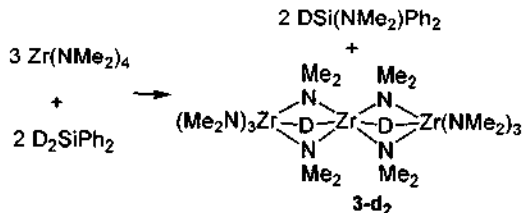


Figure 6. Preparation of an amide hydride complex.

We were also surprised to observe that the reactions of  $(\text{Me}_2\text{N})_3\text{ZrSi}(\text{SiMe}_3)_3$  with  $\text{H}_2\text{SiRNPh}$  gave an unstable hydride complex  $(\text{Me}_2\text{N})_2\text{Zr}(\text{H})\text{Si}(\text{SiMe}_3)_3$  (4) and  $\text{HSi}(\text{NMe}_2)\text{RNPh}$ , and to reach equilibria (Figure 7). This observation confirmed that the reactions of these d<sup>0</sup> amide complexes with silanes to form hydrides and aminosilanes were reversible. To our knowledge, the current study represents the first direct observation of hydrides in the reactions of transition metal amides with silanes through unusual equilibria [9].

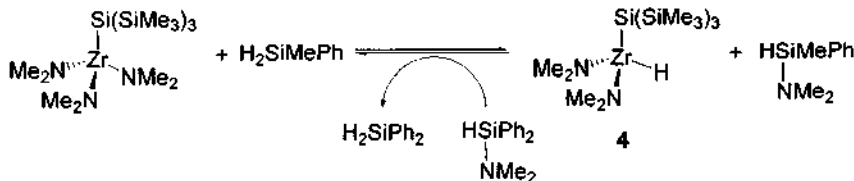


Figure 7. Reversible reactions between amides and silanes.

In CVD with  $\text{Ti}(\text{NR}_2)_4$  as precursors, C incorporation is often observed [8]. In the current studies of the CVD of Ti-Si-N films, we observed C incorporation into the films as well. Mechanistic pathways leading to C incorporation have been investigated to reduce C contamination, and initial  $\beta$ -H abstraction between two amide ligands in  $\text{M}(\text{NR}_2)_n$  to give an  $\eta^2$ -imine moiety was postulated as the first step to establish M-C bonds in C incorporation into the nitride films [8]. We have found that the reactions of  $\text{Ta}(\text{NMe}_2)_5$  with  $\text{H}_2\text{SiRPh}$  ( $\text{RN} = \text{Me, Ph}$ ) yielded an unusual bridging imine complex  $(\text{Me}_2\text{N})_3\text{Ta}(\mu\text{-H})_2(\mu\text{-N-}\eta^2\text{-N,C-CH}_2\text{NMe})\text{Ta}(\text{NMe}_2)_3$  (**5**, Figure 8) with a Ta-C bond [10]. This Ta complex is one of few structurally characterized  $\eta^2$ -imine complexes from  $\beta$ -H abstraction between amide ligands [15-16]. The formation of the bridging imine ligand is a step of mechanistic significance to the formation of M-bound carbon in CVD of metal nitride thin films [8].

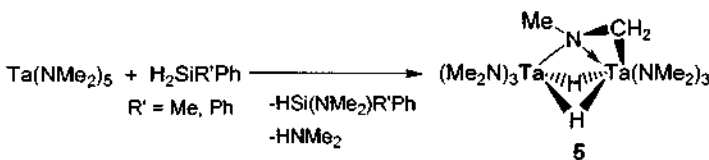
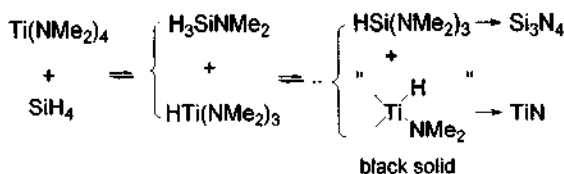


Figure 8. Formation of a  $\eta^2$ -imine complex from  $\beta$ -H abstraction between amide ligands.

## 5 Mechanistic Considerations

The current studies indicated that CVD reactions of  $\text{Ti}(\text{NMe}_2)_4$  with  $\text{SiH}_4$  to give Ti-Si-N thin films yielded black solids containing -H and -NMe<sub>2</sub> ligands, and aminosilanes  $\text{H}_n\text{Si}(\text{NMe}_2)_{4-n}$ . The role of silane here was to remove amide ligands. The black solid and  $\text{H}_n\text{Si}(\text{NMe}_2)_{4-n}$  perhaps underwent separate pathways to give  $\text{TiN}$  and  $\text{Si}_3\text{N}_4$ , respectively (Figure 9).  $\text{H}_n\text{Si}(\text{NMe}_2)_{4-n}$  have been used as precursors in chemical vapor deposition of  $\text{Si}_3\text{N}_4$  [17]. No intermediates with Ti-Si bonds were observed suggesting they were either not present or minor products. This perhaps explained in part why this CVD reaction did not give silicides  $\text{TiSi}_n$ . The observations of the equilibrium in Figure 7 suggest similar reversible reactions may occur in the reaction of  $\text{Ti}(\text{NMe}_2)_4$  with  $\text{SiH}_4$  (Figure 9), and contribute in part to the presence of unreacted -NMe<sub>2</sub> ligands in the black solid. Similar pathways may be present in the reactions of  $\text{Ti}(\text{NET}_2)_4$  with  $\text{SiH}_4$  and NH<sub>3</sub> and deposition of  $\text{TiN-Si}_3\text{N}_4$  ternary films from these reactions [6-7].



**Figure 9.** Mechanistic pathways in the formation of Ti-Si-N ternary materials.

## 6 Acknowledgements

This work was supported by the U.S. National Science Foundation and Department of Energy.

## References

1. *The Chemistry of Metal CVD*, ed. by Kodas, T. and Hampden-Smith, M. J. (VCH: Weinheim, Germany, 1994) pp. 1-43.
2. *Copper Metallization in Industry*, *MRS Bulletin* **19**(8) (August 1994) pp. 15-75 and references therein.
3. Winter, C. H., The Chemical vapor deposition of metal nitride films using modern metalorganic precursors. *Aldrichimica Acta* **33** (2000) 3-12 and references therein.
4. Mayer, J. W. and Lau, S. S. *Electronic Materials Science: For Interconnection Circuits in Si and GaAs* (Macmillan: New York, 1990) and references therein.
5. Fix, R.; Gordon, R. G. and Hoffman, D. M., Chemical vapor deposition of titanium, zirconium, and hafnium nitride thin films. *Chem. Mater.* **3** (1991) 1138-1148.
6. Smith, P. M. and Custer, J. S. Chemical vapor deposition of titanium-silicon-nitride films. *Appl. Phys. Lett.* **70** (1997) 3116-3118 and references therein.
7. Custer, J. S.; Smith, P. M.; Fleming, J. G. and Roherty-Osmun, E., Chemical vapor deposition of refractory ternary nitrides for advanced diffusion barriers. *ACS Symp. Ser.* **727** (1999) 86-99.
8. See, e.g., Fix, R. M.; Gordon, R. G. and Hoffman, D. M., Synthesis of thin films by atmospheric pressure chemical vapor deposition using amido and imido titanium(IV) compounds as precursors. *Chem. Mater.* **2** (1990) 235-241.
9. Liu, X.-Z.; Wu, Z.-Z.; Cai, H.; Yang, Y.-H.; Chen, T.-N.; Vallet, C. E.; Zuhr, R. A.; Beach, D. B.; Peng, Z.-H.; Wu, Y.-D.; Concolino, T. E.; Rheingold, A. L. and Xue, Z.-L. Reactions of tetrakis(dimethylamide)-titanium, -zirconium and -hafnium with silanes. Synthesis of unusual amide hydride complexes and mechanistic studies of titanium-silicon-nitride (Ti-Si-N) formation. *J. Am. Chem. Soc.* **123** (2001) 8011-8021 and references therein.
10. Cai, H.; Chen, T.-N.; Wang, X.-P.; Schultz, A. J.; Koetzle, T. F. and Xue, Z.-L. Direct observation of  $\eta^2$ -imine formation through  $\text{C}-\text{H}$  abstraction between amide ligands. Neutron and X-ray diffraction structure of a dihydride imine ditantalum complex. *Chem. Comm.* (2002) 230-231.
11. Miura, Y. and Fujieda, S., Structural investigation of thermally nitrided amorphous titanium silicide. *J. Appl. Phys.* **81** (1997) 6476-6478.
12. Musher, J. N. and Gordon, R. G., Atmospheric pressure chemical vapor deposition of titanium nitride from tetrakis(diethylamido)titanium and ammonia. *J. Electrochem.*

- Soc. **143** (1996) 736-744.
- 13. Creemers, H. M. J. C.; Verbeek, F. and Noltes, J. G., Studies in Group IV organometallic chemistry XXX. Synthesis of compounds containing tin-titanium and tin-zirconium bonds. *J. Organomet. Chem.* **15** (1968) 125-130.
  - 14. Kalinina, G. S.; Petrov, B. I.; Kruglaya, O. A. and Vyazankin, N. S., Bis[tris(pentafluorophenyl)silyl]mercury and -cadmium. *Zh. Obshch. Khim.* **42** (1972) 148-151.
  - 15. Berno, P. and Gambarotta, S., Formation of a metalaaziridine ring and dinitrogen fixation promoted by a niobium amide complex. *Organometallics*, **14** (1995) 2159-2161.
  - 16. Scoles, L.; Ruppa, K. B. P. and Gambarotta, S., Preparation of the first ditantalum(III) complex containing a Ta-Ta bond without bridging ligands. *J. Am. Chem. Soc.* **118** (1996) 2529-2530.
  - 17. See, e.g., Aoki, T.; Ogishima, T.; Wrobel, A. M.; Nakanishi, Y.; Hatanaka, Y. Silicon nitride film growth by remote plasma CVD using tris(dimethylamino)silane. *Vacuum* **51** (1998) 747-750.

## INFLUENCE OF CRYSTALLITE SIZE ON THE PROPERTIES OF $\text{SnO}_2$ NANOCRYSTALS

GUANGSHENG PANG, HAIYING JIN, QIANG WAN, YAN SUN, AND SHOUHUA FENG

*State Key Laboratory of Inorganic Synthesis & Preparative Chemistry, Department of Chemistry,  
Jilin University, Changchun, 130023, P. R. China  
E-mail: panggs@mail.jl.cn.*

AHARON GEDANKEN

*Department of Chemistry, Bar-Ilan University, Israel  
E-mail: gedanken@mail.biu.ac.il*

$\text{SnO}_2$  nanocrystals with a particle size ranging from 3.5 to 17.9 nm are prepared by heating a smaller  $\text{SnO}_2$  nanocrystal at different temperatures. The samples are characterized by powder X-ray diffraction, Raman spectroscopy and UV-vis diffuse reflectance spectroscopy. The Raman spectra show a surface-related vibration mode, which is dependent on the crystallite size of the  $\text{SnO}_2$  nanocrystals. The quantum confinement effect is observed. The UV-vis diffuse reflectance spectroscopic results indicate that the band gap of the  $\text{SnO}_2$  nanocrystals increases from 3.65 eV to 3.95 eV when the particle size decreases from 4.0 nm to 3.6 nm.

### 1 Introduction

$\text{SnO}_2$  is an n-type wide band gap semiconductor with a band gap of 3.6 eV. Some unique properties of  $\text{SnO}_2$  make this material useful for applications such as resistors, gas sensors, special coating for energy-conserving "low emissivity" windows, transparent heating elements, electrodes in glass melting furnaces, antistatic coating etc [1-3]. The development of reliable and reproducible methods for preparing large quantity of high crystallinity and monodispersivity of  $\text{SnO}_2$  nanocrystals remains an area of interest. High quality  $\text{SnO}_2$  nanocrystal samples are essential for most of the applications as well as the characterization of the properties in nanoscale. Sol-gel is a common method in the preparation of  $\text{SnO}_2$  nanoparticles [4-7]. Hydrous tin oxide is formed by hydrolysis of tin (IV) salts solutions with an average particle size between 1.5 and 3.0 nm, depending upon the preparation conditions [4]. In order to achieve full crystalline dehydrated product, further calcination at a high temperature is indispensable. Several strategies have been used to control the particle size of  $\text{SnO}_2$ . The use of a dopant such as  $\text{Nb}_2\text{O}_5$  can control the particle growth during the synthesis of  $\text{SnO}_2$  processed by the polymeric precursor method [8]. Changing the surface properties by replacing the hydroxyl group with methyl siloxyl surface group has been used to prevent the crystal growth [9]. Methyl siloxyl surface group decomposes in air at 350 °C resulting in  $\text{SiO}_2$  particles, which serves as the "pinning" particles.

A novel method has been developed for controlling the particle size of inorganic nanocrystals. For example, a monodispersed nanocrystalline YSZ with an average particle size of 4.7 nm is obtained by using this method [10]. A very high surface area of 165 m<sup>2</sup>/g and a significant band gap increase from 4.13 to 5.44 eV are observed. Smaller  $\text{SnO}_2$  nanocrystals are also prepared by this method [11]. Here we report the Raman spectra and UV-vis diffuse reflectance spectroscopy (DRS) results of the  $\text{SnO}_2$  nanocrystals with different particle sizes.

## 2 Experimental Section

The synthetic process is similar to the experimental procedure described in reference [11]. The reactants used for the preparation of  $\text{SnO}_2$  are  $\text{SnCl}_4 \cdot 5\text{H}_2\text{O}$ ,  $\text{Sr}(\text{NO}_3)_2$ ,  $\text{NH}_4\text{OH}$ , and  $\text{NH}_4\text{HCO}_3$ . A hydrous  $\text{SnO}_2$  precipitation is obtained by dropping ammonium hydroxide into  $\text{SnCl}_4$  solution. The precipitation is centrifuged and washed with deionized water, then dispersed in water under sonication and formed a suspension.  $\text{SrCO}_3$  nanoparticles are prepared by dropping  $\text{NH}_4\text{HCO}_3$  solution into 0.05 M  $\text{Sr}(\text{NO}_3)_2$  solution under sonication. The  $\text{SrCO}_3$  nanoparticles are washed with deionized water, then dispersed in water and formed a suspension. The  $\text{SrCO}_3$  nanoparticles suspension is added into the hydrous  $\text{SnO}_2$  suspension under stirring. The proportions of hydrous  $\text{SnO}_2$  and  $\text{SrCO}_3$  are 1:2.5 in weight. The mixture is centrifuged, dried at 120 °C, and calcined at 600 °C for 2 h.  $\text{SrCO}_3$  is washed out by dissolving it in 10 %  $\text{HNO}_3$  solution under sonication. The solid product is washed with deionized water for several times and dried in vacuum at room temperature. At this stage, the product is referred to as  $S_{\text{RT}}$ . The samples are further heated at different temperature, 200, 400, 600, 800, and 1000 °C, for 2 h and referred to as  $S_{200}$ ,  $S_{400}$ ,  $S_{600}$ ,  $S_{800}$ , and  $S_{1000}$ , respectively.

Powder X-ray diffraction (XRD) is performed on a Siemens D5005 diffractometer with  $\text{Cu K}\alpha$  radiation. The particle size is calculated from the X-Ray line broadening, using the Debye-Scherrer equation. DRS is measured by Perkin-Elmer Lambda 20 UV-visible spectrophotometer at room temperature in the wavelength region between 200 and 800 nm. Raman spectra are recorded on a Bruker RFS 100 with  $2 \text{ cm}^{-1}$  resolution.

## 3 Results and Discussion

Figure 1 shows the XRD patterns of sample  $S_{\text{RT}}$  and the samples heated at different temperature. The XRD patterns indicate that all of the samples exhibit cassiterite structure, and the line width depends on the heating temperature. The particle sizes estimated from the broadening of the XRD are 3.5, 3.6, 4.0, 5.9, 8.8, and 17.9 nm for the sample  $S_{\text{RT}}$ ,  $S_{200}$ ,  $S_{400}$ ,  $S_{600}$ ,  $S_{800}$ , and  $S_{1000}$ , respectively. Figure 2 shows the variation of the average particle size when the samples are heated at different temperature. It is worth noting that, in order to obtain fully crystalline product, the sample  $S_{\text{RT}}$  has been annealed at 600 °C while it is adhered on the surface of  $\text{SrCO}_3$  nanoparticles. The sample cannot keep the smaller particle size (3.5 nm) without the support of  $\text{SrCO}_3$  nanoparticles even at much lower temperature (200 °C). This indicates that the  $\text{SrCO}_3$  nanoparticles play important role in stabilizing the smaller size nanoparticles. The effect of  $\text{SrCO}_3$  in inhibiting particle growth is not well understood yet. But, it is clear that there should be some interaction (such as electrostatic forces) between the  $\text{SnO}_2$  particles and the surface of  $\text{SrCO}_3$ . This is also supported by the result that the decomposition temperature of  $\text{SrCO}_3$  decreased when it was mixed with hydrous  $\text{SnO}_2$  nanoparticles [11].

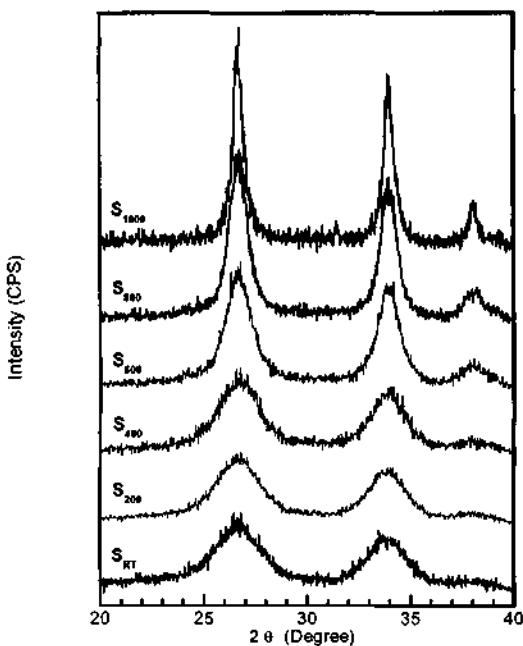


**Figure 1.** The XRD patterns of sample  $S_{RT}$  and the samples heated at different temperature.

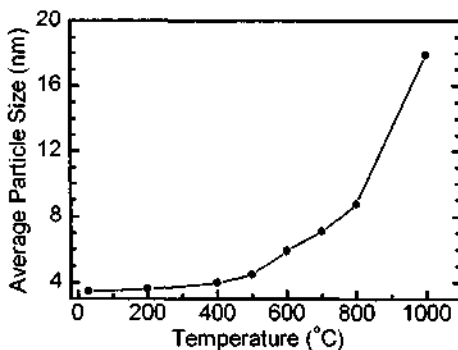


**Figure 2.** The variation of the average particle size when the samples are heated at different temperature.

Raman spectroscopy is an effective method for studying material structure. There have been several reports on the relationship between the particle size and the spectral changes in nanocrystallites of  $\text{SnO}_2$  [12, 13]. The relationship between the change of the Raman spectra of  $\text{SnO}_2$  and its crystal size has been explained by the surface layer structure of nanostructure of  $\text{SnO}_2$ . Fig 3 shows the Raman spectra of sample  $S_{RT}$  and the samples heated at different temperature. The Raman spectrum of  $S_{1000}$  (17.9 nm), which exhibit the bulk properties of Raman shift at 475, 633, and  $775 \text{ cm}^{-1}$ , is similar to that of single crystal of  $\text{SnO}_2$ . For sample  $S_{1000}$ , there is a small hump at  $572 \text{ cm}^{-1}$ , which

correspond to the surface-related vibration mode of the sample. When the particle size decreased, the intensity of Raman shift at 572 nm increased. Sample S<sub>RT</sub> with the smallest particle size has the highest intensity of Raman shift at 572 nm.

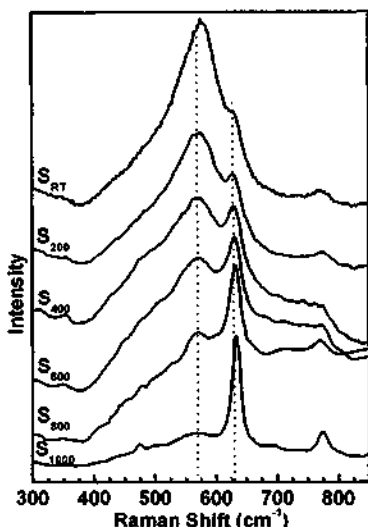


**Figure 3.** The Raman spectra of sample S<sub>RT</sub> and the samples heated at different temperature.

For semiconducting nanoparticles, the quantum confinement effect is expected, and the absorption edge will be shifted to a higher energy when the particle size decreases. The band gaps of the SnO<sub>2</sub> samples are studied by DRS. Figure 4 shows the DRS results. The Kubelka-Munk function,  $F(R) = (1-R)^2/2R$ , is used to determine the band gap by analyzing the DRS results. Figure 5 shows the plots of  $(F(R) \times h\nu)^2$  vs.  $h\nu$  of sample S<sub>RT</sub> and the samples heated at different temperature. The band gaps are defined by extrapolation of

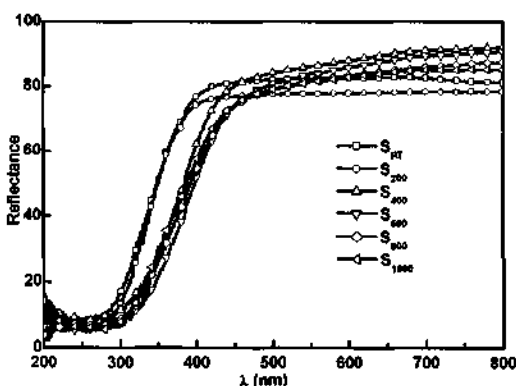


**Figure 4.** The DRS results of sample S<sub>RT</sub> and the samples heated at different temperature.

the rising part of the plots to the X-axis (dotted line in Fig. 5). The band gaps of the  $S_{RT}$ ,  $S_{200}$ ,  $S_{400}$ ,  $S_{600}$ ,  $S_{800}$ , and  $S_{1000}$  are 3.97, 3.95, 3.65, 3.62, 3.67, and 3.69 eV, respectively. The band gap of  $S_{400}$ ,  $S_{600}$ ,  $S_{800}$ , and  $S_{1000}$  (about 3.65 eV) are similar to the literature value of the bulk  $\text{SnO}_2$ .<sup>12, 18</sup> The band gap of  $\text{SnO}_2$  nanocrystals have little change when the particle size changed from 17.9 nm to 4.0 nm, but changed significantly when the particle size decrease from 4.0 nm to 3.6 nm. Band gap increases from 3.65 eV to 3.95 eV when the particle size decreases from 4.0 nm to 3.6 nm. This implies the critical size of  $\text{SnO}_2$  is in the range from 3.6 to 4.0 nm.

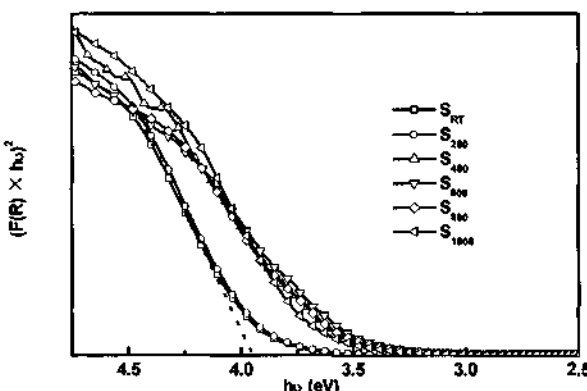


**Figure 5.** The plots of  $(F(R) \times h\nu)^2$  vs.  $h\nu$  of sample  $S_{RT}$  and the samples heated at different temperature.

#### 4 Conclusion

In summary,  $\text{SnO}_2$  nanocrystals with particle size from 3.5 to 17.9 nm are prepared by heating a smaller  $\text{SnO}_2$  nanocrystal at different temperatures. The smaller nanoparticles of  $\text{SnO}_2$  with a particle size 3.5 nm is prepared by a novel method.  $\text{SrCO}_3$  plays important roles in this method. Dispersing the hydrous  $\text{SnO}_2$  particles on a higher surface area lowers the agglomeration and oxolation during the dehydration process. The samples with different particle sizes are characterized by Powder X-ray diffraction, Raman spectrum, and UV-vis diffuse reflectance spectroscopy. The Raman spectra show a surface-related mode, which is dependent on the crystallite size of the  $\text{SnO}_2$  nanocrystals. The quantum confinement effect was observed. The UV-vis diffuse reflectance spectroscopy results indicate that the band gap of  $\text{SnO}_2$  nanocrystals increase from 3.65 eV to 3.95 eV when the particles size decrease from 4.0 nm to 3.6 nm, which implies the critical size of  $\text{SnO}_2$  is in the range from 3.6 to 4.0 nm.

## References

1. Jarzebski Z. M. and Marton J. P., Physical properties of  $\text{SnO}_2$  materials – II. Electrical properties, *Journal of the electrochemical Society, J. Electrochem. Soc.* **123** (1976) pp. 299c-310c.
2. Jarzebski Z. M. and Marton J. P., Physical properties of  $\text{SnO}_2$  materials – III. Optical properties, *J. Electrochem. Soc.* **123** (1976) pp. 333c-346c.
3. Gopel W. and Schierbaum K. D.,  $\text{SnO}_2$  sensor: current status and future prospects, *Sensors and Actuators B* **26-27** (1995) pp. 1-12.
4. Hiratsuka R. S., Pulcinelli S. H. and Santilli C. V., Formation of  $\text{SnO}_2$  gels from dispersed sols in aqueous colloidal solutions, *J. of Non-Cryst. Solids* **121** (1990) pp. 76-83.
5. Pulcinelli S. H., Santilli C. V., Jolivet J. P. and Tronc E, Morphological characterization of aqueous tin oxyhydroxide gel, *J. of Non-Cryst. Solids* **170** (1994) pp. 21-26.
6. Briois V., Santilli C. V., Pulcinelli S. H. and Brito G. E. S., EXAFS and XRD analyses of the structural evolutions involved during drying of  $\text{SnO}_2$  hydrogels, *J. of Non-Cryst. Solids* **191** (1995) pp.17-28.
7. Vincent C. A. and Weston D. G. C., Preparation and properties of semiconducting polycrystalline tin oxide, *J. Electrochem. Soc.* **119** (1972) pp. 518-521.
8. Leite E. R., Weber I. T., Longo E. and Varela, J. A. A new method to control particle size and particle size distribution of  $\text{SnO}_2$  nanoparticles for gas sensor applications, *Adv. Mater.* **12** (2000) pp. 965-968.
9. Wu N. -L., Wang S. -Y. and Rusakova I. A., Inhibition of crystallite growth in the Sol-Gel synthesis of nanocrystalline metal oxides, *Science* **285** (1999) pp. 1375-1377.
10. Pang G., Chen S., Zhu Y., Palchik. O., Koltypin. Yu., Zaban. A., Gedanken. A., Preparation and characterization of monodispersed YSZ nanocrystals, *J. Phys. Chem. B* **105** (2001) pp. 4647-4652.
11. Pang G., Chen S., Koltypin Yu., Zaban A., Feng S. and Gedanken A., Controlling the particles size of calcined  $\text{SnO}_2$  nanocrystals, *Nano Letters* **1(12)** (2001) pp.723-726.
12. Zuo J., Xu C., Liu X., Wang C., Wang C., Hu Y. and Qian Y., Study of the Raman spectrum of nanometer  $\text{SnO}_2$ , *J. Appl. Phys.* **75(3)** (1994) pp. 1835-1836
13. Xie C., Zhang L. and Mo C., Characterization of Raman spectra in nano- $\text{SnO}_2$  solids, *Phys. Stat. Sol.* **141** (1994) pp. K59-61.

# METAL SALTS AS STRUCTURE-DIRECTING AGENTS FOR $\text{SiO}_2$ AND $\text{TiO}_2$ NANOTUBES CONTAINING HIGH AMOUNTS OF ENCAPSULATED METAL

LIRONG REN,<sup>\*1,2</sup> UTE MELVILLE<sup>1</sup> AND MICHAEL WARK<sup>1,2</sup>

<sup>1</sup> Institute for Applied and Physical Chemistry, University of Bremen,  
D-28334 Bremen, Germany

<sup>2</sup> Institute for Physical Chemistry and Electrochemistry, University of Hannover,  
Callinstr. 3-3A, D-30167 Hannover, Germany  
E-mail: Michael.Wark@pci.uni-hannover.de

This paper reports on the one-step-formation of silica and titania nanotubes with a high amount of metal clusters (up to 25 wt.%) encapsulated. By a sol-gel processing very small fibers of a templating salt, e.g.  $[\text{Pt}(\text{NH}_3)_4](\text{HCO}_3)_2$ , precipitated as needles with sizes in nanometer regime, were coated with silicate or titanate species forming the tube walls. Based on the variation of the templating noble metal salts an understanding on the mechanism of the formation of the nanotubes possessing rectangular inner cross-section has been achieved.

## 1 Introduction

Since the discovery of carbon nanotubes, there has also been extensive research on the synthesis of nanotubes consisting of other materials. Nanotubes have been synthesized from oxides such as  $\text{Al}_2\text{O}_3$  [1],  $\text{MoO}_3$  [1],  $\text{V}_2\text{O}_5$  [1,2],  $\text{SiO}_2$  [1,3],  $\text{TiO}_2$  [4],  $\text{In}_2\text{O}_3$  [5] and  $\text{ZrO}_2$  [6], and other materials like BN [7,8],  $\text{MoS}_2$  or  $\text{WS}_2$  [9]. The general route of synthesis for oxidic nanotubes is based on the sol-gel processing using structure-directing templates. Due to the ability of sols and gels to adapt to given structures, the morphology of the templating agents is transferred to the ceramic oxides.

This paper describes a new synthesis route for the formation of silica and titania nanotubes filled with high amounts of Pt metal clusters up to 24.5 wt.%. To some extent, the mechanism of the synthesis has been explored.

## 2 Methods

For the preparation of e.g. platinum-filled  $\text{SiO}_2$  nanotubes 0.05 mmol  $[\text{Pt}(\text{NH}_3)_4](\text{HCO}_3)_2$  was dissolved in 2 ml distilled water. After the addition of 40 ml ethanol, some white reprecipitate appeared. Then 2 ml 0.4 M ammonia solution and 0.5 mmol tetraethylorthosilicate (TEOS) were dropwise added to the suspension. After stirring for 12 h, the solvent was removed and the precipitate was dried. Finally, the powder was calcined at 773 K (heating rate: 2 K/min) for 5 h with in a flow of argon (6L/h). The whole reaction before calcination was kept at room temperature.

Metal-filled  $\text{TiO}_2$  nanotubes can be obtained by using tetrabutylorthotitanate (TBOT) instead of TEOS. In this case the reaction was conducted at 213K for 5h.

In order to study the synthesis mechanism, several kinds of inorganic compounds have been used as templates under the same conditions, such as  $[\text{Pt}(\text{NH}_3)_4](\text{OH})_2$ ,  $[\text{Pt}(\text{NH}_3)_4]\text{Cl}_2$ ,  $[\text{Pd}(\text{NH}_3)_4]\text{Cl}_2$ ,  $[\text{Cu}(\text{NH}_3)_4]\text{SO}_4$ .

The calcined samples were investigated by transmission electron microscopy (TEM) in a Philips EM 420 instrument operated at 120 kV. The specimens were deposited on

copper grids coated with carbon films.

### 3 Results

#### 3.1 Formation of nanotubes

In case of silica nanotubes formed from TEOS and with  $[\text{Pt}(\text{NH}_3)_4](\text{HCO}_3)_2$  as templating salt, the synthesis products consist almost exclusively of nanotubes. As deduced from TEM-micrographs (Fig. 1), the portion of non-structured silica formed can be neglected. The lengths of the tubes vary between 50 nm and several  $\mu\text{m}$  and the inner diameters range from 10 nm up to 300 nm with a maximum of frequency around 50 nm. The silica walls are X-ray amorphous with a thickness of about 30-50 nm.

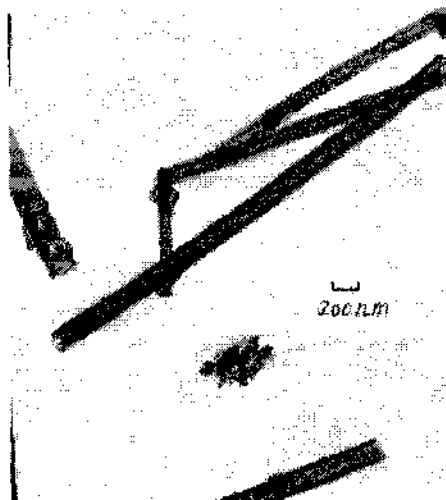


Figure 1. TEM micrograph of Pt-loaded  $\text{SiO}_2$  nanotubes. The dark spots represent Pt particles formed during calcination. The bar represents 200 nm.

The length of the longest nanotube shown in Figure 1, is around 3.6  $\mu\text{m}$ , and the width is about 180 nm. The dark spots represent Pt particles formed during calcination of the structure-directing Pt-salt.

As demonstrated in a previous paper [10], the tubes are hollow with a marked rectangular cross-section. As supposed before, the rectangular inner shape of the tubes might be a counter-plast of the templating metal salt nanofibers, precipitated in the ethanolic solution prior to the addition of TEOS. A rectangular morphology of  $[\text{Pt}(\text{NH}_3)_4](\text{HCO}_3)_2$  had been found for single crystals of this salt, carefully grown by slow evaporation of the solvent ethanol. SEM micrographs and the unit cell parameters of these single crystals were described already [10].

Figure 2 presents some SEM pictures taken directly from suspensions of the fluffy precipitate of  $[\text{Pt}(\text{NH}_3)_4](\text{HCO}_3)_2$  in ethanol before addition of TEOS and representing the formation process of the templating Pt-salt nanofibers. Figure 2a shows the salt as it was received from the supplier. The micrograph 2b was taken after dissolution of the salt in water and re-precipitation with ethanol and, finally, micrograph 2c after the addition of TEOS and calcination.

Compared with the starting salt crystals (Fig. 2a), the templating salt fibers (Fig. 2b) exhibit a drastically reduced size and a more regular morphology. Besides stick-shaped particles a large amount of needle-shaped fibers is observable. The lengths of the needles are a few micrometer and their width are far below 1  $\mu\text{m}$ . After the hydrolysis and condensation of TEOS and, in further step, the calcination in Ar, the morphology and sizes of the final silica nanotubes exhibit obviously no difference. Also in the final product there are two kinds of morphologies, sticks and needles. The needle-shaped nanotubes form aggregates making an exact determination of their size distribution difficult. However, it is obvious even from that micrograph that the sizes are comparable to that of the separated nanotubes shown in Figure 1. This demonstrates that a direct formation of the nanotubes by a coating of the needle-like  $[\text{Pt}(\text{NH}_3)_4](\text{HCO}_3)_2$  nanofibers, shown in Fig. 2b, is highly probable. The stick-like crystals are only a side-product.

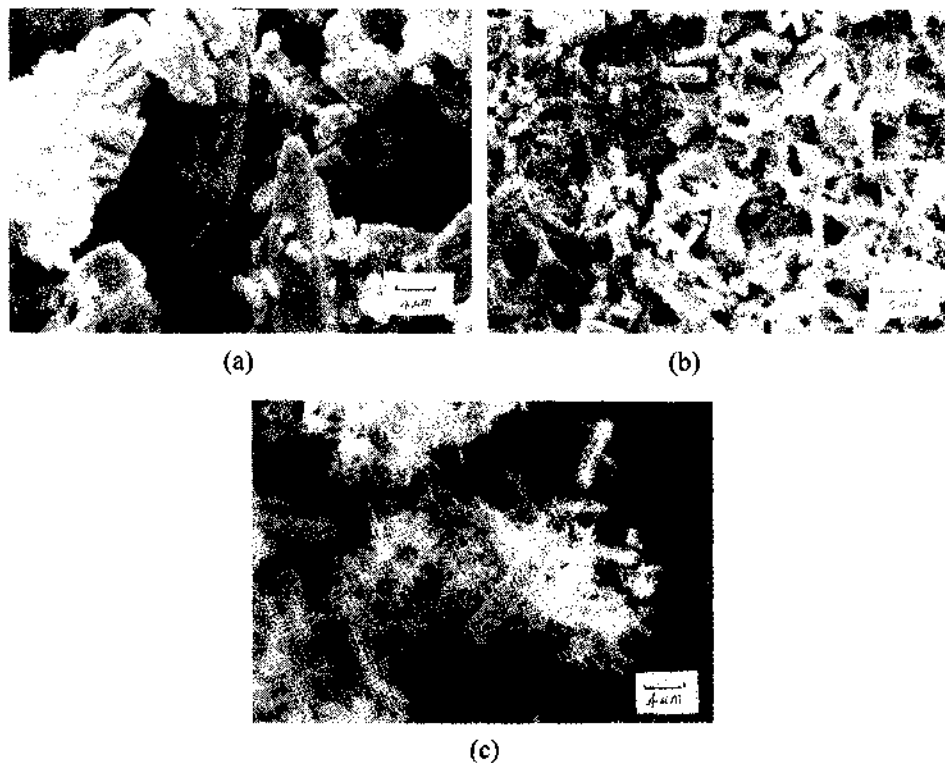


**Figure 2.** SEM representing the steps of the formation of nanofibers of  $[\text{Pt}(\text{NH}_3)_4](\text{HCO}_3)_2$ , acting as templating units for the condensation of silicate monomers forming the  $\text{SiO}_2$  nanotubes: original salt (a), after re-precipitation in ethanol and after addition TEOS and calcination. The bars represent 4  $\mu\text{m}$ .

### 3.2 Effect of the anion type on the synthesis of nanotubes

Salts of Pt-ammine cations with three different anions, *i.e.*  $[\text{Pt}(\text{NH}_3)_4](\text{HCO}_3)_2$ ,  $[\text{Pt}(\text{NH}_3)_4](\text{Cl})_2$ ,  $[\text{Pt}(\text{NH}_3)_4](\text{OH})_2$  have been used as templates. Although the cationic complex remained unchanged, the morphologies of the templating salt fibers are quite different. The salt with the anion ( $\text{HCO}_3^-$ ) exhibits mainly  $\mu\text{m}$ -long needles, with diameters around 120 nm. In contrast, with the  $\text{OH}^-$  anion predominately short sticks with

diameters around 450 nm are precipitated, and the chloride salt forms sphere-like particles whose diameter is around 130 nm. From this, it can be assumed that the size of the anion, its interaction with the cationic complex and possibly also its basic strength influence the morphology of the precipitated templating nanofibers.

In order to verify this assumption, the metal ion in the cationic complex was changed from  $\text{Pt}^{2+}$  to  $\text{Pd}^{2+}$  and as anions in the templating salts  $(\text{HCO}_3)^-$  and  $\text{Cl}^-$  were used to create nanotubes.  $[\text{Pd}(\text{NH}_3)_4](\text{HCO}_3)_2$  was synthesized from the purchased compound  $[\text{Pd}(\text{NH}_3)_4](\text{Cl})_2$  by anion exchange with an ion exchange resin.

As deduced from the TEM micrographs of the products after hydrolysis, condensation and calcination, tubular structures comparable to that found with  $[\text{Pt}(\text{NH}_3)_4](\text{HCO}_3)_2$  were only obtained by use of the complex compound  $[\text{Pd}(\text{NH}_3)_4](\text{HCO}_3)_2$ .

#### 4 Discussion

For the formation of silica nanotubes around  $[\text{Pt}(\text{NH}_3)_4](\text{HCO}_3)_2$  nanofibers, acting as templates, a coating mechanism, comparable to that given by Caruso et al. for the coating of polystyrene spheres with silica or titania [11], can be discussed.

Under the basic conditions present during the synthesis, the silicate species are partly deprotonated and negatively charged. It is assumed that an exchange of  $(\text{HCO}_3)^-$  ions with silicate anions takes place at the surface of the precipitated needle-like  $[\text{Pt}(\text{NH}_3)_4](\text{HCO}_3)_2$  crystals. The arrangement of the silicate anions around the metal salt fibers is, besides the electrostatic interaction, attracted by the formation of hydrogen bonds with the  $\text{NH}_3$  ligands of the  $[\text{Pt}(\text{NH}_3)_4]^{2+}$  complex cations.

The  $\text{SiO}_2$  walls are built up by condensation processes, for which the anchored silicate species act as nucleation points. The enrichment of the oxide at the templating crystals occurs by an Ostwald ripening mechanism; the particles grow in size at the tube walls and highly soluble very small silica particles re-dissolve to the reaction solution. The polycondensation reaction is finished within about 12 h.

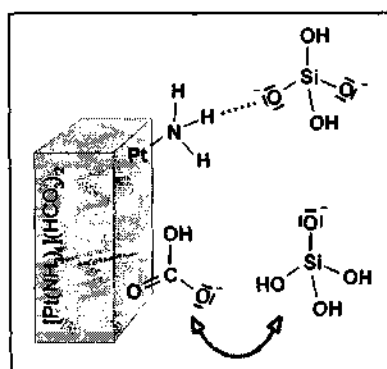


Figure 3. Interactions between the  $[\text{Pt}(\text{NH}_3)_4](\text{HCO}_3)_2$  nano-fibers and the silicate monomers.

The calcination of the precipitated nanotubes at 773 K leads to the decomposition and simultaneous reduction of the platinum salt, resulting in the formation of metallic platinum particles decorating the inner surface of the tube. The reductive decomposition of

$[\text{Pt}(\text{NH}_3)_4](\text{HCO}_3)_2$  and the following removal of  $\text{CO}_2$ ,  $\text{NH}_3$ ,  $\text{H}_2\text{O}$ ,  $\text{H}_2$  and  $\text{N}_2$  through the porous walls, generates the hollow tubes, the morphology of which is stable up to temperatures of 1073 K. This synthesis route ensures that the metal clusters formed by calcination in Ar at 773 K are located mostly in the interior of the tubes or might at the most migrate into the walls [12].

According to Figure 1 and to a large number of further micrographs, taken from thus prepared  $\text{SiO}_2$  nanotubes, it can be stated that the needle-shaped tubes possess marked rectangular cross-sections. Moreover, there exist several kinds of needle-shaped nanotubes: some are filled with Pt particles, some are empty. At the same time, there is a coexistence of nanotubes with two-open-ends, one-open-end and two-closed-ends [13]. It is reasonable that nanotube with two open ends are empty, since there is no reason for the Pt particles not to diffuse out of the tubes.

Reference experiments show that non-coated  $[\text{Pt}(\text{NH}_3)_4](\text{HCO}_3)_2$  nanofibers are not stable over long periods. They tend to agglomerate to non-regular structures. Only the rigid  $\text{SiO}_2$  layers, forming the silica walls, stabilize the needle-like structure.

The broad distribution of the lengths and diameters of the final nanotubes is probably caused by the same broad size-distribution in the templating  $[\text{Pt}(\text{NH}_3)_4](\text{HCO}_3)_2$  nanofibers. During the coating process obviously no drastic changes in the morphology occur. In order to control the size of the nanotubes, the emphasis should be put on the effort to control the precipitation of the metal-salt nanofibers.

Recent experiments demonstrated that besides Pt-filled  $\text{SiO}_2$  nanotubes also titania nanotubes can be produced by the discussed synthesis route. One has to take care that the reaction temperature is below 213 K and ceaseless stirring is achieved. But the portion of perfect  $\text{TiO}_2$  nanotubes in the products is much lower than that of ideal  $\text{SiO}_2$  nanotubes. The difficulties in the synthesis of  $\text{TiO}_2$  nanotubes result from the rapid hydrolysis and condensation of tetrabutylorthotitanate (TBOT) used as titanium source. Furthermore, a destruction of  $\text{TiO}_2$  nanotubes into amorphous structures was often observed under the high-power electron beam of the TEM microscope.

## 5 Conclusions

A novel route for the synthesis of  $\text{SiO}_2$  and  $\text{TiO}_2$  nanotubes with rectangular cross-section is developed. The high metal content and their anisotropic morphology render these tube-like nanocomposites attractive materials for nanoelectronics. In order to realize probable applications as nanowires, the synthesis route must be further optimized to obtain tubes, which are uniform in length and width.

However, in the highly attractive research area of self-assembly and structure-directing synthesis, the reported successful formation of Pt-filled  $\text{SiO}_2$  and  $\text{TiO}_2$  nanotubes is only the first step. Compared with these two kinds of nanotubes, many other metal-filled oxide nanotubes, e.g. such filled with Fe, Cu or Ni clusters, might be more applicable and attractive. In order to synthesize these other kinds of nanotubes, the thorough understanding should be explored toward those factors affecting the formation of the nanotubes. With respects to this goal, the presented variation of the anions and the central metal in the structure directing Pt-ammine salts gave first indications. It can be assumed that at least complex compounds with the general composition  $[\text{M}(\text{NH}_3)_4](\text{HCO}_3)_2$  might be useable as templates for the creation of metal oxide nanotubes. Further variations promising additional information on the formation mechanism are designed and are underway in our laboratory.

## 6 Acknowledgements

We thank Mrs. A. Toltz (University of Bremen, Germany) for her help to produce the SEM micrographs. Financial support by the Deutsche Forschungsgemeinschaft (DFG, WA 1116-5) is also gratefully acknowledged.

## References

1. Satishkumar, B.C., Govindaraj, A., Nath, M. and Rao, C.N.R., Synthesis of metal oxide nanorods using carbon nanotubes as templates, *J. Mater. Chem.* **10** (2000) pp. 2115-2120.
2. Krumeich, F.; Muhr, H.J., Niederberger, M.; Bieri, F., Schnyder, B. and Nesper, R., Morphology and topochemical reactions of novel vanadium oxide nanotubes, *J. Am. Chem. Soc.* **121** (1999) pp. 8324-8331.
3. Nakamura, H. and Matsui, Y., The preparation of novel silica gel hollow tubes, *Adv. Mater.* **7** (1995) pp. 872-874.
4. Kasuga, T., Hiramatsu, M., Hoson, A., Sekino, T. and Niihara, K., Titania nanotubes prepared by chemical processing, *Adv. Mater.* **11** (1999) pp. 1307-13221.
5. Liang, C., Meng, G., Lei, Y., Phillip, F., Zhang, L., Catalytic growth of semiconducting  $In_2O_3$  nanofibers, *Adv. Mater.* **13** (2001) pp. 1330-1333.
6. Rao, C.N.R., Satishkumar, B.C., and Govindaraj, A., Zirconia nanotubes, *J. Chem Soc., Chem. Commun.* (1997) pp. 1581-1582.
7. Hamilton, E.J.M., Dolan, S.E., Mann, C.M., Colijn, H.O., McDonald, C.A. and Shore, S.G., Preparation of amorphous boron nitride and its conversion to a turbostratic tubular form, *Science* **260** (1993) pp. 659-660.
8. Gleize, P., Schouler, M.C., Gadelle, P. and Caillet, M.J., Growth of tubular boron nitride filaments, *J. Mater. Sci.* **29** (1994) pp. 1575-1580.
9. Remskar, M., Skraba, Z., Stadelmann, R. and Levy, F., Structural stabilization of new compounds:  $MoS_2$  and  $WS_2$  micro- and nanotubes alloyed with gold and silver, *Adv. Mater.* **12** (2000) pp. 814-817.
10. Hippe C., Wark M., Lork E. and Schulz-Ekloff G., Platinum-filled oxide nanotubes, *Microporous Mesoporous Mater.* **31** (1999) pp. 235-241.
11. Caruso, R.A., Susha, A. and Caruso, F., Multilayered titania, silica and laponite nanoparticle coatings on polystyrene colloidal templates and resulting inorganic hollow spheres, *Chem. Mater.* **13** (2001), pp. 400-409.
12. Wark M., Hippe C. and Schulz-Ekloff G., Distribution of Pt clusters in  $SiO_2$  and  $TiO_2$  nanotubes, *Stud. Surf. Sci. Catal.* **129** (2000) pp. 475-482.
13. Krumeich, F., Nesper, R., Ren, L., Wark, M., Electron microscopy characterization of silica nanotubes, paper in preparation.

## TEMPERATURE EFFECTS ON FORMATION OF C-BN FILMS BY MAGNETRON SPUTTERING

B. WANG, H. ZHOU, X. H. LI, R. Z. WANG, H. WANG AND H. YAN\*

*The Key Laboratory of Advanced Functional Materials of China Education Ministry  
Beijing Polytechnic University, Beijing 100022, China  
E-mail address: hyan@bjpu.edu.cn*

The effects of substrate temperature ( $T_{sub}$ ) on cubic boron nitride (c-BN) films synthesized using magnetron sputtering were studied. Fourier transform infrared (FTIR) spectroscopy, X-ray photoelectron spectroscopy (XPS) were employed to characterize the structure and composition of the films. It is found that  $T_{sub}$  plays a crucial role on the formation of cubic phase, and an appropriate  $T_{sub}$  can lead to a high content. A tentative explanation on the mechanism of such  $T_{sub}$  effects is reported with the most details.

### 1. Introduction

Cubic boron nitride (c-BN), as one kind of important III-Nitrides, has drawn great attention both academically and industrially from 1990's due to its significant potential application. Similar with diamond, c-BN has a low density, ultrahigh hardness, high electrical resistance, excellent chemical stability, great thermal conductivity and wide optical band gap [1]. Furthermore, c-BN can be efficiently doped with both n- and p-type impurities [2]. Therefore, c-BN films hold great application potential in electronic and optic-electronic devices [3]. More promising, it is recently found to have negative electron affinity [4], which could make it well attractive in field emission devices and in field emission display (FED).

Recently, many methods in the synthesis of c-BN films were studied, which include physical vapor deposition [1,5-7] (PVD) and chemical vapor deposition [1,8,9] (CVD, such as PECVD, HFCVD, MW-ECR-CVD). Most experiments have indicated that the commercial application of c-BN films depends on enhancement and improvement in the stability and repeatability of preparation process. Generally, ion energy flow density or ion bombardment was attributed to the essential factor with the influence in the c-BN formation [1,10-13]. However, it is noted that the discrepancy between PVD and CVD maybe result from the difference in the substrate temperature ( $T_{sub}$ ). Unfortunately, the role which  $T_{sub}$  plays on the growth of cubic phase in PVD was seldom investigated systematically.

This work puts its weight on the effect of  $T_{sub}$  on the growth of c-BN films using magnetron sputtering. In experiments, a relative broad range of the experimental parameters of  $T_{sub}$  was found and relative stable synthesis of the films with high content of cubic phase was realized.

### 2. Experimental

BN films were deposited on silicon (100) wafer with resistivity (5-8 $\Omega$  cm) by a magnetron sputtering system. Sputtering target used here was a hot-pressed h-BN with 4N purity. The substrate was applied with a negative bias at 180V and 300V, respectively. Deposition was carried out with a base pressure of  $2 \times 10^{-4}$  Pa and mixed

working gas of nitrogen and argon ( $N_2$ :  $Ar=1:1$ ) under the working pressure in the range of 0.5 to 4Pa, after the substrate had been pre-sputtered for 10 min with  $Ar^+$  and  $N^+$  ions at the substrate bias of 300V. During the deposition,  $T_{sub}$  was adjusted from room temperature to 800°C and RF power was fixed at 500W. The films were primarily characterized by a Nicolet 550 FTIR in an absorption mode. During FTIR measurement, an incidence pattern normal to the substrate surface was applied. Both the composition and binding states of element of B and N were measured by a Kratos AXIS-HS XPS using Al K $\alpha$  radiation.

### 3. Results and Discussion

Definitely as reported previously, it can be concluded that the ion energy flow density was ascribed to the essential factor with influence in c-BN formation [10-13]. So, the substrate bias of 180V was here chosen to deposit c-BN films at different  $T_{sub}$ .

Figure 1 shows the FTIR absorption spectra of the films deposited at different  $T_{sub}$  under working pressure of 0.5Pa and deposition time of 0.5h. It is evident that the appearance of the peak at 1080 cm $^{-1}$  in FTIR spectra indicates the formation of cubic phase (TO mode of c-BN) even though  $T_{sub}$  is at room temperature. Note that the ratio of peak intensity at 1080cm $^{-1}$  to that at 1380cm $^{-1}$  (in-plane mode of hexagonal BN, h-BN) gradually increases, and then go down showing a tendency in the cubic phase content with the increase in  $T_{sub}$ . In the same FTIR spectra,  $I_{1080} / (I_{1080} + I_{1380})$  is usually defined as C, which could indicate the content of cubic phase [14]. The dependence of C at 1080cm $^{-1}$  picked from Figure 1 on  $T_{sub}$  is further revealed in Figure 2. It is seen that the value of C presents the trend of increasing to the peak, then going down with the increase in  $T_{sub}$ . The behavior of the c-BN content with  $T_{sub}$  is identical with that prepared at various substrate biases and working pressures, in a way similar to that reported in previous literatures [15-17]. Furthermore, the fact that result of C of 33% as  $T_{sub}$  is at room temperature demonstrates that the cubic phase can be synthesized under a lower  $T_{sub}$  than the critical one mentioned by Mirkarimi et al. [15]. When  $T_{sub}$  reaches 490°C, C as a peak in the curve is up to 64%. Moreover, under such  $T_{sub}$  the films with higher c-BN content above 75% by applying a higher bias of 225~250V or a higher working pressure of 1Pa were acquired. So, it is thought that  $T_{sub}$  near 500°C is a relative ideal parameter to reach a higher C.

The atomic ratio of N to B of all the films here by XPS measurement was almost stoichiometric. For comparison between the different BN phases, XPS spectra of B $_{1s}$  and N $_{1s}$  corresponding respectively to the higher and lower c-BN content films are plotted in Figure 3 (a) and (b). Here, the higher c-BN content film was prepared at 490°C as shown in Figure 1, and the lower c-BN content film was composed of pure hexagonal phase synthesized also by magnetron sputtering. From Figure 3, it is clear that the binding energy (E $_B$ ) of B $_{1s}$  in the higher c-BN content film shifts by 0.25eV to higher energy from that of the lower c-BN content film. In contrast the E $_B$  of N $_{1s}$  in the higher c-BN content film is 0.38eV lower than that in the lower c-BN content film. Therefore, the XPS result is consistent with the transfer charges caused by the different B-N bonding structures.

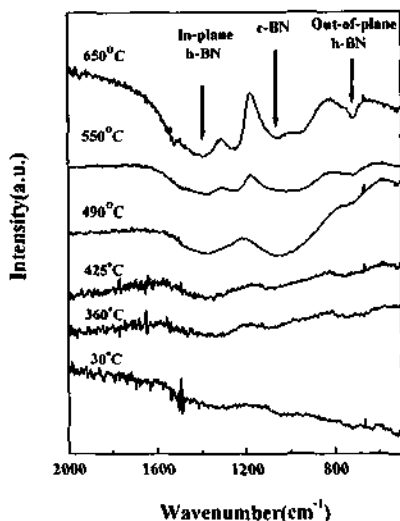


Figure 1. FTIR absorption spectra of c-BN films deposited at different  $T_{\text{sub}}$ .

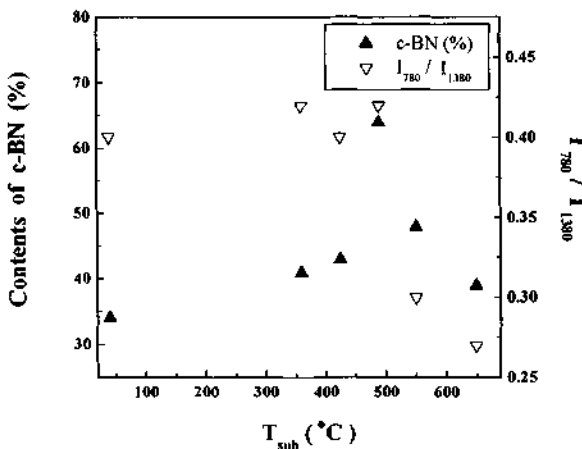
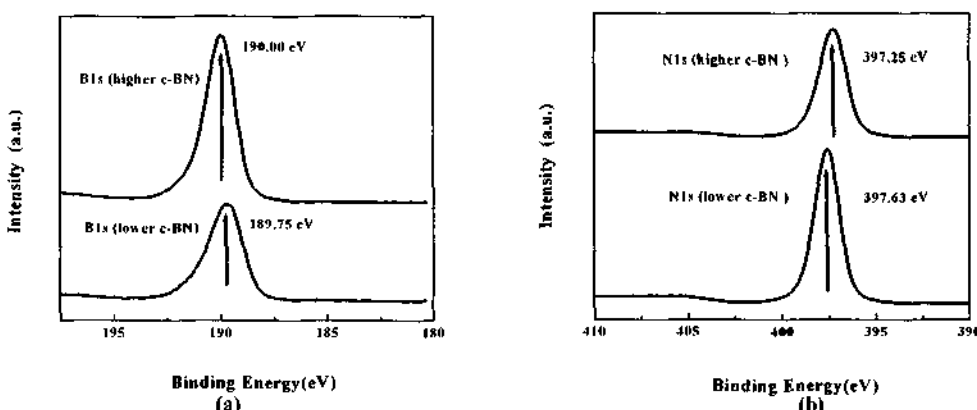


Figure 2. Dependence of c-BN content and orientation of residual h-BN grains in the films as plotted in Figure 1. on  $T_{\text{sub}}$ .

It is well known that the growth of films depends chiefly on diffusion of deposited atoms, which is mainly influenced by the kinetic energy. When the other parameters are settled, the kinetic energy of the deposited atoms consequently comes to be a function of  $T_{\text{sub}}$ . However, higher kinetic energy not only stimulates deposited atoms to diffuse faster near to c-BN critical nuclei for its further growth, but also causes more adsorption, which is disadvantageous to both stability of critical nuclei and the subsequent growth of c-BN phase. In fact, this idea about diffusion was

previously proposed [15]. When  $T_{\text{sub}}$  is relative low, the diffusivity of deposited atoms is not high enough for the further growth of c-BN nuclei. Moreover, the energy necessary for the growth of h-BN phase is lower than that of c-BN phase. Therefore, higher growth probability of h-BN phase leads to less c-BN content under low  $T_{\text{sub}}$ , as clearly seen in Figure 2. In general, the c-BN phase induced by great incoming ion bombardment forms on top of basal plane of h-BN grain when its c-axis orientation is parallel to surface [1]. Such orientation is usually due to compressive stress caused by ion bombardment. However, it is also found that a higher  $T_{\text{sub}}$  could destroy the growth of (100) oriented h-BN films (its basal plane perpendicular with the surface), as reported elsewhere [18]. Hence, when  $T_{\text{sub}}$  is relative high, greater adsorption occurs, which destabilizes critical nuclei and inhibits such favorable orientation for the formation of c-BN phase. As seen in Figure 2, the value of  $I_{1380} / I_{780}$  is, respectively, 0.3 and 0.27 corresponding to  $T_{\text{sub}}$  of 550°C and 650°C, which indicates poor (100) orientation of residual h-BN grains in the films [19]. Obviously, the c-BN content resultantly descends from a peak under higher temperatures. Consequently, appropriate kinetic energy of deposited atoms would be more beneficial to further growth of c-BN critical nuclei under a proper  $T_{\text{sub}}$  (about 500°C), because compared to the diffusion effects that of adsorption is of unimportance. Moreover, at such  $T_{\text{sub}}$ , (100) orientation of residual h-BN grains (the value of R, 0.42) mostly in the interface between Si substrate and c-BN films could be favorable to increase the cubic phase content at higher bias or working pressures, as substantiated by other works.



**Figure 3.** XPS spectra of B<sub>1s</sub> (a) and N<sub>1s</sub> (b) of the higher and lower c-BN content films, respectively.

Conclusively, ion energy flow density cannot be considered as the sole essential factor with influence in the formation of c-BN films from outcomes of the present study and others' works.  $T_{\text{sub}}$  is another important factor in such process, especially in the subsequent growth of c-BN films after rapid nucleation of cubic phase [14-17]. Namely, under any one above the critical  $T_{\text{sub}}$  (usually above room temperature) once ion energy flow density is above the threshold, cubic phase forms. And a certain  $T_{\text{sub}}$  is advantageous to increase the cubic phase content and improve quality of c-BN

films, but  $T_{\text{sub}}$  can't determine whether the cubic phase could appear, which corresponds well with the mode of ion bombardment-induced c-BN formation [10-13].

#### 4. Conclusion

Stoichiometric c-BN films were prepared by magnetron sputtering at different  $T_{\text{sub}}$  and the substrate negative bias of 180V. It is found that when ion energy flow density does not reach the threshold, h-BN film is formed. When it reaches the threshold, c-BN phase with the dependence of the content on  $T_{\text{sub}}$  is obtained. Under an appropriate  $T_{\text{sub}}$  (near 500°C) the content of c-BN phase reaches a maximum value. It is suggested that a proper  $T_{\text{sub}}$  would give rise to preferentially (100) oriented h-BN transitional layer for the formation of c-BN phase and an advantageous kinetic energy of deposited atoms for the further growth of c-BN critical nuclei.

#### 5. Acknowledgements

This work was supported in particular by Beijing Natural Science Foundation (No.2992002) and Beijing Technology New Stars Project.

#### References

- Mirkarimi P. B., McCarty K. F., Medlin D. L. et al., On the role of ions in the formation of cubic boron nitride films by ion-assisted deposition, *J. Mater. Res.*, **9** (1994) pp. 2925-2938.
- Wentorf R. H., Jr., Preparation of semiconductor cubic boron nitride, *J. Chem. Phys.*, **36** (1962) pp. 1990-1991.
- Kidner S., Taylor II C. A., Clarke R., Low energy kinetic threshold in the growth of cubic boron nitride films, *Appl. Phys. Lett.*, **64** (1994) pp. 1859-1861.
- Ronning C., Banks A. D., McCarson B. L. et al., Structure and electronic properties of boron nitride thin films containing silicon, *J. Appl. Phys.*, **84** (1998) pp. 5046-5051.
- Bewilogua K., Buth J., Hübsch H. et al., Deposition of c-BN films by DC magnetron sputtering, *Diamond Relat. Mater.*, **7** (1998) pp. 26-31.
- Litvinov D., Clarke R., Reduced bias growth of pure-phase cubic boron nitride, *Appl. Phys. Lett.*, **71** (1997) pp. 1969-1971.
- Johansson M. P., Ivanoz I. et al., Low-temperature deposition of cubic BN:C films by unbalanced direct current magnetron sputtering of a B4C target, *J. Vac. Sci. Technol. A*, **14** (1996) pp. 3100-3107.
- Yokoyama H., Okamoto M. et al., Effects of a negative self-bias on the growth of cubic boron nitride prepared by plasma chemical vapor deposition, *Jpn. J. Appl. Phys.*, **30** (1991) pp. 344-348.
- Weber A., Bringmann U. et al., Growth of cubic boron nitride and boron-carbon-nitrogen coatings using N-trimethylborazine in an electron cyclotron resonance plasma process, *Diamond Relat. Mater.*, **2** (1993) pp. 201-206.

10. Kester D. J., Messier R., Phase control of cubic boron nitride thin films, *J. Appl. Phys.*, **72** (1992) pp. 504-511.
11. Ikeda T., Cubic boron nitride films synthesized by low-energy ion-beam-enhanced vapor deposition, *Appl. Phys. Lett.*, **61** (1992) pp. 786-788.
12. Tanabe N., Hayashi T., Iwaki M., Deposition of cubic boron nitride thin films by ion-beam-enhanced deposition, *Diamond Relat. Mater.*, **1** (1992) pp. 883-890.
13. Ronning C., Felderman H., Hofsäss H., Growth, doping and applications of cubic boron nitride thin films, *Diamond Relat. Mater.*, **9** (2000) pp. 1767-1773.
14. Friedmann T. A., Mirkarimi P. B. et al., Ion-assisted pulsed laser deposition of cubic boron nitride films, *J. Appl. Phys.*, **76** (1994) pp. 3088-3101.
15. Mirkarimi P. B., Medlin D. L., McCarty K.F., Growth of cubic BN films on  $\beta$ -SiC by ion-assisted pulsed laser deposition, *Appl. Phys. Lett.*, **66** (1995) pp. 2813-2815.
16. McCarty K. F. et al., On the low-temperature threshold for cubic boron nitride formation in energetic film deposition, *Diamond Relat. Mater.*, **5** (1996) pp. 1519-1526.
17. Felderman H., Merk R., Hofsäss H., Ronning C., Zheleva T., Room temperature growth of cubic boron nitride, *Appl. Phys. Lett.*, **74** (1999) pp. 1552-1553.
18. Zhou H., Wang R. Z., Huang A. P., Wang M., Wang H., Wang B., Yan H. Dependence of oriented BN films on substrate temperature, *J. Crystal Growth*, in press.
19. Friedmann T. A., McCarty K. F., Klaus E. J. et al., Pulsed laser deposition of BN onto silicon (100) substrates at 600 °C, *Thin Solid Films*, **237** (1994) pp. 48-56.

## PHASE FORMATION AND TRANSFORMATION OF NANOSTRUCTURED TITANIA IN SOLUTION

GUANGGUO WANG, GANG LIN, YELI TU, XIANFENG YANG, JUNBIAO LONG,  
SHOUHUA FENG, RUREN XU AND MINGMEI WU

*State Laboratory of Optoelectronic Materials and Technologies, and School of Chemistry and Chemical Engineering, Sun Yat-Sen (Zhongshan) University, Guangzhou, 510275, P. R. China.*

*State Key Laboratory of Inorganic Synthesis and Preparative Chemistry, Jilin University,  
Changchun 130023, P. R. China  
Email: ceswmm@zsu.edu.cn*

Synthesis and phase transformation of nanosized titania has been paid great attention for decades. Nanoparticles of anatase and rutile with various sizes and morphologies were prepared herein in various acidic aqueous solutions via sol-hydrothermal reactions. Anatase forms first and then transforms to rutile in a certain medium. The transformation can be accelerated in acidic solution. However, the strong chemical coordination of some anions, such as  $\text{CH}_3\text{COO}^-$  ( $\text{OAc}^-$ ) and  $\text{SO}_4^{2-}$  to titanium suppresses the phase transformation. Thus, phase-pure anatase was formed in either  $\text{H}_2\text{SO}_4$  or  $\text{HOAc}$  aqueous solutions, and phase-pure rutile was formed in  $\text{HCl}$  solution, especially in concentrated  $\text{HCl}$  solutions. The phase transformation could also be facilitated by the presence of some mineralizer or initial rutile particles. Besides the crystallographic structure, the size and shape of titania could be controlled in solution. Monodisperse anatase nanocrystals were prepared in solvothermal system, which shows high photocatalysis in the decomposition of organic compounds. As microemulsion approach can confine crystal growth and lead to the yield of monodisperse nanoparticles, microemulsion-mediated hydrothermal synthesis to prepare nanoparticles of titania was proposed here. The initial shape of microemulsions of amorphous titania show crucial effect on the eventual shape of nanocrystals of titania. The reverse micelles can confine the growth of nanocrystallites in cores, while the micelles can serve as templates to direct the generation of nanoporous materials. Mesoporous titania with anatase framework was constructed through alkylamine as surfactant in aqueous solution. Upon removal of surfactants, the porous materials exhibit reversible adsorption-desorption isotherms, indicating uniform pore sizes, which would find wide application in photocatalysis. Under hydrothermal condition, the mesoporous titania can be transformed into finely dispersed nanoparticles of anatase and rutile, respectively.

### 1 Introduction

Both chemical and physical properties of nanosized materials depend on their particle sizes, morphologies, and structures. The controlled preparations of  $\text{TiO}_2$  nanomaterials are attracting great interest and showing improved importance in preparative chemistry and materials sciences. Sol-gel has provided an approach to prepare dispersed nanoparticles usually by using metal alkoxides as metal sources through hydrolysis and polycondensation in aqueous solutions. The control of hydrolysis plays a critical role in sol-gel chemistry. Titanium alkoxides have been extensively used as titanium sources in the preparation of uniform  $\text{TiO}_2$  by using alcohol or chelating agents to tailor hydrolysis and condensation [1]. During a normal procedure of the sol-gel processing, the hydrogel should be further treated to become dry gel before calcination to offer crystallization of nanosized titanium dioxide.

Hydrothermal synthesis is a nice route to prepare a phase-pure and crystalline oxide in one step. Hydrothermal synthesis of  $\text{TiO}_2$  nanoparticles has been reported in some publications [2-4]. Products with different shapes and phases have been

prepared under various conditions [2-5]. The use of organic solvent can control the hydrolysis of titanium alkoxide to prepare uniform titania particles [1,6]. In this report, some inorganic acids were used to control the hydrolysis of titanium alkoxide to form clear solution serving as the precursors of hydrothermal processing [7].

Microemulsions (or reverse micelles) can be used as microreactors to confine crystal growth to prepare uniform nanoparticles, such as  $\text{TiO}_2$  [8]. The common way is first to isolate the precursor of hydroxide or hydrate precipitate from microemulsions by using precipitating agents, followed by washing and calcinations to promote crystallization. It is surely of great interest to prepare directly well dispersed and phase-pure crystalline nanoparticles in confined microreactors without calcination. P. K. Dutta proposed a direct nucleation and growth of nanocrystals of a sodalite-structured microporous zincophosphate in reverse micelles under milder condition [9]. According to the crystallization of  $\text{TiO}_2$  in acidified aqueous solutions, a microemulsion-mediated hydrothermal synthesis is proposed to prepare uniform nanorods and spheres of  $\text{TiO}_2$  [10].

As microemulsions (or reverse micelles) can act as microreactors to confine the growth of nanocrystallites in cores, and micelles can also serve as templates to direct the formation of mesoporous silica [11]. Besides mesoporous silica oxide, a variety of non-silica oxides have been prepared [11-13]. Here we use neutral amine as surfactant to prepare mesoporous  $\text{TiO}_2$ .

Anatase, brookite and rutile are three polymorphs of titanium dioxide. Anatase is a kind of thermodynamically metastable form while rutile is a kind of stable one. Anatase can transform irreversibly to rutile at elevated temperatures ranged from 400 to 1200 °C according to particle size, morphology and additives. The solid-state phase transformation behavior has been widely investigated while the phase evolution between anatase and rutile under hydrothermal condition has been little paid attention to so far [5]. In this work, the structural evolution from anatase to rutile under milder hydrothermal conditions is proposed as well [7, 10].

## 2 Experimental Section

### 2.1 Preparation

**Sol-Hydrothermal Synthesis:** HCl,  $\text{HNO}_3$ ,  $\text{H}_2\text{SO}_4$ , and  $\text{CH}_3\text{COOH}$  (HOAc) acids were used to prepare titania hydrosol. Titanium *n*-butoxide (TNB) was dropped into a concentrated acid solution under magnetic stirring to form a clear sol mixture. This mixture was diluted by adding distilled water dropwise into to form a clear sol at a certain ratio of acid to titanium. The mixture finally was charged into a Teflon-lined vessel and tightly closed for hydrothermal crystallization. A white product was isolated after filtering, washing and drying.

**Microemulsion-Mediated Hydrothermal Synthesis:** Triton X-100 was served as the surfactant, *n*-hexanol as co-surfactant, cyclohexane as the continuous oil phase, and a solution of titanium *n*-butoxide dissolved in an acid (HCl or  $\text{HNO}_3$ ) was employed as the dispersed aqueous phase. The concentration of hydrochloric acid or nitric acid ranged from 0.5 M to 2.0 M. A transparent feedstock of microemulsions was charged into a Teflon-lined stainless autoclave and hydrothermal reaction was

conducted at temperatures in the range of 120-200 °C or 12-144 h.

**Synthesis of Mesoporous Titania:** aqueous solution of an alkylamine and alcohol of titanium butoxide was mixed under magnetic stirring and aged at a certain temperature. A yellowish powder was obtained.

**Hydrothermal Phase Transformation from Anatase to Rutile:** the phase transformation from anatase to rutile was investigated under various hydrothermal conditions by using as-hydrothermally-synthesized nanocrystals of pure anatase or mixture of anatase and rutile as starting materials.

## 2.2 Characterization

The products were characterized by X-ray diffraction using  $\text{CuK}\alpha$  radiation ( $\lambda=0.15045\text{nm}$ ). The crystal sizes of  $\text{TiO}_2$  particles were calculated from FWHM (full width at half maximum) of diffraction peaks by using Scherrer's equation. The morphology of  $\text{TiO}_2$  products was observed using a JEM-100CX transmission electron microscopy (TEM). Adsorption properties were obtained from the calculation of  $\text{N}_2$  adsorption-desorption isotherms measured at 77 K on a Micromeritics ASAP 2010 system after the samples were degassed at 150 °C overnight.

## 3 Results and Discussion

### 3.1 Sol-Hydrothermal Synthesis

Figure 1 shows the powder XRD patterns of  $\text{TiO}_2$  particles derived from different acid media at a mole concentration of 1.5 M. By using  $\text{HCl}$  medium, the product was pure rutile; while by using  $\text{HNO}_3$ , it was a mixture of rutile and anatase. Pure anatase was generated if either  $\text{H}_2\text{SO}_4$  or  $\text{HAc}$  was used. However, if the concentration of titanium was reduced to 0.25 M, the use of  $\text{H}_2\text{SO}_4$  yielded quite different result than that of  $\text{HOAc}$ . Pure anatase was still prepared in  $\text{HOAc}$  medium; while besides anatase, rutile phase was generated as the side product in  $\text{H}_2\text{SO}_4$  medium. This implied that the formation of rutile in  $\text{HOAc}$  medium was more difficult than in  $\text{H}_2\text{SO}_4$  medium. Pure anatase could be obtained more easily in  $\text{HOAc}$  medium than in others. A mixture of anatase and a trace of brookite yielded if no acid was added into a reaction medium (Figure 1a). A conclusion drawn here is that the medium favors the formation of rutile in the tendency of  $\text{HCl} > \text{HNO}_3 > \text{H}_2\text{SO}_4 > \text{HOAc}$ .

It is clearly shown that the peaks in a XRD patterns (Figure 1b or 1c) corresponding to anatase from a reaction medium of  $\text{HAc}$  or  $\text{H}_2\text{SO}_4$  are much sharper than the corresponding peaks of anatase formed from acid-free reaction (Figure 1a). It means that anatase from  $\text{HAc}$  or  $\text{H}_2\text{SO}_4$ -acidified titanium source crystallized more completely and the particle sizes were larger. The TEM



**Figure 1.** XRD patterns of nanocrystal titania samples prepared from various media: (a)  $\text{H}_2\text{O}$ , (b)  $\text{CH}_3\text{COOH}$ , (c)  $\text{H}_2\text{SO}_4$ , (d)  $\text{HNO}_3$ , and (e)  $\text{HCl}$ .

photographs in Figure 2 also reveal that an acidified medium can promote crystallization of titanium dioxide. These acids could play catalytic roles in the growth of anatase and/or rutile under hydrothermal conditions.

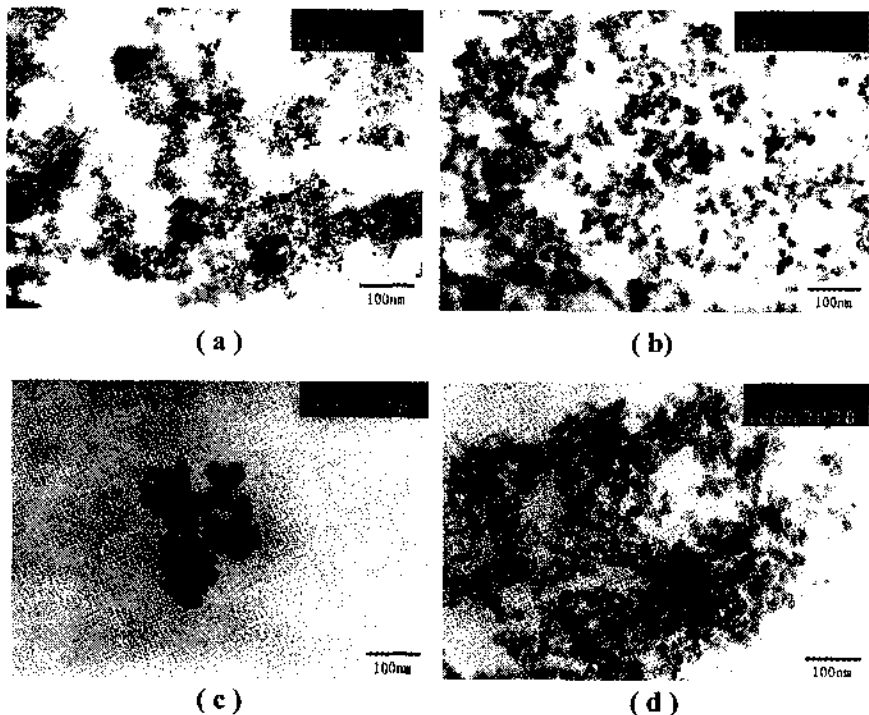


**Figure 2.** TEM images of nanocrystal titania samples prepared from various media: (a)  $\text{H}_2\text{O}$ , (b)  $\text{CH}_3\text{COOH}$ , (c)  $\text{H}_2\text{SO}_4$  and (d)  $\text{HNO}_3$ .

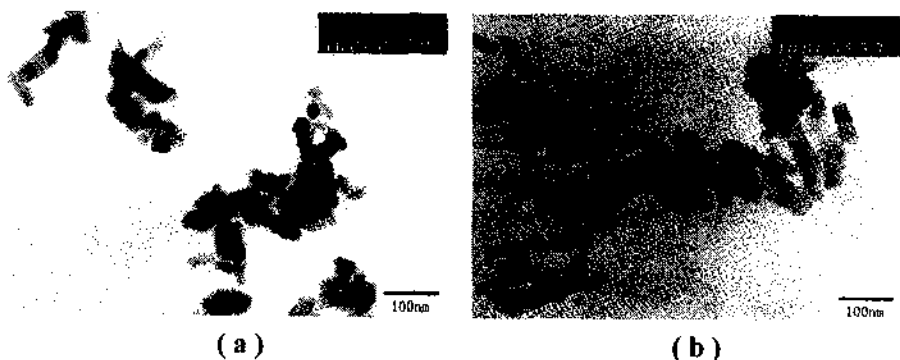


**Figure 3.** TEM images of titania powders prepared from acidified titanium sources under various hydrothermal conditions. (a) 0.50 M TNB and 1.5 M HCl, at 220°C for 10 h; (b) 0.25 M TNB and 1.5 M HCl, at 220°C for 10 h.

Different acids can be used to control the particle sizes of anatase. The anatase particles from  $\text{H}_2\text{SO}_4$  were greater than those from HOAc, indicating that using

$\text{H}_2\text{SO}_4$  could promote the growth of anatase more efficiently than using HOAc. The cause probably is that the acidity of  $\text{H}_2\text{SO}_4$  is much stronger than HOAc. Furthermore, the surface modification of anions, such as  $\text{SO}_4^{2-}$ ,  $\text{NO}_3^-$  on the particles will prevent those titania nanocrystals from aggregation. Thus, the sol-hydrothermal method using acids provides an excellent approach to obtain well-dispersed nanocrystals of pure anatase and rutile respectively. The rutile from HCl-medium was rod-like particles (Figure 3a) that were larger and longer than those from  $\text{HNO}_3$  medium (Figure 2d) as the HCl could facilitate the formation and growth of rutile most obviously. The increase of HCl concentration and/or decrease of TNB concentration favored the formation and crystal growth of rutile. (Figure 3).

### 3.2 Microemulsion-Mediated Hydrothermal Synthesis

As described above, the nature of the acid used in the aqueous phase had a significant effect on the phase composition of a  $\text{TiO}_2$  product. The feedstock was prepared as the following: mixing 3.4 ml of TNB and 4.0 or 8.0 ml acid (5.0 M or 10.0 M hydrochloric acid or nitric acid), then the mixture was added into another mixture of Triton X-100/n-hexanol/cyclohexane. The concentration of TNB and acid were kept at 0.25 M and in range of 0.5-2.0 M respectively. The XRD patterns of the products prepared in different acids with different concentrations are given in Figure 4, and TEM micrographs of some products are shown in Figure 5.

As shown in Figure 4 and Figure 5, nearly uniformed nanorods of phase-pure rutile were formed in HCl acid, and nanospheres of phase-pure anatase was yielded in  $\text{HNO}_3$ . As uniform  $\text{TiO}_2$  could be prepared in these media of microemulsions, monodispersed  $\text{TiO}_2$  nanocrystals with other morphologies were prepared in some of other organic media. That is, the organic molecules affect the morphologies of nanocrystals of  $\text{TiO}_2$ .

In comparison to Figure 1d, it was found that those organic molecules inhibited the generation of rutile. In fact, the composition of rutile in product was influenced by reaction temperature and time. Figure 6 shows us the fraction of rutile versus reaction temperature and time. The fraction of rutile is calculated according to the equation of  $f_r = 1.26I_r/(I_a + 1.26I_r)$  by taking the intensities of the strongest (110) and (101) reflections of rutile ( $I_r$ ) and anatase ( $I_a$ ) respectively.

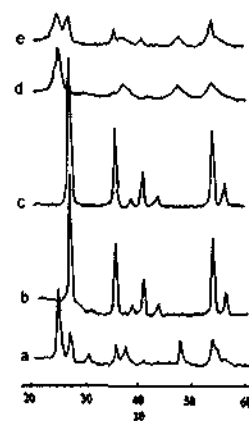
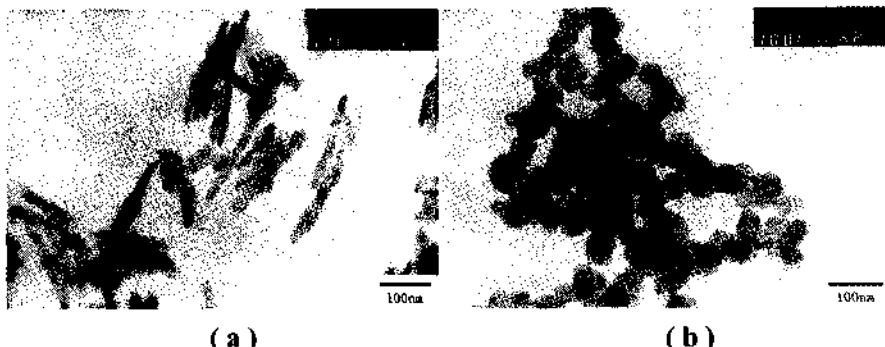
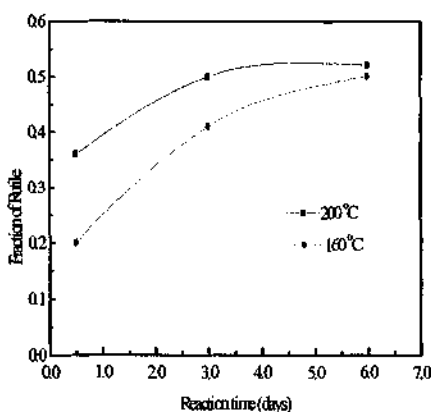


Figure 4. XRD patterns of products prepared in HCl or  $\text{HNO}_3$  at 120°C for 12 h (a) 0.5 M HCl (5.0 ml/4.0 M), (b) 1.0 M HCl (5.0 ml/8.0 M), (c) 2.0 M HCl (10.0 ml/8.0 M), (d) 0.5 M  $\text{HNO}_3$  (5.0 ml/4.0 M), (e) 1.0 M  $\text{HNO}_3$  (5.0 ml/8.0 M).



**Figure 5.** TEM micrographs of products from the microemulsion with: (a) 2.0 M HCl (10.0ml/8.0M) and (b) 0.5 M HNO<sub>3</sub> (5.0ml/4.0M).

Figure 6 implies that anatase could be transformed into rutile especially at higher temperatures. If a precursor of anatase particles prepared from hydrothermal reaction was loaded into a vessel again for aging in HCl medium, it would be transformed into a product of a mixture of anatase and rutile, even of a pure rutile phase. In the presence of rutile as a trace component, the precursor would be transformed into rutile more easily. Thus, the phase transformation from anatase to rutile could be achieved not only in solid-state reaction, but also in aqueous chemistry, especially in the medium of HCl aqueous solution, and the phase transformation in aqueous solution will be promoted with the existence of trace rutile. Some mineralizers such as NaCl also affect the phase transformation from anatase to rutile.



**Figure 6.** TEM micrographs of microemulsions containing: (a) 2.0 M HCl (10.0ml/8.0M) (b) 0.5 M HNO<sub>3</sub> (5.0ml/4.0M).

### 3.3 Preparation of nanoporous titania

Figure 7a shows the powder XRD pattern of the as-prepared mesostructured titania from titanium butoxide. The mesostructure was collapsed at 400 °C for 5 h, indicated by powder XRD diffraction and adsorption properties.

Chemical extraction is a promising method to remove amines from voids of mesostructured composites. A co-solvent of ethanol and dilute acetic acid was used to extract organic molecules from voids. After chemical leaching at room temperature for a period of time, the powder was filtered, washed, and evaporated in air. After degassed overnight, the porosity is illustrated by type-IV N<sub>2</sub> adsorption-desorption isotherm at 77 K shown in Figure 7b. The isotherm study gives the following values:

Brunauer-Emmett-Teller (BET) surface area =  $222 \text{ m}^2 \text{ g}^{-1}$ , single-point total pore volume =  $0.24 \text{ cm}^3 \text{ g}^{-1}$ , and average Barrett-Joyner-Halenda (BJH) pore diameter =  $3.0 \text{ nm}$ . Higher resolution TEM demonstrated that the nanoporous titania was constructed by a crystalline framework. If the calcination was carried out at a lower temperature, such as  $150^\circ\text{C}$ , adsorption-desorption isotherms were reversible, indicating uniform pore sizes, which would find wide application in photocatalysis, such as in the process of the degradation of acetone in air.

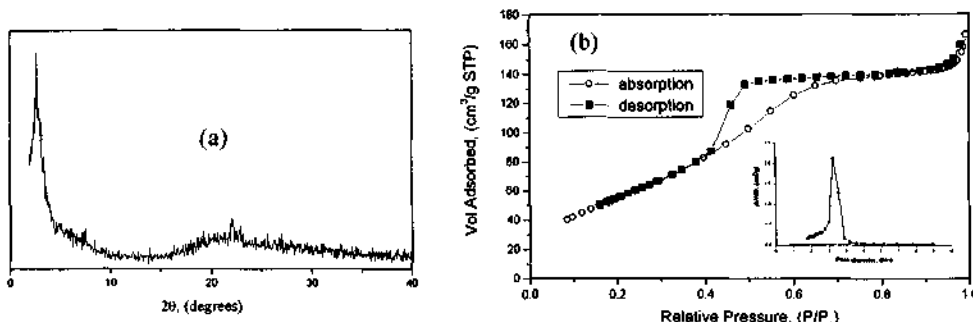


**Figure 7.** (a) Powder XRD of the as-prepared mesostructured titania and (b)  $\text{N}_2$  adsorption-desorption isotherms after chemical extractions and calcinations.

#### 4 Acknowledgements

This work was financially supported by the National Natural Science Foundation of China, the Provincial Natural Science Foundation of Guangdong, the Government of Guangzhou City. The authors would like to express great appreciation to Lu Gao for the help of BET measurements.

#### References

1. Selvaraj U., Prasadrao A. V., Komarneni S. and Roy R., Sol-gel fabrication of epitaxial and oriented  $\text{TiO}_2$  thin film. *J. Am. Ceram. Soc.*, **75** (1992) pp. 1167-1170.
2. Wang C.-C. and Ying J. Y., Sol-gel synthesis and hydrothermal processing of anatase and rutile titania nanocrystal. *Chem. Mater.*, **11** (1999) pp.3113-3120.
3. Cheng H.-M., Ma J.-M., Zhao Z.-G. and Qi L.-M., Hydrothermal preparation of uniform nanosize rutile and anatase particles. *Chem. Mater.*, **7** (1995) pp. 663-671.
4. Qian Y.-T., Chen Q.-W., Chen Z.-Y., Fan C.-G., Zhou G.-E., Preparation of ultrafine powders of  $\text{TiO}_2$  by hydrothermal  $\text{H}_2\text{O}_2$  oxidation starting from metallic Ti. *J. Mater. Chem.*, **3** (1993) pp. 203-205.
5. Kutty T. R. N., Vivekanandanand R. and Murugaraj P., Precipitation of rutile and anatase ( $\text{TiO}_2$ ) fine powders and their conversion to  $\text{MTiO}_3$  (M = Ba, Sr, Ca) by the hydrothermal method. *Mater. Chem. Phys.*, **19** (1988) pp.533-546.

6. Park H. K., Kim D. K. and Kim C. H., Effect of solvent on titania particle formation and morphology in thermal hydrolysis of  $TiCl_4$ . *J. Am. Chem. Soc.* **80** (1997), pp. 743-749.
7. Wu M.-M., Lin G., Chen D.-H., Wang G. G., He D., Feng S.-H. and Xu R.-R., Sol-hydrothermal synthesis and hydrothermally structural evolution of nanocrystal titanium dioxide. *Chem. Mater.*, **14** (2002), in press.
8. Chhabra V., Pillai V., Mishra B., Morrone A., Shah D., Synthesis, characterization, and properties of microemulsion-mediated nanoparticle  $TiO_2$  particles. *Langmuir*, **11** (1995) pp. 3307-3311.
9. Dutta P. K., Jakupca M., Reddy K. S. N., Salvati L., Controlled growth of microporous crystals nucleated in reverse micelles. *Nature*, **374** (1995), 44-46.
10. Wu M.-M., Long J.-M., Huang A.-H., Luo Y.-J., Feng S.-H., Xu R.-R., Microemulsion-mediated hydrothermal synthesis and characterization of nanosized rutile and anatase particles. *Langmuir*, **15** (1999) pp. 8822-8825.
11. Huo Q.-S., Margolese D. I., Ciesla U., Demuth D. G., Feng P.-Y., Gier T. E., Sieger P., Firouzi A., Chmelka B. F., Schüth F. and Stucky G. D., Organization of organic molecules with inorganic molecular species into nanocomposite biphasic arrays. *Chem. Mater.*, **6** (1994) pp. 1176-1191.
12. Sayari A. and Liu P., Non-silica periodic mesostructured materials: recent progress. *Microporous Mater.*, **12** (1997) pp. 149-177.
13. Ying J. P., Mehnert C. P. and Wong M. S., Synthesis and applications of supermolecular-templated mesoporous materials. *Angew. Chem. Int. Ed.*, **38** (1999) pp. 56-77.

## NOVEL SYNTHESIS OF NANOSIZED Pd/Ce<sub>x</sub>Zr<sub>1-x</sub>O<sub>2</sub> CATALYSTS

J. A. WANG,\* L. F. CHEN, J. C. GUEVARA AND L. BALDERAS-TAPIA

*Laboratorio de Catálisis y Materiales, ESIQIE, Instituto Politécnico Nacional, Col. Zacatenco, 07738 México D. F., Mexico, Email: jwang@ipn.mx*

Ceria-zirconia nanophases were synthesized by a surfactant-assisted method. The refined structural data concerning the crystallite size, lattice parameters, structural microstrain, cationic occupancy number and cationic defect concentration are reported. Zirconium addition into the cubic structure of ceria inhibits crystal sintering but leads to structure distortion. Different CO-metal bonds are formed when CO chemisorbs on Pd-loaded Ce<sub>x</sub>Zr<sub>1-x</sub>O<sub>2</sub> catalysts. Catalytic tests reveal that the lower zirconium content benefits the CO oxidation.

### 1 Introduction

Ceria has been used as an important promoter in the current three-way catalysts (TWCs) due to its high oxygen storage/release capacity [1,2]. However, ceria usually shows thermal instability at high temperatures. For example, when it is calcined above 1073K, its surface area usually reduces to less than 10 m<sup>2</sup>/g, resulting in significant decay of activity. Recently, ceria doped by zirconia has attracted much attention since it exhibits improved thermal stability, reducibility and oxygen transferring between the surface and bulk [3, 4]. The ceria-zirconia mixed oxide is, therefore, considered to be the new generation of TWC support in the near future. In the present work, a surfactant-assisted method is applied to prepare the nanophases of ceria-zirconia solid solution. The crystalline structure is refined by the Rietveld technique together with XRD analysis. The CO-chemisorptive behaviors and catalytic properties over the Pd supported catalysts are reported.

### 2 Experimental

The ceria-zirconia sample was prepared by using cerium nitrate (Ce(NO<sub>3</sub>)<sub>3</sub>·6H<sub>2</sub>O) and zirconium chloride octahydrate (ZrOCl<sub>2</sub>·8H<sub>2</sub>O) as precursors and a surfactant, cetyltrimethylammonium bromide (CH<sub>3</sub>(CH<sub>2</sub>)<sub>15</sub>N(CH<sub>3</sub>)<sub>3</sub>Br) as molecular template. As an example, for preparing Ce<sub>0.2</sub>Zr<sub>0.8</sub>O<sub>2</sub> solid, 10.70 g of Ce(NO<sub>3</sub>)<sub>3</sub>·6H<sub>2</sub>O and 30.63 g of ZrOCl<sub>2</sub>·8H<sub>2</sub>O were dissolved into a container with 1000 ml deionized water to obtain a mixed solution. This solution was added, drop by drop, into a solution of 34.98g surfactant with rapid stirring. The ratio of surfactant/cation (Ce+Zr) is about 1.2 and the pH of the mixture was maintained at 11 by adding ammonia (28 %). After aging for 24 hours, the precipitate was filtered and washed, and then dried at 573 K for two days followed by calcination at various temperatures in air. The Pd loaded catalysts were prepared by impregnating the support calcined at 600 °C with an aqueous solution of PdCl<sub>2</sub>·2H<sub>2</sub>O.

The X-ray diffraction analyses were carried out at room temperature in a Siemens D-5000 diffractometer with *Cu Kα* radiation. Intensities were obtained in the 2θ range between 20 and 110° with a step of 0.02° and a measuring time of 2.7 second each point. The crystalline structures were refined by using DBWS-9006 PC and WYRET programs by the Rietveld method. The standard deviations, showing the variation of the last figures of the corresponding number, are given in parentheses.

The CO chemisorptive properties of the Pd loaded catalysts were studied by FTIR-in situ technique. Before the adsorption the samples were thermally treated at 673K for 30 min to remove the impurities and then the adsorption cell was cooled to 473K followed by CO adsorption. The IR spectrum was recorded after adsorption for 10min. Afterwards, the temperature was reduced to 297K and the adsorption cell was evaluated. Before and after the evaluation, the IR spectra were also recorded.

Catalytic tests were carried out in a microreactor system with a catalyst loading 0.025 g. The 8% CO in N<sub>2</sub> mixing with dried air was fed into the reactor, the flow rate was 20 ml/min for CO and 40 ml/min for air. The light-off temperature, T<sub>50</sub>, is defined as the temperature at which the conversion of CO to CO<sub>2</sub> reaches 50 %.

### 3 Results and Discussion

#### 3.1 Crystalline structure

Figure 1 shows the XRD patterns of the Ce<sub>x</sub>Zr<sub>1-x</sub>O<sub>2</sub> ( $x = 0.2, 0.5$  and  $0.8$ ) samples calcined at 873 and 1073K. A Rietveld refinement plot of the 3wt.%Pd/Ce<sub>0.8</sub>Zr<sub>0.2</sub>O<sub>2</sub> sample calcined at 673K is shown in Figure 2. All the samples contain a single phase with cubic structure, indicating that the cerium and zirconium ions are uniformly distributed in the structure. The average crystallite size is in nanoscale ranging from 2 to 17 nm in the temperatures between 353 and 1073 K (Table 1). Both zirconium atomic fraction and calcination temperature affect the crystallite size. When  $x$  alters from 0.8 to 0.2, below 873K of calcination, the crystallite size decreases. However, when the calcination temperature is at 873K and 1073K, the crystallite size increases as  $x$  reduces from 0.5 to 0.2. One may compare with pure CeO<sub>2</sub> prepared by the same method, the crystalline size of ceria calcined at 1073K is 31 nm, which is two times bigger than the zirconia-doped ceria calcined at the same temperature. Therefore, relative to pure CeO<sub>2</sub>, zirconium addition to ceria effectively inhibits the crystal sintering thus enhancing its thermal stability.

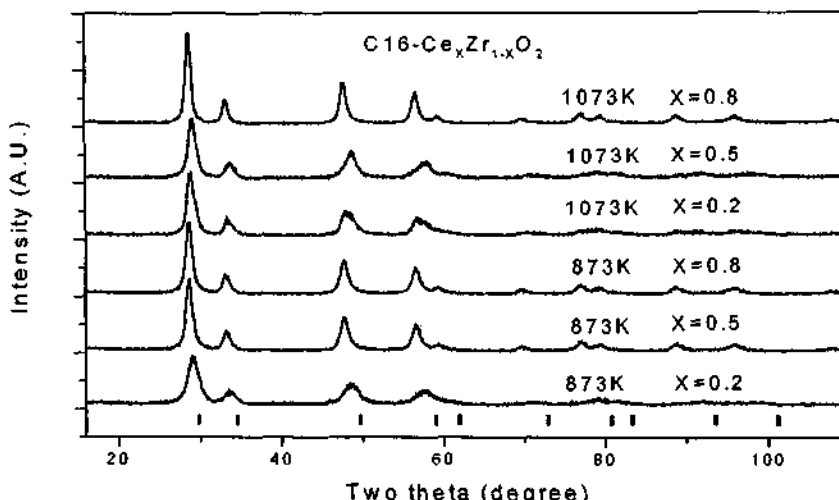
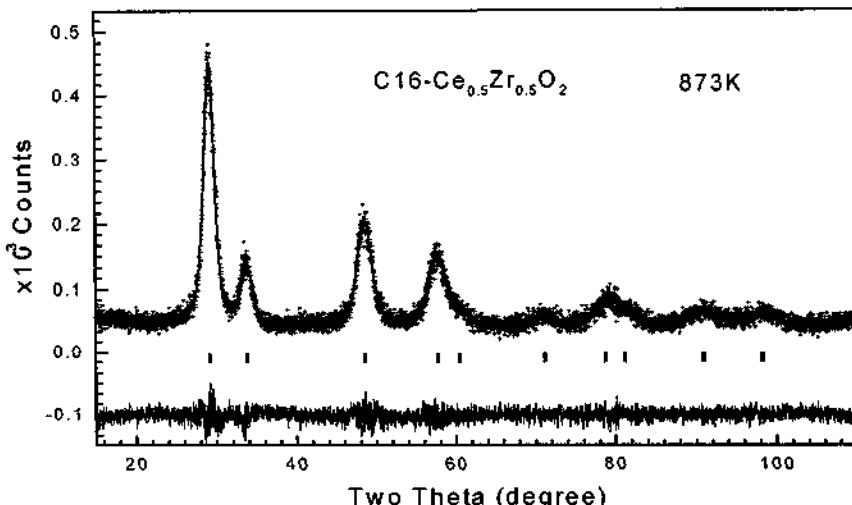


Figure 1. XRD patterns of the samples calcined at 873 and 1073K.



**Figure 2.** Rietveld plot of the sample  $C_{16}-Ce_{0.5}Zr_{0.5}O_2$  calcined at 873 K. Experimental data are indicated by crosses, while the calculated curve obtained after the refinement is indicated with a continuous line. The tick marks correspond to cubic. The continuous curve under the tick marks represents the difference between the experimental date and the calculated curve.

The lattice cell parameter also varies with the calcination temperature and zirconium atomic fraction. At the same composition, the lattice parameter generally decreases with increasing of the calcination temperature. When the samples with different compositions were calcined at a fixed temperature, the lattice parameter shows a linear reduction when  $x$  increases from 0.2 to 0.8. It is because zirconium radius is smaller than the cerium one (for 8-coordinated  $M^{4+}$ ,  $r_{Zr^{4+}}=0.84\text{ \AA}$ ;  $r_{Ce^{4+}}=0.97\text{ \AA}$ ), the substitution of larger  $Ce^{4+}$  ions by smaller  $Zr^{4+}$  ions in the structure induces a contract of the lattice cell volume, shortening the lattice distance.

The Rietveld refinements show that the crystalline structure contains microstrain that is mainly caused by the crystal distortion related to zirconium replacement. It is also found that cationic occupancy number in the crystalline structure is smaller than their normal value 0.02083 present in an ideal crystal, indicating that the crystalline structure is of cationic deficient. As far as the local environment of the cationic defect is concerned, the lattice oxygen ions around it are not fully bonded, which are mobile and more active under the reaction condition compared to the normal ones. Therefore, the creation of cationic defects in the structure is a possible origin of the unusual reducibility and high inmobility of oxygen species from bulk to surface exhibited on the ceria-zirconia solids, that are reported by other groups [5, 6].

**Table 1.** Data of crystallite size, lattice parameters, structure microstrain, cationic occupancy number and defect concentration of the  $\text{Ce}_x\text{Zr}_{1-x}\text{O}_2$  samples calcined at different temperatures.

Calc. Temp. (K)	353	473	673	873	1073
<b>Average crystalline size (Å)</b>					
$\text{Ce}_{0.8}\text{Zr}_{0.2}\text{O}_2$	76.3(1.0)	78.4(1.0)	86.1(1.1)	112.0(1.5)	148.5(2.1)
$\text{Ce}_{0.5}\text{Zr}_{0.5}\text{O}_2$	22.4(6)	43.3(9)	62.7(1.2)	86.6(1.8)	135.0(3.3)
$\text{Ce}_{0.2}\text{Zr}_{0.8}\text{O}_2$	59.4(9)	100.2(1.9)	169.0(5.2)		
<b>Lattice cell parameters (Å)</b>					
$\text{Ce}_{0.8}\text{Zr}_{0.2}\text{O}_2$	5.4125(8)	5.4027(9)	5.3979(8)	5.3899(7)	5.3848(6)
$\text{Ce}_{0.5}\text{Zr}_{0.5}\text{O}_2$	5.364(5)	5.336(3)	5.307(2)	5.298(2)	5.289(1)
$\text{Ce}_{0.2}\text{Zr}_{0.8}\text{O}_2$	5.187(2)	5.183(1)	5.332(1)		
<b>Structural microstrain (%)</b>					
$\text{Ce}_{0.8}\text{Zr}_{0.2}\text{O}_2$	1.14 (0.28)	1.70(0.22)	2.05(0.18)	2.06(0.13)	2.09(0.10)
$\text{Ce}_{0.5}\text{Zr}_{0.5}\text{O}_2$	6.38(0.25)	6.85(0.33)	6.02(0.25)	5.21(0.18)	
$\text{Ce}_{0.2}\text{Zr}_{0.8}\text{O}_2$	4.91(0.31)	4.62(0.20)	6.04(0.15)		
<b>Cationic occupancy numbers</b>					
$\text{Ce}_{0.8}\text{Zr}_{0.2}\text{O}_2$	0.01746	0.01603	0.01556	0.01647	0.01577
$\text{Ce}_{0.5}\text{Zr}_{0.5}\text{O}_2$	0.01821	0.01346	0.01332	0.01375	0.01487
$\text{Ce}_{0.2}\text{Zr}_{0.8}\text{O}_2$	0.01923	0.01920	0.02083		
<b>Cationic defect concentration (%)</b>					
$\text{Ce}_{0.8}\text{Zr}_{0.2}\text{O}_2$	16.2	23.0	25.3	20.9	24.3
$\text{Ce}_{0.5}\text{Zr}_{0.5}\text{O}_2$	12.5	35.4	36.1	34.0	28.6
$\text{Ce}_{0.2}\text{Zr}_{0.8}\text{O}_2$	7.7	7.6	0.0		

### 3.2 CO adsorption behaviour

Three adsorption bands are observed in the CO-FTIR spectra in the range between 2200 and 1800  $\text{cm}^{-1}$ , which correspond to CO association with the Pd/ceria-zirconia (the spectra are not shown here). It is well-known that two common adsorption modes of CO-Pd, linear and bridged bonds, are usually formed in the case of CO adsorption on Pd atoms or nanocrystals. The linear bond of CO-Pd usually appears around 2100  $\text{cm}^{-1}$  and the bridged one in the range of 1800-1900  $\text{cm}^{-1}$  [7]. With respect to these assignments, the bands at 2165-2177  $\text{cm}^{-1}$  and at 1900-1850  $\text{cm}^{-1}$  was respectively assigned to the linear and the bridged CO-Pd bonds. As for the one appearing in the range between the linear and bridged adsorption bands, it is suggested to be a multiple bond of CO-Pd, which is caused by the competitive adsorption of CO in linear and bridged modes.

The adsorption bands in the region between 2300 and 2250  $\text{cm}^{-1}$  are due to adsorbed  $\text{CO}_2$ . Before CO adsorption, no bands corresponding to adsorbed  $\text{CO}_2$  are observed. Therefore,  $\text{CO}_2$  must be produced in the course of CO adsorption. There are two possible pathways to produce  $\text{CO}_2$ : (i) CO reacting with lattice oxygen of the catalyst; (ii) CO disproportionating to  $\text{CO}_2$  and carbon. Since CO was introduced into the IR cell at 473K, the reaction of CO oxidation easily takes place on the catalyst surface, which is supported

by the catalytic test. On CO disproportionation, several reports have been appeared where carbon deposits are detected after CO adsorption on the Pd-Ce/Al<sub>2</sub>O<sub>3</sub> catalysts [8]. Although no straightforward evidence of carbon formation is provided in the present work, the possibility of CO<sub>2</sub> produced by CO disproportionation should be taken into account.

Both CO and CO<sub>2</sub> were easily removed from the active sites in a vacuum condition, indicating that adsorption of both reactant and product is not so strong. This benefits the CO oxidation because strong adsorption either reactant or product on catalyst surface may poison the active sites, leading to rapid deactivation.

### 3.3 Catalytic Activity

Table 2 reports the catalytic activities of CO oxidation over the different Pd-supported catalysts calcined at 873K and 1073K. In both cases, the 3wt.%Pd/Ce<sub>0.8</sub>Zr<sub>0.2</sub>O<sub>2</sub> catalyst shows the best activity when the reaction temperature is below 673K, its T<sub>50</sub> is about 383K, which is much lower than that of the other two catalysts. Particularly, its catalytic activity is maintained almost unchanged when the calcination temperature increases from 873 to 1073K. It is also found that when the catalysts were calcined at 873K, at a reaction temperature below 423K, the catalytic activity gradually decreases as zirconium content increases. For example, at 423K, the conversion of CO decreases from 61.7 % to 36.5% and 22.8% when zirconium atomic fraction increases from 0.2 to 0.5 and 0.8. This result indicates that greater fraction of cerium atoms replaced by zirconium in ceria is unfavorable to CO oxidation. It seems that the CO oxidation over the Pd-loaded catalysts is independent on the crystallite size because the Ce<sub>0.5</sub>Zr<sub>0.5</sub>O<sub>2</sub> sample calcined at 1073K shows the smallest crystallite size, however, its catalytic activity is the lower than the other two catalysts.

**Table 2.** CO oxidation activity of the different catalysts.

Catalysts (25 mg)	CO conversion (%)						
	323K	373K	423K	473K	523K	573K	623K
<b>Catalysts calcined at 873K for 4 hours</b>							
3wt.%Pd/Ce <sub>0.8</sub> Zr <sub>0.2</sub> O <sub>2</sub>	2.4	29.8	61.7	77.6	88.7	93.6	95.2
3wt.%Pd/Ce <sub>0.5</sub> Zr <sub>0.5</sub> O <sub>2</sub>	0.0	21.8	36.5	58.0	88.0	100	
3wt.%Pd/Ce <sub>0.2</sub> Zr <sub>0.8</sub> O <sub>2</sub>	0.0	0.0	22.8	71.7	95.7	96.1	100
<b>Catalysts calcined at 873K and then 1073K for 4 hours</b>							
3wt.%Pd/Ce <sub>0.8</sub> Zr <sub>0.2</sub> O <sub>2</sub>	3.9	11.1	65.3	80.2	89.2	92.4	97.7
3wt.%Pd/Ce <sub>0.5</sub> Zr <sub>0.5</sub> O <sub>2</sub>	0.0	10.6	23.7	38.7	64.2	70.9	74.3
3wt.%Pd/Ce <sub>0.2</sub> Zr <sub>0.8</sub> O <sub>2</sub>	0.0	7.4	44.6	64.9	73.2	79.5	83.3

#### 4 Conclusions

Nanosized ceria-zirconia materials with improved thermal stability can be prepared by using the surfactant-assisted method. Structural refinements confirm that the nanocrystals contain structural microstrain and cationic lattice defects. Zirconium addition to ceria suppresses the crystal sintering and imporves the thermal stability but leads to structure distortion. Both catalytic tests and CO-chemisorption show that Pd supported ceria-zirconia nanoparticles are active for CO oxidation.

#### 5 Acknowledgments

The financial support from projects CONACyT-31282-U (Mexico) and FIES-98-29-III (IMP-IPN-Mexico) is greatly appreciated. L.F.Chen would like to thank the visiting professor fellowship granted by CONACyT, Instituto Politecnico Nacional (Mexico) and Instituto del Mexicano Petroleo.

#### References

1. Trovarelli A., Catalytic Properties of ceria and CeO<sub>2</sub>-containing materials. *Catal. Rev.-Sci. Eng.* **38** (1996) pp.439-520.
2. Force C., Belzunegui, J. P., Sarnz J., Martínez-Arias A. and Soria J., Influence of precursor salt on metal particle formation in Rh/CeO<sub>2</sub> catalysts. *J. Catal.* **197** (2000) pp.192-199.
3. Fornasiero P., Balducci G., Di Monte R., Kašpar J., Sergo V., Gubitosa G., Ferrero A. and Graziani M., Modification of the Redox behaviour of CeO<sub>2</sub> induced by structural doping with ZrO<sub>2</sub>. *J. Catal.* **164** (1996) pp.173-183.
4. González-Velasco J.R., Gutierrez-Ortiz M.A., Marc J.L., Botas J.A. González-Marcos M. P. and Blanchard G., Contribution of cerium/zirconium mixed oxides to the activity of a new generation of TWC. *Appl. Catal. B: Environmental* **22** (1999) pp.167-178.
5. Fornasiero P., Kašpar J., Graziani M., Redox behaviour of high surface area Rh-loaded Ce<sub>0.5</sub>Zr<sub>0.5</sub>O<sub>2</sub> mixed oxide. *J. Catal.* **167** (1997) pp.576-580.
6. Fornasiero P., Hickey N., Kašpar J., Montuni T., Graziani M., Redox and chemisorptive properties of ex-chloride and ex-nitrate Rh/Ce<sub>0.6</sub>Zr<sub>0.4</sub>O<sub>2</sub> catalysts. *J. Catal.* **189** (2000) pp.339-348.
7. Kondarides D. I., Zhang Z.-L., Verykios X. E., Chlorine-induced alterations in oxidation state and CO chemisorptive properties of CeO<sub>2</sub>-supported Rh catalysts. *J. Catal.* **176** (1998) pp.536-544.
8. Ciuparu D., Bensalem A., Pfefferle L., Pd-Ce interaction and adsorption properties of palladium: CO and NO TPD studies over Pd-Ce/Al<sub>2</sub>O<sub>3</sub> catalysts. *Appl. Catal. B: Environmental* **26** (2000) pp.241-255.

## EFFECT OF SILICON DOPANT ON THE MICROSTRUCTURE OF TITANIUM DIOXIDE

YUHONG ZHANG

*Department of Chemistry, Zhejiang University, Hangzhou 310027, China*

*E-mail: yhzhangc@zjuem.zju.edu.cn*

OLAV BECHER AND ARMIN RELLER

*Solid State Chemistry, Institute of Physics, Augsburg University, Augsburg 86135, Germany*

*E-mail: armin.reller@physik.uni-augsburg.de*

In this report, we present the changes of the microstructure of titanium dioxide and the formation of nanotubes caused by silicon doping. The silicon-doped titania is prepared by a different sol-gel technique. The results of XRD and TEM reveal that pure titanium dioxide shows a rapid increasing of grain size, accompanied by the phase transformation of anatase-to-rutile between 600°C to 700°C. However, the grain growth of doped specimens was drastically arrested. As a result of heavy restraint of the grain growth, the silicon-doped samples show much higher surface area than that of pure titanium dioxide when heated by using the same heating program. It is very important to note that nanotubes with an outer diameter of 13 nm and an inner diameter of 3 nm are prepared in the 5 at.% and 6 at.% silicon-doped samples. The formation and composition of nanotubes are sensitively related with the silicon content.

### 1 Introduction

Titanium dioxide is an important material for a variety of applications such as catalytic devices, solar cells, and other optoelectronic devices [1-3]. The properties of titanium dioxide, especially the catalytic properties, are proved to be strongly related with its crystal structure and grain size. Titanium dioxide in the anatase phase appears to be the most active species for most substrates [4-5]. In addition, the use of titanium dioxide as a catalyst support exhibits several advantages over other classical used oxides such as alumina and silica [6-9]. One of the unique features of TiO<sub>2</sub> as a support is that it interacts strongly with the active phase of metal/metal oxide and therefore increases the catalytic activity [6-7], and the optimal catalytic activity and selectivity is achieved when the catalyst is dispersed on anatase phase of TiO<sub>2</sub> [8-9]. On the other hand, special attention has been paid to nanocrystalline titanium dioxide yielding the increased efficiencies as a result of larger band gap and surface area [10-13]. However, nanocrystalline titanium dioxide undergoes phase transformation and grain growth at relatively lower temperatures, which limits its applications in many fields such as high temperature gas separation and membrane reactors [14-15].

In nanocrystalline titanium dioxide a large fraction of atoms are situated on the surface and the surface energy is very high, therefore it is energetically favorable to increase the phase transformation rate and reduce the total surface area (grain growth). In fact, two processes are observed in the nanocrystalline titanium dioxide powders at high temperatures. One is the grain growth, and another is the rapid phase transition (the free energy of the rutile modification is less than that of the anatase). Therefore, the transition temperature of anatase-to-rutile of nanocrystalline titanium dioxide is

greatly reduced from that of the bulk value (between 700°C and 900°C) [16-17]. The analogous tendency has also been observed in other nanocrystalline system [18-19].

$\text{SiO}_2\text{-TiO}_2$  compositions have been studied as a low temperature route to ultra low expansion glasses and as a method for obtaining optical thin films [20-23]. In addition, the crystalline titanium silicas with zeolitic properties (TS-1) have enlarged the realm of zeolite catalysis [3,24-26]. In these studies, titanium is used as a dopant and silica as a host. Here we report a different sol-gel technique for the preparation of silicon-doped nanocrystalline mesoporous titanium dioxide in non-aqueous medium and present the role of silicon-doping on the phase transformation, mesoporous structure, grain growth of nanocrystalline titania and formation of nanotubes.

## 2 Methods

A sol-gel technique was used to prepare a gel. According to the required silicon amounts of 0%, 1 at.%, 2 at.%, 3 at.%, 4 at.%, 5 at.%, 6 at.%, 10 at.%, 20 at.%, 30 at.%, 50 at.%, 60 at.% and 70 at.%, the sample is labeled as TS0, TS1, TS2, TS3, TS4, TS5, TS6, TS7, TS8, TS9, TS10, TS11 and TS12. Crystallization was achieved by subsequent calcination of the dry gel at different temperatures by using the same heat-treatment program for TS0~12 in air. The crystallinity and the phase were studied on a Phillip Xpert X-ray diffractometer using  $\text{Cu K}\alpha$  radiation. The investigation of the particle morphology was performed on a CM-30 transmission electron microscopy (TEM) and the micrographs were recorded at 300 kV. The samples were prepared by dispersing the powder products as a heptane slurry, which was then deposited and dried on a holey carbon film on a Cu grid. The silicon distribution was detected by energy-dispersive X-ray (EDX mapping) which was mounted on a LEO-982 scanning electron microscope (SEM) and TEM.

## 3 Results and Discussion

The samples of the as-prepared silicon-doped titanium dioxide were examined by the energy-dispersive X-ray (EDX mapping) which was mounted on both the SEM and TEM. The results show that the silicon dopant is homogeneously distributed in the  $\text{TiO}_2$  matrix, either in the anatase or the rutile modifications.

The results of XRD show that the anatase phase is formed at a temperature of 330°C for the pure titanium dioxide, while rutile phase is formed when the calcination temperature approached 630°C, indicating the beginning of the transformation from anatase to rutile. The anatase peaks in the XRD pattern disappears during the heat treatment of bare titanium dioxide at 700°C for 1h, suggesting the end of the transformation of anatase to rutile. The evolution of both anatase and rutile starts at higher temperature for silicon doped samples. However, the transition temperature of anatase to rutile progressively elevates when the silicon content is increased. Figure 1 shows the  $2\theta$  diffraction scans for some of the samples annealed at 1000°C for 1h in air. It can be seen that the phase transition temperature

is strongly influenced by the silicon content. The 6 at.% silicon-doped sample (TS6) shows single phase of rutile, and 70 at.% silicon-doped (TS12) has a single phase of anatase. TS8 (20 at.%) and TS9 (40 at.%) are a mixture of anatase and rutile, but the ratio of anatase to rutile in TS9 is much higher than that in TS8.

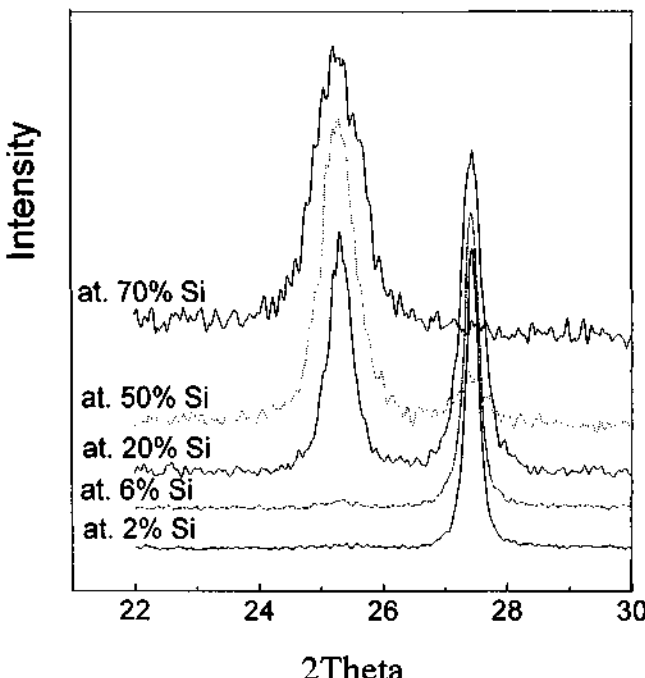


Figure 1. XRD patterns of TS2, TS6, TS8, TS9 and TS12 annealed at 1000°C.

The average grain sizes calculated from XRD peak broadening by using both the Scherrer's equation and TEM are listed in the Table 1 for the samples heated at 600°C for 1h in air. The grain size of pure titania sintered to 30 nm, whereas that of the composition containing 1 at.% silicon calcinated at the same heating program significantly maintains 17 nm. With increasing amount of silicon content, the tendency of restraining the grain growth is more manifest. The average diameter of TS7 (10 at.%) was dramatically retained at 6.2 nm after heated at 600°C for 1h in air. The analogous results are found for the samples heated at higher temperature. For example, the average grain size of TS12 is extraordinarily maintained at 7 nm after heating at 1000°C for 1h. It is evident that the silicon-doped titania shows unexpected high stability against grain growth.

**Table 1.** Average grain sizes of the product TS0 ~ TS6 calcined at 600°C for 1h and determined by XRD and TEM methods.

Sample	TS0	TS1	TS2	TS3	TS4	TS5	TS6	TS7
Size (nm)	29.8	17.2	11.9	10.6	8.7	8.1	7.2	6.2

In recent years unconventional functional materials have been generated by varying their nanoscopic forms and textures [27-28]. In our HRTEM research we found that a lot of nanotubes are co-existent with nanoparticles in some samples, especially in the samples of TS5 and TS6 calcined at 600°C for 1h. Figure 2 presents the TEM nanotube images of TS5 (5at. %) calcined at 600°C for 1h in air. The nanotubes can be observed everywhere in sample TS5. In TS6 the nanotube can still be observed, but the composition of nanotubes is less than that in TS5. A few nanotubes are found in TS4. However, only nanoparticles are observed in TS7. EDX (mounted on the TEM) mapping images reveal that titanium and silicon are homogeneously distributed in the nanotube, indicating that the nanotubes are constructed by both titania and silica. In addition, the nanotubes are not stable to the TEM beam. No nanotubes are found in the pure titania samples. Further studies are in progress for elucidating the phenomena.

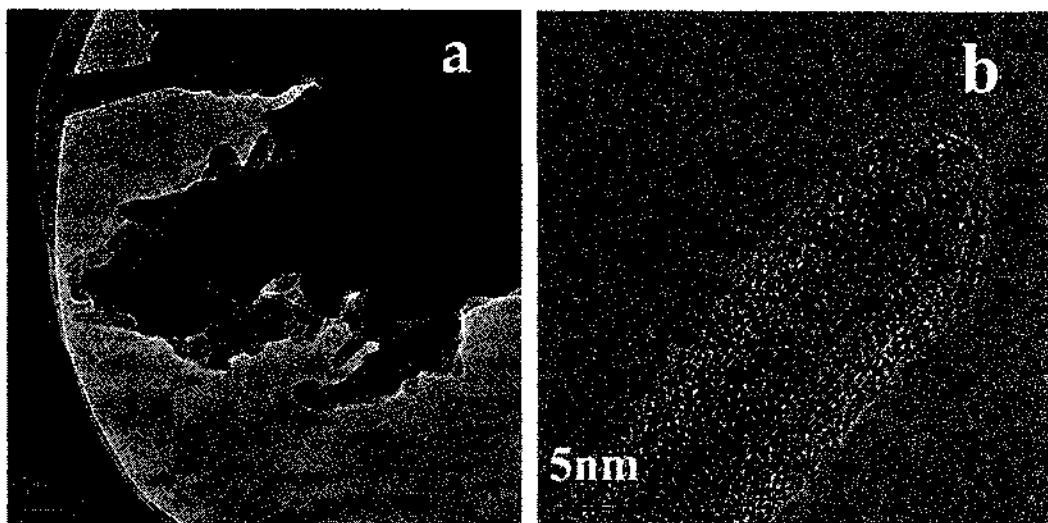


**Figure 2.** TEM micrographs of nanotubes of silicon-doped titania (TS5) calcined at 600°C for 1h in air.

#### 4 Conclusion

A series of silicon-doped nanocrystalline mesoporous titanium dioxide were prepared by a sol-gel technique. The crystal structure and phase transition of the doped specimens are strongly depended on the amount of silicon dopant. Silicon doping not only significantly retards the phase transition from anatase-to-rutile, but substantially enlarges the range of coexistence of anatase and rutile as well. The grain growth, usually happening during the treatment of nanoparticle particles at high temperatures, is significantly reduced and the mesoporous nanocrystalline structure is dramatically maintained up to higher temperature by doping silicon into the titanium dioxide matrix. In addition, the microstructure such as the shape and diameter of the pores is sensitively related to the silicon content. The HRTEM results reveal that nanotube is formed in specific silicon doped samples. The nanotubes co-exist with nanoparticles. The silicon content and the calcination temperature influence the formation of nanotubes.

#### References

1. Hoffman, M. R.; Martin, S. T.; Choi, W.; Bahneman, D. W. *Chem. Rev.* **95** (1995) pp. 6.
2. Taramasso, M., Perego, G., and Notari, B. US Patent 4,410,501, **1983**.
3. O'Regan, B.; Grätzel, M. *Nature* **353** (1991) pp. 737.
4. Rao, M. V.; Rajeshwar, K.; Verkerk, V. R.; Dubow, J. *J. Phys. Chem.* **84** (1987) pp. 1987.
5. Nishimoto, S.; Ohtani, B.; Kajiwara, H.; Kagiya, T. *J. Chem. Soc., Faraday Trans.* **81** (1985) pp. 61.
6. Chary, K. V. R.; Kishan, G.; Lakshmi, K. S.; Ramesh, K. *Langmuir*, **16** (2000) pp. 7192.
7. Topsoe, N. Y.; Topsoe, H.; Dumesic, J. A. *J. Catal.* **151** (1995) pp. 226.
8. Wachs, I. E.; Saleh, R. Y.; Chan, S. S.; Cherish, C. C. *J. Catal.* **15** (1985) pp. 339.
9. Bond, G. C.; Bruckman, K. *Faraday Discuss. Chem. Soc.* **72** (1982) pp. 235.
10. Chio, W.; Termin, A.; Hoffmann, M. R. *J. Phys. Chem.* **98** (1994) pp. 13669.
11. Nanoparticles and nanostructured films, edited by Janos H. Fendler, Wiley-VCH, 1998.
12. Fendler, J. H. *J. Phys. Chem.*, **89** (1985) pp. 2730.
13. Zhang, Y.; Reller, A. *J. Mater. Chem.*, **11** (2001) pp. 2537.
14. Anderson, M. A.; Geiselmann, M. J.; Xu, Q. *J. Membrane Sci.* **39** (1988) pp. 243.
15. Bhate, R. R. *Inorganic Membranes Synthesis, characteristics, and Applications*, Van Nostrand Reinhold, New York, 1991.
16. Melendres, C. A.; Narayanasamy, A.; Maroni, V. A.; Siegel, R. W. *J. Mater. Res.* **4** (1989) pp. 1246.
17. Ding, X. Z.; Liu, X. H. *J. Mater. Sci. Lett.* **15** (1996) pp. 1789.

18. Qadri, S..B.; Skelton, E..F.; Hsu, D.; Dinsmore, A..D.; Yang, J.; Gray, H..F.; Ratna, B..R. *Phys. Rew. B*, **60** (1999) pp. 9191.
19. Yoldas, B..E. *Am. Ceram. Soc. Bull.*, **54** (1975) pp. 286.
20. Brunauer, L..S.; Deming, L..S.; Deming, W..S.; Teller, E. *J. Am. Ceram. Soc.*, **62** (1940) pp. 1723.
21. Best, M..F.; Condrate, R..A. *J. Mater. Sci. Lett.*, **4** (1985) pp. 994.
22. Emili, M.; Incoccia, L.; Mobilio, S.; Fagherazzi, G.; Guglielmi, M. *J. Non-Cryst. Solids*, **74** (1985) pp. 129.
23. Hayashi, H.; Yamada, T.; Saito, H. *J. Mater. Sci.*, **18** (1983) pp. 3137.
24. Thangaraj, A.; Kumar, R.; Mirajkar, S..P.; Ratnasamy, P. *J. Catal.*, **130** (1991) pp. 1.
25. Gao, H.; Lu, W.; Chen, Q. *Microporous and mesoporous Mater.*, **34** (2000) pp. 307.
26. Notari, B. *Stud. Surf. Sci. Catal.*, **60** (1991) pp. 343.
27. Iijima, S. *Nature*, **354** (1991) pp. 56.
28. Kasuga, T., Hiramatsu, M., Hoson, A., Sekino, T. and Niihara, K. *Adv. Mater.*, **11** (1999) pp. 1307.

# MICROEMULSION SYNTHESIS AND MAGNETIC PROPERTIES OF Co@Pt CORE-SHELL NANOPARTICLES

YONGNAN ZHAO, XIUHONG LI, MING LI AND ZHENHONG MAI

*Institute of Physics & Condensed Matter of Physics, Chinese Academy of Sciences, Beijing 100080,  
P. R. China  
E-mail: zhaogn@263.net*

YI YU

*State Key Laboratory of Inorganic Synthesis and Preparative Chemistry, Jilin University,  
Changchun 130023, P. R. China*

Nearly monodispersed platinum coated cobalt (Co@Pt) nanoparticles with an average diameter of 5nm was prepared in microemulsion medium. The particles were characterized by powder X-ray diffraction, transmission electron microscopy and magnetic measurements. The composition of the nanoparticles was determined by energy dispersive X-ray analysis to be CoPt<sub>2</sub>. Both of the simple colsed packing calculation and the magnetic measurements give the same result of the cobalt core size of 3nm. The magnetic studies indicated its superparamagnetic behavior at room temperature and ferromagnetic state below 50k with a coercivity of 658.8Oe at 5K.

## 1 Introduction

Nanomaterials have recently been one of the most active research fields in the areas of solid-state physics, chemistry and engineering and the research is in progress from a variety of viewpoints [1]. The interest in nanomaterials derived from the needing of fabricating new materials with finer scale to continue decreasing the cost and increasing the speed of information transmission and storage. And nanomaterials display novel and often enhanced properties compared to traditional materials, which opens up possibilities for new technology applications. Nanoparticles, defined by a diameter of 1–10 nm, are creating a new category of materials, which is different from both bulk materials and atoms. For instance, magnetic and semiconductor NPs exhibit strong size dependent properties. And nanoparticles have been recognized in numerous applications, including ceramics, pigments, catalysts, electronics, medical diagnostics and other areas, especially of high technology and medicine. Single domain magnetic particles show very interesting properties such as high coercivity and remanence, which are of special interest to applications in magnetic recording and permanent magnets [2]. Interest in single domain particles immersed in non-magnetic metallic matrix has increased recently due to their giant magnetoresistance [3]. This has stimulated much research on bimetallic magnetic nanocomposites [4]. Of the three transition metals (Fe, Co, Ni), cobalt nanoparticles have the greatest potential for use due to its uniaxial. Spin-dependence tunneling in uniform cobalt nanoparticle arrays has also been reported as a model experimental system for studying magnetotransport in nanostructured materials [5]. Ferromagnetic alloys such as FePt and CoPt are of the most interest in magnetic storage due to their high coercivity [6]. This increase in coercivity is originated from exchange enhancement coupled with the very high magnetocrystalline anisotropy.

Many synthetic methods have been developed for preparing nanoparticles. Among these, microemulsion has been proved to be a promising way for preparing monodispersed nanoparticles [7]. Water-in-oil (w/o) microemulsion solutions not only act as microreactors for processing reactions but also inhibit the excess aggregation of particles. Since the platinum-group metallic nanoparticles were prepared in w/o microemulsion [8], this technique has been widely used to prepare nanoparticles of numerous materials, including metals, sulfides and selenides, borides, halides, oxides and organic polymers [9]. To investigate the magnetic properties of bimetallic composite nanoparticles, Co@Pt core-shell nanoparticles have been prepared from microemulsion medium. Here we report its synthesis and magnetic properties.

## 2 Experimental

The Co@Pt nanoparticles were synthesized in cationic microemulsions using cetyltrimethylammonium bromide (CTAB) as the surfactants, 1-butanol (BuOH) as co-surfactant and octane as the oil phase.  $\text{CoCl}_2 \cdot 6\text{H}_2\text{O}$ ,  $\text{H}_4\text{PtCl}_6 \cdot 6\text{H}_2\text{O}$  and  $\text{NaBH}_4$  were used as the starting materials. All reagents were of analytical grade and used without further purification. The procedures were performed under nitrogen atmosphere. The solvents were degassed before use. The procedure and the component are schematically shown in Figure 1. Typically, the CTAB, BuOH and octane were mixed under stirring. Aqueous solutions of  $\text{HPtCl}_4$ ,  $\text{CoCl}_2 \cdot 6\text{H}_2\text{O}$  and  $\text{NaBH}_4$  were employed to form the microemulsions. The particle sizes were determined by the ratio of water to CTAB ( $\omega$ ). The experiments were carried out in two steps. In the first step, two microemulsions were prepared using 0.5M  $\text{CoCl}_2 \cdot 6\text{H}_2\text{O}$  and 1.1M  $\text{NaBH}_4$  with  $\omega$  value of 8. Then these two types of microemulsions were mixed and reacted for one hour. The reaction led to a black colloid of Co nanoparticles. In the second step, two additional microemulsions were prepared using 0.5M  $\text{HPtCl}_4$  and 1.6M  $\text{NaBH}_4$ . The microemulsion containing  $\text{HPtCl}_4$  was dispersed into the Co colloid under vigorous stirring. Then the addition of the microemulsion containing 1.6M  $\text{NaBH}_4$  was followed and stirred for one hour. The final product was washed by 1:1 chloroform/ethanol mixture for several times to remove the surfactant and dried at room temperature.

A Rigaku D/MAX-III X-ray diffractometer was used to determine the phase in the  $2\theta$  range of  $20^\circ$ - $80^\circ$ . Transmission electron micrographs (TEM) were recorded on a JEM-200CX. The composition of the Co@Pt nanoparticles was measured using energy dispersive X-ray analysis equipped on a scanning electron microscope (Hitachi S-4200). Magnetic measurements were carried out on an MPMS-7 SQUID magnetometer.

## 3 Results and Discussion

The powder XRD profiles of the Co@Pt NPs are shown in Figure 2. All the peaks correspond to the metallic platinum diffraction. The peaks of the cobalt are hidden under the peaks of platinum due to the overlapping of their diffraction peaks. No diffraction patterns of cobalt oxides are detected. The evidence of the presence of the

cobalt is proved by the energy dispersive X-ray analysis attached on a scanning electronic microscope. The results of three samples give an average ratio of Co to Pt of 1:2. The size and morphology of the nanoparticles are studied by TEM. TEM images show nearly monodispersed spherical nanoparticles with diameter of ca.5nm (Figure 3). The cobalt core is estimated to be 3nm by the simple close packing model calculation.

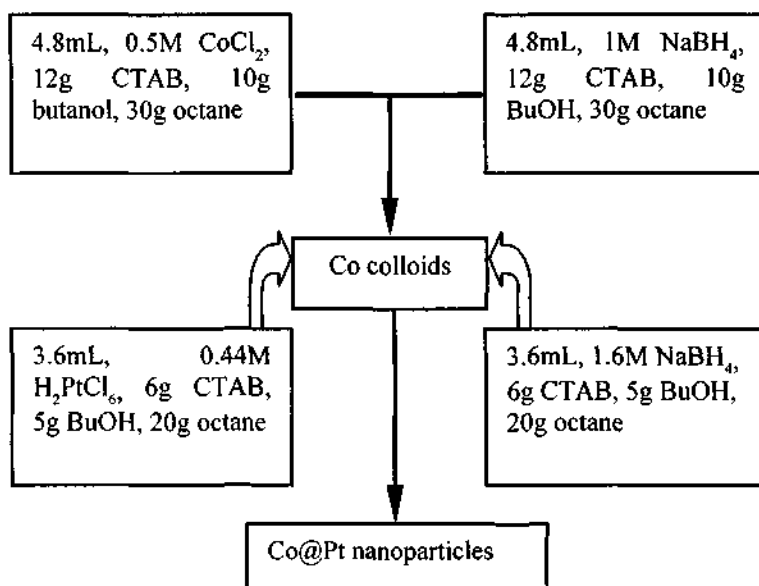


**Figure 1.** Schematic diagram showing the procedure of preparing Co@Pt nanoparticles.

Magnetic measurements of the core-shell nanoparticles were performed on a MPMS-7 SQUID magnetometer. The magnetic properties were derived from zero-field-cooled and field-cooled (ZFC/FC) magnetization as a function of temperature in a 50Oe field and from magnetization *vs.* magnetic field hysteresis loops at 5K, 50K and 300K. Figure 4 shows the ZFC/FC curves of the Co@Pt nanoparticles. At 300K, where the relaxation of the magnetic moments is faster than the characteristic experimental time, and the magnetization is linear in field following Curie-Weiss law. At low temperature, the ZFC and FC curve split at 50K and the ZFC curve declines below temperature of 50K. This phenomenon is the well-known blocking of the magnetic moments, which is caused by the anisotropy.

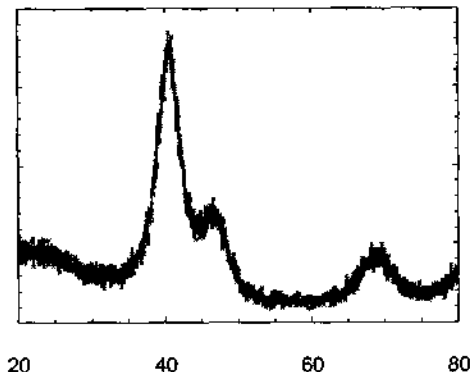


**Figure 2.** The powder XRD patterns of the Co@Pt core-shell nanoparticles.

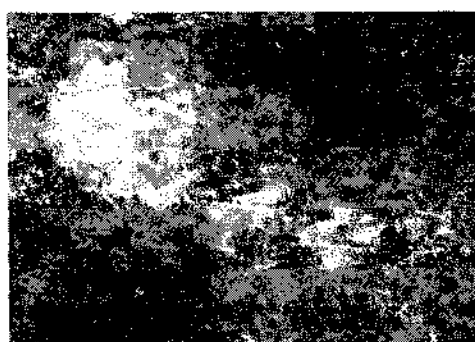


**Figure 3.** The TEM image of the Co@Pt core-shell nanoparticles. Scale bar = 50nm.

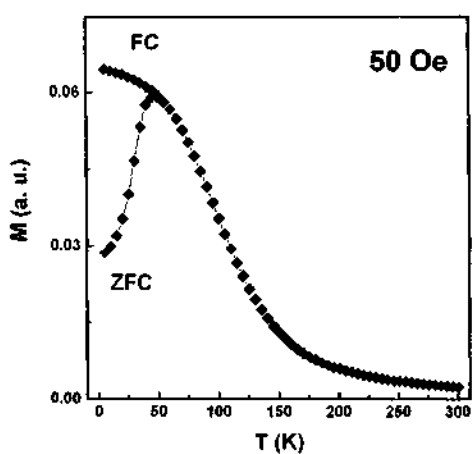


**Figure 4.** The ZFC/FC curves of the Co@Pt nanoparticles.

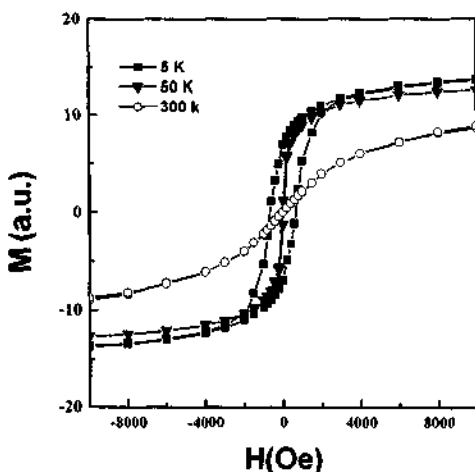


**Figure 5.** The magnetization vs the magnetic field of the Co@Pt nanoparticles at 5K, 50K and 300K.

The ZFC/FC curve also indicates the narrow size distribution of the Co@Pt NPs. In the case of a wide size distribution, a broad curve and even two shoulders were present. The results of the magnetization vs. magnetic field at different temperature were illustrated in Figure 5. The particles are characterized by superparamagnetic behavior above the blocking temperature (50K). This is originated from the reduced particle size. When the volume of the ferromagnetic particle is reduced, thermal fluctuations cause the magnetic moment of the domains to fluctuate randomly between their energy minima. Hence the particles behave like a paramagnet. No remanence and coercivity can be observed above the blocking temperature. Below 50K, the Co@Pt nanoparticles are in ferromagnetic state with a coercivity of 658.8Oe at 5K. The temperature dependence of magnetization at low temperature was shown in Figure 5. Under the weak interparticle interactions, the magnetization curve of such a superparamagnetic system with uniform particle size can be described by the Langevin equation:  $M = M_s (1 - k_B T / \mu H)$ , where  $\mu$  is the magnetic moment of a single particle with volume  $V$ . [3] For single domain particles,  $\mu = M_s V$ . Therefore, the average size of the magnetic cobalt core can be calculated assuming that the core is spherical. The diameter of the cobalt core is 3nm calculated using this model, which is in good agreement with the result calculated by the simple closed packing model.

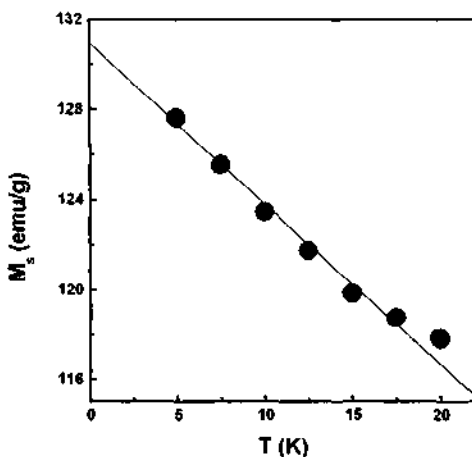


**Figure 6.** Saturation magnetization ( $M_s$ ) versus temperature for the Co@Pt nanoparticles. The solid line shows the linear relationship between the  $M_s$  and temperature.

### Acknowledgements

The authors are grateful to Dr. Hai Wang for the magnetic measurements and Dr. Dongsheng Tang for the TEM images recording.

### References

- Edelstein A. S. and Cammarata R. C., Nanomaterials: Synthesis, Properties and Applications, Institute of Physics Publishing, 1998; Shipway A. N., Katz E., and Willner I., *ChemPhysChem*, **1** (2000), 18; Toshima N. and Yonezawa T., *New J.*

- Chem.*, **1998**, 1179; Bonnemann H. and Richards R. M., *Eur. J. Inorg. Chem.*, **2001**, 2455; Schimid G., Baumle M., Geerkens M., Heim I., Osemann C., and Sawitowski T., *Chem. Soc. Rev.*, **28** (1999), 179.
2. Murdock E. S., Simmons R. F., Davison R., *IEEE Trans. Magn.*, **28** (1992), 3078; Billas I. M. L., Chatelain A., and de Heer W. A., *Science*, **265** (1994), 1682.
  3. Wang J. Q. and Xiao G., *Phys. Rev. B*, **49** (1994), 3982.
  4. Zhang Y. D., Budnick J. I., Hines W. A., Chien C. L., and Xiao J. Q., *Appl. Phys. Lett.*, **72** (1998), 2053; Paulus P. M., Bonnemann H., van der Kraan A. M., Luis F., Sinzig J., and de Jongh L. J., *Eur. Phys. J. D*, **9** (1999), 501; Park J. and Cheon J., *J. Am. Chem. Soc.*, **123** (2001), 5743; Lin J., Zhou W., Kumbhar A., Wiemann J., Fang J., Carpenter E. E., and C. J. O'Connor, *J. Solid State Chem.*, **159** (2001), 26; Carpenter E. E., Sims J. A., Wienmann J. A., Zhou W. L., and O'Connor C. J., *J. Appl. Phys.*, **87** (2000), 5615; Ely T. O., Pan C., Amiens C., Chaudret B., Dassenoy F., Lecante P., Casanove M. J., Masset A., Respaud M., and Broto J. M., *J. Phys. Chem. B*, **104** (2000), 695.
  5. Sun S. H. and Murray C. B., *J. Appl. Phys.*, **85** (1999), 4325; Black C. T., Murray C. B., Sandstrom R. L., and Sun S. H., *Science*, **290** (2000), 1131.
  6. Sun S. H., Murray C. B., Weller D., Folks L., and Moser A., *Science*, **287** (2000), 1989; Liou S. H., Huang S., Klimek E., Kirby R. D., and Y. D. Yao, *J. Appl. Phys.*, **85** (1999), 4334.
  7. Fendler J. H., *Chem. Rev.*, **87** (1987), 877; Pilani M. P., *Adv. Funct. Mater.*, **11** (2001), 323; Pilani M. P., *J. Phys. Chem.*, **97** (1993), 9661.
  8. J. H. Boutonnet., J. Kizling, P. Stenius, *Colloids Surf.*, **1982**, **5**, 209.
  9. Pilani M. P., *Langmuir*, **13** (1997), 3266; Kishida M., *J. Chem. Soc., Chem. Commun.*, **1995**, 763; Zarur A. J., Ying J. Y., *Nature*, **403** (2000), 65; Ingert D., Feltin N., and Levy L., *Adv. Mater.*, **11** (1999), 220; Cieron J., Pilani M. P., *J. Phys. Chem. B*, **101** (1997), 8887; Ayyub P., Maitra A. N., and Shah D. O., *Physica C*, **168** (1990), 571; Barnickel P. and Wokaun A., *Mol. Phys.*, **69** (1990), 1; Pillai V., Kumar P., and Shah D. O., *J. Magn. Magn. Mater.*, **116** (1992), L299; Pillai V. and Shah D. O., *J. Magn. Magn. Mater.*, **163** (1996), 243; Moumen N., Bonville P., and M. P. Pilani, *J. Phys. Chem.*, **100** (1996), 14410; Pitet P., Taleb A., Pilani M. P., *Adv. Mater.*, **10** (1998), 259, and references therein.

# PREPARATION AND CHARACTERIZATION OF NANOPOWDERS AND NANOCERAMICS OF VANADIUM OXIDES

CHENMOU ZHENG, XINMIN ZHANG AND LIUYA WEI

*Department of Chemistry, Zhongshan University, Guangzhou, 510275, P. R. China*

*E-mail: daddy200@sina.com*

SHAN HE AND DEMING LEI

*Department of physics, Zhongshan University, Guangzhou, 510275, P. R. China*

*E-mail: stslsm@zsu.edu.cn*

$V_2O_3$ ,  $VO_2$  and  $V_2O_5$  powders with nano-particles were prepared by the pyrolysis of a precursor,  $(NH_4)_5[VO_6(CO_3)_4(OH)_9] \cdot 10H_2O$ , under milder conditions. The thermoanalysis processes of the precursor were investigated respectively by TGA and DTA under various atmospheres.  $V_2O_3$  powder with spherical particles about 30nm was prepared by reductive pyrolysis of the precursor at 650°C for 1h in  $H_2$  atmosphere. A temperature of phase transition of the powder is -119.5°C on cooling or -99.2°C on heating. Amorphous, incomplete crystalline or crystalline  $VO_2$  with 10, 20, or 30nm was got at < 450°C by the pyrolysis of the precursor in  $N_2$  atmosphere. The temperature and the heat of the transition are closely related to the stoichiometry of  $VO_2$  powders.  $V_2O_5$  powders with granular shape particles from 40 to 400nm were prepared by the oxidative pyrolysis of the precursor at < 630 °C in a flow of air. The IR spectra of  $V_2O_3$  show a size effect. The  $VO_2$  ceramics with about 60nm grain exhibits an abrupt change in electrical resistivity by three orders of magnitude at about 66 °C.

## 1 Introduction

Vanadium oxides have been the subjects of many investigations.  $V_2O_3$  or  $VO_2$  shows a discontinuity of first order metal-insulator transition at about -120°C or 68°C respectively [1,2].  $V_2O_5$  is known as an *n*-type semiconductor [3]. These three oxides are all excellent catalysts and are used in conductive polymer composites and lithium batteries [4-6]. Moreover, the vanadium oxide powders obtained by various methods exhibit different properties and further influence the final function of the devices or the materials. Over two decades, many methods have been studied for preparing these oxides. For example,  $V_2O_3$  powder was prepared by reduction of  $V_2O_5$  obtained by evaporative decomposition of solutions (EDS) under pure  $H_2$  at 850°C for 6h [7].  $VO_2$  powder was generally synthesized by solid-solid reaction between  $V_2O_3$  and  $V_2O_5$  in an evacuated silica tube at high temperature. The method of EDS was also used to prepare  $VO_2$  through decomposition of dilute solution of  $VOSO_4$  in a mixed flow of  $H_2-N_2$  at ≥740°C with a spray-pyrolysis reactor [8].  $V_2O_5$  powder was prepared by heating  $V_2O_5 \cdot nH_2O$  gels [3]. However, only micropowders could be obtained by these methods.

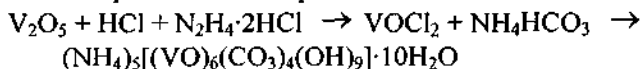
So far, only two reports have been found in the literature on the syntheses of  $V_2O_3$  and  $VO_2$  nanoparticles [6,9]. The purpose of this article is to study the probability of preparation of  $V_2O_3$ ,  $VO_2$  and  $V_2O_5$  nanopowders by pyrolysis of the precursor,  $(NH_4)_5[VO_6(CO_3)_4(OH)_9] \cdot 10H_2O$ , at lower temperatures under  $H_2$ ,  $N_2$  or air atmosphere respectively. Our investigation is aimed to prepare the ceramics of vanadium oxides with nanometer-sized grains using these powders and to observe the

properties of the ceramics. The experimental results show that the single molecular compound is a good precursor with merits as follows for preparing vanadium oxides. First, the precursor is easily synthesized. Second, nanopowders of vanadium oxides are expected to be easily obtained due to the releasing of a large amount of gases during pyrolysis. Third, the pyrolysis temperature of the precursor is lower. Moreover, the VO<sub>2</sub> ceramics with nanometer-sized grains is first prepared.

## 2 Experimental Section

### 2.1 Synthesis and Thermoanalyses of the Precursor

The synthesis route of the precursor was reported in an earlier work of ours [10]:



The sample particles of the precursor used here are about 10 μm in size. Its composition was confirmed with its molecular formula. Thermogravimetric analysis (TGA) and differential thermal analysis (DTA) were simultaneously conducted on a PCT-1 type thermoanalysis meter in H<sub>2</sub> (99.999%), and were respectively completed on a Perkin-Elmer TGS-2 and a Perkin-Elmer DTA-1700 in N<sub>2</sub>(99.99%) or air, with 5 °C min<sup>-1</sup> heating rate and a gas flow rate of 15 mL min<sup>-1</sup>.

### 2.2 Pyrolyses of the Precursor

A coarse precursor was pulverized to be about 2μm in size. Its vanadium content was higher than the calculated value by about 2.6%. The fine precursor was spread in a quartz boat. The quartz boat was placed in a silica tube. A stream of H<sub>2</sub>, N<sub>2</sub> or O<sub>2</sub> was introduced into the system to replace the air in the tube. The tube was then heated to a desired temperature and maintained for a preset time. After the reaction was completed, pull out the tube from the tube furnace and cool rapidly to room temperature.

### 2.3 Preparation of VO<sub>2</sub> ceramics

The VO<sub>2</sub> powder was pressed at a pressure and the pellets obtained were 12.0 mm in diameter and 2 mm thick. The pellets were then sintered at 950°C for 1h in a N<sub>2</sub> atmosphere.

### 2.4 Characterization of Products

V<sub>2</sub>O<sub>3</sub> or VO<sub>2</sub> sample was dissolved in a mixed solution of phosphoric-sulfuric acid for determination of V<sup>3+</sup> and total vanadium content. The content of V<sup>3+</sup> was determined using ferroin as an indicator [11]. The total vanadium content was titrated by a FeSO<sub>4</sub> solution. X-ray diffraction (XRD) experiments were carried out on a D/max-3A diffractometer using Cu K<sub>α1</sub> radiation ( $\lambda = 0.154050$  nm). The morphologies of the products were observed on a JSM-6330F field emission

scanning electron microscope (SEM) or a JEM 100-CX-II TEM. Differential scanning calorimetry (DSC) experiments were performed on a NETZSCH DSC-204 in N<sub>2</sub> atmosphere with a heating or cooling rate of 10°C min<sup>-1</sup>. The dc resistivity measurements of VO<sub>2</sub> ceramics were carried out as a function of temperature in N<sub>2</sub> gas flow using the four-probe method. The infrared spectra were recorded on a Nicolet 5DX FT-IR spectrometer.

### 3 Results and Discussion

#### 3.1 Thermoanalyses of the Precursor

The TGA and the DTA curves of the thermolysis of the precursor in H<sub>2</sub> are shown in Figure 1. The thermolysis models from the TGA curve are displayed in Scheme 1.

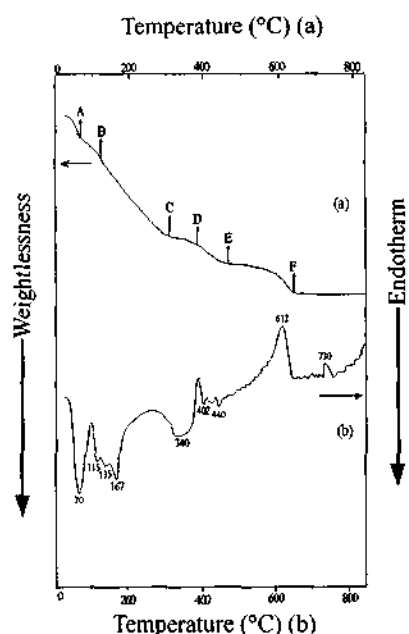


**Figure 1.** TGA and DTA curves of thermoanalysis of the precursor in H<sub>2</sub> flow: (a) TGA curve; (b) DTA curve.

(NH <sub>4</sub> ) <sub>5</sub> [{(VO) <sub>6</sub> (CO <sub>3</sub> ) <sub>4</sub> (OH) <sub>6</sub> } · 10H <sub>2</sub> O		
	—3H <sub>2</sub> O	
(NH <sub>4</sub> ) <sub>5</sub> [{(VO) <sub>6</sub> (CO <sub>3</sub> ) <sub>4</sub> (OH) <sub>6</sub> } · 7H <sub>2</sub> O	75°C <sup>a</sup>	A
(94.9%)	(94.6%) <sup>c</sup>	
	—5H <sub>2</sub> O	
(NH <sub>4</sub> ) <sub>5</sub> [{(VO) <sub>6</sub> (CO <sub>3</sub> ) <sub>4</sub> (OH) <sub>6</sub> } · 2H <sub>2</sub> O	122°C	B
(86.5%)	(86.2%)	
	—3H <sub>2</sub> O	
	—4NH <sub>3</sub>	
	—3CO <sub>2</sub>	
(NH <sub>4</sub> ) <sub>5</sub> {(VO) <sub>6</sub> (CO <sub>3</sub> ) <sub>4</sub> (OH) <sub>11</sub> }	305°C	C
(62.6%)	(62.6%)	
	—NH <sub>3</sub>	
	—CO <sub>2</sub>	
6 VO <sub>2</sub> · H <sub>2</sub> O	390°C	D
(56.9%)	(56.2%)	
	—3H <sub>2</sub> O	
6 VO <sub>2</sub> · 0.5H <sub>2</sub> O	465°C	E
(51.8%)	(50.3%)	
+ 3H <sub>2</sub>		
—6H <sub>2</sub> O		
3 V <sub>2</sub> O <sub>3</sub>	620°C	F
(42.2%)	(42.1%)	

**Scheme 1.** Thermolysis process of the precursor: (a) temperature of formation of intermediate; (b), (c) calculated and the experimental value of residual weight percentage.

The TGA data from Figure 1(a) and Scheme 1 indicate that there are five intermediates A, B, C, D, and E before V<sub>2</sub>O<sub>3</sub> (F) forms at 620°C in the reductive pyrolysis process of the precursor. It can be seen from Figure 1(b) that there are eight endothermic peaks on the DTA curve due to the thermolysis effects of the formation of the intermediates. The large exothermic peak at 612°C on the DTA curve is attributed to the exothermic effect of reduction of V<sup>4+</sup> to V<sup>3+</sup>. The small exothermic peak at 730°C on the DTA curve is attributed to the crystallization of V<sub>2</sub>O<sub>3</sub>.

Reduction of bulk particle  $V_2O_5$  was studied by thermal analysis in  $H_2$ , showing that pure  $V_2O_3$  formed at  $717^\circ C$  [12]. Obviously, this temperature is higher than that of forming  $V_2O_3$  in the thermolysis of the precursor by  $97^\circ C$ , showing that the nanoparticles in the thermolysis process have higher reduction activity than that of the  $V_2O_5$  bulk-particles. Most importantly, the difference between the formation and the crystallization temperatures ( $620$  and  $730^\circ C$ ) of  $V_2O_3$  is large enough to be detected in the thermolysis process. This is the first report for the crystallization temperature of  $V_2O_3$ .

The thermoanalysis of the precursor in  $N_2$  shows the forming and crystallization of  $VO_2$  at  $362$  and  $387^\circ C$  [13]. The thermoanalysis of the precursor in air shows the forming and melting of  $V_2O_5$  at  $358$  and  $669^\circ C$ . This melting point is lower than that of bulk particle  $V_2O_5$  due to size effect [14].

### 3.2 Pyrolysis of the precursor in $H_2$ and properties of $V_2O_3$ powder

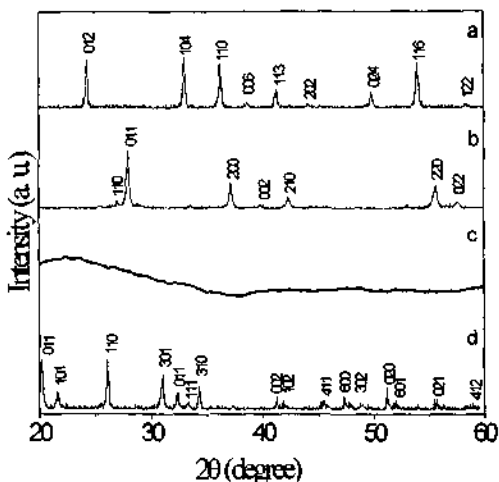


Figure 2. XRD patterns of vanadium oxides: (a)  $V_2O_3$ ; (b) crystalline  $VO_2$ ; (c) amorphous  $VO_2$ ; (d)  $V_2O_5$ .



Figure 3. SEM micrograph of  $V_2O_3$  powder ( $\times 10^5$ ).

The effects of various pyrolysis conditions including temperature, time,  $H_2$  flow rate and precursor amount on compositions of  $V_2O_3$  products are studied in the reductive pyrolysis of the precursor. The XRD pattern of the  $V_2O_3$  obtained at  $650^\circ C$  for  $1\text{ h}$  is shown in Figure 2(a), in which no peaks of impurities are observed. Figure 3 is a SEM micrograph of the same sample. One can see from the picture that the spherical particles with about  $30\text{ nm}$  size are clear and more homogeneous in distribution even if there is still trace of dispersing agent. The particle size value is consistent with the mean value  $33.2\text{ nm}$  calculated by the Scherrer equation.  $V_2O_3$  nanopowder is expected to be easily prepared by the pyrolysis of the precursor, because a large amount of gases releases and the reduction occurs during the pyrolysis. This process causes strong splitting and atomizing of the particles. Botto et al. indicated that it was very difficult to obtain pure  $V_2O_3$  even with freshly prepared samples in their

studies on  $V_2O_3$  and  $VO_2$  by IR, XPS and EPR, due to the reoxidation by the effect of air at the surface of the particles[15]. To observe the reoxidation effect of various powders, three kinds of powder were exposed to air and then their changes in composition were determined. As Figure 4 showed, the reoxidation rate of the micropowder of  $14 \times 20 \mu\text{m}^2$  size (curve (a)) is lightly slower than that of the nanopowder of  $< 100 \text{ nm}$  size (curve (b)), and the reoxidation rate of another nanopowder of about  $36 \text{ nm}$  size (curve (c)) is very fast. Obviously, nanopowders, especially obtained at lower temperature, more easily adsorb air due to their finer size and larger surface areas, causing deeper reoxidation when exposing to air. DSC of  $V_2O_3$  powder has not been determined up to now. The DSC curves of  $V_2O_3$  nanopowder in Figure 5 show that the temperatures of phase transition are  $-119.5^\circ\text{C}$  on cooling and  $-99.2^\circ\text{C}$  on heating respectively. These are consistent with the results observed by determination of electrical resistance [1]. According to the DSC, the transition heat is  $-12.55\text{J g}^{-1}$  on cooling or  $11.42\text{J g}^{-1}$  on heating, respectively, in this work.

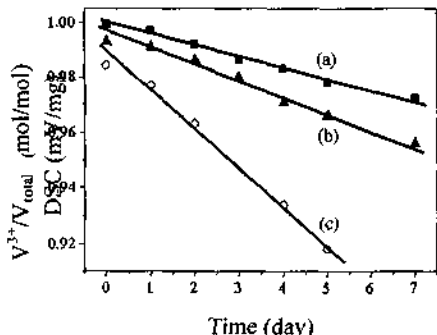


Figure 4. Reoxidation process of  $V_2O_3$  powders in air: (a) micropowder; (b) nanopowder got at  $900^\circ\text{C}$  for 5h; (c) nanopowder got at  $700^\circ\text{C}$  for 1h.

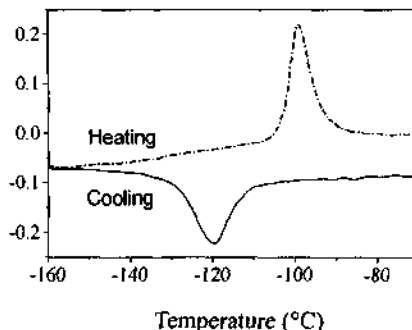


Figure 5. DSC scans of  $V_2O_3$  nanopowder.

### 3.3 Pyrolysis of the precursor in $N_2$ and properties of $VO_2$ powder

The effects of various pyrolysis conditions including temperature, time, precursor amount,  $N_2$  flow rate and flow rate of air in  $N_2$  on compositions and crystalline states of  $VO_2$  were studied in the pyrolysis of the precursor. The results show that the deviation of  $x$  of  $VO_{1.96\pm x}$  to  $VO_{2.07\pm x}$  is 0.004 and the stoichiometric and various nonstoichiometric powders can be successfully prepared under the selecting and controlling conditions. At the same time, the amorphous powder (10nm), the incomplete crystalline powder (20nm) or crystalline powder (30nm) was obtained at  $350^\circ\text{C}$ ,  $410^\circ\text{C}$  or  $450^\circ\text{C}$  for 30min. The XRD patterns of crystalline and amorphous  $VO_2$  are shown in Figure 2(b) and (c). Figure 6 is a TEM micrograph of the incomplete crystalline sample.



**Figure 6.** TEM micrograph of incomplete crystalline  $\text{VO}_2$  ( $\times 10^5$ ).

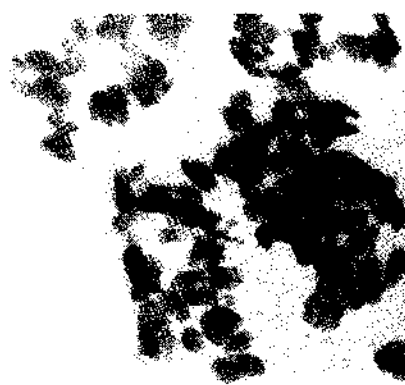


**Figure 7.** TEM micrograph of  $\text{V}_2\text{O}_5$  got at  $630^\circ\text{C}$  for 1 h ( $\times 10^4$ ).

**Table 1.** Heats and temperatures of phase transition of crystalline  $\text{VO}_2$ .

x in $\text{VO}_x$	1.96	1.98	2.00	2.01	2.02	2.03	2.04	2.05	2.07
$\Delta H(\text{J/g})$	24.2	37.9	45.6	49.1	56.8	52.5	46.4	37.8	34.0
Tt( $^\circ\text{C}$ )	60.7	68.0	68.8	68.7	70.1	69.6	69.7	70.9	69.0

The effect of various stoichiometry  $\text{VO}_2$  powders on temperature and heat of phase transition has not been reported so far. In this paper, the heats and the temperatures of transition from  $\text{VO}_{1.96}$  to  $\text{VO}_{2.07}$  in the crystalline state were measured from DSC scans. The results are listed in Table 1, indicating that the heats of the oxygen-deficient  $\text{VO}_2$  are less than those of the oxygen-rich  $\text{VO}_2$ , and the  $\text{VO}_{2.02}$  has the maximum transition heat. The transition temperature is increased about  $10^\circ\text{C}$  from  $\text{VO}_{1.96}$  to  $\text{VO}_{2.07}$ . Those results are not consistent with the results observed by determination of electrical resistivity of monocrystals reported in the literature, and the results in the literature are also contradictory [16,17]. The IR spectra of various size, crystalline state and stoichiometry  $\text{VO}_2$  are observed, showing the effects of size, crystalline state and stoichiometry [18].

### 3.4 Pyrolysis of the precursor in air or $\text{O}_2$ and properties of $\text{V}_2\text{O}_5$ powders

The pyrolysis of the precursor in air or  $\text{O}_2$  (at  $< 500^\circ\text{C}$ ) flow was carried out at various temperature and time to generate various sizes of  $\text{V}_2\text{O}_5$ . The sizes of the products obtained under various conditions are listed in Table 2. The XRD pattern is shown in Figure 2(d). The TEM micrograph of the powder obtained at  $630^\circ\text{C}$  for 1 h is shown in Figure 7, indicating its size is  $< 400 \text{ nm}$  with granular shape. Honma et al. [3] reported that  $\text{V}_2\text{O}_5$  particles with the strip-like shape of  $1 \mu\text{m} \times 4 \mu\text{m}$  were obtained at the same conditions by heating  $\text{V}_2\text{O}_5 \cdot 2.07\text{H}_2\text{O}$  gel. Only strip-like shape  $\text{V}_2\text{O}_5$  with  $0.8 \mu\text{m} \times 2.4 \mu\text{m}$  grew at  $660^\circ\text{C}$  near the melting point of  $\text{V}_2\text{O}_5$  for 1 h in this

work. Obviously,  $V_2O_5$  with finer size and granular shape is easily prepared using our method reported in this paper. The IR data of various size  $V_2O_5$  are also listed in Table 2. The results show that the absorption wavenumbers of the band decrease gradually and the absorption in  $494\text{-}518\text{cm}^{-1}$  disappears gradually as the powder size decreases. This is attributed to size effect[14].

Table 2. IR spectra of various size  $V_2O_5$  ( $\text{cm}^{-1}$ ).

Pyrolysis condition	Size (nm)	$\nu_1$	$\nu_2$	$\nu_3$	$\nu_4$	$\nu_5$
630°C, 1h	< 400	1020	838	634	518	481
600°C, 0.5h	< 200	1019	836	634	512	481
500°C, 1h	< 110	1019	831	632	512	479
500°C, 0.5h	< 80	1020	831	629	494	479
330°C, 6h	< 60	1018	830	629		478
310°C, 24h	< 40	1017	828	628		476

### 3.5 $VO_2$ Ceramics with nano-grain

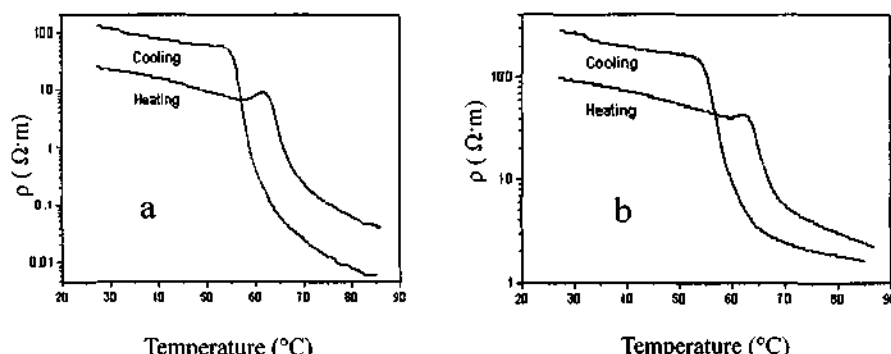


Figure 8. Temperature dependence of electrical resistivity of  $VO_2$  ceramics. (a)  $VO_{1.99}$ , (b)  $VO_{1.98}$ .

The influence of temperature on the electrical resistivity can be considered as another criterion for the phase composition of  $VO_2$ . This dependence is shown in Figure 8. The size in the jump of resistivity of  $VO_{1.99}$  ceramics in Figure 8 (a) and of  $VO_{1.98}$  ceramics in Figure 8 (b) is about  $10^4$  at  $66^\circ\text{C}$  and  $10^2$  at  $64^\circ\text{C}$ , respectively. These are consistent with the transition heats and temperatures of  $VO_2$  powders in Table 1. The research of another composition  $VO_2$  ceramic is carrying on. The results of XRD show that the size of grain in the ceramics is about 60nm.

### 4 Acknowledgement

This work was supported by the Natural Science Foundation (No. 970168) of Guangdong Province of China.

## References

1. MeWhan B.D., Mentch A., et al., Metal-insulator transitions in pure and doped V<sub>2</sub>O<sub>3</sub>. *Phys. Rev. B* **7** (1973) pp. 1920 - 1931.
2. Morin F., Oxides which show a metal to insulator transition at the Neel temperature. *Phys. Rev. Lett.* **3** (1959) pp. 34 - 36.
3. Honma K., Yoshinaka M., et al., Fabrication, microstructure and electrical conductivity of V<sub>2</sub>O<sub>5</sub> ceramics. *Mater. Res. Bull.* **31** (1996) pp. 531 - 537.
4. Baiker A., et al., Influence of grain morphology of V<sub>2</sub>O<sub>5</sub> on its reducibility and selectivity for methanol oxidation. *J. Catal.* **91** (1985) pp. 361 - 365.
5. Du W. and Du H., Mechanism of the PTC effect of V<sub>2</sub>O<sub>3</sub> - polyethylene composites. *Chin. Sci. Bull.* **37** (1992) pp. 1929 - 1932.
6. Tsang C. and Manthiram A., Synthesis of nanocrystalline VO<sub>2</sub> and its electrochemical behavior in lithium batteries. *J. Electrochem. Soc.* **144** (1997) pp. 520 - 524.
7. Sullivan J.R., Srinivasan T.T. and Newnham E.R., Synthesis of V<sub>2</sub>O<sub>3</sub> powder by evaporative decomposition of solutions and H<sub>2</sub> reduction. *J. Am. Ceram. Soc.* **73** (1990) pp. 3715 - 3717.
8. Lawton A.S., et al., Synthesis of vanadium oxide powders by evaporative decomposition of selutions. *J. Am. Ceram. Soc.* **78** (1995) PP. 104 - 108.
9. Toshiyuki O., Yasuhiro I. and Kenkyu R.K., Synthesis of SnO<sub>2</sub>, VO<sub>2</sub> and V<sub>2</sub>O<sub>3</sub> fine particles by laser-induced vapor-phase reaction. *J. Photopolym Sci. Technol.* **10** (1997) pp. 211 - 216.
10. Mak T.C.W., Li P., Zheng C. and Huang K., Synthesis and structural characterization of (NH<sub>4</sub>)<sub>5</sub>[ (VO)<sub>6</sub>(CO<sub>3</sub>)<sub>4</sub>(OH)<sub>9</sub>] · 10H<sub>2</sub>O. *J. Chem. Soc., Chem. Commun.* (1986) pp. 1597 - 1599.
11. Rao G. G. and Rao K.P., Potentiometric titration of vanadium(III) alone and in mixture with vanadium(IV). *Talata* **13** (1966) pp. 1335 - 1340.
12. Tkatchenko B. D. and Delahay G., Hydrogen temperature programmed reduction based on water analysis: Application to vanadium pentoxide. *J. Thermal Anal.* **41** (1994) pp. 1141 - 1151.
13. Zheng C., Zhang J., et al., Preparation of VO<sub>2</sub> powders by thermolysis of a precursor at low temperature. *J. Mater. Sci.* **35** (2000) pp. 3425-3429.
14. Zheng C., Zhang X., et al., Preparation and characterization of nanocrystal V<sub>2</sub>O<sub>5</sub>. *J. Solid State. Chem.* **159** (2001) pp. 181-185.
15. Botto I. L., Vasollo M.B., Baran E.J. and Minelli G. M., IR spectra of VO<sub>2</sub> and V<sub>2</sub>O<sub>3</sub>. *Mater. Chem. Phys.* **50** (1997) pp. 267 - 270.
16. Kimizuk N., Ishii M., Kawada I., Saeki M. and Nakahira M., Behavior of vanadium dioxide single crystals synthesized under the various oxygen partial pressures at 1500 K. *J. Solid State Chem.* **9** (1974) pp. 69 - 77.
17. Brückner W., Moldenhauer W., et al., The range of homogeneity of VO<sub>2</sub> and the influence of the composition on the physical properties. *Phys. Stat. Sol. (a)* **29** (1975) pp. 63 - 69.
18. Zheng C., Zhang X., et al., Preparation and characterization of VO<sub>2</sub> nanopowders. *J. Solid State Chem.* **156** (2001) pp. 274-280.

## PREPARATION OF NANOPHASE $\beta$ -Ni(OH)<sub>2</sub> POWDER FOR ELECTRODE MATERIALS

XIJIANG HAN,\* CHONGQUAN XU, CUIFEN ZHANG AND LI ZHAO

Department of Applied Chemistry, Harbin Institute of Technology, Harbin 15001, China  
E-mail: hanxj63@yahoo.com.cn

Nanophase  $\beta$ -Ni(OH)<sub>2</sub> powder for electrode materials were prepared by the coordination-precipitation method. The XRD results showed that the Ni(OH)<sub>2</sub> powder prepared was the  $\beta$  phase, which could be used as an electrode material. The TEM results showed that the  $\beta$ -Ni(OH)<sub>2</sub> powders were of nanosize in the range of 20nm to 40nm. The effect of experimental parameters, such as the concentration of the precipitating agent, the reaction temperature and the coordination agent quantity, on the particle diameter and productivity has been also discussed. The ratio of [Ni<sup>2+</sup>] to [ethylamine] was the primary factor to affect the diameter and the productivity of Ni(OH)<sub>2</sub>. The concentration of the KOH, which should be dropped into the solution with a high rate, was another important factor. The charge and discharge experiment results indicated that the electrode specific capacity was improved by 11% through the doping of the nano- $\beta$ -Ni(OH)<sub>2</sub> into the conventional micron Ni(OH)<sub>2</sub> particles.

### 1. Introduction

Increasing interest has been focused on the nano-scale science and technology in the field of chemical power sources. Some novel nano materials have been prepared whereas new synthetic methods have been designed [1,2]. The use of MH-Ni batteries decreased the pollution of the Cd-Ni battery, improving the performance of the alkaline battery. But the improvement of the properties of the cathode materials made it necessary to improve the discharge capacity of the anode materials [3-5]. The discharge capacity of anodes has been increased by 20%, and these anodes were made of  $\beta$ -Ni(OH)<sub>2</sub> nano fibers prepared by the wet chemistry method, with the diameter of 2nm~5nm and the length of 15nm~50nm [6]. In addition, the nano Ni(OH)<sub>2</sub> doped into the conventional Ni(OH)<sub>2</sub> with a particle size of several microns could also increase the anode capacity.

In this paper, the nano Ni(OH)<sub>2</sub> powders were prepared by the coordination-precipitation method. The effect of the experimental parameters on the phase composition and structure, such as the precipitating agent concentration, the reaction temperature and the coordination agent quantity has been discussed.

### 2. Experimental

Ethylamine was added into the Ni(NO<sub>3</sub>)<sub>2</sub> solution (0.1000mol/L), then the mixture was stirred for 20 minutes. A KOH solution (0.1000mol/L) was dropped into the mixture as soon as it was stirred. The Ni(OH)<sub>2</sub> precipitate was dried in a vacuum oven for 20h at 80°C.

The size and structure of the prepared Ni(OH)<sub>2</sub> was measured on a 1200EX transmission electron microscope (TEM) and a D/max-rB X-ray diffractometer (XRD), respectively.

The nano powder  $\text{Ni(OH)}_2$  was doped into the conventional micron  $\text{Ni(OH)}_2$  powder at the ratios of 5%, 8%, 12%, respectively. The mixture of the  $\text{Ni(OH)}_2$  and an adhesive was spread in the skeletal nickel, which was made as the anode. With Cd as the cathode and  $\text{Hg/HgO}$  as the reference electrode, 1C charging and discharging experiment was carried out in a 7mol/L KOH solution.

### 3. Results and Discussion

The effect of the technical parameters on the size and productivity of  $\text{Ni(OH)}_2$ , such as the KOH concentration, the reaction temperature, and the ethylamine quantity was examined. Table 1 presents the effect of the technical parameters on the size and productivity of  $\text{Ni(OH)}_2$ .

**Table 1.** Effect of technical parameters on the size and productivity of  $\text{Ni(OH)}_2$ \*.

No.	A	B	KOH (mL)	Temp (°C)	Stirring	C	D	E	X+Y
1	0.07	80	400	50	Weak	1:1	68.1	41	0.00
2	0.14	132	240	20	Weak	1:2	30.3	21	-0.16
3	0.07	132	240	50	Strong	1:2	40.9	31	-0.52
4	0.14	80	400	20	Strong	1:1	58.2	21	1.88
5	0.07	80	240	20	Strong	1:1	64.0	31	1.18
6	0.14	80	400	50	Strong	1:2	46.5	25	0.57
7	0.07	132	400	20	Weak	1:2	37.4	21	0.36
8	0.14	132	240	50	Weak	1:1	59.3	21	1.96
$\Sigma$ I	1.02	3.70	2.81	3.26	2.16	0.25			
$\Sigma$ II	4.25	1.64	2.54	2.01	3.11	5.02			
R	3.23	2.06	0.27	1.25	0.95	4.77			

\* A: KOH concentration (mol/L); B: KOH dropping rate (drops/min); C:  $[\text{Ni}^{2+}]$ : [ethylamine] ratio; D: Productivity (%); E: Particle diameter (nm)

The evaluation standard  $X+Y$  in Table 1 involves both factors of productivity and particle diameter. The productivity should be considered in future industrial production. The electrochemical activity became higher when the particle diameter became smaller [2]. However, the experiment results showed that the particle size was also larger when the productivity was higher. The  $X$  value was related to the productivity. It was defined as 5 at the highest productivity.  $X$  was calculated according to the following equation:

$$X = \frac{5}{0.68} P \quad (1)$$

where 0.68 was the highest productivity in our experiments, and  $P$  was the productivity.  $Y$  was related to the particle diameter. The  $Y$  value for the largest particles was defined as -5 because a smaller diameter was expected.  $Y$  was calculated according to the following equation:

$$Y = \frac{-5}{44} d \quad (2)$$

where 44 was the largest particle diameter in our experiments;  $d$  was the particle diameter. The value of  $\Sigma I$  and  $\Sigma II$  were the sums of  $X+Y$  at the first level and the second level, respectively.  $R$  was the difference between  $\Sigma I$  and  $\Sigma II$ , which indicated the factor effect degree. According to the cross experiment analysis, it was found that the ratio of  $[Ni^{2+}]$  to [Ethylamine] was the primary factor to affect the diameter and productivity of  $Ni(OH)_2$ , and the best value of it was 0.5. The KOH concentration was the second factor, which should be high.

Figure 1 shows the TEM images of samples No.1, No.3, No.4 and No.8. It was found that the particle diameter for the samples was about 20nm to 40nm. Figure 2 displays the XRD patterns of samples No.1, No.3, No.4 and No.8. One sees that the samples are indeed  $\beta$ - $Ni(OH)_2$ . However the location and the relative intensity of the diffraction peaks change for samples with different diameters.

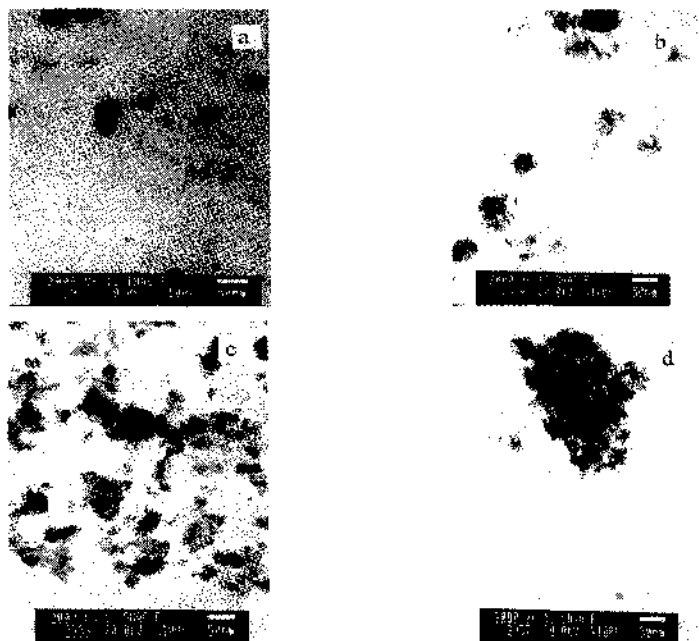
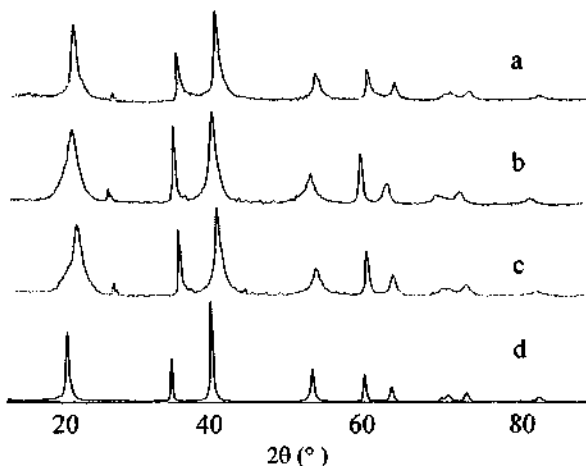
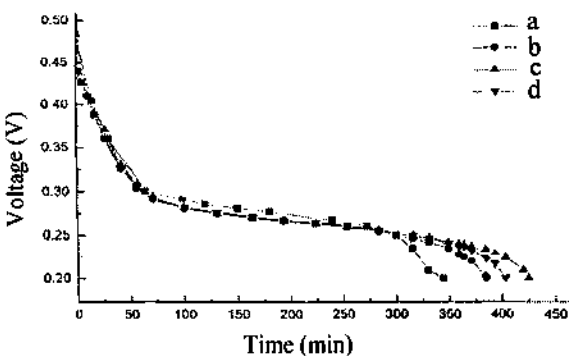


Figure 1. The TEM images for samples (a) No. 1, (b) No. 3, (c) No. 4 and (d) No. 8.



**Figure 2.** Powder XRD patterns for samples (a) No. 1, (b) No. 3, (c) No. 4 and (d) No. 8.

The No. 4 sample was doped into the conventional micron  $\beta$ -Ni(OH)<sub>2</sub> at ratios of 5%, 8% and 12%, respectively. The results of charging and discharging experiments are shown in Figure 3. The nano  $\beta$ -Ni(OH)<sub>2</sub> doping increases the electrode specific capacity, in which the 8% nano  $\beta$ -Ni(OH)<sub>2</sub> doping increased the 11% electrode specific capacity.



**Figure 3.** Results of charging and discharging experiments of samples with (a) no doping, (b) 5% doping, (c) 8% doping and (d) 12% doping.

## References

1. Chou Z., Yan J., Zhang R., *Chinese J. Inorg. Mater.*, **13** (1998) 674.
2. Zhai Q., Qiu S., Xia F., *Chinese Chem. Res. Appl.*, **10** (1998) 226.
3. Chu W., Wu Y., You J., *J. Power Tech.*, **22** (1998) 256.
4. Tan Z., Wang J., *Chinese J. Power Source Tech.*, **23** (1998) 31.
5. Reisner D. E., Salkind A. J., Strutt P. R., *J. Power Source*, **65** (1997) 231.
6. Xia X., Wei Y., *Chinese J. Inorg. Mater.*, **13** (1998) 674.

## SOLID SUPERACIDS OF SULFATED ZIRCONIA-SILICON NANOCRYSTALS

HUA YANG\* AND RONG LU

*College of Chemistry, Jilin University, Changchun, P. R. China, 130023*

*E-mail: huayang86@sina.com*

The precursors of sulfated zirconia-silicon nanocrystals were prepared by chemical methods in three steps. The precursors were calcined at different temperatures to form the  $\text{SO}_4^{2-}/\text{ZrO}_2\text{-SiO}_2$  nanocrystalline catalysts. The reaction conditions were investigated, such as  $\text{ZrO}_2$  content, volume ratio of water-ethanol, the amount of  $\text{HNO}_3$  and reactive temperature and time. The specific surface area, heat stability and structure properties of the catalysts were examined by XRD, IR and DTA. The surface areas of  $\text{ZrO}_2\text{-SiO}_2$  and  $\text{SO}_4^{2-}/\text{ZrO}_2\text{-SiO}_2$  are 800 and  $400 \text{ m}^2/\text{g}$ . They are higher than those of  $\text{ZrO}_2$  and  $\text{SO}_4^{2-}/\text{ZrO}_2$ . It is shown that there are very strong interactions between  $\text{SO}_4^{2-}$  and  $\text{ZrO}_2\text{-SiO}_2$ . The acidic properties of  $\text{SO}_4^{2-}/\text{ZrO}_2\text{-SiO}_2$  were tested by Hammett Indicator method. Through the acetic acid reaction with glycerin, it is shown that the  $\text{SO}_4^{2-}/\text{ZrO}_2\text{-SiO}_2$  catalyst has higher active sites and catalytic activity.

### 1 Introduction

The study on sulfated metal oxides, first reported in 1976 [1-2], has become an active area of research because of the high catalytic activity for carbon-cationic reactions manifested by such compositions [3-7]. It is well known that some sulfate metal oxides are strong solid superacids. It has been found [8] that superacid sites are formed during the sulfation using  $\text{H}_2\text{SO}_4$ ,  $(\text{NH}_4)_2\text{SO}_4$ ,  $\text{SO}_3$ ,  $\text{SO}_2$  or  $\text{H}_2\text{S}$ , provided that the optimal calcination temperature for each one is used. However, more research needs to be carried out in order to improve the knowledge of two aspects of these materials. The first one is the systematic study of each one of the catalyst preparation steps going from the formation of the most adequate source for metal oxide up to the final sulfated form [9-11]. The second aspect involves developing characterization techniques for measuring adequately the acidity of these materials. One representation of structure is that each sulfur atom is connected to the lattice through two tri-coordinated oxygen atoms, a rather peculiar bonding scheme [12]. Another structure model presented the sulfur bonded to three metal atoms by  $\text{S-O-M}$  bonds, and indicated that Bronsted acidity is generated by cleavage of one of these bonds by water and formation of an  $(\text{M-O})_2\text{S}(=\text{O})\text{-OH}$  group [10,12-14], which implies that the oxidation state of sulfur would be +5.

The catalytic activity of these materials depends upon the sulfur content. When the sulfur loading in the catalyst increases, structures with  $\text{S-O-S}$  bonds similar to those in pyrosulfuric or higher polysulfuric acids may exist on the surface of the catalysts.

In many cases, the components are inactive while their mixtures have a high catalytic activity. Thus, recently many kinds of mixed oxides were reported to show catalytic activity for particular reactions [15-18]. Among these solid superacids  $\text{SO}_4^{2-}/\text{ZrO}_2$  is the most outstanding one, as its acidic strength is ten thousand times higher than that of 100%  $\text{H}_2\text{SO}_4$ , and its thermal stability is rather high.  $\text{SiO}_2$  alone is impractical as a catalyst because of its low catalytic activity. However, nanocrystalline  $\text{SiO}_2$  has high specific surface area, so sulfated mixed oxide combining  $\text{ZrO}_2$  with  $\text{SiO}_2$  ( $\text{SO}_4^{2-}/\text{ZrO}_2\text{-SiO}_2$ ) will have higher surface area, more catalytically active sites, and better catalytic activity.

However, little has been reported about the acidic and catalytic properties of  $\text{SO}_4^{2-}/\text{ZrO}_2\text{-SiO}_2$ . In this paper,  $\text{SO}_4^{2-}/\text{ZrO}_2\text{-SiO}_2$  nanocrystalline catalysts were prepared by a chemical method. The structure, acidic properties and catalytic activity of the catalysts were investigated by using X-ray diffraction (XRD), IR, DTA, Hammett indicators and catalytic esterification reaction of acetic acid with glycerin.

## 2 Experimental

The  $\text{ZrO}_2\text{-SiO}_2$  nanocrystallites were prepared in two steps. First, to a  $\text{Zr}(\text{OH})_4$  gel prepared from a  $\text{ZrOCl}_2$  solution with a certain amount of surfactant of 16-alkyltrimethylammoniumbromide was added an  $\text{NH}_4\text{OH}$  solution until the solution pH was close to 10 at room temperature.  $\text{HNO}_3$  was mixed and soled with the  $\text{Zr}(\text{OH})_4$  gel in the water pool to make a  $\text{Zr}(\text{OH})_4$  sol. Second,  $\text{Zr}(\text{OH})_4\text{-Si}(\text{OH})_4$  mixed gel was prepared. The solution with a particular ratio of water-ethanol was added to a tetraethoxysilane  $\text{Si}(\text{OC}_2\text{H}_5)_4$  solution, then stirred for a certain period. The  $\text{Si}(\text{OH})_4$  solution was mixed with the  $\text{Zr}(\text{OH})_4$  sol to prepare a  $\text{Zr}(\text{OH})_4\text{-Si}(\text{OH})_4$  gel. The precipitated gel was stirred in the water pool for 5h, and then washed with deionized water. The precipitate was allowed to dry for 12h at 100°C to prepare the precursor which is the  $\text{Zr}(\text{OH})_4\text{-Si}(\text{OH})_4$  complex.

The precursors were placed in a stirred solution of 1M  $\text{H}_2\text{SO}_4$  solution for 2h. The solids,  $\text{SO}_4^{2-}/\text{ZrO}_2\text{-SiO}_2$ , were then filtered and dried at 100°C for 12h. The sulfated precursors were powdered and calcined at different temperatures for 2-6h to prepare the  $\text{SO}_4^{2-}/\text{ZrO}_2\text{-SiO}_2$  nanocrystalline catalysts.

The X-ray diffraction (XRD) patterns were collected on a RIGAKU diffractometer, operated at 30kV and 20 mA and using  $\text{CuK}\alpha$  radiation ( $\lambda=0.15405\text{nm}$ ). The specific surface areas of the catalysts were tested on a home-made analyzer, following the BET method from air isotherms determined at liquid nitrogen temperature. The structure properties of the catalysts were characterized by IR spectroscopy using a PE-783 IR spectrometer. The amount of samples were mixed with KBr in form of disks, and the spectra were taken at room temperature.

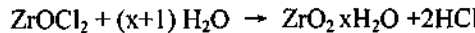
The total acidities of the samples were determined by temperature-programmed desorption of ammonia (TPD). The sample was first treated at 923K for 1h, then saturated with ammonia at 373K. Weakly adsorbed  $\text{NH}_3$  was eliminated by treatment under dry nitrogen at the same temperature, and the temperature subsequently was raised up to 923K at 10K/min under dry nitrogen. The amount of  $\text{NH}_3$  evolved from the sample was determined by conductimetry. The acid strength of the samples was measured by Hammett indicators. The samples were heated under vacuum system at 200°C for one hour, then connected with the vapor of Hammett indicators and the colors of the indicators with different  $\text{pK}_a$  were observed. Differential thermal (DTA) analysis was carried out by using a PE-1700 analyzer.

The catalytic experiments were carried out in a reactor at atmospheric pressure. A certain amount of glycerin, acetic acid and toluene were put in this reactor, and the  $\text{SO}_4^{2-}/\text{ZrO}_2\text{-SiO}_2$  catalyst was added too into the reactor. The reactor temperature was 120°C, and the conversion of this catalyst was assessed by testing the acid concentration.

## 3 Results and Discussion

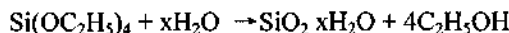
The  $\text{SO}_4^{2-}/\text{ZrO}_2\text{-SiO}_2$  nanocrystalline catalysts were prepared by a chemical method in three steps. First,  $\text{Zr}(\text{OH})_4$  sols were prepared from the  $\text{ZrOCl}_2$  solution reaction with

water. The reaction equation is as follows:



In order to facilitate the hydrolysis,  $\text{NH}_3 \cdot \text{H}_2\text{O}$  was added to the  $\text{ZrOCl}_2$  solution.  $\text{ZrO}_2 \cdot \text{xH}_2\text{O}$  or  $\text{Zr}(\text{OH})_4$  was prepared, which is a white gel containing some water, also called  $\alpha\text{-H}_4\text{ZrO}_4$  ( $\alpha$ -Zirconic acid). It can be dissolved in a dilute acid to form a transparent sol. Upon heating treatment, the gel forms a precipitate called  $\beta\text{-H}_4\text{ZrO}_4$ . It contains a small amount of  $\text{H}_2\text{O}$  and is difficult to get dissolved in any acid. In the preparation of  $\text{Zr}(\text{OH})_4$ ,  $\text{HNO}_3$  is used as a soling agent to sol for  $\text{ZrO}_2 \cdot \text{xH}_2\text{O}$ .

In the second step, tetraethoxysilane is hydrolyzed under acidic conditions as follows:



This reaction proceeds slowly at room temperature. But acids catalyze the hydrolysis.

$\alpha\text{-Zr}(\text{OH})_4$  sol and the water-ethanol solution with the tetraethoxysilane were mixed completely. The acid in the  $\text{Zr}(\text{OH})_4$  sol catalyzes the hydrolysis of the tetraethoxysilane, and the process is heated at various temperatures, so  $\beta\text{-H}_4\text{ZrO}_4$  precipitate was formed from the  $\alpha\text{-Zr}(\text{OH})_4$  sol. Because two processes of the hydrolysis and precipitate proceeded simultaneously, binary mixed oxides of  $\text{ZrO}_2\text{-SiO}_2 \cdot \text{xH}_2\text{O}$  with the hydration water were formed. It was dried at  $100^\circ\text{C}$  and calcined at different temperatures to prepare the  $\text{ZrO}_2\text{-SiO}_2$  complex oxide. In the processes of the hydrolysis and precipitate, the amount of  $\text{HNO}_3$  is an important factor. It promotes the  $\text{ZrO}_2$  to sol, and catalyzes the hydrolysis of the tetraethoxysilane. Adding different amounts of  $\text{Zr}(\text{OH})_4$  in the tetraethoxysilane is equal to add different amounts of  $\text{HNO}_3$  solution.

In the last step, the  $\text{ZrO}_2\text{-SiO}_2$  complex oxide was impregnated in a solutin of differnet concentrations of  $\text{H}_2\text{SO}_4$  solution. The impregnated concentration of  $\text{H}_2\text{SO}_4$  solution affects the catalytic conversion of acetic acid reaction with glycerin. Table 1 shows the effect of  $\text{H}_2\text{SO}_4$  concentration on the catalytic conversion of acetic acid (HAc). From Table 1, the conversion of HAc is the highest when the concentration of  $\text{H}_2\text{SO}_4$  solution is 1M. When the concentration is lower, there are few  $\text{SO}_4^{2-}$  ions on the surface of the catalysts, and there are less acidic sites and the conversion of Hac is low. When the concentration is higher, the sulfate catalysts are formed easily on the surface of the support, and the acidic sites decrease. The optimum concentration of  $\text{H}_2\text{SO}_4$  is 1M.

Table 1. Effect of  $\text{H}_2\text{SO}_4$  concentration on the conversion of Hac.

[ $\text{H}_2\text{SO}_4$ ] (M)	The conversion of HAc (%)
0.50	0.4713
0.75	0.5375
1.00	0.6254
1.25	0.5755
1.50	0.5621

Now the reactive conditions, such as  $\text{ZrO}_2$  content of catalysts, volume ratio of water-ethanol and the amount of  $\text{HNO}_3$ , are investigated.

The effect of  $\text{ZrO}_2$  content of the catalysts on the surface area of the  $\text{ZrO}_2\text{-SiO}_2$  complex is assessed. Te surface area of the sample calcined at  $500^\circ\text{C}$  is increased with

increasing  $\text{ZrO}_2$  content when it is smaller than 11.23 wt%. When the  $\text{ZrO}_2$  content of the complex oxides is 11.23 wt%, the specific surface area is the highest ( $800\text{m}^2/\text{g}$ ). It is shown that if the  $\text{ZrO}_2$  content is small, the complex oxides un-modified with  $\text{H}_2\text{SO}_4$  have higher specific surface areas. When the complex oxides are modified with  $\text{H}_2\text{SO}_4$ , more sulfated species form in the  $\text{SiO}_2$ . The catalysts modified with  $\text{H}_2\text{SO}_4$  have more acidic sites or catalytic sites.  $\text{ZrO}_2$  is dispersed uniformly in  $\text{SiO}_2$ . When the  $\text{ZrO}_2$  content of the catalysts is over 11.23 wt%, the specific surface area decreases. The specific surface area of the sulfated  $\text{ZrO}_2$  is generally  $100\text{m}^2/\text{g}$ ; whereas the specific surface areas of  $\text{ZrO}_2\text{-SiO}_2$  and  $\text{SO}_4^{2-}/\text{ZrO}_2\text{-SiO}_2$  are 800 and  $450\text{m}^2/\text{g}$ . It is shown that the specific surface area of the catalyst is increased because of the addition of  $\text{SiO}_2$ . Table 2 shows the effect of  $\text{ZrO}_2$  content on the specific surface area of  $\text{SO}_4^{2-}/\text{ZrO}_2\text{-SiO}_2$ .

Table 2. Effect of  $\text{ZrO}_2$  content on the specific surface area of  $\text{SO}_4^{2-}/\text{ZrO}_2\text{-SiO}_2$ .

$\text{ZrO}_2$ (wt%)	Specific surface area ( $\text{m}^2/\text{g}$ )
6.00	398.8
7.80	390.0
9.60	405.9
11.23	424.9
12.98	346.4
17.15	357.3
19.84	341.0
23.58	348.0

From Table 2, we see that the specific surface area of  $424.9\text{m}^2/\text{g}$  is the highest for the sample with 11.23 wt% of  $\text{ZrO}_2$ . The  $\text{ZrO}_2$  content of  $\text{SO}_4^{2-}/\text{ZrO}_2\text{-SiO}_2$  with the highest specific surface area is the same as that of  $\text{ZrO}_2\text{-SiO}_2$  complex oxides. However, the specific surface area of the modified catalysts decreases compared with that of the unmodified catalysts. It is different from single oxide modified with  $\text{H}_2\text{SO}_4$ , the specific surface area of  $\text{SO}_4^{2-}/\text{ZrO}_2$  is greater than that of pure  $\text{ZrO}_2$ .

The effect of the volume ratio of water-ethanol on the specific surface area of  $\text{ZrO}_2\text{-SiO}_2$  complex oxides is also studied. The tetraethoxysilane hydrolyzes slowly at room temperature, and it does not dissolve in water. However, it dissolves in the ethanol solution. When the amount of water-ethanol is added in the tetraethoxysilane, the uniform system of hydrolysis of tetraethoxysilane is formed. When the volume ratio of water-ethanol is 5, the specific surface area of the  $\text{ZrO}_2\text{-SiO}_2$  complex oxides and  $\text{SO}_4^{2-}/\text{ZrO}_2\text{-SiO}_2$  are greater ( $741.4$  and  $745.8\text{ m}^2/\text{g}$ , respectively). With a volume ratio of water-ethanol of 5, the water, ethanol and tetraethoxysilane are mixed and dissolved completely to form a uniform system. The system is beneficial to preparing the catalysts with higher specific surface areas and catalytic reactive sites.

The amount of  $\text{HNO}_3$  is also important to soling  $\text{Zr(OH)}_4$  and tetraethoxysilane hydrolysis because  $\text{HNO}_3$  gives  $\text{H}^+$  as an acidic catalyst in preparing  $\text{ZrO}_2\text{-SiO}_2$  and  $\text{SO}_4^{2-}/\text{ZrO}_2\text{-SiO}_2$ . The  $\text{HNO}_3$  is important to the soling of  $\text{Zr(OH)}_4$  and the hydrolysis of tetraethoxysilane, so the volume of  $\text{HNO}_3$  and soling  $\text{Zr(OH)}_4$  affects the specific surface area of the complex. When different volumes of soling  $\text{Zr(OH)}_4$  are added to the hydrolysis system of tetraethoxysilane, the amount of  $\text{HNO}_3$  is different. For preparing the catalysts with optimum specific surface area, the optimum total volume of  $\text{HNO}_3$  and soling  $\text{Zr(OH)}_4$  must be selected. In the range of 12-16mL, the  $\text{ZrO}_2\text{-SiO}_2$  has higher specific surface area, so the  $\text{ZrO}_2$  content, the volume ratio of water-ethanol and the amount of  $\text{HNO}_3$  all affect the specific surface area of  $\text{ZrO}_2\text{-SiO}_2$ .

The  $\text{ZrO}_2\text{-SiO}_2$  and  $\text{SO}_4^{2-}/\text{ZrO}_2\text{-SiO}_2$  catalysts calcined at 500°C for 2h were examined by XRD. The XRD pattern of pure  $\text{ZrO}_2$  is proved to be the tetragonal phase. This phase is characterized by a peak at  $2\theta=30.0$ , which corresponds to the (111) reflection. Some peaks indicate the presence of a mixture of tetragonal and monoclinic phase. The monoclinic form presents peaks at  $2\theta=28.0^\circ$  and  $32.0^\circ$ , which correspond to the (111) and (11-1) reflections. When the  $\text{ZrO}_2$  content of  $\text{ZrO}_2\text{-SiO}_2$  is 23.58 wt% there is a characteristic diffraction peak of tetragonal phase of  $\text{ZrO}_2$  at  $2\theta=30.0^\circ$ . We believe that the smaller particles of  $\text{ZrO}_2$  are dispersed in  $\text{SiO}_2$ . When the  $\text{ZrO}_2$  content is less than 23.58 wt%, the XRD pattern of  $\text{ZrO}_2\text{-SiO}_2$  is amorphous. The amorphous binary oxides were formed because most Zr atoms enter into the crystal lattice of  $\text{SiO}_2$ . With increasing  $\text{ZrO}_2$  content, amorphous  $\text{ZrO}_2$  transforms to tetragonal phase of  $\text{SiO}_2$  restraining the crystallization of  $\text{ZrO}_2$ . The restraining function may make the catalyst to have higher specific surface area, and the catalysts have higher catalytic activity. The structure of  $\text{SO}_4^{2-}/\text{ZrO}_2\text{-SiO}_2$  is amorphous from the XRD patterns of  $\text{SO}_4^{2-}/\text{ZrO}_2\text{-SiO}_2$ . In comparison, there are not tetragonal phases of  $\text{SO}_4^{2-}/\text{ZrO}_2\text{-SiO}_2$ . It is shown that adding  $\text{SO}_4^{2-}$  ions restrains crystallization of  $\text{ZrO}_2$  and increases the crystallization temperature of  $\text{ZrO}_2$ .

The DTA curves of  $\text{ZrO}_2\text{-SiO}_2$  and  $\text{SO}_4^{2-}/\text{ZrO}_2\text{-SiO}_2$  show an endothermic peak of dehydration at about 200°C. This may be because that water exists in the porous catalysts, and therefore, the  $\text{ZrO}_2\text{-SiO}_2$  prepared by us is a porous binary oxides. Between 400°C and 1000°C, there is no endothermic or exothermic peak, except for a smaller exothermic signal at 900°C with 23.58 wt% of  $\text{ZrO}_2$  content. This peak may correspond to the crystallization of  $\text{ZrO}_2$ . It is shown, too, that  $\text{SiO}_2$  makes the crystallization temperature of  $\text{ZrO}_2$  in the binary oxides to increase so that it improves the thermal stability of the binary oxides. The thermal stability of  $\text{SO}_4^{2-}/\text{ZrO}_2\text{-SiO}_2$  is examined by DTA. The endothermic peak of dehydration is located at 117°C. It is shown that there are some porous structures in the  $\text{SO}_4^{2-}/\text{ZrO}_2\text{-SiO}_2$  catalysts. On the other hand, another endothermic peak exists at 748°C. This may be an endothermic peak for sulfur component decomposing on the surface of the  $\text{SO}_4^{2-}/\text{ZrO}_2\text{-SiO}_2$  catalysts. It is shown that the  $\text{SO}_4^{2-}/\text{ZrO}_2\text{-SiO}_2$  has higher thermal stability, and the stability is higher than that of  $\text{SO}_4^{2-}/\text{ZrO}_2$ .

A series of  $\text{ZrO}_2\text{-SiO}_2$  and  $\text{SO}_4^{2-}/\text{ZrO}_2\text{-SiO}_2$  catalysts calimed at 500°C are examined by IR absorption. The bands at 1225, 1070 and 800  $\text{cm}^{-1}$  belong to the stretching vibrations of the Si-O bonds. The band at 470  $\text{cm}^{-1}$  is due to the bending vibration of the Si-O of  $\text{SiO}_2$ , and the band at 980  $\text{cm}^{-1}$  arises from the Si-OH vibration of  $\text{SiO}_2\cdot\text{H}_2\text{O}$ . In comparison with the IR spectra of pure  $\text{ZrO}_2$  or  $\text{SiO}_2$ , it is clear that no compound is formed between  $\text{ZrO}_2$  and  $\text{SiO}_2$  because there is no new band in the IR spectra of the  $\text{ZrO}_2\text{-SiO}_2$  complex. It is in accordance with the results of the X-ray diffraction analysis which shows no new phase is formed between  $\text{ZrO}_2$  and  $\text{SiO}_2$ . With increasing  $\text{ZrO}_2$  content, the vibration of Si-OH disappears and the stretching vibration of Si-O between 1200 and 1000  $\text{cm}^{-1}$  shifts gradually to lower wavenumbers. It is indicated that adding  $\text{ZrO}_2$  content decreases the vibration frequency of Si-O. In other words, the  $\text{ZrO}_2$  interacts with the  $\text{SiO}_2$  on a molecular level. From the site and strength shifts of the vibration bands, it can be concluded that Zr-O-Si bonds exist in the complex.

The acidic strengths of the  $\text{SO}_4^{2-}/\text{ZrO}_2\text{-SiO}_2$  catalysts with 11.23 wt% of  $\text{ZrO}_2$  after calcination at 500°C for 3h are examined using a flow Hammett indicator method in Table 3. The acidic strength of a solid is defined as the ability of the surface to convert an adsorbed neutral base into its conjugate acid. Thus, the color of suitable indicators absorbed on a surface can give a measure of its acid strength. If the color is that of the acid form of the indicator, then the value of the Hammett  $H_o$  function of the surface is equal to

or lower than the  $pK_a$  of the conjugate acid of the indicators. Lower values of  $H_o$  correspond to greater  $pK_a$ , and higher acid strength of the solid.

Table 3. The acid strength of  $\text{SO}_4^{2-}/\text{ZrO}_2\text{-SiO}_2$ .

Hammett indicator	$pK_a$ of indicator	$\text{SO}_4^{2-}/\text{ZrO}_2\text{-SiO}_2$	$\text{SO}_4^{2-}/\text{ZrO}_2$	$\text{SO}_4^{2-}/\text{SiO}_2$
Benzalacetophenone	-5.6	+	+	+
Anthraquinone	-8.2	+	+	-
p-nitro-methybenzene	-11.35	+	+	-
p-nitro-chlorbenzene	-12.70	+	+	-
2,4-dinitro-methybenzene	-13.75	+	+	-
2,4-dinitro-fluorobenzene	-14.52	±	+	-
Trichlorbenzene	-16.12	-	+	-

The acid strength of  $\text{SO}_4^{2-}/\text{SiO}_2$  is estimated to be  $H_o \leq -5.6$ , and that of  $\text{SO}_4^{2-}/\text{ZrO}_2$  is  $H_o \leq -16.12$ . Acids with a strength higher than  $H_o = -11.93$  are superacids, and this strength corresponds to that of 100%  $\text{H}_2\text{SO}_4$ . From Table 5, we can see that the acid strength of  $\text{SO}_4^{2-}/\text{ZrO}_2\text{-SiO}_2$  is  $H_o \leq -14.52$ , so that it is a solid superacid and its acid strength is lower than that of  $\text{SO}_4^{2-}/\text{ZrO}_2$ . The superacid properties are attributed to the double bond nature of the S=O in the complex formed by the interaction of  $\text{ZrO}_2\text{-SiO}_2$  with the sulfated ions. The  $\text{SO}_4^{2-}/\text{ZrO}_2\text{-SiO}_2$  catalysts show high acid strength as well as high catalytic activity.

The catalytic activities of  $\text{SO}_4^{2-}/\text{ZrO}_2\text{-SiO}_2$  catalysts are tested by the acetic acid reaction with the glycerin. Table 6 shows the effect of  $\text{ZrO}_2$  content on the conversion of HAc of the  $\text{SO}_4^{2-}/\text{ZrO}_2\text{-SiO}_2$  catalysts. The reactive conditions are as follows: 0.5g catalyst, 0.1mol glycerin, 0.4mol HAc and 20ml toluene. After the catalyst is added into the reaction system, the reaction temperature is increased into 120°C, the esterification reaction proceeds for 2h. The conversion of HAc is calculated by the amount of HAc in the system and by the acid-base titration. The results are presented in Table 6. When the  $\text{ZrO}_2$  content is lower or higher than 11.23 wt%, the conversions of HAc are lower relatively. When the  $\text{ZrO}_2$  content is 11.23 wt%, the conversion is up to 89%. It is shown that the conversion of HAc or the catalytic activity of the catalyst is a function of  $\text{ZrO}_2$  content. When the  $\text{ZrO}_2$  is added into the  $\text{SiO}_2$ , the  $\text{ZrO}_2\text{-SiO}_2$  complex which is sulfated with the  $\text{H}_2\text{SO}_4$  exhibits a remarkable increase in acidity.

#### 4 Conclusions

The  $\text{ZrO}_2\text{-SiO}_2$  precursors have been prepared in two steps, then sulfated with  $\text{H}_2\text{SO}_4$  to form the  $\text{SO}_4^{2-}/\text{ZrO}_2\text{-SiO}_2$  followed by calcination at various temperatures. The effects of the  $\text{ZrO}_2$  content, the volume ratio of water-ethanol and the amount of  $\text{HNO}_3$  on the specific surface area of  $\text{SO}_4^{2-}/\text{ZrO}_2\text{-SiO}_2$  catalysts have been assessed. The  $\text{ZrO}_2\text{-SiO}_2$  nanocrystals with a high specific surface area are prepared. The structure properties and thermal stability of the  $\text{ZrO}_2\text{-SiO}_2$  complex are examined by XRD, IR and DTA. The acid strength of the  $\text{SO}_4^{2-}/\text{ZrO}_2\text{-SiO}_2$  catalyst is slightly lower than that of  $\text{SO}_4^{2-}/\text{ZrO}_2$  and its specific surface area is about  $400\text{m}^2/\text{g}$ , higher than that of  $\text{SO}_4^{2-}/\text{ZrO}_2$  ( $100\text{m}^2/\text{g}$ ). Strong interactions exist between  $\text{SO}_4^{2-}$  and  $\text{ZrO}_2\text{-SiO}_2$ . The thermal stability of  $\text{SO}_4^{2-}/\text{ZrO}_2\text{-SiO}_2$  is equivalent to that of  $\text{SO}_4^{2-}/\text{ZrO}_2$ .

The  $\text{SO}_4^{2-}/\text{ZrO}_2\text{-SiO}_2$  has high catalytic activity for the esterification reaction between acetic acid and glycerin. The conversion of HAc reaches 89%, if the  $\text{ZrO}_2$  content is 23.11

wt%. This conversion value is much higher than that of  $\text{SO}_4^{2-}/\text{ZrO}_2$  catalyst which shows a value of 40% for the same esterification reaction.

## References

1. Tanabe K., *Preparation of Catalysts*, (1976) pp. 65.
2. Mishra H. K. and Parida K. M., *Appl. Catal. A : General*, **224** (2002) pp. 179.
3. Yamaguchi T., *Appl. Catal. A : General*, **222** (2001) pp. 237.
4. Hua W., Goeppert A. and Sommer J., *Appl. Catal. A : General*, **219** (2001) pp. 201.
5. Moreno J. A. and G. Poncelet G., *Appl. Catal. A : General*, **210** (2001) pp. 151.
6. Paál Z., Wild U. and Muhler M., *Appl. Catal. A : General*, **188** (1999) pp. 257.
7. Sassi A. and Sommer J., *Appl. Catal. A : General*, **188** (1999) pp. 155.
8. Matsuhashi H., Shibata H., Nakamura H. and Arata K., *Appl. Catal. A : General*, **187** (1999) pp. 99.
9. Matsuhashi H., Tanabe T., *Proc. Inter. Symp. Acid-base Catal. Sappora*, Tokyo: Kodanha , (1998) pp. 357.
10. Carata K., *Appl. Catal.*, **59** (1990) pp. 197.
11. Sohn J. R. and Jang H. J., *J. Mol. Catal.*, **64** (1991) pp. 349.
12. Navarrete J., Lope T. and Gomez Z. R., *Langmuir*, **12** (1996) pp. 4385.
13. Carata K., *Appl. Catal.*, **59** (1990) pp. 197.
14. Sohn J. R. and Jang H. J., *J. Mol. Catal.*, **64** (1991) pp. 349.
15. Navarrete J., Lope T. and Gomez Z. R., *Langmuir*, **12** (1996) pp. 4385.
16. Wen. M. Y., Wender I. et al., *Energy and Fuels*, **4** (1990) pp. 372.
17. Arata K. and Hino M., *Mater. Chem. Phys.*, **26** (1990) pp. 213.
18. Hino M., et al., *Appl. Catal.*, **59** (1990) pp. 197.
19. Hudson M. J. and Knowles J. A., *J. Mater. Chem.*, **6** (1996) pp. 95.
20. Lopez T., Navarrete J., et al., *Appl. Catal. A : General*, **125** (1995) pp. 217.
21. Sohn J. R., Jang H. J. et al., *J. Mol. Catal.*, **93** (1994) pp. 149.

This page is intentionally left blank

## **Part V**

### **New Synthetic Methods, Characterization and Theory**

This page is intentionally left blank

# MICROWAVE HYDROTHERMAL PARTICLE GROWTH OF COLLOIDAL SILICA

C. FALAMAKI

*Ceramics Department, Materials & Energy Research Center, P. O. Box 14155-4777, Tehran, Iran  
E-mail: cavus\_falamaki@yahoo.com*

A new method for the hydrothermal growth of dilute colloidal silica from an initial value of 3 nm to a final value up to 13 nm has been introduced. Microwave heating of the sol in a polyethylene autoclave with a net heat input of 66.3 cal s<sup>-1</sup> for less than 100 s resulted in a significant growth of the colloidal particles. The activation energy of the growth process has been calculated to be 2.92 kcal mole<sup>-1</sup>. The latter is significantly lower from the reported values for the conventional hydrothermal heating (>10 kcal mole<sup>-1</sup>). Although the SiO<sub>2</sub> / Na<sub>2</sub>O molar ratio of the sols investigated had been less than 30:1, no gelling occurred during the process. However, slight coagulation in some cases was observed. The latter was attributed, to some extent, to the memory effect of the polyethylene walls.

## 1 Introduction

Colloidal silica is a dispersion of mono or poly modal silica particles in a liquid medium (usually water) in which the particle size is within colloidal range. Different grades are produced in a large scale by several manufacturers (e.g. Ludox and Syton of Du Pont). The production process basically consists of the preparation of an initial dilute sol of less than 4 nm particle size and further growth of the particles. The initial sol is usually produced via ion exchange of a dilute sodium silica aqueous solution [1,2]. The growth process is performed in well-mixed reactors at atmospheric pressures under careful pH control [3,4] or by superatmospheric autoclaving procedures [5,6]. Considering the latter method, the activation energy for particle growth in basic solutions (pH>8.5) has been reported to be above 10 kcal mole<sup>-1</sup> [7]. The present work discloses a new method for increasing the size of dilute silica sols (3.11 wt. % SiO<sub>2</sub>) from 2-4 nm up to 13 nm applying microwave hydrothermal heating.

The use of microwave power in the synthesis of advanced materials is an emerging new technique, which is growing with a high speed. Zeolites [10] and zeolite-like materials (AlPO<sub>4</sub>-5) [11] have been successfully synthesized according to this procedure. Mesoporous and microporous alumina powders have been recently synthesized using the microwave heating technique [12].

## 2 Methods

A commercial Iranian sodium silicate solution (Sanaee Silicate Iran) with the following specifications was used: SiO<sub>2</sub> 42.03 wt. %, SiO<sub>2</sub> / Na<sub>2</sub>O 2.85 (molar ratio), Al 1.22 ppm and Fe 0.272 ppm. The latter was diluted to 3.11 wt. % SiO<sub>2</sub> by adding distilled water. Some 65 cm<sup>3</sup> of this solution was brought into contact with 30 g humidity equilibrated H-form PUROLITE C-100 (strong acid cation exchanger resin) for at least 3 minutes to get a stable pH of 2.78. The silica sol formed was filtered and its pH raised with addition of caustic soda. The final solution was introduced into a polyethylene autoclave designed appropriately (Figure 1).

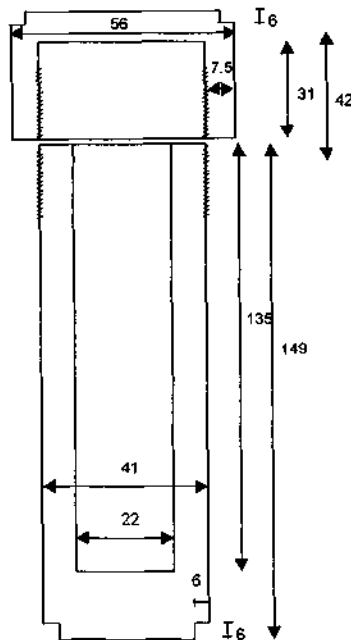


**Figure 1.** Schematic representation of the autoclave.

The sealed autoclave was put in a conventional microwave oven (BUTANE) with a nominal power of 1000 W and frequency of 2455 MHz. After heating for the predetermined period of time, the autoclave was quenched in cold water and part of the resultant sol was immediately analyzed by the Sear's method [8]. In some cases, specific area determination was performed by the BET method. For this means, the pH of the colloidal solutions were adjusted to 7 using a 0.13 N HCl solution. Then, n-propyl alcohol (with a volume equal to the colloidal solution obtained) was added. The obtained gel was allowed to dry overnight at RT. A Syton X30 sample of known specific area was used as standard. Light absorbance of the filtered samples was performed using SP6-500, PYE UNICAM spectrophotometer apparatus at a wavelength of 400 nm. Three different sets of experiments were performed with an initial pH of 8, 8.5 and 9.3 (series A, B and C, respectively). A separate set of experiments was performed to evaluate the actual heat input to the fluid in the autoclave during microwave heating. This was done by heating the autoclave for different periods of time and by evaluating the net heat input by calorimetric calculations considering the initial and final liquid temperatures. For this experiments the fluid temperature was never allowed to exceed 100 °C and the heat capacity of the polyethylene autoclave was reasonably neglected (due to short time periods employed, the temperature rise of the autoclave itself was negligible).

### 3 Results and Discussion

The following correlation has been obtained for the evaluation of the specific area by the Sear's method:

$$A = 26.595 (V - 0.25)$$

where A is the specific area ( $\text{m}^2 \text{ g}^{-1}$ ) and V the volume of the titrant (0.1 N NaOH solution). Considering the colloidal particles to be spherical, the specific area had been related to the average particle diameter using the following equation:

$$d = 2720 / A$$

where the unit of d is micron. The average particle diameter versus time of microwave heat treatment is shown on Figure 2.

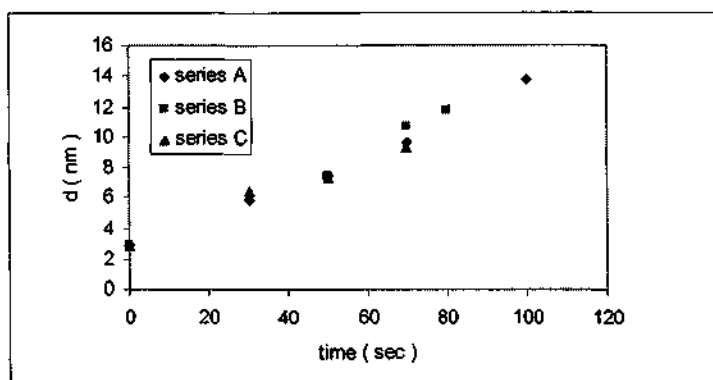


Figure 2. Average particle diameter versus hydrothermal microwave treatment time.

The trend of the curves shows an approximate linear relationship (low activation energy). An interesting observation is that particles could be grown from under 4 nm up to 13 nm in less than 2 minutes without gel formation, a phenomenon not reported earlier. Growth of silica particles of a 4 wt. %  $\text{SiO}_2$  basic solution ( $8 < \text{pH} < 10$ ) up to 12 nm in 10 minutes at 200 °C and 15 nm in 3 h at 160 °C by conventional autoclaving have been reported previously [9]. Additionally, it is observed that the initial pH has no appreciable effect on the growth process. Figure 3 shows that the solution pH undergoes a significant rise during each experiment. Although in each case a plateau in the pH value is observed, the particle growth rate seems to keep a constant value.

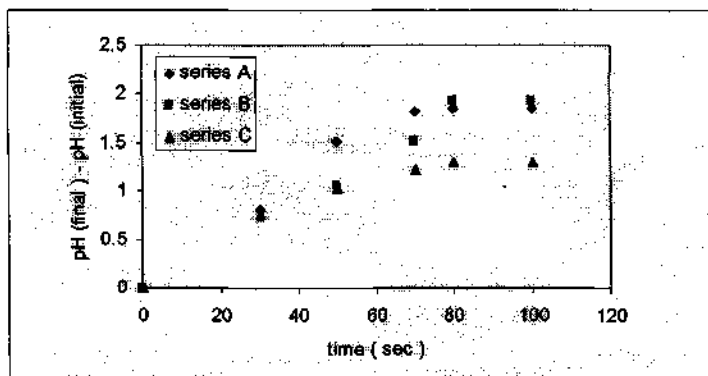


Figure 3. Variation of pH with hydrothermal treatment time.

It is noteworthy to investigate the efficiency of the BET method for the measurement of the surface area of the colloidal particles obtained in the range of 3-13 nm. Figure 4 shows that, in general, the BET method results in lower values of the specific area. This is attributed to the particle agglomeration during the transformation of the colloidal sol to solid powder. Using the results of the series A experiments and considering the net heat input power previously calculated, the pertaining temperatures had been estimated. Thereof, the activation energy of the process was estimated to be 2.92 kcal mole<sup>-1</sup> (Figure 5). This value is significantly less than the reported values for conventional hydrothermal heating (>10 kcal mole<sup>-1</sup>).

According to Table 1, the absorbance versus average particle diameter follows a nonlinear relationship. The slope change is significant for particles larger than 9 nm.

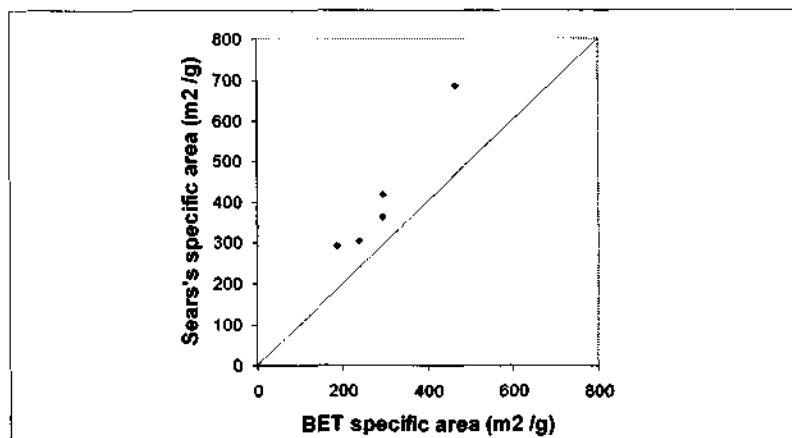


Figure 4. Comparison between the specific area evaluated by the Sera's and BET methods.

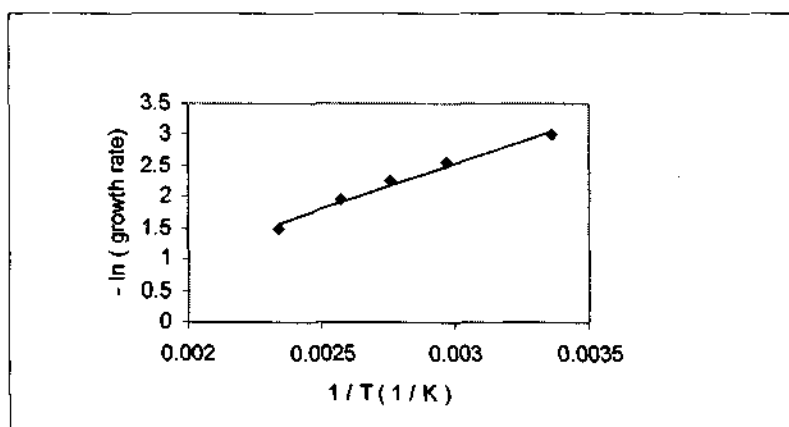


Figure 5. Variation of  $\ln$  (particle growth rate) versus reciprocal of temperature.

**Table 1.** Absorbance versus average diameter for the experiments of series A.

absorbance	.006	.028	.041	.055	.138
diameter ( $\mu\text{m}$ )	2.89	5.81	7.52	9.59	13.74

It has been observed that the final sols with an average particle diameter larger than 10 nm are contaminated with coagulated matter. The latter consisted of a threadlike or fiberlike network. Repeated experiments showed that this phenomenon was more pronounced if the inner walls of the polyethylene vessel were not completely polished before the hydrothermal process. Thus, it may be deduced that some sort of wall memory effect contributes to the formation of such fibrillar matter. On the other hand, the  $\text{SiO}_2 / \text{Na}_2\text{O}$  molar ratio of the final sols had been in the range of 20-30. It is well known that dilute sols (<6 wt. %  $\text{SiO}_2$ ) produced by ion exchange processes with a pH 8-9.5 are stable if their  $\text{SiO}_2 / \text{Na}_2\text{O}$  molar ratio is in the range of 30:1-130:1. Therefor, it is speculated that partial coagulation during the build up process of the colloidal particles might be avoided by optimizing the cation type, cation concentration and use of clean-wall autoclaves.

#### 4 Conclusions

The obtained results support the idea that the application of the microwave hydrothermal heating method might be a fast and efficient method for colloidal silica growth. It is well known that the obtained sols can be further concentrated by conventional evaporation methods to a maximum level dictated by the average particle diameter, pH and electrolyte concentration. It should be noted that, for the sols with average particle diameters larger than 12 nm, the quenching-cooling process might be partially substituted with a flashing process, during which cooling and concentration of the sol occur simultaneously.

#### References

1. Bechtold, M. F. and Snyder, O.E., *US Patent 2 574 902* (1951).
2. Mindick, M. and Reven, L. E., *US Patent 3 468 813* (1969).
3. Dirmberger, L. A. and Nelson, R.T., *US Patent 2 974 109* (1961).
4. Irani, F. A., *US Patent 3 789 009* (1979).
5. Alexander, G. B. and McWhorter, J. R., *US Patent 2 833 724* (1954).
6. Broge, E.C. and Iler, R. K., *US Patent 2 680 721* (1961).
7. Iler, R. K., The chemistry of silica, solubility, polymerization, colloid and surface properties and biochemistry (John Wiley and Sons, New York, 1979) p. 248.
8. *Ibid*, p. 353.
9. *Ibid*, p.253.
10. Jansen, J. C., Arafat, A., Barakat, A. K. and van Bekkum, H., Synthesis of microporous materials, Vol. 1, *Molecular Sieves* (van Nostrand Reinhold, New York, 1992), p. 507.
11. Girmus, I., Pohl, M. M., Mendau, J. R., Schneider, M., Noak, M., Venzke, D. and Caro, *Adv. Mater.* 7 (1995) 8, p. 711.
12. Deng, S. G. and Lin, Y. S., *J. Mater. Sci. Lett.* 16 (1997) p. 1291.

This page is intentionally left blank

# THE METHOD OF DETERMINATION OF THE SURFACE COMPOSITION OF THE Ir-Rh ALLOYS

MENGQIU JIA

*Beijing University of Chemical Technology, 15 Beisanhuan Donglu, 100029 Beijing, China*  
*E-mail: Jiamengqiu@263.net*

N. I. KUDRYASHOV AND A. MERETSKY

*D.Mendeleyev University of Chemical Technology of Russia, Miusskaya Sq. 9, Moscow 125047  
Russia*  
*E-mail: koref-gefest@mtu-net.ru*

The method of potentiodynamic pulses was applied for the study of the features of hydrogen adsorption on the iridium-rhodium alloys from sulfuric acid aqueous solutions. Hydrogen adsorption on rhodium and the alloys with all the values of Rh:Ir ratio in the range of medium surface coverage was well described by the Temkin logarithmic isotherm equation, while the features of hydrogen adsorption on the Ir- electrode are better fitted by the Freundlich isotherm equation. Hydrogen adsorption heat as a function of surface coverage for Ir-Rh –electrodes were obtained. The profile of the current-potential curve and position of the weakly bonded hydrogen adsorption on the potential scale are all related to the alloy compositions, thus can serve as the basis for the determination of the alloy surface composition.

## 1 Introduction

Hydrogen adsorption on the metals of the platinum group resulting from the hydroxonium ions discharge in the sulfuric acid solutions was under consideration in many studies [1-3]. Experimental data revealed an essential energy non-homogeneity of adsorbed hydrogen on these metals. Thus on the cathodic potentiodynamic  $i, E$ , curve for platinum and iridium electrodes, two forms of adsorbed hydrogen are observed, while on the rhodium and ruthenium, only one weakly bonded hydrogen form is manifested. Among binary systems prepared on the basis of platinum group metals, the behavior of the platinum-rhodium pair only has been studied in any detail against the hydrogen adsorption [4,5], the data on the mechanisms of hydrogen adsorption in other catalytic systems are practically absent.

In the present work, the results of the study of the adsorption properties of iridium-rhodium electrodes are presented, the features of the hydrogen adsorption process on such electrodes have never been studied before.

## 2 Experimental

Iridium-rhodium alloys were prepared in electric arc furnace in argon atmosphere by smelting refined powders of rhodium and iridium of 99.95 mass% purity. The composition of the alloys was controlled by the atomic adsorption analysis using the Perkin-Elmer spectrophotometer with HUS-72 analyzer. X-ray phase analysis indicated that all binary systems had a single-phase FCC-structure characteristic of

the substitutional solid solutions (Figure 1).

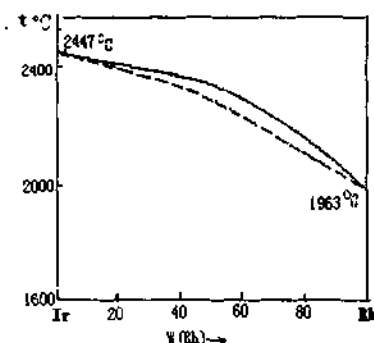


Figure 1. State diagram for the iridium-rhodium system.

The samples of 1 to 2 mm<sup>2</sup> cross-section were cut of the metal ingots by electrospark discharge method, the samples were then glass sealed so that the visible electrode surface was of 0.5 to 1 cm<sup>2</sup> [6]. The electrodes were treated on concentrated solutions of H<sub>2</sub>SO<sub>4</sub> and H<sub>2</sub>O<sub>2</sub> in order to remove mechanical and organic contaminants, repeatedly washed in distilled water and subjected to alternate anode and cathode polarization at the potential of  $E_r = 1.6$  и 0.0 V during 10-15 minutes. Thus prepared electrodes-catalysts were stored in 0.5 M H<sub>2</sub>SO<sub>4</sub> solution. Hydrogen adsorption was studied using the method of cathode potentiodynamic pulses which determines the adsorption value via the quantity of electricity passing through the electrode in the hydrogen range of the charging curve [7]. Adsorption measurements were taken using the equipment comprising PI-50-1 potentiostat, PR-8 programmer and S8-13 pulsed storage oscilloscope.

The system of potential pulses applied in this study consisted of two stages: a preparatory stage and a measuring one (Figure 2). At the preparatory stage of the potential pulses the electrode was kept at  $E_r = 1.2$  V for 20 seconds to oxidize the microimpurities adsorbed on the electrode, followed by the reduction of the oxidized surface at  $E_r = 0.0$  V for another 20 seconds. Then the electrode potential was increased to  $E_r = 0.4$  V in a step-wise way, from which a single cathode measuring pulse was applied with the potential sweep rate of 2 V/s. The quantity of electricity corresponding to the hydrogen adsorption value ( $Q_H^0$ ) was determined by integration the potential dynamic  $i, E_r$  - curve in the potential range from 0.4 to 0.0 V. On the cathode side, the area underneath the  $i, E_r$  - curve was limited by the hydrogen evolution curve extrapolated towards more positive potentials.

The values of the measured currents were transformed into currents on the unit

real electrode surface determined in the hydrogen range of the cathodic  $i, E_r$ -curve. During the calculations, it was assumed that a single-layer coverage on 1 cm<sup>2</sup> of the iridium and rhodium surface by the adsorbed hydrogen requires 210 and 220  $\mu C/s$  of electricity quantity, respectively [3,5]. In the case of binary Ir-Rh system, it was assumed that the quantity of electricity required to flow through the electrode to fill it with the monolayer of H<sub>ads</sub> changes linearly with the component compositions in the alloy.

A mercury-sulfate electrode served as a reference electrode. All electrode potentials are referred to the potential of the reversible hydrogen electrode in the same electrolyte and at the same temperature as the test electrode. Adsorption measurements were performed in the 0.5 M H<sub>2</sub>SO<sub>4</sub> solution prepared using special purity B-5 sulfuric acid and water doubly-distilled. To remove oxygen dissolved in the electrolyte, pure helium or argon was bubbled through acid solution.

### 3 Results and Discussion

Potentiodynamic  $i, E_r$ -curves of hydrogen adsorption on the Ir, Rh and their alloys in the 0.5 M H<sub>2</sub>SO<sub>4</sub> aqueous solution at 20°C are presented in Figure 2. The data demonstrates that the current-potential curve in the hydrogen adsorption region is substantially affected by the alloy composition. According to the data of [1,2], two adsorption peaks are observed for the Ir - electrode: a small maximum at  $E_r = 0.230$  V due to the strongly bonded adsorbed hydrogen, and a sharp maximum of weakly bonded hydrogen at  $E_r = 0.070$  V.

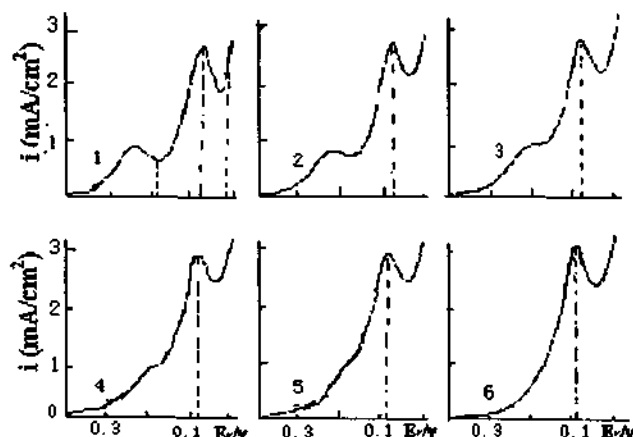


**Figure 2.** Potentiodynamic  $i, E_r$ -curves of hydrogen adsorption on the Ir (1), Rh (6) and Ir-Rh alloys, w(Rh) % : 20 (2), 40 (3), 60 (4) and 85 (5).

Incorporation of rhodium into the system results in the reduction of the adsorption maximum related to the strongly bonded hydrogen; already at 40 at % of Rh it degenerates into a shoulder. With further increase of rhodium concentration in the alloy, it practically disappears. At the same time, the current corresponding to the weakly bound hydrogen adsorption slightly increases. The position of the adsorption maximum shifts towards the anode side along the potential scale up to the value of  $E_r = 0.090$  V, typical for the Rh-electrode [3].

If the potential of the adsorption maximum of the weakly bound hydrogen is plotted on the ordinate axis, and the composition of the binary Ir-Rh system is plotted on the abscissa axis, then practically a linear dependence between these values can be traced (Figure 3).

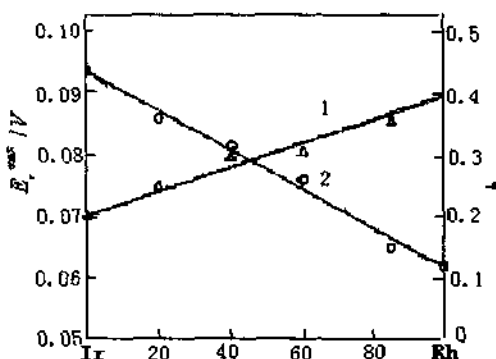


Figure 3. Dependence of the adsorption maximum of the weakly bonded hydrogen  $E_r^{\max}$  (1) and the value  $\gamma$  (2) on the alloy composition.

The increase of the rhodium contents in the alloy is accompanied by a substantial reduction of the strongly bound hydrogen portion. If we assume that the transition from one type of adsorbed hydrogen to another one occurs at  $E_r = 0.18$  V (the potential of the minimum on the cathodic  $i, E_r$  - curve of hydrogen adsorption on Ir-electrode), then we can estimate the ration of the strongly to weakly bonded hydrogen for the alloys of various compositions. The quantity of strongly bound adsorbed hydrogen corresponds to the area underneath the cathodic  $i, E_r$  - curve in the potential range from 0.40 to 0.18 V, and that of the weakly bonded hydrogen corresponds to the area limited by the potentials 0.18 and 0.0 V. As can be seen from Figure 2, the ratio of the quantities of strongly and weakly bonded hydrogen, expressed by the value  $\gamma = Q_{H,s} / Q_{H,w}$ , is a linear function of the alloy compositions.

The profile of the cathodic current-potential curve and the position of the

adsorption maximum of loosely bound hydrogen on the potential scale are practically unchanged in the course of adsorption and polarization measurements and hence are the characteristics of an alloy of specific composition. That is why the dependencies presented in Figure 2 together with the typical  $i, E_r$ -curve profile (Figure 1) can be used for a quantitative evaluation of both the bulk and the surface alloy composition.

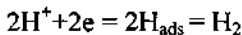
Graphical integration of the  $i, E_r$ -curve in the potential range  $0.4 - E_r, \text{V}$  is used to determine the quantity of electricity  $Q_H$  required for the hydrogen adsorption at a specified value of  $E_r$  ( $0.4 > E_r > 0.0 \text{ V}$ ). The values  $Q_H$  and  $Q_H^0$  are used to estimate the degree of the electrode surface coverage by hydrogen at a specific potential value  $E_r$ , using the formula:

$$\theta_H = \frac{Q_H}{Q_H^0} \quad (1)$$

The electrode potential value is related to the equilibrium pressure of molecular hydrogen via the equation:

$$E_r = -\frac{RT}{2F} \ln P_{H_2} \quad (2)$$

i.e. a certain value of the molecular hydrogen pressure corresponds to each potential value in the hydrogen adsorption region under the equilibrium conditions of the system:



When  $E_r$  values are calculated against equilibrium pressure values  $P_{H_2}$  using (2), the dependence  $\theta_H = f(P_{H_2})$ , shown in Figure 4, is obtained. When these dependencies are plotted, it was assumed that at any temperature, a monolayer coverage of the electrode surface with adsorbed hydrogen is achieved at  $P_{H_2} = 1 \text{ atm}$  ( $E_r = 0 \text{ V}$ ). In the range of medium coverage ( $0.2 < \theta_H < 0.8$ ) the hydrogen adsorption on the rhodium electrode is well described by the equation of Temkin logarithmic isotherm:

$$\theta_H = A + \frac{1}{f'} \ln P_{H_2} \quad (3)$$

with the surface non-homogeneity factor  $f' = 12.5$ . On the contrary, the data of adsorption measurements for Ir-electrode is better linearized in the coordinates  $\lg \theta_H - \lg P_{H_2}$ , i.e. it is described by Freundlich equation:

$$\theta_H = kP_{H_2}^{1/n'} \quad (4)$$

where  $n' = 10.5$ .

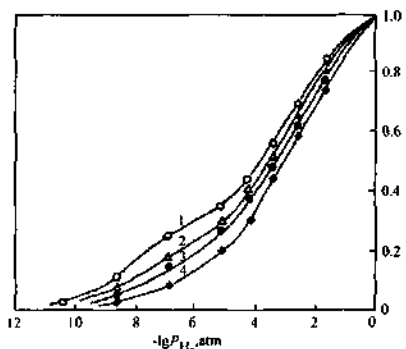


**Figure 4a.** Isotherms of hydrogen adsorption in the Coordinates  $\theta_H - \lg P_{H_2}$  at  $20^\circ\text{C}$  on Ir (1), Rh (4) and Ir-Rh alloys, w(Rh) %: 40 (2), 60 (3).

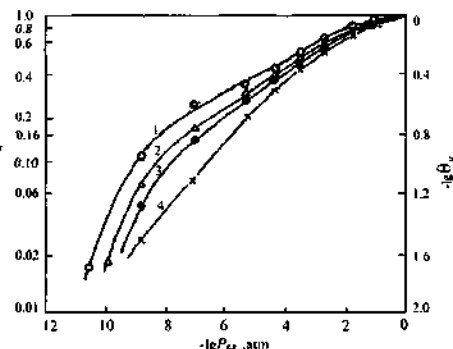


**Figure 4b.** Isotherms of hydrogen adsorption in the coordinates  $\lg \theta_H - \lg P_{H_2}$  at  $20^\circ\text{C}$  on Ir (1), Rh (4) and Ir-Rh alloys, w(Rh) %: 40 (2), 60 (3).

The relation (3) has only a limited applicability for the description of hydrogen adsorption on iridium while the equation (4) for the adsorption on rhodium. The Freundlich equation can be used to characterize the adsorption process on rhodium only for the coverage degrees  $\theta_H < 0.3$ , while Temkin isotherm is valid in the case of adsorption on iridium only at high  $\theta_H$  values. With regard to the iridium-rhodium electrodes-catalysts, from the comparison of Figure 4a and 4b, it can be noted that the Freundlich equation can well account for the features of the adsorption process only on the iridium rich alloys, while the Temkin isotherm reasonably well reproduces experimental data for the systems of any composition, both in the region of high and medium surface coverage values.

The analysis of adsorption dependencies (Figure 4) reveals that to achieve the same level of surface coverage by adsorbed hydrogen on the electrodes with higher contents of rhodium, a higher hydrogen partial pressure is required. Thus the coverage level of  $\theta_H = 0.4$  on the rhodium is achieved at the hydrogen partial pressure one order of magnitude higher than the pressure on Ir-electrode. In other words, the higher the rhodium contents in the alloy, the lower is the surface coverage by adsorbed hydrogen at the same value of  $P_{H_2}$ .

With the temperature increase from 20 to  $70^\circ\text{C}$  the region of hydrogen adsorption on the Ir-Rh alloys, and on pure iridium and rhodium becomes narrower, and the potentials of the onset of hydrogen adsorption and of the maxima of the both types of adsorbed hydrogen shift towards less positive potential values. The hydrogen quantity adsorbed on the unit electrode surface actually remains almost the same in this case.

On the basis of experimental data for Ir, Rh and their alloys, the adsorption isotherms at different temperatures have been plotted (Figure 5a). The adsorption isosteres are obtained by the intersection of the adsorption isotherms at a specified

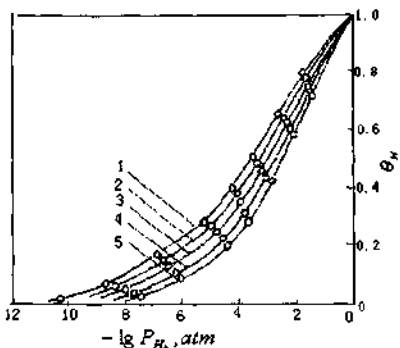


**Figure 5a.** Isotherms of the adsorption on the w(Rh)%=40 Ir-Rh alloy at different temperatures T/°C: 1 - 20; 2 - 30; 3 - 40; 4 - 55; 5 - 70.

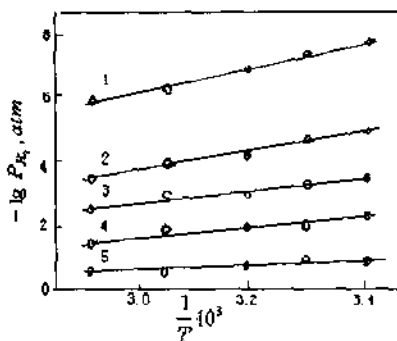


**Figure 5b.** Isosteres of the adsorption on the w(Rh)%=40 Ir-Rh alloy at different values of coverage  $\Theta_H$ : 1 - 0.1; 2 - 0.3; 3 - 0.5; 4 - 0.7; 5 - 0.9

coverage value in the  $\lg P_{H_2} = f(1/T)$  coordinates (Figure 5b), the tangent of their inclination angle in accord with the Clausius-Clapeyron equation:

$$\left( \frac{\partial \ln P_{H_2}}{\partial T} \right)_{\Theta_H} = \frac{\Delta H_{ads}}{RT^2} \quad (5)$$

is used to define the values of the differential hydrogen adsorption heat. Hydrogen adsorption heat as a function of surface coverage for the systems of various compositions is presented in Figure 6.

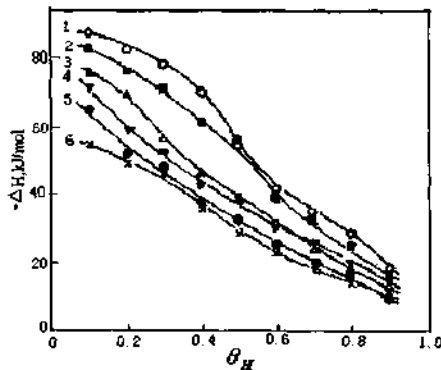


**Figure 6.** Hydrogen adsorption heat as a function of surface coverage for Ir-Rh electrodes, w(Rh)%: 1- Ir, 2- 20, 3- 40, 4-60, 5- 85, 6- Rh.

It is typical that the higher the rhodium content in the alloy, the lower is the hydrogen adsorption heat. The effect of the electrode catalyst material on the adsorption heat is substantially affected by the surface coverage by the adsorbed

hydrogen and is most pronounced in the low coverage region; the differences between adsorption heats for the alloys of different composition decrease with increasing  $\theta_H$  value. Hence the transition from the iridium to the rhodium in the region  $\theta_H = 0.1\text{-}0.2$ , the value  $\Delta H_{\text{ads}}$  drops by 30-35 kJ/mol, while at  $\theta_H = 0.7\text{-}0.8$  the differences in the hydrogen adsorption heat do not exceed 8-10 kJ/mol. At  $\theta_H \rightarrow 1.0$ , i.e. at the potentials of the onset of hydrogen evolution, the differences in the hydrogen adsorption heats of different alloys almost disappear.

#### 4 Conclusion

In conclusion it should be noted that the energy spectrum of the hydrogen adsorption in the process of hydroxonium ions discharge in sulfuric solutions is substantially different when changing from the iridium to the rhodium; the quantity of the strongly bonded hydrogen decreases, and the peak of the weakly bound hydrogen is shifted towards more positive potentials. No extreme modifications of the adsorption properties with the change of alloy composition were observed, probably due to the creation of solid solutions in the whole concentration range of the system studied. A linear dependence of the adsorption maximum on the iridium and rhodium contents in the system in the case of weakly bonded hydrogen and the profile of the cathodic  $i, E$ -curve in the region 0.4-0.0 V are specific characteristics of the Ir-Rh alloy composition and can be used to identify the surface composition of the alloy.

#### References

1. Bold W., Breiter M., Adsorption hydrogen heat measuring on activated electrodes of Pt-group in sulphuric acid. *Z. Electrochem.* 64 (1960) pp. 897-901.
2. Zakumbayeva G. D., Urumbayeva Sh. U., Sokolsky D. B., Hydrogen adsorption on the iridium in acid solutions. *J. Phys. Chem.* 47 (1973) pp. 945-949 (in Russian).
3. Meretsky A. M., Kudryashov I. V., Vasiliev Yu. B., Hydrogen and oxygen chemisorption on the rhodium monocrystal surface. *Electrokhimiya* 13 (1977) pp. 447-451 (in Russian).
4. Radushkina K. A., Burshtein R. H., Tarasevich M. R., Kuprina V. V., Chernyaeva L. L. Hydrogen and oxygen chemisorption on the platinum-rhodium alloys. *Electrokhimiya* 5 (1969) pp. 1379-1382 (in Russian).
5. Grishina T. M., Mestcheryakova E. V., Hydrogen adsorption on platinum, rhodium and their alloys at different temperatures. *J. Phys. Chem.* 60 (1986) pp. 1510-1513 (in Russian).
6. Jia M., Korenovsky N. L., Meretsky A. M., The features of hydrogen adsorption on iridium- rhodium metallurgical alloys during electrolysis of sulphuric acid solutions. *J. Phys. Chem.* 71 (1997) pp. 2044-2047 (in Russian).
7. Vasiliev Yu. B., Skundin A. M., Binary metal systems in electrocatalysis. In: *Problemy Elektrokataliza*, M., Nauka, 1980. pp. 128-160 (in Russian).

# THE USE OF OXALATES AS PRECURSORS FOR THE LOW TEMPERATURE SYNTHESIS OF $\text{LiNi}_{1-x}\text{Co}_x\text{VO}_4$

Q. Y. LAI, J. Z. LU, F. Y. YAN

*Chemical College of Sichuan University, 610064, Chengdu, China  
E-mail: laiqy@sc.homeway.com.cn*

X. Y. JI

*Analytical and Testing Center, 610064, Chengdu, China*

A kind of xerogel as a precursor composed of oxalates including lithium, nickel, cobalt and vanadium with a certain stoichiometric ratio has been obtained by the soft chemical method. The influences of sintering temperature, heat treatment and impurities on the phases, crystallinity and powder sizes of the products were studied. The results tested by TGA, DTA, XRD, TEM, IR and Raman spectra show that the cubic inverse spinel  $\text{LiNi}_{1-x}\text{Co}_x\text{VO}_4$  ( $0 \leq x \leq 0.5$ ) could be obtained through sintering xerogel at 400–500°C for 2–3h in air. The average size of the particles was about  $0.1\mu\text{m}$ . The IR spectra of the samples exhibit complex stretching vibration modes related to  $\text{VO}_4$  tetrahedra in the range of  $600\text{--}850\text{cm}^{-1}$  absorption which tended to narrow with increasing sintering temperature. The sample was unstable when quenched from 700°C. The study of cycling behavior for  $\text{Li} / \text{LiNi}_{0.7}\text{Co}_{0.3}\text{VO}_4$  cell showed that the cell polarization decreased and the cycle efficiency increased with lessening current rates.

## 1 Introduction

There are many studies about normal spinel oxides including lithium and transition-metal used as cathode active compounds for lithium ion batteries recently, especially lithium and manganese spinel oxides such as  $\text{LiMn}_2\text{O}_4$ ,  $\text{LiMn}_{2-x}\text{M}_x\text{O}_4$  ( $\text{M}=\text{Co, Ni, V, Mg}\cdots$ ) [1,2] and  $\lambda\text{-MnO}_2$ ,  $\text{Li}_2\text{Mn}_4\text{O}_9$ ,  $\text{Li}_4\text{Mn}_5\text{O}_{12}$  with some defects [3] as cathode materials have exhibited fine electrochemical properties. However there is another class of spinels, namely inverse spinels, such as  $\text{LiNiVO}_4$  used as cathode active compound for lithium secondary batteries has been proved to have a very high voltage up to 4.8V (vs Li) which is considered as the highest voltage among the all spinel oxides for lithium secondary batteries up to now [4].  $\text{LiNiVO}_4$  is a cubic crystal, all the atoms in the spinel unit cell of which occupy special positions in the space group  $Fd\bar{3}m$  (no 227), these positions are lithium and nickel (16d 1/2, 1/2, 1/2), vanadium (8a, 1/4, 1/4, 1/4) and oxygen (32e, x, x, x) [5].  $\text{LiCoVO}_4$  has a similar structure to  $\text{LiNiVO}_4$ , but having lower voltage near 4.2V (vs Li)<sup>[5,4]</sup>. In practice it is difficult to seek a kind of electrolytes with antioxidantizing ability which is appropriate for 4.8V (vs Li) of  $\text{LiNiVO}_4$ . This situation can be improved by using cobalt as a dopant to synthesize the sosoloid  $\text{LiNi}_{1-x}\text{Co}_x\text{VO}_4$  [6]. According to our knowledge, the synthesis of  $\text{LiNiVO}_4$  and  $\text{LiCoVO}_4$  has been achieved by conventional solid state reactions. For example, Wong-Ng used  $\text{LiOH}\cdot\text{H}_2\text{O}$ ,  $\text{NiCO}_3$  and  $\text{V}_2\text{O}_5$  as raw materials, sintering the mixture at 90°C for 73h to obtain  $\text{LiNiVO}_4$ , and using  $\text{LiOH}\cdot\text{H}_2\text{O}$ ,  $\text{CoO}$  and  $\text{V}_2\text{O}_5$  at 600°C for 19h, then at 650°C for 70h, at last at 800°C for 20h to obtain  $\text{LiCoVO}_4$  [7]. Fey used  $\text{Li}_2\text{CO}_3$ ,  $\text{NiO}$ ,  $\text{Co}_3\text{O}_4$  and  $\text{V}_2\text{O}_5$  as raw materials, at 800°C for many hours and used  $\text{LiOH}\cdot\text{H}_2\text{O}$ ,  $\text{Ni}(\text{NO}_3)_2\cdot 6\text{H}_2\text{O}$ ,  $\text{Co}(\text{NO}_3)_2\cdot 6\text{H}_2\text{O}$  and  $\text{NH}_4\text{VO}_3$  as raw materials through co-precipitating to obtain  $\text{LiNi}_{0.5}\text{Co}_{0.5}\text{VO}_4$ , respectively [6]. In general conventional ceramic technique takes a lot of energy and time, and co-precipitate method

is hard to gain lithium stoichiometry due to large insolubility of all the lithium salts. We obtained  $\text{LiNi}_{1-x}\text{Co}_x\text{VO}_4$  ( $0.1 \leq x \leq 0.5$ ) by means of sintering at lower temperature for a shorter time through a mild liquid route with oxalate groups as both complex agent and precipitating agent.

## 2 Experimental

$\text{Li}_2\text{CO}_3$ ,  $\text{NH}_4\text{VO}_3$ ,  $\text{NiC}_2\text{O}_4 \cdot 2\text{H}_2\text{O}$  and  $\text{CoC}_2\text{O}_4 \cdot 2\text{H}_2\text{O}$  were mixed in appropriate stoichiometric ratios, and the oxalic acid saturated solution was dropped in the mixture. A blue xerogel was gained by driving away water on the stremmer at 60-70°C. The xerogel was used as the precursor which was sintered in air at 300-700°C for 2-9h then cooled gradually and yellow powder samples could be obtained. The quenched samples were prepared by sintering the xerogel at 700°C for 4h followed by quenching to the room temperature in air.

Powder XRD patterns were obtained at room temperature on an X-ray diffractometer Japan D/max-rA, Cu K $\alpha$ , 40KV, 150mA,  $\lambda=0.15405\text{nm}$ . The shapes and the sizes of the products were analyzed by TEM photograph, transmission electron micrograph, Japan JEM-100cx model. The DTA and TGA curves were gained on an American Dupont 1090 model thermoanalysis apparatus, over the temperature range of 30-800°C at a heating rate of  $10^\circ \text{ min}^{-1}$  in air. The IR spectra of the samples were obtained on a PE16FT-IR apparatus, the wavenumber range being of  $400\text{-}4000\text{cm}^{-1}$ . The Raman spectrum of the sample was recorded by using the SPEX 1403-laser Raman spectrometer with a scanning range of  $50\text{-}2000\text{cm}^{-1}$ .

Charge and discharge tests were carried out by using the experimental cells which were assembled in an argon dry box at room temperature. The cathode was prepared from a mixture of 85wt%  $\text{LiNi}_{1-x}\text{Co}_x\text{VO}_4$  as the active materials, 12wt% acetylene black and 3wt% Teflon binder. The Li sheets were used as a reference and counter electrodes. The electrolyte solution (Japan Mitsubishi chemical Co.) was  $1 \text{ mol/dm}^3 \text{ LiPF}_6$  dissolved in a mixture solvent consisting of ethylene carbonate (EC) and diethylene carbonate (DEC) in a volume.

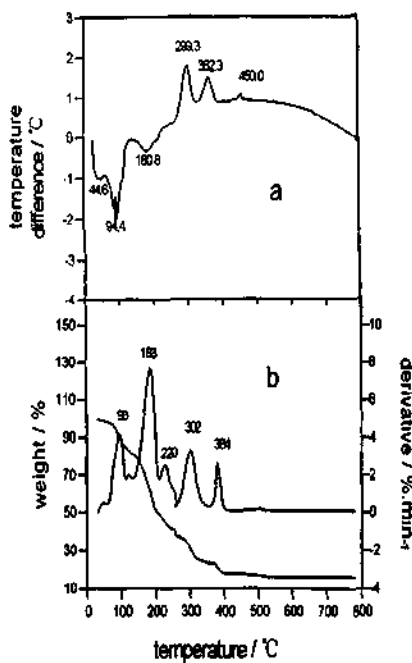
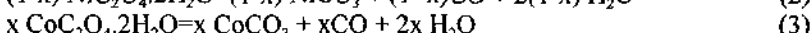
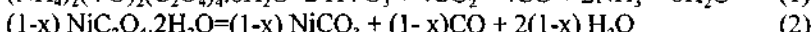
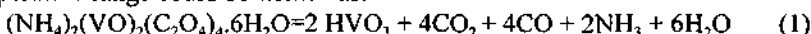


Fig.1 The thermal analysis of xerogel (Li:Ni:Co:V=1:0.7:0.3:1)  
(a)DTA Curve ,(b) TGA Curve

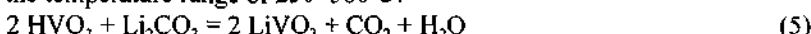
### 3 Results and Discussion

#### 3.1 The analysis of DTA and TGA for xerogel

Fig. 1 shows the curves of DTA and TGA for the xerogel with Li:Ni:Co:V=1:0.7:0.3:1 in a stoichiometric ratio. There were three endothermic peaks located at 44.6°C, 94.4°C and 180.8°C in the DTA curve, respectively. Correspondingly there was a continual weight loss about 62% in the temperature range 30-250°C in the TGA curve. This behavior can be considered as the removal of water from the xerogel, the driving away of the crystal water molecules and the decomposing into the relevant metal oxides, carbon oxides, ammonia gas and water. In fact, the xerogel used as the precursor was a mixture composed of the complex  $(\text{NH}_4)_2(\text{VO})_2(\text{C}_2\text{O}_4)_4 \cdot 6\text{H}_2\text{O}$  produced by  $\text{NH}_4\text{VO}_3$  reacting with  $\text{H}_2\text{C}_2\text{O}_4$  and the precipitates  $\text{Li}_2\text{C}_2\text{O}_4$ ,  $\text{NiC}_2\text{O}_4 \cdot 2\text{H}_2\text{O}$  and  $\text{CoC}_2\text{O}_4 \cdot 2\text{H}_2\text{O}$  prepared by  $\text{Li}_2\text{CO}_3$ ,  $\text{NiCO}_3$  and  $\text{CoCO}_3$  reacting chemically with  $\text{H}_2\text{C}_2\text{O}_4$ . Here the oxalic acid played the role of both complex agent and precipitate agent. According to the results of the thermal analysis, the correlative reactions for the xerogel after removing surface water in this temperature range could be written as:



There were three exothermic peaks in the DTA curve, two distinct peaks among which are located at 299.3°C and 362.3°C respectively. Correspondingly there exist a smaller weight loss about 16% in the temperature range of 250-380°C in the TGA curve. This phenomenon may be interpreted as the steady vanadate having been synthesized due to elevating heating temperature. The reactions below have something to do with the two bigger exothermic peaks in the DTA curve and with the smaller weight loss in the TGA curve in the temperature range of 250-380°C:



The peak located at 450°C in the DTA curve was a very small exothermic peak, but no weight loss above 400°C could be observed in the TGA. Therefore we can know that the reactions in the xerogel has basically finished and the  $\text{LiNi}_{1-x}\text{Co}_x\text{VO}_4$  has formed. The exothermic peak located at 450°C in the DTA curve can be interpreted as a kind of transformation of  $\text{LiNi}_{1-x}\text{Co}_x\text{VO}_4$  from amorphous solid into crystal solid.

#### 3.2 XRD analysis of products

The products were synthesized by sintering xerogel with various metal atom stoichiometric amounts at different temperatures for different times and by using different thermal treatments. The results measured by XRD are shown in Table 1.

It is obvious from Table 1 that the sample no.1 sintered at 300°C for 4h included mixture phases of  $\text{LiVO}_3$ ,  $\text{NiO}$  and  $\text{CoO}$ , and the sample no. 2 sintered at 400°C for 3h was also a mixture in which  $\text{CoO}$  and  $\text{NiO}$  phases disappeared. It implies that the sosoloid  $\text{LiNi}_{1-x}\text{Co}_x\text{VO}_4$  ( $x = 0.1$ ) with cobalt dopant formed but a small amount of impurity such as  $\text{LiVO}_3$  and  $\text{NiO}$  still existed in the sample. From no.3-no.5 we can know that  $\text{CoO}$  phase could not be seen with increasing of cobalt dopant amounts but only  $\text{LiNi}_{1-x}\text{Co}_x\text{VO}_4$  ( $0.1 \leq x \leq 0.5$ ) which was compared with the TGA result. The sample no.6 was a

quenched product from 700°C to the room temperature showing impurity of  $\text{Li}_3\text{VO}_4$  and  $\text{NiO}$  which were observed through the strongest peak of the XRD pattern in the percentages 4% and 2% respectively. Therefore we consider that the  $\text{LiNi}_{1-x}\text{Co}_x\text{VO}_4$  is somehow unstable when it is quenched. Fig. 2 (a) and Fig. 2 (b) are the XRD patterns of the cobalt doping and undoping samples. Compared with the undoped sample, the peak positions of the doped sample moved somewhat to lower degrees about 0.1-0.4 ( $\theta$ ) which is not easy to see with half an eye on the shrunken diagram and the intensity of the peaks (400), (422) and (440) increased to a certain degree. We believe that this is resulted from cobalt instead of nickel in the B sites of the solid solution [5] which can be expressed as  $[\text{V}]_A [\text{LiNi}_{1-x}\text{Co}_x]_B \text{O}_4$  ( $X=0.5$ ). Fig. 3 is the TEM photograph of the sample no.5. It is clear that a large proportion of the particles are cubic aggregates, and the average size of the particles is about  $0.1\mu\text{m}$ .

Table 1. The influence of synthesizing conditions on the phase of products

Sample	Li:(Ni+Co):V (in xerogel)	Temp /°C	Time / h	Cooling manners	Phase of products
1	1:(0.9+0.1):1	300	4	slow	$\text{LiVO}_3$ , $\text{NiO}$ , $\text{CoO}$
2	1:(0.9+0.1):1	400	3	slow	$\text{LiNi}_{1-x}\text{Co}_x\text{VO}_4$ ( $x=0.1$ ), $\text{NiO}$ , $\text{LiVO}_3$
3	1:(0.9+0.1):1	500	2	slow	$\text{LiNi}_{1-x}\text{Co}_x\text{VO}_4$ ( $x=0.1$ )
4	1:(0.7+0.3):1	500	2	slow	$\text{LiNi}_{1-x}\text{Co}_x\text{VO}_4$ ( $x=0.3$ )
5	1:(0.5+0.5):1	500	2-9	slow	$\text{LiNi}_{1-x}\text{Co}_x\text{VO}_4$ ( $x=0.5$ )
6	1:(0.7+0.3):1	700	4	quenching	$\text{LiNi}_{1-x}\text{Co}_x\text{VO}_4$ ( $x=0.3$ ), $\text{Li}_3\text{VO}_4$ , $\text{NiO}$

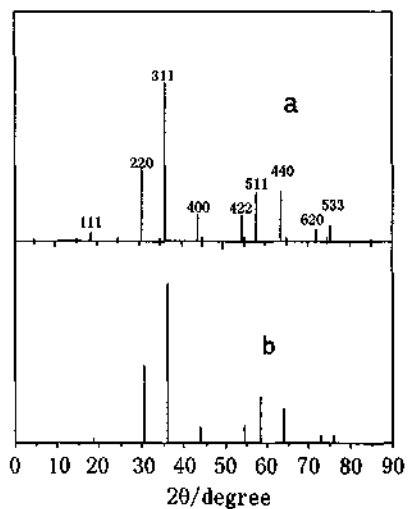


Fig. 2 XRD patterns  
for  $\text{LiNi}_{1-x}\text{Co}_x\text{VO}_4$   
(a)  $X=0.5$  (b)  $X=0$

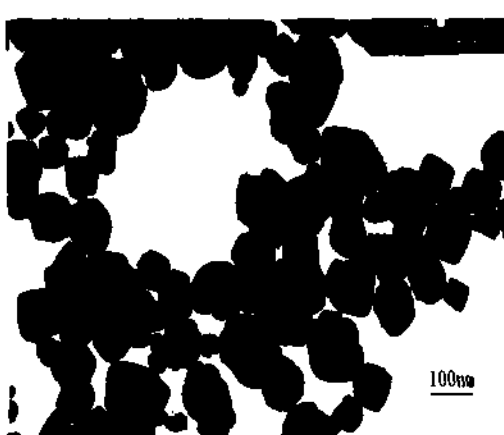


Fig. 3 TEM photograph of  
 $\text{LiNi}_{1-x}\text{Co}_x\text{VO}_4$  ( $X=0.5$ )

### 3.3 IR and Raman Analysis

Fig. 4 shows the IR spectra of the samples in wavenumber range of 400-1600 cm<sup>-1</sup>. For the curve (a) (450 °C for 2h), there is a broad absorption band of 600-850cm<sup>-1</sup> which was related to the stretching vibrations of VO<sub>4</sub> tetrahedra [8], implying the existence of vanadate with VO<sub>4</sub> tetrahedra. There are three splitting IR absorption peaks in the absorption band of 650-850cm<sup>-1</sup>, and they are located respectively at 625cm<sup>-1</sup>, 717cm<sup>-1</sup> and 810cm<sup>-1</sup> for the curve (b) of the sample sintered at 550 °C for 4h. Another three signals are located respectively at 644cm<sup>-1</sup>, 720cm<sup>-1</sup> and 804 cm<sup>-1</sup> for the curve (c) of the sample quenched from 700°C to room temperature after sintering for 4h. It is explicit to see that the positions of the three small peaks have shifted with raising temperature: 625cm<sup>-1</sup> (b) moving to 644cm<sup>-1</sup> (c) with a blue shift of 19cm<sup>-1</sup>, 717cm<sup>-1</sup> (b) moving to 720cm<sup>-1</sup> (c) with a blue shift of 3cm<sup>-1</sup> and 810cm<sup>-1</sup> (b) moving to 804cm<sup>-1</sup> (c) with a red shift of 6cm<sup>-1</sup> respectively. Because of the blue shifts accompanying by the red shift in the same absorption band, the band becomes narrower. The behaviors of the splitting peaks can be attributed to the complex vibrational modes in the VO<sub>4</sub> tetrahedron due to some asymmetry resulted from each oxygen of VO<sub>4</sub> tetrahedron bonding to three kinds of cations Li<sup>+</sup>, Ni<sup>2+</sup> and Co<sup>2+</sup>. The absorption band going narrower from the curve (a) to curve (c) can be explained in terms that the crystallinity of the products becomes better with increasing temperature. It is worth to mention that the new peak sited at 510cm<sup>-1</sup> in the curve (c) could be tentatively considered as the Li-O stretching vibrational mode, indicating that the quenched sample from 700°C is slightly unstable. This explanation agrees with the result of XRD. In addition, there are small absorption peaks in the range of 1100-1120cm<sup>-1</sup>, and they are sited at 1103cm<sup>-1</sup> for the curve (a), 1104cm<sup>-1</sup> for the curve (b) and 1118cm<sup>-1</sup> for the curve (c), respectively. Perhaps they also belong to asymmetric stretching vibrations of the VO<sub>4</sub> tetrahedra which are expected to be proved in the future research. The Raman spectrum tested in the range of 50~2000cm<sup>-1</sup> for LiNi<sub>0.7</sub>Co<sub>0.3</sub>VO<sub>4</sub> obtained by sintering the sample at 550°C for 4h is shown in Fig. 5. The two peaks of 786 and 816cm<sup>-1</sup> are much stronger and sharper than the peak at 330cm<sup>-1</sup>, corresponding to the IR absorption peaks at 717 and 810cm<sup>-1</sup> in the strong absorption band in the 650~850cm<sup>-1</sup> (see Fig. 4 b). The two stronger and sharper Raman peaks can also be

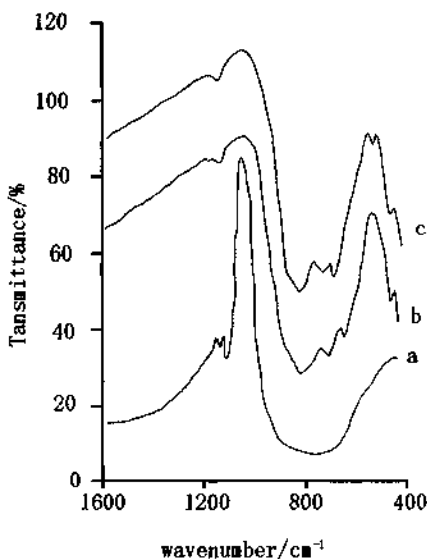


Fig. 4 IR Spectra of the samples LiNi<sub>0.7</sub>Co<sub>0.3</sub>VO<sub>4</sub> (x=0.3)  
(a) 450 °C 2h (b) 550 °C 4h  
(c) 700 °C 4h  
quenched in air

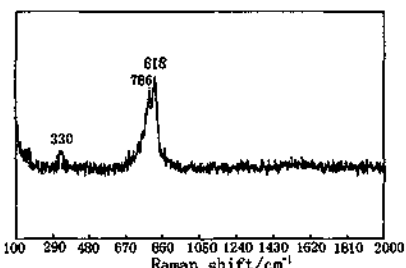


Fig. 5 Raman spectrum for LiNi<sub>0.7</sub>Co<sub>0.3</sub>VO<sub>4</sub>

considered as the stretching vibrations of  $\text{VO}_4$  tetrahadra. The  $330\text{cm}^{-1}$  signal can be attributed to the flex vibration of  $\text{VO}_4$  tetrahadra.

### 3.4 Cycling behavior

Fig. 6 indicates the cycling behavior of the first charge and discharge for  $\text{Li} / \text{LiNi}_{0.7}\text{iCo}_{0.3}\text{VO}_4$  cell with various current rates between 4.5-3.2V at room temperature. Fig. 6(a) shows that the charge capacity and the discharge capacity are 75 mAh/g and 53 mAh/g at the current rate of  $0.2\text{ mA/cm}^2$ , respectively, and the cycle efficiency of the battery is 70.7%. Fig. 6(b) shows that the charge capacity and the discharge capacity are 72 mAh/g and 43 mAh/g when the current rate increases from  $0.2\text{ mA/cm}^2$  to  $2\text{ mA/cm}^2$ , and the cycle efficiency of the battery becomes 59.7%. In Fig. 6(c), when the current rate further increases from  $2\text{ mA/cm}^2$  to  $4\text{ mA/cm}^2$ , the charge capacity and the discharge capacity are 70 mAh/g and 34 mAh/g respectively, and the cycle efficiency of the battery is 48.6 %. It is clear from Fig. 5 that the polarization of the cell increases and the cycle efficiency decreases with current rates.

## 4 Conclusions

The inverse spinel  $\text{LiNi}_{1-x}\text{Co}_x\text{VO}_4$  ( $0.1 \leq x \leq 0.5$ ) can be synthesized by the soft chemical method through the mild liquid route at lower sintering temperature  $400\text{-}500^\circ\text{C}$  for shorter sintering time 2-3h. The phases, crystallinity and particle sizes of the products were affected by the sintering temperature and thermal treatment. The average size of the particles was about  $0.1\mu\text{m}$ . The current rates have influence on the cycling behavior of the  $\text{Li} / \text{LiNi}_{0.7}\text{iCo}_{0.3}\text{VO}_4$  cell, and the polarization of the cell decreased and the cycle efficiency increased with decreasing current rates.

## 5 Acknowledgement

We gratefully acknowledge the financial support for this work by the National Natural Science Foundation of China.

## References

1. J. M. Tarascon, W. R. McKinnon, F. Coowar, T. N. Bowmer, G. Amatucci, and D. Guyomard, *J. Electrochem. Soc.* **141** (1994) pp. 1421.

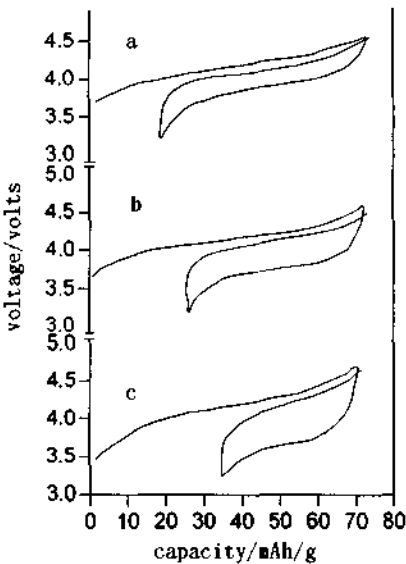


Fig. 6 cycling behaviors of  $\text{LiNi}_{0.7}\text{Co}_{0.3}\text{VO}_4$  cell between 4.5–3.2V at various current density  
 (a)  $0.2\text{ mA/cm}^2$  (b)  $2\text{ mA/cm}^2$  (c)  $4\text{ mA/cm}^2$

2. J. M. Tarascon, E. Wang, F. K. Shokoohi, W. R. McKinnon, and S. Colson, *J. Electrochem. Soc.*, **138** (1991) pp. 2859.
3. M. H. Rossow, A. DeKock, L. A. DePicciotto, M. M. Thackeray, W. I. F. David, and R. M. Iberson, *Mater. Res. Bull.*, **25** (1990) pp. 173.
4. George Ting-Kuo Fey, Wu Li, and J. R. Dahn, *J. Electrochem. Soc.*, **141** (1994) pp. 2279.
5. C. Gonzalez, M. Gaitan, M. L. Lopez, M. L. Veiga, R. Saez-Puche, and C. Pico, *J. Mater. Sci.*, **29** (1994) pp. 3458.
6. Fey Ting-Kuo, *Technical Conference Extended Abstract of China International Battery Fair 97.*, Beijing, China, (1997) pp. 4.
7. W. Wong-Ng, H. McMurdie, B. Paretzkin, C. Hubbard, and A. Dragoo, JCPDS 38-1395, 38-1396.
8. J. Preudhomme and P. Tarte, *Spectrochimica Acta*, **28** (1972) pp. 69.

This page is intentionally left blank

## INTERFACE LAYER IN COLLOID BY SAXS

ZHI HONG LI, YAN JUN GONG, MIN PU, DONG WU\* AND YU HAN SUN

*State Key Laboratory of Coal Conversion, Institute of Coal Chemistry,  
Chinese Academy of Sciences, P.O.Box 165, Taiyuan 030001, P. R. China  
E-mail: wudong@public.ty.sx.cn*

HUI ZHAO, JUN WANG AND BAO ZHONG DONG

*Facility of Synchrotron Radiation, Institute of High Energy Physics,  
Chinese Academy of Sciences, P.O.Box 918, Beijing 100039, P. R. China*

Small Angle X-ray Scattering (SAXS) can be used to determine the average thickness  $E$  of the interface layers that wrap about colloidal nuclei in colloid system by analyzing the negative deviation of the scattering data from Porod's law. Herein, a new method for determining  $E$  is presented on the basis of the analysis of the negative deviation of the slit-smeared scattering data from Debye's theory. This method was tested with experimental SAXS data of  $\text{SiO}_2$  colloids prepared under various conditions. The results were close to that derived from the negative deviation from Porod's law. With the increase of the average size of the colloidal nuclei,  $E$  reasonably decreased.

### 1 Introduction

A colloid is a suspension in which the dispersed phase (i.e. sol particle or colloidal particle) is so small (in nanoscale) that gravitational forces are negligible and interactions are dominated by short-range forces, such as van der Waals attraction and surface charges [1]. The inertia of the colloidal particle is small enough that it exhibits Brownian motion, a random walk driven by momentum imparted by collisions with molecules of the suspending medium. One of the important factors that lead the colloid to be relatively stable in a certain time is that there exists an (diffuse) interface layer between the colloidal nuclei and the dispersed medium [2,3], which prevents the colloidal nuclei from aggregation to some extent. That is to say, a colloidal particle is composed of a colloidal nucleus and an interface layer that wraps about the colloidal nucleus. The average thickness of the interface layer denoted as  $E$  is an important characteristic structural parameter of a colloid. Determination of  $E$  is difficult for usual characterizing tools, but it is easy for Small Angle X-ray Scattering (SAXS) that originates from spatial fluctuations of the electronic density within a sample [4]. The electronic density of the interface layer is usually between that of the dispersed phase and that of the dispersed medium, this results in the overall scattering showing negative deviation from Porod's law and Debye's theory (two main theories in SAXS). Based on the analysis of the negative deviation from Porod's law,  $E$  of  $\text{SiO}_2$  colloid has been measured [3]. However, can  $E$  also be directly determined from the negative deviation from Debye's theory? This paper targeted answering this question.  $\text{SiO}_2$  colloid prepared by base-catalyzed hydrolysis and condensation of alkoxides in alcohol served as tested sample. The analysis was directly based on slit-smeared SAXS data.

## 2 Determination of average thickness of the interface layer in colloid by SAXS

For an ideal two-phase system having sharply defined phase boundaries, according to Porod's law [5], the slit-smeared scattering intensity is given as [6]

$$\lim J(q) = K' q^{-3} \quad (1)$$

or

$$\ln[q^3 J(q)] = \ln K' \quad (2)$$

(see the curve I in Fig.1); according to Debye's theory [7], the slit-smeared scattering intensity is given as [8]

$$J(q) = A(1 + a_c^2 q^2)^{-3/2} \quad (3)$$

or

$$J(q)^{-2/3} = A^{-2/3} + A^{-2/3} a_c^2 q^2 \quad (4)$$

(see the curve I in Fig. 2) where  $q$  is the scattering vector,  $q = 4\pi \sin\theta/\lambda$ ,  $2\theta$  is the scattering angle,  $\lambda$  is the incident X-ray wavelength,  $J(q)$  is the slit-smeared scattering intensity,  $K'$  is Porod constant,  $A$  is a constant and  $a_c$  is the correlation distance which is a measure of phase size.

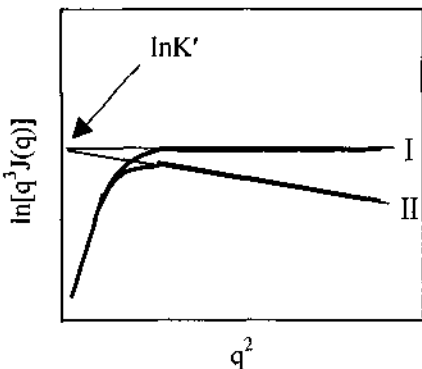


Figure 1. Typical  $\ln[q^3 J(q)]$  versus  $q^2$  plots, where I is for an ideal two-phase system, and II is for a negative deviation system.

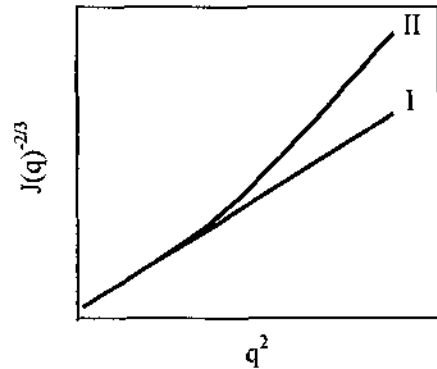


Figure 2. Typical  $J(q)^{-2/3}$  versus  $q^2$  plots, where I is for an ideal two-phase system, and II is for a negative deviation system.

For a non-ideal (pseudo) two-phase system having interface layer, the overall scattering will show negative deviation from Porod's law (see the curve II in Fig.1) and Debye's theory (see the curve II in Fig.2), thence the Porod equation (1) becomes [6,9]

$$J(q) = K' q^{-3} \exp(-\sigma^2 q^2) \quad (5)$$

where  $\exp(-\sigma^2 q^2)$  is the Fourier transform of the auto-correlation of the Gaussian smoothing function for the sigmoidal-gradient model [6] and represents the negative deviation due to the diffuse interface,  $\sigma$  is the standard deviation of the Gaussian smoothing function and is a parameter in relation to the thickness of the interfacial layer. In order to evaluate  $\sigma$ , Eq.(5) is transformed to

$$\ln[q^3 J(q)] = \ln K' - \sigma^2 q^2 \quad (6)$$

This means that plot of  $\ln[q^3 J(q)]$  versus  $q^2$  is linear in high angle range and  $\sigma$  can be derived from the slope, and then the average thickness of the interface layer  $E$  is determined as

$$E = (2\pi)^{1/2} \sigma \quad (7)$$

This is just the method that has been used for determining the value of  $E$  [9].

To the best of our knowledge, the study of the negative deviation of the scattering of colloid from Debye's theory has not been seen in the literatures up to now. Considering the physical meaning of  $\exp(-\sigma^2 q^2)$  in Eq.(5) mentioned above, it should also be used to characterize the negative deviation from Debye's theory due to the diffuse interface layer. Thus, Eq.(3) should be changed to the following formula

$$J(q) = A(1 + a_c^2 q^2)^{-3/2} \exp(-\sigma^2 q^2) \quad (8)$$

for fitting the slit-smeared scattering with a negative deviation from Debye's theory due to the diffuse interface. Here the physical meaning of  $\exp(-\sigma^2 q^2)$  is the same as that in Eq.(5).

However, comparing with Eq.(5), the unknown number in Eq.(8) (i.e.  $\sigma$ ,  $A$  and  $a_c$ ) is more than that in Eq.(5) (i.e.  $\sigma$  and  $K'$ ), and solving Eq.(8) is relatively complex and difficult. Herein, by proper deduction, Eq.(8) is transformed into a tractable form, i.e.

$$\exp(-2/3 \sigma^2 q^2) J(q)^{-2/3} = A^{-2/3} + A^{-2/3} a_c^2 q^2 \quad (9)$$

For a definite scattering system, the parameters  $\sigma$ ,  $A$  and  $a_c$  in Eq.(9) have the respective sole value, which assure plot of  $\exp(-2/3 \sigma^2 q^2) J(q)^{-2/3}$  versus  $q^2$  being (or statistically being) linear. Therefore, the method of trials can be used to solve Eq.(9). That is altering  $\sigma$  value continuously until  $\exp(-2/3 \sigma^2 q^2) J(q)^{-2/3}$  versus  $q^2$  plot is or statistically is linear. Because of  $\sigma \geq 0$ , the changing of  $\sigma$  should start from zero. Then with the increase of  $\sigma$  (with a small increment at a time, such as 0.01), the sum  $S_{ad}$  of the absolute values of the deviations of  $\exp(-2/3 \sigma^2 q^2) J(q)^{-2/3}$  versus  $q^2$  curve from the least square fitting straight line decreases continuously. Until  $S_{ad}$  is minimum, the corresponding value of  $\sigma$  is just the solution of the parameter in relation to the interface layer thickness, and then the average interface layer thickness  $E$  could be obtained using the above formula (7). Besides, the correlation distance  $a_c$ , another important parameter in SAXS [4,7,8], could also be derived from the slope and intercept of the least square fitting straight line. This process seems to be complicated, but it is actually very easy by using computer program.

### 3 Experimental

Five samples of SiO<sub>2</sub> colloids were examined. The samples were prepared by co-condensation of tetraethoxysilane (TEOS) and methyltriethoxysilane (MTES) using NH<sub>4</sub>OH as catalyst. TEOS and MTES were named precursors. The non-ionic alkyl-aryl EO<sub>10</sub> surfactant (C<sub>8</sub>H<sub>17</sub>(C<sub>6</sub>H<sub>4</sub>)(EO)<sub>10</sub>H, denoted Tx-10) was used as organic modifier. The molar ratio of precursor:H<sub>2</sub>O:C<sub>2</sub>H<sub>5</sub>OH:NH<sub>4</sub>OH was 1:2:40:0.0005. TEOS and ethanol were mixed at ambient condition for 30 min to form solution (I); certain amounts of NH<sub>4</sub>OH, H<sub>2</sub>O and Tx-10 were mixed with the same volume of

ethanol to make solution (II), which was then added into solution (I) to produce a homogeneous and transparent solution. After 30 min stirring, the solution was kept at ambient condition for some time. So-produced samples are listed in Table 1.

SAXS experiment was performed using Synchrotron Radiation as X-ray source with a long-slit collimation system at Beijing Synchrotron Radiation Faculty. The incident X-ray wavelength  $\lambda$  was 0.154nm. The scattered X-ray intensities were recorded using imagery plate technology. The air scattering and the absorption of the sample were corrected.

**Table 1.** SAXS results of  $\text{SiO}_2$  colloid systems prepared under various conditions<sup>a</sup>.

Sample	Precursor /mol%	Surfactant /mol%	Aging time /day	Porod and Debye deviation	Average diameter of colloidal nuclei /nm	Average interface layer thickness $E$	
						$E_p$ /nm	$E_d$ /nm
G1	TEOS 90%+MTES 10%		7	Negative	7.74	2.49	2.56
G2	TEOS 90%+MTES 10%		19	Negative	9.01	2.24	2.42
G3	TEOS 100%	Tx-10, 5%	7	Negative	9.61	2.19	2.32
G4	TEOS 100%	Tx-10, 5%	12	Negative	13.74	1.16	1.41
G5	TEOS 90%+MTES 10%	Tx-10, 5%	12	Negative	11.04	1.44	1.47
Estimated standard error						$\pm 9\%$	$\pm 7\%$

<sup>a</sup> EP was derived from the negative deviation from Porod's law and ED was derived from the negative deviation from Debye's theory.

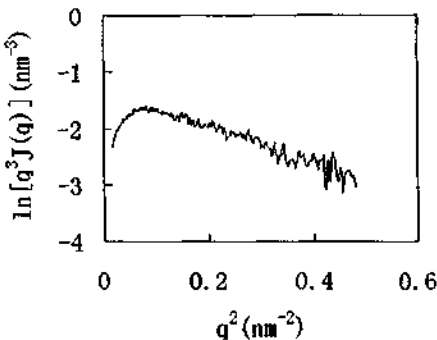
#### 4 Results and Discussion

Table 1 summarizes the SAXS results of  $\text{SiO}_2$  colloids prepared under various conditions. Obviously, the average size of the colloidal nuclei, which was derived from the curve of  $\ln[J(q)]$  versus  $q^2$  in which the negative deviation from Porod's law has been corrected [10], was in nanometer range for each sample. With the increase of the aging time, the colloidal nuclei reasonably grew gradually. The scattering of each sample showed negative deviations from both Porod's law and Debye's theory. Fig.3 and Fig.4 show the negative deviations from Porod's law and from Debye's theory for sample G2, respectively. These deviations suggested that the electron density did not change abruptly, but varied gradually over a certain range between two phases in the system. According to the theory of SAXS [6,9], this range refers to a diffuse interfacial layer, though its real composition and structure are still ambiguous for any colloid up to now.

Because the colloidal nucleus was in nanoscale, the specific surface area was very large and the specific surface free enthalpy was very high, the system was thermomechanically unstable. Thus the small colloidal nuclei could spontaneously aggregate each other to form big colloidal nuclei and to precipitate followed by separation from the dispersed medium. However, due to the high specific surface free enthalpy, each colloidal nucleus could also spontaneously adsorb some groups or

matter in the colloid system to form a diffuse interface layer, which exerted mechanical resistance to protect the inter-colliding colloidal nuclei against aggregation to a certain extent. Thus, the existence of the interface layer between the colloidal nuclei and the dispersed medium was one of the important factors that lead the colloid to be relatively stable in a certain time.

The average thickness  $E$  of the diffuse interface layer could be determined (see Table 1) by the above-mentioned two methods. The results obtained with the new method presented in this letter, i.e. by analysis of the negative deviation from Debye's theory (see Fig. 5), were denoted as  $E_D$ . The results derived from the negative deviation from Porod's law were denoted as  $E_P$ . It is obvious that  $E_D$  is close with  $E_P$  for various samples, but in each case the former is slightly higher and the reasons are thus not fully understood. With the increase of the average diameter of the colloidal nuclei,  $E$  ( $E_D$  and  $E_P$ ) reasonably increased.



**Figure 3.**  $\ln[q^3J(q)]$  versus  $q^2$  plot of G2, which shows a negative deviation from Porod's law.

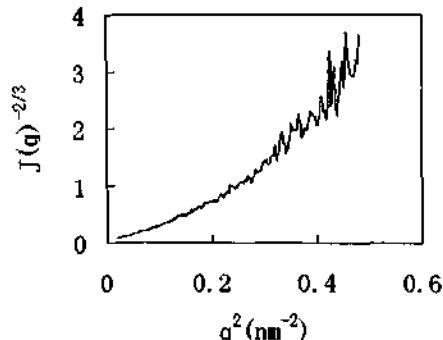


**Figure 4.**  $J(q)^{-2/3}$  versus  $q^2$  plot of G2, which shows a negative deviation from Debye's theory.

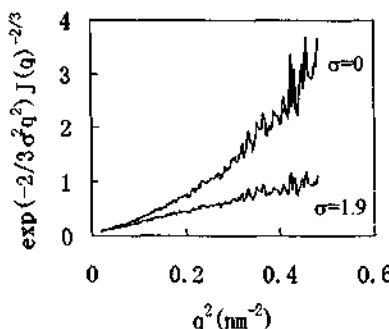


**Figure 5.** Plots of  $\exp(-2/3\sigma^2q^2)J(q)^{-2/3}$  versus  $q^2$  of G2, which shows the proceeding of the determination of the average interface layer thickness. When  $\sigma$  is 1.93 nm,  $\exp(-2/3\sigma^2q^2)J(q)^{-2/3}$  versus  $q^2$  plot is linear, and the value of  $E_D$  is 4.84 nm.

## 5 Acknowledgements

This work was supported by the National Nature Science Foundation (Grant No.29625307 and No.29973057), the National Key Basic Research Special Foundation (G20000480) and the Shanxi Provincial Nature Science Foundation (Grant No.991023).

## References

1. Jeffrey Brinker C., and Scherer G.W. Sol-gel science, The physics and chemistry of sol-gel processing (Academic Press, San Diego, CA, 1990).
2. Fu X. C., Shen W. X. and Yao T. Y. Physical Chemistry (Fourth Edition, Volume II) (Higher Education Press, Beijing, 1990).
3. Li Z. H., Sun J. H., Zhao J. P., Wu D., Sun Y. H., et al., Study of sol structure by SAXS. *Acta Physica Sinica* **49** (2000) pp. 775-780.
4. Glatter O. and Kratky O. Small angle X-ray scattering (London: Academic Press.,1982).
5. Porod G., Die rontgenkleinwinkelstreuung von dichtgepackten kolloiden system. *Kolloid-Z* **124** (1951) pp. 83-114.
6. Koberstein J. T., Morra B. and Stein R. S., The determination of diffuse-boundary thickness of polymers by small angle X-ray scattering. *J. Appl. Cryst.* **13** (1980) pp. 34-45.
7. Debye A. and Bueche A. M., Scattering by an inhomogeneous solid. II. The correlation function and its application. *J. Appl. Phys.* **20** (1949) pp. 518.
8. Brown D. S., Warner F. P. and Wetton R. E., Surface areas of fillers in Polymers by small angle X-ray scattering. *Polymer* **13** (1972) pp.575-578.
9. Hashimoto T., Fujimura M. and Kawai H., Domain-boundary structure of styrene-isoprene block copolymer films cast from solutions: 5. molecular-weight dependence of spherical microdomains. *Macromolecules* **13** (1980) pp. 1660-1669.
10. Li Z. H., Gong Y. J., Wu D., Sun Y. H., et al., A negative deviation from Porod's law in SAXS of organo-MSU-X. *Microporous Mesoporous Mater.* **46** (2001) pp. 75-80.

## WICKER-SHAPED SILVER PARTICLES PREPARED BY EXTRACTION INTERFACE REDUCTION

XUEMEI LI, SIXIU SUN AND YANZHAO YANG

*School of Chemistry and Chemical Engineering, Shandong University, Jinan 250100, China  
E-mail: ssx@sdu.edu.cn*

Wicker-shaped silver particles are obtained by interface reduction during the extraction process. The primary amine N1923 is used as extractant and reductant of silver. The silver particles were characterized by X-ray diffraction and transmission electron microscopy. It is shown that silver particles are wicker-shaped and uniformly dispersed and the wicker-shaped silver is composed by spherical particles of silver average diameter *ca.* 10nm.

### **1 Introduction**

Particles with sizes in nanometers range may possess unusual physical and chemical properties which are quite different from those of bulk materials because of their extremely small size and large specific surface area. They are expected to have many potential applications in many areas of science and technology, including catalysis, optoelectronic, chemical and biosensors, and drug delivery.

Nanometer-scale silver and other noble metals have been investigated intensively in the recent years because of their useful optical, electrical and catalytic properties. All the properties strongly depend on the choice of the shape of the nanosized materials and the preparative methods. Spherical, rod-like and wire-like silvers have been prepared and they have different optical and electric properties. Thus, it is important to control the morphologies of silver. The preparative strategies play a major role in the preparation of silver particles. A variety of preparation methods have been applied in the literature [1-4], for example, radiation chemical reduction, pulsed sonochemical method, chemical reduction with or without stabilizing agents, and template method which templates including micelle and reversed micelle, DNA, carbon nanotube, mesoporous silica, polymer films, and membrane. In the process of preparation of noble metals, especially for the gold and silver, protective agents usually be used, the protective agents include polymer, thiols and oleate et al. Diniel V. Leff et al have reported on the synthesis and characterization of amine-capped gold nanocrystals.

It is well known that silver (I) can be reduced to the metallic state with various organic substances and thus agitation of silver (I) with some extractants may reduce it. In the literature, the solvent extraction-reduction process possesses metallic ions were extracted form an aqueous solution to organic solvents and then the ions were reduced in the organic phase by reductant or radiation. In this work, we report a new strategy to prepare wicker-shaped silver. The primary amine N1923 is used as extractant and reductant.

### **2 Experimental Section**

#### **2.1 Materials**

Primary amine N1923 (its formula is  $\text{RNH}_2$ , its structure is  $\text{R}_1\text{R}_2\text{CHNH}_2$ , and the total number of carbonyl atoms is 19-23) was obtained from Shanghai Institute of Organic Chemistry of Academy Sinica and purified at the low pressure of 667 Pa. The purity of

$\text{RNH}_2$  is higher than 99%, the average value of the molecular weight is 291.8, and the density is 0.829 g/mL.  $\text{AgNO}_3$ , n-heptane and other chemicals were analytical grades. Deionized water was used in our experiments.

## 2.2 Procedure

The extraction procedure was as follows.  $\text{AgNO}_3$  was dissolved in water and added to an organic solvent containing an extractant. In the case of primary amine N1923, the condition of acidification is considered. The primary amine N1923 is acidified completely or not acidified. Then the mixed solution was shaken at 25°C for 2h. After the extraction, the organic phase is separated from the aqueous phase and then is put in dark.

## 2.3 Characterization

The structure of products was investigated with a Rigaku D/Max- $\gamma\text{A}$  X-ray diffractometer. The size and shape were observed under a JEM-100CXII transmission electron microscope.

## 3 Results and Discussion

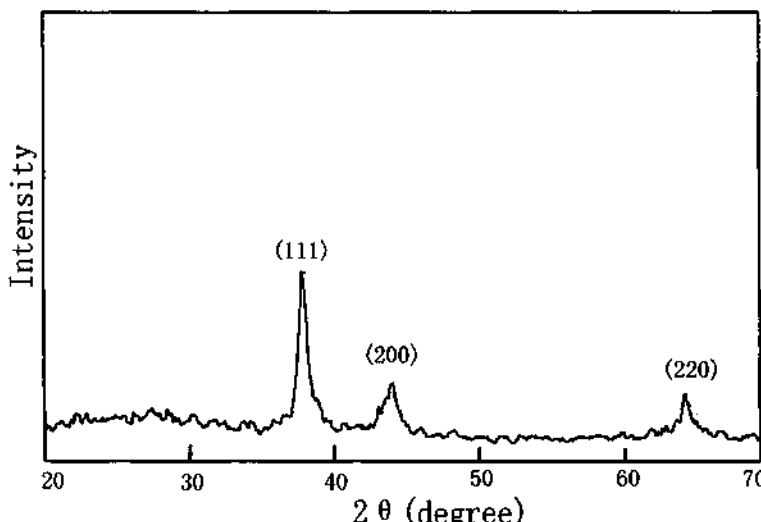
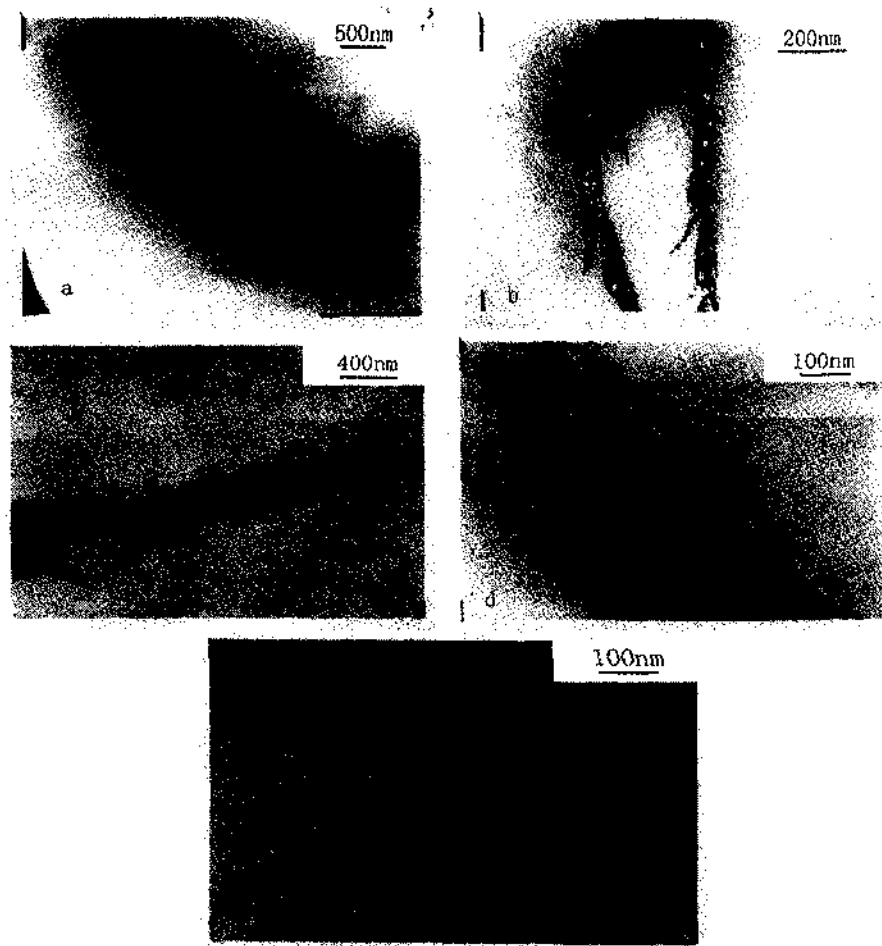


Figure 1. X-ray diffraction pattern of the silver prepared by the primary amine N1923 (not acidified).

As described in the experimental section, the products were prepared for XRD analysis. The products were washed several times with deionized water and ethanol, respectively. The products were examined on a Japan Rigaku D/Max- $\gamma\text{A}$  X-ray diffractometer using Ni-filtered  $\text{Cu K}\alpha$  radiation ( $\lambda=1.54178\text{\AA}$ ). The patterns were recorded within 20-70° (2θ). The temperature of the collection data is 25°C. Figure 1 shows the XRD patterns of the products and the peaks are indexed as 111, 200, and 220 planes, respectively, which

are in agreement with the literature (JCPDS No. 4-783) and indicates that the products is silver with a cubic symmetry.



**Figure 2.** Transmission electron micrographs of the prepared samples by unacidified N1923 (a, b, c, d) and acidified N1923 (e).

- a: the samples prepared by unacidified N1923 and kept for 2 days,
- b: the enlarged micrographs locally of a,
- c: the samples prepared by unacidified N1923 and kept for 10 days,
- d: the enlarged micrographs locally of c,
- e: the samples prepared by acidified N1923.

Transmission electron microscopic images (TEM) of the products were performed on a JEM-100CXII transmission electron microscope, under the accelerating voltage of 100kV. Figure 2 shows the results of the transmission electron investigations. The micrographs of Figure 2a-d are under the conditions that the primary amine N1923 is not acidified and the micrograph of Figure 2e is under that the extractant is acidified completely. From Figure 2 it can be seen that the morphologies of the products are quite different at different

conditions of primary amine N1923. When the primary amine is not acidified, the samples are wicker-shape. However, when the primary amine is not acidified, the samples are spherical and the average sizes of the silver are 15nm. It indicates that the acidified degree of the extractants plays an important role in controlling the shape of the products. As an extractant, the primary amine N1923 has very strong interfacial activity because both  $\text{RNH}_2$  and  $\text{RNH}_3^+$  have amphiphility in extraction system. Thus, in actual extraction system, the amine molecules are easier to aggregate to form spherical or rod-like micelles because the critical micelle concentration  $C_{\min}$  of amines is usually at the level of  $10^{-7}$ . In this work, the concentration of primary amine N1923 is 0.2mol/L, which means that the amine molecules con combines together and acted as template in the reduction of silver. The acidified amine may lead to the formation of spherical micelle while the amines which were not acidified result in rod-like micelle, making the final products to have different shapes. For the system that the amines are not acidified, there are no evident difference between the products kept for 2days (Figure 2a) and 10days (Figure 2c), which shows that the products are stable. In the meantime, in order to investigate the samples in detail, the Figure 2a and Figure 2c can be enlarged locally and got Figure 2b and Figure 2d. It can be seen that the wicker-silver are combined by spherical silver nanoparticles and the sizes of the particles are 5-30nm.

#### 4 Conclusions

In summary, the wicker-shape silver is prepared by extraction-reduction. In the process of the preparation, the primary amine N1923 act as the reductant, extractant and template and the conditions of the extractants are also important.

#### 5 Acknowledgements

This work was supported by the National Nature Science Foundation of China (No.20171029) and the Excellent Younger Scientist Research Encouragement Foundation of Shandong Province.

#### References

1. Luis M. Liz-Marzán and Isabel Lado-Touriño, Reduction and stabilization of silver nanoparticles in ethanol by nonionic surfactants. *Langmuir* **12** (1996) pp. 3585-3589.
2. H. X. Li, M.A. Lin and J. G. Hou, Electrophoretic deposition of ligand-stabilized silver nanoparticles synthesized by the process of photochemical reduction. *Journal of Crystal Growth* **212** (2000) pp. 222-226.
3. Kan-Sen Chou and Chiang-Yuh Ren, Synthesis of nanosized silver particles by chemical reduction method. *Materials Chemistry and Physics* **64** (2000) pp. 241-246.
4. S. A. Vorobyova, A. I. Lesnikovich and N. S. Sobal, Preparation of silver nanoparticles by interphase reduction. *Colloids and Surfaces A: Physicochemical and Engineering Aspects* **152** (1999) pp. 375-379.

## RHEOLOGICAL PHASE REACTION METHOD AND ITS APPLICATION

JUTANG SUN, LIANGJIE YUAN, YIYONG YANG, ZHENGYONG YUAN,  
JINLONG WANG AND KELI ZHANG

*College of Chemistry and Molecular Science, Wuhan University, Wuhan 430072, P. R. China  
E-mail: jtsun@whu.edu.cn*

In this paper the rheological phase reaction method was presented. The amorphous nanoscale MnO<sub>2</sub> with high dispersibility and good fluidity, and the single crystals of Ni(C<sub>6</sub>H<sub>5</sub>OHCO<sub>2</sub>)<sub>2</sub>·4H<sub>2</sub>O and binuclear Cu(C<sub>6</sub>H<sub>5</sub>CO<sub>2</sub>)<sub>2</sub>H were prepared by the use of the rheological phase reaction method. The charge and discharge properties of the MnO<sub>2</sub> as a positive electrode material in lithium batteries was investigated. The structures of two single crystal samples were determined, and the dependence of crystal growth on particle size of solid precursor was discussed.

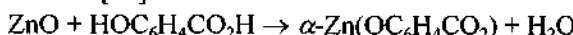
### 1 Introduction

In recent years, studies on the rheological behavior of solid-liquid suspension, electro- and magneto-rheological materials, polymer, and colloidal dispersion system are actively pursued [1-10]. Rheological techniques have been playing an important role in modern science and technology. However, rheology and chemical reaction have not yet been closely combined, and little attention has been paid to the application of rheology in synthetic chemistry.

The rheological phase reaction method is the process of preparing compounds or materials from a solid-liquid rheological mixture. That is, the solid reactants are fully mixed in a proper molar ratio, and made up by a proper amount of water or other solvents to a solid-liquid rheological body in which the solid particles and liquid substance are uniformly distributed, so that the product can be obtained under suitable experimental conditions.

In the rheological phase system there are many advantages: the surface area of solid particles can be efficiently utilized, the contact between solid particles and fluid is close and uniform, heat change is very efficient, local overheating can be avoided, and the reaction temperature can be easily controlled. In addition, many substances have greatly increased solubility and new reaction behavior in this state.

For example, in aqueous solution, salicylic acid is a monoacid and reacts with ZnO to form Zn(C<sub>6</sub>H<sub>5</sub>OHCO<sub>2</sub>)<sub>2</sub>. However, in the solid-liquid rheological phase system, its hydroxyl group can give out a proton, and it displays the property of a dibasic acid [11].



Many functional materials and compounds with new structures and properties, such as Sr[C<sub>6</sub>H<sub>5</sub>(CO<sub>2</sub>)<sub>2</sub>]:Tb<sub>x</sub>,  $\alpha$ -Zn(OC<sub>6</sub>H<sub>5</sub>CO<sub>2</sub>):Tb<sub>x</sub>, salicylate-doped zinc benzoate [Zn(Bzo)<sub>2</sub>:Sal<sub>x</sub>] luminescent materials and non-crystalline tin-based composite oxide negative electrode materials, etc. have been obtained by means of the rheological phase reaction method [11-14].

It is of interest to note that great single crystal sample of Ni(Sal)<sub>2</sub>·4H<sub>2</sub>O [Sal = C<sub>6</sub>H<sub>5</sub>(OH)CO<sub>2</sub>] has been obtained unexpectedly by rheological phase reaction method from Ni(OH)<sub>2</sub> and salicylic acid. In addition, the single crystal of Cu(C<sub>6</sub>H<sub>5</sub>CO<sub>2</sub>)<sub>3</sub>H has been prepared from CuO and benzoic acid.

In this paper, we present a new method preparing nanosized  $\text{MnO}_2$  and single crystals of  $\text{Ni}(\text{Sal})_2 \cdot 4\text{H}_2\text{O}$  and  $\text{Cu}(\text{C}_6\text{H}_5\text{CO}_2)_3\text{C}_6\text{H}_5\text{CO}_2\text{H}$ . The electrochemical property of  $\text{MnO}_2$  is investigated, and the crystal structures of two single crystal samples are characterized. It reveals the molecule identification and self-assembled functions in the rheological phase system. A new channel was inaugurated for single crystal growth. It can be predicted that the rheological phase reaction method will play an important role in synthetic chemistry, especially in the synthesis of compounds with novel structures and functional materials.

## 2 Experimental Section

$\text{Ni}(\text{OH})_2$  and  $\text{CuO}$  were self-made, the other reagents were analytical grade.

### 2.1 Nanosized $\text{MnO}_2$

An amorphous nanosized  $\text{MnO}_2$  with high dispersibility and good fluidity was synthesized by rheological phase reaction method from manganese benzoate and  $\text{KMnO}_4$ . The structure and properties were characterized by chemical titration, X-ray diffraction (XRD), BET Multipoint surface area analyses and transmission electron microscopy (TEM). The charge and discharge behaviors as positive electrode material were determined with a NEWERE cell testing apparatus.

### 2.2 Preparations and resolution of single crystal samples

The  $\text{Ni}(\text{OH})_2$  and salicylic acid in 1:2 molar ratio, the  $\text{CuO}$  and salicylic acid in 1:3 mole ratio were fully mixed, and the rheological bodies were made with a proper quantity of water, respectively. The light green  $\text{Ni}(\text{Sal})_2 \cdot 4\text{H}_2\text{O}$  and blue  $\text{Cu}(\text{C}_6\text{H}_5\text{CO}_2)_3\text{H}$  crystals were obtained from the rheological bodies in closed containers for 48 h at 60 °C and for 4 days at 90 °C, respectively. The crystal structures were determined by NONIUS KappaCCD diffractometer [for  $\text{Ni}(\text{Sal})_2 \cdot 4\text{H}_2\text{O}$ ] and RIGAKU R-AXIS IV Imaging Plate single crystal X-ray diffractometer [for  $\text{Cu}(\text{C}_6\text{H}_5\text{CO}_2)_3\text{H}$ ] with graphite-monochromatized Mo  $K\alpha$  radiation ( $\lambda = 0.71073 \text{ \AA}$ ).

## 3 Results and Discussion

### 3.1 Amorphous nanosized $\text{MnO}_2$

Figure 1 shows the TEM image of product  $\text{MnO}_2$ . In the powder XRD patterns, no diffraction peaks can be observed. This indicates that the structure of  $\text{MnO}_2$  is amorphous or amorphous-like. The average size of the particles is about 20 nm. The specific surface area is  $157.29 \text{ m}^2/\text{g}$ .

In order to obtain a discharge-charge profile of  $\text{MnO}_2$ , the electrochemical cell was assembled with a  $\text{MnO}_2$  working electrode and a lithium foil counter-electrode. The working electrodes was prepared by pressing  $\text{MnO}_2$  powders, acetylene black and polytetrafluoroethylene binder onto a nickel gauze current collector. The

electrolyte used was a 1 mol·L<sup>-1</sup> solution of LiPF<sub>6</sub> dissolved in a 50:50 mixture by volume of ethylene carbonate (EC) and diethyl carbonate (DEC). The cell was discharged and charged between 3.8 and 1.7 V vs. Li<sup>+</sup>/Li at a constant current density of 30 mA·g<sup>-1</sup>. The cell was subjected to 26 cycles, the cycling behavior is shown in Figure 2. The discharge capacity reaches to 262 mAh·g<sup>-1</sup> and the charge capacity is 285 mAh·g<sup>-1</sup>. The ratio of discharge and charge is more than 90 % and an average fade in discharge capacity of 0.83 %/cycle. These results demonstrate that the amount of inserted lithium can be reversibly extracted, and the amorphous nanosized MnO<sub>2</sub> has very fine charge and discharge properties as a positive electrode material of lithium ion battery.

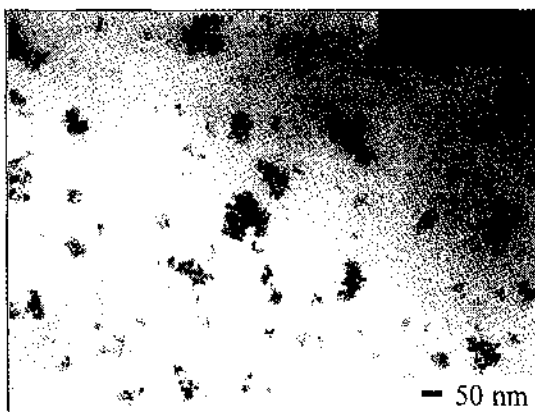


Figure 1. TEM image of the amorphous nanosized MnO<sub>2</sub>.

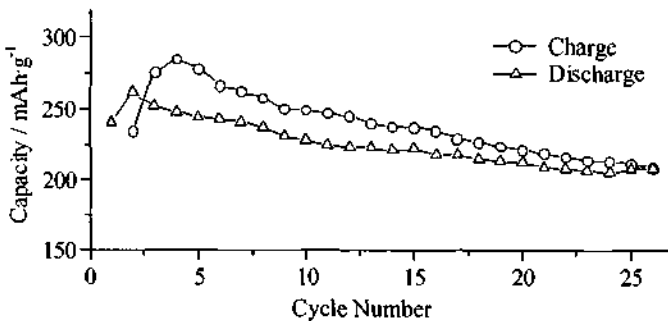


Figure 2. The variation in the discharge and charge capacity with the cycle number of MnO<sub>2</sub>/Li test cell.

### 3.2 Crystal structure of Ni(Sal)<sub>2</sub>·4H<sub>2</sub>O

Ni(Sal)<sub>2</sub>·4H<sub>2</sub>O is a monoclinic, space group  $P2_1/n$ ,  $a = 6.7874(3)$ ,  $b = 5.1591(2)$ ,  $c = 23.1330(9)$  Å,  $\beta = 90.9286(17)^\circ$ ,  $V = 809.94(6)$  Å<sup>3</sup>,  $Z = 2$ ,  $\rho_{\text{calcd}} = 1.661$  g·cm<sup>-3</sup>. Final  $R$  indices:  $R = 0.0279$  and  $wR = 0.0650$  [ $I > 2\sigma(I)$ ].

The crystallographic analysis uncovers that this compound is a molecular crystal, and the metal ion is located in the molecular symmetric center as shown in Figure 3. In the crystal cell, there are many strong hydrogen bonds between molecules as shown in Figure 4, which lead to salicylate ligands arranging each other in parallel,

and forming two-dimension layer structure along the crystallographic *a* and *b* axes. There is not chemical bond between layer and layer.

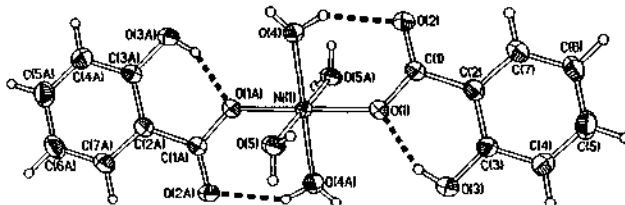


**Figure 3.** Molecular structure of  $\text{Ni}(\text{Sal})_2 \cdot 4\text{H}_2\text{O}$ .

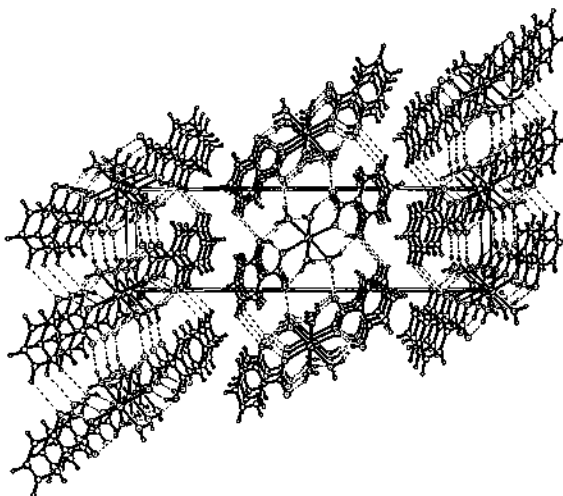


**Figure 4.** Stereoscopic view of the Packing  $\text{Ni}(\text{Sal})_2 \cdot 4\text{H}_2\text{O}$ .

### 3.3 Crystal structure of $\text{Cu}(\text{C}_6\text{H}_5\text{CO}_2)_3\text{H}$

$\text{Cu}(\text{C}_6\text{H}_5\text{CO}_2)_3\text{H}$  is a monoclinic, space group  $P2_1/n$ ,  $a = 10.799(2)$ ,  $b = 11.780(2)$ ,  $c = 15.303(3)$  Å,  $\beta = 91.35(3)^\circ$ ,  $V = 1946.1(7)$  Å<sup>3</sup>,  $Z = 4$ ,  $\rho_{\text{calcd}} = 1.460$  g·cm<sup>-3</sup>. Final *R* indices:  $R = 0.0560$  and  $wR = 0.0750$  [ $I > 2\sigma(I)$ ]. It is a molecular crystal with binuclear structure as shown in Figure 5. The distance between the two Cu atoms is 2.6249(12) Å. But there is not hydrogen bond between molecules. The molecular packing diagram is shown in Figure 6.

### 3.4 Crystal growths of $\text{Ni}(\text{Sal})_2 \cdot 4\text{H}_2\text{O}$ and $\text{Cu}(\text{C}_6\text{H}_5\text{CO}_2)_3\text{H}$

Figure 7 and 8 show the scanning picture of the crystal  $\text{Ni}(\text{Sal})_2 \cdot 4\text{H}_2\text{O}$  and  $\text{Cu}(\text{C}_6\text{H}_5\text{CO}_2)_3\text{H}$  prepared with rheological phase reaction method, and the raw material  $\text{Ni(OH)}_2$  and  $\text{CuO}$ . We discovered that the particle size of solid precursor had direct influence upon the single crystal growth. If the  $\text{Ni(OH)}_2$  and  $\text{CuO}$  granules

were very small, the great crystal could not be gained. But when the  $\text{Ni(OH)}_2$  and  $\text{CuO}$  were relatively large in size, as shown in Figure 7a and 8a, the great crystal was obtained easily. That is to say, the great single crystal can be constructed on the basis of great polymorphic blocks in the rheological phase system.

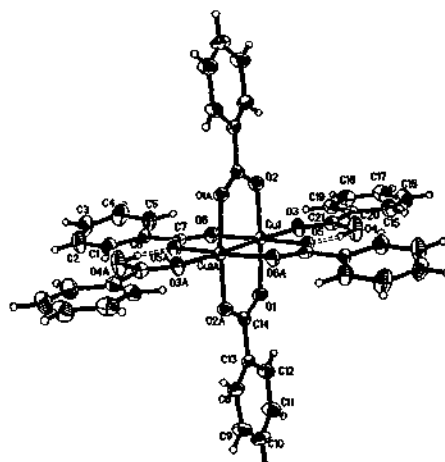


Figure 5. Molecular structure of  $\text{Cu}(\text{C}_6\text{H}_5\text{CO}_2)_3\text{H}_2\text{O}$ .

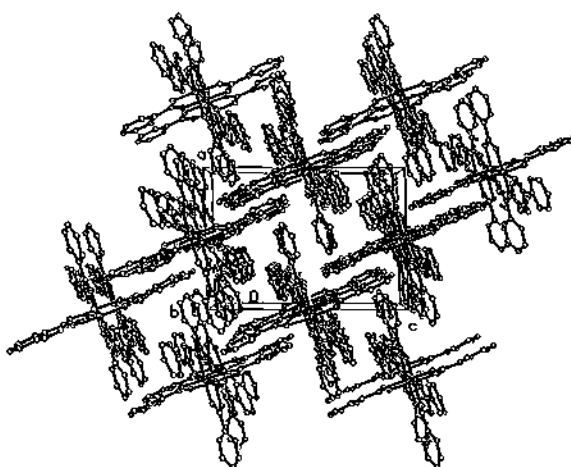


Figure 6. Stereoscopic view of the packing  $\text{Cu}(\text{C}_6\text{H}_5\text{CO}_2)_3\text{H}_2\text{O}$ .

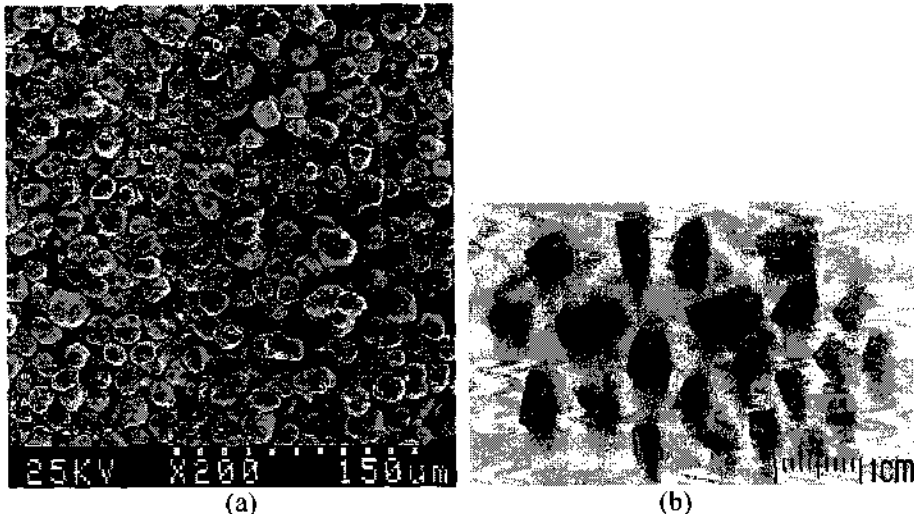


Figure 7. The SEM image of  $\text{Ni}(\text{OH})_2$  (a) and the pictures of single crystal  $\text{Ni}(\text{Sal})_2 \cdot 4\text{H}_2\text{O}$  (b).

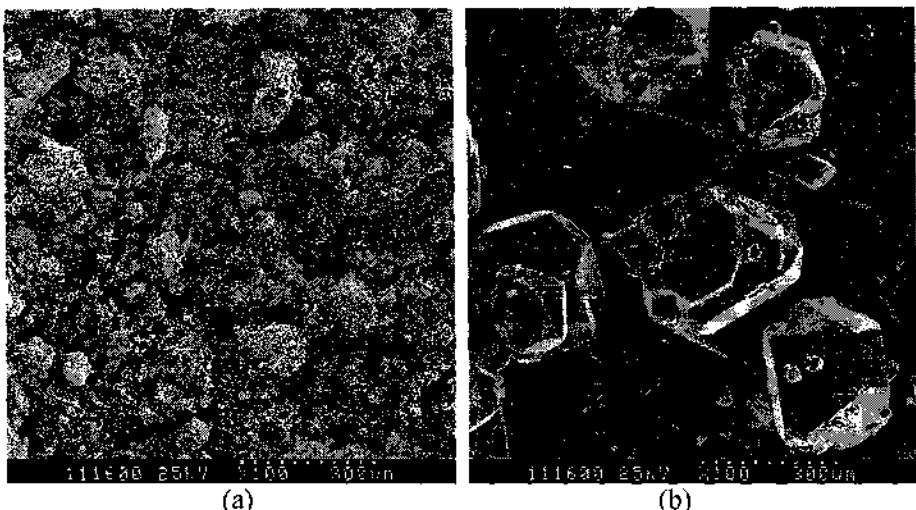


Figure 8. The SEM images of CuO (a) and single crystal  $\text{Cu}(\text{C}_6\text{H}_5\text{CO}_2)_3\text{H}$  (b).

The above results suggest that the  $\text{Ni}(\text{Sal})_2 \cdot 4\text{H}_2\text{O}$  molecule had multi-position identification function in the process of crystal building. But in the case of  $\text{Cu}(\text{C}_6\text{H}_5\text{CO}_2)_3\text{H}$  crystal, there was supermolecule identification function. In the rheological phase system, the generating  $\text{Ni}(\text{Sal})_2 \cdot 4\text{H}_2\text{O}$  or  $\text{Cu}(\text{C}_6\text{H}_5\text{CO}_2)_3\text{H}$  molecule entered into medium nearby solid  $\text{Ni}(\text{OH})_2$  or Cu granule to form quasi-free molecule. When the biggish granule of solid precursor was used, the reaction speed was slow, and the quasi-free molecule had chance to identify each other and assemble to form great crystal.

#### 4 Acknowledgement

This work was supported by The National Natural Science Foundation of China (No. 29971024).

#### References

- Bruinsma P. J., Wang Y., Li X. S., Liu J., Smith P. A. and Bunker B. C., Rheological and solid-liquid separation properties of bimodal suspensions of colloidal gibbsite and boehmite. *J. Colloid Interf. Sci.* **192** (1997) pp. 16–25.
- Fisher M. L. and Lange F. F., Rheological behavior of slurries and consolidated bodies containing mixed silicon nitride networks. *J. Am. Ceram. Soc.* **83** (2000) pp. 1861–1867.
- Yang C. Y., Shih W. Y. and Shih W. H., Celation, consolidation, and rheological properties of boehmite-coated silicon carbide suspensions. *J. Am. Ceram. Soc.* **83** (2000) pp. 1879–1884.
- Gavin H. P., The effect of particle concentration inhomogeneities on the steady flow of electro- and magneto-rheological materials. *J. Non-Newton. Fluid Mech.* **71** (1997) pp. 165–182.
- Chin B. D. and Park O. O., Rheology and microstructures of electrorheological fluids containing both dispersed particles and liquid drops in a continuous phase. *J. Rheol.* **44** (2000) PP. 397–412.
- Cho M. S., Kim J. W., Choi H. J., Webber R. M. and Jhon M. S., Electrorheological characteristics of polyaniline and its copolymer suspensions with ionic and nonionic substituents. *Colloid Polym. Sci.* **278** (2000) pp. 61–64.
- Tsitsilianis C., Katsampas I. and Sfika V., ABC heterottelechelic associative polyelectrolytes. Rheological behavior in aqueous media. *Macromolecules* **33** (2000) pp. 9054–9059.
- Manchado M. A. L., Biagiotti J. and Kenny J. M., Rheological behavior and processability of polypropylene blends with rubber ethylene propylene diene terpolymer. *J. Appl. Polym. Sci.* **81** (2001) pp. 1–10.
- Mezzasalma S. A., Koper G. J. M. and Shchipunov Yu. A., Lecithin organogel as a binary blend of monodisperse polymer-like micelles. *Langmuir* **16** (2000) pp. 10564–10565.
- Cappaere E. and Cressely R., Influence of NaClO<sub>3</sub> on the rheological behaviour of a micellar solution of CPCl. *Rheol. Acta* **39** (2000) pp. 346–353.
- Sun J., Xie W., Yuan L., Zhang K. and Wang Q., Preparation and Luminescence properties of Tb<sup>3+</sup>-doped zinc salicylates. *Mater. Sci. Eng.* **B64** (1999) pp. 157–160.
- Yuan L., Wang Q. and Sun J., Luminescence Properties of Salicylate Doped Zinc Benzoate. *Spectrosc. Lett.* **31** (1998) pp. 1733–1736.
- Sun J., Yuan L., Zhang K. and Wang D., The thermal decomposition mechanism of zinc Phthalate. *Thermochim. Acta* **343** (2000) pp. 105–109.
- Liu L., Yang H., Sun J. and Ai X., A preliminary study of the synthesis of tin-based amorphous material and its behavior on lithium intercalation. *Electrochem. (Chinese)* **4** (1998) pp. 361–364.

This page is intentionally left blank

# NONEQUILIBRIUM NONDISSIPATIVE THERMODYNAMICS AND ITS APPLICATION TO MODERN INORGANIC SYNTHESIS

JI-TAO WANG AND DAVID WEI ZHANG

*Department of Microelectronics, Fudan University, 220 Handan Road, 200433 Shanghai, China  
E-mail: jtwang@fudan.ac.cn*

ZI-KUI LIU

*Department of Materials Science and Engineering, The Pennsylvania State University, University Park, PA 16802, USA  
E-mail: zikui@psu.edu*

The nonspontaneous transformation from graphite to diamond under low pressure is driven by another simultaneous spontaneous reaction, the association of superequilibrium atomic hydrogen, in activated CVD diamond process. That is called reaction coupling or coupled reaction in modern thermodynamics. After quantitative verification of reaction coupling the classification of thermodynamics has been drastically changed. Because the equality of the second law of thermodynamics is not a sufficient and necessary condition for a system being in equilibrium, a new field of nonequilibrium nondissipative thermodynamics emerges. Theoretical calculated results in the new field can be illustrated as nonequilibrium stationary phase diagrams. Nonequilibrium stationary phase diagram in the new field of modern thermodynamics is a powerful theoretical guide for modern inorganic synthesis.

## 1 Introduction

Classical thermodynamics has played an important role in inorganic synthesis for a long time. Especially, equilibrium phase diagrams provide powerful theoretical guide for designing and optimizing the reaction processes. However, in recent years, many new processes for inorganic synthesis or processes for new inorganic materials have emerged, such as activated low pressure diamond synthesis, chemical vapor deposition of cubic boron nitride, preparation of carbon nitride, fullerenes, carbon nanotubes and so on. These processes do not take place under the conditions close to equilibrium. They may include a nonspontaneous reaction (i.e., a positive Gibbs free energy change reaction, if isothermal and isobaric conditions are concerned), so they are difficult explained on the basis of classical thermodynamics. For instance, the activated low-pressure diamond synthesis had been achieved as early as in 1970, but it was in general recognized only after 16 years. Based on classical thermodynamics the low-pressure diamond synthesis from graphite had been seemed thermodynamically impossible. It had even recently been regarded as “thermodynamic paradox” perhaps “violating the second law of thermodynamics” [1-3, 8-9]. The basic problem in classical thermodynamics is that *the equality of the second law of thermodynamics had been intuitively regarded for about 150 years as the necessary and sufficient condition for a system being in equilibrium*. After correction of the unsuitable viewpoint the classification of thermodynamics has to be drastically changed. A complete classification of modern thermodynamics is

proposed and discussed in this paper, and thus modern thermodynamics becomes a self-consistent academic discipline for teaching courses and a powerful and quantitative guide for modern inorganic synthesis.

## 2 Verification of Reaction Coupling

After the activated low-pressure diamond process was generally recognized in 1986, Spear reviewed that “*The new diamond technology has a curious history that is a story of scientific caution ... . It was perhaps influenced by the mystique that surrounds diamonds --- a mystique that has led some scientists to joke of ‘alchemy’ when discussing their investigations* (note: the former Soviet scientists’ achievement started in 1970). *The activated vapor process was first recognized in the Soviet Union, then in Japan, and finally, in the past few years, in the West.”* [12] Since then, another 16 years has passed. Sometime, the low-pressure diamond growth together with the simultaneous graphite etching or the transformation from graphite to diamond under low pressure had still been regarded as a “thermodynamic paradox” maybe “violating the second law of thermodynamics” or not a crystal growth process subordinated to “fundamental principles of thermodynamics”[1-3, 8-9]. All of these doubts are coming from classical thermodynamics, because in equilibrium phase diagram of carbon diamond is metastable while graphite is stable under low pressures. However, the activated CVD diamond growth system is typical nonequilibrium one, the classical equilibrium thermodynamics and the equilibrium phase diagram should not be used.

It is well known that superequilibrium atomic hydrogen (SAH denoted by H\*) produced by hot filament or plasma activation, as shown in Figure 1 (a) and (b), plays an important role during the diamond growth. Based on modern thermodynamics, the activated low-pressure vapor deposited diamond process can be regarded as a coupled reaction [13-19], consisting mainly of two simultaneous reactions.

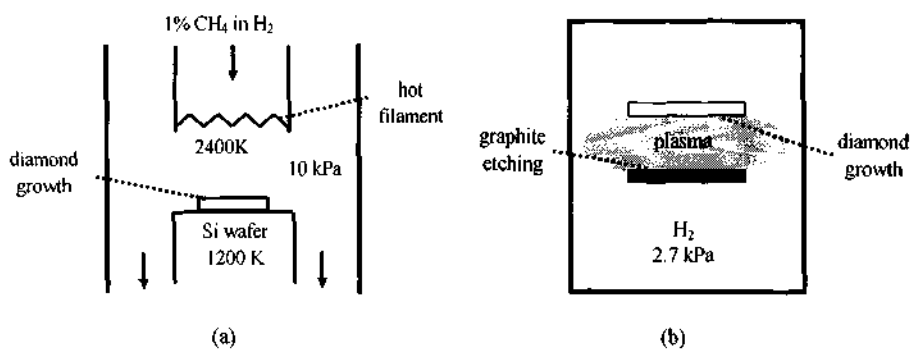
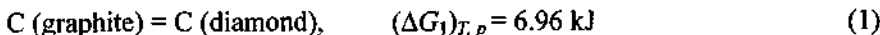
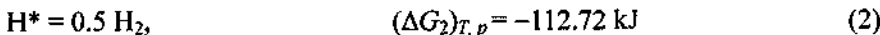


Figure 1. Activated low-pressure diamond growth from the vapor phase.

For process of the activated diamond growth at substrate temperature  $T = 1200\text{ K}$ , pressure  $p = 10\text{ kPa}$  and activation temperature  $T_{activation} = 2400\text{ K}$  the calculated results are as follows.

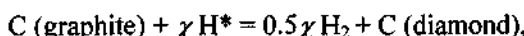


The transformation from graphite to diamond under low pressure, i.e. reaction 1, is a nonspontaneous reaction with positive molar Gibbs free energy change, which should never occur spontaneously toward the right side.



The association of SAH, i.e. reaction 2, is a strong spontaneous reaction with a big negative value of molar Gibbs free energy change. According to the empirical value of reaction rate ratio  $\chi = r_2 / r_1 = 0.28$  (from comparison with experiments), the total molar Gibbs free energy change of the overall coupled reaction 3 is negative.

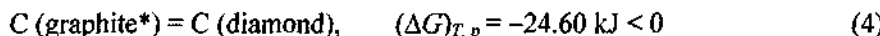
$$(1) + \chi (2),$$



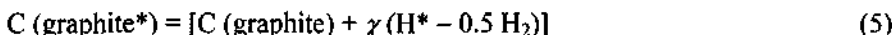
$$(\Delta G)_{T,p} = 6.96 - 0.28 \times 112.72 = -24.60 \text{ kJ} < 0 \quad (3)$$

That is, the activated low-pressure vapor deposited diamond process has been quantitatively verified as an example of thermodynamic reaction coupling, because all these data of molar Gibbs free energy changes are subordinate to criterion in modern thermodynamics for reaction coupling, i.e.  $[(\Delta G_1)_{T,p} > 0, (\Delta G_2)_{T,p} < 0 \text{ and } (\Delta G)_{T,p} \leq 0]$ .

The overall coupled reaction 3 can be rewritten as



Here,



In this way, the routine Gibbs free energy minimization program can still be used, but thermodynamic data of ordinary graphite should be substituted by thermodynamic data of activated graphite, as listed in Table 1 for the carbon-hydrogen system. The derivation of these data can be found in our previous papers and books [13-19], and will not be repeated here again.

**Table 1.** Thermodynamic Data of Activated Graphite (gra\*) during the Existence of Superequilibrium Atomic Hydrogen (Hot filament: 2400 K, Ref. Temp.: 298 K, Pressure range: 0.010-100 kPa,  $\chi = 0.28$ ).

$H_{\text{gra}^*} = 61.036 \text{ (kJ mol}^{-1}\text{)}$		
$S_{\text{gra}^*} = 29.145 \text{ (J mol}^{-1}\text{ K}^{-1}\text{)}$		
$C_p \text{ (J mol}^{-1}\text{ K}^{-1}\text{)} = A + BT 10^{-3} + CT^{-2} 10^5 + DT^2 10^{-6}$		
298-1000 K	1000-1550 K	1550-2400 K
$A = 1.7735$	$A = 27.184$	$A = 27.2366$
$B = 39.236$	$B = 0.1240$	$B = -0.6810$
$C = -1.4317$	$C = -39.064$	$C = -33.356$
$D = -17.7877$	$D = -0.2778$	$D = 0.1279$

Figure 2 is an example of our calculated nonequilibrium stationary phase diagrams for the activated diamond growth from C-H system at pressure of 4.8 kPa with filament temperature of 2400 K. The phase diagram is divided into five regions by these two gas-solid phase lines and a horizontal line. They are (i). gas phase region (no deposition region), (ii). diamond phase region (diamond growth region), (iii). diamond stable & graphite metastable region, (iv). graphite phase region, and (v) graphite stable & diamond metastable region. For low-pressure diamond growth research the regions (iii), (iv) and (v) are usually called nondiamond carbon deposition region. For understanding the characteristic of nonequilibrium stationary phase diagram, it is supposed here that the graphitization of diamond could be negligible in the range of the figure and that thermodynamic data of diamond could be extrapolated from those reported in the literature up to 1200 K.

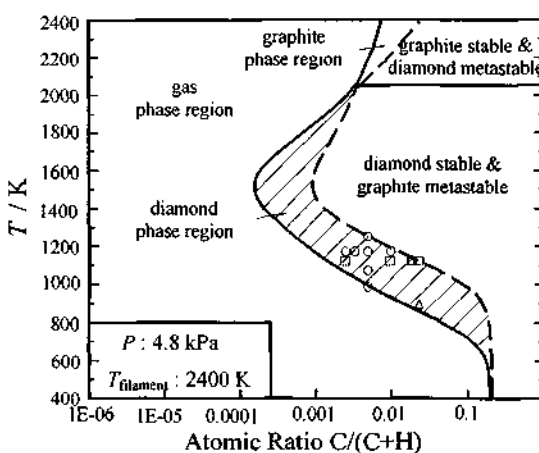


**Figure 2.** Nonequilibrium (stationary) phase diagrams for C-H system with the existence of superequilibrium concentration atomic hydrogen ( $\text{O}$ ,  $\bullet$  and  $\Delta$  are experimental data reported by Matsumoto [6], Sato[10], and Southworth [11] etc.).

In Figure 2 the intersection point ( $\sim 2050$  K) of two gas-solid phase lines is a triple (three-phase) point, if pressure is fixed. Gas phase, solid diamond phase and solid graphite phase may exist at the same time with or without phase transformation between any two phases. At this point, all compositions of these three phases and temperature have already been fixed. That agrees with the Gibbs phase rule, i.e.,  $F$  (degree of freedom) =  $K$  (number of components) -  $\Phi$  (number of phases) + 2, and here  $F = 2 - 3 + 2 = 1$ . One degree of freedom, pressure, has been fixed in Figure 2, so all compositions of these three phases and temperature have been fixed. For each of two-phase line (stable diamond gas-solid phase line at lower temperature or activated graphite gas-solid phase line at high temperature) gas phase and one solid phase (diamond or graphite) exist with or without phase transformation between phases, so one parameter (temperature or composition) can be changed. That agrees very well with the Gibbs phase rule. i.e.,  $F = 2 - 2 + 2 = 2$ . One degree of freedom, pressure, has been fixed in Figure 2, so only one parameter (temperature or composition) can be changed. In single-phase region (such as gas phase region or

diamond growth region) two parameters (such as temperature and gas composition) can be changed. That agrees also very well with the Gibbs phase rule, i.e.,  $F = 2 - 1 + 2 = 3$  here. One degree of freedom, pressure, has been fixed in Figure 2, so both temperature and composition can be changed. That is, nonequilibrium stationary phase diagrams are still subordinated to the Gibbs phase rule.

Figure 2 also shows the excellent agreement between theory and experiments reported by different research groups [6, 10-11]. The term of nonequilibrium phase diagram had been used in polymer science as shearing induced phase diagram [4] or in amorphous alloy during quenching [7]. The meanings are quite different from that in our case. However, there is no room for nonequilibrium stationary phase diagrams in classical thermodynamics. That is due to a basic problem hidden inside classical thermodynamics for about 150 years.

### 3 Classification of Modern Thermodynamics

After reaction coupling has been quantitatively verified in the activated low-pressure diamond growth from the vapor phase, the classification of thermodynamics has been drastically changed, as shown in Figure 3. The formulation of Gibbs free energy under isothermal and isobaric conditions is more familiar for most scientists, so the discussion in this paper is only based on Gibbs free energy formulation. All criteria for different fields are listed in square brackets [ ] in Figure 3. Here,  $(dG_1)_{T,p}$ ,  $(dG_2)_{T,p}$  and  $(dG)_{T,p} = [(dG_1)_{T,p} + (dG_2)_{T,p}]$  are Gibbs free energy changes of reaction 1, reaction 2 and the whole system at constant temperature and pressure, respectively.  $X$  and  $J$  represent thermodynamic force and thermodynamic flux for irreversible process, respectively.

The first order division is based on the system with or without reaction coupling, so the modern thermodynamics in a broad sense has been divided into the classical thermodynamics and the modern thermodynamics in a narrow sense. It is very clear that classical thermodynamics should only be used for simpler systems without reaction coupling, because the second law of thermodynamics, such as  $(dG)_{T,p} \leq 0$ , is only concerned with the whole system and not concerned with individual processes. That is a severe limitation of classical thermodynamics, because systems in modern inorganic synthesis and in life science are usually complex with multi-reaction processes including reaction coupling.

The second order division is based on the second law of thermodynamics for both the classical thermodynamics and the modern thermodynamics in a narrow sense. In this way, all nomenclature in classical thermodynamics can keep unchanged, but the classical nomenclature should not be used for the modern thermodynamics in a narrow sense. Thus a radically new field of nonequilibrium nondissipative thermodynamics emerges. It belongs to the equality of the second law of thermodynamics and also belongs to the nonequilibrium thermodynamics, i.e.,  $[(dG_1)_{T,p} > 0, (dG_2)_{T,p} < 0 \text{ and } (dG)_{T,p} = 0]$ , so quantitative calculation in the new field results in nonequilibrium stationary phase diagrams, as discussed for Figure 2. The inequality of the second law of the modern thermodynamics in the narrow sense, i.e.,  $[(dG_1)_{T,p} > 0, (dG_2)_{T,p} < 0 \text{ and } (dG)_{T,p} < 0]$ , should be called modern dissipative

**thermodynamics.**

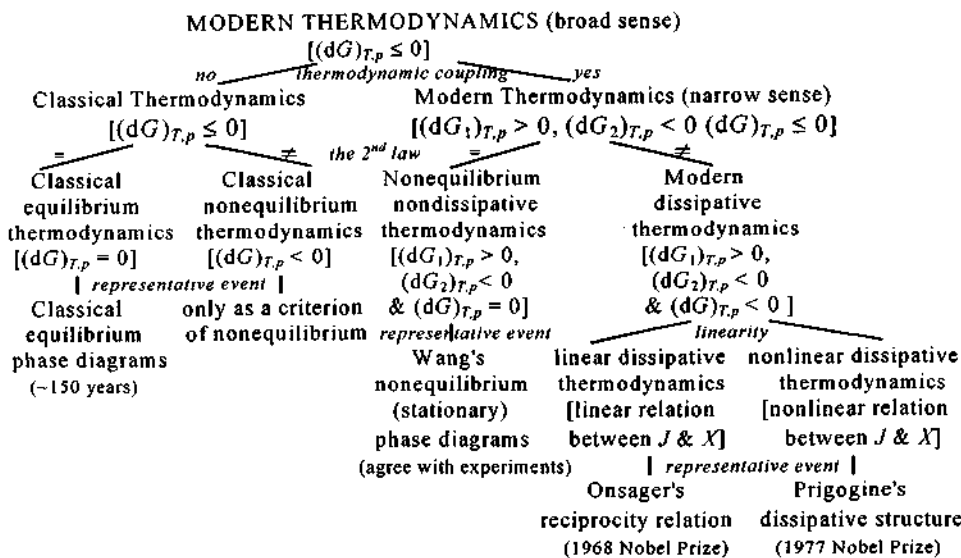


**Figure 3.** A complete systematization of modern thermodynamics. Note:  $(\Delta G_1)_{T,P}$ ,  $(\Delta G_2)_{T,P}$  and  $(\Delta G)_{T,P}$  are Gibbs free energy changes of reaction 1, reaction 2 and the whole system at constant temperature and pressure, respectively.  $X$  and  $J$  represent thermodynamic force and thermodynamic flux for irreversible process, respectively.

The third order division is based on linearity, thus the traditional terms of “linear nonequilibrium thermodynamics” and “nonlinear nonequilibrium thermodynamics” [5] should be renamed as the terms of “linear dissipative thermodynamics” and “nonlinear dissipative thermodynamics”, respectively, in the complete classification of thermodynamics.

Now definitions or frameworks of modern thermodynamics in a broad sense, of classical thermodynamics, and of modern thermodynamics in a narrow sense are very clear. Modern thermodynamics in a broad sense includes all fields of thermodynamics (both classical thermodynamics and modern thermodynamics in a narrow sense) for any macroscopic system, but modern thermodynamics in a narrow sense includes only three fields of thermodynamics, i.e., nonequilibrium nondissipative thermodynamics, linear dissipative thermodynamics and nonlinear dissipative thermodynamics. The modern thermodynamics in a narrow sense should not be called nonequilibrium thermodynamics, because the classical nonequilibrium thermodynamics is not included. Meanwhile, the classical thermodynamics should only be applied to simpler systems without reaction coupling. That is, the application of classical thermodynamics to some modern inorganic syntheses and to the life science may be not suitable. Without the self-consistent classification of modern thermodynamics it was very difficult to really accept the term of "modern thermodynamics" even only for teaching courses.

#### 4 Conclusions

The basic problem in classical thermodynamics is that *the equality of the second law of thermodynamics had been intuitively regarded for about 150 years as the necessary and sufficient condition for a system being in equilibrium.* Modern thermodynamics is a powerful and useful tool for research on modern inorganic synthesis, life science and other fields of science and technology. However, a complete classification of modern thermodynamics had not been finished for a long time. That has seriously hindered the general acceptance of modern thermodynamics and the application of modern thermodynamics. In this paper it can be found that there is a radically new field — nonequilibrium nondissipative thermodynamics in modern thermodynamics for nonequilibrium stationary phase diagrams. Theorem of nonequilibrium stationary phase diagrams may be used not only for the activated vapor deposited diamond process but also for activated vapor deposition of cubic boron nitride, carbon nitride, fullerenes, carbon nanotubes and even for biological systems.

#### 5 Acknowledgements

Project 50172011 supported by National Natural Science Foundation of China, and project supported by Chinese Ministry of Science and Technology. ZKL is supported by National Science Foundation CAREER Award under grant DMR 9983532.

#### References

1. Hwang N.M., Evidence of nanometer-sized charged carbon clusters in the gas phase of the diamond chemical vapor deposition (CVD) process. *J. Crystal Growth*, **204** (1999) 85-90.
2. Jiang H.M., Hwang N.M., Theory of the charged cluster formation in the low pressure synthesis of diamond: Part I. Charged-induced nucleation. *J. Materials Res.*, **13**(12) (1998) 3527-3535.
3. Jiang H.M., Hwang N.M., Theory of the charged cluster formation in the low pressure synthesis of diamond: Part II. Free energy function and thermodynamic stability. *J. Materials Res.*, **13**(12) (1998) 3536-3549.
4. Jou D., Casas-Vazquez J., Criado-Sancho M., Thermodynamics of fluids under flow (Springer, Heidelberg, 2000) 231 pages.
5. Kondepudi D., Prigogine I., Modern thermodynamics — from heat engines to dissipative structures (Wiley, New York, 1998) 486 pages.
6. Matsumoto S., Sato Y., Tsutsumi M., Setaka N., Growth of diamond particles from methane-hydrogen gas. *J. Mater. Sci.* **17**, (1982) pp.3106-3112.
7. Nonequilibrium phase diagrams of ternary amorphous alloys (Springer, Heidelberg, 1997) 295 pages.
8. Piekarczyk W., Crystal growth of CVD diamond and some of its peculiarities. *Cryst. Res. Technol.*, **34** (1999) pp.553-563.
9. Piekarczyk W., How and why CVD diamond is formed: a solution of the

- thermodynamic paradox, *J. of Materials Science*, **33** (1998) pp.3443-3453.
- 10. Sato Y., Kamo M., Texture and some properties of vapor-deposited diamond films. *Surface and Coatings Tech.* **39/40** (1989) pp.183—198.
  - 11. Southworth P., Buhaenko D.S., Ellis P.J., Jenkins C.E., Stoner B.R., Growth of oriented diamond films on silicon substrates. In: *Diamond Materials, 3rd Intern'l Symp. at Honolulu, Hawaii 1993*, ed. by Dismukes J.P., Ravi K.V., Spear K.E., Lux B., Setaka N. (The Electrochemical Soc., Inc., Pennington, 1993), pp. 87-94.
  - 12. Spear K.E., Growth of crystalline diamond from low-pressure gases, *Earth and Mineral Science*, **56**(4) (1987) pp.53-59.
  - 13. Wang J.-T., Modern thermodynamics for advanced materials research". In: *Eng. & Tech. Sci. 2000, Session 3 Adv. Materials, vol. 1, International Conf., Oct. 2000, Beijing, China*, eds. by Song J., Yin R. (New World Press, Beijing, 2000) pp. 864-870.
  - 14. Wang J.-T., Nonequilibrium nondissipative thermodynamics with application to low-pressure diamond synthesis (Springer, Heidelberg, 2002) 254 pages.
  - 15. Wang J.-T., Phase diagrams of stationary nonequilibrium states — Thermodynamics for low-pressure diamond growth from the vapor phase (in Chinese) (Science Press, Beijing, 2000) 202 pages.
  - 16. Wang J.-T., Carlsson J.-O., A thermochemical model for diamond growth from the vapor phase, *Surf. Coat. Technol.*, **43/44** (1990) pp.1-9.
  - 17. Wang J.-T., Ding S.-J., Zhang D.W. et al., Modern thermodynamics for activated cubic boron nitride growth from the vapor phase. In: *Eng. & Tech. Sci. 2000, Session 3 Adv. Materials, vol. 1, International Conf. Oct. 2000, Beijing, China*, eds. by Song J., Yin R. (New World Press, Beijing, 2000) pp. 871-880.
  - 18. Wang J.-T., Shen J.-Y., Zhang D.W., Modern thermodynamics in CVD of hard materials". *International J. Refractory Metals and Hard Materials*, **19**(4-6) (2001) pp.461-466.
  - 19. Wang J.-T., Wan Y.-Z., Zhang D.W., Z.-J. Liu, Z.-Q. Huang: "Calculated phase diagrams for activated low pressure diamond growth from C-H, C-O and C-H-O systems". *J. Materials Research*, **12** (12) (1997) pp.3250-3253.

# THEORETICAL STUDY ON THE REACTION MECHANISMS OF THE IMIDE FORMATION IN AN N-(O-CARBOXYBENZOYL)-L-AMINO ACID

ZHIJIAN WU, FUQIANG BAN AND RUSSELL J. BOYD \*

*Department of Chemistry, Dalhousie University, Halifax, NS, Canada B3H 4J3*

*E-mail: Russell.boyd@dal.ca*

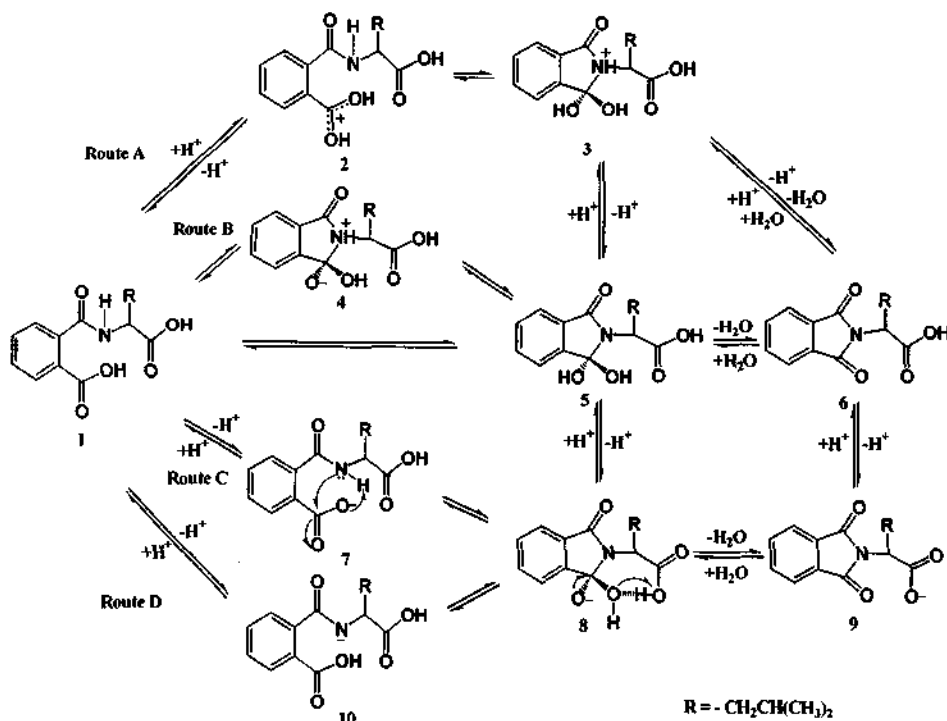
Reaction mechanisms of the imide formation in an N-(o-carboxybenzoyl)-L-amino acid have been studied using density functional theory. Our results suggest that the reaction route initiated by protonation at the oxygen of the carboxyl group of the amino acid is favored, and those initiated by deprotonation at the oxygen of carboxyl group of phthalic acid and at amidic nitrogen from the reactant are minor pathways. These conclusions are in good agreement with the experimental facts that under highly acidic conditions (hydrogen ion concentration  $< -1$ ), imide formation is the most favorable, while in the pH range 0-5, cyclization is not the dominant reaction. Our calculations also show that the carboxyl group of the amino acid is involved in the catalytic reaction in both the favored and minor pathways.

## 1 Introduction

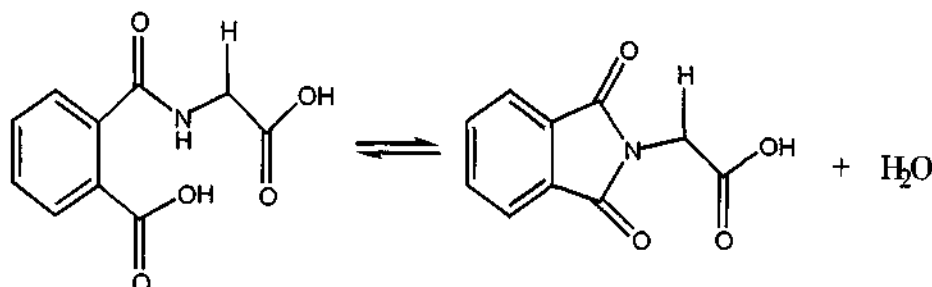
The mechanisms by which enzymatic catalysis proceeds are important, however, very perplexing in enzymology [1,2]. Carboxyl (acid) proteinases, conventionally described as aspartic proteinases [2], have a very long history in enzymology. The distinct characteristic of aspartic proteinases is their pH-dependent catalytic action with an optimal pH range 1.9–4.0. The hydrolysis of a peptide bond is catalyzed by two carboxyl groups of the aspartic residue. In fact, as models for hydrolytic enzymes, intramolecular systems containing carboxyl groups have been extensively investigated for many decades and continue to be a subject of great interest [3-9]. As can be seen experimentally, cyclization to the imide [6-9] and amide hydrolysis [3-8] are the two main types of reactions of interest that occur in the model systems. In particular, molecules containing two carboxyl groups, such as N-(o-carboxybenzoyl)-L-phenylalanine, N-(o-carboxybenzoyl)-L-leucine and N-(o-carboxybenzoyl)-L-valine [7,8], have been used to probe the catalytic activity of the neighboring carboxyl group from an amino acid that is involved in enzymatic reactions. Possible reaction mechanisms for cyclization to the imide and amide hydrolysis of N-(o-carboxybenzoyl)-L-leucine have also been presented experimentally by Nome and co-workers [8].

In this paper, we focus on the imide formation. Reaction mechanism for amide hydrolysis will be studied and presented in a separate paper. For cyclization to the imide, the three proposed routes (A, B and C in Scheme 1) correspond to different pH ranges [8]. Cyclization depends strongly on the acidity of the solution. It predominates under highly acidic conditions (hydrogen ion concentration  $< -1$ ), this corresponds to Route A ( $1 \rightarrow 2 \rightarrow 3 \rightarrow 6$  and  $1 \rightarrow 2 \rightarrow 3 \rightarrow 5 \rightarrow 6$ ), in which the intermediates are either pure cationic ( $1 \rightarrow 2 \rightarrow 3 \rightarrow 6$ ) or a mixture of cationic and neutral ( $1 \rightarrow 2 \rightarrow 3 \rightarrow 5 \rightarrow 6$ ). In the pH range 0-5, cyclization is not the dominant reaction. In Route B ( $1 \rightarrow 4 \rightarrow 5 \rightarrow 6$  and  $1 \rightarrow 5 \rightarrow 6$ ) where pH range is 0-2, the intermediates are zwitterionic or neutral. In Route C ( $1 \rightarrow 7 \rightarrow 8 \rightarrow 9 \rightarrow 6$ ), the

intermediates are monoanionic with pH range 2-5. In addition, besides the pathways presented by Nome and co-workers, previous study on N-methylphthalamic acid [6] proposed other pathways for the cyclization to the imide which have been adapted for N-(*o*-carboxybenzoyl)-L-leucine shown in Scheme 1 (but the relationship between pH ranges and pathways are not clearly assigned). These additional pathways include the routes of initiation by deprotonation at amide nitrogen (**10**) shown as Route D (**1**→**10**→**8**→**9**→**6** and **1**→**10**→**8**→**5**→**6**) and **1**→**7**→**8**→**5**→**6**. Possible routes proposed by experiments [6,8] for cyclization to the imide are summarized in Scheme 1.



Scheme 1



Scheme 2

Due to the size of the molecule and the complexity of the reaction pathways, only a few theoretical computations [10-15] have been reported for reaction mechanisms of intramolecular systems containing carboxyl groups. Most of the theoretical studies have concentrated on the pathway of amide hydrolysis. The previous theoretical studies have been carried out mainly at the Hartree-Fock (HF) level, with single point energies calculated using second-order Møller-Plesset perturbation theory (MP2). The development of density functional theory (DFT) with modern exchange-correlation functionals has paved the way to study equilibrium structures and reaction pathways for intramolecular catalysis in fairly large molecules. On the other hand, since experiment alone is usually not enough to deduce reaction mechanisms, theoretical work is necessary to gain further insight into reaction mechanisms. In this paper, we report the first theoretical study of the reaction mechanism of the imide formation shown in Scheme 1 using our model system shown in Scheme 2. Our model system with two carboxyl groups is based on previous experimental studies [7,8], and is designed to investigate intramolecular catalytic effects. The final product is produced by eliminating a water molecule through various tetrahedral intermediates. The smaller amino acid, glycine, is used in our model system (*N*-(*o*-carboxybenzoyl)-L-glycine). Density functional theory is employed on the study of reaction mechanisms of the imide formation. Solvent effects have also been considered because they often play a crucial role in biological processes.

## 2 Computational Methods

All geometry optimizations were performed with the B3LYP hybrid density functional in conjunction with the 6-31G(d,p) basis set using the GAUSSIAN 98 suite of programs [16]. The B3LYP functional is a combination of Becke's three-parameter hybrid exchange functional [17], and the Lee-Yang-Parr correlation functional [18]. Harmonic vibrational frequencies and zero-point vibrational energies (ZPVEs) were obtained at the same level of theory. Relative energies were obtained by performing single point calculations at the B3LYP level with the 6-311G(2df,p) basis set using the above optimized geometries and by including the zero-point vibrational energy i.e., B3LYP/6-311G(2df,p)//B3LYP/6-31G(d,p)+ZPVE. The entropy contributions to the free energies at 298.15 K were derived from B3LYP/6-31G(d,p) frequency calculations.

The solvent effect on the potential energy surface was investigated by single point calculations at the B3LYP/6-311G(2df,p) level using the conductor-like polarized continuum solvent model (CPCM) [19] (denoted CPCM-B3LYP/6-311G(2df,p)) on the geometries obtained by using the Onsager model [20] with a dielectric constant of 78.39 at the B3LYP/6-31G(d,p) level (denoted Onsager-B3LYP/6-31G(d,p)). The zero-point energy corrections obtained from the Onsager-B3LYP/6-31G(d,p) frequency calculations are included in the calculations of the relative energies in the solvation of water, i.e., CPCM-B3LYP/6-311G(2df,p)//Onsager-B3LYP/6-31G(d,p)+Onsager-ZPVE. The entropy contributions to the free energies in solvation at 298.15 K were derived from Onsager-B3LYP/6-31G(d,p) frequency calculations. All energies are in kJ mol<sup>-1</sup> and bond distances in angstroms (Å).

### 3 Results and Discussion

Our calculation reveals that the route of  $1 \rightarrow 2 \rightarrow 3 \rightarrow 5 \rightarrow 6$  (Route A) in Scheme 1 is the most favorable reaction route in this mechanism. This corresponds to high acidic region experimentally. Route B ( $1 \rightarrow 4 \rightarrow 5 \rightarrow 6$  and  $1 \rightarrow 5 \rightarrow 6$ ) with pH range 0-2 is not located. Other routes studied in this paper are less favorable, which corresponds to high pH ranges. These minor routes include  $1 \rightarrow 2 \rightarrow 3 \rightarrow 6$ ,  $1 \rightarrow 7 \rightarrow 8 \rightarrow 9 \rightarrow 6$  and  $1 \rightarrow 10 \rightarrow 8 \rightarrow 9 \rightarrow 6$ . The routes that most unlikely to occur are  $1 \rightarrow 7 \rightarrow 8 \rightarrow 5 \rightarrow 6$  and  $1 \rightarrow 10 \rightarrow 8 \rightarrow 5 \rightarrow 6$ . On the other hand, routes  $1 \rightarrow 7 \rightarrow 8 \rightarrow 9 \rightarrow 6$  and  $1 \rightarrow 10 \rightarrow 8 \rightarrow 9 \rightarrow 6$  are the two competitive routes. These conclusions are in consistent with the experiment [8] that at highly acidic conditions (hydrogen ion concentration < -1), the imide formation is the most favorable (Route A,  $1 \rightarrow 2 \rightarrow 3 \rightarrow 5 \rightarrow 6$ ), while in the pH range 2-5 (Route C), cyclization is not the dominant reaction. Our calculation also shows that the carboxyl group of the amino acid is involved in the reaction of both high acidic region (hydrogen ion concentration < -1) and pH range 2-5.

The energy profile in aqueous solution at only ZPVE correction and 298.15 K shows a pattern similar to those in the gas phase. Solvent effects do not have significant influence on the reaction pathways for the imide formation.

### 4 Acknowledgements

We gratefully acknowledge the Natural Sciences and Engineering Research Council of Canada and the Killam Trusts for financial support.

### References

1. Northrop, D. B. *Acc. Chem. Res.* **34** (2001) pp790-797.
2. Page, M. I.; Williams, A. *Enzyme Mechanisms*, Royal Society of Chemistry, London, 1987, pp229-239.
3. Perry, C. J. *J. Chem. Soc., Perkin Trans. 2* (1997) pp977-982.
4. Granados, A. M.; de Rossi, R. H. *J. Org. Chem.* **66**(2001) pp1548-1552.
5. Bender, M. L.; Chow, Y. -L.; Chloupek, F. *J. Am. Chem. Soc.* **80**(1958) pp5380-5384.
6. Brown, J.; Su, S. C.; Shafer, J. A. *J. Am. Chem. Soc.* **88**(1966) pp4468-4474.
7. Onofrio, A. B.; Joussef, A. C.; Nome, F. *Synth. Commun.* **29**(1999) pp3039-3049.
8. Onofrio, A. B.; Gesser, J. C.; Joussef, A. C.; Nome, F. *J. Chem. Soc. Perkin Trans. 2* (2001) pp1863-1868.
9. Fife; T. H.; Chauffe, L. *J. Org. Chem.* **65**(2000) pp3579-3586.
10. Yunes, S. F.; Gesser, J. Chaimovich, C. H.; Nome, F. *J. Phys. Org. Chem.* **10**(1997) pp461-465.
11. Barros, T. C.; Yunes, S.; Menegon, G.; Nome, F.; Chaimovich, H.; Politi, M. J.; Dias, L. G.; Cuccovia, I. M. *J. Chem. Soc. Perkin Trans. 2* (2001) pp2342-2350.
12. Park, H. Suh J.; Lee, S. *Theochem.* **490**(1999) pp47-54.

13. Hori, K.; Kamimura, A.; Ando, K.; Mizumura, M.; Ihara, Y. *Tetrahedron* **53**(1997) pp4317-4330.
14. Antonczak, S.; Ruiz-López, M. F.; Rivail, J. L. *J. Am. Chem. Soc.* **116**(1994) pp3912-3921.
15. Antonczak, S.; Ruiz-López, M. F.; Rivaíl, J. L. *J. Mol. Model.* **3**(1997) pp434-442.
16. Frisch, M. J.; Trucks, G. W.; Schlegel, H. B.; Scuseria, et. al. GAUSSIAN 98, Gaussian, Inc.: Pittsburgh, PA, 1998.
17. Becke, A. D. *J. Chem. Phys.* **98**(1993) pp1372-1377.
18. Lee, C.; Yang, W.; Parr, R. G. *Phys. Rev. B* **37**(1988) pp785-789.
19. Barone, V.; Cossi, M. *J. Phys. Chem. A* **102**(1998) pp1995-2001.
20. Onsager, L. *J. Am. Chem. Soc.* **58**(1936) pp1486-1493.

This page is intentionally left blank

## SYNTHESIS AND X-RAY CRYSTAL STRUCTURES OF LOW-DIMENSIONAL BORATES FROM HYDROTHERMAL AND SOLVOTHERMAL SYSTEMS

ZHEN-TAO YU, YI HE, YU-SHENG JIANG, ZHAN SHI, WEI CHEN  
AND JIE-SHENG CHEN\*

*State Key Laboratory of Inorganic Synthesis and Preparative Chemistry, College of Chemistry,  
Jilin University, Changchun 130023, P. R. China  
E-mail: chemcj@mail.jlu.edu.cn*

A series of new polyborates have been synthesized using hydrothermal and solvothermal techniques. The structures of these compounds were solved by single-crystal X-ray diffraction analysis. The compound  $Pb_6B_{11}O_{18}(OH)_6$  (1), which crystallized from a hydrothermal system in the trigonal  $P3_2$  space group, has a novel chiral structure consisting of infinite helical chains and finite chain fragments built up from  $BO_4$  and  $BO_3$  units. Two alkaline-earth metal borate compounds –  $Ba_3B_6O_9(OH)_6$  (2) and  $SrBO_2(OH)$  (3) were also prepared from a hydrothermal system. The structure of 2 (space group  $P2/c$ ) can be regarded as constructed from anionic borate chains of  $B_3O_3$  six-membered rings sharing B atoms, which are all tetrahedrally coordinated by oxygen atoms. In the structure of 3 (space group  $Pnma$ ), the  $Sr^{2+}$  ion is surrounded by eight oxygen atoms and the borate ion is identified as an isolated  $[BO_2(OH)]^{2-}$  group. In addition, we obtained two metal-complex containing borates –  $Zn(C_2H_5N_2)_3B_3O_7(OH)_3$  (4) and  $Co(C_2H_5N_2)_3B_3O_7(OH)_3$  (5), which are isostructural (space group  $P2_1/c$ ) with each other, from a nonaqueous system. The crystal structures of 4 and 5 are characterized by the chiral  $M(en)_3^{2+}$  ( $M = Zn, Co$ ) cations and the isolated  $B_3O_7(OH)_2^{2-}$  groups. It can be seen that the wide variability of borate crystal chemistry allows the creation of very different structure types.

### 1 Introduction

The discovery of  $\beta$ - $Ba_2B_2O_4$  (BBO) has stimulated many attempts to synthesize new borates since these compounds have enormous potential as NLO materials [1-4], as the hosts of laser and luminescent materials [5,6] and as thermoelectronic cathodal materials for microgenerators. On the other hand, the structure types of borate compounds manifest the wide variability because the boron atom is capable of being coordinated in either three-fold (trigonal) or four-fold (tetrahedral) mode. Three classes of borates are distinguished: borates containing only triangular  $BO_3$  groups, those containing only tetrahedral  $BO_4$  groups, and those where  $BO_3$  and  $BO_4$  groups are combined. On this basis, the structural chemistry of borates extends a broad spectrum from isolated species, oligomers, rings, and chains to layers and frameworks. For example,  $LiB_3O_5$  (LBO) has a chain arrangement [7] whereas  $Sr_2Be_2B_2O_7$  (SBBO) has a layered structure [8]. In the two-dimensional  $(C_2N_2H_{10})_2[(BO_{2.5})_2(GeO_2)_3]$  [9], tetrahedrally-coordinated boron is incorporated into the templated germanate network. And the three-dimensional  $Zn_4O(BO_3)_2$  [10] is the only neutral-framework borate containing micropores.

Borate minerals are common but synthesized examples are relatively rare [11]. We also notice that the borate crystals were usually grown by high temperature methods, exemplified by the high temperature flux and melt techniques [12-14]. There were a few reports on the preparation of borates by using the sol-gel technique.

Despite of applications in geochemistry and in crystal growth long before, the hydrothermal technique has only recently been exploited in the routine preparation of inorganic materials. Nevertheless, hydrothermal and related syntheses have evolved into an area of rapidly increasing importance for the preparation of new and structurally complex solid-state compounds [15-18]. It was only during the last two decades that borates synthesized by utilizing hydrothermal and related techniques have occasionally been reported [19,20].

In this work, we describe the exploratory synthesis of a series of new low-dimensional borates using hydrothermal and solvothermal techniques:  $\text{Pb}_6\text{B}_{11}\text{O}_{18}(\text{OH})_9$  (**1**) [21], two alkaline-earth metal borate compounds –  $\text{Ba}_3\text{B}_6\text{O}_9(\text{OH})_6$  (**2**) and  $\text{SrBO}_2(\text{OH})$  (**3**) [22], two metal-complex containing borates –  $\text{Zn}(\text{C}_2\text{H}_8\text{N}_2)_3\text{B}_5\text{O}_7(\text{OH})_3$  (**4**) and  $\text{Co}(\text{C}_2\text{H}_8\text{N}_2)_3\text{B}_5\text{O}_7(\text{OH})_3$  (**5**). Structure determinations show that these compounds are of different structure types.

## 2 Experimental

Compounds **1**, **2**, **3**, **4** and **5** were synthesized hydrothermally or solvothermally using  $\text{H}_3\text{BO}_3$  as the boron source. All reagents were of analytical grade. The syntheses were carried out in 20 mL Teflon-lined stainless steel vessels under autogeneous pressure with a filling capacity of approximately 70%. The sole resulting crystals were collected by filtration, washed with distilled water for **1**, **2** and **3** but with ethanol for **4** and **5**, and dried in air at ambient temperature.

Table 1 shows the optimal compositions of the initial reaction mixtures and crystallization conditions for obtaining highly crystalline single phases of the borate compounds.

**Table 1.** Typical gel compositions and crystallization conditions.

Gel composition in molar ratio <sup>a</sup>	Crystallization Time (days)	Conditions Temp. (°C)	Product
1 $\text{PbAc}_2$ : 2A: 7en: 133 $\text{H}_2\text{O}$	2	180	<b>1</b>
1 $\text{BaAc}_2$ : 0.75A: 3en: 4C: 67 $\text{H}_2\text{O}$	3	180	<b>2</b>
1 $\text{Sr}(\text{NO}_3)_2$ : 1A: 3en: 67 $\text{H}_2\text{O}$	5	180	<b>3</b>
1 $\text{ZnAc}_2$ : 10A: 20en: 124THF	30	100	<b>4</b>
1 $\text{CoAc}_2$ : 18A: 116en	24	180	<b>5</b>

<sup>a</sup> A =  $\text{H}_3\text{BO}_3$ , en =  $\text{H}_2\text{NCH}_2\text{CH}_2\text{NH}_2$ , B =  $\text{CH}_3\text{COOH}$ , C =  $\text{CH}_3\text{NH}_2$

## 3 Results and Discussion

### 3.1 $\text{Pb}_6\text{B}_{11}\text{O}_{18}(\text{OH})_9$ (**1**)

Hydrothermal and related processes are relatively complex. Many factors, such as initial reactants, starting concentration, pH value, crystallization temperature and pressure may affect the formation and crystal growth of products. The presence of ethylenediamine in the crystallization system for **1** seems to be critical for the growth

of the crystals, because without ethylenediamine, no crystals of **1** appear in the reaction product. The acetic acid is used to adjust the pH value of the reaction system. We find that the pH value is an important factor for the synthesis. When the pH value is approximately 8.5, pure colorless columnar crystals of **1** can be formed. Higher pH in the gel usually results in the formation of **1** and an unknown sheet phase. However, at lower pH value (<7), no crystallization occurs at reaction temperatures below 240 °C. In addition, at temperatures lower than 180 °C, pure phase of **1** cannot be obtained. The relative amount of the boron source also affects the crystallization of **1**. As the concentration of H<sub>3</sub>BO<sub>3</sub> increases, the crystallinity of **1** becomes poor, and impurity starts to form with **1** from the reaction system.

The chiral borate **1** is the first reported polyborate containing infinite and finite chains (Fig. 1), which crystallizes in the trigonal space group *P*3<sub>2</sub> with lattice constants  $a = 11.7691(7)$  Å and  $c = 13.3361(12)$  Å. The infinite helical chains A and B with a composition of [B<sub>4</sub>O<sub>8</sub>(OH)]<sub>n</sub><sup>5n-</sup> are composed of non-planar six-membered B<sub>3</sub>O<sub>3</sub> rings which are found to join together by sharing the tetrahedrally-coordinated B atoms. The central axis of each helical chain running along the *c* axis is a three-fold screw axis. For the chain C of the B<sub>3</sub>O<sub>7</sub>(OH)<sub>2</sub><sup>7-</sup> fragment, three B atoms are linked into a finite chain through O bridges, which comprise a triangular BO<sub>3</sub> and two distorted tetrahedral BO<sub>4</sub> units. The negative charges in **1** are compensated by the Pb<sup>2+</sup> cations residing between adjacent chains of anions. The Pb<sup>2+</sup> cations are believed to be responsible for holding the chain structures together mainly through electrostatic interactions with the chains.

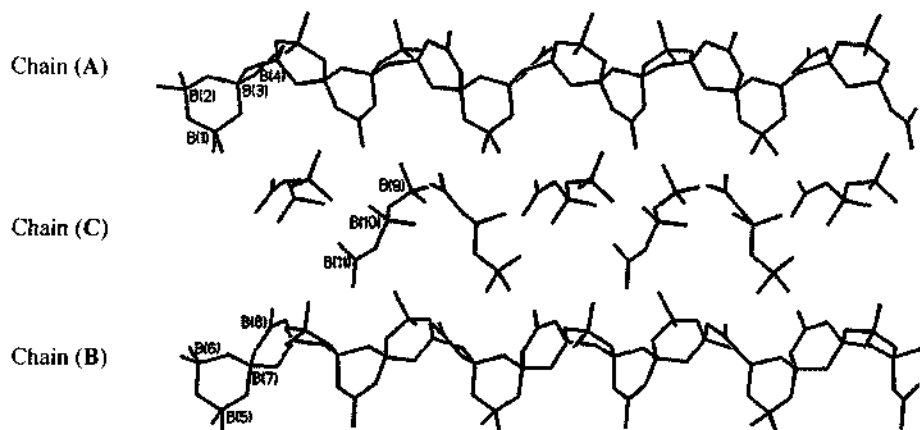


Figure 1. View of the chain structures along the *a* axis for Pb<sub>6</sub>B<sub>11</sub>O<sub>18</sub>(OH)<sub>6</sub> (**1**).

### 3.2 Two alkaline-earth metal borates Ba<sub>3</sub>B<sub>6</sub>O<sub>9</sub>(OH)<sub>6</sub> (**2**) and SrBO<sub>2</sub>(OH) (**3**)

Employing a hydrothermal technique, **2** and **3** were also synthesized in the presence of ethylenediamine and methylamine. The role of ethylenediamine and methylamine

in the crystallization systems for compounds **2** and **3** is not very clear yet, but these species seem to be indispensable to the growth of the crystals in the synthesis although they are not incorporated in the final structures. No crystals of **2** and **3** appeared in the reaction products when we tried a variety of reactant ratios and reaction conditions in the absence of the amine molecules.

In general, alkaline earth metal borates exhibit framework structures made up of  $\text{BO}_4$  tetrahedra and  $\text{BO}_3$  triangles. Only a few compounds show isolated islands, and layered structural feature and chain arrangement are absent. Moreover, most of these compounds contain both  $\text{BO}_4$  and  $\text{BO}_3$ . No chain structure of barium borate has been discovered yet prior to our work [22].

### 3.2.1 $\text{Ba}_3\text{B}_6\text{O}_9(\text{OH})_6$ (2)

This compound crystallizes in a monoclinic system with space group  $P2/c$  and cell parameters  $a = 6.9868(2)$  Å,  $b = 7.1366(2)$  Å,  $c = 11.9209(4)$  Å,  $\beta = 90.955(2)^\circ$ , and  $Z = 2$ .

The structure of  $\text{Ba}_3\text{B}_6\text{O}_9(\text{OH})_6$  can also be regarded as constructed from infinite anionic borate  $[\text{B}_6\text{O}_9(\text{OH})_6]^{6n-}$  chains (Fig. 2), the negative charges of which are compensated for by the  $\text{Ba}^{2+}$  cations located between the chains. This compound is the first reported chain borate in which all the boron atoms are tetrahedrally coordinated by oxygen atoms. The anionic infinite chains extending along the  $a$  direction are built up from non-planar six-membered  $\text{B}_3\text{O}_3$  rings which are found to join together by sharing the tetrahedrally-coordinated B atoms.

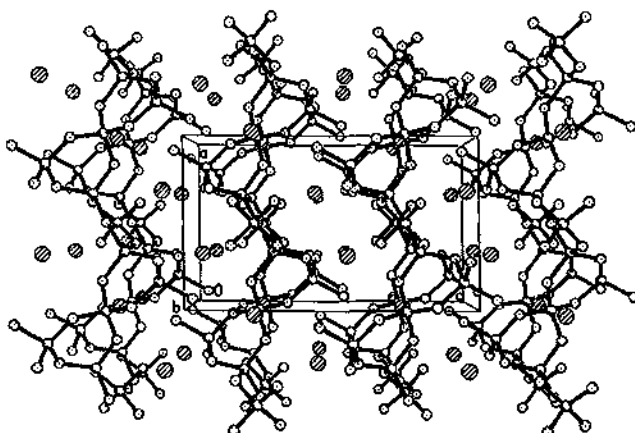


Figure 2. View of the chain structure along the  $b$  axis for  $\text{Ba}_3\text{B}_6\text{O}_9(\text{OH})_6$  (2).

### 3.2.2 $\text{SrBO}_2(\text{OH})$ (3)

$\text{SrBO}_2(\text{OH})$  (3) is crystallized in the orthorhombic space group  $Pnma$ ,  $a = 6.991(2)$  Å,  $b = 5.707(2)$  Å,  $c = 6.952(3)$  Å, and  $Z = 4$ .

Single-crystal X-ray diffraction analysis reveals that the unit cell of compound 3 contains crystallographically independent individual  $[\text{BO}_2(\text{OH})]^{2-}$  groups (Fig. 3). Three oxygens are bonded to each B to form a  $\text{BO}_3$  triangle for 3. Due to the symmetry of the space group, the  $\text{BO}_3$  groups are exactly planar and lie nearly parallel to the  $bc$  plane, and each  $\text{BO}_3$  group is surrounded by six nearest  $\text{BO}_3$  neighbors with three B-B distances, 3.52, 4.38 and 4.99 Å. For 3, the layers containing the  $\text{BO}_3$  triangles in the  $bc$  plane are stacked in such a way that the  $\text{BO}_3$  triangles in adjacent layers are in a staggered form when the structure is viewed along the  $a$  axis. The bond between the B and O(1) or O(1A) atom is stronger than that between the B and O(2) atom so that the bond length of B-O(2) is longer than that of the other two B-O bond lengths.

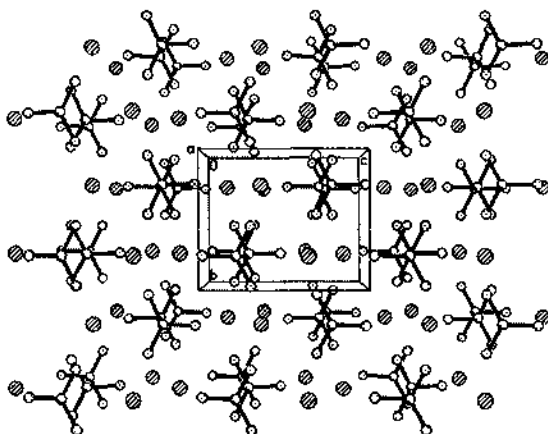


Figure 3. View of the borate anions  $[\text{BO}_2(\text{OH})]^{2-}$  along the  $a$  axis for  $\text{SrBO}_2(\text{OH})$  (3).

### 3.3 Two metal-complex containing borates $\text{Zn}(\text{C}_2\text{H}_8\text{N}_2)_3\text{B}_5\text{O}_7(\text{OH})_3$ (4) and $\text{Co}(\text{C}_2\text{H}_8\text{N}_2)_3\text{B}_5\text{O}_7(\text{OH})_3$ (5)

Solvothermal synthesis promoted by organic amines has proved to be a promising method to prepare materials with a new structure [23]. In contrast to 1, 2 and 3, 4 and 5 were prepared from a nonaqueous system. It is believed that the properties of the organic solvents have important effect on the chemistry of the reactions. In these cases, the ethylenediamine molecule acts not only as a reaction medium for adjusting the pH of the reaction systems but also as an organic ligand to form the metal complex. Structure determinations show that  $\text{Zn}(\text{C}_2\text{H}_8\text{N}_2)_3\text{B}_5\text{O}_7(\text{OH})_3$  (4) is isostructural with  $\text{Co}(\text{C}_2\text{H}_8\text{N}_2)_3\text{B}_5\text{O}_7(\text{OH})_3$  (5). Both 4 and 5 crystallize in the monoclinic space group  $P2_1/c$  with crystal data:  $a = 8.5327(17)$  Å,  $b = 23.340(5)$  Å,  $c = 9.5269(19)$  Å,  $\beta = 107.04(3)^\circ$ , and  $Z = 4$  for 4 and  $a = 8.5074(17)$  Å,  $b = 23.347(5)$  Å,  $c = 9.5181(19)$  Å,  $\beta = 107.71(3)^\circ$ , and  $Z = 4$  for 5.

The structures of 4 and 5 are both constructed by isolated borate anion groups which are charge-balanced by the chiral  $\text{M}(\text{en})_3^{2+}$  ( $\text{M} = \text{Zn}, \text{Co}$ ) cations. These borate

groups are formed by two  $B_3O_3$  cycles linked through a boron atom, which contain two groups of two  $BO_3$  triangles on each side of a  $BO_4$  tetrahedron (Fig. 4). The metal M(Zn, Co) atom is coordinated by six nitrogen atoms, leading to chiral metal complexes with two enantiomeric configurations (Fig. 4).

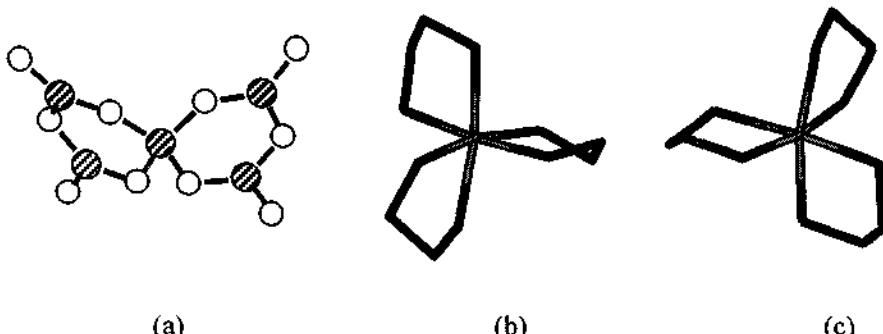


**Figure 4.** Representations of the pentaborate unit  $[B_5O_{10}]^{5-}$  (a) and the  $M(en)_3^{2+}$  ( $M = Zn, Co$ ) complexes  $\Delta - M(en)_3^{2+}$  (b) and  $\Delta - M(en)_3^{2+}$  (c) for (4) and (5).

#### 4 Conclusions

A series of new borates have been successfully prepared by varying the crystallization conditions of a hydrothermal or a solvothermal reaction system. The compounds  $Pb_6B_{11}O_{18}(OH)_9$  (1) and  $Ba_3B_6O_9(OH)_6$  (2) consist of infinite chain arrangements. Whereas the structures of  $SrBO_2(OH)$  (3),  $Zn(C_2H_8N_2)_3B_5O_7(OH)_3$  (4) and  $Co(C_2H_8N_2)_3B_5O_7(OH)_3$  (5) contain finite borate groups. It is evident that the hydrothermal and solvothermal techniques offer very effective methods for the preparation of borate materials with quite different structural features. The pH value, the solvent, the reaction temperature and the molar ratio of the reaction mixture all affect the formation of the borate compound from the reaction system. Detailed investigation in the reaction conditions will assist in the design and synthesis of target materials with specific structures and properties.

#### 5 Acknowledgements

We gratefully acknowledge the National Natural Science Foundation of China and the Education Ministry of China for financial support.

#### References

- Chen C. T., Wu Y. C. and Li R. K., The development of new NLO crystals in the borate series, *J. Cryst. Growth*, **99** (1990) pp. 790-798.

2. Becker P., Borate materials in nonlinear optics, *Adv. Mater.* **10** (1998) pp. 979-992.
3. Gopalakrishnan J., Ramesha K., Rangan K. K. and Pandey S., In search of inorganic nonlinear optical materials for second harmonic generation, *J. Solid State Chem.* **148** (1999) pp. 75-80.
4. Xue D., Betzler K., Hesse H. and Lammers D., Nonlinear optical properties of borate crystals, *Solid State Commun.*, **114** (2000) pp. 21-25.
5. Mikhail P., Hulliger J., Schnieper M. and Bill H.,  $\text{SrB}_4\text{O}_7$ :  $\text{Sm}^{2+}$ : crystal chemistry, czochralski growth and optical hole burning, *J. Mater. Chem.*, **10** (2000) pp. 987-991.
6. Diaz A. and Keszler D. A.,  $\text{Eu}^{2+}$  luminescence in the borates  $\text{X}_2\text{Z}(\text{BO}_3)_2$  ( $\text{X} = \text{Ba}, \text{Sr}; \text{Z} = \text{Mg}, \text{Ca}$ ), *Chem. Mater.* **9** (1997) pp. 2071-2077.
7. Chen C. T., Wu Y. C., Jiang A. D., Wu B. C., You G. M., Li R. K. and Lin S. J., New nonlinear-optical crystal:  $\text{LiB}_3\text{O}_5$ , *J. Opt. Soc. Am.* **6** (1989) pp. 616-621.
8. Chen C. T., Wang Y. B., Wu B. C., Wu K. C., Zeng W. L. and Yu L. L., Design and synthesis of an ultraviolet-transparent nonlinear optical crystal  $\text{Sr}_2\text{Be}_2\text{B}_2\text{O}_7$ , *Nature* **373** (1995) pp. 322-324.
9. Dadachov M. S., Sun K., Conradsson T. and Zou X. D., The first templated borogermanate  $(\text{C}_2\text{N}_2\text{H}_{10})_2[(\text{BO}_{2.5})_2(\text{GeO}_2)_3]$ : linkage of tetrahedra of significantly different sizes, *Angew. Chem. Int. Ed.* **39** (2000) pp. 3674-3676.
10. Harrison W. T. A., Gier T. E. and Stucky G. D., The synthesis and ab initio structure determination of  $\text{Zn}_4\text{O}(\text{BO}_3)_2$ , a microporous zincoborate constructed of "fused" subunits of three- and five-membered rings, *Angew. Chem. Int. Ed.* **32** (1993) pp. 724-726.
11. Thompson P. D. and Keszler D. A., Structure of  $\text{Sr}_3\text{Sc}(\text{BO}_3)_3$ , *Chem. Mater.* **6** (1994) pp. 2005-2007.
12. Penin N., Seguin L., Touboul M. and Nowogrocki G., Crystal structures of three  $\text{MB}_5\text{O}_8$  ( $\text{M} = \text{Cs}, \text{Rb}$ ) borates ( $\alpha$ - $\text{CsB}_5\text{O}_8$ ,  $\gamma$ - $\text{CsB}_5\text{O}_8$ , and  $\beta$ - $\text{RbB}_5\text{O}_8$ ), *J. Solid State Chem.* **161** (2001) pp. 205-213.
13. Thompson P. D., Huang J. F., Smith R. W. and Keszler D. A., The mixed orthoborate pyroborates  $\text{Sr}_2\text{Sc}_2\text{B}_4\text{O}_{11}$  and  $\text{Ba}_2\text{Sc}_2\text{B}_4\text{O}_{11}$ : pyroborate geometry, *J. Solid State Chem.* **95** (1991) pp. 126-135.
14. Campá J. A., Cascales C., Gutiérrez-Puebla E., Monge M. A., Rasines I. and Ruiz-Valero C., Crystal structure, magnetic order, and vibrational behavior in iron rare-earth borates, *Chem. Mater.*, **9** (1997) pp. 237-240.
15. Chen J. S., Pang W. Q. and Xu R. R., Mixed-bonded open-framework aluminophosphates and related layered materials, *Top. Catal.* **9** (1999) pp. 93-103.
16. Bontchev R. B., Do J. and Jacobson A. J., Templated synthesis of vanadium borophosphate cluster anions, *Angew. Chem. Int. Ed.* **38** (1999) pp. 1937-1940.
17. Bu X. H., Feng P. Y., Gier T. E., Zhao D. Y. and Stucky G. D., Hydrothermal synthesis and structural characterization of zeolite-like structures based on gallium and aluminum germinates, *J. Am. Chem. Soc.*, **120** (1998) pp. 13389-13397.
18. Feng P. Y., Bu X. H., Tolbert S. H. and Stucky G. D., Syntheses and

- characterizations of chiral tetrahedral cobalt phosphates with zeolite ABW and related frameworks, *J. Am. Chem. Soc.*, **119** (1997) pp. 2497-2504.
- 19. Menchetti S., Sabelli C. and Trosti-Ferroni R., The structure of sodium borate  $\text{Na}_3[\text{B}_5\text{O}_9]\text{-H}_2\text{O}$ , *Acta Crystallogr. Sect. B* **38** (1982) pp. 2987-2991.
  - 20. Byrapa K., Shekar K. V. K. and Rodriguez-Clemente R., Crystal growth and morphology of hydrothermally grown lithium borates, *J. Mater. Res.* **8** (1993) pp. 2319-2326.
  - 21. Yu Z. T., Shi Z., Jiang Y. S., Yuan H. M. and Chen J. S., A chiral lead borate containing infinite and finite chains built up from  $\text{BO}_4$  and  $\text{BO}_3$  units, *Chem. Mater.* **14** (2002) pp. 1314-1318.
  - 22. Yu Z. T., Shi Z., Chen W., Jiang Y. S., Yuan H. M. and Chen J. S., Synthesis and X-ray crystal structures of two new alkaline-earth metal borates:  $\text{SrBO}_2(\text{OH})$  and  $\text{Ba}_3\text{B}_6\text{O}_9(\text{OH})_6$ , *J. Chem. Soc. Dalton. Trans.*, (2002) in press.
  - 23. Morris R. E. and Weigel S. J., The synthesis of molecular sieves from non-aqueous solvents, *Chem. Soc. Rev.* **26** (1997) pp. 309-318.

# CALCULATION OF THE ELECTROSTATIC ENERGY $H_e(fd)$ ON $4f^{N-1}5d$ CONFIGURATION OF LANTHANIDE IONS

JINGSHENG SHI, SHIHONG ZHONG AND SIYUAN ZHANG

*Key Laboratory of Rare Earth Chemistry and Physics, Changchun Institute of Applied Chemistry,  
Chinese Academy of Sciences, Changchun, Jilin 130022, P. R. China  
E-mail: syzhang@ciac.jl.cn*

In LS coupling, the energy expressions of  $H_e(fd)$  of the chief low-energy levels of  $4f^{N-1}5d$  ( $n < 9$ ) configuration ions are calculated.  $H_e(fd)$  can be parameterized with  $F_k$  ( $k=2,4$ ) and  $G_k$  ( $k=1,3,5$ ).  $f_k$  and  $g_k$ , which are coefficients, times the corresponding parameter  $F_k$  and  $G_k$  leads to the energy expressions of  $H_e(fd)$ .

## 1 Introduction

In the past century, spectroscopic character of  $4f^N$  configuration of lanthanide ions has been studied in experiment and theory extensively. Energy level diagram of  $4f^N$  configuration for all trivalent lanthanides are represented in the energy range 0-40000cm<sup>-1</sup> [1], Wegh extended the diagram to 70000cm<sup>-1</sup> [2]. Some work has also been done on energy levels of the excited configuration  $4f^{N-1}5d$ . Several authors have revealed the energy differences of electronic configurations  $4f^{N-1}5d-4f^N$  [3], but most of the energy levels of the  $4f^{N-1}5d$  configuration are unknown, systemic research on which is still lacked. In the last several years, some spectra of the vacuum ultraviolet region for the  $4f^N-4f^{N-1}5d$  transitions of lanthanides have been reported which reveal many new results non-observed previously [4-6]. However, most of the features of the vacuum ultraviolet spectra are broad band structures, and it is very difficult to point out and to affirm the ordering of the energy levels of the  $4f^{N-1}5d$  configuration from the spectra. In addition, new materials such as the solid-state laser [7], PDP luminescence power [8] and scintillator materials [9], in which the vacuum ultraviolet emission and absorption is involved, have been studied extensively. In order to improve luminescence efficiency of the materials, the knowledge of energy levels of the  $4f^{N-1}5d$  configuration is required anxiously.

As mentioned above, it is difficult to derive the energy levels from experiment straightforward. Calculation may be a way to explore the energy levels. The  $4f^{N-1}5d$  configuration is different from the  $4f^N$  configuration. In the former, one of the 4f electrons has been excited to a d orbit so that there are several additional contributions to the free ionic Hamiltonian of the  $4f^{N-1}5d$  configuration. The free ionic Hamiltonian of the  $4f^{N-1}5d$  configuration is given by the following expression:

$$H = H_o + H_e(f) + H_e(fd) + H_{so}(f) + H_{so}(d),$$

where  $H_o$  represents the core potential. The core potential of the  $4f^{N-1}5d$  configuration is different from that of the  $4f^N$  configuration, which can be evaluated approximately in the calculation.  $H_e(f)$  is the Coulomb interaction of the 4f electrons, whose expression is given by Nielson and Koster [10].  $H_e(fd)$  is the Coulomb interaction between the 4f electrons and d electron.  $H_{so}(f)$  and  $H_{so}(d)$  are the spin-orbit interaction of the 4f electrons and the d electron respectively. The  $H_e(fd)$  is the dominating supplement for the free ionic

Hamiltonian of the  $4f^{N-1}5d$  configuration. If figuring out the supplement, we can get the energy levels of the  $4f^{N-1}5d$  configuration. In this paper, the coefficients of the electrostatic interactions between the 4f electrons and the d electron are presented.

## 2 Calculation Method

In treating configuration of the type  $4f^{N-1}5d$ , there are two coupling schemes to be chosen usually, which are Russell-Saunders (LS) coupling and j-j coupling. The resultant expression of the energy matrix for the electrostatic interactions in the LS coupling is different from that in j-j coupling, but the two types of expression can be transformed from one to the other, as discussed more fully in the 3. In this paper, all calculation is in the LS coupling.

In the LS coupling, the matrix element of the supplements of the electrostatic interactions can be written as:

$$\begin{aligned} & \langle f^{n-1}\alpha_1 S_1 L_1, sl'; SL | H_e(f5d) | f^{n-1}\alpha'_1 S'_1 L'_1, sl'; SL \rangle \\ &= \sum_k [f_k(f, d) F^k(4f, 5d)] + \sum_k [g_k(f, d) G^k(4f, 5d)], \end{aligned} \quad (1)$$

where  $H_e(fd)$  is the Hamiltonian of the electrostatic interactions between the 4f electrons and the d electron;  $F_k$  and  $G_k$  are known as direct and exchange Slater parameters for the electrostatic interactions between the 4f electrons and the d electron. To avoid the occurrence of large denominators in the calculations, the parameters  $F^k$  and  $G^k$  are substituted with  $F_k$  and  $G_k$  [10], which are related by the expression

$$F_k = \frac{F^k}{D^k} \quad \text{and} \quad G_k = \frac{G^k}{D^k},$$

the  $D^k$ 's are given by Condon and Shortley[10].

In the equation (1), the coefficients  $f_k$  and  $g_k$  for  $4f^{N-1}5d$  ( $N < 9$ ) configuration can be written: [11]

$$\begin{aligned} f_k(l, l') = & \delta(S_1, S'_1) (-1)^{L_1 + L'_1} ([l, l']) \begin{pmatrix} l & k & l' \\ 0 & 0 & 0 \end{pmatrix} \begin{pmatrix} l & k & l \\ 0 & 0 & 0 \end{pmatrix} \\ & \times \left\{ \begin{matrix} l & k & l' \\ L_1 & L & L'_1 \end{matrix} \right\} (\psi_1 \mid \mid U^{(k)} \mid \mid \psi'_1), \end{aligned} \quad (2)$$

$$\begin{aligned} g_k(l, l') = & (N-1) ([l, l']) ([S_1, L_1, S'_1, L'_1])^{1/2} (-1)^{S_1 + S'_1} \begin{pmatrix} l & k & l' \\ 0 & 0 & 0 \end{pmatrix} \\ & \times \sum_{\psi} (\psi_1 \mid \mid \bar{\psi} \mid \mid \psi'_1) \left\{ \begin{matrix} s & \bar{s} & S'_1 \\ s & S & S_1 \end{matrix} \right\} \left\{ \begin{matrix} \bar{L} & l & L'_1 \\ l & k & l' \\ L_1 & l' & L \end{matrix} \right\}, \end{aligned} \quad (3)$$

where  $\bar{L}$  and  $\bar{S}$  are the orbit quantum and spin quantum of fractions parentage for  $4f^{N-1}$  configuration,  $U^{(k)}$  is the unit tensors of the  $4f^{N-1}$  core,  $(\psi_1 \mid \mid \bar{\psi})$  represent the coefficients of fractions parentage for the  $4f^{N-1}$  configuration, which are given by Nielson and Koster [12] for all the states of the  $4f^{N-1}$  configurations( $N < 9$ ).

### 3 Results

The  $f_k$ 's and  $g_k$ 's obtained in terms of the two formulae (2), (3) are multiplied by the corresponding  $D^k$  to give the coefficients of the parameters  $F_k$  and  $G_k$ , which are presented in Table 1.

**Table 1.** The energy expressions of  $H_e(fd)$  on  $4f^{n+1}5d$  configuration: ( $t_1$  denotes the term of the  $4f^{n+1}$  core and  $t_2$  denotes the term of the  $4f^{n+1}5d$  configuration).

$N$	$t_1 t_2$	$F_2$	$F_4$	$G_1$	$G_3$	$G_5$
2	$(^2F)$	$^3H$	10	3	-15	-10
		$^3G$	-15	-22	10	-35
		$^3F$	-11	66	-6	-19
		$^3D$	6	-99	3	42
		$^3P$	24	66	-1	-24
		$^1H$	10	3	15	10
		$^1G$	-15	-22	-10	35
		$^1F$	-11	66	6	19
		$^1D$	6	-99	-3	-42
		$^1P$	24	66	1	24
3	$(^3H)$	$^4K$	10	-4	-20	-30
		$^4I$	-11	24	-6	-44
		$^4H$	-35/3	-56	6	-38/3
		$^4G$	0	182/3	-7/3	-88/3
		$^4F$	52/3	-26	3/7	316/21
		$^2K$	10	-4	10	15
		$^2I$	-11	24	3	22
		$^2H$	-35/3	-56	-3	19/3
		$^2G$	0	182/3	7/6	44/3
		$^2F$	52/3	-26	-3/14	-158/21
4	$(^3F)$	$^4H$	-10/3	-1	-9	-118/3
		$^4G$	5	22/3	-47/3	-23/3
		$^4F$	11/3	-22	3	-79/3
		$^4D$	-2	33	3	-38
		$^4P$	-8	-22	-2	12
		$^2H$	-10/3	-1	9/2	59/3
		$^2G$	5	22/3	47/6	23/6
		$^2F$	11/3	-22	-3/2	79/6
		$^2D$	-2	33	-3/2	19
		$^2P$	-8	-22	1	-6
5	$(^3P)$	$^4F$	-6	0	-38/7	-222/7
		$^4D$	21	0	-14	-6
		$^4P$	-21	0	6	-36
		$^2F$	-6	0	19/7	111/7
		$^2D$	21	0	7	3
		$^2P$	-21	0	-3	18

Table 1. (continued)

$N$	$t_1 t_2$	$F_2$	$F_4$	$G_1$	$G_3$	$G_5$
4						
( $^4D$ )						
$^5L$		4	-3	-21	-54	-21
$^5K$		-4	17	-17	-38	-101
$^3I$		-51/11	-408/11	9/11	-334/11	-2581/11
$^5H$		-5/11	408/11	12/11	-496/11	-3997/11
$^5G$		70/11	-476/33	-17/33	142/33	-14486/33
$^3L$		4	-3	7	18	7
$^3K$		-4	17	17/3	38/3	101/3
$^3I$		-51/11	-408/11	-3/11	334/33	2581/33
$^3H$		-5/11	408/11	-7/11	496/33	3997/33
$^3G$		70/11	-476/33	17/99	-142/99	14486/99
( $^4G$ )						
$^5I$		-4/11	45/11	-196/11	-524/11	-686/11
$^5H$		5/11	-585/22	-76/11	-823/22	-1910/11
$^5G$		65/154	5265/77	-141/11	-14177/308	-10895/44
$^5F$		-1/14	-585/7	13/7	113/28	-8383/28
$^5D$		-5/7	585/14	1	-569/14	-373
$^3I$		-4/11	45/11	196/33	524/33	686/33
$^3H$		5/11	-585/22	76/33	823/66	1910/33
$^3G$		65/154	5265/77	47/11	14177/924	10895/132
$^3F$		-1/14	-585/7	-13/21	-113/84	8383/84
$^3D$		-5/7	585/14	-1/3	569/42	373/3
( $^4F$ )						
$^5H$		-5	-3/2	-12	-101/2	-82
$^5G$		15/2	11	-17	-107/4	-803/4
$^5F$		11/2	-33	-3	-103/2	-1111/4
$^5D$		-3	99/2	-3	-99/2	-297
$^5P$		-12	-33	2	-12	-264
$^3H$		-5	-3/2	4	101/6	82/3
$^3G$		15/2	11	17/3	107/12	803/12
$^3F$		11/2	-33	1	103/11	1111/12
$^3D$		-3	99/2	1	33/2	99
$^3P$		-12	-33	-2/3	4	88
( $^4D$ )						
$^5G$		68/7	22/21	-53/3	-704/21	-506/3
$^5F$		-136/7	-66/7	15/7	-380/7	-902/7
$^5D$		-51/7	264/7	-9	-272/7	-209
$^5P$		17	-88	-5	10	-341
$^5S$		34	132	-21	-54	-462

Table 1. (continued)

<i>N</i>	<i>t<sub>1</sub></i>	<i>t<sub>2</sub></i>	<i>F<sub>2</sub></i>	<i>F<sub>4</sub></i>	<i>G<sub>1</sub></i>	<i>G<sub>3</sub></i>	<i>G<sub>5</sub></i>
4							
	( <sup>4</sup> D)						
	<sup>3</sup> G	68/7	22/21	53/9	704/63	506/9	
	<sup>3</sup> F	-136/7	-66/7	-5/7	380/21	902/21	
	<sup>1</sup> D	-51/7	264/7	3	272/21	209/3	
	<sup>3</sup> P	17	-88	5/3	-10/3	341/3	
	<sup>5</sup> S	34	132	7	18	154	
	( <sup>4</sup> S)						
	<sup>5</sup> D	0	0	-9	-36	-198	
	<sup>3</sup> D	0	0	3	12	66	
5							
	( <sup>5</sup> I)						
	<sup>6</sup> L	-4	3	-21	-74	-56	
	<sup>6</sup> K	4	-17	-21	-34	-19	
	<sup>6</sup> I	51/11	408/11	-126/11	-619/11	-3766/11	
	<sup>6</sup> H	5/11	-408/11	42/11	-387/11	-4704/11	
	<sup>6</sup> G	-70/11	476/33	-4/33	-856/33	-15082/33	
	<sup>4</sup> L	-4	3	21/4	37/2	14	
	<sup>4</sup> K	4	-17	21/4	17/2	49	
	<sup>4</sup> I	51/11	408/11	63/22	619/44	1883/22	
	<sup>4</sup> H	5/11	-408/11	-21/22	387/44	1176/11	
	<sup>4</sup> G	-70/11	476/33	1/11	214/33	7541/66	
	( <sup>5</sup> G)						
	<sup>6</sup> I	4/11	-45/11	-226/11	-624/11	-1437/11	
	<sup>6</sup> H	-5/11	585/22	-293/11	-1437/22	-5277/22	
	<sup>6</sup> G	-65/154	-5265/77	-438/77	-6043/308	-92563/308	
	<sup>6</sup> F	1/14	585/7	-92/7	-1557/28	-10581/28	
	<sup>6</sup> D	5/7	-585/14	47/14	-387/14	-6141/14	
	<sup>4</sup> I	4/11	-45/11	113/22	131/11	1437/44	
	<sup>4</sup> H	-5/11	585/22	293/88	1437/88	5277/88	
	<sup>4</sup> G	-65/154	-5265/77	219/154	6043/1232	92563/1232	
	<sup>4</sup> F	1/14	585/7	23/7	1557/112	10581/112	
	<sup>4</sup> D	5/7	-585/14	-47/56	387/56	6141/56	
	( <sup>5</sup> F)						
	<sup>6</sup> H	5	3/2	-39/2	-111/5	-375/2	
	<sup>6</sup> G	-15/2	-11	-12	-177/4	-825/4	
	<sup>6</sup> F	-11/2	33	-6	-261/4	-1221/4	
	<sup>6</sup> D	3	-99/2	-3/2	-57/2	-759/2	
	<sup>6</sup> P	12	33	-16	-24	-429	
	<sup>4</sup> H	5	3/2	39/8	111/20	375/8	
	<sup>4</sup> G	-15/2	-11	3	177/16	825/16	
	<sup>4</sup> F	-11/2	33	3/2	261/16	1221/16	
	<sup>4</sup> D	3	-99/2	3/8	57/8	759/8	
	<sup>4</sup> P	12	33	4	6	429/4	

Table 1. (continued)

<i>N</i>	<i>t<sub>1</sub></i>	<i>t<sub>2</sub></i>	<i>F<sub>2</sub></i>	<i>F<sub>4</sub></i>	<i>G<sub>1</sub></i>	<i>G<sub>3</sub></i>	<i>G<sub>5</sub></i>
5							
	( <sup>5</sup> D)						
	<sup>6</sup> G	-68/7	-22/21	-256/21	-1264/21	-3322/21	
	<sup>5</sup> F	136/7	66/7	-132/7	-288/7	-7314/7	
	<sup>6</sup> D	51/7	-264/7	-90/7	-125/7	-6852/7	
	<sup>6</sup> P	-17	88	-6	-79	-286	
	<sup>6</sup> S	-34	-132	24	-44	-242	
	<sup>4</sup> G	-68/7	-22/21	64/21	316/21	1661/42	
	<sup>4</sup> F	136/7	66/7	33/7	72/7	3657/14	
	<sup>4</sup> D	51/7	-264/7	45/14	125/28	1713/7	
	<sup>4</sup> P	-17	88	3/2	79/4	143/2	
	<sup>4</sup> S	-34	-132	-6	11	121/2	
	( <sup>3</sup> S)						
	<sup>6</sup> D	0	0	-12	-48	-264	
	<sup>4</sup> D	0	0	3	12	66	
6							
	( <sup>6</sup> H)						
	<sup>7</sup> K	-10	4	-21	-84	-126	
	<sup>7</sup> I	11	-24	-21	-49	-322	
	<sup>7</sup> H	35/3	56	-21	-187/3	-1288/3	
	<sup>7</sup> G	0	-182/3	-8/3	-92/3	-1373/3	
	<sup>7</sup> F	-52/3	26	18/7	-1324/21	-9697/21	
	<sup>5</sup> K	-10	4	21/5	84/5	126/5	
	<sup>5</sup> I	11	-24	21/5	49/5	322/5	
	<sup>5</sup> H	35/3	56	21/5	187/15	1288/15	
	<sup>5</sup> G	0	-182/3	8/15	92/15	1373/15	
	<sup>5</sup> F	-52/3	26	18/35	1324/105	9697/105	
	( <sup>6</sup> F)						
	<sup>7</sup> H	10/3	1	-21	-212/3	-749/3	
	<sup>7</sup> G	-5	-22/3	-58/3	-142/3	-814/3	
	<sup>7</sup> F	-11/3	22	-6	-242/3	-1166/3	
	<sup>7</sup> D	2	-33	-3	-52	-451	
	<sup>7</sup> P	8	22	-21	-24	-462	
	<sup>5</sup> H	10/3	1	21/5	212/15	749/15	
	<sup>5</sup> G	-5	-22/3	58/15	142/15	814/15	
	<sup>5</sup> F	-11/3	22	6/5	242/15	1166/15	
	<sup>5</sup> D	2	-33	3/5	52/5	451/5	
	<sup>5</sup> P	8	22	21/5	24/5	462/5	
6							
	( <sup>6</sup> P)						
	<sup>7</sup> F	6	0	-137/7	-408/7	-2244/7	
	<sup>7</sup> D	-21	0	-5	-75	-264	
	<sup>7</sup> P	21	0	-21	-39	-462	
	<sup>5</sup> F	6	0	137/35	408/35	2244/35	
	<sup>5</sup> D	-21	0	1	15	264/5	
	<sup>5</sup> P	21	0	21/5	39/5	462/5	

Table 1. (continued)

<i>N</i>	<i>t<sub>1</sub></i>	<i>t<sub>2</sub></i>	<i>F<sub>2</sub></i>	<i>F<sub>4</sub></i>	<i>G<sub>1</sub></i>	<i>G<sub>3</sub></i>	<i>G<sub>5</sub></i>
7							
	( <sup>7</sup> <i>F</i> )						
	<sup>8</sup> <i>H</i>	-10	-3	-21	-84	-252	
	<sup>8</sup> <i>G</i>	15	22	-21	-84	-462	
	<sup>8</sup> <i>F</i>	11	-66	-21	-24	-462	
	<sup>8</sup> <i>D</i>	-6	99	-21	-84	-462	
	<sup>8</sup> <i>P</i>	-24	-66	14	-84	-462	
	<sup>6</sup> <i>H</i>	-10	-3	21/6	14	42	
	<sup>6</sup> <i>G</i>	15	22	21/6	14	77	
	<sup>6</sup> <i>F</i>	11	-66	21/6	4	77	
	<sup>6</sup> <i>D</i>	-6	99	21/6	14	77	
	<sup>6</sup> <i>P</i>	-24	-66	-7/3	14	77	
8							
	( <sup>8</sup> <i>S</i> )						
	<sup>9</sup> <i>D</i>	0	0	-21	-84	-462	
	<sup>7</sup> <i>D</i>	0	0	3	12	66	

Part of the coefficients of the parameters  $F_K$  and  $G_K$  for the  $4f^{N-1}5d$  configuration presented in some papers [10,13] are consistent with the results calculated by us. All the coefficients are calculated in the LS coupling, but some of the  $4f^{N-1}5d$  configuration is closer to the j-j coupling scheme. In such cases, the matrix elements in the j-j coupling can be calculated by a transformation from the matrix elements of operators in the LS coupling into j-j coupling as the following [14].

$$\begin{aligned}
 & \langle f''(\alpha S_1 L_1) J_1, s l' j', J_2 | H_e(f5d) | f''(\alpha' S_1' L_1') J_1', s l' j'', J_4 \rangle \\
 &= \delta(J_2, J_4) ([J_1, J_1', j', j''])^{1/2} \\
 &\quad \times \sum_{S_2, L_2} ([S_2, L_2]) \left\{ \begin{array}{ccc} S_1 & s & S_2 \\ L_1 & l' & L_2 \\ J_1 & j' & J_2 \end{array} \right\} \left\{ \begin{array}{ccc} S_1' & s & S_2 \\ L_1' & l' & L_2 \\ J_1' & j'' & J_2 \end{array} \right\} \\
 &\quad \times \langle f'' \alpha S_1 L_1, s l'; S_2 L_2 | H_e(f5d) | f'' \alpha' S_1' L_1', s l'; S_2 L_2 \rangle.
 \end{aligned}$$

After the coefficients are obtained, the energy expressions of the chief low-energy levels of  $4f^{N-1}5d$  configuration can be presented explicitly. If values of the parameters  $F_K$ ,  $G_K$  can be known, the energy levels of the  $4f^{N-1}5d$  configuration for rare-earth free ions can be obtained with little difficulty. It is greatly convenient to calculate and to compare the orderings of these energy levels. Even if the calculation results are approximate values, they are advantageous to explain the vacuum ultraviolet spectra and to design new materials in which the vacuum ultraviolet emission and absorption is involved.

**References**

1. G. H. Dieke, *Spectra and Energy Levels of Rare Earth Ions in Crystals*, Wiley Interscience, New York, 1968.
2. R. T. Wegh, A. Meijerink, R. J. Lamminmaki, J. Holsa, *J. Lumin.*, 87, 1002 (2000).
3. E. Loh, *Phys. Rev.* 147, 332 (1966).
4. R. T. Wegh and A. Meijerink, *Phys. Rev. B.*, 60, 10820 (1999).
5. J. C. Krupa, M. Queffelec, *J. Alloys. Compds.*, 250, 287 (1997).
6. E. Sarantopoulou, A. C. Cefalas, M. A. Dubinskii, Z. Kollia and C. A. Nicolaides. *J. Mod. Opt.*, 41, 4767 (1994).
7. R. W. Wayant and P. H. Klein, *Appl. Phys. Lett.*, 46, 14 (1985).
8. G. Blasse and B. C. Grabmaier, *Luminescent Materials* (Springer Verlag, Berlin, 1994), Chapter 6.
9. C. W. E. van Eijk, *Proc. SPIE* 2706, 158(1996).
10. E. U. Condon and G. H. Shortley, *The Theory of Atomic Spectra*, Cambridge Univ., 1979.
11. B. G. Wybourne, *Spectroscopic Properties of Rare Earths*, John Wiley & Sons, Inc., 1965.
12. C. W. Nielson and G. F. Koster, *Spectroscopic Coefficients for the p<sup>n</sup>, d<sup>n</sup> and f<sup>n</sup> configurations*, The M. I. T. press., 1963.
13. D. S. McClure and Z. Kiss, *J. Chem. Phys.* 47, 1353 (1967).
14. B. R. Judd, *Phys Rev.* 125, 613 (1962).

# ENHANCEMENT OF IR ABSORPTION OF CO ADSORBED ON PALLADIUM NANOPARTICLES PREPARED BY SHIP-IN-A-BOTTLE IN SUPERCAGES OF NaA ZEOLITE

YAN-XIA JIANG,\* NAN DING AND SHI-GANG SUN

*State Key Laboratory for Physical Chemistry of Solid Surfaces, Department of Chemistry, Institute of Physical Chemistry, Xiamen University, China*  
E-mail: yxjiang@xmu.edu.cn

Palladium nanoparticles (nm-Pd) were synthesized by “ship-in-a-bottle” technique in supercages of NaA zeolite. The behaviors of electrodes of thin film of nm-Pd accommodated in NaA zeolite were characterized by cyclic voltammetry. The results illustrated that the nm-Pd possess particular properties for hydrogen reaction, i.e. in contrast to hydrogen absorption on massive palladium electrode, the surface processes of hydrogen adsorption-desorption become the dominant reaction on electrodes of thin film of nm-Pd. The processes of adsorption and desorption of carbon monoxide on the electrodes were studied using *in situ* electrochemical FTIR reflection spectroscopy. It has been revealed that in comparison with CO adsorbed on a massive Pd electrode, the IR absorption of CO adsorbed on nm-Pd particles accommodated in NaA zeolite has been enhanced to about 36 times.

## 1 Introduction

Platinum group metal, exhibiting high stability and activity in catalysis, is frequently used in direct fuel cells as anode for electro-oxidation of small organic molecules and as cathode for electro-reduction of oxygen [1]. The commercial applications of electrocatalyst based on platinum group metal are nevertheless limited owing to the high cost. Accordingly, one of the most important subjects of electrocatalysis is to select suitable substrate materials to disperse platinum group metals and to prepare electrocatalysts of high performance and low cost. Zeolite materials display high specific surface areas and aperture structures and are used widely as support materials in heterogeneous catalysis [2,3]. With particular techniques of preparation and using zeolites as a template, it is of great possibility to produce and stabilize metallic nanoparticles of well-defined size. The unique cages and channels of zeolites can be used extensively as “nanometer-sized microreactors” to synthesize materials at nano-scale by the method of “ship-in-a-bottle” [5], and the resulting nanostructured materials prepared in such a way can exhibit particular physical and/or chemical properties that could not be observed on corresponding massive materials [5]. Amongst the study methods employed often in electrocatalysis, the *in situ* IR spectroscopy, which can provide information at molecular level and possesses a high sensitivity to surface structure, is considered as one of the most powerful techniques to study the intrinsic relationship between surface structure and special properties [6]. In this paper, nm-Pd particles were synthesized in the supercages of NaA zeolite. Cyclic voltammetry and *in situ* electrochemical FTIR reflection spectroscopy were applied to study electrochemical and optical properties of thus formed material. A novel phenomenon of enhancement of IR absorption (EIRA) of CO adsorbed on Pd nanoparticles confined in supercages of NaA zeolite had been discovered.

## 2 Experimental

A saturated calomel electrode was served as reference electrode, and all experiments were carried out at room temperature around 20°C. Solutions were prepared with Millipore water and chemicals of analytical grade.

### 2.1 Preparation of Pd nanoparticles

1 g NaA was lightly ground using a mortar and pestle, and then dispersed in 250 ml  $1.0 \times 10^{-3}$  M  $\text{PdCl}_2$  aqueous solution for 24 h at 100 °C to accommodate  $\text{Pd}^{2+}$  into the zeolite via ion-exchange between  $\text{PdCl}_2$  and NaA zeolite. The sample was then washed carefully using chloride acid solution of pH = 5 to remove occluded materials and surface-adherent salts. They were finally rinsed with Millipore water till free of  $\text{Cl}^-$  and dried in air to produce  $\text{Pd}^{2+}\text{-NaA}$ . 20 mg prepared samples were dispersed through ultrasonic vibration in a solution of 0.3 ml of dechloroethane containing 3 mg of polyvinyl chloride (PVC) to form a suspension. A defined quantity of the suspension was applied to a clean surface of glassy carbon (GC), resulting in a thin film of around 10  $\mu\text{m}$  in thickness after drying in air for about 30 min. The  $\text{Pd}^{2+}$  ions in the film electrodes have been reduced to the metallic state by applying a potential cycling between -0.4 V to 0.0 V or maintaining a constant potential of reduction of -0.4 V. The electrode thus prepared was noted as  $\text{Pd}^0_{\text{EC}}\text{-NaA/GC}$ . CO adsorption on  $\text{Pd}^0_{\text{EC}}\text{-NaA/GC}$ , denoted as CO- $\text{Pd}^0_{\text{EC}}\text{-NaA/GC}$ , was carried out by introducing pure CO gas into the cell containing 0.1 M  $\text{Na}_2\text{SO}_4$  solution ( $\text{pH}=3.3$ ) while holding electrode potential between at -0.40 and 0 for 75 min to insure a saturation adsorption of CO. The solution CO species had been removed by bubbling the solution with pure  $\text{N}_2$  gas and holding electrode potential at -0.40 V. The Pd nanoparticles were thus formed by adsorption and desorption of CO.

### 2.2 Electrochemical *in situ* FTIR Reflection Spectroscopy

Electrochemical *in situ* FTIR reflection spectroscopic measurements were carried out on a Nexus 870 FTIR spectrometer (Nicolet) equipped with an EverGlo™ IR source and a liquid nitrogen cooled MCT-A detector. A  $\text{CaF}_2$  disk was used as IR window. The IR cell of thin layer configuration between electrode and IR window was approached by pushing electrode against the IR window before FTIR measurement [7]. The spectral resolution was 8  $\text{cm}^{-1}$ , and 100 interferograms were collected and coadded into each single-beam spectrum. The resulting spectrum is the different spectrum of potential and it represents the relative change in reflectivity. Multi-step FTIR spectroscopy (MSFTIR) technique was applied in investigation of CO adsorption, and the result spectra were calculated as,

$$\frac{\Delta R}{R}(E_S^i) = \frac{R(E_S^i) - R(E_R)}{R(E_R)} \quad (1)$$

where  $R(E_S^i)$  is the single-beam spectrum acquired at study potential  $E_S^i$ , and  $R(E_R)$  is the single-beam spectrum recorded at reference potential  $E_R$ . The

experimental procedure was designed in such a way that, after saturation adsorption of CO on the electrode and removal of all CO in the bulk solution,  $R(E'_S)$  was collected accompanied by varying the  $E'_S$  stepwise in the study potential region. The  $R(E_R)$  was taken finally at  $E_R$  at which the adsorbed CO ( $\text{CO}_{\text{ad}}$ ) had been oxidized to  $\text{CO}_2$ . It is evident that a negative-going band of IR absorption should be attributed to species at  $E_S$ , and positive-going band of IR absorption should be assigned to species at  $E_R$  in the resulting spectrum. As a consequence, only  $\text{CO}_{\text{ad}}$  at  $E_S$  and  $\text{CO}_2$  in the thin layer derived from  $\text{CO}_{\text{ad}}$  oxidation at  $E_R$  were subjected to *in situ* FTIRS investigations.

### 3 Results and Discussion

#### 3.1 Studies of Cyclic Voltammetry

Cyclic voltammograms (CV) of massive Pd electrode and  $\text{Pd}^0_{\text{EC}}\text{-NaA/GC}$  are displayed in Figure 1. We can see in Figure 1a a reduction current below -0.10 V attributed to hydrogen absorption, and a large negative current peak near 0.23 V caused by the reduction of Pd oxide formed at high potentials during the positive-going potential scan. A pair of current peaks around -0.22 V attributed to the adsorption-desorption of hydrogen, and a reduction peak near 0.20 V assigned to the reduction of Pd oxide can be observed in Figure 1 b. In contrast to hydrogen absorption on massive palladium electrode, the surface processes of hydrogen adsorption-desorption become the dominant reaction on electrodes of  $\text{Pd}^0_{\text{EC}}\text{-NaA/GC}$ , indicating that Pd nanoparticles possesses electrochemical properties different from massive Pd.

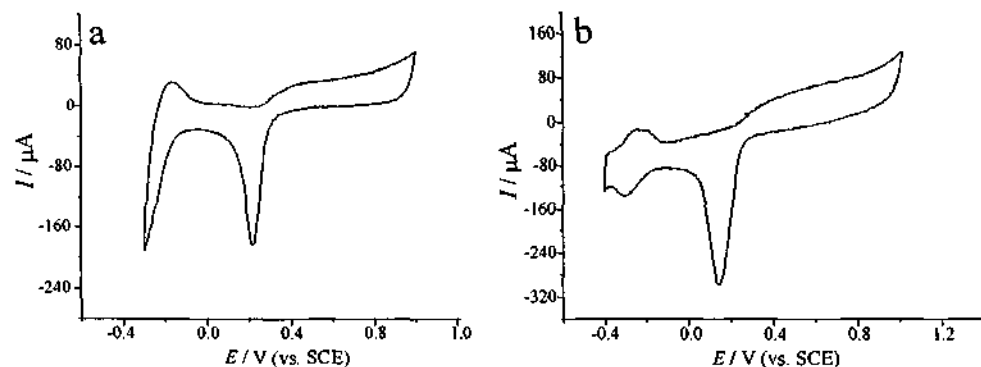


**Figure 1.** Cyclic voltammograms of (a) Pd massive electrode, (b)  $\text{Pd}^0_{\text{EC}}\text{-NaA/GC}$ , in 0.1 M  $\text{Na}_2\text{SO}_4$  ( $\text{pH}=3.3$ ), sweep rate 50 mV s<sup>-1</sup>.

### 3.2 Studies of *in situ* FTIR Reflection Spectroscopy

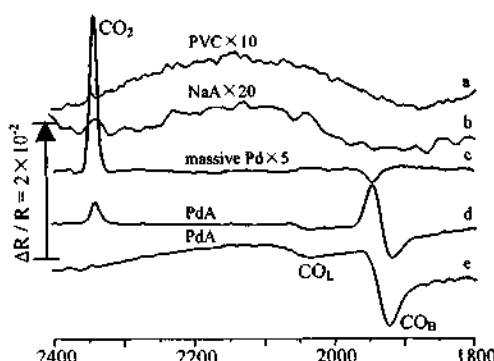


Figure 2. *In situ* FTIR spectra of  $\text{CO}_{\text{ad}}$  on different electrode, (a) PVC, (b) NaA, (c) massive Pd electrode, (d) and (e)  $\text{Pd}^0_{\text{EC}}\text{-NaA/GC}$ , in 0.1 M  $\text{Na}_2\text{SO}_4$  ( $\text{pH} = 3.3$ ),  $E_S = -0.4$  V,  $E_R = 1.0$  V (see text for details).

around  $1950 \text{ cm}^{-1}$  assigned to the IR absorption of bridge-bonded CO ( $\text{CO}_B$ ), and a positive-going band near  $2345 \text{ cm}^{-1}$  corresponding to the IR absorption of  $\text{CO}_2$  derived from the oxidation of  $\text{CO}_B$  at the reference potential. Under the present experimental conditions, the integrated intensity of the  $\text{CO}_2$  band ( $A_{\text{CO}_2}$ ) can be taken as a measure of the quantity of  $\text{CO}_{\text{ad}}$ , and the normalized intensity of  $\text{CO}_{\text{ad}}$  band is defined as  $A_{\text{CO}_{\text{ad}}} / A_{\text{CO}_2}$ , which has been measured at 0.159 from spectrum c. In contrast, we can observe three bands in spectrum d, i.e. a bipolar band of  $\text{CO}_B$  around  $1930 \text{ cm}^{-1}$ , a negative-going band of  $2040 \text{ cm}^{-1}$  assigned to IR absorption of linear bonded CO ( $\text{CO}_L$ ) and a positive-going  $\text{CO}_2$  band near  $2345 \text{ cm}^{-1}$  produced from the oxidation of  $\text{CO}_B$  and  $\text{CO}_L$ . According to formula 1, positive-going band is assigned to IR absorption at  $E_R$  in the resulting spectrum. As a result, bipolar band in spectrum d illustrates  $\text{CO}_{\text{ad}}$  has not been oxidized completely at  $E_R$  at that time. In spectrum e three bands were also observed. Different with spectrum d, a monopolar  $\text{CO}_B$  can be observed. The normalized intensity of oxidized  $\text{CO}_{\text{ad}}$  is 5.724, The enhancement factor  $\Delta$  of IR absorption of  $\text{CO}_{\text{ad}}$  is defined consequently as [8]:

$$\Delta = \frac{\left[ \frac{(\text{CO}_{\text{ad}} \text{ oxidized})}{(\text{CO}_2 \text{ produced})} \right]_{\text{CO-Pd}^0\text{-NaA/GC}}}{\left[ \frac{\text{CO}_{\text{ad}}}{\text{CO}_2} \right]_{\text{CO-Pd}}} \quad (2)$$

A value of 36 has been calculated using equation (2). The variation of the center of the  $\text{CO}_B$  band ( $v_B$ ) versus  $E_S$  for massive Pd electrode and  $\text{Pd}^0_{\text{EC}}\text{-NaA/GC}$  is plotted in Figure 3a and 3b. Two straight lines can be observed in the case of  $\text{Pd}^0_{\text{EC}}\text{-NaA/GC}$ . One is for  $E_S$  below  $-0.6$  V, which yields a Stark shift rate ( $dv_B / dE$ ) of  $52 \text{ cm}^{-1} \text{ V}^{-1}$ . The second linear part is observed in the potential range between  $-0.6$  V to  $-0.2$  V, from which a Stark shift rate of  $16 \text{ cm}^{-1} \text{ V}^{-1}$  has been evaluated. In comparison with the value of Stark shift rate of  $47 \text{ cm}^{-1} \text{ V}^{-1}$  on massive Pd electrode, the small values of Stark shift rate in Figure 3a may be attributed to the structure of Pd nanoparticles and geology in NaA zeolite.

Figure 2 shows the *in situ* FTIR spectra of  $\text{CO}_{\text{ad}}$  on the PVC and NaA film electrodes as well as massive Pd electrode and  $\text{Pd}^0_{\text{EC}}\text{-NaA/GC}$  in 0.1 M  $\text{Na}_2\text{SO}_4$  ( $\text{pH}=3.3$ ) solution, in which  $E_S = -0.40$  V,  $E_R = 1.00$  V.  $R(E_R)$  was collected immediately after collecting  $R(E_S)$  in spectra 2a ~ d, whereas  $R(E_R)$  was collected when  $\text{CO}_{\text{ad}}$  was oxidized completely in spectrum e. Spectra a and b are two featureless IR spectra, indicating that CO can not be adsorbed on PVC or NaY film electrode. In spectrum c, we can observe a negative-going band

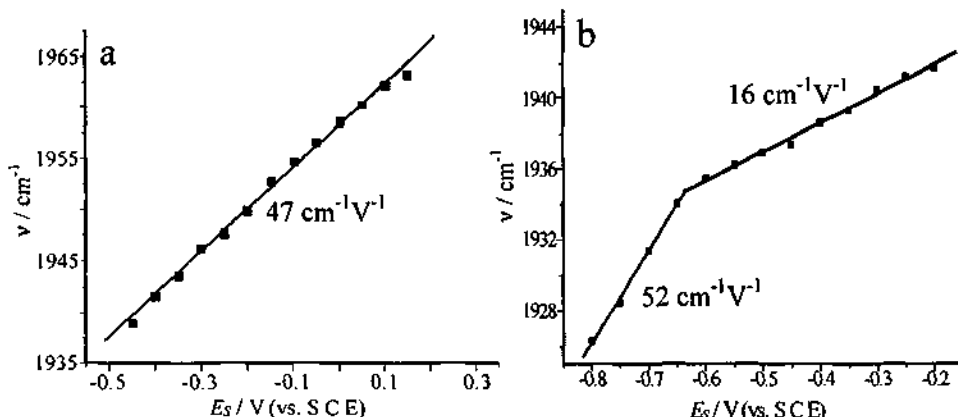


Figure 3. Potential-dependent  $\nu$  of CO<sub>B</sub> on (a) massive Pd and (b) CO-Pd<sup>0</sup><sub>EC</sub>-NaA/GC.

Similar to CO adsorbed on Pd<sup>0</sup><sub>EC</sub>-NaA/GC electrode, CO adsorbed on Pd nanoparticles loaded in Al<sub>2</sub>O<sub>3</sub> and SiO<sub>2</sub> on Pt (noted as Pd<sup>0</sup><sub>EC</sub>/Al<sub>2</sub>O<sub>3</sub>/Pt and Pd<sup>0</sup><sub>EC</sub>/SiO<sub>2</sub>/Pt) also exhibits three bands, i.e. CO<sub>B</sub>, CO<sub>L</sub> and CO<sub>2</sub>, and the enhancement of IR absorption. However, CO<sub>ad</sub> bands in the spectra of Pd<sup>0</sup><sub>EC</sub>/SiO<sub>2</sub>/Pt and Pd<sup>0</sup><sub>EC</sub>/Al<sub>2</sub>O<sub>3</sub>/Pt are much weaker. Table 1 illustrates the enhancement factors and full width at half maximum (FWHM) of the CO<sub>B</sub> band for massive Pd, Pd<sup>0</sup><sub>EC</sub>-NaA/GC, Pd<sup>0</sup><sub>EC</sub>/SiO<sub>2</sub>/Pt, and Pd<sup>0</sup><sub>EC</sub>/Al<sub>2</sub>O<sub>3</sub>/Pt. FWHMs of CO<sub>B</sub> on Pd<sup>0</sup><sub>EC</sub>-NaA/GC, Pd<sup>0</sup><sub>EC</sub>/SiO<sub>2</sub>/Pt, Pd<sup>0</sup><sub>EC</sub>/Al<sub>2</sub>O<sub>3</sub>/Pt are much

Table 1. Enhancement factors and FWHMs of CO<sub>ad</sub> in different electrodes.

	Δ	FWHM
Massive Pd	1	20
Pd <sup>0</sup> <sub>EC</sub> -NaA/GC	36	36
Pd <sup>0</sup> <sub>EC</sub> /SiO <sub>2</sub> /Pt	9.36	39
Pd <sup>0</sup> <sub>EC</sub> /Al <sub>2</sub> O <sub>3</sub> /Pt	6.44	32

larger than that measured from spectra of massive Pd electrode, implying an increase of the discreteness of vibrational energy states of CO-Pd<sup>0</sup> system in Pd nanoparticles.

Pd nanoparticles were formed in the supercages of NaA zeolite and pores between SiO<sub>2</sub> or Al<sub>2</sub>O<sub>3</sub> molecules, in which size of Pd nanoparticles was limited by the template of the used materials. According to Drozdova's work [9], Pd<sub>6</sub> core was formed in the supercages of NaA zeolite by admission and release of CO and thus possessing unique particle size. However, pores between SiO<sub>2</sub> or Al<sub>2</sub>O<sub>3</sub> molecules has broader distribution (pores' diameter of 20 ~ 100 nm representing 80% of all the apertures). Consequently, The Pd cores formed in SiO<sub>2</sub> or Al<sub>2</sub>O<sub>3</sub> [2] display a bigger particles size and a wider particles size distribution, therefore leading to a small enhancement of IR adsorption of CO<sub>ad</sub>. These results may conclude that uniform particle distribution and small particle size produce large EIIRAS.

#### 4 Conclusion

In the present study, Pd nanoparticles were synthesized in the supercages of NaA zeolite. Novel IR optical properties of CO<sub>ad</sub> adsorbed on electrodes of Pd<sup>0</sup><sub>EC</sub>-NaA/GC were revealed for the first time. In comparison with CO adsorbed on a

massive Pd electrode, IR absorption of CO adsorbed on  $Pd^0_{EC-NaA/GC}$  was enhanced to about 36 times and the FWHM of  $CO_B$  and  $CO_L$  bands significantly increased. From comparison of results of CO adsorbed on electrodes of massive Pd,  $Pd^0_{EC-NaA/GC}$ ,  $Pd^0_{EC/SiO_2/Pt}$ , and  $Pd^0_{EC/Al_2O_3/Pt}$ , it is concluded that the structure of zeolite template plays an important role in the initial Pd nanoparticles formation, and the size of the nanoparticles dominates the optical properties. The present study has been devoted to understanding the size effect of nanomaterials and to developing new electrocatalyst as well.

## 5 Acknowledgements

This work was supported financially by the National Natural Science Foundation of China (NNSFC).

## References

1. Mcnicol B. D., Rand D. A. J., Williams K. R., Direct methanol-air fuel cells for road transportation, *J. Power Sources* **83** (1999) pp.15–31.
2. Ichikawa M., “Ship-in-Bottle” Catalyst Technology, *Platinum Metals Rev.*, **44** (2000) pp. 3–14.
3. Beck A., Horvath A., Szucs A., Schay Z., Horvath Z. E., Zsoldos Z., Dekany I., Guczi L., Pd nanoparticles prepared by “controlled colloidal synthesis” in solid/liquid interfacial layer on silica. I. Particle size regulation by reduction time, *Catal. Lett.* **65** (2000) pp. 33–42.
4. Schmid G., Maihack V., Lautermann F., Peschel S., Ligand-stabilized metal clusters and colloids: properties and applications, *J. Chem. Soc. Dalton Trans.* (1996) pp. 589–595.
5. Zhang Z., Chen H., Sachiler W. M. H., Migration and coalescence of Pd carbonyl clusters in zeolite Y, *J. Chem. Soc. Faraday Trans.*, **87** (1991) pp. 1413–1418.
6. Haberland H., Clusters of Atoms and Molecules, Vol. I, 2nd ed., Springer, Berlin, 1995.
7. Iwasita T., Nart F. C., In situ infrared spectroscopy at electrochemical interfaces, *Prog. Surf. Sci.*, **55** (1997) pp. 271–340.
8. Sun S. G., Yang D. F., Tian Z. W., In situ FTIR studies on the adsorption and oxidation of n-propanol and isopropanol at a platinum electrode, *J. Electroanal. Chem.* **289** (1990) pp. 177–189.
9. Jiang Y X, Sun S G, Ding N, Novel phenomenon of enhancement of IR absorption of CO adsorbed on nanoparticles of Pd confined in supercages of Y-zeolite, *Chem. Phys. Lett.*, **344** (2001) pp. 463–470.
10. Drozdova, L., Novakova J., Schulz-Ekloff G., Jaeger N. I. Ship-in-bottle synthesis of palladium carbonyl complexes in NaY and NaX zeolites via the direct carbonylation of  $Pd(NH_3)_4^{2+}$ , *Microp. Mesop. Mater.* **28** (1993) pp. 395–403.

## SYNTHESSES OF MIXED LAYERED NICKEL HYDROXIDE MANGANESE OXIDES BY HYDROTHERMAL INTERCALATION REACTION AND EXFOLIATION-RESTACKING HYDROTHERMAL REACTION

YAOHUA XU, SHOUHUA FENG AND WENQIN PANG

*Department of Chemistry, Jilin University, Changchun, 130023, P. R. China*

QI FENG

*Department of Advanced Materials Science, Faculty of Engineering, Kagawa University, 2217-20  
Hayashi-cho, Takamatsu, 761-0396 Japan*

KOJI KAJIYOSHI AND KAZUMICHI YANAGISAWA

*Research Laboratory of Hydrothermal Chemistry, Faculty of Science, Kochi University, Akebono-cho, Kochi-shi, 780-8520 Japan*

A series of  $\text{Ni(OH)}_2$ -manganese oxide (NMO) compounds with a mixed layered structure were synthesized by inserting nickel hydroxide into layered manganese oxides, Na-birnessite ( $\text{NaBir}$ ) and Ni-birnessite ( $\text{NiBir}$ ), under hydrothermal conditions. The hydrothermal intercalation reaction and the NMO compounds were investigated.  $\text{Ni(OH)}_2$  is preferentially formed in the interlayer space of the birnessites rather than as free  $\text{Ni(OH)}_2$ . The mixed layered  $\text{Ni(OH)}_2$ -manganese oxide with  $\text{Ni(OH)}_2$  content up to  $\text{Ni/Mn}=1/2$  can be obtained by using the hydrothermal intercalation method and  $\text{Ni/Mn}=1$  by exfoliation-restacking hydrothermal reaction method.  $\text{Ni(OH)}_2$  was more easily inserted into  $\text{NiBir}$  than into  $\text{NaBir}$  under the hydrothermal conditions when the molar ratio of  $\text{Ni/Mn}$  is in some extent. A mechanism of topotactic insertion reaction was proposed for the formation of the mixed layered compounds. The mixed layered NMO can be also prepared by hydrothermal treatment of  $\text{NaBir}$  in  $\text{Ni}(\text{Ac})_2$  solution below  $250^\circ\text{C}$ . The NMO compounds were stable up to  $300^\circ\text{C}$  in air, and transformed to other phases over this temperature.

### 1 Introduction

Layered metal oxides show interesting chemical properties, such as ion-exchange, intercalation, catalysis and adsorption, as well as physical properties such as conductivity and magnetism. These compounds can be used as adsorbents, cathodic materials for batteries, precursors for syntheses of organic/inorganic composites and new compounds [1-10]. The development of a new technique for synthesis of mixed layered compounds is interesting in the preparation of new materials with special physicochemical properties [11-15]. Since the mixed layered compounds are made up by alternately stacking two or more kinds of structural unit layers, their properties can be predicted from the stacking structures as well as the properties of the structural unit layers, which means the design of the properties is possible.

Since in most cases the mixed layered compounds are metastable phase, they are not easy to be synthesized by using a normal method. Soft chemical method is a powerful method for the synthesis of such metastable phases. Some mixed layered compounds have been synthesized by insertion of metal hydroxides into clay compounds with cation-exchange and pH titration methods, and it has been also found that these mixed layered compounds exhibit characteristics differing from the metal hydroxides and the clay precursors [15-17]. However, only a few studies have been reported on the synthesis of mixed layered metal oxides. Recently, we have synthesized a mixed layered manganese

oxide from a birnessite-type manganese oxide with a layered structure by using a hydrothermal soft chemical process [13].

Asbolanes are naturally occurring manganese oxide minerals with uncontinuous metal hydroxide layers, such as  $\text{Ni}(\text{OH})_2$ ,  $\text{CoOOH}$  or  $\text{Co}(\text{OH})_3$ ,  $\text{Mn}(\text{OH})_2$ , and  $\text{Cu}(\text{OH})_2$  in the interlayer spaces of layered manganese oxide [18, 19]. Very recently we have successfully synthesized a mixed layered nickel hydroxide-manganese oxide (NMO) from a Ni-birnessite by using a hydrothermal intercalation method, and found that the mixed layered compound can be used as a precursor for the synthesis of a  $\text{LiNi}_x\text{Mn}_{1-x}\text{O}_2$  layered compound which is an attractive material as an alternative of  $\text{LiCoO}_2$  cathodic material in lithium rechargeable batteries. In this paper, we present the intercalation reactions of nickel hydroxide into Ni-birnessite and Na-birnessite in various solutions under hydrothermal and room temperature conditions, and propose a formation mechanism of the mixed layered compounds.

## 2 Experimental

### 2.1 Preparation of materials

A  $\text{Na}^+$ -form of birnessite-type manganese oxide (NaBir), which was used as a precursor, was prepared as described in literature [6]. A  $\text{Ni}^{2+}$ -form of birnessite-type manganese oxide (NiBir) and a  $\text{H}^+$ -form of birnessite-type manganese oxide (HBir) were prepared from NaBir by ion-exchanging

Mixed layered  $\text{Ni}(\text{OH})_2$ -manganese oxides (NMO) were prepared by three methods. In the first method, NiBir or NaBir was dispersed into a stoichiometric  $\text{Ni}(\text{NO}_3)_2$  solution, and added NaOH solution until  $\text{pH}=11\text{-}12$ , then the mixture was filtered and washed with distilled water, and was autoclaved in distilled water at 150–200°C for 1–3 days. In the second method, NaBir was directly hydrothermally treated in  $\text{Ni}(\text{Ac})_2$  solution at 150 and 200°C for 1 day. The third one is exfoliation-restacking hydrothermal method. HBir was dispersed in 0.05 M tetramethylammonium hydroxide (TMAOH) solution with molar ratio of TMA/Mn=5/2 under stirring to exfoliate the layered manganese oxide into a nanosheet colloidal suspension solution. A solution with stoichiometric amount of  $\text{Ni}(\text{NO}_3)_2$  was dropwise added into the exfoliated suspension solution under vigorous stirring. A black-brown precipitate was obtained with a final pH value between 11 and 14. After 4 hours stirring, the precipitate was filtered and washed with distilled water until the pH was between 7 and 8. Then this precipitate was autoclaved in water at 150 to 200°C for 1 to 3 days.

### 2.2 pH titration

A pH titration of the suspension solutions of NaBir or NiBir in  $\text{Ni}(\text{NO}_3)_2$  solution was carried out similarly as that for preparation of  $\text{Ni}(\text{OH})_2$ -montmorillonite mixed layered compound described by Yamanaka et al. [15]. Separate NaBir and NiBir (dried at 80°C) were dispersed in  $\text{Ni}(\text{NO}_3)_2$  solution (0.1M), and agitated by ultrasonic vibration for 30 min. Then these suspensions were potentiometrically titrated with a NaOH solution. The pH value at each stage of the titration was measured by a HORIBA F-22 pH meter. The titrated suspension was stirring for 10 min before the pH measurement at each stage of the titration before  $\text{pH}=8$ , 5 min before  $\text{pH}=10$ , and 2 min to the end. A pure water and one with dispersed NiBir as well as a pure  $\text{Ni}(\text{NO}_3)_2$  solution were also similarly titrated for comparison.

### 2.3 Chemical analysis.

The contents of sodium, nickel and manganese in the samples were determined by Seiko Instruments SPS7000A induced couple plasma (ICP) spectrometer after dissolved in a mixed solution of HCl and H<sub>2</sub>O<sub>2</sub>.

### 2.4 Physical analysis.

Powder X-ray diffraction (XRD) patterns of the samples were carried out on a Rigaku RTP300-RC X-ray diffractometer with Cu K $\alpha$  ( $\lambda=1.5418\text{\AA}$ ) radiation. Infrared spectra (IR) were recorded by the KBr method on a Perkin-Elmer 1600 Series FTIR infrared spectrometer. Thermogravimetric (TG) and differential thermal analysis (DTA) curves were obtained at a heating rate of 10°C/min in air on a Seiko SSC5200 thermal analyzer. Scanning electron microscopy (SEM) was performed on a Hitachi S-530 scanning electron microscope.

## 3 Results and Discussion

### 3.1 Preparation of NaBir and NiBir

The XRD pattern of NaBir prepared as the precursor is shown in Figure 1A. The XRD pattern of NiBir (Figure 1B) shows two main diffraction peaks at 0.97 and 0.49 nm, which is very similar to that of buserite [20]. This fact suggests that the layered structure of the birnessite retains after the ion-exchange reaction, while the basal spacing increases from 0.72 nm to 0.97 nm. However, there is a hump at the right side of the first diffraction peak (large d-spacing) and the intensity of peak at 0.49 nm is as strong as that at 0.97 nm. This is perhaps due to the partial formation of mixed layered NMO.

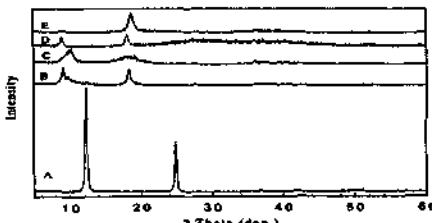


**Figure 1.** The XRD patterns of (A) NaBir, (B) NiBir, (C) sample obtained by pH titration of NaBir in Ni(NO<sub>3</sub>)<sub>2</sub> with NaOH at room temperature, (D) Ni(OH)<sub>2</sub>-NiBir mixture with Ni/Mn=1/2, and (E) hydrothermally treated sample (D) at 200°C for 2 days.

### 3.2 Intercalation of Ni(OH)<sub>2</sub> into birnessites by pH titration

The intercalation reaction of Ni(OH)<sub>2</sub> into NiBir and NaBir at room temperature was investigated by pH titration method. When NaOH solution was added into Ni(NO<sub>3</sub>)<sub>2</sub> solution without the presence of the birnessites, the pH of the solution increased from pH 5.6 to 7.2, immediately, and then increased very slowly (Figure 2D). This was accompanied the formation of Ni(OH)<sub>2</sub> precipitate at the same time. The Ni(NO<sub>3</sub>)<sub>2</sub>

solution showed the end-point of the titration at pH=9.5, around which pH increased rapidly.

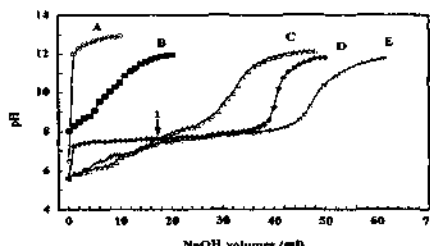


**Figure 2.** The pH titration curves of (A) blank, (B) distilled water with NiBir, (C) 0.1M  $\text{Ni}(\text{NO}_3)_2$  solution with NaBir, (D) 0.1M  $\text{Ni}(\text{NO}_3)_2$  solution, and (E) 0.1M  $\text{Ni}(\text{NO}_3)_2$  solution with NiBir.

The titration curve of NaBir- $\text{Ni}(\text{NO}_3)_2$  system showed dibase behavior (Figure 2C), which was different from that of  $\text{Ni}(\text{NO}_3)_2$  solution. The titration curve C can be separated into two stages, before the point (1) crossing with curve D and after that. Before the point (1), the pH values are lower than that of curve D, which corresponds to the formation of  $\text{Ni(OH)}_2$  precipitate in the interlayer space of NaBir. After the point (1), the pH values are higher than those of curve D, which corresponds to the formation of free  $\text{Ni(OH)}_2$  precipitate. The amount of  $\text{Ni(OH)}_2$  inserted into NaBir by the titration estimated from the amount of NaOH at the point (1) is 2.03 meq/g of NaBir ( $\text{Ni/Mn}=1.6/14$  in mole). The added amount of NaOH at the end-point ( $\text{pH}=9.5$ ) of the titration curve C is less than that of the curve D. The difference of the added NaOH amounts between the end points of curves C and D is 1.53 meq/g of NaBir, which is attributed to the amount of nickel ion that is inserted into NaBir by  $\text{Ni}^{2+}/\text{Na}^+$  exchange reaction during the titration [15]. Since the  $\text{Na}^+$  content in NaBir is 2.84 meq/g, so only 54% of  $\text{Na}^+$  was exchanged by  $\text{Ni}^{2+}$  ion after the titration. The XRD study on the  $\text{Ni(OH)}_2$ -NaBir sample obtained by titration indicated that the basal spacing of the layered structure increased from 0.72 nm of NaBir to 0.87 nm after the titration, revealing that  $\text{Ni(OH)}_2$  was inserted into the interlayer space of NaBir, and NMO was formed (Figure 1C). The small peak at 0.46 nm is attributed to the free  $\text{Ni(OH)}_2$ . The titration result suggests that  $\text{Ni(OH)}_2$  is precipitated preferentially in the interlayer space of NaBir rather than as free  $\text{Ni(OH)}_2$ , and partial  $\text{Na}^+$  in NaBir was exchanged by  $\text{Ni}^{2+}$  during the titration.

The titration curve of NiBir- $\text{Ni}(\text{NO}_3)_2$  system also shows a dibase behavior similar to that of NaBir- $\text{Ni}(\text{NO}_3)_2$  system (Figure 2E). In the first stage, the pH value increases with the increasing of the amount of NaOH with almost the same manner as that of curve C until it approaches the point (1), which can be attributed to the formation of  $\text{Ni(OH)}_2$  in the interlayer space of NiBir. The amount of  $\text{Ni(OH)}_2$  inserted into NiBir is 2.33 meq/g of NiBir ( $\text{Ni/Mn}=1.9/14$ ). In the second stage (after the point (1)), the curve E shows a similar behavior to the curve D, which can be ascribed to the formation of free  $\text{Ni(OH)}_2$ . It is interesting that the amount of NaOH required to complete the titration is more than that of  $\text{Ni}(\text{NO}_3)_2$  solution (curve D). To clear this phenomenon, a titration of distilled water containing NiBir and a blank titration were performed. The pH value increases rapidly with the addition of NaOH in a blank titration (Figure 2A), but with the presence of NiBir, the titration curve shows a different behavior (Figure 2B), implying that  $\text{Ni}^{2+}$  ions in NiBir

transformed to  $\text{Ni(OH)}_2$ , and some  $\text{Na}^+$  ions were inserted into NiBir to balance the charge during the titration.

The amount of inserted  $\text{Na}^+$  is 0.77 meq/g of NiBir based on the difference of the added NaOH amounts between the end points of curves D and E. Since more amount of  $\text{Ni(OH)}_2$  was formed in NiBir- $\text{Ni(NO}_3)_2$  system than that in  $\text{Ni(NO}_3)_2$  solution only, more amount of NaOH was required to complete the titration in NiBir- $\text{Ni(NO}_3)_2$  system than that in  $\text{Ni(NO}_3)_2$  solution.

### 3.3 Hydrothermal intercalation of $\text{Ni(OH)}_2$ into NiBir

Although  $\text{Ni(OH)}_2$  can be inserted into the birmessites by the pH titration at room temperature, the titration needs a relatively long time to reach the reaction equilibrium, and the amount of inserted  $\text{Ni(OH)}_2$  is very little. A hydrothermal method was used in the preparation of NMO. In the hydrothermal intercalation, NiBir (or NaBir) was firstly dispersed in a  $\text{Ni(NO}_3)_2$  solution, and a NaOH solution was then added in the NiBir- $\text{Ni(NO}_3)_2$  system to prepare a  $\text{Ni(OH)}_2$ -NiBir mixture. The mixture was hydrothermally treated in distilled water to intercalate free  $\text{Ni(OH)}_2$  into the NiBir.

Figure 1D shows the XRD pattern of the  $\text{Ni(OH)}_2$ -NiBir mixture with a molar ratio of  $\text{Ni/Mn}=1/2$ . The broad peak between 20 and 40° is attributed to amorphous phase of the free  $\text{Ni(OH)}_2$ . After hydrothermal treatment in distilled water at 200°C for 2 days, the intensity of peak at 0.46 nm increased while that at 0.92 nm decreased (Figure 1E), and the broad peak of the free  $\text{Ni(OH)}_2$  disappeared. This suggests that the free  $\text{Ni(OH)}_2$  is inserted into NiBir under the hydrothermal conditions.

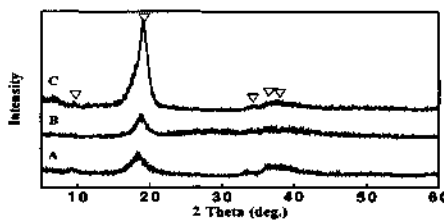


Figure 3. XRD patterns of (A) as-prepared  $\text{Ni(OH)}_2$ -manganese oxide precipitate and hydrothermally treated samples for (B) 7h and (C) 4 days at 150 °C.

To synthesize NMO with high Ni content, we used the exfoliation-restacking hydrothermal method. In this method, the mixed layered NMO was stepwise synthesized from HBir. Firstly, HBir was treated with TMAOH solution to exfoliate the layered manganese oxide into manganese oxide nanosheet colloidal solution, and then a  $\text{Ni(NO}_3)_2$  solution was added in the colloidal solution. When  $\text{Ni(NO}_3)_2$  solution was added in the colloidal solution, a black-brown precipitate of  $\text{Ni(OH)}_2$ -manganese oxide was formed, immediately. Figure 3(A) shows the XRD patterns of the as-prepared  $\text{Ni(OH)}_2$ -manganese oxide precipitate. The precipitate shows a weak broad diffraction peak at 0.48 nm, suggesting the manganese oxide nanosheets retain the sheet structure, but they are in low ordering arrangement in the precipitate. An IR study indicated that there is some free amorphous  $\text{Ni(OH)}_2$  in the precipitate. The precipitate can be crystallized to the mixed layered NMO under hydrothermal conditions. Figures 3(B) and (C) show the XRD

patterns of the hydrothermally treated samples in distilled water at 150°C. After the hydrothermal treatment, the diffraction peak at 0.48 nm shifted to 0.46 nm, and the intensity increased with increasing the reaction time. The hydrothermally treated samples show same XRD pattern as the NMO prepared by hydrothermal intercalation method, but the diffraction peaks are broad. This fact revealed that the NMO can be prepared by the exfoliation-restacking hydrothermal method, and the layered structure is in low ordered arrangement. IR analysis shows that there is no free  $\text{Ni(OH)}_2$  in the hydrothermally treated samples, meaning all  $\text{Ni(OH)}_2$  is accommodated into the layered structure. The formation of the NMO from the manganese oxide nanosheets solution is a restacking process of manganese oxide nanosheets, which accompanies accommodation of  $\text{Ni(OH)}_2$  into the layered manganese oxide.

### 3.4 Morphology of NMO

The SEM photographs for NMO-2/7 and NMO-1/2 samples are shown in Figure 4. All these samples have similar sheety crystal morphology as that of NaBir precursor [21]. This result suggests that the hydrothermal insertion of  $\text{Ni(OH)}_2$  is a topotactic reaction, in which almost no dissolution-deposition of NaBir or NiBir occurs. The sheety crystal morphology also suggests that the  $\text{Ni(OH)}_2$  inserted samples have a layered structure.



**Figure 4.** SEM micrographs of microstructures of (A) NMO-2/7 and (B) NMO-1/2.

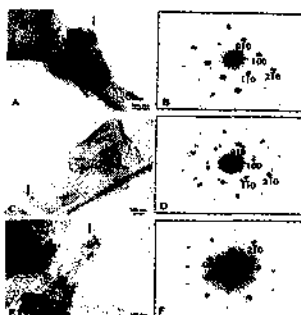


**Figure 5.** TEM images and selected-area electron diffraction (SAED) patterns from the c axis direction (perpendicular to the basis plane of the plate-like crystal particle) for NMO-6 (A, B), NMO-5 (C, D), and NMO-3 (E, F), respectively.

To confirm the structure of NMO, TEM observation and selected-area electron diffraction (SAED) studies were carried out on NMO samples. NMO-6 has a plate-like particle morphology (Figure 5(A)). When the electron beam is perpendicular to the basis plane, the SAED pattern contains two incommensurate hexagonal networks of  $(h k 0)$

reflections (Figure 5(B)). The diffraction pattern is in agreement with that of asbolane, a nature mineral with mixed layered  $\text{Ni(OH)}_2$ -manganese oxide structure. The mixed layered structure can be described by two sublattices (sublattices I and II) having different hexagonal unit-cell parameters in the ab plane but a common periodicity perpendicular to them along c. The sublattice I with small a corresponds to the sublattice of  $\text{MnO}_6$  octahedral layer, and sublattice II with large a to the sublattice of  $\text{Ni(OH)}_6$  octahedral layer. The SAED patterns for NMO-5 and NMO-3 are similar to that for NMO-6 (Figure 5), but with larger a than that for NMO-6. The relative intensity of sublattice II reflections decreases in an order of NMO-6>NMO-5>NMO-3, which is in agreement with the decreasing order of  $\text{Ni(OH)}_2$  content in the samples, indicating that sublattice II corresponds to the sublattice of  $\text{Ni(OH)}_2$  layer in the mixed layered structure.

#### 4 Conclusions

In the weak basic solution,  $\text{Ni(OH)}_2$  is preferentially formed in the interlayer space of birnessite rather than as free  $\text{Ni(OH)}_2$  from  $\text{Ni}^{2+}$  containing solution. Hydrothermal intercalation method is favored the formation of a mixed layered  $\text{Ni(OH)}_2$ -manganese oxide, in which the  $\text{Ni(OH)}_2$  insertion into the birnessites is topotactic reaction.

#### References

1. Y. -F. Shen, S. L. Suib, C. -L. O'Young, *J. Am. Chem. Soc.* **116** (1994) pp. 11020.
2. S. -T. Wong, S. Cheng, S. *Inorg. Chem.* **31** (1992) pp 1165-1169.
3. K. Domen, A. Kudo, A. Shinozaki, A. Tanaka, K. Maruya, T. Onishi, T. *J.C.S., Chem. Commun.* (1986) pp. 356.
4. R. E. Schaak, T. E. Mallouk, *Chem. Mater.* **12**(9) (2000) pp. 2513.
5. A. J. Jacobson, *Mater. Sci. Forum* **152-153** (1994) pp. 1.
6. Q. Feng, K. Yanagisawa, N. Yamasaki, *J. Porous Mater.* **5** (1998) pp. 153.
7. A. R. Armstrong, P. G. Bruce, *Nature* **381**(6) (1996) pp. 499.
8. J. Kim, A. Manthiram, A. *Nature* **390**(20) (1997) pp. 265.
9. J. M. Paulsen, C. L. Thomas, J. R. Dahn, *J. Electrochem. Soc.* **146**(10) (1999) pp3560.
10. J. M. Paulsen, C. L. Thomas, J. R. Dahn, *J. Electrochem. Soc.* **147**(3) (2000) pp. 861.
11. S. W. Keller, H. -N. Kim, T. E. Mallouk, *J. Am. Chem. Soc.* **116** (1994) pp. 8817.
12. G. Decher, *Science* **277** (1997) pp. 1232.
13. Q. Feng, C. Honbu, K. Yanagisawa, N. Yamasaki, *Chem. Mater.* **11** (1999) pp. 2444.
14. E. R. Kleinfeld, G. S. Ferguson, *Science* **265** (1994) pp. 370.
15. S. Yamanaka, G. W. Brindley, *Clays and Clay Minerals* **26**(1) (1978) pp. 21.
16. K. Ohtsuka, M. Suda, M. Tsunoda, M. Ono, *Chem. Mater.* **2** (1990) pp. 511.
17. S. Yamanaka, K. Senda, *Clay Science* **9** (1993) pp. 99.
18. F. V. Chukhrov, *International Geology Review* **25** (1983) pp. 838.
19. A. Manceau, A. I. Gorshkov, V. A. Drts, *American Mineralogist* **77** (1992) pp. 1144.
20. Q. Feng, H. Kanoh, K. Ooi, *J. Mater. Chem.* **9** (1999) pp. 319.
21. Q. Feng, L. Liu, K. Yanagisawa, *J. Mater. Sci. Lett.* **19** (2000) pp. 1567.

This page is intentionally left blank

## Author Index

- Aoki, K. 97  
 Attfield, M. P. 177  
 Balderas-Tapia, L. 461  
 Ban, F. Q. 549  
 Bausk, N. V. 91  
 Beach, D. B. 427  
 Becher, O. 467  
 Boyd, R. J. 549  
 Cai, H. 427  
 Cai, J. W. 361  
 Cai, Z. 85  
 Cao, R. 311, 333  
 Caspi, E. N. 13  
 Che, P. 97  
 Chen, C. T. 103  
 Chen, J. -S. 555  
 Chen, L. F. 461  
 Chen, T. N. 427  
 Chen, W. 555  
 Chu, L. 185  
 Cui, H. -N. 369  
 Cui, X. F. 377  
 Ding, N. 571  
 Dong, B. Z. 523  
 Dong, J. X. 233  
 Dou, T. 227  
 Du, G. T. 383  
 Du, Z. L. 415  
 Fajula, F. 197  
 Falamaki, C. 501  
 Fan, J. 283  
 Fan, Y. 415  
 Feng, C. -Q. 125  
 Feng, J. 91, 361, 159  
 Feng, Q. 577  
 Feng, S. H. 39, 435, 453, 577  
 Feng, X. H. 415  
 Feng, X. -L. 361  
 Feng, Y. B. 85  
 Fu, L. S. 73  
 Fu, Q. X. 167  
 Fujita, K. 91, 97  
 Fukuda, T. 97  
 Gan, F. -X. 143  
 Gao, Q. M. 391  
 Gao, S. 399  
 Ge, Z. H. 275  
 Gedanken, A. 435  
 Gobin, P. F. 197  
 Gong, Y. J. 523  
 Greenblatt, M. 13  
 Gu, Y. L. 27  
 Guevara, J. C. 461  
 Guo, Y. H. 249  
 Guo, Y. -R. 137  
 Han, E. S. 421  
 Han, X. J. 487  
 Harvey, H. G. 177  
 He, S. 479  
 He, Y. 555  
 Hong, M. C. 311, 333  
 Hong, P. -J. 265  
 Hou, Y. -L. 399  
 Hu, C. W. 249, 405  
 Hu, S. F. 79  
 Hu, X. -P. 361  
 Hu, Z. G. 415  
 Huang, J. -W. 53  
 Huang, W. -X. 143  
 Ikorskii, V. N. 91  
 Jang, L. Y. 79  
 Ji, L. -N. 53  
 Ji, X. Y. 515  
 Jia, M. -K. 125  
 Jia, M. Q. 507  
 Jiang, Q. 377  
 Jiang, Y. -S. 555  
 Jiang, Y. X. 191  
 Jiang, Y. -X. 571  
 Jin, H. Y. 435  
 Jin, J. 303  
 Jorgensen, J. D. 13  
 Kajiyoshi, K. 577  
 Kamegashira, N. 47, 91, 97, 159  
 Kang, Z. H. 405  
 Kinomura, N. 219, 257

- Kitagawa, S. 355  
 Kobayashi, M. 47  
 Kudryashov, N. I. 507  
 Kumada, N. 219, 257  
 Lai, Q. Y. 515  
 Lai, Z. H. 211  
 Lee, J. F. 79  
 Lefevre, B. 197  
 Lei, D. M. 479  
 Li, C. Y. 149  
 Li, H. R. 73  
 Li, J. C. 377, 411  
 Li, J. P. 233  
 Li, M. 241, 473  
 Li, Q. W. 275  
 Li, T. 53  
 Li, W. B. 203  
 Li, X. C. 211  
 Li, X. H. 447, 473  
 Li, X. -J. 143  
 Li, X. M. 529  
 Li, X. N. 275  
 Li, Y. 39, 295  
 Li, Y. G. 405  
 Li, Z. H. 523  
 Li, Z. -H. 137, 265  
 Li, Z. M. 191  
 Liang, Y. G. 339  
 Liao, D. -Z. 317  
 Lin, G. 453  
 Lin, J. 65  
 Liu, D. 383  
 Liu, D. L. 383  
 Liu, F. Y. 73  
 Liu, G. H. 233  
 Liu, J. H. 241  
 Liu, K. Q. 211  
 Liu, L. 415  
 Liu, R. S. 79  
 Liu, S. Z. 415  
 Liu, T. 103  
 Liu, X. Q. 167  
 Liu, X. T. 59  
 Liu, X. Z. 427  
 Liu, Z. -K. 541  
 Long, J. B. 453  
 Lu, J. Z. 515  
 Lu, R. 491  
 Lu, W. Q. 85  
 Luan, R. 421  
 Luo, C. G. 191  
 Luo, J. H. 333  
 Luo, L. T. 211  
 Luo, Y. Q. 59  
 Ma, H. 131  
 Ma, Y. 383  
 Mai, Z. H. 473  
 Martin, T. 197  
 Mathmura, Y. 219  
 Mazalov, L. N. 91  
 Melville, U. 441  
 Meng, G. Y. 167  
 Meng, J. 91, 97, 159  
 Meretsky, A. 507  
 Mori, T. 97  
 Munshiyeva, M. K. 321  
 Ni, C. -L. 53  
 Niu, S. Y. 303  
 Ong, H. C. 383  
 Pang, G. S. 435  
 Pang, W. Q. 577  
 Peng, D. K. 167  
 Pu, M. 523  
 Qi, W. 131  
 Qian, Y. -T. 27  
 Qian, B. 265  
 Qin, J. G. 103  
 Range, K. -J. 117  
 Rao, C. N. R. 3  
 Reller, A. 467  
 Ren, L. R. 441  
 Ren, P. 103  
 Rustamov, M. I. 321  
 Saito, J. -I 47  
 Sasai, R. 97  
 Satoh, H. 91, 97, 159  
 Shen, R. F. 109  
 Shi, C. S. 59  
 Shi, J. S. 563  
 Shi, Q. 311  
 Shi, Y. H. 39  
 Shi, Z. 555

- Shishido, T. 97  
 Si, S. -F. 317  
 Slater, B. 177  
 Sokolov, V. V. 91  
 Song, X. M. 411  
 Sttckl, A. C. 117  
 Su, Q. 149  
 Suib, S. L. 391  
 Sun, D. F. 311  
 Sun, J. T. 339, 533  
 Sun, S. -G. 571  
 Sun, S. X. 529  
 Sun, Y. 435  
 Sun, Y. H. 523  
 Tagiyev, D. B. 321  
 Takano, M. 257  
 Takei, T. 257  
 Tang, H. 125  
 Teixeira, V. 369  
 Tian, Y. -L. 143  
 Tong, Z. F. 191  
 Tu, B. 283  
 Tu, X. -Y. 265  
 Tu, Y. L. 453  
 Vallet, C. E. 427  
 Veith, G. M. 13  
 Wan, Q. 435  
 Wang, B. 411, 447  
 Wang, C. Y. 79  
 Wang, D. 219, 257  
 Wang, E. B. 249, 405  
 Wang, F. Y. 109  
 Wang, G. G. 453  
 Wang, G. P. 327  
 Wang, H. 411, 447  
 Wang, J. 73, 523, 149  
 Wang, J. A. 461  
 Wang, J. L. 533  
 Wang, J. P. 159  
 Wang, J. -T. 541  
 Wang, J. Z. 383  
 Wang, L. M. 283  
 Wang, M. 411  
 Wang, Q. -L. 317  
 Wang, R. H. 333  
 Wang, R. Z. 447  
 Wang, S. B. 149  
 Wang, X. Q. 383  
 Wang, X. Z. 227  
 Wang, Y. 295  
 Wang, Y. W. 39  
 Wark, M. 441  
 Wei, L. Y. 479  
 Wei, W. P. 59  
 Wei, Y. -D. 137  
 Wehrich, R. 117  
 Wen, G. -H. 399  
 Wu, D. 523  
 Wu, M. M. 453  
 Wu, Y. C. 103  
 Wu, Z. J. 549  
 Wu, Z. Z. 427  
 Xie, D. M. 59  
 Xie, R. 109  
 Xiong, J. H. 59  
 Xu, C. Q. 487  
 Xu, F. C. 109  
 Xu, J. 143  
 Xu, R. R. 295, 453  
 Xu, X. Y. 167  
 Xu, Y. H. 577  
 Xue, C. F. 233  
 Xue, Z. L. 427  
 Yan, C. X. 241  
 Yan, F. Y. 515  
 Yan, H. 411, 447  
 Yanagisawa, K. 219, 577  
 Yang, G. D. 303  
 Yang, H. 491  
 Yang, R. 241  
 Yang, S. J. 339  
 Yang, S. R. 383  
 Yang, X. F. 203, 453  
 Yang, X. T. 383  
 Yang, Y. 249, 265  
 Yang, Y. H. 427  
 Yang, Y. Y. 533  
 Yang, Y. Z. 529  
 Yang, Z. -M. 265  
 Yashima, T. 219  
 Ye, L. 303  
 Yu, C. Z. 283  
 Yu, J. -F. 399  
 Yu, J. H. 295  
 Yu, M. 65

- Yu, R. B. 219, 257  
Yu, X. Q. 339  
Yu, Y. 473  
Yu, Z. -T. 555  
Yuan, L. J. 533  
Yuan, Z. Y. 533  
  
Zhang, C. F. 487  
Zhang, D. W. 541  
Zhang, H. J. 73  
Zhang, K. L. 533  
Zhang, K. -L. 125  
Zhang, S. -H. 265  
Zhang, S. Y. 563  
Zhang, X. M. 479  
Zhang, X. X. 399  
Zhang, Y. 53, 203  
Zhang, Y. H. 467  
Zhang, Y. -M. 185  
Zhang, Y. T. 383  
  
Zhao, D. Y. 283  
Zhao, H. 523  
Zhao, L. 487  
Zhao, Q. 411  
Zhao, X. H. 131  
Zhao, Y. J. 333  
Zhao, Y. N. 473  
Zheng, C. M. 479  
Zheng, L. -M. 345  
Zhong, B. 227  
Zhong, S. H. 563  
Zhou, B. -B. 137  
Zhou, C. H. 275  
Zhou, H. 447  
Zhu, L. G. 327  
Zhu, L. -G. 355  
Zhuang, G. X. 59  
Zou, Y. -Q. 143  
Zuhr, R. A. 427

## Subject Index

- Activation energy 501
- Adsorption 249
- Alkaline earth metal 555
- Alloy surface composition 507
- Aluminophosphates 295
- Aluminum diphosphonates 177
- Amides 427
- n*-Amyl cinnamate 339
- Anion Cl 109
- Anode 79
- Anode material 167
- Antiferromagnetism 47
- Asbolane 577
- Assembly 283
- AuSb<sub>2</sub>-SiP<sub>2</sub> 117
- BaLn<sub>2</sub>Mn<sub>2</sub>O<sub>7</sub> 91
- BaTb<sub>2</sub>Mn<sub>2</sub>O<sub>7</sub> 159
- BaTiO<sub>3</sub> 85
- Bentonite 191
- Binuclear Ni(II) complex 303
- Birnessite 391, 577
- Bi-system superconductor 109
- Borates 555
- Calcosilicate 233
- Carbon monoxide 571
- CAS-1 233
- Catalyst 211, 265, 321, 461, 339
- Catalytic alkylation 275
- Cat-CVD 411
- Cathode 79
- Cathode materials 125
- Cationic surfactant 241
- Cavity 311
- Ceramic 149
- Ceria-zirconia 461
- Cerium dioxide 241
- Cerium material 257
- Characterization 191, 233, 415, 479
- Charge transfer 117
- Charge-orbital ordering 13
- Chemical reduction 399
- Chemical synthesis 59
- Chemical vapor deposition 541
- Chiral metal complex 295
- Chiral recognition 295
- Chiral transference 295
- Ciprofloxacin 327
- Clathrate 361
- Co cation 109
- CO oxidation 461
- Co@Pt 473
- Cobalt 515
- Colloidal silica 501
- Compression 265
- Conductivity 137, 369
- Confined fluids 197
- Coordination precipitate method 487
- Co-permeation 137
- Copper 345, 355
- Copper benzoate 533
- Copper bismuth vanadate 39
- Copper(II) complex 327
- Core-shell 473
- Crystal 219
- Crystal growth 97
- Crystal structure 47, 257, 317, 327, 345, 355, 361, 555
- Crystal structure determination 177
- Crystallite size 435
- Cu complexes 311
- Cubic boron nitride 447
- Curie temperature 377
- CVD 427
- Cyanide bridge 317
- Cyclic voltammetry 571
- Damping 197
- Debye's theory 523
- Defect 143
- Density functional computer calculations 177
- Design 311
- DFT band structure calculations 117
- Diamine ligands 333
- Diamond synthesis 541
- Dielectric 85
- Diffuse reflectance spectroscopy 435
- Diffusion barriers 427
- Dislocations 143
- Doping 125
- Double-mesopore silica 227
- Dye 249

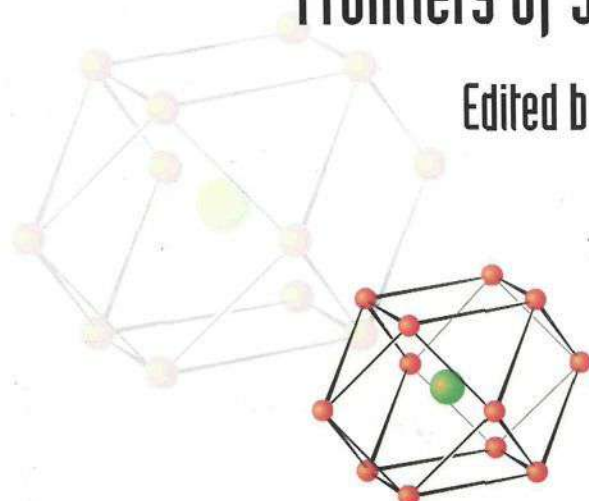
- Electrical conductivity 167
- Electrode material 487
- Electron spin resonance 149
- Electronic structure 91
- Electrostatic interactions 563
- Energy calculation 295
- Energy expression parameter 563
- Energy level 563
- Energy storage 149
- EPMA 143
- Esterification 339
- Ethylene oligomerization 321
- Exfoliation 577
- Extraction-reduction 529
- Ferroelectric 85, 377
- Fluoroquinolone 327
- Framework 345
- Fréedericksz transition 53
- Functionalization 197
- Grafting 321
- Growth 501
- Heterogeneous 321
- Heteropoly acid 185
- Heteropoly compounds 339
- Heteropolymolybdophosphate 415
- Hexagonal boron nitride 447
- Hierarchy 3
- Host/guest 355
- Hybrid 415
- Hybrid materials 73
- Hydrogen adsorption 507
- Hydrogen bonding 355
- Hydrophobicity 197
- Hydrothermal 501, 555
- Hydrothermal crystallization 453
- Hydrothermal synthesis 39, 185, 257
- Hydroxyl-Zr 191
- Imidazolate-bridged 303
- Imide formation 549
- Infrared 103
- Inorganic compounds 59
- Inorganic-organic hybrid materials 177
- Intercalation 391, 577
- Interface layer thickness 523
- Interlayer distance 191
- Inverse spinel 515
- Ion-doping 109
- Ionic conductivity 39
- IR spectra 311
- Iridium-rhodium alloys 507
- Iron 399
- ITO films 369
- Keggin anion 185
- $\text{KHgBr}_3\text{H}_2\text{O}$  103
- Ladder structure 3
- Lanthanum gallate 167
- Lanthanide ions 563
- Large area devices 369
- Layered 391
- Layered manganates 159
- LB films 415
- Ligand exchange 321
- Li-ion battery 79
- Lithium 515
- Lithium battery 125
- Lithium manganese oxide 125
- $\text{LiVMo}_6$  79
- Long lasting phosphorescence 149
- Low-dimensional 555
- Luminescence 65, 73
- Luminescent mechanism 59
- Luminescent property 59
- Macrocyclic complex 333
- Macroporous 249
- Magnetic properties 345, 473
- Magnetism 303, 317, 399
- Magnetoresistance 13
- Magnetron sputtering 369, 447
- Manganates 91
- Manganese 317
- Manganese dioxide 533
- Manganese oxide 391, 577
- Manganese titanium oxide 47
- MCM-41 73, 197
- Mechanism 227
- Mesoporous 197, 203
- Mesoporous material 185, 241, 283
- Metal carboxylate 311
- Metal clusters 333, 441
- Metal-organic 333
- Metal-oxalates 3
- Metal phosphates 3
- Metal salts 441

- Metastable phase 131  
 Metastable structure 27  
 Method of potentiodynamic pulses 507  
 Microemulsion 421  
 Microemulsion synthesis 473  
 Microwave heating 501  
 Mineralizer 219  
 Mixed layered compound 577  
 Mixed surfactants 203  
 MOCVD 383  
 Modeling 549  
 Modern thermodynamics 541  
 Modification 227  
 Molecular sieves 283  
 Molecular simulations 295  
 Molybdate 249  
 Montmorillonite 275
- NaA zeolite 571  
 1,5-Naphthalenedisulfonate 361  
 Nano grain ceramics of VO<sub>2</sub> 479  
 Nanocrystal and nanoporous 453  
 Nanocrystals 435  
 Nanomaterials 27  
 Nanometer 391  
 Nanoparticle 283, 377, 399, 405, 473, 529  
 Nanophase 487  
 Nanopowders of vanadium oxides 479  
 Nanorods 405  
 Nanosize 487  
 Nanosized materials 533  
 Nanosized titania 467  
 Negative deviation 523  
 Nematic liquid crystal 53  
 Network 355  
 Ni(OH)<sub>2</sub> powders 487  
 Nickel hydroxide 577  
 Nickel 515  
 Nickel-organic complexes 321  
 Nickel salicylate 533  
 Nickel sulfide 421  
 Nitroprusside 317  
 Noble metal 441  
 N-(o-carboxybenzoyl)-L-amino acid 549  
 Non-aqueous synthesis 219  
 Nondissipative thermodynamics 541  
 Nonlinear optical 103  
 Non-oxides 27  
 Nucleation 411  
 One-dimensional 3
- Open-framework 3  
 Optical transmittance 369  
 Orthorhombic phase 131  
 Oxalates 515  
 Oxide 79
- Palladium nanoparticles 571  
 Particle size distribution 85  
 Patterning 65  
 Pd electrode 571  
 Perovskite 47  
 Perovskite layers 13  
 Perovskite structure 167  
 Phase diagram 541  
 Phase transition 159  
 Phosphonate 345  
 Phosphor film 65  
 Photoluminescence 383  
 Pillared layered clays 275  
 Polyethylene glycol 241  
 Polyoxometalate 405  
 POMs 137  
 Porod's law 523  
 Porous material 275, 361  
 Porphyrinatozinc( II) 53  
 Postsynthesis hydrothermal treatment 227  
 Powder X-ray diffraction 435  
 Powder XRD 131  
 Praseodymium 59  
 Pre-carbonization 411  
 Precipitation 241  
 Precursor 491, 515  
 Precursor route synthesis 131  
 Preparation 191, 211, 391, 415, 479  
 Primary amine N1923 529  
 PrMnO<sub>3</sub> 97  
 Protocatechuate 355  
 Purolite C-100 501
- Quantum confinement effect 435
- Raman spectrum 435  
 Rare earth 47  
 Rare earth elements 137  
 Rare earth vanadate 65  
 Reaction coupling 541  
 Reaction mechanism 549  
 Reverse micelles 529  
 Rheological phase reaction 125, 533

- Rietveld refinement 13  
 Rock salt layers 13  
 Route of precursor 479  
 $\text{Ru/TiO}_2$  265  
 Ruddlesden Popper phases 13
- Salt-gel reaction 185  
 SAXS 523  
 Schiff base 317  
 Sear's method 501  
 Second harmonic generation 103  
 Selected area electron diffraction 131  
 Self-assembly 3  
 SHELXL program 97  
 Ship-in-a-bottle 571  
 Silanes 427  
 Silica nanotubes 441  
 Silicon dopant 467  
 $\beta\text{-SiC}$  411  
 Single crystal growth 533  
 $\text{SiO}_2$  colloid 523  
 Size dependence 377  
 Sn cation 109  
 $\text{SnO}_2$  435  
 Soft lithography 65  
 Sol-gel technique 85  
 Sol-gel 65, 211, 249, 441  
 Solid oxide fuel cells 167  
 Solid state reaction 79, 405  
 Solid superacids 491  
 Solvent extraction 185  
 Solvothermal 399, 555  
 Solvothermal synthesis 27  
 Spatial structure 91  
 Specific surface area 191, 265, 491  
 Spectra 303  
 Spinel 125  
 Sr- and Mn-doped 167  
 SRXWT 143  
 Stack effect 327  
 Stress area 143  
 Strongly bonded hydrogen 507  
 Structural characterization 39  
 Structural refinement 461  
 Structure 219, 303, 311, 391, 549  
 Structure analysis 97, 159  
 Structure-directing agents 441  
 Substrate temperature 447  
 Succinic acid 265
- Sulfated zirconia-silicon nanocrystals 491  
 Sulfation 491  
 Superfine  $\text{BaTiO}_3$  211  
 Superparamagnetic 473  
 Supramolecular chemistry 333  
 Surface 321  
 Surface total acidity 191  
 Surfactant 421  
 Surfactant-assisted synthesis 461  
 Synchrotron X-ray radiation 177  
 Syngas 211  
 Synthesis 227, 233, 303, 327, 339, 515
- $\text{TbMnO}_3$  97  
 Template 283, 529  
 Templating 249  
 Terbium 159  
 $p\text{-Tert butyl catechol}$  275  
 Thermal stability 203, 241  
 Thermoluminescence 149  
 $\text{TiSiW}_{12}\text{O}_{40}/\text{TiO}_2$  339  
 Titania 203, 453  
 Titania nanotubes 441, 467  
 Transition metal 415  
 Transition metal oxide 13
- Ultrafine particles 421  
 Ultraviolet 383
- Vanadium 515  
 Variable valence cation 109
- Weakly bound hydrogen 507  
 Wet-oxidation 265  
 Wicker-shaped silver 529
- XANES 91, 167  
 Xerogel 515  
 X-ray absorption 91  
 X-ray four-circle diffraction 97
- $\text{YVO}_4$  crystal 143
- Zero flux surface 117  
 Zirconia 203  
 Zirconium phosphate 219  
 $\text{ZnO}$  383  
 $\delta'\text{-ZrW}_{1.6}\text{Mo}_{0.4}\text{O}_8$  131

# Frontiers of Solid State Chemistry

Edited by S. H. Feng and J. S. Chen



[www.worldscientific.com](http://www.worldscientific.com)  
5056 hc

ISBN 981-238-105-8



9 789812 381057